



The Optimization of Initial Treatment of Seaweed *Ulva reticulata* Using CEM Synthesizer Method for Bioethanol Production

Sefrinus Maria Dolfi Kolo^{1*} , Noviana Mery Obenu¹, Patrisius Maryanto Bria¹, Helena Abi¹, Benedikta Balok Seran¹, Deana Wahyuningrum²

¹Department of Chemistry, Faculty of Agricultural, Science and Health, University of Timor, 85614, Kefamenanu, Indonesia

²Organic Chemistry Research Group, Institut Teknologi Bandung, Jl. Ganesha 10, Bandung, 40132, Indonesia

Abstract: Research has been carried out on the optimization of initial treatment and hydrolysis using CEM microwave synthesizer and the production of bioethanol from *Ulva reticulata* seaweed. Optimization in the initial treatment was carried out by varying the concentration of HCl and H₂SO₄ (each in 1; 3; 5; and 7%), variations in time (30; 40; 50; and 60 minutes), temperature (100; 150; 200 and 250 °C), and electrical power (100; 150; 200; and 250 W). Fermentation was carried out anaerobically at 10% inoculum concentration and a production time of 6 days. Characterization of reducing sugar using DNS method and characterization of ethanol using GC-FID and HPLC. The results of the initial lignocellulosic analysis obtained the lignin content of 10.03%, cellulose 14.38% and hemicellulose 22.29%. After the initial treatment, the lignin content decreased to 3.86%, while cellulose increased to 24.50% and hemicellulose to 41.57%. The reducing sugar content produced using HCl is 97.10 g/L at optimum temperature 200 °C, for 60 minutes, using 7% concentration of HCl and 200 W of power, while the optimum reducing sugar content using H₂SO₄ is 76.40 g/L at optimum temperature 200 °C, time for 50 minutes, using 3% concentration of H₂SO₄ and 200 W of power. Production of bioethanol through fermentation and distillation processes obtained a bioethanol level of 43.89% (GC) or 18.89% (HPLC) for optimum conditions using H₂SO₄, whereas for optimum conditions using HCl, the bioethanol level is 44.29% (GC) or 18.09% (HPLC).

Keywords: *Ulva reticulata*, CEM microwave synthesizer, Hydrolysis, Fermentation, Bioethanol

Submitted: August 7, 2023. **Accepted:** December 3, 2023.

Cite this: Kolo SMD, Obenu NM, Bria PM, Abi H, Seran BB, Wahyuningrum. The Optimization of Initial Treatment of Seaweed *Ulva reticulata* Using CEM Synthesizer Method for Bioethanol Production. JOTCSA. 2024;11(2):403-12.

DOI: <https://doi.org/10.18596/jotcsa.1336106>

*Corresponding author. E mail: sefrichem@unimor.ac.id

1. INTRODUCTION

Bioethanol can be produced through a fermentation process using raw materials that contain carbohydrates. The available raw materials are broken down into four main types. The first generation of bioethanol is mostly edible food crops such as rice, wheat, potatoes, corn, and sugar cane, so it competes with food consumption (1). Second generation bioethanol utilizes lignocellulosic biomass such as paper pulp, rice straw, corn cobs, and sugar cane bagasse. However, pretreatment is required which is expensive and difficult while producing large amounts of residue. Alternative raw materials with residues rich in monosaccharides or even polysaccharides other than lignin are needed. In this context, third generation bioethanol production from macroalgae is an alternative raw material solution to replace vegetable starch and lignocellulosic biomass. This is mainly due to the fast growth rate of macroalgae, the absence of competition with agricultural land, the high

carbohydrate content and the relatively simple processing steps compared to lignocellulosic biomass (2).

Ulva macroalgae is considered to be a third generation renewable energy source because it contains carbohydrates and lipids (3). In contrast to the high starch or sugar content found in first-generation feedstocks, second-generation bioethanol typically utilizes non-edible feedstocks (4), such as lignocellulosic materials and agricultural forest residues (e.g., macroalgae) (5). Yu-Qing et al. (2016) state that *Ulva* seaweed contains carbohydrates in the form of heteropolysaccharides of glucose, arabinose, rhamnose and xylose which are very abundant (6). This type of seaweed is widely spread in the East Timor Sea (East Nusa Tenggara). However, *Ulva Reticulata* has not been utilized by the people on Timor Island so it has become garbage that reduces the aesthetics of the coast. On the other hand, seaweed is not used as food, so it does not compete with food.

Ulva reticulata conversion is carried out through initial treatment, hydrolysis, fermentation, and distillation (purification) (7). The use of acid catalysts during hydrolysis is very influential on the production of reducing sugar. The effectiveness of the HCl type of catalyst is higher producing glucose at the same temperature, concentration and time compared to H₂SO₄. This is because the nature of HCl is stronger with higher reactivity compared to H₂SO₄. In addition, one alternative tool in the initial treatment (delignification and hydrolysis) is the use of CEM microwave synthesizer which has many advantages, such as a short hydrolysis time compared to conventional methods, a rate of starch hydrolysis reactions to glucose that increases 50-100 times, is cost-effective, and is environmentally friendly because the acid concentration used is lower (4).

Kolo et al. (2021) reported that hydrolysis of *Ulva reticulata* seaweed with 2% H₂SO₄ for 50 minutes could maximize reducing sugar production of 33.4 g/L and a bioethanol concentration of 5.02% at an inoculum concentration of 10% for 6 days (8). Research by Kolo et al. (2022) also reported that the hydrolysis of *Ulva reticulata* macroalgae through variations in temperature and reaction time using H₂SO₄ catalyst obtained a sugar content of 27.79 g/L and a bioethanol content of 7.76% (9). Furthermore, research by Kolo et al. (2023) reported that hydrolysis of *Ulva reticulata* using the HNO₃ catalyst obtained a sugar content of 86.5 g/L and a bioethanol content of 37.2% (10). The three previous studies that used the macroalgae *Ulva reticulata* had not optimized the fermentation process, so the researchers tried to optimize the fermentation process to increase bioethanol levels.

The main problem in the fermentation process in an effort to find alternative energy is finding the right fermentation time and inoculum concentration so as to get the highest bioethanol concentration. The novelty value of this research lies in optimizing the initial treatment converting *Ulva reticulata* into bioethanol using the CEM synthesizer, and refining fermentation time and inoculum concentration to obtain the highest bioethanol content. This research aims to determine the optimum reducing sugar concentration using HCl and H₂SO₄ catalysts through variations in time, temperature, and concentration and to obtain the highest levels of bioethanol through variations in fermentation time and inoculum concentration. According to Febriani et al. (2020) using an inoculum concentration that is too high (>15%) can cause a

decrease in cell viability. Apart from that, too high levels of bioethanol resulting from long fermentation will be toxic to cells so that cells die and their viability decreases (11). This research also provides information for industry to increase the economic value of *Ulva reticulata* macroalgae as a renewable energy source in the future.

2. EXPERIMENTAL SECTION

2.1. Material and Tools

Materials: H₂SO₄ (Merck), NaOH (technical), HCl (technical), glucose (Merck), ethanol (Merck), acetic acid (Merck). Inoculum media consisted of *Saccharomyces cerevisiae* inoculum media (yeast extract 5 g/L; peptone 5 g/L; glucose 20 g/L as carbon source), fermentation media consisted of yeast extract 5 g/L; peptone 5 g/L; KH₂PO₄ 5 g/L; MgSO₄·7H₂O 0.4 g/L; NH₄SO₄ 0.5 g/L; glucose hydrolysate.

Tools: Glassware, analytical balance, pH meter, autoclave, 37 °C temperature incubator, water bath, CEM Microwave Synthesizer, GC-FID, HPLC, UV-Vis Spectrophotometer, fermenter and SEM equipment, magnetic stirrer, loop wire, falcon tube.

2.2. *Ulva reticulata* Macroalgae Preparation

The preparation of *Ulva reticulata* sp. involve two steps: drying and milling. The product is, then sieved using ± 100 mesh sieve to obtain *Ulva reticulata* sp. powder. The powder of *Ulva reticulata* sp. was analysed for lignocellulosic content using Surajit Method (4).

2.3. *Ulva reticulata* Macroalgae Powder Saccharification

The saccharification stage of *Ulva reticulata* powder aims to hydrolyze cellulose into monosaccharides such as glucose. Saccharification was carried out with various concentrations of HCl and H₂SO₄, temperature, time, and power using a CEM microwave synthesizer (**Table 1**).

Acid hydrolysis was carried out in the following way: 10 g of *Ulva reticulata* powder and 100 ml of HCl or H₂SO₄ 1; 3; 5; and 7% (v/v) were put into a 250 ml heating flask, then sterilized. The medium is then cooled to room temperature. The heating results are then filtered, and the glucose content analysis is carried out using UV-Vis, while the hydrolysis residues are surface analyzed using SEM (12). The optimum results in the hydrolysis process are then used to produce bioethanol.

Table 1: Optimization of *Ulva reticulata* sp. powder hydrolysis with HCl or H₂SO₄ as catalysts.

Treatment	Optimization (HCl or H ₂ SO ₄)			
	% (v/v)	Time (minute)	Temperature (°C)	Power (Watt)
1.	1; 3; 5; 7	40	100	100
2.	Result 1	30; 40; 50; 60	100	100
3.	Result 1	Result 2	100; 150; 200; 250	100
4.	Result 1	Result 2	Result 3	100; 150; 200; 250

Bioethanol Production with Optimum Concentration, Time, Temperature, and Power

2.4. The making of Fermentation Medium

The fermentation medium used was 100 ml of hydrolysates in a 250 ml Erlenmeyer for each research treatment. The first step in making the starter was to inoculate the yeast culture of *S. cerevisiae* from the liquid culture into 100 ml of the fermentation medium, which was then incubated at room temperature for 24 hours (13).

2.5. Bioethanol Production

Fermentation was carried out using *S. cerevisiae*. The fermentation volume for the hydrolysate medium is 200 mL. The hydrolysate of *Ulva reticulata* powder was put in the fermentation medium and sterilized at 121 °C for 15 minutes. The fermentation medium used demineralized water as a solvent. Fermentation is set at pH 4.5 and a temperature of 30 °C. The inoculum concentration was 10% (v/v), and the fermentation time was 6 days (14).

2.6. Analysis of the Chemical Content of Lignocellulose *Ulva reticulata*

A total of 1 g of *Ulva reticulata* powder was suspended in 150 mL H₂O and then refluxed for 2 hours at 100 °C. The heating results are then filtered to separate the residue and filtrate. The dried residue was then refluxed again for 2 hours with 150 mL of 0.5 M H₂SO₄ at 100 °C. The dried sample residue was immersed in 10 mL of 72% (v/v) H₂SO₄ solution at room temperature for 4 hours, then diluted to 0.5 M H₂SO₄, refluxed at 100 °C for 2 hours, and dried. The residue was filtered and washed with demineralized water until neutral. The residue was then dried in an oven at a temperature of 105 °C until the weight was constant and counted as weight (d). After that, the residue was smoked into ash and weighed (e). The composition of the lignocellulosic components of *Ulva reticulata* sample was determined by the following calculations:

$$\text{Hemicellulose (\%)} : \frac{b-c}{a} \times 100\% \quad (1)$$

$$\text{Cellulose (\%)} : \frac{c-d}{a} \times 100\% \quad (2)$$

$$\text{Lignin (\%)} : \frac{d-e}{a} \times 100\% \quad (3)$$

Note: a is the initial weight of dry powder of *Ulva reticulata* sample; b is the weight of the dry sample residue after refluxing with hot water; c is the residual weight of the sample after refluxing with 0.5 M H₂SO₄; and d is the residual weight of the sample after being treated with 72% (v/v) H₂SO₄ solution (4).

2.7. Surface Texture Analysis of *Ulva reticulata* Powder

The results of the hydrolysis are filtered and then neutralized for further processing. The solid fraction was examined for its surface texture by SEM, while the liquid fraction was analyzed for reducing sugar content using the DNS method.

2.8. Reducing Sugar Analysis (3,5-dinitrosalicylic acid (DNS) method)

The hydrolysis solution of *Ulva reticulata* powders were analyzed for reducing sugar content using the DNS method. The analysis of reducing sugars was determined using a UV-VIS spectrophotometer (9), with the following steps:

Standard glucose solutions were made with concentrations of 1000, 2000, 3000, 4000, and 5000 ppm.

Take 1 mL of each solution, and then add 1.75 mL of DNS reagent.

The solutions were homogenized and heated in boiling water for 5 minutes.

The cold solution was diluted 5 times and homogenized again.

The absorbance was measured using a spectrophotometer at a wavelength of 540 nm, then a standard curve was made to obtain a linear regression equation.

The measurement of the reducing sugar content in the sample is carried out in the same way at points b to e.

2.9. Bioethanol Product Analysis

Ethanol analysis was carried out using Gas Chromatography-Flame Ionization Detector (GC-FID) and High Performance Liquid Chromatography (HPLC) with detector temperature 40 °C, column temperature 60 °C, mobile phase flow rate 0.6 mL/minute, Phenomenex ROA Organic Acid column and RI detector (Refractive Index).

3. RESULTS AND DISCUSSION

3.1. *Ulva reticulata* Powder Morphology before and after Pretreatment

Ulva reticulata macroalgae powder used as raw material in this study contains cellulose, hemicellulose, and lignin as the main components (4). However, before carrying out the initial treatment process, it is necessary to know the composition of the lignocellulosic constituents. It is necessary to develop an effective method for converting cellulose components into simple sugars and also as a basis for selecting suitable microorganisms to convert sugars into bioethanol. Therefore, the structural carbohydrate content of *Ulva reticulata* powder was determined before and after the initial treatment both by analyzing the surface morphology and by measuring the chemical content of *Ulva reticulata* powder. After initial treatment using CEM microwave synthesizer, the mixture was then filtered to separate the filtrate and *Ulva reticulata* residue. The filtrate was used for analysis of reducing sugar content, while the residue was washed until neutral pH and then dried for analysis of powder surface texture using SEM. The results of the morphological characterization of *Ulva reticulata* powder are shown in **Figure 1**.

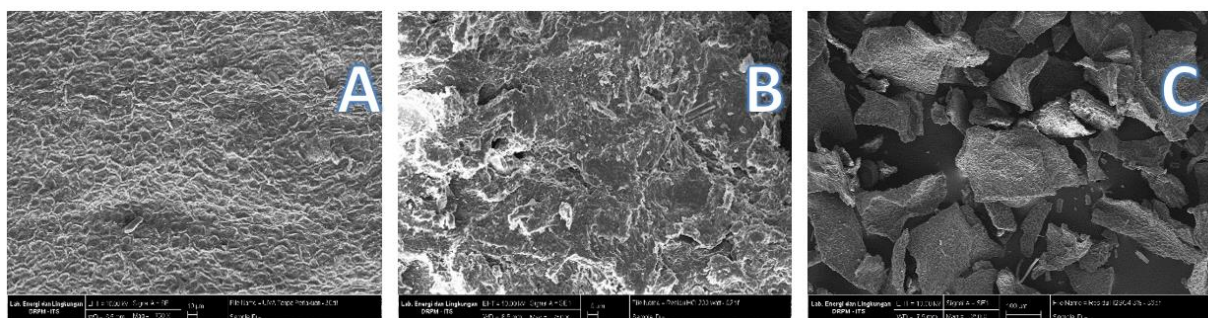


Figure 1: The morphology of *Ulva reticulata* powder: A. Without initial treatment; B. After CEM Synthesizer (HCl), and C. After CEM Synthesizer (H₂SO₄).

The surface morphology of *Ulva reticulata* macroalga showed that the powder surface was dense and stiff before initial treatment and acid hydrolysis (**Figure 1(A)**). The initial treatment process removes acetyl and other acid substitutions in lignin, and hemicellulose protecting the cellulose. The SEM results revealed that the macroalga powder was broken and suffered significant damage after the initial treatment using HCl and H₂SO₄ (**Figure 1 (B and C)**). These results indicate that both treatments succeeded in degrading the lignin portion of the lignocellulosic part of *Ulva reticulata* powder.

The lignin is not a sugar polymer, so it cannot be used as a substrate for bioethanol production through microbial fermentation. Lignin will also inhibit microbial growth during the fermentation process (15). Lignin is broken down and released from the structure of cellulose and hemicellulose due to initial treatment with dilute acid combined with the help of microwave (CEM Synthesizer synthesizer). Acid hydrolysis is required to degrade the -1,4-glycosidic bonds of linear glucan-cellulose chains or -1,4-D-pyranosyl linkage of heterogeneous hemicellulose polysaccharides into sugar monomers, such as glucose, xylose, galactose, arabinose, and mannose (4). The initial treatment process combined with the CEM Synthesizer synthesizer helps to degrade and release lignin from

cellulose or hemicellulose materials. Lignin is not a sugar polymer, cannot be used as a raw material for bioethanol production and inhibits microbial growth during fermentation (15).

3.2. Chemical Ingredients of *Ulva reticulata* Macroalga Powder

The results of the analysis of the lignocellulose content of *Ulva reticulata* showed that the cellulose content after initial treatment using microwave-assisted techniques increased from 14.38% to 24.50%, hemicellulose increased from 22.29% to 41.57%, while the lignin content decreased from 10, 03% to 3.86% (**Table 2**).

The use of CEM synthesizer in the alkaline delignification process increased the cellulose content obtained in this study. This indicates that the alkaline delignification process with microwave-assisted treatment has succeeded in breaking the structural bonds between lignin and polysaccharides, thereby releasing free cellulose into the solution. Kolo et al., (2020), also reported that the cellulose and hemicellulose content decreased after acid hydrolysis, because this process would also break down the glycosidic bonds of cellulose or the -1,4-D-pyranosyl bonds of hemicellulose, resulting in monosaccharides (4).

Table 2: Lignocellulose content of *Ulva reticulata* powder.

Process	Water content (%)	Hemicellulose (%)	Cellulose (%)	Lignin (%)
Pre-treatment	53.15	22.29	14.38	10.03
Treatment (CEM Synthesizer)	29.95	41.57	24.50	3.86

Sari et al. (2014) reported that the treatment of 100.0 g of *Sargasum duplicatum* macroalga yielded 15.08 g of cellulose (16). Meanwhile, in our study, 100.0 g of *Ulva reticulata* macroalga yielded 24.50 g of cellulose. Adini et al., (2015) also reported that 100 g of *Gracilaria* sp. macroalga contains 19.7 g of cellulose (17). Wadi et al. (2019) used alkaline delignification (NaOH) for the pretreatment of *Euclidean cottonii*. They reported that 50.2 g of cellulose was converted to 6.1% bioethanol using the SSF method (18). The use of microwave irradiation can increase the rate of hydrolysis of starch into glucose by 100 times (9).

3.3. Reducing Sugar Content in *Ulva reticulata* Powder

The reducing sugar content in the sample was analyzed using a UV-Vis spectrophotometer at a wavelength of

540 nm with 3,5-dinitrosalicylic acid (DNS) reagent. The hydrolyzed filtrate was determined based on the formation of a brownish red reduced product when the sugar in the sample was reduced from 3,5-dinitrosalicylate to 3-amino-5-nitrosalicylic acid during heating. The brownish red color will be absorbed maximally at a wavelength of 540 nm. The reaction of glucose with DNS reagent will produce absorbance values that can be measured spectrophotometrically (19).

The initial treatment process in this study was combined with microwave irradiation techniques using a CEM synthesizer. The use of this technique is to increase the efficiency of the hydrolysis reaction to obtain a higher reducing sugar content. The results of the hydrolysis of *Ulva reticulata* powder using CEM synthesizer are presented in **Table 3**. The optimum

yield of reducing sugar using HCl was influenced by microwave irradiation, as indicated by the concentration of reducing sugar increasing with increasing acid concentration, temperature, time, and microwave irradiation power (**Table 3**).

3.4. Variation of Temperature, Time, Power, and Concentration of HCl

The optimization results of the initial treatment are presented in **Table 3**, showing the analysis of reducing sugars from the hydrolysate of *Ulva reticulata* powder using HCl.

Table 3: Results of *Ulva reticulata* powder reducing sugar using HCl.

Temp (°C)	GP (g/L)	WR (Min)	GP (g/L)	HCl (% v/v)	GP (g/L)	DI (Watt)	GP (g/L)
100	19.5	30	24.7	1	46.4	100	79.7
150	75.1	40	43.0	3	56.4	150	86.1
200	79.6	50	56.3	5	68.3	200	97.1
250	74.0	60	84.7	7	84.7	250	90.9

Abbreviations: HCl: Hydrochloric Acid; GP: Reducing Sugar; WR: Reaction Time; Temp: Temperature; DI: Irradiation Power.

The results of the hydrolysis in **Table 3** show an increase in reducing sugars with an increase in the concentration of hydrochloric acid used and the hydrolysis time. However, it was different for the hydrolysis temperature, which increased from 100 °C to 200 °C and then decreased at 250 °C. Likewise, the irradiation power increases from 100 to 200 W and then decreases at 250 W of power. This condition is caused by an increase in temperature and excess power, so sugar products will be converted into secondary compounds such as furfural and hydroxymethylfurfural (HMF) (20). The most optimal conditions for hydrolysis of *Ulva reticulata* macroalga using hydrochloric acid (HCl) combined with CEM synthesizer are an acid concentration of 7% (v/v) with an irradiation power of 200 watts for 60 minutes at 200 °C, which produces reducing sugars of 97.10 g/L. This result is higher than the study conducted by Kolo et al., (2021), which produced a reducing sugar content of 33.4 g/L obtained at a concentration of 2% H₂SO₄ at a temperature of 150 °C with a reaction time of 50 minutes using a Kirin type household microwave.

3.5. Variation of Temperature, Time, Power and Concentration of H₂SO₄

The results of the optimization of the initial treatment, obtained by analyzing the reducing sugars from the hydrolysate of *Ulva reticulata* powder using H₂SO₄ are shown in **Table 4**. The results of the hydrolysis in **Table 4** show an increase in reducing sugars with the increase in the concentration of acid used, hydrolysis time, temperature, and irradiation power of CEM synthesizer. Kolo et al., (2022) reported that

hydrolysis of acid (H₂SO₄) in *Ulva reticulata* using a Kirin type microwave with a combination of delignification and hydrolysis through variations in hydrolysis time and temperature obtained an optimum reducing sugar of 27.97 g/L at 150 °C, a concentration of 2% H₂SO₄, and a hydrolysis time of 50 minutes. These results are still low compared to those obtained in this study. Optimum conditions for hydrolysis of *Ulva reticulata* macroalga using sulfuric acid (H₂SO₄) combined with CEM synthesizer at an acid concentration of 5% (v/v) with an irradiation power of 200 W for 50 minutes at 200 °C, produce reducing sugars of 76.40 g/L.

Based on the variation of reaction time and hydrolysis temperature, it was seen that there was a color change in the *Ulva reticulata* hydrolysate. The longer the heating time at high temperatures, the darker the color of the hydrolysate. This indicates that there has been a complete degradation of hemicellulose and cellulose into glucose (21), but if the hydrolysis process is continued at high temperatures, charcoal will form on the flask wall (**Figure 2**). This proves that the resulting glucose is damaged or burned, and the caramelization is formed (Kolo et al., 2022). In addition, the longer reaction time causes the formation of secondary compounds such as hydroxymethylfurfural (HMF), which then reacts to form formic acid (22). The use of CEM synthesizer is considered to be more advantageous than the standard reflux method and simple microwave due to the shorter reaction time (in minutes), less solvent, and higher reducing sugar product.

Table 4: Results of *Ulva reticulata* powder reducing sugar using H₂SO₄

Temp (°C)	GP (g/L)	WR (Min)	GP (g/L)	H ₂ SO ₄ (% v/v)	GP (g/L)	DI (Watt)	GP (g/L)
100	7.3	30	3.1	1	63.0	100	56.8
150	12.0	40	19.2	3	64.7	150	60.0
200	23.7	50	33.4	5	61.3	200	76.4
250	17.1	60	28.0	7	59.7	250	69.9

Abbreviations: H₂SO₄: Sulfuric Acid; GP: Reducing Sugar; WR: Reaction Time; Temp: Temperature; ID: Irradiation Power.



Figure 2: Hydrolysis results using CEM synthesizer (personal documentation).

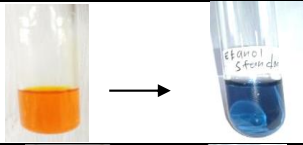
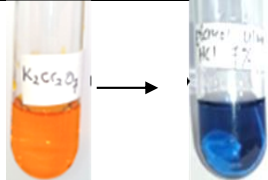
3.6. *Ulva reticulata* Powder Hydrolysate Fermentation

The result sugar is then utilized in the fermentation process by selecting the optimum conditions of the two catalysts used, namely HCl and H₂SO₄. The optimum condition of glucose hydrolysate used during the fermentation process was 3% H₂SO₄ treatment at a temperature of 150 °C for 50 minutes. Meanwhile, the glucose hydrolysate in the HCl treatment had 7% HCl concentration at a temperature of 150 °C and a reaction time of 50 minutes. The fermentation process uses *Ulva reticulata* powder hydrolysate as a substrate using the yeast *Saccharomyces cerevisiae*. *S. cerevisiae* was chosen because it has various advantages, including a high survival rate and the ability to produce alcohol in sufficient quantities (23). Before proceeding with the gas chromatography and HPLC testing, we performed a qualitative analysis using

potassium dichromate (K₂Cr₂O₇) to ensure that the sample from the graded distillation yielded ethanol. The results of the analysis are presented in **Table 5**. The results of purification after fermentation are shown in **Table 6**.

The results of the qualitative test showed that there was a color change from orange to bluish green in both standard ethanol and fermented samples. According to Kolo et al., (2023), stated that a positive test for the presence of ethanol was indicated by a change in the color of potassium dichromate from orange to bluish green. So, it can be concluded that in the fermented sample there has been a change in glucose to ethanol, which is marked by a change in the color of the potassium dichromate solution from orange to bluish green when the fermented sample is added (10).

Table 5: Qualitative test results using K₂Cr₂O₇.

Sample	Test Result	Picture
Pure ethanol	+	
Bioethanol of <i>Ulva reticulata</i> powder	+	

3.7. Ethanol Analysis Using Gas Chromatography

The quantitative analysis of bioethanol content in *Ulva reticulata* powder samples was carried out using a gas chromatography instrument. Analysis using GC was carried out to determine the presence of ethanol produced from the fermentation process. The compound used as an internal standard is toluene to create a perfect separation between the sample peaks and the measurement of compound levels is not influenced by other compounds. Toluene was chosen as the internal standard because it has a molecular formula similar to that of ethanol. With this similarity, the solubility between the two solutions

is easy to know based on the principle of like dissolved like (24).

The GC chromatogram in **Figure 3** shows that the fermented sample contains 3 peaks with different retention times, namely at retention times of 2.950, 3.216, and 4.288 minutes where the compound that comes out or evaporates as a peak is hexane, then

followed by ethanol and toluene. Sample chromatograms were confirmed using standard ethanol chromatograms which were detected at a retention time of 3.214 minutes. The peak of the hexane compound comes out first because hexane has the lowest boiling point (68.7 °C) compared to ethanol (78.3 °C) and toluene (110.6 °C) (8). This is because the components of the mixture in the sample will separate or come out according to their boiling point. The component that has a lower boiling point will evaporate first, so it will come out as the first peak on the chromatogram. In this study, hexane was used as a solvent to dissolve ethanol and toluene before being injected into the GC. Hexane is used as a solvent because it is a non-polar compound and is a good organic solvent because it has a low boiling point (volatile), harmless, non-toxic, not explosive or flammable, inexpensive and inert (does not react with solutes) (24).

The chromatogram obtained can be used to calculate the concentration of bioethanol in the sample by

comparing the area of the ethanol peak with the area of the standard. The obtained calculation show that the optimum concentration of ethanol, at an inoculum concentration of 10% using glucose hydrolysate from optimization of H_2SO_4 was 43.8% and 44.2% from optimization using HCl. The low concentration of bioethanol produced in this study was caused by several factors, such as the fact that not all glucose molecules were converted into ethanol, and also because during the hydrolysis process using acid, hydroxymethylfurfural (HMF) compounds were usually formed, where this compound was an inhibitor compound that could inhibit the growth of microorganisms in the fermentation process. In addition, it is also caused by the slow fermentation process due to the small amount of nutrients in the

medium. This situation is also due to the fact that ethanol has been oxidized to acetic acid either during the filtering process or when transferring the distillate sample from the distillation flask to the reagent bottle. According to Azizah et al., (2012), the products of the fermentation process include, in addition to ethanol, acetic acid, fassel oil, and acetaldehyde (25). Another factor that causes low concentrations of bioethanol is the presence of contaminants such as lactic acid bacteria, and acetic acid bacteria which are capable of being inhibitors in the fermentation process (26). Another influencing factor is the presence of residual water content in the distillation sample.

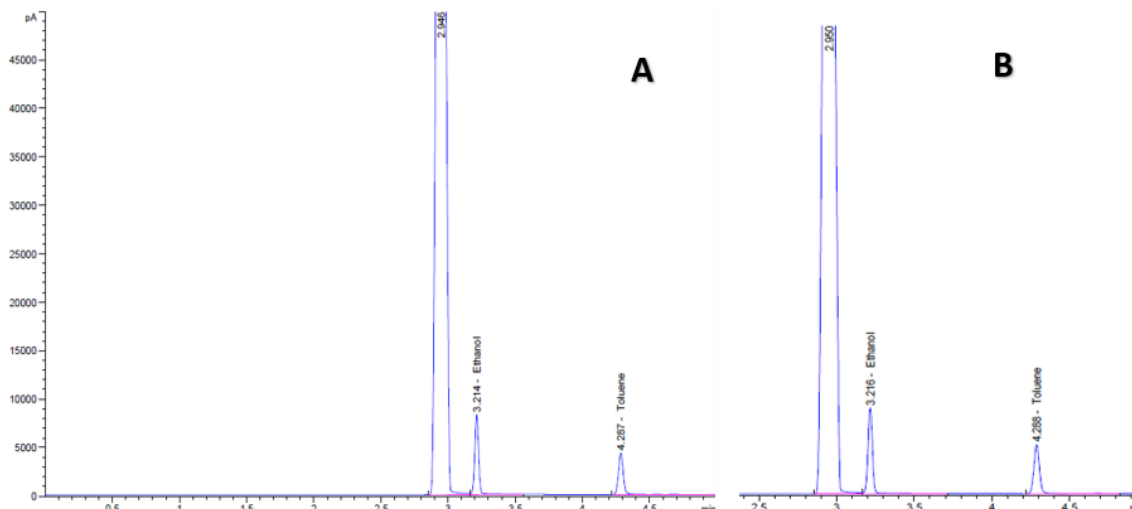


Figure 3: Chromatogram (GC): A. Ethanol standard, B. Bioethanol sample.

3.8. Ethanol Analysis Using High Performance Liquid Chromatography (HPLC)

The production of bioethanol is carried out through a fermentation process using an inoculum concentration of 10% for 6 days. The results of HPLC analysis of the content of ethanol and acetic acid in the product after fermentation are presented in **Figures 4** and **5**. Ethanol and acetic acid in the product after

fermentation were confirmed by comparing the retention times of standard ethanol and acetic acid with the fermentation samples. Concentrations of ethanol and acetic acid were calculated using HPLC chromatogram analysis data. The area data of each ethanol and acetic acid were entered into the standard regression equation of ethanol and acetic acid.

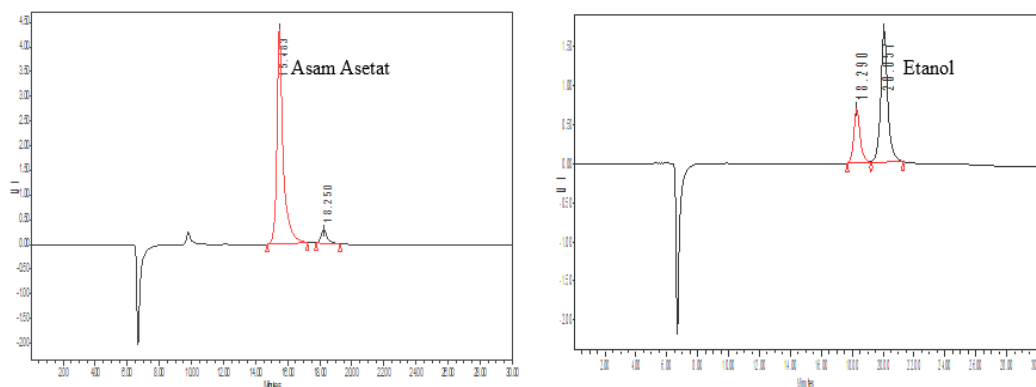


Figure 4: Standard Chromatogram of Acetic acid and Ethanol.

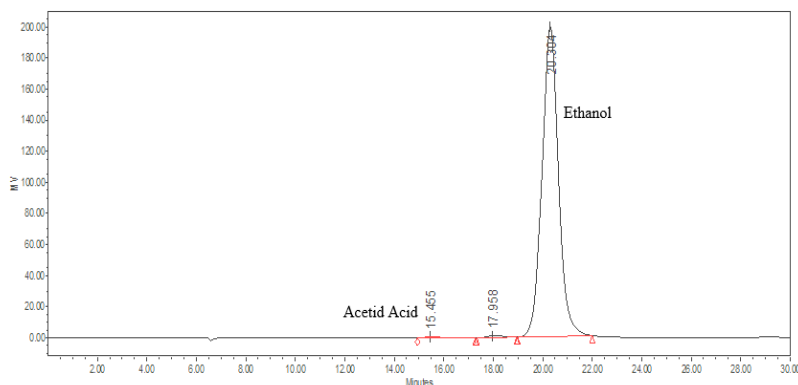


Figure 5: Chromatogram of Acetic acid and Ethanol in Fermentation Products.

The peak area of the ethanol product in the HPLC analysis chromatogram was then entered into the standard regression equation of ethanol and acetic

acid as a variable (y) to obtain the concentration (x), as follows:

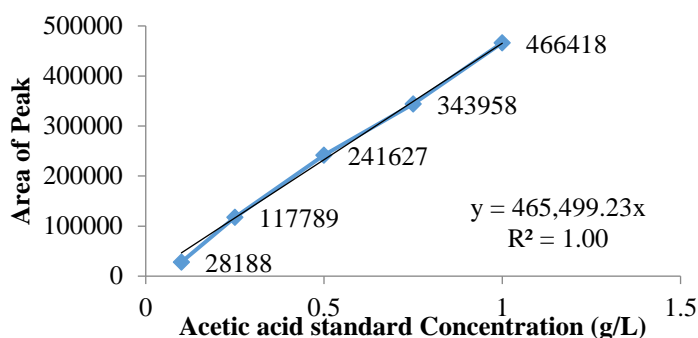


Figure 6: Linear plot between area in chromatogram and concentration of acetic acid.

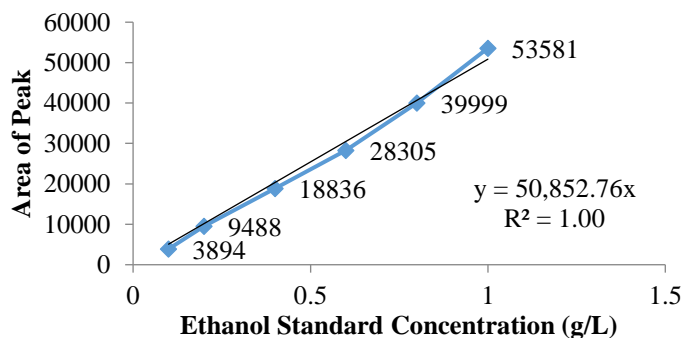


Figure 7: Linear plot between area in chromatogram and ethanol concentration.

Ethanol concentration (x): $\frac{y-b}{a}$

Ethanol concentration (g/L): Ethanol conc. (%) × ρ × 10 (correction factor) (4)

The initial concentration of glucose, obtained directly from the initial treatment process of *Ulva reticulata* macroalga was 97.1 g/L. The hydrolyzate at the optimum conditions of H₂SO₄ was then fermented and obtained optimal concentrations of

bioethanol and acetic acid of 18.8% and 0.013%, respectively, by using a 10% inoculum concentration for 6 days of fermentation. Under these conditions, the bioethanol yield was 23%, with the highest productivity rate of 0.2 g/L per day. Fermentation efficiency reaches a level of 34.41% and substrate conversion efficiency is 56.38%.

Table 6: Bioethanol yield from *Ulva reticulata*.

Optimum Hydrolysis	Inoculum (%)	Fermentation time (days)	Ethanol content (%)		Acetic Acid content (%)
			GC	HPLC	
H ₂ SO ₄ 3%, 150 °C, 50 min	10	6	43,8	18.8	0.013
HCl 7%, 150 °C, 50 min	10	6	44,2	18.0	0.012

Yadav et al. (2011) reported the results of research on the topic of bioethanol production from rice straw hydrolyzate using co-cultures, namely *Sacharomyces cerevisiae* and *Pichia stipitis*, and obtained an ethanol concentration of 1.2% and an ethanol productivity rate of 0.33 g/L a day (14). Kolo et al. (2020) reported a research on the topic of bioethanol production from Hydrolyzed Elephant Grass using 2 types of yeast, namely *Sacharomyces cerevisiae-Pichia stipitis*, and the resulting ethanol concentration was 10.97 g/L with a productivity rate of 0.45 g/L per hour and fermentation efficiency reaching 69.48%. Based on the results of ethanol and the parameters determined, it

can be concluded that the highest ethanol concentration was obtained by fermentation using an inoculum concentration of 10% to produce 44.2% ethanol with a fermentation time of 6 days. The ethanol content was then used to calculate the fermentation efficiency, yield, productivity rate, and substrate conversion (**Table 7**). When viewed from the effectiveness and efficiency of the use of materials and time in this study, it is necessary to optimize the fermentation process to determine the best inoculum concentration and fermentation time so as to increase the yield and ethanol content obtained.

Table 7: Substrate parameters and fermentation products.

Initial treatment	EF (%)	Y _{p/s} (%)	Rate (g/L.day)	Ks (%)
H ₂ SO ₄ 3%, 150 °C, 50 min	23.68	24.59	0.13	40.68
HCl 7%, 150 °C, 50 min	19.35	19.35	0.13	53.68

Description: Ks = Total substrate conversion (%), Y_{p/s} (%) = Yield or yield (ethanol/substrate), Theoretical yield = 51%, Rate(g/L,days) = ethanol productivity rate/day, EF= Fermentation efficiency(%).

4. CONCLUSION

In this study, the biomass content after pretreatment using the CEM synthesizer technique was 24.50% cellulose, 41.57% hemicellulose, and 3.86% lignin. The reducing sugar content obtained was 97.1 g/L at the optimum conditions of 5% HCl; 200 °C; 200 Watts of irradiation power; and a 60 minutes of hydrolysis time. Bioethanol production

through fermentation and distillation processes resulted in bioethanol levels of 43.89% (GC) or 18.89% (HPLC) under optimum conditions with H₂SO₄ and 44.29% (GC) or 18.09% (HPLC) under optimum conditions with HCl. The efficiency of fermentation is 23.68%, the optimal rate of ethanol productivity is 0.13 g/L/day and the substrate conversion is 53.68%.

5. CONFLICT OF INTEREST

The authors declare there is no potential conflict of interest with respect to the research, authorship, and/or publication of this article.

6. ACKNOWLEDGMENT

The author expresses his deepest gratitude to the Director of Research, Technology, and Community Service (DRTPM Kemendikbud Ristek), LPPM Timor University, Chemistry Laboratory Timor University and the Bandung Institute of Technology for facilitating this research through budget and facilities.

7. REFERENCES

- Halder P, Azad K, Shah S, Sarker E. Prospects and technological advancement of cellulosic bioethanol ecofuel production. *Advances in Eco-Fuels for a Sustainable Environment*. Elsevier Ltd.; 2018. 211–236 p. Available from: [<URL>](#)
- Robak K, Balcerek M. Review of second generation bioethanol production from residual biomass. *Food Technol Biotechnol*. 2018;56(2):174–87. Available from: [<URL>](#)
- Mathimani T, Pugazhendhi A. Utilization of Algae for Biofuel, Bio-products and Bio-remediation. Vol. 17, *Biocatalysis and Agricultural Biotechnology*. Elsevier Ltd; 2019. 326–330 p. Available from: [<URL>](#)
- Kolo SMD, Wahyuningrum D, Hertadi R. The Effects of Microwave-Assisted Pretreatment and Cofermentation on Bioethanol Production from Elephant Grass. *Int J Microbiol*. 2020;2020:1–11. Available from: [<URL>](#)
- Tse TJ, Wiens DJ, Reaney MJT. Production of bioethanol—a review of factors affecting ethanol yield. *Fermentation*. 2021;7(4):1–18. Available from: [<URL>](#)
- Yu-Qing T, Mahmood K, Shehzadi R, Ashraf MF. *Ulva Lactuca* and Its Polysaccharides: Food and Biomedical Aspects. *J Biol Agric Healthc*. 2016;6(1):140–51. Available from: [<URL>](#)
- Park JH, Hong JY, Jang HC, Oh SG, Kim SH, Yoon JJ, et al. Use of *Gelidium amansii* as a promising resource for bioethanol: A practical approach for continuous dilute-acid hydrolysis and fermentation. *Bioresour Technol*. 2012;108:83–8. Available from: [<URL>](#)

8. Kolo SMD, Presson J, Amfotis P. Produksi Bioetanol sebagai Energi Terbarukan dari Rumput Laut *Ulva reticulata* Asal Pulau Timor. *ALCHEMY Jurnal Penelitian Kimia*. 2021;17(2):159. Available from: [<URL>](#)
9. Kolo SMD, Obenu NM, Tuas MYC. Pengaruh Pretreatment Makroalga *Ulva Reticulata* Menggunakan Microwave Irradiation Untuk Produksi Bioetanol. *Jurnal Kimia*. 2022;16(2):212. Available from: [<URL>](#)
10. Kolo SMD, Obenu NM, Kefi L, Fuel FF. Optimasi Proses Hidrolisis Rumput Laut *Ulva Reticulata* dengan Pelarut HNO₃ untuk Produksi Bioetanol. *Jurnal Riset Kimia*. 2023;14(1):12–23. Available from: [<URL>](#)
11. Febriani Y, Sidharta BR, Pranata FS. Produksi Bioetanol Pati Umbi Talas (*Colocasia esculenta* (L.) Schott) dengan Variasi Konsentrasi Inokulum dan Waktu Fermentasi *Zymomonas mobilis*. *Biota: Jurnal Ilmiah Ilmu-Ilmu Hayati*. 2020;5(2):92–8. Available from: [<URL>](#)
12. Susmiati Y. Detoksifikasi hidrolisat asam dari ubi kayu dengan metode arang aktif untuk produksi bioetanol. *Agrointek*. 2011;5(1):9–15. Available from: [<URL>](#)
13. Samsuri M, Gozan M, Mardias R, M. Baiquni M, Hermansyah H, Wijanarko A, et al. Pemanfaatan Selulosa Bagas Untuk Produksi Ethanol Melalui Sakarifikasi Dan Fermentasi Serentak Dengan Enzim Xylanase. *MAKARA of Technology Series*. 2012;11(1):17–24. Available from: [<URL>](#)
14. Yadav KS, Naseeruddin S, Prashanthi GS, Sateesh L, Rao LV. Bioethanol fermentation of concentrated rice straw hydrolysate using co-culture of *Saccharomyces cerevisiae* and *Pichia stipitis*. *Bioresour Technol*. 2011 Jun;102(11):6473–8. Available from: [<URL>](#)
15. Wang H, Maxim ML, Gurau G, Rogers RD. Microwave-assisted dissolution and delignification of wood in 1-ethyl-3-methylimidazolium acetate. *Bioresour Technol*. 2013;136(2013):739–42. Available from: [<URL>](#)
16. Sari RN, Bandol Utomo BS, Tambunan AH. Kondisi Optimum Produksi Bioetanol Dari Rumput Laut Coklat (*Sargassum duplicatum*) Menggunakan *trichoderma Viride* dan *Pichia angophorae*. *Jurnal Pascapanen dan Bioteknologi Kelautan dan Perikanan*. 2014 Dec 3;9(2):121. Available from: [<URL>](#)
17. Adini S, Kusdiyantini E, Budiharjo A. Produksi Bioetanol Dari Rumput Laut dan Limbah Agar *Gracilaria sp* . dengan Metode Sakarifikasi Yang Berbeda Abstrak. *Bioma*. 2015;16(2):65–75. Available from: [<URL>](#)
18. Wadi A, Ahmad A, Tompo M, Hasyim H, Tuwo A, Nakajima M, et al. Production of Bioethanol from Seaweed, *Gracilaria verrucosa* and *Euclima cottonii*, by Simultaneous Saccharification and Fermentation Methods. *J Phys Conf Ser*. 2019;1341(3):1–9. Available from: [<URL>](#)
19. Galung FS. ANALISIS KANDUNGAN KARBOHIDRAT (GLUKOSA) PADA SALAK GOLLA – GOLLA. *Journal of Agritech Science*. 2021;5(1):10–4. Available from: [<URL>](#)
20. Tongtummachat T, Akkarawatkhoosith N, Kaewchada A, Jaree A. Conversion of Glucose to 5-Hydroxymethylfurfural in a Microreactor. *Front Chem*. 2020;7(January):1–9. Available from: [<URL>](#)
21. Widyastuti P. Pengolahan Limbah Kulit Singkong Sebagai Bahan Bakar Bioetanol melalui Proses Fermentasi. *Jurnal Kompetensi Teknik*. 2019;11(1):41–6. Available from: [<URL>](#)
22. Menegazzo F, Ghedini E, Signoretto M. 5-Hydroxymethylfurfural (HMF) production from real biomasses. *Molecules*. 2018;23(9):1–18. Available from: [<URL>](#)
23. Jayus J, Noorvita IV, Nurhayati N. Produksi Bioetanol Oleh *Saccharomyces cerevisiae* FNCC 3210 Pada Media Molases Dengan Kecepatan Agitasi Dan Aerasi Yang Berbeda. *Jurnal Agroteknologi*. 2016;10(02):184–92. Available from: [<URL>](#)
24. Solikha DF. Analisis Kandungan p-Xilena pada Pertamina dan Pertamina Plus dengan Teknik Kromatografi Gas (GC-PU 4600) Menggunakan Standar Internal. *Jurnal Ilmiah Indonesia*. 2017;2(8):1–15. Available from: [<URL>](#)
25. Azizah N, Al-bAARI A, Mulyani S. Pengaruh Lama Fermentasi Terhadap Kadar Alkohol, pH, dan Produksi Gas pada Proses Fermentasi Bioetanol dari Whey dengan Substitusi Kulit Nanas. *Jurnal Aplikasi Teknologi Pangan*. 2012;1(2):72–7. Available from: [<URL>](#)
26. Micelyn Amelia Ngamput H, Herrani R. The effect of differentiation of hydrolysis time towards ethanol levels produced through *ulva lactuca* fermentation. *J Phys Conf Ser*. 2019;1241(1):1–8. Available from: [<URL>](#)



Production and Activity Characterization of Lipase from *Bacillus flexus* InaCC-B486

Azra Zahrah Nadhirah Ikhwani^{1*} , Idris Idris¹ , Rizki Rabeca Elfirta¹ ,
Pamungkas Rizki Ferdian² 

¹National Research and Innovation Agency, Republic of Indonesia (BRIN), Research Organization for Life Sciences and Environment, Research Center for Applied Microbiology, Bogor, 16911, Indonesia

² National Research and Innovation Agency, Republic of Indonesia (BRIN), Research Organization for Life Sciences and Environment, Research Center for Applied Zoology, Bogor, 16911, Indonesia

Abstract: Lipases are widely used in a variety of industries, both to develop products and to improve process efficiency. The need for lipase increased along with the wider application of this enzyme. Therefore, studies related to the search for potential lipase-producing microbes that answer the needs of the industry are required to be carried out continuously. Enzymes produced by microbes are preferred because they can be produced quickly compared to other sources. *Bacillus flexus* InaCC-B486 was used to produce lipase in this study with olive oil as substrate. This research aimed to observe the production of lipase from *B. flexus* InaCC-B486 and characterize its activity. The result shows that the production of *B. flexus* InaCC-B486 lipase was optimal at day-4 which was 11.983 ± 0.101 U/mL. The activity of *B. flexus* InaCC-B486 lipase was optimal at an incubation time of 15 minutes (2.810 U/mL), pH of 8.0 (3.173 U/mL), and a temperature of 35 °C (3.173 U/mL). These findings can be used for further applications, both in research and industry, that use *B. flexus* InaCC-B486 as a resource for lipase production or any related applications.

Keywords: *Bacillus flexus* InaCC-B486, lipase enzyme, production optimization.

Submitted: July 28, 2023. **Accepted:** November 1, 2023.

Cite this: Ikhwani AZN, Idris. I, Elfirta RR, Ferdian PR A. Production and Activity Characterization of Lipase from *Bacillus flexus* InaCC-B486. JOTCSA. 2024;11(2):413-20.

DOI: <https://doi.org/10.18596/jotcsa.1333916>

***Corresponding author.** Email: azra001@brin.go.id

1. INTRODUCTION

The touch of biotechnology has contributed to the development of industry. One application in the field of biotechnology is the use of enzymes in industry, both in the process of making a product and in the use of enzymes as ingredients of a product. There are potential industries using enzymes, such as food and beverages (dairy, bakery, fruit juices, beer, and wine) (1), cosmetics, detergents, and oil-mining industries (2). Moreover, the enzyme has already been applied in the ecological services industry as an agent to eliminate pollutants. One enzyme widely applied is lipase. Lipase works to break down the ester bond in acyl-glycerols to glycerol and free fatty acids by hydrolysis process. This versatile enzyme enhances flavors, pharmaceuticals, and cosmetics. Moreover, it serves as an essential component in wastewater treatment, including oil-

pollutant removal, detergent cleaning, and other water-wastes elimination (3,4).

Research on lipase, especially in production, has been conducted for a long time and is still interesting today. Lipase production must be efficient in process and cost so that it can be more applicable. Lipase is naturally present in the human stomach and pancreas, as well as in other animal species, to digest fats and lipids. Other than that, lipase is also produced by microbes such as bacteria, yeast, and fungi. We can use microbial as the source of lipase to enhance and optimize production. Microbial enzymes contribute to approximately 90% of the global lipase market and industry. Moreover, the use of microbes tends to support sustainability since the microbes are relatively easy to grow and reproduce (5–7). Many microorganisms have been reported to produce lipase, such as *Bacillus*, *Burkholderia*,

Corynebacterium, *Geobacillus*, *Idiomarina*, *Oceanobacillus*, *Pseudomonas*, *Staphylococcus*, and *Virgibacillus* (8). *Bacillus* sp. were found to be predominant in the production of enzymes because of their shorter generation time, and the ease of genetic and environmental manipulation (9). *Bacillus* sp. is known to produce extracellular enzymes such as amylase, lipase, and protease (10,11). Roy et al. (10), reported that *Bacillus flexus* is a potential source of lipase, protease, amylase, and cellulase. The strain *B. flexus* KP1-14 cultivated in NB medium supplemented with 1% (v/v) Tween 80 was reported to have the highest lipase activity ($29.68 \pm 0.80 \text{ U mL}^{-1}$) by using p-nitrophenyl butyrate (8). The pathogenicity test performed in blood agar did not show any halo zone formation, thus indicating that *B. flexus* is non-pathogenic (10). So, lipase produced by *B. flexus* is safe to be used in the food and beverage industry as well as for other commercial needs. Other than that, the activity optimization of lipase needs to be conducted since the artificial environment applied, such as temperature, pH, activator, inhibitor, or other factors, can significantly influence the work of the enzyme itself.

The research on lipase from *B. flexus* needs to be enriched to fill the knowledge gap so that the further use of lipase could be complete and comprehensive enough to be applied in industry. Furthermore, the various collections of *B. flexus* exist and can be obtained from any culture collection organization. One of them is the collection of *B. flexus* from the Indonesian Culture Collection (InaCC), Indonesia. There was no report regarding the production and activity characterization of lipase from *B. flexus* collection from InaCC. Only a few isolates of *B. flexus* from Indonesia have been reported to have lipolytic activity, namely strains C₁₃ and C₁₄ (12) as well as SS5 (13). However, all these isolates have not been studied further regarding their lipase activity. Therefore, this research was designed to investigate the production and characterize the activity of lipase produced by *Bacillus flexus* InaCC-B486. The lipase production was monitored daily for a 7-day period. Subsequently, activity characterization was systematically conducted, focusing on some parameters, including incubation time, pH, and temperature.

2. EXPERIMENTAL

2.1. Materials

The materials employed in this research included glucose, peptone, yeast extract, NaCl, K₂HPO₄, MgSO₄·7H₂O, (NH₄)₂SO₄, p-nitrophenyl palmitate (p-NPP), triton X-100, Arabic gum, acetone, ethanol, olive oil, aquadest, and a bacterial isolate of *B. flexus* InaCC-B486, obtained from the collection of the Indonesia Culture Collection (InaCC).

2.2. Media Preparation

Specific media was prepared for the growth of *B. flexus* InaCC-B486, following Soleymani et al., (14). The media was formulated to support lipase

production. The media was made for 1 L and consisted of glucose and peptone (10 g), yeast extract and NaCl (5 g), K₂HPO₄ (1 g), CaCl₂ (2 g), MgSO₄·7H₂O (0.2 g), (NH₄)₂SO₄ (2 g). The pH was adjusted to 7.0 and then sterilized using an autoclave at 121°C for 15 minutes. A total of 20 mL of olive oil that had been sterilized by filtering was added afterward to the media.

2.3. Lipase Production

The 24-hour starter of *B. flexus* InaCC-B486 inoculated in nutrient broth was added to the prepared media as much as 1% (v/v). The mixture was then incubated in a rotary shaker with an agitation time of 110 rpm at room temperature. The production was conducted in triplicate. The lipase was obtained by centrifugating the culture at 4 °C, 5000 rpm, and 20 minutes. The supernatant was collected since the lipase was soluble in the supernatant. The lipase was collected each day within 7 days for testing the activity of lipase. The incubation time with the highest lipase activity value is used as the production time for the next stage, which is the effect of reaction incubation time, pH, and temperature.

2.4. Effect of Incubation Time, pH, and Temperature on Lipase Activity Assay

Lipase obtained from the production process was used to characterize the lipase activity in several parameters. These observations were conducted sequentially for incubation time, pH, and temperature. The base temperature and pH were 35°C and 7.0. The incubation time varied between 0 and 60 minutes, with an interval of 15 minutes. After gaining the highest lipase activity during the incubation time, the effect of pH was observed. The pH was varied between 5 and 10, with an interval of 1 scale. In the third step, the effect of temperature on lipase activity was observed. The highest lipase activity of incubation time and pH was used to observe the effect of temperature. The temperature varied between 25°C and 50°C with an interval of 5°C. Experiments to determine each parameter were carried out in triplicate.

2.5. Lipase Activity Assay

The lipase activity was measured using p-nitrophenyl palmitate (p-NPP) as a substrate. The substrate was prepared by dissolving 6.6 mg of p-nitrophenyl palmitate (p-NPP) in 1 mL of isopropanol, which was then added to a detergent solution. The detergent solution was prepared from 200 µL Triton X-100 dissolved in a 20 mL buffer to which 11 mg of Arabic gum had been added. The reaction solution consisted of 250 µL of substrate and 500 µL of crude lipase (culture-free supernatant). The reaction solution was homogenized using a vortex and then incubated at 35°C for 15 minutes. The reaction was stopped with 250 µL of acetone: ethanol (1:1) solution. The absorbance of the sample was read at a wavelength of 410 nm (15). Lipase activity was determined by measuring the concentration of p-nitrophenol (p-NP) released during the hydrolysis reaction, utilizing the standard curve of p-NP. One unit of enzyme

activity using this method was defined as the amount of enzyme liberating 1 μmol of p-nitrophenol per minute.

2.6. Standard Curve of p-Nitrophenol (p-NP)

Standard series of p-NP were prepared in concentrations of 10, 20, 30, 40, 50, and 60 μmol . The absorbance was measured at a wavelength of 410 nm. The linear curve was drawn with the y-axis as absorbance and the x-axis as the concentration of p-NP. The formula and linear regression of the curve were determined to calculate the lipase activity (15).

2.7. Data Analysis

Data were analyzed using one-way ANOVA, and if the results were significant, they were then continued with Duncan's Multiple Range Test (DMRT) at a 95% confidence level. The data was processed using Microsoft Excel 2013.

3. RESULTS AND DISCUSSION

Bacillus is well known as the best lipase-producing source (1,3). The microbial lipases are mostly extracellular enzymes secreted into the lipase production medium. Submerged fermentation (liquid fermentation system) was widely used as a technique to produce lipase enzymes from microorganisms. This is a method of cultivation of microorganisms in a liquid broth medium that

breaks down the supplied nutrients into a compound (3). In this study, olive oil was used as a lipidic substrate. Zarevúcka (16) reported that the use of olive oil in lipase production can enhance the lipase yield compared to other oil sources.

3.1. Lipase Production Time

Lipase production from *B. flexus* InaCC-B486 using olive oil as a substrate gave the best results on day 4, with a value of 11.983 ± 0.101 U/mL, which was a significant difference compared to the three first days and day 5. Lipase production was first detected on the first day of incubation and continued to increase until the fourth day of incubation. Lipase production began to decrease on the fifth day. On the sixth and seventh day, there was a slight increase in lipase production, but it was not significantly different from the previous day. (Fig. 1). Another study also reported that the optimum production of lipase time by *B. subtilis* PCSIR NL-38 was found on day 4, but with an activity value of 8.8 U/mL at 32°C (17). Meanwhile, the highest lipase production from *B. cereus* ATA179 was obtained on day 2 with a value of 6.6 U/mL (18). The decrease in lipase activity observed after a longer incubation time could be attributed to decreased nutrient availability (19). Furthermore, the presence of proteolytic activity, which can decompose enzyme proteins, caused a decrease in enzyme activity (20,21).

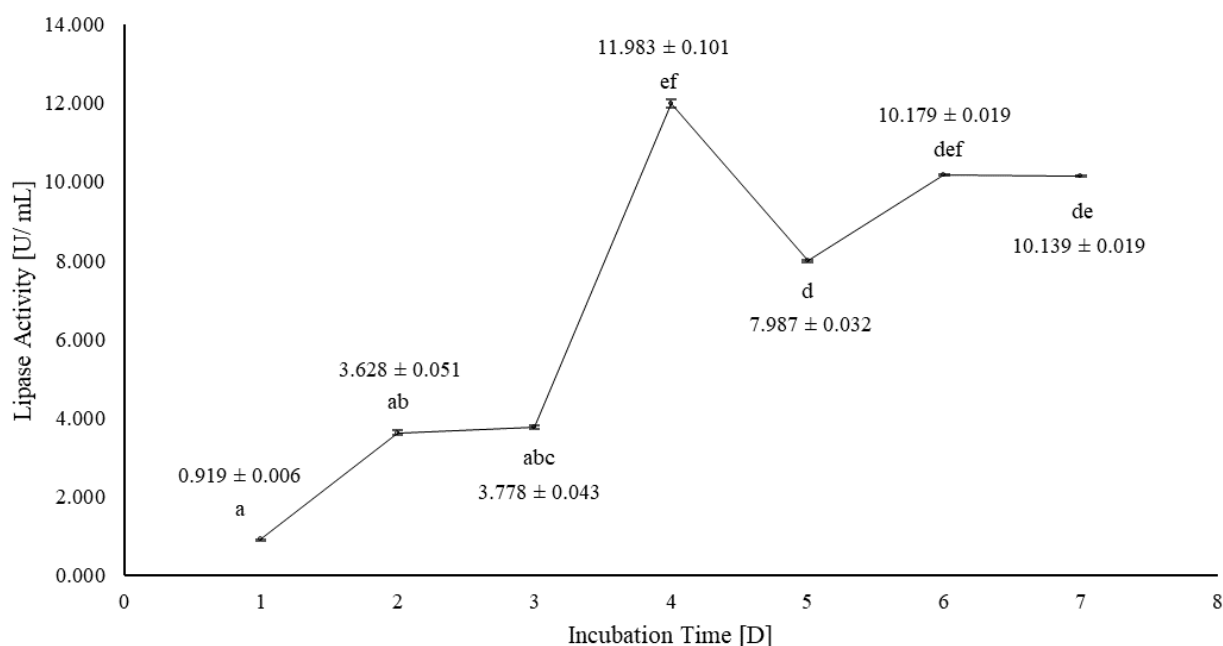


Figure 1. Lipase production time from *Bacillus flexus* InaCC-B486 on lipase activity.

The difference in lowercase symbols between treatments indicated a significantly different ($P < 0.05$) of lipase activity value according to Duncan's Multiple Range Test (DMRT).

3.2. Effect of Incubation Time, pH, and Temperature on Lipase Activity Assay

The lipase activity assay in this study followed the spectrophotometric method using p-nitrophenyl palmitate (p-NPP) as the substrate. The assay was carried out based on the colorimetric principle with

the hydrolysis of the ester substrate from palmitate by lipolytic enzymes, which had an effect on the release of the para-nitrophenol (p-NP) chromogenic product (22). This reaction produces the yellow-colored product of p-NP, which is measurable spectrophotometrically at 410 nm. One unit of

enzyme activity was defined as the amount of enzyme liberating 1 μmol of p-nitrophenol per minute. This method was advantageous because of its short reaction time and the result can be read using spectrophotometric analyses (23). The standard p-NP curve in this study was linear in the range of 0.147–0.819 μmol , with a determination

coefficient (R^2) of 99.95% (Fig. 2). The equation of this standard curve will be able to predict the concentration of p-NP products released by the reaction that occurs, which then the lipase activity can be calculated.

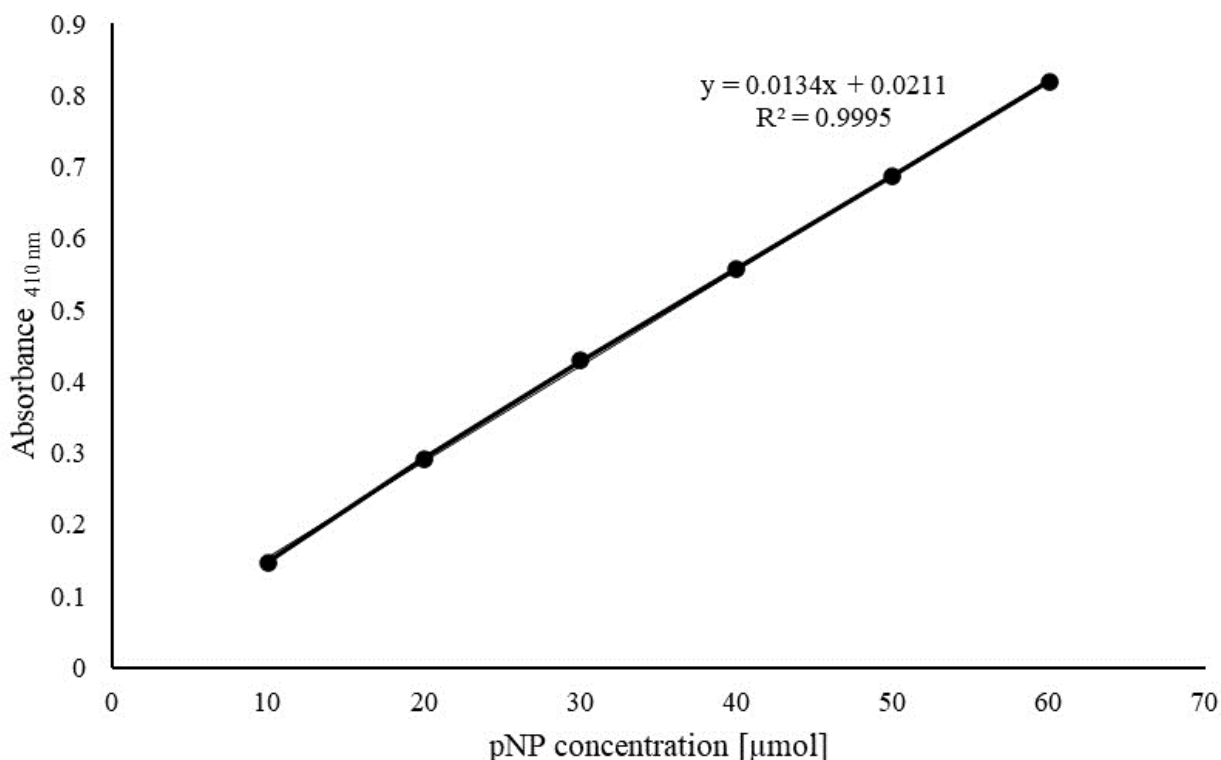


Fig. 2. Standard curve of p-NP.

Mostly, the active sites of bacterial lipases are covered by an alpha-helical flexible “flap” that can change from closed to open conformation when the lipase enzyme is absorbed by the lipid–water interface. The phenomenon of increased lipase activity at the lipid–water interface is referred to as interfacial activation (24–26).

The characterization of lipase activity began with the search for the best reaction time. The data obtained showed that the reaction had not occurred

initially (minute 0) and the best lipase activity with a value of 2.810 ± 0.106 U/mL was found at the 15th, minute which was significantly different from the incubation time of other observation times. The lipase activity after 15 minutes of incubation continuously decreases until 60 minutes of observation (Fig. 3). The decrease in enzyme activity can be caused by denaturation, structural modification, or dwindling substrate availability, which eventually triggers the repression of enzyme action (27).

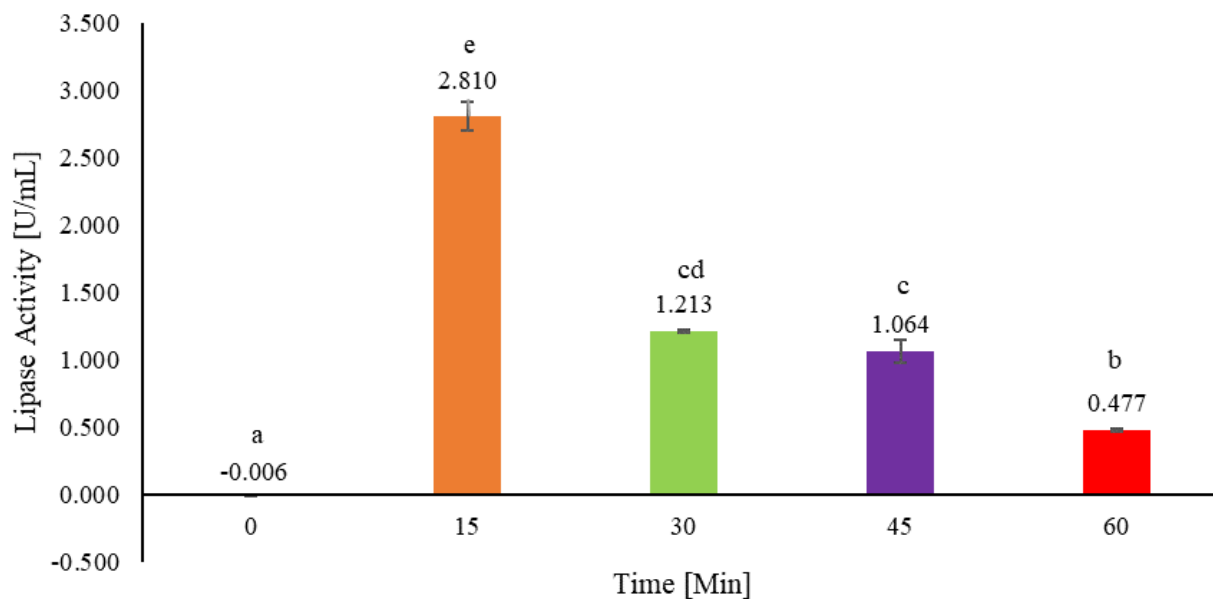


Fig. 3. Effect of reaction time conditions of lipase activity assay.

The difference in lowercase symbols between treatments indicated a significantly different ($P < 0.05$) of lipase activity value according to Duncan's Multiple Range Test (DMRT).

Subsequently, the effect of pH on lipase activity was observed. The highest lipase activity was obtained at pH 8, with a value of 3.173 ± 0.070 U/mL, which was significantly different from the other pH conditions tested (Fig. 4). This finding indicates that the lipase enzyme produced by *B. flexus* InaCC-B486 is of alkaline nature (alkaliphilic). The ionization of groups at the enzyme's active site and on the substrate can change as the pH changes, influencing the rate of substrate binding to the active site (28). Different *B. flexus* strains also showed the highest activity at alkaline pH, which was even higher at 10 (21). Generally, lipase enzymes produced from bacteria have good yields if produced under alkaline and neutral pH conditions (3). However, the lipases produced by fungi have an optimum yield if produced at acidic pH conditions (29,30). Tambekar et al. (11) reported that *B. flexus* isolated from Lonar Lake was able to produce extracellular lipase enzymes, and the optimum activity was recorded at pH 9. Lipase from *Bacillus cereus* NC7401 was also reported to be optimal at pH 8.0 and stable in the pH range of 5–10 (31). *B. subtilis* DR8806 that has been reported, exhibiting a pH optimum of 8.0 (32). Another alkaliphilic bacterial lipase has been reported from *Cohnella* sp. A01 exhibited maximum activity at pH 8.5 and was stable in the pH range of 8.5–10.0 (25). The alkaline lipases have great potential for use in food and beverage, detergent, flavoring, leather processing, pharmaceutical, and cosmetic industries (33). Alkaline lipases from bacteria are now popularly explored for a large variety of industrial purposes (34,35).

The optimum temperature that showed the highest lipase activity was found at 35°C (Fig. 5). The lipase

activity decreased dramatically when temperature increased to 40°C and 45°C. Interestingly, lipase activity was seen to increase again at 50°C but was lower than at 35°C. Increasing temperature enhances the rate of reaction at a certain point. On the other hand, higher temperatures denature enzyme proteins that change the shape of the active site of the enzyme, reducing or eliminating its activity (36). Another study found that lipase purified from *B. methylotrophicus* PS3 showed maximum activity at 55°C and was stable at 35°C (37). Bora et al. (38) reported that alkaline lipase has optimum activity at 30°C–65°C. The low optimum temperature can save an industry's production costs because it does not require high energy. According to its optimum temperature, the lipase produced by *B. flexus* InaCC-B486 belongs to the mesophilic family of enzymes. Mesophilic lipase has been used in several industrial applications, such as detergents, food processing, and waste treatment (39).

The results of the study in this article are limited to obtaining a determination of lipase activity from *Bacillus flexus* InaCC-B486, which was produced using olive oil as a substrate, by observing the influence of incubation time, pH, and temperature using p-nitrophenyl palmitate (p-NPP) during the reaction. The use of olive oil with the main components being oleic acid (C_{18}) and p-NPP (C_{16}) can provide an overview of the work of the lipase enzyme in breaking down fats with ester bonds from long chain fatty acids, in contrast to esterase, which prefers short chain fatty acids (40). Further research needs to be carried out, including enzyme purification and characterization, and then it can be tested for specific application purposes.

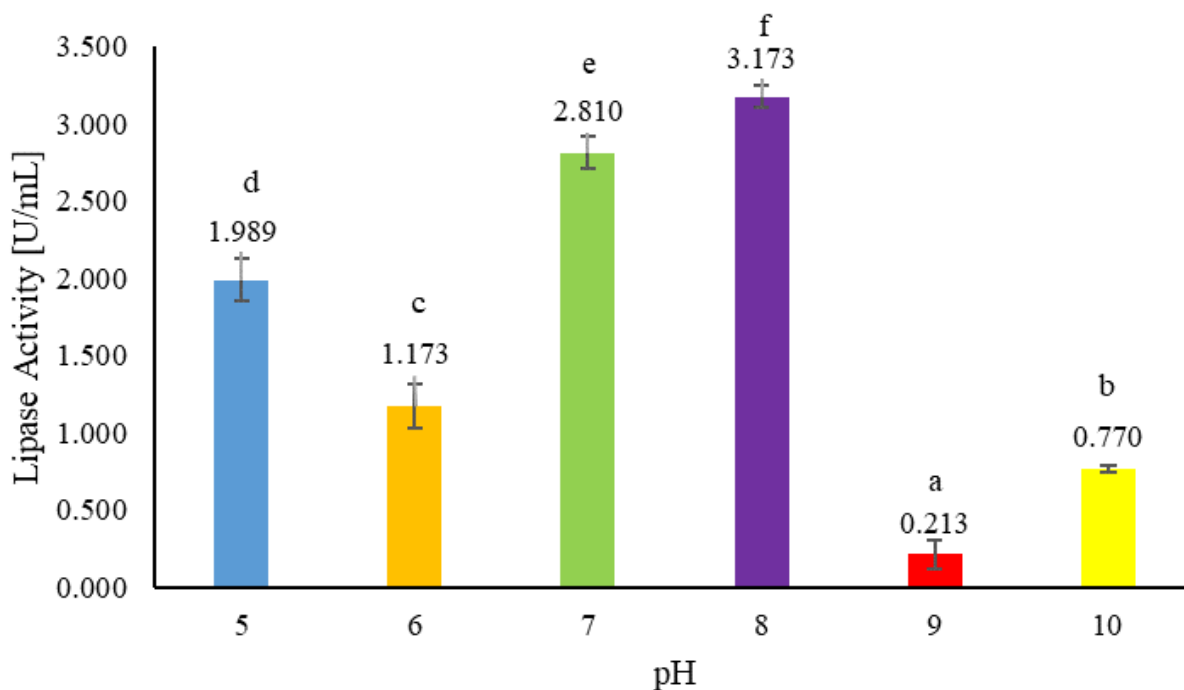


Fig. 4. Effect of reaction pH solutions of lipase activity assay.

The difference in lowercase symbols between treatments indicated a significantly different ($P < 0.05$) of lipase activity value according to Duncan's Multiple Range Test (DMRT).

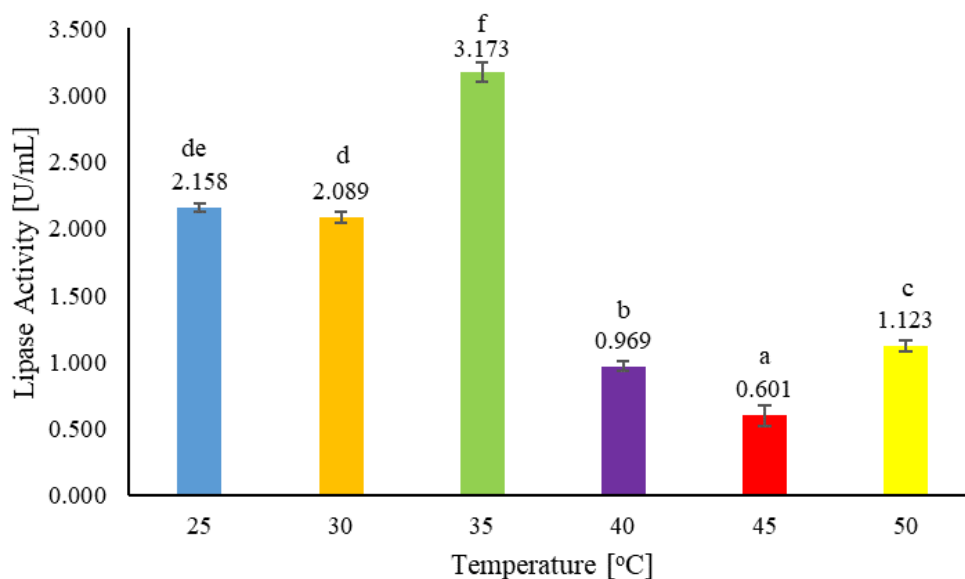


Fig. 5. Effect of reaction temperature of lipase activity assay.

The difference in lowercase symbols between treatments indicated a significantly different ($P < 0.05$) of lipase activity value according to Duncan's Multiple Range Test (DMRT).

4. CONCLUSION

Lipase production from *Bacillus flexus* InaCC-B486 was successfully achieved, reaching its optimum on day 4 with the addition of olive oil to the growth medium. We found that the lipase from *B. flexus*, InaCC-B486, has optimum activity at the first 15 minutes of incubation, a pH of 8, and a temperature of 35°C. These findings can hopefully be used as a reference for further research or industry

requirements, mainly in the use of lipase from *B. flexus* InaCC-B486.

5. CONFLICT OF INTEREST

The authors declare that there is no conflict of interest regarding the publication of this paper.

6. ACKNOWLEDGMENTS

This research project is funded by the National Research and Innovation Agency (NRIA), Republic of Indonesia.

7. REFERENCES

- Coelho ALS, Orlandelli RC. Immobilized microbial lipases in the food industry: a systematic literature review. *Crit Rev Food Sci Nutr*. 2021 May 31;61(10):1689–703. Available from: [<URL>](#).
- Negi S. Lipases: A Promising Tool for Food Industry. In: Parameswaran B, Varjani S, Raveendran S, editors. *Green Bio-processes: Enzymes in Industrial Food Processing*. Singapore: Springer Singapore; 2019. p. 181–98. Available from: [<URL>](#).
- Bharathi D, Rajalakshmi G. Microbial lipases: An overview of screening, production and purification. *Biocatal Agric Biotechnol*. 2019;22:101368. Available from: [<URL>](#).
- Ismail AR, Baek KH. Lipase immobilization with support materials, preparation techniques, and applications: Present and future aspects. *Int J Biol Macromol*. 2020;163:1624–39. Available from: [<URL>](#).
- Raveendran S, Parameswaran B, Ummalyma SB, Abraham A, Mathew AK, Madhavan A, et al. Applications of microbial enzymes in food industry. Vol. 56, *Food Technology and Biotechnology*. University of Zagreb; 2018. p. 16–30. Available from: [<URL>](#).
- Guerrand D. Lipases industrial applications: Focus on food and agroindustries. In: *OCL - Oilseeds and fats, Crops and Lipids*. EDP Sciences; 2017. Available from: [<URL>](#).
- Pessione E. The Less Expensive Choice: Bacterial Strategies to Achieve Successful and Sustainable Reciprocal Interactions. Vol. 11, *Frontiers in Microbiology*. Frontiers Media S.A.; 2021. Available from: [<URL>](#).
- Daroonpant R, Saeng-in P, Tanasupawat S. Identification and lipolytic activity of *Bacillus* and *Staphylococcus* strains from shrimp paste (Ka-pi). *J Appl Pharm Sci*. 2019 Apr 1;9(4):24–9. Available from: [<URL>](#).
- Mukesh kumar DJ, Andal Priyadharshini D, Suresh K, Saranya G, Rajendran K, Kalaichelven P. Production, purification and characterization of α -amylase and alkaline protease by *Bacillus* sp. HPE 10 in a concomitant production medium. *Asian Journal of Plant Science and Research*. 2012;2(3):376–82.
- Roy P, Chatterjee S, Saha NC, Gantait VV. Characterization of a Starch Hydrolysing *Bacillus flexus* U8 Isolated from Rhizospheric Soil of the Paddy Plants. *Proceedings of the National Academy of Sciences, India Section B: Biological Sciences*. 2020;90(5):1075–81. Available from: [<URL>](#).
- Tambekar DH, Tambekar SD, Jadhav AS, Kharat PA. Alkaliphilic *Bacillus flexus*: A potential source of lipase producer for industrial and medical application. *Int J Pharm Sci Res*. 2017;8(10):11. Available from: [<URL>](#).
- Setyati WA, Martani E, Triyanto, Subagiyo, Zainuddin M. Selection, identification and optimization of the growth water probiotic consortium of mangrove ecosystems as bioremediation and biocontrol in shrimp ponds. *Indonesian Fisheries Processing Journal*. 2014;17(3):243–53. Available from: [<URL>](#).
- Sarastiti S, Suminto, Sarjito. Molecular identification bacteria as probiotic candidates isolated from intestinal tract of vaname shrimp (*Litopenaeus vannamei*) collected from Subang, West Java. *Journal of Coastal and Marine Resources Management*. 2020;4(1):9–15.
- Soleymani S, Alizadeh H, Mohammadian H, Rabbani E, Moazen F, Sadeghi HM, et al. Efficient Media for High Lipase Production: One Variable at a Time Approach. Vol. 9. Available from: [<URL>](#).
- Picazo-Espinosa R. Lipase activity assay: improvements to the classical p-nitrophenol palmitate spectrophotometrical method. In: 41st International Conference of the Slovak Society of Chemical Engineering (SSCHE). Tatranské Matliare; 2014. Available from: [<URL>](#).
- Zarevúcka M. Olive Oil as Inductor of Microbial Lipase. In: Boskou D, editor. *Olive Oil - Constituents, Quality, Health Properties and Bioconversion*. Rijeka: InTech; 2012 [cited 2023 Jul 17]. p. 457–70. Available from: [<URL>](#).
- Abbas N, Javed J, Abbas Z, Choudry S, Ali S. Lipase production from *Bacillus subtilis* using various agricultural waste. *International Journal of Advanced engineering, Management and Science*. 2017;3(5):405–9. Available from: [<URL>](#).
- Demirkan E, Aybey Çetinkaya A, Abdou M. Lipase from new isolate *Bacillus cereus* ATA179: Optimization of production conditions, partial purification, characterization and its potential in the detergent industry. *Turkish Journal of Biology*. 2021;45(3):287–300. Available from: [<URL>](#).
- Barik A, Sen SK, Rajhans G, Raut S. Purification and Optimization of Extracellular Lipase from a Novel Strain *Kocuria flava* Y4. Basheer C, editor. *Int J Anal Chem*. 2022;2022:6403090. Available from: [<URL>](#).
- Bora L, Bora M. Optimization of extracellular thermophilic highly alkaline lipase from thermophilic *Bacillus* sp. isolated from hot spring of Arunachal Pradesh, India. *Brazilian Journal of Microbiology*. 2012;43:30–42. Available from: [<URL>](#).
- Niyonzima FN, More S. Biochemical properties of the alkaline lipase of *Bacillus flexus* XJU-1 and its detergent compatibility. *Biologia (Bratisl)*. 2014;69(9):1108–17. Available from: [<URL>](#).
- Jaeger KE, Kovacic F. Determination of Lipolytic Enzyme Activities. In: Filloux A, Ramos JL, editors. *Pseudomonas Methods and Protocols*. New York, NY: Springer New York; 2014. p. 111–34. Available from: [<URL>](#).
- Vardar-Yel N. Investigation of the activity of lipase variants on different 4-nitrophenyl esters by spectrophotometric assay. *Caucasian Journal of Science*. 2021 Dec 31;8(2):292–303. Available from: [<URL>](#).
- Cheng M, Angkawidjaja C, Koga Y, Kanaya S. Requirement of lid2 for interfacial activation of a family I.3 lipase with unique two lid structures. *FEBS Journal*. 2012 Oct;279(19):3727–37. Available from: [<URL>](#).
- Golaki BP, Aminzadeh S, Karkhane AA, Yakhchali B, Farrokh P, Khaleghinejad SH, et al. Cloning, expression, purification, and characterization of lipase 3646 from

- thermophilic indigenous *Cohnella* sp. A01. Protein Expr Purif. 2015 May 1;109:120–6. Available from: [<URL>](#).
26. Zhang W, Yang H, Liu W, Wang N, Yu X. Improved performance of magnetic cross-linked lipase aggregates by interfacial activation: A robust and magnetically recyclable biocatalyst for transesterification of jatropha oil. Molecules. 2017 Dec 1;22(12). Available from: [<URL>](#).
27. Sooch BS, Singh Kauldhar B. Influence of Multiple Bioprocess Parameters on Production of Lipase from *Pseudomonas* sp. BWS-5. Braz Arch Biol Technol. 2013;56(5):711–21. Available from: [<URL>](#).
28. Gusniah A, Veny H, Hamzah F. Activity and stability of immobilized lipase for utilization in transesterification of waste cooking oil. Bull Chem React Eng Catal. 2020 Apr 1;15(1):242–52. Available from: [<URL>](#).
29. Taskin M, Ucar MH, Unver Y, Kara AA, Ozdemir M, Ortucu S. Lipase production with free and immobilized cells of cold-adapted yeast *Rhodotorula glutinis* HL25. Biocatal Agric Biotechnol. 2016 Oct 1;8:97–103. Available from: [<URL>](#).
30. Turati DFM, Almeida AF, Terrone CC, Nascimento JMF, Terrasan CRF, Fernandez-Lorente G, et al. Thermotolerant lipase from *Penicillium* sp. section *Gracilentia* CBMAI 1583: Effect of carbon sources on enzyme production, biochemical properties of crude and purified enzyme and substrate specificity. Biocatal Agric Biotechnol. 2019;17:15–24. Available from: [<URL>](#).
31. Akhter K, Karim I, Aziz B, Bibi A, Khan J, Akhtar T. Optimization and characterization of alkaliphilic lipase from a novel *Bacillus cereus* NC7401 strain isolated from diesel fuel polluted soil. PLoS One. 2022 Aug 30;17(8):e0273368. Available from: [<URL>](#).
32. Emtenani S, Asoodeh A, Emtenani S. Molecular cloning of a thermo-alkaliphilic lipase from *Bacillus subtilis* DR8806: Expression and biochemical characterization. Process Biochem. 2013;48(11):1679–85. Available from: [<URL>](#).
33. Salihi A, Alam MdZ. Solvent tolerant lipases: A review. Process Biochemistry [Internet]. 2015;50(1):86–96. Available from: [<URL>](#).
34. Hu J, Cai W, Wang C, Du X, Lin J, Cai J. Purification and characterization of alkaline lipase production by *Pseudomonas aeruginosa* HFE733 and application for biodegradation in food wastewater treatment. Biotechnol Biotechnol Equip. 2018 May 4;32(3):583–90. Available from: [<URL>](#).
35. Huang J, Yang Z, Zhu R, Qian X, Wang Y, Li Y, et al. Efficient heterologous expression of an alkaline lipase and its application in hydrolytic production of free astaxanthin. Biotechnol Biofuels. 2018;11(1):181. Available from: [<URL>](#).
36. Robinson PK. Enzymes: principles and biotechnological applications. Essays Biochem. 2015 Nov 15;59:1–41. Available from: [<URL>](#).
37. Sharma P, Sharma N, Pathania S, Handa S. Purification and characterization of lipase by *Bacillus methylotrophicus* PS3 under submerged fermentation and its application in detergent industry. J Genet Eng Biotechnol. 2017;15(2):369–77. Available from: [<URL>](#).
38. Bora L, Gohain D, Das R. Recent advances in production and biotechnological applications of thermostable and alkaline bacterial lipases. J Chem Technol Biotechnol. 2013 Nov 1;88(11):1959–70. Available from: [<URL>](#).
39. Kumar V, Yedavalli P, Gupta V, Rao NM. Engineering lipase A from mesophilic *Bacillus subtilis* for activity at low temperatures. Protein Eng Des Sel. 2014 Mar;27(3):73–82. Available from: [<URL>](#).
40. Fojan P, Jonson PH, Petersen MTN, Petersen SB. What distinguishes an esterase from a lipase: A novel structural approach. Biochimie. 2000;82:1033–41. Available from: [<URL>](#).



DFT Calculations of Trilayer Heterostructures from MoSe₂, PtS₂ Monolayers in Different Orders with Promising Optoelectronic Properties

Jassim M. Al-Issawe¹ , Idrees Oreibi^{1,*} 

¹Directorate of Education Babylon, Ministry of Education, Iraq

Abstract: Van der Waals (vdW) heterostructures have taken the dominant place in commercialization of the optoelectronic devices. MoSe₂ and PtS₂ are two-dimensional semiconductors, Using first-principles computations, the optical and electronic characteristics of trilayer van der Waals (vdW) heterostructures with four distinct orders were investigated. We demonstrate that all innovative heterostructures investigated are semiconductors. In addition, it should be emphasized that the indirect band gaps of the ABA, BAA, ABB, and BAB orders (where A is MoSe₂ and B is PtS₂) are approximately 0.875, 0.68, 0.595, and 0.594 eV, respectively. Positively, the optical characteristics reveal that the trilayer heterostructures strongly absorb light with energies ranging from infrared to ultraviolet. Therefore, these heterostructures can be utilized in optoelectronic devices in these regions.

Keywords: DFT, heterostructures, trilayer, optoelectronic

Submitted: May 11, 2023. **Accepted:** December 26, 2023.

Cite this: Al-Issawe JM, Oreibi I. DFT Calculations of Trilayer Heterostructures from MoSe₂, PtS₂ Monolayers in Different Orders with Promising Optoelectronic Properties. JOTCSA. 2024; 11(2): 421-30.

DOI: <https://doi.org/10.18596/jotcsa.1295960>.

***Corresponding author. E-mail:** idrees114af@gmail.com

1. INTRODUCTION

Shortly after the discovery of graphene, two-dimensional (2D) materials became the focus of material research (1). The effectiveness of using graphene in nanotechnology and nanodevices has started a thorough investigation and study into layered low-dimensional materials (2). Graphene has spurred substantial research into two-dimensional (2D) materials such as TMDs (3), silicene (4), MX₂ Janus (5), germanene (6), III-group monochalcogenides (7, 8), phosphorene (9), and stanene (10).

Vertical heterostructures comprised of transition metal dichalcogenides (TMDs) monolayers are attractive prospects for next-generation optoelectronic and thermoelectric devices (11). These materials are more adaptable as candidates for thin, flexible device applications and are beneficial for numerous applications, including

photovoltaic devices (12, 13), transistors (14), Electrochemical Energy Systems (15, 16), lubrication (17, 18), lithium-ion batteries (16, 19), optoelectronic nanodevices (20), and thermoelectric devices (21). Transition metal dichalcogenide (TMDs) semiconductors and their bi-layer/tri-layer heterostructures have attracted significant attention because of their rich electronic/photonic properties such as a high carrier mobility (22), indirect to direct band gap transition (23), and abundance of multiexcitons (24), as well as importance for fundamental research and novel device applications (25, 26). TMDs monolayers are the most researched 2D semiconductors, with substantial exciton states and accessibility to the valley degree of freedom (27). TMDs materials are atomically 2D MX₂ semiconductors of the type MX₂, with M a transition metal atom (Mo, W, etc.) and X a chalcogen atom (S, Se, or Te), Many of these materials have been made in the laboratory, such as MoS₂ (28, 29), MoSe₂ (30), GeSe₂ (31), PtS₂ (32), MoTe₂ (33), and

WS₂ (34)...etc. Specifically, PtS₂ and MoSe₂ monolayers, among other TMDs materials, have become a focus of study in recent years due to their remarkable features, which make them ideal materials for transistors (35, 36), solar energy applications (37), and electrocatalysts (38). PtS₂ monolayer is a semiconducting material with a bandgap of about 1.7 eV (39). On the other hand, MoSe₂ monolayer is also a semiconducting material with a bandgap of about 1.5 eV (40).

Moreover, to my knowledge, no investigation into the optical and band structure characteristics of trilayer vdW heterostructures has ever been published. We shall thus study these characteristics of trilayer vdW heterostructures. The density functional theory was utilized to examine the optoelectronic characteristics of the heterostructures composed of three monolayers of PtS₂ and MoSe₂. Because the orders that form in the heterostructures may have a significant influence in determining the properties of the heterostructures, the examined properties are studied with four orders of trilayer vdW heterostructures. Our research could lead to a material that could be used to make optoelectronic devices.

2. COMPUTATIONAL METHODS

In this study, we calculate the optical and electronic properties of the trilayer heterostructures by first-principles calculations using castep code (41), with the generalized gradient approximations (GGA) (42). In the current work, the exchange-correlation

energy function developed by Perdew, Burke, and Ernzerhof (PBE) has been applied. The interaction of valence electrons is defined by the ultrasoft pseudopotential (43). The cutoff energy for plane-wave basis was taken to be 500 eV. The 4×4×1 supercell is the model system used in this work to replicate the heterostructure. The relativistic treatment follows out via the function of Koelling-Harmon. The self-consistent energy tolerance in the calculations was deemed to be converged at 4×10⁻⁶ eV/atom, while the force's convergence threshold was established at 1.5×10⁻² eV/Å. A vacuum gap of 25 Å along the perpendicular direction to the surface was utilized to exclude the interaction between two adjacent layers. To compute the geometry optimization and optical characteristics, respectively, the Brillouin zone is integrated with a 12×12×1 and 30×30×1 Monkhorst-Pack k-point mesh (44).

3. RESULTS AND DISCUSSION

3.1. Structural and Electronic Properties

Fig. 1 shows the geometrical atomic structures of MoSe₂ and PtS₂ monolayers from various angles. At equilibrium, MoSe₂ and PtS₂ monolayers correspond to the space group P-6m2 and P-3m1, respectively. the lattice constant of the single-layer MoSe₂ is a = b = 3.29 Å, c = 18.25 Å and the length of Mo-Se (d) is 2.522 Å, while the lattice constant of the single-layer PtS₂ is a = b = 3.58 Å, c = 17.56 Å and the length of Pt-S (d) is 2.418 Å, These results are in good agreement with previous experimental and theoretical data (45-49).

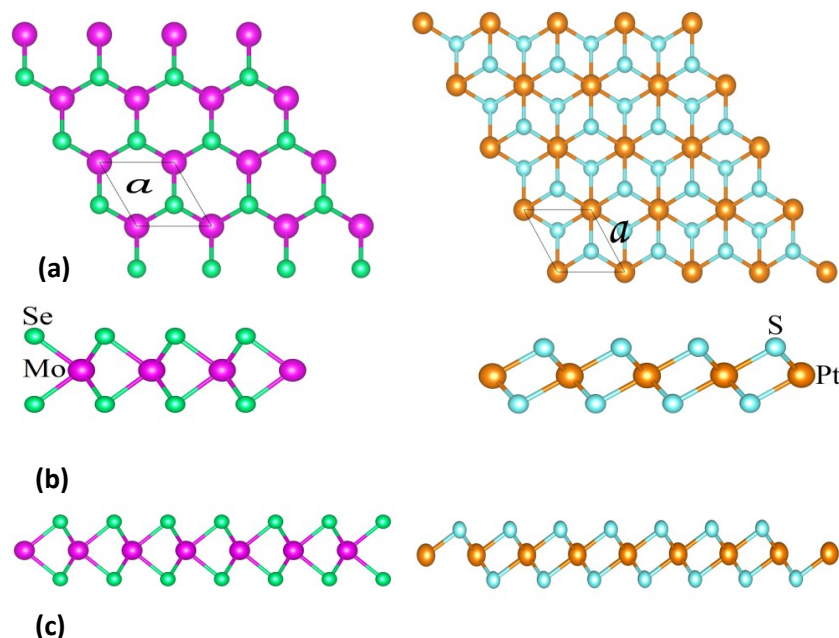


Figure 1: The top (a), side (b), and front(c) views of MoSe₂ and PtS₂ monolayers.

The three-layer heterostructures include four different arrangements where the monolayers are arranged perpendicular in the z-direction. These

arrangements are; ABA, AAB, ABB, and BAB (where A is MoSe₂ and B is PtS₂) as shown in Fig. 2. The calculated interlayer distances (h), lattice constants

(a), bond lengths (d), formation energy, and bind energy have been summarized in Table 1. These values are comparable with the mean value of monolayers MoSe_2 and PtS_2 . Our findings suggest that the arrangement of trilayer heterostructures has a significant effect on structural properties. The

formation and bind energies were calculated to identify the stability of ABA, BAA, ABB, and BAB orders. Manifestly, all the formed orders are stable due to their possessing formation energies with negative values.

Table 1: The computed structural and electronic properties of trilayer heterostructures.

Orders	a=b(Å)	h_1 (Å)	h_2 (Å)	$D_{\text{Mo-Se}}$ (Å)	$D_{\text{Pt-S}}$ (Å)	Formation energy(eV)	binding energy (eV)
ABA	3.387	3.928	4.258	2.544	2.385	-20.43	0.47
BAA	3.385	4.005	3.976	2.729	2.385	-20.41	0.49
ABB	3.491	4.391	4.240	2.570	2.4	-18.33	0.57
BAB	3.489	4.388	4.104	2.571	2.4	-18.31	0.58

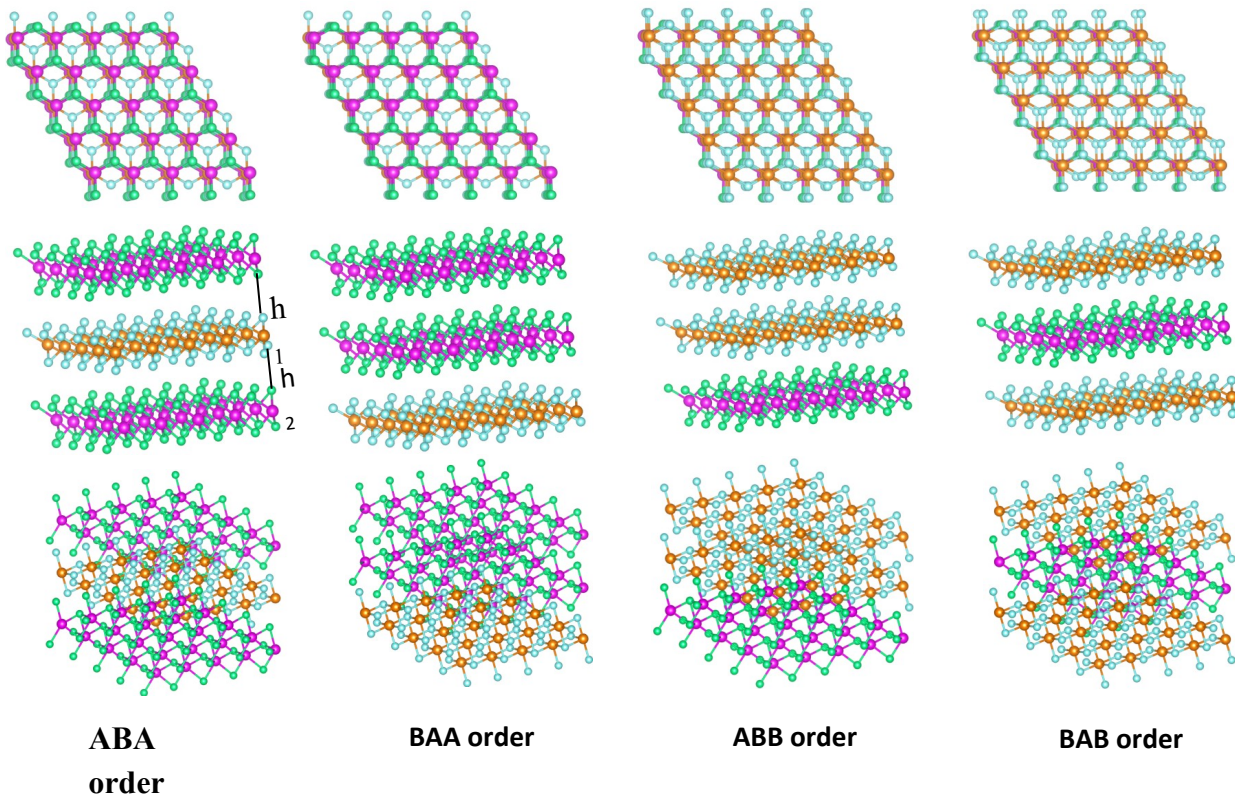


Figure 2: Atomic structures of trilayer heterostructures by different orders where A and B are MoSe_2 and PtS_2 , respectively.

The calculations of band structure show that the MoSe_2 monolayer has a direct bandgap (1.489 eV) lying at Γ point and is very comparable with previous experimental data (50, 51). On the other hand, the PtS_2 monolayer having the properties of a semiconductor with indirect bandgap (1.776 eV), the conduction band minimum (CBM), and valence band maximum (VBM) placed in the Γ -M and K- Γ paths, respectively, as exhibited in Fig. 3. This result is found to be in a very good agreement with previous reports (46, 52).

Figure 4 shows the phonon dispersion of the trilayer heterostructures. We note that the BAA order is the most dynamically stable, as it is devoid of any negative values, unlike the ABA order, which shows one branch that shows negative values that may indicate instability or numerical noise. As for the ABB and BAB orders, we notice that there are few negative values at Γ , which is mostly due to numerical noise.

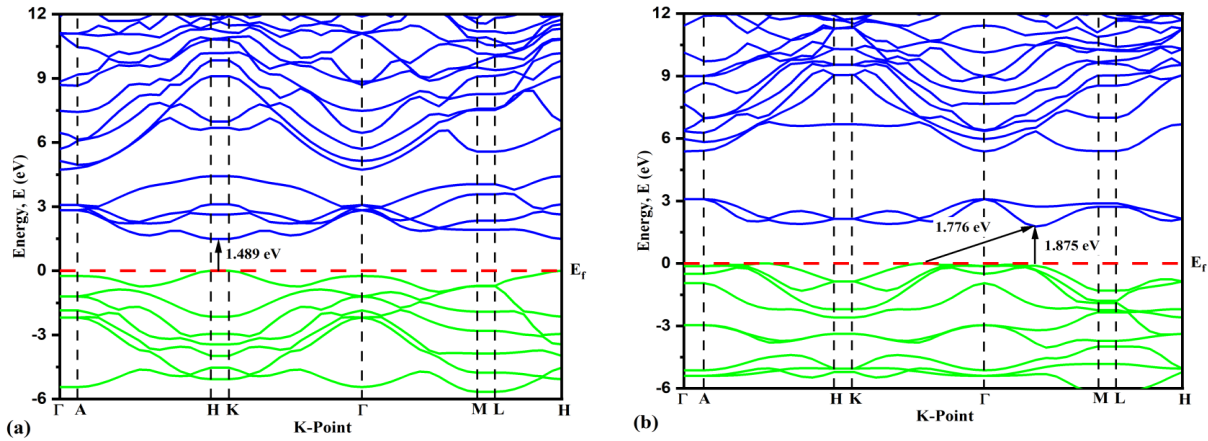


Figure 3: The band structure of the monolayers (a) MoSe₂, (b) PtS₂.

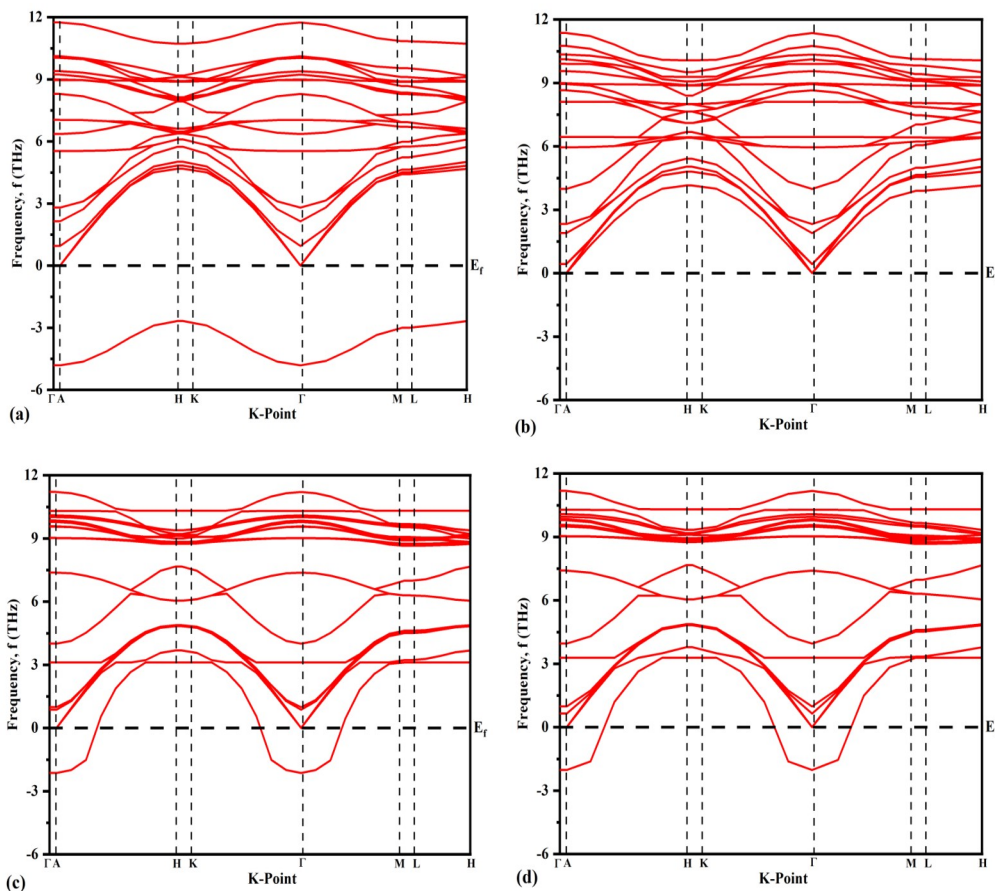


Figure 4: Phonon dispersions of trilayer heterostructures (a) ABA, (b) BAA, (c) ABB, (d) BAB orders.

Figure 5 depicts the band structure of trilayer heterostructures. The bandgaps are 0.875 eV (ABA), 0.68 eV (BAA), 0.595 eV (ABB), and 0.594 eV (BAB). These values are corresponded to the wavelengths, 1416.96 nm, 1823.29 nm, 2083.77 nm, and 2087.27 nm, respectively. From the band structure of ABA, BAA, ABB, and BAB orders, it can be seen that ABA and BAA orders have a lot in common when it comes to their direct and indirect energy gaps. The same is true for ABB and BAB orders. It should be pointed out that the VBM for all trilayers is positioned at Γ

point whereas CBM is placed in (ABA and BAA) ABB and BAB orders at (K- Γ path) Γ path. However, the sites of VBM are unchanged irrespective of the heterostructure order in contrast to CBM, which depends on the heterostructure type. Although the values of bandgaps of ABB and BAB heterostructures are very comparable, the values are much smaller than those in MoSe₂ and PtS₂ monolayers counterparts. More precisely, the construction of trilayer heterostructures reduces the energy gap to nearly a third of its value. In another

development, there a direct bandgaps for ABA, BAA, ABB, and BAB orders are positioned at r path with comparable values; 1.22, 1.16, 1.013, and 1.014 eV, respectively. This indicates that the values of the direct bandgap are approximately twice the indirect bandgap. Based on these values, we can unambiguously deduce that the bandgaps are situated in the infrared (IR) range. These findings revealed that there is a high probability of utilizing heterostructures as promising materials as photovoltaic devices.

This suggests that controlling the number and arrangement of the monolayers to form the triple layers leads us to obtain a band structure with

different energy gaps. This is the important feature of the triple layers that make them preferable to the monolayers that are involved in their formation. In addition, we computed the total and partial densities of state (TDOS and PDOS), and the results are shown in Fig. 6, It can be observed that the valence band (VB) and conduction band (CB) near the Fermi level (near zero) are composed of the p orbitals of sulfur and selenium atoms and the d orbitals of molybdenum and platinum atoms. The far region (-12 to -15 eV) of the valence band (VB) is dominated by the 3 s and 4 s orbitals of sulfur and selenium, whereas the far region of the conduction band (VB) is dominated by the s and p orbitals of platinum and selenium. This data provides the strongest support for the band structure results.

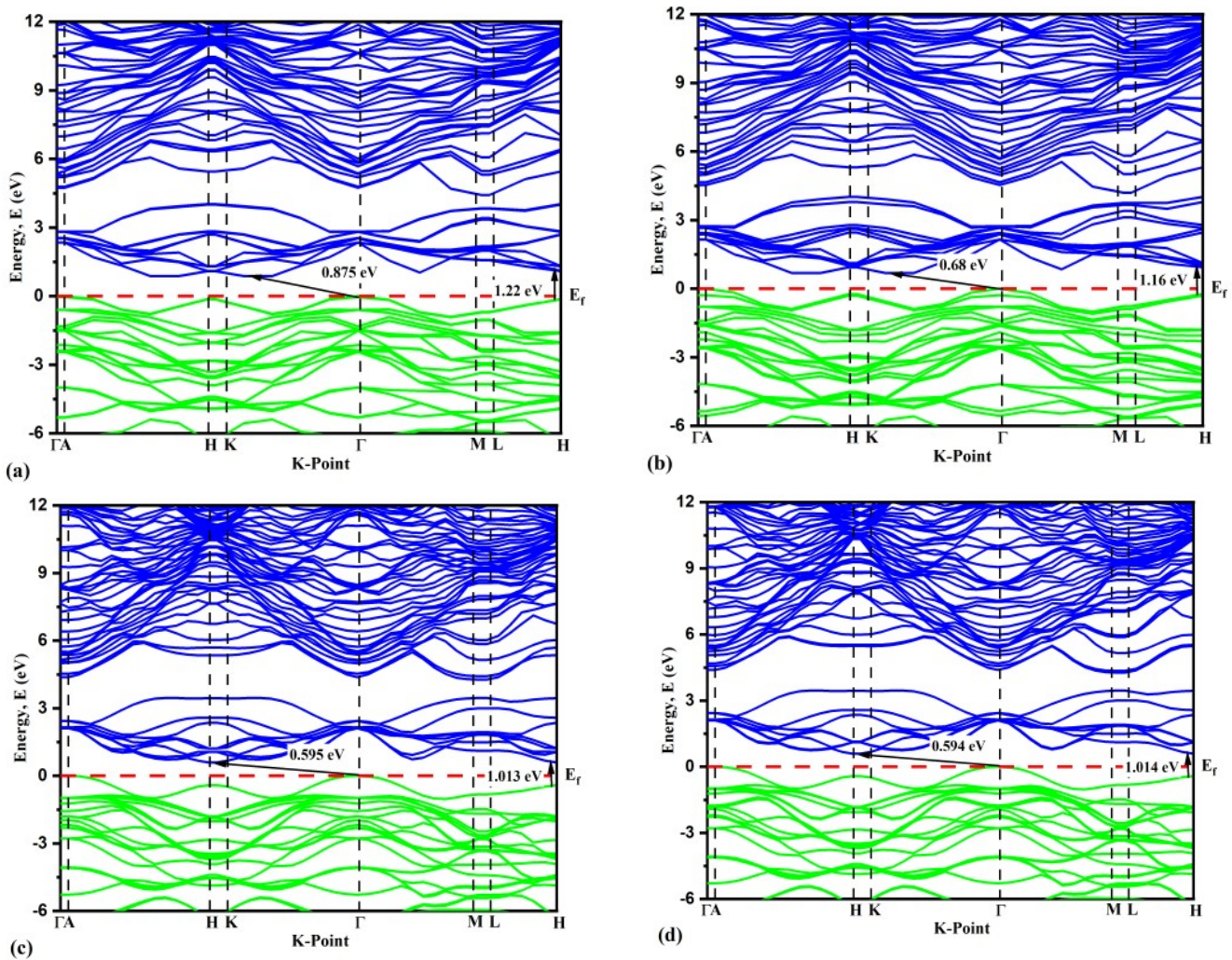


Figure 5: The band structure of trilayer heterostructures (a) ABA, (b) BAA, (c) ABB, (d) BAB orders.

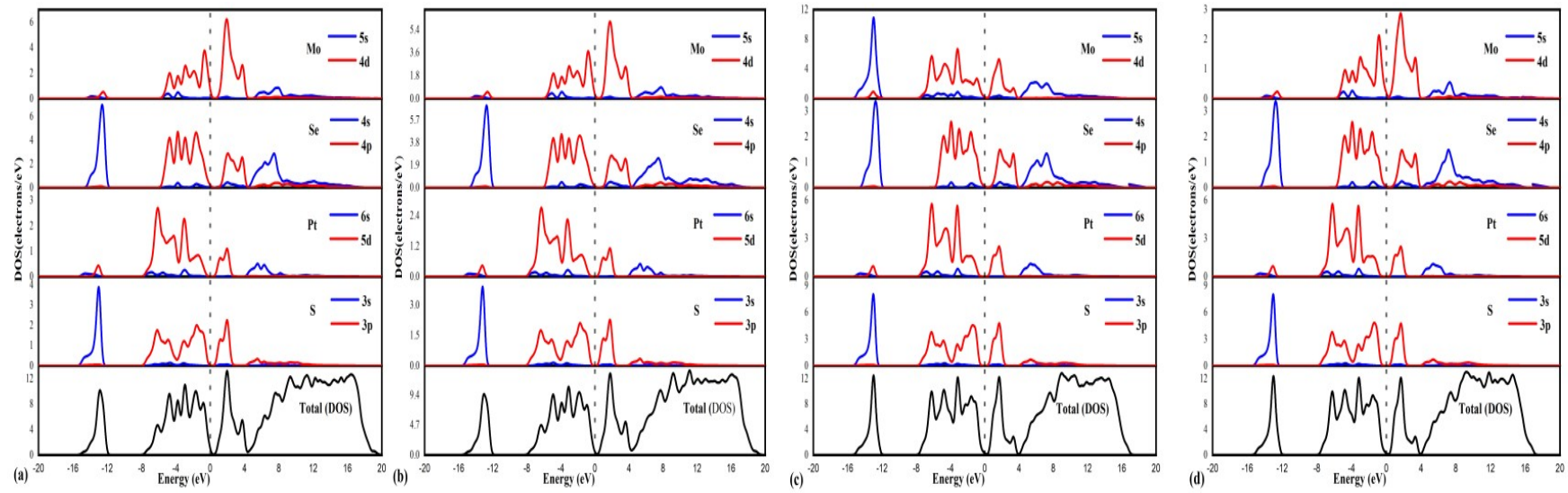


Figure 6: TDOS and PDOS of trilayer heterostructures (a) ABA, (b) BAA, (c) ABB, (d) BAB orders.

3.2. The Optical Properties

To determine the possible uses of a material in optical detection and electronic devices, its optical properties are crucial. Within the energy range of up to 30 eV, the optical properties of the layers were determined in the current study.

To employ a material in high-performance solar cells and other photovoltaic devices, it is necessary to understand its optical absorption, which offers essential information on how efficiently it transforms solar energy. The absorption coefficient (α) of trilayer heterostructures is illustrated in Fig. 7(a). After a careful analysis, we notice that the beginning of α in the infrared (IR) range, then, α increases with the growth of photon energy. This rise continues up to the highest value of α ; 15.2×10^4 , 15×10^4 , 15×10^4 , and $14.9 \times 10^4 \text{ cm}^{-1}$, for ABB, ABA, BAA, and BAB orders, respectively, all these values are positioned in the ultraviolet region. To be precise, this does not mean neglecting the value of the absorption coefficient in other regions, as its value in the visible region is also very high and equal to $8 \times 10^4 \text{ cm}^{-1}$. In addition, the absorption coefficient of the ABA and BAA have two peaks, not three as in ABB and BAB orders.

Reflectivity as a function of phonon energy is depicted in Fig. 7(b). Clearly, the static reflectivity of ABA, BAA, ABB, and BAB orders at zero energy is 22.5%, 22.2%, 21.9%, and 21.5%, respectively. However, the maximum values of reflectivity are 33.1% (ABA), 33% (BAA), 32.9% (ABB), and 32.7% (BAB); hence, the maximum values of reflectivity cannot exceed 33.1% for all trilayer vdW heterostructures. In addition, there are two peaks of reflectivity for ABA and BAA orders and three peaks for ABB and BAB orders, with the principal peaks for ABA, BAA, ABB, and BAB orders occurring in the visible range at energies of 2.67, 2.78, 2.78, and 2.67 eV, respectively. Reflectivity demonstrated a notable amount of anisotropy in the energy range of 0 to 21 eV, which decreases gradually to zero above 27 eV. Trilayer vdW heterostructures can therefore be used as coating nanomaterials in the visible and ultraviolet spectrum. The optical conductivity (σ) versus the photon energy of heterostructures described in Fig. 7(c). Clearly, there are two main peaks for ABA and

BAA orders and three main peaks for ABB and BAB orders. Although the conductivity commences from the IR region, their main peaks are positioned at the end of the infrared region and the beginning of the visible light region. Precisely, the uppermost values of conductivity are 2.8, 2.77, 2.65, and 2.6, positioned at 1.6 eV for all orders. After about 13.5 eV, the optical conductivity begins to decrease with the growth of photon energy.

The real ($\text{Re } \epsilon$) and imaginary ($\text{Im } \epsilon$) components of the dielectric function are computed and depicted in Fig. 7(d) and (e). The results of the ($\text{Re } \epsilon$) portion indicate that the topmost peaks of heterostructures are 9.66 (ABA), 9.58 (BAA), 9.45 (ABB), and 9.23 (BAB) at phonon energies of approximately 1.47 eV, 1.53 eV, 1.58 eV, and 1.64 eV, respectively. After about 21 eV, the ($\text{Re } \epsilon$) part becomes constant. Generally, it is notable that the superior ($\text{Re } \epsilon$) part is located in the visible region. In contrast, the results indicate that for all cases, the imaginary parts ($\text{Im } \epsilon$) of the dielectric function have one maximum peak in visible light. Nevertheless, the ($\text{Re } \epsilon$) and ($\text{Im } \epsilon$) peaks of the dielectric function of ABA layers are always greater than those of other layers. These peaks demonstrate that there is no additional transition between the valence and conduction bands. Because the number of peaks increases or decreases with the amount of electron transitions, when the number of peaks increases, more electrons are transferred between the valence and conduction bands.

Materials' optoelectronic properties are substantially influenced by the refractive index. Fig. 7(f) depicts the refractive index as a function of phonon energy (f). At zero photon energy, the static refractive indices of the real part for the ABA, BAA, ABB, and BAB orders are 2.82, 2.80, 2.77, and 2.72, respectively. For all trilayers, the maximum refractive index occurs near 2 eV. Beyond these values, the refractive index decreases gradually as photon energy increases. The refractive index remains constant after approximately 21 eV. In other words, after 21 eV, these heterostructures become anisotropic. These trilayers can be used as an internal layer coating between the substrate and ultraviolet absorbing layer due to their high refractive indices.

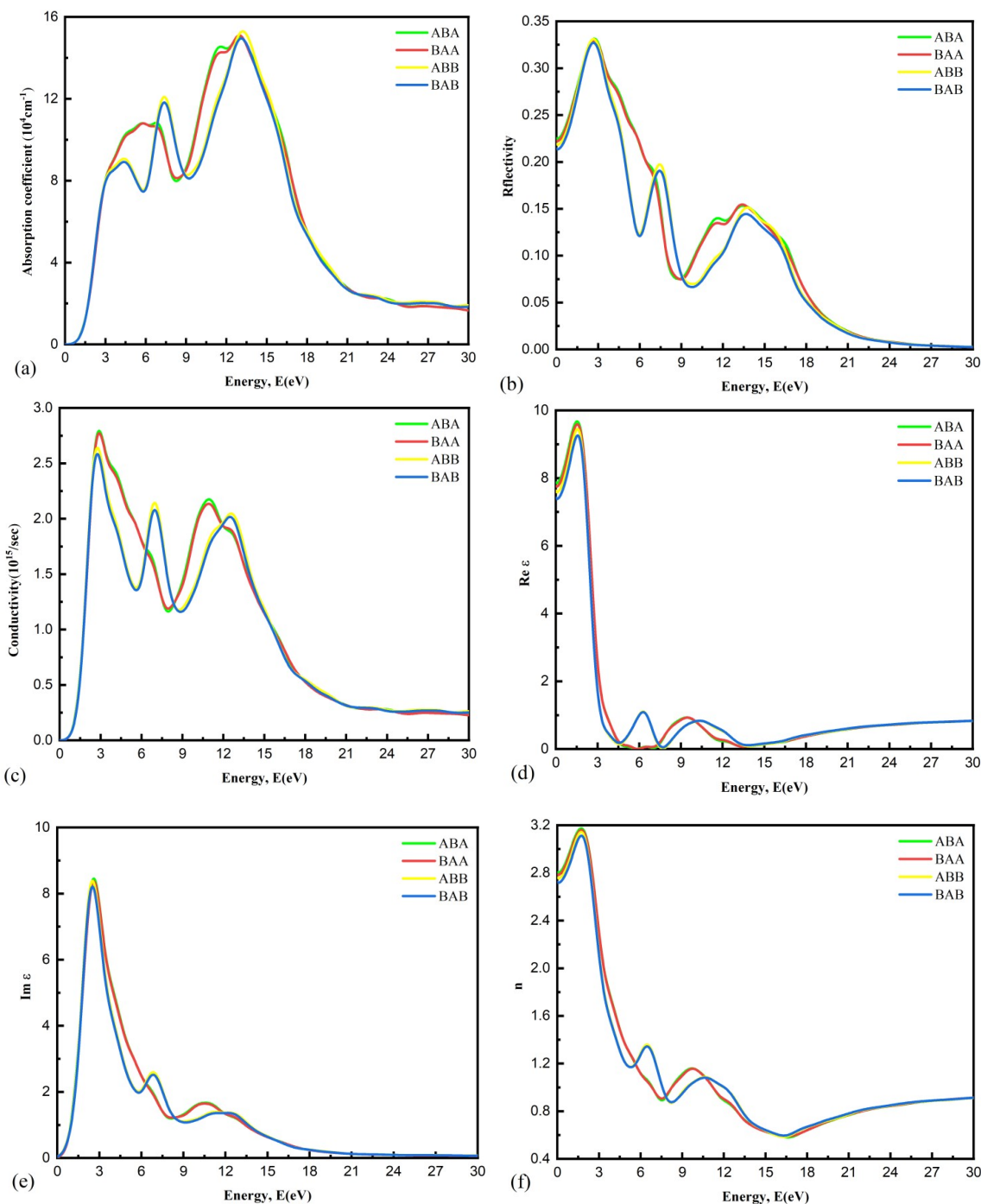


Figure 7: The optical characteristics of triple-layer heterostructures (a) the Absorption coefficient, (b) the reflectivity, (c) the conductivity, (d) the real part of the dielectric function, (e) the imaginary part of the dielectric function, (f) the refraction index.

4. CONCLUSIONS

In summary, we studied four orders of trilayer heterostructure. Using the PBE method the band gaps of All trilayers are between 0.594 to 0.875 eV, appealing for applications in nanoelectronics. Additionally, their direct energy gaps are nearly twice as great as their indirect energy gaps. On the other hand, it is found that the bandgaps of the

trilayer heterostructures are much smaller than those in the monolayer counterpart. the VB and CB near the Fermi level are composed of the p orbitals of S and Se atoms and the d orbitals of Mo and Pt atoms. According to optical simulations, the absorption coefficient of these unique trilayer heterostructures is extremely high in the visible light spectrum. ABA and BAA orders have higher optical property values in lower energy regions

before 6 eV. Due to the unique optical and electronic features of trilayer vdW heterostructures, it is hypothesized that these heterostructures can be utilized in optoelectronics and nanoelectronics applications.

5. CONFLICT OF INTERESTS

The authors declare that they have no conflict of interests.


6. REFERENCES

- Nandi P, Rawat A, Ahammed R, Jena N, De Sarkar A. Group-IV (A) Janus dichalcogenide monolayers and their interfaces straddle gigantic shear and in-plane piezoelectricity. *Nanoscale*. 2021;13(10):5460-78. Available from: [<URL>](#).
- Nguyen HT, Vu TV, Binh NT, Hoat D, Hieu NV, Anh NT, et al. Strain-tunable electronic and optical properties of monolayer GeSe: promising for photocatalytic water splitting applications. *Chemical Physics*. 2020;529:110543. Available from: [<URL>](#).
- Naguib M, Mochalin VN, Barsoum MW, Gogotsi Y. 25th anniversary article: MXenes: a new family of two-dimensional materials. *Advanced materials*. 2014;26(7):992-1005. Available from: [<URL>](#).
- Vogt P, De Padova P, Quaresima C, Avila J, Frantzeskakis E, Asensio MC, et al. Silicene: compelling experimental evidence for graphenelike two-dimensional silicon. *Physical review letters*. 2012;108(15):155501. Available from: [<URL>](#).
- Zhang Y, Ye H, Yu Z, Liu Y, Li Y. First-principles study of square phase MX₂ and Janus MXY (M= Mo, W; X, Y= S, Se, Te) transition metal dichalcogenide monolayers under biaxial strain. *Physica E: Low-dimensional Systems and Nanostructures*. 2019;110:134-9. Available from: [<URL>](#).
- Liu C-C, Feng W, Yao Y. Quantum spin Hall effect in silicene and two-dimensional germanium. *Physical review letters*. 2011;107(7):076802. Available from: [<URL>](#).
- Li P, Appelbaum I. Symmetry, distorted band structure, and spin-orbit coupling of group-III metal-monochalcogenide monolayers. *Physical Review B*. 2015;92(19):195129. Available from: [<URL>](#).
- Ren C, Wang S, Tian H, Luo Y, Yu J, Xu Y, et al. First-principles investigation on electronic properties and band alignment of group III monochalcogenides. *Scientific Reports*. 2019;9(1):1-6. Available from: [<URL>](#).
- Koenig SP, Doganov RA, Schmidt H, Castro Neto A, Özyilmaz B. Electric field effect in ultrathin black phosphorus. *Applied Physics Letters*. 2014;104(10):103106. Available from: [<URL>](#).
- Zhu F-f, Chen W-j, Xu Y, Gao C-l, Guan D-d, Liu C-h, et al. Epitaxial growth of two-dimensional stanene. *Nature materials*. 2015;14(10):1020-5. Available from: [<URL>](#).
- Bassman L, Rajak P, Kalia RK, Nakano A, Sha F, Aykol M, et al. Efficient discovery of optimal N-layered TMDC heterostructures. *Mrs Advances*. 2018;3(6-7):397-402. Available from: [<URL>](#).
- Flöry N, Jain A, Bharadwaj P, Parzefall M, Taniguchi T, Watanabe K, et al. A WSe₂/MoSe₂ heterostructure photovoltaic device. *Applied Physics Letters*. 2015;107(12):123106. Available from: [<URL>](#).
- Bastonero L, Cicero G, Palumbo M, Re Fiorentin M. Boosted Solar Light Absorbance in PdS₂/PtS₂ Vertical Heterostructures for Ultrathin Photovoltaic Devices. *ACS applied materials & interfaces*. 2021;13(36):43615-21. Available from: [<URL>](#).
- Wu D, Li W, Rai A, Wu X, Movva HC, Yogeesh MN, et al. Visualization of local conductance in MoS₂/WSe₂ heterostructure transistors. *Nano letters*. 2019;19(3):1976-81. Available from: [<URL>](#).
- Soares DM, Mukherjee S, Singh G. TMDs beyond MoS₂ for electrochemical energy storage. *Chemistry-A European Journal*. 2020;26(29):6320-41. Available from: [<URL>](#).
- Prabhu P, Jose V, Lee J-M. Design strategies for development of TMD-based heterostructures in electrochemical energy systems. *Matter*. 2020;2(3):526-53. Available from: [<URL>](#).
- Fan X, Li X, Zhao Z, Yue Z, Feng P, Ma X, et al. Heterostructured rGO/MoS₂ nanocomposites toward enhancing lubrication function of industrial gear oils. *Carbon*. 2022;191:84-97. Available from: [<URL>](#).
- Feng P, Ren Y, Li Y, He J, Zhao Z, Ma X, et al. Synergistic lubrication of few-layer Ti₃C₂T_x/MoS₂ heterojunction as a lubricant additive. *Friction*. 2022:1-15. Available from: [<URL>](#).
- Liu H, Huang Z, Wu G, Wu Y, Yuan G, He C, et al. A novel WS₂/NbSe₂ vdW heterostructure as an ultrafast charging and discharging anode material for lithium-ion batteries. *Journal of Materials Chemistry A*. 2018;6(35):17040-8. Available from: [<URL>](#).
- Pham KD, Hieu NN, Bui LM, Phuc HV, Hoi BD, Tu LT, et al. Vertical strain and electric field tunable electronic properties of type-II band alignment C₂N/InSe van der Waals heterostructure. *Chemical Physics Letters*. 2019;716:155-61. Available from: [<URL>](#).
- Zhao X, Tang G, Li Y, Zhang M, Nie Y. Biaxial strain improving the thermoelectric performance of a two-dimensional MoS₂/WS₂ heterostructure. *ACS Applied Electronic Materials*. 2021;3(7):2995-3004. Available from: [<URL>](#).
- Xia C, Xiong W, Du J, Wang T, Peng Y, Li J. Universality of electronic characteristics and photocatalyst applications in the two-dimensional Janus transition metal dichalcogenides. *Physical Review B*. 2018;98(16):165424. Available from: [<URL>](#).
- Mak KF, Lee C, Hone J, Shan J, Heinz TF. Atomically thin MoS₂: a new direct-gap semiconductor. *Physical review letters*. 2010;105(13):136805. Available from: [<URL>](#).
- Imani Yengejeh S, Wen W, Wang Y. Mechanical properties of lateral transition metal dichalcogenide heterostructures. *Frontiers of Physics*. 2021;16(1):1-7. Available from: [<URL>](#).
- Dong R, Kuljanishvili I. Progress in fabrication of transition metal dichalcogenides heterostructure systems. *Journal of Vacuum Science & Technology B, Nanotechnology and Microelectronics: Materials, Processing, Measurement, and Phenomena*. 2017;35(3):030803. Available from: [<URL>](#).
- Datta K, Shadman A, Rahman E, Khosru QD. Trilayer TMDC heterostructures for MOSFETs and nanobiosensors. *Journal of Electronic Materials*. 2017;46(2):1248-60. Available from: [<URL>](#).
- Jin C, Ma EY, Karni O, Regan EC, Wang F, Heinz TF. Ultrafast dynamics in van der Waals heterostructures. *Nature nanotechnology*. 2018;13(11):994-1003. Available from: [<URL>](#).

28. Naseri M. First-principles prediction of a novel cadmium disulfide monolayer (penta-CdS₂): Indirect to direct band gap transition by strain engineering. *Chemical Physics Letters*. 2017;685:310-5. Available from: [<URL>](#).
29. Lee YH, Zhang XQ, Zhang W, Chang MT, Lin CT, Chang KD, et al. Synthesis of large-area MoS₂ atomic layers with chemical vapor deposition. *Advanced materials*. 2012;24(17):2320-5. Available from: [<URL>](#).
30. Wang X, Gong Y, Shi G, Chow WL, Keyshar K, Ye G, et al. Chemical vapor deposition growth of crystalline monolayer MoSe₂. *ACS nano*. 2014;8(5):5125-31. Available from: [<URL>](#).
31. Yumigeta K, Brayfield C, Cai H, Hajra D, Blei M, Yang S, et al. The synthesis of competing phase GeSe and GeSe₂ 2D layered materials. *RSC advances*. 2020;10(63):38227-32. Available from: [<URL>](#).
32. Zhao D, Xie S, Wang Y, Zhu H, Chen L, Sun Q, et al. Synthesis of large-scale few-layer PtS₂ films by chemical vapor deposition. *AIP Advances*. 2019;9(2):025225. Available from: [<URL>](#).
33. Meng L, Xu C, Li H, Wang X, Yan X. Controlled synthesis and frictional properties of 2D MoTe₂ via chemical vapor deposition. *Chemical Physics Letters*. 2019;728:156-9. Available from: [<URL>](#).
34. Meng L, Hu S, Yan W, Feng J, Li H, Yan X. Controlled synthesis of large scale continuous monolayer WS₂ film by atmospheric pressure chemical vapor deposition. *Chemical Physics Letters*. 2020;739:136945. Available from: [<URL>](#).
35. Ghiasi TS, Quereda J, Van Wees BJ. Bilayer h-BN barriers for tunneling contacts in fully-encapsulated monolayer MoSe₂ field-effect transistors. *2D Materials*. 2018;6(1):015002. Available from: [<URL>](#).
36. Han G, Kaniselvan M, Yoon Y. Photoresponse of MoSe₂ transistors: A fully numerical quantum transport simulation study. *ACS Applied Electronic Materials*. 2020;2(11):3765-72. Available from: [<URL>](#).
37. Xiong R, Hu R, Zhang Y, Yang X, Lin P, Wen C, et al. Computational discovery of PtS₂/GaSe van der Waals heterostructure for solar energy applications. *Physical Chemistry Chemical Physics*. 2021;23(36):20163-73. Available from: [<URL>](#).
38. Chen C, Cao J, Yin W, Zhang Q, Yao Y, Wei X. Single transition metal atom modified MoSe₂ as a promising electrocatalyst for nitrogen fixation: A first-principles study. *Chemical Physics Letters*. 2021;780:138939. Available from: [<URL>](#).
39. Liu G, Gan Y, Quhe R, Lu P. Strain dependent electronic and optical properties of PtS₂ monolayer. *Chemical Physics Letters*. 2018;709:65-70. Available from: [<URL>](#).
40. Wasey AA, Chakrabarty S, Das G. Substrate induced modulation of electronic, magnetic and chemical properties of MoSe₂ monolayer. *AIP Advances*. 2014;4(4):047107. Available from: [<URL>](#).
41. Clark SJ, Segall MD, Pickard CJ, Hasnip PJ, Probert MI, Refson K, et al. First principles methods using CASTEP. *Zeitschrift für kristallographie-crystalline materials*. 2005;220(5-6):567-70. Available from: [<URL>](#).
42. Perdew JP, Burke K, Ernzerhof M. Generalized gradient approximation made simple. *Physical review letters*. 1996;77(18):3865. Available from: [<URL>](#).
43. Vanderbilt D. Soft self-consistent pseudopotentials in a generalized eigenvalue formalism. *Physical review B*. 1990;41(11):7892. Available from: [<URL>](#).
44. Monkhorst HJ, Pack JD. Special points for Brillouin-zone integrations. *Physical review B*. 1976;13(12):5188. Available from: [<URL>](#).
45. Mir SH, Chakraborty S, Wärnå J, Narayan S, Jha PC, Jha PK, et al. A comparative study of hydrogen evolution reaction on pseudo-monolayer WS₂ and PtS₂: insights based on the density functional theory. *Catalysis Science & Technology*. 2017;7(3):687-92. Available from: [<URL>](#).
46. Yao W, Guan H, Zhang K, Wang G, Wu X, Jia Z. Nb-doped PtS₂ monolayer for detection of C₂H₂ and C₂H₄ in on-load tap-changer of the oil-immersed transformers: A first-principles study. *Chemical Physics Letters*. 2022:139755. Available from: [<URL>](#).
47. Li Y, Feng Z, Sun Q, Ma Y, Tang Y, Dai X. Electronic, thermoelectric, transport and optical properties of MoSe₂/BAS van der Waals heterostructures. *Results in Physics*. 2021;23:104010. Available from: [<URL>](#).
48. Hu X, Zhang Q, Yu S. Theoretical insight into the hydrogen adsorption on MoS₂ (MoSe₂) monolayer as a function of biaxial strain/external electric field. *Applied Surface Science*. 2019;478:857-65. Available from: [<URL>](#).
49. Wu Q, Fu X, Yang K, Wu H, Liu L, Zhang L, et al. Promoting a weak coupling of monolayer MoSe₂ grown on (100)-faceted Au foil. *ACS nano*. 2021;15(3):4481-9. Available from: [<URL>](#).
50. Zhang Y, Chang T-R, Zhou B, Cui Y-T, Yan H, Liu Z, et al. Direct observation of the transition from indirect to direct bandgap in atomically thin epitaxial MoSe₂. *Nature nanotechnology*. 2014;9(2):111-5. Available from: [<URL>](#).
51. Yadav VK, Kumar PP, Singh V. Effect of different precursors on morphology of CVD synthesized MoSe₂. *Materials Today: Proceedings*. 2022;56:3786-9. Available from: [<URL>](#).
52. Tao W-L, Mu Y, Hu C-E, Cheng Y, Ji G-F. Electronic structure, optical properties, and phonon transport in Janus monolayer PtSSe via first-principles study. *Philosophical Magazine*. 2019;99(8):1025-40. Available from: [<URL>](#).



Sorption of Mn(II) Ions From Wastewater Using Dried and Blended Water Hyacinth (*Eichhornia crassipes*) Roots: Adsorption-Desorption Studies and Kinetics

Godswill Okeoghene Tesi^{1*} , Onome Ejeromedoghene² , Bridget Kpomah³ ,
Ayodele R. Ipeaiyeda⁴ 

¹University of Africa, Department of Chemical Sciences, Toru-Orua, Nigeria.

²Southeast University, School of Chemistry and Chemical Engineering, 211189 Nanjing, Jiangsu Province, P. R. China.

³Delta State University, Department of Chemistry, Abraka, Nigeria.

⁴University of Ibadan Department of Chemistry, Ibadan, Nigeria.

Abstract: This study examined the sorption of Mn(II) ions from waste using dried and blended water hyacinth root (WHR). It focused on how the major process parameters influenced the sorption process. Mathematical models were proposed to explain both the equilibrium and kinetics of biosorption. A desorption study was conducted using different HNO₃ and NaOH concentrations. An application study using actual industrial effluent was evaluated to analyze the fitness of the biosorbent at optimal batch conditions. The results demonstrated that the increasing initial Mn(II) ion concentration decreased Mn(II) ion removal, while an increase in the sorbent dosage increased its removal. For the rate of biosorption, the contact time was rapid between 15 and 45 min, and the maximum Mn(II) ion was removed within the initial 60 min. Equilibrium sorption was attained at pH 7, where maximum Mn(II) ion uptake was 94 %. The results also showed that Mn(II) ion biosorption at 30 °C and pH 7 for water hyacinth roots could be modeled by Langmuir and Freundlich isotherms and the pseudo-2nd order model. Furthermore, an effective desorption of Mn(II) was obtained with solutions of both NaOH and HNO₃. The results also showed that the percentage biosorption and desorption of Mn(II) from the industrial wastewater were 64.68 and 27.95 %, respectively.

Keywords: Biosorption; Biosorbent; Wastewater; Water Hyacinth; Desorption.

Submitted: July 9, 2022. **Accepted:** November 28, 2023.

Cite this: Tesi GO, Ejeromedoghene O, Kpomah B, Ipeaiyeda AR. Sorption of Mn(II) Ions From Wastewater Using Dried and Blended Water Hyacinth (*Eichhornia crassipes*) Roots: Adsorption-Desorption Studies and Kinetics. JOTCSA. 2024;11(2):431-40.

DOI: <https://doi.org/10.18596/jotcsa.1142283>

***Corresponding author's E-mail:** godswillinfodesk@yahoo.com

1. INTRODUCTION

Water, a vital natural resource, is progressively being contaminated by urbanization and industrialization (1). Contamination of water is occurring due to the continuous discharge of both industrial effluents from chemical and textile industries, compromising the biotic and abiotic components of the ecosystem (2). Consequently, problems like alteration of the chemical oxygen demand (COD) by aquatic organisms, and reduced availability of potable water for human consumption have been on the increase due to the increased toxicity of the discharge of colored substances into water bodies from the textile, pulp, dye, and pigment industries (3,4).

These colored substances contain a significant amount of heavy metal ions that pose several toxicity risks to the adjoining water bodies (5).

Over the years, conventional wastewater treatment processes, which include membrane filtration, oxidation, precipitation, and coagulation, have been employed to remove toxic heavy metals from wastewater (6–8). However, adsorption has been recognized and reported to be a cost-effective and economical choice for the exclusion of metals from industrial effluents via the use of low-cost biosorbent materials with high adsorption capability and minimizing waste dispersal problems (9).

There has been increased attention on an aquatic plant, the water hyacinth (*Eichhornia crassipes*), for use in the adsorption of contaminants, especially toxic metal ions, from aquatic environments due to its rapid proliferation resulting from its absorption efficiency, higher than normal growth rate, low operation cost, and renewability (10, 11). The plant has been well studied, and literature has it that *E. crassipes* is capable of improving the quality of effluent from oxidation ponds. *E. crassipes* is also reported to play a key role in the treatment of industrial, agricultural, municipal, and agricultural wastewaters of any sort (12, 13). *E. crassipes* have been reported to thrive in profoundly polluted water and thus possess a high capability for the accumulation of metal ions (14). The dried root of the plant is reported to possess a strong affinity to adsorb metal ions like lead (Pb), copper (Cu), cadmium (Cd), chromium (Cr), and zinc (Zn) from aqueous media, with varying sorption performance for each metal, its solution chemistry and concentration (15-17). With many studies reporting on heavy metal adsorption onto water hyacinth biomass (18), there is currently no literature relating to the biosorption of Mn(II) ions exploitation of powdered roots of water hyacinth. Herein, the kinetics and adsorption-desorption studies on Mn(II) ion sorption from industrial wastewater with the roots of water hyacinth as a biosorbent were investigated and reported.

2. EXPERIMENTAL DETAILS

2.1. Preparation of Water Hyacinth Roots (WHR) Adsorbent

E. crassipes employed in this experiment were derived from wild specimens growing in Oba Dam, Ibadan. The collected plant root was washed several times with tap water, air-dried, and ground into powder using an electric blender, and thereafter sieved using a 2 mm sieve before being used directly as a biosorbent without further pretreatment. The morphology of the dried WHR was captured on an FEI-110730002486 SEM instrument.

2.2. Preparation of Adsorbate

A stock solution of Mn (II) ions was made in a 1L flask by dissolving 3.0766 g of MnSO₄.H₂O in distilled water. The prepared Mn(II) stock solution was standardized with a standard EDTA solution using suitable indicators and buffer solution at different pH. Working solutions of Mn(II) ion were made from the stock by serial dilution. Each sample was analyzed in triplicate to reduce experimental error and obtain reproducible results.

2.3. Batch Adsorption Experiments

The adsorption of Mn (II) ion on WHR, desorption studies and application to real industrial wastewater, isotherms modeling, and kinetics of the sorption process were done using procedures and model equations previously described (13, 18-20).

2.3.1. Effect of pH

The effect of the sorbent pH was determined by providing 25 mL of Mn(II) ions working solution in a flask and adding 1.0 g of the powdered WHR to it.

The mixture was gently stirred using a rotary shaker at 30 °C, for 1 h and then filtered using Whatman No.1 filter paper. The Atomic Absorption Spectrophotometer (AAS), Perkin Elmer (Analyst 200) was used to determine the concentration of filtrate of the Mn(II) ions. The pH of these suspensions was adjusted to a range between 4.0, and 9.0 with a 2M HCl or 2M NaOH solution.

2.3.2. Effect of contact time

The effect of the contact time was studied and determined at different time intervals, 15, 30, 45, 60, 75, and 90 min. 1.0 g of powdered WHR was weighed into different flasks for the different contact time intervals. 25 mL of the prepared Mn(II), at pH 7 and containing equal concentrations (5 mg/L), was added and mixed at 30 °C. At 15 min, the bottle was withdrawn, and the mixture was filtered by gravity using Whatman No.1 filter paper. This was repeated for the different time intervals, and the metal ion concentrations of the filtrate were determined using AAS.

2.3.3. Effect of initial metal concentration

Several standard solutions containing equal concentrations of Mn(II) ions were prepared, and 1.0 g of the biosorbents was weighed into several flasks. Thereafter, 25 mL of the prepared Mn(II) (pH 7) containing an equal concentration of 5 mg/L was added to the flask and mixed thoroughly for 1 h using a rotary shaker at 30 °C. At 15 mins, the flask was withdrawn, and the mixture was filtered by gravity using Whatman No.1 filter paper. This was repeated for the different time intervals, and the metal ion concentrations of the filtrate were determined using AAS.

2.3.4. Effect of dosage

The effect of the sorbent dosage was determined at different concentrations (0.2, 0.4, 0.6, 0.8, 1.0, and 1.2 g) of powdered WHR with 25 mL of Mn(II) (pH 7) in each volumetric flask. The mixture was stirred for 1 h at 30 °C with a rotary shaker to ensure equilibrium. At each time interval, the flask was withdrawn, and the mixture was filtered by gravity using Whatman No.1 filter paper. The concentrations of the metal ions in the filtrate were determined using AAS.

2.4. Desorption Studies

The desorption study was conducted at 2, 4, and 6 M concentrations of NaOH and HNO₃ solutions. A 25 mL mixture of the adsorbent and adsorbate was shaken for 1 h and left undisturbed for 24 h; thereafter, the solution was filtered. AAS was used to measure the concentration of Mn(II) ions. The percentage desorption was computed as follows:

$$\text{Desorption Efficiency (\%)} = \frac{\text{Released metal concentration}}{\text{Initially sorbed metal concentration}} \times 100 \quad (1)$$

2.5. Application to Real Industrial Wastewater

Industrial wastewater was obtained from along the Omi-Asoro river, Ilesa, Nigeria, 25 mL of which was introduced to a tightly closed flask wherein 1.0 g of the sorbents was added. The pH of these suspensions was regulated to 7 and the mixture was gently

shaken with a rotary shaker at 30 °C for 1 h. Thereafter, the mixture was filtered using Whatman No.1 filter paper, and AAS was used to measure the concentration of Mn(II) ions. The desorption study for the water sample was also carried out as discussed in Section 3.3.5 above using 4M HNO₃.

2.6. Calculation of Mn(II) Ions Concentration Removal by the Sorbent

A series of batch examinations was done, and the amount of Mn(II) sorbed was determined using the mass balance equation expressed below:

$$q_e = \frac{V}{M}(C_0 - C_e) \quad (2)$$

Where,

q_e = Metal concentration on biosorbent (mg/g) at equilibrium

C_e = Metal concentration in solution (mg/L) at equilibrium

V = Volume of initial metal solution used (mL)

M = Mass of adsorbent used (g)

More so, the percentage removal of Mn(II) ions was calculated using the following equations,

$$CR = C_0 - C_e \quad (3)$$

$$\% R = \frac{C_r}{C_e} \times 100 \quad (4)$$

Where,

R = Removal

C_0 = Initial metal ion concentration in solution (mg/L)

C_e = Metal ion concentration removed or adsorbed by adsorbent (mg/L)

2.7. Equilibrium Sorption, Adsorption Isotherms, and Kinetics of Mn(II) Removal

The sorption equilibrium offers vital physicochemical information for estimating the applicability of the physisorption processes as a unit operation typically defined by isotherm models, whose parameters express the affinity and surface properties of the sorbent at a fixed pH and temperature. The sorption data were tested against two adsorption isotherm models: the Freundlich model and the Langmuir model.

The Langmuir equation was elected for use in the estimation of maximum adsorption capacity equivalent to the biosorbent surface saturation. The linearized equation after reshuffling is given in the equation below:

$$\frac{C_e}{q_e} = \frac{1}{Q_m K_a} + \frac{C_r}{Q_m} \quad (5)$$

Where,

Q_m is the maximum sorption upon complete saturation of the biosorbent surface (mg/g).

K is a constant related to the adsorption/desorption energy (L/mg).

The experimental data was fitted into equation (4) by

plotting C_e/q_e against C_e .

The slope and intercepts were used to obtain the constants.

For the Freundlich model, it was selected for use to estimate the intensity of adsorption by the biosorbent powder. The linear form of the equation is represented below:

$$\log q_e = \log K_f + \frac{1}{n} (\log C_e) \quad (6)$$

Where,

q_e = Metal ion uptake/ adsorption density per unit weight of WHR powder (mg/g).

C_e = concentration of a metal ion in solution at equilibrium (mg/l).

The Freundlich constants are n and K_f

K_f measures the degree of adsorption, while 'n' signifies the affinity of the sorbent for the biosorbent powder.

A plot of $\log q_e$ against $\log C_e$ in equation (5) yielding a straight line is an indication of a positive confirmation of the Freundlich adsorption isotherm. The constant 'n' can be obtained from the slope and K_f from the intercept.

Furthermore, prediction of the rate of sorption is a requisite in the design of batch sorption systems. The kinetics of the solute is also an essential requisite when choosing the optimal operational environment for the batch process. This data is often collected from pseudo-first- and second-order kinetic models. These models are correlative solute uptake, a vital component when forecasting the reactor volume. These models are clarified below.

The pseudo-first-order equation is expressed as follows:

$$\frac{dq_t}{dt} = k_1(q_e - q_t) \quad (7)$$

Where,

q_e = sorption capacity (mass of metal ion adsorbed) at equilibrium (mg/g).

q_t = sorption capacity (mass of metal ion sorbed) at time t (mg/g).

k_1 = pseudo-first order sorption rate constant (L/min)

Following the application of boundary conditions and integration, $q_t = 0$ to $q_t = q_t$ at $t = 0$ to $t = t$; the modified equation (6) is:

$$\log(q_e - q_t) = \log(q_e) - \frac{k_1}{2.303} t \quad (8)$$

This equation applies only to experimental outcomes but differs from a true first-order equation in the following ways.

- $k_1 (q_e - q_t)$ does not epitomize the summation of the existing sites.

- $\log(q_e)$ is modifiable. It is most often different from the intercept of a plot of $\log(q_e - q_t)$ against 't', even though $\log(q_e)$ should be equal to the intercept of a plot of $\log(q_e - q_t)$ against 't' in a true first-order sorption reaction.

To fit the equilibrium sorption capacity (q_e) in equation (7) with the experimental data, q_e must be known. Where ' q_e ' is unknown (as in most cases), and as chemisorption tends to be unhurried, the expanse sorbed is significantly lower than the equilibrium volume. Moreover, there needs to be a method for inferring the experimental data to $t = \infty$, with the assumption that q_e can be resolved by trial and error. It is thus vital to use trial and error to attain the equilibrium sorption capacity (q_e) and to analyze the pseudo-first-order model kinetics. The slope of the plot between $\log(q_e - q_t)$ versus time, t , and a linear plot confirms this model and hence can be used to obtain the pseudo-first-order rate constant k_1 .

Moreover, if the rate of sorption follows the second-order mechanism, the pseudo-second-order chemisorption kinetic rate equation is expressed as,

$$\frac{dq_t}{dt} = k(q_e - q_t)^2 \quad (9)$$

Where; q_e = sorption capacity at equilibrium (mg/g).

q_t = sorption capacity at time t (mg/g)

k = rate constant of pseudo-second order sorption (g/mg/min)

For the boundary conditions $q_t = 0$ to $q_t = q_t$ at $t = 0$ to $t = t$; the modified equation (8) becomes:

$$\frac{1}{q_e - q_t} = \frac{1}{q_e} + kt \quad (10)$$

The linear form below is used:

$$\frac{t}{q_t} = \frac{1}{kq_e^2} + \frac{1}{q_e} t \quad (11)$$

Where t is contact time (min)

q_e is solute adsorbed at equilibrium (mg/g)

q_t is solute adsorbed at time, t (mg/g).

Equation (10) has no problem assigning an effective q_e . If pseudo-second-order kinetics is appropriate, the plot of t / q_t against t in equation (10) would display a linear relationship, from which q_e and K can be deduced from the intercept and slope even when there are no other earlier known parameters.

3. RESULTS AND DISCUSSION

3.1. Morphological Studies

Figure 1 gives the result of the morphology of the sorbent material. Typically, plant roots are critical as they facilitate plant growth, and are responsible for the absorption of water, inorganic salts, and other nutrients. However, WHRs are characterized by tap- and fibrous root systems with potential voids that are capable of adsorbing toxic pollutants (21). This is because these voids could develop into air passages, with numerous support mechanisms for Mn (II) sorption. The water hyacinth powder obtained in this study demonstrated a pore-like spherical morphology that could serve as channels for trapping Mn(II) ions in the wastewater owing to the large space between the root and water (22).

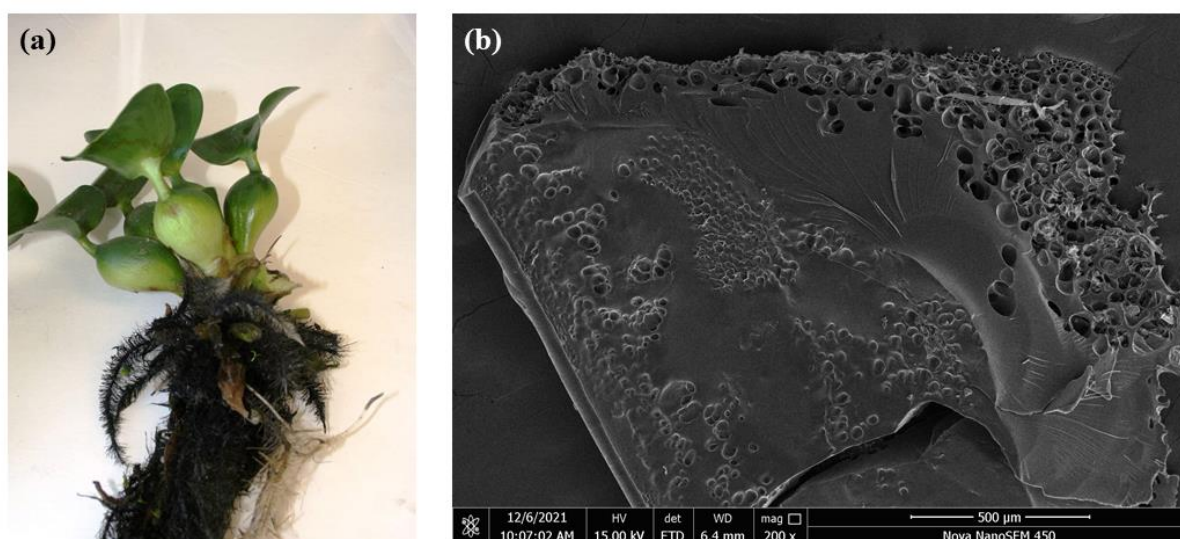


Figure 1: (a) WHR (b) SEM micrograph of dried WHR.

3.2. Effect of pH

It has been established that pH influences the solubility and concentrations of metal ions and counters, respectively on functional groups in the cell walls of the sorbent. It also impacts metal speciation in the solution, calcium carbonate solubility, and the

protonation of metal binding sites (23). Therefore, pH is a key factor to be considered when dealing with sorption. Figure 2 shows the impact pH has on the sorption of Mn(II) ions.

From observation, a rise in pH from 4 – 7, influenced

the uptake of Mn(II) by WHR, but beyond a pH of 7, the uptake efficiency is almost insignificant (24). The ion-exchange mechanism of sorption explains the effect of pH, and it uses ligands with cation exchange characteristics. At low pH, Mn (II) removal was repressed. This could be contingent upon the interaction of hydrogen and Mn (II) at the sorption spots, with an ostensible superiority of H⁺ restricting

the action of Mn(II) ion as a result of the action of the abhorrent force. With increasing pH, the oxygen-containing compounds would be exposed, thereby resulting in a total negative charge density on the sorbent and also enhancing the magnetism of positively charged metal ions, permitting sorption (25, 26).

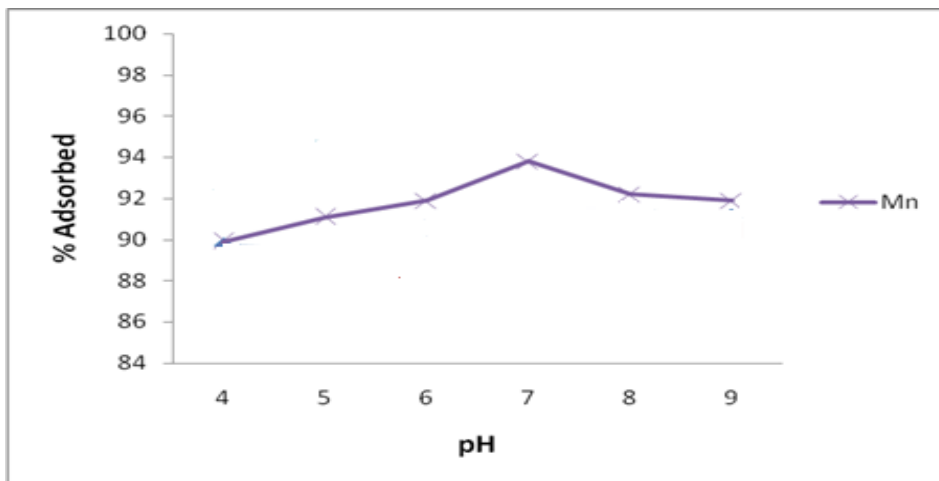


Figure 2: Effect of pH on sorption of Mn(II) by WHR.

3.3. Influence of Contact Time

Contact time influence on the biosorption capacity of Mn(II) with the biosorbent is displayed in Figure 3. By increasing the time of contact from 15 to 90 min, there was a resultant increase in Mn(II) removal from 89.5 % to 91.3 %. The result indicates a higher adsorption rate at the beginning, which resulted from the WHR's many active sites. As the experiment progresses, these sites are used up, and the uptake rate becomes a function of the Mn (II) transportation rate from the outward to the innermost sites of the WHR (27). The highest removal was reached within

the first 60 min with no significant change in sorption thereafter. Therefore, the following sorption experiments were limited to a 60 min contact time. This study uses a lower equilibrium time for the adsorbents compared to some reported in the literature. This equilibrium time is significant as it is of vital importance when considering economical water, and wastewater applications. In process applications, swift biosorption is advantageous since the shorter contact time directly results in fewer contact pieces of equipment and ultimately lower processing and operational costs (9).

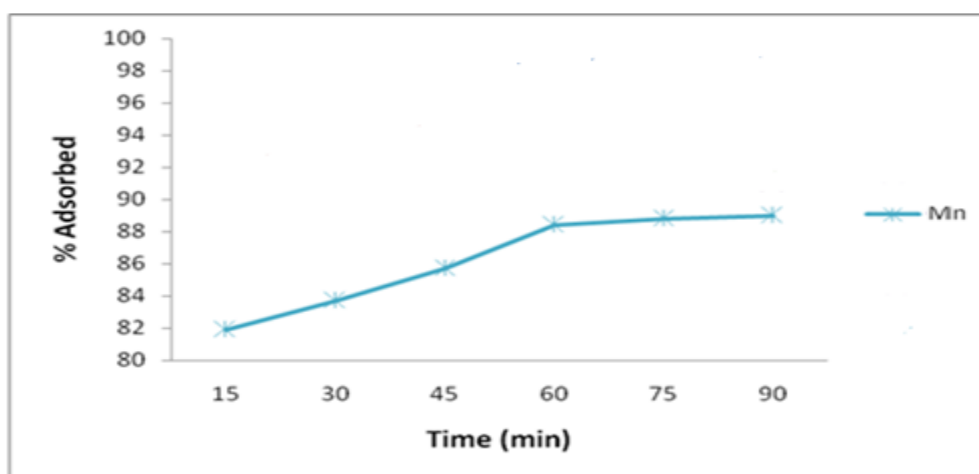


Figure 3: Contact time as a function of Mn(II) removal by WHR.

3.4. Impact of Mn(II) Ion Concentrations

The practicability and effectiveness of biosorption depend both on the absorbate concentration in the solution and the biosorbent properties. The initial absorbate concentration is a vital factor needed to conquer the resisting mass transfer between the aqueous phase and the solid (28). Figure 4 displays the effect of initial Mn (II) ion concentration on the

sorption process. As the strength of the Mn(II) ion increased, there was a decrease in Mn(II) removal from 95.9 % to 90.1 %. Certain factors are thought to play a contributing role, including ensuring that adsorption sites stay unsaturated throughout the reaction. However, an accumulation of adsorbent particles at higher concentrations could be a vital contributing factor. Such accumulation causes a

reduction of the available surface area needed for adsorption, thereby resulting in length extension of the diffusional path (29, 30). At lower concentrations, however, Mn (II) ions in solution could lead to interactions between the Mn(II) and the

binding sites, resulting in a greater sorption percentage compared to a higher metal ion concentration. A lower adsorption yield at higher concentrations is a result of active site saturation.

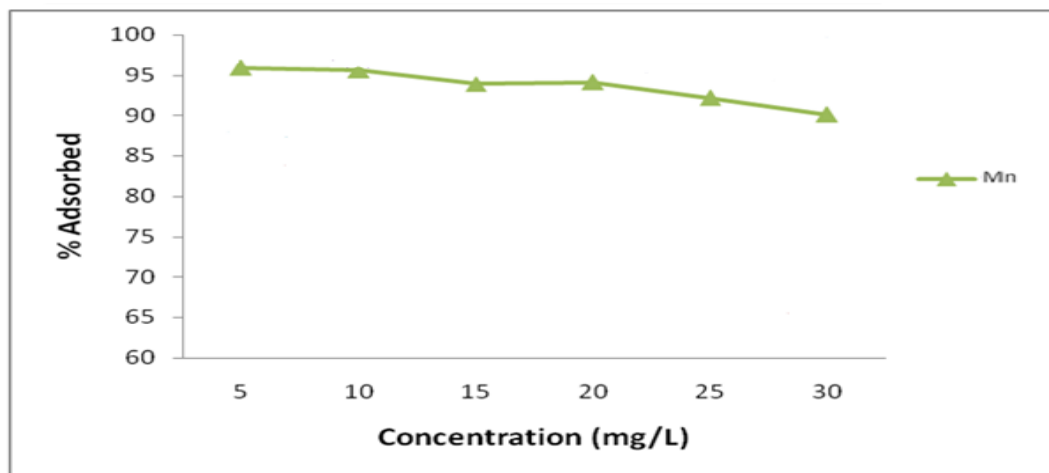


Figure 4: Initial metal ion concentration as a function of Mn(II) removal by WHR.

3.5. Effect of Dosage

The adsorbent dosage has a significant influence on the biosorption process. This was obtained by varying the adsorbent dosage. Figure 5 below clearly displays the removal efficiency. The Mn(II) removal increased with an increase in the WHR mass. The

increase in sorption is probably a consequence of the binding site number and the increasing sorbent surface area (16). The removal efficiency increased from 99.5 % to 99.9 % with an increase in dosage from 0.2 g to 1.2 g.

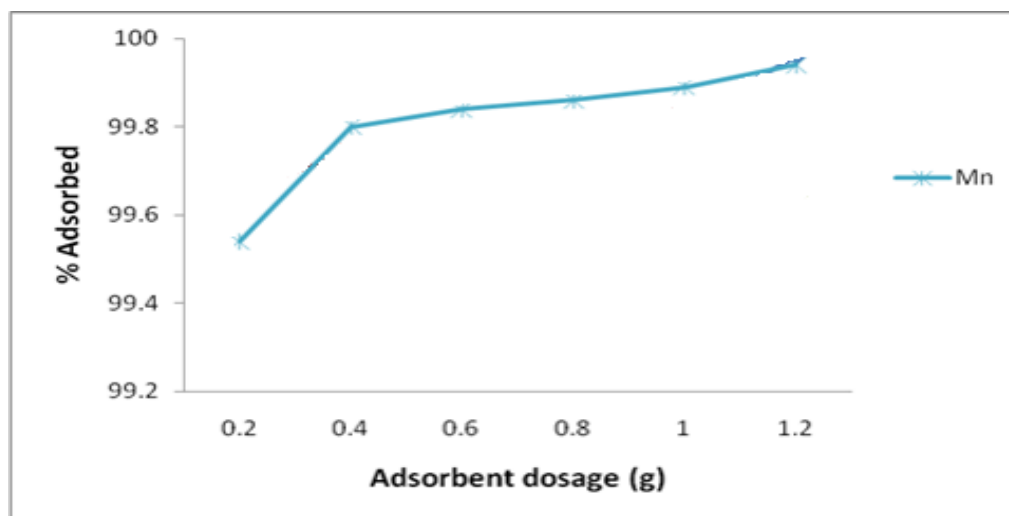


Figure 5: Effect of WHR dosage on Mn(II) removal.

3.6. Adsorption Equilibrium

A plot of C_e/q_e against C_e for Mn(II) for the adsorbent (Figure 6a) with the regression coefficient (R^2) and Langmuir isotherm parameters Q_m , K_a , and K_R , is given in Table 1. The adsorption of Mn (II) ions by WHR fits well into the Langmuir model, as evidenced by the obtained R^2 value of 0.986. The sorption process follows the Langmuir adsorption equation, suggesting that the uptake of Mn(II) ions occurs independently of the type of binding site (31). The adsorption of Mn(II) by WHR ensues principally because of the ion exchange at the surface level. It is therefore expected that the tendency of adsorption will be greatly influenced by the electronegativity of Mn(II) (1.55) (20). However, the adsorption affinity

of the metal observed arising from the sorption capacity (Q_m) values opposes the order of electronegativity. It is also known that the removal of metals of greater ionic radius is superior to that of lesser ionic radius. Besides, other factors such as the ionic radius and the initial metal ion may be responsible for the sorption of Mn(II) onto WHR. This infers that initial metal ions and several factors play a role in the sorption process.

The adsorption coefficient K_a (l/mg) about the energy of sorption is given in Table 1. The results show that the energy of sorption is significantly favorable for the adsorbents, with a K_a value of 0.65. The separation factor (K_R) is a crucial property of the

Langmuir isotherm. For this study, the values of K_R obtained revealed that the adsorption of Mn(II) ions

by WHR is favorable, as the K_R value obtained was greater than 0 but less than 1 (32).

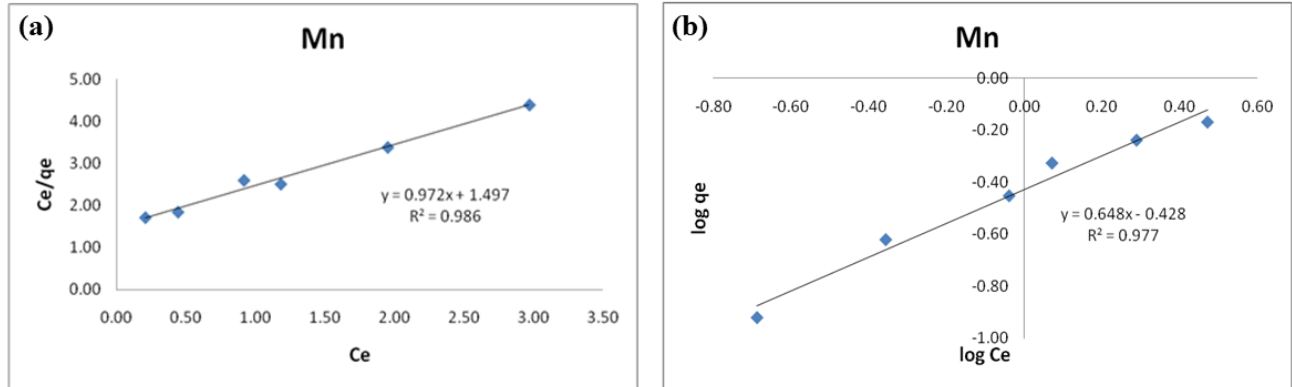


Figure 6: Langmuir (a) and Freundlich (b) isotherms for Mn(II) adsorption by WHR.

Furthermore, a plot of $\log q_e$ against $\log C_o$ is shown in Figure 6b. The linear plot of the $\log q_e$ against $\log C_o$ shows that Mn(II) ion adsorption by WHR fits well with the Freundlich model. The Freundlich isotherm parameters R^2 , n , $1/n$, and K_f of the Mn(II) ion and WHR are shown in Table 1. The R^2 (0.977) value obtained for WHR adsorption of Mn(II) ions showed

that the Freundlich model is an ideal model for Mn(II) ion adsorption by WHR. In this study, the $1/n$ value obtained was < 1 suggesting that there is significant adsorption at lower concentrations (33). The adsorption capacity K_f (0.36) obtained for the Mn(II) ion and adsorbent was appreciable.

Table 1: Freundlich isotherms and Langmuir parameters for the adsorption of Mn(II) ions by WHR.

	Langmuir isotherm parameters				Freundlich isotherm parameters			
	K_a	Q_m	K_R	R^2	$1/n$	n	K_f	R^2
Mn	0.65	1.03	0.24	0.986	0.65	1.54	0.37	0.977

3.7. Kinetics of Sorption

The plots of $\log(q_e - q_t)$ versus t and of t/q_t against t for the adsorption of Mn(II) are shown in Figure 7, while the kinetic data are presented in Table 2. The regression value (0.088) obtained for the 1st order model indicates that the 1st order model is not fitting

when describing the process of adsorption of Mn(II) by WHR. The q_e value (calculated) for the adsorbent differs greatly from that of the experimental. This is predictable, as the pseudo-1st order is not an ideal model to describe the process (34).

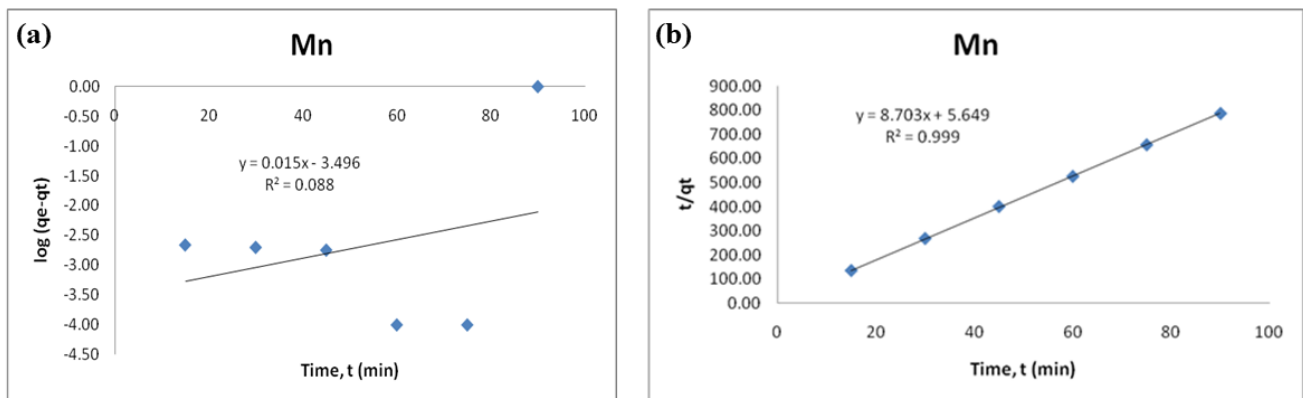


Figure 7: Sorption Kinetics of Mn (II) removal by WHR (a) Pseudo 1st order (b) Pseudo 2nd order.

Table 2: Obtained kinetic data for the biosorption process.

	Experimental q_e (mg/g)	Calculated q_e (mg/g)	k_1 (1/min)	k_2 (g/mg.min)	h (mg/g.min)	R^2
Pseudo-1 st order	0.1141	3.19×10^{-4}	-0.03	-	-	0.088
Pseudo-2 nd order	0.1141	0.11490	-	13.41	0.18	0.999

However, Figure 7b shows an exceptional fit between the data points. It shows ideal linearity in the experimental data. The R^2 value (0.999) obtained for the 2nd order model was very high, and the q_e (calculated) and q_e (experimental) were very close. These signify that the 2nd order model is fitting when describing the process of adsorption of Mn(II) by WHR and supporting the proposal that chemisorption is the rate-determining stage (35).

3.8. Desorption Studies

Land disposal and incineration are possibilities for discarding used adsorbent. These methods, however, result in pollution of the environment, whether directly or indirectly. A less used possibility would be the regeneration of Mn from the used adsorbent. With the regeneration of Mn, there would be the option of recycling Mn and WHR, hence contributing to the possible protection of the environment. Desorption studies aid in clarifying the adsorption pathway and recovering metals from adsorbent and wastewater (36). Table 3 gives the desorption efficiencies (DE) of the Mn (II) ion from the WHR.

The desorption efficiency increased from 4.58 % to 4.84 % as NaOH concentration increased from 2M to 4M. However, as NaOH concentration increased from 4M to 6M, the DE decreased to 2.05 %. Concerning HNO₃, the DE increased from 32.26 % to 33.22 % as HNO₃ concentration increased from 2 M to 6 M. Overall, effective desorption of Mn(II) was obtained with both NaOH and HNO₃ solutions. The resulting desorption phenomenon seen in both HNO₃ and NaOH is due to ion exchange interaction rather than chemisorption (37). The results indicated that HNO₃ and NaOH are satisfactorily beneficial in desorbing Mn (II) from WHR.

Table 3: Desorption of Mn(II) loaded water hyacinth roots adsorbent.

	Percentage desorption (%)
Strength of NaOH (M)	
2	4.58
4	4.84
6	2.05
Strength of HNO ₃ (M)	
2	32.26
4	33.01
6	33.22

3.9. Application Studies Using Real Industrial Wastewater

Further investigation on real industrial wastewater was conducted to examine the fittingness of the adsorbent at optimal batch conditions. The obtained result demonstrates a 64.68 % adsorption of Mn(II) by the adsorbent and a substantial percentage desorption of Mn(II) from WHR of 27.95 %. The result of the desorption study has a similar trend to that obtained for the aqueous solution of synthetic wastewater.

4. CONCLUSION

WHR has been effectively applied as an adsorbent for removing Mn(II) ions from wastewater. The results showed that with an increasing initial Mn(II) ion concentration, there was a decrease in Mn(II) ion removal while increasing sorbent dosage increased Mn (II) ion removal. Equilibrium sorption was attained at pH 7 within the first 60 min. The mechanism of sorption suited Freundlich and Langmuir isotherms, while the kinetics suited the pseudo-2nd order model. Effective desorption of Mn(II) was obtained with both NaOH and HNO₃ solutions, however, desorption was more suited for HNO₃. Appreciable results were also obtained for real industrial wastewater applications.

5. REFERENCES

1. Nnamonu L, Ogidi O, Eneji I. Assay of Heavy Metals in Water Hyacinth (*Eichhornia crassipes*) Growing in River Benue, Nigeria and Its Safety as Food. *Int Res J Pure Appl Chem* [Internet]. 2015 Jan 10;9(1):1-9. Available from: [<URL>](#).
2. Shahul Hameed K, Muthirulan P, Meenakshi Sundaram M. Adsorption of chromotrope dye onto activated carbons obtained from the seeds of various plants: Equilibrium and kinetics studies. *Arab J Chem* [Internet]. 2017 May;10:S2225-33. Available from: [<URL>](#).
3. Raveendra R, Prashanth P, Malini B, Nagabhushana B. Adsorption of Eriochrome black-T azo dye from aqueous solution on low cost activated carbon prepared from *tridax procumbens*. *Res J Chem Sci* [Internet]. 2015 [cited 2023 Dec 28];5(3):9-13. Available from: [<URL>](#).
4. Velusamy S, Roy A, Sundaram S, Kumar Mallick T. A Review on Heavy Metal Ions and Containing Dyes Removal Through Graphene Oxide-Based Adsorption Strategies for Textile Wastewater Treatment. *Chem Rec* [Internet]. 2021 Jul 4;21(7):1570-610. Available from: [<URL>](#).
5. Chang Y, Yang D, Li R, Wang T, Zhu Y. Textile Dye Biodecolorization by Manganese Peroxidase: A Review. *Molecules* [Internet]. 2021 Jul 21;26(15):4403. Available from: [<URL>](#).
6. Rajasulochana P, Preethy V. Comparison on efficiency of various techniques in treatment of waste and sewage water – A comprehensive review. *Resour Technol* [Internet]. 2016 Dec;2(4):175-84. Available from: [<URL>](#).
7. Pohl A. Removal of Heavy Metal Ions from Water and Wastewaters by Sulfur-Containing Precipitation Agents. *Water, Air, Soil Pollut* [Internet]. 2020 Oct 28;231(10):503. Available from: [<URL>](#).
8. Sylwan I, Thorin E. Removal of Heavy Metals during Primary Treatment of Municipal Wastewater and Possibilities of Enhanced Removal: A Review. *Water* [Internet]. 2021 Apr 19;13(8):1121. Available from: [<URL>](#).

9. Qasem NAA, Mohammed RH, Lawal DU. Removal of heavy metal ions from wastewater: a comprehensive and critical review. *npj Clean Water* [Internet]. 2021 Jul 8;4(1):36. Available from: [<URL>](#).
10. Rezanian S, Ponraj M, Talaiekhosani A, Mohamad SE, Md Din MF, Taib SM, et al. Perspectives of phytoremediation using water hyacinth for removal of heavy metals, organic and inorganic pollutants in wastewater. *J Environ Manage* [Internet]. 2015 Nov;163:125–33. Available from: [<URL>](#).
11. Patel S. Threats, management and envisaged utilizations of aquatic weed *Eichhornia crassipes*: an overview. *Rev Environ Sci Bio/Technology* [Internet]. 2012 Sep 8;11(3):249–59. Available from: [<URL>](#).
12. Huynh AT, Chen Y-C, Tran BNT. A Small-Scale Study on Removal of Heavy Metals from Contaminated Water Using Water Hyacinth. *Processes* [Internet]. 2021 Oct 11;9(10):1802. Available from: [<URL>](#).
13. Mary Lissy A, Madhu G. Removal of heavy metals from waste water using water hyacinth. *ACEEE Int J Transp Urban Dev* [Internet]. 2011 [cited 2023 Dec 29];1(1):48–52. Available from: [<URL>](#).
14. Jones JL, Jenkins RO, Haris PI. Extending the geographic reach of the water hyacinth plant in removal of heavy metals from a temperate Northern Hemisphere river. *Sci Rep* [Internet]. 2018 Jul 23;8(1):11071. Available from: [<URL>](#).
15. Gupta A, Balomajumder C. Removal of Cr(VI) and phenol using water hyacinth from single and binary solution in the artificial photosynthesis chamber. *J Water Process Eng* [Internet]. 2015 Sep;7:74–82. Available from: [<URL>](#).
16. Zheng J-C, Liu H-Q, Feng H-M, Li W-W, Lam MH-W, Lam PK-S, et al. Competitive sorption of heavy metals by water hyacinth roots. *Environ Pollut* [Internet]. 2016 Dec;219:837–45. Available from: [<URL>](#).
17. Mahamadi C. Water hyacinth as a biosorbent: A review. *African J Environ Sci Technol* [Internet]. 2012 Dec 29;5(13):1137–45. Available from: [<URL>](#).
18. Murithi G, Onindo CO, Wambu EW, Muthakia GK. Removal of Cadmium(II) Ions from Water by Adsorption using Water Hyacinth (*Eichhornia crassipes*) Biomass. *BioResources* [Internet]. 2014 May 1;9(2):3613-31. Available from: [<URL>](#).
19. Ipeaiyeda AR, Tesi GO. Sorption and Desorption Studies on Toxic Metals From Brewery Effluent Using Eggshell as Adsorbent. *Adv Nat Sci* [Internet]. 2014;7(2):15. Available from: [<URL>](#).
20. Najem AM. Evaluation the Biosorption Capacity of Water Hyacinth (*Eichhornia crassipes*) Root for Some Heavy Metals. *Najem Iraqi J Sci*. 2015;56(4A):2846–52. Available from: [<URL>](#).
21. Zhou J, Jiang Z, Qin X, Zhang L, Huang Q, Xu G. Effects and Mechanisms of Calcium Ion Addition on Lead Removal from Water by *Eichhornia crassipes*. *Int J Environ Res Public Health* [Internet]. 2020 Feb 2;17(3):928. Available from: [<URL>](#).
22. Feng W, Xiao K, Zhou W, Zhu D, Zhou Y, Yuan Y, et al. Analysis of utilization technologies for *Eichhornia crassipes* biomass harvested after restoration of wastewater. *Bioresour Technol* [Internet]. 2017 Jan;223:287–95. Available from: [<URL>](#).
23. Mwandira W, Nakashima K, Kawasaki S, Arabelo A, Banda K, Nyambe I, et al. Biosorption of Pb (II) and Zn (II) from aqueous solution by *Oceanobacillus profundus* isolated from an abandoned mine. *Sci Rep* [Internet]. 2020 Dec 3;10(1):21189. Available from: [<URL>](#).
24. Tangahu BV, Sheikh Abdullah SR, Basri H, Idris M, Anuar N, Mukhlisin M. A Review on Heavy Metals (As, Pb, and Hg) Uptake by Plants through Phytoremediation. *Int J Chem Eng* [Internet]. 2011;2011: 939161. Available from: [<URL>](#).
25. Abbas MN, Abbas FS. Utilization of Iraqi Rice Husk in the Removal of Heavy Metals from Wastewater. *Res J Environ Earth Sci* [Internet]. 2013 Jul 20;5(7):370–80. Available from: [<URL>](#).
26. Caporale AG, Violante A. Chemical Processes Affecting the Mobility of Heavy Metals and Metalloids in Soil Environments. *Curr Pollut Reports* [Internet]. 2016 Mar 23;2(1):15–27. Available from: [<URL>](#).
27. Senthil Kumar P, Kirthika K. Kinetics and equilibrium studies of Zn²⁺ ions removal from aqueous solutions by use of natural waste. *Electron J Environ Agric Food Chem* [Internet]. 2010;9(1):264–74. Available from: [<URL>](#).
28. Kanamarlapudi SLRK, Chintalpudi VK, Muddada S. Application of Biosorption for Removal of Heavy Metals from Wastewater. In: *Biosorption* [Internet]. InTech; 2018. Available from: [<URL>](#).
29. Sheta M, Yousry B, Zattot A, Taha NA. Optimization of Chitosan Surface Response Methodology (Natural and Commercial) Used for Chromium Ion Removal from Wastewater across Different Parameters. *Sustainability* [Internet]. 2021 Dec 6;13(23):13494. Available from: [<URL>](#).
30. Rápó E, Tonk S. Factors Affecting Synthetic Dye Adsorption; Desorption Studies: A Review of Results from the Last Five Years (2017–2021). *Molecules* [Internet]. 2021 Sep 6;26(17):5419. Available from: [<URL>](#).
31. Lee AYW, Lim SF, Chua SND, Sanaullah K, Bains R, Abdullah MO. Adsorption Equilibrium for Heavy Metal Divalent Ions (Cu²⁺, Zn²⁺, and Cd²⁺) into Zirconium-Based Ferromagnetic Sorbent. *Adv Mater Sci Eng* [Internet]. 2017;2017: 1210673. Available from: [<URL>](#).
32. Meroufel B, Benali O, Benyahia M, Benmoussa Y, Zenasni MA. Adsorptive removal of anionic dye from aqueous solutions by Algerian kaolin:

- Characteristics, isotherm, kinetic and thermodynamic studies. *J Mater Environ Sci*. 2013;4(3):482–91. Available from: [<URL>](#).
33. Rajurkar NS, Gokarn AN, Dimya K. Adsorption of Chromium(III), Nickel(II), and Copper(II) from Aqueous Solution by Activated Alumina. *CLEAN – Soil, Air, Water* [Internet]. 2011 Aug 3;39(8):767–73. Available from: [<URL>](#).
34. Revellame ED, Fortela DL, Sharp W, Hernandez R, Zappi ME. Adsorption kinetic modeling using pseudo-first order and pseudo-second order rate laws: A review. *Clean Eng Technol* [Internet]. 2020 Dec;1:100032. Available from: [<URL>](#).
35. Kumar PS, Vincent C, Kirthika K, Kumar KS. Kinetics and equilibrium studies of Pb²⁺ in removal from aqueous solutions by use of nano-silversol-coated activated carbon. *Brazilian J Chem Eng* [Internet]. 2010 Jun;27(2):339–46. Available from: [<URL>](#).
36. Indhumathi P, Sathiyaraj S, Koelmel JP, Shoba SU, Jayabalakrishnan C, Saravanabhavan M. The Efficient Removal of Heavy Metal Ions from Industry Effluents Using Waste Biomass as Low-Cost Adsorbent: Thermodynamic and Kinetic Models. *Zeitschrift für Phys Chemie* [Internet]. 2018 May 24;232(4):527–43. Available from: [<URL>](#).
37. Al-Ghouti MA, Al-Absi RS. Mechanistic understanding of the adsorption and thermodynamic aspects of cationic methylene blue dye onto cellulosic olive stones biomass from wastewater. *Sci Rep* [Internet]. 2020 Sep 28;10(1):15928. Available from: [<URL>](#).



Synthesis of Some New 1,3,4-Thiadiazole Derivatives Derived from Cholic Acid and Evaluation of their Biological Activity

Intisar Q. Mahmood Al-araj^{1*} , Rana A. Saeed² , Linda R. Abdul-Raheem¹ ,
Amena A. Ahmed¹ 

¹ Chemistry Dept, College of Education for Pure Science, University of Mosul, Mosul, Iraq.

² Pharmacy Dept, Mosul Technical Institute, Mosul, Iraq.

Abstract: In this work, several oxadiazole, thiadiazole, and triazole derivatives, as well as new Schiff bases, were prepared. Cholic acid was used as a starting material to prepare the five-membered heterocyclic compounds. The synthesized compounds were identified by FTIR and ¹H,¹³C-NMR spectroscopy, which elucidated and confirmed the structure of the target molecules. Estimation of the biological activity of the newly produced compounds has been conducted against two types of Gram-positive and Gram-negative pathogenic bacteria.

Keywords: Cholic acid, heterocyclic, Schiff bases, thiadiazoles, oxadiazoles, pathogenic bacteria

Submitted : October 8, 2023. **Accepted :** December 6, 2023.

Cite this: Al-araj IQM, Saeed RA, Abdul-Raheem LR, Ahmed AA. Synthesis of some new 1,3,4-thiadiazole derivatives derived from cholic acid and evaluation of their biological activity, JOTCSA. 2024;11(2):441-8.

DOI: <https://doi.org/10.18596/jotcsa.1371936>

*Corresponding author E-mail: mahmood_intisar@uomosul.edu.iq

1. INTRODUCTION

Cholic acid is an essential biliary acid and has a chemical name 4-(3,7,12-trihydroxy-10,13-dimethylhexa-decahydro-1H-cyclopenta[a] phenanthren-17-yl) pentanoic acid (1). It is a kind of endogenous steroid that naturally occurs in many animals, including humans (2). It is being studied increasingly as a structural element in supramolecular chemistry. It has been discovered that the liver is where this acid is typically generated (3). Additionally, they function as surfactants to make vitamins and lipids soluble, so they may be absorbed in the colon (4). This occurs by combining with taurine or glycine to create water-soluble salt, and then micelles are formed around molecules that are attracted to lipophilicity (5). Cholic acid with chenodeoxycholic acid, known as an important primary bile acid, is synthesized by cholesterol, and it is also produced in the liver. The concentration of these two acids is equal in humans, and they are converted to amino biliary acids (6). Figure (1) gives An illustration of intestinal bacteria further transforming deoxycholic acid and lithocholic acid, respectively, into biliary acid (7,8).

1,3,4-Oxadiazoles are interesting compounds (10-12). The unique structure of these compounds has attracted researchers' interest in finding new therapeutic molecules (13). It has been found that these compounds have a great range of biological applications, which include antiviral (14), anticonvulsant (15), anti-inflammatory (16), anti-tubercular (17), antimicrobial, anti-allergic, antineoplastic, analgesic, antiproliferative, monoamine oxidase and tyrosine kinase inhibitory effects (18). Thiadiazols are also heterocyclic moieties consisting of one sulfur atom with two nitrogen atoms (19). Thiadiazols and their analogs are interesting chemical compounds due to their bioactivity effect, such as anti-tubercular and antimicrobial activity (20,21). Recently, it was found that 1,3,4-thiadiazole sulfonamide derivatives work as a modulator of anticancer treatment when joined with some cytotoxic substances. It can also be a lead molecule in treating new diseases, for instance, COVID-19 and black fungus infection (22).

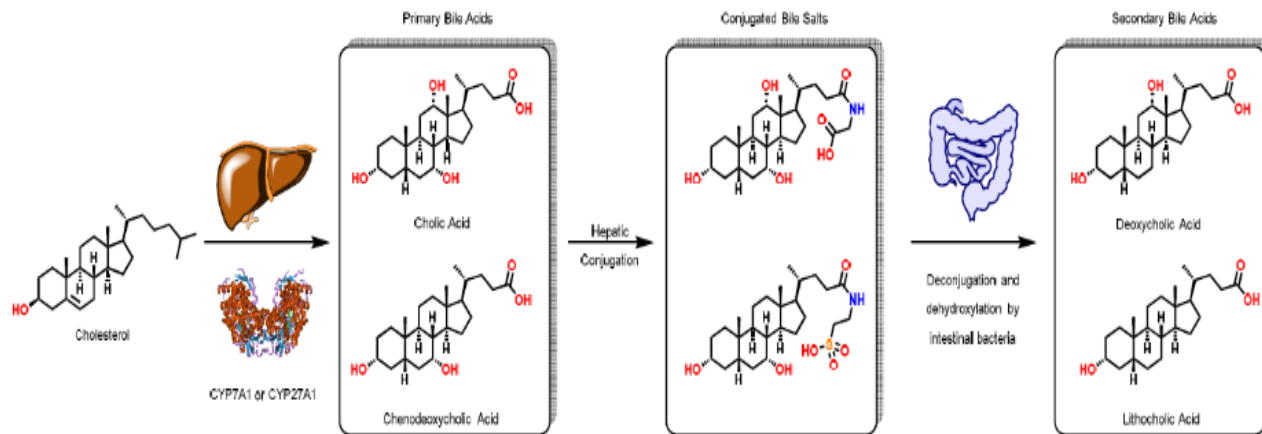


Figure 1: The Production of Biliary Acids from Cholesterol (9)

Nowadays, compounds based on 1,3,4-thiadiazoles have been shown to have activity against various cancers by focusing on unchecked DNA replication and cell division, and malignancies in vitro and in vivo can be reduced (23). Furthermore, heteroatoms in thiadiazoles can form interactions with biological targets, including key kinases involved in tumorigenesis (24). Triazoles are good examples of heterocyclic compounds due to the exhibition of high aromatic stability compared to other organic compounds (25,26). Triazoles can form hydrogen bonds suitable for many biologically active molecules (27). Medicinal chemists emphasize the anticancer activity of such compounds (28) due to their crucial roles in the design of anticancer drugs (29). Biological studies have shown that the five-membered triazole heterocycles have a broad and potent biological activity (30), notably in antiviral activities such as those against the human immunodeficiency virus (HIV)(31), the hepatitis C virus (HCV), the hepatitis B virus (HBV)(32), the influenza virus (IV), the herpes simplex virus (HSV), the hepatitis A virus (HAV), the varicella-zoster virus (VZV), and the human cytomegalovirus (HCMV) (33). Currently, other molecules, such as Schiff bases derived from heterocycles, are the subject of many investigations because of their diverse range of biological functions (34). They are very important in various biological systems and have found applications in different industries (35). Schiff bases derived from various sources exhibit the ability to fight against several biological problems, including cancer, inflammation, and allergies. These can be treated using antibacterial, antifungal, antitumor, and antiviral substances containing Schiff bases. (36,37). In addition, the field of research dealing with Schiff-base chemistry has expanded greatly nowadays(38).

2. EXPERIMENTAL SECTION

2.1 General

Sigma Aldrich provided the cholic acid, while BDH and Fluka companies supplied the other reagents. All chemicals were used without further purification. Melting points (MP) were determined on the Electro Thermal IA1900. IR spectrometer with a 4000–400 cm^{-1} range was utilized using KBr disks on a Shimadzu FT-IR-8400. ^1H and ^{13}C NMR spectra were recorded using a Varian Agilent USA 400 MHz spectrometer at Laboret Center, University of Tehran. Thin layer chromatography (TLC) was performed on TLC aluminum sheets to verify the purity of the compounds.

2.1.1 Synthesis of compound (1)

A mixture of cholic acid (0.01 mol) and conc. sulfuric acid (10 mL) was stirred in an ice bath. Then, the solution was heated in a steam bath 10 hrs until one distinct spot on TLC. This hot mixture was poured onto crushed ice, and ammonium hydroxide was concentrated to precipitate the free base. It recrystallized from ethanol to give a brown solid, m.p.: 116–118 $^{\circ}\text{C}$ and 78% yield. ν_{max} : 3560, 3380, 2929, 2852, 1665, 1107, 1050 cm^{-1} .

2.1.2 Synthesis of compound (2)

0.01 mol of compound (1), ethyl alcohol (50 mL), and 4-aminoacetophenone (0.01 mol) were refluxed together for 5 hrs and then cooled down to room temperature when TLC showed the end of the reaction. The resulting precipitate was filtered and then dried. Ethyl alcohol was used to recrystallize the product to produce a bright yellow solid m.p.: 107–109 $^{\circ}\text{C}$ and 70% yield. ν_{max} : 3541, 3376, 3050–3117, 1686–1661 cm^{-1} .

2.1.3 Synthesis of compound (3)

0.01 mol of compound (2) was dissolved in absolute EtOH (50 mL), bromoethyl acetate (0.01 mol) and sodium bicarbonate (3 g) were added. The mixture of reaction was refluxed for 8 hrs, and the mixture was monitored via TLC. Crushed ice was added to the residue after the solvent was evaporated, and the solution was extracted with dry ether (2x30 mL). The

mixture was then filtered, concentrated, and given a dark brown solid with m.p: 112 °C and 71% of yield. ν_{\max} : 3310, 2927, 2855, 1741, 1411, 1372 cm^{-1} .

2.1.4 Synthesis of compound (4)

A mixture of 10 mL of hydrazine hydrate (85%) and 0.01 mol of compound (3) in 50 mL abs. ethyl alcohol was refluxed for 3.5 hrs. TLC was used to follow the reaction, and then evaporation was done to obtain acid hydrazide (4); it produced a white solid after recrystallization from ethanol m.p: 200–201 °C and 92% yield. ν_{\max} : 3360, 2957, 2862, 1669, 1531, 1581, 1462 cm^{-1} .

2.1.5 Synthesis of compound (5)

0.01 mol of acid hydrazide (4) and ammonium thiocyanate (0.01 mol) were combined and dissolved in absolute ethanol (50 mL). Hydrochloric acid (8 mL) was added to the reaction mixture and then recondensed for 2 hrs. Product formation was monitored using TLC. After the primary compounds disappeared from TLC, the crude product was combined with silica gel after the solvent had been evaporated under decreased pressure, and it was then purified using column chromatography, eluting with petroleum ether/EtOAc (1:1) gave pale brown solid, m.p: 145–147°C and 77% of yield ν_{\max} : 3314, 3012, 1667, 1583, 1549, 1420, 1210 cm^{-1} .

2.1.6. Synthesis of compound (6)

Refluxing of substituted thiosemicarbazide (5) (0.01 mol) with $\text{NH}_2\text{NH}_2 \cdot \text{H}_2\text{O}$ 85% (12 mL, 0.2 mol) for 2 hrs gave a solid that was isolated, dried, and recrystallized from ethyl alcohol to give yellow solid, m.p: 143–145 °C and 52% of yield. ν_{\max} : 3419, 3320, 3054, 2923, 1620 cm^{-1} .

2.1.7. Synthesis of compound (7)

A solution containing ten drops of glacial acetic acid and 0.01 mol of chlorobenzaldehyde in 15 mL of ethanol was added to a mixture containing 0.01 mol of compound (6) in ethanol (30 mL) and refluxed for 3 hrs when TLC revealed no starting material, the resultant solution is concentrated to half, the residue was then added to crushed ice. The product is filtered and washed with water to give a white solid, m.p.: 165–167 °C and 79% yield; recrystallization from methanol gave the desired compound. ν_{\max} : 3035, 1706, 1430–1544, 688 cm^{-1} .

2.1.8. Synthesis of compound (8)

A mixture of 0.01 mol thiosemicarbazide (5) and 0.01 mol HgO in 25 mL of methanol was refluxed for 6 hrs, the reaction was observed using TLC, and the mixture was filtered while still hot. The solvent was evaporated and purified via column chromatography using petroleum ether/EtOAc (5:2) as eluent gave a deep yellow solid, m.p: 210–211 °C and 64% of yield. ν_{\max} : 3424, 3162, 3055, 2926, 2850, 1612, 1164, 1033 cm^{-1} .

2.1.9. Synthesis of compound (9)

The mixture of five drops of glacial acetic acid and 0.01 mol chlorobenzaldehyde was combined with compound (8) (0.01 mol) in 30 mL of ethanol. The same procedure of compound (7) was followed to prepare compound (9), column chromatography with $\text{CH}_2\text{CH}_2/\text{MeOH}$ (5:1) as eluent was used for purification to give a white solid, m.p: 222–224 °C and 69% of yield. ν_{\max} : 3032, 1663, 1544, 1433, 687 cm^{-1} .

2.1.10. Synthesis of compound (10)

A substituted thiosemicarbazide (5) (0.01 mol) was added to a round-bottomed flask along with 10 mL of concentrated H_2SO_4 and refluxed in a water bath at 90 °C for (2 hrs), then the mixture was neutralized using a solution of concentrated NH_4OH with cooling. The resulting precipitation was filtered, washed, dried, and recrystallized from benzene to offer a white solid, m.p.: 214–215 °C and 71% of yield, ν_{\max} : (3421–3370), 1623, 3053, and 1034 cm^{-1} .

2.1.11. Synthesis of compound (11)

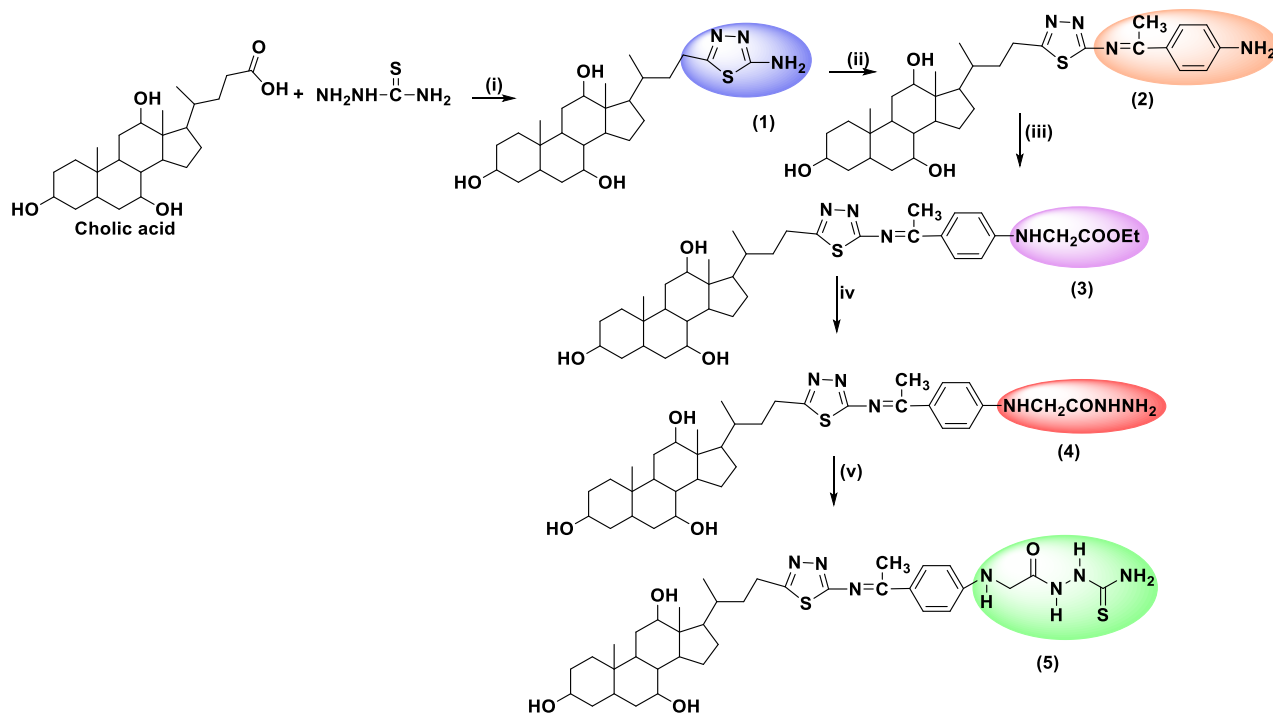
Compound (10) (0.01 mol) was dissolved in ethyl alcohol (30 mL) and then added to a solution comprising five drops of glacial acetic acid with chlorobenzaldehyde (0.01 mol). The synthesis conditions of compound (7) were employed to obtain the title compound (10), which gave a pale green solid, m.p: 230–231°C, and 74% yield. ν_{\max} 3025, 2922, 2850, 1670, 1544, 1433, 687 cm^{-1}

3. RESULT AND DISCUSSION

The preparation of new substituted oxadiazoles, thiadiazols, triazoles, and Schiff bases starting from cholic acid, hydrazide, and substituted thiosemicarbazide, as well as their antibacterial evaluation, have been carried out according to a known protocol. Firstly, treating cholic acid with thiosemicarbazide gave 2-choly-5-amino-1,3,4-thiadiazol (1). The structure was confirmed by IR, which gave absorption at 3380, 1665, 1107, 1050 cm^{-1} related to N-H, C=N, and C-S-C, respectively. Compound (1) was then treated with 4-aminoacetophenone and conc. HCl in ethyl alcohol to produce hydrazone (2), F.T-IR spectrum for compound (2) showed absorption for the C=N group at 1686–1661 cm^{-1} and for the aromatic C-H at 3050–3117 cm^{-1} . The $^1\text{H-NMR}$ spectrum showed two doublets at 7.41 and 6.68 ppm, which belong to aromatic protons of para-substitution, a singlet at 5.49 for the NH_2 group and a singlet at 2.42 for (3H) corresponding to methyl (CH_3) group of hydrazone. The ester compound (3) was then synthesized through the reaction between hydrazone (2) with ethyl 2-bromoacetate. The structure of the product was elucidated and confirmed by IR spectrum, which gave an absorption band at 1741 cm^{-1} for the carbonyl group; also $^1\text{H-NMR}$ recognized the structure by demonstrating a quartet at 4.15 ppm for methylene group (CH_2) and a triplet at 1.36 ppm for methyl group (CH_3). $^{13}\text{C-NMR}$ gave two

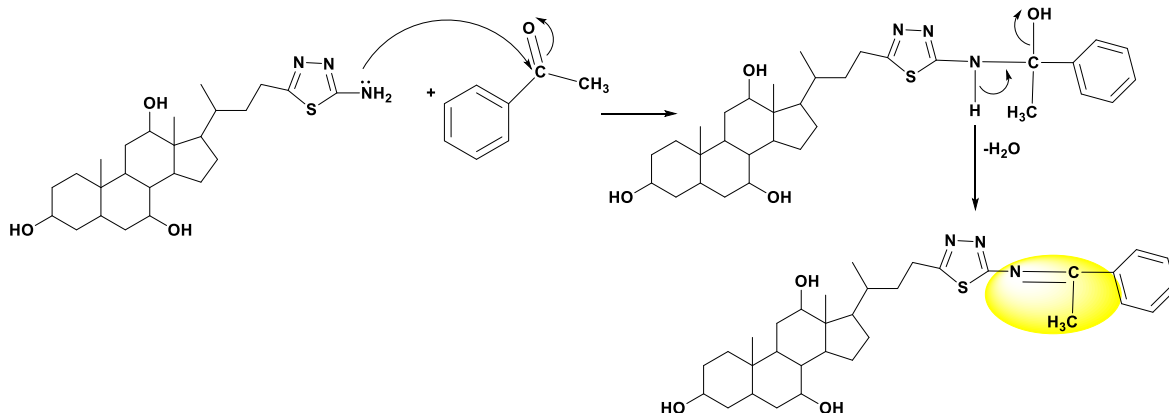
distinguished peaks belong to carbonyl at 170.2 ppm and 60.6 ppm for the carbon of methylene group. The conversion of ester (**3**) to acid hydrazide (**4**) was completed via the reaction with $N_2H_4 \cdot H_2O \setminus EtOH$. The structure of (**4**) presented bands in IR spectroscopy at 3360 and 1669 cm^{-1} for (N-H) and (C=O) groups, respectively. 1H NMR gave two peaks at 7.10 and 2.63 ppm for NH and NH_2 . The substituted thiosemicarbazide

(**5**) was prepared via the reaction of acid hydrazide and ammonium thiocyanate, which clearly showed IR absorbance at 3314 (N-H), 1667 (C=O) and 1210 (C=S) cm^{-1} . The 1H -NMR exhibited a signal at 6.18 ppm for NH_2 next to the (C=S) group, and ^{13}C -NMR appeared peaks at 181.3 and 169.6 ppm for (C=S) and (C=O), respectively. All spectral data confirmed the structure formation of the compound (**5**).



Reagents and conditions: (i) Cholic acid, conc. H_2SO_4 , steam bath (ii) EtOH, 4-aminoacetophenone, refl. (iii) abs. EtOH, bromo ethyl acetate, $NaHCO_3$, refl (iv) $N_2H_4 \cdot H_2O$ 85% abs. EtOH, refl (v) ammonium thiocyanate abs. EtOH, HCl, refl.

The following steps showed the suggested mechanism for the Schiff base formation reaction (39).



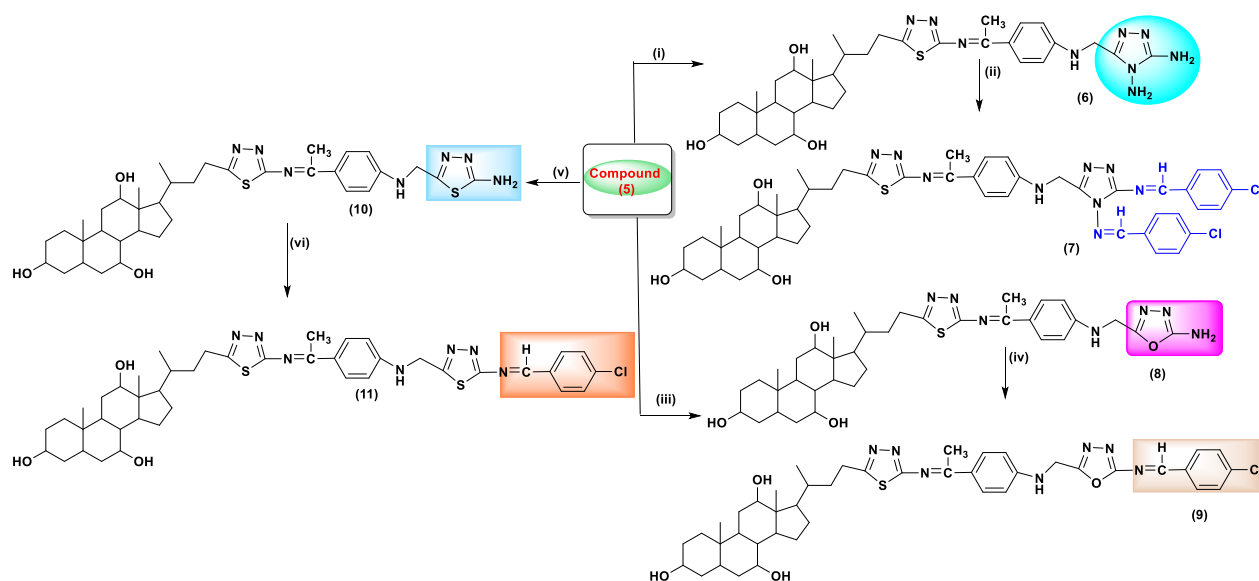
The substituted thiosemicarbazide (**5**) was then divided into three portions, which were converted to substituted 1,2,4-triazole (**6**), 1,3,4-oxadiazole (**8**), and 1,3,4-thiadiazole (**10**) via the reaction with hydrazine hydrate, mercuric oxide, and concentrated

sulfuric acid, respectively. The IR spectral data of substituted 1,2,4-triazole (**6**) presented absorption at $3419, 3320\text{ cm}^{-1}$ due to (NH) and 1620 cm^{-1} belonging to the (C=N) group. The 1H NMR gave signals for two NH_2 groups at 5.42 and 4.56 ppm, respectively. The

cyclization of (**5**) was successfully accomplished to offer the corresponding compounds [substituted 1,3,4-oxadiazole (**8**) and substituted 1,3,4-thiadiazole (**10**)]. Infrared spectrum gave absorbance in cm^{-1} at 3382, 3289 (NH_2), 1620 ($\text{C}=\text{N}$), 1110 ($\text{C}-\text{O}-\text{C}$) for compound (**8**) while compound (**10**) offered 3385, 3278 (NH_2), 1635 ($\text{C}=\text{N}$), 1096 ($\text{C}-\text{S}-\text{C}$). Finally, a series of Schiff bases (**7**, **9**, and **11**) were synthesized successfully via the reaction of substituted 1,2,4-triazole (**6**), 1,3,4-oxadiazole (**8**), and 1,3,4-thiadiazole (**10**) with 4-chlorobenzaldehyde and concentrated hydrochloric acid in ethanol. Again, the structure of the prepared Schiff bases was characterized by IR, compound (**7**) showed bands at 3035 cm^{-1} related to aromatic C-H, 1706 cm^{-1} for $\text{C}=\text{N}$ and 688 cm^{-1} due to C-Cl, the $^1\text{H-NMR}$ confirmed the structure of the desired product by presenting two singlets at 8.83 (1H) and 8.66 (1H) ppm related to protons in two azo-methane $\text{CH}=\text{N}$ groups, in addition, $^{13}\text{C-NMR}$ gave peaks at 167.7 and 160.7 ppm for carbon atoms in two $\text{CH}=\text{N}$ groups, peaks at 138.6,

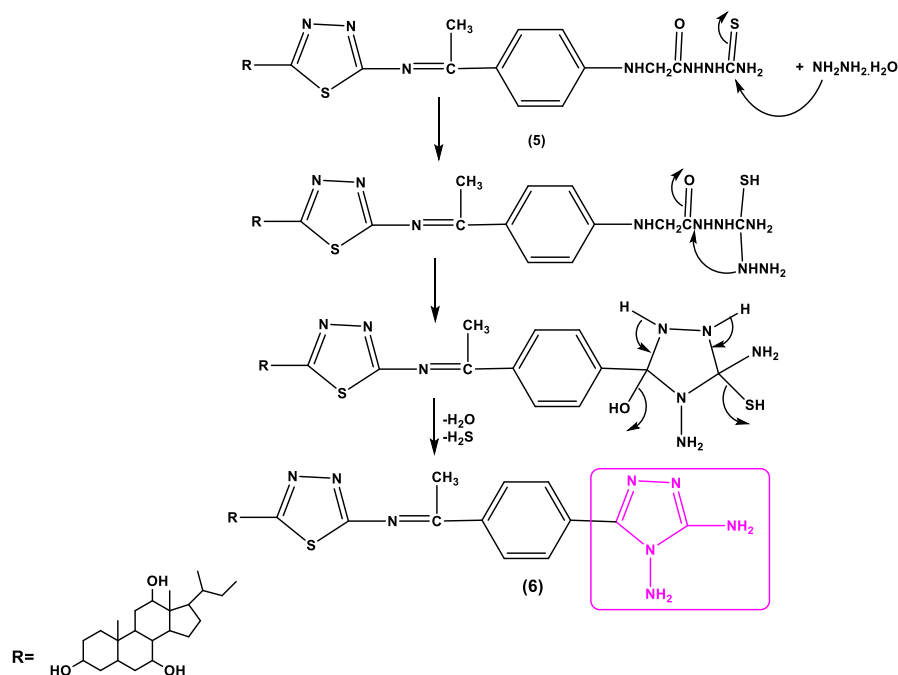
138.5 ppm were also obtained for C-Cl. The IR spectrum proved the structure of compounds **8** and **10** by the disappearance of the stretching bands belonging to the carbonyl and thione groups. However, it was demonstrated absorption in cm^{-1} at (3424-3162), (3421-3370), 1612, 1623, 3055, 3053, (1164-1033), and 1034 corresponding to the following groups NH , $\text{C}=\text{N}$, aromatic C-H, C-O-C, and C-S-C respectively. For compounds (**8** and **10**), the structures were also verified by NMR data. Also, characteristic peaks that are required to approve the chemical structure of compounds (**9** and **11**) were shown by $^1\text{H-NMR}$ spectrum, which exhibited multiple in the range of 7.02-8.28 ppm related to aromatic protons, singlet of $\text{CH}=\text{N}$ proton at (8.34 ppm/ comp. 9), (876 ppm/ comp 11) respectively.

The proposed mechanism below shows the steps for the cyclization of substituted thiosemicarbazides (**5**) to substituted 1,2,4-triazole (**6**).



Scheme 2: Preparation of compounds (6-11).

Reagents and conditions: (i) $\text{N}_2\text{H}_4 \cdot \text{H}_2\text{O}$ 85% refl., (ii) EtOH, glacial acetic acid, chlorobenzaldehyde, refl.; (iii) HgO , MeOH, refl (iv) EtOH, glacial acetic acid, chlorobenzaldehyde, refl; (v) conc. H_2SO_4 , 90°C (vi) EtOH, glacial acetic acid, chlorobenzaldehyde, refl.



4. THE BIOLOGICAL STUDY

In the current work, the two bacteria *S. aureus* and *P. aeruginosa* have been used in sensitivity tests by the disc diffusion method for the synthesized compounds (**2**, **5**, **7**, **8**, and **11**), with the results shown in Table 1. These different compounds have shown antibacterial activities against the bacteria mentioned above and can inhibit the growth of these two types. The species

S. aureus was inhibited at a concentration of 200 mg/mL for compound **11** (23 mm) and (21 mm) for compound **8**, while compounds **2**, **5**, and **7** have inhibition zones (15, 20, and 19 mm), respectively. The species *P. aeruginosa* was inhibited at a 200 mg/mL concentration for compounds **5**, **8**, and **11** (21, 20, and 18 mm), respectively. Compounds **7** and **2** at 200 mg/mL have (16 and 14 mm), respectively.

Table 1: Biological activity of some prepared compounds.

Compound No.	Concentration mg/mL	Bacteria	
		<i>S. aureus</i>	<i>P. aeruginosa</i>
2	200	15	14
	100	12	11
	50	7	8
	25	7	5
	12.5	0	0
5	200	20	21
	100	17	14
	50	15	13
	25	13	8
	12.5	8	0

7	200	19	16
	100	16	12
	50	9	9
	25	0	5
	12.5	9	0
8	200	21	20
	100	17	17
	50	9	17
	25	0	8
	12.5	0	0
11	200	23	18
	100	19	14
	50	15	11
	25	12	8
	12.5	6	0
Amikacin (amk)	20 mg/dick	21	20

5. CONCLUSION

The target compounds, including 1,3,4-oxadiazoles, 1,3,4-thiadiazoles, 1,2,4-triazoles, and Schiff bases, were successfully synthesized utilizing cholic acid as the initial substance. The chemical structures developed have been elucidated and confirmed using

FTIR and ^1H , ^{13}C -NMR spectroscopy. A preliminary assessment of bio-activity has indicated that several chemicals (refer to Table 1) exhibit noteworthy action against specific pathogenic organisms. In addition, the synthesized chemicals could be examined for a range of further bio-applications.

6. CONFLICT OF INTEREST

In relation to this study, the authors declare that they have no competing interests.

7. ACKNOWLEDGMENTS

For all the assistance and resources provided during the project, we would like to convey our profound gratitude and appreciation to Mosul University and the chemistry department of College of Education for pure Science.

8. REFERENCES

- Sievänen E. Exploitation of Bile Acid Transport Systems in Prodrug Design. *Molecules* [Internet]. 2007 Aug 16;12(8):1859–89. Available from: [<URL>](#)
- Lee S, Lee MS, Chang E, Lee Y, Lee J, Kim J, et al. Mulberry Fruit Extract Promotes Serum HDL-Cholesterol Levels and Suppresses Hepatic microRNA-33 Expression in Rats Fed High Cholesterol/Cholic Acid Diet. *Nutrients*. 2020 May 21;12(5):1499. [<URL>](#)
- Sahoo S, Ghosh P, Banerjee S, De P. Recent Advances in Biomedical Applications of Cholic Acid-Based Macromolecules. *ACS Appl Polym Mater*. 2021 Apr 9;3(4):1687–706. [<URL>](#)
- Anwar S, Shamsi A, Kar RK, Queen A, Islam A, Ahmad F, et al. Structural and biochemical investigation of MARK4 inhibitory potential of cholic acid: Towards therapeutic implications in neurodegenerative diseases. *Int J Biol Macromol*. 2020 Oct;161:596–604. [<URL>](#)
- Yadav K, Kumar S, Mishra D, Asad M, Mitra M, Yavvari PS, et al. Deciphering the Role of Intramolecular Networking in Cholic Acid–Peptide Conjugates on the Lipopolysaccharide Surface in Combating Gram-Negative Bacterial Infections. *J Med Chem*. 2019 Feb 28;62(4):1875–86. [<URL>](#)
- Pheiffer F, Schneider Y, Hansen E, Andersen J, Isaksson J, Busche T, et al. Bioassay-Guided Fractionation Leads to the Detection of Cholic Acid Generated by the Rare *Thalassomonas* sp. *Mar Drugs*. 2022 Dec 20;21(1):2. [<URL>](#)
- Kumar S, Thakur J, Yadav K, Mitra M, Pal S, Ray A, et al. Cholic Acid-Derived Amphiphile which Combats Gram-Positive Bacteria-Mediated Infections via Disintegration of Lipid Clusters. *ACS Biomater Sci Eng*. 2019 Sep 9;5(9):4764–75. [<URL>](#)
- Uchida N, Yanagi M, Hamada H. Anionic Technol PG-Based Nanoparticles Prepared Using Cholic Acid-Derived Surfactants. *Nat Prod Commun*. 2022 May 13;17(5) [<URL>](#)
- Knudtson CA, Dias JR. Recent methods for diversification of bile acids and related steroids towards supramolecular. *Steroids*. 2019 Nov;151:108442. [<URL>](#)
- Shetnev A, Baykov S, Kalinin S, Belova A, Sharoyko V, Rozhkov A, et al. 1,2,4-Oxadiazole/2-Imidazoline Hybrids: Multi-target-directed Compounds for the Treatment of Infectious Diseases and Cancer. *Int J Mol Sci*. 2019 Apr 5;20(7):1699. [<URL>](#)
- Li Z, Zhan P, Liu X. 1,3,4-Oxadiazole: A Privileged Structure in Antiviral Agents. *Mini-Reviews in Medicinal Chemistry*. 2011;11(13). [<URL>](#)
- Ahmed AA, Mahmood IQ, Aziz HS. Synthesis and Characterization of Few New Substituted 1,3,4-Oxadiazoles 1,2,4-Triazoles and Schiff Bases via Chalcone Compounds. *INTERNATIONAL JOURNAL OF DRUG DELIVERY TECHNOLOGY*. 2022 Jun 30;12(03):1087–92. [<URL>](#)
- Luczynski M, Kudelko A. Synthesis and Biological Activity of 1,3,4-Oxadiazoles Used in Medicine and Agriculture. *Applied Sciences*. 2022 Apr 8;12(8):3756. [<URL>](#)
- Nazar S, Siddiqui N, Alam O. Recent progress of 1,3,4-oxadiazoles as anticonvulsants: Future horizons. *Arch Pharm (Weinheim)*. 2020 Jul 21;353(7):1900342. [<URL>](#)
- Rezki N, Al-Yahyawi A, Bardaweel S, Al-Blewi F, Aouad M. Synthesis of Novel 2,5-Disubstituted-1,3,4-thiadiazoles Clubbed 1,2,4-Triazole, 1,3,4-Thiadiazole, 1,3,4-Oxadiazole and/or Schiff Base as Potential Antimicrobial and Antiproliferative Agents. *Molecules*. 2015 Sep 2;20(9):16048–67. [<URL>](#)
- Torosyan, S. A., et al. "Synthesis of New 1, 3, 4-Oxadiazole and 1, 2, 3-Triazole Derivatives of Thieno [3, 2-b] pyrrolicarboxylic Acid." *Russian Journal of Organic Chemistry* 59.2 (2023): 328-331. [<URL>](#)
- K. Ajay Kumar* PJGVK. International Journal of ChemTech Research CODEN(USA): IJCRGG ISSN: 0974-4290 Vol.4, No.4, pp 1782-1791, Oct-Dec 2012 Comprehensive Review On The Chemistry Of 1,3,4-Oxadiazoles And Their Applications. *Int J Chemtech Res*. [<URL>](#)
- Ebenezer O, Shapi M, Tuszynski JA. A Review of the Recent Developments of Molecular Hybrids Targeting Tubulin Polymerization. *Int J Mol Sci*. 2022 Apr 4;23(7):4001. [<URL>](#)
- Sonar JP, Pardeshi SD, Dokhe SA, Kharat KR, Zine AM, Kotai L, et al. SYNTHESIS AND ANTIPROLIFERATIVE SCREENING OF NEW THIAZOLE COMPOUNDS. *European Chemical Bulletin*. 2020 Apr 20;9(4-6):132. [<URL>](#)
- Dhotre B et al. An Efficient and One Spot Synthesis of Silica Supported Synthesis of Fluorinated 1, 3, 4-Thiadiazole Derivative Under Microwave Irradiation. *Chem. J*. 2020;2. [<URL>](#)
- Ibraheem H, Al-Majedy Y, Al-Amiery A. 4-Thiadiazole: The Biological Activities. *Systematic Reviews in Pharmacy*. 2018 Jul 31;9(1):36–40. [<URL>](#)
- Alminderej, Elganzory, El-Bayaa, Awad, El-Sayed. Synthesis and Cytotoxic Activity of New 1,3,4-Thiadiazole Thioglycosides and 1,2,3-Triazolyl-1,3,4-Thiadiazole N-glycosides. *Molecules*. 2019 Oct 16;24(20):3738. [<URL>](#)
- Çevik UA, Osmaniye D, Levent S, Sağlık BN, Çavuşoğlu BK, Özkay Y, et al. Synthesis and characterization of a new series of thiadiazole derivatives as potential anticancer agents. *Heterocycl Comm*. 2020 Mar 10;26(1):6–13. [<URL>](#)
- Hussain SJS and MA. Synthesis and antimicrobial activities of 1, 2, 4-triazole and 1, 3, 4-thiadiazole derivatives

Al-araj IQM et al. JOTCSA. 2024;11(2):441-448.

of 5-amino-2-hydroxybenzoic acid. E-Journal of Chemistry .
[<URL>](#)

25. Abu-Hashem AA, Al-Hussain SA. Design, Synthesis of New 1,2,4-Triazole/1,3,4-Thiadiazole with Spiroindoline, Imidazo[4,5-b]quinoxaline and Thieno[2,3-d]pyrimidine from Isatin Derivatives as Anticancer Agents. Molecules. 2022 Jan 27;27(3):835. [<URL>](#)

26. Cai BG, Bao YP, Pei C, Li Q, Li L, Koenigs RM, et al. Photochemical synthesis of 1,2,4-triazoles *via* addition reaction of triplet intermediates to diazoalkanes and azomethine ylide intermediates. Chem Sci. 2022;13(44):13141-6. [<URL>](#)

27. Zazharskiy V et al. Synthesis, structure, physicochemical properties and antibacterial activity of 1,2,4-triazoles-3-thiols and furan derivatives. Voprosy Khimii i Khimicheskoi Tekhnologii. 2019 Nov;(6):74-82. [<URL>](#)

28. Aggarwal R, Sumran G. An insight on medicinal attributes of 1,2,4-triazoles. Eur J Med Chem. 2020 Nov;205:112652. [<URL>](#)

29. Asif M. Antiviral and antiparasitic activities of various substituted triazole derivatives: A mini. Chem Int. [<URL>](#)

30. Gupta O, Pradhan T, Chawla G. An updated review on diverse range of biological activities of 1,2,4-triazole derivatives: Insight into structure activity relationship. J Mol Struct. 2023 Feb;1274:134487. [<URL>](#)

31. El-Sebaey SA. Recent Advances in 1,2,4-Triazole Scaffolds as Antiviral Agents. ChemistrySelect. 2020 Oct 8;5(37):11654-80. [<URL>](#)

RESEARCH ARTICLE

32. Tawfik SS, Liu M, Farahat AA. Antiviral activity of thiadiazoles, oxadiazoles, triazoles and thiazoles. Arkivoc. 2020 Aug 18;2020(1):180-218. : [<URL>](#)

33. Iacopetta D, Ceramella J, Catalano A, Saturnino C, Bonomo MG, Franchini C, et al. Schiff Bases: Interesting Scaffolds with Promising Antitumoral Properties. Applied Sciences. 2021 Feb 20;11(4):1877. [<URL>](#)

34. Mukhtar S, Hassan A, Morsy N, Hafez T, Hassaneen H, Saleh F. Overview on Synthesis, Reactions, Applications, and Biological Activities of Schiff Bases. Egypt J Chem. 2021 Jun 19;0(0):0-0. [<URL>](#)

35. Troschke EMO and IKI. Schiff-bases for sustainable battery and supercapacitor electrodes. Exploration. [<URL>](#)

36. Panda J et al. Retracted: Green Chemistry Approach for Efficient Synthesis of Schiff Bases of Isatin Derivatives and Evaluation of Their Antibacterial Activities. Journal of Nanoparticles. 2015 Dec 17;2015:1-1. [<URL>](#)

37. Ibrahim MN, and SES. Synthesis, characterization and use of Schiff bases as fluorimetric analytical reagents. E-journal of Chemistry. [<URL>](#)

38. Surendar P et al. Organic Quasi-Liquid Schiff Bases from Biomolecules: Synthesis, Structure and Quantum Mechanical Studies. Biointerface Res Appl Chem. 2022 Mar 24;13(2):107. [<URL>](#)

39. Sani U, Na'ibi HU, Dailami SA. In vitro antimicrobial and antioxidant studies on N-(2-hydroxybenzylidene) pyridine-2-amine and its M (II) complexes. Nigerian Journal of Basic and Applied Sciences. 2017;25(1):81-8. [<URL>](#)



The Parasitic Plant *Cistanche violacea* (Desf.) Beck from Ghardaïa (Algeria): A Source of Biologically Active Compounds

Nadjette Djemouai ^{ID}^{1,2*}, Somia Saad ^{ID}^{3,4}, Faiza Baali ^{ID}², Hassina Meguellati ^{ID}³,
Hanane BenZetta ^{ID}⁵, Abdelhamid Foughalia ^{ID}⁴

¹Université de Ghardaia, Faculté des Sciences de la Nature et de la Vie et Sciences de la Terre, Département de Biologie, Ghardaïa, 47000, Algeria

²Ecole Normale Supérieure de Kouba, Laboratoire de Biologie des Systèmes Microbiens (LBSM), Algiers, 16308, Algeria

³Université des Sciences et de la Technologie Houari Boumediene, Faculté des Sciences Biologiques, Laboratoire de Recherche sur les Zones Arides (LRZA), Algiers, 16111, Algeria

⁴Centre de Recherche Scientifique et Technique sur les Régions Arides (CRSTRA), Biskra, 07000, Algeria

⁵Centre de Recherche en Agropastoralisme CRAPast, Université Ziane Achour, Djelfa, 17000, Algeria

Abstract: The present study aims to determine the contents of total polyphenol (TPC) and total flavonoid (TFC) and evaluate the antioxidant and antimicrobial activities of *Cistanche violacea* (Desf.) Beck. The extraction of bioactive compounds from the whole plant of *C. violacea* (Desf.) Beck was carried out by three different methods, including maceration, Soxhlet, and ultrasound, with ethanol and water as solvents. The results showed that the ultrasound ethanolic extract recorded the greatest amounts of TPC with $188.95 \pm 2.2 \mu\text{g}$ gallic acid equivalent/mg dry extract, while for TFC, it was the maceration ethanolic extract with $40.26 \pm 6.02 \mu\text{g}$ quercetin equivalent/mg dry extract. The High-Performance Liquid Chromatography (HPLC) results showed the presence of phenolic compounds, with 32 identified compounds in the ethanolic and aqueous extracts. The different extracts showed antioxidant capacities for DPPH, ABTS, phenanthroline, and reducing power assays. The highest antioxidant ability was observed with the ethanolic extract obtained by the maceration method ($\text{IC}_{50} 33.35 \pm 1.4$ and $\text{IC}_{50} < 12.5 \mu\text{g/mL}$ for DPPH and ABTS tests). The antimicrobial investigation on seven microbial strains revealed that the ethanolic extract ultrasound showed moderate antibacterial activity ($18.66 \pm 1.1\text{mm}$) against only *Staphylococcus aureus* ATCC25923, while the other extracts showed weak or no antimicrobial activity. This work suggests that *C. violacea* (Desf.) Beck has antioxidant properties of natural origin, which justify its traditional use in treating many conditions related to oxidative stress.

Keywords: *Cistanche violacea*, extracts, phenolic compounds, HPLC, antioxidant potential, antimicrobial activity.

Submitted: May 04, 2023. **Accepted:** December 06, 2023.

Cite this: Djemouai N et al. The Parasitic Plant *Cistanche violacea* (Desf.) Beck from Ghardaïa (Algeria): A Source of Biologically Active Compounds. JOTCSA. 2024; 11(2): 449-68.

DOI: <https://doi.org/10.18596/jotcsa.1291696>.

*Corresponding author. Email: djemouai.nadjette@univ-ghardaia.dz

1. INTRODUCTION

The *Orobanchaceae* family comprises more than 2000 species in about 100 genera and contains the most significant number of parasitic angiosperm plants (1, 2). This family comprises facultative or obligate parasite plants distributed in all climatic zones and continents except Antarctica (2, 3).

The genus *Cistanche* Hoffmanns. & Link (1813) includes around 25 species of obligate parasite

plants, meaning they cannot complete their life cycles without host plants¹ (4). As a result, they have lost their photosynthetic abilities and are thus called holoparasites (5). They are found in different environments, including halophytic habitats and semi-arid and arid zones across Eurasia and North Africa (4). Long underground stolons, fleshy stems and colored inflorescences characterize the *Cistanche* species. Generally, species belonging to the *Cistanche* genus grow on the roots of plants of the following families: *Plumbaginaceae*, *Zygophyllaceae*, *Chenopodiaceae*, and *Tamaricaceae* (6).

In the Algerian flora, three species of *Cistanche* are reported, namely *C. tubulosa* in Tassili N'Ajjer (Central Sahara of Algeria), *C. tinctoria* (Desf.) Beck a species with a Saharo-Mediterranean distribution and *C. violacea* (Desf.) Beck² (1893), the holoparasitic endemic species of North Africa (7). In Algerian popular medicine, the locally known plant Danoun (*C. tinctoria* (Desf.) Beck) is traditionally used to treat diabetes, diarrhea, and abdominal pains. In addition, this plant is used as an aphrodisiac, analeptic and, for muscle contractions, bruises and as a lactation stimulant (8). On the other hand, *C. phelypaea* (L.) synonym of *C. tinctoria* (Desf.) Beck is used in North African traditional medicine for diarrhea, diabetes, intestinal troubles, infection, and as a diuretic. In addition, several species of *Cistanche* are used in traditional Chinese medicine as food additives and tonics. Moreover, they are used to treat conditions like renal deficiency, impotence, infertility, profuse metrorrhagia and chronic constipation (9).

Information about the traditional use of *C. violacea* is lacking in Algeria, but a few studies have been conducted on its phytochemical and biological properties. Indeed, Bougandoura et al. (10) revealed the chemical constituents and the anti-inflammatory activity of the ethanolic extract of the aerial parts of *C. violacea* collected from southwest Algeria. Furthermore, Alia et al. (11) studied the extent to which host plant variation affected the natural product extracts of *C. violacea* (Desf.) Beck growing in the Oued Souf region (southeast Algeria). In Tunisia, Debouba et al. (12) have shown that the flowers and bulbs of *C. violacea* collected from the seashore of Hassi Jerbi village, located in the southeast of Tunisia, had important amounts of total phenolic compounds. In addition, Ben Attia et al. (13) highlighted the antioxidant and cytotoxic activities of *C. violacea* collected from Tataouine (southeast Tunisia). Finally, the recent study of Bouzayani et al. (14) for samples collected from Sfax (southeast of Tunisia) showed important phenolic content and antioxidant activities for polar extracts, while evaluating the antimicrobial activity indicated that the methanol extracts had the highest activities. However, the methanol and ethanol extracts of *C. violacea* collected from the Qassim region of Saudi Arabia exhibited no or weak antimicrobial activity, except for *Staphylococcus epidermidis*, which had good activity (15).

As part of our project to study the Algerian desert flora and search for plants with therapeutic value, we were interested in studying *C. violacea* (Desf.) Beck growing in a spontaneous state in Ghardaïa Province. This work aims to evaluate the chemical composition of different extracts (ethanolic and aqueous) obtained by three extraction methods: maceration, Soxhlet, and ultrasound of the whole plant of *C. violacea* (Desf.) Beck. We explored the phenolic and flavonoid contents, antioxidant properties and antimicrobial activities of the obtained extracts. In addition, we evaluated the relationship and correlation between the phytochemical contents of the different extracts and the tested antioxidant activity.

2. EXPERIMENTAL SECTION

2.1. Plant Material

Whole plants of *C. violacea* (Desf.) Beck were collected from Noumerate (32°23'30.7"N 3°46'03.3"E) at the campus of the University of Ghardaïa. This region is characterized by a semi-arid climate and is located in the Septentrional Sahara (16). First, the freshly collected plants are washed with running tap water and put to dry in the laboratory. Then, the samples were grounded using a mechanical grinder (Sayona Electric, France) and finally stored pending subsequent analysis.

2.2. Extraction Methods

Bioactive compounds were extracted from the analyzed plants by three extraction methods. The conventional methods used were maceration and Soxhlet and the unconventional method was ultrasound-assisted extraction.

For the maceration method, 10 g of the plant powder was macerated in 100 mL of ethanol (70%) or water under magnetic stirring for 24 h. The extracts were filtered, and the ethanol was evaporated using the rotavaporator R-210 (Buchi, Switzerland), while water was eliminated by the lyophilizer (Telstar IyoQuest, Spain). For the Soxhlet extraction, 10 g of the plant powder was placed in a Soxhlet cartridge. The extraction was performed using a Soxhlet apparatus with a 500 mL flask containing 100 mL of ethanol (70%) or water and the extraction cycle lasted 4 h, and the temperature was fixed at 60 °C or 100 °C, respectively. Then, the resulting ethanolic solutions were evaporated using the rotavaporator R-210 and a lyophilizer was used for removal of water. The ultrasound-assisted extraction was carried out in a Sonorex Digetec DT 514 (Bandelin, Germany) using a 250 W power and 35 kHz frequency. Ten grams of plant powder was put separately in a beaker and put through a 1 h extraction with 100 mL of ethanol or water. Then, the obtained extracts were evaporated using the rotavaporator R-210 and a lyophilizer. Finally, the yield (%) of each extract was determined after weighing and then stored in a refrigerator at 4 °C pending further analysis.

¹ <http://www.gbif.org>

² <http://www.gbif.org>

2.3. Total Phenols Content (TPC)

The determination of Total Phenols Content (TPC) was performed according to the Folin-Ciocalteu method described by Singleton et al. (17). First, 20 μL of each extract was added to 100 μL of Folin-Ciocalteu reagent (diluted 10-fold with distilled water). Next, the mixtures were shaken and then added to 75 μL of sodium carbonate (7.5% Na_2CO_3) and allowed to incubate in the dark at room temperature for 2 h. The absorbance was measured at 765 nm using a 96-well microplate reader (Thermo Scientific™ Multiskan Sky, France). Finally, the results are expressed in μg gallic acid equivalent/mg dry extract (μg GAE/mg DE) with reference to the calibration curve of different concentrations of gallic acid.

2.4. Total Flavonoids Content (TFC)

The Total Flavonoids Content (TFC) of the plant extracts was evaluated by the method described by Zhishen et al. (18). First, 50 μL of each extract was added to 50 μL of 2% aluminum chloride hexahydrate. Next, the mixtures were stirred and then 150 μL of 5% (w/v) sodium acetate was added and incubated in the dark at room temperature for 2.5 h. After incubation, absorbance was determined at 440 nm using a 96-well microplate reader. The results were expressed in μg quercetin equivalent/mg dry extract (μg QE/mg DE) by referring to the calibration curve of different concentrations of quercetin.

2.5. High-Performance Liquid Chromatography (HPLC) Analysis

In order to characterize the phenolic composition of the various extracts of *C. violacea* (Desf.) Beck, a high-performance liquid chromatography system (Agilent 1100) was used, as described in Meguellati et al. (19). For this, a Hypersil BDS C18 analytical column (4.6 X 250 mm and 5 μm particle size, a UV Diode Array Detector (DAD) ranging from 200 to 400 nm and equipped with a quaternary rapid separation pump were used. The injected sample volumes were 5 μL and the flow rate of the mobile phase was 1.5 mL/min. Acetic acid (0.2% in water) as solvent A and acetonitrile as solvent B in a linear gradient for 30 min were used as the mobile phase. The analysis started with 95% of solvent A and finished with 100% of solvent B. Comparing the obtained retention times of the compounds with the standards that were injected under the same conditions revealed the identity of the compounds in the extracts.

2.6. Antioxidant Assays

The evaluation of the antioxidant activity was carried out on the different extracts using four different methods.

2.6.1. DPPH radicals scavenging assay

The free radical scavenging activity was carried out using the 2,2-diphenyl-1-picrylhydrazyl (DPPH) assay described by Blois et al. (20). Forty microliters of each extract were diluted to 12.5, 25, 50, 100, 200, 400, and 800 $\mu\text{g}/\text{mL}$ concentrations. Then, they were blended with 160 μL of a methanolic DPPH solution (0.1 mM). After 30 min of incubation in the dark, the absorbance was measured at 517 nm using a microplate reader. Butylated hydroxytoluene (BHT)

and ascorbic acid were used as positive controls and the results were expressed as % Inhibition and IC_{50} values in $\mu\text{g}/\text{mL}$.

$$\% \text{ Inhibition} = [(A_c - A_s / A_c)] \times 100.$$

Where A_c and A_s were the absorbance of the negative control and the absorbance of the sample at 30 min, respectively. IC_{50} ($\mu\text{g}/\text{mL}$) corresponds to half the maximal inhibitory concentration.

2.6.2. ABTS^{•+} scavenging activity

ABTS radical-scavenging activities were carried out based on the method of Re et al. (21). $\text{ABTS}^{\bullet+}$ was prepared by combining 5 mL of a 7 mM ABTS solution with 5 mL of a 2.45 mM potassium persulfate solution. The resulting mixture was then stored in a dark environment in a refrigerator at 4 °C for 16 h. Subsequently, the mixture was modified using distilled water till achieving an absorbance of 0.700 ± 0.020 at a wavelength of 734 nm. Sample solutions at different concentrations were prepared with distilled water (12.5, 25, 50, 100, 200, 400, and 800 $\mu\text{g}/\text{mL}$). Then 40 μL of sample solutions were mixed with 160 μL of $\text{ABTS}^{\bullet+}$ solution. After 10 min of incubation, the absorbance was recorded at 734 nm using a 96-well microplate reader. Results were expressed as inhibition percentage (%) and as IC_{50} values ($\mu\text{g}/\text{mL}$). BHT and ascorbic acid were used as the positive controls and the inhibition of ABTS free radical was determined as below;

$$\% \text{ Inhibition} = [(A_0 - A_1 / A_0)] \times 100.$$

Where A_0 is the absorbance of the negative control, A_1 is the absorbance of the sample at 10 min. IC_{50} ($\mu\text{g}/\text{mL}$) corresponds to half of the maximal inhibitory concentration.

2.6.3. Reducing antioxidant Power (RP) assay

The reducing antioxidant power (RP) assay was carried out according to the Oyaizu (22) method. Ten microliters of the different concentrations of the extracts (3.125, 6.25, 12.5, 25, 50, 100, and 200 $\mu\text{g}/\text{mL}$) were added to 40 μL of 0.2 M phosphate buffer (pH 6.6) and 50 μL of 1% potassium ferricyanide. The plate was incubated at 50 °C for 20 min. Then, 50 μL of tricarboxylic acid (TCA, 10%), 40 μL of distilled water and 10 μL of ferric chloride (FeCl_3 0.1%) were added to each mixture. The absorbance was measured in the microplate reader at 700 nm. BHT and ascorbic acid were used as positive controls. Results were expressed as absorbance against a reagent blank and $A_{0.5}$ values ($\mu\text{g}/\text{mL}$) corresponding to the concentration indicating 0.50 absorbance intensity.

2.6.4. Phenanthroline activity

Phenanthroline activity (Phen) was determined according to the method of Szydłowska-Czerniak et al. (23). Ten microliters (10 μL) of the extracts, 50 μL of FeCl_3 (0.2% in water) and 30 μL of phenanthroline (0.5% in methanol) were placed in a 10 mL volumetric flask and then 110 μL of methanol were added. The obtained solution was homogenized and put in the dark at room temperature. The

absorbance of the resulting solution was measured at 510 nm after 20 min against a reagent blank that consisted of 1 mL of FeCl₃ (0.2%) and 0.5 mL of Phen (0.5%). BHT and ascorbic acid were used as positive controls. Results were expressed as absorbance against a reagent blank and A_{0.5} values (µg/mL) corresponding to the concentration indicating 0.50 absorbance intensity.

2.7. Antimicrobial Activity

2.7.1. Preparation of microbial suspensions

In order to evaluate the antibacterial activity of the extracts, six bacterial strains were used in this study. The Gram-negative strains were *Escherichia coli* (ATCC 25922), *Salmonella typhimurium* (ATCC 14028) and *Pseudomonas aeruginosa* (ATCC 27853) and the Gram-positive bacteria were *Listeria monocytogenes* (ATCC 35152), *Bacillus cereus* (ATCC 14579) and *Staphylococcus aureus* (ATCC 25923). One yeast, namely *Candida albicans* (ATCC 10231), was used to test the antifungal activity. Bacterial and fungal suspensions were prepared using a sterile saline solution.

2.7.2. Disk diffusion assay

The antimicrobial activity of *C. violacea* extracts was investigated using the disk diffusion method (24). The Mueller–Hinton and Sabouraud chloramphenicol agar plates were surface inoculated using the bacterial and fungal suspensions containing 10⁶ and 10⁸ CFU/mL, respectively. Then, 6 mm sterile discs (Whatman filter papers) were soaked with the extracts (dissolved in 2.5% DMSO and sterilized through 0.22 µm filters) and placed on the surface of the inoculated agar plates. DMSO was used as a negative control, while gentamicin and fluconazole were used as positive controls for antibacterial and antifungal activities, respectively. The plates were then incubated at 37 °C for 24 h for bacteria and 28

°C for 48 h for fungi and the diameters of the inhibition zones were measured using a Vernier caliper. The experiment was performed in triplicate.

2.8. Statistical Analysis

Results are expressed as mean values ($n = 3$) with standard deviation (SD). Data were analyzed by Statistica software. An analysis of variance (ANOVA) followed by testing the significance of differences using a Tukey LSD test ($p \leq 0.05$) was applied. Correlations between the variables were determined with a Hierarchical Cluster Analysis (HCA) and a Principal Component Analysis (PCA). Pearson correlation analysis was performed based on the results of the TPC, TFC, DPPH, ABTS, RP and Phen tests.

3. RESULTS

3.1. Phytochemical Composition

The present study shows the contents of total phenolics and flavonoids in the ethanolic and aqueous extracts of *C. violacea* (Desf.) Beck (Table 1). The content of total phenolics was the highest for the ultrasound extraction method, with a value of 188.95 ± 0.4 µg GAE/mg DE, followed by the maceration extraction (183.51 ± 2.2 µg GAE/mg DE) and the Soxhlet extraction (159.17 ± 3.3 µg GAE/mg DE) for ethanolic extracts. In contrast, the lowest results were obtained with the aqueous extraction for TPC. In the same manner, the highest results of the total flavonoids contents were obtained for ethanolic extracts, with contents of 40.26 ± 6.02 µg QE/mg DE for maceration, 27.73 ± 0.8 µg QE/mg DE for ultrasound and 19.76 ± 3.7 µg QE/mg DE for Soxhlet. In addition, we did not obtain a significant difference in the total flavonoids contents for the three types of extraction methods for the aqueous extract of *C. violacea* (Desf.) Beck.

Table 1: Quantitative analyses of total phenolics (µg GAE/mg DE) and total flavonoids (µg QE/mg DE) contents of the ethanolic and aqueous extracts from *Cistanche violacea* (Desf.) Beck.

Extract	Extraction method	TPC (µg GAE/mg DE)	TFC (µg QE/mg DE)
Ethanolic extract	Maceration	183.51 ± 2.2 ^b	40.26 ± 6.02 ^c
	Soxhlet	159.17 ± 3.3 ^d	19.76 ± 3.7 ^{ab}
	Ultrasound	188.95 ± 0.4 ^b	27.73 ± 0.8 ^b
Aqueous extract	Maceration	79.48 ± 2.4 ^a	17.05 ± 0.1 ^a
	Soxhlet	107.22 ± 5.7 ^c	17.45 ± 0.2 ^a
	Ultrasound	71.48 ± 5.3 ^a	18.35 ± 0.3 ^a

Values are the mean of three replicates ($n = 3$) ± SD. Results with different superscript letters are significantly different ($p \leq 0.05$).

In the HPLC analysis, the retention times of the samples and standards were identified. The composition of the obtained extracts was recorded in Table 2 and the chromatograms (280, 300 and 355 nm) were presented in Figure 1. The different HPLC profiles showed many peaks corresponding to different phenolic compounds. A total of 32 compounds were identified in the six extracts, with 29 compounds each in maceration, Soxhlet and ultrasound for the ethanolic extracts, while we recorded 22 compounds in maceration and Soxhlet and 20

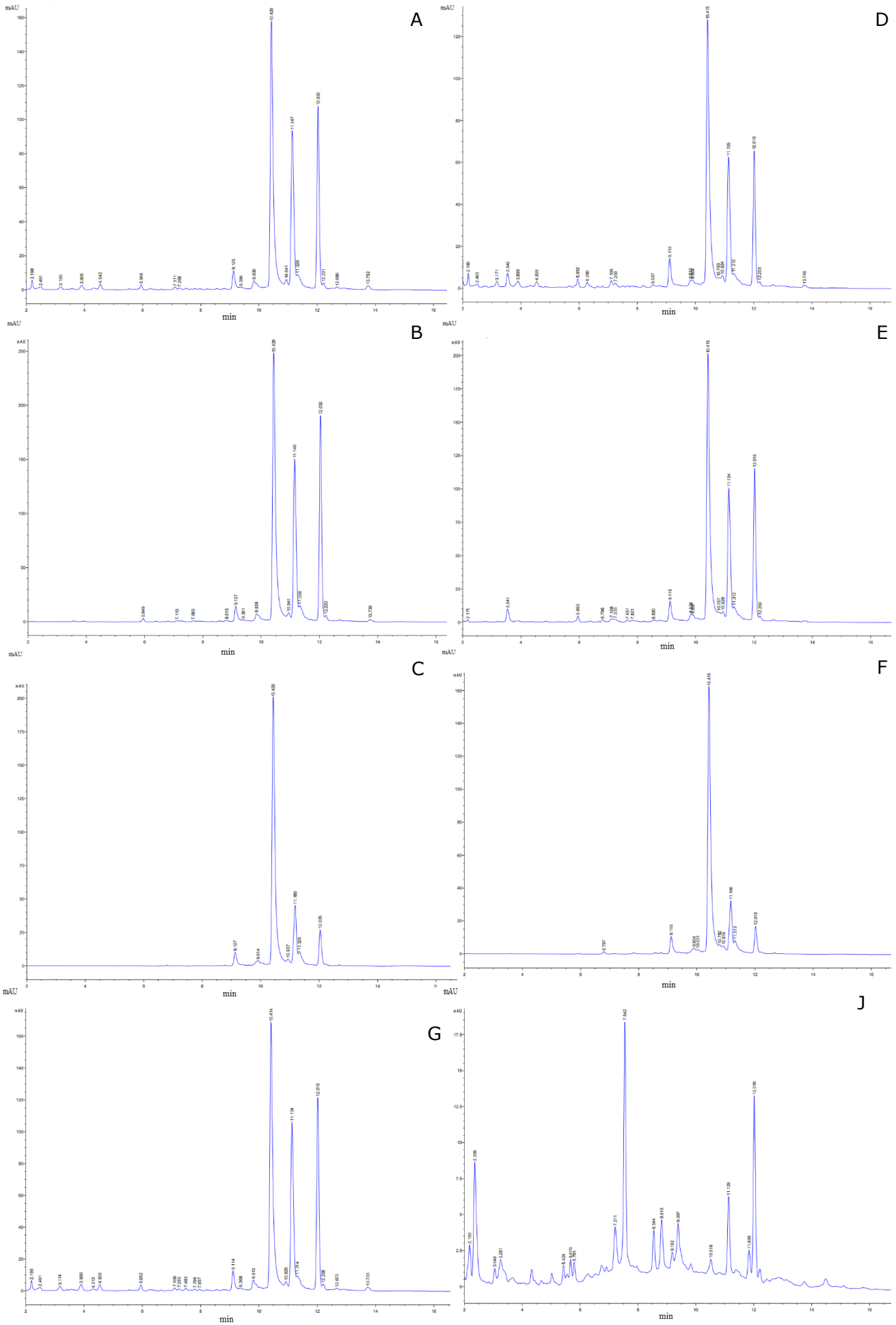
compounds in ultrasound for the obtained aqueous extracts. The phenolic acids included hydroxybenzoic acids like salicylic and gallic acids and hydroxycinnamic acid derivatives such as trans-cinnamic and caffeic acids. Some of the identified phenolic acids were ferulic, syringic, vanillin, m-anisic, cinnamic, and 3, 4, 5-trimethoxybenzoic acids. The flavonoids included, for example, luteolin-7-glycoside, apigenin-7-glycoside and rutin. Also, other phenolic compounds were identified, like resorcinol and hydroxyquinone.

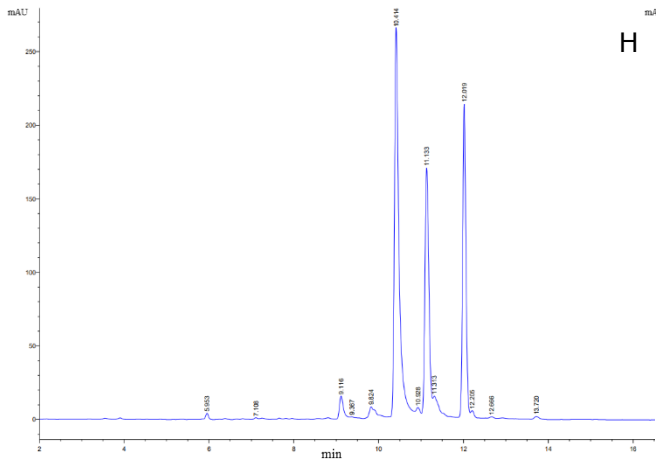
Table 2: HPLC results of the ethanolic and aqueous extracts from *Cistanche violacea* (Desf.) Beck.

Compound number	Identified compound	Ethanolic extract			Aqueous extract		
		Maceration (retention time in min)	Soxhlet (retention time in min)	Ultrasound (retention time in min)	Maceration (retention time in min)	Soxhlet (retention time in min)	Ultrasound (retention time in min)
1	Ascorbic acid	+(2.197)	+(1.963)	+(2.197)	+(2.180)	+ (1.950)	+ (1.997)
2	Gallic acid	+(3.180)	+(3.171)	+(3.174)	+(3.251)	+ (3.209)	+ (3.220)
3	Hydroxyquinone	+(3.906)	+(3.542)	+(3.900)	/	+(3.553)	+(4.327)
4	Tannic acid	/	+(3.899)	/	+(3.048)	+(3.553)	+(3.046)
5	Resorcinol	+(4.542)	+(4.539)	+(4.539)	+(5.424)	/	+(5.031)
6	p-hydroxybenzoic acid	+(5.852)	+(6.280)	+(8.855)	+(5.545)	+(6.282)	+(5.546)
7	1,2 dihydroxybenzene	+(5.948)	+(6.280)	+(5.952)	+(5.794)	+(6.281)	+(5.672)
8	Dihydroxycinnamic acid	+(7.111)	+(7.105)	+(7.106)	+(7.211)	/	/
9	Caffeic acid	+(7.113)	+(7.108)	+(7.108)	+(7.210)	/	(7.653)
10	Syringic acid	+(7.268)	+(7.250)	+(7.265)	/	/	/
11	p-hydroxybenzaldehyde	/	/	+(7.799)	+(7.542)	/	+(7.531)
12	Isovanillic acid	+(7.276)	+(7.255)	/	+(7.539)	/	+(7.516)
13	Sinapic acid	+(8.815)	+(9.115)	+(9.116)	+(8.816)	+(9.115)	+(9.118)
14	Vanillin	+(9.125)	+(8.537)	+(9.114)	+(8.544)	+(9.113)	+(8.543)
15	n-hydroxy cinnamic acid	+(9.127)	+(8.550)	/	/	/	+(8.532)
16	Rutin	+(9.127)	+(9.115)	+(9.116)	/	+(9.115)	/
17	Ferulic acid	(9.381)	/	+(9.367)	+(9.390)	+(9.832)	+(9.382)
18	Salicylic acid	+(9.830)	+(9.830)	+(9.813)	+(9.387)	+(9.832)	+(9.380)
19	3-hydroxy-4-methoxycinnamic acid	+(9.839)	+(9.830)	+(9.824)	/	+(9.833)	/
20	Luteolin-7-glycoside	+(9.914)	+(9.904)	+(9.901)	+(9.401)	+(9.912)	/
21	Quercetin-3-B-glucoside	/	+(10.031)	(10.024)	/	/	/
22	Rosmarinic acid	+(10.429)	+(10.415)	+(10.414)	+(10.526)	+(10.430)	/
23	Naringenin-7-glucoside	+(10.429)	+(10.415)	+(10.414)	+(10.518)	+(10.430)	+(10.493)
24	Apigenin-7-glycoside	+(10.429)	+(10.415)	+(10.414)	/	+(10.430)	/
25	Myricetin	+(10.937)	+(10.918)	+(10.924)	+(11.130)	+(11.184)	/

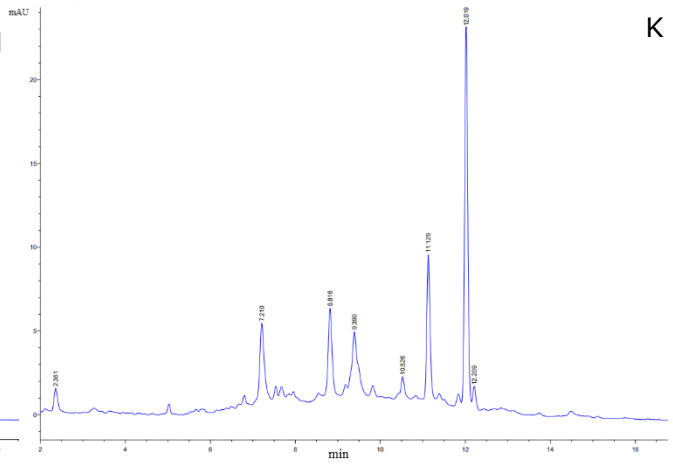
Compound number	Identified compound	Ethanollic extract			Aqueous extract		
		Maceration (retention time in min)	Soxhlet (retention time in min)	Ultrasound (retention time in min)	Maceration (retention time in min)	Soxhlet (retention time in min)	Ultrasound (retention time in min)
26	3, 4, 5 trimethoxybenzoic acid	+(10.946)	+(10.909)	/	/	+(11.009)	+(11.336)
27	Spiracocide	+(11.180)	+(10.782)	+(11.167)	/	+(11.328)	/
28	Coumarin	+(12.032)	+(12.016)	+(12.019)	+(11.839)	+(12.026)	+(11.848)
29	m-anisic acid	+(12.032)	+(12.016)	+(12.019)	+(12.019)	+(12.026)	+(11.846)
30	3,4,5-trimethoxy-trans cinnamic acid	+(12.220)	+(12.202)	+(12.666)	+(12.209)	/	+(12.223)
31	Rosmarinic acid	+(13.739)	/	+(13.720)	/	+(10.430)	/
32	Cinnamic acid	+(13.752)	+(13.746)	+(13.735)	/	/	/
Total		29	29	28	21	22	20

/: non detected, +: present.

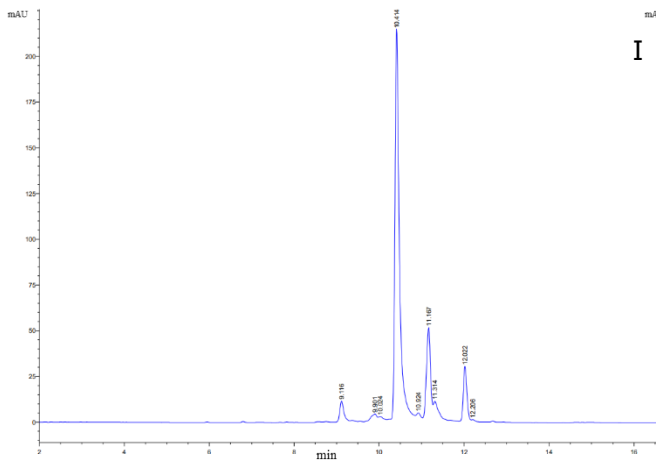




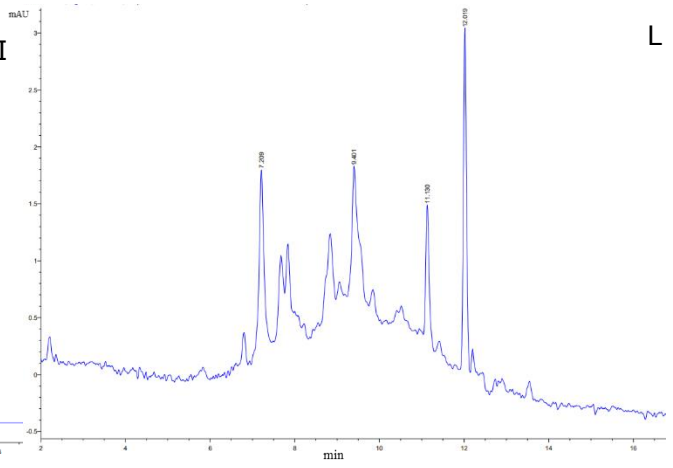
H



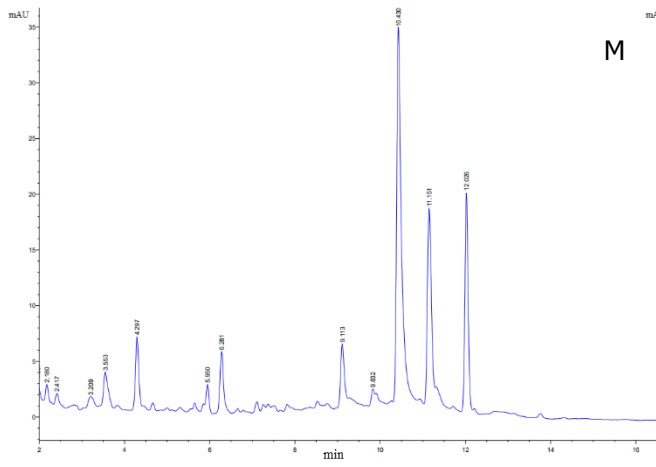
K



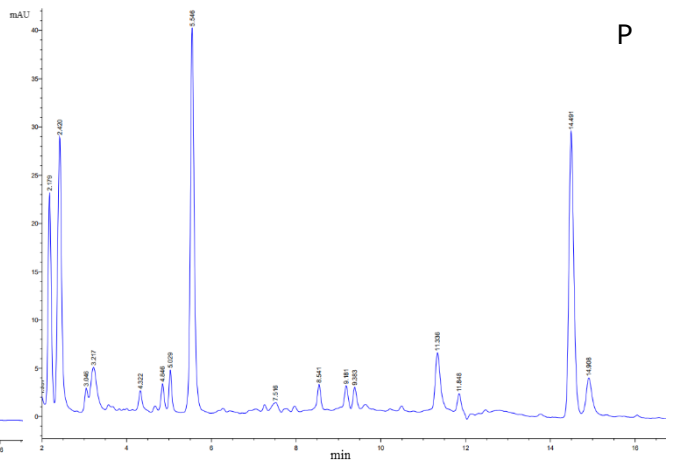
I



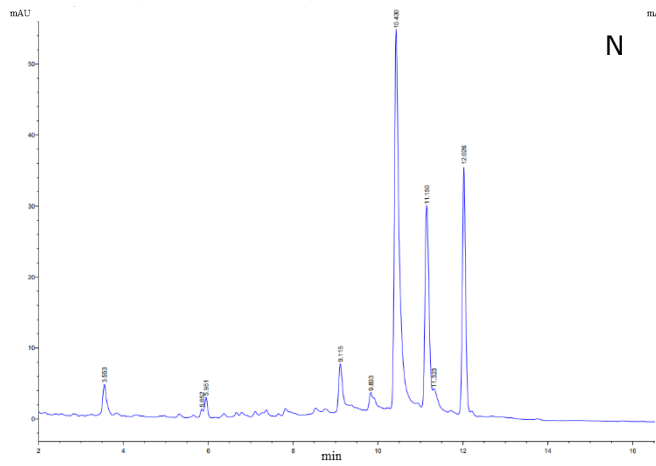
L



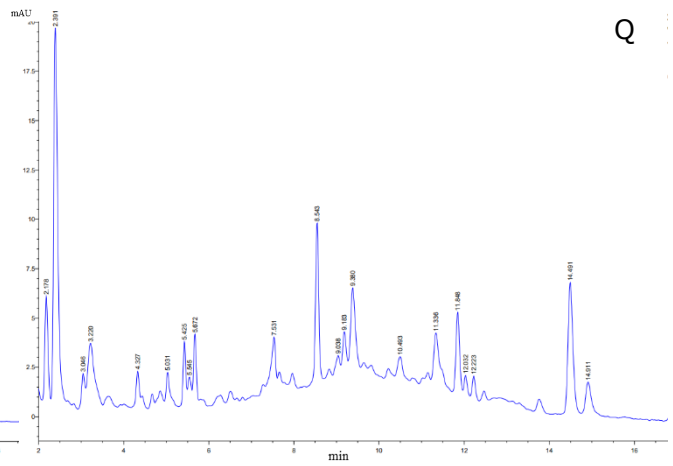
M



P



N



Q

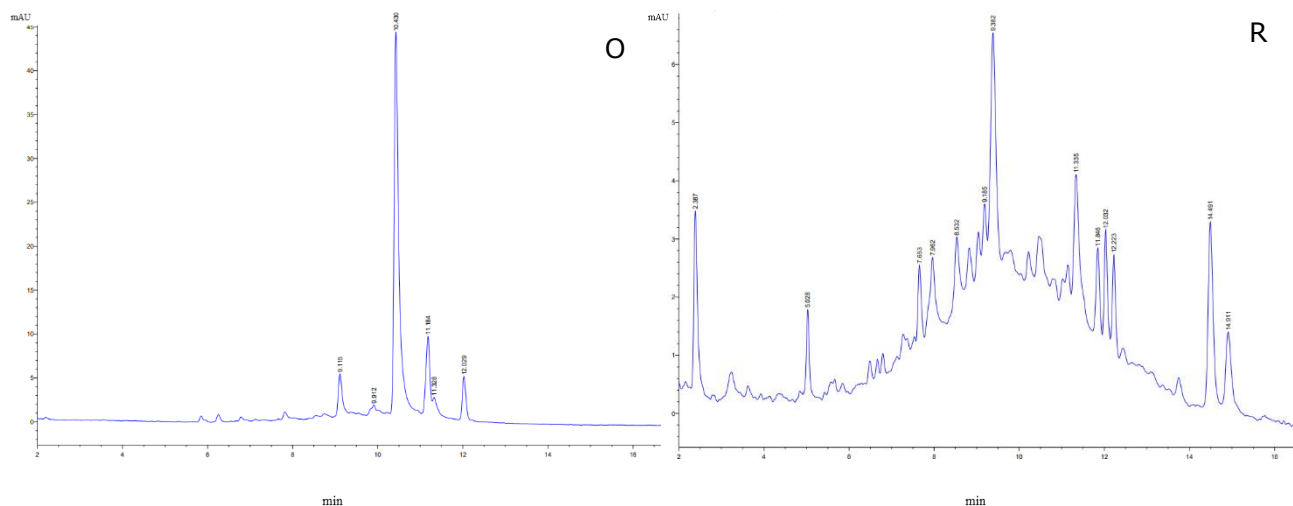


Figure 1: HPLC chromatograms of *Cistanche violacea* (Desf.) Beck extracts. A, B and C: Ethanolic extract.

Maceration; D, E and F: Aqueous extract Maceration; G, H and I: Ethanolic extract Soxhlet; J, K and L: Aqueous extract Soxhlet; M, N and O: Ethanolic extract Ultrasound; P, Q and R: Aqueous extract Ultrasound at 280, 300 and 355nm.

3.2. Antioxidant Activity

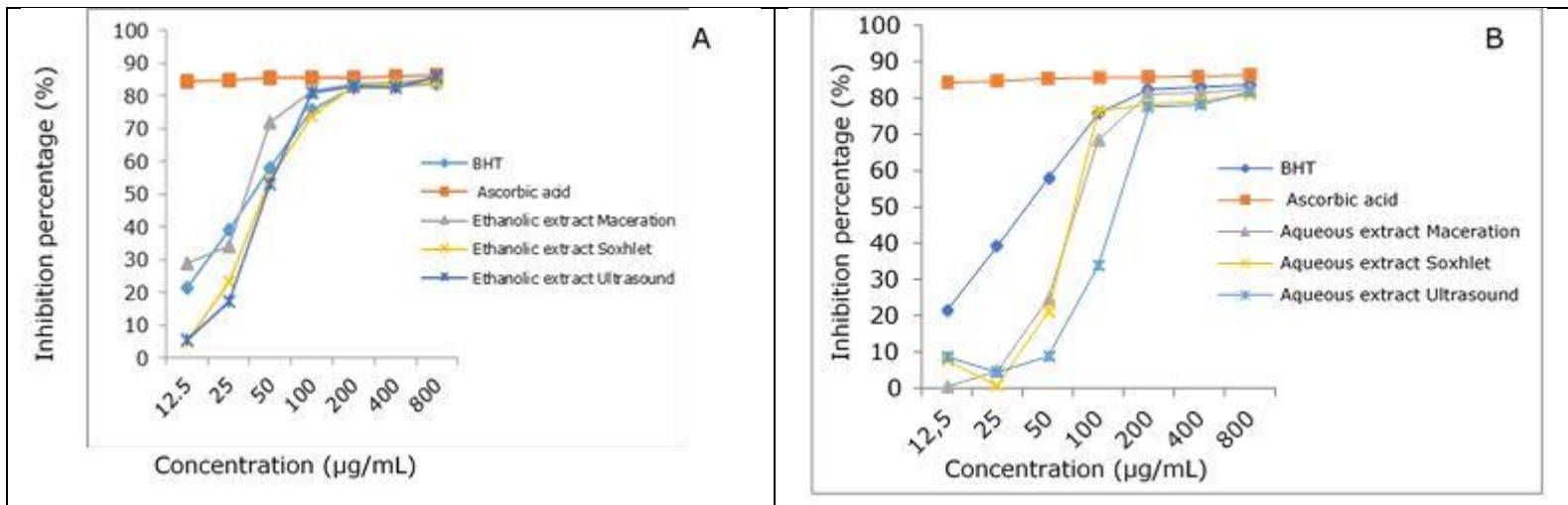
The results of the antioxidant activity of *C. violacea* (Desf.) Beck extracts are presented in Table 3 and Figure 2.

Table 3: Antioxidant activity of *Cistanche violacea* (Desf.) Beck extracts.

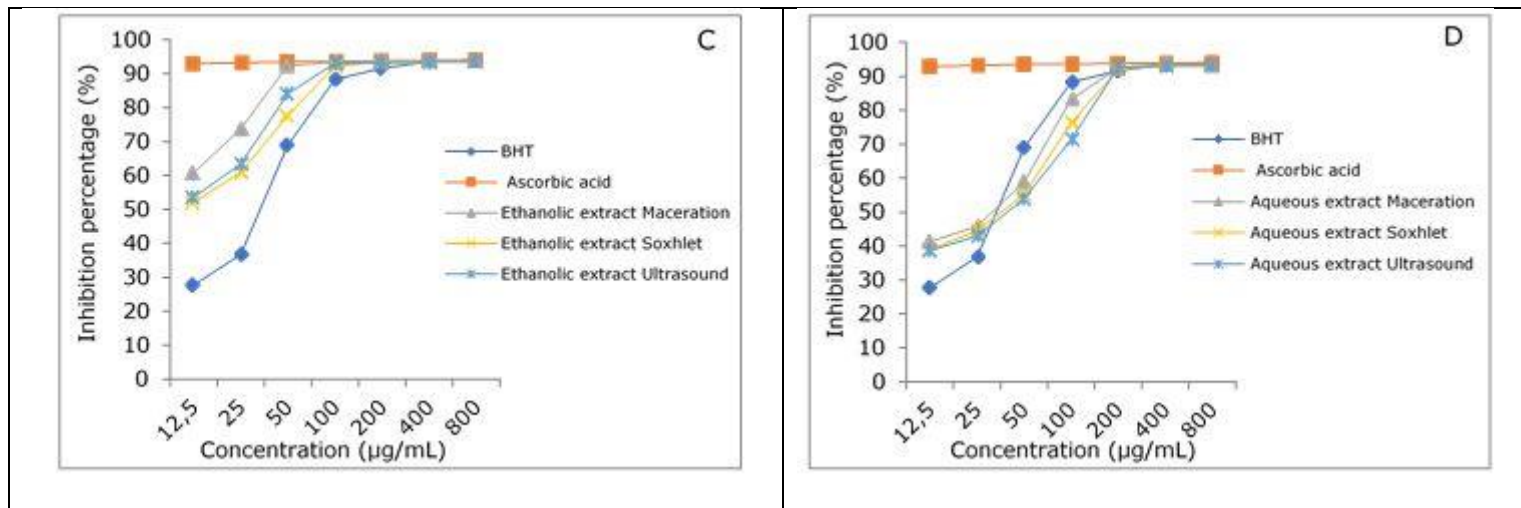
Standard/ extract	Extraction technique	IC ₅₀			A _{0.5}
		DPPH (µg/mL)	ABTS (µg/mL)	Phen (µg/mL)	RP (µg/mL)
BHT	/	42.60 ± 2.3 ^e	35.52 ± 1.05 ^c	8.84 ± 0.7 ^f	10.73 ± 0.7 ^f
Ascorbic acid		<12.5 ^g	<12.5 ^e	<3.125 ^g	1.48 ± 0.5 ^g
Ethanolic extract	Maceration	33.35 ± 1.4 ^f	<12.5 ^e	24.79 ± 1.9 ^e	38.67 ± 1.2 ^f
	Soxhlet	46.29 ± 0.7 ^{de}	<12.5 ^e	36.34 ± 0.7 ^{cd}	103.73 ± 0.5 ^b
	Ultrasound	48.39 ± 1.1 ^d	<12.5 ^e	32.71 ± 2.9 ^d	60.61 ± 3.3 ^e
Aqueous extract	Maceration	78.73 ± 1.4 ^c	32.91 ± 0.6 ^d	42.71 ± 1.9 ^c	69.35 ± 2.7 ^d
	Soxhlet	90.62 ± 2.5 ^b	38.09 ± 1.1 ^b	53.41 ± 4.88 ^b	84.26 ± 2.1 ^c
	Ultrasound	138.43 ± 1.5 ^a	42.82 ± 0.3 ^a	62.23 ± 2.38 ^a	142.63 ± 3.8 ^a

Values are the mean of three replicates ($n = 3$) ± SD. Results with different superscript letters are significantly different ($p \leq 0.05$). BHT: Butylated hydroxytoluene, DPPH: 2,2-diphenyl-1-picryl-hydrazyl, ABTS: 2,2'-azino-bis(3-ethylbenzothiazoline-6-sulfonic acid), Phen: phenanthroline, RP: reducing power. IC₅₀ (mg/mL): concentration at which 50% is inhibited. A_{0.5} (mg/mL): concentration indicating 0.50 absorbance intensity.

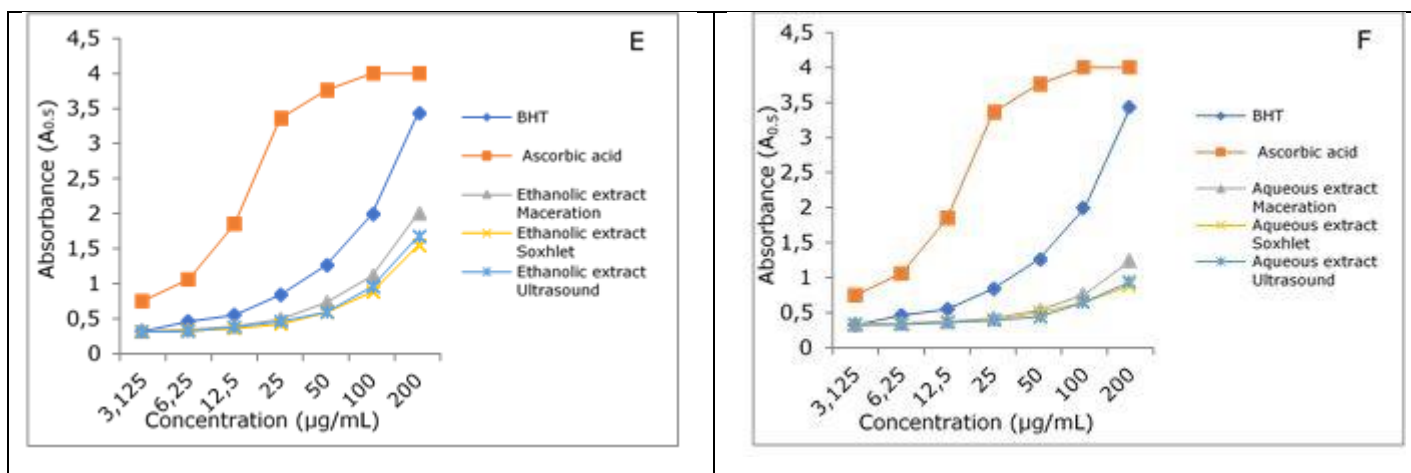
DPPH



ABTS



Phen



RP

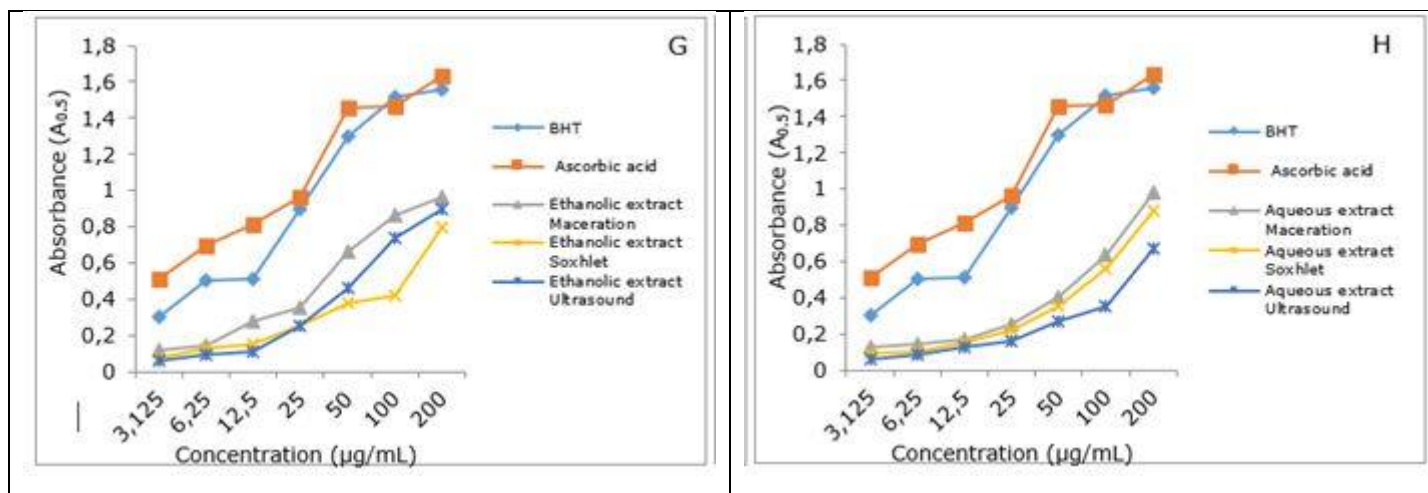


Figure 2: DPPH and ABTS scavenging effects and absorbance values in phenanthroline and reducing power assays of different extracts of *Cistanche violacea* (Desf.) Beck with BHT and ascorbic acid were used as the positive controls. BHT: Butylated hydroxytoluene, A and B: DPPH (2,2-diphenyl-1-picrylhydrazyl) for ethanolic and aqueous extracts, C and D: ABTS (2,2'-azino-bis(3-ethylbenzothiazoline-6-sulfonic acid) for ethanolic and aqueous extracts, E and F: Phen (phenanthroline assay) for ethanolic and aqueous extracts and G and H: RP (reducing power assay) for ethanolic and aqueous extracts.

The DPPH and ABTS scavenging effects of *C. violacea* (Desf.) Beck extracts were evaluated. From Table 3, the obtained results show that the IC₅₀ values of the DPPH assay were variable for the different extracts. Furthermore, we noted that the IC₅₀ value was found to be $33.35 \pm 1.4 \mu\text{g/mL}$ for the maceration ethanolic extract, which was higher than the ascorbic acid (IC₅₀ < $12.5 \mu\text{g/mL}$) and lower than BHT (IC₅₀ = $42.60 \pm 2.3 \mu\text{g/mL}$). So, we conclude that the maceration ethanolic extract had an important antioxidant activity than BHT. For ABTS results, the IC₅₀ values were < $12.5 \mu\text{g/mL}$ for the three extraction methods of the ethanolic extract. Thus, these different extracts had important antioxidant capacities when compared to BHT (IC₅₀ = $35.52 \pm 1.05 \mu\text{g/mL}$).

The phenanthroline and reducing power assays were used to determine the potential of the different obtained extracts of *C. violacea* (Desf.) Beck to reduce metallic ions. However, all the tested extracts were less efficient than BHT ($A_{0.5} = 8.84 \pm 0.7 \mu\text{g/mL}$ and $A_{0.5} = 10.73 \pm 0.7 \mu\text{g/mL}$) and the ascorbic acid ($A_{0.5} = < 3.125 \mu\text{g/mL}$ and $A_{0.5} = 1.48 \pm 0.5 \mu\text{g/mL}$) for the phenanthroline as well as the reducing power assays, respectively. Hence, BHT and ascorbic acid had more important antioxidant activities than our six analyzed extracts.

The antioxidant activity of *C. violacea* (Desf.) Beck is also presented in Figure 2 for the ethanolic and aqueous extracts. On one hand, the obtained results showed that the inhibition percentage increased with increasing fraction concentrations for the six extracts for DPPH and ABTS scavenging effects. On the other hand, the results of the phenanthroline and reducing power assay showed that the absorbance values of various extracts of *C. violacea* (Desf.) Beck increased with increasing fractions.

Overall, the results showed that the ethanolic extracts obtained by the three extraction methods from *C. violacea* (Desf.) Beck exhibited interesting high scavenging activities against DPPH and ABTS

free radicals, while all the extracts showed weaker antioxidant properties than the used standards.

3.3. Antimicrobial Activity

The results of the antimicrobial activity of *C. violacea* (Desf.) Beck extracts are summarized in Table 4 and shown in Figure 3.

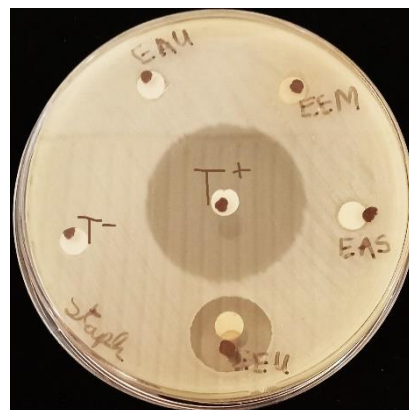


Figure 3: Representative photo showing *S. aureus* ATCC25923 (Staph) susceptibility to *Cistanche violacea* (Desf.) Beck extracts with negative and positive controls. EEM: Ethanolic extract Maceration, EEU: Ethanolic extract Ultrasound, EAU: Aqueous extract Ultrasound, EAS: Aqueous extract Soxhlet. T⁻: negative control, T⁺: positive control.

The antimicrobial activity of *C. violacea* (Desf.) Beck extracts revealed that the aqueous extract Soxhlet had mild antibacterial activity against *S. aureus* ATCC25923 with an inhibition zone of $18.66 \pm 1.1 \text{ mm}$. In addition, a weak antifungal activity against *C. albicans* ATCC10231 was obtained by the ethanolic extract Soxhlet and the aqueous extract ultrasound with inhibition zones of $7.33 \pm 0.5 \text{ mm}$. The other tested microorganisms did not show any susceptibility to the tested extracts.

Table 4: Antimicrobial activity of *Cistanche violacea* (Desf.) Beck extracts.

Control /Extract	Extraction technique	<i>E. coli</i> ATCC25922	<i>P. aeruginosa</i> ATCC27853	<i>S. typhimurium</i> ATCC14028	<i>S. aureus</i> ATCC25923	<i>B. cereus</i> ATCC14579	<i>L. monocytogenes</i> ATCC35152	<i>C. albicans</i> ATCC10231
Positive control	/	19.1 ± 0.7	31.44 ± 1.1	22 ± 0.9	30.11 ± 0.9	33.22 ± 0.8	33 ± 0.7	19.55 ± 0.7
Ethanol extract	Maceration	6 ± 0.00*	6 ± 0.00*	6 ± 0.00*	6 ± 0.00*	6 ± 0.00*	6 ± 0.00*	6 ± 0.00*
	Soxhlet	6 ± 0.00*	6 ± 0.00*	6 ± 0.00*	6 ± 0.00*	6 ± 0.00*	6 ± 0.00*	7.33 ± 0.5*
	Ultrasound	6 ± 0.00*	6 ± 0.00*	6 ± 0.00*	6 ± 0.00*	6 ± 0.00*	6 ± 0.00*	6 ± 0.00*
Aqueous extract	Maceration	6 ± 0.00*	6 ± 0.00*	6 ± 0.00*	6 ± 0.00*	6 ± 0.00*	6 ± 0.00*	6.66 ± 0.5*
	Soxhlet	6 ± 0.00*	6 ± 0.00*	6 ± 0.00*	18.66 ± 1.1*	6 ± 0.00*	6 ± 0.00*	6.66 ± 0.5*
	Ultrasound	6 ± 0.00*	6 ± 0.00*	6 ± 0.00*	6 ± 0.00*	6 ± 0.00*	6 ± 0.00*	7.33 ± 0.5*

Values are the mean of three replicates ($n = 3$) ± SD. * $p < 0.001$ is significant compared to the positive control (one-way ANOVA followed by Tukey's test). Zone diameter equals 6 mm = no inhibition. In **bold** represents the highest antibacterial activity.

Table 5: Matrix of correlation between TPC, TFC and antioxidant assays.

	TFC	DPPH	ABTS	Phen	RP
TPC	0.74*	-0.87*	-0.94*	-0.84*	-0.62*
TFC	1.00	-0.65*	-0.65*	-0.73*	-0.69*
DPPH		1.00	0.93*	0.95*	0.79*
ABTS			1.00	0.92*	0.59*
Phen				1.00	0.81*

*Significant correlation with $p < 0.05$. TPC: Total Phenolics Content, TFC: Total Flavonoids Content, DPPH: 2,2-diphenyl-1-picrylhydrazyl, ABTS: 2,2'-azino-bis(3-ethylbenzothiazoline-6-sulfonic acid), Phen: phenanthroline, RP: reducing power.

3.4. Correlation between total phenolics and flavonoids contents and antioxidant activity

Pearson correlation was used to analyze the relationship between the total phenolics and

The obtained results showed strong correlations between the DPPH, ABTS and Phen antioxidant assays, indicating the antioxidant properties of the tested extracts ($r = 1$, $p < 0.05$). Significant negative correlations were also found between the TPC of the extracts and their ABTS radical scavenging ($r = -0.94$, $p < 0.05$), DPPH radical scavenging ($r = -0.87$, $p < 0.05$), Phen ($r = -0.84$, $p < 0.05$) and RP ($r = -0.62$, $p < 0.05$) activities. Also, TFC showed a negative correlation with all the antioxidant activities measured by ABTS ($r = -0.65$, $p < 0.05$), DPPH ($r = -0.65$, $p < 0.05$), RP ($r = -0.69$, $p < 0.05$) and Phen ($r = -0.73$, $p < 0.05$) assays. On the other hand, a positive correlation was found between the DPPH and RP ($r = 0.79$), ABTS ($r = 0.93$) and Phen ($r = 0.92$). These findings indicated that TFC and TPC are not the key determinants associated with the antioxidant activity of the different extracts of *C. violacea* (Desf.) Beck.

flavonoid contents and the antioxidant activity of *C. violacea* (Desf.) Beck extracts (Table 5).

3.5. Multivariate Analyses

Based on TFC and TPC as well as the antioxidant activity results from *C. violacea* (Desf.) Beck, multivariate analyses, including HCA and PCA, were conducted on the different extracts used in this study. These analyses were used to differentiate the different extraction methods and the used solvents on the TFC, TPC and antioxidant activities of the studied plant. HCA is a classification method that is frequently used to identify homogeneous groups based on the assessed variables. The dendrogram that results from the HCA analysis is based on Ward's linkage algorithm and Euclidean distances.

Based on the extraction method and the solvents used, HCA dendrogram (Figure 4) showed that *C. violacea* (Desf.) Beck extracts were clearly divided into three main clusters. The first cluster contained the ethanol extracts obtained by the three extraction methods. The second cluster contained the aqueous extracts after maceration and Soxhlet extractions, while the third cluster was the aqueous extract obtained by the ultrasound extraction method.

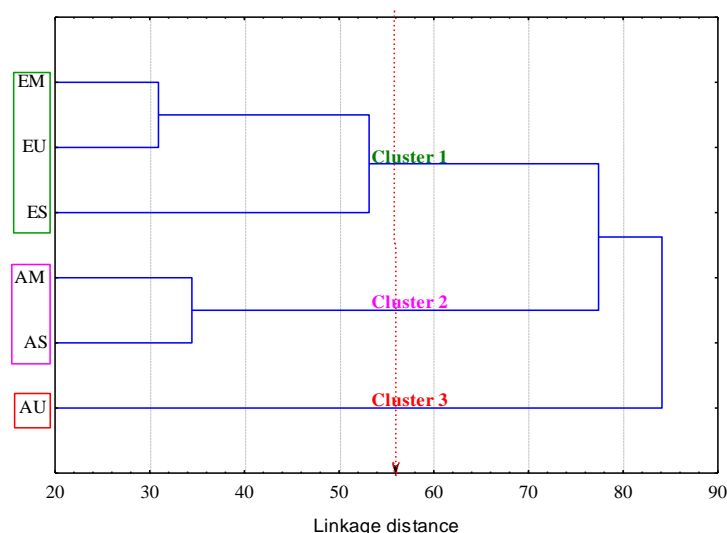


Figure 4: Hierarchical clustering analysis for the different extracts of *Cistanche violacea* (Desf.) Beck based on TFC, TPC as well as ABTS, DPPH, RP and Phen antioxidant activities. EM: Ethanolic extract Maceration; AM: Aqueous extract Maceration; ES: Ethanolic extract Soxhlet; AS: Aqueous extract Soxhlet; EU: Ethanolic extract Ultrasound; AU: Aqueous extract Ultrasound.

A score plot was used to assess the similarities and differences between the different extracts of *C. violacea* (Desf.) Beck. It was clear that the ethanolic extract using the maceration method was distinguished from the other extracts. Since the highest component with eigen values larger than 1.0 was chosen, two factors were retrieved. Our research revealed that factor 1 accounted for up to 83.53% of the total variation and factor 2 accounted for up to 8.90% of the total variance, totaling 92.43%. Therefore, the test samples were divided into factor 1 and

factor 2 based on the PCA loading plot (Figure 5A), which showed differences in the test samples' TFC, TPC, and antioxidant activities as determined by the ABTS, DPPH, RP and Phen assays.

The PCA plot's first two principal components axes accounted for 92.43% of the total variance. PC1 described 83.53% of the total variability, while PC2 accounts only for 8.9%. According to the loading plot of PCA, two principal components PC1 and PC2 were applied to supply a convenient visual aid for recognizing

the dissimilarity in the data and to show how strongly each characteristic (or variable) influences a principal component. The results showed that the main contributors to the first component were TPC and TFC. The second component (PC2) was associated with DPPH, ABTS, RP and Phen antioxidant activities. The ethanolic extracts of *C. violacea* (Desf.) Beck were distinguished from the aqueous extracts based on their polyphenolic content and antioxidant activities by representing factor 1 vs factor 2 in the scatter plot (Figure 5B). Therefore, PC1 and PC2 explained the relation between the phenolic composition and the antioxidant activity of different extracts of *C. violacea* (Desf.) Beck. According to the results of HCA and PCA, polyphenolic composition and antioxidant activities can be used to distinguish between the different extracts of *C. violacea* (Desf.) Beck.

4. DISCUSSION

The phytochemical study, antioxidant capacity and antimicrobial activity of the ethanolic and aqueous extracts of *C. violacea* (Desf.) Beck obtained by maceration, Soxhlet and ultrasound extraction methods were investigated in this study.

4.1. Phytochemical Study

Many phenolic compounds found in plants have a positive effect on counteracting the oxidation process

and function as reducing agents and antioxidants. To characterize *C. violacea* (Desf.) Beck, the TPC and TFC were determined for the different extracts obtained by two solvents (water and ethanol) and three different extraction methods (maceration, Soxhlet and ultrasound). The obtained results show that TPC in the ethanolic extracts were significantly higher ($p < 0.05$) than those in the aqueous extracts, ranging from 159.17 ± 3.3 to 188.95 ± 0.4 mg GAE/mg DE and from 71.48 ± 5.3 to 107.22 ± 5.7 mg QE/mg DE, respectively. Furthermore, ultrasound and maceration extractions were significantly higher for TPC than the obtained results for Soxhlet extraction when using ethanol as an extraction solvent. In contrast, Soxhlet extraction gave significant results compared to maceration and ultrasound extraction methods when using water as a solvent. For TFC, Highly significant results were obtained for maceration after using ethanol as an extraction solvent (40.26 ± 6.02 μ g QE/mg DE), followed by ultrasound extraction (27.73 ± 0.8 μ g QE/mg DE) and finally, Soxhlet (19.76 ± 3.7 μ g QE/mg DE). No significant differences between the extraction methods for the aqueous extracts were observed despite the high TFC content of the ultrasound aqueous extract (18.35 ± 0.3 μ g QE/mg DE).

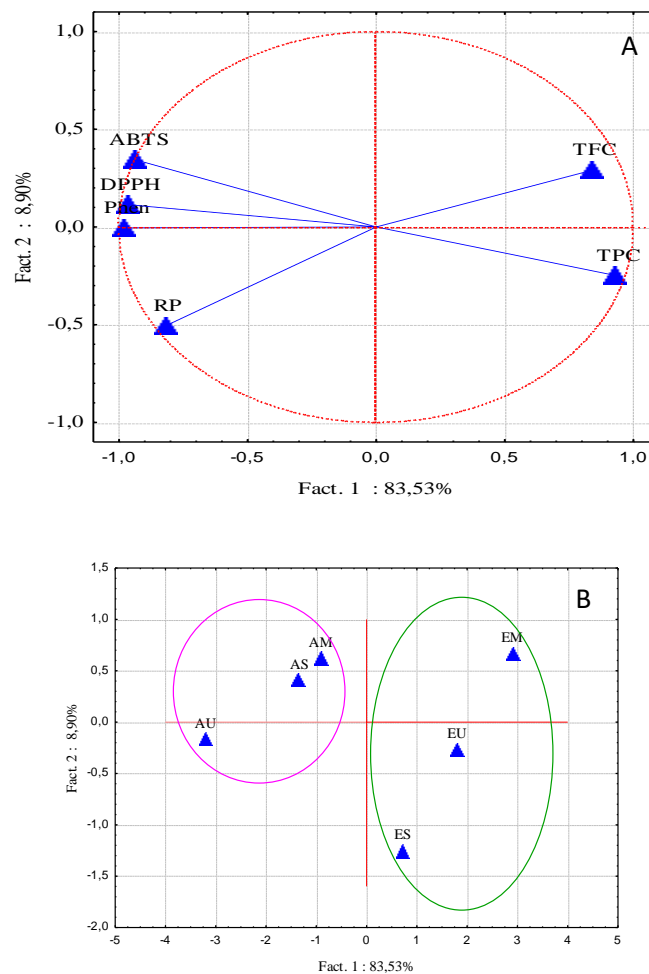


Figure 5: Principal component analysis loading plot (A) and score plot (B) for the different extracts of *Cistanche violacea* (Desf.) Beck based on TFC, TPC as well as ABTS, DPPH, RP and Phen antioxidant assays.

EM: Ethanol extract Maceration; AM: Aqueous extract Maceration; ES: Ethanol extract Soxhlet; AS: Aqueous extract Soxhlet; EU: Ethanol extract Ultrasound; AU: Aqueous extract Ultrasound.

A study conducted by Alia et al. (11) showed that the TPC and TFC of the methanolic extract of *C. violacea* collected from Oued Souf region (southeast of the Algerian Sahara) were 19.055 ± 0.197 mg GAE/mg DE and 5.769 ± 0.353 μ g QE/mg DE, respectively. As was observed, our results were higher than those obtained by Alia et al. (11). This difference can be explained by the Folin-Ciocalteu reagent used in dosage, the biogenetic, geographical and environmental factors (25, 26). In addition, the composition of phenolic compounds is influenced by the solvent used and the extraction method. This fact was also reported by Ben Attia et al. (13), who showed that a cascade maceration using different solvents with increasing polarity (n-hexane, ethyl acetate, acetone, methanol, and water) gave different TFC and TPC contents for *C. violaceae* collected from Tataouine (southeastern Tunisia). According to Bouzayani et al. (14), *C. violaceae* (Desf) Hofmanns & Link, all extracts of the aerial parts and underground stems collected from Sfax, in the southeast of Tunisia, were rich in phenolic compounds, particularly the acetone-water extracts of the aerial parts (877 mg GAE/g DW) and the underground stems (814 mg GAE/g DW). Flowers were the most enriched in TPC compounds (394 mg GAE/g DW) compared to bulbs (116 mg GAE/g DW) in the study of Debouba et al. (12) on *C. violacea* collected from the seashore of Hassi Jerbi village located in the southeast of Tunisia. According to Piwowarczyk et al. (4), the quantity of polyphenolic compounds found in the stems and flowers of *Cistanche* was very diverse and depended on the host plant. *Cistanche armena* samples that were collected from southeastern Armenia gave a quantity of polyphenols of 568 mg/100 g (4).

In contrast to our TFC results, Bouzayani et al. (14) proved that *C. violaceae* extracts were rich in TFC. In their study, the highest TFC (342 mg QE/g DE) was derived from the underground stems acetone-water (8-2, v/v) extract, followed by 303 mg QE/g DE recorded in the underground stems methanol extract. In addition, Debouba et al. (12) showed that *C. violacea* flowers were the lowest enriched in TFC (95 mg QE/g DW) to bulbs (287 mg QE/g DW) but still higher than our TFC results. Our results are higher than those obtained by Ben Attia et al. (13), who reported that the highest TFC was observed in acetone and ethyl acetate for *C. violaceae* with 0.8 ± 0.08 and 0.79 ± 0.03 mmol CE/g, respectively.

The chemical variation between the different extracts of *C. violacea* (Desf.) Beck revealed that all the extracts are rich in phenolic compounds after HPLC analysis. Approximately twenty-nine compounds were revealed in each of the obtained extracts using ethanol as the solvent, while a lower number was obtained for the different aqueous extracts. Constituents including *para*-hydroxybenzaldehyde (phenolic aldehyde), cinnamic acid, dihydroxycinnamic, *n*-hydroxycinnamic, 3-hydroxy, 4-methoxycinnamic, 3, 4, 5-trimethoxy-trans-cinnamic, salicylic, and gallic

acids (phenolic acids), and apigenin-7-glycoside, luteolin-7-glycoside, spiracoside and rutin (flavonoids) were detected. In addition, other compounds like resorcinol and hydroxyquinone were revealed. Rutin and gallic acid were also reported in the study of Alia et al. (11) on the crude extract of *C. violaceae*, whereas they also reported the presence of chlorogenic acid and naringin. On the other hand, Piwowarczyk et al. (4) identified polyphenolic compounds based on MS and MS/MS data of *C. armena*, revealing phenylethanoids and their glycosides in morphological parts (flowers and stem with tubers separately). In the phytochemical study carried out by Beladjila et al. (9) on *C. phelypaea* *n*-butanol extract, four new phenylethanoid glycosides (1- β -p-hydroxyphenyl-ethyl-3,6-di- α -L-rhamnopyranosyl-4-p-coumaroyl- β -D-glu-copyranoside, 1- β -p-hydroxyphenyl-ethyl-3,6-O-di- α -L-rhamnopyranosyl- β -D-glucopyranoside, 1- β -p-hydroxy-phenyl-ethyl-2-O-acetyl-3,6-di- α -L-rhamnopyranosyl-4-p-coumaroyl- β -D-glucopyranoside and 1- β -p-hydroxy-phenyl-ethyl-2-O-acetyl-3,6-di- α -L-rhamnopyranosyl- β -D-glu-copyranoside) and the three known compounds brandioside, pinosresinol 4-O- β -D-glucopyranoside and apigenin 7-O- β -glucuronopyranoside were reported. This last compound was also revealed in our study.

Several studies have indicated that many of the identified compounds in our extracts have been isolated from various plants and have a wide range of biological effects, including anti-inflammatory, antioxidant, antimicrobial, antitumor, and others (27-35).

From the 32 identified compounds, ten were found in our six extracts, namely ascorbic acid, gallic acid, *para*-hydroxybenzoic acid, 1, 2 dihydroxybenzene, sinapic acid, vanillin, salicylic acid, naringenin-7-glucoside, coumarin, and *m*-anisic acid. These compounds were studied by many researchers and reported to possess many biological and pharmacological effects. Ascorbic acid, which was recorded in all analyzed extracts, is a known potent antioxidant and free-radical scavenger. It acts primarily as a donor of single hydrogen atoms, and the radical anion monodehydroascorbate reacts mainly with radicals (29). Gallic acid is a low molecular weight tri-phenolic molecule that has outstanding anti-inflammatory, antioxidant, antitumor, antidiabetes, antiobesity, antimicrobial, and anti-myocardial ischemia properties (31). *p*-hydroxybenzoic acid and its derivatives have been reported by Singab et al. (33) to have potential antimicrobial, antiviral action against SARS-CoV-2, antimutagenic, anti-inflammatory, antioxidant, hypoglycemic, antiestrogenic, and antiplatelet aggregating activities. This compound can be chemically synthesized or recovered from various plants (33). Sinapic acid is a prevalent component of the human diet since it is found in a wide variety of dietary and medicinal plants. The antioxidant, antibacterial, anti-inflammatory, anticancer, and anti-anxiety properties of sinapic acid are demonstrated by Nićiforović and

Abramovič (27). This compound has been recommended for potential use in food processing, cosmetics, and the pharmaceutical industry, mostly due to its antioxidative action (27). Vanillin is a well-known natural aromatic flavoring compound that is widely used in foods, drinks, pharmaceuticals, perfumes, and cosmetics. Many studies have documented the pharmacological effects of vanillin, including its diuretic, anticancer, antidiabetic, antioxidant, antisickling, antibacterial and anti-inflammatory properties (34). Salicylic acid is a phenolic derivative that is widely present in plants. It is known to be a regulator of several physiological and biochemical processes, including thermogenesis, plant signalling or plant defense, and response to biotic and abiotic stresses. Salicylic acid plays an important role in protection against pathogens and has anti-inflammatory and antioxidant effects (28). Coumarins are naturally and widely occurring in plants and have been reported to possess varied biological actions like antitumor, anti-HIV, antimicrobial, anti-inflammatory and anticoagulant properties, as well as triglycerides lowering and stimulant effects on the central nervous system (30). *p*-hydroxybenzaldehyde found in the maceration of the aqueous extract and the ultrasound for both aqueous and ethanolic extracts has various pharmacological effects, such as antioxidant, anti-inflammatory, vasodilation effects, and a protective effect on transient focal cerebral ischemia in normal rats (35). Moreover, it has been demonstrated that other polyphenols reported in different plants, including quercetin, apigenin, syringic acid, caffeic acid, rutin, and ferulic acid, boost the plant's antioxidant capacity by altering antioxidant processes and preventing lipid peroxidation (32). Some of the identified compounds were not found in the obtained extracts from our study. This can be explained by the fact that the production of secondary metabolites by plants is a very complex process that depends on many factors, including internal developmental genetic circuits (regulated genes and enzymes), as well as aspects related to external environmental factors (light, temperature, water, salinity, etc.) (36).

On the other hand, some of the peaks were not identified in our study. This is due to the lack of standards; thus, it could be interesting to search for phenylethanoid glycosides as Deyama et al. (37) revealed their isolation from many *Cistanche* species, including *C. deserticola*, *C. salsa*, *C. tubulosa*, *C. sinensis* and *C. phelypaea*.

4.2. Biological Activities Study

It is known that plants develop defense mechanisms to survive in their ecosystems, and hence, they represent a rich source of antimicrobial agents and other compounds of pharmaceutical interest. As the biological activities of *C. violaceae* are largely unknown and not all its active substances are identified, we assessed the antioxidant (DPPH, ABTS, reducing power and phenanthroline) and antimicrobial capacities of six different extracts.

Many antioxidant tests are employed for the assessment of the antioxidant properties of plant extracts.

This is caused by the complicated composition of bioactive molecules, which react differently to different assay techniques (38). Four *in vitro* antioxidant assays were employed in our study to assess the scavenging and reducing the potential of the aqueous and ethanolic extracts from *C. violaceae* for this purpose. The obtained results showed mild antioxidant capacities of the analyzed extracts. The ethanolic extracts exhibited important antioxidant activities compared to the aqueous extracts, with the highest activity recorded for the ABTS test (IC₅₀ values of < 12.5 µg/mL). These differences in the antioxidant activity between the extracts could result from the difference in the composition (39).

Generally, the antioxidant activity of our extracts was of average values, which was comparable to the obtained results of Alia et al. (11). Ben Attia et al. (13) evaluated the antioxidant activity by DPPH, ABTS and Ferric Reducing Antioxidant Power (FRAP) assays of hexane, ethyl acetate, acetone, methanol, and water extracts obtained by sequential maceration. Their results revealed that the highest antioxidant activity, based on all the tests combined, was obtained with *C. violacea*. Bouzayani et al. (14) used five complementary methods to assess the antioxidant activity of *C. violacea*, namely DPPH, ABTS, Nitric Oxide (NO), Total Antioxidant Capacity (TAC), and FRAP. These authors showed that most tested extracts displayed notable antioxidant capacities for aerial and underground parts. Our results are not comparable with those obtained by Debouba et al. (12), who reported that *Cistanche* flowers had the highest free radical scavenging activity and the strongest reducing power while *Cistanche* bulb was the most efficient in chelating ferrous ions.

Different extracts made from other *Cistanche* species presented relevant antioxidant properties. For example, Rahim et al. (38) showed that the aqueous extract of *C. phelypaea* roots presented an interesting antioxidant potential related to the synergistic effects of several antioxidant compounds. Similarly, Aboul-Enein et al. (40) tested the DPPH scavenging abilities of the aqueous and ethanolic extracts from the whole *C. phelypaea* plants from Egypt and found that the aqueous extract produced better results. Moreover, the water extracts of roots and flowers exhibited the highest antioxidant capacity for *C. phelypaea*, which was collected from Ludo, Ria Formosa (Portugal) (41). According to the study of Wang et al. (42), all tested extracts had good dose-dependent inhibitory activity against the DPPH radical test. However, all of them were less potent than the reference antioxidants Trolox and ascorbic acid for *C. deserticola* from China.

For the antimicrobial activity, only one extract showed mild antibacterial activity against *S. aureus*. This last, when compared to the positive control that was tested under identical conditions, was less active in absolute terms with a high significant difference.

The activity against *S. aureus* can be explained by the presence of phenylethanoid glycosides, as suggested by Deyama et al. (37), who isolated them

from many *Cistanche* species, including *C. deserticola*, *C. salsa*, *C. tubulosa*, *C. sinensis* and *C. phelypaea* and reported their anti-*Staphylococcus* activity.

Our results corroborate those obtained by Hamed and El-Kamali (43) for the methanolic extract of *C. phelypaea* roots that did not show any activity against the tested bacteria. On the other hand, Keymanesh et al. (44) revealed mild antimicrobial activity of hydro-alcoholic extract of *C. tubulosa* aerial parts collected in Iran. The only antibacterial activity of *C. violacea* methanol and ethanol extracts was recorded against *S. epidermidis* ATCC® 12228™ in the study of Abdallah (15), while for the other microorganisms, the results showed weak activity or not at all. In contrast to our results, the study of Ullah et al. (45) revealed that the crude methanolic extract and aqueous, chloroform, *n*-hexane, *n*-butanol and ethyl acetate fractions of *C. tubulosa* from Pakistan were active against six tested bacterial strains. Also, the butanolic extract of *C. tubulosa* at concentrations of 2 and 4 mg/mL showed mild inhibition against *E. coli* (46). Bouzayani et al. (14) revealed that the aerial parts and underground stems of *C. violacea* had good efficiency against the tested bacterial strains. These authors showed that the methanolic extract at the concentration of 10 mg/mL was active against *S. aureus* with an inhibition zone of 15 mm.

4.3. Correlation

The DPPH and ABTS assays use a similar mechanism of action, which is a scavenging activity that may be the reason for the correlation between them. Similar studies have reported a strong relationship between the antioxidant capacity using these tests, including Bouzayani et al. (14), Fidrianny et al. (47) and Ali et al. (48). Also, Wang et al. (49) showed that the different antioxidant tests like DPPH scavenging capacity, Trolox Equivalent Antioxidant Capacity (TEAC), and RP correlated well with each other. Therefore, the antioxidant effect of the extracts may be assigned to phenolic compounds and flavonoids. Furthermore, positive correlations were observed in the study of Bouzayani et al. (14) between the TPC, TFC and CT and antioxidant activity of *C. violacea*. Other studies reported that the mechanism of action of flavonoids is through scavenging or chelating processes (50). In addition, Kalia et al. (51) and Amri et al. (52) reported that the potential antioxidant activity of an extract depends on its content in polyphenols and flavonoids.

5. CONCLUSIONS

This study was conducted to valorize a parasitic plant from the south of Algeria, *C. violacea*. This research revealed that the plant had phenolics and flavonoids contents, antioxidant and antimicrobial activities. Furthermore, statistical methods using HCA, PCA, and Pearson correlation were employed based on the results to highlight the existing correlation between the TPC, TFC and antioxidant activity. Furthermore, the composition of the parasitic plant, identified using HPLC analysis, testifies to the plant's potential properties as for example, the presence of active ingredients, including ascorbic acid, that possesses a

strong antioxidant activity. Thus, our findings support the role and value of the parasitic plant *C. violacea* as a source of bioactive compounds from the harsh climate conditions of Ghardaia Province (Algeria). Further studies on the isolation and purification of bioactive components from this plant are highly recommended to verify their practical use.

6. CONFLICT OF INTEREST

There is no actual or potential conflict of interest in relation to this article.

7. ACKNOWLEDGMENTS

The authors acknowledge the Ministry of Higher Education and Scientific Research of Algeria (MESRS) and the General Direction of Scientific Research and Technological Development (DGRSDT), the Center for Scientific and Technical Research on Arid Regions (CRSTRA), Biskra, Algeria and the University of Ghardaia, Ghardaia, Algeria.

8. REFERENCES

- Bennett JR, Mathews S. Phylogeny of the parasitic plant family Orobanchaceae inferred from phytochrome A. *American Journal of Botany*. 2006 Jul;93(7):1039-1051. [<URL>](#).
- Mutuku JM, Cui S, Yoshida S, Shirasu K. Orobanchaceae parasite-host interactions. *New Phytologist*. 2021 Apr;230(1):46-59. [<URL>](#).
- Heide-Jørgensen HS. Introduction: the parasitic syndrome in higher plants. In: Joel D, Musselman LJ, Gressel J, editors. *Parasitic Orobanchaceae*. Heidelberg: Springer Berlin; 2013 Jan. P. 1-20. [<URL>](#).
- Piwowarczyk R, Ochmian I, Lachowicz S, Kapusta I, Sotek Z, Błaszak M. Phytochemical parasite-host relations and interactions: A *Cistanche armena* case study. *Science of The Total Environment*. 2020 May;716,137071. [<URL>](#).
- Westwood JH, Yoder JI, Timko MP, de Pamphilis CW. The evolution of parasitism in plants. *Trends in Plant Science*. 2010 Apr;15(4):227-235. [<URL>](#).
- Piwowarczyk R, Sánchez Pedraja Ó, Moreno Moral G, Fayvush G, Zakaryan N, Kartashyan N, Aleksanyan A. Holoparasitic Orobanchaceae (*Cistanche*, *Diphelypaea*, *Orobanche*, *Phelipanche*) in Armenia: distribution, habitats, host range and taxonomic problems. *Phytotaxa*. 2019 Jan;386(1):001-106. [<URL>](#).
- Quezel P, Santa S. Nouvelle flore d'Algérie et des régions désertiques méridionales. Tomes 2. Edition CNRS; Paris; 1963. 1170p. ISBN: IF5841. [<URL>](#).
- Hammiche V, Maiza K. Traditional medicine in Central Sahara: Pharmacopoeia of Tassili N'ajjer. *Journal of Ethnopharmacology*. 2006 May;105:358-367. [<URL>](#).
- Beladjila KA, Berrehal D, De Tommasi N, Granchi C, Bononi G, Braca A, De Leo M. New phenylethanoid glycosides from *Cistanche phelypaea* and their activity as inhibitors of monoacylglycerol lipase (MAGL). *Planta Medica*. 2018 Jan;84:710-715. [<URL>](#).
- Bougandoura A, D'Abrosca B, Ameddah S, Scognamiglio M, Mekkiou R, Fiorentino A, Benayache S, Benayache F.

Chemical constituents and in vitro anti-inflammatory activity of *Cistanche violacea* Desf. (Orobanchaceae) extract. *Fitoterapia*. 2016 Mar;109:248-253. [<URL>](#).

11. Alia F, CHouikh A, Djahra AB, Bousbia Brahim A, Nani S, Tliba A. Comparative study of some physicochemical and biological properties of effect host species variation on the relationship Saharan parasitic plant *Cistanche violacea* (Desf.) Beck. *Notulae Scientia Biologicae*. 2021 Nov;13(4):11054. [<URL>](#).

12. Debouba M, Balti R, Hwiwi S, Zouari S. Antioxidant capacity and total phenols richness of *Cistanche violacea* hosting *Zygophyllum album*. *International Journal of Phytomedicine*. 2012; 4(3):399-402. [<URL>](#).

13. Ben Attia I, Zucca P, Marincola FC, Nieddu M, Piras A, Rosa A, Rescigno A, Chaieb M. Evaluation of the antioxidant and cytotoxic activities on cancer cell line of extracts of parasitic plants harvested in Tunisia. *Polish Journal of Food and Nutrition Science*. 2020 Mar;70(3):253-263. [<URL>](#).

14. Bouzayani B, Koubaa I, Frikha D, Samet S, Ben Younes A, Chawech R, Maalej S, Allouche N, Mezghani Jarraya R. Spectrometric analysis, phytoconstituents isolation and evaluation of in vitro antioxidant and antimicrobial activities of Tunisian *Cistanche violacea* (Desf). *Chemical Papers*. 2022 Jan;76(5):3031-3050. [<URL>](#).

15. Abdallah, EM. Antimicrobial evaluation of flowering stalks of *Cistanche violacea*, a holoparasitic plant collected from arid region in Qassim, Saudi Arabia. *Pharmaceutical and Biological Evaluations*. 2017 Dec;4(6):239-244. [<URL>](#).

16. Mihoub R, Chabour N, Guermoui M. Modeling soil temperature based on Gaussian process regression in a semi-arid-climate, case study Ghardaia, Algeria. *Geomechanics and Geophysics for Geo-Energy and Geo-Resources*. 2016 Jul;2:397-403. [<URL>](#).

17. Singleton VL, Orthofer R, Lamuela-Raventos RM. Analysis of total phenols and other oxidants substrates and antioxidants by means of Folin-Ciocalteu reagent. *Methods in Enzymology*. 1999;299:152-178. [<URL>](#).

18. Zhishen J, Mengcheng T, Jianming W. Research on antioxidant activity of flavonoids from natural materials. *Food Chemistry*. 1999 Mar;64:555-559. [<URL>](#).

19. Meguellati H, Ouafi S, Saad S, Harchaoui L, Djemouai N. Phytochemical characterization, *in vivo* and *in vitro* biological activities of *Atriplex lindleyi* Moq. subsp. *inflata*. *Journal of Ethnopharmacology*. 2024 Jan;117333. [<URL>](#).

20. Blois MS. Antioxidant determinations by the use of a stable free radical. *Nature*. 1958;181(4617):1119-1200. [<URL>](#).

21. Re R, Pellegrini N, Proteggente A, Pannala A, Yang M, Rice-Evans C. Antioxidant activity applying an improved ABTS radical cation decolorization assay. *Free Radical Biology and Medicine Journal*. 1999 May;26(98):1231-1237. [<URL>](#).

22. Oyaizu M. Studies on products of browning reaction: Antioxidative activities of products of browning reaction prepared from glucosamine. *The Japanese Journal of Nutrition and Dietetics*. 1986;44(6):307-315. [<URL>](#).

23. Szydłowska-Czerniak A, Dianoczki C, Recseg K, Karlovits G, Szlyk E. Determination of antioxidant capacities of vegetable oils by ferric-ion spectrophotometric methods. *Talanta*. 2008 Aug;76(4):899-905. [<URL>](#).

24. Pérez C, Agnese AM, Cabrera JL. The essential oil of *Senecio graveolens* (Compositae): Chemical composition and antimicrobial activity tests. *Journal of Ethnopharmacology*. 1999 Jul;66(1):91-96. [<URL>](#).

25. Miliuskas G, Venskutonis PR, Van Beek, TA. Screening of radical scavenging activity of some medicinal and aromatic plant extract. *Food chemistry*. 2004 Apr;85(2):231-237. [<URL>](#).

26. Ebrahimi NS, Hadian J, Mirjalili MH, Sonboli A, Yousefzadi M. Essential oil composition and antibacterial activity of *Thymus caramanicus* at different phenological stages. *Food Chemistry*. 2008 Oct;110(4):927-931. [<URL>](#).

27. Nićiforović N, Abramović H. Sinapic acid and its derivatives: Natural sources and bioactivity. *Comprehensive Reviews in Food Science and Food Safety*. 2014 Jan;13(1):34-51. [<URL>](#).

28. Sharma A, Sidhu GP, Araniti F, Bali AS, Shahzad B, Tripathi DK, Brestic M, Skalicky M, Landi M. The role of salicylic acid in plants exposed to heavy metals. *Molecules*. 2020 Jan;25(3):540. [<URL>](#).

29. Njus D, Kelley PM, Tu Y, Schlegel HB. Ascorbic acid: The chemistry underlying its antioxidant properties. *Free Radical Biology and Medicine*. 2020 Nov;159:37-43. [<URL>](#).

30. Küpeli Akkol E, Genç Y, Karpuz B, Sobarzo-Sánchez E, Capasso R. Coumarins and coumarin-related compounds in pharmacotherapy of cancer. *Cancers*. 2020 Jul;12(7):1959. [<URL>](#).

31. Bai J, Zhang Y, Tang C, Hou Y, Ai X, Chen X, Zhang Y, Wang X, Meng X. Gallic acid: Pharmacological activities and molecular mechanisms involved in inflammation-related diseases. *Biomedicine & Pharmacotherapy*. 2021 Jan;133:110985. [<URL>](#).

32. Purba R, Paengkoum S, Paengkoum P. Development of a simple high-performance liquid chromatography-based method to quantify synergistic compounds and their composition in dried leaf extracts of *Piper sarmentosum* Roxb. *Separations*. 2021 Sep;8(9):152. [<URL>](#).

33. Singab RA, Elleboudy NS, Elkhatib WF, Yassein MA, Hassouna NA. Improvement of caffeic acid biotransformation into para-hydroxybenzoic acid by *Candida albicans* CI-24 via gamma irradiation and model-based optimization. *Biotechnology and Applied Biochemistry*. 2021 Apr;69(2):469-478. [<URL>](#).

34. Olatunde A, Mohammed A, Ibrahim MA, Tajuddeen N, Shuaibu MN. Vanillin: A food additive with multiple biological activities. *European Journal of Medicinal Chemistry Reports*. 2022 Aug;5: 100055. [<URL>](#).

35. Xiao T, Yang L, Chen P, Duan X. Para-hydroxybenzaldehyde against transient focal cerebral ischemia in rats via mitochondrial preservation. *Experimental and Therapeutic Medicine*. 2022 Oct;24(6):716. [<URL>](#).

36. Li Y, Kong D, Fu Y, Sussman M R, Wu H. The effect of developmental and environmental factors on secondary metabolites in medicinal plants. *Plant Physiology and Biochemistry*. 2020 Mar;148:80-89. [<URL>](#).

37. Deyama T, Kobayashi(Late) H, Nishibe S, Tu P. Isolation, structure elucidation and Bioactivities of phenylethanoid glycosides from *Cistanche*, *Forsythia* and *Plantago* plants. *Studies in Natural Products Chemistry*. 2006 Mar;33:645-674. [<URL>](#).

38. Rahim, Meriem Z., Bhakti Prinsi, Luca Espen, Tarek Benabdelkader, Mohamed Nabiev, and Karim Houali. Comparative analysis of the chemical constituents and in vitro antioxidant activities of different aqueous extracts of *Cistanche phelypaea* (L.) Cout. from Algeria. *South African Journal of Botany*. 2022 August;148:259-267. [<URL>](#).
39. Kabtni S, Sdougua D, Bettaib Rebey I, Save M, Trifi-Farah N, Fauconnier ML, Marghali S. Influence of climate variation on phenolic composition and antioxidant capacity of *Medicago minima* populations. *Scientific reports*. 2020 May;10(1):1-15. [<URL>](#).
40. Aboul-Enein AM, El-Ela FA, Shalaby EA, El-Shemy HA. Traditional medicinal plants research in Egypt: Studies of antioxidant and anticancer activities. *Journal of Medicinal Plant Research*. 2012 Feb;6(5):689-703. [<URL>](#).
41. Trampetti F, Pereira C, Rodrigues MJ, Celaj O, D'Abrosca B, Zengin G, Mollica A, Stefanucci A, Custódio L. Exploring the halophyte *Cistanche phelypaea* (L.) Cout as a source of health promoting products: In vitro antioxidant and enzyme inhibitory properties, metabolomic profile and computational studies. *Journal of Pharmaceutical and Biomedical Analysis*. 2019 Feb;165:119-128. [<URL>](#).
42. Wang X, Wang J, Guan H, Xu R, Luo X, Su M, Chang X, Tan W, Chen J, Shi Y. Comparison of the chemical profiles and antioxidant activities of different parts of cultivated *Cistanche deserticola* using ultra performance liquid chromatography-quadrupole time-of-flight mass spectrometry and a 1, 1-diphenyl-2-picrylhydrazyl-based assay. *Molecules*. 2017 Nov;22(11):2011. [<URL>](#).
43. Hamed SEM, EL-Kamali HH. Antibacterial properties of methanolic and aqueous extracts of some plants against some Enterobacteriaceae species. *Open Access Library Journal*. 2016 Mar;3:e2488. [<URL>](#).
44. Keymanesh K, Hamedi J, Moradi S, Mohammadipanah F, Sardari S. Antibacterial and antifungal and toxicity of rare Iranian plants. *International Journal Pharmacology*. 2009;5(1):81-85. [<URL>](#).
45. Ullah N, Rehman A, Ahmad S, Samad N, Andaleeb H, Ahmad W, Ahmad K, Haroon M, Maqbool S, Altaf A, Raza N. Antimicrobial assay and minimum inhibitory concentration values of *Cistanche tubulosa*. *International Journal of Current Microbiology and Applied Sciences*. 2016 Feb;5(2):380-388. [<URL>](#).
46. Adnan M, Bibi R, Mussarat S, Tariq A, Shinwari ZK. Ethnomedicinal and phytochemical review of Pakistani medicinal plants used as antibacterial agents against *Escherichia coli*. *Annals of Clinical Microbiology and Antimicrobials*. 2014 Aug;13(1):40. [<URL>](#).
47. Fidrianny I, Rizkiya A, Ruslan K. Antioxidant activities of various fruit extracts from three *Solanum* sp. using DPPH and ABTS method and correlation with phenolic, flavonoid and carotenoid content. *Journal of Chemical and Pharmaceutical Research*. 2015 Jan;7(5):666-672. [<URL>](#).
48. Ali A, Shahu R, Balyan P, Kumari S, Ghodmare R, Jobby R, Jha P. Antioxidation and antiglycation properties of a natural sweetener: *Stevia rebaudiana*. *Sugar Tech*. 2022 Mar-Apr; 24(2):563-575. [<URL>](#).
49. Wang C, Cheng D, Cao J, Jiang W. Antioxidant capacity and chemical constituents of Chinese jujube (*Ziziphus jujuba* Mill.) at different ripening stages. *Food Science and Biotechnology*. 2013 Jun;22(3):639-644. [<URL>](#).
50. Pourmorad F, Hosseinimehr S J, Shahabimajid N. Antioxidant activity, phenol and flavonoid contents of some selected Iranian medicinal plants. *African Journal of Biotechnology*. 2006 Jun;5(11): 1142-1145. [<URL>](#).
51. Kalia K, Sharma K, Singh HP, Singh B. Effects of extraction methods on phenolic contents and antioxidant activity in aerial parts of *Potentilla atosanguinea* Lodd. and quantification of its phenolic constituents by RP-HPLC. *Journal of Agricultural and Food Chemistry*. 2008 Oct;56(21):10129-10134. [<URL>](#).
52. Amri O, Elguiche R, Tahrouch S, Zekhnini A, Hatimi A. Antifungal and antioxidant activities of some aromatic and medicinal plants from the southwest of Morocco. *Journal of Chemical and Pharmaceutical Research*. 2015 Jul;7(7):672-678. [<URL>](#).



Determination of Limonene Chirality in Oils Obtained from Different Types of Citrus Waste Peels in Türkiye

Barış Güzel^{1*} , Oltan Canlı¹ , Beyza Yüce¹ , Selda Murat Hocaoğlu¹ 

¹TUBITAK Marmara Research Center, Climate Change and Sustainability Vice Presidency, Water Management and Treatment Technologies Research Group, Kocaeli, 41470, Türkiye.

Abstract: Limonene constitutes a significant amount in citrus oils. It has a chiral structure and has two different optically active isomers, R-limonene and S-limonene, which are symmetrical to each other. Determining the chiral configurations of limonene plays an important role in determining the beneficial use areas of essential oils. Citrus oils are used in a wide variety of industrial areas, depending on their limonene content. This paper presents the analytical method optimization, validation, and chirality studies of limonene in the citrus oils acquired from different citrus waste peels in Türkiye. An inlet temperature of 250 °C and an injection volume of 2 µL were decided as the optimal conditions for the most accurate measurement of both limonenes in the citrus oil. This method produced results for linearity, sensitivity (LODs and LOQs), repeatability, and reproducibility that were acceptable within the scope of the validation studies. The chirality of limonene was investigated in twenty-six citrus oils (fifteen orange oils, six lemon oils, four mandarin oils, and one grapefruit oil) in Türkiye. While the content of R-limonene in orange oil varied between 56.39% and 72.85%, the content of S-limonene changed from 2.53% to 5.71%. Whereas the constituent of R-limonene in lemon oils ranged from 54.73% to 73.99%, the content of S-limonene varied between 3.78-4.79%. In mandarin oils, the content of R-limonene was determined to be 58.02% and 65.05%, while the content of S-limonene was found as 3.05% and 4.87%. In single grapefruit oil, R-limonene content was 60.69% and S-limonene content was 3.12%.

Keywords: Chirality, Citrus peel, Essential oil, Gas Chromatography, Mass Spectrometry, Limonene.

Submitted: September 20, 2023. **Accepted:** December 22, 2023.

Cite this: Güzel B, Canlı O, Yüce B, Murat Hocaoğlu S. Determination of Limonene Chirality in Oils Obtained from Different Types of Citrus Waste Peels in Türkiye. JOTCSA. 2024;11(2):469-76.

DOI: <https://doi.org/10.18596/jotcsa.1363425>

***Corresponding author's E-mail:** guzelbaris08@gmail.com

1. INTRODUCTION

Limonene is a naturally occurring compound found in the peels of citrus fruits such as lemons, mandarins, oranges, and grapefruits. It is commonly used as a flavoring agent in food and beverages, as well as a fragrance in cosmetics and cleaning products (1). The limonene molecule (C₁₀H₁₆) has a chiral structure and has two enantiomers, which are mirror images of each other (Figure 1). R-limonene (or D) and S-limonene (or L), which are symmetrical to each other (2,3). R-limonene is one of the enantiomers of limonene that is the naturally occurring form and has a fresh citrus aroma, often described as orange-like. This enantiomer is commonly found in citrus fruits and is used in various applications, including flavoring agents, fragrances, and cleaning products. S-limonene is a specific enantiomer of limonene, which is a naturally occurring compound found in the peels of citrus fruits. They have the same chemical

formula but differ in their spatial arrangement. In terms of its potential beneficial uses, S-limonene shares similar properties and potential health benefits as limonene in general (5,6).

There is a significant amount of scientific research conducted on limonene in citrus oils due to its wide range of applications and potential health benefits. Here are a few examples of scientific research studies related to limonene in citrus oils: (a) "Anticancer activity of citrus peel oil components limonene". The researchers found that these compounds exhibited anti-tumor activity against various types of cancer cells (7-9). (b) "Antioxidant and anti-inflammatory roles of limonene". Limonene's potential therapeutic applications in the prevention and treatment of several diseases are also highlighted (10-13). (c) "Limonene and its role in chronic diseases". Researchers are looking into limonene's potential for use in the treatment and prevention of chronic

illnesses like diabetes, obesity, and cardiovascular diseases. They discuss the mechanisms of action and the potential health benefits of limonene (14). (d) "Antimicrobial activity of the citrus fruit peel oils against pathogenic bacteria". The studies investigated the antimicrobial activity of citrus fruit peel oils, including limonene, against various pathogenic bacteria. The results showed that these

oils exhibited significant antimicrobial effects, suggesting their potential use as natural antimicrobial agents (15,16). (e) "Limonene inhalation reduces stress and improves immune function". The researchers found that limonene inhalation reduced stress-induced behaviors and improved immune function, suggesting its potential as a natural stress-relieving agent (17,18).

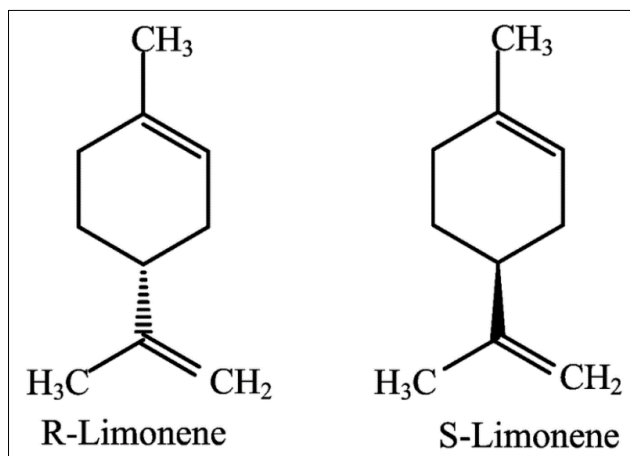


Figure 1: The chemical structure of limonene enantiomers (4).

The detection of limonene in citrus oils can be done using various analytical techniques. Here are a few commonly used methods: (a) Gas Chromatography (GC): GC is a widely used instrumental technique for analyzing volatile compounds like limonene. It involves separating the components of a sample based on their volatility and then detecting and quantifying them. GC coupled with a flame ionization detector (FID) or a mass spectrometer (MS) is commonly used for limonene analysis (19). (b) High-Performance Liquid Chromatography (HPLC): HPLC is another technique used for the analysis of limonene in citrus oils. It involves separating the components of a sample based on their chemical properties using a liquid mobile phase. Detection can be done using UV-Vis spectroscopy or other detectors (20). (c) Fourier Transform Infrared Spectroscopy (FTIR): FTIR spectroscopy can be used to identify and quantify limonene in citrus oils based on the characteristic absorption bands of the compound. It provides information about the functional groups present in the sample (21). (d) Nuclear Magnetic Resonance (NMR) Spectroscopy: NMR spectroscopy can be used to identify and quantify limonene in citrus oils. It provides information about the chemical structure and can be used to differentiate between different isomers of limonene (22). These are just a few examples of the techniques used for the detection of limonene in citrus oils. The choice of method depends on factors such as sensitivity, selectivity, and the equipment available in the laboratory.

In this study, we present the analytical method optimization, validation, and chirality studies of limonene in the citrus oils obtained from different citrus waste peels in Türkiye. It is thought that this study will contribute to the accurate chiral identification of limonene in citrus oils and different plant-based oils. The authors believed that the results of method optimi-

zation and validation studies would provide significant support for analytical method studies in this field.

2. EXPERIMENTAL SECTION

2.1. Reagents and Chemicals

Single standards ($\geq 99.9\%$ purity) of S-limonene (1000 $\mu\text{g/mL}$ in isopropanol) and R-limonene (1000 $\mu\text{g/mL}$ in isopropanol) in ampoule form were purchased from Dr. Ehrenstorfer (Augsburg, Germany). To make the corresponding stock solutions, Merck (Darmstadt, Germany) provided hexane with the highest analytical purity (GC gradient grade). By combining the aforementioned standards at equal concentrations (100 and 250 $\mu\text{g/mL}$ stock solutions in hexane), the desired concentrations were formed. The dilution of the required solutions for matrix-matched calibration curves or validation assays in hexane was conducted progressively.

2.2. Analytical Method Optimization

GC is a programmable analytical technique to successfully separate relative analytes in an analysis. Some GC parameters were optimized to get the best MS and analysis conditions in the experiments in this study. Thus, trial runs were carried out on the inlet temperature and injection volume parameters of the GC-MS device to determine the optimal conditions for the sensitive and accurate determination of enantiomers of limonene.

2.3. GC-MS Analytical Condition

Within the scope of this study, the determination of chirality of limonene (the amounts of R-limonene and S-limonene) was done by using GC-MS with Cyclosil-B column (length 30 m, id. 0.250 mm, film thickness 0.250 μm ; Agilent Technologies) as chiral column. Analytical separation was carried out by

temperature-programmed analysis and detection by electron ionization MS in full-scan mode. Details of the GC analysis program for chirality testing of limonene in citrus oils are presented in Table 1.

Table 1: GC analysis program for chirality testing of limonene in citrus oils.

Instrument	Agilent 6890N GC Single Quadropole MS		
Carrier Gas	Helium		
Carrier Gas Flow	1.1 mL/min.		
Column	Cyclosil-B		
Column Length	30 m		
Column Inner Diameter	0.25 mm		
Film Thickness	0.25 µm		
Detector Type	MS		
Detector Temperature	220 °C		
Electron Energy	70 eV		
Injection Volume	2 µL		
Auxiliary Temperature	230°C		
Oven Temperature Program	Ratio (°C/min)	Temperature (°C)	Retention Time (min.)
Initial		50	3
	10	100	5
	20	220	5

2.4. Sample Collection and Sample Preparation

The sampling studies were carried out to determine the chirality of limonene content in twenty-six citrus oils (fifteen orange oils (POR), six lemon oils (LİM), four mandarin oils (MAN), and one grapefruit oil (GREY)) from Anadolu Etap Agriculture and Food Products Industry and Trade Inc. obtained from Türkiye at different times. Citrus peels were used in the cold-pressed extraction process to produce the citrus oils that were provided. The TÜBITAK MAM laboratories received these oils in tightly sealed 1L containers with a cold chain. Up until the end of the studies, all samples were kept at +4 °C.

The water content in the citrus oil samples was eliminated by passing them through a sodium sulfate column before GC/MS analysis was performed on them. About 0.5 g of citrus oil samples were added into a glass tube and the samples were then spiked with 4.5 mL of hexane. In an ultrasonic bath, they were mixed for ten minutes. Finally, 2 µL of the sample in hexane was injected into the GC-MS after the mixture was diluted to 1 mL and put into a vial.

2.5. Performance of GC-MS method

The validation of the optimized GC-MS method involved conducting various studies, including an assessment of parameters such as linearity, sensitivity (limit of detections (LODs) and the limit of quantifications (LOQs)), repeatability, and reproducibility. This validation process adhered with EURACHEM Guidelines (23) and the Guidelines for Standard Method Performance Requirements (24).

3. RESULTS AND DISCUSSION

3.1. Assessment of Analytical Method Performance Studies

In this study, the retention times of R-limonene and S-limonene were determined in the GC chromatogram, at first. Figure 2 shows the GC-MS chromatogram obtained from the analysis of a mixture of R-limonene and S-limonene at a concentration of 10.0 mg/L. The retention times (min.) of S-limonene and R-limonene were 8.07 and 8.23, respectively.

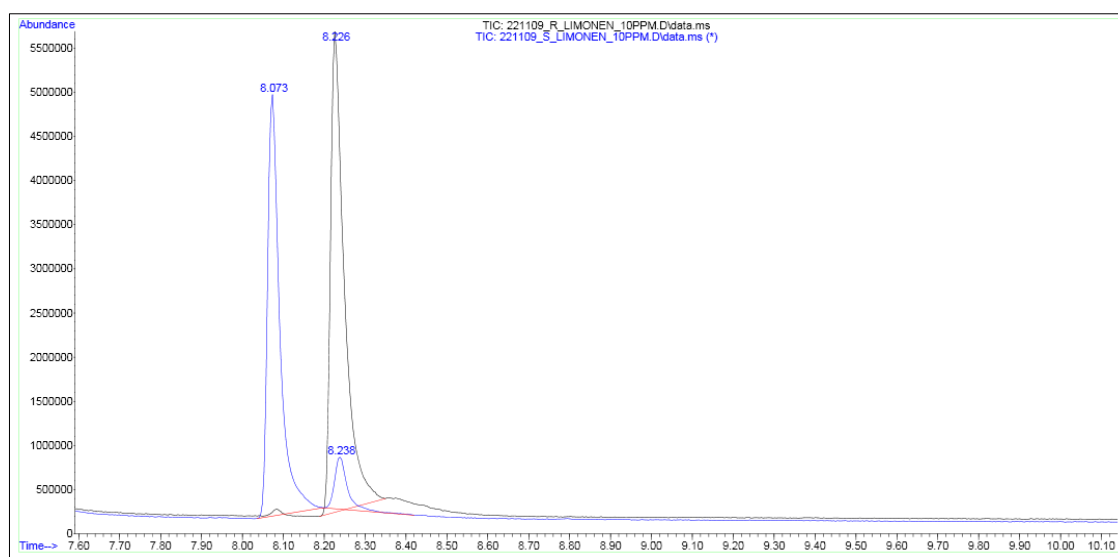


Figure 2: GC-MS chromatogram of R-limonene and S-limonene.

The method optimization stage aims to find the most suitable conditions for the most successful chromatographic separation of both limonenes. Considering the volatility of limonene, the determination of optimum conditions of the analytical method was conducted depending on the parameters of inlet temperature and injection volume of the GC-MS. First, the behaviour of terpenes was studied at five different inlet temperatures (230 °C, 240 °C, 250 °C, 260 °C, and 270 °C) (Figure 3a). After

determining the ideal inlet temperature, the signal efficiency of the limonene on the GC system was assessed at four different injection volumes (0.5 µL, 1 µL, 1.5 µL, and 2 µL) (Figure 3b). In accordance with the graphical results in Figure 3, an inlet temperature of 250 °C and an injection volume of 2 µL were decided as the optimal conditions for the most accurate measurement of both limonenes in the citrus oil.

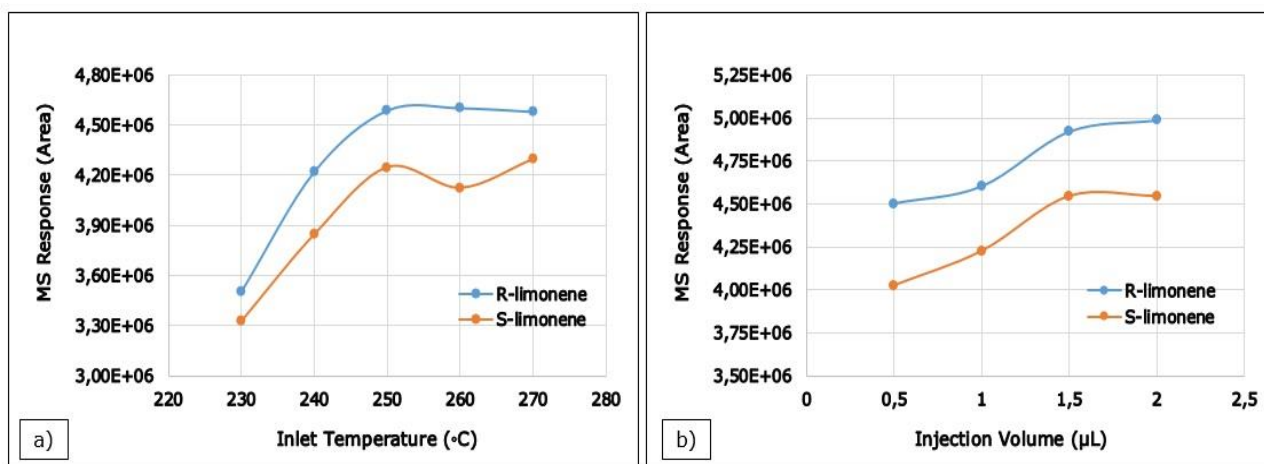


Figure 3: Effect of a) inlet temperature (°C), and b) injection volume (µL) on MS measurement of R-limonene and S-limonene.

Table 2 demonstrates information about the analytical method performance results of limonene enantiomers in citrus oils. Seven different concentration levels of each limonene - 1.00 mg/L, 2.00 mg/L, 5.00 mg/L, 10.0 mg/L, 25.0 mg/L, 50.0 mg/L, and 100 mg/L - were used to form the calibration curves for each one (Figure 4). The linear dynamic range of measurements for both was from 1.00 mg/L to 100 mg/L. As seen in Figure 4, the calibration coefficients (R^2) of S-limonene and R-

limonene were 0.9991 and 0.9976, respectively. In accordance with other comparable method validation studies in the literature (25-30), the correlation coefficient of a calibration curve denotes a good linear regression if it is greater than 0.99. In this regard, the values (R^2) of S-limonene and R-limonene indicate that the relevant calibration graphs have good linearity for accurate measurement.

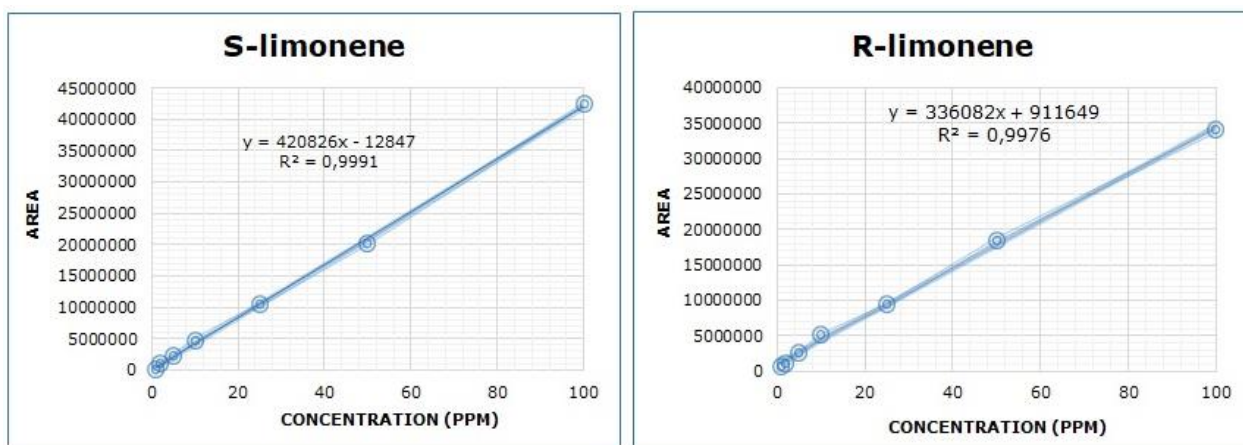


Figure 4: The linearity of calibration graphs of R-limonene and S-limonene.

To determine the LOD and LOQ of both limonenes, six injections of the mixture of relevant standards at different concentrations (1.00 mg/L and 2.00 mg/L) were made. The LODs were calculated taking into consideration the limonene peaks, which are clearly visible over the background noise in the chromatogram of the GC system. The LOD and LOQ values of both limonenes correspond to the signal-

to-noise ratio multiplied by 3 and 10. The LODs of R-limonene and S-limonene were found to be 0.08 mg/L and 0.09 mg/L, while their LOQs were calculated as 0.24 mg/L and 0.26 mg/L, respectively. As seen in Table 2, the values of LODs and LOQs of both limonenes are at a level comparable to studies in the literature in this field (31-33).

Table 2: Analytical method performance results of limonene enantiomers in citrus oils.

Parameters		R-limonene	S-limonene
Linear dynamic range (mg/L)		1-100	1-100
LOD (mg/L)		0.08	0.09
LOQ (mg/L)		0.24	0.26
Accuracy (5 mg/L)	Recovery (%)	90.82	4.86
	RSD (%)	2.21	5.28
	Mean Conc. (%)	8.86 ± 0.31	9.00 ± 0.26
Repeatability (10 mg/L; n=6)	Recovery (%)	88.62	89.98
	RSD (%)	3.58	2.98
	Mean Conc. (%)	4.40 ± 0.05	4.55 ± 0.10
(Reproducibility (5 mg/L; n=6))	Day-1 Recovery (%)	88.02	91.09
	Day-1 RSD (%)	1.07	2.11
	Day-1 Mean Conc. (%)	4.56 ± 0.07	4.48 ± 0.10
	Day-2 Recovery (%)	91.28	89.53
	Day-2 RSD (%)	1.54	2.24
	Day-2 Mean Conc. (%)		

RSD: Relative Standard Deviation

The accuracy test involved injecting a standard solution with a concentration of 5 mg/L into the mixture of citrus oils and taking six measurements to calculate the recovery of each limonene. The accuracy of the optimized method was required to be between 70 and 120% (accepted recovery range) (34, 35). Table 3 indicates that the mean recovery of R-limonene and S-limonene was 88.62% and 89.92% with an RSD of 2.21% and 5.28%, respectively. These results are within the acceptance range specified above, indicating that the method is sufficient in terms of measurement accuracy.

Six consecutive measurements at a concentration of 10.0 mg/L of each limonene were used to determine the precision's repeatability. Six consecutive measurements at a concentration of 5.00 mg/L on two different days were used to actualize the reproducibility of one person. In the precision test, it is considered acceptable if the results of repeatability and reproducibility are 15% lower in terms of RSD (34, 36). As shown in Table 2, the RSDs of both limonenes in the repeatability test were between 3.58% and 2.98%. In the reproducibility test, the RSDs of R-limonene changed from 1.07% to 1.54%, whereas the RSDs of S-limonene varied from 2.11% to 2.24%. The optimized method possesses a

satisfactory precision compared to the other research in the literature (34, 36-38).

3.2. Determination of Chirality of Limonene in Citrus Oils

The chirality of limonene in citrus oils made from various citrus waste peels was ascertained using the optimized and validated GC-MS method. The details of the chirality test results of limonene in different types of citrus oils in Türkiye by GC-MS are presented in Table 3. The results for total limonene content in relevant citrus oils were taken from previous work (19). R-limonene and S-limonene contents were calculated proportionally based on these results. The chirality of limonene was investigated in twenty-six citrus oils in Türkiye. While the content of R-limonene in orange oil varied between 56.39% and 72.85%, the content of S-limonene changed from 2.53% to 5.71%. Whereas the content of R-limonene in lemon oils ranged from 54.73% to 73.99%, the content of S-limonene varied between 3.78-4.79%. In mandarin oils, the content of R-limonene was determined to be 58.02% and 65.05%, while the content of S-limonene was found to be 3.05% and 4.87%. In single grapefruit oil, R-limonene content was 60.69% and S-limonene content was 3.12%.

Table 3: Chirality test results of limonene in different citrus oils in Türkiye.

Type of Citrus Oil / Ingredient	Total Limonene (%)	R-limonene (%)	S-limonene (%)
LIM-1	62.54	57.75	4.79
LIM-2	58.56	54.73	3.83
LIM-3	62.29	58.51	3.78
LİM-4	69.92	65.94	3.98
LİM-5	74.67	70.55	4.12
LİM-6	78.08	73.99	4.09
MAN-1	62.89	58.02	4.87
MAN-2	66.31	63.26	3.05
MAN-3	69.91	65.05	4.86
MAN-4	67.82	63.05	4.77
GREY-1	63.81	60.69	3.12
POR-1	70.48	67.09	3.39
POR-2	66.88	61.69	5.19
POR-3	68.25	62.70	5.55
POR-4	70.32	65.98	4.34
POR-5	60.49	56.39	4.10
POR-6	66.14	62.79	3.35
POR-7	74.27	68.56	5.71
POR-8	73.17	69.22	3.95
POR-9	71.31	66.95	4.36
POR-10	75.12	72.59	2.53
POR-11	67.67	63.41	4.26
POR-12	66.87	61.46	5.41
POR-13	67.58	63.09	4.49
POR-14	65.36	62.11	3.25
POR-15	78.06	72.85	5.21

4. CONCLUSION

This paper presented detailed information about the analytical method optimization, validation, and chirality studies of limonene in the citrus oils obtained from different citrus waste peels in Türkiye. An analytical method containing a chiral column (Cyclosil-B) in the GC-MS was optimized for the simultaneous determination of R-limonene and S-limonene in citrus oils (orange oil, lemon oil, mandarin oil, and grapefruit oil) at first. Then, the validation of the optimized GC-MS method was performed with some studies in accordance with the related international guidelines. Finally, the amount of both limonenes in citrus oils was measured with the optimized and validated GC-MS method. At the end of the determination of optimal conditions, an inlet temperature of 250 °C and an injection volume of 2 µL were determined as the optimal conditions in the measurement of both limonenes in the citrus oil, precisely. This method produced the results for linearity, sensitivity (LODs and LOQs), repeatability, and reproducibility that were desirable. In Türkiye, while the content of R-limonene in orange oil varied between 56.39% and 72.85%, the content of S-limonene changed from 2.53% to 5.71%. Whereas the content of R-limonene in lemon oils ranged from 54.73% to 73.99%, the content of S-limonene varied between 3.78-4.79%. In mandarin oils, the content of R-limonene was determined as 58.02% and 65.05%, while the content of S-limonene was found as 3.05% and 4.87%. In single grapefruit oil, R-limonene content was 60.69% and S-limonene content was 3.12%. The study provides a significant alternative method for the sensitive, accurate, and

simultaneous identification of limonene in citrus oils and different plant-based oils in terms of literature. With the analytical method's optimum conditions, it will prevent analytical devices from losing performance in a shorter time by providing significant savings in energy and time.

5. CONFLICT OF INTEREST

The authors declare that they have no known competing financial interests or personal relationships that could have appeared to influence the work reported in this paper.

6. ACKNOWLEDGMENTS

This work was performed within the development of a process for the production of a bio-based, two-component epoxy resin from renewable raw materials project - CORNET multi-collaboration program, funded by TUBITAK with Project Number: 220N255.

7. REFERENCES

1. Pourbafrani M, Forgács G, Horváth IS, Niklasson C, Taherzadeh MJ. Production of biofuels, limonene and pectin from citrus wastes. *Bioresour Technol* [Internet]. 2010 Jun;101(11):4246–50. Available from: [<URL>](#).
2. Ciriminna R, Lomeli-Rodriguez M, Demma Carà P, Lopez-Sanchez JA, Pagliaro M. Limonene: a versatile chemical of the bioeconomy. *Chem Commun* [Internet]. 2014;50(97):15288–96. Available from: [<URL>](#).

3. Siddiqui SA, Pahmeyer MJ, Assadpour E, Jafari SM. Extraction and purification of d-limonene from orange peel wastes: Recent advances. *Ind Crops Prod* [Internet]. 2022 Mar;177:114484. Available from: [<URL>](#).
4. Wei F, Xu Y, Guo Y, Liu S, Wang H. Quantitative Surface Chirality Detection with Sum Frequency Generation Vibrational Spectroscopy: Twin Polarization Angle Approach. *Chinese J Chem Phys* [Internet]. 2009 Dec 1;22(6):592–600. Available from: [<URL>](#).
5. Friedman L, Miller JG. Odor Incongruity and Chirality. *Science* (80-) [Internet]. 1971 Jun 4;172(3987):1044–6. Available from: [<URL>](#).
6. Boelens MH, Boelens H, Van Gemert LJ. Sensory properties of optical isomers. *Perfum Flavorist* [Internet]. 1993;18(6):1–16. Available from: [<URL>](#).
7. Chaudhary S, Siddiqui M, Athar M, Alam MS. D-Limonene modulates inflammation, oxidative stress and Ras-ERK pathway to inhibit murine skin tumorigenesis. *Hum Exp Toxicol* [Internet]. 2012 Aug 8;31(8):798–811. Available from: [<URL>](#).
8. Hakim IA, Harris RB, Ritenbaugh C. Citrus Peel Use Is Associated With Reduced Risk of Squamous Cell Carcinoma of the Skin. *Nutr Cancer* [Internet]. 2000 Jul 18;37(2):161–8. Available from: [<URL>](#).
9. Lu X-G, Zhan L-B, Feng B-A, Qu M-Y, Yu L-H, Xie J-H. Inhibition of growth and metastasis of human gastric cancer implanted in nude mice by d - limonene. *World J Gastroenterol* [Internet]. 2004;10(14):2140–4. Available from: [<URL>](#).
10. Hirota R, Roger NN, Nakamura H, Song H, Sawamura M, Suganuma N. Anti-inflammatory Effects of Limonene from Yuzu (Citrus junos Tanaka) Essential Oil on Eosinophils. *J Food Sci* [Internet]. 2010 Apr 5;75(3):H87–92. Available from: [<URL>](#).
11. Rufino AT, Ribeiro M, Sousa C, Judas F, Salgueiro L, Cavaleiro C, et al. Evaluation of the anti-inflammatory, anti-catabolic and pro-anabolic effects of E-caryophyllene, myrcene and limonene in a cell model of osteoarthritis. *Eur J Pharmacol* [Internet]. 2015 Mar;750:141–50. Available from: [<URL>](#).
12. Yoon W-J, Lee NH, Hyun C-G. Limonene Suppresses Lipopolysaccharide-Induced Production of Nitric Oxide, Prostaglandin E2, and Pro-inflammatory Cytokines in RAW 264.7 Macrophages. *J Oleo Sci* [Internet]. 2010;59(8):415–21. Available from: [<URL>](#).
13. Yu L, Yan J, Sun Z. D-limonene exhibits anti-inflammatory and antioxidant properties in an ulcerative colitis rat model via regulation of iNOS, COX-2, PGE2 and ERK signaling pathways. *Mol Med Rep* [Internet]. 2017 Mar;15(4):2339–46. Available from: [<URL>](#).
14. Pizzino G, Irrera N, Cucinotta M, Pallio G, Mannino F, Arcoraci V, et al. Oxidative Stress: Harms and Benefits for Human Health. *Oxid Med Cell Longev* [Internet]. 2017;2017:8416763. Available from: [<URL>](#).
15. Mizrahi B, Shapira L, Domb AJ, Hour-Haddad Y. Citrus Oil and MgCl₂ as Antibacterial and Anti-Inflammatory Agents. *J Periodontol* [Internet]. 2006 Jun;77(6):963–8. Available from: [<URL>](#).
16. Naveed R, Hussain I, Tawab A, Tariq M, Rahman M, Hameed S, et al. Antimicrobial activity of the bioactive components of essential oils from Pakistani spices against Salmonella and other multi-drug resistant bacteria. *BMC Complement Altern Med* [Internet]. 2013 Dec 14;13(1):265. Available from: [<URL>](#).
17. Asikin Y, Shimizu K, Iwasaki H, Oku H, Wada K. Stress amelioration and anti-inflammatory potential of Shiikuwasha (Citrus depressa Hayata) essential oil, limonene, and γ-terpinene. *J Food Drug Anal* [Internet]. 2022 Sep 14;30(3):454–65. Available from: [<URL>](#).
18. Eddin LB, Jha NK, Meeran MFN, Kesari KK, Beiram R, Ojha S. Neuroprotective Potential of Limonene and Limonene Containing Natural Products. *Molecules* [Internet]. 2021 Jul 27;26(15):4535. Available from: [<URL>](#).
19. Güzel B, Canlı O, Murat Hocoğlu S. Method development and validation for accurate and sensitive determination of terpenes in bio-based (citrus) oils by single quadrupole gas chromatography-mass spectrometry (GC/MS). *Microchem J* [Internet]. 2023 Aug;191:108903. Available from: [<URL>](#).
20. Bernart MW. Ultra-High Performance Liquid Chromatography (UHPLC) Method for the Determination of Limonene in Sweet Orange (Citrus sinensis) Oil: Implications for Limonene Stability. *J AOAC Int* [Internet]. 2015 Jan 1;98(1):94–7. Available from: [<URL>](#).
21. Agatonovic-Kustrin S, Ristivojevic P, Gegechkori V, Litvinova TM, W. Morton D. Essential Oil Quality and Purity Evaluation via FT-IR Spectroscopy and Pattern Recognition Techniques. *Appl Sci* [Internet]. 2020 Oct 19;10(20):7294. Available from: [<URL>](#).
22. Marti G, Boccard J, Mehl F, Debrus B, Marcourt L, Merle P, et al. Comprehensive profiling and marker identification in non-volatile citrus oil residues by mass spectrometry and nuclear magnetic resonance. *Food Chem* [Internet]. 2014 May;150:235–45. Available from: [<URL>](#).
23. Magnusson B, Örnemark U. Eurachem Guide: The Fitness for Purpose of Analytical Methods – A Laboratory Guide to Method Validation and Related Topics. 2014; Available from: [<URL>](#).
24. AOAC. Guidelines for Standard Method Performance Requirements Appendix F. 2016; Available from: [<URL>](#).
25. Al-Alam J, Baroudi F, Chbani A, Fajloun Z, Millet M. A multiresidue method for the analysis of pesticides, polycyclic aromatic hydrocarbons, and

- polychlorinated biphenyls in snails used as environmental biomonitors. *J Chromatogr A* [Internet]. 2020 Jun;1621:461006. Available from: [<URL>](#).
26. Canlı O, Oktem Olgun E, Güzel B, Kaplan M. Sensitive and accurate determination of 168 micropollutants including pharmaceuticals and pesticides in surface water and wastewater samples with direct injection using jet stream ESI LC-MS/MS. *Int J Environ Anal Chem* [Internet]. 2022 Mar 23;(Article in Press):1–27. Available from: [<URL>](#).
27. Canlı O, Güzel B, Çetintürk K. Determination of Ethylenediaminetetraacetic acid (EDTA) levels in surface waters by high performance liquid chromatography (HPLC)-Ultraviolet/Visible (UV/VIS) detector. *Turkish J Anal Chem* [Internet]. 2022 Dec 29;4(2):76–9. Available from: [<URL>](#).
28. Güzel B, Canlı O, Öktem Olgun E. Gas Chromatography Method Validation Study for Sensitive and Accurate Determination of Volatile Aromatic Hydrocarbons (VAHs) in Water. *Cumhur Sci J* [Internet]. 2018 Dec 24;39(4):970–82. Available from: [<URL>](#).
29. Güzel B. Method validation for the sensitive and simultaneous detection of fifty-five volatile organic compounds (VOCs) with human health hazards in environmental waters. In: Çoğun HY, Parlar İ, Üzmuş H, editors. *Current Debates on Natural and Engineering Sciences 9* [Internet]. Bilgin Kültür Sanat Yayınları; 2023. p. 456–74. Available from: [<URL>](#).
30. de Souza SVC, Junqueira RG. A procedure to assess linearity by ordinary least squares method. *Anal Chim Acta* [Internet]. 2005 Nov;552(1–2):25–35. Available from: [<URL>](#).
31. Giese MW, Lewis MA, Giese L, Smith KM. Method for the Analysis of Cannabinoids and Terpenes in Cannabis. *J AOAC Int* [Internet]. 2015 Nov 1;98(6):1503–22. Available from: [<URL>](#).
32. Nguyen T-D, Riordan-Short S, Dang T-TT, O'Brien R, Noestheden M. Quantitation of Select Terpenes/Terpenoids and Nicotine Using Gas Chromatography–Mass Spectrometry with High-Temperature Headspace Sampling. *ACS Omega* [Internet]. 2020 Mar 17;5(10):5565–73. Available from: [<URL>](#).
33. Ponce-Rodríguez HD, Herráez-Hernández R, Verdú-Andrés J, Campíns-Falcó P. Quantitative Analysis of Terpenic Compounds in Microsamples of Resins by Capillary Liquid Chromatography. *Molecules* [Internet]. 2019 Nov 10;24(22):4068. Available from: [<URL>](#).
34. Huang C, Bian C, Wang L, Zhou W, Li Y, Li B. Development and validation of a method for determining d-limonene and its oxidation products in vegetables and soil using GC–MS. *Microchem J* [Internet]. 2022 Aug;179:107470. Available from: [<URL>](#).
35. Sayed R, Hussein OE, Omran AA. Method optimization and validation for the determination of mancozeb in chamomile by modified QuEChERS and liquid chromatography–tandem mass spectrometry. *J Food Compos Anal* [Internet]. 2022 Aug;111:104646. Available from: [<URL>](#).
36. Ibrahim E, Wang M, Radwan M, Wanas A, Majumdar C, Avula B, et al. Analysis of Terpenes in Cannabis sativa L. Using GC/MS: Method Development, Validation, and Application. *Planta Med* [Internet]. 2019 Mar 15;85(05):431–8. Available from: [<URL>](#).
37. Emberger ME, Lin J, Pika J, Christ I, Eigenbrodt B. Automated Solid-Phase Microextraction GC-MS/MS Method for Quantification of Volatile Limonene Oxidation Products in Encapsulated Orange Oil. *Flavour Fragr J* [Internet]. 2019 Jan 5;34(1):52–62. Available from: [<URL>](#).
38. Marine SS, Clemons J. Determination of Limonene Oxidation Products Using SPME and GC-MS. *J Chromatogr Sci* [Internet]. 2003 Jan 1;41(1):31–5. Available from: [<URL>](#).



Sonochemical Synthesis of Copper Borates: Effect of Reaction Conditions on the Characteristic Properties

Fatma Tuğçe Şenberber Dumanli¹ , Sibel Kavci Karaagac² , Azmi Seyhun Kipcak² ,
Emek Moroydor Derun^{2*} 

¹Istanbul Nisantasi University, Department of Civil Engineering, Istanbul, 34398, Turkey

²Yildiz Technical University, Department of Chemical Engineering, Istanbul, 34210, Turkey

Abstract: The effect of ultrasonic treatment on liquid-state production and the characteristic features of synthesized powder were studied in liquid-state conditions. In sonochemical synthesis, the operation parameters of mole ratio, reaction temperature, and time were optimized. The synthesis was achieved in moderate conditions such as mole ratio of copper: sodium: boron (Cu: Na: B) 1:2:1, 70°C and 2.5 minutes. The prepared samples were identified as copper borate ($\text{Cu}(\text{BO}_2)_2$) with the powder diffraction file number "00-001-0472". The reaction yields were also increased from 50% to 71.5% with the modification of the experimental procedure. The specific FT-IR peaks were observed at 1090, 985, 872, 781 and 731 cm^{-1} band values. In the morphological analyses, the agglomerations of multi-angular particles were seen. The results showed the affirmative effects of the possible use of the ultrasonic treatment on both the practical synthesis and the increase of characteristics.

Keywords: Copper; Borate; X-ray methods; Spectroscopy; SEM; Ultrasound.

Submitted: August 9, 2023. **Accepted:** November 20, 2023.

Cite this: Şenberber Dumanli FT, Kavci Karaagac S, Kipcak AS, Moroydor Derun E. Sonochemical Synthesis of Copper borates: Effect of Reaction Conditions on the Characteristic Properties. JOTCSA. 2024;11(2):477-82.

DOI: <https://doi.org/10.18596/jotcsa.1342058>

***Corresponding author.** E-mail: moroydor@yildiz.edu.tr

1. INTRODUCTION

Metal borates are defined as compounds including metal atoms, boron, oxygen, and hydrogen, if any. Commonly, three coordinated trigonal and four coordinated tetragonal groups of boron and oxygen are bonded to metal atoms. The metal borates can be defined according to the metal atom in structure (1). As a member of the borate family, copper borates occur from the different combinations of copper and boron atoms such as CuBO_2 , $\text{Cu}(\text{BO}_2)_2$, $\text{Cu}_3\text{B}_2\text{O}_6$, and $3\text{CuO}\cdot 2\text{B}_2\text{O}_3\cdot 6\text{H}_2\text{O}$ (2). The fabrication of copper borates draws attention because of their unique crystallographic structures, and they exhibit electrical, magnetic, and optical features (3). Among the delafossite group compounds, copper borates have the largest band gap (4,5). Copper borates are mostly utilized in linear and non-linear optical devices, hydrogen generation systems, and photocatalytic reactions. Also, this type of borate has applications in fire retardants, wood preservation, the design of ion exchange materials,

and lubricant additives (6–9). These characteristics make their synthesis important. Different procedures were experimented with to synthesize the copper borate at different compositions and characteristics, such as supercritical, hydrothermal, solvothermal, and solid-state (10–12). With the optimization of reaction conditions, the modified particle fabrication of copper borates could be probable (13,14).

Alp et al. indicated the effects of pH on the colorimetric features of synthesized powder, and the darker samples were prepared in alkaline conditions (2). Pisarev et al. characterized the piezoelectric form of copper borate in tetragonal lattice (6). Kahalili et al. studied the catalytic activities of boron-containing copper complexes in organic reactions (15). Kipcak et al. studied the effect of copper and boron sources on the prepared sample using a traditional hydrothermal method (16).

The studies on copper borate clarified the importance of optimizing the parameters to obtain the sample at the highest reaction yield and crystallinity. As a developing technology, ultrasound treatment can be used to increase contact of raw material in liquid-state conditions. With the use of ultrasound treatment in the synthesis procedure, the required reaction time and temperature can be decreased, whereas the reaction yield and crystallinity of the sample can be increased (17). In this paper, it is aimed to investigate the suitability of sonochemical synthesis for copper borate fabrication without using any modification agent. Also, the effect of reaction conditions on the characteristics of prepared copper borate was studied by using the techniques of X-ray diffraction (XRD), Fourier Transform Infrared Spectroscopy (FT-IR), and Scanning Electron Microscope (SEM).

2. EXPERIMENTAL SECTION

2.1. Materials

The copper source used in the experiments was copper sulphate pentahydrate ($\text{CuSO}_4 \cdot 5\text{H}_2\text{O}$) purchased from Sigma Aldrich at a minimum purity

of %98. Boron source of boric acid (H_3BO_3), with a minimum purity of %99, was provided by Eti Mine Boron Works in the region of Bandirma, Turkey. Sodium hydroxide (NaOH) was obtained from Merck Chemicals at the minimum purity of %97.

2.2. Synthesis

In liquid-state conditions, the probable reaction can be seen in Eq. 1, and the experimental design is presented in Figure 1. The experimental procedure could be explained in two steps. In the first step, the starting materials were dissolved in distilled water and reacted with the effect of ultrasound at 80°C for 5 minutes. For the sonochemical synthesis, an ultrasonic probe of Bandelin was employed. The determined molar ratios of $\text{CuSO}_4 \cdot 5\text{H}_2\text{O}$: NaOH: H_3BO_3 were 1:2:0.8, 1:2:1, 1:2:1.33, 1:2:2, and 1:2:4. In the second step of the synthesis, the effect of temperature and time were examined. The samples were prepared at the reaction temperatures of 70, 80, and 90°C for the reaction times of 2.5, 5, 10, and 15 minutes. After the reaction was completed, the solutions were washed, filtered, and dried in an Ecocell incubator.

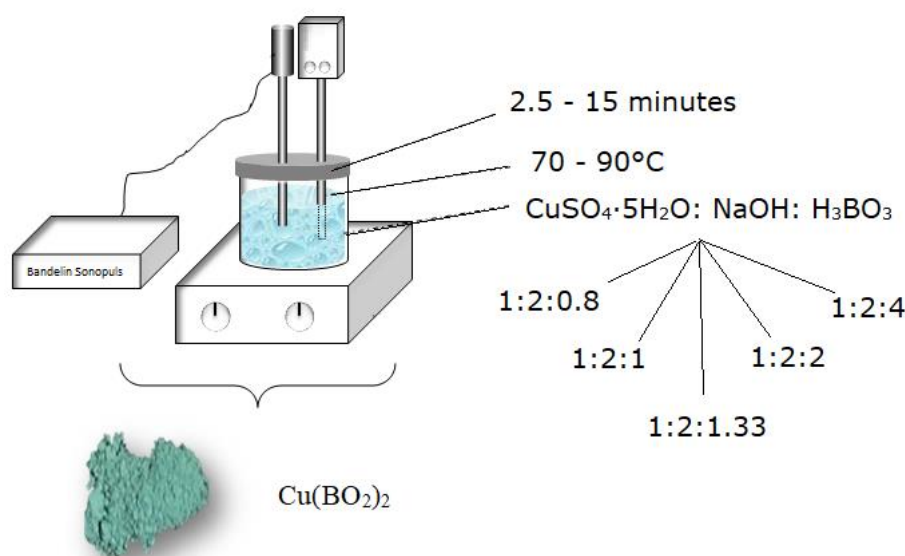
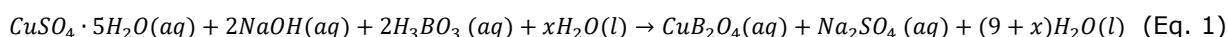


Figure 1: The experimental design for the sonochemical synthesis of copper borates

2.3. Characterization of the Synthesized Samples

The prepared powders underwent X-ray diffraction analysis for the identification of obtained phases by using a PANalytical Xpert Pro X-Ray Diffractometer at the operating conditions of 45 kV, 40 mA, and in the 2θ range of $10 - 70^\circ$. In the characterization of functional groups of structure, the samples were subjected to Fourier Transform Infrared (FT-IR) Spectroscopy by using a Jasco 6000 Fourier Transform Infrared Spectrometer. For the morphological characterization, the Scanning Electron Microscope of Tescan Vega 3 (SEM) was used at the operating conditions of 15 kV and magnification values of 400 X.

In estimating reaction yields, $\text{CuSO}_4 \cdot 5\text{H}_2\text{O}$ was identified as the key component in the experiments. Typically, the product moles at the last stage, N_P , were divided by the consumed moles of the key reactant, A, to calculate the overall yield, Y. The moles of A that were consumed were determined by using the reactant's final (N_A) and initial (N_{A0}) moles. For a batch system, the calculation of reaction yield was given in Eq. 2 (18).

$$Y = \frac{N_P}{N_{A0} - N_A} \quad (\text{Eq. 2})$$

3. RESULTS AND DISCUSSION

3.1. XRD Results

In the XRD analyses, the obtained phases matched $Cu(BO_2)_2$ with the powder diffraction file number "00-001-0472". XRD patterns of the mole ratio experiments are shown in Figure 2. XRD patterns indicated the lower peaks formation of crystalline

phase in the mole ratio (Cu: Na:B) of 1:2:0.8. At the 1:2:1 ratio, the characteristic peaks were observed at the 2θ values of 13.82° , 16.71° , 22.90° , 28.13° , 33.67° , 35.74° and 52.89° . Counts of the obtained peaks were in decline at the higher ratios of boric acid, and the sample was identified as amorphous at the ratio of 1:2:4.

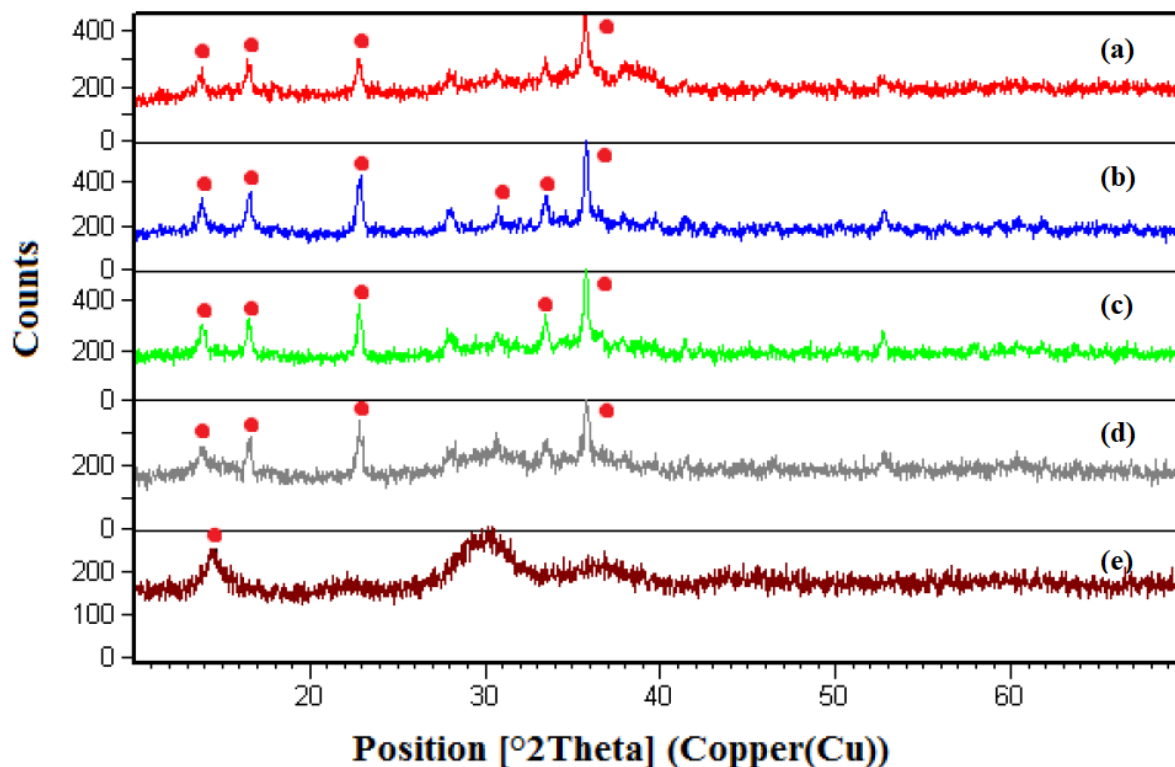


Figure 2: XRD patterns of the mole ratio experiments (a) 1:2:0.8, (b) 1:2:1, (c) 1:2:1.33, (d) 1:2:2, and (e) 1:2:4.

At the mole ratio of 1:2:1, the XRD scores of the samples at different temperatures and times are given in Table 1. According to the XRD results, the optimum reaction conditions were determined to be $70^\circ C$ and 2.5 minutes. Compared with the

traditional hydrothermal synthesis procedure, ultrasonic treatment in the experimental procedure positively affected the formation and decreased the reaction time (16).

Table 1: XRD scores of the samples at different temperatures and times.

Temperature ($^\circ C$)	Time (min)	XRD Score
90	2.5	38
	5.0	*
	10	25
	15	*
80	2.5	30
	5.0	13
	10	25
	15	40
70	2.5	41
	5.0	27
	10	*
	15	*

3.2. The Results of Reaction Yields

The plots of reaction yield percentages with the changing reaction parameters, such as mole ratios, reaction time, and temperature, can be seen in Figure 3. The effect of the mole ratio of the sources can be seen in the reaction yield as well as crystallinity (Figure 3 (a)). The calculated reaction yield percentages were in the range of 50 – 71.5%. Among the different mole ratios, the highest reaction yield percentage was obtained at the ratio of 1:2:1. In Figure 3 (b), minor increases were obtained with increasing temperature and time. The highest reaction yield was estimated to be 71.5% at the reaction temperature of 90°C and 15 mins.

3.3. FT-IR results

The characteristic band values observed in the IR range of the prepared sample at 70°C and 2.5 minutes were presented in Figure 4. According to the FT-IR results, the peaks between 1090 and 985 cm^{-1} are related to the asymmetrical stretching of four-coordinate boron to oxygen bands [$\nu_{as}(\text{B}_{(4)}\text{-O})$]. The stretching observed at 872 cm^{-1} can be explained by the symmetrical stretching of three-coordinate boron to oxygen bands [$\nu_s(\text{B}_{(3)}\text{-O})$]. The characteristic band values in the range of 781 and 731 cm^{-1} indicated the symmetrical stretching of four-coordinate boron to oxygen bands [$\nu_s(\text{B}_{(4)}\text{-O})$].

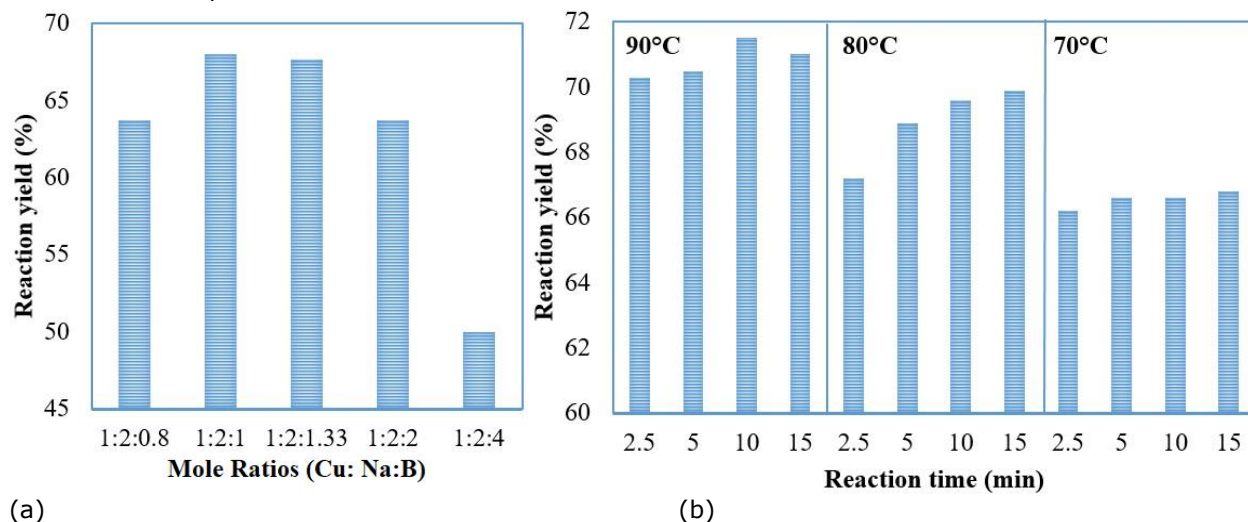


Figure 3: Reaction yields at (a) different mole ratios (1:2:0.8, 1:2:1, 1:2:1.33, 1:2:2, and 1:2:4) and (b) different reaction temperatures and times (70, 80, and 90°C; 2.5, 5, 10, and 15 minutes).

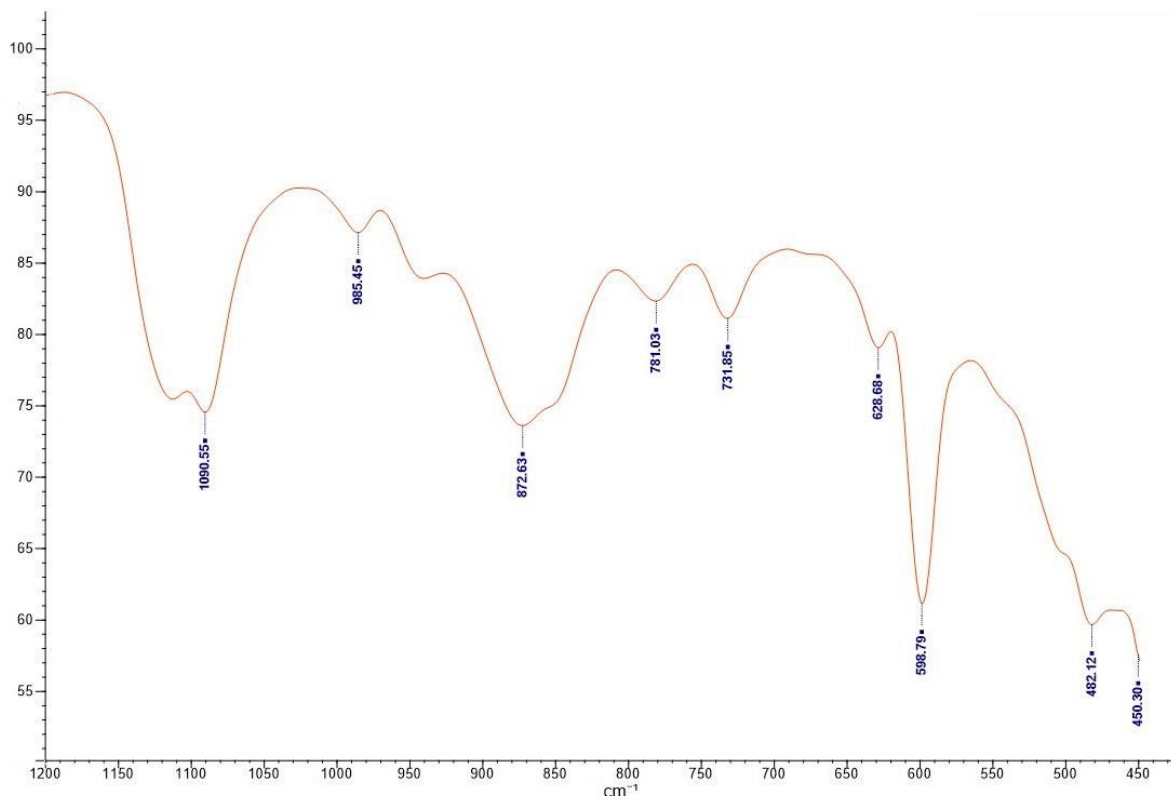


Figure 4: FT-IR spectrum of the prepared sample at 70°C and 2.5 minutes.

From the spectral results obtained, it is seen that the specific boron to oxygen bands were achieved in the preparation and that these B to O bands are in good agreement with Zheng et al. and Yongzhong et al. (14, 19).

3.4. SEM results

The morphology of the prepared sample at 70°C and 2.5 minutes was given in Figure 5. With the effect of intramolecular hydrogen bonding, the agglomeration of sub-micron scale particles could be seen in the SEM results. The multi-angular particle formation could explain the morphology of the sample.

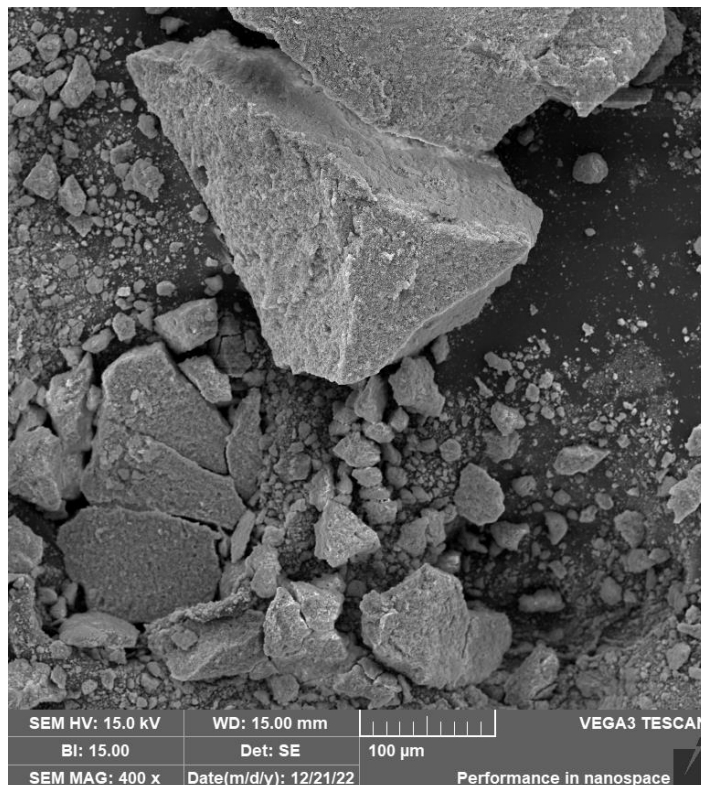


Figure 5: Morphology of the prepared sample at 70°C and 2.5 minutes.

The obtained morphology was in good agreement with the previous studies. Compared with the traditional liquid-state synthesis method, homogeneity in the surface was observed (16).

4. CONCLUSION

The copper borate (CuBO_2)₂ was successfully synthesized in moderate liquid-state conditions with the help of ultrasonic treatment. The reaction conditions were optimized for the modified experimental procedure, and the possible reaction mechanism was estimated. The optimum reaction parameters can be summarized as the mole ratio (Cu:Na:B) of 1:2:8, the reaction temperature of 70°C, and a reaction time of 2.5 minutes. The experimental results indicated the beneficial effects of ultrasonic treatment on the characteristic features of the prepared sample. The temperature also increased the reaction yield; however, the crystallinity decreased. This situation can be interpreted as being temperature-sensitive to the obtained phases. The reaction time was decreased, and the fabricated powder's crystallinity was increased with the help of ultrasonic treatment. The obtained characteristic band values of FT-IR were in good agreement with the previous studies.

5. CONFLICT OF INTEREST

The author declares no conflict of interest.

6. REFERENCES

1. Senberber FT, Derun EM. Thermal Kinetics and Thermodynamics of the Dehydration Reaction of Inyoite ($\text{Ca}_2\text{B}_6\text{O}_6(\text{OH})_{10} \cdot 8\text{H}_2\text{O}$). *Glass Phys Chem.* 2020;46(1):64-71. Available from: [<URL>](#)
2. Alp B, Atakul Savrik S, Balkose D. Preparation and Characterization of Copper Borates as Lubricant Additives. *J Mater Sci Eng B.* 2014;4(4). Available from: [<URL>](#)
3. Thatribud A, Tungsurat T, Pengpan T. First-principles study on electronic and optical properties of transparent conducting oxide CuBO_2 . *Comput Mater Sci.* 2014;81:601-6. Available from: [<URL>](#)
4. Zia W, Siraj K, Faiz H, Firdos A. A facile synthesis of single phase delafossite CuBO_2 powders. *Mater Res Express.* 2019; 6(9):096314. Available from: [<URL>](#)
5. Santra S, Das NS, Maiti S, Chattopadhyay KK. Wide band gap p-type CuBO_2 nanostructures by hydrothermal route and fabrication high quality p- CuBO_2 /n-ZnO nano-heterojunction. *Chem Phys Lett.* 2014;604:97-100. Available from: [<URL>](#)

6. Pisarev RV, Boldyrev KN, Popova MN, Smirnov AN, Davydov VYu, Bezmaternykh LN, vd. Lattice dynamics of piezoelectric copper metaborate CuB_2O_4 . *Phys Rev B*. 2013;88(2):024301. Available from: [<URL>](#)
7. Liu LL, Zhu D, Cao LL, Stephan DW. N-Heterocyclic carbene stabilized parent sulfenyl, selenenyl, and tellurenyl cations (XH^+ , X = S, Se, Te). *Dalton Trans*. 2017;46(10):3095-9. Available from: [<URL>](#)
8. Soylu M, Al-Ghamdi AA, Omran SB, Yakuphanoglu F. Rectifying structure with high voltage operation based on CuBO_2 as an UV photocatalyst. *J Alloys Compd*. 2014;617:602-8. Available from: [<URL>](#)
9. Zhang HH, Kong N, Wang J, Liu ZH. Thermodynamic properties of microporous materials for two copper borates, $\text{MCuB}_7\text{O}_{12}\cdot\text{H}_2\text{O}$ (M=Na,K). *J Chem Thermodyn*. 2015;89:164-8. Available from: [<URL>](#)
10. Hu ZS, Dong JX, Chen GX, Lou F. Preparation of nanometer copper borate with supercritical carbon dioxide drying. *Powder Technol*. 1999;102(2):171-6. Available from: [<URL>](#)
11. Szwagierczak D, Synkiewicz-Musialska B, Kulawik J, Pałka N. Sintering, Microstructure, and Dielectric Properties of Copper Borates for High Frequency LTCC Applications. *Materials*. 2021;14(14):4017. Available from: <https://www.mdpi.com/1996-1944/14/14/4017>
12. Wang JJ, Wei Q, Yang BF, Yang GY. Two New Copper Borates with Mesoscale Cubic Supramolecular Cages Assembled from $\{\text{Cu}_4\text{@B}_{20}\}$ Clusters. *Chem - Eur J*. 2017;23(12):2774-7. Available from: [<URL>](#)
13. Ursu D, Dabici A, Miclau M, Miclau N. Low-temperature hydrothermal synthesis of hierarchical flower-like CuB_2O_4 superstructures. *Process Appl Ceram*. 2020;14(2):113-8. Available from: [<URL>](#)
14. Zheng Y, Wang Z, Tian Y, Qu Y, Li S, An D, vd. Synthesis and performance of 1D and 2D copper borate nano/microstructures with different morphologies. *Colloids Surf Physicochem Eng Asp*. 2009;349(1-3):156-61. Available from: [<URL>](#)
15. Khalili D, Evazi R, Neshat A, Aboonajmi J. Copper(I) Complex of Dihydro Bis(2-Mercapto Benzimidazolyl) Borate as an Efficient Homogeneous Catalyst for the Synthesis of 2 *H* -Indazoles and 5-Substituted 1 *H* -Tetrazoles. *Chemistry Select*. 2021;6(4):746-53. Available from: [<URL>](#)
16. Kipcak AS, Senberber FT, Aydin Yuksel S, Derun EM, Piskin S. Synthesis, characterisation, electrical and optical properties of copper borate compounds. *Mater Res Bull*. 2015;70:442-8. Available from: [<URL>](#)
17. Senberber Dumanli FT, Moroydor Derun E. A comparative study of ultrasonic-assisted methods to synthesise spinel (CoAl_2O_4) nanoparticles. *Ceram Int*. 2022;48(13):19047-55. Available from: [<URL>](#)
18. Fogler HS. Elements Of Chemical Reaction Engineering. Prentice Hall India; 1999. 1004 s.
19. Yongzhong J, Shiyang G, Shuping X, Jun L. FT-IR spectroscopy of supersaturated aqueous solutions of magnesium borate. *Spectrochim Acta A Mol Biomol Spectrosc*. 2000;56(7):1291-7.



Ecological Risk Assessment of Potentially Toxic Metals in Arable Soils around Adudu Lead–Zinc Mine, North-Central Nigeria

Jude Chinedu Onwuka^{1*}, Enebi Estella Jasper², Gladys Nkeiruka Onwuka³

¹Department of Science Laboratory Technology, Federal University of Lafia, PMB 146, Nasarawa – Nigeria.

²Department of Chemical Sciences, Dennis Osadebe University, Asaba, Delta State, Nigeria.

³Department of Biochemistry, Federal University of Lafia, PMB 146, Lafia, Nasarawa – Nigeria.

Abstract: Mining is a major source of toxic heavy metals into the soil when mine wastes are discharged into the nearby farmlands used for the cultivation of food crops. This study investigated the influence of Pb–Zn mining on the quality and ecological risk of arable soils around active mining sites in Adudu, Nasarawa State, Nigeria. Composite soil samples were collected at 0–20 cm depth, pulverized, and analyzed for heavy metal (Al, As, Cr, Cu, Fe, Mn, Pb, and Zn) concentration using X-ray fluorescence technique. Enrichment factor, geo-accumulation index, improved Nemerow index (IIN), contamination factor (CF), degree of contamination (Cd), pollution load index (PLI), and ecological risk assessment (ERA) were used to evaluate the effect of the mining activities on the environment. Results showed elevated levels of Pb, Zn, Cu, Fe, Mn, and Cr in arable soils around the mine and lower levels of these metals in the control soil. IIN, Cd, and PLI showed that the mine and the nearby arable soils were the most deteriorated, and soil quality improved away from the mining vicinity. ERA revealed that the mine and the closest arable soils (sites F1 and F4) have significant to high ecological risk index as a result of the dominant presence of Pb, Zn, and Cu at the sites. Thus, arable soils which are disposal channels for mine wastes are not good for growing food crops. This study clearly shows that Pb–Zn mining activities introduced heavy metals into the arable soils surrounding the mine.

Keywords: Mining; Heavy metal; Ecological risk; Soil contamination; Arable soils.

Submitted: September 15, 2023. **Accepted:** January 3, 2024.

Cite this: Onwuka JC, Jasper EE, Onwuka GN. Ecological Risk Assessment of Potentially Toxic Metals in Arable Soils around Adudu Lead – Zinc Mine, North-Central Nigeria. JOTCSA. 2024;11(2):483-98.

DOI: <https://doi.org/10.18596/jotcsa.1360723>

***Corresponding author's E-mail:** emperor20062003@yahoo.com

1. INTRODUCTION

Globally, harnessing mineral resources (solid, liquid, and gas) significantly contributes to economic growth development and sustainability through income generation from increased business and foreign exchange earnings, provision of industrial raw materials, enhanced employment opportunities, poverty alleviation, etc. (1, 2). Mineral exploitation is of great importance in a developing nation like Nigeria because of its economic potential. This is why it is on the exclusive list of the Federal Government of Nigeria. Nigeria is endowed with about fifty (50) economically potential solid minerals across all states of the country (3). Nigeria's dependence on oil caused the decline of solid mineral exploitation and consequently, the country's economy became a mono-product economy (3). The recent global decline in crude oil prices due to the COVID-19 pandemic has intensified the efforts of the Federal Government of Nigeria to diversify the country's

economy from crude oil exploration to solid mineral exploration. Consequently, the Federal Government has introduced various policies such as tax holidays for miners, waivers on imported mining equipment, financial assistance to artisanal miners, etc., to encourage investors in the mining sector. However, the authorities pay little attention to the adverse environmental and health impacts of these mining activities on the host communities.

The impacts of mineral exploration and processing activities on the environment are similar globally depending on the chemical attributes of the ore, method of extraction, and environmental conditions (4, 5). It is a global concern because they cause physical degradation of the ecosystem (6) and more importantly, they produce large amounts of tailings and wastes (7) which are principal anthropogenic sources of heavy metals (such as Pb, Zn, Cd, Mn, Cr, Co, Cu, Ni, Hg, As, Al and Fe) that have adverse effect on the environment (8). Studies have recorded

higher concentrations of heavy metals in soils around the Pb–Zn mine in Enyigba, southeastern Nigeria (9), Ameri, Abakaliki (10), Mkpuma Ekwoku, southeastern Nigeria (11), Abakaliki, Lower Benue Trough, Nigeria (12) and various sites, southeast Missouri, USA (13). Similarly, Oyebamiji et al (5) and Eludoyin et al. (14) reported elevated concentrations of heavy metals in soils around tantalum-niobium and gold mining sites of Iludun–Oro and Itagunmodi communities respectively, in southwestern, Nigeria.

Elevated levels of these heavy metals (pollutants) can have severe negative effects on human and animal health, water quality, aquatic life, land use and agriculture, and other aspects of ecosystem imbalance (15). The elevated levels of these heavy metals increase the risk of soil pollution in and around the mining site, depending on their mobility and bioavailability. Their mobility and bioavailability in the environment are determined by some physicochemical characteristics of the soil such as pH, textural characteristics, organic matter content, speciation or chemical form, and electrical conductivity (16).

Nasarawa State is located in the north-central region of Nigeria and is known as “The Home of Solid Minerals” because it is blessed with abundant solid minerals that are of high economic significance. The prominent mineral deposits of the State are coal, barytes, salt, limestone, clays, glass, tantalite, columbite, cassiterite, copper, iron ore, lead, and zinc (17). The rocks in Nasarawa State are the host to gold in Wamba; baryte at Azara, Wuse, and Alosi; coals (of the highest rank in Nigeria) at Obi, Jangerigeri, Jangwa, and Shankodi; Tantalite at Afu, Udege Beki, and Wamba; Gemstone in Keffi; Nasarawa Eggon and Kokona; salt deposits in Ribi, Keana, and Awe; Limestone deposits at Adudu, and Jangwa; at Keffi, Akwanga, Nasarawa Eggon, Tudu Uku, etc. (18). Thus, illegal, indiscriminate and unregulated mining are issues bedeviling several villages/towns in Nasarawa State which are endowed with these solid minerals. It was reported that out of 64 active mining licenses in Nasarawa State, only ten

(10) had environmental impact assessments (19). Surface mining such as open-cast mining is predominantly employed in the mining of these solid mineral resources because the solid minerals do not seem to lie deep beneath the earth. Open-cast mining involves the excavation of vegetation (topsoil) with heavy equipment and hard implements to mine a target mineral (20). During this process, pits and dumps are created which causes physical degradation of the land (21). The excavation of soil causes atmospheric depositions of metals and also generates huge quantities of wastes (such as waste rocks, tailings mine wastewater, etc. that contain harmful minerals and chemicals that pollute the environment) which are discharged directly into nearby farmlands, streams, and river channels. Thus, open-cast mining has serious adverse consequences on the environment of the host communities.

Pb–Zn ores are mined using the open cast mining method, in the Adudu community, Awe, North – central Nigeria. This situation has persisted for decades, resulting in the presence of abandoned mines and the generation of significant amounts of mine waste, including waste rocks, tailings, and mine wastewater. These wastes have been haphazardly and indiscriminately disposed of in farmlands (as shown in Figure 1), streams, and river channels.

These increased the possibility of elevated levels of heavy metals in the arable soils around the mine. The community dwellers are ignorant of the adverse consequences of these mining activities on their health and environment. Obasi et al. (22) reported that health challenges such as miscarriages, selenosis in infants, the decline in infertility, and physiological and mental imbalance, were common among inhabitants around Pb–Zn mine in Enyigba community, southeastern Nigeria. Yet until this research, no study has been carried out on the environmental risk of heavy metal-polluted agricultural soils around the Pb–Zn mining site in the Adudu community.



Figure 1: Pb–Zn Mine at Adudu Showing Mine Wastewater Discharged or pumped to Nearby Farmlands (a) and the Pb–Zn ore (b) being mined.

Therefore, this research investigated the influence of opencast mining activities on the heavy metal pollution and environmental risk of arable soils around the Pb-Zn mine site at Adudu, North Central, Nigeria.

2. EXPERIMENTAL SECTION

2.1. Description of Study Area

Adudu is a community in Obi Local Government Area in Nasarawa State. However, geographical coordinates show that the Adudu Pb-Zn mine is located in Awe Local Government Area although it is a boundary between the Obi and Awe Local Government Areas of Nasarawa. The geographical coordinates of the Pb-Zn mine lie within latitude 08°13'83.3"N and longitude 009°01'00.0"E and 169 m above sea level.

Adudu is a low-income community with farming, mining, cattle rearing, and trading as the sources of income. The predominant land uses in the community are agriculture and mining. Mining is the second source of income for the inhabitants of this community. The average temperature of the area is 32 °C. Awe has two distinct seasons which are the dry and the rainy seasons. The soil varies from loam to sandy loam which is good for crop production and crops such as yam, maize, and rice grown in substantially large quantities.

Adudu is located within the middle region of Benue Trough of Nigeria which contains up to 6000 M of

Cretaceous-Tertiary Sediment (23). Adudu is within the southern part of Nasarawa State which is part of the low plains of Benue origin and volcanic cones (24) and is also the sedimentary part of the State as the area is covered by sedimentary rocks of Cretaceous-Tertiary ages (2).

2.2. Sample Collection and Preparation

Eleven (11) study sites were investigated in this study. The study sites include the mining site, nine (9) cultivated arable farms around the Pb-Zn active mining site, and one (1) cultivated arable farm located about 3 km away from the active mining site which serves as the control. The cultivated arable farms around the mining site are not less than 150 m apart from each other and 100 m from the mine. Ten (10) composite soil samples were collected from each of the study sites using soil auger. Thus, a total of 110 composite samples were collected and analyzed. At each location in each studied site (active mining site and cultivated arable farms), six (6) quadrats were marked and, in each quadrat, four (4) core soil samples were collected randomly at depth of 0-20 cm and mixed to give a composite sample of that location in the studied site. Foreign materials such as waste polythenes and plastics, plant debris, pebbles, etc were removed from the soil samples. The soil samples were air-dried for 10 days, pulverized, sieved to less than 2 mm, and then, stored in plastic containers for analysis. The coordinates of the sample locations were marked with a handheld global positioning system (GPS) and are shown in Figure 2.

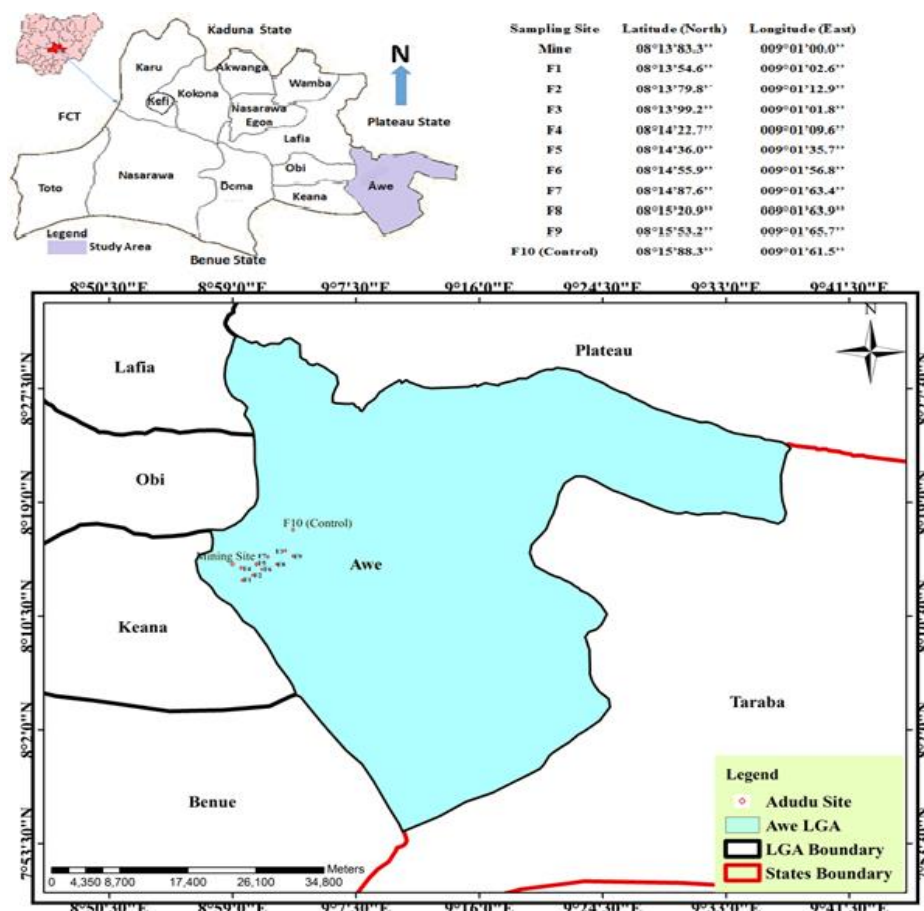


Figure 2: Maps of Nigeria, Nasarawa State and Awe Local Government Area Showing Location of Sampling Sites with Their Coordinates

2.3. Heavy Metal Analysis

About 5 g of the finely ground soil sample was pelletized at a pressure of about 19.4 kg/m² using a pelletizing machine. The pelletized sample was placed in a standard sample holder and loaded into the energy dispersive X-ray fluorescence (EDXRF) spectrometer (Minipal 4 model) [Detection limit: 0.0001 % (1 ppm) – 99.9999 %]. The EDXRF spectrometer was switched on and allowed to stabilize for 2 hours. It was set at the default mode to analyze the compositions of the soil samples by irradiating the sample with X-rays generated from the Rh tube (Maximum power: 9 W; window: 75 μm Be; maximum high voltage: 30kV; maximum current: 300 μA; cooling medium: air). A recovery test was carried out on the EDXRF machine as a quality control measure by spiking analyses to ensure the reliability of the result.

2.4. Environmental Risk Assessment

2.4.1. Enrichment factor (EF)

EF is used to differentiate the natural and anthropogenic sources of the heavy metals in the soils by normalizing the heavy metal concentration in the sample concerning a reference heavy metal [6]. The most commonly used reference elements are Sc, Mn, Ti, Al, and Fe (25). The EF of the analyzed heavy metals in the investigated soil samples from the study area was calculated using Eq.1:

$$EF = \left[\frac{C_n(\text{sample})/C_{\text{ref}}(\text{sample})}{B_n(\text{Background})/B_{\text{ref}}(\text{Background})} \right] \quad (1)$$

Where, $C_n(\text{sample})$ is the concentration of the investigated heavy metal "n" in the study site, $C_{\text{ref}}(\text{sample})$ is the concentration of the reference heavy metal in the study site; $B_n(\text{background})$ is the background concentration of the investigated heavy metal (usually the average shale value of the investigated heavy metal) and $B_{\text{ref}}(\text{background})$ is the background concentration of the reference heavy metal (usually the average shale value of the reference heavy metal). In this study, Fe is the most naturally abundant element in all the studied soils and thus, was used as the reference heavy metal while the average shale value described by Turekian and Wedepohl, (26) was adopted as the reference value.

2.4.2. Geo-accumulation index (I_{geo}) and improved Nemerow index (I_{IN})

I_{geo} is a single-factor contamination index proposed by Muller (27) for qualitative assessment of heavy metal pollution in soils using Eq. 2.

$$I_{\text{geo}} = \log_2 \left[\frac{C_n}{1.5B_n} \right] \quad (2)$$

Where C_n is the concentration of the heavy metal "n" in the sample; B_n is the geochemical background concentration for heavy metal "n" which is either directly measured in fossil argillaceous sediments of the area or adopted from literature (world average shale value); 1.5 is a correction factor used to reduce the possible geogenic effect on the variations in background concentration of a given metal. The world average shale values of the analyzed heavy metals as provided by Turekian and Wedepohl (26) were adopted in this study as shown in Table 1.

I_{IN} is a comprehensive index method employed for general assessment of the pollution integrity of the study area (28,29). It was computed using Eq. 3 proposed by Nemerow (30).

$$I_{\text{IN}} = \sqrt{\frac{(I_{\text{geomax}}^2 + I_{\text{geoave}}^2)}{2}} \quad (3)$$

Where I_{IN} is the comprehensive contamination index of a sample, I_{geomax} is the maximum I_{geo} value of such sample, and I_{geoave} is the arithmetic mean value of I_{geo} .

2.4.3. Contamination factor (CF), degree of contamination (C_d), and pollution load index (PLI)

The extent of soil contamination by each of the analyzed heavy metals was determined using the contamination factor (CF). It was calculated using Eq. 4.

$$CF = \frac{C_n}{C_b} \quad (4)$$

Where C_n is the concentration of the heavy metal "n" in the sample, C_b is the background concentration of the heavy metal "n". Nigerian Directorate of Petroleum Resources (31) target values for heavy metals in soils (Table 1) were adopted as the background values " C_b ".

The sum of all contaminants factors of the various heavy metals is referred to as the degree of contamination (C_d) (32). The generalized form of Hakanson's (33) equation for computing C_d was used in this study. It is given in Eq. 5:

$$C_d = \sum_{i=1}^{n=8} (CF_i) \quad (5)$$

Where n is the number of heavy metals studied and CF_i is the contamination factor for heavy metal "i" in the sample.

Pollution Load Index (PLI) was used to estimate the magnitude of contamination by the simultaneous presence of analyzed heavy metals in a sampling site (5). PLI was calculated using Eq. 6 as proposed by Tomlinson *et al.* (34).

$$PLI = (CF_1 \times CF_2 \times CF_3 \times CF_4 \times \dots \times CF_n)^{1/n} \quad (6)$$

Where n is the number of metals and CF is the contamination factor of each heavy metal.

2.4.4. Ecological risk assessment

Potential hazard(s) from soil heavy metal contamination were quantified using ecological risk factor (Er) and ecological risk index (RI).

Er is a single index quantitative expression of the potential ecological risk of a given contaminant (heavy metal) (33). It was calculated using Eq. 7

$$Er = Tr \times CF \quad (7)$$

Tr is the toxic response factor suggested by Hakanson (33) and presented in Table 1 while CF is the contamination factor of the heavy metal.

The potential ecological risk index (RI) index evaluates the general pollution caused by the simultaneous presence of the eight analyzed heavy metals. It was calculated using the expression in Eq. 8

$$RI = \sum_i^n Er \quad (8)$$

n is the number of the heavy metals considered; Er and RI are potential ecological risk factors of individual and multiple metals respectively.

3. RESULTS AND DISCUSSION

3.1. Heavy Metal Concentration

Table 1 presents the concentrations of the analyzed heavy metals in the investigated soils. Results showed that concentrations of the analyzed heavy metals in the investigated soils varied significantly away from the mine. The highest concentrations of Mn, Pb, and Zn were obtained in the soil from the mine which also recorded significant levels of Cr, Cu, and Fe. However, the control soil (collected 3 km away from the mining site) showed the least Cr, Cu, Fe, and Mn concentrations and also, lower concentrations of Pb and Zn compared to other investigated soils. This is evidence that the concentrations of analyzed heavy metals in the investigated arable soils around the mine, increased beyond their natural levels due to anthropogenic activities from Pb–Zn mineral exploration and processing. Overall, the studied sites (mining and arable sites) showed high concentrations of Al, Cr, Cu, Fe, Mn, and Zn. This is an indication that mine waste is leached under acidic conditions which are induced by acid mine drainage.

Table 1 showed that Al concentration in the studied soils ranged between 7039.12 ± 157.04 to 31754.81 ± 338.65 mg/kg and thus, are below average shale (26) reference value of 80000 mg/kg for Al. This suggests geogenic or lithogenic origin as the possible major source of Al. The mine and control site contained the lowest and highest Al concentrations respectively. Hence, the Al concentration obtained at the mine is appreciably low compared to those of the studied arable farms (F1–F10) which are away from the mine. This implies that weathering and mineralization of the geochemical composition of the rocks in the study area is a major contributing factor to the presence of Al. Human exposure to Al is inevitable as it naturally occurs in soil, water, air, and food (35). Chronic exposure to free Al cation (Al^{3+}) is a huge concern as it has been reported to be essentially toxic and may aggravate the risk of developing Alzheimer's disease and breast cancer (36). Obiora *et al.* (37) reported a similar range of Al level and decline in Al close to the Pb–Zn mine in Enyigba, southeastern Nigeria. According to Abraham and Susan (38), precipitation of metals in the acidic mined zone could be responsible for Al decline near a Cu mine in western Uganda.

The levels of arsenic (As) in the studied sites are below the instrumentation limit of detection (i.e., 1 mg/kg). Consequently, the level in the study area is below the average shale reference value (26) and its acceptable limit for arable soil (31). This is an indication that As presence in the study area may be associated with natural processes such as weathering of rock, volcanic eruptions, geothermal activities, etc (39). Commonly referred to as king of poison (40), occurs naturally in the earth's crust (41).

Low As level was similarly recorded in most of the arable soils around Pb–Zn mining sites of Abakaliki, Lower Benue Trough, Nigeria (12), and Abuni town, Nasarawa State, Nigeria (42). However, elevated range As (6.9–7.7 mg/kg) was reported in stream sediments around the Pb–Zn mining vicinity of Enyigba, southeastern Nigeria (37). Exposure to AS is a global concern as studies that it is inimical to human health. Human exposure to inorganic As increases the risk of skin cancer and other internal tumors of the bladder, liver, kidney, and lung (43, 44), congenital malformations, low birth weight, spontaneous abortion, genotoxicity, mutagenicity, and teratogenicity (45).

In the present study, soil from the mine showed lower Cr concentration than the investigated arable soils (except control soil) (Table 1). This could be attributed to the leaching of mine wastes to the surrounding arable farms under acidic conditions in addition to the dissolution of Cr through Pb–Zn mineralization of the study area. The concentration of Cr varied between 102.63–649.99 mg/kg. Except for the control soil (F10), soils from the mine and the studied arable farms, showed Cr concentrations above the DPR (31) threshold limit for arable soil (100 mg/kg) and the average shale (26) reference value (90 mg/kg). An indication that Cr concentration is related to the mineralization of the Pb–Zn ores in the study area. Cr usually exists in three main forms; Cr, Cr^{3+} , and Cr^{6+} . Cr^{3+} is less toxic and required in minute quantity for human health. Thus, it has little or no adverse effect on human health (46). However, Cr^{6+} is highly toxic and can cause several human health problems such as anemia, cancer, irritations and ulcers in the small intestine and stomach, damage to sperm and the male reproductive system, and possibly death (47). Cr concentration obtained in this study exceeded values reported by Obiora *et al.* (9) for agricultural soils around Pb–Zn mining localities in Enyigba, southeast Nigeria. However, it is less than the Cr range (1112.60–1127.57 mg/kg) recorded for agricultural soils in Ameri, Abakaliki Pb–Zn mining area, Ebonyi State, southeast Nigeria (10).

Cu levels in soils from the mine site (3594.91 ± 79.48 mg/kg) and site F4 (6710.50 ± 134.02 mg/kg) are appreciably higher compared to other studied sites (Table 1). Thus, the maximum Cu level obtained in site F4 could be attributed to introductions from chalcopyrite, bornite, and azurite through the disposal of mine wastes (such as waste rocks or gangues, tailings, mine wastewater, etc.) at the site. The Cu level is significantly lower in the control site (F10) than in other studied sites but its level in all

the studied sites greatly exceeded its average shale (26) reference value and DPR (31) acceptable limit for arable soils. This implies that anthropogenic activities from Pb–Zn mining are not the only sources of soil contamination with Cu in the area; the underlying geology and mineralization of Pb–Zn ores in the area are significant contributors. The high level of Cu at the mine suggests that Cu-bearing mineral ores associated with Pb–Zn ores such as chalcopyrite (CuFeS₂), bornite (Cu₅FeS₄), azurite

[Cu₃(CO₃)₂(OH)₂], etc., are among the principal ores exploited in the study area. The Cu range obtained in this study is higher than those reported for agricultural soils around Pb–Zn mines by other researchers (9–12, 22, 37). Overdose of Cu can have adverse effects on human health such as irritations, dizziness, vomiting, stomach cramps, diarrhea, nausea, liver and kidney damage, and even death (48).

Table 1: Mean concentrations (mg/kg) of the analysed heavy metals in the investigated soils.

Sampling Site	No of Samples Per Site	Data Presentation	Al	As	Cr	Cu	Fe	Mn	Pb	Zn
Mine	10.00	Mean ± SD	7039.12 ±157.04	BDL	102.63 ±10.80	3594.91 ±79.48	123167.44 ±3503.58	4956.49 ±18.26	24786.02 ±368.36	13979.01 ±521.93
F1	10.00	Mean ± SD	20243.69 ±376.21	BDL	410.52 ±21.04	958.64 ±65.17	75012.54 ±1758.22	2323.35 ±63.49	4455.91 ±89.22	401.70 ±16.52
F2	10.00	Mean ± SD	18311.93 ±201.03	BDL	444.73 ±8.63	734.96 ±36.96	118446.37 ±1948.22	1858.68 ±59.71	BDL	241.02 ±7.91
F3	10.00	Mean ± SD	14395.51 ±286.62	BDL	342.10 ±16.99	798.87 ±21.04	112081.67 ±2417.74	3020.36 ±65.97	BDL	BDL
F4	10.00	Mean ± SD	13231.17 ±477.12	BDL	338.68 ±20.59	6710.50 ±134.02	169259.06 ±4193.55	2865.47 ±34.82	BDL	457.93 ±24.07
F5	10.00	Mean ± SD	14231.23 ±191.88	BDL	280.52 ±9.44	798.87 ±18.47	212867.75 ±6218.37	3330.14 ±57.02	BDL	BDL
F6	10.00	Mean ± SD	16009.71 ±173.36	BDL	478.94 ±35.82	734.96 ±33.33	120264.86 ±3618.81	1703.79 ±48.17	BDL	BDL
F7	10.00	Mean ± SD	29108.57 ±387.11	BDL	342.10 ±27.33	615.13 ±16.62	25144.06 ±221.64	1936.13 ±37.11	BDL	BDL
F8	10.00	Mean ± SD	10611.40 ±161.29	BDL	649.99 ±25.70	878.76 ±39.05	137155.80 ±2531.77	1703.79 ±66.28	BDL	241.02 ±13.42
F9	10.00	Mean ± SD	26118.33 ±218.74	BDL	441.73 ±31.08	519.26 ±218.59	34201.52 ±510.06	3020.36 ±71.24	BDL	BDL
F10 (Control)	10.00	Mean ± SD	31754.81 ±338.65	BDL	BDL	375.47 ±13.32	7204.00 ±95.41	1471.46 ±42.87	BDL	BDL
Average Shale Values*			80000.00	13.00	90.00	45.00	47200.00	850.00	20.00	96.00
DPR Target Values (31)			NA	1.00	100.00	36.00	38000.00	850.00	85.00	140.00
Tr**			NA	10.00	2.00	5.00	NA	1.00	5.00	1.00

Keys: SD = Standard Deviation; NA = Not Available; BDL = Below Detectable Limit; DPR = Department of Petroleum Resources (Nigeria); Tr = Toxic Response Factor; * = (26); ** = (33)

Iron (Fe) is the most abundant heavy metal found in all the investigated soils (except in soil from the control arable site which has Al as the most abundant). This suggests that Fe-rich mineral ores such as chalcopyrite (CuFeS₂), bornite (Cu₅FeS₄), siderite (FeCO₃), pyrite (FeS₂), marcasite (FeS₂), etc., are probably among the principal ores exploited in the area. The studied sites showed varied Fe concentrations ranging from 7,204±95.41 to 212,867.75±6218.37 mg/kg (Table 1). The lowest Fe concentration was obtained in the control soil (F10) while most of the investigated soils (except F7, F9, and F10) showed Fe concentration above the DPR (31) regulatory limit for arable soil and the average shale (26) reference value. These observations, especially the high concentration of Fe in sites located away from the mine (sites F4, F5, and F8), suggest possible introductions from chalcopyrite and bornite, siderite, and pyrite via combined effects of the Pb–Zn mining activities in addition to geologic processes and Pb–Zn mineralization of the area. The Fe range obtained in this study falls within the range reported by Obiora *et al.* (37) for stream sediments

around the Pb–Zn mine in Enyigba, southeastern Nigeria.

Table 1 shows that Mn level varied between 1471.46±42.87 – 4956.49±18.26 mg/kg. The maximum and minimum Mn levels were obtained in soils from the mine and control site (F10) respectively. However, Mn levels in all the studied sites are above 850 mg/kg which is the average shale (26) reference value and DPR (31) tolerance level for Mn in arable soils. Thus, Mn sources could be of geogenic and anthropogenic origin. The high Mn concentration obtained could be ascribed to the dissolution of Mn from the sulfide and carbonate ores (such as chalcopyrite, bornite, siderite, etc.) which underlie the study area (49). Also, anthropogenic sources such as used batteries, discarded metal scraps, machinery parts, automobile exhaust fumes, and wastes from welding works and spray paintings of the vehicles (50), could have also contributed to the high level of Mn observed in the control soil due to its proximity to the highway. Mn exists in natural deposits as oxides, sulfides, carbonates, and silicates (51). It is an essential element for humans and

animals and is also a global concern because studies have shown that at an elevated level, it can cause Parkinson's disease-like syndrome of tremour, gait disorder, postural, instability, and cognitive and neurological disorder (52).

Lead (Pb) is a prominent toxic heavy metal and highly persistent in the environment due to its non-biodegradable nature. Hence, on continuous exposure, it accumulates to a toxic level (53). Its toxicity causes negative effects on humans such as high blood pressure, brain and kidney damage, miscarriage, anemia, learning deficit, reduced fertility, and behavioral disorders (53–55). A high concentration of Pb was observed only in soils from the mine (24786.02 ± 368.36 mg/kg) and site F1 (4455.91 ± 89.22 mg/kg) which are above the Pb permissible limit for arable soils (31). The other studied sites (F2–F10) had very low Pb concentrations that were below the instrumentation limit of detection (1 mg/kg). The very high concentration of Pb at the mine is evidence that galena (Pbs) is one of the major mineral components explored at the mine. Also, the continuous disposal/dumping of mine wastes and tailings to the nearby arable farm (F1) explains the appreciable level of Pb in the site. The drastic decrease in Pb concentration in studied sites (F2–F9) that are farther away from the mine, could be attributed to the immobility nature of Pb in soil (56), density settling, and elemental precipitation (37) and poor solubility of Pb in water (57, 58). The low solubility of Pb in water affects its amount in the mine wastewater that is discharged or leached to the surroundings while Pb immobility nature makes it difficult for it to be transported via the soil, to a distance farther from the mine. Similarly, at high pH, Pb precipitates thereby reducing the amount of Pb in the leaching effluents. Ambo *et al.* (42) and Obiora *et al.* (37) reported similar drastic decreases in Pb at locations away from the Pb–Zn mine at Abuni town Nasarawa State and Enyigba, southeastern, Nigeria; respectively.

Similar to Pb, the Zinc (Zn) level at the mine (13979.01 ± 521.93 mg/kg) was found to be significantly high compared to other studied arable soils. Also, soils from arable sites (F1 and F4) which serve as disposal channels for mine wastes showed higher levels of Zn (401.70 ± 16.52 mg/kg and 457.93 ± 24.07 mg/kg respectively) than the other studied arable soils (BDL – 241.02 ± 13.42 mg/kg). Hence, the Zn level in the mining site and a few studied arable sites (F1, F2, F4, and F8) exceed the average shale (26) value and DPR (31) tolerance limit of Zn for arable soils. The elevated Zn level at the mine site is an indication that sphalerite (ZnS) which occurs in close association with galena (PbS), is a principal component of the minerals exploited in the area. Elueze (59) reported that sphalerite and galena are often mined together because of their strong association of occurrence. Unlike Pb, a high amount of Zn was observed at some of the studied sites located farther away from the mine. Thus, in addition to site F1, sites F2, F4, and F8 showed significant levels of Zn which can be attributed to the solubility of Zn in water (57, 58). Aloh *et al.* (10)

observed elevated Zn levels in agricultural soils in Ameri, Abakaliki Pb–Zn mining area, Ebonyi State, southeast Nigeria. Zn is an essential element to both humans and animals but is toxic in overdose.

3.2. Environmental Risk Assessment

The quality of the investigated soils and their effect on the environment was evaluated using enrichment factor (EF), geo-accumulation index (I_{geo}), contamination factor (CF), degree of contamination (C_d), pollution load index (PLI), ecological risk (Er) and potential ecological risk index (RI) models.

3.2.1. Enrichment factor (EF)

EF is always used to differentiate between natural and anthropogenic sources of metals (60). The EF values close to unity indicate crusted origin, those less than 1.0 suggest a possible depletion of metals, whereas $EF > 1.0$ indicates that the element is of anthropogenic origin (61). EF values for the analyzed heavy metals are displayed in Table 3 and enrichment levels proposed by Birth (62) (Table 2) were used to classify the level of enrichment of these heavy metals in the investigated soils.

The result shows that the mine is deficient in Al and Cr. However, it is enriched with Pb and Zn at extremely severe levels, and Cu and Mn at very severe and minimal levels respectively (Table 3). This is supporting evidence that Pb–Zn–Cu bearing ores are major components of the minerals explored at the mine. The highest enrichments of Al, Cu, and Mn are observed at the control site. Consequently, the control site is found to be severely and minimally enriched with Mn and Al respectively, and most enriched with Cu at an extremely severe level. This shows that anthropogenic sources of these metals (Al, Cu, and Mn) in the investigated soils, are a consequence of the geological nature and mineralization of the study area. The EF values signify anthropogenic sources ($EF > 2$) for Pb, Zn, Cu, and Mn as well as lithogenic sources ($EF < 1$) for Al and Cr presence at the mine.

EF value for arsenic (As) was not evaluated because As concentration was not empirically ascertained as it is below the instrumentation limit of detection. Fe was used as a reference element in this study. Except for the control site (F10), the studied sites showed no Al enrichment and deficient to moderate levels of Cr enrichment. Cu is the most enriched element in each of the studied sites (i.e., F2–F10) except the mine and site F1. It is enriched at moderate to extremely severe levels in the studied sites. Some of the studied sites (F2, F4, F5, F6, and F8) showed no Mn enrichment while others showed minimal to severe Mn enrichment. Pb enrichment of the mine and site F1 (close to the mine), is at an extremely severe level while it could be deficient at other studied sites (F2–10). Zn is enriched at an extremely severe level at the mine, minimally enriched at sites (F1 and F4) close to the mine, and deficient at the remaining sites. High EF values (> 1) of Pb, Zn, Mn, Cu, and Cr at some of the studied sites are an indication of significant anthropogenic contributions from mining activities. Thus, the result shows that the combined effects of Pb–Zn mining activities with

the underlying geology and Pb–Zn mineralization of the study area are the sources of these analyzed heavy metals in the investigated soils.

Table 2: Classes of EF, I_{geo} , IIN, CF, Cd, Er, and RI concerning enrichment, pollution, contamination level, contamination degree, potential ecological risk, and ecological risk levels, respectively (6, 32).

EF Classes	Enrichment Level	Igeo value Classes	Pollution Level
EF < 1	No enrichment	0 ; $I_{geo} \leq 0$	Practically Unpolluted
EF = 1 – 3	Minor enrichment	1 ; $I_{geo} = 0 - 1$	Unpolluted to moderately polluted
EF = 3 – 5	Moderate enrichment	2 ; $I_{geo} = 1 - 2$	Moderately polluted
EF = 5 – 10	Moderate severe enrichment	3 ; $I_{geo} = 2 - 3$	Moderately to Strongly polluted
EF = 10 – 25	Severe enrichment	4 ; $I_{geo} = 3 - 4$	Strongly polluted
EF = 25 – 50	Very severe enrichment	5 ; $I_{geo} = 3 - 5$	Strongly to extremely polluted
EF > 50	Extremely severe enrichment	6 ; $I_{geo} > 5$	Extremely polluted
IIN Classes	Contamination Level		
0 ; $0 < IIN \leq 0.5$	Uncontaminated		
1 ; $0.5 < IIN \leq 1$	Uncontaminated to moderately contaminated		
2 ; $1 < IIN \leq 2$	Moderately contaminated		
3 ; $2 < IIN \leq 3$	Moderately to heavily contaminated		
4 ; $3 < IIN \leq 4$	Heavily contaminated		
5 ; $4 < IIN \leq 5$	Heavily to extremely contaminated		
6 ; $IIN > 5$	Extremely contaminated		
CF Classes	Contamination Level	Cd Classes	Degree
CF < 1	Low contamination	$Cd < 8$	low degree of contamination
CF = 1 – 3	Moderate contamination	$Cd = 8 - 16$	Moderate degree of contamination
CF = 3 – 6	Considerable contamination	$Cd = 16 - 32$	Considerable degree of contamination
CF > 6	High contamination	$Cd \geq 32$	Very high degree of contamination
Er Classes	Er Level	RI Classes	Risk Levels
Er < 40	Low potential ecological risk	RI < 150	Low ecological risk
Er = 40 – 80	Moderate potential ecological risk	RI = 150 – 300	Moderate ecological risk
Er = 80 – 160	Significant potential ecological risk	RI = 300 – 600	Significant ecological risk
Er = 160 – 320	High potential ecological risk	RI > 600	High ecological risk
Er > 320	Very high potential ecological risk		

Table 3: Enrichment Factor (EF) of the Analysed Heavy Metals in the Investigated Soils.

Sampling Site	Al	As	Cr	Cu	Fe	Mn	Pb	Zn
Mine	0.03	-	0.44	30.61		2.23	474.92	55.80
F1	0.16	-	2.87	13.40		1.72	140.19	2.63
F2	0.09	-	1.97	6.51		0.87	-	1.00
F3	0.08	-	1.60	7.48		1.50	-	-
F4	0.05	-	1.05	41.58	Used as Reference Element	0.94	-	1.33
F5	0.04	-	0.69	3.94		0.87	-	-
F6	0.08	-	2.09	6.41		0.79	-	-
F7	0.68	-	7.14	25.66		4.28	-	-
F8	0.05	-	2.49	6.72		0.69	-	0.86
F9	0.45	-	6.82	15.92		4.90	-	-
F10 (Control)	2.60	-	-	54.67		11.34	-	-

Key: - = Not Calculated

Table 4: Geo-accumulation index (I_{geo}) of the Analysed Heavy Metals and Improved Nemerow Index (I_{IN}) of the Studied Sites.

Sampling Site	Al	As	Cr	Cu	Fe	Mn	Pb	Zn	I_{geo} ave I_{geo} max I_{IN}		
Mine	-4.09	-	-0.40	5.74	0.80	1.96	9.69	6.60	2.54	9.69	7.08
F1	-2.57	-	1.60	3.83	0.08	0.87	7.22	1.48	1.56	7.22	5.22
F2	-2.71	-	1.72	3.45	0.74	0.54	-	0.74	0.56	3.45	2.47
F3	-3.06	-	1.34	3.57	0.66	1.24	-	-	0.47	3.57	2.55
F4	-3.18	-	1.33	6.64	1.26	1.17	-	1.67	1.11	6.64	4.76
F5	-3.18	-	1.06	3.57	1.59	1.39	-	-	0.55	3.57	2.55
F6	-2.91	-	1.83	3.45	0.76	0.42	-	-	0.44	3.45	2.46
F7	-2.04	-	1.34	3.19	-1.49	0.60	-	-	0.20	3.19	2.26
F8	-3.50	-	2.27	3.70	0.95	0.42	-	0.74	0.57	3.70	2.65
F9	-2.20	-	1.72	2.94	-1.05	1.24	-	-	0.33	2.94	2.09
F10 (Control)	-1.92	-	-	2.48	-3.30	0.21	-	-	-0.32	2.48	1.77

Key: - = Not Calculated

Table 5: Contamination Factor (CF), Degree of Contamination (Cd), and Pollution Load Index (PLI) of the Investigated Soils.

Sampling Site	Al	As	Cr	Cu	Fe	Mn	Pb	Zn	Cd		PLI
Mine	0.09	-	1.03	99.89	3.24	5.83	291.60	99.85	501.53	6.89	
F1	0.25	-	4.11	26.63	1.97	2.73	52.42	2.87	90.98	3.49	
F2	0.23	-	4.45	20.42	3.12	2.19	-	1.72	32.13	1.99	
F3	0.18	-	3.42	22.19	2.95	3.55	-	-	32.29	1.86	
F4	0.17	-	3.39	186.40	4.45	3.37	-	3.27	201.05	2.92	
F5	0.17	-	2.81	22.19	5.60	3.92	-	-	34.69	1.98	
F6	0.20	-	4.79	20.42	3.16	2.00	-	-	30.57	1.83	
F7	0.36	-	3.42	17.09	0.66	2.28	-	-	23.81	1.54	
F8	0.13	-	6.49	24.41	3.61	2.00	-	1.72	38.36	2.00	
F9	0.33	-	4.45	14.42	0.90	3.55	-	-	23.65	1.69	
F10 (Control)	0.40	-	-	10.43	0.19	1.73	-	-	12.75	1.04	

Key: - = Not Calculated

Table 6: Ecological Risk (Er) and Potential Ecological Risk Index (RI) of the Analysed Heavy Metals and Investigated Soils.

Sampling Site	Er								RI
	Al	As	Cr	Cu	Fe	Mn	Pb	Zn	
Mine	-	-	2.06	499.45	-	5.83	1458.00	99.85	2065.19
F1	-	-	8.22	133.15	-	2.73	262.10	2.87	409.07
F2	-	-	8.90	102.10	-	2.19	-	1.72	114.91
F3	-	-	6.84	110.95	-	3.55	-	-	121.34
F4	-	-	6.78	932.00	-	3.37	-	3.27	945.42
F5	-	-	5.62	110.95	-	3.92	-	-	120.49
F6	-	-	9.58	102.10	-	2.00	-	-	113.68
F7	-	-	6.84	85.45	-	2.28	-	-	94.57
F8	-	-	12.98	122.05	-	2.00	-	1.72	138.75
F9	-	-	8.90	72.10	-	3.55	-	-	84.55
F10 (Control)	-	-	-	52.15	-	1.73	-	-	53.88

Key: - = Not Calculated

3.2.2. Geo-accumulation index (I_{geo}) and improved Nemerow index (I_{IN})

I_{geo} and I_{IN} values for the analyzed heavy metals studied sites respectively are given in Table 4. I_{geo} evaluation for the analyzed heavy metals is used to determine the level of contamination of the study area by individual heavy metals (28, 63).

Using Muller's (27) classification presented in Table 2, I_{geo} values show that the mine is extremely polluted by Pb, Zn, and Cu ($I_{geo} > 5$) and unpolluted by Al and Cr ($I_{geo} < 0$). However, the control site is unpolluted by Al and Fe but moderately to strongly polluted by Cu and unpolluted to moderately polluted by Mn. All studied sites are unpolluted by Al but are polluted by Cu at moderate to extreme levels ($I_{geo} > 2$). Most of the investigated arable soils are moderately polluted by Cr (Class 2). The level of Fe and Mn pollution in the studied sites ranges from unpolluted to moderately polluted. Sites close to the mine are extremely and moderately polluted by Pb (F1) and Zn (F1 and F4) respectively. These observations ascertained that of all the analyzed heavy metals, Pb and Zn are the most accumulated heavy metals at the mine while Cu is the most accumulated heavy metal in all the studied sites except at the mine and site F1 where Pb is the most accumulated heavy metal. This suggests that Pb, Zn, and Cu could be absorbed by food crops grown in the mine, sites F1 and F4 where they will be accumulated. The concentrations of Cr, Pb, and Zn at the control site are below 1 mg/kg suggesting that the site could also be unpolluted by these metals in addition to the unpollution of the site by Al and Fe that was ascertained by the result. These show that human activities from Pb-Zn ore mining and processing increase the geological concentrations of these heavy metals in the arable soils (via diffuse pollution, wet and dry deposition of metals, erosion and leaching of mine wastes, etc.) within the study area which leads to the increase in geo-accumulation of the heavy metals over time (63).

I_{IN} gives a comprehensive description of the pollution status of the study area because it considers input from all other pollution indices (28, 29). According to Fostner *et al.* (64) categorization, the mine and site

F1 are extremely contaminated (Class 6) while site F4 is heavy to extremely contaminated. These can be attributed to Pb-Zn mining activities at the mine and releases from mine wastes dumped or disposed of at sites F1 and F4. Other studied sites are moderately to heavily contaminated (Class 3) except the control site which is moderately contaminated. The descending sequence for contamination of the studied sites is as follows: mine > F1 > F4 > F8 > F3 and F5 > F2 > F6 > F7 > F9 > F10. Thus, the mining site is the most contaminated while the control is the least contaminated indicating the influence of mining activities.

3.2.3. Contamination factor (CF), degree of contamination (C_d), and pollution load index (PLI)

CF of the analyzed heavy metals, C_d , and PLI of the investigated soils are summarised in Table 5 and interpreted using levels and classes proposed by Hakanson (33) which is presented in Table 2. The mine site is highly contaminated (CF > 6) by Pb, Cu, and Zn, considerably contaminated by Fe and Mn and moderately contaminated by Cr. Thus, contamination of the mine is dominated by Pb, Cu, and Zn. However, the control site showed low contamination by Al and Fe, moderate contamination by Mn, and high contamination by Cu.

All studied sites showed low (CF < 1) and high (CF > 6) contamination of Al and Cu respectively. Most of the studied sites are considerably contaminated by Cr (CF = 3 – 6). The sites showed low to considerable levels of Fe contamination as well as moderate to considerable levels of Mn contamination. The mine and site F1 are highly contaminated by Pb while other studied sites are assumed to be lowly contaminated by Pb since their Pb content is below 1 mg/kg. Zn contaminates the mine at a very high level but the studied arable sites showed low to moderate Zn contamination. The high CF value (>1) for Pb, Zn, Cu, Mn, Cr, and Fe in different studied sites of the study area, is attributed to anthropogenic activities associated with Pb-Zn ore mining and processing which increase the geologic concentration of the heavy metals in arable soil around the mine.

C_d gives the summation of the contamination factor (CF) for all contaminants in a given sampling site (32). Table 5 shows that the studied sites are contaminated in the following decreasing order; mine > F4 > F1 > F8 > F5 > F3 > F2 > F6 > F7 > F9 > F10. This indicates that the mining and control sites are the most and least contaminated respectively. The contamination degrees of most studied sites (mine, sites F1, F2, F3, F4, F5, and F8) are very high ($C_d > 32$). Their contamination is dominated by Cu (all sites), Pb (mine and site F1 only), and Zn (mine only). The control site shows a moderate degree of contamination dominated by Cu.

A PLI value under zero indicates unpolluted soils; zero indicates perfection; a value of one or unity indicates the presence of only baseline levels of pollutants and values above one would indicate progressive deterioration of the site soil quality (34, 65). PLI values in this study (Table 5) are high (PLI > 1) except the control site with PLI value of approximately one. This indicates that the control site is considered unpolluted since the result suggests that the pollutants at this site are present at baseline levels. PLI values show that pollution of the studied sites follows a descending order: mine > F1 > F4 > F8 > F2 > F5 > F3 > F6 > F9 > F7 > F10. Thus, the mining site is the most polluted due to the Pb-Zn mineral exploration on this site.

3.2.4. Ecological risk assessment

The persistent nature of heavy metals results in their excessive accumulation in arable soils which affects food quality and safety because plants can absorb and store these heavy metals in their tissues. Consequently, when consumed by humans heavy metals increase the risks of severe diseases, such as cancer, leukemia, and kidney or liver damage (66). Soils contaminated by toxic heavy metals can enter the human body via different exposure routes (such as oral ingestion, inhalation, and dermal contact) and cause serious ecological and human health risks (67). Thus, it is necessary to evaluate the ecological risk factor (Er) of the individual analyzed heavy metals and the ecological risk index (RI) of the studied sites.

Er and RI were calculated to estimate the toxicity of the analyzed heavy metals in investigated soils. Er and RI classifications as specified by Hakanson (33) and reported in Table 2, were applied in the interpretation of Er and RI values of the analyzed heavy metals shown in Table 6. At the mine, Cu and Pb pose a very high ecological risk ($Er > 320$) while Zn has a significant potential for ecological risk. This implies that food crops, animals, and mine workers are exposed to a high risk of Pb, Zn, and Cu poisoning at the mine site (68). However, a low risk of contamination from Cr, Mn, Pb, and Zn and a moderate contamination risk from Cu was observed at the control site.

The Er of Al, As, and Fe were not evaluated because Al and Fe have no certified toxic response factor (Tr) while the levels of As in the investigated soils were below the instrumentation limit of detection. The result shows that the potential ecological risk factors

of Cr and Mn in all the studied sites are low ($Er < 40$). Thus, Cr and Mn do not pose any ecological risk to the environment. Cu has a very high potential ecological risk factor at mine and site F4 ($Er > 320$) and ranges between moderate to significant levels at other studied sites with the least Er of Cu observed at the control site. There is a very high and high potential risk of Pb contamination at the mine and site F1 respectively. Contamination risk from Pb at other studied sites could be assumed to be low due to the low level of Pb in these sites (< 1 mg/kg). Zn has a significant level of potential ecological risk at the mine ($Er = 80-160$) and low potential ecological risk at the studied arable soils.

The RI values of the analyzed metals in the investigated soils showed that the mine and control site had the highest and lowest risks of contamination respectively. This indicates that Pb-Zn mining activities affect the risk of contamination of the study area by these heavy metals. The mine and site F4 showed a high ecological risk index (RI > 600) while site F1 is considered to be at risk of contamination with a significant ecological risk index. This signifies that mine workers and Adudu dwellers close to the mine and arable farms used as disposal channels for mine wastes (i.e., sites F1 and F4) are exposed to toxic levels of Pb, Zn, and Cu through inhalation and dermal contact with the soils from the sites. Also, food crops grown on these sites are at high risk of being contaminated by Pb, Zn, and Cu which will be inimical to human health when consumed (6). A low risk of contamination was observed at the other studied arable sites (F2, F3, F5, F6, F7, F8, F9, and F10) due to their low ecological risk index (RI < 150). The high risk of contamination observed in arable sites F1 and F4 could be attributed to the discharge of mine wastes and tailings to these sites due to their proximity to the mine. The decreasing sequence of potential ecological risk index (RI) of the studied sites from the analyzed heavy metals is as follows: mine > F4 > F1 > F8 > F3 > F5 > F2 > F6 > F7 > F9 > F10. This sequence shows a direct relationship between RI and degree of contamination (C_d) due to their similar trends.

4. CONCLUSION

This study clearly showed that Pb-Zn-Cu bearing ores such as galena, sphalerite, chalcopyrite, bornite, smithsonite, cerussite, and azurite are principal minerals exploited in the mine because of the elevated concentrations of Cu, Fe, Mn, Pb, and Zn at the mining site. Concentrations of the analyzed heavy metals varied greatly away from the mine. Thus, the levels of these heavy metals in the arable soils are related to the Pb-Zn mining activities such as washing and erosion of tailings, discharge, and leaching of mine wastewater, atmospheric deposition (wet and dry) of metals, etc. Weathering or fragmentation of the geochemical composition of the rocks in the study area is a significant contributing factor to the source of these heavy metals. In soil quality assessment, the EF, I_{geo} , and CF showed that the mining site is very severely to extremely severely enriched, extremely polluted, and highly contaminated respectively Pb, Zn, and Cu. I_{IN} , C_d ,

and PLI showed that the mine and the nearby arable farms are the most deteriorated (contaminated and polluted) and the quality of soil improves away from the mining vicinity. Er revealed that the level of Pb, Zn, and Cu at the mine present a significant to very high risk of contamination. Cr and Mn in all the investigated soils pose no ecological risk but Cu poses moderate to very high ecological risk in the studied sites. RI showed that the presence of the analyzed heavy metals at the mine and the close arable farms (sites F1 and F4) can have serious adverse effects on plants, animals, and humans on the sites. However, the control and other studied sites had a low ecological risk index. Therefore, anthropogenic activities from Pb–Zn mining and natural processes (geologic weathering and Pb–Zn mineralization of the area) are the sources of these analyzed heavy metals in the arable soils around the mine site. This study has shown that the arable soils within the vicinity of the Pb–Zn mine, are not good for growing food crops because these heavy metals will enter the food chain via their uptake from soil.

5. CONFLICT OF INTEREST

The authors declare that they have no competing interests. All authors have endorsed the publication of this research.

6. ACKNOWLEDGMENTS

The authors appreciate the efforts of Dr Ombugadu Akwashiki, during the sample collection, especially in taking the GPS coordinates of sampling sites. We also thank Mr Esua D. Yaharo of the National Geological Survey, Kaduna State, Nigeria; for aiding in sample analysis.

7. REFERENCES

1. Oelofse SHH, Hobbs PJ, Rascher J, Cobbing JE. The pollution and destruction threat of gold mining waste on the Witwatersrand: A West Rand case study. In: 10th International Symposium on Environmental Issues and Waste management in Energy and Mineral Production (SWEMP, 2007), Bangkok. Citeseer; 2007. p. 11–3.
2. Adewumi T, Salako KA. Delineation of mineral potential zone using high resolution aeromagnetic data over part of Nasarawa State, North Central, Nigeria. *Egypt J Pet* [Internet]. 2018 Dec 1;27(4):759–67. Available from: [<URL>](#).
3. Obaje NG. Geology and Mineral Resources of Nigeria Development Options for Economic Growth and Social Transformation. In: 2nd Inaugural Lecture, Nigeria: Nasarawa State University, Keffi; 2008 (Unpublished).
4. Yan X, Liu M, Zhong J, Guo J, Wu W. How Human Activities Affect Heavy Metal Contamination of Soil and Sediment in a Long-Term Reclaimed Area of the Liaohe River Delta, North China. *Sustainability* [Internet]. 2018 Jan 29;10(2):338. Available from: [<URL>](#).
5. Oyebamiji A, Amanambu A, Zafar T, Adewumi AJ,

Akinyemi DS. Expected impacts of active mining on the distribution of heavy metals in soils around Iludun-Oro and its environs, Southwestern Nigeria. Fantke P, editor. *Cogent Environ Sci* [Internet]. 2018 Jan 1;4(1):1495046. Available from: [<URL>](#).

6. Mandeng EPB, Bidjeck LMB, Bessa AZE, Ntomb YD, Wadjou JW, Doumo EPE, et al. Contamination and risk assessment of heavy metals, and uranium of sediments in two watersheds in Abiete-Toko gold district, Southern Cameroon. *Heliyon* [Internet]. 2019 Oct;5(10):e02591. Available from: [<URL>](#).

7. Islam K, Murakami S. Global-scale impact analysis of mine tailings dam failures: 1915–2020. *Glob Environ Chang* [Internet]. 2021 Sep 1;70:102361. Available from: [<URL>](#).

8. Yang CL, Guo RP, Yue QL, Zhou K, Wu ZF. Environmental quality assessment and spatial pattern of potentially toxic elements in soils of Guangdong Province, China. *Environ Earth Sci* [Internet]. 2013 Oct 12;70(4):1903–10. Available from: [<URL>](#).

9. Obiora SC, Chukwu A, Davies TC. Heavy metals and health risk assessment of arable soils and food crops around Pb–Zn mining localities in Enyigba, southeastern Nigeria. *J African Earth Sci* [Internet]. 2016 Apr 1;116:182–9. Available from: [<URL>](#).

10. Aloh G, Aloh H, Obasi A, Chukwu K. Evidence of Heavy Metal Contamination of Agricultural Soil in Ameri, Abakaliki Lead-Zinc Mining Area, Ebonyi State Southeast Nigeria: An Indication for Phytoremediation. *Nutr Food Technol Open Access* [Internet]. 2017;3(3):1–5. Available from: [<URL>](#).

11. Chukwu A, Oji KK. Assessment of Pb, Zn, As, Ni, Cu, Cr and Cd in Agricultural Soils around Settlements of Abandoned Lead-Zinc Mine in Mkpuma Ekwoku, South-eastern, Nigeria. *J Appl Sci Environ Manag* [Internet]. 2018 Nov 27;22(9):1485–8. Available from: [<URL>](#).

12. Obasi PN, Akudinobi BEB. Pollution status of arable soils and stream sediments in mining areas of Abakaliki, Lower Benue Trough, Nigeria. *Int J Environ Sci Technol* [Internet]. 2019 Dec 22;16(12):7869–84. Available from: [<URL>](#).

13. Potra A, Dodd JW, Ruhl LS. Distribution of trace elements and Pb isotopes in stream sediments of the Tri-State mining district (Oklahoma, Kansas, and Missouri), USA. *Appl Geochemistry* [Internet]. 2017 Jul 1;82:25–37. Available from: [<URL>](#).

14. Eludoyin AO, Ojo AT, Ojo TO, Awotoye OO. Effects of artisanal gold mining activities on soil properties in a part of southwestern Nigeria. Nzeadibe T, editor. *Cogent Environ Sci* [Internet]. 2017 Jan 1;3(1):1305650. Available from: [<URL>](#).

15. Canlı O, Çetintürk K, Güzel B. A comprehensive assessment, source input determination and distribution of persistent organic pollutants (POPs) along with heavy metals (HMs) in reservoir lake sediments from Çanakkale province, Türkiye. *Environ Geochem Health* [Internet]. 2023 Jun

- 11;45(6):3985–4006. Available from: [<URL>](#).
16. Zhang W, You M, Hu Y. The distribution and accumulation characteristics of heavy metals in soil and plant from Huainan coalfield, China. *Environ Prog Sustain Energy* [Internet]. 2016 Jul 22;35(4):1098–104. Available from: [<URL>](#).
17. Idzi AA, Olaleke AM, Shekwonyadu I, Christian EA. Geochemical studies of mineral bearing ores from Nasarawa Eggon and Udege Beki areas of Nasarawa State, Nigeria. *Int J Basic Appl Chem Sci* [Internet]. 2013;3(1):93–108. Available from: [<URL>](#).
18. Jauro A, Obaje NG, Agho MO, Abubakar MB, Tukur A. Organic geochemistry of Cretaceous Lamza and Chikila coals, upper Benue trough, Nigeria. *Fuel* [Internet]. 2007 Mar 1;86(4):520–32. Available from: [<URL>](#).
19. Attah S. Governor Sule assures of repositioning mining sector [Internet]. *Business Day Newspaper*. 2020 [cited 2020 Oct 23]. Available from: [<URL>](#).
20. Ezeaku PI. Evaluating the influence of open cast mining of solid minerals on soil, landuse and livelihood systems in selected areas of Nasarawa State, North-Central Nigeria. *J Ecol Nat Environ* [Internet]. 2012 Feb 12;4(3):62–70. Available from: [<URL>](#).
21. Okolo CC, Akamigbo FOR, Ezeaku PI, Nwite JN, Nwite JC, Ezeudo VC, et al. Impact of open cast mine land use on soil physical properties in Enyigba, Southeastern Nigeria and the implication for sustainable land use management. *Niger J Soil Sci* [Internet]. 2015;25:95–101. Available from: [<URL>](#).
22. Obasi NA, Obasi SE, Elom SO, Kalu KM, Alope C, Igwenyi IO, et al. Health Risk Assessment of Heavy Metals in Ameri Lead-Zinc Mining Community Via Consumption of Cassava (*Manihot esculenta* Cruz) in Ikwo L.G.A., Ebonyi State, Nigeria. *Am J Sustain Agric* [Internet]. 2017 [cited 2024 Jan 11];11(6):22–30. Available from: [<URL>](#).
23. Benkhelil J, Guiraud M, Ponsard JF, Saugy L. The Bornu-Benue Trough, the Niger Delta and its offshore: Tectono-sedimentary reconstruction during the Cretaceous and Tertiary from geophysical data and geology. In: *Geology of Nigeria*, 2nd ed. Rock view, Jos. 1989 (Unpublished).
24. *Physica Setting of Nasarawa State*. [cited 2003 May 2]; Available from: [<URL>](#).
25. Sutherland RA. Bed sediment-associated trace metals in an urban stream, Oahu, Hawaii. *Environ Geol* [Internet]. 2000 Apr 18;39(6):611–27. Available from: [<URL>](#).
26. Turekian KK, Wedepohl KH. Distribution of the Elements in Some Major Units of the Earth's Crust. *Geol Soc Am Bull* [Internet]. 1961;72(2):175–92. Available from: [<URL>](#).
27. Muller G. Index of geoaccumulation in sediments of the Rhine River. *GeoJournal*. 1969;2(3):108–18.
28. Guan Y, Shao C, Ju M. Heavy Metal Contamination Assessment and Partition for Industrial and Mining Gathering Areas. *Int J Environ Res Public Health* [Internet]. 2014 Jul 16;11(7):7286–303. Available from: [<URL>](#).
29. Nwankwoala HO, Ememu AJ. Contamination Indices and Heavy Metal Concentrations in Soils in Okpoko and Environs, Southeastern Nigeria. *J Environ Sci Public Heal* [Internet]. 2018;2(2):77–95. Available from: [<URL>](#).
30. Nemerow NL. *Stream, lake, estuary, and ocean pollution*, 2nd edition [Internet]. New York: Van Nostrand Reinhold Publishing Co.; 1985 [cited 2024 Jan 11]. Available from: [<URL>](#).
31. Egaspin DPR. Environmental Guidelines and Standards for the Petroleum Industry in Nigeria (EGASPIN). Department of Petroleum Resources, Lagos, Nigeria. 2002; Available from: [<URL>](#).
32. Güzel B, Canlı O, Aslan E. Spatial distribution, source identification and ecological risk assessment of POPs and heavy metals in lake sediments of Istanbul, Turkey. *Mar Pollut Bull* [Internet]. 2022 Feb 1;175:113172. Available from: [<URL>](#).
33. Hakanson L. An ecological risk index for aquatic pollution control. a sedimentological approach. *Water Res* [Internet]. 1980 Jan 1;14(8):975–1001. Available from: [<URL>](#).
34. Tomlinson DL, Wilson JG, Harris CR, Jeffrey DW. Problems in the assessment of heavy-metal levels in estuaries and the formation of a pollution index. *Helgoländer Meeresuntersuchungen* [Internet]. 1980 Mar;33(1–4):566–75. Available from: [<URL>](#).
35. Agency for Toxic Substances and Disease Registry (ASTDR). Public Health Statement, Aluminum. *Dep Heal Hum Serv Public Heal Serv Div Toxicol Environ Med Atlanta CAS#7429 – 90 – 5* 2008.
36. Exley C. The toxicity of aluminium in humans. *Morphologie* [Internet]. 2016 Jun;100(329):51–5. Available from: [<URL>](#).
37. Obiora SC, Chukwu A, Davies TC. Contamination of the Potable Water Supply in the Lead-Zinc Mining Communities of Enyigba, Southeastern Nigeria. *Mine Water Environ* [Internet]. 2019 Mar 19;38(1):148–57. Available from: [<URL>](#).
38. Abraham MR, Susan TB. Water contamination with heavy metals and trace elements from Kilembe copper mine and tailing sites in Western Uganda; implications for domestic water quality. *Chemosphere* [Internet]. 2017 Feb 1;169:281–7. Available from: [<URL>](#).
39. Nriagu JO, Pacyna JM. Quantitative assessment of worldwide contamination of air, water and soils by trace metals. *Nature* [Internet]. 1988 May;333(6169):134–9. Available from: [<URL>](#).
40. Nriagu JO, Bhattacharya P, Mukherjee AB, Bundschuh J, Zevenhoven R, Loeppert RH. Arsenic in

- soil and groundwater: an overview. In: Trace Metals and other Contaminants in the Environment [Internet]. Elsevier; 2007. p. 3–60. Available from: [<URL>](#).
41. Cullen WR, Reimer KJ. Arsenic speciation in the environment. *Chem Rev* [Internet]. 1989 Jun 1;89(4):713–64. Available from: [<URL>](#).
42. Ambo AI, Etonihu C, Iyakwari S, Ogara JI. Assessment of Metal concentrations in Lead- Zinc mines and Near-by soils, plants and water in Abuni Town Awe Local Government Area, Nasarawa State, Niheria. *NSUK J Sci Technol*. 2012;2(1&2):232–41.
43. Wu M-M, Kuo T-L, Hwang Y-H, Chen C-J.. Dose-response relation between arsenic concentration in well water and mortality from cancers and vascular diseases. *Am J Epidemiol* [Internet]. 1989 Dec 1;130(6):1123–32. Available from: [<URL>](#).
44. Chen C-J, Chen C, Wu M-M, Kuo T-L. Cancer potential in liver, lung, bladder and kidney due to ingested inorganic arsenic in drinking water. *Br J Cancer* [Internet]. 1992 Nov;66(5):888–92. Available from: [<URL>](#).
45. Agency for Toxic Substances and Disease Registry (ATSDR). Toxicological Profile for Arsenic. U. S. Department of Health & Human Services, Public Health Service, Division of Toxicology 1600, Atlanta, GA 30333. 1999;
46. Agency for Toxic Substances and Disease Registry (ATSDR). Toxicological profile for Chromium. Division of Toxicology and Human Health Sciences, Environmental Toxicology Branch, Atlanta, Georgia. 2012;
47. Azeh Engwa G, Udoka Ferdinand P, Nweke Nwalo F, N. Unachukwu M. Mechanism and Health Effects of Heavy Metal Toxicity in Humans. In: Karcioğlu O, Arslan B, editors. *Poisoning in the Modern World - New Tricks for an Old Dog?* [Internet]. IntechOpen; 2019. Available from: [<URL>](#).
48. Agency for Toxic Substances and Disease Registry (ATSDR). Toxicological profile for Cobalt. U.S. Department of Health and Human Services, Public Health Service, Division of Toxicology 1600, Atlanta, GA 30333. 2004;
49. Clewell HJ, Lawrence GA, Calne DB, Crump KS. Determination of an Occupational Exposure Guideline for Manganese Using the Benchmark Method. *Risk Anal* [Internet]. 2003 Oct 12;23(5):1031–46. Available from: [<URL>](#).
50. Anapuwa OS. Heavy Metal Contamination and Physicochemical Characteristics of Soils from Automobile Workshops in Abraka, Delta State, Nigeria. *Int J Nat Sci Res* [Internet]. 2014;2(4):48–58. Available from: [<URL>](#).
51. Keen CL, Ensunsa JL, Lönnerdal B, Zidenberg-Cherr S. Manganese. In: Caballero B, Allen L, Prentice A, editors. *Encyclopedia of Human Nutrition* [Internet]. Elsevier; 2013. p. 148–54. Available from: [<URL>](#).
52. Obasi PN, Akudinobi BB. Potential health risk and levels of heavy metals in water resources of lead-zinc mining communities of Abakaliki, southeast Nigeria. *Appl Water Sci* [Internet]. 2020 Jul 7;10(7):184. Available from: [<URL>](#).
53. Wani AL, Ara A, Usmani JA. Lead toxicity: a review. *Interdiscip Toxicol* [Internet]. 2015 Jun 1;8(2):55–64. Available from: [<URL>](#).
54. Sokol RZ, Berman N. The effect of age of exposure on lead-induced testicular toxicity. *Toxicology* [Internet]. 1991 Jan 1;69(3):269–78. Available from: [<URL>](#).
55. Rubin R, Strayer DS. Environmental and Nutritional pathology. In: Rubin's pathology: clinicopathologic foundations of medicine. Philadelphia: Lippincott Williams & Wilkins; 2008.
56. El-Alfy MA, El-Amier YA, El-Hamid HTA. Soil quality and health risk assessment of heavy metals in agricultural areas irrigated with wastewater from Kitchener Drain, Nile Delta, Egypt. *J Sci Agric* [Internet]. 2017 Jun 20;1:158–70. Available from: [<URL>](#).
57. Burgos P, Madejón E, Pérez-de-Mora A, Cabrera F. Spatial variability of the chemical characteristics of a trace-element-contaminated soil before and after remediation. *Geoderma* [Internet]. 2006 Jan 1;130(1–2):157–75. Available from: [<URL>](#).
58. Conesa HM, Robinson BH, Schulin R, Nowack B. Metal extractability in acidic and neutral mine tailings from the Cartagena-La Unión Mining District (SE Spain). *Appl Geochemistry* [Internet]. 2008 May 1 [cited 2024 Jan 11];23(5):1232–40. Available from: [<URL>](#).
59. Elueze AA. Geochemistry of the Ilesha granite gneiss in the basement complex of southwestern Nigeria. *Precambrian Res* [Internet]. 1982 Oct 1;19(2):167–77. Available from: [<URL>](#).
60. Charzyński P, Plak A, Hanaka A. Influence of the soil sealing on the geoaccumulation index of heavy metals and various pollution factors. *Environ Sci Pollut Res* [Internet]. 2017 Feb 16;24(5):4801–11. Available from: [<URL>](#).
61. Szefer P, Szefer K, Glasby GP, Pempkowiak J, Kaliszan R. Heavy-metal pollution in surficial sediments from the Southern Baltic sea off Poland. *J Environ Sci Heal Part A Environ Sci Eng Toxicol* [Internet]. 1996 Nov;31(10):2723–54. Available from: [<URL>](#).
62. Birth GA. A scheme for assessing human impacts on coastal aquatic environments using sediments. In: Woodcoffe CD, Furness RA, editors. *Coastal GIS 2003*. Wollongong: Wollongong University Papers; 2003.
63. Santos-Francés F, Martínez-Graña A, Alonso Rojo P, García Sánchez A. Geochemical Background and Baseline Values Determination and Spatial Distribution of Heavy Metal Pollution in Soils of the Andes Mountain Range (Cajamarca-Huancavelica,

- Peru). *Int J Environ Res Public Health* [Internet]. 2017 Jul 31;14(8):859. Available from: [<URL>](#).
64. Förstner U, Ahlf W, Calmano W, Kersten M. Sediment Criteria Development. In: Heling D, Rothe P, Förstner U, Stoffers P, editors. *Sediments and Environmental Geochemistry* [Internet]. Berlin, Germany: Springer; 1990 [cited 2024 Jan 11]. p. 311–38. Available from: [<URL>](#).
65. Chakravarty M, Patgiri AD. Metal Pollution Assessment in Sediments of the Dikrong River, N.E. India. *J Hum Ecol* [Internet]. 2009 Jul 24;27(1):63–7. Available from: [<URL>](#).
66. Suresh G, Sutharsan P, Ramasamy V, Venkatachalapathy R. Assessment of spatial distribution and potential ecological risk of the heavy metals in relation to granulometric contents of Veeranam lake sediments, India. *Ecotoxicol Environ Saf* [Internet]. 2012 Oct 1;84:117–24. Available from: [<URL>](#).
67. Dong X, Li C, Li J, Wang J, Liu S, Ye B. A novel approach for soil contamination assessment from heavy metal pollution: A linkage between discharge and adsorption. *J Hazard Mater* [Internet]. 2010 Mar 15;175(1–3):1022–30. Available from: [<URL>](#).
68. Lo Y-C, Dooyema CA, Neri A, Durant J, Jefferies T, Medina-Marino A, et al. Childhood Lead Poisoning Associated with Gold Ore Processing: a Village-Level Investigation—Zamfara State, Nigeria, October–November 2010. *Environ Health Perspect* [Internet]. 2012 Oct;120(10):1450–5. Available from: [<URL>](#).



Synthesis of Ternary Chalcogenides in Cu-As-Se Systems by the Solvothermal Method in Organic Medium and Production of Nano-and Microparticles

Turac Suleymanova¹ 

¹Y.H. Mamedaliyev's Institute of Petrochemical Processes of the Ministry of Science and Education, AZ 1025, Baku, Azerbaijan

Abstract: Ternary selenides CuAsSe_2 and Cu_3AsSe_3 were synthesized by the solvothermal method from H [CuCl₂]-As₂Se₃-C₂H₆O₂ system. Nano and microparticles were obtained, and their physical and chemical properties were studied. During syntheses, sodium metaarsenite and copper (I) chloride are mixed in ethylene glycol, and a solution of Na₂SeSO₃ is added as a selenidation reagent according to stoichiometry. These solutions were added to an experimental vessel, placed in a Teflon cuvette, sealed, and placed in a microwave electric heater. The samples are kept in the oven at 413-443 K for 10 hours. After the process, the precipitate is filtered through a glass filter, washed first with dilute hydrochloric acid and distilled water, and finally with ethyl alcohol, and dried in a vacuum at 333-343 K. The productivity of the samples was 90-92 %. Compounds formed at a temperature of 453-473 K dissolve. Nanoparticles of compounds obtained at a temperature of 413-433 K have an irregular shape. Nanoparticles obtained at a temperature of 443 K are in the form of plates. The results of the X-ray phase analysis showed that the compounds correspond to cubic zirconia and belong to the Pm3m spatial structure. Lattice parameters of CuAsSe_2 compound: $a = 5.513 \text{ \AA}$, $Z = 2$ and lattice parameters of Cu_3AsSe_3 compound: $a = 5.76 \text{ \AA}$, $Z = 1$. Based on DTA results, the CuAsSe_2 compound melts congruently at 743 K, while the Cu_3AsSe_3 compound decomposes at 773 K.

Keywords: Solvothermal method, Nanoparticles, Scanning electron microscope, XRF, Melting point, Unit cell

Submitted: January 10, 2023. **Accepted:** November 29, 2023.

Cite this: Suleymanova T. Synthesis of Ternary Chalcogenides in Cu-As-Se Systems by the Solvothermal Method in Organic Medium and Production of Nano-and Microparticles. JOTCSA. 2024;11(2):499-506.

DOI: <https://doi.org/10.18596/jotcsa.1231804>

*Corresponding author. E-mail: teimxkl@gmail.com

1. INTRODUCTION

Three-component copper chalcogenides are among the promising functional materials of modern technology. Multicomponent crystalline and amorphous materials of Cu-, Ag-, Ge-, In-, As-, and Sb-based chalcogenides reveal a significant combination of electrical, optical,

magnetic, mechanical, and other physical properties. The study of physical processes in amorphous chalcogenide semiconductor layers has expanded to nanostructures in the recent decade. Despite a wide range of compositions in binary, ternary, and more complex systems of

chalcogenide glasses, the problem of smooth or abrupt modification of parameters still exists. These modifications are performed partially by particular technologies (cooling rate, thin film deposition) or by creating complex artificial structures as known in microelectronic technology. Following the example of microelectronics turning to nanoelectronics on the way to the smaller and more efficient devices exploiting new properties of the crystalline semiconductors at the nano-scale, scientists drew attention to amorphous materials (1-7).

This work demonstrates a simple and elegant strategy for the synthesis of CuInSe_2 with improved control over the chemical composition.

The reaction proceeds via a redox-induced phase transformation of the line compound copper diselenide (CuSe_2) upon incremental addition of elemental indium. Given the chemical and structural similarity between CuSe_2 and CuInSe_2 , stepwise direct transformation of the CuSe_2 structural template into $(1-x)\text{CuSe}_2 / x\text{CuInSe}_2$ nanocomposites without the formation of unwanted binary or ternary indium phases is demonstrated. By X-ray diffraction and transmission electron microscopy, CuInSe_2 particles in size range from 5 to 50 nm of the structural template provided by CuSe_2 are formed (Figure 1) (8).

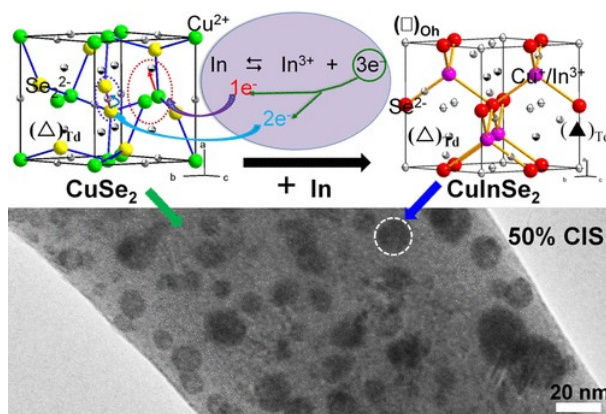


Figure 1: Formed particles of CuInSe_2 in the 5-50 nm size range of the structural template provided by CuSe_2 by X-ray diffraction and transmission electron microscopy.

The $\text{Cu}_5\text{As}_{46.25}\text{Se}_{48.75}$ samples were prepared from arsenic (As) pieces (99.9999 %), selenium (Se) pellets (99.999 + %), and highly enriched copper ^{65}Cu (99.73 % ^{65}Cu and 0.27 % ^{63}Cu) or ^{63}Cu (99.89 % ^{63}Cu and 0.11 % ^{65}Cu) isotopes. The elements were weighed in the correct proportions in a high-purity argon-filled glove box using a balance of precision ± 0.1 mg to give a total sample mass of ≥ 3 g. They were then sealed under vacuum ($\leq 10^{-5}$ torr) in cleaned silica ampoules (5 mm inner diameter and 1 mm wall thickness), heated slowly in a rocking furnace to 870 °C, maintained at this temperature for 6 hours, and finally cooled to 500 °C before quenching in an ice/salt-water mixture. The samples, therefore, are processed in the same fashion to aid materials with identical compositions (9).

($\text{Te}_{85}\text{Se}_{15}$) $_{60-0.6x}\text{As}_{40-0.4x}\text{Cu}_x$ ($x = 0, 10, 16.7, 20, 25$) glasses (TEA1, TEA2, TEA3, TEA4, and TEA5 respectively) were prepared using the melt quenching method. Appropriate amounts of high purity (5N) raw materials Te, Se, As mixed with Cu and sealed in evacuated ($\sim 10^{-3}$ Pa) silica

tubes and melted in a rocking furnace at 1023 K for 10 hours. Then, the glasses were quenched in water and annealed at 5 K lower than their glass transition temperature T_g for 3 hours to relieve internal stresses (10).

The phase diagram $\text{Cu}_2\text{Se}-\text{As}_2\text{Se}_3$ was investigated using thermal and X-ray methods. Cu_2Se has a limited solubility for As_2Se_3 (5 mole % at 769 K). The stoichiometric compound Cu_3AsSe_3 exists between 696 and 769 K. $\text{Cu}_4\text{As}_2\text{Se}_5$, a phase at 66.6 mole % Cu_2Se , decomposes peritectically at 746 K. The narrow homogeneity range (4 mole % at 683 K) extends far into the ternary space. CuAsSe_2 also decomposes peritectically at 683 K. A degenerated eutectic between CuAsSe_2 and As_2Se_3 was found at 641 K. Single crystals of $\text{Cu}_4\text{As}_2\text{Se}_5$ were grown in a salt melt. A metastable modification of the high-temperature phase Cu_3AsSe_3 can be obtained by quenching. $\text{Cu}_4\text{As}_2\text{Se}_5$ (space group $R\bar{3}$, lattice constants $a = 1404.0(1)$ pm, $c = 960.2(1)$ pm), $\text{Cu}_6\text{As}_4\text{Se}_9$, obtained by Cambi and Elli, and $\text{Cu}_7\text{As}_6\text{Se}_{13}$ of Takeuchi and Horiuchi are different versions of a

sphalerite-type compound with a broad homogeneity range in the system Cu-As-Se. CuAsSe_2 is possibly monoclinic with lattice parameters of $a = 946.5(1)$ pm, $b = 1229.3(1)$ pm, $c = 511.7(1)$ pm, and $\beta = 98.546(4)$. The enthalpy of mixing Cu_2Se and As_2Se_3 in the liquid state is endothermic (11).

Analysis of the literature shows that CuAsSe_2 and Cu_3AsSe_3 compounds were obtained from elemental substances only by the bulb synthesis method, with no material about obtaining nano- and microparticles. In our study, the synthesis of glassy ternary chalcogenide semiconductors from the $\text{H}[\text{CuCl}_2]\text{-As}_2\text{Se}_3\text{-C}_2\text{H}_6\text{O}_2$ system containing CuAsSe_2 and Cu_3AsSe_3 by a new, inexpensive method was presented. The influence of the conditions of obtaining nano- and micro-particles of those compounds was studied, and several physicochemical properties were studied.

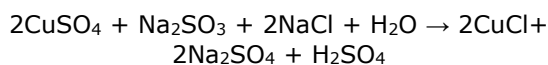
2. EXPERIMENTAL SECTION

2.1. Materials

Ternary copper chalcogenide compounds synthesized from copper (I) chloride and sodium metaarsenite under solvothermal conditions. Sodium selenium sulfate in an ethylene glycol medium is used as a selenizing reagent and the number of reagents taken by stoichiometry.

Preparation of copper (I) chloride and sodium selenosulfate:

Copper (I) chloride is a white tetrahedral crystalline substance that forms salt in the open air and turns blue quickly. CuCl is slightly soluble in water (0.0062 % at 293 K). It is soluble in NH_4OH , hot solid HCl , and chloride solutions of alkali metals. The preparation was obtained according to the following reaction equation using Na_2SO_3 to reduce Cu^{2+} ions from CuSO_4 :



250 g of $\text{CuSO}_4 \cdot 5\text{H}_2\text{O}$ and 125 g of NaCl are dissolved and filtered by heating in 900 ml of water. 240 g of Na_2SO_3 dissolved in 530 ml on an aqueous and filtered added to the filtrate heated until a light blue color formed. Separated CuCl is mixed with 40 ml of 2 % hydrochloric acid solution in a bunsen tube and filtered with suction. In this manner, washing continued until the sulfate ions were exhausted. Then, the sediment was washed several times with ethyl alcohol, spread in a thin layer on a porcelain bowl, and dried at 110 °C with occasional stirring (12).

Preparation of sodium selenosulfate from sodium sulfite and elemental selenium. Elemental

selenium reacts with sodium sulfite to form sodium selenosulfate according to the equation: $\text{Na}_2\text{SO}_3 + \text{Se} \rightarrow \text{Na}_2\text{SeSO}_3$. Typically, to prepare a 50 mM solution of Na_2SeSO_3 , 0.0987 g of Se powder refluxed with 0.5 g Na_2SO_3 in 20 mL distilled water in a round bottom flask fitted with an air condenser for 3-4 h. An excess concentration of Na_2SO_3 is necessary to prevent the decomposition of Na_2SeSO_3 back into Se and Na_2SO_3 . After cooling, the solution was filtered and diluted to 25 mL in a standard measuring flask. This solution is used immediately for the synthesis (13, 14).

2.2. The Method of Obtaining CuAsSe_2

First, the stoichiometry, sodium metaarsenite and copper (I) chloride are mixed in 20 ml of ethylene glycol, and then the selenizing agent sodium selenosulfate (pH = 7-5) is added. The mixture is heated in a sealed glass ampoule in an electric microwave oven (Speedwave four BERGHOF - Germany). The sample was kept in a heater between 413 and 443 K for 6 hours. The resulting precipitate is filtered through a glass filter, washed with the dilute hydrochloric acid solution, ultrapure water, and ethyl alcohol, and dried in a vacuum at 333-343 K.

2.3. Synthesis method of Cu_3AsSe_3

The composition is synthesized from CuCl , NaAsO_2 , and sodium selenosulfate under solvothermal conditions. The mixture is stirred in 20 ml of ethylene glycol sodium selenosulfate (pH = 7-5) and heated in a sealed glass bulb in an electric microwave oven. The sample is kept in a heater at a temperature of 413-443 K for 6 hours.

The yield of both substances is 90-92 %. At a temperature (453-473 K), the resulting precipitate of CuAsSe_2 and Cu_3AsSe_3 partially dissolves in a solution (ethylene glycol). The composition of the obtained compound (Cu-As-Se ratio) was determined in a NETZSCH STA 449F349F3 (Germany) thermal analyzer and chemical analysis. Differential thermal analysis (DTA) was carried out with an HTP-70 pyrometer, Thermoscan-2 unit, in an inert atmosphere. The phase analysis of CuAsSe_2 and Cu_3AsSe_3 nano- and microparticles was studied using a Bruker D8 ADVANCE X-ray diffractometer ($\text{CuK}\alpha$, $\lambda = 1.5406 \text{ \AA}$, $0 < 2\theta < 80^\circ$). Morphological studies were performed using scanning electron microscopy TM3000 (Hitachi, Japan).

3. RESULTS AND DISCUSSION

3.1. TG Analysis

It is known that, depending on the conditions of acquisition, chalcogenides in the organic or aqueous mediums of various synthesized

compositions CuAsSe_2 , Cu_3AsSe_3 , $\text{Cu}_4\text{As}_2\text{Se}_5$, $\text{Cu}_8\text{As}_2\text{Se}_7$ etc. with different stoichiometry. Therefore, thermogravimetric analysis was carried out using the hydrothermal method in the NETZSCH STA 449F349F3 instrument. The results of the reacher are shown in Figure 2.

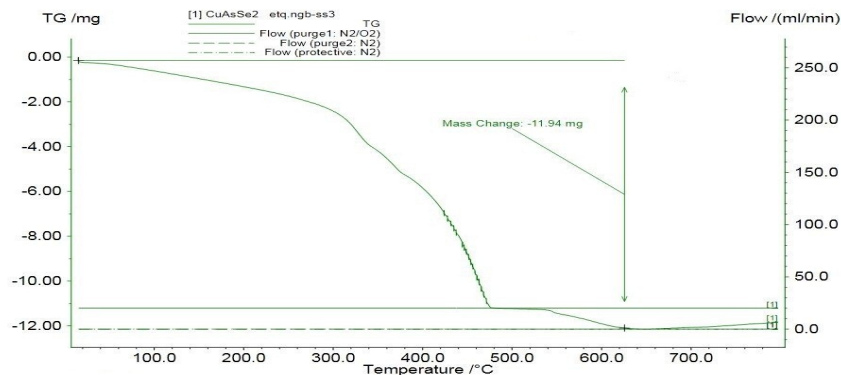


Figure 2: TGA diagrams of CuAsSe_2 .

They were within 20 - 800 °C, and the air supply rate was 40 ml/min. Weight loss at a temperature of 20 - 625 °C is 11.94 mg. A sample weighing 14.95 mg was taken for analysis. The theoretically contains 3.78 mg of arsenic and 7.95 mg of selenium (total 3.78 + 7.95 = 11.73 mg). The weight loss (11.94 mg in the experiment) occurred due to As and Se, and

this number is consistent with the theoretically calculated amounts. The remainder (3.01 mg) coincides with the theoretically calculated amount of copper (3.12 mg). All this shows that the formula for the CuAsSe_2 compound is correct. The thermal differential analysis of the CuAsSe_2 alloy indicated congruent melting at 480 °C.

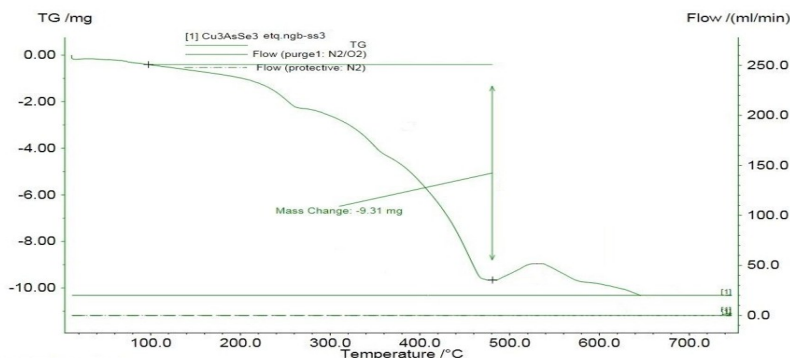


Figure 3: TGA diagrams of Cu_3AsSe_3 .

The heating of the samples was carried out within the temperature range of 20 - 750 °C. A sample weighing 15 mg was taken for analysis. In the Cu_3AsSe_3 sample at a temperature of 20-480 °C, the weight loss is 9.31 mg (Figure 3), which corresponds to the theoretically calculated amount of arsenic and selenium (2.23 mg As + 7.05 mg Se = 9.28 mg). The remaining 5.69 mg corresponds to the content of copper (5.71 mg) in the sample. The results obtained confirm the

correctness of the formula for the compound Cu_3AsSe_3 .

Endo effects observed at 220 °C, 480 °C, 560 °C in TGA of Cu_3AsSe_3 compound. The thermal effect at 220 °C corresponds to the decomposition of Cu_3AsSe_3 into CuAsSe_2 , the effect at 480 °C corresponds to the oxidation of Cu_2O , and the effect at 560 °C corresponds to the oxidation of Cu_2O to CuO .

According to the DTA results, the CuAsSe_2 compound melts congruently at 470°C , and the Cu_3AsSe_3 compound melts with decomposition at 500°C .

3.2. X-Ray Structure Determination

X-ray phase analysis of the compound CuAsSe_2 and Cu_3AsSe_3 studied patterns showed that the CuAsSe_2 and Cu_3AsSe_3 compounds crystallize into the cubic crystal system (CuAsSe_2 sp. gr.: $a = 5.513 \text{ \AA}$), Cu_3AsSe_3 (sp. gr.: $a = 5.758 \text{ \AA}$) (Figure 4, 5).

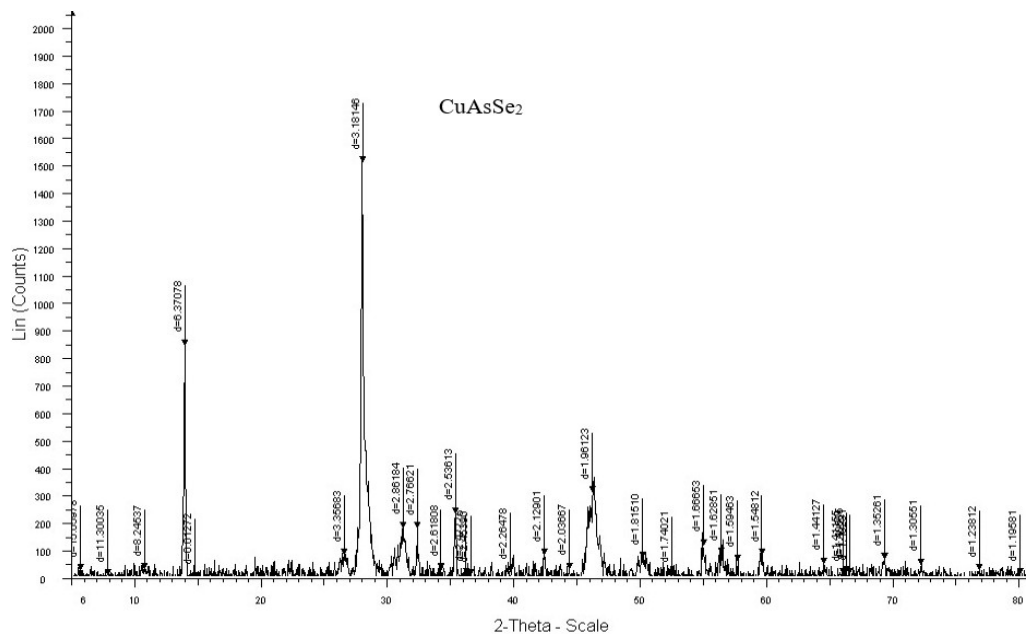


Figure 4: X-ray diffraction pattern of CuAsSe_2 .

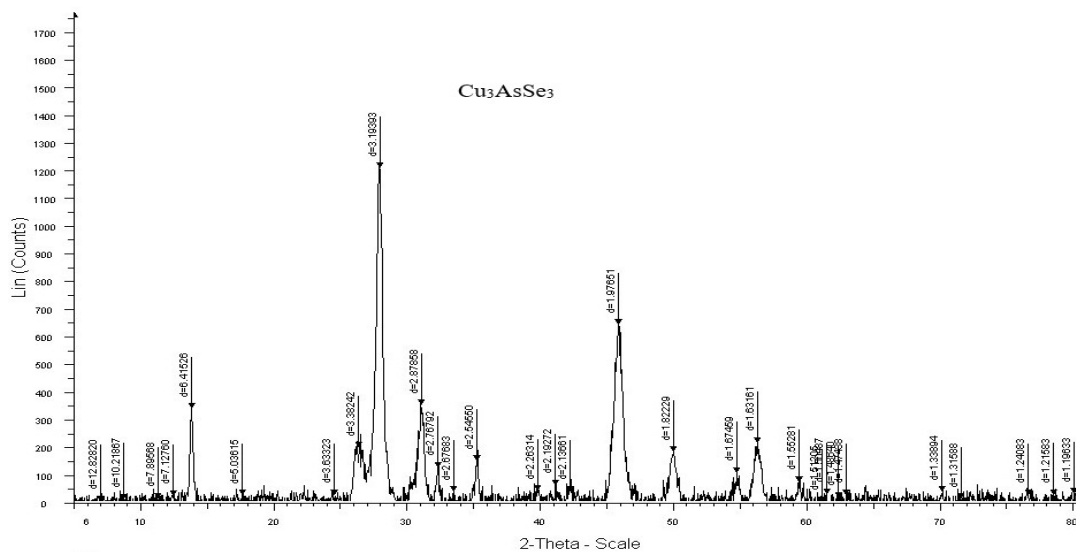


Figure 5: X-ray diffraction pattern of Cu_3AsSe_3 .

X-ray diffraction pattern of arsenic copper selenide (CuAsSe_2 , Cu_3AsSe_3) intensity and position of the developing peaks fully comply with the standards (PDF 00-012-0379).

3.3. SEM analysis

The effect of temperature growth and formation of nano and microparticles synthesized by the solvothermal method was studied, and the sizes of these particles were taken in an electron

microscope (Figure 6, 7). As the temperature changes from 413 K to 443 K, they gradually transform into different formations. It can be seen from the picture that the CuAsSe_2 and

Cu_3AsSe_3 nanoparticles obtained at the temperature of 413 K have an irregular shape (Figure 6 a, b).

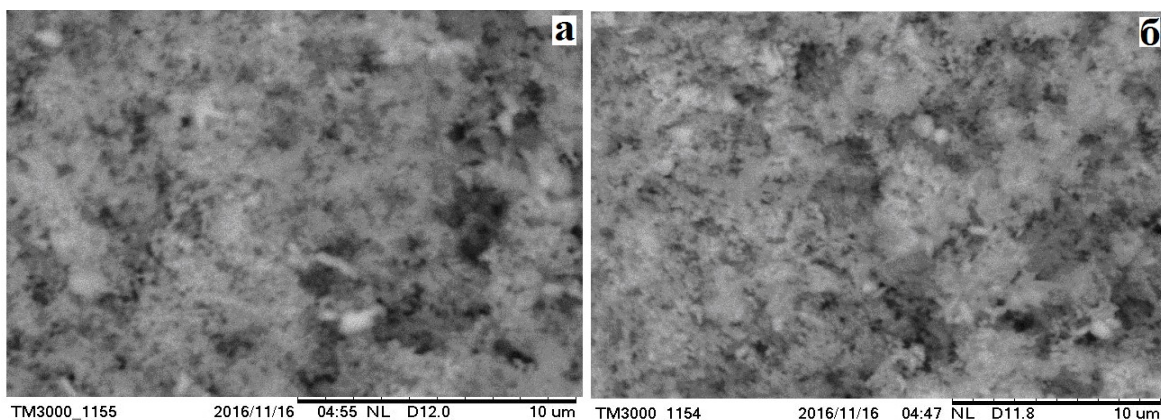


Figure 6: SEM photographs of CuAsSe_2 (a) and Cu_3AsSe_3 (b) nanoparticles at 413 K.

Furthermore, at a temperature of 443 K, formed nano and microplates (Figure 7 a, b). nanoparticles (CuAsSe_2 and Cu_3AsSe_3) are

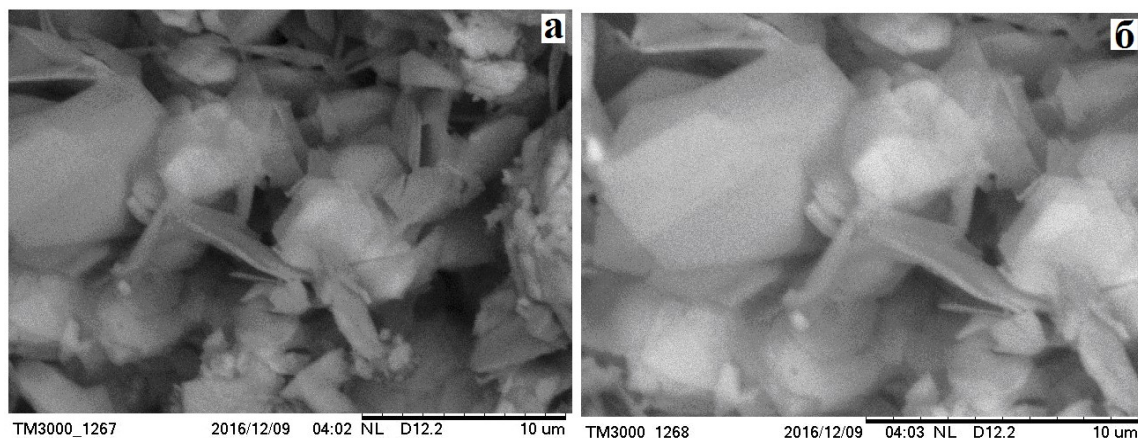


Figure 7: SEM photographs of CuAsSe_2 (a) and Cu_3AsSe_3 (b) nanoparticles at 443 K.

It was determined that the formation of nano- and microparticles depends on temperature and time in the liquid phase. Thus, when As^{3+} and Se^{2-} interact in an ethylene glycol medium, a dark brown precipitate (pH=10) is formed. After heating for 10 hours, a coagulated black settled in the reaction vessel.

3.4. Thermal Properties

The DTA thermograms show that one endothermic peak was observed on the curves (Figure 8 a, b).

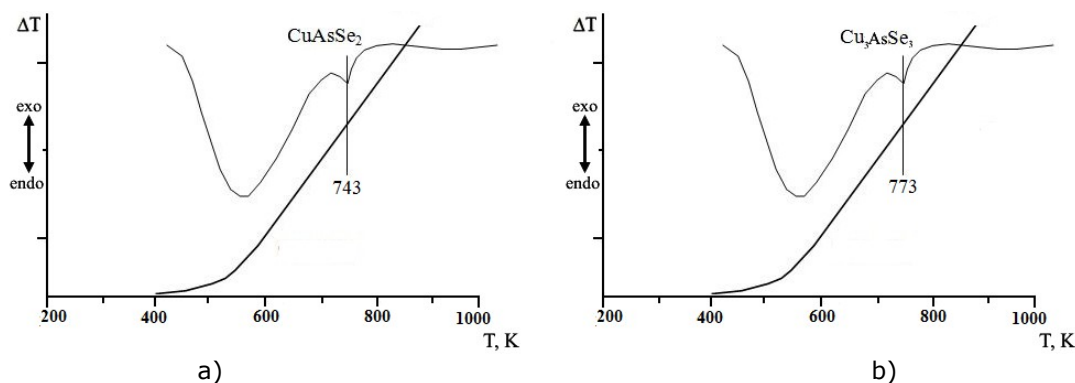


Figure 8: DTA curves of CuAsSe_2 (a) and Cu_3AsSe_3 (b) samples.

The melting temperature of CuAsSe_2 is (endotherm point) 743 K, and the melting point of Cu_3AsSe_3 is 773 K. When examined by differential thermal analysis, the CuAsSe_2 compound melts congruently at 743 K, the Cu_3AsSe_3 compound decomposes at 773 K melts.

3.5. Chemical Analysis

Chemical analysis of the samples (CuAsSe_2 , Cu_3AsSe_3) was performed in an atomic absorption spectrophotometer (The Thermo Scientific AA Spectrometer ICE 3500 - a True Dual Atomizer AAS). **COPPER**, 1000 mg/L. A minimum of 1.000 g of copper metal was dissolved in (1+1) HNO_3 . Dilute to 1 liter with 1 % (v/v) HNO_3 . **ARSENIC**, 1000 mg/L. 1.320 g of arsenic oxide (As_2O_3) was dissolved in 25 mL of 20 % (w/v) KOH solution. Neutralize with 20 % (v/v) H_2SO_4 to the

phenolphthalein endpoint. Dilute to 1 liter with 1 % (v/v) H_2SO_4 . **SELENIUM**, 1000 mg/L. Dissolve 1.000 g of selenium metal in a minimum volume of concentrated HNO_3 . Evaporate to dryness, add 2 mL of water, and evaporate to dryness 2 or 3 more times. Dissolve in 10 % (v/v) HCl and dilute to 1 liter with 10 % (v/v) HCl (15).

A sample weighing 0.1-2.0 g was placed in an Erlenmeyer flask, and a certain amount of concentrated HNO_3 acid was added and kept in a mechanical shaker for about 15 minutes. The sample is then heated at the selected temperature for 30 minutes to several hours, filtered through a glass filter with deionized water or dilute acid solution, filtered into a 50 ml volumetric flask, and diluted again to 50 ml. The data results are shown in Table 1.

Table 1. Results of chemical analysis of the compound CuAsSe_2 and Cu_3AsSe_3 .

Sample, g	Number of elements, g					
	Cu		As		Se	
	Theor.	Pract.	Theor.	Pract.	Theor.	Pract.
CuAsSe_2 , 0.1482	0.0319	0.0315	0.0374	0.0369	0.0788	0.0781
Cu_3AsSe_3 , 0.1467	0.0559	0.0552	0.0218	0.0213	0.0388	0.0380

As can be seen from the data in the table, the chemical analysis of the compounds also confirms the formula of the compounds - CuAsSe_2 and Cu_3AsSe_3 .

4. CONCLUSION

The simple synthesis methods were developed for ternary copper chalcogenides in an ethylene glycol medium without polluting the environment. CuAsSe_2 and Cu_3AsSe_3 compounds were synthesized from copper (I) chloride, sodium metaarsenite, and sodium selenosulfate. These

compounds (nanoparticles) were obtained in the temperature range of 413-443 K for 10 hours (pH = 7-5). 90-92 % of the results were obtained. Nanoparticles of compounds obtained at a temperature of 413-433 K have an irregular shape. Nanoparticles obtained at a temperature of 443 K are in the form of plates. SEM analysis of compounds was not found in the literature, so it is possible to look for the first time in our research. X-ray phase analysis was performed, and it was determined that the compounds correspond to cubic syconia and belong to the Pm3m spatial structure position of the developing

peaks is consistent (PDF 00-012-0379) (11). According to the DTA results, the CuAsSe_2 compound congruently at 743 K, and the Cu_3AsSe_3 compound decomposes at 773 K melts. The stoichiometric compound Cu_3AsSe_3 exists between 696 and 769 K. CuAsSe_2 was also peritectic at 683 K, and eutectic composition between CuAsSe_2 and As_2Se_3 was found at 641 K (11). Thermogravimetric analysis was performed. The thermal differential of the CuAsSe_2 alloy showed congruent melting at 753 K. Endo effects were observed at 493 K, 753 K, and 833 K in the TGA of the Cu_3AsSe_3 compound. Thermal differential analysis at 493 K corresponds to the decomposition of Cu_3AsSe_3 to CuAsSe_2 , 753 K to the oxidation of Cu_2O , and 833 K to the oxidation of Cu_2O to CuO .

Among copper metal-doped chalcogenide glasses, ternary selenides attracting more attention for their potential applications in semiconductor technology, nano- and microelectronics. Therefore, the development of the technology of semiconductor devices and the expansion of the class of combinations with parameters, which allows controlling their physical properties, is envisaged.

5. ACKNOWLEDGMENTS

Based on the presentation on the framework of scientific and cultural relations between Kyrgyzstan and Azerbaijan, organized by the Elger Science and Education Center, the conference held with Kyrgyz Jusup Balasagun Kyrgyz National University XXXIII International Scientific Symposium.






6. REFERENCES

1. Keiji T, Koichi S. Amorphous chalcogenide semiconductors and related materials. Springer. 2011;195-228. Available from: [<URL>](#)
2. Melnikova NV, Mollaev AY, Kheifets OL, et al. Influence of high pressures on electrical and thermoelectric properties of Cu-Ge-As-Se glasses. Azerbaijan Journal of Physics 2015;21:3-8. ISSN 1028-8546.
3. Kumar V, Tripathy SK, Jha V. Second-order nonlinear optical properties of $\text{A}^{\text{I}}\text{B}^{\text{III}}\text{C}_2^{\text{VI}}$ chalcopyrite semiconductors. Appl. Phys. Lett. 2012 Nov 08;101:192105. Available from: [<URL>](#)

4. Saipulaeva LA, Gabibov FS, Melnikova NV, et al. Photoelectric and electric properties of four-component copper chalcogenides. J. Exp. Theor. Phys. 2012 Nov;115:918-924. Available from: [<URL>](#)
5. Melnikova NV, Saipulaeva LA, Khokhlachev PP, et al. Effect of pressures on the electrical properties of multicomponent copper and silver chalcogenides. Phys. Solid State 2015 Nov 28;57:2025-2029. Available from: [<URL>](#)
6. Zeng Y, Joo PH, Yang K, et al. Computation-motivated design of ternary plasmonic copper chalcogenide nanocrystals. Chem. Mater. 2021;33:117-125. Available from: [<URL>](#)
7. Kokenyesi S. Amorphous chalcogenide nanomultilayers: research and development. Journal of Optoelectronics and Advanced Materials. 2006 Dec;8:2093-2096. Available from: [<URL>](#)
8. Alan O, Pranati S, Stephanie T, et al. Topochemical Solid-State Reactivity: Redox-Induced Direct Structural Transformation from CuSe_2 to CuInSe_2 . Chem. Mater. 2015 Oct 2;27(20):7179-7186. Available from: [<URL>](#)
9. Shuqin X, Jian L, Philip SS. Structure of Cu-As-Se glasses investigated by neutron diffraction with copper isotope substitution. Physical review. B, Condensed matter. 2008 Aug.;78(6):064207-8. Available from: [<URL>](#)
10. Cui S, Boussard C, Calvez L, et al. Comprehensive study of tellurium-based glass ceramics for thermoelectric application. Advances in Applied Ceramics. 2015;114:42-47. Available from: [<URL>](#)
11. Blachnik R, Kurz G. Compounds in the system Cu_2Se and As_2Se_3 . Journal of Solid State Chemistry 1984 Nov;55:218-224. Available from: [<URL>](#)
12. Rzayev BZ. New studies in the field of sulfur compounds of arsenic. Baku: Elm, 2002;94 p.
13. Cynthia GZ. Handbook of Electrochemistry. New Mexico, USA, 2007;879. Available from: [<URL>](#)
14. Suleymanova T. Production of nanoparticles of AgAsSe_2 and Ag_3AsSe_3 compounds. Journal of the Turkish Chemical Society, Section A: Chemistry. 2018;4:103-10. Available from: [<URL>](#)
15. Analytical Methods for Atomic Absorption Spectroscopy. 1996. The Perkin-Elmer Corporation. Printed in the United States of America. Manual Part No. 0303-0152.310 p.



In-depth Hirschfeld Surface Analysis, Interaction Energy, Molecular Docking, and DFT Investigations of Electronic Properties of 2,4-dimethyl-1-nitrobenzene

Youcef Megrouss*^{1,2} , Salem Yahiaoui^{2,3} , Nourdine Boukabcha^{1,2} ,
 Mansour Azayez¹ , Sid Ahmed Kaas⁴ , Abdelkader Chouaih² ,
 Mokhtaria Drissi^{2,5} 

¹ Chemistry Department, Faculty of Exact Sciences and Informatic, Hassiba Benbouali University, Chlef 02000, Algeria.

² Laboratory of Technology and Solid Properties (LTPS), Abdelhamid Ibn Badis University of Mostaganem, BP 227, Mostaganem, 27000, Algeria

³ Higher Normal School, Mostaganem 27000, Algeria.

⁴ Department of material science, faculty of science and technology, Tissemsilt University Algeria.

⁵ Laboratory of synthesis and catalyze, University IbnKhalidoun of Tiaret, 14000 Tiaret, Algeria

Abstract: Quantum-chemical calculations, molecular docking, and Hirshfeld surface analysis of a structure of 2,4-dimethyl-1-nitrobenzene constitute the main aspects of this work. The crystal structure of the title compound which is liquid at room temperature, was obtained by in situ cryo crystallization. The crystal packing is stabilized by C5–H5···O2 and C7–H7C···N1 intermolecular hydrogen bonds. The analysis of the obtained results of the density functional theory calculations is in good agreement with the experimental data. The analysis of global chemical reactivity descriptors shows that the compound exhibits more stability and less reactivity at high polar media. Hirshfeld surface and 2D-fingerprint plots analysis shows that the H...H, O...H/H...O, C...C, and C...H/H...C contacts are the significant contributors stabilizing the crystal structure of 2,4-dimethyl-1-nitrobenzene. The RDG-NCI analysis of the molecule was performed to determine the non-covalent interactions present within the molecule. In addition, the compound under investigation presents a biological activity when it is docked into the protein (PDB ID: 4Y0S) with the binding energy system of -6.6 kcal/mol.

Keywords: Molecular docking, Hirschfeld surface analysis, DFT, RDG, Interaction energy, ELF, LOL analysis

Submitted: March 19, 2023. **Accepted:** December 12, 2023.

Cite this: Megrouss Y, Yahiaoui S, Boukabcha N, Azayez M, Kaas SA, Chouaih A, Drissi M. In-depth Hirschfeld surface analysis, interaction energy, molecular docking, and DFT investigations of electronic properties of 2,4-dimethyl-1-nitrobenzene. JOTCSA. 2024;11(2):507-24.

DOI: <https://doi.org/10.18596/jotcsa.1259444>

***Corresponding author.** E-mail: y.megrouss@univ-chlef.dz ,youcefmegrouss@gmail.com

1. INTRODUCTION

Nitrobenzene is an organic compound with the chemical formula $C_6H_5NO_2$. It comes in the form of colorless liquid or yellow crystals depending on the temperature. The structure of nitrobenzene has been subject to several modifications, of which the hydrogen atoms of

the benzene ring can be substituted either in the ortho, meta, or para position by electrophilic or nucleophilic groups (1). Nitrobenzene and its derivatives have a wide application in industry because they are versatile intermediates in organic synthesis such as the production of aniline and, the synthesis of dyes, pesticides, and rubbers (2-

4). Nitrobenzene can also be used as a solvent for cellulose ester (2) and as an organochlorine fungicide for control of various fungal diseases caused by *Rhizoctonia solani*, *Botrytis* spp., *Aspergillus* spp., *Penicillium* spp., and *Tilletia caries* (5-6). Nitrobenzene is extremely toxic in large quantities which has a great impact on the human body (4). Nitro derivatives of benzene always demonstrate excellent heat resistance and insensitivity, because of their well-known π - π stacking (7). In recent years, nitrobenzene and its derivatives have been the subject of many theoretical studies by quantum chemical calculations (8-12). These latter are very powerful tools to reveal the structure-performance relationship and to give information about the electronic and structural properties of these materials with acceptable accuracy (13-14). A complete report of structural, electronic, and intermolecular interactions of methylated derivatives of nitrobenzene is shown in this work through X-ray diffraction data analysis, quantum chemical calculations, and Hirshfeld surface analysis of 2,4-dimethyl-1-nitrobenzene. This compound is a deep yellow-green color clear liquid with having characteristic odor. The experimental section was carried out by using the X-ray diffraction method, the structure of the compound studied has been deposited in the CCDC database under the CCDC references: [1017641](#) where the theoretical study is provided using density functional theory (DFT) with traditional hybrid functional (B3LYP) to exhibit its reactivity and discuss their physical and chemical properties. The biological properties of 2,4-dimethyl-1-nitrobenzene were investigated, by predicting the relative orientation of this compound when bound with an active site of a host molecule (protein) to form a stable complex. Hirshfeld surface analysis and the associated two-dimensional fingerprint plots are performed to understand what types of interatomic contacts are responsible for the stability of the crystal structure. The intermolecular interaction energies were calculated to understand and quantify the intermolecular interactions in a crystal lattice which drive the organization of the crystal packing in materials. The topological analyses of the electron localization function (ELF) and the localized orbital locator (LOL) analyses are exhibited for covalent bond analysis as they highlight parts of the surface of the molecular structure that have a high potential for a possible pair of electrons to be located.

2. COMPUTATIONAL DETAILS, DOCKING PROCESS, AND HIRSHFELD SURFACE ANALYSIS

The molecular geometry of the studied compound was optimized using B3LYP exchange-correlation functional (15,16) implemented in the Gaussian 09 package (17), which consists of the Lee-Yang Parr correlation functional in conjunction with a hybrid exchange functional first proposed by Becke. It is known that the reaction mechanism for such molecules is directly linked to their electrostatic environment. So, Fukui functions and the molecular electrostatic potential were calculated at the same level of calculation to predict the reactive sites for the electrophilic or nucleophilic attack for the compound under investigation. The Hirshfeld surface analysis was performed using the Crystal Explorer 17.5 program (18), where intermolecular interaction was quantitatively investigated based on the two-dimensional fingerprint plots. The ELF, LOL, and topological analysis were modeled using the Multiwfn 3.7 package (19). Finally, Auto dock-vina software was utilized for the docking process of 2,4-dimethyl-1-nitrobenzene into the protein receptor (PDB ID: 4Y0S), with choosing the dimensions $52 \times 74 \times 46 \text{ \AA}^3$ as grid box sizes.

3. RESULTS AND DISCUSSION

3.1. Molecular Geometry

The geometric of 2,4-dimethyl-1-nitrobenzene is optimized at DFT/B3LYP level using 6-31G (d,p) as the basis set, which is compared by those obtained experimentally by X-ray diffraction. When the X-ray structure of 2,4-dimethyl-1-nitrobenzene is compared with its optimized counterparts, slight conformational discrepancies are observed between them (Figure 1). For example, the calculated C-C within rings, C-N, and N-O bonds lengths values are in the ranges 1.3852-1.409, 1.4714, and 1.2324-1.2328 \AA , agree with the correspondent experimental values ranging of 1.3697-1.3945, 1.4812, and 1.2074-1.2175 respectively. Whereas, the maximum deviations of valence angle values from theoretical and experimental data do not exceed 1.35° . We thus note that the experimental results and the theoretical calculations are in good agreement as reflected by low values of root mean square deviations (RMSD) (Table 1).

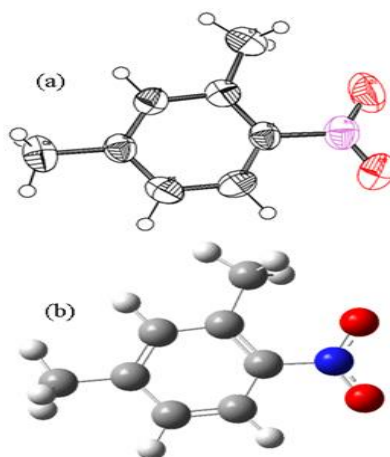


Figure 1: (a) Experimental structure and (b) optimized structure of 2,4-dimethyl-1-nitrobenzene.

3.2. Hirshfeld Surface Analysis and Intermolecular Contacts

The Hirshfeld surface analysis is a very efficient technique to quantify the intermolecular interactions among molecular crystals. Hirshfeld surfaces and the fingerprint plots illustrated in this work have been performed with the Crystal Explorer 17.5 (18). The distance of normalized contact (d_{norm}), is based on d_e and d_i and has been calculated by the following expression:

$$d_{norm} = \frac{d_i - r_i^{vdw}}{r_i^{vdw}} + \frac{d_e - r_e^{vdw}}{r_e^{vdw}}$$

where d_e is the distance from a point on the surface to the nearest nucleus outside the surface and d_i is defined as the distance from a point on the surface to the nearest nucleus inside the surface; with r_i^{vdw} present the van der Waals radius of the atom inside the Hirshfeld surface, whereas r_e^{vdw} corresponds to the van der Waals radius of the atom outside the Hirshfeld surface (20, 21).

The view of the three-dimensional Hirshfeld surface traced on d_{norm} in Figure 2 reveals two red dots, representing the contacts of the hydrogen with each oxygen atom of the nitro group. Hirshfeld surface analysis of the crystal along with d_{norm} , d_i , d_e , shape index, curvedness, and fragment patch is plotted in

Figure 3 and depicts the electron density interaction for the chosen compound with its neighboring molecule. From Figure 3, on the shape index map, we can see that the molecules are connected by π - π stacking interactions which are denoted by the adjacent red and blue triangles (highlighted by red circles), the triangles colored blue are convex areas that signify the existence of aromatic carbon atoms in the inside surface, whereas the red colored triangles signify concave areas due to the carbon atoms of the π -stacked molecule over it. The existence of the π - π clustering is distinctly seen in the curvedness surface. The wide green areas indicate a flat surface, and the blue areas exhibit curvature. Figure 4 displays the two-dimensional (2D) fingerprint plot that reflects the different intermolecular interaction contributions overlapping in the entire fingerprint and individual from each interaction. The highest significant numbers of interactions are the H...H interactions amounting to 47.5 %, because of a high quantity of hydrogen on the molecule surface. The second most important contribution was attributed to H...O/O...H interactions with 22.8%. other contributions may take place; these are fairly weak contacts C...C (7.8%), C...H/H...C (5.2%), N...C/C...N (3.5%), C...O/O...C (1.7%), N...H/H...N (1.2%), O...O (0.4%) illustrated in Figure 4.

Table 1: Bond distances and angles of atoms by X-ray and theoretical calculation.

Bond distances (Å)		X-ray	B3LYP/6-31G(d,p)	RMSD	
				0.055	
O1	N1	1.2074	1.2328		
O2	N1	1.2175	1.2324		
N1	C1	1.4812	1.4714		
C1	C2	1.3912	1.4090		
C1	C6	1.3806	1.3989		
C2	C3	1.3945	1.4032		
C2	C7	1.5025	1.5089		
C3	H3	0.9494	1.0867		
C3	C4	1.3851	1.3970		
C4	C5	1.3869	1.4027		
C4	C8	1.5113	1.5083		
C5	H5	0.9498	1.0862		
C5	C6	1.3697	1.3852		
Bond angles (°)				0.673	
O1	N1	O2	122.65	123.62	
O1	N1	C1	119.28	118.57	
O2	N1	C1	118.06	117.81	
N1	C1	C2	121.09	122.08	
N1	C1	C6	116.69	116.09	
C2	C1	C6	122.21	121.83	
C1	C2	C3	115.27	115.95	
C1	C2	C7	127.00	125.65	
C3	C2	C7	117.72	118.39	
C2	C3	C4	124.14	123.61	
C3	C4	C5	117.67	118.20	
C3	C4	C8	120.90	121.10	
C5	C4	C8	121.43	120.59	
C4	C5	C6	120.43	120.27	
C1	C6	C5	120.27	120.14	
Torsion (°)				3.65	
O1	N1	C1	C2	0.05	6.67
O1	N1	C1	C6	179.63	-173.35
O2	N1	C1	C2	179.29	-173.53
O2	N1	C1	C6	-1.03	6.44
N1	C1	C2	C3	179.37	179.98
C6	C1	C2	C7	-179.80	-179.58
N1	C1	C6	C5	179.78	179.73
C2	C1	C6	C5	0.11	-0.29
C1	C2	C3	C4	-1.26	0.31
C7	C2	C3	C4	179.44	179.93
C2	C3	C4	C8	179.71	179.56

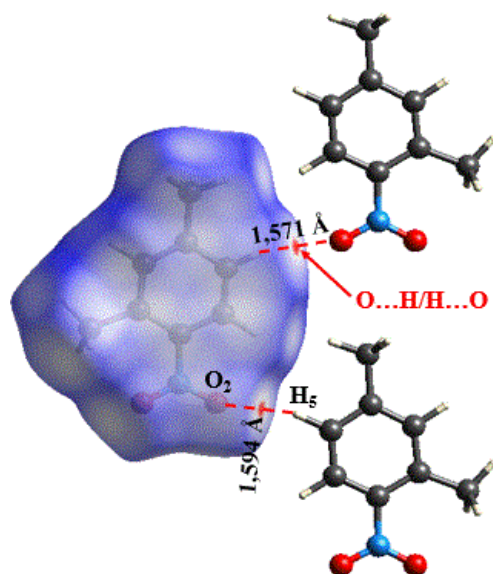


Figure 2: The view of the three-dimensional Hirshfeld surface plotted over d_{norm} .

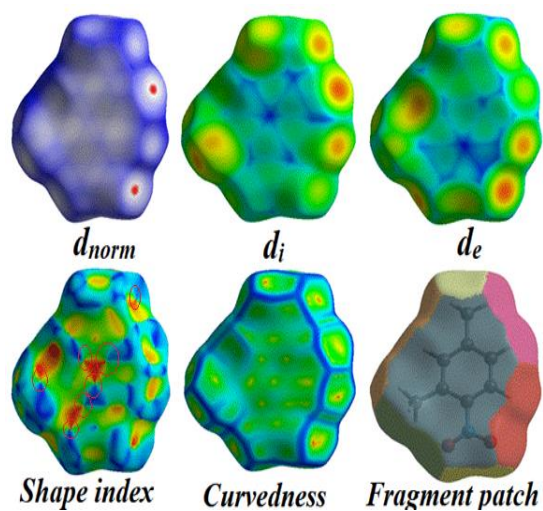


Figure 3: Hirshfeld surface analysis of the compound with d_{norm} , d_i , d_e , shape index, curvedness, and fragment patch.

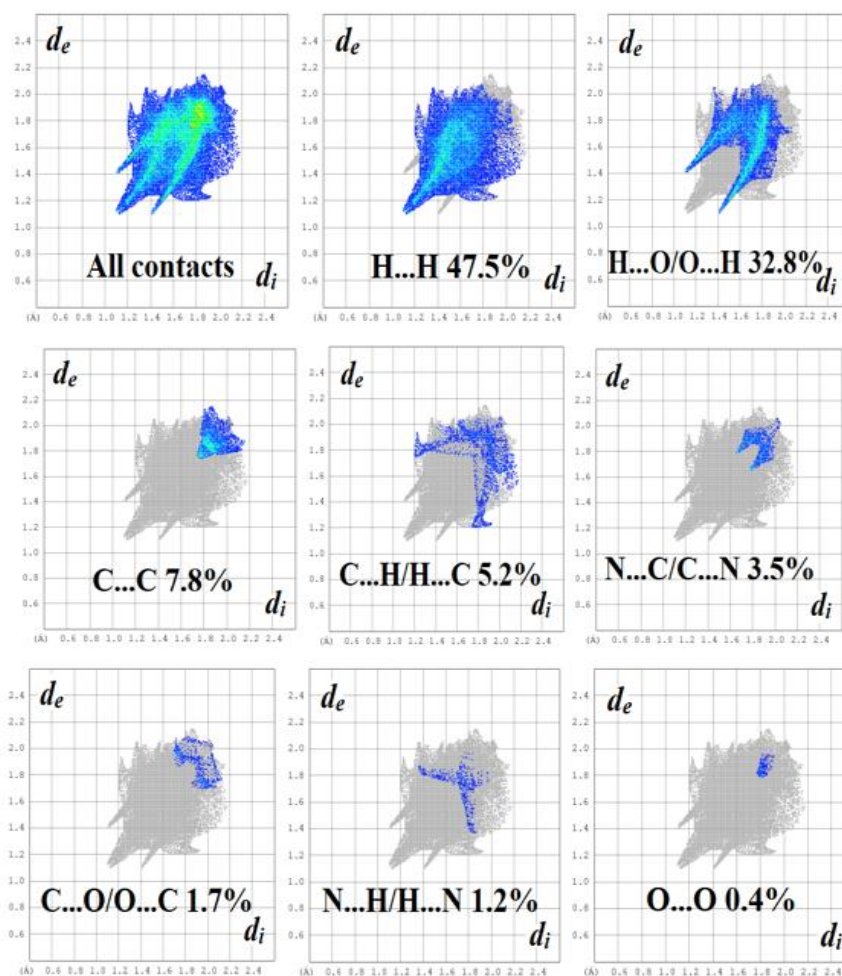


Figure 4: The 2D- Fingerprint plots showing the overall contribution to the total HS area and the individual percentages of the diverse intermolecular contacts of the molecule.

3.3. Interaction Energy and 3D energy frameworks

To understand and quantify the intermolecular interactions in a crystal lattice, including repulsion, electrostatics, dispersion, and polarization interactions energy, which occur and drives the organization of the crystal packing, the interaction energy was evaluated with the method CE-B3LYP/6-31G(d,p); energy model available in Crystal Explorer 17.5 software. The energy framework concept is a computational graphical tool for representing the magnitudes of interaction energies within

the crystal packing. Full interaction energy has been calculated by generating a cluster radius of 3.8 Å around the molecule. The energy framework represents the coulomb energy (in red tube), dispersion energy (green tube), and total energy (blue tube) (Figure 5). The energies have been calculated using a method for scaling different energy frameworks, indicating that the scaling factors for electrostatics, dispersion, polarization, and repulsion are 1.057, 0.740, 0.871, and 0.618, respectively (22).

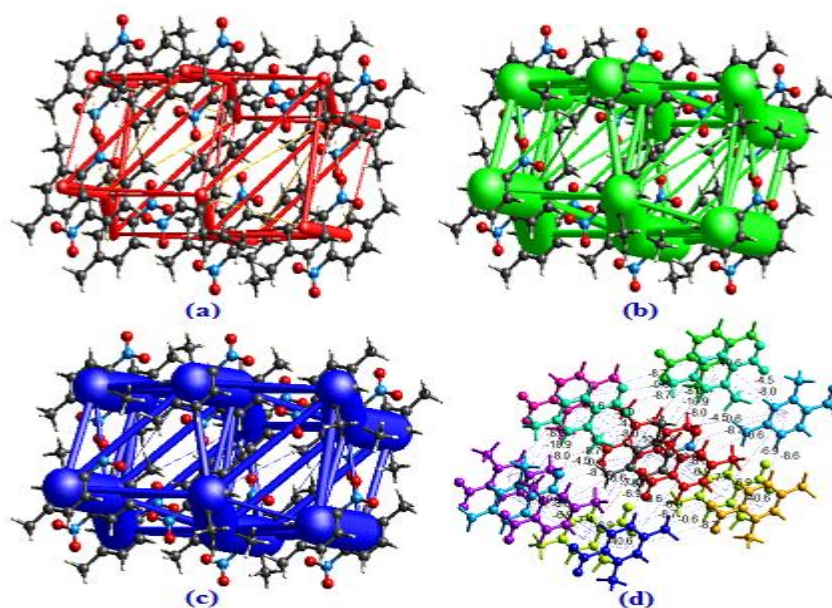


Figure 5: Energy frameworks calculated for 2,4-dimethyl-1-nitrobenzene, showing the (a) Coulomb energy (b) dispersion force (c) total energy, and (d) total energy diagram.

Table 2 demonstrates the IE calculation results for the component molecule given by respective colors. Whereas the global energies of the intermolecular interactions possible in the crystal cluster are in the range [-0.6, -40.6]

kJ/mol. The overall interaction energies are electrostatic ($E_{ele} = -29.5$ kJ/mol), polarization ($E_{pol} = -9.7$ kJ/mol), dispersion ($E_{dis} = -105.5$ kJ/mol), repulsion ($E_{repl} = 54.7$ kJ/mol), total interaction energy ($E_{tot} = -96.2$ kJ/mol).

Table 2: Energy framework detail of molecular interaction energies with symmetry operations (symop) for the compound. (distances between molecular centroids (R) in Å, interaction energies in kJ/mol, and number of pair-wise fragments (N)).

	N	Symop	R	Electron Density	E_ele	E_pol	E_dis	E_rep	E_tot
	2	x, -y+1/2, z+1/2	3.52	B3LYP/6-31G(d,p)	-12.0	-1.5	-48.0	24.2	-40.6
	1	-x, -y, -z	7.42	B3LYP/6-31G(d,p)	-3.3	-1.2	-4.1	0.8	-7.4
	2	-x, y+1/2, -z+1/2	7.69	B3LYP/6-31G(d,p)	-2.6	-1.5	-8.4	6.9	-6.9
	1	-x, -y, -z	7.51	B3LYP/6-31G(d,p)	-6.2	-1.4	-7.4	4.9	-10.9
	2	-x, y+1/2, -z+1/2	7.62	B3LYP/6-31G(d,p)	-2.2	-1.2	-10.6	7.3	-8.0
	2	x, y, z	9.74	B3LYP/6-31G(d,p)	-4.7	-1.4	-4.5	1.9	-8.7
	1	-x, -y, -z	7.71	B3LYP/6-31G(d,p)	-0.9	-0.8	-12.1	5.6	-8.6
	2	x, -y+1/2, z+1/2	10.56	B3LYP/6-31G(d,p)	1.4	-0.2	-3.2	1.4	-0.6
	1	-x, -y, -z	7.80	B3LYP/6-31G(d,p)	1.0	-0.5	-7.2	1.7	-4.5

3.4. Topological Analysis of Electronic Density (AIM) and Noncovalent Interactions Reduced Density Gradient (NCI-RDG) Analysis

Topological analysis has been performed to investigate the weak interactions of various materials with a more comprehensive approach. The theory of atoms in molecules (AIM) is greatly taken into account to evaluate the electron density of binding critical points (BCP) as well as to identify the various forms of interactions present in a molecular system (23). The hydrogen bonding properties were determined according to topological parameters including electron density $\rho(r)$, lagrangian kinetic energy $G(r)$, laplacian electron density $\nabla^2\rho(r)$, hamiltonian energy $H(r)$, and potential energy density $V(r)$, all these parameters are measured by atomic unit. The geometrical optimized structure has been applied to obtain the critical intramolecular bonding points (BCP) inside the crystal structure. The molecular graph of bond critical points for the title compound is illustrated in Figure 6, and the results of the calculations have been processed using the Multiwfn software. The topological parameters of the hydrogen-bonded interaction for the molecule are listed in Table 3. The electron density $\rho(r)$ and the laplacian $\nabla^2\rho(r)$ are significant in determining the type of interactions. In general, the large values of the electron density $\rho(r)$ and its laplacian $\nabla^2\rho(r)$ demonstrate strong hydrogen interactions. Positive laplacian $\nabla^2\rho(r)$ values are associated with a weak charge in the

interatomic region, while the negative readings could indicate the expression of a strong covalent nature (24). In this study, the electron density value (ρ_{BCP}) was found to be 0.01645 au and the Laplacian value was 0.06793 au. To determine the stability of the molecular structure, molecular interactions are involved. These interactions were able to be detected by reduced density gradient (RDG) analysis, based on the analysis of non-covalent interactions (NCI) present in the system (25). The NCI-RDG analysis is illustrated in Figure 7. The reduced density gradient (RDG) is a basic number consisting of the density and its first derivative, which is given by the formula below (26):

$$RDG(r) = \frac{1}{2(3\pi^2)^{\frac{1}{3}}} \frac{|\nabla\rho(r)|}{\rho(r)^{\frac{4}{3}}}$$

From Figure 7, the interaction between the different components is situated by an isosurface RDG around their proper area; the red dots reflect the repulsive effect. The greatest steric repulsion effect within the crystal has been seen at the center of the aromatic rings related to the π - π stacking interactions. The mixed red and green color zone surrounding (H7A, O1) and (O2, H6) between the aromatic ring and the nitro group represents a repulsive zone. The result of the NCI-RDG of the compound is in good agreement with the results of the Hirshfeld surface analysis (HAS) and XRD-packing.

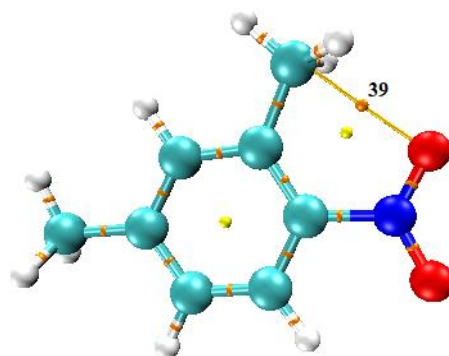


Figure 6: Molecular graph showing the bond critical point of the molecule.

Table 3. Topological parameters of hydrogen-bonded interaction for the title molecule.

Parameters	Ring critical point (RCP)
Electron density (ρ_{BCP}) (a.u)	0.01645
Laplacian of electron density (a.u)	0.06793
Lagrangian Kinetic Energy $G(r)$ (a.u)	0.01510
Hamiltonian Kinetic Energy $K(r)$ (a.u)	-0.00187
Potential energy density $V(r)$ (a.u)	-0.01322
Eigen Value λ_1	0.08624
Eigen Value λ_2	-0.1106
Eigen Value λ_3	-0.78841
H-Bond energy (kcal. Mol ⁻¹)	-0.00724

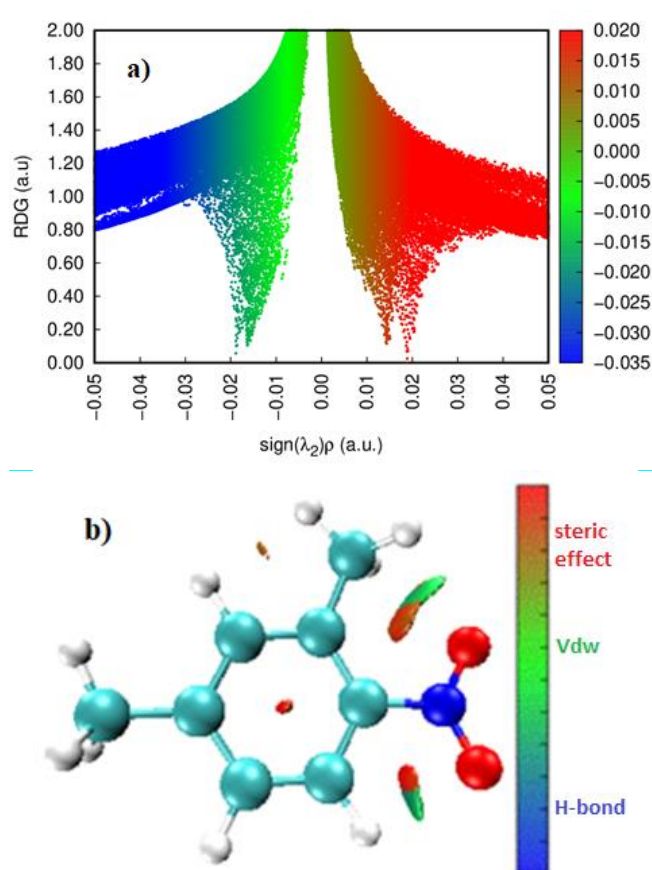


Figure 7: The scatter diagram (a) and the gradient isosurfaces (b) for the molecule.

3.5. ELF and LOL analysis

The topological analysis of the electron localization function (ELF) and the localized orbital locator (LOL) analysis are important methods for covalent bond analysis as they highlight parts of the surface of the molecular structure that have a high potential for a possible pair of electrons to be located. The ELF and LOL were modeled using the Multiwfn 3.7 package (19). ELF provides an understanding of the electron pair density and LOL provides an account of the maximum overlap of localized orbitals due to the orbitals gradient (27). The ELF chart is established within the interval 0.0 up to 1.0, although the area lower than 0.5 exhibits a delocalized electron region and the LOL achieves high values exceeding 0.5 in the areas of electron density localization dominance (28). The colors of the ELF and LOL maps shown in Figures 8 and 9 demonstrate the existence of binding and non-binding electrons,

with the red color surrounding the hydrogen atoms denoting the occurrence of both binding and non-binding electrons. High values of ELF or LOL shown in red surrounding hydrogen atoms are indicative of a strong electron localization caused by a covalent bond, a single electron pair, or a nucleus shell being present in that area. The color blue surrounding the carbon atoms of the dimethylbenzene group indicates the presence of a delocalized electron cloud. The two lone pairs of oxygen atoms are marked by weakly highlighted blue circles that mark less where the electrons are supposed to be delocalized. The region of hydrogen atoms has a relatively higher degree, which denotes the availability of localized bonding and non-bonding electrons. The middle zone in the hydrogen atom is white in the LOL because the electron density surpasses the maximum level of the color range.

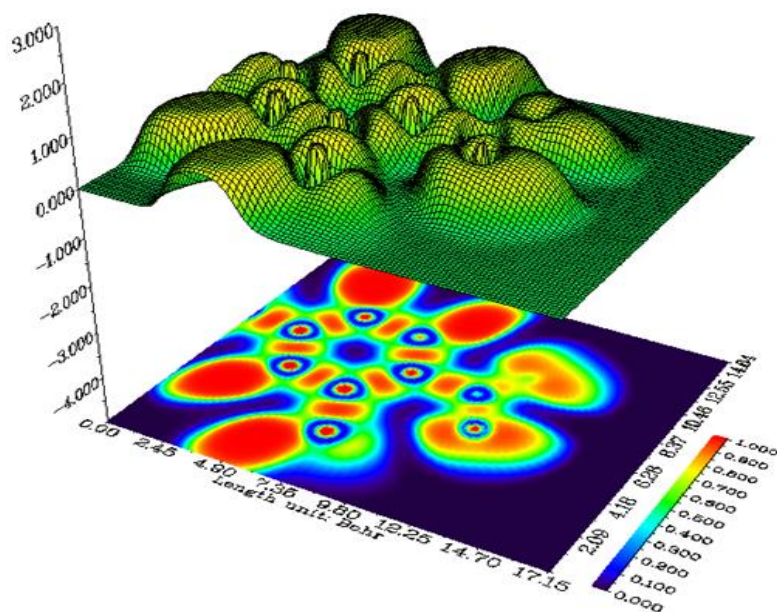


Figure 8: The relief map with a projection of ELF for the molecule.

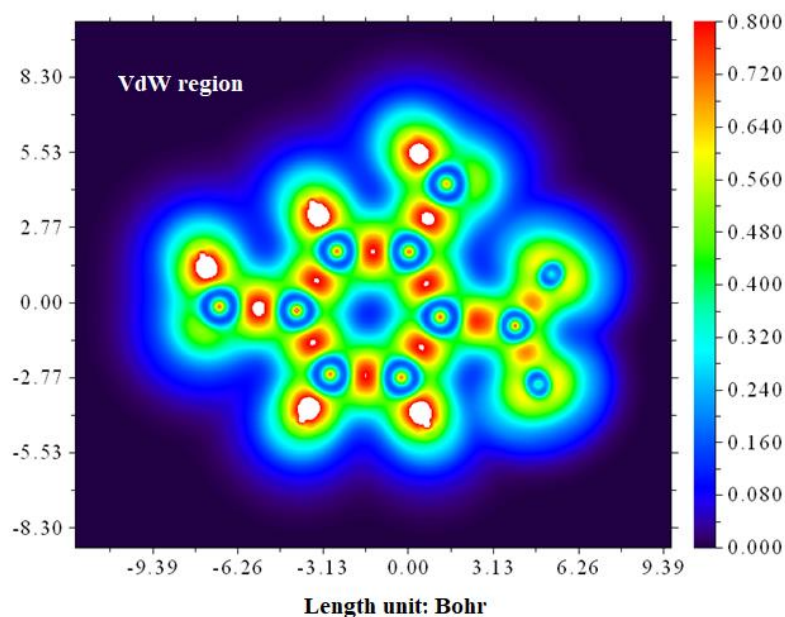


Figure 9: Contour LOL map of the molecule.

3.6. Frontier Molecular Orbitals, Global and Local Chemical Reactivity Descriptors Analysis

Molecular frontier orbitals provide a means of predicting the relative reactivity of a molecular system according to the electronic structure properties found in its structure. The molecular chemical properties in the molecule were controlled via its valence orbitals, thus nucleophilic attacks could be detected using the HOMO orbital, while the electrophilic attacks are checked through the LUMO orbital. The energy gap between HOMO (π donor) and LUMO (π acceptor) is taken as a measure of molecular structure stability (29). In the present research,

the HOMO as well as LUMO energies have been estimated using the Berny method (30-32) with a 6-31G(d,p) base set. Judging by the results given in Table 4, the gap energy between HOMO and LUMO is a critical parameter for the determination of the electrical transmission in the title molecule. The energy levels and allocations of the orbitals (HOMO \rightarrow LUMO) and (HOMO-1 \rightarrow LUMO+1) of the investigated molecule are depicted in Figure 10. Therefore, their molecular gap boundary values (ΔE_{gap}) were revealed to be 4.8 and 6.9245 eV in each case. The highest occupied molecular orbital (HOMO) is positioned above the nitro group which acts as an electron donor, whereas the

lowest unoccupied molecular orbital (LUMO) is located above the nitrobenzene.

Table 4: Energies of frontier orbitals of 2,4-dimethyl-1-nitrobenzene.

Energies (eV)	B3LYP /6-31G(d,p)
E_{HOMO}	-7.2466
E_{LUMO}	-2.4398
$E_{HOMO}-E_{LUMO}$ gap	4.80
E_{HOMO-1}	-7.3769
E_{LUMO+1}	-0.47
$E_{HOMO-1}-E_{LUMO+1}$ gap	6.9245

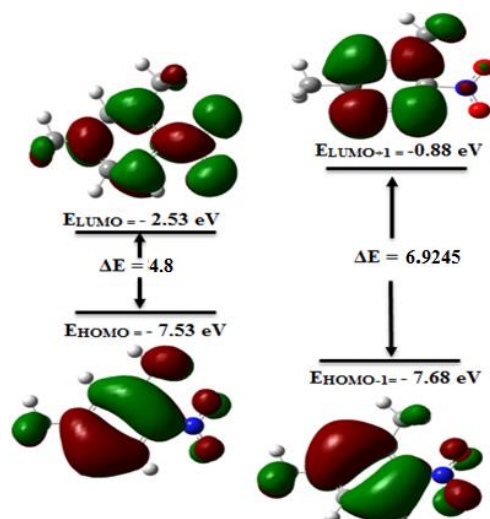


Figure 10: The frontier molecular orbitals for the molecule obtained by using the B3LYP method.

As it is well known, a high-value energy gap (ΔE) indicates that the molecular structure has higher kinetic stability, and a lower chemical reactivity (33). This approach is suitable to determine the properties of electrical transfer throughout the whole molecular structure. Thus, the values calculated of the global chemical reactivity descriptors, expressed below

(34-39), for 2,4-dimethyl-1-nitrobenzene are given in Table 5.

$$I = -E_{HOMO}; \eta = 1/2 (E_{LUMO} - E_{HOMO});$$

$$\eta = 1/2 (E_{LUMO} - E_{HOMO}); S = 1/2 \eta;$$

$$\mu = 1/2 (E_{LUMO} + E_{HOMO}); \omega = \frac{\mu^2}{2\eta};$$

$$\Gamma = E_{LUMO} - 2E_{HOMO} + E_{HOMO-1};$$

$$S^{(2)} = -\frac{\Gamma}{\eta^3}$$

Table 5: Global chemical reactivity descriptors of 2,4-dimethyl-1-nitrobenzene.

Parameters (eV)	DFT/B3LYP/6-31G(d,p)	
	In vacuum	In DMSO medium
Ionization potential (I)	7.246	6.93
Chemical hardness (η)	2.4	2.36
Chemical softness (s)	0.208	0.208
Chemical potential (μ)	-4.88	-4.57
Electrophilicity index (ω)	4.84	4.42
Hyper-hardness (Γ)	4.766	4.32
Hyper-softness ($S^{(2)}$)	-0.344	-0.328

A low value of ionization potential is observed in the DMSO medium indicating that this compound has the highest electron donor

character. The global chemical hardness values have increased and the global softness values have decreased in the presence of the high

polar solvent; 2,4-dimethyl-1-nitrobenzene exhibits less reactive properties with a low probability of intramolecular charge transfer in this medium. The value electrophilicity index in a vacuum medium is higher compared to that calculated in the gas state; this result indicates that this compound exhibits a low electrophile character in the polar environment. To characterize the reactivity or stability, the hyperhardness descriptor (Γ) has already inserted. Therefore, the positive values of hyperhardness in both media (4.766 and 4.32 eV) point to quite that the compound is stable and less reactive.

The local reactivity descriptor like the Fukui function indicates the preferred regions where a chemical species will amend its density when the numbers of electrons are modified or it indicates the tendency of the electronic density to deform at a given position upon accepting or donating electrons (40). Using NBO analysis of the neutral, cation, and anion state of the molecule, Fukui Functions are calculated using the following relations:

$$f_k^+ = [q(N+1) - q(N)] \text{ for nucleophilic attack}$$

$$f_k^- = [q(N) - q(N-1)] \text{ for electrophilic attack}$$

Where N, N-1, and N+1 are total electrons present in the neutral, cation, and anion states of the molecule, respectively.

In addition to these functions, local softness (s_k^+ , s_k^-) and local electrophilicity indices (ω_k^+ , ω_k^-) are also used to describe the reactivity of atoms in molecules. The local softness condensed to an atom location defined by (41):

$$s_k^+ = S f_k^+, \quad s_k^- = S f_k^-$$

and local electrophilicity indices (42) defined by

$$\omega_k^+ = \omega f_k^+, \quad \omega_k^- = \omega f_k^-$$

In the histogram shown in Figures 11 and 12 of the title compound, the relatively high value of local reactivity descriptors (f_k^+ , ω_k^+ , s_k^+) at C₅, C₁, and O₂ indicates that these sites are more prone to nucleophilic attack whereas the relative values of local reactivity descriptors (f_k^- , ω_k^- , s_k^-) at N indicate that this site is more prone to electrophilic attack.

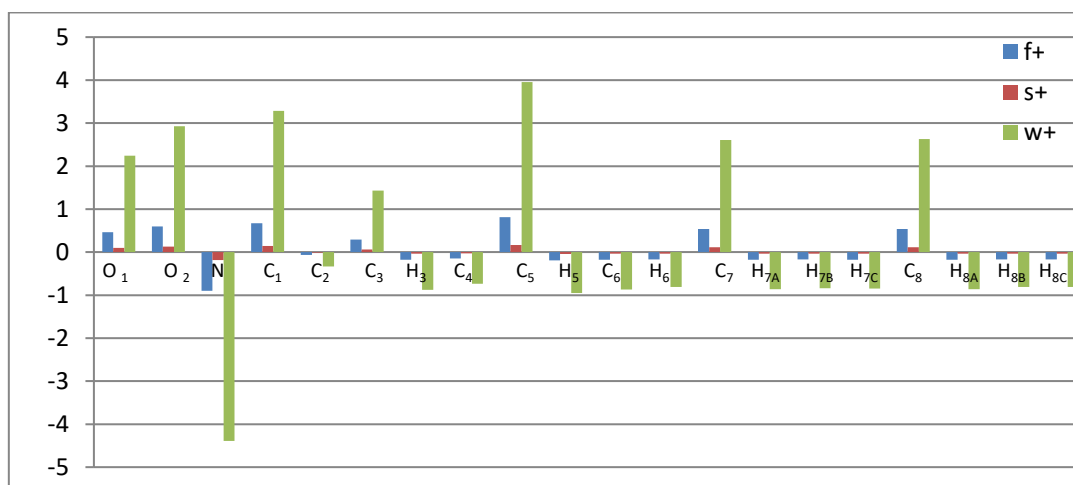


Figure 11: Local reactivity descriptors (f_k^+ , ω_k^+ , s_k^+) in eV for atomic sites of the molecule using NBO population analysis at B3LYP/6-31G(d,p) level.

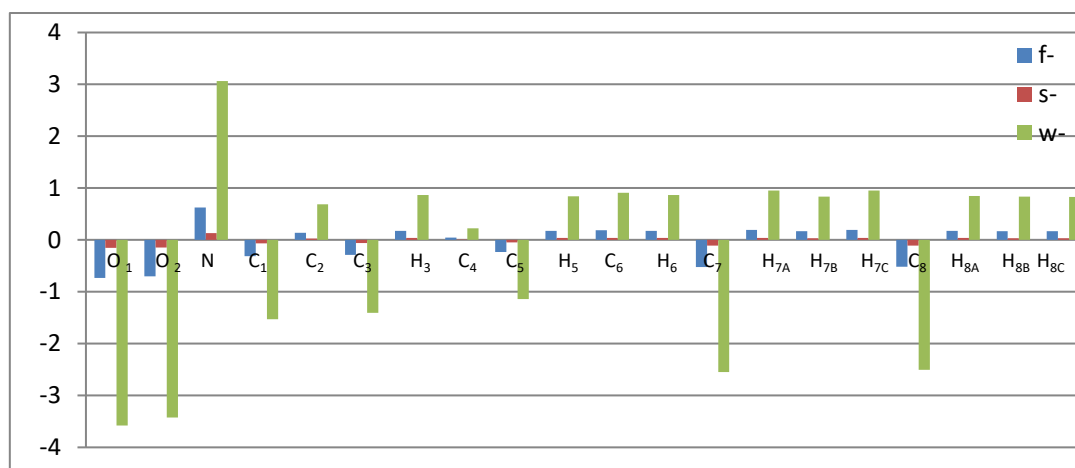


Figure 12: Local reactivity descriptors (f_k^- , ω_k^- , s_k^-) in eV for atomic sites of the molecule using NBO population analysis at B3LYP/6-31G(d,p) level.

3.7. Molecular Electrostatic Potential Analysis

An analysis of the molecular electrostatic potential surface (MEPS) has been affected to validate the evidence about the reactivity of 2,4-dimethyl-1-nitrobenzene. The MEPS can therefore provide information on the sign of different molecular regions. Colors red and blue in MEPS represent the most electron-rich

regions and those poor in electrons respectively. The compared x-ray and the DFT results led to an estimation of a similar electrostatic potential around the molecule (Figure 13). It thus was observed that the region is negative around the nitro groups (NO_2); the favored site for electrophilic attack, while for the blue zones, around the methyl group, nucleophilic attacks are taking place.

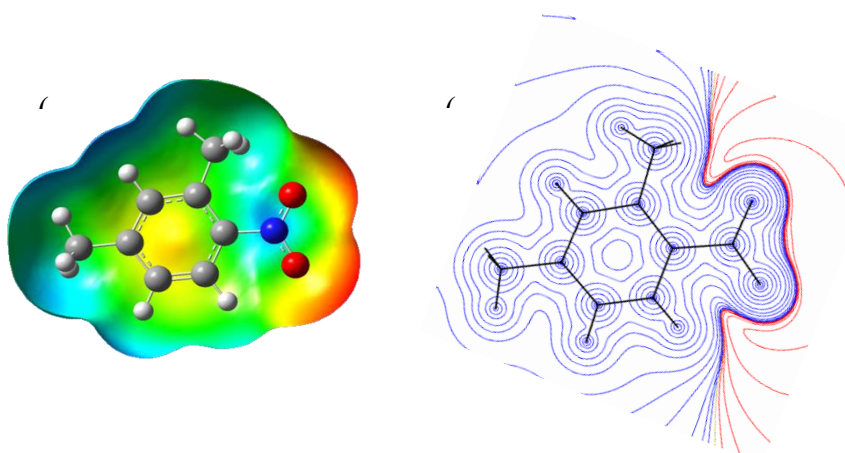


Figure 13: Electrostatic potential maps around the molecule. Panel (a) shows the DFT calculation of the electrostatic potential distribution, and panel (b) displays the electrostatic potential distribution predicted from the experimental X-ray diffraction data

3.8. Pass Analysis And Molecular Docking Studies

3.8.1. PASS analysis

The PASS tool allows us to explore the possible biological properties of compounds, based on their chemical formula. The potential biological properties of the selected compounds were investigated through the PASS web server (43). It uses 2D molecular fragments known as multilevel atom neighbor descriptors that suggest the biological activity of a chemical

compound based on its molecular structure. It gives the prediction score for biological properties on the ratio of probability to be active (P_a) and probability to be inactive (P_i). A higher P_a means the compound possesses more probability for the biological property (44). The exploration of biological activities of the selected compounds through the PASS analysis resulted in similar kinds of biological activities, the title compound was found to have great potential for biological activity as an Antibiotic Glycopeptide-like, with P_a ranging from 0,937

to 0,734 when $P_a > P_i$. The probability of the biological activities of our compound is collected in Table 6. The title compound could have a potential inhibitory effect against beta-lactoglobulin binding protein, in the current study. This protein was chosen based on the high P_a value ($P_a = 0.937$). The crystal structure of this target protein (PDB ID: 4Y0S) was obtained from the protein data bank (45). β -lactoglobulin (LG) is a protein belonging to the lipocalin family (46).

Lipocalins are often involved in the binding, storage, and transport of low-molecular-weight hydrophobic ligands (47). The ability to bind small molecules has made lipocalins an interesting target for utilization as a new class of drug transporters (48). Several proteins from this family have been modified and engineered to bind molecular targets with high specificity and selectivity (49,50).

Table 6: PASS prediction for the activity spectrum of the title compound. P_a represents the probability to be active and P_i represents the probability to be inactive.

PA	PI	Biological activity
0.937	0.001	Antibiotic Glycopeptide-like
0.909	0.005	Ubiquinol-cytochrome-c reductase inhibitor
0.811	0.007	Glucan endo-1,6-beta-glucosidase inhibitor
0.795	0.021	Acrocyllindropepsin inhibitor
0.795	0.021	Chymosin inhibitor
0.795	0.021	Saccharopepsin inhibitor
0.760	0.049	Phobic disorders treatment
0.746	0.020	Acylcarnitine hydrolase inhibitor
0.746	0.007	Pterin deaminase inhibitor
0.734	0.004	Mannan endo-1,4-beta-mannosidase inhibitor

3.8.2. Molecular docking

Molecular docking is a method that predicts the relative orientation of one molecule (ligand) when bound with an active site of another molecule (protein) to form a stable complex such that the free energy of the overall system is minimized. In the current study, we can recognize the transfer of a molecule known as ligand 2,4-dimethyl-1-nitrobenzene in biological complex systems. Autodock-Vina software (51) was utilized and the title molecule was docked into the protein receptor (PDB ID: 4Y0S). The active site of the protein was determined with the following dimensions: grid box sizes: $52 \times 74 \times 46$ Å; x, y, z centers: -3, 8, and 21 respectively. The ligand has a better docking ability to protein when its binding energy has a minimum value (52). The binding affinities and

their root-mean-square deviation (RMSD) values for different poses in 4Y0S inhibitors are reported in Table 7. Generally, the docked conformation with the lowest binding energy is selected as the best pose for molecular docking (53). From Table 7 it can be seen that the best docking pose was determined with the binding energy system (ligand-protein) of -6.6 kcal/mol in mode number 1. This value is lower compared to the binding energy of previous works, using the same target protein (PDB ID: 4Y0S) and the same active site. The docking results were visualized by Accelrys Discovery Studio (version 4.1) software, The lowest energy pose for the compound (2,4-dimethyl-1-nitrobenzene in the protein binding site was shown in Figure 14.

Table 7: Docking results of the binding affinity and RMSD values of different poses in 4Y0S inhibitor of the title compound.

mode	Affinity (Kcal/mol)	RMSD l.b	RMSD u.b.
1	-6.6	0.000	0.000
2	-6.3	1.845	2.577
3	-6.1	1.837	2.779
4	-5.4	2.544	3.416
5	-5.1	3.862	5.055
6	-4.8	3.390	4.413
7	-4.6	6.934	8.379
8	-4.4	5.077	6.427
9	-4.4	6.989	8.243

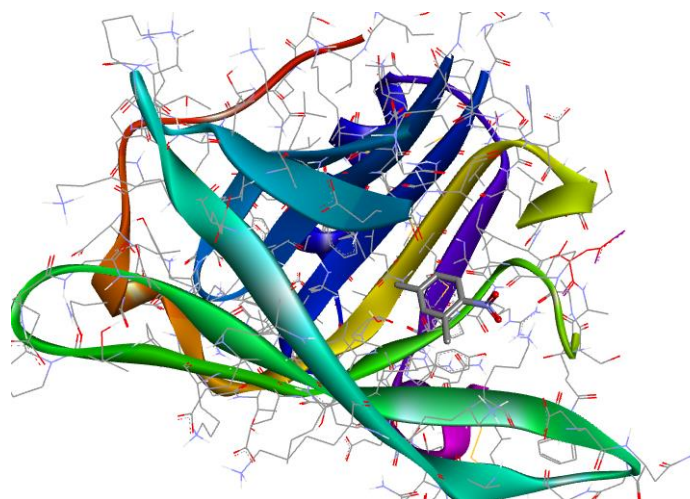


Figure 14: Best-scored docking pose of the title compound inside active sites of the 4Y0S protein.

The intermolecular interactions, linking the structure of our ligand and the 4Y0S protein, are represented in Figure 15 with two forms (form A: 2D and form B: 3D). On the other

hand, the types of intermolecular interactions existing between the residues of the 4Y0S protein and the ligand studied are illustrated in Table 8.

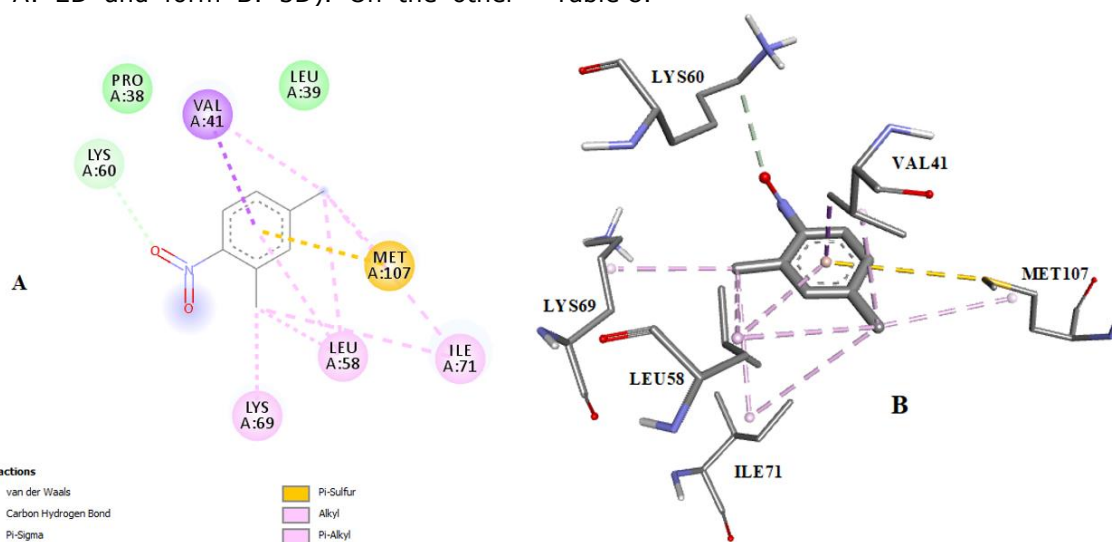


Figure 15: Two forms of intermolecular interactions, linking the structure of the ligand with the protein 1NTK (A 2D and B 3D).

Table 8: Distances, types, and location of intermolecular interactions formed from the residues of the protein C-met (PDB ID: 4Y0S) and the title molecule.

Protein	Residues	Compound	Atom/group of compound	Category	Types	Distance (Å)
PDB (ID : 4Y0S)	A:LYS60	2,4-dimethyl-1-nitrobenzene	O2	Hydrogen Bond	Carbon Hydrogen Bond	3.525
	A:VAL41		aromatic ring	Hydrophobic	Pi-Sigma	3.469
	A:MET107		aromatic ring	Miscellaneous	Pi-Sulfur	5.196
	A:LEU58		C8	Hydrophobic	Alkyl	5.027
	A:LEU58		aromatic ring	Hydrophobic	Pi-Alkyl	5.403
	A:LEU58		C7	Hydrophobic	Alkyl	4.579
	A:LYS69		C7	Hydrophobic	Alkyl	4.146
	A:ILE71		C8	Hydrophobic	Alkyl	5.313
	A:ILE71		C7	Hydrophobic	Alkyl	4.909
	A:MET107		C8	Hydrophobic	Alkyl	4.648

4. CONCLUSION

In the present work, DFT calculations, molecular docking, and Hirshfeld surface analysis of 2,4-dimethyl-1-nitrobenzene were reported. B3LYP function with 6-31G(d,p) basis set calculations of geometry optimization shows that the obtained theoretically optimized bond lengths and bond angles are in good agreement with the corresponding experimental ones. The variation of global chemical reactivity descriptors of E-TPDN in two media showed that this compound exhibits a high reactivity in the gaseous phase, while it exhibits a good electrophile character in a polar solvent such as DMSO medium. The general conclusion from the estimation of the electrostatic potential of the 2,4-dimethyl-1-nitrobenzene molecule in both experimental and theoretical studies is that the region of the nitro around the nitro group is a favored site for electrophilic attack while the methyl groups region is electropositive. The Hirshfeld surface analysis and the subsequent 2D-fingerprint plots have indicated that the crystal is principally stabilized by two types of interactions; H...H contacts with 47.5 % and H...O/O...H interactions with 22.8%. This study reveals that the title molecule has a significant hyperpolarizability and can be used to develop NLO materials. The RDG-NCI analysis of these molecules was performed to determine the non-covalent interactions present within the molecules. According to the results, we can say that the molecule is the most reactive. The title under investigation presents a biological activity (Antibiotic Glycopeptide-like), its ability of docking into the protein 4Y0S is confirmed with the binding energy system (ligand-protein) of -6.6 kcal/mol.

5. ACKNOWLEDGMENTS

We thank the Ministry of Higher Education and Scientific Research and the General Directorate

of Scientific Research and Technological Development (DG-RSDT) for their support We also thank the laboratory: Crystallography Laboratory, Department of Physics, Ondokuz Mayıs University, , Samsun, TURKEY in which the data collection was carried out.

6. REFERENCES

1. Minasyan YV, Degtyarenko AI, Kosmacheva KD, Plekhovich SD, Zelentsov SV. Effect of Acceptor and Donor Substituents in The ortho, meta, and para Positions in the Nitrobenzene Molecule on the Reaction of Interaction with Ethylene. Multidisciplinary Digital Publishing Institute Proceedings. 2018;9(1):50. Available from: [<URL>](#)
2. Program NT. Report on carcinogens, 2011. National Toxicology Program, US Department of Health and Human Services, Washington, DC. 2011.
3. Services UDoHaH. Hazardous substances data bank (HSDB, online database). National Toxicology Information Program, National Library of Medicine, Bethesda, MD. 1993. Available from: [<URL>](#)
4. Atsdr U. Agency for toxic substances and disease registry. Case Studies in environmental medicine <http://www.atsdr.cdc.gov/HEC/CSEM/csem.html>. 1997.
5. Arora PK, Sasikala C, Ramana CV. Degradation of chlorinated nitroaromatic compounds. Applied microbiology and biotechnology. 2012;93:2265-77. Available from: [<URL>](#)
6. Tas DO, Pavlostathis SG. Occurrence, toxicity, and biotransformation of pentachloronitrobenzene and chloroanilines. Critical Reviews in Environmental Science and Technology. 2014;44(5):473-518. Available from: [<URL>](#)
7. Zhang J, Mitchell LA, Parrish DA, Shreeve JnM. Enforced layer-by-layer stacking of energetic salts towards high-performance insensitive energetic materials. Journal of the American Chemical Society. 2015;137(33):10532-5. Available from: [<URL>](#)

8. Cardenuto MH, Champagne B. The first hyperpolarizability of nitrobenzene in benzene solutions: investigation of the effects of electron correlation within the sequential QM/MM approach. *Physical Chemistry Chemical Physics*. 2015;17(36):23634-42. Available from: [<URL>](#)
9. Soto J, Algarra M. Electronic structure of nitrobenzene: A benchmark example of the accuracy of the multi-state CASPT2 theory. *The Journal of Physical Chemistry A*. 2021;125(43):9431-7. Available from: [<URL>](#)
10. Millán R, Soriano MD, Cerdá Moreno C, Boronat M, Concepción P. Combined spectroscopic and computational study of nitrobenzene activation on non-noble metals-based mono-and bimetallic catalysts. *Nanomaterials*. 2021;11(8):2037. Available from: [<URL>](#)
11. Boubegra N, Megrouss Y, Boukabcha N, Chouaih A, Hamzaoui F. The electrostatic properties of 1, 2-dimethyl-3-nitrobenzene compound: ab initio calculation and X-ray charge density analysis. *Rasayan Journal of Chemistry*. 2016;9(4). Available from: [<URL>](#)
12. Kumar MS, Vibhanjali M, Tripathi P, Adil KM. Quantum Chemical Descriptors Based QSTR Study of Nitrobenzene Derivatives against *Tetrahymena Pyriformis*. *Research Journal of Chemical Sciences*. ISSN.2231:606X. Available from: [<URL>](#)
13. Krishnakumar S, Das AK, Singh PJ, Shastri A, Rajasekhar B. Experimental and computational studies on the electronic excited states of nitrobenzene. *Journal of Quantitative Spectroscopy and Radiative Transfer*. 2016;184:89-99. Available from: [<URL>](#)
14. Seshadri S, Padmavathy M. Structure, characterization and DFT studies of 1, 2-Dichloro-4-fluoro-5-Nitrobenzene. 2018. Available from: [<URL>](#)
15. Lee C, Yang W, Parr RG. Development of the Colle-Salvetti correlation-energy formula into a functional of the electron density. *Physical review B*. 1988;37(2):785. Available from: [<URL>](#)
16. Becke AD. Density-functional exchange-energy approximation with correct asymptotic behavior. *Physical review A*. 1988;38(6):3098. Available from: [<URL>](#)
17. Caricato M, Frisch MJ, Hincococks J. Gaussian 09: IOps Reference: Gaussian Wallingford, CT, USA; 2009. Available from: [<URL>](#)
18. Turner M, McKinnon J, Wolff S, Grimwood D, Spackman P, Jayatilaka D, et al. *CrystalExplorer* (Version 17.5). University of Western Australia. 2017.
19. Lu T, Chen F. Multiwfn: A multifunctional wavefunction analyzer. *Journal of computational chemistry*. 2012;33(5):580-92. Available from: [<URL>](#)
20. Kanmazalp SD, Macit M, Dege N. Hirshfeld surface, crystal structure and spectroscopic characterization of (E)-4-(diethylamino)-2-((4-phenoxyphenylimino) methyl) phenol with DFT studies. *Journal of Molecular Structure*. 2019;1179:181-91. Available from: [<URL>](#)
21. Kansız S, Dege N. Synthesis, crystallographic structure, DFT calculations and Hirshfeld surface analysis of a fumarate bridged Co (II) coordination polymer. *Journal of Molecular Structure*. 2018;1173:42-51. Available from: [<URL>](#)
22. Turner MJ, Grabowsky S, Jayatilaka D, Spackman MA. Accurate and efficient model energies for exploring intermolecular interactions in molecular crystals. *The journal of physical chemistry letters*. 2014;5(24):4249-55. Available from: [<URL>](#)
23. Bader R. *A quantum theory*. Clarendon: Oxford, UK. 1990.
24. Johnson ER, Keinan S, Mori-Sánchez P, Contreras-García J, Cohen AJ, Yang W. Revealing noncovalent interactions. *Journal of the American Chemical Society*. 2010;132(18):6498-506. Available from: [<URL>](#)
25. Aouad MR, Messali M, Rezki N, Said MA, Lentz D, Zubaydi L, et al. Hydrophobic pocket docking, double-proton prototropic tautomerism in contradiction to single-proton transfer in thione \rightleftharpoons thiol Schiff base with triazole-thione moiety: Green synthesis, XRD and DFT-analysis. *Journal of Molecular Structure*. 2019;1180:455-61. Available from: [<URL>](#)
26. Agarwal P, Bee S, Gupta A, Tandon P, Rastogi V, Mishra S, et al. Quantum chemical study on influence of intermolecular hydrogen bonding on the geometry, the atomic charges and the vibrational dynamics of 2, 6-dichlorobenzonitrile. *Spectrochimica Acta Part A: Molecular and Biomolecular Spectroscopy*. 2014;121:464-82. Available from: [<URL>](#)
27. Jacobsen H. Localized-orbital locator (LOL) profiles of chemical bonding. *Canadian Journal of Chemistry*. 2008;86(7):695-702. Available from: [<URL>](#)
28. Silvi B, Savin A. Classification of chemical bonds based on topological analysis of electron localization functions. *Nature*. 1994;371(6499):683-6. Available from: [<URL>](#)
29. Jensen F. *Introduction to computational chemistry*: John wiley & sons; 2017.
30. Cohen HD, Roothaan C. Electric dipole polarizability of atoms by the Hartree-Fock method. I. Theory for closed-shell systems. *The Journal of chemical physics*. 1965;43(10):S34-S9. Available from: [<URL>](#)
31. Demirtaş G, Dege N, İçbudak H, Yurdakul Ö, Büyükgüngör O. Experimental and DFT Studies on Poly [di- μ 3-acesulfamato-O, O: O'; O': O, O-di- μ -acesulfamato-O, O; N-di- μ -aqua-dicalcium (II)] Complex. *Journal of Inorganic and Organometallic Polymers and Materials*. 2012;22:671-9. Available from: [<URL>](#)
32. Evecen M, Tanak H, Tinmaz F, Dege N, İlhan İÖ. Experimental (XRD, IR and NMR) and theoretical investigations on 1-(2-nitrobenzoyl) 3, 5-bis (4-methoxyphenyl)-4, 5-dihydro-1H-pyrazole. *Journal of*

- Molecular Structure. 2016;1126:117-26. Available from: [<URL>](#)
33. Aihara J-i. Reduced HOMO– LUMO gap as an index of kinetic stability for polycyclic aromatic hydrocarbons. The Journal of Physical Chemistry A. 1999;103(37):7487-95. Available from: [<URL>](#)
34. Fuentealba P, Parr RG. Higher-order derivatives in density-functional theory, especially the hardness derivative $\partial \eta / \partial N$. The Journal of chemical physics. 1991;94(8):5559-64. Available from: [<URL>](#)
35. Mulliken RS. A new electroaffinity scale; together with data on valence states and on valence ionization potentials and electron affinities. The Journal of Chemical Physics. 1934;2(11):782-93. Available from: [<URL>](#)
36. Pearson RG. Hard and soft acids and bases. Journal of the American Chemical society. 1963;85(22):3533-9. Available from: [<URL>](#)
37. Pearson RG. Absolute electronegativity and hardness correlated with molecular orbital theory. Proceedings of the National Academy of Sciences. 1986;83(22):8440-1. Available from: [<URL>](#)
38. Chattaraj PK, Roy DR. Update 1 of: electrophilicity index. Chemical reviews. 2007;107(9):PR46-PR74. Available from: [<URL>](#)
39. Ayers PW, Parr RG. Beyond electronegativity and local hardness: Higher-order equalization criteria for determination of a ground-state electron density. The Journal of chemical physics. 2008;129(5). Available from: [<URL>](#)
40. Demircioğlu Z, Kaştaş ÇA, Büyükgüngör O. Theoretical analysis (NBO, NPA, Mulliken Population Method) and molecular orbital studies (hardness, chemical potential, electrophilicity and Fukui function analysis) of (E)-2-((4-hydroxy-2-methylphenylimino) methyl)-3-methoxyphenol. Journal of Molecular structure. 2015;1091:183-95. Available from: [<URL>](#)
41. Lee C, Yang W, Parr RG. Local softness and chemical reactivity in the molecules CO, SCN– and H₂CO. Journal of Molecular Structure: Theochem. 1988;163:305-13. Available from: [<URL>](#)
42. Chattaraj PK, Maiti B, Sarkar U. Philicity: a unified treatment of chemical reactivity and selectivity. The Journal of Physical Chemistry A. 2003;107(25):4973-5. Available from: [<URL>](#)
43. Filimonov D, Lagunin A, Glorizova T, Rudik A, Druzhilovskii D, Pogodin P, et al. Prediction of the biological activity spectra of organic compounds using the PASS online web resource. Chemistry of Heterocyclic Compounds. 2014;50:444-57. Available from: [<URL>](#)
44. Thomas R, Hossain M, Mary YS, Resmi K, Armaković S, Armaković SJ, et al. Spectroscopic analysis and molecular docking of imidazole derivatives and investigation of its reactive properties by DFT and molecular dynamics simulations. Journal of Molecular Structure. 2018;1158:156-75. Available from: [<URL>](#)
45. Loch JI, Bonarek P, Polit A, Jablonski M, Czub M, Ye X, Lewinski, K. Goat beta-lactoglobulin complex with pramocaine (GLG-PRM) PDB May 25, 2020. Available from: [<URL>](#)
46. Sawyer L, Kontopidis G. The core lipocalin, bovine β -lactoglobulin. Biochimica et Biophysica Acta (BBA)-Protein Structure and Molecular Enzymology. 2000;1482(1-2):136-48. Available from: [<URL>](#)
47. Flower DR. The lipocalin protein family: structure and function. Biochemical journal. 1996;318(1):1-14. Available from: [<URL>](#)
48. Richter A, Eggenstein E, Skerra A. Anticalins: exploiting a non-Ig scaffold with hypervariable loops for the engineering of binding proteins. FEBS letters. 2014;588(2):213-8. Available from: [<URL>](#)
49. Gilbreth RN, Koide S. Structural insights for engineering binding proteins based on non-antibody scaffolds. Current opinion in structural biology. 2012;22(4):413-20. Available from: [<URL>](#)
50. Loch JI, Bonarek P, Polit A, Jabłoński M, Czub M, Ye X, et al. β -Lactoglobulin interactions with local anaesthetic drugs–Crystallographic and calorimetric studies. International journal of biological macromolecules. 2015;80:87-94. Available from: [<URL>](#)
51. Li H, Wang H-Y, Kang S, Silverman RB, Poulos TL. Electrostatic control of isoform selective inhibitor binding in nitric oxide synthase. Biochemistry. 2016;55(26):3702-7. Available from: [<URL>](#)
52. Mumit MA, Pal TK, Alam MA, Islam MA-A-A-A, Paul S, Sheikh MC. DFT studies on vibrational and electronic spectra, HOMO–LUMO, MEP, HOMA, NBO and molecular docking analysis of benzyl-3-N-(2, 4, 5-trimethoxyphenyl)methylene) hydrazinecarbodithioate. Journal of molecular structure. 2020;1220:128715. Available from: [<URL>](#)
53. Guerroudj AR, Boukabcha N, Benmohammed A, Dege N, Belkafouf NEH, Khelloul N, et al. Synthesis, crystal structure, vibrational spectral investigation, intermolecular interactions, chemical reactivity, NLO properties and molecular docking analysis on (E)-N-(4-nitrobenzylidene)-3-chlorobenzeneamine: A combined experimental and theoretical study. Journal of Molecular Structure. 2021;1240:130589. Available from: [<URL>](#)



Evaluation of Heavy Metal Pollution in commonly consumed mollusc (*Crassostrea gasar*) from Elechi Creek, River State, Nigeria and the Health Risk Implications

Ibienebo Chris Davies^{1*}, Emeka Donald Anyanwu², Evelyn Godwin Amaewhule³

¹Department of Fisheries, University of Port Harcourt, East/West Road, PMB 5323 Choba, Rivers State, Nigeria.

²Department of Zoology and Environmental Biology, Michael Okpara University of Agriculture, Umudike, Nigeria.

³Department of Animal and Environmental Biology, Rivers State University, Nkpolu – Oroworukwo P.M.B. 5080, Rivers State, Nigeria.

Abstract: Marine biotas are used to assess potential adverse human health risks associated with consuming protein-rich aquatic organisms. Heavy metal content of Mangrove oysters (*Crassostrea gasar*) was evaluated between January and June 2022 in 3 stations. Six heavy metals (copper, cadmium, zinc, lead, arsenic and iron) were determined using standard methods. Target Hazard Quotient (THQ) and Hazard Index (HI) were used for the non-carcinogenic assessment while Target Cancer Risk (TR) was used for the carcinogenic assessment of the potential human health risk of consuming the oysters. The heavy metal values recorded were Cu (473.2 – 596.7 mg/kg), Cd (2.33 – 3.84 mg/kg), 209.02 – 246.41 mg/kg, Pb (6.16 – 12.07 mg/kg), As (0.012 – 0.016 mg/kg) and Fe (1609.0 – 1846.0 mg/kg). All the heavy metals were above the acceptable limits except arsenic. Stations 2 and 3 had relatively higher values; attributed to anthropogenic activities. The THQ and HI values were less than 1 in all the metals and stations while TR for Pb and arsenic were within the negligible range in all the stations. However, Cd was unacceptable among the children in station 2. Station 3 had relatively higher values while the children were more vulnerable to both non-carcinogenic and carcinogenic risks. In conclusion, the consumption of oysters from Elechi Creek is considered safe based on acceptable levels of the THQ, HI and TR; though Cd-TR for children (Station 2) was unacceptable.

Keywords: Heavy metals, Mangrove oysters, Health risks, Hazard Quotient, Carcinogenic assessment.

Submitted: August 18, 2023. **Accepted:** December 6, 2023.

Cite this: Davies IC, Anyanwu ED, Amaewhule EG. Evaluation of Heavy Metal Pollution in commonly consumed mollusc (*Crassostrea gasar*) from Elechi Creek, River State, Nigeria and the Health Risk Implications. JOTCSA. 2024;11(2):525-32.

DOI: <https://doi.org/10.18596/jotcsa.1345416>

***Corresponding author's E-mail:** davies.chris@uniport.edu.ng

1. INTRODUCTION

Estuaries are transitional zone between rivers and marine environments found in coastal zones across the world (1). Due to intense socio-economic activities, estuaries are subjected to severe perturbation (2-4); serving as sinks for pollutants, including heavy metals. The constant mixture of fresh and saltwater in the estuaries provides for the remobilization of heavy metals (5). Heavy metals are discharged into the aquatic environment via natural and anthropogenic sources (6, 7).

In the aquatic environment, heavy metals are easily distributed and accumulated in the tissues of aquatic

biota; leading to deleterious effects (8, 9). Aquatic organisms are rich in protein content, low in saturated fats and provide different health advantages (10). They are a ready source of nutrients for local residents (11). The nutritional content of seafood has increased its ever-increasing demand (12).

However, contamination of seafood especially by heavy metals elicits great interest because they can be accumulated in the surrounding environment (8, 13), which raises the issue of food safety globally. A number of marine organisms have been used as bioindicators in the evaluation of potential adverse

human health risks associated with the consumption of contaminated marine biota (14-17).

Oysters are increasingly being studied as indicators of heavy metal pollution because of their wide distribution in coastal environments, susceptibility to pollution, abundance and ease of collection as well as sessile habit and low enzymatic activity level (4, 8, 9, 11, 18, 19).

In the Niger Delta, rivers have become targets for waste disposal due to their open and accessible nature (20). Agricultural, industrial, and municipal wastes are frequently discarded directly into rivers, turning them into convenient landfills (17, 21). Artisanal crude oil refineries have been reported to be a critical anthropogenic activity currently polluting the Niger Delta environment (22-24).

In view of the foregoing, there is a need to understand heavy metal dynamics and accumulation in oysters in Elechi Creek; bearing in mind that it is one of the commonest sources of protein in the area. The aim of this study is to evaluate the heavy metal content of mangrove oysters (*Crassostrea gasar*) and the potential non-carcinogenic and carcinogenic human health risks associated with its consumption.

2. MATERIALS AND METHODS

2.1. Description of Sample Stations

The study was carried out in Elechi Creek, Port Harcourt, Rivers State, Nigeria. It discharges into the

Bonny Estuary and is brackish in nature. It extends from Eagle Island to the Illoabuchi Street waterfront. The creek had varied widths and was surrounded by mangrove trees. Some anthropogenic activities observed around the stations include industrial discharges, urbanization and stormwater runoff, agricultural activities, mangrove degradation, shipping and transportation, waste disposal, and industrial and construction activities.

Station one is located on a sand-filled area known as Eagle Island (Latitude N04°47.149'; Longitude E006°58.958'). It is located around an abandoned artisanal refinery site. The dominant vegetation in the area is Nipa palm (*Nypa fruticans*) with scattered patches of white mangrove (*Laguncularia racemosa*) and red mangrove (*Rhizophora mangle*) and elephant grass (*Pennisetum purpureum*). Station two is located at the Sawmill area (Latitude N04°47.28'; Longitude E006°59.255'); about 2.14 km downstream of station 1. It is around an active artisanal refinery site.

The dominant vegetation is Nipa palm (*Nypa fruticans*). Station three is located in the Appa area (Latitude N04°47.047'; Longitude E006°59.362'); about 2.21 km downstream of station 2. It is located around crude oil and refined products storage areas used by illegal refiners. Nipa palm (*Nypa fruticans*) is also the dominant vegetation though a large expanse has been destroyed. A large stormwater canal also discharges into the area.

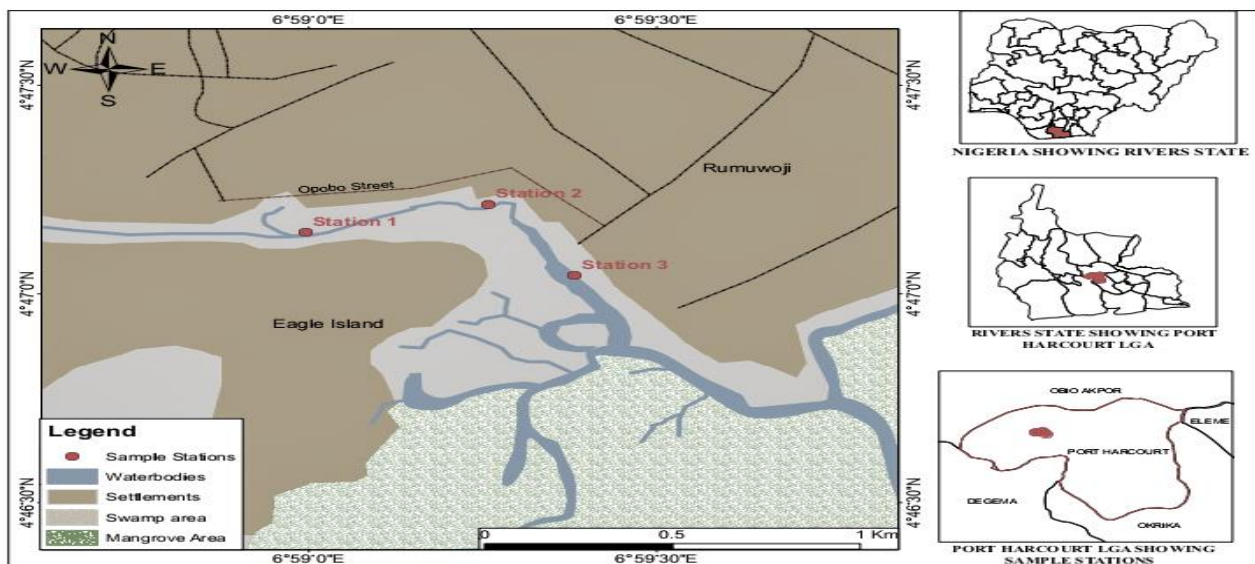


Figure 1: Showing the map of the study area and sampling stations.

2.2. Collection of Oyster Samples

Each station collected ten (10) Mangrove oysters (*Crassostrea gasar*). A total of 180 samples were collected between January and June 2022. The oysters were harvested from the prop roots of the mangrove tree during the low tide. The samples were immediately transported to the laboratory for analysis in an ice chest. The soft tissues from 8 to 10 individuals were dissected, dried, and stored in clean, clearly labelled plastic containers.

2.3. Sample Preparation and Digestion

The tissue samples, each weighing $0.5 \pm 0.01\text{g}$, were placed straight into Teflon digestion containers that had been cleaned with acid. Each vessel received 10 ml of ultra-pure nitric acid, which was then heated to 100°C using an XT-9800 pre-treatment heater until nearly all the nitrogen dioxide was released.

In order to prepare the sample for microwave digestion, a 4 mL aliquot of concentrated HNO_3 : HF (1:1 v/v) acid solution was added. Every digestion batch had a minimum of one reagent blank, one

representative reference standard, and generally, one sample replication to assess homogeneity and procedure effectiveness.

There were three stages to microwave digestion: 1.5 MPa for 1 min, 1.0 MPa for 2 min, and 1.5 MPa for 3 min. The digested sample was transferred to a graduated plastic test tube and allowed for an hour to cool and the volume was made up to 100 mL with Milli-Q water (25, 26).

2.4. Quality Assurance and Control

After microwave digestion, each metal's certified reference materials (CRMs) from Sigma-Aldrich were employed for atomic absorption spectroscopy (AAS). The metals - cadmium (Cd), iron (Fe), arsenic (As), lead (Pb), zinc (Zn), and copper (Cu) were analysed in the oyster samples in triplicates. The apparatus was calibrated using atomic absorption standards for numerous dangerous metals that were buck-certified in order to create an analytical curve.

To avoid equipment drift, 10 samples were analysed before a reagent blank. According to calculations, the percentage recovery (%R) for metals was Fe (89.0%), Pb (98.7%), Cd (100%), As (99.6%), Zn (84.5%), and Cu (97.6%). An atomic absorption spectrophotometer (Model 210 VGP, Buck Scientific) was used to determine the metal contents in the samples.

2.5. Human Health Risk Assessment

The Non-Carcinogenic Risk Assessment and Individual Lifetime Cancer Risk were applied in this study. The Target hazard quotient (THQ) for each heavy metal was calculated in order to assess the potential health risk of consuming Oysters (*Crassostrea gasar*) collected from the study area (27). It was calculated using Equation 1:

$$THQ = \frac{ED \times IR \times EF \times CW}{RfD \times BW \times AT} \times 10^{-3} \quad (1)$$

Where ED is the Exposure duration - 70 years (adults) and 10 years (children); IR is the daily ingestion rate - 0.3 mg/kg/person/day (adults) and 0.15 mg/kg/person/day (children) (28); EF is the exposure frequency (365 days/year); CW is the concentration of respective heavy metal (mg/kg) in the oysters; RFD is the reference oral dose in mg/kg/day (0.001 for Cd, 0.004 for Pb, 0.3 for Zn, 0.0003 for As, 0.7 for Fe and 0.04 for Cu); BW is body weight - 70 kg (adult) and 25 kg (children) and AT (ED x EF) is the average time of the exposure - 25550 days (adult) and 3650 days (children) (29). THQ > 1 points to adverse non-carcinogenic effects that cannot be overlooked but acceptable levels are at HQ < 1.

2.6. Hazard Index (HI)

Hazard index (HI) is the cumulative potential for non-carcinogenic effects from more than one heavy metal through ingestion pathways and can be estimated from equation 2 (30).

$$HI = \sum_{i=1}^n THQ \quad (2)$$

Where HI is the hazard index for the overall toxic risk and n equals the total number of metals under consideration. If HI for non-carcinogenic adverse effects due to ingestion exposures is lower than one (HI < 1.0), then no chronic risks are expected to occur but if HI is greater than one (HI > 1.0), possible chronic risk arising from the ingestion exposures could manifest (31).

2.6. Carcinogenic Risk

Target Cancer Risk (TR) was used to determine the carcinogenic risk (8). Target cancer risk (TR) posed by the assessed heavy metals was determined with Equation 3 (35):

$$TR = \frac{ED \times IR \times EF \times CW \times CSF}{BW \times AT} \times 10^{-3} \quad (3)$$

Where CSF is the Cancer Slope Factor while other input parameters have been previously defined in Equation 1. The acceptable range for carcinogenic risks is between 10^{-4} and 10^{-6} and values > 10^{-4} will likely result in cancer (8). The cancer slope factors (CSF) were Cd (6.3 mg/kg/day), Pb (0.0085 mg/kg/day) and As (1.5 mg/kg/day).

2.7. Statistical Analysis

One-way Analyses of variance (ANOVA) and descriptive statistics were carried out using SPSS version 16 while the Duncan Multiple Range Test was used to differentiate significant means at 0.05.

3. RESULTS AND DISCUSSION

Concentrations of heavy metals in Oysters

(*Crassostrea gasar*): The mean concentrations of the heavy metals in the oysters in the different stations are presented in Table 1. Copper ranged from 473.2 - 596.7 mg/kg. The lowest value was recorded in station 1 while the highest was recorded in station 3. Station 1 was significantly ($p < 0.05$) lower than the others and all the values exceeded the limit (3.09 mg/kg) set by (32). The Copper values recorded in the oysters exceeded the limit (3.09 mg/kg) set by (32) by a wide margin. Copper is a critical metal that is easily taken up by aquatic organisms; which could be responsible for relatively high values recorded in the oysters (4). Copper is also a nutritional component of oysters (11) and has been reported to accumulate in oysters with zinc (4, 8).

Lower values were recorded in related studies. Mean values of 11.93 mg/kg (Mundaú/Manguaba lagoon complex) and 14.33 mg/kg (Meirim River) were recorded by (18) in Alagoas, Brazil, 0.97 mg/kg by (19) in Muar River, Johor, Malaysia, 0.34 - 1.16 mg/kg by (4) in Bonny Estuary, Nigeria and 3.80 mg/kg by (11) in Paranaguá Estuarine System, Brazil. The lowest value recorded in Station 1 and the highest in Station 3 could be attributed to anthropogenic activities especially artisanal refining activities (24, 23, 24). Station 1 was located in an abandoned artisanal refinery site while station 3 was located around crude oil and refined product storage site. Station 3 also received discharges from the activities upstream in Stations 1 and 2.

Table 1: Mean concentrations of the heavy metals in the oysters (mg/kg).

Metals	Station 1	Station 2	Station 3	IAEA*
Cu	473.2±61.8 ^b	531.0±81.1 ^a	596.7±69.1 ^a	3.09
Cd	2.33±0.8 ^b	3.84±0.7 ^a	2.59±27 ^b	0.18
Zn	215.44±19.9 ^a	209.02±19.3 ^a	246.41±20.4 ^a	66.4
Pb	6.16±2.9 ^a	8.51±2.7 ^{ab}	12.07±2.5 ^b	0.10
As	0.012±0.002 ^a	0.013±0.002 ^a	0.016±0.002 ^a	13.3
Fe	1609.0±130.2 ^b	1634.0±132.1 ^b	1846.0±216.4 ^a	146.0

* International Atomic Energy Agency (2003, 2022)

Cadmium ranged between 2.33 and 3.84 mg/kg. The lowest value was also recorded in station 1 while the highest was in station 2. Stations 1 and 3 were significantly ($p < 0.05$) lower than station 2 and all the values exceeded the limit (0.18 mg/kg) set by (32). Cadmium values also exceeded the limit (0.18 mg/kg) set by (32). Higher mean values of 4.65 mg/kg (Mundaú/Manguaba lagoon complex) and 4.21 mg/kg (Meirim River) were recorded by (18) in Alagoas, Brazil, while lower values: 1.29 mg/kg was recorded by (19) in Muar River, Johor, Malaysia, 0.005 – 0.040 mg/kg by (4) in Bonny Estuary, Nigeria and 0.16 mg/kg by (11) in Paranaguá Estuarine System, Brazil. The lowest and highest values recorded in stations 1 and 2 could be attributed to anthropogenic activities in the watershed as in Cu.

Zinc ranged from 209.02 – 246.41 mg/kg. The lowest value was recorded in station 2 while the highest was recorded in station 3. There was no significant difference in all the stations and all the values in the stations exceeded the limit (66.4 mg/kg) set by (32). However, Zinc values were higher than 66.4 mg/kg set by (32) with a wide margin and exhibited the same trend as copper because they undergo the same processes (11). Zn is also a natural component of oysters and high concentrations have also been reported with copper (4, 8, 11). Zinc is necessary for good health, but elevated concentrations can be harmful because excessive intake will lead to the suppression of the intake of copper and iron (18).

Higher mean values of 413.58 mg/kg (Mundaú/Manguaba lagoon complex) and 401.43 mg/kg (Meirim River) were recorded by (18) in Alagoas, Brazil, while lower values: 1.02 mg/kg was recorded by (19) in Muar River, Johor, Malaysia, 0.87 – 7.62 mg/kg by (4) in Bonny Estuary, Nigeria and 250.3 mg/kg by (11) in Paranaguá Estuarine System, Brazil. The highest value was also recorded in station 3, though the lowest was in station 2; attributed to anthropogenic impact.

Lead ranged from 6.16 – 12.07 mg/kg. The lowest value was recorded in station 1 while the highest was recorded in station 3. Station 3 was significantly ($p < 0.05$) different from station 1; though all values exceeded the limit (0.10 mg/kg) set by (32). However, Lead values were also higher than the 0.10 mg/kg set by (32). Lower values were recorded elsewhere. 0.52 mg/kg was recorded by (19) in Muar River, Johor, Malaysia and 0.017 – 0.24 mg/kg by (4) in Bonny Estuary, Nigeria. The lowest and highest values were also recorded in stations 1 and 3 respectively as observed in copper.

Arsenic ranged from 0.012– 0.016 mg/kg. The lowest value was also recorded in station 1 while the highest was recorded in station 3. All the values in the stations were within the limit (13.3 mg/kg) set by (32). There was no significant ($p > 0.05$) difference. Arsenic values were within the acceptable limit (13.3 mg/kg) set by (32). (8) recorded a higher value of 0.72 mg/kg in oysters in Hangzhou Bay, China and 0.96 mg/kg by (11) in Paranaguá Estuarine System, Brazil. The lowest and highest values were also recorded in stations 1 and 3 respectively as observed in copper and lead.

Iron ranged between 1609.0 and 1846.0 mg/kg. The lowest value was recorded in station 1 while the highest was recorded in station 3. Stations 1 and 2 were significantly ($p < 0.05$) lower than station 3 but all the values exceeded the limit (146.0 mg/kg) set by (32).

Iron values were higher than the limit (146.0 mg/kg) set by (32) with a wide range. It is the metal that recorded the highest concentration; attributed to anthropogenic impact and environmental stress (9). Lower mean values of 278.06 mg/kg (Mundaú/Manguaba lagoon complex) and 203.18 mg/kg (Meirim River) were recorded by (18) in Alagoas, Brazil, 0.56 mg/kg by (19) in Muar River, Johor, Malaysia and 2.44–227.72 mg/kg by (9) in Pattani Bay, Thailand. The lowest and highest values were also recorded in stations 1 and 3 respectively as observed in copper, lead and Arsenic.

Health Risk Assessment: The Target Hazard Quotients (THQs) of the heavy metals evaluated in *C. gasar* are presented in Table 2. All THQs for the heavy metals were less than 1. The THQs for children were generally higher than that of adults in all the metals and stations. The lowest Cd – THQ was recorded among adults (Station 1) while the highest was among children (Station 2) while Pb and Cu – THQs had the lowest values among adults (Station 1) and the highest among children (Station 3). On the other hand, the lowest Zn and Fe – THQs were recorded among adults (Stations 1 and 2) and the highest among children (Station 3). For As, the lowest THQ values were recorded in Station 1 (adult and children), stations 2 and 3 (adults) while the highest values (equal to the reference dose) were recorded among the children in Stations 2 and 3. All HI values were lower than 1; though values among the children were relatively higher and increased spatially from stations 1 to 3 (Table 2).

Table 2: Target Hazard quotients (THQs) of the heavy metals in *C. gasar*.

Heavy metals	Station 1		Station 2		Station 3		Reference Dose
	Adult	Children	Adult	Children	Adult	Children	
Cd	1.00E-02*	1.40E-02	1.60E-02	2.30E-02**	1.10E-02	1.60E-02	4.00E-02
Pb	7.00E-03*	9.00E-03	9.00E-03	1.30E-02	1.30E-02	1.80E-02**	1.00E-03
Zn	3.00E-03*	4.00E-03	3.00E-03*	4.00E-03	4.00E-03	5.00E-03**	3.00E-01
Fe	1.00E-02*	1.40E-02	1.00E-02*	1.40E-02	1.10E-02	1.60E-02**	4.00E-03
As	2.00E-04*	2.00E-04*	2.00E-04*	3.00E-04**	2.00E-04*	3.00E-04**	3.00E-04
Cu	5.10E-02*	7.00E-02	6.00E-02	8.00E-02	6.00E-02	9.00E-02**	7.00E-01
ΣTHQ (HI)	8.12E-02	1.11E-01	9.82E-02	1.34E-01	9.92E-02	1.45E-01	

Key: * = Lowest THQs; ** = Highest THQs

All THQs were less than 1; suggesting that the consumption of oysters from Elechi Creek would not cause any adverse effects (4, 19). However, (11) record THQs greater than 1 in some stations and arsenic; suggesting health risks in consuming the oysters from their study area. THQs should not be overlooked even when they are lower than 1 because cumulative effects could occur when combined with other exposure routes (33). However, when the value is greater or equal to the reference dose, there is a tendency that the population will experience health risks (29).

This trend was observed in Pb and Fe (adults and children in all the stations) and As (children in stations 2 and 3). The THQs for children were generally higher than that of adults in all the metals and stations. This could be attributed to their assimilation level (34). Children have been reported to have high metabolic rates which translates to high assimilation. (8) recorded THQs greater than 1 among children. The higher THQs in Station 3 could be attributed to the anthropogenic activities around the station. All HI values were also lower than 1 in all the stations and both adults and children as observed by (8). With $HI < 1$, it is unlikely that consumption of the oysters from Elechi Creek will have significant risks to human health (9).

However, excessive consumption of oysters should be discouraged to prevent deleterious health risks arising from exposure to multiple heavy metals (9). (34) further reported that frequency of exposure is one of the factors that determine the extent of toxicity of heavy metals. (11) recorded hazard index values greater than one; an indication of potentially-high health risks, which was attributed to zinc and arsenic with high THQs. The TR values were used to assess the carcinogenic human health risks associated with the consumption of oysters from Elechi Creek.

Carcinogenic Human Health Risk:

The carcinogenic human health risks resulting from the consumption of oysters collected from Elechi Creek were determined using TR values. The TR values for the three carcinogens evaluated are presented in Table 3. The TR values for Pb and As were within the acceptable limits ($1.00E-04 - 1.00E-06$) among the adults and children in all the stations while Cd had a value greater than $1.00E-04$ among the children in Station 2. Stations 2 and 3 had relatively higher values. The children's values were also higher in all metals and stations as observed in the non-carcinogenic assessment.

Table 3: Target Cancer Risk (TR) values of consuming *C. gasar*.

Heavy metals	Station 1		Station 2		Station 3	
	Adult	Children	Adult	Children	Adult	Children
Cd	6.30E-05	8.80E-05	1.00E-04	1.50E-04	7.00E-05	9.80E-05
Pb	2.20E-07	3.10E-07	3.10E-07	4.30E-07	4.40E-07	6.20E-07
As	7.70E-08	1.10E-07	8.40E-08	1.20E-07	1.00E-07	1.40E-07

The TR values of $1.00E-04 - 1.00E-06$ were considered acceptable. However, Cd had a value greater than $1.00E-04$ among the children in Station 2; which is unacceptable (14). (9) reported that Cd is of carcinogenic concern among children. The TR values for Pb and As were lower than $1.00E-06$ among the adults and children in all the stations; considered negligible (11). Stations 2 and 3 had relatively higher values attributed to anthropogenic impacts. Children were more susceptible in line with previous studies (8, 15).

4. CONCLUSION

All the heavy metals were above the acceptable limits except arsenic. Stations 2 and 3 had relatively higher values; attributed to anthropogenic activities. The THQ and HI values were less than 1 in all the metals and stations while TR for Pb and arsenic were within the negligible range in all the stations. TR - Cd was unacceptable among the children in station 2. Station 3 had relatively higher values while the children were more vulnerable to both non-carcinogenic and carcinogenic risks. The consumption of oysters from

Elechi Creek is considered safe based on acceptable levels of the THQ, HI and TR; though Cd-TR for children (Station 2) was unacceptable.

5. CONFLICT OF INTEREST

No potential conflicts of interest exist between the authors' authorship and the publishing, they disclose.

6. ACKNOWLEDGMENTS

The authors wish to thank the Centre for Marine Pollution Monitoring and Seafood Safety, University of Port Harcourt, Nigeria, for providing the environment, which enabled the conducting of this research.

7. REFERENCE

- van Maanen B, Sottolichio A. Hydro- and sediment dynamics in the Gironde estuary (France): Sensitivity to seasonal variations in river inflow and sea level rise. *Cont Shelf Res* [Internet]. 2018 Aug 1;165:37–50. Available from: [<URL>](#).
- Zhang Y, Lu X, Wang N, Xin M, Geng S, Jia J, et al. Heavy metals in aquatic organisms of different trophic levels and their potential human health risk in Bohai Bay, China. *Environ Sci Pollut Res* [Internet]. 2016 Sep 1;23(17):17801–10. Available from: [<URL>](#).
- Barletta M, Lima ARA, Costa MF. Distribution, sources and consequences of nutrients, persistent organic pollutants, metals and microplastics in South American estuaries. *Sci Total Environ* [Internet]. 2019 Feb 15;651:1199–218. Available from: [<URL>](#).
- Dike CS, Vincent-Akpu IF, Babatunde BB, Sikoki FD. Investigation of the Concentration of some Metals in Blood Cockle (*Senilia senilis*) and Oyster (*Crassostrea gasar*) from Bonny Estuary and Assessment of the Human Health Risk Associated with their Consumption. *J Appl Sci Environ Manag* [Internet]. 2022 Apr 30;26(4):667–76. Available from: [<URL>](#).
- Noegrohati S. Sorption-desorption characteristics of heavy metals and their availability from the sediment of Segara anakan estuary. *Indones J Chem* [Internet]. 2010 Jun 15;5(3):236–44. Available from: [<URL>](#).
- Rajaram R, Ganeshkumar A, Vinothkannan A. Health risk assessment and bioaccumulation of toxic metals in commercially important finfish and shellfish resources collected from Tuticorin coast of Gulf of Mannar, Southeastern India. *Mar Pollut Bull* [Internet]. 2020 Oct 1;159:111469. Available from: [<URL>](#).
- Anyanwu ED, Adetunji OG, Ezekiel NI, Alexander RN. Heavy metal concentrations and health risk assessment of a rural multipurpose stream, Southeast Nigeria. *Nat Resour Sustain Dev* [Internet]. 2022;12(2):285–302. Available from: [<URL>](#).
- Noman MA, Feng W, Zhu G, Hossain MB, Chen Y, Zhang H, et al. Bioaccumulation and potential human health risks of metals in commercially important fishes and shellfishes from Hangzhou Bay, China. *Sci Rep* [Internet]. 2022 Mar 17;12(1):4634. Available from: [<URL>](#).
- Tanhan P, Lansubsakul N, Phaochoosak N, Sirinupong P, Yeesin P, Imsilp K. Human Health Risk Assessment of Heavy Metal Concentration in Seafood Collected from Pattani Bay, Thailand. *Toxics* [Internet]. 2022 Dec 26;11(1):18. Available from: [<URL>](#).
- Kennedy A, Martinez K, Chuang CC, LaPoint K, McIntosh M. Saturated Fatty Acid-Mediated Inflammation and Insulin Resistance in Adipose Tissue: Mechanisms of Action and Implications. *J Nutr* [Internet]. 2009 Jan 1;139(1):1–4. Available from: [<URL>](#).
- Silva Lima L, Silva Vieira K, Freitas Delgado J, Antônio Baptista Neto J. Human Health risk assessment associated with the consumption of oysters (*Crassostrea gasar*) in Paranaguá Estuarine System/Brazil and its Salinity gradient as a tool to understand the contaminants assimilation dynamic. 2023 Jan 24; Available from: [<URL>](#).
- Sacchetti G, Castellini G, Graffigna G, Hung Y, Lambri M, Marques A, et al. Assessing consumers' attitudes, expectations and intentions towards health and sustainability regarding seafood consumption in Italy. *Sci Total Environ* [Internet]. 2021 Oct 1;789:148049. Available from: [<URL>](#).
- Chris D, Ekperusi A. Evaluation of Heavy Metal Concentrations in Water, Sediment and Fishes of New Calabar River in Southern Nigeria. *J Limnol Freshw Fish Res* [Internet]. 2021 Dec 30;7(3):207–18. Available from: [<URL>](#).
- Baki MA, Hossain MM, Akter J, Quraishi SB, Haque Shojib MF, Atique Ullah AKM, et al. Concentration of heavy metals in seafood (fishes, shrimp, lobster and crabs) and human health assessment in Saint Martin Island, Bangladesh. *Ecotoxicol Environ Saf* [Internet]. 2018 Sep 15;159:153–63. Available from: [<URL>](#).
- Liu Q, Liao Y, Shou L. Concentration and potential health risk of heavy metals in seafoods collected from Sanmen Bay and its adjacent areas, China. *Mar Pollut Bull* [Internet]. 2018 Jun 1;131:356–64. Available from: [<URL>](#).
- Pandion K, Khalith SBM, Ravindran B, Chandrasekaran M, Rajagopal R, Alfarhan A, et al. Potential health risk caused by heavy metal associated with seafood consumption around coastal area. *Environ Pollut* [Internet]. 2022 Feb 1;294:118553. Available from: [<URL>](#).
- Davies DICC, Anyanwu ED. Assessment of some Heavy Metals and Health Risks in Water and Shrimps from a Polluted Mangrove Swamp, Niger Delta, Nigeria. *Pollution* [Internet]. 2023 Oct 1;9(4):1653–65. Available from: [<URL>](#).

18. Azevedo JAM, Barros AB, Miranda PRB de, Costa JG da, Nascimento VX. Biomonitoring of Heavy Metals (Fe, Zn, Cu, Mn, Cd and Cr) in Oysters: *Crassostrea rhizophorae* of Mangrove Areas of Alagoas (Brazil). *Brazilian Arch Biol Technol* [Internet]. 2019 Oct 24;62:e19180211. Available from: [<URL>](#).
19. Ashykin N, Razak A, Abdullah S. Analysis of Heavy Metals Concentration in Fish and Crustaceans from Muar River. *Enhanc Knowl Sci Technol* [Internet]. 2021 Jul 29;1(2):109–15. Available from: [<URL>](#).
20. Numbere AO, Maduiké EM. The Impact of Unsustainable Exploitation of Forest and Aquatic Resources of the Niger Delta, Nigeria. In: Izah SC, editor. *Biodiversity in Africa: Potentials, Threats and Conservation* [Internet]. Springer, Singapore; 2022. p. 239–65. Available from: [<URL>](#).
21. Akankali JA, Davies IC, Blessing DI. Assessment of Sawmill and other Associated Wastes on the Water Quality of Ilo-abuchi Creek, Rivers State, Niger Delta. *Asian J Fish Aquat Res* [Internet]. 2022 May 6;17(4):1–13. Available from: [<URL>](#).
22. Sibe L, Osuji LC, Hart AI. Physico-Chemical Alterations of Interstitial Water Quality by Artisanal Refining Operations at K-Dere Coastal Plain, South-Eastern Nigeria. *Int J Sci Eng Res*. 2019;10(12):194.
23. Ikezam P, Elenwo EI, Oyegun CU. Effects of Artisanal Refinery on the Environment, Public Health and Socio-Economic Development of Communities in the Niger Delta Region. *Environ Manag Sustain Dev* [Internet]. 2021 Aug 11;10(3):97. Available from: [<URL>](#).
24. Onuh PA, Omenma TJ, Onyishi CJ, Udeogu CU, Nkaku NC, Iwuoha VO. Artisanal refining of crude oil in the Niger Delta: A challenge to clean-up and remediation in Ogoniland. *Local Econ J Local Econ Policy Unit* [Internet]. 2021 Sep 30;36(6):468–86. Available from: [<URL>](#).
25. Yi Y, Yang Z, Zhang S. Ecological risk assessment of heavy metals in sediment and human health risk assessment of heavy metals in fishes in the middle and lower reaches of the Yangtze River basin. *Environ Pollut* [Internet]. 2011 Oct 1;159(10):2575–85. Available from: [<URL>](#).
26. Anyanwu BO, Ibienebo Chris D. Human health hazard implications of heavy metals concentration in swimming crab (*Callinectes amnicola*) from polluted creeks in Rivers State, Nigeria. *Case Stud Chem Environ Eng* [Internet]. 2023 Jun 1;7:100325. Available from: [<URL>](#).
27. Biswas C, Soma SS, Rohani MF, Rahman MH, Bashar A, Hossain MS. Assessment of heavy metals in farmed shrimp, *Penaeus monodon* sampled from Khulna, Bangladesh: An inimical to food safety aspects. *Heliyon* [Internet]. 2021 Mar 1;7(3):e06587. Available from: [<URL>](#).
28. Markmanuel DP, Amos-Tautau BMW, Songca SP. Tin Concentrations and Human Health Risk Assessment for Children and Adults in Seafood and Canned Fish commonly consumed in Bayelsa State, Nigeria. *J Appl Sci Environ Manag* [Internet]. 2022 Jul 31;26(7):1263–9. Available from: [<URL>](#).
29. USEPA. Risk Assessment Guidance for Superfund Volume I: Human Health Evaluation Manual (Part E). U.S. Environmental Protection Agency. 2004; Available from: [<URL>](#).
30. Sharma S Das. Risk assessment via oral and dermal pathways from heavy metal polluted water of Kolleru lake - A Ramsar wetland in Andhra Pradesh, India. *Environ Anal Heal Toxicol* [Internet]. 2020 Sep 28;35(3):e2020019. Available from: [<URL>](#).
31. Moldovan A, Hoaghia MA, Kovacs E, Mirea IC, Kenesz M, Arghir RA, et al. Quality and Health Risk Assessment Associated with Water Consumption—A Case Study on Karstic Springs. *Water* [Internet]. 2020 Dec 14;12(12):3510. Available from: [<URL>](#).
32. IAEA. Certification of trace elements and methylmercury mass fractions in fish flesh homogenate (IAEA-407A). IAEA Analytical Quality in Nuclear Applications Series No. 68 (IAEI/AQ/68). International Atomic Energy Agency, Vienna, Austria. 2022; Available from: [<URL>](#).
33. Giandomenico S, Cardellicchio N, Spada L, Annicchiarico C, Di Leo A. Metals and PCB levels in some edible marine organisms from the Ionian Sea: dietary intake evaluation and risk for consumers. *Environ Sci Pollut Res* [Internet]. 2016 Jul 4;23(13):12596–612. Available from: [<URL>](#).
34. Orisakwe OE, Nduka JK, Amadi CN, Dike DO, Bede O. Heavy metals health risk assessment for population via consumption of food crops and fruits in Owerri, South Eastern, Nigeria. *Chem Cent J* [Internet]. 2012 Dec 1;6(1):77. Available from: [<URL>](#).
35. Bonsignore M, Salvagio Manta D, Mirto S, Quinci EM, Ape F, Montalto V, et al. Bioaccumulation of heavy metals in fish, crustaceans, molluscs and echinoderms from the Tuscany coast. *Ecotoxicol Environ Saf* [Internet]. 2018 Oct 30;162:554–62. Available from: [<URL>](#).



New 8-Heterocyclic Xanthine Derivatives as Antiproliferative Agents: Synthesis and Biological Evaluation

Bilgesu Onur Sucu^{1,2} 

¹Istanbul Medipol University, Department of Pharmaceutical Chemistry, Faculty of Pharmacy, Istanbul, Turkey

²Istanbul Medipol University, Center of Drug Discovery and Development, Research Institute for Health Sciences and Technologies (SABITA), Istanbul, Turkey

Abstract: This research focuses on the synthesis, characterization, and evaluation of the anti-cancer activity of novel 8-aryl substituted 1,3-diethylxanthine derivatives. The anti-proliferative activities of all the compounds were assessed using an MTT assay on four human cancer cell lines: breast cancer MCF7, human lung cancer A549, human brain cancers LN229, and U87. One of the derivatives of 1,3-diethylxanthine with a thiazole structure displayed strong anti-proliferative activity. 1,3-Diethyl-8-(thiazol-4-yl)-3,7-dihydro-1*H*-purine-2,6-dione (5) exhibited the strongest activity against A549, MCF7, LN229, and U87 cell lines, with IC₅₀ values of 16.70, 78.06, 22.07, and 25.07 μM, respectively. Furthermore, the scratch assay was conducted to evaluate the effect of compound 5 on the inhibition of cell migration in A549 cells. The consistent results demonstrate that compound 5 exhibits potent anti-cancer activity, which could be further investigated to enhance its biological potential.

Keywords: Xanthine, Heterocyclic compounds, Antiproliferative activity, Anti-cancer, MTT.

Submitted: August 9, 2023. **Accepted:** November 20, 2023.

Cite this: Sucu BO. New 8-Heterocyclic Xanthine Derivatives as Antiproliferative Agents: Synthesis and Biological Evaluation. JOTCSA. 2024;11(2):533-40.

DOI: <https://doi.org/10.18596/jotcsa.1340105>

***Corresponding author.** E-mail: bsucu@medipol.edu.tr

1. INTRODUCTION

Cancer is a widespread public health problem that affects people of all ages, and it's caused by uncontrolled cell growth and spread, which can invade almost any tissue in the body (1). Despite significant advancements in the discovery and use of anticancer drugs, there are several challenges. These include the non-selectivity and high toxicity of the drugs (2). That's why studies aimed at developing new and effective cancer drugs are crucial. Many classes of organic compounds can be highly effective. Specifically, nitrogen-containing compounds are notable for their wide range of biological activities (3–6).

Xanthine (3,7-dihydropurine-2,6-dione) (Fig. 1) consists of a pyrimidine ring fused with an imidazole ring. They are purine alkaloids containing a nitrogen atom at the 1-, 3-, 7-, and 9 positions and a carbonyl group at the 2- and 6 positions. Different natural and synthetic xanthine derivatives are important therapeutic agents with a wide range

of biological effects, such as antiasthmatic (7,8), antagonization of adenosine receptor (9), antibacterial (10), anti-inflammatory (11), antioxidant (12,13) and antitumor activity (14). The 8-(4-pyrazolyl)-xanthine derivative (Fig. 1) was found to be a selective and high-affinity A2B AdoR antagonist. It was determined to be safe and well tolerated in two phase 1 clinical studies (15). It has been reported as beneficial in various diseases, including asthma, chronic obstructive pulmonary disease, and pulmonary fibrosis (16,17). Theophylline, a xanthine derivative compound, is reported to have anti-asthma, anti-inflammatory, and immunomodulatory effects (18,19). Additionally, it has been reported to induce apoptosis in chronic lymphocytic leukemia cells and inhibit Bcl-2 expression in leukemic cells (20). According to reports, methylxanthines like theobromine and caffeine demonstrate strong anti-cancer activity (21–24). Studies have reported that xanthine derivatives induce apoptosis (25). Hence, it is crucial to explore the antiproliferative potential of derivatives of xanthine-containing compounds.

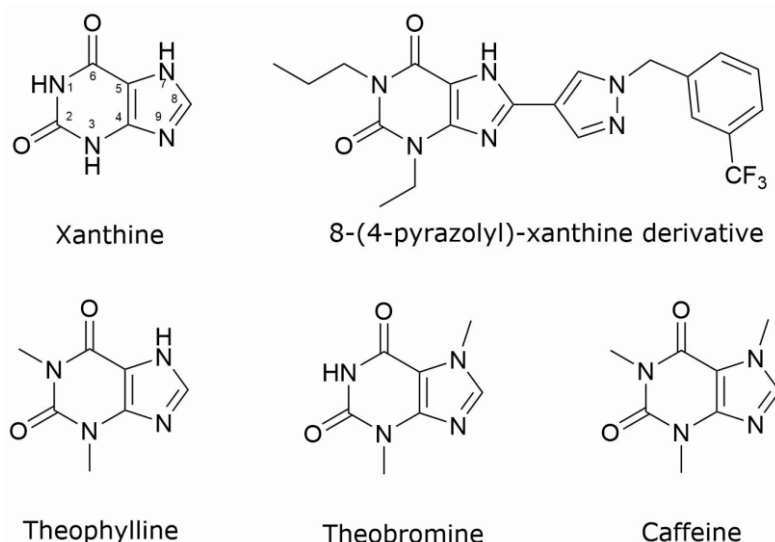


Figure 1: Structures of xanthine derivatives.

Xanthine provides many substitution possibilities, so it is possible to synthesize a wide variety of derivatives. Research indicates that the incorporation of substituents at positions 1, 3, and 8 can lead to the synthesis of more potent compounds (26). Some of the synthesized 8-(substituted)aryloxycaffeine derivatives showed strong inhibitory activity against the tested gram-negative (-) bacteria *Salmonella enteritidis*, while others also showed strong inhibitory activity against topoisomerase II (27). 8-(3-phenylpropyl)-1,3,7-triethylxanthine compound is reported to be a potent potential adenosine A1 receptor antagonist as a result of *in vitro* and *in vivo* activity studies (28). According to studies, incorporating specific groups at the 8th position can significantly enhance the stability and pharmaceutical properties of xanthines (29).

In line with the literature studies mentioned above, a new 1,3-diethyl xanthine derivative with heterocyclic structures substituted at C8 was synthesized and characterized to search for new anti-cancer agents. The anti-cancer activities of these compounds on the proliferation of lung cancer cell line (A-549), breast cancer cell line (MCF-7), and glioblastoma cancer cell lines (LN229 and U87) were determined by MTT assay. In addition, the pharmacokinetic properties of the derivatives were analyzed to evaluate their potential as drug candidates, which showed that all compounds conformed to Lipinski's rule of five.

2. EXPERIMENTAL SECTION

2.1. Materials and Methods

All chemicals and reagents were obtained from Merck, Sigma-Aldrich, and TCI. Reactions were monitored by thin-layer chromatography (TLC). The purity of the compounds was checked on TLC. Column chromatography purifications were performed on Merck Silica gel 60. Melting points were taken in open capillary tubes using a SRS

OptiMelt apparatus. High-resolution mass Spectra (HRMS) were measured using the Thermo ORBITRAP Q-EXACTIVE instrument. The ^1H and ^{13}C (APT) nuclear magnetic resonance (NMR) spectra were measured in CDCl_3 on Agilent 500 MHz NMR spectrophotometer. MCF7 (ATCC, HTB-22), A549 (ATCC, CCL-185), LN229 (ATCC, CRL-2611), and U87 (ATCC, HTB-14) cells were available in our laboratory. *In vitro* experiments were conducted using fetal bovine serum (FBS), high and low glucose Dulbecco's Modified Eagle Medium (DMEM), Penicillin-Streptomycin, L-Glutamine, and Trypsin/EDTA 0.25%. Antiproliferative activities were performed using the 3-(4,5-Dimethylthiazol-2-yl)-2,5-Diphenyltetrazolium Bromide (MTT) Sigma-Aldrich.

2.2. Chemistry

2.2.1. General procedure for the synthesis of xanthine analogues (5-7): 5,6-diamino-1,3-diethyl-2,4(1*H*,3*H*)-pyrimidinedione hydrochloride (1 mmol) was dissolved in a minimum amount of dioxane/ H_2O (1:1). EDC.HCl (1.3 mmol) and the corresponding carboxylic acid (1 mmol) were added. The reaction was stirred for 2 h at room temperature. The reaction was neutralized with the addition of 1 N NaOH. The reaction was then heated at reflux for 2 h at room temperature. The precipitate formed after cooling was filtered and washed with water (30). The obtained crude material was purified by SiO_2 column using Ethyl Acetate/*n*-Hexane as eluent.

2.2.2. 1,3-diethyl-8-(thiazol-4-yl)-3,7-dihydro-1*H*-purine-2,6-dione (5):

1,3-thiazole-4-carboxylic acid **2** (0.129 g, 1 mmol) was treated with 5,6-diamino-1,3-diethyl-2,4(1*H*,3*H*)-pyrimidinedione hydrochloride **1** (0.235 g, 1 mmol) and processed as described in the general procedure section. White solid; yield 62%; m.p. 258-260 °C; R_f : 0.3 (4:1 EtOAc:*n*-hexane); ^1H NMR (500 MHz, CDCl_3) δ 12.03 (s,

1H), 8.92 (d, $J = 2.1$ Hz, 1H), 8.22 (d, $J = 2.0$ Hz, 1H), 4.26 (q, $J = 7.1$ Hz, 2H), 4.19 (q, $J = 7.0$ Hz, 2H), 1.40 (t, $J = 7.1$ Hz, 3H), 1.32 (t, $J = 7.1$ Hz, 3H). ^{13}C NMR (126 MHz, CDCl_3) δ 155.29, 154.37, 150.92, 149.11, 146.12, 146.01, 119.48, 107.72, 39.05, 37.06, 13.61. HRMS-ESI (m/z) calc. for $\text{C}_{12}\text{H}_{13}\text{N}_5\text{O}_2\text{S}$ $[\text{M}+\text{H}]^+$: 292.08682, found: 292.08588.

2.2.3. 1,3-diethyl-8-(3-methylisoxazol-5-yl)-3,7-dihydro-1H-purine-2,6-dione (**6**):

3-methylisoxazole-5-carboxylic acid **3** (0.127 g, 1 mmol) was treated with 5,6-diamino-1,3-diethyl-2,4(1H,3H)-pyrimidinedione hydrochloride **1** (0.235 g, 1 mmol) and processed as described in the general procedure section. White solid; yield 56%; m.p. 274 °C (decomposed); R_f : 0.48 (4:1 EtOAc:*n*-hexane); ^1H NMR (500 MHz, CDCl_3) δ 6.95 (s, 1H), 4.27 (q, $J = 7.1$ Hz, 4H), 2.42 (s, 3H), 1.38 (dt, $J = 16.6, 7.1$ Hz, 6H). ^{13}C NMR (126 MHz, CDCl_3) δ 160.39, 159.54, 155.68, 150.25, 148.96, 139.95, 108.49, 105.12, 39.07, 37.29, 13.27, 13.18, 11.32. HRMS-ESI (m/z) calc. for $\text{C}_{13}\text{H}_{15}\text{N}_5\text{O}_3$ $[\text{M}+\text{H}]^+$: 290.12531, found: 290.12433.

2.2.4. 1,3-diethyl-8-(oxazol-5-yl)-3,7-dihydro-1H-purine-2,6-dione (**7**):

Oxazole-5-carboxylic acid **4** (0.113 g, 1 mmol) was treated with 5,6-diamino-1,3-diethyl-2,4(1H,3H)-pyrimidinedione hydrochloride **1** (0.235 g, 1 mmol) and processed as described in the general procedure section. White solid; yield 26%; m.p. 262 °C; R_f : 0.3 (4:1 EtOAc:*n*-hexane); ^1H NMR (500 MHz, CDCl_3) δ 13.42 (s, 1H), 8.05 (s, 1H), 8.00 (s, 1H), 4.26 (dq, $J = 21.5, 7.1$ Hz, 4H), 1.41 (t, $J = 7.1$ Hz, 3H), 1.37 (t, $J = 7.1$ Hz, 3H). ^{13}C NMR (126 MHz, CDCl_3) δ 155.97, 151.91, 150.45, 149.54, 142.62, 141.10, 127.83, 108.10, 39.37, 37.49, 13.57, 13.39. HRMS-ESI (m/z) calc. for $\text{C}_{12}\text{H}_{13}\text{N}_5\text{O}_3$ $[\text{M}-\text{H}]^-$: 274.09402, found: 274.09467; $[\text{M}+\text{Na}]^+$: 298.09161, found: 298.09076.

2.3. Biological evaluation

2.3.1. Cell Culture

A549, MCF7, LN229, and U87 were used for cell viability analysis. Cell lines were cultured with high glucose Dulbecco's Modified Eagle (DMEM) containing 10% FBS, 1% Penicillin- Streptomycin, and 1% L-Glutamine. Cells were grown on a 10 cm petri dish at 37 °C in a 5% CO_2 incubator. It was removed from the flask with 0.25% trypsin/EDTA to perform cell viability experiments. A549, MCF7, LN229, and U87 were seeded in 96-well black plates at a cell density of 9×10^3 , 6.5×10^3 , 7×10^3 and 7.5×10^3 cells per well, respectively.

2.3.2. Assay for antiproliferative effect

To explore the anti-proliferative potential of compounds, an MTT assay was performed using different cell lines. Cells were seeded in 96-well black plates and cultured for 24 hours at 37 °C in 5% CO_2 incubator. The growth medium was withdrawn, and the cells were treated with varied concentrations of novel compounds (6.25, 12.5,

25, 50, 100, and 200 μM). After 48 hours of treatment, MTT solution (5 μl , 5 mg/mL in PBS) was added to each well and incubated for 3 h. MTT solution was aspirated, and 200 μl DMSO was added to dissolve the formazan crystals. UV-Vis spectrophotometer was used to measure the optical density at 570 nm. The relative cell viability was expressed as a percentage relative to Tween 20 treated cells as 0% viable and untreated control cells as 100% viable (31). GraphPad Prism software was used to calculate the IC_{50} values.

2.3.3. Scratch Assay

A549 cells were seeded on a 35 mm plate at 6×10^5 per well for the scratch assay. The seeded cells were incubated. Then, the cells were scraped off with a p100 pipette tip. The culture medium was withdrawn, and the cells were treated with 10 μM compound **5** and equal concentrations of DMSO solvent for 48 hours. Markings were made close to the drawn area to obtain the same area during image acquisition. Images of the determined reference points were taken at 0, 24, and 48 hours under the microscope. Images were analyzed with ImageJ software.

2.3.4. ADME Properties

The ADME properties of the synthesized compounds were predicted using the SwissADME online property calculator (32). Molecular weight, number of rotatable bonds, topological polar surface area (TPSA), the logarithm of the partition coefficient (XLOGP3), and Lipinski's rule of five criteria were calculated.

2.3.5. Statistical Analysis

The experiments were carried out in three sets. All statistical comparisons were made using the Student's t-test. The differences were declared statistically significant at $*p < 0.0001$. The data was expressed as a standard error of the mean (SEM).

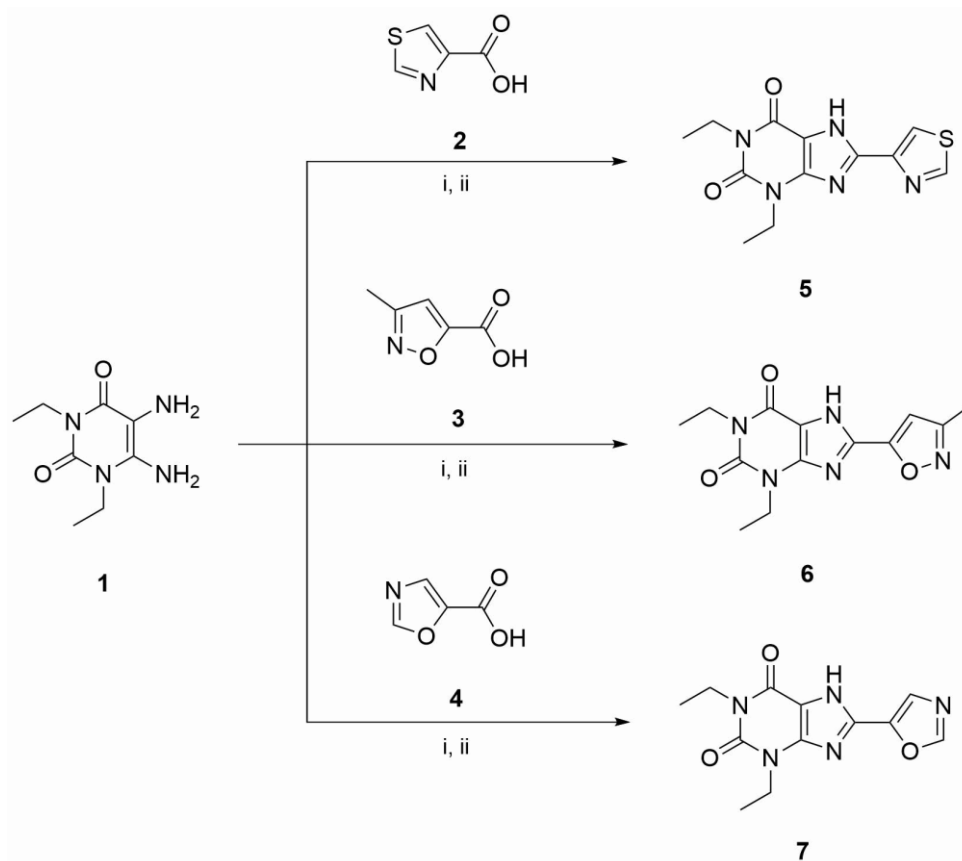
3. RESULTS AND DISCUSSION

3.1. Chemistry

The target xanthine derivatives, compounds **5-7** were synthesized as described in Scheme 1. 5,6-diamino-1,3-diethyl-2,4(1H,3H)-pyrimidinedione hydrochloride **1** was reacted with a carboxylic acid (1,3-thiazole-4-carboxylic acid **2**, 3-methylisoxazole-5-carboxylic acid **3** and oxazole-5-carboxylic acid **4**) in the presence of the dehydrating agent *N*-(3-Dimethylaminopropyl)-*N'*-ethylcarbodiimide hydrochloride (EDC.HCl) to yield the corresponding intermediary amides. Ring closure was achieved by heating the intermediate amides with aqueous NaOH (1 N), yielding the corresponding 1,3-dialkyl-7H-xanthine analogs (**5-7**). All compounds were characterized using ^1H NMR, ^{13}C (APT) NMR, and HRMS analysis as cited in the Supplementary material. The methyl peaks of the ethyl groups at the 1- and 3-positions of the xanthine nucleus are observed as triplets between 1.32 - 1.41 ppm in the ^1H NMR spectra, and between 13.18 - 13.81 ppm in the ^{13}C (APT) NMR

spectra. The methylene peaks are between 4.19 - 4.27 ppm in the ^1H NMR spectra, and between 39.37 - 37.06 ppm in the ^{13}C (APT) NMR spectra. The methyl group at the 3-position of the isoxazole ring in compound **6** was observed as a singlet at 2.42 ppm in the ^1H NMR and 11.32 ppm in the ^{13}C

(APT) NMR spectra. Aromatic protons showed between 6.25–8.92 ppm. In compounds **5** and **7**, a characteristic peak for the -NH group was also observed at ~ 12-13.5 ppm in ^1H -NMR.



Scheme 1: Synthetic pathway to xanthine derivatives **5-7**. Reagents and conditions: (i) EDC.HCl, dioxane:H₂O (1:1); (ii) NaOH (aq), reflux.

3.2. Biological evaluation

Compounds **5-7** were evaluated for their antiproliferative activity against four cancer cell lines, lung carcinoma (A549), breast cancer cell line (MCF-7), and glioblastoma (GB) cell lines (LN229 and U87) using MTT assay, and tamoxifen citrate was used as the reference compound. Graph Pad Prism software was used to calculate the median inhibition concentration (IC₅₀) for all

compounds. Results are illustrated in Table 1. Compounds **6** and **7**, containing isoxazole and oxazole moieties, respectively, displayed weak antiproliferative activity against all cancer cell lines. Compound **5**, which has a thiazole moiety at the 8-substitution in the xanthine nucleus, exhibited significant antiproliferative activity in all cell lines.

Table 1: IC₅₀ values (μM) for compounds against the selected cancer cell lines.

Compound	Antiproliferative activity IC ₅₀ (μM)			
	A549	MCF7	U87	LN229
5	16.70	78.06	22.07	25.07
6	123.0	148.3	>200	159.8
7	190.6	182.8	>200	171.2
Tamoxifen citrate	15.0	15.78	12.68	13.44

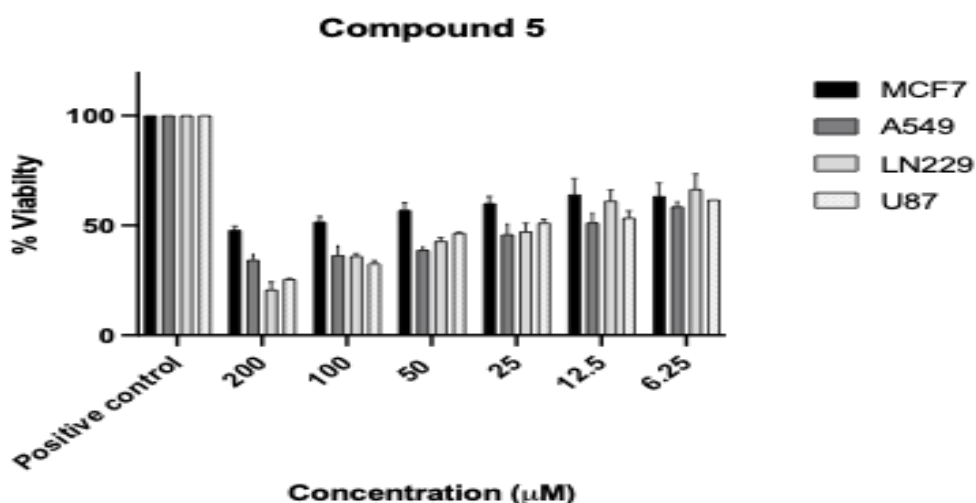


Figure 2: Cell viability results of compound 5 on cancer cells. The error bars show SEM.

Scratch assay was performed to evaluate the inhibition of cell migration in A549 cells treated with compound **5**. Images at various time points, along with the wound closure rate of cells treated with 10 μM compound **5** compared to the control, are presented in Figure 2. The wound closure rate

in A549 control cells and cells treated with compound **5** for 48 hours was 85 % and 28 %, respectively. The data demonstrate that cell migration was considerably inhibited in A549 cells treated with compound **5** for 48 hours.

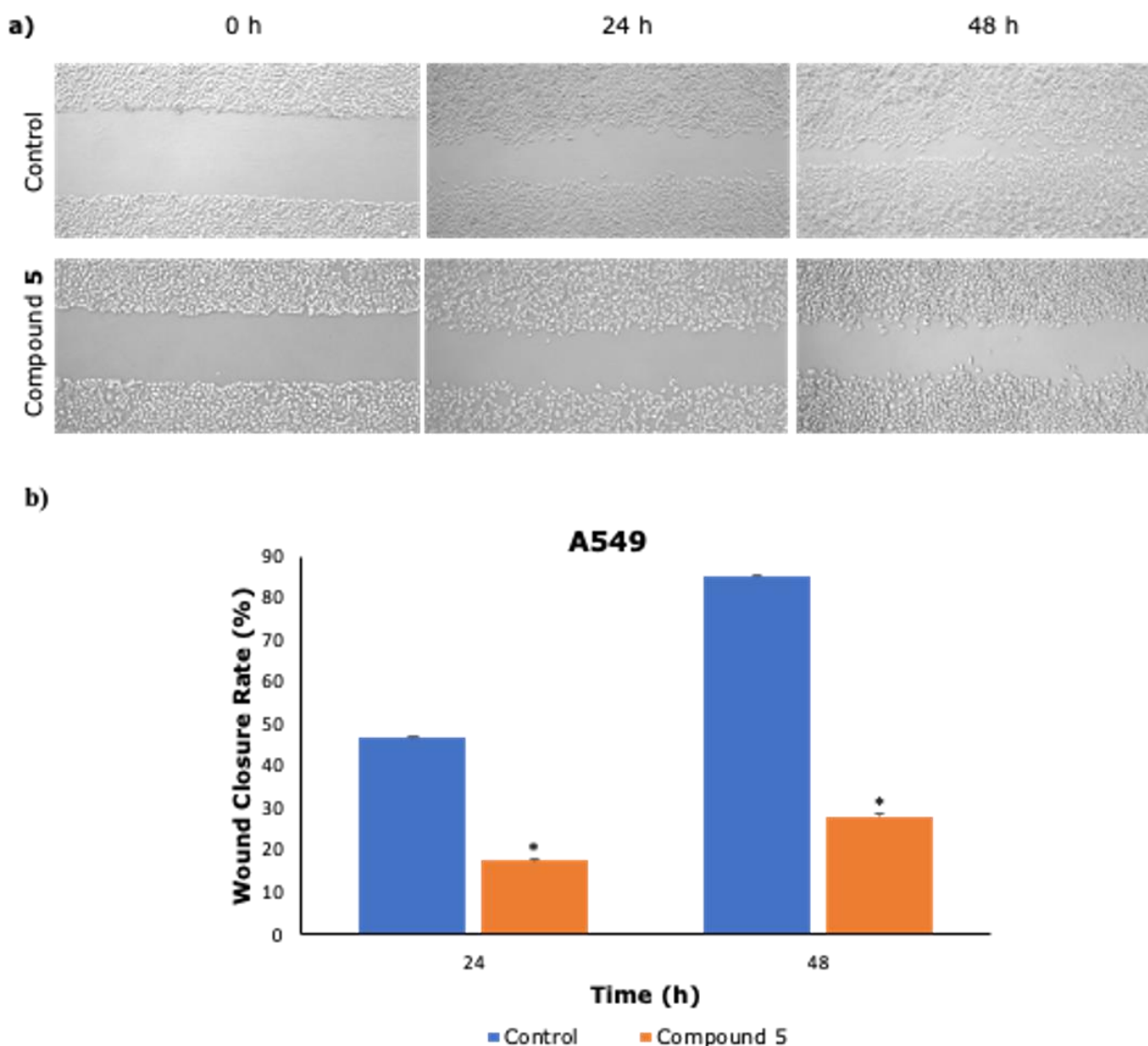


Figure 3: Results of Scratch Assay. Image of A549 cells treated with 10 μ M compound **5** for 24 h and 48 h (a). Quantification of the scratch area by using ImageJ analysis (b). Control cells were treated with equal concentrations of DMSO solvent. Differences were considered statistically significant at * $p < 0.0001$, and the error bars were calculated by SEM.

Evaluating pharmacokinetic properties such as solubility, permeability, and bioavailability is crucial for conducting clinical testing during the drug development process. Lipinski's "rule of five" defines physicochemical parameters that are important for the understanding of molecular properties in the design of new drug candidates (33). The bioavailability and potency of the novel compounds were calculated using the SwissADME calculator, and the results are shown in Table 2. All of the novel compounds adhered to the Lipinski

rules, including the number of hydrogen bond donors ($n\text{-OH/NH} < 5$), number of hydrogen bond acceptors ($n\text{-ON} < 10$), molecular weight of the compounds ($M_w < 500$ Dalton), octanol-water partition coefficient ($\log P < 5$), and the topological polar surface area (TPSA) of the compounds. These data showed that each of the molecules has good cell permeability and drug-like properties. In addition, most of the synthesized compounds were classified as soluble.

Table 2: *In silico* prediction of some pharmacokinetic properties for compounds 5-7.

Compound	Mw g/mol	#rotatable bonds	n-OH/NH	n-ON	Log P	Tpsa Å ²	Lipinski's Violation
5	291.33	3	1	4	2.00	13.81	0
6	289.29	3	1	5	1	98.71	0
7	275.26	3	1	5	1.38	98.71	0

MW: Molecular weight. #Rotatable bonds: number of rotatable bonds, determines flexibility, must be less than 9. N-OH/NH: The number of H-bond donors must be less than 5. n-ON: the number of H-bond acceptors must be less than 10. LogP: The partition coefficient between n-octanol and water calculated by XLOGP3 method, determines lipophilicity, must be between -0.7 and +5.0. TPSA: Topological Polar Surface Area, determines polarity, must be between 20 and 130 Å².

4. CONCLUSION

In the current work, synthesized new xanthine derivatives and characterized utilizing diverse spectroscopic methods like HRMS, ¹H NMR, and ¹³C (APT) NMR. The cytotoxic activity of the target compounds against several cancer cell lines (A549, MCF7, LN229, and U87) was investigated using the MTT test. Compound **5**, containing thiazole, exhibited more antiproliferative activity compared to the tested aryl groups (oxazole, isoxazole, and thiazole). The predicted ADME properties of the new compounds followed Lipinski's rule, indicating that they have sufficient bioavailability and drug-likeness for further biological investigations.

5. CONFLICT OF INTEREST

The author declares no competing interests.

6. REFERENCES

- Siegel RL, Miller KD, Wagle NS, Jemal A. Cancer statistics. CA: A Cancer Journal for Clinicians. 2023 Jan;73(1):17–48. Available from: [<URL>](#)
- Ioele G, Chieffallo M, Occhiuzzi MA, De Luca M, Garofalo A, Ragno G, et al. Anticancer Drugs: Recent Strategies to Improve Stability Profile, Pharmacokinetic and Pharmacodynamic Properties. Molecules. 2022 Aug;27(17):5436. Available from: [<URL>](#)
- Pal R, Teli G, Matada GSP, Dhiwar PS. Designing strategies, structural activity relationship and biological activity of recently developed nitrogen containing heterocyclic compounds as epidermal growth factor receptor tyrosinase inhibitors. Journal of Molecular Structure. 2023 Nov;1291:136021. Available from: [<URL>](#)
- Taruneshwar Jha K, Shome A, Chahat, Chawla PA. Recent advances in nitrogen-containing heterocyclic compounds as receptor tyrosine kinase inhibitors for the treatment of cancer: Biological activity and structural activity relationship. Bioorganic Chemistry. 2023 Sep;138:106680. Available from: [<URL>](#)
- Sharma PC, Bansal KK, Sharma A, Sharma D, Deep A. Thiazole-containing compounds as therapeutic targets for cancer therapy. European Journal of Medicinal Chemistry. 2020 Feb;188:112016. Available from: [<URL>](#)
- Roy A, Kumar Bahe A, Chanderiya A, Dangi H, Mishra P, Mishra AK, et al. Synthesis of Nitrogen-and Oxygen-Containing Heterocyclic Compounds Using Nanocatalyst: A Review. Journal of the Turkish Chemical Society Section A: Chemistry. 2021 Aug;8(3):851-862. Available from: [<URL>](#)
- Persson C. Development of safer xanthine drugs for treatment of obstructive airways disease. Journal of Allergy and Clinical Immunology. 1986 Oct;78(4):817–24. Available from: [<URL>](#)
- Persson CGA, Kjellin G. Enprofylline, a Principally New Antiasthmatic Xanthine. Acta Pharmacol Toxicol (Copenh). 1981 Oct;49:313-316. Available from: [<URL>](#)
- Müller CE, Jacobson KA. Xanthines as Adenosine Receptor Antagonists. Handbook of Experimental Pharmacology. 2011 200:151-99. Available from: [<URL>](#)
- Hayallah AM, Elgaher WA, Salem OI, Abdel Alim AAM. Design and synthesis of some new theophylline derivatives with bronchodilator and antibacterial activities. Archives of Pharmacal Research. 2011 Jan;34(1):3–21. Available from: [<URL>](#)
- Singh N, Kumar Shreshtha A, Thakur MS, Patra S. Xanthine scaffold: scope and potential in drug development. Heliyon. 2018 Sep;4:829. Available from: [<URL>](#)
- Bhat VB, Madyastha KM. Antioxidant and radical scavenging properties of 8-oxo derivatives of xanthine drugs pentoxifylline and lisofylline. Biochemical and Biophysical Research Communications. 2001 Nov;288(5):1212–7. Available from: [<URL>](#)
- Sierakowska A, Jasiewicz B, Piosik Ł, Mrówczyńska L. New C8-substituted caffeine derivatives as promising antioxidants and cytoprotective agents in human erythrocytes. Scientific Reports. 2023 Dec 1;13(1): 1785. Available from: [<URL>](#)
- Hisham M, Youssif BGM, Osman EEA, Hayallah AM, Abdel-Aziz M. Synthesis and biological evaluation of novel xanthine derivatives as potential apoptotic antitumor agents. European Journal of Medicinal Chemistry. 2019 Aug;176:117–28. Available from: [<URL>](#)
- Kalla R V., Zablocki J. Progress in the discovery of selective, high affinity A2B adenosine receptor antagonists as clinical candidates. Purinergic Signalling. 2009 Mar;5:21–9. Available from: [<URL>](#)
- Sun CX, Zhong H, Mohsenin A, Morschl E, Chunn JL, Molina JG, et al. Role of A2B adenosine receptor

- signaling in adenosine-dependent pulmonary inflammation and injury. *Journal of Clinical Investigation*. 2006 Aug;116(8):2173–82. Available from: [<URL>](#)
17. Hayallah AM, Elgaher WA, Salem OI, Abdel Alim AAM. Design and synthesis of some new theophylline derivatives with bronchodilator and antibacterial activities. *Archives of Pharmacal Research*. 2011 Jan;34(1):3–21. Available from: [<URL>](#)
18. Yasui K, Komiyama A. New clinical applications of xanthine derivatives: Modulatory actions on leukocyte survival and function. *International Journal of Hematology*. 2001 Jan;73(1):87–92. Available from: [<URL>](#)
19. Onan D, Güven Um, Demirtürk E, Çevikelli T. Preparation, characterization and in-vitro evaluation of theophylline loaded microemulsion formulations. *Journal of Pharmaceutical Technolgy*. 2020 Apr;1(1):7–12. Available from: [<URL>](#)
20. Mentz F, Mossalayi M, Ouaz F, Baudet S, Issaly F, Ktorza S, et al. Theophylline synergizes with chlorambucil in inducing apoptosis of B- chronic lymphocytic leukemia cells. *Blood*. 1996 Sep;88(6):2172–82. Available from: [<URL>](#)
21. Xu H, Wang L, Shi B, Hu L, Gan C, Wang Y, et al. Caffeine inhibits the anticancer activity of paclitaxel via down-regulation of α -tubulin acetylation. *Biomedicine and Pharmacotherapy*. 2020 Sep;129:110441. Available from: [<URL>](#)
22. Tilaoui M, Ait Mouse H, Zyad A. Update and New Insights on Future Cancer Drug Candidates From Plant-Based Alkaloids. *Frontiers in Pharmacology*. 2021 Dec;12. Available from: [<URL>](#)
23. Sinn B, Tallen G, Schroeder G, Grassl B, Schulze J, Budach V, et al. Caffeine confers radiosensitization of PTEN-deficient malignant glioma cells by enhancing ionizing radiation-induced G1 arrest and negatively regulating akt phosphorylation. *Molecular Cancer Therapeutics*. 2010 Feb;9(2):480–8. Available from: [<URL>](#)
24. Tokusoglu O. Food and Beverage Methylxanthines, Glycoalkaloids, Pyrolizidines and Phenolic Alkaloids: Processing Effects. *Journal of Food Health and Technology Innovations*. 2019 Sep;2(5):130–133.
25. Hisham M, Youssif BGM, Osman EEA, Hayallah AM, Abdel-Aziz M. Synthesis and biological evaluation of novel xanthine derivatives as potential apoptotic antitumor agents. *European Journal of Medicinal Chemistry*. 2019 Aug;176:117–28. Available from: [<URL>](#)
26. Yadav K, Yadav D, Bhandari DD, Yadav R. Identification of 1,3-(Dimethyl / Propyl)-8-Substituted (Cinnamic acid/Furan) Xanthine Derivatives with Anti-bronchospasmodic Activity Using in silico and in vivo Techniques. *ChemistrySelect*. 2022 May;7(17). Available from: [<URL>](#)
27. Kadi AA, El-Tahir KEH, Jahng Y, Rahman AFMM. Synthesis, biological evaluation and Structure Activity Relationships (SARs) study of 8-(substituted)aryloxycaffeine. *Arabian Journal of Chemistry*. 2019 Dec;12(8):2356–64. Available from: [<URL>](#)
28. Van Der Walt MM, Terre'Blanche G. 1,3,7-Triethyl-substituted xanthines - Possess nanomolar affinity for the adenosine A1 receptor. *Bioorganic & Medicinal Chemistry*. 2015 Oct;23(20):6641–9. Available from: [<URL>](#)
29. Baraldi PG, Fruttarolo F, Tabrizi MA, Romagnoli R, Preti D. Novel 8-heterocyclyl xanthine derivatives in drug development - an update. *Expert Opinion on Drug Discovery*. 2007 Sep;2(9):1161–83. Available from: [<URL>](#)
30. Van Der Walt MM, Terre'Blanche G, Petzer A, Lourens ACU, Petzer JP. The adenosine A2A antagonistic properties of selected C8-substituted xanthines. *Bioorganic Chemistry*. 2013 July;49:49–58. Available from: [<URL>](#)
31. Demiral A, Verimli N, Goralı Sİ, Yılmaz H, Çulha M, Erdem SS. A Rational design of multi-functional nanoplatfrom: Fluorescent-based "off-on" theranostic gold nanoparticles modified with D- α -Tocopherol succinate. *Journal of Photochemistry and Photobiology B: Biology*. 2021 Sep;222:112261.
32. Daina A, Michielin O, Zoete V. SwissADME: A free web tool to evaluate pharmacokinetics, drug-likeness and medicinal chemistry friendliness of small molecules. *Scientific Reports*. 2017 Mar;7:42717. Available from: [<URL>](#)
33. Walters WP. Going further than Lipinski's rule in drug design. *Expert Opinion on Drug Discovery*. 2012 Jan;7:99–107. Available from: [<URL>](#)



Effect of 3-Amino-1,2,4-Triazole-5-Carboxylic Acid on Human Blood Erythrocyte Catalase

Kübra Çıkrıkçı¹ , Nahit Gençer^{1*} 

¹Balikesir University, Department of Chemistry, Faculty of Art and Sciences, 10145, Balikesir, Turkey

Abstract: Catalase is an antioxidant enzyme with great therapeutic potential that scavenges hydrogen peroxide, a reactive oxygen species produced during cellular metabolism. Substances containing 1,2,4-triazole structures are biologically important heterocyclic compounds found in the structure of many pharmaceutical drugs used in drug discovery studies against various types of diseases in the human body. In this study, the effect of phosphate buffer prepared at different pHs and 3-amino-1,2,4-triazole-5-carboxylic acid (ATZc) on catalase enzyme activity in human blood erythrocytes was determined. It was determined that the catalase enzyme was inhibited by ATZc at different pH levels. The weakest inhibition was observed at pH 5.5 (IC₅₀:49.01 µM), whereas the strongest inhibition was observed at pH 7.5 (IC₅₀:23.21 µM).

Keywords: 3-amino-1,2,4-triazole-5-carboxylic acid, Catalase, enzyme inhibition

Submitted: October 26, 2023. **Accepted:** January 9, 2024.

Cite this: Çıkrıkçı K, Gençer N. Effect of 3-Amino-1,2,4-Triazole-5-Carboxylic Acid on Human Blood Erythrocyte Catalase. JOTCSA. 2024;11(2):541-6.

DOI: <https://doi.org/10.18596/jotcsa.1381362>

***Corresponding author.** E-mail: ngencer@balikesir.edu.tr

1. INTRODUCTION

Heterocyclic compounds are commonly found in nature and are the composition of various biologically active molecules, effective modern drugs, and plant protection products (1). Nitrogen-containing heterocycles have been found to have a significant impact on the discovery of new structures for pharmaceutical applications. These compounds are commonly seen in metabolic systems that are vital for living organisms. 1,2,4-triazoles, which have particularly unique structures and properties among various nitrogen-containing heterocycles, are used in various fields such as pharmaceutical chemistry, agricultural chemistry, materials science, and organic catalysts (2). Triazoles are five-membered rings containing three heteroatoms, a nitrogen atom, and two carbon atoms that can interact with various proteins, enzymes, and receptors in organisms through weak interaction bonding. Therefore, they can be viewed as bioisosteres of amides, esters, and carboxylic acids. Triazoles have various biological activities such as anticancer, antibacterial, antifungal, anti-inflammatory, antiviral, antioxidative, and anti-HIV. These triazole

compounds show their biological activities through the inhibition of some other enzymes such as dihydrofolate reductase, DNA polymerase, DNA gyrase, and catalase (3).

Catalase is one of the most fundamental oxidoreductases in the human body and is a vital antioxidant enzyme involved in the catalytic removal of reactive oxygen species (ROS), prevention of cell damage, and inhibition of tumor cell growth (4). This enzyme catalyzes the breakdown of H₂O₂, which is highly toxic, into water and oxygen, thus protecting cells against toxic oxidants. Inactivation of the catalase enzyme has some side effects and can lead to various diseases such as cancer, hypertension, Parkinson's disease, and Alzheimer's disease. Human blood erythrocyte catalase is a large (240 kDa) enzyme with a tetrameric structure containing iron and four heme groups. This large structure facilitates its interaction with the substrate H₂O₂ (5). There are known inhibitors of catalase activity, such as azide, cyanide, and cyanogen bromide, but these inhibitors are not specific to the enzyme and can

inhibit different enzymes. 3-amino-1,2,4-triazole (ATZ) causes irreversible inhibition of the enzyme by covalent binding to the active center of the tetrameric form of catalase in the presence of H_2O_2 , and this inhibitor is specific for catalase (6). Catalase is primarily localized in the liver. Given that the liver is the organ responsible for metabolizing and detoxifying drugs, this enzyme plays a crucial role in determining the potential side effects of medications (7). Erythrocytes are also a good model for investigating the toxicological effects of xenobiotics (drugs, pesticides, etc.) entering the human body (8). Because inhibition studies are important to investigate drug-enzymes interactions, understand the mechanisms involved in the body, and determine the effective concentration and toxicity of drugs, we aimed to determine the effect of ATZc on catalase activity in human erythrocytes. In addition, the investigation of interactions at different pH levels can aid in understanding the effects of this compound in various cellular environments. Such studies can be valuable in biomedical research for the discovery and development of potential therapeutic agents.

2. MATERIALS AND METHODS

2.1. Materials

Hydrogen peroxide (H_2O_2), dipotassium phosphate (K_2HPO_4), dihydrogen phosphate (KH_2PO_4), 3-amino-1,2,4-triazole-5-carboxylic acid were obtained from Sigma-Aldrich. The study was approved by the local ethics committee (Balikesir University Faculty of Medicine Clinical Research Ethics Committee, Balikesir/Turkey, Decision No:2022/44 and Date:09.03.2022).

2.2. Preparation of Hemolysate

A 20-mL blood sample was collected from healthy volunteers, and the supernatant was separated by centrifugation at 5000 rpm for 20 min at +4 °C. Then, it was washed three times with 0.9% NaCl. The blood sample was then hemolyzed with three times the volume of cold water. The hemolysate was centrifuged again at 15000 rpm for 40 min at +4 °C.

2.3. Catalase Activity Determination

Enzyme activity was determined by the spectrophotometric method by measuring the absorbance decrease at 240 nm during the conversion of H_2O_2 to water and oxygen in the experimental environment (9). For activity determination, 30 mM H_2O_2 substrate solution was used and 50 mM phosphate activity buffer was prepared at different pH ranges (5-5.5-6-6.5-7-7.5-8-8.5).

2.4. Determination of the Inhibition Effect of 3-amino-1,2,4-triazole-5-carboxylic acid on Catalase

The inhibition study of ATZc (inhibitor) was performed at different pHs and constant substrate concentrations. A total reaction volume of 3 mL was created by taking 0.1 mL of hemolysate and different volumes of inhibitor (0.01 M) solution. First, enzyme activity was found in the inhibitor-free environment and this value was accepted as 100% activity. The change in absorbance at 240 nm in one minute was recorded. From the absorbance values obtained, % activity-inhibitor graphs were drawn, and IC_{50} values were calculated from their slopes.

3. RESULTS AND DISCUSSION

Triazoles are attracting increasing attention because of their broad biological activities. In particular, ATZ derivatives have received special attention because they demonstrate a broad range of bioactivity, including potential applications against thrombotic disorders, fibrotic, autoimmune diseases, central nervous system disorders, obesity, and diabetes (10). Today, there are triazole ring-containing drugs with different properties and in use for various therapeutic purposes. These drugs are used as antifungals, such as fluconazole, itraconazole, and voriconazole; as antidepressants, including triazolam, alprazolam, and estazolam; and as antivirals, such as ribavirin. The drugs letrozole, anastrozole, and vorozole, which are also aromatase enzyme inhibitors used in breast cancer treatment, contain a 1,2,4-triazole ring (11). At the same time, many compounds derived from triazole are effective in inhibiting various enzymes such as phosphatase, lactamase, butyrylcholinesterase, acetylcholinesterase, alpha-amylase, and alpha-glucosidase (12).

Catalase, an antioxidant enzyme, plays an important role in the defense system to eliminate the destructive effects of ROS. Therefore, any factor that can weaken the activity of this enzyme can cause ROS accumulation and oxidative damage to proteins, causing many diseases. ATZ is a specific inhibitor that covalently binds to the active site of catalase (13). Therefore, the catalase enzyme is the most suitable enzyme for studying the inhibition properties of triazole derivatives.

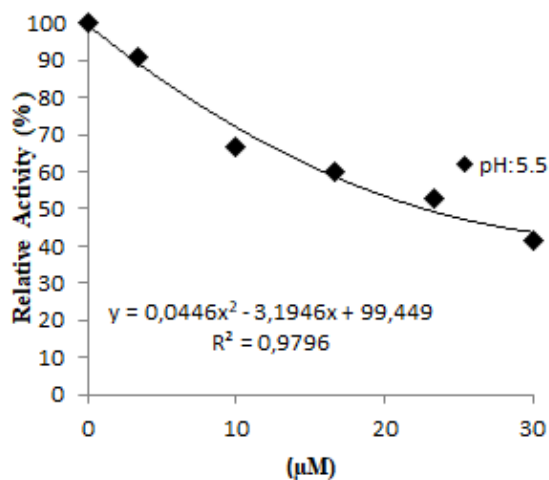
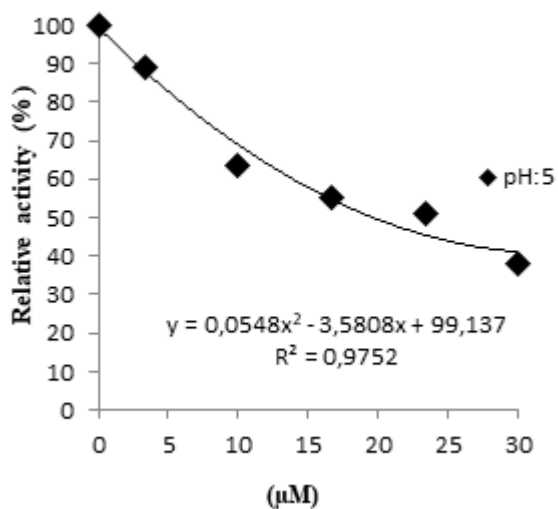
In this study, the inhibition effect of ATZc on catalase was investigated at different pH values. For this purpose, %activity-inhibitor graphs were plotted (Figure 1). IC_{50} values were calculated from the slopes of these graphs; the strongest inhibition was observed at pH:7.5 (IC_{50} : 23.21 μ M) and the weakest inhibition was observed at pH:5.5 (IC_{50} : 49.01 μ M). It was found to have stronger inhibition at high pHs, whereas it had weaker inhibition at low pHs (Table 1). The pH of the medium has a significant impact on enzyme performance (14). Catalase exhibits activity in a broad optimum pH:5-10 range (15).

Table 1: IC₅₀ values of 3-amino-1,2,4-triazole-5-carboxylic acid determined at different pH ranges.

pH (Buffer Solution)	IC ₅₀ (μ M)
5	45.74
5.5	49.01
6	26.16
6.5	27.92
7	24.56
7.5	23.21
8	27.88
8.5	26.52

In the present experiment, the inhibition effect of ATZc in two forms (ATZ-carboxylic acid and ATZ-carboxylate) on catalase under different pH conditions was investigated. Carboxylic acid converts to carboxylate as pH increases, and carboxylate converts to carboxylic acid as pH decreases. Therefore, inhibition of ATZc was

observed between pH:5-8.5. This inhibitor showed weak inhibition at pH 5-5.5 but strong inhibition in the basic form at pH 7.0-8.5. Thus, it shows that the active part of this inhibitor interacts with the chemical group of the enzyme, which is approximately 7–7.5 pKa.



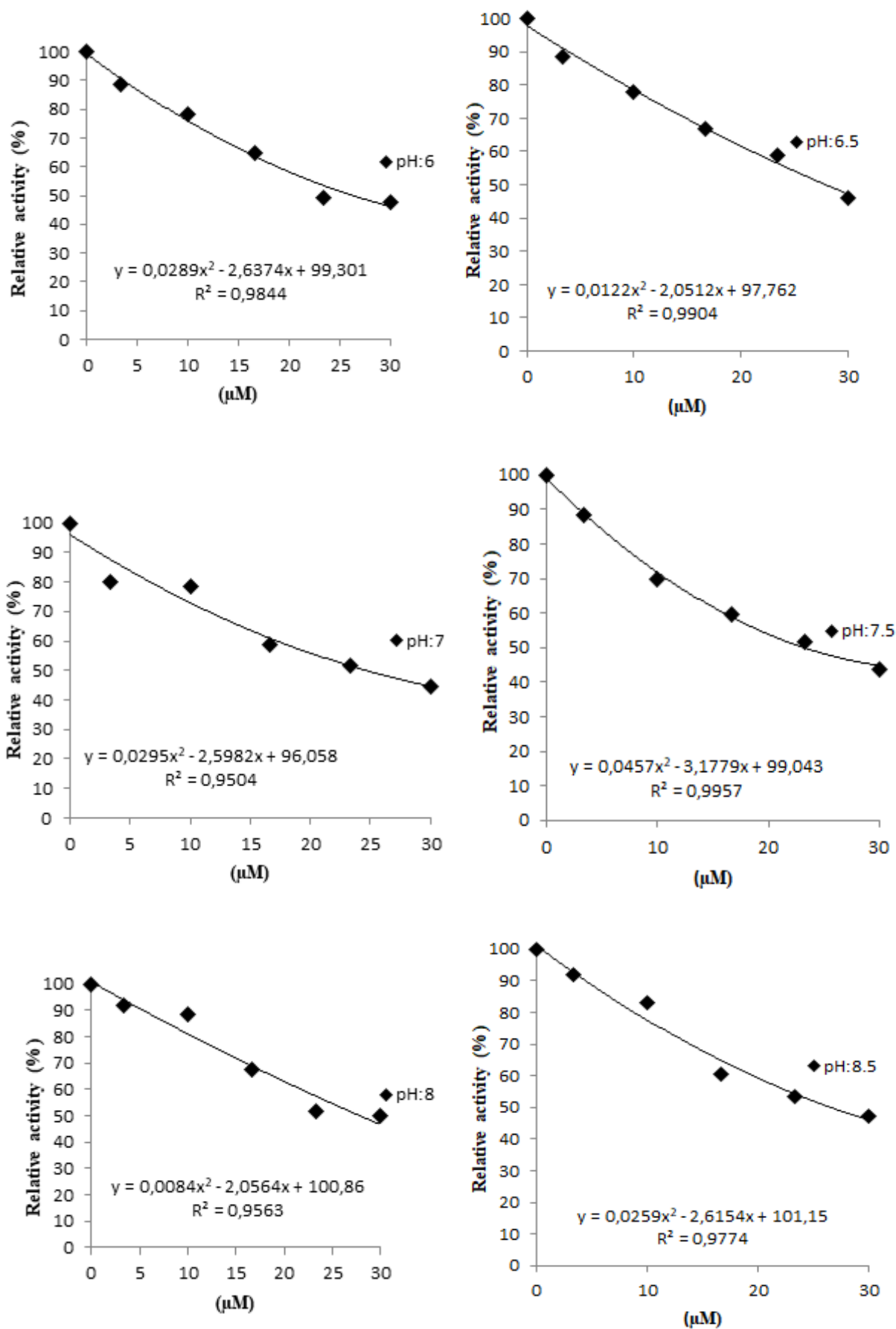


Figure 1: Inhibition graphs of 3-amino-1,2,4-triazole-5-carboxylic acid at different pHs.

In the literature, the inhibitory effect of ATZ on chicken liver catalase activity was reported as IC_{50} :3 mM at pH:7 (16), whereas in this study the strongest inhibition of human blood erythrocyte catalase activity was found at pH: 7.5 IC_{50} :23.21

μ M. These pH values, on the other hand, are close together, but the inhibitor we used in our study contains a carboxyl (-COOH) group, unlike the ATZ compound (Figure 2c).

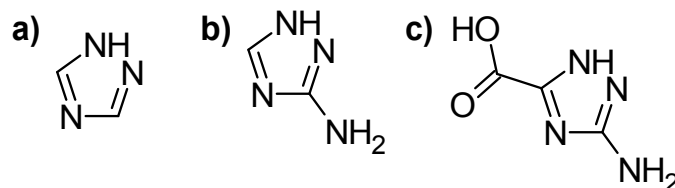


Figure 2: a) 1,2,4-triazole b) 3-amino-1,2,4-triazole (ATZ) c) 3-amino-1,2,4-triazole-5-carboxylic acid (ATZc).

In another study, it was found that ATZ infused peripherally in spontaneously hypertensive rats (SHR) disrupted sympathetic activity and also increased antisympathetic activity. Additionally, it has been found to have a vascular relaxation effect and reduce arterial pressure in SHRs (17). Tada et al. reported that the ATZ is a competitive inhibitor of imidazole glycerol phosphate dehydratase (18).

4. CONCLUSION

In conclusion, in this study, the pH-dependent effect of ATZc on human erythrocyte catalase enzyme activity was determined. There have been no inhibition studies on catalase and 3-amino-1,2,4-triazole-5-carboxylic acid in the literature. An important part of the active substances used for therapeutic purposes are drugs that act as enzyme inhibitors. Therefore, determining the effect of ATZc, which has a 1,2,4-triazole structure, on the catalase enzyme is crucial for drug development research, but it should be supported by *in vivo* studies for its use in treatment.

5. CONFLICT OF INTEREST

The authors declare that they have no known competing financial interests or personal relationships that could have appeared to influence the work reported in this paper.

6. ACKNOWLEDGMENTS

This study has been supported by Balıkesir University (BAUN) Research Projects with the project (No:2023/134).

7. REFERENCES

1. Yuriy K, Kusdemir G, Volodymyr P, Tüzün B, Taslimi P, Karatas OF, et al. A biochemistry-oriented drug design: synthesis, anticancer activity, enzymes inhibition, molecular docking studies of novel 1,2,4-triazole derivatives. *J Biomol Struct Dyn*. 2023 Sept;1-17. Available from: [<URL>](#)
2. Nasri S, Bayat M, Kochia K. Strategies for synthesis of 1,2,4-triazole-containing scaffolds using 3-amino-1,2,4-triazole. *Mol Divers*. 2022 Feb;26(1):717-39. Available from: [<URL>](#)

3. Tian G, Song Q, Liu Z, Guo J, Cao S, Long S. Recent advances in 1,2,3- and 1,2,4-triazole hybrids as antimicrobials and their SAR: A critical review. *Eur J Med Chem*. 2023 Nov;259:115603. Available from: [<URL>](#)
4. Xu D, Wu L, Yao H, Zhao L. Catalase-Like Nanozymes: Classification, Catalytic Mechanisms, and Their Applications. *Small*. 2022 Sept;18(37):2203400. Available from: [<URL>](#)
5. Shahraki S, Shiri F, Razmara Z. Improving enzymatic performance of antioxidant enzyme catalase in combination with [Mn (phen)₂ Cl.H₂O]Cl.tu complex. *Appl Organomet Chem*. 2023 Apr;37(4):e7061. Available from: [<URL>](#)
6. Margoliash E, Schejter A. Kinetics of the Irreversible Inhibition of Catalase by 3-Amino-1,2,4-triazole in the Presence of Hydrogen Peroxide and Catalase-Hydrogen Peroxide Complex I Hydrogen Donors. *J Biol Chem*.1962 Jly;237(7):2359-63. Available from: [<URL>](#)
7. Koohshekan B, Divsalar A, Saiedifar M, Saboury AA, Ghalandari B, Gholamian A, et al. Protective effects of aspirin on the function of bovine liver catalase: A spectroscopy and molecular docking study. *J Mol Liq*. 2016 Jun;218:8-15. Available from: [<URL>](#)
8. Quds R, Iqbal Z, Arif A, Mahmood R. Mancozeb-induced cytotoxicity in human erythrocytes: enhanced generation of reactive species, hemoglobin oxidation, diminished antioxidant power, membrane damage and morphological changes. *Pestic Biochem Physiol*. 2023 Jun;193:105453. Available from: [<URL>](#)
9. Aebi H, Suter H, Feinstein RN. Activity and stability of catalase in blood and tissues of normal and acatalasemic mice. *Biochem. Genet*. 1968 Aug;2:245-251. Available from: [<URL>](#)
10. Grytsai O, Valiashko O, Penco-Campillo M, Dufies M, Hagege A, Demange L, et al. Synthesis and biological evaluation of 3-amino-1,2,4-triazole derivatives as potential anticancer compounds. *Bioorganic Chem*. 2020 Nov;104:104271. [<URL>](#)
11. Küçükgül ŞG, Çıkla-Süzgün P. Recent advances bioactive 1,2,4-triazole-3-thiones. *Eur J Med Chem*. 2015 Jun;97:830-70. Available from: [<URL>](#)
12. Akhtar T, Zafar W, Sumrra S. A Review on the Assessment of Enzyme Inhibition Activity by 1, 2, 4-Triazole Derivatives (Review). *South J of Res*. 2022 Jly;2(2):189-203. Available from: [<URL>](#)

13. Galasso M, Gambino S, Romanelli MG, Donadelli M, Scupoli MT. Browsing the oldest antioxidant enzyme: catalase and its multiple regulation in cancer. *Free Radic Biol Med.* 2021 Aug;172:264-72. Available from: [<URL>](#)
14. Costa SA, Tzanov T, Filipa Carneiro A, Paar A, Gübitz GM, Cavaco-Paulo A. Studies of stabilization of native catalase using additives. *Enzyme Microb Technol.* 2002 Mar;30(3):387-91. Available from: [<URL>](#)
15. Goyal MM, Basak A. Human catalase: looking for complete identity. *Protein Cell.* 2010 Oct;1(10):888-97. Available from: [<URL>](#)
16. Aydemir T, Kuru K. Purification and partial characterization of catalase from chicken erythrocytes and the effect of various inhibitors on enzyme activity. *Turk J Chem.* 2003;27(1):85-97. Available from: [<URL>](#)
17. Pontes RB, Colombari DSA, De Paula PM, Colombari E, Andrade CAF, De Luca LA, et al. Sympathetic and angiotensinergic activity in spontaneously hypertensive rats treated with 3-amino-1,2,4-triazole. *Auton Neurosci.* 2023 Sept;248:103107. Available from: [<URL>](#)
18. Tada S, Hatano M, Nakayama Y, Volrath S, Cuyer D, Ward E, and Ohta D. Insect Cell Expression of Recombinant Imidazoleglycerolphosphate Dehydratase of Arabidopsis and heat and Inhibition by Triazole Herbicides. *Plant Physiol.* 1995;109:153-159. Available from: [<URL>](#)



The Influence of *Hibiscus tiliaceus* Leaf Extract as Capping Agent on the Zinc Oxide Properties and its Photo-simultaneous Performance

Riki Subagyo¹ , Elfirza Zain¹ , Siyam Martina^{2,3} , Saepurahman² ,
Yuly Kusumawati^{1,*} 

¹Department of Chemistry, Faculty of Science and Data Analytics, Institut Teknologi Sepuluh Nopember, Kampus ITS Keputih, 60111, Sukolilo, Surabaya, Indonesia

²Research Center for Chemistry, National Research and Innovation Agency (BRIN), Gd. 452 KST BJ Habibie, Serpong, Tangerang Selatan, Banten, 15314, Indonesia

³Department of Chemistry, Faculty of Mathematics and Natural Sciences, Universitas Negeri Semarang, Gd. D6 Kampus Sekaran Gunungpati, Semarang, 50229, Indonesia

Abstract: Polyol method, as one alternative in ZnO synthetic methods, have been developed and generated a nano-ZnO. However, the produced nano-ZnO is unstable due to its small particle size. To overcome the problems, we added *Hibiscus tiliaceus* leaves' extract during the ZnO (EZnO) synthesis to change the water content and hydrolysis ratio of Zn²⁺/water. The addition of *H. tiliaceus* extract resulted in a shifting peak at (101) plane compared to ZnO synthesized without extract addition (WZnO). The use of *H. tiliaceus* extracts leads to the formation of large and non-uniform particles compared to the one prepared without the extract, which is in agreement with the intensity of diffraction pattern. The use of *H. tiliaceus* extracts shifted the bandgap energy to visible range. The performance of WZnO and EZnO samples was tested for simultaneous photo-oxidation of methylene blue and photo-reduction of Cr(VI) ions under UV-C irradiation. The EZnO is equally active as WZnO for Cr(VI) ion photo-reduction but less active for photo-oxidation of methylene blue. The presence of retained organic material in EZnO is plausibly affected by the adsorption and subsequent photo-oxidation of the bulky MB leading to a lower photo-oxidation performance. However, the activity of EZnO was a little bit lower than that of WZnO, revealing that the synergistic of particle size and band gap energy is a crucial factor in photo-removal process. In addition, the presence of phenolic compounds on the EZnO surface might change the nature properties of WZnO, which influence its performance.

Keywords: Zinc oxide, polyol, *Hibiscus tiliaceus*, Cr(VI), methylene blue, clean water

Submitted: October 8, 2023. **Accepted:** January 4, 2024.

Cite this: Subagyo R, Zain E, Martina S, Saepurahman, Kusumawati Y. The Influence of *Hibiscus tiliaceus* Leaf Extract as Capping Agent on the Zinc Oxide Properties and its Photo-simultaneous Performance. JOTCSA. 2024;11(2):547-556.

DOI: <https://doi.org/10.18596/jotcsa.1372145>

***Corresponding author.** E-mail: y_kusumawati@chem.its.ac.id

1. INTRODUCTION

Zinc oxide has been extensively utilized for pollutant photocatalysis due to its good properties, such as bandgap in UV region (3.2 eV), chemically stable, un-toxic, and cheap (1,2). The technique of synthesis of ZnO (i.e., polyol methods) has been developed in order to generate their size in nanoscale. ZnO nano-sized particles exhibit a high specific surface area, allowing fast reactions due to the high number of reaction sites (3,4). Nonetheless, ZnO nanoparticles are unstable due

to their small particle size, which is attributed to their high surface energy. The high surface energy leads to particle agglomeration; regulating particle size, morphology, and microstructure becomes hard to observe. Particles' agglomeration was caused by sintering processes and Ostwald ripening (5). To overcome this issue, the stabilization of ZnO nano-sized particles has to be considered via particle immobilization on a supporting material or addition of capping agents (6–8).

Introducing capping agents (e.g., surfactants, polysaccharides, dendrimers, and polymers) during the ZnO synthesis has been observed and utilized due to the organic nature of the capping agent materials that serve on the ZnO nano-sized surface (9). Besides, the addition of capping agent also improves the compatibility of ZnO nano-sized with another phase or improves the functionalities (10). For instance, the influence of various capping agents has been studied in ZnO synthesis, including polyethylene glycol (PEG) and polyvinyl pyrrolidone (PVP) by coprecipitation method (11). The presence of PEG and PVP during the synthesis altered the crystallographic surface energy, promoting the anisotropic growth of nanosized ZnO. In order to minimize the utilization of chemicals as capping agents, plant extracts have been used due to their low cost and availability (12–14). *H. tiliaceus* is a tropical plant that has been used for various applications. The leaves' extracts of *H. tiliaceus* have been utilized for ZnO synthesis, as reported by Putri et al., showing good antioxidant activity (15). The compounds in the extract (including phenolic compounds) altered the formation of ZnO. The phenolic compound would act as a reduction agent and capping agent.

Here, we synthesized the ZnO using polyol methods. *H. tiliaceus* leaf extract was used to change the water contained in the polyol methods. The activity of the obtained ZnO (EZnO) was evaluated for simultaneous photo-oxidation of methylene blue and photo-reduction of chromium (Cr(VI)) ions under UV-C light irradiation. ZnO without *H. tiliaceus* extracts (WZnO) was also produced and utilized for simultaneous removal to compare their activities.

2. EXPERIMENTAL SECTION

2.1. Preparation of *Hibiscus tiliaceus* leaves extract

H. tiliaceus leaves were collected, washed using a water-ethanol solution, and dried in an oven set at 80 °C for three days until the leaves changed color from dark green to brown. The brown *H. tiliaceus* leaves were crushed using a blender and sieved to obtain a uniform size (100 mesh). The *H. tiliaceus* leaves' powder was mixed with aqua DM and stirred for 30 minutes at 70°C. The obtained filtrates were separated using centrifugation at 10000 rpm.

2.2. ZnO synthesis

The ZnO nanoparticles were synthesized using a polyol method utilizing a reflux system, as reported in ref. (1,16). $Zn(CH_3COO)_2 \cdot H_2O$, NaOH, Aqua DM, and DEG were mixed at a mol ratio of 1:2:1. The reflux system was operated for one hour at 161°C. The obtained solids were separated using centrifugation at 10,000 rpm, followed by washing with ethanol and acetone. The obtained solid was then left for 3 days at 60 °C. The dried solid was collected and labeled as WZnO. In order to investigate the influence of *H. tiliaceus* leaf extract, the aqua DM was replaced with *H. tiliaceus*

leaf extract. The obtained solid was labeled as EZnO.

2.3. Characterization

The WZnO and EZnO photocatalysts were characterized using several instruments to observe their characteristics. The structural properties of WZnO and EZnO photocatalysts were investigated using X-ray diffractometer (XRD, PANalytical, $2\theta = 5-90^\circ$), fourier transform infrared spectrophotometer (FTIR, Shimadzu, $\nu = 4000-400\text{ cm}^{-1}$), and field emission scanning electron microscope (FESEM, JEOL). Transmission electron microscope (TEM, Hitachi7700) was utilized to observe the nanostructure of WZnO. The optical properties of WZnO and EZnO were analyzed using ultraviolet-visible diffuse reflectance spectrophotometer (DR-UV-Vis, Agilent Cary 60, $\lambda=200-800\text{ nm}$).

2.4. Photocatalytic Activity Test

Photocatalytic activity of EZnO and WZnO was tested for simultaneous photo-oxidation of methylene blue and photo-reduction of Cr(VI) ions under UV-C irradiation. Briefly, 50 mg EznO or WZnO was dispersed in 12 mL Milli-Q water, followed by ultrasonication for 10 minutes. In a 300 mL crystallizing dish with a diameter of 9.5 cm, 18 mL of MB at 40 ppm and 20 mL of Cr(VI) ions at 40 ppm solutions were added, followed by the EZnO or WZnO dispersion. The final MB and Cr(VI) ions concentration was 14.4 and 16 ppm, respectively, and the [MB]/[Cr(VI)] ratio was 0.9. The crystallizing dish was put inside a $59.5 \times 49.5 \times 50\text{ cm}^3$ UV-C chamber containing a Philips TUV 15W/G15 T8 lamp emitting a UV-C ($\lambda = 254\text{ nm}$) light. The dish was separated at 14.5 cm from the lamp. The dish was irradiated for 60 min and after that $2 \times 1.5\text{ mL}$ of sample was taken, centrifuged at 7000 rpm for at least 10 min. 1 mL of clear solution was analyzed for its MB concentration by directly measuring its absorbance at 665 nm wavelength. Another 1 mL of clear solution was tested for its Cr(VI) ion concentration. The Cr(VI) ion concentration was determined colorimetrically by mixing 1 mL of the clear solution with 9 mL of MilliQ water, 200 μL of $H_2SO_4\ 6N$, and 1 mL of 1,5-diphenylcarbazide in acetone solution. The mixture was incubated for 10 min and the absorbance was measured at 540 nm wavelength using a Cary-60 UV-Vis spectrophotometer. To simulate MB and Cr(VI) ions removal due to adsorption, similar experiments for EZnO and WZnO were performed with the lamp turned off. An exact solution composition without photocatalysts was prepared and used as a reference. The percentage of removal is calculated as the difference between the absorbance of the solution after photo-oxidation or photo-reduction (A_t) and the absorbance of the reference (A_0) following Eq. 1.

$$\text{Removal efficiency (\%)} = 100 \times \frac{A_0 - A_t}{A_0} \quad \text{Eq. 1}$$

The kinetic study of simultaneous photocatalytic of MB and Cr(VI) was performed in similar method by the variation of time irradiation. The addition of

scavenger agent was also performed as well as the preliminary test.

3. RESULTS AND DISCUSSION

The structural properties of EZnO and WZnO samples were investigated using XRD analysis and FTIR analysis. The diffraction pattern of EZnO and WZnO samples is shown in Figure 1 (a). All samples exhibit characteristic peaks of hexagonal wurtzite ZnO at 31.67, 34.39, 36.15, 47.57, 56.61, 62.81, 66.34, 67.88, 69.14, 72.49, and 76.92° which corresponded to (100), (002), (101), (102), (110), (103), (200), (112), (201), (004), and (202) planes, respectively. This result was similar to our previous study reported by Hosni et al. (16) and Zakiyah et al. (1). The intensity peaks of EZnO are higher than that of WZnO, indicating that *H. tiliaceus* leaves' extract increases the crystallinity

of EZnO. The (101) plane has the highest intensity for all samples, implying that the ZnO samples grew strongly along the (101) direction, which reveals a high alignment degree along the c-axis and can be vital for tuning the aspect ratio. Figure 1 (b) showed an enlarged XRD peak of (101) plane showing a peak shift with the addition of *H. tiliaceus* leaves' extract, which was associated with the variant in residual strain developed in the crystal lattice. The strain induced shift along (101) direction might be a crucial factor in controlling the equatorial and axial growth of ZnO nanostructure. With the addition of *H. tiliaceus* leaves' extract, the (101) plane was slightly shifted to left compared to ZnO photocatalyst prepared without adding *H. tiliaceus* leaves' extract (WZnO). This suggests that c-axis growth is reduced by the addition of *H. tiliaceus* leaves' extract.

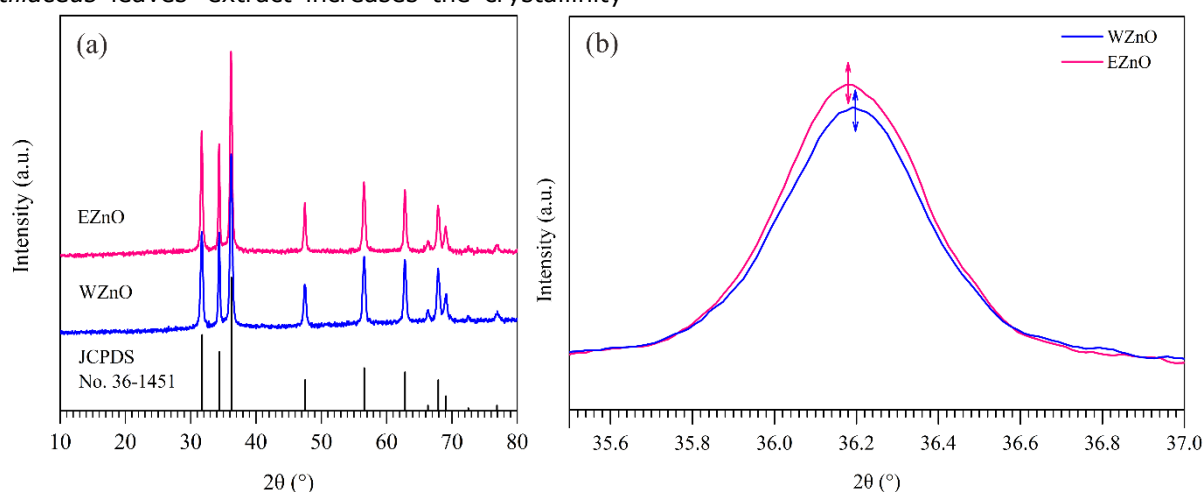


Figure 1: (a) diffraction pattern and (b) enlarged (101) peak of samples

FTIR analysis was carried out to analyze the presence of functional groups in WZnO and EZnO photocatalysts. Both WZnO and EZnO exhibit bands at 3430, 2922, 1564, 1407, and 500–400 cm^{-1} as shown in Figure 2. The band at 3430 cm^{-1} is attributed to the O–H (17), indicating the presence of physically adsorbed water. The band at 2922 cm^{-1} is attributed to the stretching vibration of –CH, confirming the presence of CH_2 and CH_3 groups (18). The absorption bands at 1564 and 1407 cm^{-1} are assigned to the symmetric and asymmetric stretching vibrations of C=O (19). The presence of bands at 2922, 1564, and 1407 cm^{-1} implies that both WZnO and EZnO contain organic material retained on their surface. The intensity of those bands is somewhat less pronounced in WZnO than in EZnO, suggesting that the EZnO retains

more organic material than the WZnO. The organic compound in WZnO and EZnO is retained since the formation of ZnO did not use the calcination process. The presence of organic compounds might be correlated to the presence of DEG and flavonoid compounds extracted from *H. tiliaceus* leaves. The stretching vibration of Zn–O is observed at 500–400 cm^{-1} . In addition to the mentioned bands above, unlike WZnO, EZnO also exhibits prominent bands at 1300–1100 cm^{-1} . These bands are likely due to the presence of other functional groups contributed by the *H. tiliaceus* leaf extract such as polyphenolic compounds adsorbed on the surface of EZnO via π -electron interaction of carbonyl group with the free orbital of Zn (20).

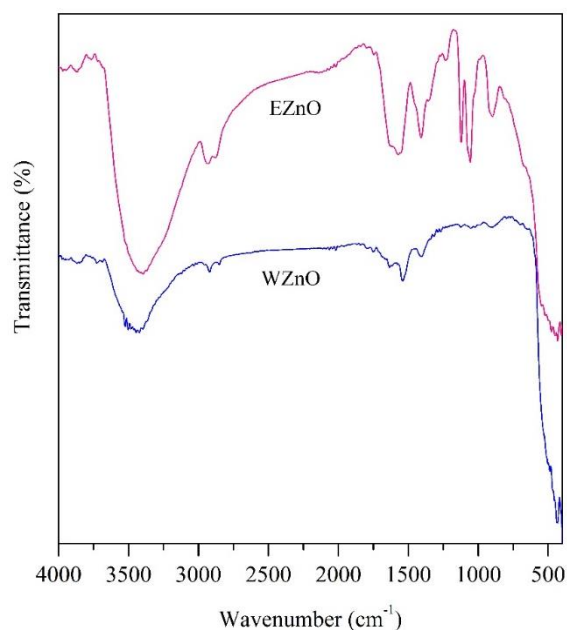


Figure 2: FTIR spectra of samples

The morphology of WZnO and EZnO photocatalysts is depicted in Figure 3. The WZnO photocatalysts formed a uniform nanosize rods-like morphology. The nanorods' morphology is a one-dimensional structure that enables a highly efficient charge carrier mobility due to decreased grain boundaries, disorder, discontinuous interface, and surface defects. In order to clarify the morphology of WZnO, TEM analysis has been carried out. As shown in Fig. 3b, it can be seen that the dominant morphology of WZnO is nanorods. However,

several morphologies are also observed in WZnO, including hexagonal and sphere. The particle has a nano-size of 20 – 200 nm. Unlike the WZnO photocatalyst, the EZnO photocatalyst exhibits nanosize non-uniform morphology. It can be seen that adding the *H. tiliaceus* leaves' extract altered the ZnO formation, leading to the formation of non-uniform ZnO morphology. The difference is possibly due to the competitive interaction among DEG, *H. tiliaceus* leaf extract, and Zn²⁺ ions, which led to the formation of non-uniform structures.

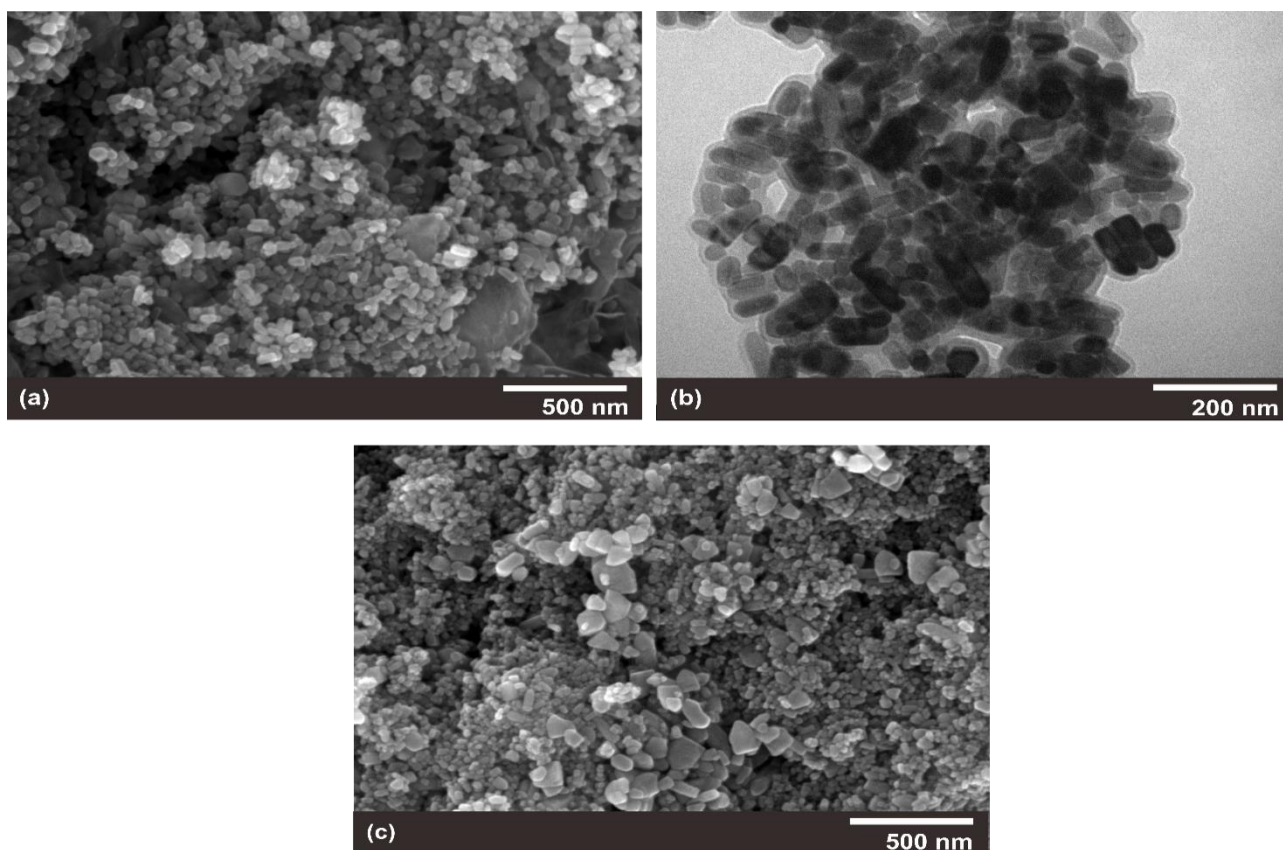


Figure 3: (a) FESEM and (b) TEM image of WZnO. (c) is FESEM image of EZnO

The optical properties of WZnO and EZnO photocatalysts were analyzed using UV-Vis DRS. The UV-Vis spectra of WZnO and EZnO are displayed in Figure 4. The WZnO exhibits a high absorption in UV region compared to the EZnO photocatalyst. The red shift in the absorption edge is observed after the addition of *H. tiliaceus* leaf extract, which is associated with bandgap-shifting. The band gap energies of WZnO and EZnO photocatalysts were calculated using the Tauc plot following Eq. (2).

$$(ah\nu)^{1/n} = A(h\nu - E_g) \quad \text{Eq. (2)}$$

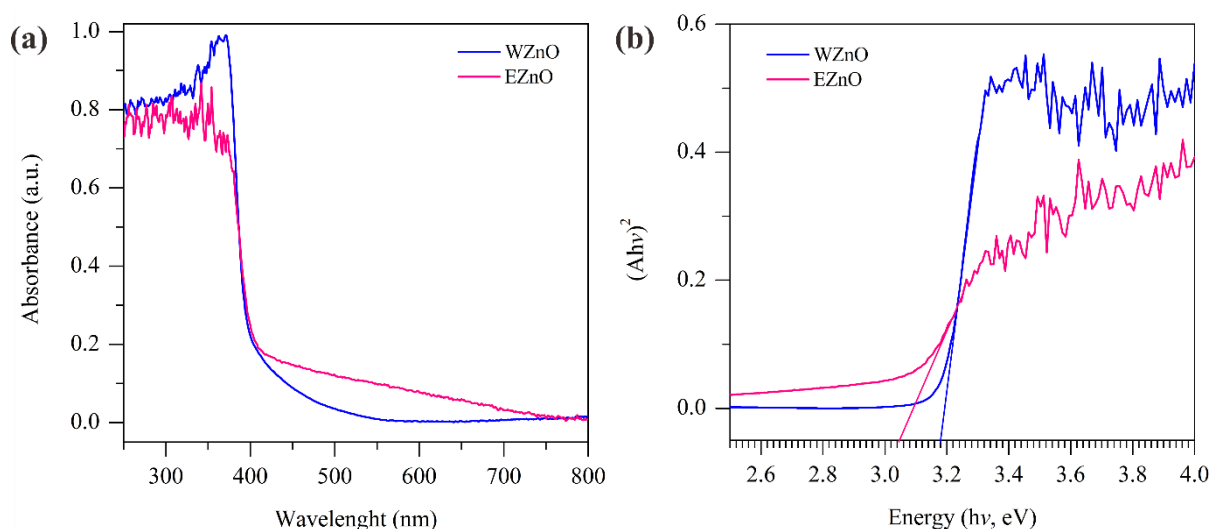


Figure 4: (a) Spectra UV-Vis and (b) Tauc plot of samples

The performance of the WZnO and EZnO photocatalysts in simultaneous photo-oxidation of MB and photo-reduction of Cr(VI) ions is illustrated in Figure 5. Dark experiments showed that the MB removal by the WZnO and EZnO photocatalysts is minor, implying that MB removal via adsorption is negligible (less than 4% after 60 min). The MB removal by WZnO photocatalyst was significantly increased under UV-C irradiation, where the MB removal reached 33.45% after only 10 min illumination and further increased to 72.30% after 60 min UV-C exposure (Figure 5 (left)). The MB removal by EZnO photocatalyst behaved similarly. However, the MB removal by the EZnO photocatalyst was slightly lower at 18.91 and 47.58% after 10- and 60-min UV-C illumination, respectively. This implies that the WZnO photocatalyst had better MB photo-oxidation performance than the EZnO photocatalyst. The performance of the WZnO and EZnO photocatalysts for Cr(VI) ion photoreduction is shown in Figure 5 (right). The removal Cr(VI) ions in the dark was negligible (maximum was 6.60% after 60 min). The Cr(VI) ions' removal reached 20% after 10 min UV-C illumination and 63% after 60 min. Unlike the MB removal, there was no significant differences in the performance of the WZnO and EZnO photocatalysts for Cr(VI) ion photoreduction.

where A is a constant of proportionality, a is the photon absorption coefficient, $h\nu$ is the energy of photons, and E_g is the band gap energy. As shown in Figure 4b, the band gap energies of WZnO and EZnO are 3.18 eV and 3.05 eV, respectively. This result implies there was a red shift in the absorption edge. The red shift of the absorption edge is attributed to the position of the band level in the ZnO. The addition of *H. tiliaceus* leaf extract might have changed the position of the band level due to the presence of various organic compounds that affected the generation of EZnO. As a result, the band gap decreased.

While the performance of WZnO and EZnO photocatalysts for MB photo-oxidation displayed a significant difference, their performance for Cr(VI) ion photoreduction exhibited no difference. This implies that the MB photo-oxidation is affected by the surface characteristics of the photocatalysts. As mentioned before, the EZnO sample contained more retained organic material as compared to the WZnO sample, as supported by the FTIR analyses. The presence of the organic material might have affected the bulky MB adsorption and subsequently photo-oxidation of MB, leading to a lower performance displayed by the EZnO. For Cr(VI) ion photoreduction, on the other hand, due to its smaller ionic diameter, the Cr(VI) ions might have no restriction to reach active sites in both WZnO and EZnO and underwent photo-reduction.

However, the efficiency of MB removal using EZnO is lower than that using WZnO. While the Cr(VI) removal using WZnO is slightly enhanced compared with what EZnO did. Compared with WZnO, EZnO particle size is smaller, reducing the active sites for dyes and leading to a decrease in photocatalytic performance, even though the band gap energy of EZnO is narrower than that of WZnO. It can be seen that the synergy of ZnO properties (nano-sized, surface area, band gap)

must be generated in order to obtain the optimum photocatalytic performance of ZnO. Nonetheless, the addition of *H. tiliaceus* leaves' extract to the ZnO synthesis can be a good candidate to alter the

bandgap energy of ZnO in the visible region, with further development to achieve the synergistic nature of its properties for optimum activity performance.

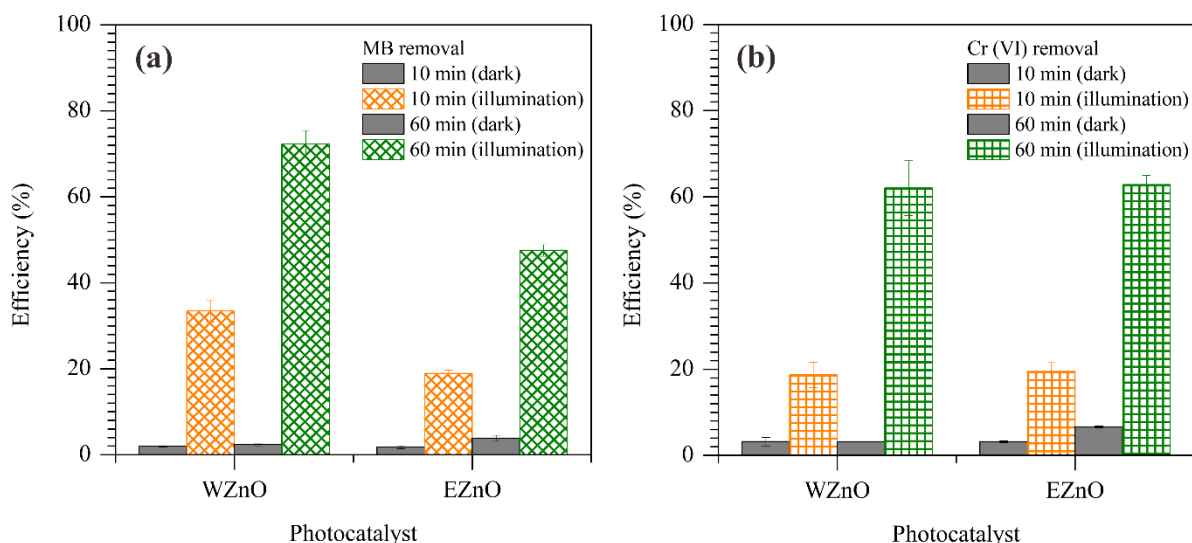


Figure 5: Simultaneous (a) photo-oxidation of MB efficiency and (b) photo-reduction efficiency of Cr (VI) ions by WZnO and EZnO photocatalysts under dark and illuminated conditions.

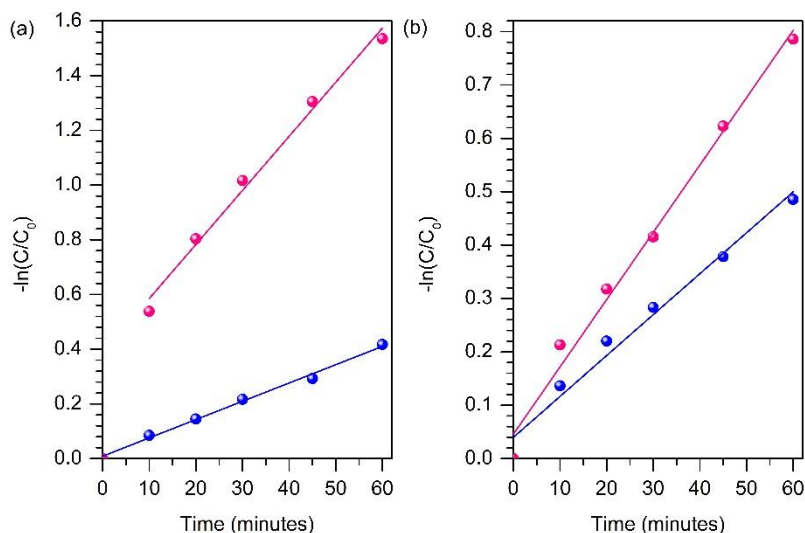


Figure 6: Kinetic study of simultaneous (a) photo-oxidation of MB efficiency and (b) photo-reduction efficiency of Cr (VI) ions by WZnO and EZnO photocatalysts.

Table 1: Summary of pseudo-first order kinetic of simultaneous photocatalytic of MB and Cr(VI)

Material	WZnO		EZnO	
	MB	Cr(VI)	MB	Cr(VI)
R^2	0.9868	0.9856	0.9936	0.9737
K_1 (min^{-1})	0.0198	0.0126	0.0067	0.0077
r (M min^{-1})	0.2851	0.2016	0.0965	0.1232

The kinetics of simultaneous photocatalytic reactions of Cr and MB have been determined by the pseudo-first order reaction. As shown in Figure 6, the kinetics of the simultaneous photocatalysis of Cr(VI) and MB are in agreement with the pseudo-first order. In the MB kinetic study, especially for WZnO, the kinetic study was plotted from 10 min to 60 min since the large improvement of MB removal from the initial to the 10 minutes correlated with the adsorption process

of MB on the surface of WZnO. The pseudo-first order parameter was tabulated in Table 1. The reaction rate of WZnO is faster than that of EZnO. This result demonstrates that WZnO has a good ability to remove MB and Cr(VI). Besides, the MB reaction rate by WZnO is faster than the Cr(VI) reaction rate of WZnO, indicating that WZnO is more effective for MB photocatalysis. In contrast, the reaction rate of Cr(VI) by EZnO is faster compared to the reaction rate of MB by EZnO,

revealing that EZnO is suitable for photoreduction of Cr(VI). The presence of functional groups in organic compounds of *H.tiliaceus* leaves' extract might facilitate the photoreduction of Cr(VI) than the photooxidation of MB molecules. The K_1 value of WZnO and EZnO for Cr(VI) photoreduction is higher compared to the previous study using ZnO/graphene (21) and ZrO_2 (22), indicating that WZnO and EZnO have excellent ability to reduce Cr(VI) to Cr(III). However, the K_1 value of MB photooxidation is slightly low compared to previous studies using biosynthesis ZnO (23) and mesoporous ZnO (24). It can be due to the simultaneous photocatalytic process, leading to reaction competition between Cr(VI) and MB.

The mechanism of simultaneous photocatalysis of Cr(VI) and MB is proposed in Figure 7a. Upon light illumination, the electrons in the VB of ZnO are

excited to the CB of ZnO. As a result, the equivalent number of holes was formed in the VB of ZnO. Both charge carriers diffused into the surface of ZnO, and a redox reaction took place. According to Butler and Ginley equation, the VB and CB levels of ZnO can be calculated following Eqs. (3) and (4) (25).

$$E_{VB} = X - E^e + \frac{1}{2}E_g \quad \text{Eq. (3)}$$

$$E_{CB} = E_{VB} - E_g \quad \text{Eq. (4)}$$

E_{VB} , E_{CB} , and E_g are the VB level, CB level, and band gap of ZnO. E^e and X are the free electron energy on hydrogen scale (4.5 eV) and the electronegativity of ZnO (5.79 eV). The calculated VB and CB levels of WZnO are 2.88 eV and -0.3 eV, respectively, whereas the VB and CB levels of EZnO are 2.82 eV and -0.24 eV, respectively.

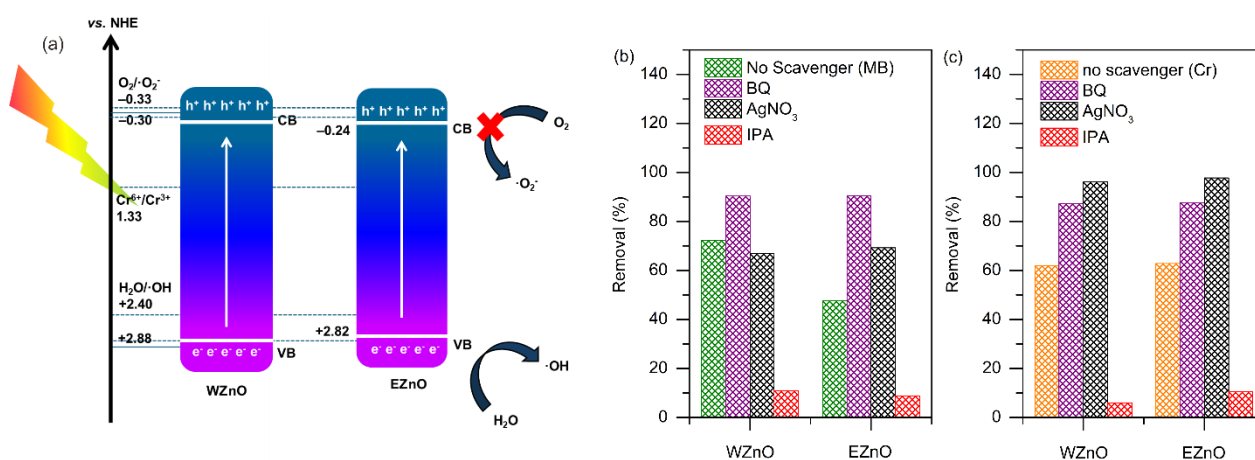


Figure 7: (a) Mechanism of photocatalytic by WznO and EZnO and (b, c) is the removal of MB and Cr(VI) after the addition of scavenger agent

The CB level of both ZnO is more negative compared to reduction potential of Cr(VI)/Cr(III) ($E^0 = +1.33$ eV vs. NHE), indicating that the photoreduction of Cr(VI) to Cr(III) is feasible. Besides, the VB level of both ZnO is more positive than that of oxidation potential of OH⁻/·OH ($E^0 = +2.40$ eV vs. NHE), revealing that the oxidation reaction OH⁻ by h⁺ easily occurred (24,26). However, the oxidation potential of O₂/·O₂⁻ ($E^0 = -0.33$ eV vs. NHE) is more negative compared to CB level of both ZnO, demonstrating that ·O₂⁻ is impossible to generate. Since pH of the used Milli-Q water is under 7, the main species of Cr(VI) ions is HCrO₄⁻ or Cr₂O₇²⁻ which require three and six electrons to reduce to Cr(III), respectively. Scavenger agents were added during the photocatalytic process to assess the presence of radical active species. The scavenger agents, including isopropanol (IPA), silver(I) nitrate (AgNO₃), and p-benzoquinone (BQ), were used to inhibit the activity of ·OH (27), e⁻ (28), and ·O₂⁻ (29), respectively. As shown in Figure 7b and 7c, the addition of IPA decreased the photocatalytic activity of ZnO whereas adding BQ and AgNO₃ improved the photocatalytic activity. The improvement of photocatalytic activity by adding

BQ and AgNO₃ might reveal that BQ and AgNO₃ can act as electron sinks. Specifically for AgNO₃, its presence during the irradiation can induce the formation of a Schottky junction, thereby enhancing electron transfer and facilitating the photoreduction process (30). Therefore, it can be noted that ·OH is an active species during the photocatalytic process.

4. CONCLUSION

H. tiliaceus leaves' extract influenced the properties of ZnO (EZnO). EZnO generated a crystalline structure and a large particle size compared with WZnO. Nevertheless, EZnO exhibited narrow bandgap energy in the visible region. However, the efficiency of MB removal using EZnO is lower than that using WZnO. While the Cr (VI) removal using EZnO is slightly reduced compared with WZnO. The synergy of ZnO properties (nano-sized, surface area, band gap) must be generated in order to obtain the optimum photocatalytic performance of ZnO. Nonetheless, the addition of *H. tiliaceus* leaves' extract in the ZnO synthesis can be a good candidate to alter bandgap energy of ZnO in the visible region, with

further development to achieve the synergistic nature of its properties for optimum activity performance.

5. CONFLICT OF INTEREST

There is no conflict of interest.

6. ACKNOWLEDGMENTS

The authors gratefully acknowledge financial support from the Institut Teknologi Sepuluh Nopember for this work, under the project scheme of the Publication Writing and IPR Incentive Program (PPHKI) 2024.

7. REFERENCES

- Zakiah A, Anindika GR, Kusumawati Y. Synthesis of zinc oxide (ZnO) nanoparticles by polyol method and its application on photocatalytic reduction of paracetamol concentration. *AIP Conf Proc.* 2021;2349.
- Subagyo R, Kusumawati Y, Widayatno WB. Kinetic study of methylene blue photocatalytic decolorization using zinc oxide under UV-LED irradiation. *AIP Conf Proc.* 2020;2237(June).
- Maaza M, Ngom BD, Achouri M, Manikandan K. Functional nanostructured oxides. *Vacuum [Internet].* 2015;114:172–87. Available from: [<URL>](#)
- Wellia DV, Kusumawati Y, Diguna LJ, Amal MI. Introduction of Nanomaterials for Photocatalysis. In: Khan MM, Pradhan D, Sohn Y, editors. *Nanocomposites for Visible Light-induced Photocatalysis.* Springer S. Springer, Cham; 2017. p. 1–17. Available from: [<URL>](#)
- Mateo-Mateo C, Vázquez-Vázquez C, Pérez-Lorenzo M, Salgueiriño V, Correa-Duarte MA. Ostwald ripening of platinum nanoparticles confined in a carbon nanotube/silica-templated cylindrical space. *J Nanomater.* 2012;2012.
- Villa A, Schiavoni M, Prati L. Material science for the support design: A powerful challenge for catalysis. *Catal Sci Technol.* 2012;2(4):673–82.
- Morsbach E, Spéder J, Arenz M, Brauns E, Lang W, Kunz S, et al. Stabilizing catalytically active nanoparticles by ligand linking: Toward three-dimensional networks with high catalytic surface area. *Langmuir.* 2014;30(19):5564–73.
- Villa A, Dimitratos N, Chan-Thaw CE, Hammond C, Veith GM, Wang D, et al. Characterisation of gold catalysts. *Chem Soc Rev [Internet].* 2016;45(18):4953–94. Available from: [<URL>](#)
- Campisi S, Schiavoni M, Chan-Thaw CE, Villa A. Untangling the role of the capping agent in nanocatalysis: Recent advances and perspectives. *Catalysts.* 2016;6(12):1–21.
- Neouze MA, Schubert U. Surface modification and functionalization of metal and metal oxide nanoparticles by organic ligands. *Monatshfte fur Chemie.* 2008;139(3):183–95. Available from: [<URL>](#)
- Javed R, Usman M, Tabassum S, Zia M. Effect of capping agents: Structural, optical and biological properties of ZnO nanoparticles. *Appl Surf Sci [Internet].* 2016;386:319–26. Available from: [<URL>](#)
- Ahmed S, Annu, Chaudhry SA, Ikram S. A review on biogenic synthesis of ZnO nanoparticles using plant extracts and microbes: A prospect towards green chemistry. *J Photochem Photobiol B Biol.* 2017;166:272–84. Available from: [<URL>](#)
- Singh A, Singh NB, Hussain I, Singh H, Yadav V, Singh SC. Green synthesis of nano zinc oxide and evaluation of its impact on germination and metabolic activity of *Solanum lycopersicum*. *J Biotechnol.* 2016;233:84–94. Available from: [<URL>](#)
- Zare M, Namratha K, Thakur MS, Byrappa K. Biocompatibility assessment and photocatalytic activity of bio-hydrothermal synthesis of ZnO nanoparticles by *Thymus vulgaris* leaf extract. *Mater Res Bull.* 2019;109(May 2018):49–59. Available from: [<URL>](#)
- Putri OK, Syafdhani H, Holilah, Fadlan A, Kusumawati Y, Santoso M, et al. Antioxidant and antibacterial activities of phytosynthesised ZnOs by hibiscus tiliaceus leaf extract against four pathogenic bacteria. *Rasayan J Chem.* 2022;15(4):2835–43.
- Hosni M, Kusumawati Y, Farhat S, Jouini N, Pauporté T. Effects of oxide nanoparticle size and shape on electronic structure, charge transport, and recombination in dye-sensitized solar cell photoelectrodes. *J Phys Chem C.* 2014;118(30):16791–8.
- Meshram J V., Koli VB, Phadatare MR, Pawar SH. Anti-microbial surfaces: An approach for deposition of ZnO nanoparticles on PVA-Gelatin composite film by screen printing technique. *Mater Sci Eng C [Internet].* 2017;73:257–66. Available from: [<URL>](#)
- Johnson MK, Powell DB, Cannon RD. Vibrational spectra of carboxylato complexes-I. Infrared and Raman spectra of beryllium(II) acetate and formate and of zinc(II) acetate and zinc(II) acetate dihydrate. *Spectrochim Acta Part A Mol Spectrosc.* 1981;37(10):899–904.
- Anandan M, Dinesh S, Krishnakumar N, Balamurugan K. Improved photocatalytic properties and anti-bacterial activity of size reduced ZnO nanoparticles via PEG-assisted precipitation route. *J Mater Sci Mater Electron.* 2016;27(12):12517–26.
- Nasrollahzadeh M, Issaabadi Z, Sajadi SM. Green synthesis of Pd/Fe₃O₄ nanocomposite using *Hibiscus tiliaceus* L. extract and its application for reductive catalysis of Cr(VI) and nitro compounds. *Sep Purif Technol [Internet].* 2018;197(January):253–60. Available from: [<URL>](#)
- Chen Z, Luo Y, Huang C, Shen X. In situ assembly of ZnO/graphene oxide on synthetic molecular receptors: Towards selective photoreduction of Cr(VI) via interfacial synergistic catalysis. *Chem Eng J [Internet].* 2021;414(January):128914. Available from: [<URL>](#)
- Aziz FFA, Jalil AA, Hassan NS, Hitam CNC, Rahman AFA, Fauzi AA. Enhanced visible-light driven multi-photoredox Cr(VI) and p-cresol by Si and Zr interplay in fibrous silica-zirconia. *J Hazard Mater [Internet].* 2021;401(March 2020):123277. Available from: [<URL>](#)
- Gawade V V., Sabale SR, Dhabbe RS, Kite S V., Garadkar KM. Bio-mediated synthesis of ZnO nanostructures for efficient photodegradation of methyl orange and methylene blue. *J Mater Sci Mater Electron*

[Internet]. 2021;32(24):28573–86. Available from: [<URL>](#)

24. Prasetyoko D, Sholeha NA, Subagyo R, Ulfa M, Bahruji H, Holilah H, et al. Mesoporous ZnO nanoparticles using gelatin – Pluronic F127 as a double colloidal system for methylene blue photodegradation. *Korean J Chem Eng.* 2023;40(1):112–23.

25. Subagyo R, Tehubijuluw H, Prasetyo Utomo W, Dwi Rizqi H, Kusumawati Y, Bahruji H, et al. Converting red mud wastes into mesoporous ZSM-5 decorated with TiO₂ as an eco-friendly and efficient adsorbent-photocatalyst for dyes removal. *Arab J Chem.* 2022;15(5):103754. Available from: [<URL>](#)

26. Azami MS, Jalil AA, Hassan NS, Hussain I, Fauzi AA, Aziz MAA. Green carbonaceous material-fibrous silica-titania composite photocatalysts for enhanced degradation of toxic 2-chlorophenol. *J Hazard Mater [Internet].* 2021;414(December 2020):125524. Available from: [<URL>](#)

27. Zulfa LL, Ediati R, Hidayat ARP, Subagyo R, Faaizatunnisa N, Kusumawati Y, et al. Synergistic effect of modified pore and heterojunction of MOF-derived α -Fe₂O₃/ZnO for superior photocatalytic degradation of methylene blue. *RSC Adv.* 2023;13(6):3818–34.

28. Lam SM, Jaffari ZH, Sin JC, Zeng H, Lin H, Li H, et al. Surface decorated coral-like magnetic BiFeO₃ with Au nanoparticles for effective sunlight photodegradation of 2,4-D and *E. coli* inactivation. *J Mol Liq.* 2021;326:115372. Available from: [<URL>](#)

29. Yong ZJ, Lam SM, Sin JC, Zeng H, Mohamed AR, Jaffari ZH. Boosting sunlight-powered photocatalytic fuel cell with S-scheme Bi₂WO₆/ZnO nanorod array composite photoanode. *Inorg Chem Commun.* 2022;143(August):109826. Available from: [<URL>](#)

30. Subagyo R, Yudhowijoyo A, Sholeha NA, Hutagalung SS, Prasetyoko D, Birowosuto MD, et al. Recent advances of modification effect in Co₃O₄-based catalyst towards highly efficient photocatalysis. *J Colloid Interface Sci.* 2023;650(PB):1550–90. Available from: [<URL>](#)



Mechanical, Optical, and Thermal Properties of SnS₂-Filled PVA Composites

Volkan Uğraşkan^{1*} 

¹Yıldız Technical University, Chemistry Department, Istanbul, 34220, Turkey.

Abstract: The effects of tin disulfide (SnS₂) addition on the mechanical, thermal, and optical characteristics of polyvinyl alcohol (PVA) were determined in this study. The solvent-casting approach was used to create composite films with varying SnS₂ weight ratios. Mechanical testing revealed that the addition of SnS₂ raised the tensile strength (TS) of the virgin PVA from 32.10 MPa to 47.50 MPa, while the elongation at break (EB) increased from 78.40% to 108.80%. Optical investigations revealed that PVA and SnS₂ had intermolecular interactions. Furthermore, the contribution of SnS₂ resulted in a drop in energy bandwidth from 5.310 eV to 4.821 eV. Thermal investigations revealed that PVA/SnS₂ had greater stability than the virgin polymer. Given the data obtained, it was obtained that the addition of SnS₂ simultaneously enhanced the mechanical, thermal, and optical properties of PVA.

Keywords: Polyvinyl alcohol, tin disulfide, polymer, composite.

Submitted: July 8, 2023. **Accepted:** January 23, 2024.

Cite this: Uğraşkan V. Mechanical, Optical, and Thermal Properties of SnS₂-Filled PVA Composites. JOTCSA. 2024;11(2):557-64.

DOI: <https://doi.org/10.18596/jotcsa.1324711>

***Corresponding author's E-mail:** ugraskan@yildiz.edu.tr

1. INTRODUCTION

There has been a recent interest in thermoplastic composites filled with various fillers that are used to improve the physicomaterial properties and provide desirable properties to composites used in food packaging, drug delivery, automation, aerospace, textile, and so on applications (1). These composites have the features of organic polymers, such as lightweight and good moldability, as well as the inorganic materials' high strength, thermal stability, and chemical resistance (2).

Polyvinyl alcohol (PVA) is a semi-crystalline organic polymer produced by vinyl acetate polymerization. Because of its excellent film-forming, adhesion, emulsification, and chemical stability, it could potentially be employed in a variety of pharmaceutical, cosmetic, or biological applications such as drug administration, tissue engineering, tissue regeneration, or replacement. It should be noted that PVA is difficult to melt because of its strong inter/intra hydrogen bonding, yet the many hydroxyl groups in the molecular structure supply PVA with exceptional water solubility, making it ideal for casting (3-5). Furthermore, virgin PVA films display low dielectric permittivity and weak conductivity behavior across a wide frequency range,

proving their suitability as low-dielectric ecologically friendly, transparent compounds. The customizable usability of these polymers' composites with diverse fillers has proven them as particularly suitable for the construction of a wide range of flexible and lightweight biodegradable microelectronic, organoelectronic, and optoelectronic technologies (6).

Tin disulfide (SnS₂) is a 2.2 eV moderate bandgap CdI₂-type multilayer semiconducting material. It has recently piqued the interest of researchers for use in a variety of applications such as lithium batteries, pigments, gas sensors, photoconductors, solar cells, optoelectronics, photoluminescence, and so on due to its plentiful source components, simple synthesis, cost-effectiveness, non-toxicity, strong stability, and comparatively strong visible-light photocatalytic activity (7-10). However, there is no study reported on the mechanical properties of SnS₂ and its composites in the literature.

In this work, the mechanical, optical, electrical, and thermal properties of SnS₂-filled PVA composites were examined.

2. EXPERIMENTAL SECTION

2.1. Materials

PVA (Mowiol 40-88), tin (II) chloride dehydrate (98%), thiourea ($\geq 99.0\%$), and ethylene glycol (99.8%) were purchased from Sigma Aldrich, Germany.

2.2. Synthesis of SnS₂

The synthesis of SnS₂ was carried out as described in the literature (8). To begin, tin(II) chloride dehydrate and thiourea was grounded in a mortar at a mole ratio of 0.2:0.5. The powder combination was then transferred to a porcelain crucible and heated at 170 °C for 2 h. Lastly, the resulting yellowish SnS₂ was rinsed with distilled water to eliminate impurities and dried overnight in an oven at 90 °C.

2.3. Preparation of The Composite Films

PVA/SnS₂ composites were produced by incorporating several weight ratios of SnS₂ such as 0.5%, 1%, 3%, 5%, 7%, and 10% into a 10% w/v PVA solution. The combinations were then cast on glass templates. The composite films were formed following drying at 60 °C under vacuum.

2.4. Characterization

The instruments used in this study are listed in Table 1.

Table 1: The instruments used in this study.

Instruments	Model
FTIR-ATR	Nicolet IS10 Thermo FTIR
SEM	Zeiss EVO LS10
XRD	Panalytical Empyrean
UV-vis	Shimadzu UV2600
TGA and DSC	NETZSCH STA 449F3
Tensile tests	ZONHOW, DZ-106

3. RESULTS AND DISCUSSION

XRD spectra of the virgin PVA, SnS₂, and PVA/SnS₂ containing 3% SnS₂ were given in Fig. 1. The pattern of the virgin PVA film displayed two peaks at 19.5° and 41.4°, which correspond to the semi-crystalline structure kept together by intramolecular and intermolecular H-bonding (11) (Fig. 1a). The diffraction pattern's reflections are all well-matched with characteristic SnS₂ crystals and showed the hexagonal SnS₂ phase. The acquired XRD results are consistent with the literature (JCPDPS card no. 22-0951) (7). In the pattern of the PVA/SnS₂, no significant change was observed compared to the virgin PVA, which was due to the homogenous distribution of SnS₂ particles in the composite structure (12).

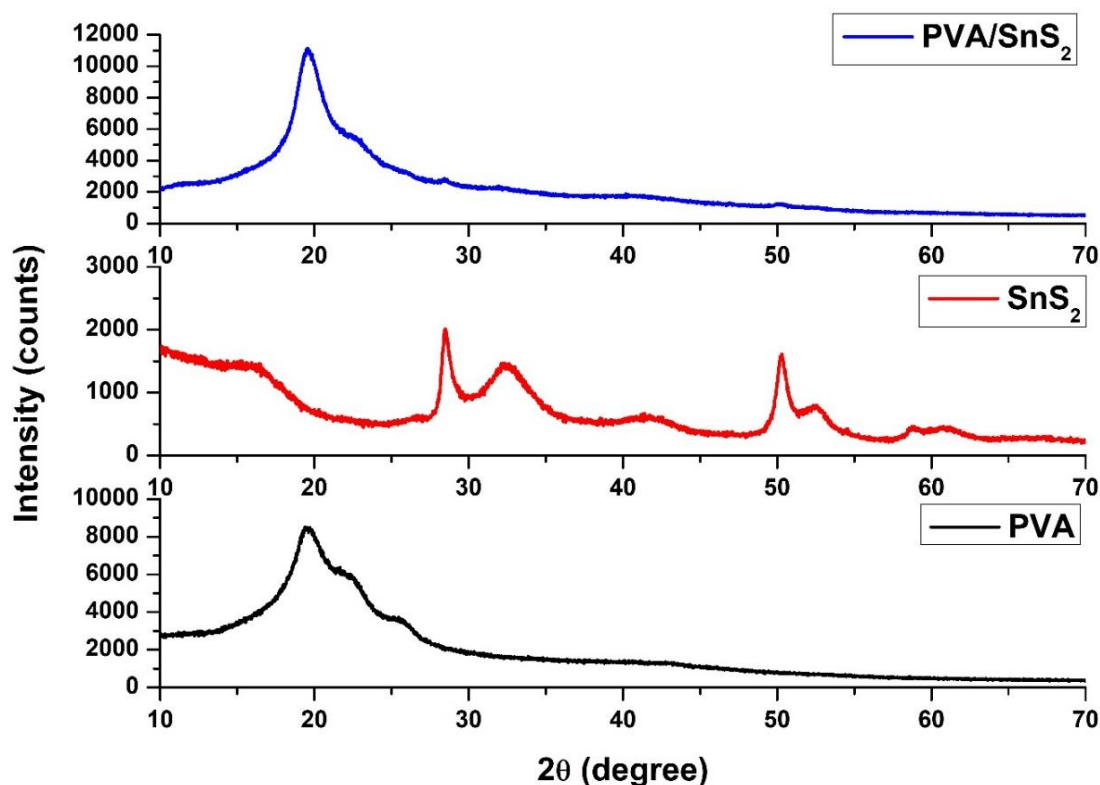


Figure 1: XRD patterns of the virgin PVA, SnS₂, and PVA/SnS₂ containing 3% SnS₂.

Fig. 2 showed the SEM images of SnS₂, and a cross-sectional view of the films of the virgin PVA, and PVA/SnS₂ containing 3% SnS₂. It was observed that the virgin PVA film had a smooth surface, while the composite surface was rough. Additionally, the homogenous distribution of the SnS₂ particles

without any significant agglomeration in the composite structure was observed (Fig. 2a, c, d). The micrograph of SnS₂ revealed the porous flower-like hierarchical structures formed by interpenetrated sheets (8).

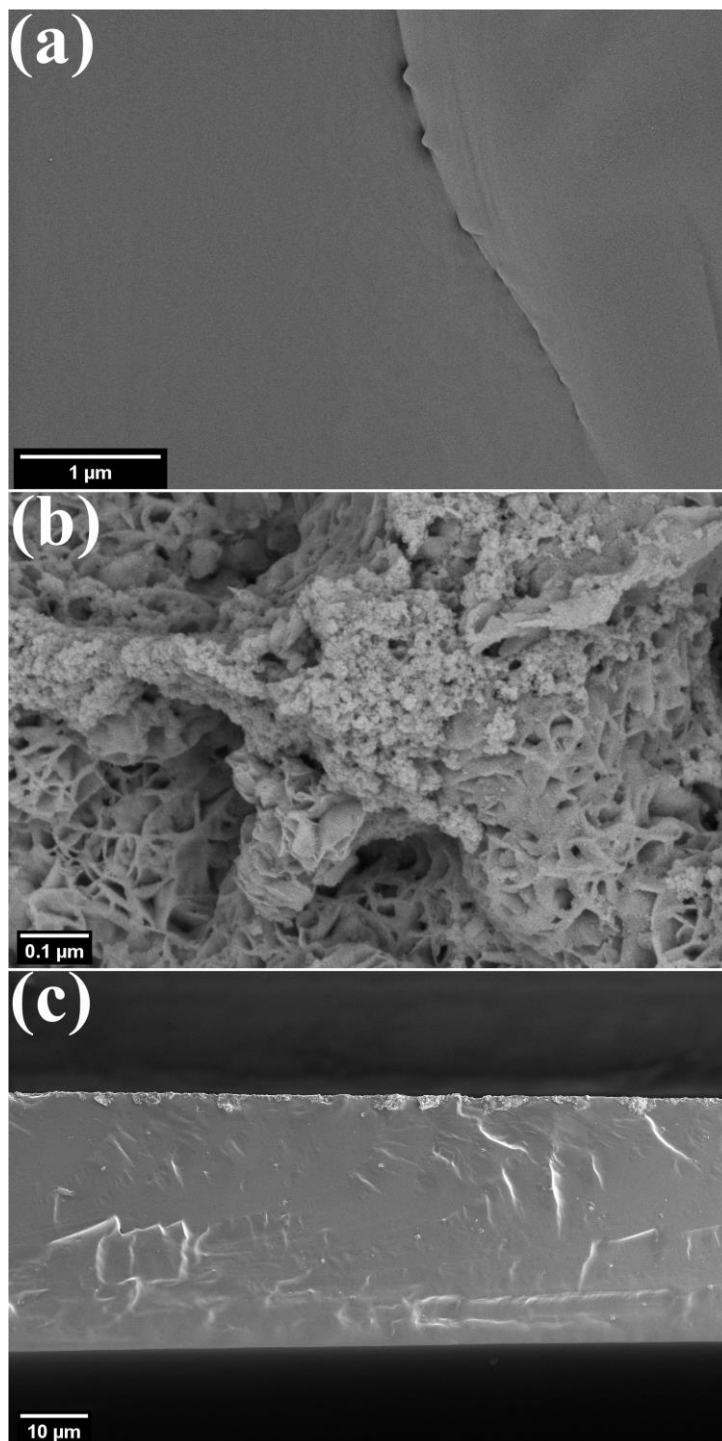


Figure 2: SEM images of the samples; cross-sectional view of the virgin PVA film (a), SnS₂ (b), cross-sectional view of the PVA/SnS₂ containing 3% SnS₂.

FTIR-ATR spectra of the virgin PVA, SnS₂, and PVA/SnS₂ containing 3% SnS₂ were given in Fig. 3 whereas the peak assignments were given in Table 2. For the PVA/SnS₂, a spectrum similar to that of virgin PVA was obtained, with the peak observed at 1628 cm⁻¹ originating from SnS₂. Additionally, shifts in peak values were observed, which were attributed to the interaction of the SnS₂ particles with the PVA matrix.

UV-vis spectra of the virgin PVA and PVA/SnS₂ containing different weight ratios of SnS₂ were illustrated in Fig. 4. The virgin PVA exhibited a peak

at 277 nm, which corresponded to n-n* transitions in the polymer backbone. In addition, a significant decrease in absorbance is noticed in the 200-240 nm range, which is related to the sample's band gap, suggesting the semi-crystalline structure of PVA as revealed by XRD analysis (14). The spectra of the PVA/SnS₂ were identical to those of the virgin PVA, however, the peaks corresponding to the n-n* transitions moved to higher wavelengths. The establishment of a strong intermolecular interaction between the SnS₂ particles and the polar unit of PVA caused a shift in the peak locations of PVA/SnS₂ to the higher wavelengths (15).

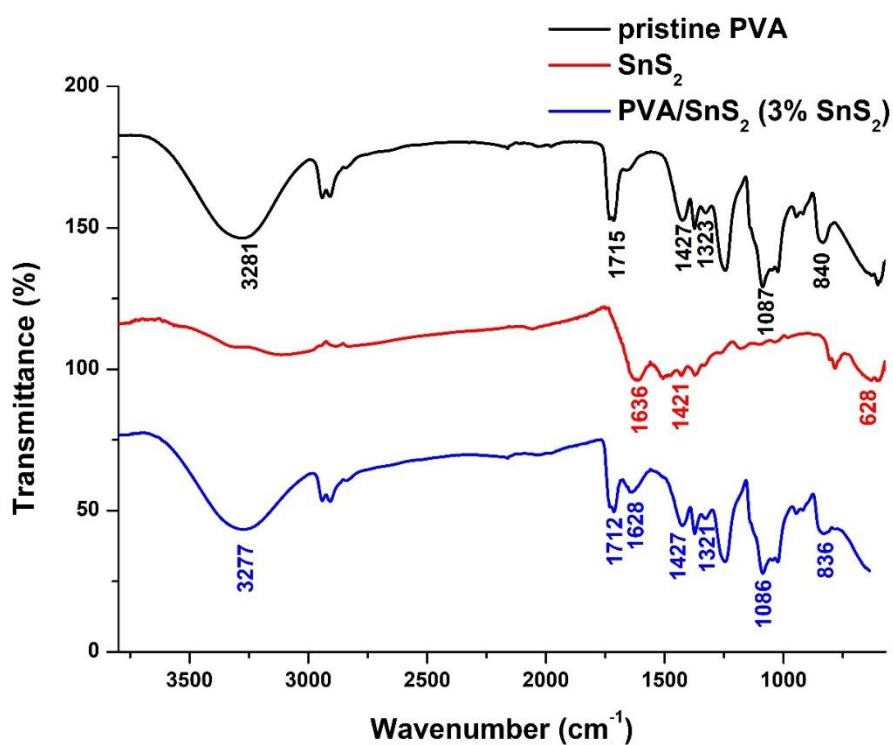


Figure 3: FTIR-ATR spectra of the virgin PVA, SnS₂, and PVA/SnS₂ containing 3% SnS₂.

Table 2: The FTIR-ATR data of the samples [7] [13].

Wavenumber (cm ⁻¹)	Functional group
3281	O-H stretchings
1715	C=O stretchings
1427	C-H bending
1323	C-H deformation
1087	C-O stretchings
840	C-C stretchings
1636	C-H stretchings
1421	C-O stretchings
628	Sn-S band

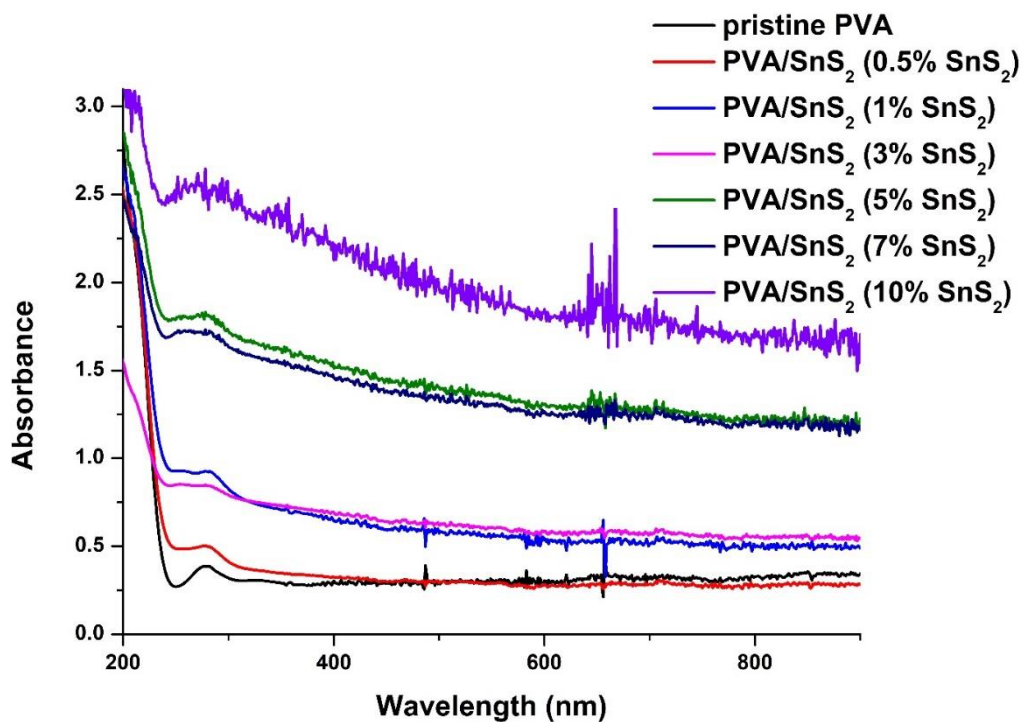


Figure 4: UV-VIS spectra of the virgin PVA, SnS₂, and PVA/SnS₂.

Knowing the absorption coefficients would allow you to calculate the optical energy band gaps (E_g), which are the most significant characteristics of organic and inorganic materials. The Tauc relation is utilized to calculate the films' energy band gap:

$$(\alpha h\nu) = B(h\nu - E_g)^{1/n}$$

where $1/n$ defines the type of electronic transition and is related to the density of state distribution. B is a constant, connected to the probability of

transition. Following that, optical band gaps were calculated by graphing $(\alpha h\nu)^2$ against $(h\nu)$. The energy bandwidth of the composites reduced from 5.310 to 4.767 eV when compared to pristine PVA film, indicating that SnS_2 might raise the amount of energy states between PVA's valence and conduction bands, leading to a change in the electronic structure of the PVA matrix (Fig. 5). The change in the optical bandgap is caused by the localized electronic states in the band gaps of PVA created by SnS_2 as trapping and recombination centers (16).

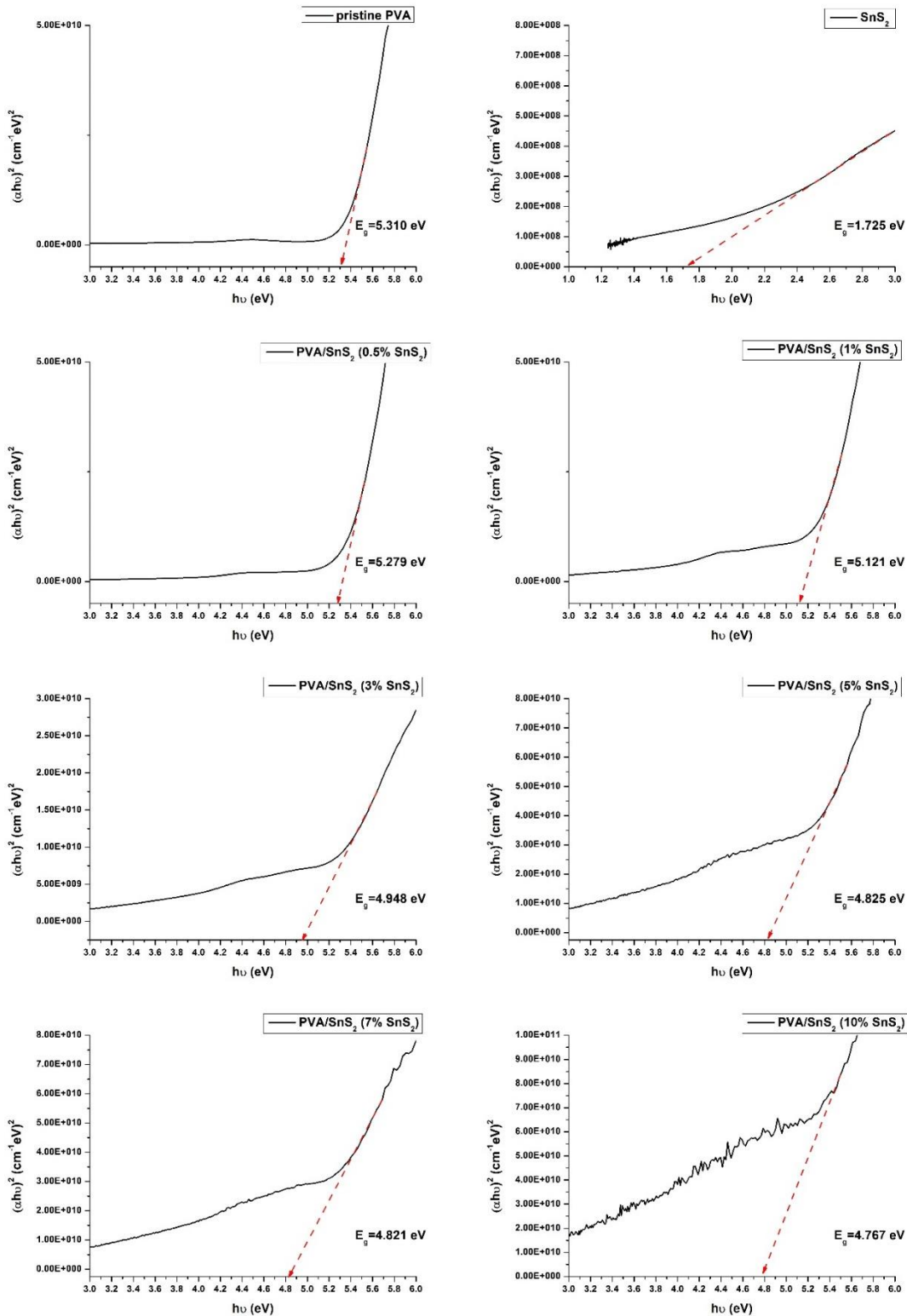


Figure 5: $(\alpha h\nu)^2$ against $(h\nu)$ plots of the pristine PVA, SnS_2 , and PVA/ SnS_2 composites.

The TGA spectra of the virgin PVA and PVA/SnS₂ containing 3% SnS₂ were shown in Fig. 6. The weight losses observed in all samples below 100 °C indicated the removal of the absorbed water molecules from the structure (17). SnS₂ was thermally stable and showed a 7.2 wt% weight loss between 260 and 460 °C. The spectra of the virgin PVA and PVA/SnS₂ revealed a two-stage decomposition trend. While the samples began to deteriorate at roughly 260 °C, they were completely

decomposed at around 460 °C. Additionally, the breakdown temperature of PVA/SnS₂ (270 °C) is greater than that of virgin PVA (260 °C). Besides, according to the DSC data, it was observed that the melting temperature of the virgin PVA increased from 187.5 °C to 189.1 °C with the addition of 3% SnS₂. The rise in the thermal stability was ascribed to SnS₂ particles' superior temperature stability and interfacial interactions with the PVA matrix (18).

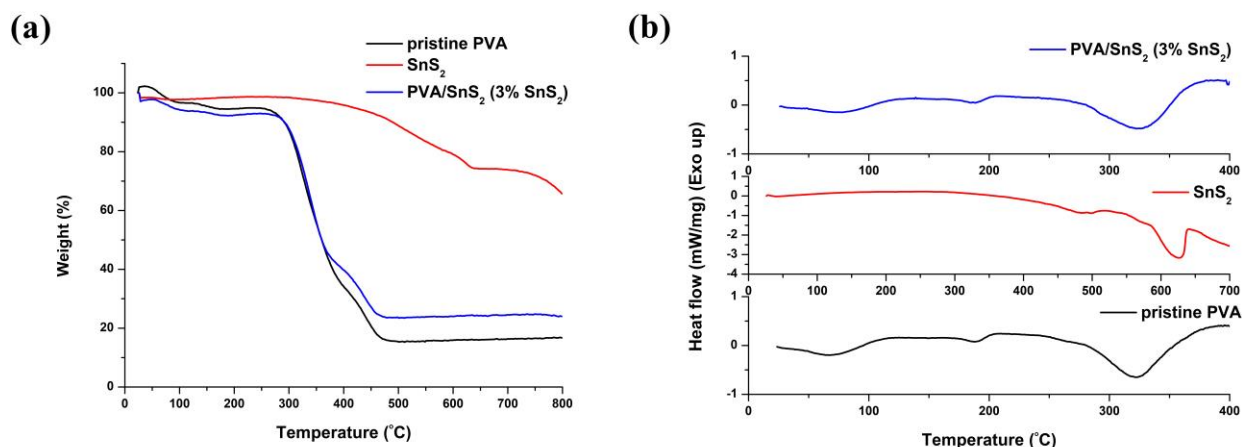


Figure 6: TGA spectra (a) and DSC curves (b) of the virgin PVA, SnS₂, and PVA/SnS₂ containing 3% SnS₂.

Fig. 7 depicts the stress-strain curves of the virgin PVA and PVA/SnS₂, whereas Table 3 lists the TS, Young's modulus, and EB. Tensile testing revealed that the virgin PVA's TS increased from 32.10 MPa to 47.50 MPa with the addition of 3% SnS₂. The composites demonstrated linear stress-strain behavior up to failure and plastic deformation, as well

as equivalent curve morphologies for plain and nanofiller composites (19). Additionally, the simultaneous enhancement in the tensile strength and elongation was ascribed to the homogeneous dispersion of SnS₂ particles in the PVA/SnS₂ structure (20).

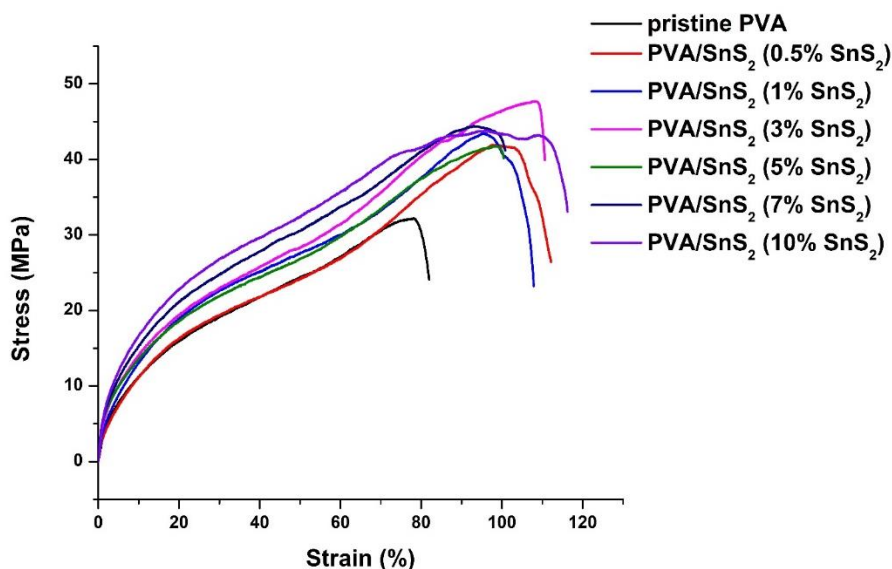


Figure 7: Stress-strain curves of the virgin PVA, SnS₂, and PVA/SnS₂.

Table 3: Tensile properties of the virgin PVA and PVA/SnS₂ films.

Sample	TS (MPa)	EB (%)	Young Modulus (GPa)
Virgin PVA	32.10	78.40	1.80
PVA/SnS ₂ (0.5% SnS ₂)	42.00	97.20	3.01
PVA/SnS ₂ (1% SnS ₂)	43.60	95.80	3.04
PVA/SnS ₂ (3% SnS ₂)	47.50	108.80	3.42
PVA/SnS ₂ (5% SnS ₂)	42.55	99.13	2.78
PVA/SnS ₂ (7% SnS ₂)	44.50	92.32	3.11
PVA/SnS ₂ (10% SnS ₂)	43.56	94.86	3.86

4. CONCLUSION

The mechanical, thermal, and optical features of SnS₂-filled PVA composites were examined in this work. Firstly, SnS₂ was synthesized, and then composite films with varied SnS₂ weight ratios were made using the solvent-casting process. Mechanical testing revealed that the addition of SnS₂ raised the TS of the virgin PVA from 32.10 MPa to 47.50 MPa, while the EB increased from 78.40% to 108.80%. Optical investigations revealed that the intermolecular interactions between PVA and SnS₂. Thermal investigations revealed that PVA/SnS₂ are more stable than virgin PVA.

5. CONFLICT OF INTEREST

The authors declare that they have no conflict of interest.

7. REFERENCES

- Kohli D, Garg S, Jana AK. Physical, mechanical, optical and biodegradability properties of polyvinyl alcohol/cellulose nanofibrils/kaolinite clay-based hybrid composite films. *Indian Chem Eng* [Internet]. 2021 Jan 1;63(1):62–74. Available from: [<URL>](#).
- Chen T, Wu Z, Wei W, Xie Y, Wang X (Alice), Niu M, et al. Hybrid composites of polyvinyl alcohol (PVA)/Si–Al for improving the properties of ultra-low density fiberboard (ULDF). *RSC Adv* [Internet]. 2016;6(25):20706–12. Available from: [<URL>](#).
- Cavalu S, Fritea L, Brocks M, Barbaro K, Murvai G, Costea TO, et al. Novel Hybrid Composites Based on PVA/SeTiO₂ Nanoparticles and Natural Hydroxyapatite for Orthopedic Applications: Correlations between Structural, Morphological and Biocompatibility Properties. *Materials (Basel)* [Internet]. 2020 May 1;13(9):2077. Available from: [<URL>](#).
- Rathinavel S, Saravanakumar SS. Development and Analysis of Silver Nano Particle Influenced PVA/Natural Particulate Hybrid Composites with Thermo-Mechanical Properties. *J Polym Environ* [Internet]. 2021 Jun 2;29(6):1894–907. Available from: [<URL>](#).
- Yao Y, Jin S, Wang M, Gao F, Xu B, Lv X, et al. MXene hybrid polyvinyl alcohol flexible composite films for electromagnetic interference shielding. *Appl Surf Sci* [Internet]. 2022 Mar;578:152007. Available from: [<URL>](#).
- Sengwa RJ, Dhatarwal P. Nanofiller concentration-dependent appreciably tailorable and multifunctional properties of (PVP/PVA)/SnO₂ nanocomposites for advanced flexible device technologies. *J Mater Sci Mater Electron* [Internet]. 2021 Apr 13;32(7):9661–74. Available from: [<URL>](#).
- Umar A, Akhtar MS, Dar GN, Abaker M, Al-Hajry A, Baskoutas S. Visible-light-driven photocatalytic and chemical sensing properties of SnS₂ nanoflakes. *Talanta* [Internet]. 2013 Sep;114:183–90. Available from: [<URL>](#).
- Wei H, Hou C, Zhang Y, Nan Z. Scalable low temperature in air solid phase synthesis of porous flower-like hierarchical nanostructure SnS₂ with superior performance in the adsorption and photocatalytic reduction of aqueous Cr(VI). *Sep Purif Technol* [Internet]. 2017 Dec;189:153–61. Available from: [<URL>](#).
- Kiruthigaa G, Manoharan C, Raju C, Dhanapandian S, Thanikachalam V. Synthesis and spectroscopic analysis of undoped and Zn doped SnS₂ nanostructure by solid state reaction method. *Mater Sci Semicond Process* [Internet]. 2014 Oct;26:533–9. Available from: [<URL>](#).
- Kiruthigaa G, Manoharan C, Raju C, Jayabharathi J, Dhanapandian S. Solid state synthesis and spectral investigations of nanostructure SnS₂. *Spectrochim Acta Part A Mol Biomol Spectrosc* [Internet]. 2014 Aug;129:415–20. Available from: [<URL>](#).
- Aziz S, Abdulwahid R, Rasheed M, Abdullah O, Ahmed H. Polymer Blending as a Novel Approach for Tuning the SPR Peaks of Silver Nanoparticles. *Polymers (Basel)* [Internet]. 2017 Oct 4;9(12):486. Available from: [<URL>](#).
- Morimune S, Nishino T, Goto T. Poly(vinyl alcohol)/graphene oxide nanocomposites prepared by a simple eco-process. *Polym J* [Internet]. 2012 Oct 18;44(10):1056–63. Available from: [<URL>](#).
- Kharazmi A, Faraji N, Mat Hussin R, Saion E, Yunus WMM, Behzad K. Structural, optical, opto-thermal and thermal properties of ZnS–PVA nanofluids synthesized through a radiolytic approach. *Beilstein J Nanotechnol* [Internet]. 2015 Feb 23;6:529–36. Available from: [<URL>](#).
- Aslam M, Kalyar MA, Raza ZA. Fabrication of nano-CuO-loaded PVA composite films with enhanced optomechanical properties. *Polym Bull* [Internet]. 2021 Mar 21;78(3):1551–71. Available from: [<URL>](#).
- Ramesan MT, Jayakrishnan P, Anilkumar T, Mathew G. Influence of copper sulphide nanoparticles on the structural, mechanical and dielectric properties of poly(vinyl alcohol)/poly(vinyl pyrrolidone) blend nanocomposites. *J Mater Sci Mater Electron* [Internet]. 2018 Feb 28;29(3):1992–2000. Available from: [<URL>](#).

16. Abdolrahimi M, Seifi M, Ramezanzadeh MH. Study the effect of acetic acid on structural, optical and mechanical properties of PVA/chitosan/MWCNT films. Chinese J Phys [Internet]. 2018 Feb;56(1):221–30. Available from: [<URL>](#).
17. Zhang L, Yu P, Luo Y. Dehydration of caprolactam–water mixtures through cross-linked PVA composite pervaporation membranes. J Memb Sci [Internet]. 2007 Dec;306(1–2):93–102. Available from: [<URL>](#).
18. Wu H, Xiao D, Lu J, Li T, Jiao C, Li S, et al. Preparation and Properties of Biocomposite Films Based on Poly(vinyl alcohol) Incorporated with Eggshell Powder as a Biological Filler. J Polym Environ [Internet]. 2020 Jul 4;28(7):2020–8. Available from: [<URL>](#).
19. Koteswararao J, Satyanarayana SV, Madhu GM, Venkatesham V. Estimation of structural and mechanical properties of Cadmium Sulfide/PVA nanocomposite films. Heliyon [Internet]. 2019 Jun;5(6):e01851. Available from: [<URL>](#).
20. Singh H, Kumar D, Sawant KK, Devunuri N, Banerjee S. Co-doped ZnO–PVA Nanocomposite for EMI Shielding. Polym Plast Technol Eng [Internet]. 2016 Jan 22;55(2):149–57. Available from: [<URL>](#).



Investigation of Electronic and Molecular Features of Zn₃S₃/PEG4000 Composite Using the DFT Method

Manahil A. Hraja¹ , Aula M. Al Hindawi¹ , Nagham M. Shiltagh^{2*} 

¹Department of Chemistry, College of Education for Pure Science, University of Kerbala, Karbala, Iraq.

²Department of Physics, College of Science, University of Kerbala, Karbala, Iraq.

Abstract: Molecular geometry structures were accurately optimized to low convergence energy thresholds for the Zn₃S₃ cluster before and after adding Polyethylene Glycol (PEG4000). Density functional theory DFT/ B3LYP calculations with 6-11G (d, p) basis set were employed to investigate structural and electronic properties of Zn₃S₃/PEG4000 composite. The FTIR spectral lines were analyzed where an agreement of FTIR spectra of titled molecules was evaluated between experimental and theoretical findings of the active peaks of O-H, C-H, C=O, C-O-C, and Zn-S functional groups. The vibrational modes frequencies were systematically analyzed on the distribution basis of potential energy around the range 0–4000 cm⁻¹ and observed 12 modes of vibrations for the Zn₃S₃ molecule, while 36 modes for the Zn₃S₃/PEG4000 compound. Frontier high occupied, and low unoccupied molecular orbitals (HOMO&LUMO) were calculated and plotted to obtain the energy gap (*E_g*) resulting from the difference between those orbitals. The promising indicator was obtained at increasing *E_g* from (4.031 to 4.459) eV after adding PEG4000, pointing out the effect of polymer on the ZnS surface as a capping agent. Additionally, electronic features of the mentioned structures, such as IP, EA, Ef, *E_g*, *C_p*, *χ*, η, S, and ω, were calculated. Finally, the molecular electrostatic potential (MEP) diagram of Zn₃S₃ and Zn₃S₃/PEG4000 and charge densities of isosurface and contour diagrams were estimated, showing the nucleophilic and electrophilic attack of these compounds.

Keywords: PEG4000 polymer, ZnSNPs, HOMO&LUMO, Vibrational frequencies, DFT.

Submitted: September 7, 2023. **Accepted:** January 24, 2024.

Cite this: Hraja MA, Al Hindawi AM, Shiltagh NM. Investigation of Electronic and Molecular Features of Zn₃S₃/PEG4000 Composite Using the DTF Method. JOTCSA. 2024;11(2):565-74.

DOI: <https://doi.org/10.18596/jotcsa.1356389>

***Corresponding author's E-mail:** nagam.altememi@uokerbala.edu.iq

1. INTRODUCTION

Zinc sulfide (ZnS) is a substantial compound with a wide range of applications due to its unique optical and structural features. ZnS nanomaterials have a relatively large bandgap of 3.6 eV, which increases with decreasing particle size (1). In addition, 3D-Zn-VI used in semiconductors has drawn wide attention due to their applications in short-wavelength light-emitting devices. 3D-ZnS is one such binary compound that appears in two structures: the Wurtzite (WZ) structure at high temperatures and a cubic zinc alloy (ZB) structure at low temperatures and ambient pressures (2-4). Zinc is widely used on electrodes in the deposition process industry with other metals like Sn-alloy (5). The preparation of nanomaterials occupies a

significant position in research centers, and the preparation methods have been varied, either physically or chemically, according to their application (6-8). Recently, polymers have played a vital role in improving and enhancing the characterizations of nanoparticles' surfaces (9,10). Polyethylene Glycol (PEG4000) is one of these polymers that is an ethereal compound belonging to the family of polymers with high molecular weight (11); some other names for the PEG4000 polymer include polyglycol, poly (ethylene oxide) (PEO), and poly (oxyethylene) (POE) (12). PEG is the most popular among the three types and the best among them to employ in the field of medicine and refers to polymers with molecular masses less than 20,000 g/mol. For instance, PEG 4000 is a safe and more effective drug compared to lactulose for the

treatment of constipation in children (13), where several clinical studies have demonstrated that PEG 4000 is effective in the treatment of constipation in adults and children (14,15). In addition, PEG 4000 acts as an osmotic agent that increases fecal water content. PEG4000 is nontoxic and non-immunogenic (16). Thanks to the feature of PEG4000, it is flexible and soluble in water, so that it can work at high osmotic pressures (17,18). It has been proven that nanoparticles have the advantages of mass production and high stability, so the manufacture of smart or stimuli-responsive polymers has been achieved. Either from natural or synthetic resources, one of the most important natural polymers used in the manufacture of medical preparations is dextrose gelatin. In contrast, synthetic polymers use polyethylene glycol (19,20). Density Functional Theory (DFT), which is an algorithm of quantum mechanical modeling utilized in the chemical and physical fields to discover electronic structure (21), has established itself as a valuable research tool to validate experimental conclusions or characterize those possibilities left open (22).

Computational processes offer precisely superior scales in chemical interactions and combinations phenomena, particularly (DFT) method, which theoretically presents predictions of material design through the geometrical structures (23) in addition to the low cost. Furthermore, the more quantitative predictions of phenomena that are made and confirmed by experiment, the more the overall theory is accepted when the theoretical investigation is "confirmed" for that specific experiment (24). Nevertheless, several theoretical studies have been relied on and taken into account in practical applications such as gas sensors (25).

DFT theory was recently employed to study the structural and electronic properties of ZnS molecules as a nanotube in different numbers of ZnS atoms (26,27), or by ab initio/DFT to study electronic and spectroscopic properties of ZnO-NPs. Furthermore, an investigation of Polyethylene Glycol (PEG) was based on a nanocomposite by DFT study to use as a drug in medical applications (23). On the other hand, to study the effect of polymers on nanoparticle behaviors, the structural and electronic properties of ZnS nanoparticles with the presence of PEG4000 have been investigated experimentally in our recent work (28). However, their structural, electronic, and vibrational features have not been theoretically investigated.

Therefore, this work could be promising for gaining more knowledge for this composite over theoretical study using the DFT theory.

2. COMPUTATIONAL DETAILS

The development of the quantum mechanical technique has been influenced by the density functional theory (DFT), which has been used to study the electronic structure and behavior of many electron systems. Disciplines of physics and chemistry employ functional analysis to gain an understanding of the electron density distribution. A many-electron system's ground state (GS) and other features can be identified using DFT, as demonstrated by this study. The most popular and adaptable method in computational physics and chemistry disciplines is, by far, DFT. Additionally, it has proven to be quite efficient at estimating the properties of materials in their ground state. The approach in this work uses DFT theory with hybrid B3LYP (Becke, three parameters, Lee-Yang-Parr) and a basis set with 6-311G**. Where the first asterisk above basis G represents the polarization set d-function for heavy atoms. However, the second sign indicates the polarization of p-functions of hydrogen atoms or sometimes must be written as 6-311G (d, p) (29,30). Because of the accuracy of this basis set, it was powerfully used to calculate energetic and electronic features in multiple phases (31). All those equations and theories were involved by Gaussian 09 and Gaussian View 6.0 software (32).

To achieve accurate results, the geometries of molecules were optimized precisely to lower the convergence thresholds. Furthermore, Frequencies of normal vibrations were calculated to confirm the minimal energy at geometric optimization by solving the self-consistent field (SCF) equation.

Figure (1-a) demonstrates the molecular structure of a cluster of three Zn atoms and three S atoms (Zn_3S_3); either (1-b) clarifies the cluster of Zn_3S_3 after adding PEG4000 polymer (C_2H_4O)_n, as adsorption process experimentally on PEG surface. These structures were optimized geometrically at the following conditions: maximum force, RMS force, max. displacement and RMS displacement converged at several steps, 0.000076, 0.000021, 0.000104, and 0.000099, respectively. Figure (2) shows the steps of geometrical optimization.

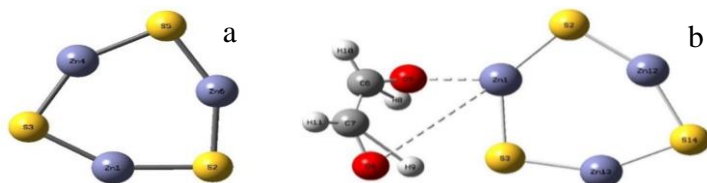


Figure 1: The optimized structures of ZnSNPs (Zn_3S_3) before adding PEG4000 (a), and after adding the polymer (b) using the DFT method with basis set 6-311G**.

The electronic features of the mentioned molecules were computed, which are Fermi level energy (E_f), Energy of bandgap (E_g), and Ionization potential (IP) that represents the amount of energy needed to break the structural unit of the weakest electron bond to the nucleus. The greater the ionization energy, the more difficult it is to extract the electron and electron affinity (EA), which is the amount of energy released when an electron is added to a gaseous atom, after identifying the Highest Occupied Molecular Orbital (HOMO) and Lowest Unoccupied Molecular Orbital (LUMO) energies by the following equations (33,34):

$$E_g = E_{LUMO} - E_{HOMO} \quad (1)$$

$$IP = -E_{HOMO} \quad (2)$$

$$EA = -E_{LUMO} \quad (3)$$

$$E_f = (E_{HOM} + E_{LUMO}) / 2 \quad (4)$$

In addition, to describe the chemical reactivity of the studied system between polymer-NPs, the quantum molecular identifiers (C_p , χ , η , S , and ω) were employed. These descriptors involved are generally: the chemical potential (C_p) is the energy that can be absorbed or released due to a change in the number of particles, and it can be known as the ferry energy in a semiconductor when a system of electrons at a temperature of absolute zero, electronegativity (χ) is a measure of an atom's ability to attract electrons in a chemical bond; the global hardness (η), the softness (S), and the electrophilicity index (ω) are by the following equations (35, 36):

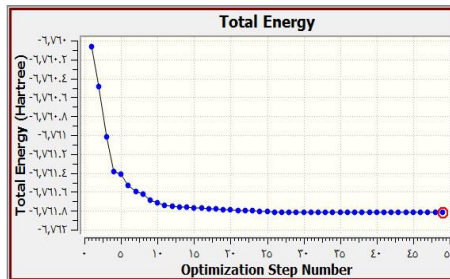
$$C_p = -\chi \quad (5)$$

$$\chi = IP + EA / 2 \quad (6)$$

$$\eta = IP - EA / 2 \quad (7)$$

$$S = 1 / \eta \quad (9)$$

$$\omega = -\chi^2 / 2\eta \quad (10)$$



Optimization Step Number = 49, Total Energy (Hartree) = -6761.821012

Figure 2: Steps of geometrical optimization with minimal energy DFT study using B3LYP-D/6-311 G.

3. RESULTS AND DISCUSSION

3.1. Vibrational Frequencies & FTIR spectra

Any way of connection with Ethylene Glycole polymer is a planar structure of the C1 point symmetry group. According to the equation (3N-6) for non-linear molecules, the number of normal vibration modes can be calculated, where N is the number of atoms. Hence, twelve vibrational modes were obtained for the Zn_3S_3 molecule, which consists of 6 atoms. These frequencies have been arranged in Table (1) from the lowest frequency of the patterns to the highest mode. The highest frequency modes are (11 and 12) in the range (408.23-408.89) cm^{-1} . In comparison, 36 modes were obtained for the $Zn_3S_3/PEG4000$ structure, including 14 atoms. The strongest modes at high frequencies are (33, 34, 35, and 36) at frequencies (3175.62, 3244.59, 3450.37, 374.07) cm^{-1} , respectively, as shown in Table (2).

On the other hand, the IR spectra of the studied structure were calculated at the range (0 – 4000) cm^{-1} using DFT- B3LYP levels with the 6-311G** basis set. The comparison of the FT-IR spectra between theoretical and experimental spectra is illustrated in Figure (3) for Zn_3S_3 and Zn_3S_3/PEG , observing a strong agreement between them.

Table 1: The range of normal vibrational modes for Zn_3S_3 from lowest to highest frequency.

No. Mode	Frequency/ cm^{-1}	No. Mode	Frequency/ cm^{-1}
MODE 1	89.33	MODE7	297.88
MODE2	90.87	MODE8	298.05
MODE3	106.96	MODE9	327.78
MODE4	107.06	MODE10	387.43
MODE5	146.05	MODE11	408.23
MODE6	170.53	MODE12	408.89

Commented [YB1]: The total energy (Hartree) axis is written in Indian language. Please convert into normal (Arabic) numbers.

Table 2: The range of normal vibrational modes for Zn₃S₃/PEG400 from lowest to highest frequency.

No. Mode	Frequency/cm ⁻¹	No. Mode	Frequency/cm ⁻¹	No. Mode	Frequency/cm ⁻¹
MODE 1	16.59	MODE 13	278.38	MODE 25	945.70
MODE 2	37.60	MODE 14	297.00	MODE 26	964.47
MODE 3	67.18	MODE 15	309.08	MODE 27	1138.66
MODE 4	80.75	MODE 16	335.13	MODE 28	1271.64
MODE 5	87.68	MODE 17	372.38	MODE 29	1322.46
MODE 6	98.75	MODE 18	393.31	MODE 30	1393.98
MODE 7	105.80	MODE 19	416.68	MODE 31	1407.61
MODE 8	120.49	MODE 20	431.47	MODE 32	1713.20
MODE 9	130.08	MODE 21	530.63	MODE 33	3175.62
MODE 10	154.22	MODE 22	666.68	MODE 34	3244.59
MODE 11	167.68	MODE 23	721.17	MODE 35	3450.37
MODE 12	257.22	MODE 24	767.55	MODE 36	3764.07

It was found that the broad peaks at frequency 3760 cm⁻¹ (DFT) and frequency 3480 cm⁻¹ belong to the black line (ZnS/PEG4000 (exp.)), indicating to the OH-stretching vibrations band (37, 38). This stretching vibration is significantly attributed to the hydrogen bonding (39). Meanwhile, this band for ZnS (exp.) in the pink line has red-shifted to the short frequency 3221 cm⁻¹ (long wavelength) due to the confinement quantum of phonon (26). This could be evidence of the effect of polymer that enhances the nano properties of ZnS particles.

In addition, the peaks of (1120 and 1110) cm⁻¹ for Zn₃S₃/PEG4000 (DFT) and ZnS/PEG4000 (Exp),

respectively, indicate the C–O–C band stretching vibrations (40). Other signed Peaks at (660, 657, and 648) cm⁻¹ are attributed to the stretching vibrations of the Zn–S bond and belong to the Zn₃S₃/PEG4000 (DFT), ZnS/PEG4000 (Exp), and Zn₃S₃ (DFT) respectively (41, 42). It was observed that the peaks of vibration bands at regions (416, 416, and 420) cm⁻¹ belong to (ZnS/PEG4000 (exp.), Zn₃S₃/PEG 4000 (DFT), and ZnS (exp.), respectively. Also, it is located at the range around 600 cm⁻¹, where the range of the appearance of the Zn–S bond is located around the range 450–1000. Agrees with Liu et. Al.'s work (43). Table (3) presents this comparison of FTIR spectra of mentioned molecules.

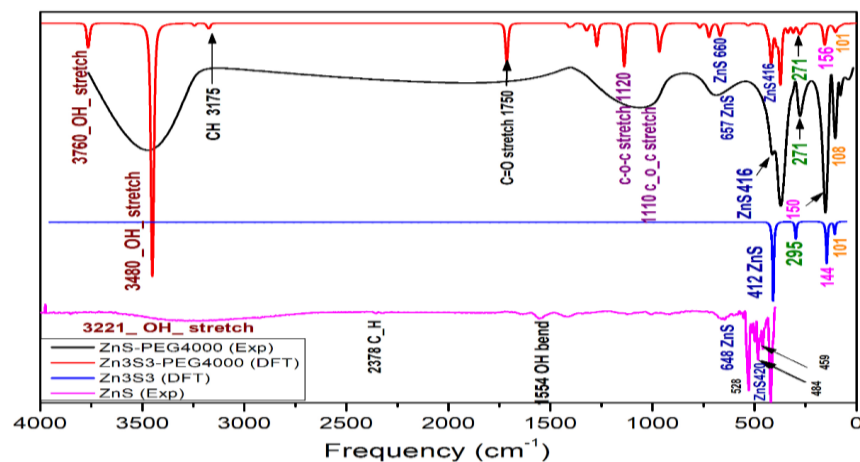
**Figure 3:** Comparison of the FTIR spectra for ZnSNPs before and after adding PEG polymer theoretically and experimentally showing remarkable agreement between them.

Table 3: Comparison of FTIR of studied structures between experimental and theoretical spectra for ZnSNPs before and after adding PEG polymer clarifying the range of functional groups.

ZnS/PEG (Exp)		Zn ₃ S ₃ /PEG (DFT)		ZnS (Exp)		Zn ₃ S ₃ (DFT)	
Functional group	The range	Functional group	The range	Functional group	The range	Functional group	The range
Zn - S	657-416	Zn-S	660-416	Zn - S	648-416	Zn - S	412
C - O - C	1110	C - O - C	1120				
O - H	3760	O - H	3480	O - H	3221		

3.2. Electronic Properties

Molecular orbital theory (MOT) is a significantly sophisticated model that covers comprehensive aspects relating to the bonding of orbitals, energies, chemical reactions, and their characterizations. From these orbitals are the highest occupied molecular orbital (HOMOs) which occupies by electrons in it and have the highest energy. The other one is the lowest unoccupied molecular orbital (LUMO), which has no electrons and the lowest energy. The values of those molecular orbitals were computed for ZnSNPs before and after adding PEG polymer using the DFT method with a 6-113G** basis set. By determining the HOMO, LUMO energies and the HOMO-LUMO (E_g) that are a valuable index of the interaction system, electronic properties IP , EA , E_f , E_g , C_p , χ , η , S and ω , were calculated using the (1-10) Equations. Table (4) demonstrates the electronic properties of ZnS-NP clusters before and after adding PEG4000 at room temperature. It was observed an agreement of E_g experimentally and theoretically around 4.2 (grey shaded) and 4.03 eV, respectively, for the ZnS cluster. Similarly, there are (4.5 eV - exp) and (4.459 eV - DFT) concerning ZnS-PEG. Figure (4) clarifies HOMO and LUMO MOs for mentioned molecules, where the energy gap (E_g) increases with adding polymer, indicating the effect of the PEG molecule on the ZnS particles as a capping agent, indicating the quantum confinement concept strongly, the greater value for the band gap (the smallest nanoparticle diameter) (44).

Table 4: Computed electronic features of ZnSNPs before and after adding PEG polymer at room temperature.

Properties	Zn ₃ S ₃ (DFT)	Zn ₃ S ₃ /PEG (DFT)
E_{HOMO}	- 7.0199	- 6.7014
E_{LUMO}	- 2.9886	- 2.2323
E_f / eV	- 5.0043	- 4.4668
E_g / eV	4.0310	4.4599
E_g / eV	4.2000 (Exp)	4.5000 (Exp)
IP / eV	7.0199	6.7014
EA / eV	2.9886	2.2323
C_p / eV	- 5.0043	- 4.4668
χ / eV	5.0043	4.4668
η / eV	2.0156	2.2323
S / (eV) ⁻¹	0.4961	0.4479

ω / eV	- 6.2122	- 4.4691
---------------	----------	----------

3.3. Molecular Electrostatic Potential

To evaluate the connections and interactions of non-covalent inside molecules with intermolecular distance and to examine the attractive or repulsive interactions, nonlocalized dispersion among the structures reactions, molecular electrostatic potential (MEP) diagram, and densities of the electron with charge were utilized (45) using B3LYP calculations with basis set 6-311G(d,p). The zones of these interactions were described in Figure (5) for a titled molecule to visualize three interaction areas based on the electron density function (46).

The being of hydrogen bonding is presented in blue zones. Red patches indicate the repulsive interactions and the green zones refer to the Van der Waals bonding (VdW) (46). Figure (5) shows the transformation of the colored from a cluster of Zn₃S₃ into Zn₃S₃/PEG4000 (a to b), respectively. Furthermore, The advantage of the molecular electrostatic potential scheme is that it is a useful tool for investigating reactivity to electrophilic or nucleophilic attacks in the studied systems depending on the charge distribution. The colored line shown in the upper edge in Fig. (5) is color-coded of the system referring to two regions (the range from -8.065×10^{-2} (red) to 8.065×10^{-2} (blue) and from -4.036×10^{-4} to 4.036×10^{-4} for ZnS cluster and Zn₃S₃-PEG-4000 surfaces respectively; the negative charge densities in red color represent the acceptor of the H-bonding of molecules. Meanwhile, the second zone demonstrates positive charge densities in the blue ruler for the donor of the H-bonding (47).

On the other hand, If all Zn₃S₃/PEG4000 surfaces are plotted with all iso-surface values, only the top surface will be seen. To see all the studied molecules' surfaces, it can simply plot each surface as a contour around the molecule, as shown in Figures (5- c and d) for the Zn₃S₃ cluster and Zn₃S₃/PEG4000 surface, respectively.

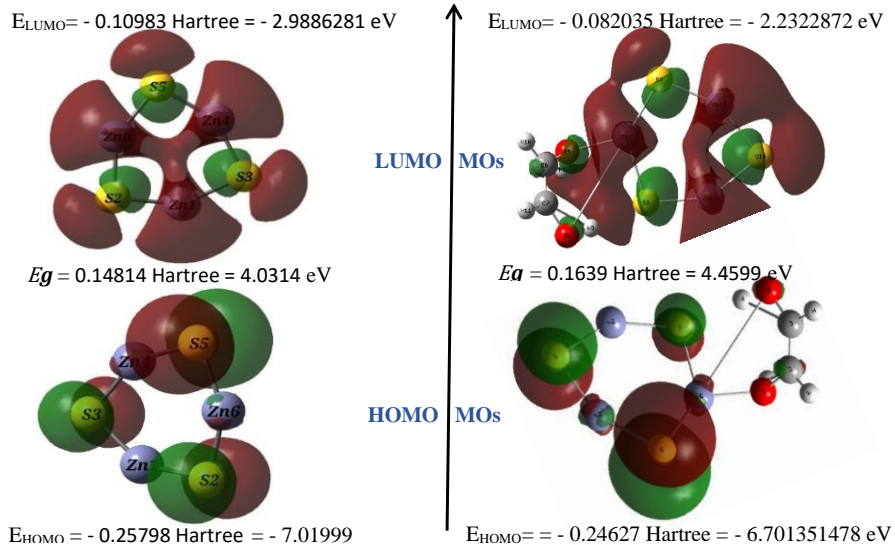


Figure 4: Frontier molecular (HOMO&LUMO) orbitals and E_g of ZnSNPs cluster (on left), for Zn_3S_3 /PEG4000 (on right). An increase in E_g around 0.43 eV with adding PEG polymer indicates the enhancement for nano features.

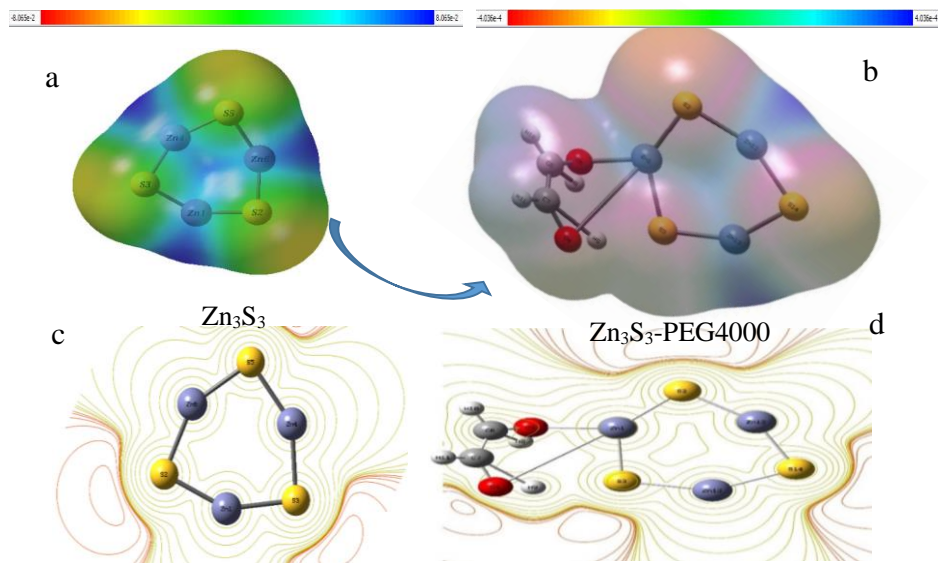


Figure 5: Charge density distribution as color-coded ruler in upper edge (red color for negative charge and blue for positive), MEP surface surfaces diagram of Zn_3S_3 (a) Zn_3S_3 _PEG4000 (b), MEP contour surface of Zn_3S_3 (c) Zn_3S_3 _PEG4000 (d).

4. CONCLUSION

Structural and electronic features of a cluster of three atoms of Zn and three atoms of S (Zn_3S_3) have been calculated theoretically for the first time using the DFT computations with the hybrid B3LYP and 6-311G (d, p) basis set. The same calculations have been conducted for the mentioned molecule after adding the PEG4000 polymer ($Zn_3S_3/PEG4000$). The spectral lines, such as FTIR spectra, were analyzed, and a comparison has been made between the two structures experimentally and theoretically. A strong agreement of active peak position between experimental and theoretical spectra was found.

Vibrational frequencies assigned around the range 0–4000 cm^{-1} were systematically analyzed, and 12 modes of vibration of the Zn_3S_3 molecule and 36 modes of the $Zn_3S_3/PEG4000$ compound were observed. In addition, the energies of HOMO and LUMO orbitals were calculated and illustrated to evaluate the Energy gap (E_g). A remarkable effect of the polymer after adding to the ZnS cluster was noticed on the Energy gap, where the gap increases from (4.031 to 4.459) eV, and these findings are in agreement with the experimental value indicating the quantum confinement concept strongly, the greater value for the band gap (the smallest nan particle diameter). The molecular electrostatic potential (MEP) diagram and charge densities of isosurface and contour diagrams were estimated, showing these compounds' nucleophilic and electrophilic attack.

5. ACKNOWLEDGMENTS

The authors would like to thank the Department of Chemistry, College of Education for Pure Science, University of Kerbala, and the Department of Physics, College of Science, University of Kerbala, for supporting this work.

6. CONFLICTS OF INTEREST

The authors declared no conflict of interest.

7. REFERENCES

- Hamad S, Catlow CRA. Computational study of the relative stabilities of ZnS clusters, for sizes between 1 and 4nm. *J Cryst Growth* [Internet]. 2006 Aug 15;294(1):2–8. Available from: [<URL>](#).
- Lashgari H, Boochani A, Shekaari A, Solaymani S, Sartipi E, Mendi RT. Electronic and optical properties of 2D graphene-like ZnS: DFT calculations. *Appl Surf Sci* [Internet]. 2016 Apr 30;369:76–81. Available from: [<URL>](#).
- Abd-Alameer Jawad S, Ali Ahmed H. Synthesis, Characterization and Study of Amide Ligand Type N_2S_2 and Metal Complexes with Di Valance Manganese, Zinc and tri Valance Iron. *Ann Rom Soc Cell Biol* [Internet]. 2021 Apr 2;25:8511–20. Available from: [<URL>](#).
- Wang Z, Daemen LL, Zhao Y, Zha CS, Downs RT, Wang X, et al. Morphology-tuned wurtzite-type ZnS nanobelts. *Nat Mater* [Internet]. 2005 Dec 1;4(12):922–7. Available from: [<URL>](#).
- Alesary HF, Ismail HK, Shiltagh NM, Alattar RA, Ahmed LM, Watkins MJ, et al. Effects of additives on the electrodeposition of Zn Sn alloys from choline chloride/ethylene glycol-based deep eutectic solvent. *J Electroanal Chem* [Internet]. 2020 Oct 1;874:114517. Available from: [<URL>](#).
- Turki ZT, Al Hindawi AM, Shiltagh NM. Green Synthesis of CdS Nanoparticles using Avocado Peel Extract. *NanoWorld J* [Internet]. 2022;08(03). Available from: [<URL>](#).
- Shiltagh NM, Ridha NJ, Hindawi AM Al, Tahir KJ, Madlol RA, Alesary HF, et al. Studying the optical properties of silver nitrates using a pulsed laser deposition technique. In: *AIP Conference Proceedings* [Internet]. American Institute of Physics Inc.; 2020. p. 050059. Available from: [<URL>](#).
- Al Hindawi AM, Obaid NH, Juadah I, Shiltagh N, Tahit KJ. Fabrication and Characterization of Silver Nanoparticles Using Plant Extract. *Int J Pharm Res* [Internet]. 2020 Mar 1;12(2):985–8. Available from: [<URL>](#).
- Jawad RA, Shiltagh N, Aboud LH, Watkins MJ. The Effect of Silver Nanoparticles on a Mixture of MB-dye/PVA-Polymer as Determined by Absorption and Emission Spectra Measurements. *NanoWorld J* [Internet]. 2021;7(1):13–21. Available from: [<URL>](#).
- Tahir KJ, Obeed HH, Shiltagh NM. Study optical properties of R6G dye doped in polymer PVA. *J Phys Conf Ser* [Internet]. 2019 Jul 1;1234(1):012048. Available from: [<URL>](#).
- Brittain WJ, Minko S. A structural definition of polymer brushes. *J Polym Sci Part A Polym Chem* [Internet]. 2007 Aug 15;45(16):3505–12. Available from: [<URL>](#).
- Almashhadani NJH. UV-Exposure effect on the mechanical properties of PEO/PVA blends. *Iraqi J Sci* [Internet]. 2021 Jul 2;62(6):1879–92. Available from: [<URL>](#).
- Wang Y, Wang B, Jiang X, Jiang M, Xu C, Shao C, et al. Polyethylene glycol 4000 treatment for children with constipation: A randomized comparative multicenter study. *Exp Ther Med* [Internet]. 2012 May 17;3(5):853–6. Available from: [<URL>](#).
- Corazziari E, Badiali D, Habib FI, Reboa G, Pitto G, Mazzacca G, et al. Small volume isosmotic polyethylene glycol electrolyte balanced solution (PMF-100) in treatment of chronic nonorganic constipation. *Dig Dis Sci* [Internet]. 1996 Aug;41(8):1636–42. Available from: [<URL>](#).
- Pashankar DS, Bishop WP. Efficacy and optimal dose of daily polyethylene glycol 3350 for treatment of constipation and encopresis in children. *J Pediatr* [Internet]. 2001 Sep 1;139(3):428–32. Available from: [<URL>](#).
- Keerthana M, Komala G, Nagaraju R. Polymeric Micelles of Oregano - Formulation and In-Vitro Evaluation. *Curr Trends Biotechnol Pharm* [Internet]. 2023 Feb 20;17(1):660–70. Available from: [<URL>](#).
- Chen X, Liu G, Zhao L, Du L, Xie J, Wei D. *Lactiplantibacillus plantarum* X7022 ameliorates loperamide-induced constipation and modulates gut microbiota in mice. *Food Bioeng* [Internet]. 2022 Dec 2;1(3–4):252–63.

Available from: [<URL>](#).

18. Wu LC, Zheng ED, Sun HY, Lin XZ, Pan JY, Lin XX. Observation of the application effect of low-volume polyethylene glycol electrolyte lavage solution (PEG-ELS) combined with ascorbic acid tablets in bowel preparation for colonoscopy in hospitalized patients. *Front Oncol* [Internet]. 2023 Apr 14;13:1038461. Available from: [<URL>](#).

19. Yu Z, Shen X, Yu H, Tu H, Chittasupho C, Zhao Y. Smart Polymeric Nanoparticles in Cancer Immunotherapy. *Pharmaceutics* [Internet]. 2023 Feb 26;15(3):775. Available from: [<URL>](#).

20. Figueiredo AQ, Rodrigues CF, Fernandes N, de Melo-Diogo D, Correia IJ, Moreira AF. Metal-Polymer Nanocojugates Application in Cancer Imaging and Therapy. *Nanomaterials* [Internet]. 2022 Sep 13;12(18):3166. Available from: [<URL>](#).

21. Rahimi R, Solimannejad M. Empowering hydrogen storage performance of B_4C_3 monolayer through decoration with lithium: A DFT study. *Surfaces and Interfaces* [Internet]. 2022 Apr 1;29:101723. Available from: [<URL>](#).

22. Huang EW, Lee WJ, Singh SS, Kumar P, Lee CY, Lam TN, et al. Machine-learning and high-throughput studies for high-entropy materials. *Mater Sci Eng R Reports* [Internet]. 2022 Jan 1;147:100645. Available from: [<URL>](#).

23. Adekoya OC, Adekoya GJ, Sadiku RE, Hamam Y, Ray SS. Density Functional Theory Interaction Study of a Polyethylene Glycol-Based Nanocomposite with Cephalexin Drug for the Elimination of Wound Infection. *ACS Omega* [Internet]. 2022 Sep 27;7(38):33808–20. Available from: [<URL>](#).

24. Huang B, von Lilienfeld OA, Krogel JT, Benali A. Toward DMC Accuracy Across Chemical Space with Scalable Δ -QML. *J Chem Theory Comput* [Internet]. 2023 Mar 28;19(6):1711–21. Available from: [<URL>](#).

25. Alaa Hussein T, Shiltagh NM, Kream Alaarag W, Abbas RR, Jawad RA, Abo Nasria AH. Electronic and optical properties of the BN bilayer as gas sensor for CO_2 , SO_2 , and NO_2 molecules: A DFT study. *Results Chem* [Internet]. 2023 Jan 1;5:100978. Available from: [<URL>](#).

26. Hussein MT, Thjeel HA. Vibration Properties of ZnS nanostructure Wurtzoids: ADFT Study. *J Phys Conf Ser* [Internet]. 2019 Feb 1;1178(1):012015. Available from: [<URL>](#).

27. Hussain MT, Thjeel HA. Study of geometrical and electronic properties of ZnS wurtzoids via DFT. *Chalcogenide Lett* [Internet]. 2018;15(10):523–8. Available from: [<URL>](#).

28. Hraja MA, Al Hindawi AM, Shiltagh NM. Synthesis, Characterization And Studying The Optical Properties Of Zinc Sulfide Nanoparticles In The Presence Of Peg4000. *J Aeronaut Mater*. 2023;43:37–48.

29. Becke AD. Density-functional thermochemistry. III. The role of exact exchange. *J Chem Phys*. 1993 Apr 1;98(7):5648–52. Available from: [<URL>](#).

30. Lee C, Yang W, Parr RG. Development of the Colle-Salvetti correlation-energy formula into a functional of the electron density. *Phys Rev B Condens Matter* [Internet]. 1998;37:785–9. Available from: [<URL>](#).

31. Sadoon AM. Theoretical Investigation of the Structures and Energetics of (MX)-Ethanol Complexes in the Gas Phase. *J Turkish Chem Soc Sect A Chem* [Internet]. 2023 Feb 28;10(1):47–54. Available from: [<URL>](#).

32. Pople JA, Gill PMW, Johnson BG. Kohn–Sham density-functional theory within a finite basis set. *Chem Phys Lett* [Internet]. 1992 Nov 20;199(6):557–60. Available from: [<URL>](#).

33. Parey V, Jyothirmai MV, Kumar EM, Saha B, Gaur NK, Thapa R. Homonuclear B_2/B_3 doped carbon allotropes as a universal gas sensor: Possibility of CO oxidation and CO_2 hydrogenation. *Carbon N Y* [Internet]. 2019 Mar 1;143:38–50. Available from: [<URL>](#).

34. Huang Y, Rong C, Zhang R, Liu S. Evaluating frontier orbital energy and HOMO/LUMO gap with descriptors from density functional reactivity theory. *J Mol Model* [Internet]. 2017 Jan 8;23(1):3. Available from: [<URL>](#).

35. Kaufman GB. *Inorganic chemistry: principles of structure and reactivity*, 4th ed. (Huheey, James E.; Keiter, Ellen A.; Keiter, Richard L.). *J Chem Educ*. 1993 Oct 1;70(10):A279. Available from: [<URL>](#).

36. De Proft F, Geerlings P. Conceptual and Computational DFT in the Study of Aromaticity. *Chem Rev* [Internet]. 2001 May 1;101(5):1451–64. Available from: [<URL>](#).

37. Kaur J, Sharma M, Pandey OP. Photoluminescence and photocatalytic studies of metal ions (Mn and Ni) doped ZnS nanoparticles. *Opt Mater (Amst)* [Internet]. 2015 Sep 1;47:7–17. Available from: [<URL>](#).

38. Kharazmi A, Faraji N, Mat Hussin R, Saion E, Yunus WMM, Behzad K. Structural, optical, opto-thermal and thermal properties of ZnS–PVA nanofluids synthesized through a radiolytic approach. *Beilstein J Nanotechnol* [Internet]. 2015 Feb 23;6:529–36. Available from: [<URL>](#).

39. Abdelmoula H, Ghalla H, Nasr S, Bahri M, Bellissent-Funel MC. Hydrogen-bond network in liquid ethylene glycol as studied by neutron scattering and DFT calculations. *J Mol Liq* [Internet]. 2016 Aug 1;220:527–39. Available from: [<URL>](#).

40. Pretsch E, Bühlmann P, Badertscher M. *Structure Determination of Organic Compounds*. Berlin, Heidelberg: Springer Berlin Heidelberg; 2020. Available from: [<URL>](#).

41. Yang H, Holloway PH, Ratna BB. Photoluminescent and electroluminescent properties of Mn-doped ZnS nanocrystals. *J Appl Phys* [Internet]. 2003 Jan 1;93(1):586–92. Available from: [<URL>](#).

42. Nanaki SG, Kyzas GZ, Tzereme A, Papageorgiou M, Kostoglou M, Bikiaris DN, et al. Synthesis and characterization of modified carrageenan microparticles for the removal of pharmaceuticals from aqueous solutions. *Colloids Surfaces B Biointerfaces*. 2015 Mar;127:256–65. Available FROM: [<URL>](#).

43. Liu LN, Dai JG, Zhao TJ, Guo SY, Hou DS, Zhang P, et al. A novel Zn(II) dithiocarbamate/ZnS nanocomposite for highly efficient Cr^{6+} removal from aqueous solutions. *RSC Adv* [Internet]. 2017 Jul 12;7(56):35075–85. Available from: [<URL>](#).

44. Bhargava RN, Gallagher D, Hong X, Nurmiikko A. Optical properties of manganese-doped nanocrystals of ZnS. *Phys*

Hraja MA et al. JOTCSA. 2024; 11(2): 565-574

RESEARCH ARTICLE

Rev Lett [Internet]. 1994 Jan 17;72(3):416-9. Available from: [<URL>](#).

45. Shamim M, Perveen M, Nazir S, Hussnain M, Mehmood R, Khan MI, et al. DFT study of therapeutic potential of graphitic carbon nitride (g-C₃N₄) as a new drug delivery system for carboplatin to treat cancer. J Mol Liq [Internet]. 2021 Jun 1;331:115607. Available from: [<URL>](#).

46. Noureddine O, Issaoui N, Medimagh M, Al-Dossary O, Marouani H. Quantum chemical studies on molecular

structure, AIM, ELF, RDG and antiviral activities of hybrid hydroxychloroquine in the treatment of COVID-19: Molecular docking and DFT calculations. J King Saud Univ - Sci [Internet]. 2021 Mar 1;33(2):101334. Available from: [<URL>](#).

47. Adekoya OC, Adekoya GJ, Sadiku ER, Hamam Y, Ray SS. Application of DFT Calculations in Designing Polymer-Based Drug Delivery Systems: An Overview. Pharmaceutics [Internet]. 2022 Sep 19;14(9):1972. Available from: [<URL>](#).



Competitive Inhibition and Synergistic Effects of Nutraceutical and Metabolite Molecules on Anti-Acetylcholinesterase Activity

Munteha Girgin¹ , Shirin Tarbiat¹ , Sevim Isik^{2,3} , Nigar Kantarci-Carsibasi^{1*} 

¹Department of Chemical Engineering, Uskudar University, Uskudar, Istanbul, Turkey.

²Department of Molecular Biology and Genetics, Uskudar University, Uskudar, Istanbul, Turkey

³Uskudar University, Stem Cell Research and Application Center (USKOKMER), Istanbul, Turkey.

Abstract: The rapidly increasing prevalence of Alzheimer's disease (AD) poses a significant global public health threat. While medications such as Donepezil, Galantamine, and Rivastigmine are used, their serious side effects and limited healing fail to provide a definite cure. Consequently, combination therapies are being explored to enhance the efficacy of existing drugs. This study aims to evaluate the anti-acetylcholinesterase activities of previously identified nutraceutical and metabolite compounds, namely Queuine, Etoperidone, and Thiamine. Combined use of Queuine with Donepezil, Etoperidone, and Thiamine on acetylcholinesterase enzyme inhibition is also evaluated. The effects of the drug combinations on cell viability and acetylcholinesterase inhibition were investigated by using safe doses determined for each drug. The cytotoxic effect of drug combinations was investigated on the SH-SY5Y cell line using the RTCA method. All the individual or drug combinations were non-toxic to neuronal cells. Anti-acetylcholinesterase activities were estimated by Ellman's method yielding the inhibition percentages as 70%, 61%, 45%, and 51% for Donepezil, Etoperidone, Queuine, and Thiamine, respectively. When drug combinations were analyzed, competitive inhibition resulted for Queuine+Donepezil and Queuine+Thiamine, the enzyme inhibition percentages being diminished to 47% and 21%, respectively. A significant synergistic effect was observed for Queuine+Etoperidone with the highest inhibition of 74%. This study provides the first evidence of the nutraceutical molecule Queuine's impact on acetylcholinesterase inhibition and the synergistic effect of Queuine and Etoperidone as a potent drug combination surpassing the effectiveness of Donepezil. Queuine and Etoperidone synergism may serve as a potential AD treatment by further in vivo validations.

Keywords: Alzheimer's Disease (AD), Acetylcholinesterase (AChE), Ellman assay, Queuine, Etoperidone.

Submitted: September 28, 2023. **Accepted:** January 14, 2024.

Cite this: Girgin M, Tarbiat S, Isik S, Kantarci Carsibasi N. Competitive Inhibition and Synergistic Effects of Nutraceutical and Metabolite Molecules on Anti-Acetylcholinesterase Activity. JOTCSA. 2024;11(2):575-84.

DOI: <https://doi.org/10.18596/jotcsa.1367877>

***Corresponding author's E-mail:** nigar.carsibasi@uskudar.edu.tr

1. INTRODUCTION

Alzheimer's disease (AD) is a neurodegenerative disorder posing a significant challenge in identifying effective treatments due to its intricate etiology. While the exact cause of the disease is unknown, recent insights into disease progression have led to several hypotheses such as the cholinergic hypothesis which is reflected by reduced levels of acetylcholine due to overexpression of acetylcholinesterase enzyme (AChE), amyloid beta (A β) related cascade which involves plaque aggregation, neurofibrillary tangle formation, mitochondrial dysfunction, metal toxicity, and generation of reactive oxygen species. Current therapeutic drug options for AD patients include; Donepezil, Galantamine, and Rivastigmine which are marketed

as AChE inhibitors, and Memantine which is the N-Methyl-D-aspartate receptor antagonist, as approved by the FDA. Donepezil is a synthetic drug, while Galantamine and Rivastigmine are obtained from natural sources.

Emerging studies reported a close correlation between these disease-related hypotheses. Castro and Martinez (2006) showed that other than the cholinergic function, AChE owns a secondary non-cholinergic function which is controlling A β deposition (1). It is suggested that the interaction of AChE with A β protein may enhance the aggregation of insoluble plaques in AD patients (2,3). AChE enzyme possesses two crucial binding sites: peripheral anionic site (PAS) and catalytic active site (CAS). Drugs that bind to CAS and PAS are reported to have

a dual effect of boosting acetylcholine levels and at the same time preventing A β plaque formation (4,5). In another study, the generation of A β plaques was reported to promote the glutamate receptors and increase calcium ion expression leading to neural loss (6). Deposition of A β aggregates may also trigger oxidative damage and inflammation contributing to AD progression (7). Hence, there is an emerging need for a dual-site multi-target drug that would impact two main concerns: AChE inhibition through interacting with the CAS and preventing A β plaque aggregation through interacting with the PAS. Drugs that bind to the PAS of AChE may also hinder substrate binding by blocking the entrance of the gorge of the active site as well (8). Recent studies have suggested that targeting various pathways, having fewer side effects, and demonstrating long-term therapeutic effects, make natural-derived active compounds promising approaches in Alzheimer's disease (AD) treatment (9). A new road to AD pharmacological treatment is thus designing dual-binding site natural origin inhibitors. Stemming from this emergence of new generation AChE inhibitors, a recent study conducted to inhibit plaque aggregation through AChE inhibition by natural compounds curcumin and piperine demonstrated promising neuroprotective effects in SH-SY5Y cells. Furthermore, the combined use of these compounds achieved a synergistic effect with a better outcome than individual usage (10).

Nutraceuticals are derived from isolated phytochemicals, often in their pure form or as mixtures of flavonoids (e.g. Quercetin, Epigenin, and anthocyanins), phenolic acids (e.g. Catechins, Gallic Acids, curcumin, resveratrol, and epigallocatechin-3-gallate), and alkaloids (e.g. morphine, strychnine, quinine, ephedrine, and nicotine). Several studies have demonstrated the effects of natural phytochemicals on Alzheimer's disease treatment and nutraceutical-based drug discovery (11). However, more research is needed to explore the synergistic effects of these isolated metabolites. A recent study was conducted to examine the synergistic effect of herbal extracts on anti-acetylcholinesterase activity. Compounds that are extracted such as gallic acid, palmatine, berberine, etc. were tested for their inhibitory activity. Palmatine and berberine combined use was reported to have a synergistic effect by binding to the PAS region, blocking the gorge, and hindering enzymatic activity (8). In another recent study, it was demonstrated that the crude extract exhibited a promising cholinesterase inhibitory and neuroprotective effect against A β 25-35 cytotoxicity, in comparison to the fractions containing Hinokinin and Cubebin lignan (12). Choi et al. (2013) investigated the neuroprotective effects of flavonoids against amyloid beta (A β) and discovered that flavonoids inhibited A β aggregation and A β -induced cytotoxicity in PC12 neuronal cells. (13). They specifically studied two isolated flavonoids, daidzein, and baicalein, and observed that while they individually exhibited similar anti-A β properties, their combination significantly reduced A β aggregation. This finding suggests the potential of baicalein and daidzein as promising approaches in developing nutraceuticals for Alzheimer's disease

treatment in the future. Coqueiro et al. (2023) studied the AChE inhibitory effect of the alkaloid fraction obtained from *Pterogyne nitens*. (14). They identified three isoprenylated guanidine alkaloids (Galegine, Ptero-gynidine, and Pterogynine) from the ethanol extract of leaves of *P. nitens*, all of which exhibited potential anti-acetylcholinesterase activity. The highest inhibition was observed with Pterogynidine.

Hybridization of the available drugs such as donepezil and tacrine by combining indanone and quinoline heterocyclic scaffolds was also studied. Several hybrid ligands were synthesized and tested for their cholinergic and non-cholinergic functions. Promising hybrid new leads that serve as modifying agents against AD by increasing the cholinergic function, decreasing the A β toxicity, and promoting neurite outgrowth were discovered (15). In another recent study individual and drug combinations of donepezil, tacrine, berberine, and galantamine were investigated and it was found that the berberine + galantamine drug combination produced the most potent synergism and reduced the total drug dose by 72% (16).

Recently, we conducted a systematic in silico strategy with in vitro evaluation to identify natural-derived molecules as potential AChE inhibitors in AD treatment. Three lead compounds namely, Queuine, Thiamine, and Etoperidone were identified as promising AChE inhibitors and interactions were compared with FDA-approved synthetic and natural source drugs namely Donepezil and Galantamine (17). Queuine and Thiamine (Vitamin B₁) are classified as nutraceuticals, while Etoperidone is a metabolite. These compounds yielded good docking scores and performed essential interactions with CAS and PAS sites of AChE that are crucial for the enzyme functioning. These interactions were prolonged as monitored by molecular dynamics simulations. Previous literature studies have already demonstrated the inhibitory effect of Thiamine on AChE (18, 19). However, Etoperidone and Queuine have not been evaluated for AChE inhibitory activity yet. Previous literature studies reported that Etoperidone was inter-linked to tau-hyperphosphorylation and Queuine was engaged in an amyloid-beta-related cascade (20-22) Hence in our previous work two new promising AChE inhibitors: Queuine and Etoperidone that may have a multi-target activity were proposed for the first time.

Considering the putative role of both CAS and PAS regions of AChE in managing disease control, it is evident that dual-binding site inhibitors may acquire importance for AD treatment. Thus, in the present study, we aim to further support our previous findings with enzyme inhibition assays and obtain a relative comparison for AChE inhibition among our lead molecules both individually and in combined use forms. The results of the present study are hoped to pave the way to propose drug or drug combinations of natural origin, namely Queuine, Etoperidone, and Thiamine, that would have dual-site binding to AChE and result in high enzyme inhibition. In short, we aim to shed light on the combined use of a PAS-effective

drug with a CAS-effective one. Would this lead to a synergistic effect which in turn would result in a boosted inhibitory action as compared to individual use of both drugs or contrary to what we expect would facilitate a competitive antagonism and hinder the individual inhibitory activities? In the present study, we tested both individuals and combinations of Queuine with other lead compounds using RTCA cell culture assay and Ellman's method for AChE assay (23) to address these issues. This research aims to propose novel drugs and drug combinations with low-risk and dual-action properties that may have therapeutic potential to address AD.

2. EXPERIMENTAL SECTION

2.1. Chemicals and Reagents

The chemical compounds used in the experiments, namely Donepezil hydrochloride (Catalog No: D6821) and Galantamine hydrobromide (Catalog No: G1660), Thiamine hydrochloride (Catalog No: T1270), were purchased from Sigma-Aldrich. Etoperidone hydrochloride (Catalog No: sc-211494) and Queuine hydrochloride (Catalog No: sc-394021) were obtained from Santa Cruz Biotechnology. The other chemical compounds used in the study were purchased from Sigma-Aldrich Co. (St. Louis, MO, USA). This study utilized SH-SY5Y (human neuroblastoma) cell lines. The SH-SY5Y cell line (CRL-2266) was provided by ATCC.

2.2. Cell Culture

After dissolving the cell line stored in a nitrogen tank for long-term use, the cells were removed from the culture dish with a 0.25 Trypsin/EDTA solution when they reached 70% density in the culture flasks. The cells were incubated in DMEM (Capricorn) supplemented with 10% heat-inactivated fetal bovine serum (FBS) and 0.1 mg/mL of penicillin at 37°C with 5% CO₂. The medium was refreshed every 48 hours, and passages were made every 5 days based on cell confluency.

2.3. Real Time Cell Analysis (RTCA) of Candidate Drugs in SH-SY5Y Cell Line

In our previous study, the optimal safe doses were determined for Donepezil, Thiamine, Queuine, and Etoperidone. In this study, we evaluated the competitive effects of Queuine in combination with Donepezil, Etoperidone, and Thiamine on cell growth and viability in cell culture using real-time cell analysis (RTCA, xCELLigence). The RTCA system is an analytical technique that enables real-time monitoring of cellular events, such as proliferation, by measuring the electrical impedance passing through microelectrodes integrated beneath specialized plates. A 16-well e-plate compatible with the RTCA device, consisting of two plates with eight wells each, was used. Initially, 100 µL of DMEM containing 15% FBS was added to cell culture to the wells to obtain the background density. Subsequently, 3x10⁴ cells were seeded in the culture medium at 100 µL. After 24 hours, the determined concentration ranges were applied individually and in combination. Previous studies on Donepezil indicated no significant impact on cell viability up to 10 µM, but a decline in cell viability was observed after reaching

15 µM (24). Referring to our previous study, we administered the safe dose of 15 µM for Donepezil on the SH-SY5Y cell line (17). Similarly, we used our previously determined safe doses on SH-SY5Y cell lines for the rest of the drugs as well. The safe doses were: Queuine (1.25 µM), Etoperidone (70 µM) and Thiamine exhibited no toxicity even at high doses. Referring to our previous study, we applied a concentration of 600 µM for Thiamine (17). To assess the synergistic effects of Queuine with Donepezil, Etoperidone, and Thiamine on cell viability, we administered a combination of Queuine at a safe concentration of 1.25 µM, Donepezil at 15 µM, Etoperidone at 70 µM, and Thiamine at 600 µM. Each selected dose was applied to two different wells. The first two wells were assigned as the control group without drug treatment. The growth curve was obtained from the data generated by the RTCA device 48 hours after drug administration. The RTCA experiments were repeated three times for each drug group.

2.4. Protein Estimation Assay

The required proteins for the Ellman method (23-25) were obtained from the SH-SY5Y cell line. A cell seeding of 1.2 x 10⁶ cells per petri dish was performed. After 24 hours of seeding, drug administration was carried out at predetermined doses. Following a 48-hour incubation period with the drugs, the petri dishes were washed with PBS and 100 µL of RIPA cell lysis buffer were added. The proteins were collected by scraping the petri dish surface. The protein quantity was determined using the BCA (Bicinchoninic Acid) (26) method.

2.5. Acetylcholinesterase Enzyme (AChE) Inhibition Assay

Ellman's method involves the hydrolysis of acetylthiocholine iodide by AChE enzyme or butyrylthiocholine chloride by BChE enzyme, resulting in the formation of thiocholine. Thiocholine then reacts with the Ellman's reagent, 5,5'-dithiobis (2-nitrobenzoic acid) (DTNB), producing a yellow-colored 2-nitro-5-thiobenzoate (TNB) which can be detected at 405 nm. The rate of yellow color production is measured at 405 nm to indicate enzyme activity. AChE activity was determined using a 96-well microplate reader (OMEGA). A 200 µL protein solution (2 mg/mL, 0.1 M phosphate buffer, pH 8.0) as enzyme source was mixed with a 100 µL solution of DTNB (3.3 mM, 0.1 M phosphate-buffered solution, pH 7.0) containing NaHCO₃ (6 mM), and 500 µL phosphate buffer (pH 8.0). After incubating for 3 minutes at 25 °C, AChE activity was evaluated by measuring the change in absorbance at 405 nm using a spectrophotometer. This experiment was repeated three times.

2.6. Statistical Analysis

All analysis data obtained from the RTCA device and the data read by the microplate reader (OMEGA) were documented using the MARS application. RTCA data were analyzed using GraphPad Prism 9.5.1 software to determine the significance compared to the control group. Statistical analysis was performed using one-way ANOVA with multiple comparisons using the Tukey test.

3. RESULTS AND DISCUSSION

3.1. Interactions of Drug Molecules with AChE

In our previous study, we conducted systematic simulations including virtual screening, natural database generation, molecular docking, molecular dynamics, MM-GBSA binding free energy

calculations, and ADMET analysis to propose promising natural molecules with anti-acetylcholinesterase activity. The identified compounds were Thiamine, Queuine, and Etoperidone which interact with important binding sites and possess dual binding properties to CAS and PAS of AChE (Figure 1).

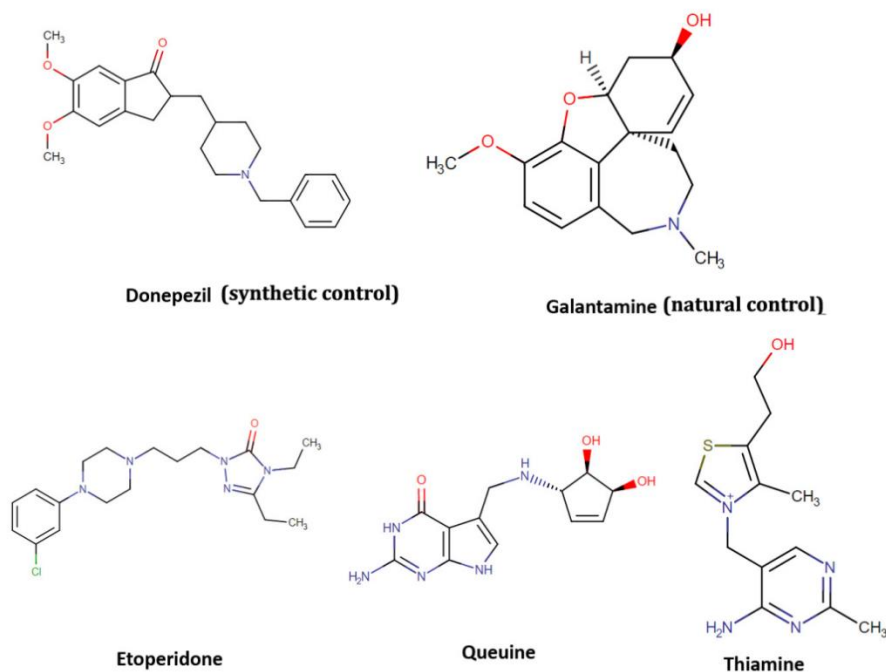


Figure 1: Structures of AChE inhibitors investigated in the present study.

The details about the methodology can be found in Girgin et al. (2023) (17). The docking scores for AChE and half inhibitory concentration (IC₅₀) of each compound were determined on SH-SY5Y cell lines. The docking scores obtained were -10.1, -10.1, and -13.4 kcal/mol for Queuine, Thiamine, and Etoperidone, respectively which may be compared to two control benchmark drugs namely Donepezil and Galantamine yielding -14.8 and -8.1 kcal/mol, respectively. The interactions with CAS and PAS regions of AChE were also investigated by molecular docking and molecular dynamics simulations. Results revealed that Queuine interacts mainly with PAS similar to Galantamine, while Etoperidone and Thiamine interact with both CAS and PAS of AChE similar to Donepezil (Figure 2). As depicted in Figure 2, the CAS residues of AChE are His 447 and Ser 203 and PAS residues consist of Asp 72, Asp74, Tyr124, Ser 125, Trp 286, Tyr 337, and Tyr 341.

IC₅₀ values that reflect the relative potencies of each drug were determined by in vitro cell culture assay on SH-SY5Y cells using RTCA and MTT assays. IC₅₀ values were 70.9, 712.8, 18780.3, 222.2, and 556.0 μM for Queuine, Etoperidone, Thiamine, Donepezil and Galantamine, respectively. Among these Queuine has the highest potency with a much lower IC₅₀ value as compared to both Donepezil and Galantamine. In light of this work, we further supported these findings with individual and combined drug use experiments on SH-SY5Y cell lines and enzyme inhibition tests to explore

synergistic and/or competitive effects on anti-acetylcholinesterase activity.

3.2. RTCA Assay: Effects of the Reagents on Cell Viability

The effects of Donepezil, Etoperidone, and Thiamine as well as the combinations of Queuine with Donepezil, Etoperidone, and Thiamine on cell growth and proliferation were determined using the xCELLigence Real-Time Cell Analysis (RTCA) system on the human neuroblastoma SH-SY5Y cell line. For this purpose, SH-SY5Y cells were exposed to safe concentrations determined in our previous study: Donepezil (15 μM), Etoperidone (70 μM), and Thiamine (600 μM), as well as Queuine (1.25 μM). Additionally, the combinations of Queuine with FDA-approved Donepezil and our candidate compounds Thiamine and Etoperidone were tested at the following concentrations: Queuine with Donepezil (1.25 μM - 15 μM), Queuine with Etoperidone (1.25 μM - 70 μM), and Queuine with Thiamine (1.25 μM - 600 μM). After 48 hours of exposure, the relative cell viability was calculated. The synergistic effects of Queuine with Donepezil, Etoperidone, and Thiamine were evaluated using the xCELLigence RTCA system, and the cell index percentage graphs obtained are presented in Figure 3. In Figure 3, the cell indices are as follows: Donepezil (15 μM) 86%, Etoperidone (70 μM) 79%, Thiamine (600 μM) 88%, Queuine (1.25 μM) 92%, Queuine with Donepezil 90%, Queuine with Etoperidone 91%, and Queuine with Thiamine 101%. When comparing the RTCA results of the two

studies for the safe doses we found in our previous study and used in this study, which are Donepezil (15 μ M), Etoperidone (70 μ M), Thiamine (600 μ M), and Queuine (1.25 μ M), the results were consistent with each other (17). According to the percentage cell

density graph presented in Figure 3, no significant cytotoxicity of the candidates on the cell line was observed with * $P < 0.05$, ** $P < 0.01$, and *** $P < 0.001$ levels of significance.

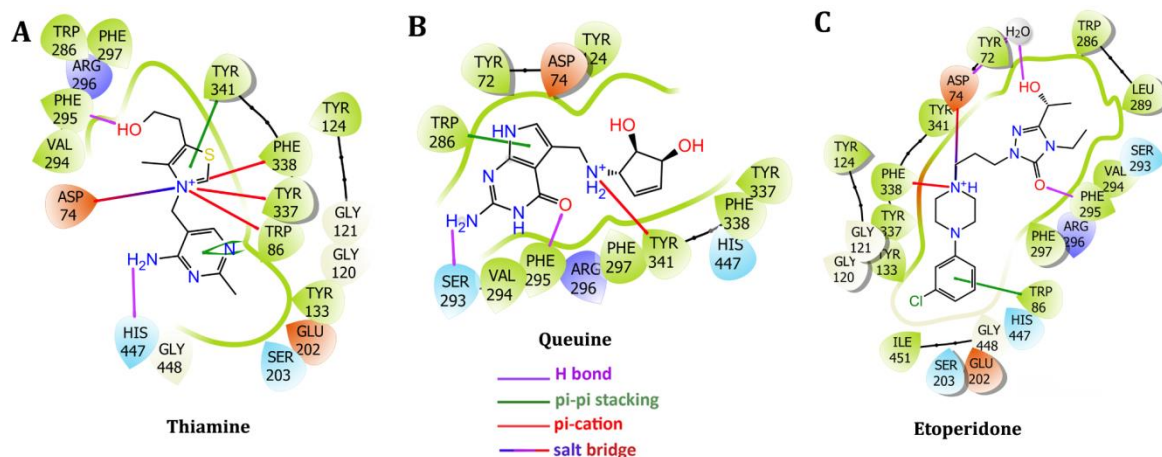


Figure 2: Binding site interactions of lead compounds Thiamine (A), Queuine (B), and Etoperidone (C) with AChE active site.

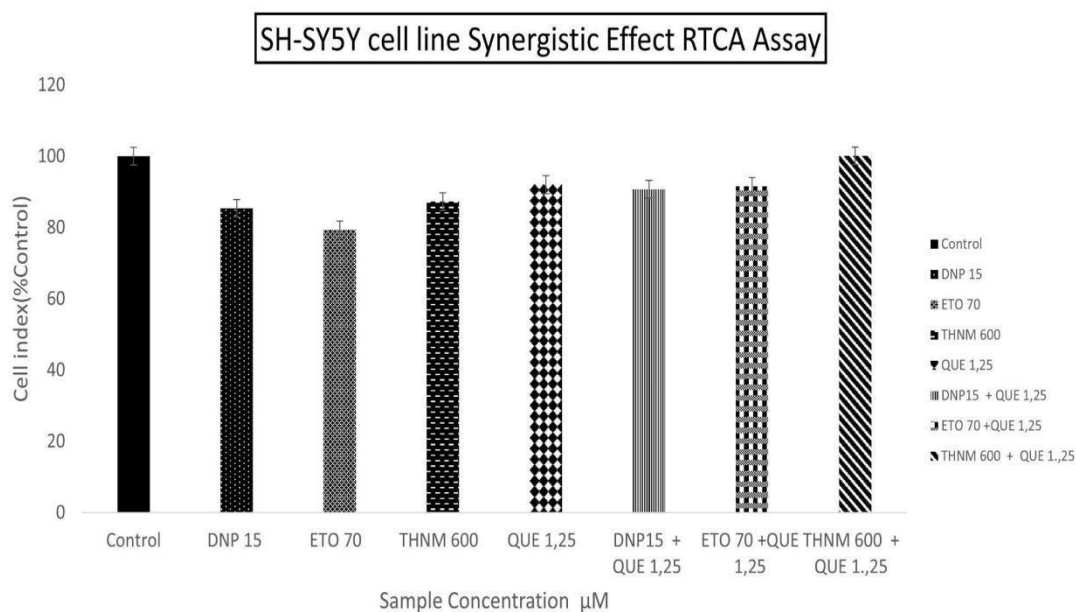


Figure 3: Viability of SH-SY5Y cells as a percentage graph compared to the control group after exposure to selected concentrations: Donepezil (15 μ M), Etoperidone (70 μ M), Thiamine (600 μ M), and Queuine (1.25 μ M). The last three columns represent the percentage graph of cell viability for the synergistic effects of Queuine with Donepezil, Etoperidone, and Thiamine. Sequentially, cell index (Control%): Donepezil (15 μ M) 86%, Etoperidone (70 μ M) 79%, Thiamine (600 μ M) 88%, Queuine (1.25 μ M) 92%, Queuine with Donepezil 90%, Queuine with Etoperidone 91%, and Queuine with Thiamine 101%. The results represent the average \pm SEM of experiments repeated three times at different time points with the same concentration ranges. When compared to the control, * $P < 0.05$, ** $P < 0.01$, and *** $P < 0.001$ indicate significant differences.

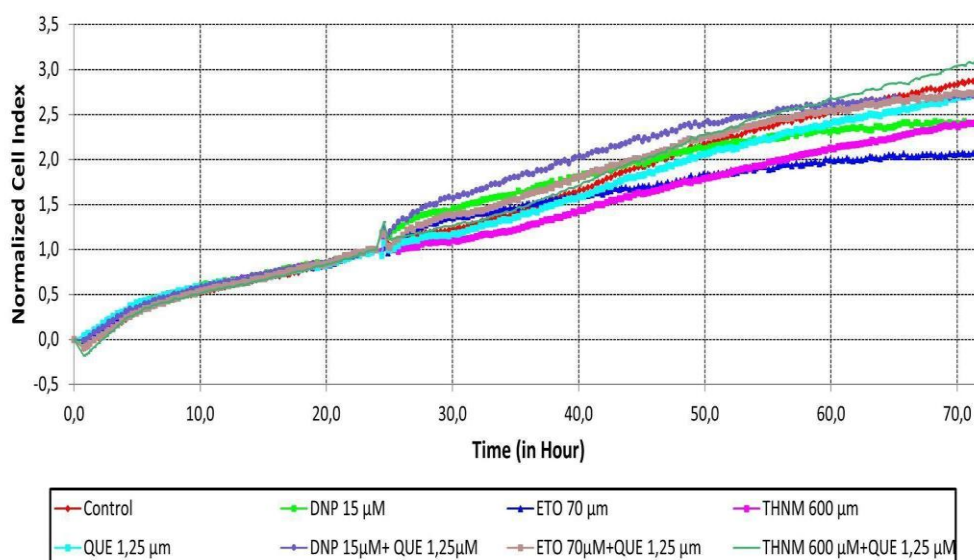


Figure 4: The results of the RTCA analysis: The cells were not treated with any drug for the first 24 hours. After 24 hours, different concentrations of drugs, both individually and in combination with Queuine, Donepezil, Etoperidone, and Thiamine at their respective safe concentrations, were applied. Following drug application, the cell index was measured continuously for 48 hours.

The cell index graphs obtained from the xCELLigence RTCA system were shown separately for Donepezil, Etoperidone, Thiamine, Queuine, and the combinations of Queuine with Donepezil, Etoperidone, and Thiamine in Figure 4. The safe dose ranges were consistent with the previous study, and no cytotoxicity was observed. Additionally, there was no significant toxic effect on cell viability and proliferation with the combination of Queuine with Donepezil, Etoperidone, and Thiamine.

3.3. Measurement of Acetylcholinesterase (AChE) Levels Using the Ellman’s Method

The enzyme inhibition results are shown in Figure 5. Our synthetic control group, Donepezil achieved 70% inhibition on AChE, while our natural-sourced control group Galantamine showed 44% inhibition. Among our three lead candidates, Etoperidone, Queuine, and Thiamine provided 61%, 45%, and 51% inhibition, respectively. When Queuine combined with Donepezil, Etoperidone, and Thiamine their synergistic effect on AChE inhibition was examined, resulting in 47%, 74%, and 21% inhibitions, respectively.

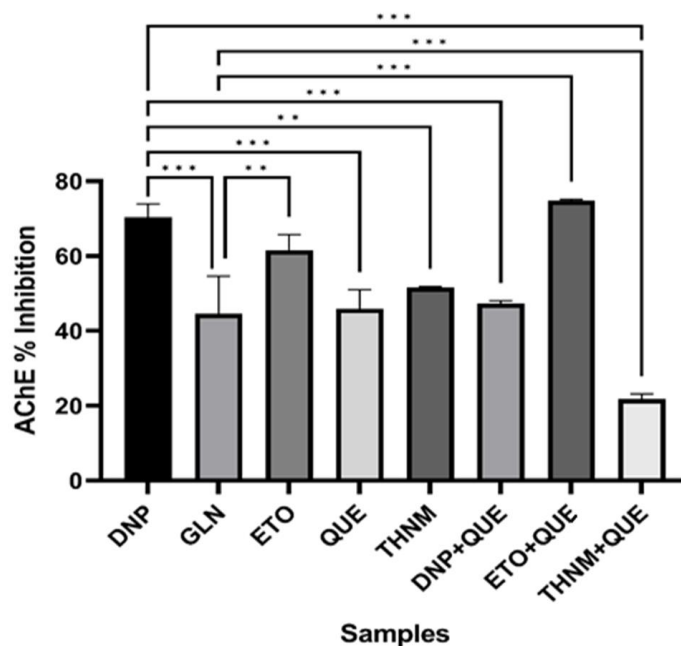


Figure 5: Percentage inhibition of AChE by study samples using Ellman’s Method. Values are mean ± standard deviation, n=3. Samples were compared with controls Donepezil (DNP) and Galantamine (GLN), and the differences between the bar pairs marked with ** (p<0.005) and *** (p<0.001) were statistically significant. DNP: Donepezil; GLN: Galantamine; ETO: Etoperidone; QUE: Queuine; THNM: Thiamine.

When evaluating the percentage of AChE enzyme inhibition graphs, a significant difference was observed between Donepezil and Thiamine at ($p < 0.005$). Significant differences were found between Donepezil and all candidate groups except for Thiamine at ($p < 0.001$). Additionally, a significant difference was observed between Galantamine and Etoperidone at ($p < 0.005$). The difference was also significant between Galantamine and the groups of Queuine+Etoperidone and Queuine+Thiamine at ($p < 0.001$).

Enzyme inhibition percentages are presented in Table 1. The values reveal that Queuine and Galantamine exhibit similar AChE inhibitory activity with inhibition percentages of 45% and 44% respectively. Regarding Queuine, its impact on amyloid has been reported in a previous study conducted on the microglia cell line (22). Additionally, it is suggested that Queuine may possess cholinergic activity through AChE inhibition. These findings support us in silico studies. Hence, we propose Queuine as a candidate multi-target nutraceutical compound probably being involved both in cholinergic and non-cholinergic amyloid-related mechanisms.

Table 1: % AChE enzyme inhibition values

Samples	% AChE inhibition	SEM +/-
Donepezil	70	3.52
Galantamine	44	10.04
Etoperidone	61	4.09
Queuine	45	5.16
Thiamine	51	0.24
Donepezil+Queuine	47	0.71
Thiamine+Queuine	21	1.36
Etoperidone+Queuine	74	0.23

In clinical trials, it has been reported that Etoperidone can inhibit the reuptake of serotonin, norepinephrine, and dopamine in the central transmission of serotonin (27,28). It has been indicated that several clinical trials involving etoperidone and its derivatives (trazodone, haloperidol) are primarily focused on the treatment of sleep disorders and Alzheimer's disease (AD) (20,21,29,30). However, the precise molecular mechanism underlying this treatment has not been fully understood. In this study, the inhibition of AChE by Etoperidone is demonstrated. Etoperidone produces a comparable inhibitory action with Donepezil, the AChE inhibition values being 61% and 70% for Etoperidone and Donepezil, respectively. These results substantiate the accuracy of our previous in silico study. To elucidate the combined effect of PAS-effective and CAS-effective drugs, we conducted combined drug use experiments with Queuine specifically. It is worth noting that the combined use of Queuine with Donepezil, and Queuine with Thiamine produced a competitive inhibition by hindering the individual inhibition values. This may stem from the fact that when Queuine binds to PAS, it may prevent the entry of Donepezil and Thiamine into the active site gorge, leading to a competitive antagonism. Contrarily, we observed a significant synergistic effect for the combined use of Queuine and Etoperidone, which resulted in a boosted inhibitory value as compared to individual use of both drugs. The highest % AChE inhibition value was obtained for this combined use

of Queuine+Etoperidone, which may be suggested as a promising drug therapy for AD treatment.

In previous literature studies investigating combined therapies, it has been noted that drugs binding to the peripheral anionic site (PAS) of acetylcholinesterase (AChE) could impede substrate binding by blocking the entrance to the active site gorge (8,16). Consequently, Queuine may obstruct the entry of both Donepezil and Thiamine into the gorge towards the catalytic anionic site (CAS), preventing their interaction with both CAS and PAS. This interference may hinder the individual inhibitory actions of Donepezil and Thiamine in the presence of Queuine. On the other hand, the scenario may differ with Etoperidone, as it could potentially enter the gorge before Queuine. As a result, Etoperidone might interact with the CAS, while Queuine simultaneously interacts with PAS. This dual interaction could lead to an enhanced inhibitory action. Upon analyzing the raw data from our previous molecular dynamics (MD) simulation results (17), comparing binding types and residues involved in binding interactions, we can assert the following: Queuine and Etoperidone, where a synergistic effect was observed, do not exhibit overlapping binding positions that would interfere with each other over the 100 ns MD simulation period. While Queuine shows a more active binding in the PAS region, Etoperidone demonstrates a stronger binding in the CAS. Despite the overlapping nature of these results, it is crucial to note that the synergistic effect presented in this study is highlighted for the first time, and thus its

implications need further comprehensive clarification through additional experimentation consistent with the results obtained from the Ellman method.

4. CONCLUSION

Queuine and Etoperidone were previously suggested to have neuroprotective effects in amyloid-beta plaque accumulation and tau-hyperphosphorylation, respectively (20-22). Neither of them has been mentioned as AChE inhibitors until now. In this study, we propose Queuine and Etoperidone as potential AChE inhibitors in addition to previously discovered amyloid-beta-related functions. Queuine is a nutraceutical molecule performing similar interactions and comparable enzyme inhibition values with Galantamine in the AChE PAS region. However, when their effectiveness in terms of dosages was compared, the IC50 value for Queuine was determined as 70.9 μM , while for Galantamine it was 556.0 μM . This indicates that Queuine provides its therapeutic effect at a lower dose, i.e. more potent than Galantamine. Queuine may serve as a multi-target drug that is effective both in cholinergic and amyloidogenic mechanisms and Queuine alone may serve as a strong drug candidate to replace Galantamine.

We suggest that the AChE interaction of Queuine in the PAS may be the basis of its effect on amyloid-related action. Etoperidone also has similar interactions and comparable enzyme inhibition values with Donepezil. Both can bind to CAS and PAS at the same time. However, Donepezil was found to be more potent than Etoperidone, with IC50 values being 712.8 and 222.2 μM , respectively. For this reason, Etoperidone alone is not as effective as Donepezil. Considering the synergistic effect studies, the combined use of Queuine and Etoperidone creates a significant synergistic effect, resulting in a higher enzyme inhibition than Donepezil, which also has not been reported in the literature before. Queuine and Etoperidone are of nutraceutical and metabolite origin, while Donepezil is a synthetic drug. This fact may be another advantage of substituting Donepezil with this drug combination as economic and toxicity issues are concerned. The results of the present study suggest alternative low-risk novel natural drugs and drug combinations having therapeutic potential and dual-action to combat AD.

5. CONFLICT OF INTEREST

The authors declare no conflict of interest.

6. REFERENCES

1. Castro A, Martinez A. Targeting Beta-Amyloid Pathogenesis Through Acetylcholinesterase Inhibitors. *Curr Pharm Des* [Internet]. 2006 Nov 1;12(33):4377–87. Available from: [<URL>](#).
2. Colovic MB, Krstic DZ, Lazarevic-Pasti TD, Bondzic AM, Vasic VM. Acetylcholinesterase Inhibitors: Pharmacology and Toxicology. *Curr Neuropharmacol* [Internet]. 2013;11(3):315–35. Available from: [<URL>](#).
3. Breijyeh Z, Karaman R. Comprehensive Review on Alzheimer's Disease: Causes and Treatment. *Molecules* [Internet]. 2020 Dec 8;25(24):5789. Available from: [<URL>](#).
4. Johnson G, Moore S. The Peripheral Anionic Site of Acetylcholinesterase: Structure, Functions and Potential Role in Rational Drug Design. *Curr Pharm Des* [Internet]. 2006 Jan 1;12(2):217–25. Available from: [<URL>](#).
5. Piazzzi L, Rampa A, Bisi A, Gobbi S, Belluti F, Cavalli A, et al. 3-(4-([Benzyl(methyl)amino]methyl)phenyl)-6,7-dimethoxy-2 H -2-chromenone (AP2238) Inhibits Both Acetylcholinesterase and Acetylcholinesterase-Induced β -Amyloid Aggregation: A Dual Function Lead for Alzheimer's Disease Therapy. *J Med Chem* [Internet]. 2003 Jun 1;46(12):2279–82. Available from: [<URL>](#).
6. Zhang Y, Li P, Feng J, Wu M. Dysfunction of NMDA receptors in Alzheimer's disease. *Neurol Sci* [Internet]. 2016 Jul 12;37(7):1039–47. Available from: [<URL>](#).
7. Penke B, Bogár F, Fülöp L. β -Amyloid and the Pathomechanisms of Alzheimer's Disease: A Comprehensive View. *Molecules* [Internet]. 2017 Oct 10;22(10):1692. Available from: [<URL>](#).
8. Balkrishna A, Pokhrel S, Tomer M, Verma S, Kumar A, Nain P, et al. Anti-Acetylcholinesterase Activities of Mono-Herbal Extracts and Exhibited Synergistic Effects of the Phytoconstituents: A Biochemical and Computational Study. *Molecules* [Internet]. 2019 Nov 18;24(22):4175. Available from: [<URL>](#).
9. Khan H, Marya, Amin S, Kamal MA, Patel S. Flavonoids as acetylcholinesterase inhibitors: Current therapeutic standing and future prospects. *Biomed Pharmacother* [Internet]. 2018 May 1;101:860–70. Available from: [<URL>](#).
10. Abdul Manap AS, Wei Tan AC, Leong WH, Yin Chia AY, Vijayabalan S, Arya A, et al. Synergistic Effects of Curcumin and Piperine as Potent Acetylcholine and Amyloidogenic Inhibitors With Significant Neuroprotective Activity in SH-SY5Y Cells via Computational Molecular Modeling and in vitro Assay. *Front Aging Neurosci* [Internet]. 2019 Aug 27;11:471888. Available from: [<URL>](#).
11. Chiu H-F, Venkatakrishnan K, Wang C-K. The role of nutraceuticals as a complementary therapy against various neurodegenerative diseases: A mini-review. *J Tradit Complement Med* [Internet]. 2020 Sep 1;10(5):434–9. Available from: [<URL>](#).
12. Tarbiat S, Unver D, Tuncay S, Isik S, Yeman KB, Mohseni AR. Neuroprotective effects of Cubebin and Hinokinin lignan fractions of Piper cubeba fruit in Alzheimer's disease in vitro model. *Turkish J Biochem* [Internet]. 2023 Jul 19;48(3):303–10. Available from: [<URL>](#).
13. Choi RCY, Zhu JTT, Yung AWY, Lee PSC, Xu SL, Guo AJY, et al. Synergistic Action of Flavonoids, Baicalein, and Daidzein in Estrogenic and Neuroprotective Effects: A Development of Potential Health Products and Therapeutic Drugs against Alzheimer's Disease. *Evidence-Based Complement Altern Med* [Internet]. 2013;2013:1–10. Available from: [<URL>](#).
14. Coqueiro A, Fernandes DC, Danuello A, Regasini LO, Cardoso-Lopes EM, Young MCM, et al. Nematostatic activity of isoprenylated guanidine alkaloids from *Pterogyne nitens* and their interaction with acetylcholinesterase. *Exp Parasitol* [Internet]. 2023 Jul 1;250:108542. Available from: [<URL>](#).

15. Chierrito TPC, Pedersoli-Mantoani S, Roca C, Requena C, Sebastian-Perez V, Castillo WO, et al. From dual binding site acetylcholinesterase inhibitors to allosteric modulators: A new avenue for disease-modifying drugs in Alzheimer's disease. *Eur J Med Chem* [Internet]. 2017 Oct 20;139:773–91. Available from: [<URL>](#).
16. Amat-ur-Rasool H, Ahmed M, Hasnain S, Carter WG. Anti-Cholinesterase Combination Drug Therapy as a Potential Treatment for Alzheimer's Disease. *Brain Sci* [Internet]. 2021 Feb 2;11(2):184. Available from: [<URL>](#).
17. Girgin M, Isik S, Kantarci-Carsibasi N. Proposing novel natural compounds against Alzheimer's disease targeting acetylcholinesterase. Al-Karmalawy AA, editor. *PLoS One* [Internet]. 2023 Apr 27;18(4):e0284994. Available from: [<URL>](#).
18. Gibson GE, Hirsch JA, Fonzetti P, Jordan BD, Cirio RT, Elder J. Vitamin B1 (thiamine) and dementia. *Ann N Y Acad Sci* [Internet]. 2016 Mar 11;1367(1):21–30. Available from: [<URL>](#).
19. Liu D, Ke Z, Luo J. Thiamine Deficiency and Neurodegeneration: the Interplay Among Oxidative Stress, Endoplasmic Reticulum Stress, and Autophagy. *Mol Neurobiol* [Internet]. 2017 Sep 5;54(7):5440–8. Available from: [<URL>](#).
20. Koppel J, Jimenez H, Adrien L, Greenwald BS, Marambaud P, Cinamon E, et al. Haloperidol inactivates AMPK and reduces tau phosphorylation in a tau mouse model of Alzheimer's disease. *Alzheimer's Dement Transl Res Clin Interv* [Internet]. 2016 Jun 21;2(2):121–30. Available from: [<URL>](#).
21. Brauer R, Lau WCY, Hayes JF, Man KKC, Osborn DPJ, Howard R, et al. Trazodone use and risk of dementia: A population-based cohort study. Brayne C, editor. *PLOS Med* [Internet]. 2019 Feb 5;16(2):e1002728. Available from: [<URL>](#).
22. Richard P, Kozlowski L, Guillorit H, Garnier P, McKnight NC, Danchin A, et al. Queuine, a bacterial-derived hypermodified nucleobase, shows protection in in vitro models of neurodegeneration. Witt SN, editor. *PLoS One* [Internet]. 2021 Aug 11;16(8):e0253216. Available from: [<URL>](#).
23. Ellman GL, Courtney KD, Andres V, Featherstone RM. A new and rapid colorimetric determination of acetylcholinesterase activity. *Biochem Pharmacol* [Internet]. 1961 Jul 1;7(2):88–95. Available from: [<URL>](#).
24. Das JR, Tizabi Y. Additive Protective Effects of Donepezil and Nicotine Against Salsolinol-Induced Cytotoxicity in SH-SY5Y Cells. *Neurotox Res* [Internet]. 2009 Oct 20;16(3):194–204. Available from: [<URL>](#).
25. Tarbiat S, Türütoğlu AS, Ekingen M. Acetylcholinesterase Inhibitory Potential and Antioxidant Activities of Five Cultivars of Rosa Damascena Mill. From Isparta, Turkey. *Curr Top Nutraceutical Res* [Internet]. 2020;18(4):354–9. Available from: [<URL>](#).
26. He F. BCA (Bicinchoninic Acid) Protein Assay. *Bio-Protocol* [Internet]. 2011;1(5):1–2. Available from: [<URL>](#).
27. Lisciani R, Baldini A, Benedetti D, Campana A, Barcellona PS. Acute Cardiovascular toxicity of trazodone, etoperidone and imipramine in rats. *Toxicology* [Internet]. 1978 Jan 1;10(C):151–8. Available from: [<URL>](#).
28. Caldwell GW, Wu WN, Masucci JA. Evaluation of the absorption, excretion and metabolism of [¹⁴C] etoperidone in man. *Xenobiotica* [Internet]. 2001 Jan 22;31(11):823–39. Available from: [<URL>](#).
29. Albert-Gasco H, Smith HL, Alvarez-Castelao B, Swinden D, Halliday M, Janaki-Raman S, et al. Trazodone rescues dysregulated synaptic and mitochondrial nascent translomes in prion neurodegeneration. *bioRxiv* [Internet]. 2023 Jun 7; Available from: [<URL>](#).
30. Wichniak A, Wierzbicka A, Jarema M. Treatment of insomnia – effect of trazodone and hypnotics on sleep. *Psychiatr Pol* [Internet]. 2021 Aug 31;55(4):743–55. Available from: [<URL>](#).



New Drug Design to Suppress Nonalcoholic Steatohepatitis

Soykan Agar^{1*}, Barbaros Akkurt², Engin Ulukaya³

¹Kocaeli Health and Technology University, Faculty of Pharmacy, Kocaeli 41275, Türkiye.

²Istanbul Technical University, Faculty of Science and Letters, Department of Chemistry, Istanbul 34469, Türkiye.

³Istinye University Medical Faculty, Department of Clinical Biochemistry, Istanbul 34010, Türkiye.

Abstract: A *de novo* designed biomolecule called INASHD was utilized through computer-aided drug design techniques to specifically target β 2-spectrin, effectively suppressing and preventing NASH disease. Advanced computational software tools concerning the technologies of molecular docking and molecular dynamics (MD), were employed to showcase the drug's remarkable ability to efficiently suppress and control the α -helical topology of β 2-spectrin. This protein is a vital component within the disease pathway. We successfully devised an effective design suppressing β 2-spectrin, exhibiting an inhibition score surpassing any other molecule documented in scientific literature. With robust support from validated computational software, this bioorganic structure holds significant value and can be applied for a patent due to its innovative design. It shows promising potential for delivering positive outcomes in various stages, including *in vitro*, *in vivo*, *ex vivo*, and human phase studies.

Keywords: Nonalcoholic steatohepatitis, *in silico* drug design, molecular docking, molecular dynamics, β 2-spectrin.

Submitted: November 24, 2023. **Accepted:** January 23, 2024.

Cite this: Agar S, Akkurt B, Ulukaya E. New Drug Design to Suppress Nonalcoholic Steatohepatitis. JOTCSA. 2024;11(2):585-90.

DOI: <https://doi.org/10.18596/jotcsa.1395403>

***Corresponding author's E-mail:** soykan.agar@kocaelisaglik.edu.tr

1. INTRODUCTION

Nonalcoholic fatty liver disease (NAFLD) is one of the most widespread disorders in the world. NAFLD is defined as a spectrum disorder affecting the liver that leads to hepatic steatosis. Nonalcoholic steatohepatitis (NASH) is described as an inflammatory subtype of NAFLD. In this condition, steatosis is accompanied by inflammation and hepatocyte damage, with or without fibrosis. It is also known that NASH can progress to cirrhosis in time, although it initially remains silent (1-5).

In a recent study by Rao *et al.*, β 2-spectrin (SPTBN1) stimulates sterol regulatory element-binding protein (SREBP)-related lipogenesis, and in this way, it promotes hepatic cancer development in an *in vivo* model. This study also reveals that SPTBN1 silencing in hepatocytes protects from lipid accumulation, fibrotic tissue formation, and hepatic damage in the same animal model. Furthermore, clinical samples from NASH patients indicate elevated SPTBN1 expression (6). Thus, SPTBN1 silencing and/or downregulation could provide a valuable route to

develop novel therapeutic strategies for treating NASH. To completely eradicate NASH, it is essential to explore strategies such as gene silencing of SPTBN1, suppressing the expression of β 2-spectrin, or inhibiting its overexpression. The initial approach involves regioselective drug design aimed at targeting particular repetitive nucleotide bases within the extensive 220,000-nucleotide sequence of SPTBN1 on chromosome 2 (7). Nevertheless, this proves to be a formidable challenge due to the demanding nature of modeling and simulation studies, requiring an immense amount of computational power, potentially involving thousands of GPUs in supercomputers, and spanning several months, if not years.

As an alternative approach to addressing the issue, a potential solution lies in the development of a siRNA-based drug that targets and suppresses the expression of β 2-spectrin. However, caution must be exercised as this approach carries some risks, particularly concerning potential drug counter-indications. Spectrin proteins play a crucial role in maintaining the structural stability of cell membranes

and cell morphology. Excessive suppression of spectrin could lead to cell membrane instability and loss of cell structure (6,8,9).

A third strategy involves dealing with NASH, where there is an excessive accumulation of β 2-spectrin due to inflammation. In this case, complete elimination of β 2-spectrin, as proposed in the second approach, may not be desirable. Alternatively, *de novo* drug design can be employed to both inhibit and regulate the activity of β 2-spectrin, enabling effective management of NASH symptoms and addressing the inflammatory issues within the affected tissue.

A new drug compound named INASHD has been computer-aided and designed with *in silico* techniques to specifically target β 2-spectrin and effectively combat NASH disease. Computational software tools, including molecular docking and molecular dynamics (MD), were employed to demonstrate the drug's exceptional efficiency in suppressing and controlling the α -helical topology of β 2-spectrin. This protein plays a crucial role in the progression of the disease.

Overall, we have successfully designed the molecule with a pharmaceutical organic formulation, and its inhibitory capabilities surpass those of any molecule documented in scientific literature. By substantiating the chemistry of this molecule with extensively validated computational software, it becomes a valuable bioorganic structure that was sent for patenting. Its innovative design holds the potential to yield promising results in various stages of testing, including *in vitro*, *in vivo*, *ex vivo*, etc.

2. MATERIALS AND METHODS

2.1. Theoretical Geometric Optimization

To accurately determine the active sites of a molecule and investigate its interactions with receptors, it is essential to establish its optimal geometric structure. In our present study, we utilized INASHD as the ligand's organic chemical structure and analyzed its most stable molecular geometry using the Gaussian 09 program (10) with density functional theory (DFT)/B3LYP functional (11) and the 6-31G(d,p) basis set. This process resulted in the formation of the most stable molecular structures of INASHD with β 2-spectrin (PDB ID: isolated from 6M3P, AnkG was removed), intended for further computational and simulation-based research, as depicted in Figures 1 and 2. To prepare input files for molecular docking, molecular dynamics computations, and post-processing of output files, we employed GaussView 6.0 and Avogadro 1.95 softwares (12,13).

2.2. Molecular Docking Procedure

Molecular docking simulations were conducted using AutoDock Vina 1.1.2 software (14), renowned for its exceptional precision and accuracy in biochemical docking simulations. A total of 800 poses were generated, comprising 100 poses for each simulation. Blind docking was employed, and the grid box dimensions were set to $80 \times 80 \times 100 \text{ \AA}^3$ (as the

x , y , and z grid parameters, respectively). The ligand INASHD, designed *de novo*, was studied for its interactions with the receptor structure of β 2-spectrin, which was downloaded with the PDB id of 6M3P and then isolated from the protein complex for analysis. Gauss View 6.0 and Avogadro 1.95 software were utilized for the optimization of the ligands and 1BNA structures. The simulations effectively illustrated the interactions and binding of the drug to the receptor, with the docking scores represented in kcal/mol signifying the Gibbs free binding energy. From all the simulations, the initial structure and input file for the subsequent molecular dynamics (MD) simulations were selected as the docking pose with the most accurate and favorable binding energy, identified within the best-clustered data.

2.3. Molecular Dynamics (MD) Simulations

The initial structures for the MD simulations were chosen based on the docking poses with the most favorable binding energies (15–18), as previously reported in scientific literature. The molecular dynamics (MD) simulations were conducted using Schrödinger's Maestro Desmond software (19), each spanning 50 ns with 5000 poses at 10 ps intervals. To ensure accuracy, each MD simulation was repeated five times with different seed numbers, confirming the correctness of the simulation parameters and the structures of the INASHD- β 2 spectrin complexes formed.

During the MD simulations, the dynamic properties of the ligand-receptor complexes were continuously evaluated over time. The simulation area was defined by a grid box measuring $130 \times 130 \times 130 \text{ \AA}^3$ with a spacing of 0.5 \AA , providing an extensive grid area for the simulations. TIP3P-type water molecules were included within the box, and 0.15 M NaCl ions were added to neutralize the system. The temperature and pressure conditions were set as follows: NPT at 310 K with Nose-Hoover temperature coupling (20) and a constant pressure of 1.01 bar using Martyna Tobias-Klein pressure coupling (21). The system was unconstrained, and the default fitting for OPLS 3.0 standards provided the initial velocity values for the forcefield calculations.

Furthermore, the formation of hydrogen bonds during the interaction of ligands with β 2 spectrin was investigated during the MD simulations.

3. RESULTS AND DISCUSSION

This *in silico* study offers a further comprehension of the non-covalent interactions between the drug and protein, aiming to unveil the inhibition efficiency and the role of hydrogen bonding in the drug binding mechanism.

The objective is to initiate the research using computational and simulation tools to effectively illustrate how the drug aligns with the domains of β 2-spectrin (Figure 1) and subsequently assess the protein binding affinity, inhibition, binding mechanism, and overall efficacy of the drug.

To reach this objective, it is essential to understand

that the efficacy of interactions seems to rely on several factors, such as the drug's external groups' affinity towards the protein and the binding topology.

The primary concept involves the simulation and calculation of the theoretical stability of β 2-spectrin under inflammatory conditions within a liver cell, specifically at a pH of 7.3. This stability will then be compared to the $\Delta(\Delta G)$ (Gibbs free energy change) when β 2-spectrin forms a complex with INASHD, leading to INASHD- β 2-spectrin.

Figure 2 illustrates the main pose of the INASHD- β 2-

spectrin, taken under 3D video within Schrödinger's Maestro Desmond MD software, where each MD run had 5000 frames. INASHD is strongly attached to the groove active site of β 2-spectrin. Along with the MD results in Schrödinger's Maestro Desmond and according to the cluster analyses of 100 posed trials from the molecular docking studies in Autodock Vina, it forms strong H-bonds β 2-spectrin, and the obtained docking energies are around -14 kcal/mol. The drug bends the morphological alpha-helical structures of β 2-spectrin. INASHD inhibits and bends the alpha-helical structure and morphology of β 2-spectrin via very strong H-bonds.

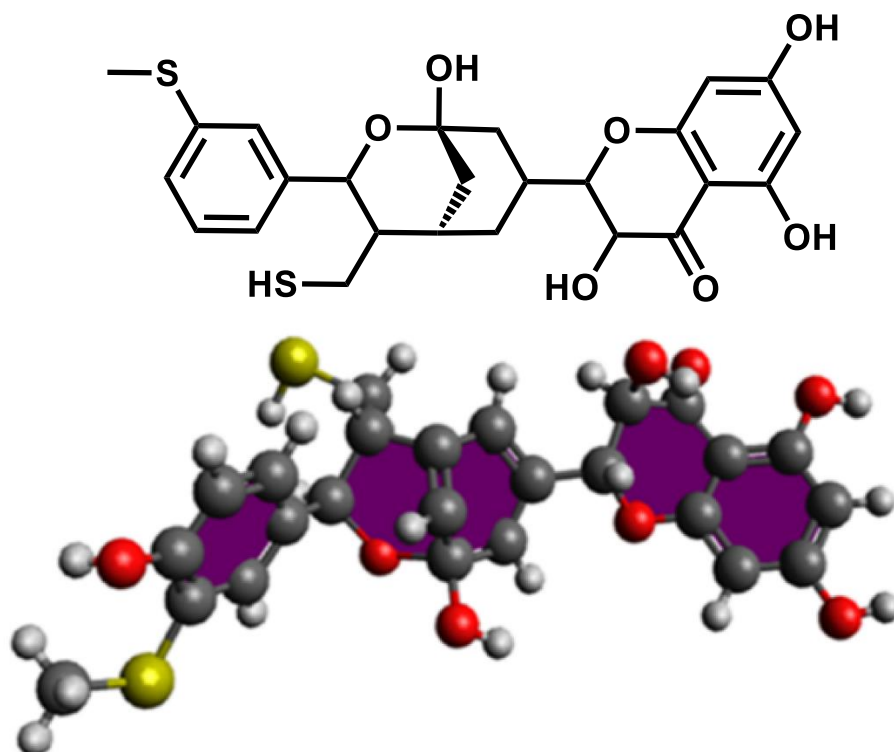


Figure 1: *De novo* designed INASHD (patent pending) with 2D and 3D illustrations, geometrically optimized under OPLS 3.0 Force field and a pH of 7.3 to suppress NASH disease.

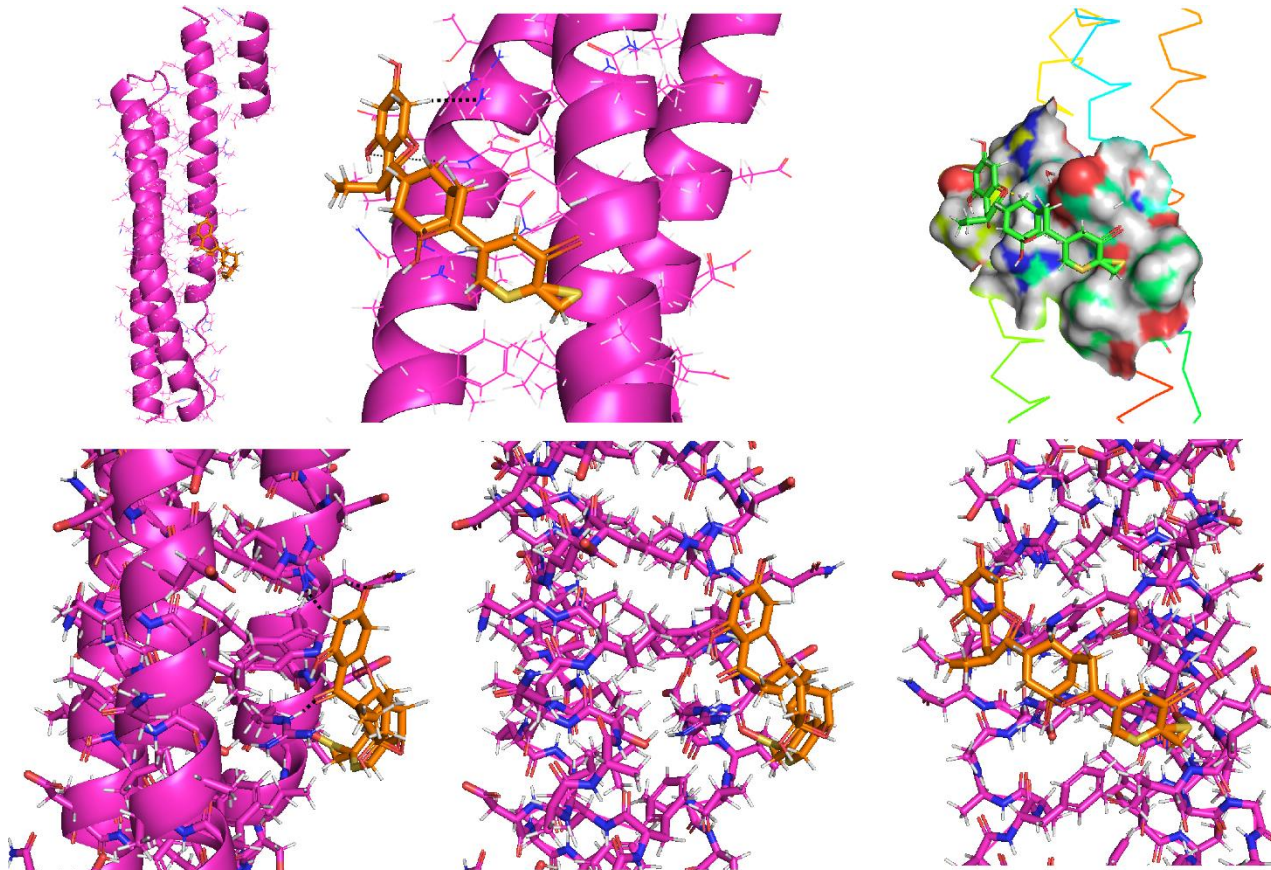


Figure 2: INASHD-β2-spectrin complex with the inhibition $\Delta(\Delta G)$ binding energy of -13.9 kcal/mol.

Depending on the cluster analyses in Figure 3, there were two main clusters, which are good result indicators and expected to happen for strong binding, inhibiting drugs as in the scientific literature. The two main clusters have similar binding energies that are around -14 kcal/mol.

With such a high docking score, α -helical modulation, and a bioactive molecule, along with great cluster depending on the data at hand and our research paper publishing past in this area, the molecular formula should be patented before going into further pre-clinical and clinical studies.

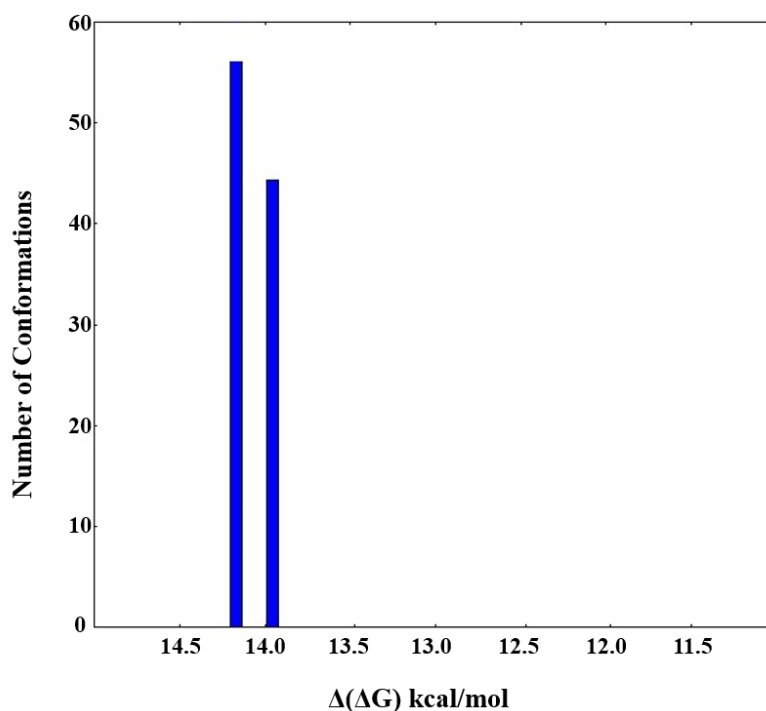


Figure 3: The cluster analysis of all the docked poses.

4. CONCLUSION

A new drug compound called INASHD was created using computer-based techniques to specifically target β 2-spectrin and effectively combat NASH disease. Computational tools, including molecular docking and molecular dynamics (MD), were employed to demonstrate the drug's remarkable efficiency in inhibiting and regulating the α -helical topology of β 2-spectrin, a protein critical in the disease pathway.

In conclusion, we successfully designed this molecule with a pharmaceutical organic formulation, and its inhibitory potential surpasses that of any molecule documented in scientific literature. Given the strong support from validated computational software, this bioorganic structure holds significant value and has already been sent for patenting. Its innovative design shows promising potential for success in various stages, including *in vitro*, *in vivo*, *ex vivo*, and human phase studies.

5. ACKNOWLEDGMENTS

i. Funding statement

This study was funded by Molecular Cancer Research Association at ISTU under the oncology & medical biochemistry team of Prof. Dr. EU (M.D. Ph.D.).

ii. Patent application

The patent application was done for the drug molecule and its mechanism within the research article via Technology Transfer Office of IU with the application number of P23-0899, and it was accepted.

iii. Any conflict of interest

The authors, Assistant Professor SA (Ph.D.), Teaching & Research Fellow BA (Ph.D.), and Prof. Dr. EU (M.D. Ph.D.), declare that there is no conflict of interest for this research paper and its datasets.

iv. How the ethical issue was handled (name the ethical committee that approved the research)

All *in silico* data was studied and represented with honest work, and since it was an *in silico* study and not an experimental study, there was no need for ethical committee approval for this research paper, which is compatible with the laws of the national ethical committee.

v. Authors contribution

SA: Writing the draft, methodology and *in silico* simulations; BA: Writing the draft, proofreading; EU: Conceptualization, checking the draft.

vi. Availability of data (if apply to your research)

It can be shared with open access in case of journal asks of us.

6. REFERENCES

- Lahmi A, Oryan S, Eidi A, Rohani AH. Comparative effects of thymol and vitamin E on nonalcoholic fatty liver disease in male Wistar rats. *Brazilian J Biol* [Internet]. 2024;84:e268781. Available from: [<URL>](#).
- Maldonado FHR, Mega PF, Germano CW, Dias LLC, Callejas GH, Gestic MA, et al. Impact of pre-operative weight loss on non-alcoholic fatty liver disease histopathology and insulin resistance in individuals undergoing bariatric surgery: a propensity matched cross-sectional comparison. *Sao Paulo Med J* [Internet]. 2024;142(1):e2022663. Available from: [<URL>](#).
- Tabaeian SP, Rezapour A, Azari S, Martini M, Saran M, Behzadifar M, et al. Prevalence of Non-alcoholic Fatty Liver Disease in Iran: A Systematic Review and Meta-analysis. *J Clin Exp Hepatol* [Internet]. 2024 Jan 1;14(1):101209. Available from: [<URL>](#).
- Manne V, Handa P, Kowdley K V. Pathophysiology of Nonalcoholic Fatty Liver Disease/Nonalcoholic Steatohepatitis. *Clin Liver Dis* [Internet]. 2018 Feb 1;22(1):23–37. Available from: [<URL>](#).
- Sheka AC, Adeyi O, Thompson J, Hameed B, Crawford PA, Ikramuddin S. Nonalcoholic Steatohepatitis. *JAMA* [Internet]. 2020 Mar 24;323(12):1175–83. Available from: [<URL>](#).
- Rao S, Yang X, Ohshiro K, Zaidi S, Wang Z, Shetty K, et al. β 2-spectrin (SPTBN1) as a therapeutic target for diet-induced liver disease and preventing cancer development. *Sci Transl Med* [Internet]. 2021 Dec 15;13(624):eabk2267. Available from: [<URL>](#).
- Bennett V, Lorenzo DN. Spectrin- and Ankyrin-Based Membrane Domains and the Evolution of Vertebrates. In: *Current Topics in Membranes* [Internet]. Academic Press; 2013. p. 1–37. Available from: [<URL>](#).
- Bennett V, Lorenzo DN. An Adaptable Spectrin/Ankyrin-Based Mechanism for Long-Range Organization of Plasma Membranes in Vertebrate Tissues. In: *Current Topics in Membranes* [Internet]. Academic Press; 2016. p. 143–84. Available from: [<URL>](#).
- De Matteis MA, Morrow JS. Spectrin tethers and mesh in the biosynthetic pathway. *J Cell Sci* [Internet]. 2000 Jul 1;113(13):2331–43. Available from: [<URL>](#).
- Frisch MJ, Trucks GW, Schlegel HB, Scuseria GE, Robb MA, Cheeseman JR, et al. Gaussian 09, Revision D.01. Wallingford, CT: Gaussian, Inc.; 2009.
- Becke AD. Density-functional thermochemistry. III. The role of exact exchange. *J Chem Phys* [Internet]. 1993 Apr 1;98(7):5648–52. Available from: [<URL>](#).
- Dennington R, Keith TA, Millam JM. GaussView Version 6. 2019.

13. Hanwell MD, Curtis DE, Lonie DC, Vandermeersch T, Zurek E, Hutchison GR. Avogadro: an advanced semantic chemical editor, visualization, and analysis platform. *J Cheminform* [Internet]. 2012 Dec 13;4(1):17. Available from: [<URL>](#).
14. Gaillard T. Evaluation of AutoDock and AutoDock Vina on the CASF-2013 Benchmark. *J Chem Inf Model* [Internet]. 2018 Aug 27;58(8):1697–706. Available from: [<URL>](#).
15. Şenel P, Agar S, Sayin VO, Altay F, Yurtsever M, Gölcü A. Elucidation of binding interactions and mechanism of Fludarabine with dsDNA via multispectroscopic and molecular docking studies. *J Pharm Biomed Anal* [Internet]. 2020 Feb 5;179:112994. Available from: [<URL>](#).
16. Şenel P, Agar S, İş YS, Altay F, Gölcü A, Yurtsever M. Deciphering the mechanism and binding interactions of Pemetrexed with dsDNA with DNA-targeted chemotherapeutics via spectroscopic, analytical, and simulation studies. *J Pharm Biomed Anal* [Internet]. 2022 Feb 5;209:114490. Available from: [<URL>](#).
17. Cheraghi S, Şenel P, Dogan Topal B, Agar S, Majidian M, Yurtsever M, et al. Elucidation of DNA-Eltrombopag Binding: Electrochemical, Spectroscopic and Molecular Docking Techniques. *Biosensors* [Internet]. 2023 Feb 21;13(3):300. Available from: [<URL>](#).
18. Şenel P, Agar S, Yurtsever M, Gölcü A. Voltammetric quantification, spectroscopic, and DFT studies on the binding of the antineoplastic drug Azacitidine with DNA. *J Pharm Biomed Anal* [Internet]. 2024 Jan 5;237:115746. Available from: [<URL>](#).
19. Desmond D. Desmond. New York: Shaw Research; 2017.
20. Evans DJ, Holian BL. The Nose-Hoover thermostat. *J Chem Phys* [Internet]. 1985 Oct 15;83(8):4069–74. Available from: [<URL>](#).
21. Martyna GJ, Tobias DJ, Klein ML. Constant pressure molecular dynamics algorithms. *J Chem Phys* [Internet]. 1994 Sep 1;101(5):4177–89. Available from: [<URL>](#).



Investigation of the Effects of Different H₂SO₄, HCl, HNO₃ and HClO₄ Liquid Acid Media on the Synthesis of CdTe Semiconductor Thin Films for Solar Cells

Ayça Kiyak Yıldırım¹ , Veli Şimşek^{2*} 

¹Vocational School of Health Services, Department of Medical Services and Techniques, Bilecik Şeyh Edebali University, 11230 Bilecik, Turkey

²Faculty of Engineering, Chemical Engineering Department, Bilecik Seyh Edebali University, 11230 Bilecik, Turkey

Abstract: The main target of the present paper is to investigate the effect of different acidic aqueous media (DAAM) on the synthesis of cadmium telluride thin films (CdTeTFm). The synthesis of CdTeTFm was carried out by the electrochemical deposition method (EDM) in DAAM. The chronoamperometry method of electrodeposition (ED) was used for the production of CdTeTFm. Furthermore, the electrochemical behaviors of the solutions were studied using cyclic voltammetry. The experiments were carried out with 3 electrodes (a working electrode (WE), a reference electrode (CE), and a counter electrode (RE)) using the electrochemical cell potentiostatic method. The experimental conditions of the acidic aqueous CdTe solution have been determined to be pH 3.56-3.57, the temperature of the solution is 85°C, the concentration of CdTe 2.45x10⁻¹ M, and the reaction time is 25 minutes. The physical properties of CdTeTFm were determined by XRD, SEM/EDX, FT-IR, and UV-VIS analysis methods. According to the results of the analysis, it was observed that acidic aqueous media have an important role in the synthesis of CdTeTFm. The bandgap ranges and Cd/Te ratios of the synthesized thin films were obtained as 1.42, 1.48, 1.50, 1.58 eV, 0.65, 0.587, 0.79 and 0.738, respectively.

Keywords: CdTe; Solar cells; HClO₄; Electrochemical deposition method; Thin film.

Submitted: April 18, 2023. **Accepted:** January 24, 2024.

Cite this: Kiyak Yıldırım A, Şimşek V. Investigation of the Effects of Different H₂SO₄, HCl, HNO₃ and HClO₄ Liquid Acid Media on the Synthesis of CdTe Semiconductor Thin Films for Solar Cells. JOTCSA. 2024; 11(2): 591-600.

DOI: <https://doi.org/10.18596/jotcsa.1285341>.

***Corresponding author. E-mail:** veli.simsek@bilecik.edu.tr.

1. INTRODUCTION

The production of CdTe thin films has been very attractive because they can be useful in lasers, biosensors, photoelectric diodes, and protein markers, among other application fields (1,2) solar cells (SCs) (1-3). Moreover, CdTe cells have emerged as the most widely used commercialized thin film photovoltaic technology (4, 5). CdTe is now the only thin film technology in the top ten global producers. This is because CdTe is a very strong and extremely chemically stable material that can be deposited using a wide range of processes, making it perfect for large-scale production (5). Semiconductors (SmC) and nanocrystals (NCs) also have interesting electrochemical behavior. However, the applications in this area are currently limited by the low solubility

of most of the NCs in watery media and the lack of a complete explanation of redox mechanisms (6-8). SmC devices based on thin films (such as CdTe) strongly depend on their structural and optical properties (OPs) (9,10). Moreover, the OPs of thin films depend on surface characteristics, shape, crystallite size, and other variables such as doping (11).

The highly efficient SC material "II-VI compound SmC," such as CdTeTFm is well known (12,13) and thought to be convenient due to its energy matching to the solar emitting spectrum and larger AC (absorption coefficient) natural structure (because of the direct transition energy band diagram and their values also are 1.45 eV and 1.5eV). It is almost optimum for photovoltaic SCs. Moreover, CdTe has a

wide optical AC ($> 105 \text{ cm}^{-1}$) compared to a-Si. So, something that has only a few microns of CdTe can absorb as high as 90% of photons (14).

Different growth methods, such as MBE (molecular beam epitaxy) (15) sputtering (16), ED (17-19), MOVPE (metal-organic chemical vapor deposition) (20) and chemical vapor deposition (21) have been improved. However, the ED of compound SmC thin films has some advantages. For example, (a) it is easy to check the electrical features of obtained films by managing deposition potential (DP) and adding impurities to the deposition films. (b) Because of the ease of device construction, it enables the production of wide-area films, and (c) it does not contain hazardous metal-organic reagents (for example, $\text{Ga}(\text{CH}_3)_3$; trimethylgallium). (d) It can be obtained at a low cost and with environmentally friendly energy. Furthermore, it was previously stated that 1.5 eV is the direct transition energy bandgap of CdTe (22). Moreover, that is the only material that can check the conduction sort and conductivity of II-VI materials by controlling impurity addition and exploiting ED.

Until now, the correlation between the electric features and the deposition conditions (which is the main carrier density (CD) and conduction sort) of CdTeTFm has been manufactured and explained openly by controlling the film composition and the DP. When the films are at a negative DP of more than -0.40 V versus Ag/AgCl on the positive part. In this case, CdTe is of the Te-rich p-type, while in the negative part, it is of the Cd-rich n-type (23). The CD of electro-deposited CdTeTFm is at most 10^{16} to 10^{17} cm^{-3} (24). On the other hand, it is too low to obtain high-efficiency SCs that require more than 10^{20} cm^{-3} . Thus, they researched the deposition method for CdTe thin films to control the transmission sort and CD, and stated the correlation between coating conditions and film features with Cu-doped CdTe (24, 25) where Cu works as a single acceptor. In the literature, it was observed that different methods carried out the synthesis of CdTeTFm. In this research, the synthesis of CdTeTFm was performed by EDM in different acids aqueous solutions, and with low pH values. Hence, a comparison of CdTeTFms obtained using four different acid solutions was made for the first time. Furthermore, one of the important

points of this study, CdTeTFm, was obtained by the electrochemical deposition method with perchloric acid (HClO_4). HClO_4 is a chlorine oxoacid which is a water-soluble, colorless liquid.

In this work, CdTeTFm were obtained by using ED device of IVIUM VERTEX different acidic aqueous media. Furthermore, in the development of physical and chemical properties of synthesized CdTeTFm, mixing speed, duration, concentration, pH and temperature were investigated. Physical properties of obtained CdTeTFm were determined by XRD, SEM/EDX, FT-IR, and UV-VIS analysis methods.

Finally, according to the analysis (SEM, XRD, etc.) results, it was observed that synthesized CdTeTFm with HClO_4 acid is smoother than synthesized CdTeTFm with other acids (H_2SO_4 and HNO_3). Moreover, SEM images of CdTeTFm don't have pinholes on the surface.

2. EXPERIMENTAL

2.1. Synthesis of CdSe Thin Films

In this investigation, CdTeTFm was synthesized by using an ED device of IVIUM VERTEX in different acidic aqueous media. A 3-electrode ED cell was used for the deposition of $\text{Cd}(\text{NO}_3)_2$ containing ITO (indium-doped tin oxide as a WE), platinum wire (CE), and Ag/AgCl (RE). First, ITO-coated glass substrates (GSs) were washed with $\text{C}_3\text{H}_6\text{O}$ and H_2O during a certain time to ensure that no pollution was left on the GSs. Second, Deposition baths consisted of $2.45 \times 10^{-1} \text{ M Cd}(\text{NO}_3)_2$, Na_2TeO_3 , 0.1 M KCl, and 3 drops of a solution of acid (HCl , H_2SO_4 , HClO_4 , and HCO_3). The cathodic potential was used to be -0.45eV. $\text{Cd}(\text{NO}_3)_2$ and Na_2TeO_3 were used as Cd and Te sources, respectively. H_2SO_4 , HCl , HClO_4 , and HNO_3 acids were used to facilitate ion transfer in the solution medium. Synthesis conditions of CdTeTFm are shown in Table 1. CdTeTFm were called CdTe (HCl), CdTe (H_2SO_4), CdTe (HClO_4), and CdTe (HNO_3), respectively. When the bath temperature reached 85°C , the film was formed $\text{Cd}(\text{NO}_3)_2$ and Na_2TeO_3 covered on ITO-coated GSs during the depositions. Hence, analysis of current densities (CDs) time curves for different acidic aqueous media of samples was carried out using EDM for 25min. The experimental scheme is given in Figure 1.

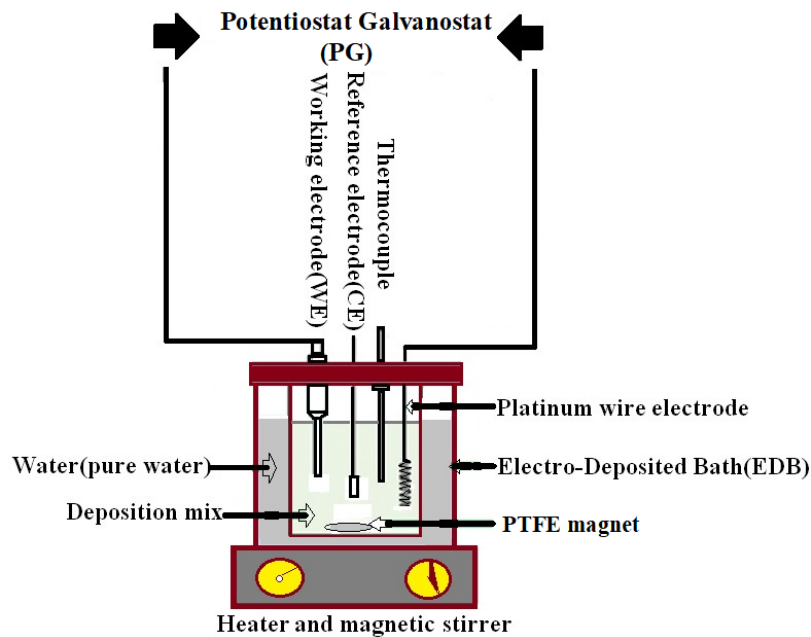


Figure 1: The experimental scheme of CdTeTFm.

Table 1: The synthesis parameters and chemicals of CdTe thin films.

Experiments	HCl	H ₂ SO ₄	HClO ₄	HNO ₃
Concentration (M)	2.45×10 ⁻¹ M	2.45×10 ⁻¹ M	2.45×10 ⁻¹ M	2.45×10 ⁻¹ M
Cathodic potential (V)	-0.45	-0.45	-0.45	-0.45
Analysis time (min.)	25	25	25	25
pH	3.56	3.57	3.56	3.57
Acid type	HCl	H ₂ SO ₄	HClO ₄	HNO ₃
Temperature (°C)	85	85	85	85
Source of Cd	(CdNO ₃) ₂	(CdNO ₃) ₂	(CdNO ₃) ₂	(CdNO ₃) ₂
Source of Te	Na ₂ TeO ₃	Na ₂ TeO ₃	Na ₂ TeO ₃	Na ₂ TeO ₃
Revolutions per minute (rpm)	800	800	800	800

2.2.Characterization studies

In this paper, FT-IR spectra of CdTeTFm were obtained in the range of 650-4000 cm⁻¹(the Perkin Elmer model IR). XRD analyses of CdTe also were performed using 0.066 step size, CuKα (λ=1.540 Å) radiation with 30V (tension), 40kV (current), and over the range 0°<2θ<70°(Panalytical Empyran HT-XRD). SEM and EDX mapping analyses were performed to obtain the surface morphology and the elemental composition of Cd and Te using the Zeiss SUPRA V 40. To determine the bandgap and adsorption wavelength features (OPs) of CdTeTFm was used, A JASCO V-530 double-beam UV-Vis spectrophotometer.

3. RESULTS AND DISCUSSION

Figure 1 illustrates UV-Vis analyses of the CdTeTFm. Hence, the OPs of CdTeTFm deposited versus acidic aqueous media were determined with A JASCO V-530 double-beam UV-Vis spectrophotometer. Band gaps of thin films have important effects on their performance such as solar cells. Therefore, the transmittance spectra of CdTeTFm are worth studying. It with different acidic aqueous media are given in Fig.2(b). It reports that CdTeTFm can absorb (Fig. 2(a)) almost all photons with a wavelength from 550 nm to 1000 nm (26).

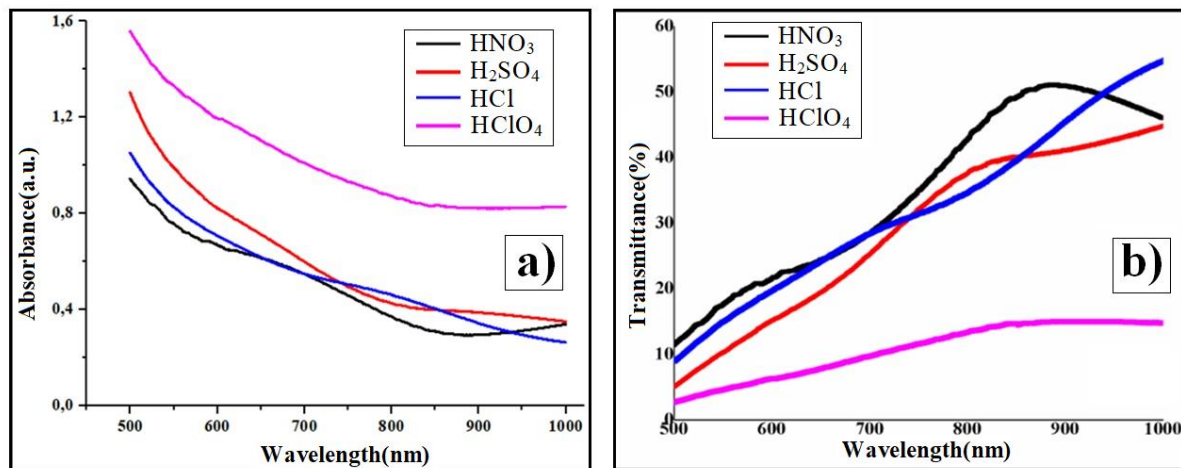


Figure 2: OPs of CdTe thin films deposited at versus acidic aqueous media a) Absorbance, b) Transmittance.

Figure 3 shows the CdTeTFm current densities. The current density depends on the thin film thickness and particle size (27).

At 85 °C, average CDs were obtained at 0.05 mA/cm². In addition, it was determined that the CDs increased proportionally by as much as 1.1 mA/cm² while the temperature value increased from 58 to 98°C. Therefore, it can be said that the reaction rate (RR) increases with temperature. It was observed that when the deposition temperature is increased,

the molecular collision increases; thus, RR increases (28). Based on literature data, syntheses were performed at 85°C.

SEM images showed they agreed with the film particle sizes varying depending on the CD values (Fig. 3, 6 (a)). Besides the high CD values of HNO₃, the particles of CdTeTFm synthesized with HNO₃ were larger than the other thin films (Fig. 3, 6).

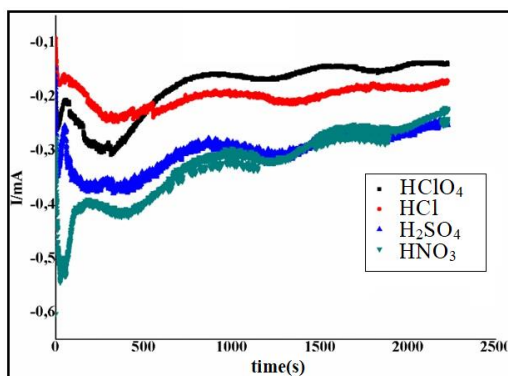


Figure 3: CD and time curves for different acidic aqueous media.

Figure 4 illustrates the XRD samples of synthesized CdTeTFm with diverse acidic aqueous media. The spherical-shaped grains structure of CdTeTFm was identified by the diffraction patterns between $2\theta = 20^\circ - 90^\circ$ with main 5 peaks, which correspond to $2\theta = 111, 220, 311, 440,$ and 112 of ordered hexagonal structures. All CdTeTFm had a clear ($d_{111}, 220$ and 311) CdTe main Bragg peaks occurring at $2\theta = 23.72^\circ, 30.51^\circ, 39.22^\circ, 45.20^\circ, 55.52^\circ$ and 59.89° (29). The crystallite sizes corresponding to different aqueous media were calculated using the Scherrer equation (28, 30).

$$D = \frac{k\lambda}{B(\text{radian})\cos(\theta_B)} \quad (1)$$

In the above expression of the Scherrer equation, "D" (the average size of the crystallites), particle shape factor "k" was taken to be 0.94, the wavelength of the X-ray is " λ " ($\lambda = 0.1542$ nm), "B" is the FWHM intensity, and θ_B is the Bragg angle. To determine the average nanoparticle crystalline size of CdTeTFm, the values associated with the $2\theta = d_{(111)}$ plane in the Scherrer equation were replaced.

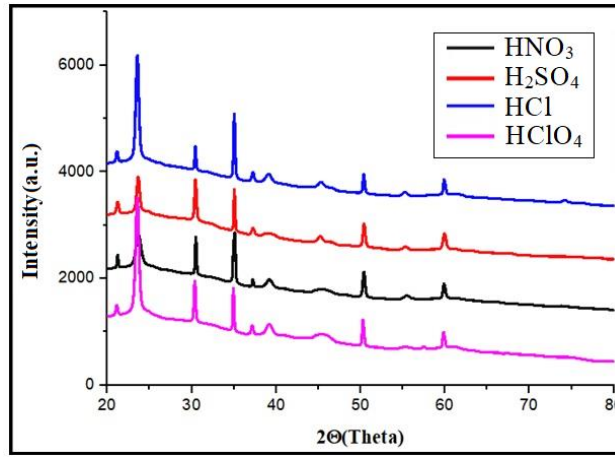


Figure 4: The XRD spectra of CdTeTFm deposited under different acid solutions HNO₃, H₂SO₄, HCl and HClO₄.

Despite very few shifts in the XRD d(111) main peaks, the crystallite sizes and FWHM(°) values of all thin films were 35.66 and 0.2378, respectively (Table 2 and Fig. 4). However, film thickness affects the intensity of XRD peaks. Furthermore, XRD peaks of thick films have a low intensity (Fig. 4, d(111)). However, if thin films have high sensitivity, these films are said to crystallize very well. When well-crystallized films are used as a permeable layer in solar cells, light can pass easily. This facilitates the passage of the photons between “n” and “p” regions. It allows the formation of electron-hole pairs. Moreover, it is preferred for solar cell applications.

Optical absorption measurements of thin films coated on glass were made. The photon energy, depending on the absorption coefficient, was calculated with the Tauc formula and can be expressed as follows:

$$\alpha h\nu = A(h\nu - g)n \tag{2}$$

The graphs of the thin films were drawn (Figure 4), and the band gaps were determined (Table 2). Here, the photon energy is $h\nu$, the absorption coefficient is α , A constant, and E_g band gap, $n=1/2$ for the direct band gap. The “n” of the indirect band gap, on the other hand, is assumed to be 2 ($n = 2$). For thin films, it also depends on the thickness of the film(31,32). The direct transitions CdTeTFm are used(29).

The calculated band gaps of CdTe (HClO₄, HNO₃, H₂SO₄ and HCl) thin films were obtained as 1.42, 1.48, 1.58, and 1.50 eV, respectively (Figure 3 and Table 2). As expected, CdTe(HClO₄) thin films with small particle sizes have been determined to have lower forbidden energy band gap values. This situation can be explained by the relationship between matter and the light used.

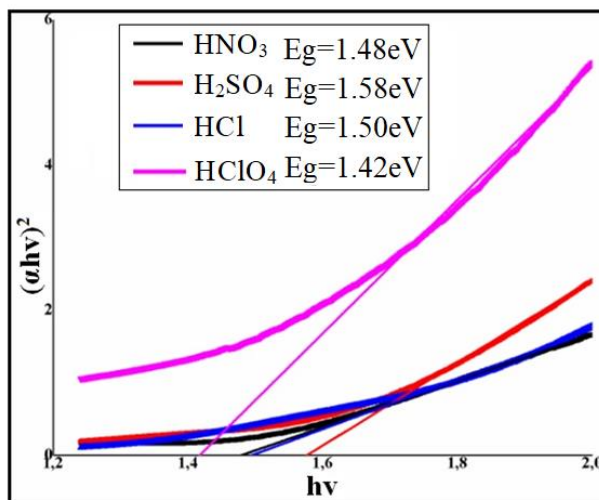


Figure 5: Tauc's plot curves of CdTeTFm.

Table 2: Physical properties of CdTeTFm.

Experiments	HNO ₃	H ₂ SO ₄	HCl	HClO ₄
Crystallite Size(nm)	11	20	20	17
FWHMβ(°)	0.2378	0.2378	0.2378	0.2378
Band gap(eV),(Tauc's plot)	1.48	1.58	1.50	1.42

FWHMβ(°) (full width at half-maximum).

Figure 6 shows the SEM images of the CdTeTFm (30kx magnifications). The surface morphology results of CdTeTFm showed different surface morphologies in different acidic aqueous media. Nitric acid-synthesized CdTe thin films had more clear spherical shaped grains (25) and were larger than others (Figures 6 and 7(a and c)). Furthermore, as

the acidity of the solution decreased, the surfaces of the synthesized thin films became smooth (Fig. 7 (a, c)). According to EDX analysis results, Cd/Te ratios of CdTe thin films synthesized in different aqueous media were obtained as 0.65, 0.587, 0.79, and 0.738, respectively (Fig. 6 and 7(b and d)).

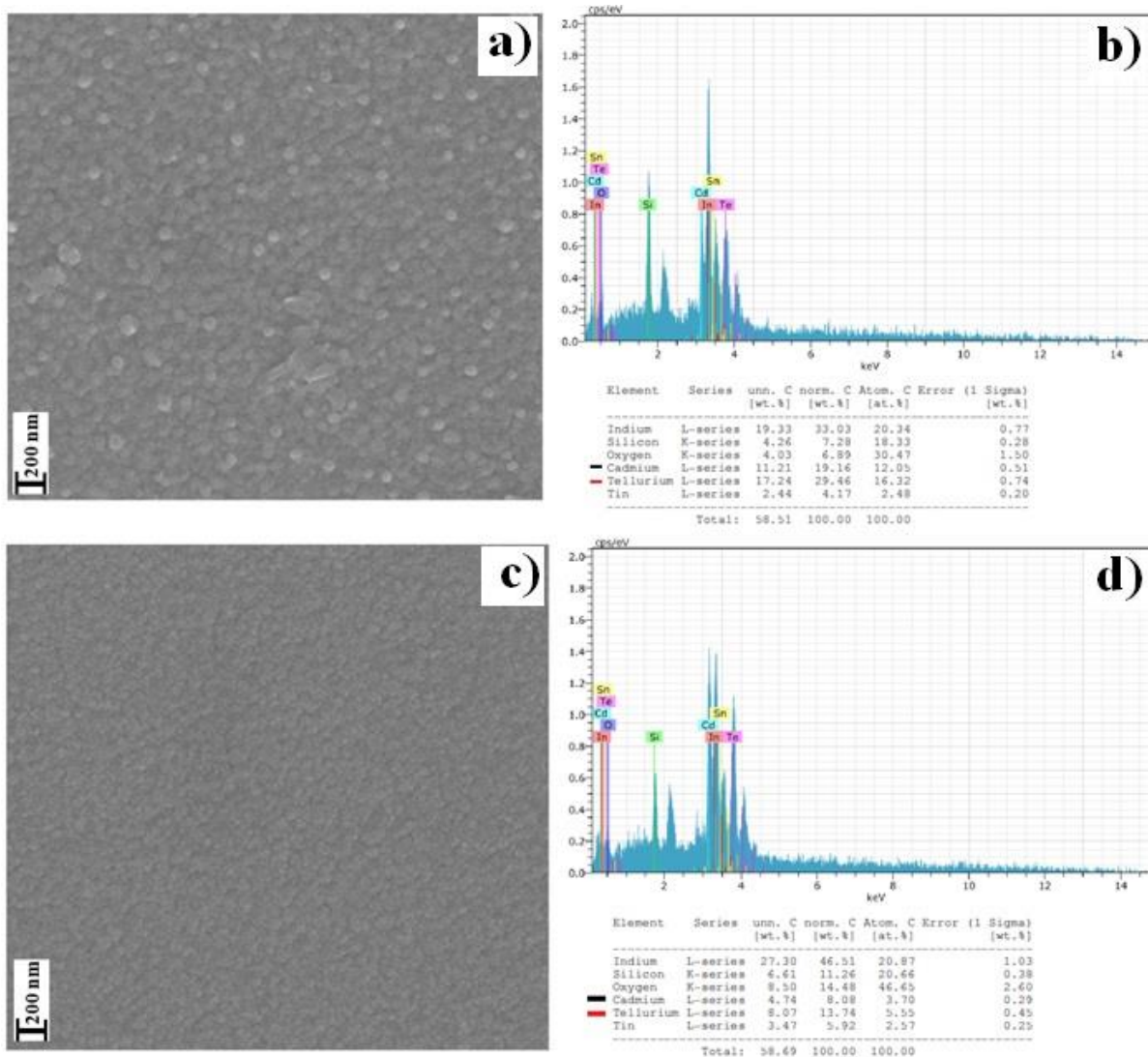


Figure 6: SEM images and EDX results of CdTeTFm deposited under different acid solutions (a, b) HNO₃, (c,d) H₂SO₄.

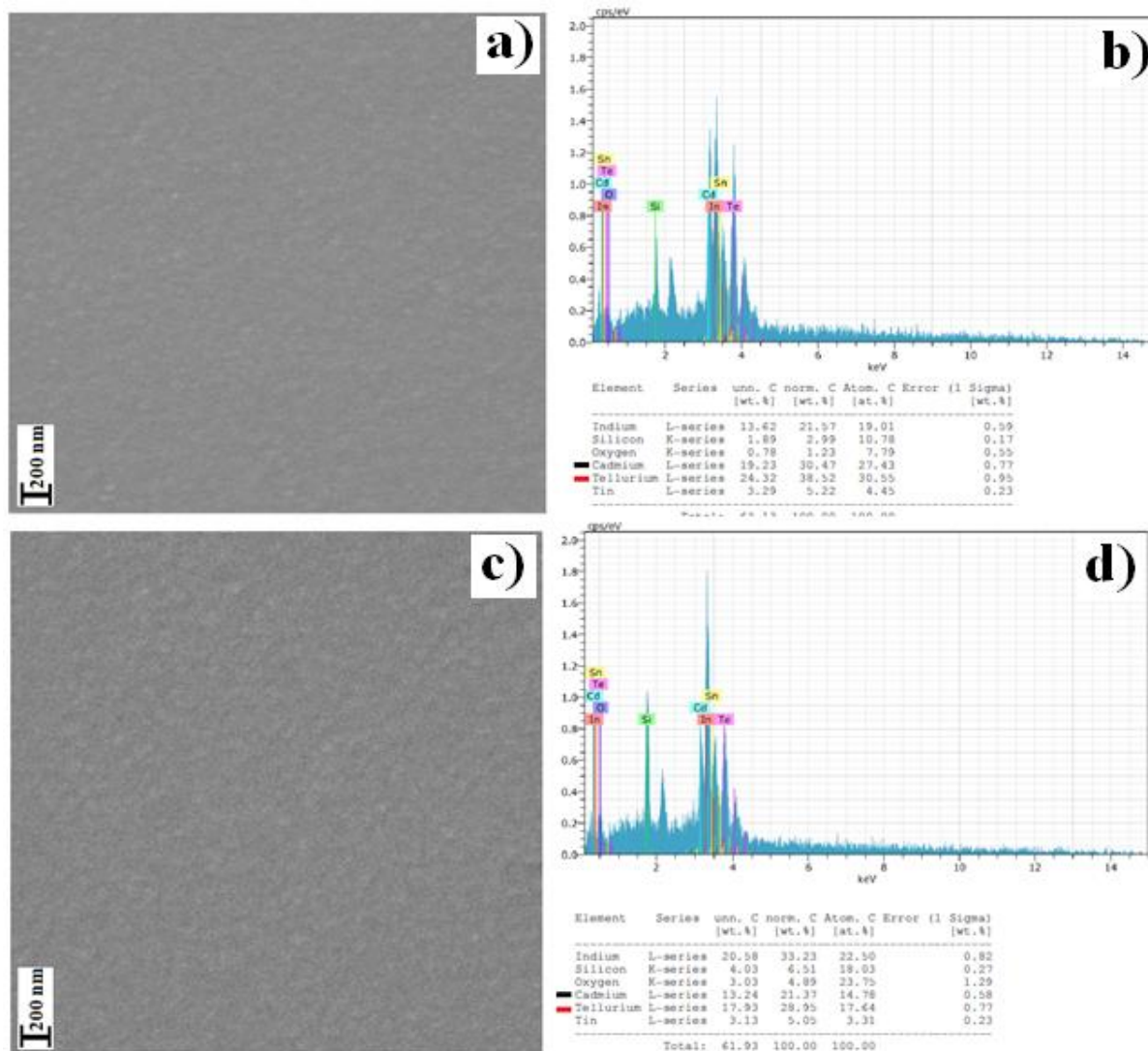


Figure 7: SEM images and EDX results of CdTeTFm deposited under different acid solutions (a, b) HCl, (c, d) HClO₄.

The thick films are not desirable in solar cells. However, the high absorbance of the films is desirable if it can be applied to gas sensors. The flatness of the obtained thin films does not scatter the photons. That is, this property increases the permeability of the films. If the surfaces of the synthesized films are rough, they cause the scattering of photons, reduce permeability, and increase absorption. Moreover, thin films to be used in solar panels should have an optimum 1.5eV and high permeability and absorption values. These properties can be obtained as a result of easier penetration of rays into the P semiconductor region.

In addition, surface characterizations of the obtained thin films were determined with the ImageJ(Fiji-win64-Fiji.app) program. The surface plot, 3D surface plot, and SurfChar1 q programs were used for the surface morphologies of the thin films. The results obtained are given in Figure 8. According to SurfCar1 q analysis results, roughness values were obtained as 11.9880, 10.6749, 8.6264, and 6.9208nm, respectively. It has been observed that these results are compatible with surface plots and 3D surface plot images. It was determined that the thin film synthesized with HCl was less rough and the grain sizes were more homogeneous (Figure 9).

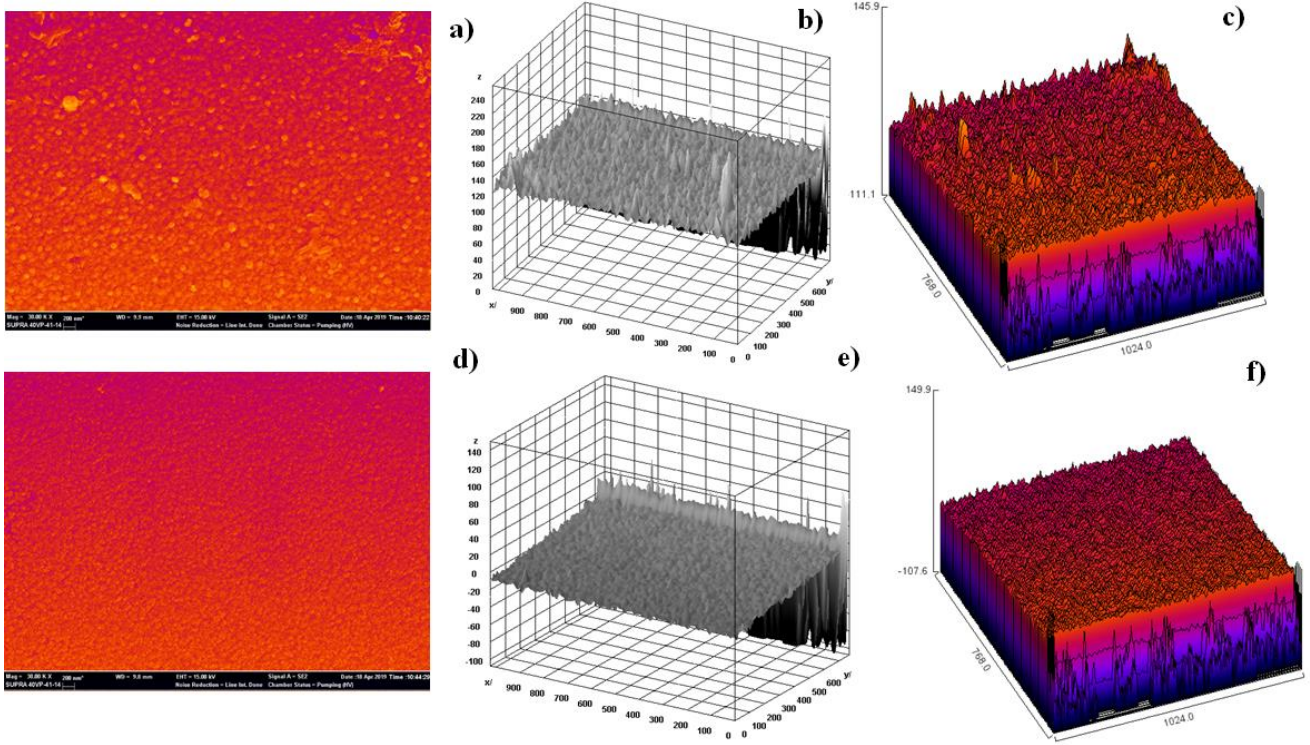


Figure 8: ImageJ analyses of CdTe (a, b, c are HNO₃ and d, e, f are H₂SO₄).

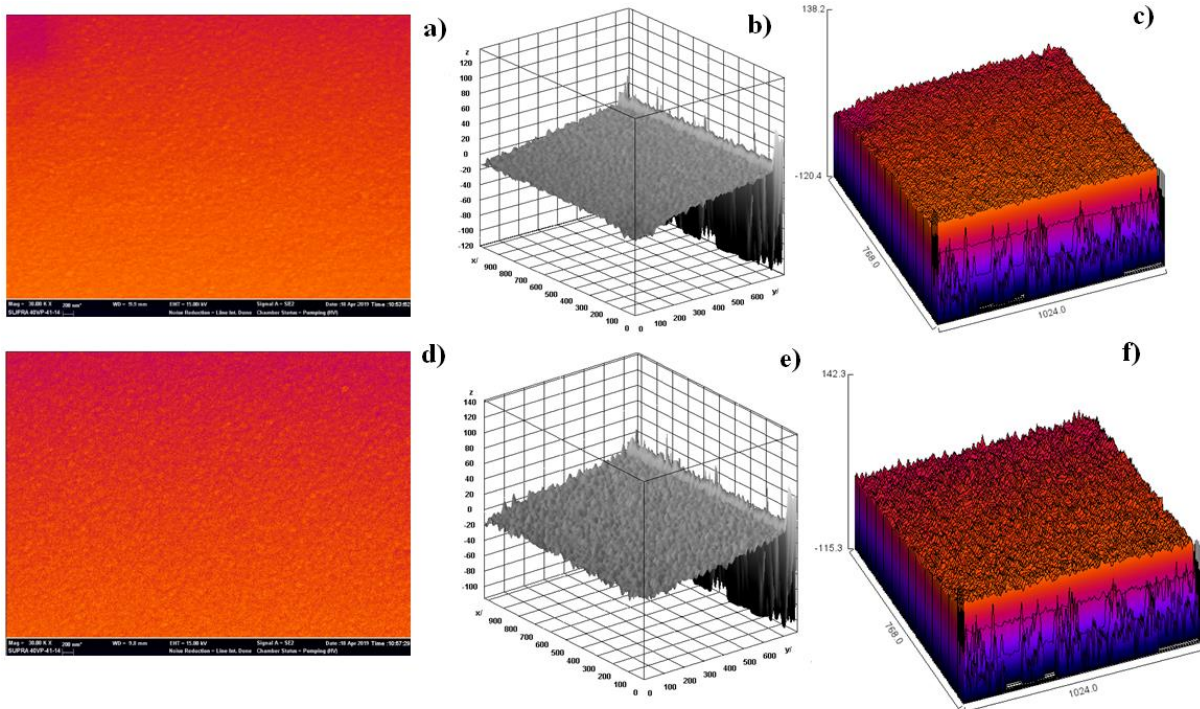


Figure 9: ImageJ analyses of CdTe (a, b, c are HCl and d, e, f are HClO₄).

4. CONCLUSION

CdTe thin films were obtained by the electrochemical deposition method. The effects of DAAM (such as HCl, H₂SO₄, HClO₄, and HNO₃) on the film surface, the structural morphology, and the OPs of the thin films obtained were investigated by XRD, SEM/EDX, FT-IR, and UV analysis methods. Moreover, a novel investigation of synthesized CdTeTFm with HClO₄

acidic aqueous media has been reported in the literature. By investigating the OPs of semiconductors, information regarding the behavior of electrons and holes in the material, as well as band structures, can be gleaned. Each material emits varied and distinct wavelengths. Similarly, the wavelengths absorbed by each substance will differ from those of other materials. The amount of light absorbed can have positive effects on optical

properties. Therefore, the surfaces, shapes, and crystal sizes of the synthesized thin films are important. It was observed that SEM images of CdTeTFm obtained with nitric acid were rough compared to other films. However, no pinholes were observed on the film surfaces. The permeability of the beams, which is thought to be due to the film thickness, was low. Despite the low transmittance of HClO₄, the current density and absorbance value were higher than other thin films. It was observed that the surface of the CdTe thin film synthesized with HClO₄ was smoother than the films obtained with HCl and H₂SO₄, and also that the Cd/Te ratio was higher. This result is predicted to be due to the grain size thickness of CdTeTFm synthesized with HClO₄. We think that since HClO₄ has a higher acidity than other solvents, it causes thinner smooth thin films to be obtained. The grain size and film thickness of HClO₄ were calculated as 105 and 344 nm, respectively. Moreover, it has the lowest forbidden band gap. Solar cells can store energy more efficiently with thin films of low transmittance and high absorbance. As a result, it has been seen that CdTeTFm prepared with HClO₄ is a good candidate for solar panels with the lowest transmittance and highest absorbance value.

5. CONFLICT OF INTEREST

The authors confirm that this article's content has no conflict of interest.

6. REFERENCES

- Gong T, Liu J, Liu X, Liu J, Xiang J, Wu Y. A sensitive and selective sensing platform based on CdTe QDs in the presence of L-cysteine for detection of silver, mercury and copper ions in water and various drinks, *Food Chem.* 2016; 213: 306–312.
- Romeo A, Artegiani E. CdTe-Based Thin Film Solar Cells: Past, Present and Future, *Energies.*2021; 14: 1684. <https://doi.org/10.3390/en14061684>
- Kosyachenko L, Lashkarev G, Grushko E, Ievtushenko A, Sklyarchuk V, Mathew X and Paulson PD. Spectral distribution of photoelectric efficiency of thin-film CdS/CdTe heterostructure. *Acta Physica Polonica A.*2009; 116: 862.
- Scarpulla MA, McCandless B, Phillips AB, Yan Y, Heben MJ, Wolden C, Xiong G, Metzger WK, Mao D, Krasikov D, Sankin I, Grover S, Munshi A, Sampath W, Sites JR, Bothwell A, Albin D, Reese MO, Romeo A, Nardone M, Hayes S M, CdTe-based thin film photovoltaics: Recent advances, current challenges and future prospects, *SolarEnergyMaterials&SolarCells,* 2023;255: 112289.
- Romeo A, Artegiani E. CdTe-Based Thin Film Solar Cells: Past, Present and Future. *Energies.* 2021; 14(6):1684. <https://doi.org/10.3390/en14061684>.
- Silva FO, Carvalho MS, Mendonça R, Macedo WAA, Balzuweit K, Reiss P, Schiavon MA. Effect of surface ligands on the optical properties of aqueous soluble CdTe quantum dots, *Nanosc. Res. Lett.* 2012; 7: 1–10.
- Farghaly OA, Hameed, RSA, Abu-Nawwas AAH. Analytical Application Using Modern Electrochemical Techniques, *Int. J. Electrochem. Sci.*2014;9: 3287–3318.
- Sanny WMMC, Charlene R S M, Tiago BSS, Anne MGPS, Luiz P C, Eliana M S, Iara F G. Study on the preparation of CdTe nanocrystals on the surface of mesoporous silica and evaluation as modifier of carbon paste electrodes *Journal of Porous Materials.* 2019; 26: 1157–1169, <https://doi.org/10.1007/s10934-018-00717-3>.
- Zakharov O, Rubio A, Cohen ML. Calculated structural and electronic properties of CdSe under pressure, *Physical Review B.*1995; 51: 4926-4930.
- Sarmah K, Sarma R, Das HL. Correlative assessment of structural and photoelectrical properties of thermally evaporated CdSe thin films, *Journal of Non-Oxide Glasses.*2009; 1: 143-156.
- Tohidi T, Jamshidi-Ghaleh K, Namdar A and Abdi-Ghaleh R. Comparative studies on the structural, morphological, optical, and electrical properties of nanocrystalline PbS thin films grown by chemical bath deposition using two different bath compositions. *Materials Science in Semiconductor Processing.*2014; 25: 197-206.
- Tobin SP, Vernon SM, Bajger C, Wojtczuk SJ, Melloch MR, Keshavarzi A, Stellwag TB, Lundstrom MS, Emery KA. Assessment of MOCVD- and MBE grown GaAs for high-efficiency solar cell applications. *IEEE Trans Electron Devices.*1990; 37: 467–477.
- Chu TL, Chu SS. Thin film II-VI photovoltaics. *Solid State Electron.*1995; 38: 533–549.
- Huang J, Yang D, Li W, Zhang J, Wu L, Wang W. Copassivation of polycrystalline CdTe absorber by CuCl thin films for CdTe solar cells, *Applied Surface Science.*2019; 484: 1214–1222.
- Chu TL, Chu SS, Ferekides C, Britt J, Wu CQ. Thin-film junctions of cadmium telluride by metalorganic chemical vapor deposition. *J Appl Phys.*1992; 71: 3870–3876.
- Ringel SA, Smith AW, MacDougal MH, Rohatgi A. The effects of CdCl₂ on the electronic properties of molecular-beam epitaxially grown CdTe/CdS heterojunction solar cells. *J Appl Phys.*1991; 70:881–889.
- Compaan AD, Gupta A, Lee S, Wang S, Drtaton J. High efficiency, magnetron sputtered CdS/CdTe solar cells. *Sol Energy.*2004; 77: 815–822.
- Uosaki K, Takahashi M, Kita H. The photoelectrochemical behavior of electrochemically deposited CdTe films. *Electrochem Acta.* 1984; 29: 279–281.
- Jeon S-H, Choi W-I, Song G-D, Son Y-H, Hur DH. Influence of Surface Roughness and Agitation on the Morphology of Magnetite Films Electrodeposited on Carbon Steel Substrates. *Coatings.* 2016; 6(4):62. <https://doi.org/10.3390/coatings6040062>.
- Nishio T, Takahashi M, Wada S, Miyauchi T, Wakita K, Goto H, Sato S and Sakurada O. Preparation and Characterization of Electrodeposited In-Doped CdTe Semiconductor Films, *Electrical Engineering in Japan,*2008; 164: 3.
- Kenta H, Toru W and Hitoshi H. Electric Current in Rate Equation for Parallel Plate Plasma-Enhanced Chemical Vapour Deposition of SiC_xN_yO_z Film without Heat Assistance. *ECS Journal of Solid State Science and Technology.* 2020; 9(2): 024001.

Kiyak Yıldırım A, Şimşek V. 2024; 11(2): 591-600

22. Takahashi M, Uosaki K, Kita H. Effects of heat treatment on the composition and semiconductivity of electrochemically deposited CdTe films. *J Appl Phys.*1985; 58: 4292–4295.

23. Takahashi M, Uosaki K, Kita H. Composition and electronic properties of electrochemically deposited CdTe films. *J Appl Phys.* 1984; 55: 3879–3881.<https://doi.org/10.1063/1.332904>.

24. Nagaoka A, Kuciauskas D, Scarpulla MA, Doping properties of cadmium-rich arsenic-doped CdTe single crystals: evidence of metastable AX behavior, *Appl. Phys. Lett.* 2017; 111, 232103. <https://doi.org/10.1063/1.4999011>.

25. Takahashi M, Muramatsu M, Watanabe M, Wakita K, Miyuki T, Ikeda S. Preparation and characterization of Cu-doped p-CdTe films grown by cathodic electrodeposition. *J Electrochem Soc.* 2002; 149: C311–C316.**DOI** 10.1149/1.1470660

26. Li C, Wang F, Chen Y, Wu L, Zhang J, Li W, He X, Li Bing. Characterization of sputtered CdSe thin films as the window layer for CdTe solar cells. *Materials Science in Semiconductor Processing.*2018; 83: 89–95.

27. Mogro-Campero A, Turner LG. Film Thickness Dependence of Critical Current Density for YBa₂CuO₇ Films Post-annealed at a Low Oxygen Partial Pressure, *Journal of Superconductivity.*1993; 6:1.

28. Kiyak A, Altıokka B. An investigation of effects of bath temperature on CdO films prepared by electrodeposition *Appl Nanosci.*2017;7: 513–518.

29. Shaabana ER, Afify N, El-Taher A. Effect of film thickness on microstructure parameters and optical constants of CdTe thin films, *Journal of Alloys and Compounds* .2009; 482: 400–404.

30. Şimşek V, Çağlayan MO. Nanocrystalline PbS thin film produced by alkaline chemical bath deposition: effect of inhibitor levels and temperature on the physicochemical properties, *Int. J. Mater. Res.* 2023; 114(12): 1047–1057.

31. Saleh W R, Saeed NM, Twej W A and Alwan M. Synthesis sol-gel derived highly transparent zno thin films for optoelectronic applications, *Advances in Materials Phy. and Chemistry.* 2012; 2: 11–16.

32. Sardela M. Practical materials characterization, Springer, New York. 2014; ISBN:978-1-4614-9280-1.



A Review on Different Analytical Techniques for Quantification of Moxidectin

Kommu Aarthi¹  and Raja Sundararajan^{1*} 

¹GITAM (Deemed to be University), Department of Pharmaceutical Quality Assurance, GITAM School of Pharmacy, Visakhapatnam, Pin-code: 530045, Andhra Pradesh (State), India.

Abstract: Moxidectin, a macrocyclic lactone of the milbemycin class, is a fermentation by-product of the bacteria *Streptomyces cyanogriseus subsp. non-Cyanogenus*. Moxidectin is a semi-synthetic derivative of nemadectin. River blindness, also known as onchocerciasis, is treated with moxidectin in patients 12 years of age and older. This condition is brought on by the parasitic worm *Onchocerca volvulus* and is subjected to intense itching, skin conditions that are disfiguring, and impaired vision brought on by the larvae of the worm. Some of the most common internal and exterior parasites are killed by moxidectin by selectively binding to their glutamate-gated chloride ion channels. In this review article, various pieces of equipment, such as a UV spectrometer, HPLC, LC-MS, and UPLC-MS, are used to determine moxidectin as well as its related compounds. The QuEChERS method was also used in the sample preparation according to the literature survey. The report also offers an overview of the pharmacodynamics, pharmacokinetics, and medication interactions of moxidectin.

Keywords: Moxidectin, Anthelmintic, River Blindness, Macrocyclic Lactones

Submitted: February 27, 2023. **Accepted:** January 29, 2024.

Cite this: Aarthi K, Sundararajan R. A Review on Different Analytical Techniques for Quantification of Moxidectin. JOTCSA. 2024; 11(2): 601-14.

DOI: <https://doi.org/10.18596/jotcsa.1257065>.

***Corresponding author. E-mail:** sraja61@gmail.com.

1. INTRODUCTION

The drug moxidectin (MOX) is a member of the macrocyclic lactones (MLs) class. It is created by the bacteria *Streptomyces cyanogriseus* or *S. hygroscopicus* and is primarily used in veterinary medicine to treat a variety of parasite infections in animals used for food production. Various regulatory organizations have defined maximum residue limits and tolerance limits for veterinary drugs to protect humans from being exposed to harmful residual levels through the consumption of edible products produced from treated animals. The liver and other tissues including the kidney and the muscle regulate the maximum levels of these drugs. (1) Because MLs are harmful, the European Union Council decided to set a maximum residual level for this substance out of concern for consumer safety. To identify ML residues in goods of animal origin, extremely sensitive and selective procedures are needed because the concentration of interest was frequently quite low. (2).

1.1. Pharmacodynamics

Moxidectin has been reported to be extremely effective against *Onchocerca volvulus* than other drugs. Moxidectin remains to be more efficient than a variety of Ivermectin-resistant nematode species when given to infected individuals. While still safe to be utilized in mass drug administration, the levels of microfilaria were reduced to undetectable levels, and moxidectin's efficacy is significantly higher when compared to other drugs. (4)

1.2 Pharmacokinetics

Moxidectin was more quickly absorbed from the injection site than other drugs (absorption half-life = 0.7 days). Moxidectin's highest plasma concentration (C_{max}) had occurred much earlier ($T_{max} = 0.4$ days). However, moxidectin's mean residence time was longer than doramectin's (9.4 days) and had a higher region under the concentration-time curve (475 ng day/mL) than doramectin's (198 ng day/mL) (4). No variations in C_{max} values were seen. Moxidectin has a

shorter T_{max} but a longer C_{max} and AUC. It has limited oral bioavailability and this small species' early emergence of resistance may be connected. (5)

1.3 Drug interaction studies

1.3.1. Clinical Study using Midazolam (CYP3A4 substrate)

In healthy individuals, taking moxidectin tablets in combination with a single 8 mg dosage had no impact on the pharmacokinetics of midazolam. Moxidectin and CYP3A4 substrates can be administered together. (5)

2. HIGH-PERFORMANCE LIQUID CHROMATOGRAPHIC (HPLC) METHOD

HPLC is used to separate the complex molecular mixtures that can be found in biological and chemical systems so that each function of the component can be thoroughly understood. The HPLC method can achieve the required precision and has great selectivity. The drug has been analyzed by using HPLC with UV, MS, or MS/MS detection modes. Utilizing high-performance liquid chromatography-based techniques, Animal tissues like liver, muscle, and fat as well as milk, urine, feces, and plasma have been found to contain moxidectin. (1) The following table 1 lists the results of the quantitative measurement of moxidectin using HPLC techniques.

Table 1: Determination of moxidectin by HPLC method.

Sr No	Drug	Mobile phase	Stationary phase	Parameters	Reference
1.	Moxidectin	Acetonitrile, ethyl acetate, and Water (90:4:6 v/v/v)	Waters Sun Fire C ₈ column (150 mm x 4.6 mm, 5 μm, Waters, USA)	Selectivity, linearity, trueness, LOD, LOQ, decision limit (CC _α), and detection capability (CC _β).	1
2.	Moxidectin	85% Methanol and 15% water	Waters PAH C ₁₈ (50 mm x 4.6 mm x 3 μm from Waters Mild ford, MA, USA)	Recovery, trueness, precision, decision limit, and detection capability	2
3.	Moxidectin	Acetonitrile and water (90:10 v/v), Acetonitrile and Isopropyl alcohol (85:15 v/v)	Zorbax Eclipse XDB-C ₁₈ column (150mm x 4.6 mm x 1.8 μm, Agilent, USA)	Linearity, LOD, LOQ, decision limit, detection capability, precision	3
4.	Moxidectin	Acetic acid - Methanol - Acetonitrile (4:15:31, v/v/v).	a Supelcosil C ₈ column	Linearity, precision, recovery, LOD, LOQ	6
5.	Moxidectin	Tetrahydrofuran-Acetonitrile-Water (40:38:22 v/v/v)	Alltech Ultra sphere C ₁₈ (5μm, 4.6 x 250 mm) column	Selectivity, precision, accuracy, recovery, linearity	7
6.	Moxidectin	0.2% Acetic acidic in water/methanol Acetonitrile (1.6:60:38.4, v/v/v)	Reverse Phase C ₁₈ column (5 μm, 4.6 mm x 250 mm)	C_{max} , T_{max} , $t_{1/2}$, AUC, standard deviation	8
7.	Moxidectin	Acetonitrile and Water (94/6, v/v)	Merck Lichrospher 100RP-18E, (5 μm, 125mm x 4 mm)	Recovery test, LOD, LOQ, precision	9
8.	Moxidectin	Acetic Acid: Methanol: Acetonitrile (20:40:40, v/v/v).	Supelcosil C ₁₈ column (5 μm, 4.6mm x150mm)	Recovery, radiopurity	10

9.	Moxidectin	Acetonitrile: methanol: water (55:27:18, v/v/v)	Gemini C ₁₈ column (150 mm × 4.60 m, 5 μm)	Precision, accuracy, recovery tests, robustness	11
10.	Moxidectin	Acetic acid-methanol-acetonitrile	Supelcosil C ₁₈ column (5 μm 150 mm × 4.6 mm)	C _{max} , T _{max} , mean residence time (MRT)	12
11.	Moxidectin	Acetonitrile (A) and water (B)	Luna C ₈ (150 mm × 3.0 mm, 5 μm)	Specificity, linearity, recovery, precision, LOD, LOQ	13
12	Moxidectin	Acetonitrile, Tetrahydrofuran, water (52:25:23 v/v/v).	C ₁₈ column (150 × 5mm, 5 μm)	LOD, recovery, correlation coefficient	LOQ, 14

Fabio Macedo et al. developed and verified a method for measuring four macrocyclic lactones in butter simultaneously by combining liquid chromatography (LC) with fluorescence detection. The mobile phase consisted of 10 ml of a (90:4:6 v/v/v) ACN, ethyl acetate, and water solution. For the separation, a Sun Fire C₈ (150 × 4.6 mm, 5 μm) column was used. The examined samples had ML residues, according to the method's applicability to actual samples. The recovery, repeatability, within-laboratory reproducibility, and LOD values were satisfactory for the intended application. The technique proved straightforward to apply and performed well for the simultaneous measurement of Macrocyclic lactone residues in butter. (1)

David Pimentel-Trapero et al. established a procedure employing QuEChERS and HPLC with fluorescence detection to measure the macrocyclic lactones in the liver of cows. An analytical Waters PAH C₁₈ column of (50 mm × 4.6 mm, 3 μm) was used for the separation. Methanol comprised about 85% of the mobile phase and 15% of it was water. The analytes' fluorescent derivatives were generated by subjecting the sample extracts to a mixture of trifluoroacetic anhydride, triethylamine, and 1-methylimidazole. Results for recovery of analytes, trueness, repeatability, LOD, and LOQ were found to be following EU Decision 2002/657's requirements. (2)

Ana Maria de Souza Santos et al. created and verified a very sensitive analytical technique for the detection of five macrocyclic lactone residues in cheese. For the separation, a Zorbax Eclipse XDB-C₁₈ column (150 mm × 4.6 mm, 1.8 μm) has been used. ACN and water made up the mobile phase (ACN: H₂O, 90:10 v/v), and acetonitrile and isopropyl alcohol made up the reaction mixture (ACN: ISOPROH, 85:15 v/v) (B). Excellent mean recoveries, repeatability, limits of quantification, and intermediate precisions were obtained. (3)

Bengone-Ndong et al. analyzed the kinetics of the plasma of moxidectin and doramectin in zebu gobra in the field settings following cutaneous application of available commercial formulations for cattle at 0.2 mg/kg. When compared to doramectin, the highest plasma concentration of moxidectin was achieved significantly earlier. The C_{max} values were constant, but moxidectin had a larger area under the concentration-time curve (475 ng day/ml) than doramectin (198 ng day/ml) and its average residence time was extended (13.4 days) than doramectin's (9.4 days). The outcomes revealed information about the bioavailability of doramectin and moxidectin in zebu gobra, which have a pharmacological property similar to that of other cattle. (4)

Escudero et al. investigated how doramectin and moxidectin act pharmacologically in goats and followed by oral or subcutaneous at a dosage of 0.2 mg/kg. Both compartmental and non-compartmental approaches were employed to analyze the data on drug plasma concentration over time. The maximal plasma concentrations of moxidectin were reached to a greater extent than doramectin. Moxidectin's mean residence time (MRT), when delivered subcutaneously or orally did not differ significantly. This small species' early emergence of resistance and its low oral bioavailability may be related. These findings should be compared to efficacy research to optimize the dosage needs for endectocides in this species. (5)

Alvinerie et al. reported that using fluorescence-enhanced high-performance liquid chromatography as a technique to detect moxidectin in plasma. By using this technique, moxidectin can be converted into a fluorescent derivative rapidly. Using a Supelcosil C₈ column with fluorescence detection, the separation was performed, and the mobile phase consisted of acetic acid/methanol/ACN (4:15:31, v/v/v). The limitations of the analyte recovery, precision, linearity, and quantification limits were found to be within the expected limits. The approach

has worked well for the pharmacokinetic study of moxidectin administered to cows subcutaneously. (6)

Dennis Kitzman et al. devised an HPLC approach for the detection of ivermectin and moxidectin in human plasma that is precise, sensitive, and selective and separates the parent drug from metabolites. The mobile phase consisted of tetrahydrofuran/acetonitrile/water (40:38:22 v/v/v) for separation on an Alltech ultra-sphere C₁₈ (5µm, 4.6 × 250 mm) column. For all concentrations, the assay was linear over the range of 80% and above. With the coefficient of variation, it showed excellent precision. Studies on precision and storage stability were within acceptable limits. This technique was reliable and appropriate for pharmacokinetic clinical research. (7)

Mercedes Lloberas et al. worked to determine the drug concentrations in plasma, target tissues, and parasites were measured by HPLC. An RP C₁₈ (5µm, 4.6 mm × 250 mm) column with a mobile phase of 0.2% of acetic acid in water/methanol/ACN (1.6:60:38.4, v/v/v) was used for the separation at a flow rate of 1.5 ml/min. Moxidectin concentrations showed a longer plasma persistence (P < 0.05). By using the least squares linear regression analysis, calibration curves were developed. Correlation coefficients and coefficient of variation were determined, and the results were found to be within the limits. (8)

Hsiu-Kuan chou et al. developed a technique for simultaneously determining the compound residue quantities (abamectin, doramectin, moxidectin, ivermectin, milbemycin) using HPLC and fluorescence detection in bovine muscle. The mobile phase consisted of 940 mL of acetonitrile and 60 mL of water (94/6, v/v). Acetonitrile was used to extract the samples, and then a C₁₈ column (5 µm, 125mm × 4 mm) was employed for solid phase extraction to clean them up. The quantification thresholds are below the specified limit residue threshold for each compound. The detection limits and recovery studies both were within accepted limits. Hence, the suggested method can be utilized to quickly screen for macrocyclic lactones in cow muscle. (9)

Alvinerie et al. examined how the enzyme cytochrome P450 contributes to the *in vitro* metabolism of moxidectin in homogenates of adult *Haemonchus contortus* stages. After phosphate buffer homogenization, 2 ml of the homogenates were cultured with 5 microorganisms, MOX, at 37 °C for 24 hours. To separate MOX and its metabolites, HPLC with Supelcosil C₁₈ (5 µm, 4.6 mm × 150 mm) column with radio detection online was utilized. The mobile phase consisted of acetic acid/ methanol/ acetonitrile (20:40:40, v/v/v), and was pumped at a flow rate of 1 ml/min. One molecule was found, and carbon monoxide prevented the formation of that metabolite. The results showed that the cytochrome P450 system in the milbemycin-resistant *H. contortus* metabolizes moxidectin. (10)

Roseanne Andrade Teixeira et al. conducted comprehensive research on Poly (1-vinyl imidazole-co-trimethyl propane trimethacrylate) which was employed in pipette-tip nanostructured polymeric solid phase extraction as a selective adsorbent. For the chromatographic separation, the mobile phase was comprised of acetonitrile, methanol, and water (55:27:18, v/v/v), and the analytical Phenomenex® Gemini C₁₈ column was employed (150 mm × 4.60 mm, 5 µm). The stability, robustness, recovery, sensitivity, precision, and accuracy performance criteria have been evaluated and were determined to be within the suggested limits. The results demonstrated the good potential of the HPLC-UV coupled PT-MIP-SPE technique for the extraction of macrocyclic lactones from water, grape juice, and other substances. (11)

Patricia Esmeralda Vazquez-Quintal et al. developed a method using spectrofluorometry and HPLC with fluorescence detection to measure moxidectin (MOX) and abamectin (ABA) levels in bovine plasma. The separation was carried out on a supelcosil C₁₈ column (150 mm × 4.6 mm, 5 µm) with acetic acid, methanol, and acetonitrile serving as the mobile phase. The developed procedures' total analysis time was comparable to or less than that of the published analytical procedures. The linear range and recovery studies were within the ranges. (12)

Roberta Galarini et al. developed a technique for simultaneously detecting the anti-parasitic veterinary drugs (abamectin, doramectin, emamectin, ivermectin, and moxidectin) in foods and feed. With the help of a Luna C8 (150mm × 3.0mm, 5 µm) column, the separation was accomplished. Acetonitrile (A) and water made up the mobile phase (B). The recovery studies, repeatability, and reproducibility within the lab were satisfactory. Since it completely satisfies the criteria, national control strategies for both food and feed have effectively used this multi-analyte strategy. (13)

Craven et al. investigated if the composition of the animal body at the time of treatment affected the pharmacokinetics of both MOX and IVM. Following a 300 g/kg intravenous infusion of IVM or MOX, samples of blood were collected regularly, and the plasma was analyzed using fluorescence-HPLC on a C₁₈ column (150 × 5 mm, 5 µm) eluted with the mobile phase consisting of acetonitrile, tetrahydrofuran, and water (52:25:23 v/v/v). IVM kinetics showed significant differences from MOX kinetics regardless of body composition, allowing MOX to be detectable in plasma for more than 40 days. MOX had more extended distribution and elimination half-lives than IVM, as well as a slower clearance rate. In this investigation, changes in body composition had no noticeable effect on the kinetic distribution of IVM. MOX was dispersed more evenly inside the lean animals and eliminated quickly than from fat animals, even though still there was no change in the area under the curve and the volume of dispersion. (14)

3. LIQUID CHROMATOGRAPHY-MASS SPECTROSCOPY (LC-MS)

One of the most significant developments of the preceding part of the twentieth century is the combination of mass spectrometry and liquid chromatography. It has become the preferred method for analytical sustenance during several

stages of pharmaceutical quality control and assurance. It has been demonstrated that tandem mass spectrometry (MS/MS) was a useful method for describing the structural characteristics of unknown compounds. (15) The quantitative measurement of moxidectin using LC-MS methods is listed in the following table 2.

Table 2: Determination of moxidectin using LC-MS/MS.

Sr No	Drug	Mobile phase	Stationary phase	Parameters	Reference
1.	Moxidectin	Methanol and water	Whatman RAC I1 Partisil5-C ₈ (4.6 mm x 10 cm)	Concentration ion	15
2.	Moxidectin	78% acetonitrile, 22% water, 0.1% triethylamine	3 mm 'Luna' C ₁₈ stationary phase	Recovery studies, CC _α , CC _β , precision	16
3.	Moxidectin	3mM ammonium formate or 0.05% formic acid prepared in pure water.	Luna C ₈ column (30 × 2.0 mm, 3 μm particle size, 100 Å)	Accuracy, precision, selectivity, sensitivity, linearity	17
4.	Moxidectin	The mixture of (A) 0.05% TEA in acetonitrile and (B) 0.05% TEA in water (70:30 v/v)	C ₁₈ (5 μm, 2.1 × 150 mm, Waters, Milford, MA, USA).	Specificity, selectivity, precision, stability, ruggedness, CC _α , CC _β	18
5.	Moxidectin	50% water (A), 45% ACN (B), and 5% 50 mM ammonium acetate buffer pH 5 (C)	Phenomenex Luna C ₁₈ column (150 mm x 2.1 mm, 5 μm)	LOD, LOQ, selectivity, retention, CC _α , CC _β	19
6.	Moxidectin	Acidic: contained 4 mM ammonium formate and 0.1% formic acid in methanol and water. Basic: 10 mM ammonium acetate in methanol and water	Aqueous C ₁₈ column (3 μm, 100 x 2.1 mm)	Accuracy, linearity, precision, ruggedness, CC _α , CC _β	20
7.	Moxidectin	(A) MeOH: ACN (1:1) with 0.1% formic acid, and eluent (B) ammonium formate solution with 0.1% formic acid.	A Waters Acquity UPLC BEH C ₁₈ column (100 mm x 2.1 mm, 1.7 μm)	Selectivity, linearity, retention, accuracy, precision, LOD, LOQ, CC _α , CC _β	21
8.	Moxidectin	Methanol/water (90:10 v/v)	Agilent Zorbax SB-C ₁₈ (3 mm × 150 mm, 3.5 μm)	Average recovery, %RSD	22

9.	Moxidectin	Ammonium acetate: methanol	water:	Whatman RACII Partisil 5-C ₈ (10 cm x 4.6 mm)	Linearity, recovery, RSD	%	23
10.	Moxidectin	ACN: water (50:50 v/v)		Waters Xterra RP ₁₈ , (3.5micron, 3 mm x 100 mm)	CC α , CC β , LOD, LOQ, %recovery, sensitivity, precision.		24
11.	Moxidectin	50 mM ammonium acetate buffer: acetonitrile (5:95, v/v)		Luna C ₁₈ column (50 mm x 2.1 m, i.d., 5 μ m)	Precision, accuracy, CC α , CC β , LOQ, LOD, recovery test		25
12.	Moxidectin	(A) ACN and (B) MeOH: H ₂ O (50:50 v/v) and TEA		Reverse phase analytical column C ₁₈ (50 x 2.1 mm, 2.7 μ m)	Linearity, sensitivity, selectivity, precision, accuracy		26
13.	Moxidectin	A- methanol B- ammonium formate	10mM	Kinetex EVO C ₁₈ (100mm x 4.6mm, 5 μ m)	Linearity, precision, accuracy, stability		27
14.	Moxidectin	0.1% acetic acid and methanol-acetonitrile (1:1, v/v)		ACE C ₁₈ (50x 3.0 mm, 3 μ m)	Precision, RSD, correlation coefficient, linear range		28

J. Steven Stout et al. utilized significant amounts of metabolites produced *in vitro* from incubations of liver microsomes to study the *in vivo* metabolism of moxidectin in cattle, sheep, and rats. To estimate the molecular weight of the unidentified metabolites using liquid chromatography/tandem mass spectroscopy and to produce daughter ion spectra of molecular species, both metabolites produced *in vitro* and *in vivo* were characterized. It was discovered that the principal metabolites of moxidectin originate from the monohydroxylation of the parent. Less commonly occurring processes were O-demethylation, monohydroxylation, and dihydroxylation. Little metabolic differences have been observed between the species. (15)

Howells et al. established a multi-residue technique for measuring and verifying the presence of avermectins as well as moxidectin residues in the liver of cattle. Using C₈ solid-phase cartridges, the target analytes were isolated from the liver homogenate and detected by using an atmospheric pressure chemical ionization (APCI) interface and ion-trap mass spectrometry in the negative ion mode. The approach allowed for the detection of abamectin, doramectin, moxidectin, and ivermectin at levels of 3.1, 3.2, 2.2, 4.0, and 3.2 ng g⁻¹ liver, respectively, which is lesser than each of their respective maximum residue levels. (16)

Daniela Hofmann et al. developed a method using LC-MS to compare the levels of moxidectin from human blood collected using capillary sampling and the micro-sampling technology mitra® to blood and plasma collected using venous samples. Using a Luna C₈ (30 x 2.0 mm, 3 μ m) column, moxidectin was discovered. The mobile phase consisted of 3 mM

ammonium formate or formic acid (mitra®) produced in ultrapure water at a concentration of 0.05%. For venous and capillary blood, the quantification limits were 0.5 and 2.5 ng/ml respectively. All of the following were validated: sensitivity, selectivity, linearity, stability, recovery, and haematocrit effect. It has been shown that the quick and efficient capillary method using mitra® micro-sample is suitable for moxidectin pharmacokinetic research. (17)

Herlinde Noppe et al. established a selective and precise approach for the simultaneous evaluation of one milbemycin (MOX) and five avermectins in fish, beef meat, and pig liver. Acetonitrile was used for extraction, while C₁₈ SPE was employed for purification. A mixture of 70% A: 30% B, consisting of (A) Triethylamine (TEA) in acetonitrile and (B) TEA in water, made up the mobile phase. A negative-mode LC-MS equipped with APCI was employed for detection. Considering the application of analytical techniques and interpretation of outcomes, the method has been verified according to the standards stated in EC/2002/657 Commission Decision. Additionally, all compounds showed good precision results, linear response, detection limits, and quantification limits. (18)

Gabriel Rubensam et al. detected the presence of ivermectin and milbemycin residues in cattle muscle by (LC-MS/MS) and (LC-FL) detection by using easy and affordable sample preparation, a solvent extraction-based process that is followed by low-temperature clean-up. Using Phenomenex Luna C₁₈ column (150 mm x 2.1 mm, 5 μ m), the separation process occurs that involves the use of a solvent, made up of (A) 50% water, (B) 45% ACN and 5%

ammonium acetate buffer pH 5 (C). The recovery studies, variation coefficient for repeatability and reproducibility, and precision led to satisfactory results. A total of 760 samples were analyzed in total, but none of them revealed residual concentrations above those permitted by the current regulations. (19)

Chris Sack et al. did collaborative validation of the QuEChERS technique for LC-MS/MS detection of pesticides in food to detect 173 pesticides in under 20 minutes, seven FDA pesticide laboratories worked together. For the examination of oranges, carrots, and spinach, the LC-MS/MS method was employed. Aqueous C₁₈ column was employed, and the mobile phases were basic (10 mM ammonium acetate in methanol and water) and acidic (4 mM ammonium formate and 0.1% formic acid). Recoveries of the pesticides were found to be satisfactory. Thus, the method was suitable to detect pesticides in food. (20)

Ioulia Moschou et al. utilized the LC-ESI-MS/MS method to simultaneously estimate avermectins and moxidectin in fish tissue. Using the Waters Acquity UPLC BEH C₁₈ (100 mm × 2.1 mm, 1.7 μm) column, the target analytes were separated and the mobile phase was made up of (A) 0.1% HCOOH in ACN-MeOH and (B) 0.1% HCOOH in 1 mM HCOONH₄. The LOD and relative standard deviations were all within the acceptable ranges, indicating the method's excellent sensitivity. Fish samples from aquaculture were successfully processed using the established technology. (21)

Sherri Turnipseed et al. used a variety of ionization methods, such as atmospheric pressure photoionization (APPI), to detect ivermectin, doramectin, and moxidectin residues in milk. Using Agilent Zorbax SB-C₁₈ column (3 mm × 150 mm, 3.5 μm) and (90:10 v/v) methanol/water was the mobile phase used to achieve separation. Electrospray, APPI, Atmospheric Pressure Chemical Ionization (APCI), and a combination of APPI and APCI were all used to determine the ionization responses of these chemicals. The responses of these compounds were evaluated by operating the APCI/APPI source in positive ion mode without supplying the corona needle with any discharge current. An MS-MS approach was developed using this mode of ionization to track the ions of sodiated molecular salt product ion scans utilizing an ion trap apparatus. Relative standard deviations and good recovery studies were observed for the residues. (22)

Khunachak et al. used liquid chromatography-mass spectrometry with fluorescence detection to determine moxidectin in cattle tissue using Whatman RACII Partisil 5-C₈ column (10 mm × 4.6 mm) and the solvent was made up of ammonium acetate/water/methanol. Following the ACN-hexane partitioning phase, the underivatized parent compound was identified using the LC/MS confirmatory method with an average recovery of 108% at the 250 ppb level in cow fat. (23)

David Durden. quantified antiparasitic endectocide medicines (abamectin, doramectin, and ivermectin) in milk with LC-MS-MS techniques using positive and negative electrospray. The mobile phase consisted of ACN: water (50:50 v/v) which was employed on Waters Xterra RP₁₈ (3 mm × 100 mm, 3.5 μm) column for separation. The LOD results were obtained within the limits. The positive ion signals were stronger and had low detection limits, the negative ion technique produced more linear responses and more accurate performance. (24)

Gabriel Rubensam et al. created a method and validated it using liquid chromatography with fluorescence detection to examine the macrocyclic lactones in cow's milk. Using an isocratic mobile phase made up of 50 mM ammonium acetate buffer: acetonitrile (5:95, v/v), the separation was accomplished on the Luna C₁₈ (50 mm × 2.1 mm, 5 μm) column. The quantification limits were much lesser than the maximum allowable limits, and the recovery rates fell within the ranges. The suggested approach has proven to be simple and inexpensive, enabling for high-volume analysis of several samples per day. (25)

Rafaela Baptista et al. established a method using high-performance liquid chromatography-electrospray ionization-tandem mass spectrometry for detecting MOX in lamb serum. For the chromatographic separation, a reverse phase C₁₈ (50 mm × 2.1 mm, 2.7 μm) analytical column was employed. The sample solvent was made up of ACN, MeOH: H₂O (50:50 v/v), and TEA was added in required quantities to achieve a pH of 8. The outcomes of precision, accuracy, LOD, and LOQ were found to be within the limits, according to the method validation. (26)

Subbarao et al. validated a rapid bioanalytical approach for the determination of moxidectin in cattle hair. Using a liquid-liquid extraction, moxidectin was isolated from cow hair using methyl tert-butyl ether as the solvent and Sorenson's buffer as the digesting solvent for incubation. The separation was achieved using a Kinetex EVO C₁₈ (100 mm × 4.6 mm, 5 μm) column and the sample solvent made up of methanol: 10 mM ammonium formate. Studies on validation characteristics like linearity, accuracy, precision, and stability have provided reliable results. The method for calculating the amount of moxidectin in cattle hair was successfully utilized. (27)

Yashpal singh chonker et al. created a bioanalytical LC-MS technique to identify moxidectin in mouse, monkey, and human plasma. On the ACE C₁₈ (50 mm × 50 mm, 3 μm) column, the separation has been accomplished using the sample solvent made of methanol: acetonitrile (1:1, v/v) and 0.1% acetic acid. With a correlation coefficient of 0.997 or above, over the range of 0.1-1000 ng ml⁻¹, MS/MS response was linear in plasma. The accuracy and precision were within acceptable bounds. A study of moxidectin's in vitro metabolic stability using this technique proved effective. (28)

4. UV- SPECTROPHOTOMETRIC METHOD

Spectrophotometry is the quantitative measurement of a material's wavelength-dependent transmission or reflection properties. The advantage of these

methods is that it requires minimal time and effort. These methods also offer good precision. The following table 3 lists the quantitative measurements of moxidectin made using UV spectrophotometric techniques.

Table 3: Determination of moxidectin using UV spectrophotometer.

SR No:	Drug	Instrument	λ max (nm)	Parameters	References
1.	Moxidectin	UV spectrophotometer	244.89 nm	Linearity, Accuracy, Precision, LOD, LOQ, Specificity, Assay	29

Sathish Babu et al. developed a sensitive, accurate, and validated UV spectrophotometry method to determine moxidectin in bulk drug and synthetic mixture. With a correlation coefficient of 0.9994, the calibration curve was plotted in the range of 8-22 g/ml. LOD and LOQ findings were within the expected range. The RSD for the method's precision was found to be less than 2% as a percentage. A 100.8% assay percentage was discovered. The newly developed method's linearity, accuracy, precision, and specificity were all validated following the ICH requirements. (29)

5. ULTRA HIGH-PERFORMANCE LIQUID CHROMATOGRAPHY (UHPLC)

Liquid chromatographic separations using columns that encapsulate particles smaller than the commonly used HPLC particle size range of 2.5-5 μ m are referred to as "ultra-high-performance liquid chromatography". Similarly, to HPLC, UHPLC operates under the governing principle that efficiency and therefore, resolution increase with a decrease in the column packing particle size. In the modern world, all chromatographic techniques that support separations using shorter columns, faster flow rates for high speed, and better resolution and sensitivity are available through UHPLC. (30) The following table 4 lists the results of the quantitative analysis of moxidectin using UHPLC.

Table 4: Determination of moxidectin using the UHPLC method.

Sr. No	Drug	Mobile Phase	Stationary Phase	Parameters	Reference
1.	Moxidectin	5 mM ammonium formate solution + 0.1% formic acid (A) and acetonitrile + 0.1% formic acid (B)	Zorbax Eclipse Plus C ₁₈ RRHD column (1.8 μ m, 2.1 mm x 50 mm)	Linearity, sensitivity, precision, accuracy, CC α , CC β , LOQ and LOD	30
2.	Moxidectin	Ammonium acetate: acetonitrile (10:90, v/v)	Acquity UPLC BEH C ₁₈ analytical column (2.1 x 50 mm, 1.7 μ m)	Linearity, precision, LOD, LOQ, accuracy.	31
3.	Moxidectin	5 mM ammonium formate in water with 0.1% formic acid and B acetonitrile: in water with 0.1% formic acid	Acquity UPLC [®] BEH C ₁₈ column (50 mm x 2.1 mm, 1.7 μ m)	Linearity, selectivity, matrix effect, CC α , CC β , LOD, LOQ, accuracy, precision, robustness	32
4.	Moxidectin	(A) water: acetonitrile (98:2, v/v), containing 10 mmol L ⁻¹ aqueous ammonium formate, and (B) methanol:	Waters Acquity UPLC [™] analytical column HSS-T3 (100 x 2.1 mm, 1.8 μ m particle size)	Accuracy, precision, CC α , CC β , linearity, RSD.	33

Sr. No	Drug	Mobile Phase	Stationary Phase	Parameters	Reference
5.	Moxidectin	acetonitrile (75:25, v/v), with 0.1% formic acid. Acetonitrile and methanol	Acquity BEH C ₁₈ column (50 × 2.1 mm, dp: 1.8 μm) and an Acquity HSS-T3 column (100 × 2.1 mm)	Linearity, LOD, LOQ, precision, accuracy, carry-over, specificity, stability	34
6.	Moxidectin	0.1% solution of formic acid in water (A)/acetonitrile (B)	RP ACQUITY UPLC BEH C ₁₈ (1.7 μm, 100 mm × 2.1 mm).	Precision, CC _α , CC _β , % recovery	35
7.	Moxidectin	A consisted of a 5 mM ammonium formate in water and acetonitrile: water (95:5 v/v) with 0.1% formic acid	Acquity UPLC® BEH C ₁₈ column (50 mm × 2.1 m, 1.7 μm)	Linearity, selectivity, CC _α , CC _β , accuracy, precision, LOD, LOQ,	36
8.	Moxidectin	Mobile phase A, 0.01% HOAc in water: MeCN (90:10, v/v) and Mobile phase B, 5 mM ammonium formate in MeOH: MeCN (75:25, v/v).	A stainless steel HSS T3 analytical column (100 mm × 2.1 mm, particle size 1.8 μm)	Sensitivity, linearity, precision, accuracy, CC _α , CC _β ,	37
9.	Moxidectin	5 mM and 10 mM ammonium buffer and 0.1% formic acid	C ₁₈ column	Precision, LOD, LOQ, recoveries	38
10.	Moxidectin	5 mM ammonium formate + 0.01% formic acid, pH 4.00) and mobile phase B (acetonitrile: mobile phase A, 95:5 v/v)	Waters Acquity BEH UPLC® C ₁₈ column (100 × 2.1 mm ID, 1.7 μm)	Selectivity, linearity, CC _α , CC _β , recovery, LOD, LOQ	39
11.	Moxidectin	A- Water B- Methanol	Poroshell 120 EC-C ₁₈ , (150 mm × 3.0 m, 2.7 μm column)	LOD, LOQ, precision, recovery, linearity, trueness	40

Michelle Del Bianchi Cruz et al. established a throughput approach (UHPLC-ESI-MS/MS) for the identification of moxidectin residues in the target tissues of lambs. The sample was prepared using a modified QuEChERS technique to increase the analyte's high recovery from the matrices. Using Zorbax Eclipse Plus C₁₈ (1.8 μm, 2.1 mm × 50 mm) column and a linear gradient program were used to carry out the chromatographic separation. The sample solvent was made up of (A) 5 mM ammonium formate solution + formic acid and (B) acetonitrile + 0.1% formic acid. Results for the method's linearity, accuracy, and precision were found to be adequate. (30)

Fabrcio de Oliveira Ferreira et al. reported a technique for determining the presence of moxidectin residues in soils using online SPE-UHPLC-TMS and extraction from solids. Using Acquity UPLC BEH C₁₈ (2.1 mm × 50 mm, 1.7 μm) analytical column was used for separation. The optimal conditions were: a sample solvent of water: methanol (40:60, v/v); a solvent of water/methanol (96:4, v/v); a sample volume of 2 × 250 μL; and with the back flush of mobile phase composed of 5 mmol l ammonium acetate/ ACN (10:90, v/v), eluting the analytes retained on the SPE column. Results from this method were within the acceptable ranges in terms of accuracy, precision, linearity, LOD, and LOQ. (31)

Guilherme Resende da Silva et al. created and validated a multi-residue approach by combining QuEChERS extraction and UHPLC-MS/MS to identify avermectins, benzimidazoles, and nitroimidazoles in bovine muscle tissue. The separation was achieved on the Waters Acquity UPLC BEH C₁₈ (50 mm × 2.1 mm, 1.7 μm) column. Mobile phase (A) was made up of 5 mM ammonium formate in water with 0.1% formic acid and ACN/water (95:5 v/v) with 0.1% formic acid was used as mobile phase (B) with a flow rate of 0.4 ml/min at a column temperature of 35 °C. All the studied analytes performance results, including those for accuracy, linearity, selectivity, LOD, LOQ, precision, and robustness, were satisfactory. (32)

Tiele Rizzetti et al. developed a straightforward and quick multi-class technique for detecting veterinary drugs in the muscle, liver, and kidney of cattle. Using the sample solvent made up of water/ACN (98:2, v/v), with 10 mol/l of ammonium formate; (B) methanol: acetonitrile (75:25, v/v), with formic acid, separation was carried out on Waters Acquity UPLC™ analytical column HSS-T3 (100 mm × 2.1 mm, 1.8 μm particle size). The results of linearity, accuracy, precision, detection limits, and capability limits fell within the acceptance limits. According to European Commission Directive 2002/657, the approach has been verified and provided satisfactory results for 69 veterinary pharmaceuticals in the liver and 68 chemicals in the muscle and kidney. (33)

Gemechu Zeleke et al. created a quick, accurate, and safe UHPLC-MS/MS technique for determining moxidectin simultaneously in bovine plasma. For the chromatographic separation of the analytes in plasma, two RP UPLC columns, the BEH C₁₈ column (50 × 2.1 mm, 1.8 μm) and the Acquity HSS-T3 column (100 mm × 2.1 mm, 1.8 μm), were assessed with mobile phase made up of 0.01% acetic acid in ACN and methanol. All the analytes had limits for quantification of 1 ng/ml, although the detection limits of IVER, DORA, and MOX were 0.02 ng/ml, 0.03 ng/ml, and 0.58 ng/ml, respectively. The intraday (RSD 6.50%) and inter-day (RSD 8.10%) results were proved to be within the limits. (34)

Bayer et al. conducted a study to establish the MS/MS detection parameters to assess the application of UHPLC-MS and to specify the validation requirements for the investigation of the residual content of avermectins and moxidectin in milk. The samples were chromatographed in gradient mode using the Acquity UPLC BEH C₁₈ (100 mm × 2.1 mm, 1.7 μm) RP analytical column and a system of formic acid solution in water (A) and acetonitrile (B). The data collected to evaluate the results' suitability, accuracy, and reproducibility complies with the European Directive's (2002/657/EC) standards. The effective UHPLC-MS technology, which has been devised and adopted for widespread use in veterinary medicine laboratories, enables the detection of residual levels of the five avermectins used in animal breeding to prevent helminthiasis. (35)

Victor Pastore et al. utilized a QuEChERS technique to establish a quantitative and confirmatory approach to measure the macrocyclic lactone residues, monensin, and fipronil present in the liver of cattle. The separation was accomplished by Acquity UPLC® BEH C₁₈ (50 mm × 2.1 mm, 1.7 μm) column. The mobile phase (A) was ammonium formate in water at a concentration of 5 mM, while the mobile phase (B) was ACN and water at a ratio of (95:5 v/v) with 0.1% formic acid. The method presented linearity and selectivity with a coefficient of correlation, LOD and LOQ were within the ranges. The accuracy, precision, CC_α, CC_β, and uncertainty results showed a satisfactory level of performance. The method proved successful in determining MLs, monensin, and fipronil residues in the livers of chickens and cattle. (36)

Michelle Whelan et al. devised and tested a modified QuEChERS-type extraction technique to detect 38 anthelmintic medication residues, including benzimidazoles and avermectins, in milk. For the separation, a stainless steel HSS T3 (100 mm × 2.1 mm, 1.8 μm) analytical column was utilized and the mobile phase (A) was made up of 0.01% HOAc in water: MeCN (90:10, v/v) and mobile phase (B) was composed of 5 mM ammonium formate in MeOH/MeCN (75:25, v/v). The decision limits of the method were found to be within the limits. By taking part in a proficiency study, the method's effectiveness for benzimidazoles and levamisole was successfully confirmed. (37)

Mirta Zrncic et al. established a method to investigate the presence of 10 anthelmintic medications in surface water using quadrupole linear ion trap mass spectrometry linked to UHPLC (UHPLC-QqLIT-MS). To achieve chromatographic separation, a C₁₈ column was employed. The organic phase contains 0.1% formic acid in methanol or ACN, whereas the aqueous phase is made up of 5 mM and 10 mM ammonium buffers. At two concentration levels, most of the analytes displayed analyte recoveries from spiked samples > 75%. The devised technique was applied to study the anthelmintics in the Lobregat River and its principal tributaries. All the samples were analyzed, and eight of the 10 anthelmintics were found at quantities below the ngl (-1) threshold. The technique covers a gap in analytical methods for environmental anthelmintic drug identification. (38)

Marianna Ramos dos Anjos et al. developed a method using QuEChERS for extraction and clean-up, coupled with detection and quantification by UPLC-MS/MS, for the evaluation of moxidectin, abamectin, doramectin, ivermectin, and aflatoxin M1 in whole raw milk. The Waters Acquity BEH UPLC C₁₈ (100 mm × 2.1 mm ID, 1.7 μm) column was used for chromatographic separation. The mobile phase (A) was made up of 5 mM ammonium formate/ formic acid and the mobile phase B was ACN: mobile phase (A) (95:5 v/v). Within the suggested working ranges of recovery studies, standard deviation, LOD, and LOQ, it was shown that this technique was suitable for measuring these analytes. Animals treated with abamectin, doramectin, and ivermectin samples were analyzed using an established method. (39)

Heng Zhou et al. devised a technique for qualitative screening and quantitative analysis of 569 pesticides in honeysuckle utilizing UHPLC with quadrupole-orbitrap high-resolution mass spectrometry and an internal executable chemical database that contains theoretical masses of precursor and fragment ions and retention times. A Poroshell C₁₈ column (150 mm × 3.0 mm, 2.7 μm) from the infinity lab was used for the separation. Water and methanol were employed as the mobile phases, and both contained 5 mM ammonium formate and 0.1% formic acid. The method showed good repeatability, linearity, and precision. Among the 82 samples analyzed, pesticides were found in 75 of them, with some of the most severely polluted samples having pesticide amounts as high as 4116.9 g/kg. To analyze honey, and suckle samples both qualitatively and quantitatively, UHPLC-Full MS/ddMS2 was thought to be the best procedure. (40)

6. CONCLUSION

Onchocerciasis is treated with moxidectin, a potent second-generation endectocide macrocyclic lactone (river blindness). For the assessment of moxidectin in pharmacological dose forms, various analytical methods, including UV, HPLC, and hyphenated techniques such as LC-MS/MS and UPLC-MS/MS were reported. Among these techniques, LC-MS and UPLC-MS yielded successful results due to their greater resolution and sensitivity. Also, the HPLC methods were desirable due to no sample preparation or extraction step. Of all the HPLC methods, David Pimentel-Trapero et al. established a greener method compared to others by using methanol and water as mobile phase and also the use of the QuEChERS method made it much more productive. The use of the QuEChERS method made the analytical technique minimize the usage of chemical solvents and a non-labor-intensive process. Additionally, there were more HPLC methods available for evaluating moxidectin in pharmaceutical dosage forms that are available in bulk. Among the UHPLC methods, Heng Zhou et al. developed a greener method compared to others using methanol and water as mobile phase. The current study provides a brief overview of the analytical techniques used to evaluate moxidectin in pharmaceutical formulations.

7. CONFLICT OF INTEREST

The authors declare no competing interests.

8. ACKNOWLEDGMENTS

The authors are thankful to the management of GITAM (Deemed to be University), Visakhapatnam, Andhra Pradesh, India, for providing the necessary facilities for carrying out the review work.

7. REFERENCES

1. Macedo F, Marsico E. T, Conte-Júnior C, A et al. Development and validation of a method for the determination of low-ppb levels of macrocyclic lactones in

butter, using HPLC-fluorescence. *Food chemistry*. 2015; 179: 239–245.

2. Pimentel-Trapero D, Sonseca-Yepes A, Moreira-Romero S, et al. Determination of macrocyclic lactones in bovine liver using QuEChERS and HPLC with fluorescence detection. *Journal of Chromatography B: Analytical Technologies in the Biomedical and Life Sciences*. 2016; 166-172.

3. Cheibub A. M. S. S, Lyra E. S, Netto A. D. P. Development and validation of a method for simultaneous determination of trace levels of five macrocyclic lactones in cheese by HPLC-fluorescence after solid-liquid extraction with low-temperature partitioning. *Journal of Food Chemistry*. 2019; 272: 148-156.

4. Bengone-Ndong T, Mvouaka S. K, Alvinerie M, et al. A comparative kinetic study of doramectin and moxidectin in zebu gobra cattle (*Bos indicus*). *Journal of Parasitology Research*. 2013; 103(6): 1465-7.

5. Escudero E, Carceles C. M, Alvinerie M, et al. Pharmacokinetics of moxidectin and doramectin in goats. *Research in Veterinary Science*. 1999; 67(2):177-81.

6. Alvinerie M, Sutra J. F, Badri M, et al. Determination of moxidectin in plasma by high-performance liquid chromatography with automated solid-phase extraction and fluorescence detection. *Journal of Chromatography B*. 1995; 674; 119-124.

7. Dennis K, She-Yi W, Lawrence F, et al. Liquid chromatographic assay of ivermectin in human plasma for application to clinical pharmacokinetic studies. *Journal of Pharmaceutical and Biomedical Analysis*. 2006, Mar 3; 40(4): 1013-20.

8. Mercedes L, Alvarez L, Entrocasso C, Virkel G, et al. Comparative tissue pharmacokinetics and efficacy of moxidectin, abamectin, and ivermectin in lambs infected with resistant nematodes. *International Journal for Parasitology: Drugs and Drug Resistance*. 2013; 3: 20–27.

9. Chou H. K, Lai C. Y, Chen T. H, et al. "A multiresidue method for the determination of abamectin, doramectin, moxidectin, ivermectin, milbemycin A3, and A4 residues in bovine muscle using HPLC with fluorescence detection," *Journal of Food and Drug Analysis*. 2004; 12(2): 146-153.

10. Alvinerie M, Dupuy J, Sutra J, et al. In vitro metabolism of moxidectin in *Haemonchus contortus* adult stages. *Parasitology Research*. 2001; 87(9): 702-4.

11. Teixeira R. A, Flores D. H. A, Silva R. C. S, et al. Pipette-tip solid-phase extraction using poly (1-vinyl imidazole-co-trimethylolpropane trimethacrylate) as a new molecularly imprinted polymer in determination of avermectins and milbemycins in fruit juice and water samples. *Journal of Food Chemistry*. 2018; 262: 86-93.

12. Vazquez-Quintal P. E, Rodríguez-Vivas R.I, Muñoz-Rodríguez D. Liquid-liquid extraction for the spectrofluorimetric determination of moxidectin or abamectin in bovine plasma. *Chemical Papers*. 2022; 76: 7441–7449.

13. Galarini R, Saluti G, Moretti S, et al. Determination of macrocyclic lactones in food and feed. *Food Additives & Contaminants: Part A: Chemistry, Analysis, Control, Exposure & Risk Assessment*. 2013; 30(6): 1068-79.

14. Craven J, Hennessy D, Nansen P, et al. Pharmacokinetics of moxidectin and ivermectin following intravenous injection in pigs with different body

- compositions. *Journal of Veterinary Pharmacology and Therapeutics*. 2001; 24(2): 99-104.
15. Stout S. J, de Cunha A. R, Afzal J, et al. Moxidectin: Characterization of Cattle, Sheep, and Rat in Vitro and in Vivo Metabolites by Liquid Chromatography/Tandem Mass Spectrometry. *Journal of Agricultural and Food Chemistry*. 1994; 42(2): 388-392.
 16. Howells L, Sauer M. J. Multi-residue analysis of avermectins and moxidectin by ion-trap LC-MSn© Crown copyright. *Analyst*. 2001; 126: 155-160.
 17. Hofmann D, Sayasone S, Keiser J. Development and validation of an LC-MS/MS method for the quantification of the anthelmintic drug moxidectin in a volumetric absorptive micro-sample, blood, and plasma: Application to a pharmacokinetic study of adults infected with *Strongyloides stercoralis* in Laos. *Journal of Chromatography B: Analytical Technologies in the Biomedical and Life Sciences*. 2021, 1166: 122556.
 18. Noppe H, Verheyden K, Bussche J V, et al. Detection of macrocyclic lactones in the porcine liver, meat, and fish tissue using LC-APCI-MS-MS. *Food Additives and Contaminants*. 2009; 26(9): 1232-1238.
 19. Rubensam G, Barreto F, Pizzolato T. M, et al. Determination of avermectins and milbemycin residues in bovine muscle by liquid chromatography-tandem mass spectrometry and fluorescence detection using solvent extraction and low-temperature clean-up. *Food Control*. 2013; 29(1): 55-60.
 20. Chris Sack, Chamkasem N, Masse C, et al. Collaborative Validation of the QuEChERS Procedure for the Determination of Pesticides in Food by LC-MS/MS. *Journal of Agricultural and Food Chemistry*. 2011; 59(12): 6383-6411.
 21. Moschou I. C, Dasenaki M. E, Thomaidis N. S. Ionization study and simultaneous determination of avermectins and milbemycins in fish tissue by LC-ESI-MS/MS. *Journal of Chromatography B*. 2019; Volume 1104: 134-140.
 22. Turnipseed S. B, Roybal J. E, Andersen W. C, et al. Analysis of avermectins and moxidectin residues in milk by liquid chromatography-tandem mass spectrometry using an atmospheric pressure chemical ionization/atmospheric pressure photoionization source. *Analytica Chimica Acta*. 2005; 529(1-2): 159-16.
 23. Khunachak A, Aacunha R, Stout S. J. Liquid Chromatographic Determination of Moxidectin Residues in Cattle Tissues and Confirmation in Cattle Fat by Liquid Chromatography/Mass Spectrometry. *Journal of AOAC International*. 1993; 76(6): 1230-5.
 24. Durden A. D. Positive and negative electrospray LC-MS-MS methods for quantitation of the antiparasitic endectocide drugs, abamectin, doramectin, emamectin, eprinomectin, ivermectin, moxidectin and selamectin in milk. *Journal of Chromatography B*. 2007; 850: 134-146.
 25. Rubensam G, Barreto F, Hoff R. B, et al. A liquid-liquid extraction procedure followed by a low-temperature purification step for the analysis of macrocyclic lactones in milk by LC-TMS. *Analytica Chimica Acta*. 2011; 705(1-2): 24-9.
 26. Baptista R. C, Maria Fernandes A. M, Susana G, et al. Determination of Moxidectin in Serum by Liquid Chromatography-Tandem Mass Spectrometry and Its Application in Pharmacokinetic Study in Lambs. *Journal of the Brazilian Chemical Society*. 2017; 28(2): 250-256.
 27. Subbarao N, Mupeksha M, Ashma S, Ashwini K, et al. Sensitive, Rapid Estimation of Moxidectin in Cattle Hair by LC-MS-MS. *LCGC Supplements, Special Issues*. 2016; 14(3): 27-31.
 28. Yashpal Chhonker. S, Richard S, Daryl Murry J. Bioanalytical method development and validation of moxidectin in plasma by LC-MS/MS: Application to in-vitro metabolism. *Journal of Biomedical chromatography*. 2019; 33(2): e4389.
 29. Babu P. S, Babu K. A, Revathi D, and Chitra K. Method development and validation of moxidectin in synthetic mixture using UV-Spectrophotometry. *World Journal of Pharmaceutical Research*. 2015; 4(7): 904-912.
 30. Michelle Del Bianchi Cruz A, Maria Fernandes A. M, Braga P. A. C, et al. Moxidectin residues in lamb tissues: Development and validation of analytical method by UHPLC-MS/MS. *Journal of Chromatography B*. 2018; 1072: 390-396.
 31. Oliveira Ferreira F, Rodrigues-Silva C, Susanne R. Online Solid-Phase Extraction-Ultra High-Performance Liquid Chromatography-tandem mass spectrometry for the determination of avermectins and milbemycin in soils. *Journal of Chromatography A*. 2016; 1471(4): 118-125.
 32. Silva G. R. D, Lima J. A, Santos F. A, et al. Multiresidue method for identification and quantification of avermectins, benzimidazoles and nitroimidazoles residues in bovine muscle tissue by ultra-high performance liquid chromatography tandem mass spectrometry (UHPLC-MS/MS) using a QuEChERS approach. *Talanta*. 2017; 171: 307-320.
 33. Tiele Rizzetti M, Martha Adaime B, Renato Zanella, et al. Optimization of sample preparation by central composite design for multi-class determination of veterinary drugs in bovine muscle, kidney, and liver by ultra-high-performance liquid chromatographic-tandem mass spectrometry. *Food chemistry*. 2018; 246: 404-413.
 34. Zeleke G, Devreese M, Suleman S, et al. Development and Validation of a Reliable UHPLC-MS/MS Method for Simultaneous Quantification of Macrocyclic Lactones in Bovine Plasma. *Molecules*. 2022; 27(3): 998.
 35. Bayer O. V, Kaminska O. V, Skoromna O. I, et al. Evaluation of Ultra-High-Performance Liquid Chromatography-Tandem Mass Spectrometry for Determination of Avermectins Residues in Milk. *Ukrainian Journal of Ecology*. 2019; 9(4): 521-526.
 36. Victor Pastore A. A, Flávio Santos A, Guilherme Silva R, et al. Development and Validation of a Multiresidue Method for the Determination of Macrocyclic Lactones, Monensin, and Fipronil in Bovine Liver by UHPLC-MS/MS Using a QuEChERS Extraction. *Food analytical methods*. 2022; 15: 3177-3188.
 37. Whelan M, Kinsella B, Danaher M, et al. Determination of anthelmintic drug residues in milk using ultra-high performance liquid chromatography-tandem mass spectrometry with rapid polarity switching. *Journal of Chromatography A*. 2010; 1217(27): 4612-22.
 38. Zrncic M, Babic S, Kastelan-Macan M, et al. Analysis of anthelmintics in surface water by ultra-high performance liquid chromatography coupled to quadrupole linear ion trap tandem mass spectrometry. *Chemosphere*. 2014; 99: 224-32.

39. Dos Anjos M. R, Castro I. M, de Aquino-Neto F. R, et al. Multiresidue method for simultaneous analysis of aflatoxin M₁, avermectins, organophosphate pesticides, and milbemycin in milk by ultra-performance liquid chromatography coupled to tandem mass spectrometry. *Food Additives & Contaminants: Part A: Chemistry, Analysis, Control, Exposure & Risk Assessment*. 2016; 33(6): 995-1002.

40. Zhou H, Cao Y. M, Miao S, Chen M, et al. Qualitative screening and quantitative determination of 569 pesticide residues in honey suckle using UHPLC coupled to quadrupole-orbitrap high-resolution mass spectrometry. *Journal of Chromatography A*. 2019; 1606:460374.



Biogenic Synthesis and Characterization of Gold Nanoparticles from *Morus alba* L. Leaves by Microwave Extraction Method

Gönül SERDAR* 

¹*Karadeniz Technical University, Central Research Laboratory, Trabzon, Turkey.

Abstract: The aim of this study was to investigate the rapid, simple, and inexpensive biosynthesis and characterization of gold nanoparticles (AuNPs) an extract from leaves of *Morus alba* L. The generated gold nanoparticles were characterized by UV-Vis spectroscopy, TEM, FT-IR and zeta-sizer. For the biogenesis of gold nanoparticles, *Morus alba* L. (Mulberry) leaves and $\text{HAuCl}_4 \cdot 3\text{H}_2\text{O}$ solution were utilized as the starting ingredients. Fresh leaves of *Morus alba* L. were collected from Turkey (Trabzon). 100 mL of distilled water was mixed with 10 g of dried material for 120 minutes. The mixture was then extracted using a laboratory microwave for 4 minutes at 600 W. For the biosynthesis of AuNPs, different amounts 100 ml of (0.5 mM, 1 mM) aqueous $\text{HAuCl}_4 \cdot 3\text{H}_2\text{O}$ solution of leaf extract (0.5 and 1 mL) were mixed with $\text{HAuCl}_4 \cdot 3\text{H}_2\text{O}$ solution, and then the mixture was placed in a household microwave at 90 W for 1 to 30 minutes. UV-vis spectroscopy, TEM, FT-IR and zeta-sizer were performed to characterize the produced gold nanoparticles. UV-Vis absorption spectra was measured using a Shimadzu UV-1240 UV-Vis spectrophotometer with a wave length range of 300 to 800 nm. The development of AuNPs was indicated by the mixture's purple-red colour. From the results of zetasizer study, the average particle size of the AuNPs was 78.95 ± 0.57 nm, the zeta potential was 12.9 ± 0.808 mV, and the polydispersity index was 0.321 ± 0.004 . When the AuNP solutions were kept in the refrigerator, their UV-Vis absorption spectra rarely changed and remained stable for around 2 to 2.5 months.

Keywords: Mulberry (*Morus alba* L.) leaf, Au nanoparticle, Microwave extraction, UV-Vis spectroscopy, TEM.

Submitted: October 06, 2023. **Accepted:** January 29, 2024.

Cite this: Serdar G. Biogenic Synthesis and Characterization of Gold Nanoparticles from *Morus Alba* L. Leaves by Microwave Extraction Method. JOTCSA. 2024; 11(2): 615-22.

DOI: <https://doi.org/10.18596/jotcsa.1372302>.

***Corresponding author. E-mail.** gonulhatipoglu@hotmail.com.

1. INTRODUCTION

The capacity to translate this structure into applications by introducing a new product in several scientific fields, including materials science, biology, and chemistry, is what makes nanotechnology one of the most promising branches of nanoscience and nanotechnology in the modern era (1). The definition of nanoparticles, which constitute the fundamental units of nanotechnology, may change depending on the application area, studies, and the properties of the corresponding materials, and they are commonly known as particles that range in size from 1 to 100 nm (2). Nanoparticles are particles composed of carbon, metal, metal oxides, or

organic substances (3,4). Most crucially, one of the things that distinguish nanotechnology from other technologies is that the surface and volume properties of the material are linked at the nanometer scale, and the ratio of surface to volume rises (5). Surface molecules can cause high hardness in metals and also make electronic devices and drugs highly efficient (1). Nanoparticles in nanotechnology in medicine and pharmaceuticals Electrics/electronics, food, textiles, environment and energy, materials and manufacturing industries (3, 7-9). Nanomaterials can provide solutions to various environmental problems through technological innovations and advances in energy storage, medicine, and wastewater treatment (9-12).

Modern extraction techniques, like microwave-assisted and supercritical fluid extraction, have improved as a result of the shortcomings of conventional approaches, especially when working with medicinal plants, as modern techniques are needed that minimize the use of organic solvents, reduce extraction time, and are environmentally friendly. More recently, "green synthesis" (13,14) has been used to overcome limitations such as expensive chemicals and equipment, extreme reaction conditions, potentially hazardous and negative environmental impact, and biocompatibility (15). "Biogenic synthesis," an alternative production method recognized as an ecological approach for the production of various nanomaterials and plant extracts (16-18), environmentally friendly approaches have been developed and used, including the application of natural and renewable materials. Plant materials containing biological extracts are employed as reducing and capping agents in green synthesis, which is quite inexpensive because it greatly lowers the cost of the synthesis process (19) overall and produces more symmetrical and stable nanoparticles (14, 20). Biological synthesis was preferred due to its environmental and economic advantages (21). Because they are produced using a single approach, biologically produced nanoparticles are one step more convenient and stable and have the characteristic of having dimensions (22).

Plant extracts have been suggested in recent years as a straightforward and practical alternative to chemical and physical approaches for producing nanoparticles due to their advantages. One of the most investigated metallic NPs is gold. Due to their good stability, optical properties, biocompatibility, antifungal, antidiabetic and antibacterial effects in nanoparticle research, researchers have become interested in Au nanoparticles in numerous crucial application areas for many chemical, biological, and environmental sectors (21, 23-25). AuNPs with a wide range of sizes and shapes have exceptional properties that can facilitate the development of new devices for a variety of biomedical applications. Important biomedical applications of AuNPs include targeted drug release, cancer therapy, contrast agents in medical imaging, molecular imaging in living cells, antimicrobial and antibacterial activities, antiviral treatments, biosensors and intracellular analysis, photothermal therapy, and hyperthermal effects (23, 24).

In this research, using *Morus alba* L. leaves extract as a coating and reducing agent, it has been reported that gold nanoparticles can be biosynthesized in under 30 minutes. Mulberry, a multifunctional agro-forestry plant from the Moraceae family, is frequently used as a silkworm diet (26). *Morus alba* sometimes referred to as white mulberry, common mulberry, and silkworm mulberry. It is widely cultivated and does well all year long in China, India, Japan, and Korea (27). Mulberry and its parts are frequently utilized to generate a variety of functional foods, including

mulberry leaf-carbonated beverages and healthy beverages, due to their high bioactivities. Due to its low toxicity and effective therapeutic properties, it is also consumed in China and Japan as a traditional herbal medicine and substitute tea (28, 29).

This study's objectives were to research the quick, simple, and affordable biosynthesis and characterisation of AuNPs utilizing an extract made from *Morus alba* L. leaves. UV-Vis spectroscopy, TEM, and Zeta-sizer were used to characterize the produced gold nanoparticles.

2. EXPERIMENTAL SECTION

2.1. Preparation of *Morus alba* L. leaves extract

For the biogenesis of gold nanoparticles, *Morus alba* L. leaves and $\text{HAuCl}_4 \cdot 3\text{H}_2\text{O}$ solution were utilized as the starting materials. *Morus alba* L. leaves were gathered from the Eastern Black Sea region of Turkey (61 m, Trabzon, Turkey) at the end of June 2022. The plant material has been placed at the Herbarium of the Department of Forest Engineering Faculty at Karadeniz Technical University in Trabzon, Turkey (KATO:19271), after Prof. Dr. Salih TERZİOĞLU verified the taxonomic identity of the plant sample. And then cleaned with de-ionized water, dried in the shade and finely ground in a grinder. 10 g of dried material was combined with 100 mL of purified water and left for 120 minutes. The flask was shaken before being placed inside a lab microwave, where it was extracted at 600 W for 4 minutes before being allowed to cool (30). To filter the mixture, Whatman filter paper was employed. The extracted solution was kept for future use in a refrigerator. Analytical grade 99.9% $\text{HAuCl}_4 \cdot 3\text{H}_2\text{O}$ Sigma Aldrich Chemical Reagent Co. Ltd. was purchased. Using *Morus alba* L. leaf extract as a reducing and stabilizing agent in an aqueous solution, gold nanoparticles were easily created by reducing $\text{HAuCl}_4 \cdot 3\text{H}_2\text{O}$.

2.2. Production of AuNP

In a typical synthesis procedure, 100 ml of (0.5 mM, 1 mM) aqueous $\text{HAuCl}_4 \cdot 3\text{H}_2\text{O}$ solution were combined with a specified volume (0,5 mL–1 mL) of mulberry leaves extract. The mixture was then microwaved at 90 W for 1–30 minutes, indicating the creation of gold nanoparticles. There were three iterations of each technique. The gold nanoparticles were then gathered, removed from the mulberry leaf extract using centrifugation, and then dried at 40 °C for an additional 18 hours.

2.3. AuNP characterization

UV-Vis spectroscopy makes it simple to see how gold nanoparticles are made by reducing gold ion solution with mulberry leaf extract. Using a Shimadzu UVP-1240 spectrophotometer, the

absorption spectra of reaction solutions at various mulberry leaf extract concentrations and $\text{HAuCl}_4 \cdot 3\text{H}_2\text{O}$ solution concentrations were captured with a resolution at wavelengths between 300 nm and 800 nm. Water that had been double-distilled used as a blank solution.

To determine the shape of nanoparticles, a transmission electron microscope (TEM) was used. A Hitachi HT-7700 Tecnai transmission electron microscopy instrument was used for the TEM observations, and it was run at an accelerating voltage of 40–120 kV. The condition of a nanoparticle in polar liquids is determined by its zeta potential, which also provides specific details about the dispersion mechanisms. Using the DLS technique (Malvern Zetasizer Nano ZSP), light source He-Ne laser 633nm, Max 10mW, 100VA maximum power, temperature range $0^\circ\text{C} - 90^\circ\text{C} \pm 0.1$, zeta potentials, polydispersity indices (PI), and average particle sizes of Au nanoparticles are calculated.

3. RESULTS AND DISCUSSION

3.1. Characterization of Gold Nanoparticles

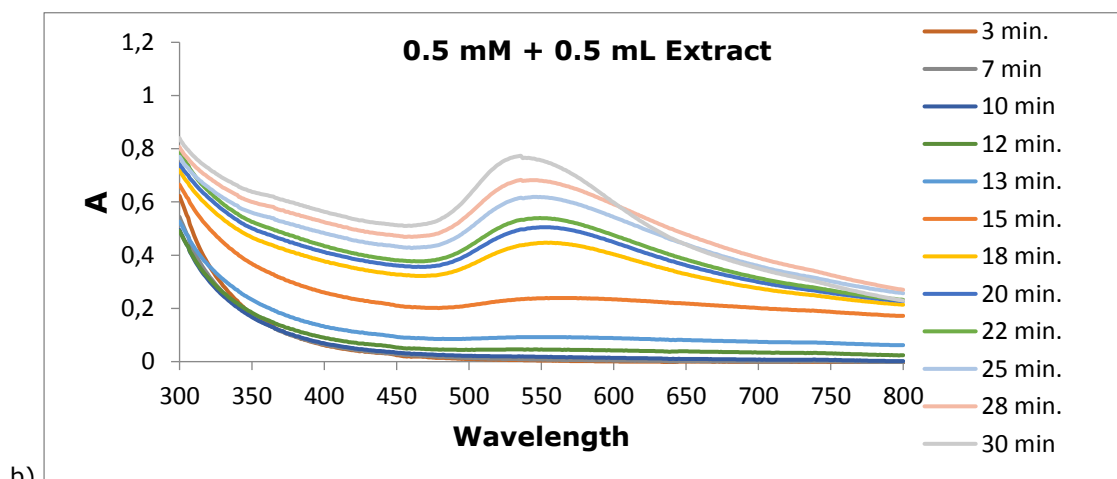
As stated before, the transition from light yellow to dark purple is a certain indicator that nanoparticle manufacturing has taken place (Figure 1).



Figure 1. (a) Before microwave treatment, color change of $\text{HAuCl}_4 \cdot 3\text{H}_2\text{O}$ solution and Mulberry leaf extract mixture, (b) and (c) after microwave treatment, purple pink color indicating the formation of Au-NPs.

The mulberry leaf extract was employed as a capping and reducing agent to create nano gold colloid. Using UV-vis spectroscopy, which is an effective spectroscopic technique for finding metallic nanoparticles, it was possible to confirm the creation of gold nanoparticles.

a)



b)

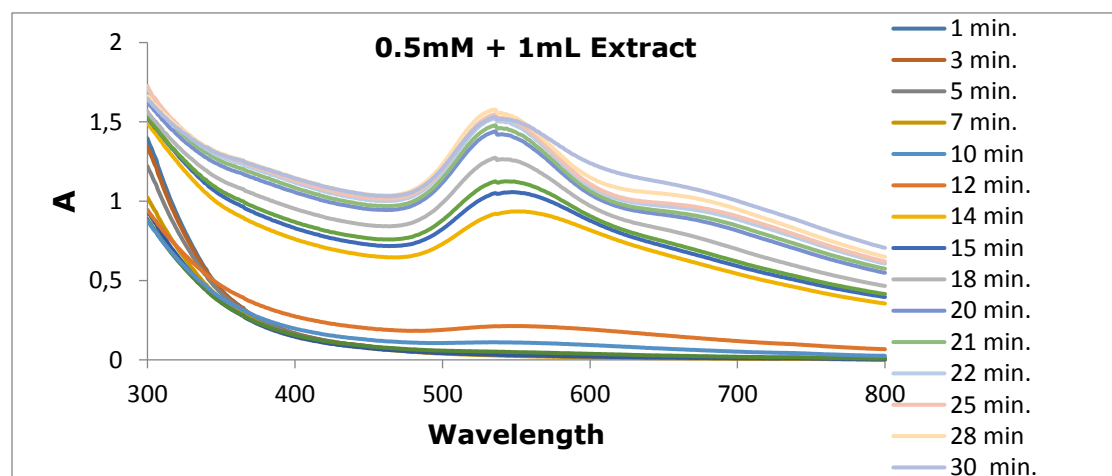
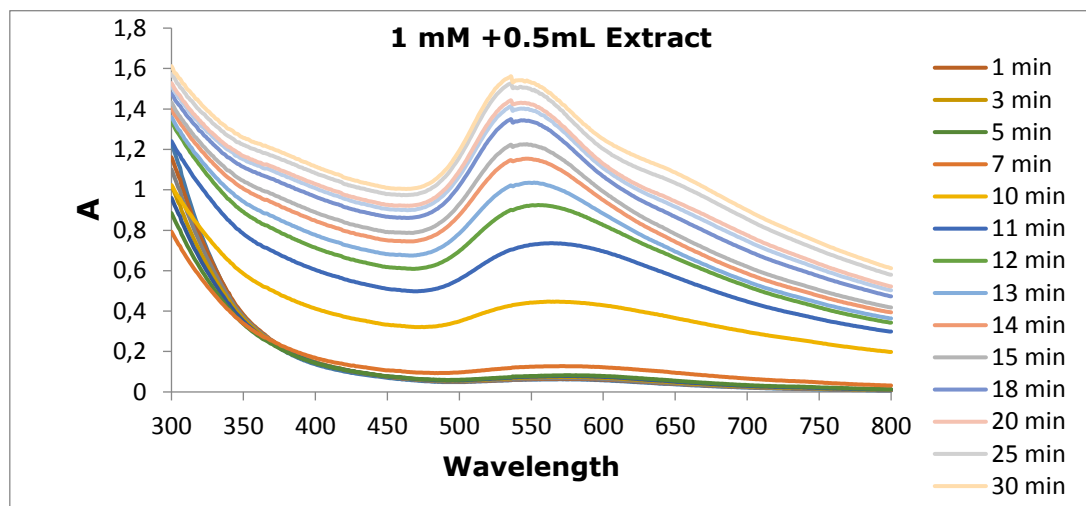


Figure 2. SPR absorption spectra of gold nanoparticles produced at a concentration of 0.5 mM (a [0,5 ml]-b [1 ml]) $\text{HAuCl}_4 \cdot 3\text{H}_2\text{O}$.

According to Figure 2a, which shows a distinctive resonance band about 530-580 nm after 18 minutes of exposure, which is the typical absorption band of spherical gold nanoparticles, it appears that AuNPs were successfully produced with 0.5 mL mulberry leaves extract. After 30

minutes of microwave treatment at 90 W power, the band reached its highest point. The size and form of the gold nanoparticles are related to the absorption band, which is the surface plasmon absorption of gold nano colloids.

a)



b)

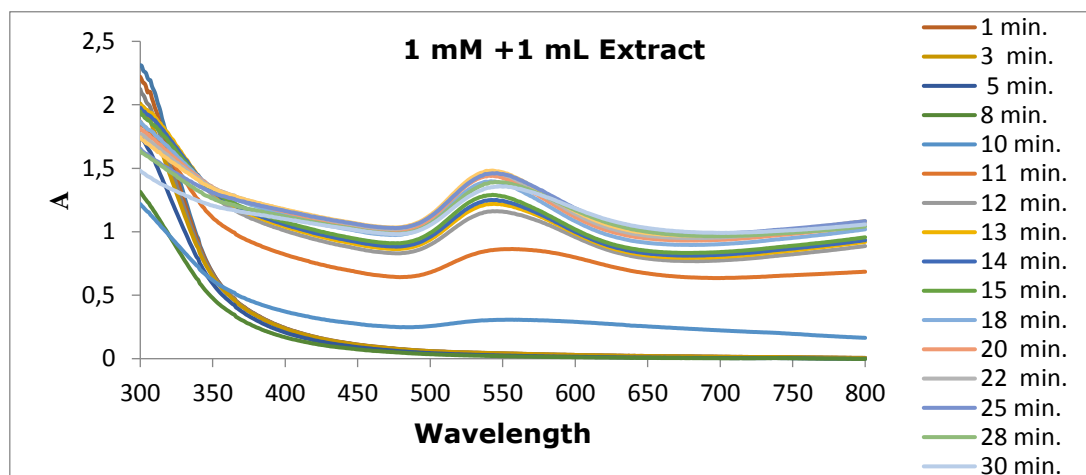


Figure 3: SPR absorption spectra of gold nanoparticles produced at a concentration of 1 mM (a [0.5 ml]-b [1 ml] $\text{HAuCl}_4 \cdot 3\text{H}_2\text{O}$).

The amount of nanoparticles was undoubtedly increased by the larger extract volume (1 mL). For 14 and 30 minutes, the surface plasmon resonance (SPR) absorption band was very strong and wide. However, significant agglomeration caused the particle size to be high. The hue of the reaction mixture revealed it. After the exposure period, the

colloidal solution had turned dark purple and cloudy. A higher concentration of $\text{HAuCl}_4 \cdot 3\text{H}_2\text{O}$ led to more AuNP generation (Figure 3a and b). There must be a limit to the bioactive components reductive power. On the other hand, even after an 11-minute microwave treatment, 1 mL of mulberry leaves extract appears to yield AuNPs (Figure. 3a and 2b). A notable band peak shift to the 600 nm region was also noted (Figure 3).

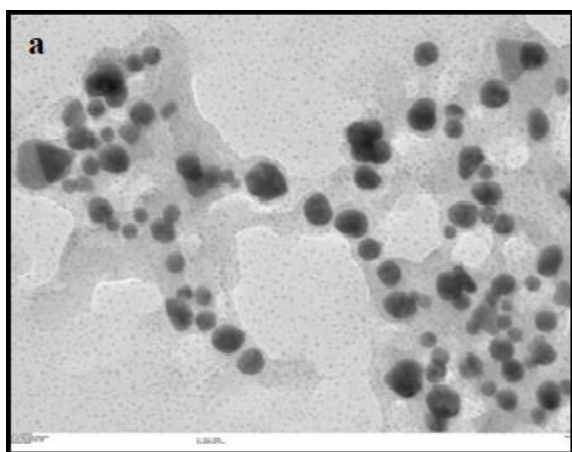


Figure 4. TEM images of Au nanoparticles were produced using the microwave extraction method with 0.5 mM $\text{HAuCl}_4 \cdot 3\text{H}_2\text{O}$ (100 nm).

Through TEM analysis, the morphology of the biosynthesized AuNPs was further confirmed. Figures 4. demonstrated the creation of a few irregularly shaped particles as well as three different magnifications of almost spherical AuNPs.

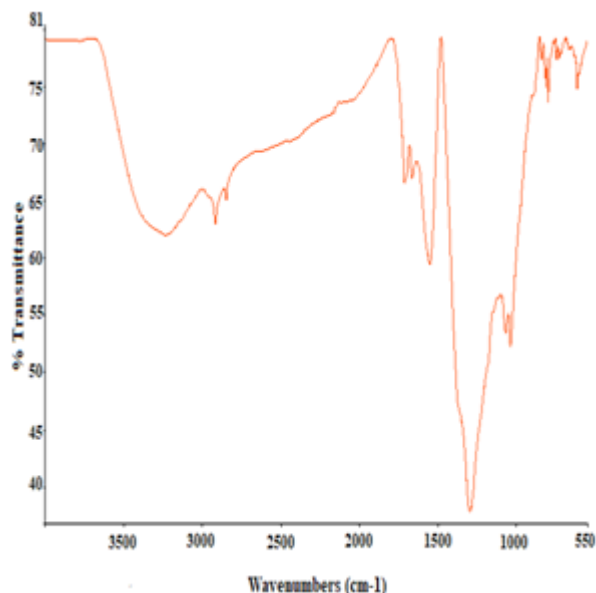


Figure 5. FT-IR spectrum of synthesized AuNPs.

The potential biomolecules responsible for capping and effective stabilization of the Au-NPs produced with mulberry leaf extract were determined using FT-IR studies. The biosynthesized AuNPs demonstrate strong bands at 3228 cm^{-1} , 2917 cm^{-1} , 1551 cm^{-1} , 1290 cm^{-1} , 1071 cm^{-1} , 1041 cm^{-1} , 616 cm^{-1} . This shows the various functional groups of biomolecules that have been adsorbed on the surface of the nanoparticles and also shows the impact of organic moieties on the synthesis of AuNPs and their ability to withstand the aqueous medium. The strong band seen at 3228 cm^{-1} is due to amine group stretching vibrations on the side of the hydroxyl group. It is possible to attribute the signal at 2917 cm^{-1} to C-H stretching vibrations of the methyl, methoxy, and methylene groups. The properties of C-OH protein vibrations and the C-O-C bending mode are represented by the peaks at

1071 cm^{-1} and 1041 cm^{-1} , respectively. The N-H groups of proteins' plane-bending vibrations could be the cause of the band at 661 cm^{-1} . According to the findings of FTIR spectral analysis, the biomolecules in the extract of Mulberry leaf served as the agents in reducing, stabilizing of AuNPs.

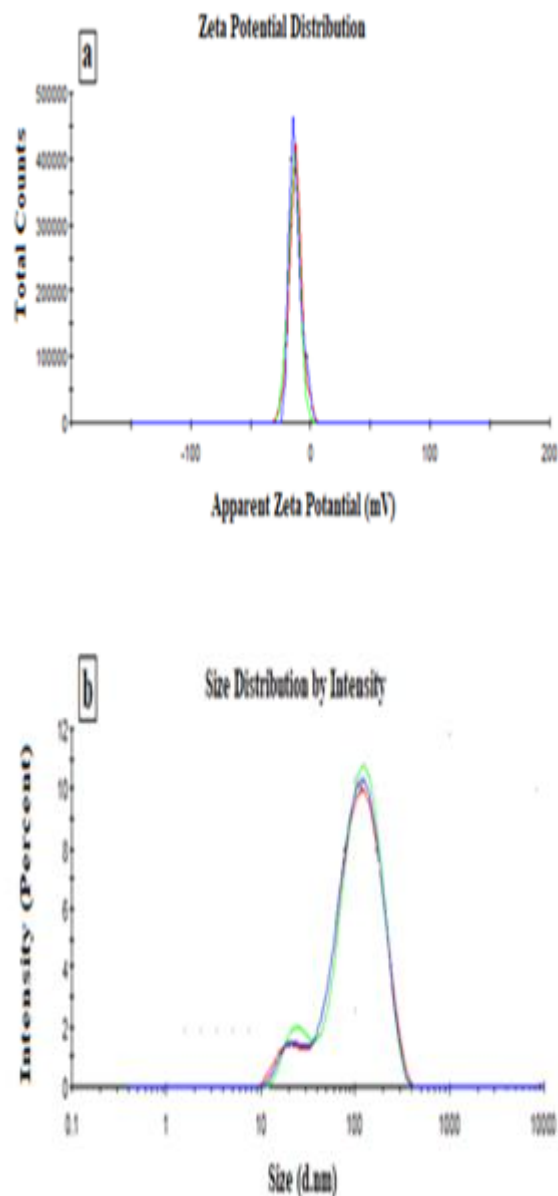


Figure 6. Zeta potential (a) and size distribution (b) of Au nanoparticles produced by microwave extraction using 0.5 mM $\text{HAuCl}_4 \cdot 3\text{H}_2\text{O}$ and 0.5 mL mulberry leaves extract, respectively.

The size of the metallic core and the thickness of the capping or stabilizing substance surrounding the metallic nanoparticles are determined using the dynamic light scattering (DLS) technique (31). Using DLS measurements, Figure 6(a) displays the particle size distribution of the biosynthesized AuNPs. Au-NPs were discovered to have an average particle size of $78.95 \pm 0,57\text{ nm}$. The ZP value of $-12,9 \pm 0,808\text{ mV}$ and a polydispersity index of $0,321 \pm 0,004$ are shown in Figure 6(b),

which points to colloidal AuNPs' increased stability. These findings were found to be comparable with the literature carried out by Adavallan and Krishnakumar (2014) (31). Adavallan and Krishnakumar (2014) synthesized gold nanoparticles from Mulberry leaf extracts using chemical synthesis and biosynthesis and used the zeta-sizer method for their characterization. They found the zeta potential and the average particle size of the biosynthesized AuNPs gold nanoparticles were -16 mV, 50 nm, respectively. Zeta potential (ZP) values provide details on the stability and surface charge of biosynthesized AuNPs (32). It's possible that the mulberry leaf extract's abundant protein content is what causes the metal ions to be reduced and the biosynthesized nanoparticles to be stabilized effectively (32).

4. CONCLUSION

The study describes a straightforward, innovative, and productive method for creating gold nanoparticles that uses *Morus alba* L. leaf extract as a reducing and stabilizing agent for gold. The surface plasmon resonance of biosynthesized AuNPs was validated by UV-visible spectrum spectroscopy. For bio-synthesized AuNPs, the zeta potential value was $-12,9 \pm 0,808$ mV, confirming the stability of the nanoparticles. Gold nanoparticle preparation is illustrated utilizing a straightforward, quick, and environmentally friendly method that uses mulberry leaf extract as a capping and reducing agent. In the proposed technique, when the extract volume is 0,5 mL and the $\text{HAuCl}_4 \cdot 3\text{H}_2\text{O}$ concentration is 0,5 mmol/L, it takes 30 minutes to synthesis gold nanoparticles in MAE. The production of size particles depends on several factors, including the quantity of extract, the concentration of $\text{HAuCl}_4 \cdot 3\text{H}_2\text{O}$, and time.

5. CONFLICT OF INTEREST

There are no disclosed conflicts of interest for this author. The research study complies with publication and research ethics.

6. ACKNOWLEDGMENTS

The author would like to thank the Karadeniz Technical University, Atatürk University Central Research Laboratories and Prof.Dr. Salih Terzioğlu from Karadeniz Technical University, Faculty of Forestry.

7. REFERENCES

1. Keikhaie KR, Saeidi S, Forghani F, Khajeh H. Green Synthesis of Nano Silver: Review. *Journal of Nano Drug Science*.2018; 1(1): 18-21.
2. Yokoyama T. et al. Basic Properties and Measuring Methods of Nanoparticles. In *Nanoparticle Technology Handbook*, Elsevier. 2018. 3–47. Available from: [<DOI>](#).
3. Güven OC. (2022), Bakır (Cu) Nanoçiçeklerinin Yeşil Sentez Yöntemi Kullanılarak Sentezlenmesi, Karakterizasyonu, Fotokatalitik, Antimikrobiyal Ve Antioksidan Aktivitesinin Belirlenmesi [Master Thesis]. Nevşehir Hacı Bektaş Veli University.2022.
4. Başarı H. *Hibiscus Sabdariffa* L. Ekstraktı Kullanılarak Sentezlenen Gümüş Nanopartiküllerin Sentez Parametrelerinin Antimikrobiyal Aktiviteye Etkisinin Değerlendirilmesi [Master Thesis]. Necmettin Erbakan University.2022.
5. Beykaya M, Çağlar A. An Investigation on Synthesis of Silver-Nanoparticles (AgNP) and their Antimicrobial effectiveness by using Herbal Extracts. *Afyon Kocatepe Univ. J. Sci. Eng.* 2016; 16(3):631–641.
6. Bila D, Radwan Y, Dobrovolskaia MA, Panigaj M, Afonin KA. The Recognition of and Reactions to Nucleic Acid Nanoparticles by Human Immune Cells. *Molecule*. 2021; 26:4231. Available from: [<DOI>](#).
7. Ferreira MC, Pimentel B, Andrade V, Zverev V, Gimaev RR, Pomorov AS, Pyatakov A, Alekhina Y, Komlev A, Makarova L, et al. Understanding the Dependence of Nanoparticles Magnetothermal Properties on Their Size for Hyperthermia Applications. A Case Study for La-Sr Manganites. *Nanomaterials*. 2021;11: 1826. Available from: [<DOI>](#).
8. Kukushkina EA, Hossain SI, Sportelli MC, Ditaranto N, Picca RA, Cioffi N. Ag-Based Synergistic Antimicrobial Composites. A Critical Review. *Nanomaterials*.2021; 11: 1687. Available from: [<DOI>](#).
9. Vankdoth S, Velidandi A, Sarvepalli M, Vangalapati M. Role of plant (tulasi, neem and turmeric) extracts in defining the morphological, toxicity and catalytic properties of silver nanoparticles. *Inorganic Chemistry Communications*.2022; 140:109476. Available from: [<DOI>](#).
10. Mallakpour S, Radfar Z, Hussain CM. Current advances on polymer-layered double hydroxides/metal oxides nanocomposites and bionanocomposites: Fabrications and applications in the textile industry and nanofibers. *Appl. Clay Sci.*, 2021; 206: 106054. Available from: [<DOI>](#).

11. Mazari SA, Ali E, Abro R, Khan FSA, Ahmed I, Ahmed M, Nizamuddin S, Siddiqui TH, Hossain N, Mubarak NM, Shah A. Nanomaterials: Applications, waste-handling, environmental toxicities, and future challenges - A review. *J. Environ. Chem. Eng.* 2021; 9: 105028. Available from: [<URL>](#).
12. Khodakarami, M., Bagheri, M. Recent advances in synthesis and application of polymer nanocomposites for water and wastewater treatment. *J. Clean. Prod.* 2021; 296:126404. Available from: [<DOI>](#).
13. Velidandi A, Sarvepalli M, Pabbathi NPP, Baadhe RR. Biogenic synthesis of novel platinum-palladium bimetallic nanoparticles from aqueous *Annona muricata* leaf extract for catalytic activity. *3, Biotech.* 2021. 11, 1-14. Available from: [<DOI>](#).
14. Castillo-Henríquez L, Alfaro-Aguilar K, Ugalde-Álvarez J, Vega-Fernández L, de Oca-Vásquez GM, Vega-Baudrit JR. Green synthesis of gold and silver nanoparticles from plant extracts and their possible applications as antimicrobial agents in the agricultural area. *Nanomaterials.* 2020; 10,1-24. Available from: [<DOI>](#).
15. Varadavenkatesan T, Selvaraj R, Vinayagam R. Green synthesis of silver nanoparticles using *Thunbergia grandiflora* flower extract and its catalytic action in reduction of Congo red dye. *Mater. Today Proc.*, 2019;23:39-42.
16. Jebiril S, Khanfir Ben Jenana R, Dridi C. Green synthesis of silver nanoparticles using *Melia azedarach* leaf extract and their antifungal activities: In vitro and in vivo. *Mater. Chem. Phys.* 2020; 248:122898. Available from: [<DOI>](#).
17. İçoglu Aksakal F, Yilmaz A, Koc K, Ozdemir S. A comparative study on aquatic toxicity of chemically-synthesized and green synthesis silver nanoparticles on daphnia magna. *Int. J. Environ. Health Res.* 2021; 1-11. Available from: [<DOI>](#).
18. Garibo D, Borbón-Nuñez HA, de León JND, García Mendoza E, Estrada I, Toledano-Magaña Y, Tiznado H, Ovalle-Marroquin M, Soto-Ramos AG, Blanco A, Rodríguez JA, Romo OA, Chávez-Almazán LA, Susarrey-Arce A. Green synthesis of silver nanoparticles using *Lysiloma acapulcensis* exhibit high-antimicrobial activity. *Sci. Rep.* 2020. 10, 1-11.
19. Selvaraj R, Pai S, Murugesan G, Pandey S, Bhole R, Gonsalves D, Varadavenkatesan T, Vinayagam R. Green synthesis of magnetic α -Fe₂O₃ nanospheres using *Bridelia retusa* leaf extract for Fenton-like degradation of crystal violet dye. *Appl. Nanosci.* 2021; 11: 2227-2234. Available from: [<DOI>](#).
20. Velidandi A, Dahariya S, Pabbathi NPP, Kalivarathan D, Baadhe RR. A Review on Synthesis, Applications, Toxicity, Risk Assessment and Limitations of Plant Extracts Synthesized Silver Nanoparticles. *Nano World J.* 2020;6:35-60. Available from: [<DOI>](#).
21. Du J, Zhou Z, Zhang X, et al. Biosynthesis of gold nanoparticles by flavonoids from *lilium casa blanca*. *J. Clust. Sci.* 2017;28(6): 3149-3158. Available from: [<DOI>](#).
22. Parveen K, Banse V, Ledwani L. Green synthesis of nanoparticles: Their advantages and disadvantages. in *AIP Conference Proceedings.* 2016;1724. Available from: [<DOI>](#).
23. Liu XY, Wang JQ, Ashby Cr, Zeng L, Fan YF, Chen ZS. Gold nanoparticles: synthesis, physiochemical properties and therapeutic applications in cancer. *Drug Discovery Today.* 2021;26(5): 1284-92. Available from: [<DOI>](#).
24. Hammami I, Alabdallah NM, Jomaa AA, Kamoun M. Gold nanoparticles: Synthesis properties and applications. *Journal of King Saud university - Science.* 2021; 33(7). Available from: [<DOI>](#).
25. Siddiqi K, Husen A. Recent advances in plant-mediated engineered gold nanoparticles and their application in biological system. *J. Trace Elem. Med. Bio.* 2017;40: 10-23. Available from: [<DOI>](#).
26. Yuan QX, Xie YF, Wang W. et al. (2015). *Carbohydrate Polymers*[J]. 2015; 128: 52. Available from: [<DOI>](#).
27. Zhang Y, Ren CJ, Lu GB. et al. *Regulatory Toxicology Pharmacology*[J]. 2014; 70(3): 687.
28. Chunfa D, Fei C, Xianglin Z, Xiangjie W, Xiuzhi Y, Bin Y. Rapid and Green Synthesis of Monodisperse Silver Nanoparticles Using Mulberry Leaf Extract. *Rare Metal Materials and Engineering.* 2018; 47(4):1089-1095. Available from: [<DOI>](#).
29. Thirugnanasambandham K, Sivakumar V, Maran JP. Microwave-assisted extraction of polysaccharides from mulberry leaves. *International Journal of Biological Macromolecules*[J]. 2015;72: 1-5. Available from: [<DOI>](#).
30. Serdar G. Green Synthesis of Gold Nanoparticles Using Mulberry Leaf Extract. 3rd International Congress On Analytical And Bioanalytical Chemistry, ss.73, 22-26 March 2021, Elazığ, Turkey.
31. Adavallan K, Krishnakumar N. Mulberry leaf extract mediated synthesis of gold nanoparticles and its antibacterial activity against human pathogens. *Adv. Nat. Sci.: Nanosci. Nanotechnol.* 2014;5, 025018. Available from: [<DOI>](#).

32. Sukirtha R, Priyanka KM, Antony JJ, Kamalakannan S, Thangam R, Gunasekaran P, Krishnan M, Achiraman S. Cytotoxic effect of Green synthesized silver nanoparticles using *Melia azedarach* against *in vitro* HeLa cell lines and lymphoma mice model. *Process Biochem.*, 2012; 47: 273. Available from: [<DOI>](#).



De novo Drug Design to Suppress Coronavirus RNA-Glycoprotein via PNA-Calcitonin

Soykan Agar^{1*} , Barbaros Akkurt² , Levent Alparslan³ 

¹Kocaeli Health and Technology University, Faculty of Pharmacy, Yeniköy Mahallesi Ilıca Caddesi No:29, Başiskele/Kocaeli, Türkiye

²Istanbul Technical University, Faculty of Science and Letters, Department of Chemistry, Istanbul 34469, Türkiye

³Istinye University, Faculty of Pharmacy, Pharmaceutical Technology Department, Istanbul 34010, Türkiye

Abstract: *De novo* drug design has been studied utilizing the organic chemical structures of Salmon Calcitonin 9 - 19 and Peptide Nucleic Acid (PNA) to suppress Coronavirus Ribonucleic Acid (RNA)-Glycoprotein complex. PNA has a polyamide backbone and thymine pendant groups to bind and selectively inhibit adenine domains of the RNA-Glycoprotein complex. While doing so, molecular docking and molecular dynamics studies revealed that there is great inhibition docking energy (-12.1 kcal/mol) with significantly good inhibition constant (124.1 μ M) values confirming the efficient nucleotide-specific silencing of Coronavirus RNA-Glycoprotein complex.

Keywords: Salmon Calcitonin, Coronavirus RNA, Coronavirus Glycoprotein, Molecular Docking, Molecular Dynamics, Hydrogen Contact Mapping

Submitted: December 18, 2023. **Accepted:** January 29, 2024.

Cite this: Agar S, Akkurt B, Alparslan L. De novo Drug Design to Suppress Coronavirus RNA-Glycoprotein via PNA-Calcitonin. JOTCSA. 2024; 11(2): 623-32.

DOI: <https://doi.org/10.18596/jotcsa.1406290>.

***Corresponding author. E-mail:** soykan.agar@kocaelisaglik.edu.tr

1. INTRODUCTION

A widespread disease emerged in December 2019 and caused a major health problem worldwide after its sudden strike in China (1-3). SARS-CoV-2, also known as the novel coronavirus, is the human pathogen that caused a global pandemic with well over 100,000 diagnosed patients across the world, from China to Europe and all the way to the U.S.A., and yet still, there is no efficient halt to this spread currently. There is now quite an effort within the industrial and scientific community to find an inhibition mechanism for SARS-CoV-2 via varying strategies to save millions of lives (4-8). There are far more than 350 genome sequences of SARS-CoV-2; however, 30,000 base-pair genomes of SARS-CoV-2 is quite a different strain from SARS-CoV which was a beta coronavirus infecting mankind that caused a major health problem in 2003 and 2004 (9,10).

Under these terms, especially in silico drug discovery and drug repurposing settings have become rapidly even more popular than they used to be and are utilized quite often since the beginning of this disease. SARS-CoV-2 enters into the human host cells through its spike subunit S1's binding to the host

cell's ACE2 transport protein. The modulation of the spike S1 protein (which is bound to S2 protein where it is attached to the surface membrane SARS-CoV-2) occurs in such a way that its trimeric structure accepts homodimer ACE2 proteins, and the binding occurs in Figure 1. ACE2 is a type 1 membrane protein known to be highly expressed within the respiratory cells. The S1 is known to be an excellent cell surface receptor binder in terms of binding affinity and efficiency. Specific anti-viral drugs from pharmaceutical synthetic and pharmacological origins are being re-examined in terms of their binding mechanisms to the ACE-2 enzyme and S1 subunit protein of coronavirus. Several drugs are being used together in the patients currently instead of solely using a drug to be able to keep them alive. Chloroquine, Arbidol, Favipiravir, Remdesivir, and an anti-asthmatic drug, Zafirlukast, and several other antibiotics and antifungal drugs Itrazol, Fazadinium, Troglitazone, Gliquidone, Idarubicin, and Oxacillin are also being tested in clinical trials effective immediately. Sending spike proteins (S1 analogs) as the drug to bind them to ACE2 receptors was the first strategy, Figure 2a, in hand. Since these spike protein analogs will block all ACE2 receptors, SARS-CoV-2 cannot bind to any ACE2. Thus, there will be no viral infection, and the immune system will be able

to recognize these non-harmful spike proteins and develop a response to the SAR-CoV-2 in time. However, blocking a protein channel such as ACE2 might cause some side effects. In Figure 2b, scientists also thought of a similar approach. Utilizing antibodies instead of the spike proteins would yield a similar outcome since the outcome of permanently blocking all ACE2 receptors might have adverse side

effects for the patients in the long run (11-13). According to Figure 2c, sending an inhibitory protein or drug such as Favipiravir to inhibit the S1 domains of SAR-CoV-2 directly might be an efficient route. With the spike proteins on the SAR-CoV-2 surface blocked, they can no longer get into interaction with ACE2 receptors (14).

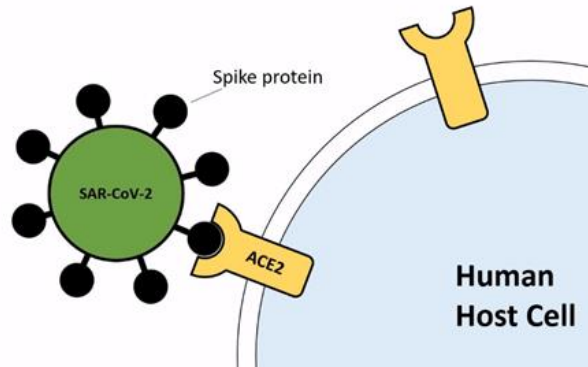


Figure 1: The binding illustration of the S1 subunit spike protein of SAR-CoV-2 and ACE2 transport protein of human host cell.

Nanobodies, also known as therapeutic antibodies, can serve the same purpose as stated in Figure 2d. A further advantage of these might be the choice of DNA sequences within the nanobodies. The choice of sequence might be beneficial for further intra-cellular mechanisms from the immune system perspective and aid in initiating the neutralizing immune response (15-17).

Rather than choosing these strategies to suppress coronavirus activity as the other scientists tried within the scientific literature, a significant *de novo* design (strategy Figure 3) was made via the complex of Calcitonin and Peptide Nucleic Acids (PNA) since the Calcitonin domain is essential for blood circulatory system bioavailability. In contrast, PNAs can be used to silence virus RNAs. Thus, the significance of Calcitonin and PNA should be mentioned. Calcitonin, a 32-amino-acid peptide, is secreted by the C-cells of the thyroid in mammals and by the ultimobranchial glands in sub-mammals. As a therapeutic agent for metabolic bone disease, Salmon calcitonin (SCT) has been in use for over three decades, and it has received approval for the treatment of postmenopausal osteoporosis in more than 90 countries. It is also approved for other indications such as Paget's disease, bone-associated pain conditions, and emergency treatment of hypercalcemia using injectable salmon calcitonin. The hormone's bioavailability within the bloodstream plays a crucial role in its mechanism. Initially identified in 1961 for its blood calcium-lowering properties, synthetic or recombinant Calcitonins from various species, including human, porcine, eel-derived, and SCT, have been employed for medical purposes. Over the past 15 years, new insights have emerged regarding the effects of SCT in preserving bone quality, particularly trabecular microarchitecture, which may contribute to its anti-fracture efficacy. SCT is the most widely used

preparation in clinical practice, owing to its 40-50 times higher intrinsic potency compared to human calcitonin and its improved analgesic properties. Nonetheless, despite being discovered 45 years ago, the physiological role of calcitonin remains not entirely understood and continues to be the subject of ongoing research (18-24).

Peptide Nucleic Acids (PNAs) were originally designed as DNA-binding agents that target the major groove domain of DNA, similar to triplex-forming oligonucleotides. Instead of using the sugar-phosphate backbone found in oligonucleotides, PNAs were created with a pseudopeptide backbone (25). Upon synthesis, it became evident that PNAs, with their backbone and nucleobase linkers, closely mimic the structure of DNA and RNA. They can form stable duplex structures with complementary DNA, RNA, or other PNA oligomers (26-28). The synthesis of PNA oligomers can be done through standard solid-phase manual or automated peptide synthesis, using either tBoc or Fmoc-protected PNA monomers (29-31). After synthesis, the oligomers are deprotected and separated from the polymer using TFMSA/TFA (for tBoc) or purified through reversed-phase HPLC. Characterization of the oligomers can be done using MALDI-TOF or proton NMR. PNA oligomers can be easily labeled with fluorophores or biotin. In cellular uptake experiments conducted *in vitro* and *in vivo*, PNA oligomers are used as antisense or antigen agents, typically consisting of 12-18 nucleobases and having molecular weights of 3000-4000 amu. These hydrophilic structures have applications as antigens, antibacterial, and antiviral agents. These oligomers demonstrated intriguing characteristics in a complex formed by the interaction of polyamide nucleic acid with purine and pyrimidine bases attached to it. Notably, they exhibit high stability in human serum and cell extracts and exhibit antisense activity and suppress HIV virus RNA (32-37).

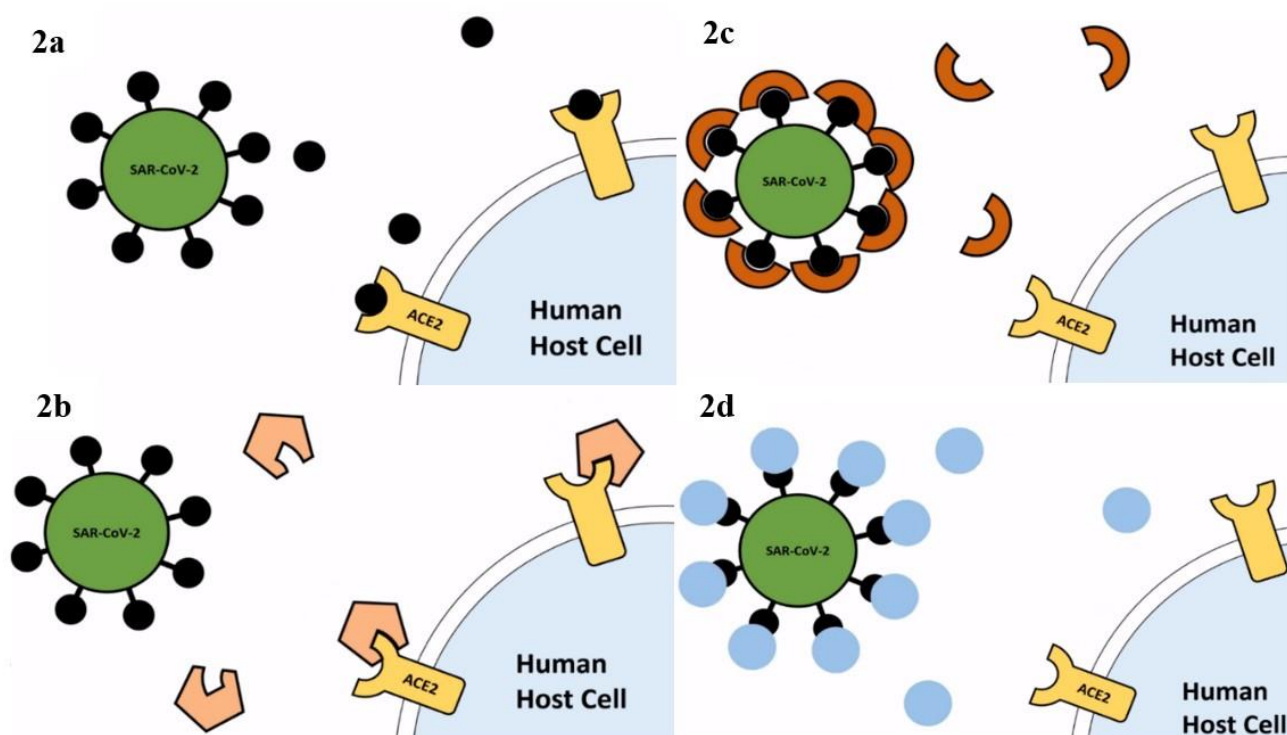


Figure 2: Strategy 2a: Occupying the ACE2 Receptors with ACE2 binding drugs (spike proteins); Strategy 2b: Occupying the ACE2 Receptors with ACE2 binding drugs (antibodies); Strategy 2c: Blocking SARS-CoV-2 directly via inhibitory drugs; Strategy 2d: Blocking SARS-CoV-2 directly via nanobodies.

Hence, studying the antiviral complementary suppression activity of Polyamide-backed PNA combined with the superior bioavailability features of SCT is the primary goal of this research paper. For the sake of argument, we can call our designed ligand (drug) Peptide Polyamide Nucleic Acid complexed with Salmon Ligand, or in short, PPNASL, which will serve as an Adenine binder and inhibitor of RNA of Coronavirus along with its attached Glycoprotein.

2. MATERIALS AND METHODS

2.1. Geometric Optimization

An accurate determination of its geometrically optimal structure is essential to determine the active sites of any molecule and investigate its interactions with receptors. In our current study, the ligand designed to inhibit Coronavirus RNA-glycoprotein was determined using our group's vast organic/pharmaceutical chemistry knowledge. These organic chemical structures, with their most stable molecular geometries, went under the processing of the Gaussian 09 software (38) with density functional theory (DFT)/B3LYP functional (39). Using the 6-31G(d,p) principle, the most stable molecular structures of polyamide-g-thymine and calcium molecules were formed for computational and simulation further research, as can be seen in Figure 1. GaussView 6.0 and Avogadro 1.95 software (40) was used to prepare the input files for the molecular

docking and molecular dynamics computations as well as for the post-processing of the output files.

2.2. Molecular Docking Procedure

All molecular docking simulations were performed via AutoDock Vina 1.1.2. and PyRx 0.8 software (41), both of which are widely used and accepted for their great precision and accuracy in biochemical docking simulations. The docking simulations took 50 posed simulations to 100 posed simulations in each run, totaling 800 poses. The drug complex of PPNASL has two domains. Its PNA (Polyamide-g-Thymine) part was de novo designed. In contrast, its Calcitonin part, along with the receptor structure of Coronavirus RNA-Glycoprotein, was downloaded from the Zinc Database with the following IDs of 2GLG and 7ACT, respectively. The optimizations were done using Gauss View 6.0 and Avogadro 1.95 and run, illustrating the interaction and binding of the drug to the receptor. The docking scores of all simulations were in kcal/mol as units stating the Gibbs free binding energy. The docking poses with the most accurate and favorable binding energy within the best-clustered data were chosen to be used as the initial structure and input file for MD simulations in each simulation with different seed numbers.

2.3. Molecular Dynamics (MD) Simulations

The docking poses possessing the best and most favorable binding energy concerning the docking results were used as the initial structure for the MD simulations (42,43). Utilizing Schrödinger's Maestro

Desmond software (44), all the ligands were run for molecular dynamics (MD) simulations with 50 ns total time periods per each new seeded run, including 5000 poses with 10 ps time intervals, respectively. Each molecular dynamics simulation was repeated 3 times with different seed numbers to ensure the simulation parameters and structure of the PPNASL (ligand) bound Coronavirus RNA-Glycoprotein (receptor) complexes were correct. MD simulations were run to evaluate the dynamic properties of the drug-receptor complexes over time. The grid box in which the system was created was set to $150 \times 150 \times 150 \text{ \AA}^3$ and with the spacing of 0.5 \AA choice for this large receptor. TIP3P-type water molecules were placed in the box, and 0.15 M NaCl ions were also added to neutralize the system. As the temperature and pressure parameters, NPT was employed at 310 K with Nose-Hoover temperature coupling (45) and at the constant pressure of 1.01 bar via Martyna Tobias–Klein pressure coupling (46). There were not any constraints on the systems, and the initial velocity values for the force field calculations were used as default fitting for OPLS 3.0 standards.

2.4. Post Molecular Dynamics Characterizations

The trajectory datasets of MD results were used for "Hydrogen contact mapping analyses" so that atom by atom, the complexes' binding effects and the drug's efficiency could be verified. The "Event Analyses" modules of Schrödinger's Maestro Desmond software were used for this purpose, where these results can be compared to the inhibition constant values.

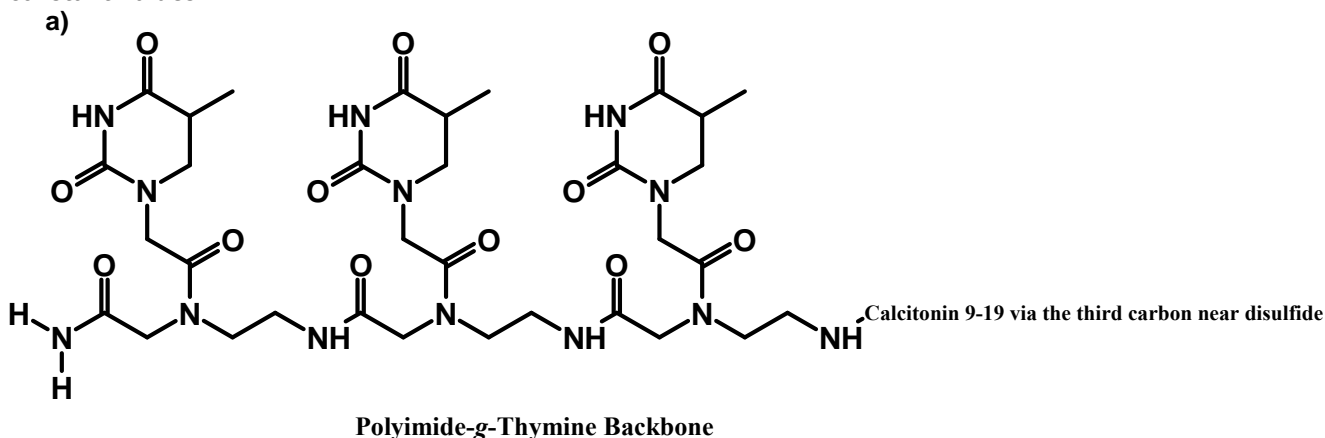


Figure 3: The de novo drug's chemical structure.

The second issue that should be referred to is that in terms of pharmacokinetics, the addition of Calcitonin to the ligand structure is significantly beneficial due to its good bioavailability within the blood circulatory system. In our *in silico* studies, referring to a published research paper of the Ph.D. thesis (51) of our group, which had the experimental *in vitro* and *in vivo* findings, the half-life of Calcitonin had the range of 50 to 80 minutes while its protein binding rate is 30-40%. Due to its peptide-based structure, Calcitonin is easily broken down in the gastrointestinal tract. Hence, it can be administered parenterally or intranasally. The plasma concentrations of $0.1\text{-}0.4 \text{ ng/mL}$ were obtained after 200 units of subcutaneous administration. While

3. RESULTS AND DISCUSSION

To achieve the goal of suppressing the activity of Coronavirus RNA-Glycoprotein by silencing its RNA to block its expression, one should know the pharmaceutical chemistry tendencies of functional groups and the genetic engineering aspects of the nucleotide-specific silencing on the receptors and its bioactivity features. The effectiveness of interactions appears to depend on various factors, including the affinity of the drug's pendant Thymine domains to RNA and the topology of the binding.

In our strategy to suppress Coronavirus, shown in Figure 3, the organic chemical structure of the designed drug (ligand) can be seen at pH 7.4. By merging PNA (Polyamide-g-Thymine) with Salmon Calcitonin 9-19, the efficiency of the ligand was planned to be increased in terms of chemical Hydrogen bond affinity towards the receptor since the mode of binding and the nucleotide regioselectivity plays a pivotal role in the inhibition and suppression mechanism.

Triple Thymine groups were chosen to bind to the Adenine groups of Coronavirus RNA-Glycoprotein, which has multiple repeating Adenines. This PNA oligomer possessing a Polyamide backbone with Thymine grafts is especially the right fit for the job in terms of RNA silencing (37, 48-50). For the first time here, we use it to silence Coronavirus RNA.

there is an immediate effect after intravenous administration, the effect is observed 15 minutes after intramuscular or subcutaneous administration. Salmon Calcitonin has the greatest effect approximately 4 hours after intramuscular or subcutaneous administration. While the effect after intravenous administration lasts between 30 minutes and 12 hours, it lasts for about 8-24 hours after intramuscular and subcutaneous administration.

In Figure 4, the organic chemical structure of the receptor target, Coronavirus RNA-Glycoprotein, is illustrated. Since the glycoprotein and RNA domains are merged within the nuclei of Coronaviruses, it is best to study the inhibition of the whole complex.

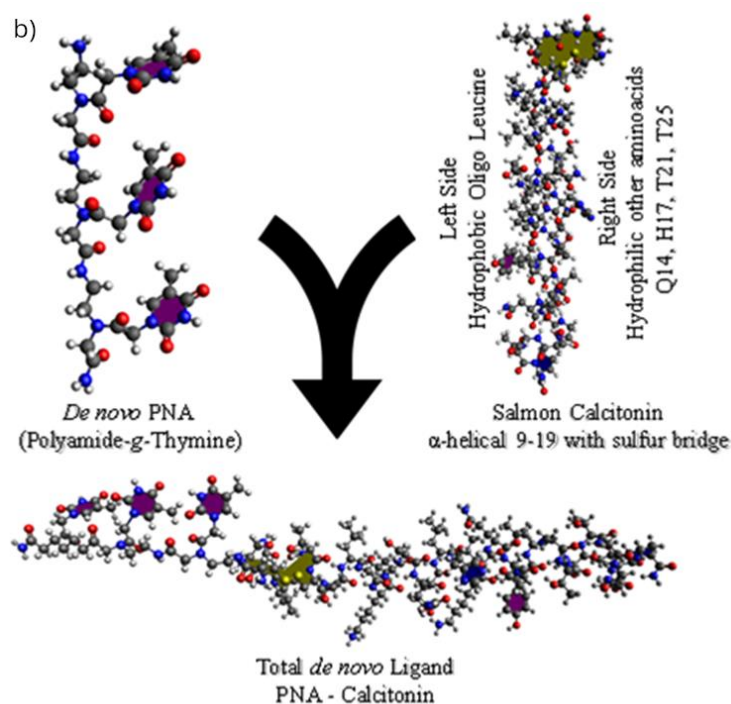


Figure 4: a) Chemical structure of PPNASL. b) *De novo* strategy for designing the biochemical organic structure of PPNASL.

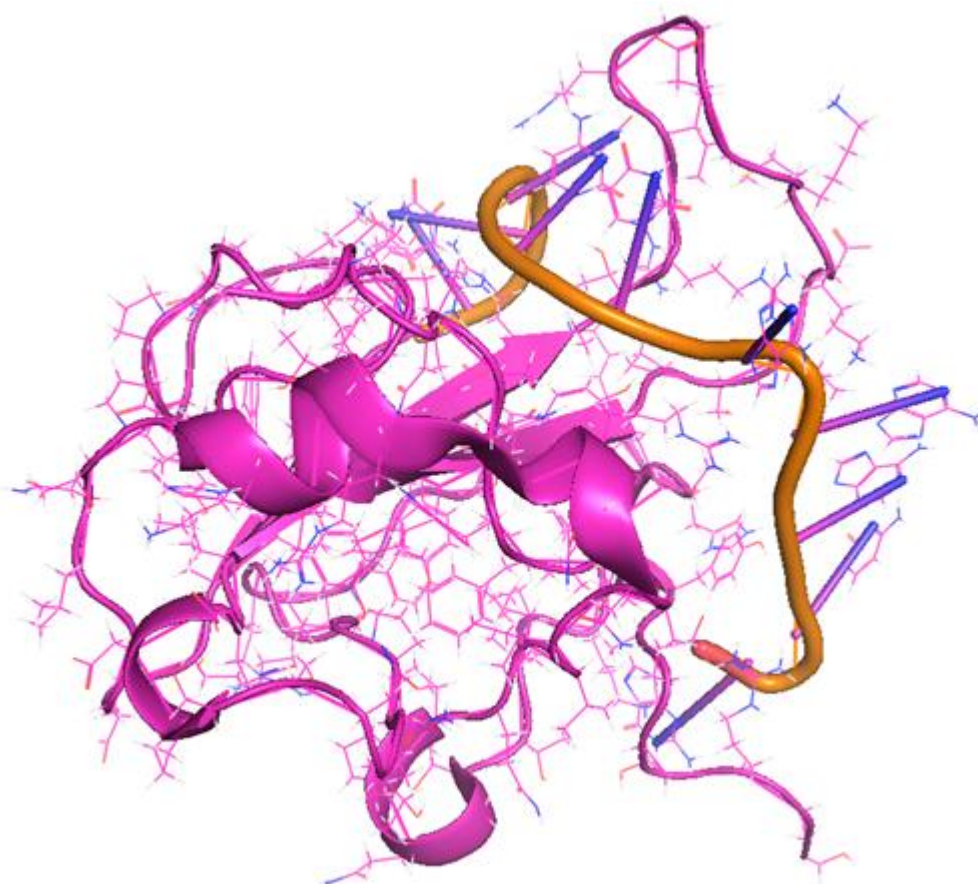


Figure 5: The receptor molecule: 3-D chemical structure of Coronavirus RNA-Glycoprotein.

The 3-D chemical structure of Coronavirus RNA-Glycoprotein was optimized using Gauss view and Avogadro. It was seen that the steric hindrance of RNA is not as much as one can expect, which is a

good starting point. Since its nucleotides, especially recurring Adenine triplets, are exposed, and the Polyamide-g-Thymine triplets of PPNASL can find the affinity and availability towards these sites easily and

docks onto them efficiently with $\Delta(\Delta G)$ of -12.1 kcal/mol and significantly good inhibition constant of 124.1 μM .

By simulating and computing the theoretical stability and binding energies of PPNASL docked onto Coronavirus RNA-Glycoprotein, Figure 6 illustrates one of the main poses of the PPNASL, taken under 3D video within Schrodinger's Maestro Desmond MD software, where the MD run had 5000 frames. The

thymine pendant groups on polyamide PNA selectively chose the adenine triplet of coronavirus RNA and silenced it.

Another detailed close-up shot of the docked pose of the ligand to Coronavirus RNA can be seen Ligand-receptor complex equilibrium and stabilization occur in Figure 7. The Thymine-Adenine binding of the ligand-receptor complex can be observed clearly.

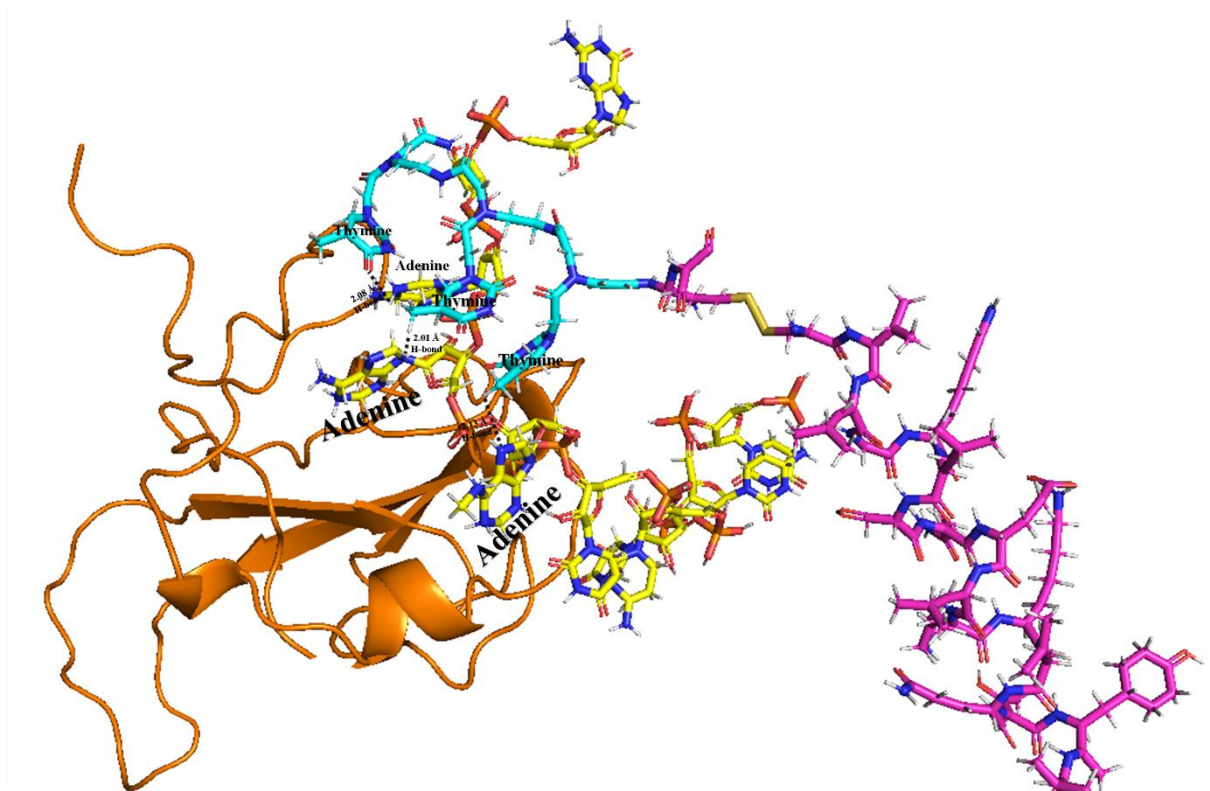


Figure 6: The best favored MD pose of PPNASL docked onto Coronavirus RNA-Glycoprotein.

Table 1: The Post-Molecular Dynamics Hydrogen bond contact mapping analyses of PPNASL

RNA domains	% of H-Bonds Thymines choose RNA	Binding Energy (kcal/mol)	H-Bond Distance (Å)
Adenine (1)	30.4	-12.4	2.08
Adenine (2)	32.3	-11.9	2.01
Adenine (3)	31.8	-12.0	2.13
The Rest	5.5	-	-

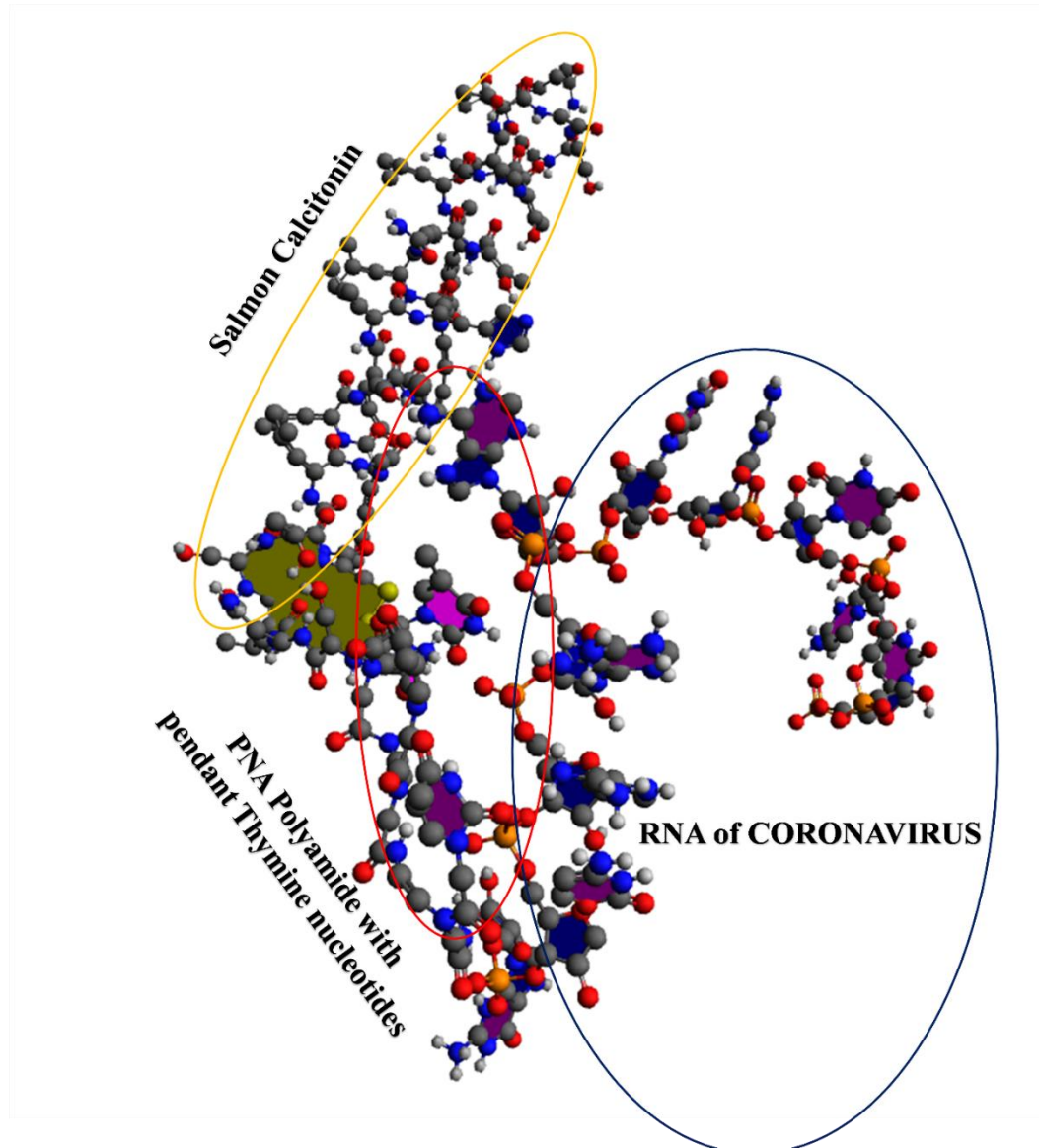


Figure 7: The close-up shot of the best favored MD pose of PPNASL docked onto Coronavirus RNA.

After conducting 3D motion trajectory analyses, Table 1 presents a subsequent investigation using Schrödinger Maestro Desmond's Event Analyses tools. The aim was to compute all potential interactions between functional groups on drugs and RNA domains. This intricate affinity and binding study involved examining all hydrogen bonds among thousands of atoms based on the matrix data from the MD study's trajectory files.

Matrix matches were manually performed for each atom to analyze the post-MD Hydrogen contact mapping. Additionally, a machine learning pre-coded script was utilized to determine the regioselectivity of Thymine groups of Polyamide PNA towards the Adenine domains of RNA. This approach was adopted to calculate the percentages of tendencies for functional group bindings.

The drug aligns and maneuvers itself onto the Adenine domains regioselectively, and strong Hydrogen forces (2.08, 2.01, 2.13 Å) take place there, maintaining inhibitory $\Delta(\Delta G)$ energies (-12.4, 11.9, -12.0 kcal/mol) so that PPNASL suppresses the RNA-Glycoprotein activity.

In Figure 8, it can be seen that after around 30 nanoseconds, the whole complex begins to reach an equilibrium in the yellow color compared to the non-bound pristine receptor (target molecule) of Coronavirus RNA, indicating lower oscillations and a stable structure form in the ligand-receptor bound situation. However, as can be seen from the blue Coronavirus RNA illustration, the oscillations among the atoms of the RNA structure go on around 2Å and do not diminish.

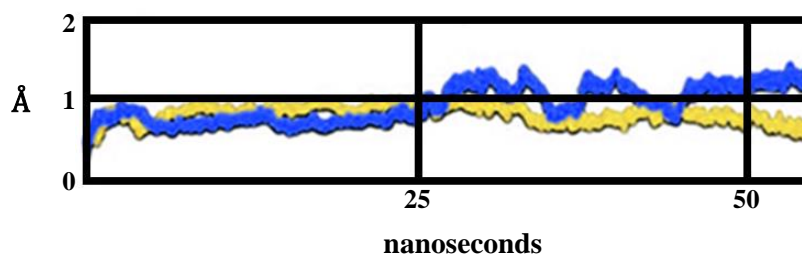


Figure 8: The Root Mean Square Deviation plot (R.M.S.D.) of all atoms studied under the force field of OPLS 3.0; PNA-Thymine in complex with RNA in yellow and non-bound receptor Coronavirus RNA (pristine) in blue respectively.

4. CONCLUSIONS

This research study has explored de novo drug design methods by utilizing the organic chemical structures of Salmon Calcitonin 9 - 19 and PNA to target the Coronavirus Ribonucleic Acid (RNA)-Glycoprotein complex. PNA, with its polyamide backbone and Thymine pendant groups, has been employed to selectively bind and inhibit the Adenine domains of the RNA-glycoprotein complex. Molecular docking, molecular dynamics, and post-MD characterization studies were conducted, revealing a highly favorable inhibition total docking energy of -12.1 kcal/mol and a significantly good inhibition constant of 124.1 μM . These findings confirm the effective and regioselective suppression of the Coronavirus RNA-Glycoprotein complex at the nucleotide level. This also proves the achievement of the Molecular Dynamics

5. CREDIT AUTHORSHIP CONTRIBUTION STATEMENT

Soykan Agar, Ph.D.: Computer-Aided Drug Design, Computational Experimenting and Writing the original draft and full paper. Barbaros Akkurt, Ph.D.: Writing the original draft and full paper, proofreading. Levent Alparslan, Ph.D.: Investigation, Supervision.

6. DECLARATION OF COMPETING INTEREST

The authors declare that they have no known competing financial interests or personal relationships that could have appeared to influence the work reported in this paper.

7. DATA AVAILABILITY

Data will be made available on request.

8. REFERENCES

- Dong L, Hu S, Gao J. Discovering drugs to treat coronavirus disease 2019 (COVID-19). *DD&T*. 2020 Feb 29;14(1):58–60. Available from: [<DOI>](#).
- Commission NH, others. Guidelines for the Prevention, Diagnosis, and Treatment of Novel Coronavirus-Induced Pneumonia. National Health Commission, Beijing, China; 2020.
- Jin Z, Du X, Xu Y, Deng Y, Liu M, Zhao Y, et al. Structure of M pro from COVID-19 virus and discovery of its inhibitors [Internet]. *Biochemistry*; 2020 Feb [cited 2023 Nov 7]. Available from: [<DOI>](#).
- Senathilake K, Samarakoon S, Tennekoon K. Virtual Screening of Inhibitors Against Spike Glycoprotein of SARS-CoV-2: A Drug Repurposing Approach [Internet]. *LIFE SCIENCES*; 2020 Mar [cited 2023 Nov 7]. Available from: [<DOI>](#).
- Chan JFW, Yuan S, Kok KH, To KKW, Chu H, Yang J, et al. A familial cluster of pneumonia associated with the 2019 novel coronavirus indicating person-to-person transmission: a study of a family cluster. *The Lancet*. 2020 Feb;395(10223):514–23. Available from: [<DOI>](#).
- Lu R, Zhao X, Li J, Niu P, Yang B, Wu H, et al. Genomic characterisation and epidemiology of 2019 novel coronavirus: implications for virus origins and receptor binding. *The Lancet*. 2020 Feb;395(10224):565–74. Available from: [<DOI>](#).
- Liu C, Zhou Q, Li Y, Garner LV, Watkins SP, Carter LJ, et al. Research and Development on Therapeutic Agents and Vaccines for COVID-19 and Related Human Coronavirus Diseases. *ACS Cent Sci*. 2020 Mar 25;6(3):315–31. Available from: [<DOI>](#).
- Wan Y, Shang J, Graham R, Baric RS, Li F. Receptor Recognition by the Novel Coronavirus from Wuhan: an Analysis Based on Decade-Long Structural Studies of SARS Coronavirus. Gallagher T, editor. *J Virol*. 2020 Mar 17;94(7):e00127-20. Available from: [<DOI>](#).
- Xu X, Chen P, Wang J, Feng J, Zhou H, Li X, et al. Evolution of the novel coronavirus from the ongoing Wuhan outbreak and modeling of its spike protein for risk of human transmission. *Sci China Life Sci*. 2020 Mar;63(3):457–60. Available from: [<DOI>](#).
- Huentelman MJ, Zubcevic J, Hernández Prada JA, Xiao X, Dimitrov DS, Raizada MK, et al. Structure-Based Discovery of a Novel Angiotensin-Converting Enzyme 2 Inhibitor. *Hypertension*. 2004 Dec;44(6):903–6. Available from: [<DOI>](#).
- Khaerunnisa S, Kurniawan H, Awaluddin R, Suhartati S, Soetjipto S. Potential Inhibitor of COVID-19 Main Protease (Mpro) From Several Medicinal Plant Compounds by Molecular Docking Study [Internet]. *MEDICINE & PHARMACOLOGY*; 2020 Mar [cited 2023 Nov 7]. Available from: [<DOI>](#).
- Chang KO, Kim Y, Lovell S, Rathnayake A, Groutas W. Antiviral Drug Discovery: Norovirus Proteases and Development of Inhibitors. *Viruses*. 2019 Feb 25;11(2):197. Available from: [<DOI>](#).
- Li JY, You Z, Wang Q, Zhou ZJ, Qiu Y, Luo R, et al. The epidemic of 2019-novel-coronavirus (2019-nCoV) pneumonia and insights for emerging infectious diseases in the future. *Microbes and Infection*. 2020 Mar;22(2):80–5. Available from: [<DOI>](#).

14. Delang L, Abdelnabi R, Neyts J. Favipiravir as a potential countermeasure against neglected and emerging RNA viruses. *Antiviral Research*. 2018 May;153:85–94. Available from: [<DOI>](#).
15. Xu Z, Peng C, Shi Y, Zhu Z, Mu K, Wang X, et al. Nelfinavir was predicted to be a potential inhibitor of 2019-nCoV main protease by an integrative approach combining homology modelling, molecular docking and binding free energy calculation [Internet]. *Pharmacology and Toxicology*; 2020 Jan [cited 2023 Nov 7]. Available from: [<DOI>](#).
16. Gopal Samy B, Xavier L. Molecular docking studies on antiviral drugs for SARS. *International Journal*. 2015;5(3):75–9.
17. Peng C, Zhu Z, Shi Y, Wang X, Mu K, Yang Y, et al. Computational study of the strong binding mechanism of SARS-CoV-2 spike and ACE2 [Internet]. *Chemistry*; 2020 Feb [cited 2023 Feb 22]. Available from: [<DOI>](#).
18. Copp DH, Cameron EC. Demonstration of a Hypocalcemic Factor (Calcitonin) in Commercial Parathyroid Extract. *Science*. 1961 Dec 22;134(3495):2038–2038. Available from: [<DOI>](#).
19. Azria M, Copp DH, Zanelli JM. 25 Years of salmon calcitonin: From synthesis to therapeutic use. *Calcif Tissue Int*. 1995 Dec;57(6):405–8. Available from: [<DOI>](#).
20. Woodrow J, Noseworthy C, Fudge N, Hoff A, Gagel R, Kovacs C. Calcitonin/calcitonin gene-related peptide protect the maternal skeleton from excessive resorption during lactation. *Journal of bone and mineral research*. 2003. p. S37–S37.
21. Hoff A, Thomas P, Cote G, Qiu H, Bain S, Puerner D, et al. Generation of a calcitonin knockout mouse model. *Bone*. 1998;23(suppl 5):S164.
22. Hirsch PF, Baruch H. Is Calcitonin an Important Physiological Substance? *ENDO*. 2003;21(3):201–8. Available from: [<DOI>](#).
23. Hoff AO, Catala-Lehnen P, Thomas PM, Priemel M, Rueger JM, Nasonkin I, et al. Increased bone mass is an unexpected phenotype associated with deletion of the calcitonin gene. *J Clin Invest*. 2002 Dec 15;110(12):1849–57. Available from: [<DOI>](#).
24. Zaidi M, Inzerillo AM, Troen B, Moonga BS, Abe E, Burckhardt P. Molecular and Clinical Pharmacology of Calcitonin. In: *Principles of Bone Biology* [Internet]. Elsevier; 2002 [cited 2023 Nov 7]. p. 1423–40. Available from: [<DOI>](#).
25. Nielsen PE, Egholm M, Berg RH, Buchardt O. Sequence-Selective Recognition of DNA by Strand Displacement with a Thymine-Substituted Polyamide. *Science*. 1991 Dec 6;254(5037):1497–500. Available from: [<DOI>](#).
26. Wittung P, Nielsen PE, Buchardt O, Egholm M, Nordén B. DNA-like double helix formed by peptide nucleic acid. *Nature*. 1994 Apr;368(6471):561–3. Available from: [<DOI>](#).
27. Jensen KK, Ørum H, Nielsen PE, Nordén B. Kinetics for Hybridization of Peptide Nucleic Acids (PNA) with DNA and RNA Studied with the BIAcore Technique. *Biochemistry*. 1997 Apr 1;36(16):5072–7. Available from: [<DOI>](#).
28. Egholm M, Buchardt O, Christensen L, Behrens C, Freier SM, Driver DA, et al. PNA hybridizes to complementary oligonucleotides obeying the Watson–Crick hydrogen-bonding rules. *Nature*. 1993 Oct;365(6446):566–8. Available from: [<DOI>](#).
29. Christensen L, Fitzpatrick R, Gildea B, Petersen KH, Hansen HF, Koch T, et al. Solid-Phase synthesis of peptide nucleic acids. *Journal of Peptide Science*. 1995 May;1(3):175–83. Available from: [<DOI>](#).
30. Dueholm KL, Egholm M, Behrens C, Christensen L, Hansen HF, Vulpius T, et al. Synthesis of peptide nucleic acid monomers containing the four natural nucleobases: thymine, cytosine, adenine, and guanine and their oligomerization. *The Journal of Organic Chemistry*. 1994;59(19):5767–73. Available from: [<DOI>](#).
31. Thomson SA, Josey JA, Cadilla R, Gaul MD, Fred Hassman C, Luzzio MJ, et al. Fmoc mediated synthesis of Peptide Nucleic Acids. *Tetrahedron*. 1995 May;51(22):6179–94. Available from: [<DOI>](#).
32. N. Ganesh K, E. Nielsen P. Peptide Nucleic Acids: Analogs and Derivatives. *Current Organic Chemistry*. 2000 Sep 1;4(9):931–43. Available from: [<DOI>](#).
33. Eldrup AB, Dahl O, Nielsen PE. A Novel Peptide Nucleic Acid Monomer for Recognition of Thymine in Triple-Helix Structures. *J Am Chem Soc*. 1997 Nov 1;119(45):11116–7. Available from: [<DOI>](#).
34. Ljungström T, Knudsen H, Nielsen PE. Cellular Uptake of Adamantyl Conjugated Peptide Nucleic Acids. *Bioconjugate Chem*. 1999 Nov 1;10(6):965–72. Available from: [<DOI>](#).
35. Cutrona G, Carpaneto EM, Ulivi M, Roncella S, Landt O, Ferrarini M, et al. Effects in live cells of a c-myc anti-gene PNA linked to a nuclear localization signal. *Nat Biotechnol*. 2000 Mar;18(3):300–3. Available from: [<DOI>](#).
36. Mologni L. Additive antisense effects of different PNAs on the in vitro translation of the PML/RARalpha gene. *Nucleic Acids Research*. 1998 Apr 15;26(8):1934–8. Available from: [<DOI>](#).
37. Mayhood T, Kaushik N, Pandey PK, Kashanchi F, Deng L, Pandey VN. Inhibition of Tat-Mediated Transactivation of HIV-1 LTR Transcription by Polyamide Nucleic Acid Targeted to TAR Hairpin Element. *Biochemistry*. 2000 Sep 1;39(38):11532–9. Available from: [<DOI>](#).
38. Frisch MJ, Trucks GW, Schlegel HB, Scuseria GE, Robb MA, Cheeseman JR, et al. *Gaussian 09, Revision D.01*. Wallingford, CT: Gaussian, Inc.; 2009.
39. Becke A. Density-Functional Thermochemistry. III. The Role of Exact Exchange. *J Chem Phys*. 1993;98:5648–52.
40. Dennington R, Keith TA, Millam JM. *GaussView 5.0*. Wallingford, CT: Gaussian, Inc.; 2009.
41. Gaillard T. Evaluation of AutoDock and AutoDock Vina on the CASF-2013 Benchmark. *J Chem Inf Model*. 2018 Aug 27;58(8):1697–706. Available from: [<DOI>](#).
42. Şenel P, Agar S, İş YS, Altay F, Gölcü A, Yurtsever M. Deciphering the mechanism and binding interactions of Pemtrexed with dsDNA with DNA-targeted chemotherapeutics via spectroscopic, analytical, and simulation studies. *Journal of Pharmaceutical and Biomedical Analysis*. 2022 Feb;209:114490. Available from: [<DOI>](#).
43. Cheraghi S, Şenel P, Dogan Topal B, Agar S, Majidian M, Yurtsever M, et al. Elucidation of DNA-Eltrombopag Binding: Electrochemical, Spectroscopic and Molecular

Docking Techniques. Biosensors. 2023 Feb 21;13(3):300.
Available from: [<DOI>](#).

44. Desmond D. Shaw Research: New York. NY; 2017.

45. Evans DJ, Holian BL. The Nose-Hoover thermostat. The Journal of Chemical Physics. 1985 Oct 15;83(8):4069-74. Available from: [<DOI>](#).

46. Martyna GJ, Tobias DJ, Klein ML. Constant pressure molecular dynamics algorithms. The Journal of Chemical Physics. 1994 Sep 1;101(5):4177-89. Available from: [<DOI>](#).

47. Mestre B, Arzumanov A, Singh M, Boulmé F, Litvak S, Gait MJ. Oligonucleotide inhibition of the interaction of HIV-1 Tat protein with the trans-activation responsive region (TAR) of HIV RNA. Biochimica et Biophysica Acta (BBA) - Gene Structure and Expression. 1999 Apr;1445(1):86-98. Available from: [<DOI>](#).

48. Mhashilkar AM, Biswas DK, LaVecchio J, Pardee AB, Marasco WA. Inhibition of human immunodeficiency virus type 1 replication in vitro by a novel combination of anti-Tat single-chain intrabodies and NF-kappa B antagonists. J Virol. 1997 Sep;71(9):6486-94. Available from: [<DOI>](#).

49. Hirschman SZ, Chen CW. Peptide nucleic acids stimulate gamma interferon and inhibit the replication of the human immunodeficiency virus. J Investig Med. 1996 Aug;44(6):347-51. Available from: [<URL>](#).

50. Alparslan AL, Yildiz Türkyilmaz G, Kozaci LD, Karasulu E. Thermoreversible Gel Formulation for the Intranasal Delivery of Salmon Calcitonin and Comparison Studies of In Vivo Bioavailability. tjps. 2023 Jun 1;20(3):127-40. Available from: [<DOI>](#).

51. Şenel P, Agar S, Sayin VO, Altay F, Yurtsever M, Gölcü A. Elucidation of binding interactions and mechanism of Fludarabine with dsDNA via multispectroscopic and molecular docking studies. Journal of Pharmaceutical and Biomedical Analysis. 2020 Feb;179:112994. Available from: [<DOI>](#).



Degradation of Tolonium Chloride Dye by Phosphate Ion in Aqueous Acidic Solution: Kinetic Approach

Patricia Ese Umoru^{1*} , Mohammad Lawal¹, Oluwayemisi Abiodun Babatunde¹, Yusuf Sahabi² 

¹Faculty of Science Nigerian Defence Academy, Department of Chemistry, Kaduna, +234 Nigeria.

²Faculty of Science Usman Danfodio University, Department of Chemistry, Sokoto, +234 Nigeria.

Abstract: The degradation of tolonium chloride (TC^+) dye by phosphate ion (PO_4^{3-}) in an aqueous acidic solution was studied using spectrophotometric analysis at 301 K, $I = 1.0$ M, $[TC^+] = 1.5 \times 10^{-5}$ M, $[H^+] = 1.0 \times 10^{-3}$ M, and λ_{max} 600 nm. To determine the potency and rate of the reactant species, an aqueous acidic medium was employed. The reaction's direction and tendency were predicted using a thermodynamic analysis at an interval of 5.0 K and a temperature range of 301-321 K. Without the presence of intermediate complex/free atoms formation, a reaction that produced phenyl sulphoxide, phenylamine, and HPO_3^{2-} as products of the reaction was obtained with a molar ratio of 1:1 for both reactants. First-order tolonium chloride reactivity was found in the reaction and first-order for the phosphate ion, resulting in a second-order reaction overall. The reaction process accelerated as the concentration of hydrochloric acid rose. The response time decreased with an increase in ionic strength concentration and added Ca^{2+} and Cl^- did catalyze the reaction positively. A straight line that went through the origin was produced by plotting $1/k_o$ vs PO_4^{3-} concentration. The spectroscopic analysis showed no discernible shift from λ_{max} of 600 nm. Additionally, an increase in temperature accelerated the reaction process. The reaction has a negative free energy change, G (-3.13–1.12 KJ/mol) which indicates that it is spontaneous and that the reactants have more free energy than that of the products. While the enthalpy of activation, H is positive and indicates that the reaction was endothermic and followed an associative path, the entropy of activation, S , is also negative (-7.45–1.10 KJ/mol), indicating that the reaction is less disordered. Due to the added ions catalysis and absence of free atoms during the course of the reaction, an outer-sphere mechanism was suggested for the reaction.

Keywords: Degradation, Tolonium chloride, Phosphate ion, Acidic Medium.

Submitted: September 19, 2023. **Accepted:** February 14, 2024.

Cite this: Umoru PE, Lawal M, Babatunde OA, Sahabi Y. Degradation of Tolonium Chloride Dye by Phosphate Ion in Aqueous Acidic Solution: Kinetic Approach. JOTCSA. 2024;11(2):633-42.

DOI: <https://doi.org/10.18596/jotcsa.1362644>

***Corresponding author's E-mail:** peumoru@nda.edu.ng

1. INTRODUCTION

An acidophilic metachromatic dye called tolonium chloride, hereafter referred to as TC^+ only stains acidic tissues (1). Since TC^+ has a strong affinity for nucleic acids, it can bind to tissues rich in DNA and RNA as well as nuclear material (2,3). Water and alcohol only partially dissolve TC^+ (2-4), which exists as the 3 isoforms ortho-, para-, and meta-toluidine (3). To do a quick microscopic inspection of a specimen, frozen sections are routinely stained with it. With TC^+ , frozen sections can be quickly dyed and examined (3) as well the identification of mast cells (5). It is utilized in forensic examination (6) and renal pathology (7). In premalignant lesions, the surgeons

utilize the dye to help highlight areas of mucosal dysplasia (8).

Tolonium chloride is used to stain cellular nuclei, making it beneficial for detecting cancerous tissue that has a greater nuclear-to-cytoplasmic ratio and increased DNA concentration (9). It can be an aid in the routine screening of people at risk and is useful in the assessment and representation of subtle oral mucosal changes. It is possible to utilize it to guide a brush biopsy without interfering with the computer-assisted cytological analysis of these tissues (10). It was reported that for many years, tolonium chloride has been successfully used as a key stain and a tool in the early diagnosis of oral cancer, cancer of the oral mucosa, and cancer of the upper aerodigestive tract (11). It is advised to use TC^+ in addition to

chemiluminescence or other methods as a diagnostic tool (12). The ability to detect early oral squamous cell carcinoma (SCC) and high-grade dysplasias using TC⁺ is also well documented (13–16).

The naturally occurring form of the element phosphorus, known as phosphates (PO₄³⁻), is present in numerous phosphate minerals. A rock or mineral that contains phosphate ions is referred to as phosphate. Phosphorus is extracted from inorganic phosphates for use in industrial and agricultural purposes (17). They are phosphorus medicinal salts, and the hygroscopic anhydrous form of phosphate is easily soluble in water but insoluble in alcohol (18). Phosphate makes up the majority of the phosphorus in living things (19). Phosphates are often made by neutralizing phosphoric acid, either completely or partially, with sodium carbonate or sodium hydroxide (20). The resulting solution within the container can then be evaporated to produce crystals of the particular hydrate. The hydrate is stable over a wide temperature range (21). Usually, inorganic phosphate is produced during the synthesis of a substance like sucrose (22). PO₄³⁻ plays fundamental functions in biochemistry, biogeochemistry, and ecology, making them very useful (17). Some phosphates are effective in treating urinary tract infections and preventing the formation of calcium stones in the urinary system. For patients who cannot acquire enough phosphorus in their diet daily, they utilize phosphates as dietary supplements (23). PO₄³⁻ is used in a wide variety of food and water treatment processes (24). For instance, sodium phosphates are frequently employed as leavening agents, thickeners, and emulsifiers in baked goods. They are additionally utilized to regulate the pH of processed foods (25). It is known that phosphate can help with constipation and can get the bowels ready for surgery (25). They are effective anti-rust agents and are used in detergents to soften water (25). They serve a variety of purposes, including those related to antimicrobials (26), pH control agents (buffers), boiling water additions, cleansers, coagulants, leaving agents, stabilizers, emulsifiers, texturizers, minerals, and dietary supplements. In meals, mono- and tri-sodium phosphate is employed as a buffering salt. The main application is to maintain the pH of food systems for fruit and vegetable products (27). They are employed as an acidulent (18), as an excipient in pharmaceuticals, and saline solutions (18). The shelf life of soy products is said to be extended by the addition of phosphates (28). Despite not affecting gram-negative bacteria like *Salmonella typhimurium*, phosphorus is bacteriostatic in that it suppresses the growth of some gram-positive bacteria (29–31). To increase the stability, water holding capacity, and sausage emulsion of emulsified sausages, phosphate mixtures are used (31,32). When used in compliance with GMP, the U.S. Food and Drug Administration has designated food phosphates as generally safe (33). Phosphates may be included in meat products, minced meat, and meat preparations (34). Phosphorus peroxide (P₂O₅), alone or in combination, is allowed in final products at a rate of 5 g/kg according to European law (35). Phosphates are frequently utilized in the meat processing industry according to (36). Utilizing the

right quantity and combination of phosphates can increase the finished products' ability to hold moisture, hold water, protect color, delay oxidation, extend shelf life, stabilize and improve structure, and more. Phosphates aid in the restoration of periodontal deficiencies, enhancement of alveolar bone, sinus lifts, tooth substitutes, and restoration of significant bone defects brought on by cancers (37–43). In tissue engineering, they are also utilized as scaffolds for the regeneration of bone or dentin (43–47). To reduce the bioactivity of the phosphates and the metal's strength, calcium phosphates in particular are utilized as injectable cements (48,49) and as coatings on titanium and titanium alloy implants (50,51).

Due to its uses in inorganic chemistry and living beings, phosphate reaction is one of the most cutting-edge fields of study. It is advantageous for plant development and has various potential uses in outstanding chemical processes in the pharmaceutical, food, and detergent sectors. In addition, the potential applications of tolonium chloride as a basic stain in the early detection of oral cancer (9) and the widespread use of phosphate in manufacturing and agriculture sparked our interest in the study of the degradation of tolonium chloride with phosphate ion. Literature has reported works done on TC⁺ but little is known about its degradation by phosphate ion which prompted this research. The purpose therefore of this research is to see how phosphate ions can degrade tolonium chloride in an acidic medium. It is expected that TC⁺ will be degraded to other forms to prevent pollution of water bodies by TC⁺ when used as a dye in textile industries. We are confident that the information gleaned from this reaction will contribute to a better understanding of the bioactivities of the phosphate ion and the redox behavior of tolonium chloride.

2. EXPERIMENTAL SECTION

2.1. Materials/Chemicals

Chemicals from A.J. Chemical Company Kaduna were used throughout. All chemicals are of analytical grade and were used throughout the research without further purification. Distilled water was used to prepare all solutions. The chemicals used are: Tolonium chloride (CAS Number= 92-31-9), potassium phosphate (CAS Number= 7778-77-0), calcium nitrate (CAS Number= 10124-37-5), sodium chloride (CAS Number= 7647-15-5), hydrochloric acid (CAS Number= 7647-01-0) and barium chloride (CAS Number= 10361-37-2).

2.2. Methods

2.2.1. Stoichiometric and product scrutiny

Molar ratio calculations were used to determine the reaction's stoichiometry. The concentration of the TC⁺ was at 1.0×10⁻⁶ M, the concentration of the hydrogen ion was at 1.0×10⁻³ M, the ionic strength was at 1.0 M, and the concentration of PO₄³⁻ was changed between (1.0-7.5)×10⁻⁶ M within an interval of 0.5×10⁻⁶ M. After 24 hours, when the reaction mixture had become colorless (52), the ultimate absorbance of each reacting mixture was measured,

and an absorbance versus concentration plot was made. Two drops of dilute lead acetate solution and two drops of acetic acid were added to the 2 mL of resultant colorless mixture to examine the presence of HPO_3^{2-} (53). Bromine water was further added to another 2 mL of the reaction solution to determine the presence of phenylamine as another reaction product.

2.2.2. Kinetic inquiry

The concentration of PO_4^{3-} was produced to surpass that of $[\text{TC}^+]$ by at least 15.33 times at $[\text{TC}^+] = 1.5 \times 10^{-5} \text{ M}$, $[\text{PO}_4^{3-}] = (2.3-3.6) \times 10^{-4} \text{ M}$ in an interval of $0.3 \times 10^{-4} \text{ M}$, $[\text{H}^+] = 1.0 \times 10^{-3} \text{ M}$, $I = 1.0 \text{ M}$, $T = 301 \text{ K}$, and $\lambda_{\text{max}} = 600 \text{ nm}$. Using a UV/visible spectrophotometer spectrum lab 725s, the reduction in the absorbance of the reaction with time was detected due to the alteration in the concentration of the reacting species. It was possible to get kinetic plots of $\log (A_t - A_\infty)$ where A_t is Absorbance at the time "t" and A_∞ , Absorbance at infinity vs time (s) and $\log k_o$ (observed rate constant) versus $\log [\text{PO}_4^{3-}]$ which was used to evaluate the order of the reaction (54,55).

2.2.3. Change in the concentration of hydrochloric acid

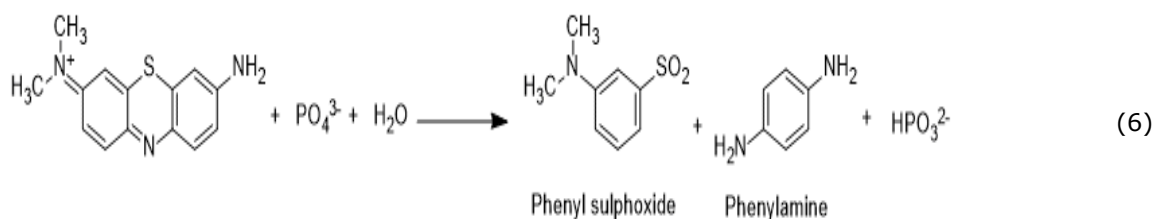
Change in the concentration of hydrochloric acid was investigated between $(0.4-1.0) \times 10^{-3} \text{ M}$ within a range of $0.2 \times 10^{-3} \text{ M}$ intervals with $\text{TC}^+ = 1.5 \times 10^{-5} \text{ M}$, $[\text{PO}_4^{3-}] = 2.9 \times 10^{-4} \text{ M}$, $I = 1.0 \text{ M}$, $T = 301 \text{ K}$, and $\lambda_{\text{max}} = 600 \text{ nm}$. A \log of k_2 vs $[\text{H}^+]$ plot was produced (56).

2.2.4. Study of ionic strength

The study of ionic strength for the reaction was observed by making the concentration of $\text{TC}^+ = 1.5 \times 10^{-5} \text{ M}$, $[\text{PO}_4^{3-}] = 2.9 \times 10^{-4} \text{ M}$, $[\text{H}^+] = 1.0 \times 10^{-3} \text{ M}$, $I = 1.0 \text{ M}$, $T = 301 \text{ K}$ and $\lambda_{\text{max}} = 600 \text{ nm}$ while that of ionic strength was varied between $(0.4-2.0) \text{ M}$ (56,57) within an interval of 0.2 M after which plot of \log of k_2 versus \sqrt{I} was attained.

2.2.5. Effect of added Ca^{2+} and Cl^- on the reaction rate

The effect of added Ca^{2+} and Cl^- on the reaction rate was investigated by adding $(2.0-3.5) \times 10^{-2} \text{ M}$ of Ca^{2+} and Cl^- respectively. The concentration of toluim chloride, hydrogen ion, ionic strength, and PO_4^{3-} were kept constant (57).



This result is not in agreement with the reports of (59-61) for the autocatalyzed reaction between phenyl hydrazine and toluidine blue in aqueous solution. Redox reaction of bis-(2-pyridinealdoximato)dioxomolybdate(IV) complex with thiosulphate ion in aqueous acidic and surfactant media, the study of Piszkiwicz's and Berezin's models on the redox reaction of

2.2.6. Consequence of temperature variation on reaction speed

At intervals of 5.0 K, the effect of temperature fluctuation on reaction speed was examined between 301 and 321 K. Other parameters such as $[\text{TC}^+] = 1.5 \times 10^{-5} \text{ M}$, $[\text{PO}_4^{3-}] = 2.9 \times 10^{-4} \text{ M}$, $[\text{H}^+] = 1.0 \times 10^{-3} \text{ M}$, $I = 1.0 \text{ M}$, and $\lambda_{\text{max}} = 600 \text{ nm}$ had constant concentrations. It was possible to plot the reciprocal of temperature ($1/T \text{ K}^{-1}$) against the \log computed speed constant ($\log k_{\text{cal}}$). Equation 1 was used to compute the speed constant from the measured speed constant k_o , and Equation 2 was used to determine the activation energy (58):

$$k_{\text{cal}} = \frac{k_o}{[\text{PO}_4^{3-}][\text{H}^+][I]} \quad (1)$$

$$E_a; \text{ Slope} = \frac{-E_a}{2.303 \times R} \quad (2)$$

Where $R =$ gas constant

2.2.7. Thermodynamic exploration

The equations employed for the investigation of the common changes in free energy (G), enthalpy (H), and entropy (S) are given in (Equations 3, 4, and 5) respectively (58).

$$\Delta G; = -2.303 \times R \times T \times \log k_{\text{cal}} \quad (3)$$

$$\Delta H; \text{ Slope} = \frac{-\Delta H}{R \times T} \quad (4)$$

$$\Delta S; \Delta G - \Delta H \quad (5)$$

2.2.8. Intermediate complex investigation and data analysis

The intermediate complex was examined using the formula; $1/k_o$ versus $1/[\text{PO}_4^{3-}]$ plot. The data collected underwent statistical analysis to determine their mean and standard deviation.

3. RESULTS AND DISCUSSION

3.1. Stoichiometry and Product Scrutiny

As demonstrated in (Equation 6), one mole of PO_4^{3-} was consumed by one mole of TC^+ Equation 6 is a representation of the degradation of TC^+ to phenyl sulphoxide and phenylamine.

allylthiourea and bis-(2-pyridinealdoximato)dioxomolybdate(IV) complex in an aqueous acidic medium respectively. When lead acetate solution was added to the colorless reaction mixture, a white precipitate resulted, which became soluble in two drops of acetic acid to reveal HPO_3^{2-} as one of the reaction's end products (53). In addition to two drops of bromine

water to the reaction mixture, the bromine water was decolorized and a white precipitate was formed confirming the presence of phenylamine as another product of the reaction.

3.2. Kinetic Inquiry

The graph of $\log (A_t - A_\infty)$ versus time (s) has an R^2 of 0.995 Figure 1, indicating that it is linear and is first-order about $[TC^+]$. The kinetic plot of $\log k_o$ vs $\log [PO_4^{3-}]$ in Figure 2 was also linear with a slope of

0.9972 which is almost unity, indicating also a first-order reaction concerning $[PO_4^{3-}]$. The second-order speed constants k_2 were computed by dividing the values of k_o with the concentration of PO_4^{3-} , and the values were discovered to be fairly constant (Table 1). The rate law for the reaction is displayed In (Equation 7).

$$\frac{-d[TC^+]}{dt} = k_2[TC^+][PO_4^{3-}] \quad (7)$$

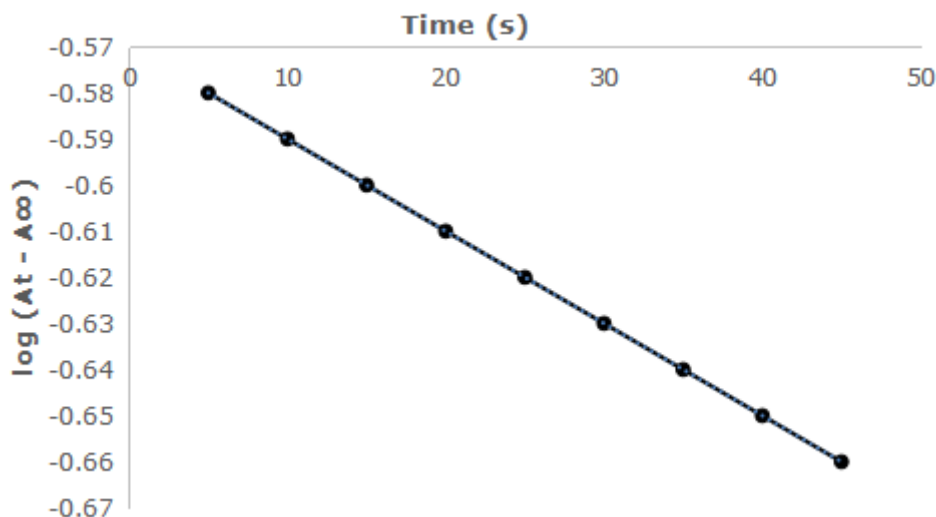


Figure 1: Graph for the Redox Reaction of TC^+ and PO_4^{3-} at $[TC^+] = 1.5 \times 10^{-5} M$, $[H^+] = 1 \times 10^{-3} M$, $I = 1.0 M$, $\lambda_{max} = 600 \text{ nm}$ and $T = 301 K$.

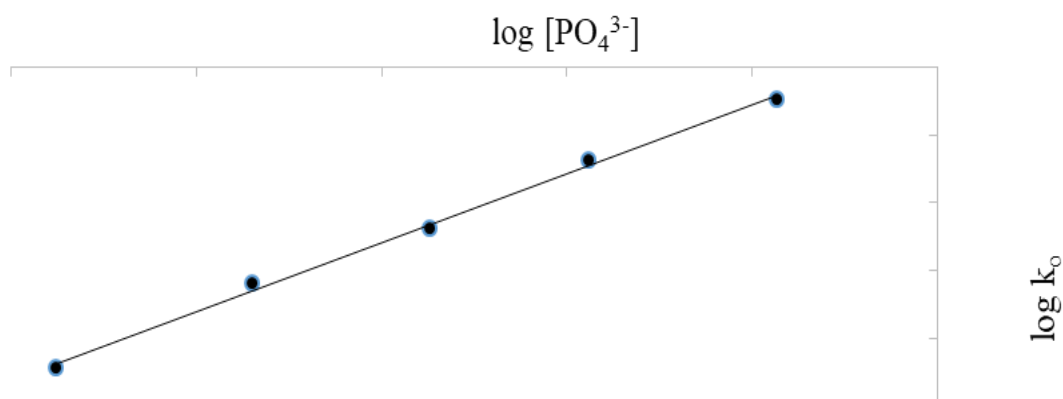


Figure 2: Plot of $\log k_o$ versus $\log [PO_4^{3-}]$, $[TC^+] = 1.5 \times 10^{-5} M$, $[H^+] = 1 \times 10^{-3} M$, $I = 1.0 M$, $\lambda_{max} = 600 \text{ nm}$ and $T = 301 K$

Table 1: Speed constant for the reduction of TC^+ by PO_4^{3-} at 301 k, $I = 1.0 M$, $[TC^+] = 1.5 \times 10^{-5}$, $[H^+] = 1.0 \times 10^{-3} M$, $[PO_4^{3-}] = (2.3-3.6) \times 10^{-4}$ and $\lambda_{max} = 600 \text{ nm}$.

$10^4 [PO_4^{3-}] M$	$I = 1.0 M$	$[H^+] = 1.0 \times 10^{-3} M$	$10^3 k_o/s$	$k_2 \text{ dm}^3/\text{mol.s}$
2.30	1.00	1.00	5.99	26.04
2.60	1.00	1.00	6.80	26.15
2.90	1.00	1.00	7.59	26.17
3.20	1.00	1.00	8.40	26.25
3.60	1.00	1.00	9.44	26.22
2.90	0.40	1.00	7.60	26.21
2.90	0.60	1.00	5.99	20.66
2.90	0.80	1.00	4.84	16.69
2.90	1.00	1.00	3.76	12.97
2.90	1.00	0.40	4.14	14.28
2.90	1.00	0.60	5.07	17.48
2.90	1.00	0.80	6.22	21.45
2.90	1.00	1.00	7.60	26.21

3.3. Change in The Concentration of Hydrochloric Acid

It was discovered that by increasing the concentration of hydrochloric acid in the reaction, the rate of reaction was observed to increase (Figure. 3). The relationship between k_2 and $[H^+]$ was linear, with a $5.955 \text{ dm}^6/\text{mol}^2.\text{s}$ intercept on the k_2 axis. This suggests that the protonated and non-protonated forms are in a quick state of pre-equilibrium, this also suggests that both forms are reactive (62). This is in contrast with the finding reported by (63), which showed that the kinetics and mechanism of the redox

interaction between toluidine blue and nitrite ions in an aqueous acidic medium did not exhibit any intercept. The rate laws are depicted in Equations 8 and 9:

$$k_2 = (a + b[H^+]) \quad (8)$$

$$\frac{-d[TC^+]}{dt} = (a + b[H^+])[TC^+][PO_4^{3-}] \quad (9)$$

Where 'a' the intercept = $5.955 \text{ dm}^6/\text{mol}^2.\text{s}$ and 'b' the slope = $1.985 \text{ dm}^3/\text{mol}.\text{s}$

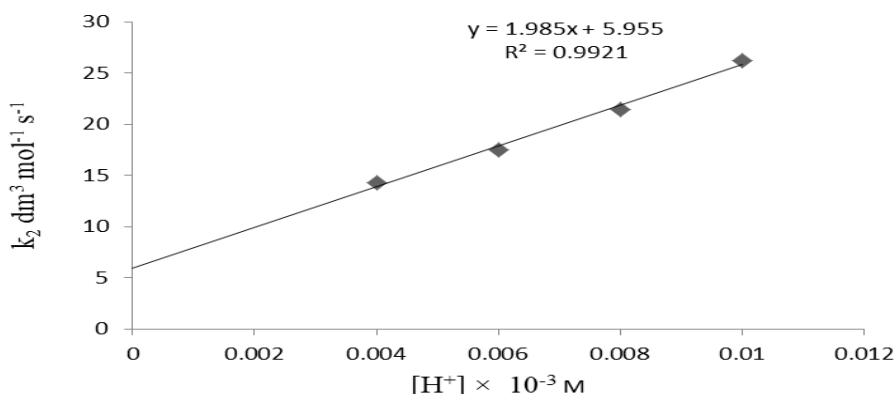


Figure 3: Plot of k_2 versus $[H^+]$ for the reduction of phosphate ion at $[TC^+] = 1.5 \times 10^{-5} \text{ M}$, $[PO_4^{3-}] = 2.9 \times 10^{-4} \text{ M}$, $[H^+] = (0.4 - 1.0 \times 10^{-3} \text{ I} = 1.0 \text{ M}$, $\lambda_{\text{max}} = 600 \text{ nm}$ and $T = 301 \text{ K}$.

3.4. Study of Ionic Strength

As the ionic strength concentration was raised, the rate of reaction between TC^+ and PO_4^{3-} was observed to decrease. According to this, the transfer of electrons takes place when two dissimilar charges are in action. The findings are in contrast to that reported by (64) regarding the kinetics and

mechanism of the oxidation of indigo carmine by permanganate ion in an aqueous acidic medium which showed that the reaction rate was unaffected as the ionic strength concentration was increased. The system plot was linear, as depicted in Figure 4's $\log k_2$ versus \sqrt{I} plot.

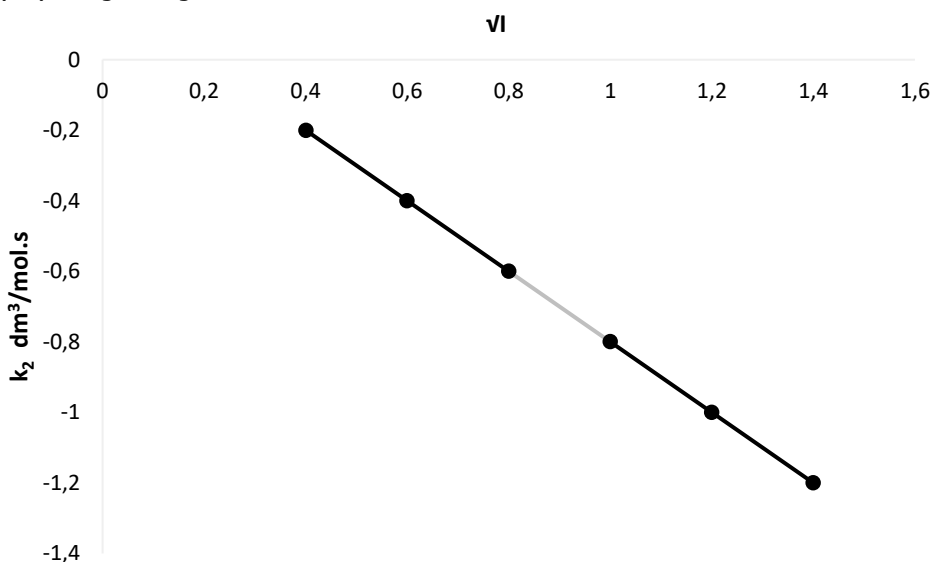


Figure 4: Plot of $\log k_2$ versus \sqrt{I} for the Reduction of TC^+ by PO_4^{3-} , $[PO_4^{3-}] = 2.9 \times 10^{-4} \text{ M}$, $[TC^+] = 1.5 \times 10^{-5} \text{ M}$, $[H^+] = 1 \times 10^{-3} \text{ M}$, $I = 1.0 \text{ M}$, $\lambda_{\text{max}} = 600 \text{ nm}$ and $T = 301 \text{ K}$.

3.5. Effect of Added Ca^{2+} and Cl^-

The addition of Ca^{2+} and Cl^- to the reaction mixture increased the rate of reaction (Table 2). This suggests that the reaction probably follows an outer-sphere mechanism.

3.6. Consequence of Temperature Variation on the Speed of Reaction

The results demonstrated that the speed constant, k_o , increased as the temperature rose (Table 3). It was possible to create a linear graph (Figure 5) with a slope of -1.671 by plotting $\log k_{\text{cal}}$ against the

temperature reciprocal ($1/T \text{ K}^{-1}$). The activation energy (E_a) yielded a value of 31.99 KJ/mol.

3.7. Thermodynamic Exploration

According to Table 4, the reaction's free energy, or G , was negative (-3.13 1.12 KJ/mol), meaning that the reactants had greater free energy than the

products. Additionally, it indicates that the reaction was unplanned (65,66). The entropy of activation, or S , is also negative, showing that the reaction is less disordered, while the enthalpy of activation, or H , is positive (4.32 0.10 KJ/mol), suggesting that the reaction is endothermic and follows an associative path.

Table 2: Pseudo First Order and Second Order Rate Constants for the effect of added Ca^{2+} and Cl^- for TC^+ by PO_4^{3-} at $[\text{TC}^+] = 1.5 \times 10^{-5} \text{ M}$, $[\text{PO}_4^{3-}] = 2.9 \times 10^{-4} \text{ M}$, $[\text{H}^+] = 1.0 \times 10^{-3} \text{ M}$, $I = 1.0 \text{ M}$, $T = 301 \text{ K}$ and $\lambda_{\text{max}} = 600 \text{ nm}$.

Ion	$10^2 [\text{Ion}] \text{ M}$	$10^2 k_0/\text{s}$	$k_2 \text{ dm}^3/\text{mol.s}$
Ca^{2+}	2.0	2.810	1.405
	2.5	3.690	1.476
	3.0	5.200	1.733
	3.5	6.399	1.828
Cl^-	2.0	3.286	1.643
	2.5	4.368	1.747
	3.0	6.388	2.129
	3.5	7.531	2.152

Table 3: Consequence of temperature variation on the speed of reaction.

Temp. K	$10^3 1/T \text{ K}^{-1}$	$10^4 [\text{PO}_4^{3-}] \text{ M}$	$10^3 [\text{H}^+] \text{ M}$	$10^7 k_0$	$k_{\text{cal}} \text{ MS}$	$\log k_{\text{cal}}$
301	3.32	2.9	1.00	5.97	2.06	0.31
306	3.27	2.9	1.00	7.91	2.73	0.44
311	3.22	2.9	1.00	9.59	3.31	0.52
316	3.16	2.9	1.00	10.52	3.63	0.56
321	3.12	2.9	1.00	13.94	4.81	0.68

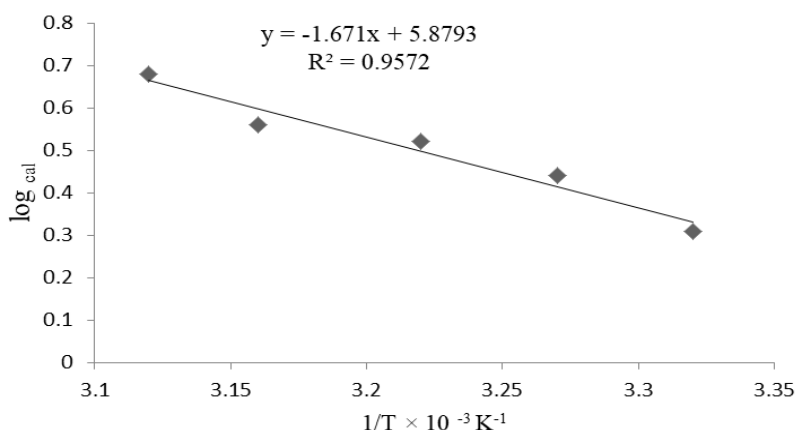


Figure 5: Plot of $\log k_{\text{cal}}$ versus $1/T$ for the reduction of phosphate ion at $[\text{TC}^+] = 1.5 \times 10^{-5} \text{ M}$, $[\text{PO}_4^{3-}] = 2.9 \times 10^{-4} \text{ M}$, $[\text{H}^+] = (0.4-1.0) \times 10^{-3} \text{ M}$, $I = 1.0 \text{ M}$, $\lambda_{\text{max}} = 600 \text{ nm}$ and $T = 301-321 \text{ K}$.

Table 4: Thermodynamic exploration.

Temp. K	$\log k_{\text{cal}}$	$\Delta G \text{ kJ/mol}$	$\Delta H \text{ kJ/mol}$	$\Delta S \text{ kJ/mol}$
301	0.31	-1.79	4.18	-5.97
306	0.44	-2.58	4.25	-6.83
311	0.52	-3.10	4.32	-7.42
316	0.56	-3.39	4.39	-7.78
321	0.68	-4.81	4.46	-9.27

3.8. Intermediate Complex Investigation

The graph of $1/k_0$ versus $1/[\text{PO}_4^{3-}]$, which produced a straight line from the origin (Figure 6), indicates that there were no intermediate complex/free atoms

formed during the course of TC^+ the degradation process. As a result, it supports an outer-sphere mechanism for the reaction by pointing to the lack of intermediate complex formation.

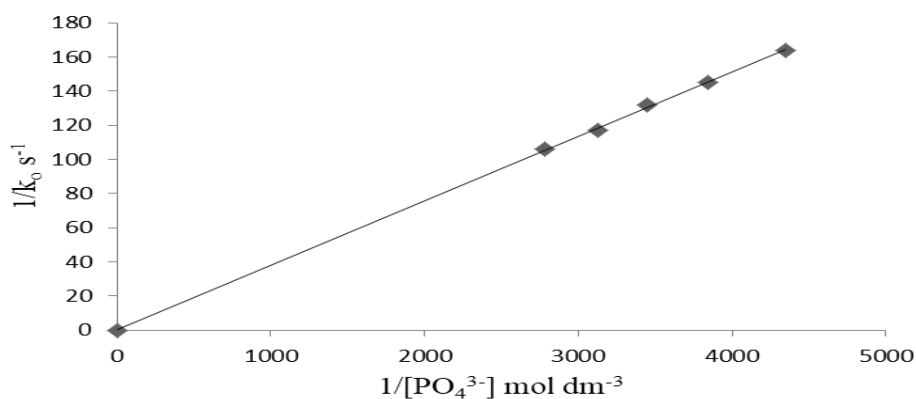
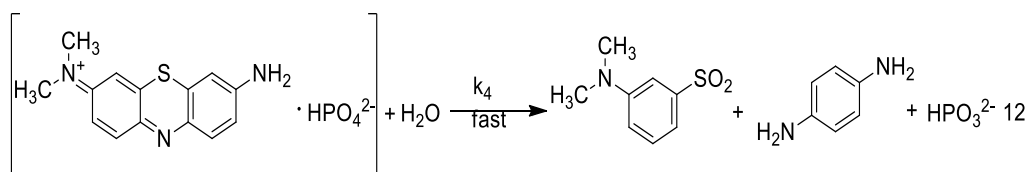
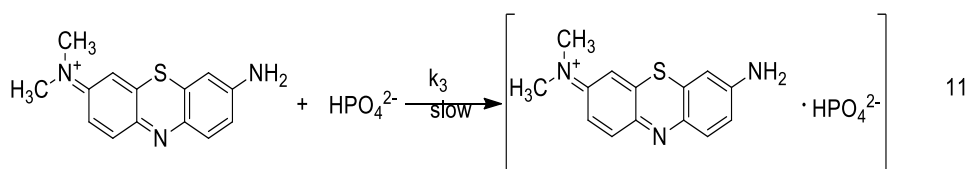
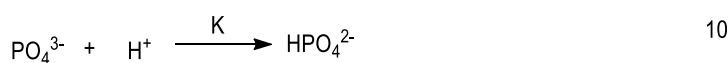


Figure 6: Plot of $1/k_1$ versus $1/[\text{PO}_4^{3-}]$, $[\text{TC}^+] = 1.5 \times 10^{-5} \text{ M}$, $[\text{PO}_4^{3-}] = (2.3\text{--}3.6) \times 10^{-4} \text{ M}$, $[\text{H}^+] = 1 \times 10^{-3} \text{ M}$, $I = 1.0 \text{ M}$, $\lambda_{\text{max}} = 600 \text{ nm}$ and $T = 301 \text{ K}$.

Mechanism of Reaction for Totonium Chloride (TC) and Phosphate ion (PO_4^{3-})



$$\text{Rate} = k_3[\text{TC}^+][\text{HPO}_4^{2-}] \quad 13$$

from equation 10

$$[\text{HPO}_4^{2-}] = K[\text{PO}_4^{3-}][\text{H}^+] \quad 14$$

Substituting equation 14 into 13;

$$\text{Rate} = Kk_3[\text{TC}^+][\text{PO}_4^{3-}][\text{H}^+] \quad 15$$

$$\text{Therefore; Rate} = k[\text{TC}^+][\text{PO}_4^{3-}] \quad 16$$

Equation 16 is similar to equation 9

4. CONCLUSION

The degradation of tolonium chloride by phosphate ion (PO_4^{3-}) in an aqueous acidic solution was studied and the results revealed a molar ratio of 1:1. The reaction exhibited acid and ionic strength dependence which could account for TC's quick detection of and attachment to biological systems. The results of the examination into intermediate complexes showed a straight line from the origin, indicating the lack of any intermediates. Alternatively, it's possible that the intermediate complex was created so quickly during the redox reaction that it was not visible. Thermodynamic analysis showed that a temperature rise sped up the reaction time. Free energy is spontaneous and has a negative sign, indicating that the reactants have more free energy than the products have.

Additionally, the activation entropy is negative, demonstrating that the reaction is less disordered, and the activation enthalpy is positive, demonstrating that the reaction was endothermic and continues via an associative pathway. The movement towards an outer-sphere mechanistic pathway has been influenced by the catalysis of added Ca^{2+} and Cl^- and the absence of an observable intermediate complex formation.

5. CONFLICT OF INTEREST

The authors affirm that they do not have any conflict of interest to disclose that is pertinent to the article's subject matter.

6. ACKNOWLEDGMENTS

We appreciate the Nigerian Defence Academy (NDA) and the entire NDA Chemistry Laboratory personnel for their assistance in making this effort successful.

7. REFERENCES

- Epstein JB, Scully C, Spinelli J. Toluidine blue and Lugol's iodine application in the assessment of oral malignant disease and lesions at risk of malignancy. *J Oral Pathol Med* [Internet]. 1992 Apr 28;21(4):160-3. Available from: [<URL>](#).
- Epstein JB, Oakley C, Millner A, Emerton S, van der Meij E, Le N. The utility of toluidine blue application as a diagnostic aid in patients previously treated for upper oropharyngeal carcinoma. *Oral Surgery, Oral Med Oral Pathol Oral Radiol Endodontology* [Internet]. 1997 May 1;83(5):537-47. Available from: [<URL>](#).
- Sridharan G, Shankar AA. Toluidine blue: A review of its chemistry and clinical utility. *J Oral Maxillofac Pathol* [Internet]. 2012 May;16(2):251-5. Available from: [<URL>](#).
- Gandolfo S, Pentenero M, Broccoletti R, Pagano M, Carozzo M, Scully C. Toluidine blue uptake in potentially malignant oral lesions in vivo: Clinical and histological assessment. *Oral Oncol* [Internet]. 2006 Jan 1;42(1):88-94. Available from: [<URL>](#).
- Carson, FL, Hladik, C. *Histotechnology: A Self-Instructional Text* (3 ed.). Hong Kong: American Society for Clinical Pathology Press. 2009, 188. ISBN 978-0-89189-581-7.
- Olshaker J, Smock. A. *Forensic Emergency Medicine*. Philadelphia: Lippincott Williams and Williams; 2001. 94-97 p.
- Nicholas SB, Basgen JM, Sinha S. Using Stereologic Techniques for Podocyte Counting in the Mouse: Shifting the Paradigm. *Am J Nephrol* [Internet]. 2011 Jun 1;33(Suppl. 1):1-7. Available from: [<URL>](#).
- Scully C. ABC of oral health: Swellings and red, white, and pigmented lesions. *BMJ* [Internet]. 2000 Jul 22;321(7255):225-8. Available from: [<URL>](#).
- Clinical Gastrointestinal Endoscopy* (Second Edition). 2012;385-99.
- Ephros HD. Toluidine blue staining. *J Oral Maxillofac Surg* [Internet]. 2004 Aug 1;62:1. Available from: [<URL>](#).
- Siddiqui IA, Farooq MU, Siddiqui RA, Rafi SMT. Role of Toluidine Blue in Early Detection of Oral Cancer. *Pakistan J Med Sci* [Internet]. 2006;22(2):184-7. Available from: [<URL>](#).
- Mills S. How effective is toluidine blue for screening and diagnosis of oral cancer and premalignant lesions? *Evid Based Dent* [Internet]. 2022 Mar 25;23(1):34-5. Available from: [<URL>](#).
- Mashberg A, Samit A. Early diagnosis of asymptomatic oral and oropharyngeal squamous cancers. *CA Cancer J Clin* [Internet]. 1995 Nov 1;45(6):328-51. Available from: [<URL>](#).
- Onofre MA, Sposto MR, Navarro CM, Paulo S. Reliability of toluidine blue application in the detection of oral epithelial dysplasia and in situ and invasive squamous cell carcinomas. *Oral Surgery, Oral Med Oral Pathol Oral Radiol Endodontology* [Internet]. 2001 May 1;91(5):535-40. Available from: [<URL>](#).
- Epstein JB, Feldman R, Dolor RJ, Porter SR. The utility of toluidine blue rinse in the diagnosis of recurrent or second primary cancers in patients with prior upper aerodigestive tract cancer. *Head Neck* [Internet]. 2003 Nov 23;25(11):911-21. Available from: [<URL>](#).
- Martin I., Kerawala C., Reed M. The application of toluidine blue as a diagnostic adjunct in the detection of epithelial dysplasia. *Oral Surgery, Oral Med Oral Pathol Oral Radiol Endodontology* [Internet]. 1998 Apr 1;85(4):444-6. Available from: [<URL>](#).
- Phosphate Primer". Florida Industrial and Phosphate Research Institute. Florida Polytechnic University. Archived from the original on 29 August 2017. Retrieved 30 March 2018.
- Budavari S. *Merck Index*. White house station, NJ. Merck & Co; 1996.
- Yang Y, Yu H, York D, Elstner M, Cui Q. Description of Phosphate Hydrolysis Reactions with the Self-Consistent-Charge Density-Functional-Tight-Binding (SCC-DFTB) Theory. 1. Parameterization. *J Chem Theory Comput* [Internet]. 2008 Dec 9;4(12):2067-84. Available from: [<URL>](#).
- Ashford RD. *Ashford's Dictionary of Industrial Chemicals*. London: Wavelength Publishers, Ltd.; 1994.
- Gard DR. Phosphoric acids and phosphates in Kroschwitz J. I., (ed) *Kirk-Othmer Encyclopedia of chemical Technology*, (4thed) 1996;18: 669-719. New York: John Wiley & sons.
- Encyclopedia of Biological chemistry*, (Second Edition) (2013).
- Phosphate Supplement (Oral Route, Parenteral Route) (2020). Description and Brand Names - Mayo Clinic "www.mayoclinic.org. Retrieved 2020-11-20.
- Schrödter K, Bettermann G, Staffel T, Wahl F, Klein T, Hofmann T. Phosphoric Acid and Phosphates. In: *Ullmann's Encyclopedia of Industrial Chemistry* [Internet]. Wiley; 2008. Available from: [<URL>](#).
- Lampila LE. Applications and functions of food-grade phosphates. *Ann N Y Acad Sci* [Internet]. 2013 Oct 26;1301(1):37-44. Available from: [<URL>](#).
- Davidson PM. Antimicrobial compounds in FJ, Francis (ed) *Encyclopedia of Food Science and*

Technology. New York: Wiley. 2000;1:63-75.

27. Fennema O. (ed). Principles of Food Chemistry Ed. New York: Dekker, 1985.

28. Amin SR. Petition to the National Organic Standards Board to amend the National List of Allowed Substances to include sodium phosphates for use in food and beverage products formulated with soymilk and dry soymilk similar to or equivalent to dairy products. Farmingdale NY: Carousel Foods of America, 2001.

29. Buňková L, Pleva P, Buňka F, Valášek P, Kráčmar S. Antibacterial effects of commercially available phosphates on selected microorganisms. Acta Univ Agric Silvic Mendel Brun [Internet]. 2008;56:19-24. Available from: [<URL>](#).

30. Dickson JS, Nettles Cutter CG, Siragusa GR. Antimicrobial Effects of Trisodium Phosphate Against Bacteria Attached to Beef Tissue. J Food Prot [Internet]. 1994 Nov 1;57(11):952-5. Available from: [<URL>](#).

31. Feiner G. Meat products handbook Practical science and technology. Cambridge, England: Woodhead Publishing Limited; 2006.

32. Zayas JF. Functionality of Proteins in Food. Berlin, Heidelberg: Springer Berlin Heidelberg; 1997.

33. Code of Federal Regulations Title 21. Food and drugs. Parts 182. Office of the Federal Register, National Archives, and Records Administration, Washington, D.C Codex Stan 2003;3:456-468.

34. Regulation E. C. No 853/2004. Regulation (EC) No 853/2004 of the European Parliament and of the Council of 29 April laying down specific hygiene rules for the hygiene of foodstuffs. 2004;

35. Directive No 95/2/EC - Annex IV. Other permitted additives 2006; European parliament and council directive No 95/2/EC of 20 February 1995 on food additives other than colours and sweeteners, amended by directive 98/72/EC of the European parliament and council of 15 October, 1998.

36. Long NHBS, Gál R, Buňka F. Use of phosphates in meat products. African J Biotechnol [Internet]. 2011 Dec 30;10(86):19874-82. Available from: [<URL>](#).

37. Jarcho M. Calcium Phosphate Ceramics as Hard Tissue Prosthetics. Clin Orthop Relat Res [Internet]. 1981;157:259-78. Available from: [<URL>](#).

38. Metsger DS, Driskell TD, Paulsrud JR. Tricalcium Phosphate Ceramic—A Resorbable Bone Implant: Review and Current Status. J Am Dent Assoc [Internet]. 1982 Dec 1;105(6):1035-8. Available from: [<URL>](#).

39. LeGeros RZ. Properties of osteoconductive biomaterials: calcium phosphates. Clin Orthop Relat Res [Internet]. 2002;395:81-98. Available from: [<URL>](#).

40. Froum SJ, Tarnow DP, Wallace SS, Rohrer MD, Sang-Choon C. Sinus Floor Elevation Using Anorganic Bovine Bone Matrix (OsteoGraf/N) with and Without Autogenous Bone: A Clinical, Histologic, Radiographic, and Histomorphometric Analysis--Part 2 of an Ongoing Prospective Study. Int J Periodontics Restorative Dent. 1998;18(6):528-43. Available from: [<URL>](#).

41. Christian S, Doris M, Alexis S, Georgios L, Else S, Franz K, et al. The fluorohydroxyapatite (FHA) FRIOS® Algipore® is a suitable biomaterial for the reconstruction of severely atrophic human maxillae. Clin Oral Implants Res [Internet]. 2003 Dec 14;14(6):743-9. Available from: [<URL>](#).

42. Uchida A, Araki N, Shinto Y, Yoshikawa H, Kurisaki E, Ono K. The use of calcium hydroxyapatite ceramic in bone tumour surgery. J Bone Joint Surg Br [Internet]. 1990 Mar 1;72-B(2):298-302. Available from: [<URL>](#).

43. Schwarz F, Bieling K, Latz T, Nuesry E, Becker J. Healing of intrabony peri-implantitis defects following application of a nanocrystalline hydroxyapatite (Ostim™) or a bovine-derived xenograft (Bio-Oss™) in combination with a collagen membrane (Bio-Gide™). A case series. J Clin Periodontol [Internet]. 2006 Jul 1;33(7):491-9. Available from: [<URL>](#).

44. Gronthos S, Brahim J, Li W, Fisher LW, Cherman N, Boyde A, et al. Stem Cell Properties of Human Dental Pulp Stem Cells. J Dent Res [Internet]. 2002 Aug 13;81(8):531-5. Available from: [<URL>](#).

45. Hubbell JA. Biomaterials in Tissue Engineering. Nat Biotechnol [Internet]. 1995 Jun 1;13(6):565-76. Available from: [<URL>](#).

46. Arinze TL, Tran T, Mcalary J, Daculsi G. A comparative study of biphasic calcium phosphate ceramics for human mesenchymal stem-cell-induced bone formation. Biomaterials [Internet]. 2005 Jun 1;26(17):3631-8. Available from: [<URL>](#).

47. Livingston TL, Gordon S, Archambault M, Kadiyala S, Mcintosh K, Smith A, et al. Mesenchymal stem cells combined with biphasic calcium phosphate ceramics promote bone regeneration. J Mater Sci Mater Med [Internet]. 2003 Mar 1;14(3):211-8. Available from: [<URL>](#).

48. Brown WE, Chow LC. Combinations of sparingly soluble calcium phosphates in slurries and pastes as mineralizers and cements [Internet]. Google Patents; 1986. Available from: [<URL>](#).

49. Bohner M. Physical and chemical aspects of calcium phosphates used in spinal surgery. Eur Spine J [Internet]. 2001 Oct 1;10:S114-21. Available from: [<URL>](#).

50. Geesink RGT. Osteoconductive Coatings for Total Joint Arthroplasty. Clin Orthop Relat Res. 2002;395:53-65. Available from: [<URL>](#).

51. Barrère F, van der Valk CM, Dalmeijer RAJ, Meijer G, van Blitterswijk CA, de Groot K, et al. Osteogenicity of octacalcium phosphate coatings

- applied on porous metal implants. *J Biomed Mater Res Part A* [Internet]. 2003 Sep 15;66A(4):779–88. Available from: [<URL>](#).
52. Idris SO, Suleman JO, Iyun JF, Osunlaja AA. Reduction of 3, 7-Bis(dimethylamino) Phenazothionium Chloride by Benzenethiol in Aqueous Nitric Acid Medium: A Mechanistic Approach. *Am Chem Sci J* [Internet]. 2015 Jan 10;5(4):313–21. Available from: [<URL>](#).
53. Jeffery G, Bassett J, Mendham J, Denney RC. *Textbook of Quantitative Chemical Analysis*. Longman Scientific & Technical Wiley; 1989. 359 p.
54. Onu AD, Iyun JF, Idris OS. Kinetics and stoichiometry of the reduction of hydrogen peroxide by an aminocarbonylactocobaltate(II) complex in aqueous medium. *J Inorg Chem*. 2015;5(4):75–82. Available from: [<URL>](#).
55. Umoru PE, Effiong UI. Kinetics and Mechanism of the Reduction of Tartrazine by Nitrite Ion in Aqueous Acid Phase. *Acad J Chem* [Internet]. 2022 Mar 22;7(71):10–6. Available from: [<URL>](#).
56. Dennis CR, van Zyl GJ, Fourie E, Basson SS, Swarts JC. A kinetic study of the oxidation of the tetrakisoxalatouranate(IV) ion by the hexacyanoferrate(III) ion in an oxalate buffer medium. *React Kinet Mech Catal* [Internet]. 2021 Apr 14;132(2):599–615. Available from: [<URL>](#).
57. Nkole IU, Idris SO, Onu AD. Redox reactions of tris-(1,10-phenanthroline)iron(III) complex with thiourea and N-methylthiourea in an aqueous acidic medium: Kinetics and mechanism. *Inorg Chem Commun* [Internet]. 2021 Nov 1;133:108930. Available from: [<URL>](#).
58. Nyong BE, Abeng FE, Ushie OA, Bassey BJ, Edim MM. Kinetics Mechanism and Thermodynamic Study of the Oxidation of Iodide Ion by Dichromate Ion in Acidic Medium. *J Appl Sci Environ Manag* [Internet]. 2020 Jun 24;24(5):821–6. Available from: [<URL>](#).
59. Jonnalagadda SB, Nattar K. Kinetics and Mechanism of Autocatalyzed Reaction between Phenyl Hydrazine and Toluidine Blue in Aqueous Solution. *Int J Chem Kinet* [Internet]. 1999;31(2):83–8. Available from: [<URL>](#).
60. Nkole IU, Idris SO, Abdulkadir I, Onu AD. Redox reaction of bis-(2-pyridinealdoximato)dioxomolybdate(IV) complex with thiosulphate ion in aqueous acidic and surfactant media. *Inorg Chem Commun* [Internet]. 2022 Jun 1;140:109468. Available from: [<URL>](#).
61. Nkole IU, Idris SO, Onu AD, Abdulkadir I. The study of Piszkiwicz's and Berezin's models on the redox reaction of allylthiourea and bis-(2-pyridinealdoximato)dioxomolybdate(IV) complex in an aqueous acidic medium. *Beni-Suef Univ J Basic Appl Sci* [Internet]. 2022 Dec 16;11(1):68. Available from: [<URL>](#).
62. Iyun J, Onu A. Kinetics and mechanism for oxidation of rosaniline monochloride by nitrite ion in aqueous media. *Niger J Chem Res* [Internet]. 2006 May 20;3(1):24–7. Available from: [<URL>](#).
63. Hamza SA, Iyun JF, Idris SO. Kinetics and mechanism of the redox reaction of toluidine blue and nitrite ions in aqueous acidic medium. *Arch Appl Sci Res* [Internet]. 2012;4(1):10–8. Available from: [<URL>](#).
64. Falodun SO, Idris SO, Ojo EO, Iyun JF. Kinetics and Mechanism of the Oxidation of Indigo Carmine by Permanganate Ion in Aqueous Acidic Medium. *Int J Chem Biomol Sci* [Internet]. 2015;1(4):255–9. Available from: [<URL>](#).
65. Eddy NO, Ameh PO, Essien NB. Experimental and computational chemistry studies on the inhibition of aluminium and mild steel in 0.1 M HCl by 3-nitrobenzoic acid. *J Taibah Univ Sci* [Internet]. 2018 Sep 3;12(5):545–56. Available from: [<URL>](#).
66. Ikpi ME, Abeng FE, Obono OE. Adsorption and Thermodynamic studies for the corrosion of inhibition of API 5L X-52 Steel in 2 M HCl solution by moxifloxacin. *World News Nat Sci* [Internet]. 2017;9:52–61. Available from: [<URL>](#).



Enhancing Biogas Production with The Addition of Nano-catalysts

Fatih Mehmet Emen^{1*}, Aslıhan Cesur Turgut², Şevkinaz Doğan³

¹Burdur Mehmet Akif Ersoy University, Department of Chemistry, Burdur, 15003, Türkiye.

²Burdur Mehmet Akif Ersoy University, Department of Plant and Animal Production, Burdur Vocational School of Food, Agriculture and Livestock, Burdur, 15030, Türkiye.

³Burdur Mehmet Akif Ersoy University, Department of Fundamentals of Nursing, Faculty of Health Sciences, Burdur, 15030, Türkiye.

Abstract: The province of Burdur is at the forefront of the livestock industry, especially with dairy cattle. It is a necessity for Burdur province to use animal manure, convert it into methane gas, and use it as fuel. In this study, a laboratory-scale biodigester was set up to produce biogas from cattle feces taken from Burdur Mehmet Akif Ersoy University Cattle Farm. γ -Fe₂O₃, meso-Fe₂O₃, and meso-Co₃O₄ nanoparticles (NPs) were synthesized and used as catalysts for biogas production. Structural characterizations of catalysts were carried out via FT-IR and XRD techniques. The TEM was used to investigate particle size distributions and morphology. The average particle sizes of the nanoparticles were determined to be in the range of 20-165 nm. The bio-digester was kept at a constant temperature of 35 °C for 20 days. It has been determined that the obtained biogas has a high methane content of 83–86%. The biogas volume was obtained to be 1.360 L/kg for γ -Fe₂O₃, 1.390 L/kg for meso-Fe₂O₃, and 625-1.250 L/kg for Co₃O₄.

Keywords: Biogas, Cattle Manure, Digester, Methane, hydrothermal method, Fe₂O₃, Co₂O₃.

Submitted: September 28, 2023. **Accepted:** February 18, 2024.

Cite this: Emen FM, Cesur Turgut A, Doğan Ş. Enhancing Biogas Production with The Addition of Nano-catalysts. JOTCSA. 2024;11(2):643-54.

DOI: <https://doi.org/10.18596/jotcsa.1368040>

***Corresponding author's E-mail:** femen@mehmetakif.edu.tr

1. INTRODUCTION

Renewable energy helps solve environmental problems and support sustainable development. Renewable energy sources reduce climate change by emitting little greenhouse gas (1). They boost energy security by diversifying the energy mix and minimizing fossil fuel imports. Renewable energies improve air quality and health (2). They also boost economic growth, investment, and job creation (3). Renewable energy technology advances improves efficiency, and lowers costs, making it more accessible and profitable. Renewable energies are crucial to the climate and ecological goals of the Green Deal, such as the European Green Deal. By 2050, it wants to make Europe the first climate-neutral continent by focusing on renewable energy and energy efficiency. The Green Deal encourages renewable energy use to reduce greenhouse gas emissions and boost economic growth. It supports renewable energy development and implementation through policies, financing, and research. Countries can fight climate change and promote sustainability by supporting the Green Deal (4). Biomass energy is

a term that encompasses bioenergy and biofuels. Bioenergy refers to solid biomass used for domestic uses (heating, cooking) and industrial applications (heat and power). Biofuels mainly refer to liquid biofuels (biodiesel and bioethanol) used in road transportation but also include biogas. Biomass energy is a renewable resource that has the potential to contribute significantly to the world's energy needs. Anaerobic digestion (AD) of agricultural waste, food waste, and sewage sludge produces biogas. Waste management, renewable energy generation, methane emission reduction, and nutrient recycling are its benefits. Methane in biogas is used to generate energy. Electricity, heating, and cooking can be made from biogas. The energy performance of biogas production can be assessed using parasitic energy demand, biogas utilization efficiency, and energy output relative to feedstock solid mass. These indicators reveal biogas plant energy efficiency and performance. Producing biogas from organic waste has many benefits. Organic waste serves as a valuable substrate for anaerobic digestion, a natural process mediated by a diverse array of microorganisms. Anaerobic digestion

converts organic residues into biogas, and volatile fatty acids, which hold potential as clean energy sources. The anaerobic digestion process comprises four interconnected steps wherein microorganisms in each step sequentially convert substrates for utilization by subsequent microbial communities (5-7). It is a complex process in which a diverse consortium of microorganisms uses organic waste as a substrate to initiate an integrated and multifaceted cascade of biochemical reactions in single-stage batch reactors, including hydrolysis, acidogenesis, acetogenesis, and methanogenesis. After this procedure, biogas—an infinite source of renewable energy that can be used for thermal applications—is produced (8). Biogas installations number 132,000 worldwide, excluding 50 million micro-scale digesters (9). Nanoscale particles or structures make up nanocatalysts. These catalysts have unique features and advantages due to their compact size and high surface area-to-volume ratio. In recent years, nanocatalysis has advanced, with many types of nanocatalysts being studied for various uses (10). In a research press mud as a substrate for anaerobic digestion with a CuO/Cu₂O nanocatalyst to improve biogas. The aqueous extract of PM and SCB used as a reducing agent was used to make CuO/Cu₂O nanocatalyst. Using 1.0 % CuO/Cu₂O nanocatalyst in the AD process, a total biogas of 224.7 mL CH₄ /g VS was reported after 42 days (11). In a different study, water is divided electrochemically using a nanocatalyst and an external energy source to produce hydrogen and oxygen. Copper (Cu) based nanostructures have been found to have an impact on the stability, immobilization, and recovery of enzymes among a variety of investigated nanomaterials (12). Furthermore, the inclusion of Cu-based nanomaterials may have improved the CAZymes' (carbohydrate-active enzymes) functional activity, which raises the efficiency of cellulose degradation during the enzymatic hydrolysis reaction (13). Platinum-based nanocatalysts can boost water-splitting efficiency. These nanocatalysts increase electrochemical reaction activity and energy conversion by providing many active sites. Other research examines nanocatalysts in organic processes. Gold nanoparticles have been widely investigated as organic transformation catalysts. Gold nanoparticles promote selective and sustained reactions due to their unique electrical and structural features. Energy applications like fuel cells use nanocatalysts. Platinum-based nanocatalysts are frequently used in fuel cell technologies due to their excellent catalytic activity and stability. These nanocatalysts aid electrochemical reactions that convert chemical energy to electricity. Research has also focused on nanocatalyst synthesis and design. Various approaches have been developed to alter nanocatalyst size, shape, and composition for customized characteristics and better catalytic performance. Support materials like carbon nanotubes or metal oxides can improve nanocatalyst stability and reactivity. Nanocatalysts' small size and high surface area-to-volume ratio allow them to improve catalytic processes. They are promising for water splitting, chemical processes, fuel cells, and more. Nanocatalysis research could improve energy generation, environmental cleanup, and chemical

synthesis (14-18). Nanocatalysts can contribute to the production efficiency of biogas and other biofuels. Nanocatalysts accelerate the degradation of organic waste and the creation of methane, the main component of biogas. They boost catalytic activity, selectivity, and stability. Bharathi et al. (2022) (19) employed iron oxide nanoparticles to boost bacterial growth, minimize retention time, and produce biogas from food waste. Nanocatalysts' high surface area and reactivity help convert organic waste into biogas. They can boost conversion efficiency, product yield, and byproduct reduction. Nanocatalysts can be optimized for specific processes and feedstocks by changing size, content, and structure. However, nanocatalysts for biogas production are still being studied. Further research is needed on catalyst production, loading optimization, and nanocatalyst-microbial community interactions. Nanocatalysts' environmental impact and cost-effectiveness in large-scale biogas generation should also be evaluated (20).

In this study, it was aimed to examine the contribution of magnetic nanoparticles to the production of biogas from cattle manure. Few studies are using mesoporous Fe₂O₃. However, studies on biogas production using mesoporous Co₃O₄ as a catalyst have not been found. For this purpose, γ -Fe₂O₃, meso-Fe₂O₃, and meso-Co₃O₄ NPs were synthesized and characterized. The laboratory-scale biodigester was designed and set up to produce biogas from cattle feces taken from Burdur Mehmet Akif Ersoy University Cattle Farm.

2. EXPERIMENTAL SECTION

2.1. Materials

In the synthesis of metal oxide NPs, iron (III) chloride hexahydrate (FeCl₃.6H₂O, Merck), cobalt (III) chloride hexahydrate (CoCl₃.6H₂O), ethylene glycol (99%, Merck), polyethylene glycol (PEG, 1000, Merck), sodium acetate trihydrate (CH₃COONa. 3H₂O, Sigma Aldrich), and sodium hydroxide (NaOH, Merck) were used.

2.2. Instrumentations

A Bruker AXS-D8 advanced model instrument was used in X-ray powder diffraction (XRD) analyses performed to elucidate the structures of the synthesized metal oxide nanoparticles. X-ray diffraction (XRD) studies were performed using a nickel filter (0.2 mm) and copper tube (Cu-K α) radiation at 40 kV. XRD data were recorded at a scan step of 0.02° and angles of 10° ≤ θ ≤ 90°. FT-IR spectra were recorded in the range of 4000-400 cm⁻¹ using the Shimadzu IRTracer-100 spectrometer. A JEOL-JEM-1400 PLUS model Transmission Electron Microscopy (TEM) system was used for particle size and morphological examinations. 7890A GC 5975C MS gas chromatography system combined with the Agilent 7697A Headspace was used to determine the percentage of methane in the biogas content. The headspace vial which contains activated carbon was used for sampling.

2.3. Method

2.3.1. Preparation of nanoparticles

Generally, in the hydrothermal synthesis method, metal oxide nanoparticles are synthesized in an aqueous solution of metal salts. The resulting oxide is obtained from water as a reservoir. However, in this study, the water source during the reaction is $\text{FeCl}_3 \cdot 6\text{H}_2\text{O}$ and $\text{CoCl}_3 \cdot 6\text{H}_2\text{O}$. Additionally, polyethylene glycol (PEG) added to this reaction is used as an oxidant, surfactant, and anti-aggregation agent. Thus, it prevents particle accumulation and ensures the formation of high surface area Fe_2O_3 and Co_3O_4 .

Synthesis of $\gamma\text{-Fe}_2\text{O}_3$ nanoparticles

The hydrothermal synthesis method was used to synthesize $\gamma\text{-Fe}_2\text{O}_3$ nanoparticles (21). $\text{FeCl}_3 \cdot 6\text{H}_2\text{O}$ (0.99 g) was mixed with ethylene glycol (40 mL) until dissolved. Sodium acetate (CH_3COONa) (3.6 g) and polyethylene glycol (PEG-1000) (1 g) were added and mixed for 45 minutes. The mixture was transferred into a Teflon-lined (50 mL) stainless steel autoclave and heated in an oven at 190°C for 5 hours. The resulting black product was collected by decantation, and the product was washed several times with ethanol. Then it was dried at 70°C for 12 hours.

Synthesis of mesoporous Co_3O_4 nanoparticles

Mesoporous Co_3O_4 was synthesized by modifying the method given in the literature (22). $\text{CoCl}_3 \cdot 6\text{H}_2\text{O}$ (0.99 g) was dissolved in 40 mL of Ethylene glycol. Sodium acetate (CH_3COONa) (3.6 g) and polyethylene glycol (PEG-1000) (1 g) were added to the first solution and mixed for 45 minutes. The mixture was transferred into a Teflon-lined (50 mL) stainless steel autoclave and heated in an oven at 190°C for 5 hours. The resulting black product was collected by decantation, and the product was washed several times with ethanol. Then it was dried at 70°C for 12 hours.

Preparation of mesoporous Fe_2O_3 nanoparticles

Mesoporous Co_3O_4 was synthesized by modifying the method given in the literature (23). 0.5 g of hexadecyltrimethylammonium bromide (CTAB) was solved in 96 mL of deionized water. Then 34 mL of ethanol and 10 mL of NH_3 were added and mixed for

5 minutes. Finally, 2 mL of tetraethylorthosilicate (TEOS) was added and stirred at room temperature for 3 hours. Then, it was heated in a muffle furnace at 550°C for 10 hours. MCM-41 was immersed in the previously prepared 1.0 M of $\text{Fe}(\text{NO}_3)_3$ solution. MCM-41- Fe_2O_3 was heated again at 550°C and then treated with a 10 M NaOH solution to remove SiO_2 . The obtained mesoporous Fe_2O_3 nanoparticles were washed with deionized water and dried.

2.3.2. Experimental design of AD process

Collection of samples

Animal feces with urine were collected from the slurry pit at Burdur Mehmet Akif Ersoy University (MAKU) Cattle Farm and used for the AD process without delay. The pH value was checked before biogas production.

Biogas production in a laboratory-scale biodigester system

A laboratory-scale biodigester (total volume is 5.0 L) with a 1.0 L working volume was used (Figure 1). The outer wall of the biodigester, which was developed for this study, contains a water jacket, and the ambient temperature is kept under control by keeping the water temperature constant with a heater. In light of all these explanations, the working temperature was determined to be 35°C , and the temperature was kept constant during fermentation. 500 g of feces were taken and diluted with water. The final %TS value of the mixture in the bioreactor was set up as 20% for each trial and three replicates were performed. The pH value of the feces used in the study was 7.35, and the temperature value was 16.5°C . Nanocatalysts were added to the bioreactor and mixed at a constant temperature for 20 days. To disrupt microbial cells and increase the biodegradation efficiency of the feces, the aqueous feces were mixed at a speed of 6 rpm per minute with the propeller mixer mounted on the system under mesophilic conditions (35°C) so as not to precipitate. This phase lasted 20 days. The catalyst amounts and waiting times used were taken from the literature, and the study was completed (24). 0.3 g/L catalyst was used in each bioreactor.



Figure 1: Biogas digester system.

A headspace vial which contains activated carbon was used for sampling. In the Headspace system, the gases are released from activated carbon and they were analyzed by Headspace-GC-MS. The amount of methane in the resulting biogas was analyzed using the 7890A GC 5975C MS gas chromatography system combined with the Agilent 7697A Headspace. The analysis method is detailed below (25):

Column temperature program: After waiting at 35°C for 5 minutes, it reaches 150 °C with an increase of 5 °C per minute and is kept at this temperature for 5 minutes. Detector and injector temperatures: 200 °C and 180 °C, Flow Rate: 25 psi (He), Needle:

90 °C, transfer line: 120 °C, Vial oven: 85 °C, Thermostat time: 5 minutes, pressurize time: 0.5 minutes, inject time: 0.08 minutes, Withdraw time: 0.5 minutes.

The amount of methane in the biogas content obtained without catalyst and with catalyst (γ -Fe₂O₃, Meso-Fe₂O₃, and Meso-Co₃O₄) in the biodigester was calculated from the peak area using the gas chromatogram. In addition, the MS detector connected to the system was used to determine which compound the relevant peak belonged to. A representative gas chromatogram is given in Figure 2.

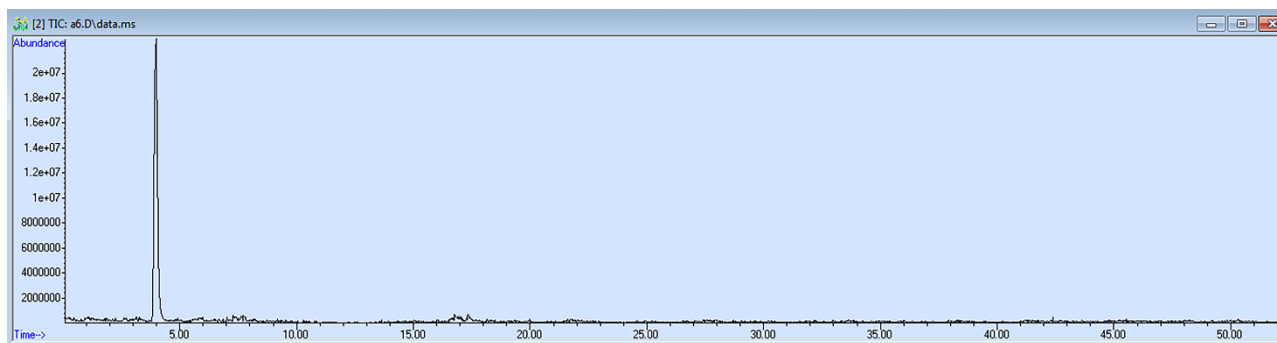


Figure 2: Gas chromatogram showing methane content in biogas.

2.4.3. Chemical characterization

The amount of dry matter, volatile solids, crude protein, and crude oil was determined in the collected biomass samples (26). Feces samples were dried at 105 °C for 24 hours and the amount of dry matter was calculated. After the dry matter was digested at 550 °C for 3 hours, the amount of Volatile solid was determined by taking the difference between the dry matter and ash components. Total Kjeldahl nitrogen (TKN) composition was determined according to the standard method (27), and crude protein nitrogen composition was determined by multiplying the TKN value by 6.25. The crude oil was determined by dissolving the substrates in diethyl ether according to the Soxhlet method (28).

3. RESULTS AND DISCUSSION

3.1. Characterization of Nanoparticles

3.1.1. XRD results of the nanoparticles

XRD powder patterns of the nanoparticles were recorded in the range of 10-90°. The XRD powder pattern of γ -Fe₂O₃ nanoparticles is given in Figure 3. The peaks with (206), (119), (0012), (1115), and (4012) hkl values correspond to γ -Fe₂O₃ nanoparticles which are in the maghemite structure formed (PDF card no: 00-025-1402). These results are compatible with the literature (29). The crystal system of γ -Fe₂O₃ is tetragonal, the space group is P43212(96) and the cell parameters are a=b=8.34

Å, c=25.02 Å, $\alpha=\beta=\gamma=90^\circ$, V=140.28 Å³. The fact that no impurity peaks were found in the powder pattern shows that γ -Fe₂O₃ was synthesized as a single phase.

The XRD powder pattern of mesoporous Fe₂O₃ nanoparticles is given in Figure 4. In the XRD pattern, the peaks obtained with (306), (134), (128), (220), (1010), (300), (214), (018), (116), (024), (113), (110), (104) and (012) hkl values. These results indicate that Fe₂O₃ is formed in the hematite structure (PDF Card no: 00-033-0664) (23). Fe₂O₃ was obtained in a rhombohedral crystal system with an R-3c (167) space group. Cell parameters are a=b= 5.03560 Å, c= 13.74890 Å, $\alpha=\beta=\gamma=90^\circ$, V= 301.93 Å³. There are no impurity peaks were found in the powder pattern showing that mesoporous-Fe₂O₃ was synthesized as a single phase.

The XRD powder pattern of mesoporous Co₃O₄ NPs is given in Figure 5. All peaks in the XRD pattern show that the Co₃O₄ structure (PDF card no: 00-042-1467) is formed in pure form and does not contain any impurity peaks (22). The crystal system of Co₃O₄ is cubic, the space group is Fd-3m (227) and the cell parameters are a=b=c= 8.03730 Å, $\alpha=\beta=\gamma=90.0^\circ$, V=524.24 Å³.

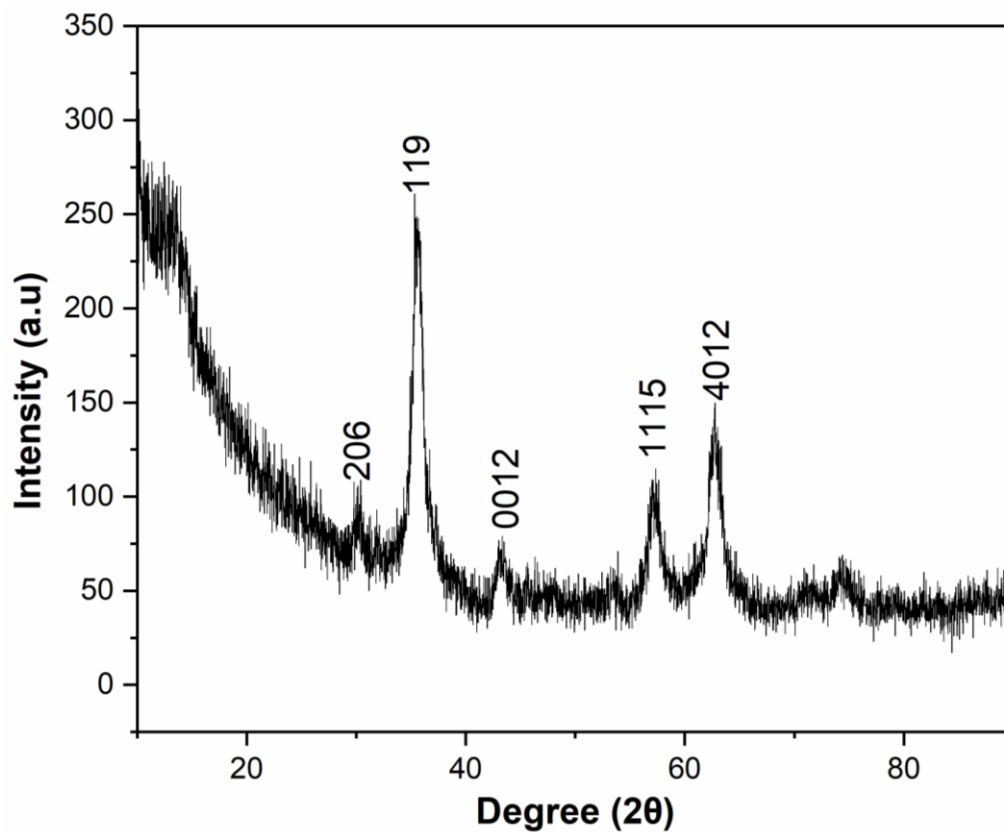


Figure 3: XRD powder pattern of γ -Fe₂O₃ nanoparticles.

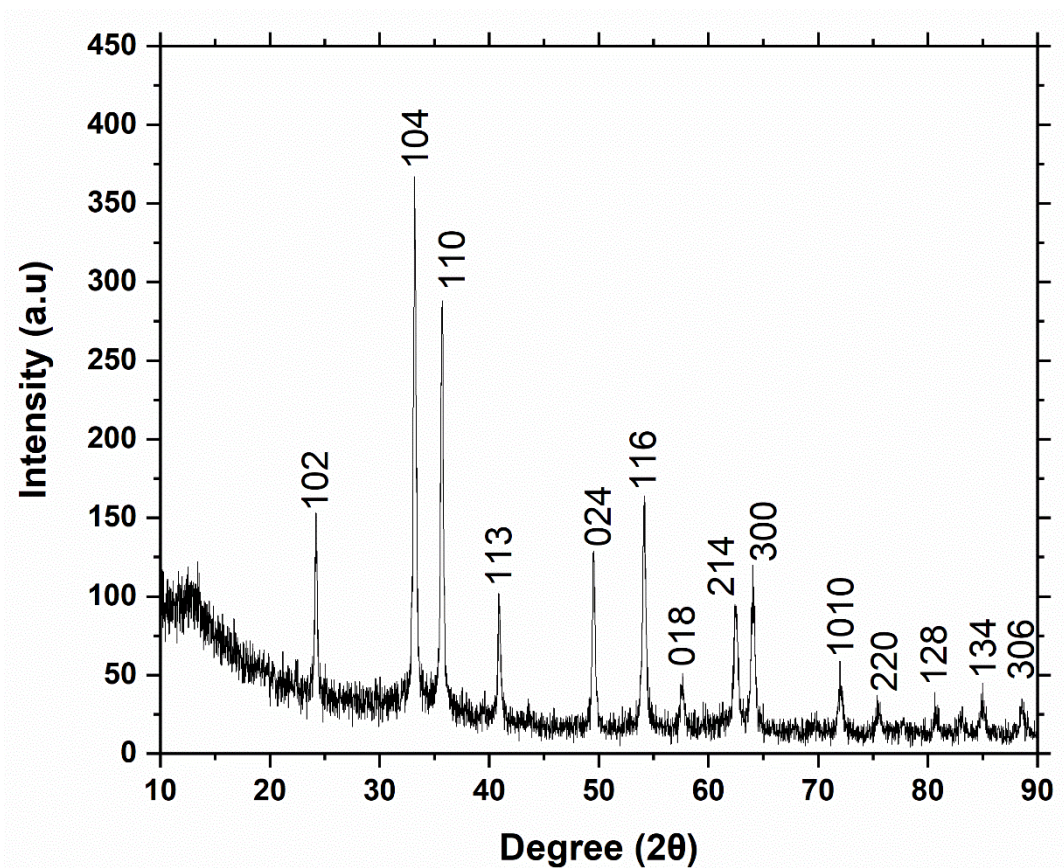


Figure 4: XRD powder pattern of mesoporous Fe₂O₃ nanoparticles.

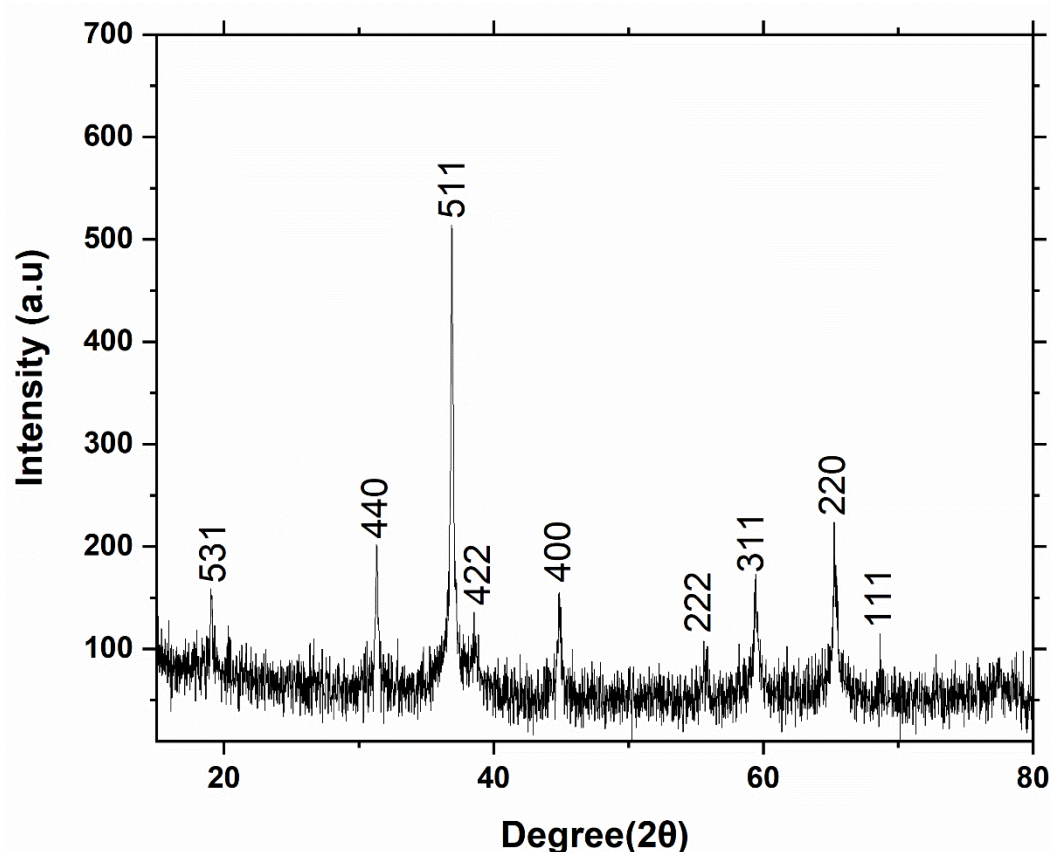


Figure 5: XRD powder pattern of meso- Co_3O_4 NPs.

3.1.2. FT-IR results of the nanoparticles

The FTIR spectra of the synthesized nanoparticles were taken in the range of $4000\text{--}400\text{ cm}^{-1}$ using KBr pellets. The FT-IR spectra of $\gamma\text{-Fe}_2\text{O}_3$ and mesoporous- Fe_2O_3 nanoparticles are given in Figures 6 and 7. FT-IR spectra of $\gamma\text{-Fe}_2\text{O}_3$ and mesoporous- Fe_2O_3 nanoparticles are identical because the vibrations of the same elements are analyzed. Three peaks were observed in the FT-IR spectrum of the

nanoparticles at 543 , 1637 , and 3428 cm^{-1} . The peak observed at 543 cm^{-1} corresponds to the symmetric vibrations of Fe-O bonds. Water molecules are adsorbed on the surfaces of Fe_2O_3 nanoparticles (30). Therefore, the peaks observed at 3428 and 1630 cm^{-1} in the FTIR spectrum belong to the stretching and bending vibrations of water molecules, respectively.

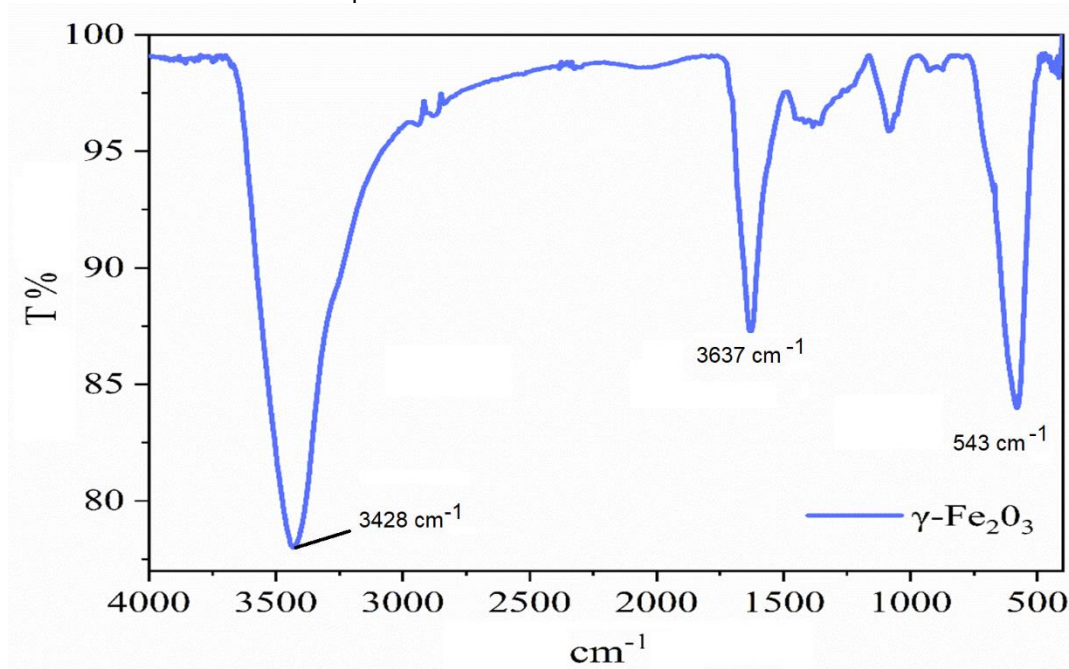


Figure 6: FTIR spectrum of $\gamma\text{-Fe}_2\text{O}_3$ NPs.

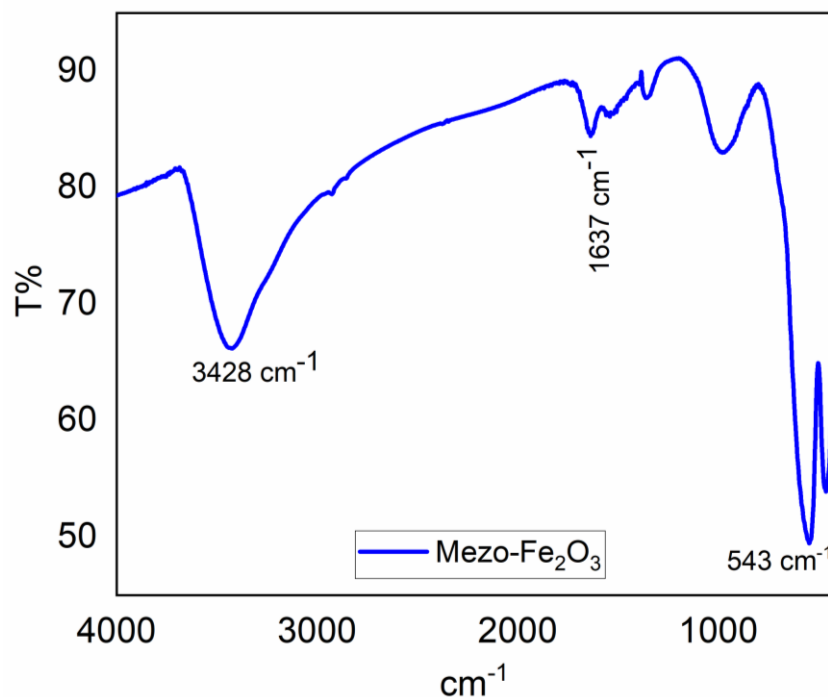


Figure 7: FTIR spectrum of meso-Fe₂O₃ NPs.

FT-IR spectrum of mesoporous Co₃O₄ NPs is given in Figure 8. Water molecules are adsorbed on the surfaces of Co₃O₄ nanoparticles. Therefore, the peaks observed at 3430 and 1635 cm⁻¹ in the FTIR spectrum belong to the stretching and bending vibrations of water molecules, respectively. The

broad peaks in the absorption bands around 673 and 580 cm⁻¹ are due to the stretching vibration of the metal-oxygen bond and the IR absorptions of Co₃O₄. The presence of this band indicates that cobalt is in a hexagonal oxygen octahedral environment and thus Co₃O₄ is formed (31).

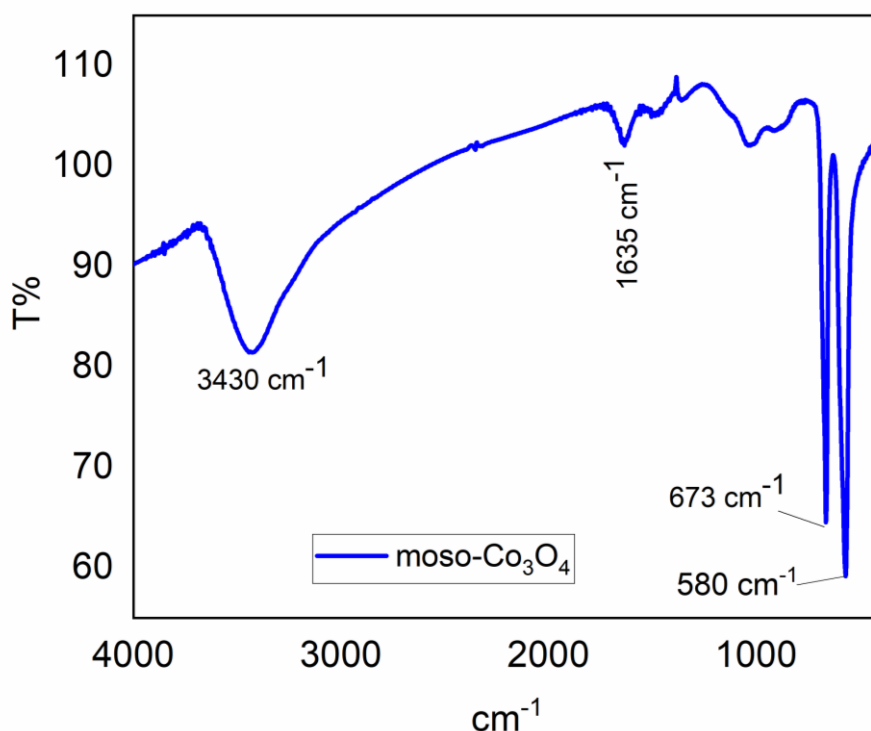


Figure 8: FTIR spectrum of meso-Co₃O₄ NPs.

3.1.3. Transmission Electron Microscope (TEM) Results

TEM micrographs of meso-Fe₂O₃ and meso-Co₃O₄ NPs used in the study are shown in Figures 9 and 10, respectively. In TEM micrographs, it is seen that the nanoparticles have a spherical morphology and spongy structure. This confirms the mesoporous

structure of the particles. The advantage of these structures is that their catalytic efficiency increases due to their large surface area. Particle size analyses show that the average grain sizes of meso-Fe₂O₃ and meso-Co₃O₄ NPs are in the range of 21.37-64.15 nm and 164.65 nm, respectively.

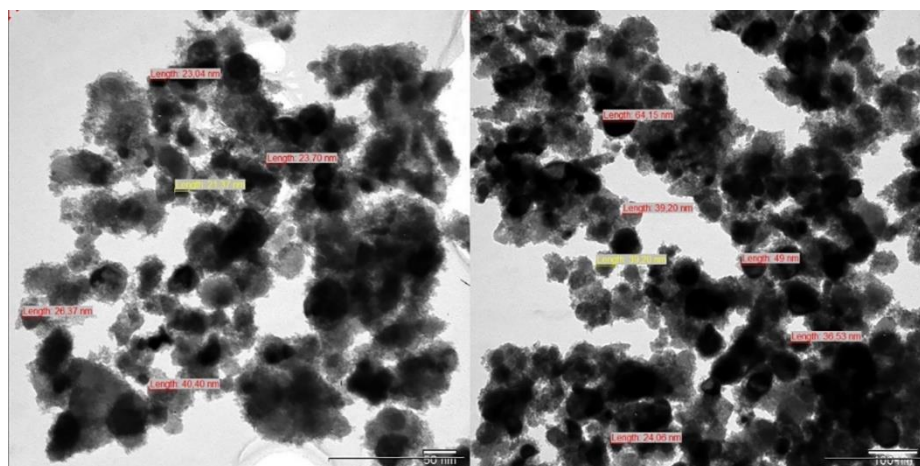


Figure 9: TEM images of meso-Fe₂O₃ NPs.

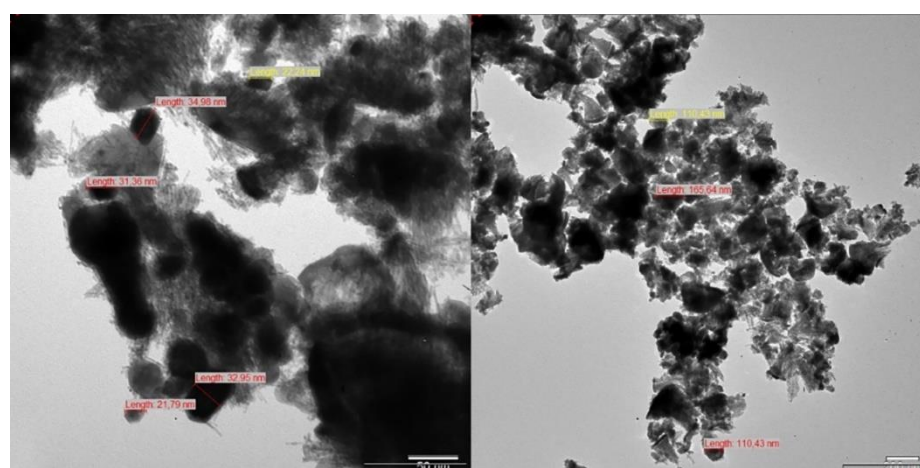


Figure 10: TEM images of meso-Co₃O₄ NPs.

3.2. AD studies

3.2.1. Chemical content analysis

In addition to the type of raw material used in biogas production (cattle, buffalo, etc.), parameters such as dry matter content, volatile solids, nitrogen, crude protein, and crude fat ratio are also important. Chemical analyses of organic feces were performed, and the results are given in Table 1.

Table 1: Chemical composition of feces.

Parameters	Feces (%)
Dry matter	8.16
Volatile solids	6.75
Ash	1.24
Total nitrogen (TKN)	1.86
Crude protein	11.63
Crude fat	1.67
pH	7.35

An important factor affecting biogas production is the solids rate, and the ideal rate for solids concentration has been reported as 7%–9% (31). In this study, the dry solids (DM) rate was calculated at 8.16%, and the ideal solids rate was achieved.

The Biogas production process comprises different stages and each stage encompasses numerous microbial flora to generate methane gas (32-33). Foremost, the mechanism of this process depends on the hydrolysis of complex organic material such as

carbohydrates, lipids, and proteins, and convert them into solubilized, simple, and monomeric forms of sugar, fatty acids, and amino acids by hydrolytic enzymes produced by most of *Firmicutes* and *Bacteroides* phyla such as *clostridium* (34). Acidogenesis was followed by hydrolysis as an intermediary step by acidogenic bacteria such as *Advenella faeciporci*, *Alkalitalea saponilacus*, *Bacteroides caccae*, *Bifidobacterium animalis*, and *Cloacibacillus porcorum* etc. The solubilized product after hydrolysis was converted into alcohol and volatile fatty acids (35). Later on, further catabolism took place by acetogenic bacteria such as *Anaerovorax odorimutans*, *Hydrogenophaga carboriunda*, and *Macellibacteroides fermentans*, etc, which convert alcohols and volatile fatty acids into acetate and hydrogen (H₂) by organic acid and CO₂ known as acetogenesis. The final step in gas production is methanogenesis which refers to the production of methane from acetate, hydrogen (H₂), and CO₂ by special types of microbes (36). These methanogenic archaeas are categorized as hydrogenotrophic, acetoclastic, and methylotrophic, which utilized H₂ and formate, acetate, and methyl-containing compounds such as methyl sulfate, methylamines, and methanol respectively to produce methane CH₄ (37). During the process of production of clean energy, these above-mentioned four different groups of bacteria and archaea cooperate and strictly depend on each other to complete this cycle. However, to enhance the production of biogas,

nanoparticles are used to develop microbes-to-microbes communication during catalytic reactions. Nanoparticles play an important role by rapidly donating or accepting electrons by direct interspecies electron transfer (DIET) (38) or mediated interspecies electron transfer (MIET) mechanism (39). However, studies on DIET showed that lag time decreased the level of hydraulic retention time and increased the stage of methanogenesis to enhance the yield of biogas by improving the CH₄ purity and lowering the inhibitor resistance between microbes. In addition, it was found that the addition of metallic nanoparticles activates hydrogenotrophic methanogens and hydrogen-producing bacteria during methanogenesis, which significantly optimize traditional anaerobic digestion into a well-established energy production technology by enhancing CH₄ generation via CO₂ reduction at the electron acceptor step supported by methanogenic archaea (40, 41).

During the biogas production process, heavy metals, minerals, and detergents have toxic effects on the growth of microorganisms depending on their concentration. Low concentrations of ammonium, calcium, sodium, potassium, magnesium, and sulfur contribute to the proliferation of microorganisms. Likewise, chromium, copper, iron, etc. while heavy metals contribute to the development of microorganisms at very low levels, they have a toxic effect at high levels and reduce methane production efficiency. It has been reported that the use of Fe₃O₄, especially magnetic metal oxide, as a catalyst, increases biogas yield (42). It has been reported that the activity of autotrophic bacteria increases in the presence of a magnetic field between small magnetic NPs [43]. The slower proliferation of autotrophic bacteria is important for their growth and enrichment in the reactor. It has also been noted that interactions between magnetic NPs can involve activated sludge to create an anoxic environment favored by heterotrophic bacteria and eventually increase their activity [44]. The stimulatory effects of Fe₃O₄ NPs are attributed to the cellular uptake of NPs in methanogens and their association with metabolic intermediates and enzyme activity involved in manure hydrolysis, acidification, and methanation. It has also been reported that the shape and size of nanoparticles have an impact on nanoparticle-cell interactions and cellular uptake [45]. Cellular uptake of spherical nanoparticles with uniform particle size distribution is 500% higher than rod-shaped nanoparticles because the membrane wrapping time is longer for longer particles. Nanoparticle size strongly affects membrane receptor binding, activation, and protein expression [46]. Based on the literature, 0.3 g of catalyst was used in this study (15). The volume of biogas produced without using a catalyst was measured as 1.060 L/kg on the 20th day. The biogas volume obtained when a 0.3 g/L catalyst was used was determined to be 1.360 L/kg for γ -Fe₂O₃, 1.390 L/kg for meso-Fe₂O₃ and 625-1.250 L/kg for Co₃O₄. These results showed that the magnetic nanoparticles used led to increased anaerobic digestion and therefore higher methane production and organic matter processing. It has also been reported that the release of iron ions from magnetic NPs may be responsible for the increased

bacterial activities [47]. In this study, γ -Fe₂O₃, meso-Fe₂O₃ and meso-Co₃O₄ magnetic nanoparticles used as catalysts cause the release of iron and cobalt ions into the reactor. This situation is also compatible with the literature [47].

3.2.2. Methane analysis in biogas

The methane amounts in the biogas content obtained without catalyst and with catalyst (γ -Fe₂O₃, Meso-Fe₂O₃, and Meso-Co₃O₄) in the biodigester are given in Table 2.

Table 2: Methane amounts in biogas content.

Sample	Methane (%)
- Fe ₂ O ₃	85.3
Meso- Fe ₂ O ₃	85.7
Meso-Co ₃ O ₄	83.4
Without catalyst	75.4

An increase in methane production was observed when the catalyst was used under the same experimental conditions. This increase was determined as 9.9%, 10.3%, and 8% for γ -Fe₂O₃, Meso-Fe₂O₃ and Meso-Co₃O₄ catalysts, respectively. The different effects of γ -Fe₂O₃ and Meso-Fe₂O₃ catalysts under the same conditions can be explained by the increase in the surface area of the mesoporous structure.

4. CONCLUSION

It is important to utilize watery animal feces on cattle farms by turning them into products. Especially biogas production is a good alternative to meet the increasing energy need. The biogas obtained can be used for heating purposes as well as for electricity generation. Burdur province is at the forefront of the livestock sector, especially with dairy cattle farming, and ranks first in Türkiye in terms of the average amount of milk obtained from an animal. To avoid wasting hydrocarbons, Burdur province must increase the number of facilities where farm wastes are used and converted into methane gas.

In this study, a laboratory-scale biodigester was designed to produce biogas from cattle feces taken from Burdur Mehmet Akif Ersoy University Cattle Farm and was produced as a prototype for a local company. Structural characterizations of the catalysts were carried out using FT-IR and XRD techniques. XRD powder patterns show that γ -Fe₂O₃ is formed in a maghemite structure in a tetragonal crystal system with P43212(96) space group (PDF card no: 00-025-1402). The mesoporous Fe₂O₃ nanoparticles are formed in the hematite structure in a rhombohedral crystal structure and an R-3c (167) crystal system (PDF Card no: 00-033-0664). Co₃O₄ nanoparticles are formed in a cubic crystal system with an Fd-3m space group (227) (PDF card no: 00-042-1467). The average particle sizes of nanoparticles were determined to be in the range of 20-165 nm. The biodigester was kept at a constant temperature of 35 °C for 20 days, and the volume of gas released was measured. The obtained biogas in the biodigester was absorbed into the adsorbent material (activated carbon) and analyzed with the headspace-GC-MS combined system. In this study, it

was observed that spherical $\gamma\text{-Fe}_2\text{O}_3$, meso- Fe_2O_3 and meso- Co_3O_4 magnetic nanoparticles used as nanocatalysts improved biogas and methane production. The amount of methane in the biogas obtained without using a catalyst was found to be 75.4%. When $\gamma\text{-Fe}_2\text{O}_3$, meso- Fe_2O_3 , and meso- Co_3O_4 nanoparticles were used as catalysts, the methane ratio was calculated as 85.3, 85.7, and 83.4, respectively. The results obtained from the study showed that in addition to $\gamma\text{-Fe}_2\text{O}_3$ used as a catalyst in biogas production, meso- Fe_2O_3 and meso- Co_3O_4 nanoparticles also have the potential to be used for this purpose.

5. CONFLICT OF INTEREST

The authors declare no conflict of interest.

6. ACKNOWLEDGMENTS

This study was supported by Burdur Mehmet Akif Ersoy University Scientific Research Projects Coordinatorship with Project No: 0715-MP-21. The authors also would like to thank Assoc. Prof. Dr. Ruken Esra Demirdöğen for her valuable contribution.

7. REFERENCES

- Kona A, Bertoldi P, Kılış Ş. Covenant of Mayors: Local Energy Generation, Methodology, Policies and Good Practice Examples. *Energies* [Internet]. 2019 Mar 13;12(6):985. Available from: [<URL>](#).
- Dabe SJ, Prasad PJ, Vaidya AN, Purohit HJ. Technological pathways for bioenergy generation from municipal solid waste: Renewable energy option. *Environ Prog Sustain Energy* [Internet]. 2019 Mar 25;38(2):654–71. Available from: [<URL>](#).
- Mikalauskiene A, Štreimikis J, Mikalauskas I, Stankūnienė G, Dapkus R. Comparative Assessment of Climate Change Mitigation Policies in Fuel Combustion Sector of Lithuania and Bulgaria. *Energies* [Internet]. 2019 Feb 7;12(3):529. Available from: [<URL>](#).
- Holdmann GP, Wies RW, Vandermeer JB. Renewable Energy Integration in Alaska's Remote Islanded Microgrids: Economic Drivers, Technical Strategies, Technological Niche Development, and Policy Implications. *Proc IEEE* [Internet]. 2019 Sep;107(9):1820–37. Available from: [<URL>](#).
- Viancelli A, Schneider TM, Demczuk T, Delmoral APG, Petry B, Collato MM, et al. Unlocking the value of biomass: Exploring microbial strategies for biogas and volatile fatty acids generation. *Bioresour Technol Reports* [Internet]. 2023 Sep;23:101552. Available from: [<URL>](#).
- Havukainen J, Uusitalo V, Niskanen A, Kapustina V, Horttanainen M. Evaluation of methods for estimating energy performance of biogas production. *Renew Energy* [Internet]. 2014 Jun;66:232–40. Available from: [<URL>](#).
- Yusuf MOL, Ify NL. The effect of waste paper on the kinetics of biogas yield from the co-digestion of cow dung and water hyacinth. *Biomass and Bioenergy* [Internet]. 2011 Mar;35(3):1345–51. Available from: [<URL>](#).
- Koniuszewska I, Korzeniewska E, Harnisz M, Czatkowska M. Intensification of biogas production using various technologies: A review. *Int J Energy Res* [Internet]. 2020 Jun 25;44(8):6240–58. Available from: [<URL>](#).
- Barozzi M, Contini S, Raboni M, Torretta V, Casson Moreno V, Copelli S. Integration of Recursive Operability Analysis, FMECA and FTA for the Quantitative Risk Assessment in biogas plants: Role of procedural errors and components failures. *J Loss Prev Process Ind* [Internet]. 2021 Jul;71:104468. Available from: [<URL>](#).
- Shakil Hussain SM, Kamal MS, Hossain MK. Recent Developments in Nanostructured Palladium and Other Metal Catalysts for Organic Transformation. *J Nanomater* [Internet]. 2019 Oct 20;2019:1562130. Available from: [<URL>](#).
- Srivastava N, Srivastava KR, Bantun F, Mohammad A, Singh R, Pal DB, et al. Improved production of biogas via microbial digestion of pressmud using CuO/Cu₂O based nanocatalyst prepared from pressmud and sugarcane bagasse waste. *Bioresour Technol* [Internet]. 2022 Oct;362:127814. Available from: [<URL>](#).
- Ribeaucourt D, Bissaro B, Guallar V, Yemloul M, Haon M, Grisel S, et al. Comprehensive Insights into the Production of Long Chain Aliphatic Aldehydes Using a Copper-Radical Alcohol Oxidase as Biocatalyst. *ACS Sustain Chem Eng* [Internet]. 2021 Mar 29;9(12):4411–21. Available from: [<URL>](#).
- Ozyilmaz E, Alhiali A, Caglar O, Yilmaz M. Preparation of regenerable magnetic nanoparticles for cellulase immobilization: Improvement of enzymatic activity and stability. *Biotechnol Prog* [Internet]. 2021 Mar 22;37(4):e3145. Available from: [<URL>](#).
- Watanabe T, Takawane S, Baba Y, Akaiwa J, Kondo A, Ohba T. Superior Thermal Stability and High Photocatalytic Activity of Titanium Dioxide Nanocatalysts in Carbon Nanotubes. *J Phys Chem C* [Internet]. 2023 Aug 31;127(34):16861–9. Available from: [<URL>](#).
- Gómez-Gualdrón DA, McKenzie GD, Alvarado JFJ, Balbuena PB. Dynamic Evolution of Supported Metal Nanocatalyst/Carbon Structure during Single-Walled Carbon Nanotube Growth. *ACS Nano* [Internet]. 2012 Jan 24;6(1):720–35. Available from: [<URL>](#).
- Bhanja P, Bhaumik A. Materials with Nanoscale Porosity: Energy and Environmental Applications. *Chem Rec* [Internet]. 2019 Feb 2;19(2–3):333–46. Available from: [<URL>](#).
- Zhou L, Zheng J, Ye E, Liu Y, He C. Nanocatalysis with sustainability. In: Li Z, Zheng J, Ye E, editors. *Nanoscience and Nanotechnology Series, Sustainable Nanotechnology* [Internet]. London:

- 10.1039/9781839165771; 2022. p. 220–54. Available from: [<URL>](#).
18. Touchy AS, Siddiki SMAH. Green Chemical Synthesis in the Presence of Nanoparticles as Catalysts. In: Singh NB, Susan ABH, Chaudhary RG, editors. Emerging Applications of Nanomaterials. Millersville: Materials Research Forum LLC; 2023. p. 42–74.
19. Bharathi P, Dayana R, Rangaraju M, Varsha V, Subathra M, Gayathri, et al. Biogas Production from Food Waste Using Nanocatalyst. R L, editor. J Nanomater [Internet]. 2022 Jul 31;2022:7529036. Available from: [<URL>](#).
20. Awogbemi O, Kallon DV Von. Recent advances in the application of nanomaterials for improved biodiesel, biogas, biohydrogen, and bioethanol production. Fuel [Internet]. 2024 Feb;358:130261. Available from: [<URL>](#).
21. Jayanthi SA, Nathan DMGT, Jayashainy J, Sagayaraj P. A novel hydrothermal approach for synthesizing α -Fe₂O₃, γ -Fe₂O₃ and Fe₃O₄ mesoporous magnetic nanoparticles. Mater Chem Phys [Internet]. 2015 Jul;162:316–25. Available from: [<URL>](#).
22. Li D, Wu X, Xiao T, Tao W, Yuan M, Hu X, et al. Hydrothermal synthesis of mesoporous Co₃O₄ nanobelts by means of a compound precursor. J Phys Chem Solids [Internet]. 2012 Feb;73(2):169–75. Available from: [<URL>](#).
23. Zhang L, Papaefthymiou GC, Ying JY. Synthesis and Properties of γ -Fe₂O₃ Nanoclusters within Mesoporous Aluminosilicate Matrices. J Phys Chem B [Internet]. 2001 Aug 1;105(31):7414–23. Available from: [<URL>](#).
24. Demir Ö, Ateş N. Manyetik Nanopartiküllerin Anaerobik Çürütücüde Biyogaz Üretimi Üzerine Etkileri. Çukurova Üniversitesi Mühendislik Fakültesi Derg [Internet]. 2021 Aug 16;36(2):283–96. Available from: [<URL>](#).
25. Yılmaz M, Seçilmiş H. Gaz kromatografisi headspace sistemi ile süt ürünlerinde bazı aroma bileşenlerinin analizi. In: Türkiye 9 Gıda Kongresi. 2006. p. 24–6.
26. Omoniye TE, Olorunnisola AO. Experimental characterisation of bagasse biomass material for energy production. Int J Eng Technol. 2014;4(10):582–9. Available from: [<URL>](#).
27. Beutler M, Wiltshire KH, Meyer B, Moldaenke C, Luring C, Meyerhofer M, Hansen UP. APHA (2005), Standard Methods for the Examination of Water and Wastewater, Washington DC: American Public Health Association. 2014;
28. Huang Y, Zhang D, Oshita K, Takaoka M, Ying M, Sun Z, et al. Crude oil recovery from oily sludge using liquefied dimethyl ether extraction: A comparison with conventional extraction methods. Energy and Fuels [Internet]. 2021 Nov 4 [cited 2024 Feb 27];35(21):17810–9. Available from: [<URL>](#).
29. Parsianpour E, Gholami M, Shahbazi N, Samavat F. Influence of thermal annealing on the structural and optical properties of maghemite (γ -Fe₂O₃) nanoparticle thin films. Surf Interface Anal [Internet]. 2015 May 12;47(5):612–7. Available from: [<URL>](#).
30. Mishra D, Arora R, Lahiri S, Amritphale SS, Chandra N. Synthesis and characterization of iron oxide nanoparticles by solvothermal method. Prot Met Phys Chem Surfaces [Internet]. 2014 Sep 12;50(5):628–31. Available from: [<URL>](#).
31. Jagadale AD, Kumbhar VS, Lokhande CD. Supercapacitive activities of potentiodynamically deposited nanoflakes of cobalt oxide (Co₃O₄) thin film electrode. J Colloid Interface Sci [Internet]. 2013 Sep;406:225–30. Available from: [<URL>](#).
32. Wang S, Jena U, Das KC. Biomethane production potential of slaughterhouse waste in the United States. Energy Convers Manag [Internet]. 2018 Oct;173:143–57. Available from: [<URL>](#).
33. Wang P, Wang H, Qiu Y, Ren L, Jiang B. Microbial characteristics in anaerobic digestion process of food waste for methane production—A review. Bioresour Technol [Internet]. 2018 Jan;248:29–36. Available from: [<URL>](#).
34. Nguyen D, Khanal SK. A little breath of fresh air into an anaerobic system: How microaeration facilitates anaerobic digestion process. Biotechnol Adv [Internet]. 2018 Nov;36(7):1971–83. Available from: [<URL>](#).
35. Hendriks ATWM, van Lier JB, de Kreuk MK. Growth media in anaerobic fermentative processes: The underestimated potential of thermophilic fermentation and anaerobic digestion. Biotechnol Adv [Internet]. 2018 Jan;36(1):1–13. Available from: [<URL>](#).
36. Li Y, Chen Y, Wu J. Enhancement of methane production in anaerobic digestion process: A review. Appl Energy [Internet]. 2019 Apr;240:120–37. Available from: [<URL>](#).
37. Venkiteshwaran K, Bocher B, Maki J, Zitomer D. Relating Anaerobic Digestion Microbial Community and Process Function: Supplementary Issue: Water Microbiology. Microbiol Insights [Internet]. 2015 Jan 20;8(S2):37–44. Available from: [<URL>](#).
38. Bai X, Zong R, Li C, Liu D, Liu Y, Zhu Y. Enhancement of visible photocatalytic activity via Ag@C₃N₄ core-shell plasmonic composite. Appl Catal B Environ [Internet]. 2014 Apr;147:82–91. Available from: [<URL>](#).
39. Appels L, Baeyens J, Degève J, Dewil R. Principles and potential of the anaerobic digestion of waste-activated sludge. Prog Energy Combust Sci [Internet]. 2008 Dec;34(6):755–81. Available from: [<URL>](#).
40. Cuetos MJ, Martinez EJ, Moreno R, Gonzalez R, Otero M, Gomez X. Enhancing anaerobic digestion of poultry blood using activated carbon. J Adv Res

- [Internet]. 2017 May;8(3):297–307. Available from: [<URL>](#).
41. Tsapekos P, Alvarado-Morales M, Tong J, Angelidaki I. Nickel spiking to improve the methane yield of sewage sludge. *Bioresour Technol* [Internet]. 2018 Dec;270:732–7. Available from: [<URL>](#).
42. Abdelsalam E, Samer M, Attia YA, Abdel-Hadi MA, Hassan HE, Badr Y. Influence of zero valent iron nanoparticles and magnetic iron oxide nanoparticles on biogas and methane production from anaerobic digestion of manure. *Energy* [Internet]. 2017 Feb;120:842–53. Available from: [<URL>](#).
43. Łebkowska M, Rutkowska-Narożniak A, Pajor E, Pochanke Z. Effect of a static magnetic field on formaldehyde biodegradation in wastewater by activated sludge. *Bioresour Technol* [Internet]. 2011 Oct;102(19):8777–82. Available from: [<URL>](#).
44. Ni SQ, Ni J, Yang N, Wang J. Effect of magnetic nanoparticles on the performance of activated sludge treatment system. *Bioresour Technol* [Internet]. 2013 Sep;143:555–61. Available from: [<URL>](#).
45. Verma A, Stellacci F. Effect of Surface Properties on Nanoparticle–Cell Interactions. *Small* [Internet]. 2010 Jan 4;6(1):12–21. Available from: [<URL>](#).
46. Jiang W, Kim BYS, Rutka JT, Chan WCW. Nanoparticle-mediated cellular response is size-dependent. *Nat Nanotechnol* [Internet]. 2008 Mar 2;3(3):145–50. Available from: [<URL>](#).
47. Liu Y, Zhang Y, Quan X, Chen S, Zhao H. Applying an electric field in a built-in zero valent iron – Anaerobic reactor for enhancement of sludge granulation. *Water Res* [Internet]. 2011 Jan;45(3):1258–66. Available from: [<URL>](#).



Biosorption of Methyl Orange Dye in Single, Binary and Ternary System onto Gingerbread Plum Seed Shell Activated Carbon

Musa Husaini^{1*} , Bishir Usman¹ , Muhammad Bashir Ibrahim¹ 

¹Department of Pure and Industrial Chemistry, Faculty of Physical Sciences College of Natural and Pharmaceutical Sciences, Bayero University Kano (BUK), P.M.B. 3011, Kano, Nigeria.

Abstract: The research investigated the potential of gingerbread plum seed shell activated to function as a biosorbent for eliminating methyl orange (MO) dye from water in various dye combinations, including single, binary, and ternary systems alongside methylene blue (MB) and Congo red (CR) dyes. The characteristics of the adsorbent were analyzed through techniques like Scanning Electron Microscopy, Fourier Transform Infrared spectroscopy, and pH point of zero charges. Batch adsorption tests were conducted to examine the adsorption processes' equilibrium behaviors, thermodynamics, and kinetics. The collected data were subjected to different isotherm and kinetics equations. The pseudo-second-order kinetics model provided the best fit for all the sorption systems, irrespective of composition differences, with higher rate constants observed for binary MO+MB= 0.031 g/mg/min system and lower for binary MO+CR= 0.028 g/mg/min and ternary MO+MB+CR= 0.029 g/mg/min systems compared to the single system MO= 0.030 g/mg/min. The maximum monolayer capacity of the adsorbent for methyl orange demonstrated synergistic interaction with the presence of methylene blue and antagonistic interaction with the presence of Congo red dye. The findings indicated that the adsorption processes varied based on the system's composition; they were all spontaneous (with ΔG values ranging from -1.146 to -10.415 kJ/mol) and exothermic (with ΔH values between -17.94 and -54.63 kJ/mol). Additionally, randomness decreased, as reflected by ΔS values of -054.43 and -382.62 J/K for the entire process.

Keywords: Adsorption, Equilibrium study, Kinetic study, Thermodynamic study, Synergistic effect, and antagonistic effect.

Submitted: October 8, 2023. **Accepted:** February 5, 2024.

Cite this: Husaini M, Usman B, Ibrahim MB. Biosorption of Methyl Orange Dye in Single, Binary and Ternary System onto Gingerbread Plum Seed Shell Activated Carbon. JOTCSA. 2024;11(2):655-64.

DOI: <https://doi.org/10.18596/jotcsa.1372995>

***Corresponding author's E-mail:** musahusaini36@gmail.com

1. INTRODUCTION

Dye contaminants in wastewater are a notable environmental hazard due to their enduring and detrimental characteristics, posing risks to human health and marine ecosystems (1). The discharge of dye-containing wastewater, even in minimal concentrations, is aesthetically displeasing and environmentally troublesome, especially when originating from textile industries. Therefore, effectively removing dyes from such wastewater is essential to address ecological, biological, and industrial challenges (2). Numerous approaches have been developed to address this issue, such as chemical ion exchange, membrane filtration, physical adsorption, photocatalysis, and biological methods.

Adsorption stands out among these methods as a promising approach thanks to its simplicity, high

effectiveness, and cost-efficiency (3). The choice of adsorbent significantly impacts the effectiveness of adsorption processes. Cost-effective adsorbents that possess a high adsorption capacity and can be easily reused are preferred (4).

Due to its favorable characteristics like high yield during production, cost-effectiveness, eco-friendliness, and effective adsorption capabilities, activated carbon derived from carbon-rich organic materials has been extensively studied for removing pollutants from wastewater (5,6). Activated carbon from various waste sources, such as sugarcane bagasse and peanut biomass, have been investigated for their potential in dye removal from water (7,8). However, industrial wastewater typically contains multiple dyes concurrently. The adsorption behavior of one dye may change when other dyes are present (9). While there is a substantial body of research on

adsorption involving single components (10,11) or binary combinations (12,13), knowledge regarding the removal of dyes in complex mixtures is more limited (14,15).

The lack of research in this area adds complexity to understanding the adsorption process for industrial wastewater with multiple components. While some agricultural waste materials have been tested for the removal of a single dye, very few have been explored for the removal of multiple dyes. This study specifically focuses on utilizing activated carbon derived from gingerbread plum seed shells to adsorb Congo red in a competitive environment. The potential of this agricultural waste in removing the dye in a competitive setting has not been investigated previously.

2. METHODOLOGY

2.1 Activated Carbon Preparation

The adsorbent sample was prepared following the method outlined in references (16,17). Gingerbread plum seed shell samples were collected and cleaned with tap water to remove impurities. Afterward, they were allowed to naturally air-dry for 72 hours. The dried samples were then finely ground to achieve a granular texture and immersed in a solution containing 30% phosphoric acid (CAS 7663-38-2) for 24 hours. After impregnation, the samples were dried and subjected to carbonization in a furnace at a temperature of 400 °C for 2 hours. The resulting activated samples underwent a thorough rinsing process using distilled water until a neutral solution was attained. They were then dried in an oven at 105 °C until a consistent weight was reached.

Subsequently, the samples were sieved and stored in an airtight container (17,18).

2.2 Adsorbent Characterization

To analyze the characteristics of activated carbon derived from gingerbread plum seed shells, its infrared spectra were recorded before and after dye absorption using an FTIR spectrophotometer spanning from 4000 cm^{-1} to 600 cm^{-1} . The surface morphology of the adsorbent was assessed through scanning electron microscopy (19,20). The adsorbent's point of zero charge (pH_{zpc}) was determined following the procedure outlined (8). This involved adding 0.1 g of the adsorbent to a 40 mL solution of 0.1 M NaNO_3 (CAS 7631-99-4) with a predefined initial pH (pH_i). In separate adsorbent flasks, initial pH levels were adjusted using 0.1 M NaOH (CAS 1310-73-2) or HCl (CAS 7647-01-0). After agitating the flasks for 24 hours, the final pH (pH_f) was measured using a pH meter. Plotting the change in pH ($\text{pH}_i - \text{pH}_f$) against the initial pH yields the pH_{zpc} , where the plot intersects the horizontal axis (21).

2.3 Preparing the Adsorbate

The main substance under adsorption investigation is an anionic dye named Methyl Orange (MO) (CAS 547-58-0), provided by Sigma Aldrich. Different aqueous solutions of MO dye were made using varying concentrations from the dye's original solution (1000 mg/L) in the case of the single dye system. In the binary system, either Methylene Blue (MB) (CAS 61-73-4) dye or Congo Red (CR) (CAS 573-58-0) dye was mixed with predefined concentrations of the primary adsorbate. All three dyes were mixed in the ternary system. Figure 1 displays the chemical structure of these three dyes.

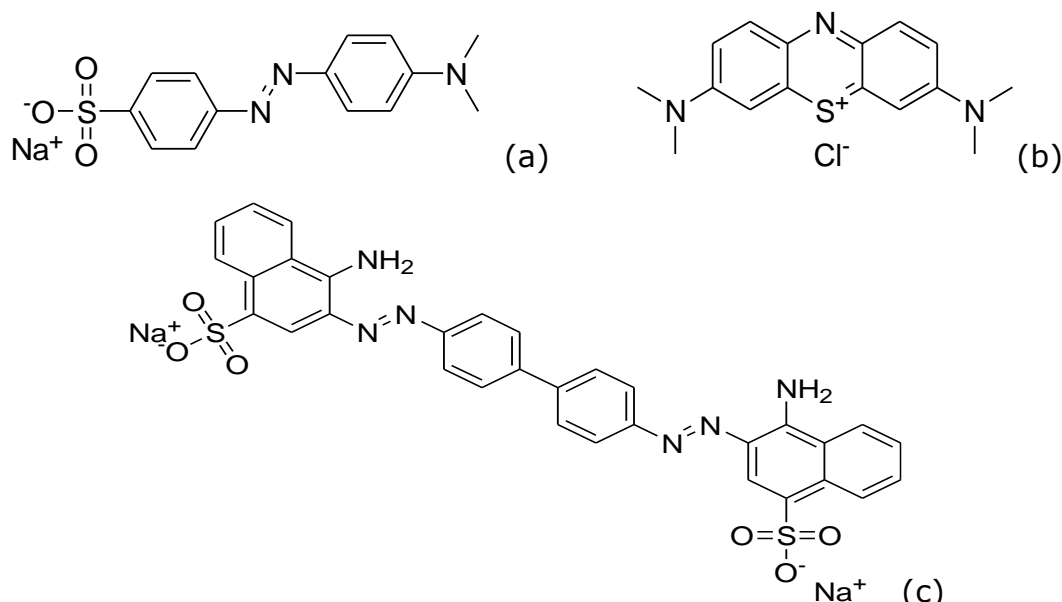


Figure 1: Structure of the Dyes (a) Methyl orange b) Methylene blue c) Congo red.

2.4 Batch Adsorption Experiment

Various solutions of methyl orange dye with differing concentrations and volume (50 mL each) were introduced into clearly labeled glass bottles containing a fixed amount of the adsorbent. These bottles were sealed with lids and placed in a

thermostat-controlled horizontal mechanical shaker that maintained a consistent speed, temperature, and pH until equilibrium. Further rounds of batch experiments were conducted to explore the effects of adsorbent quantity (0.1 – 0.6 g), contact time (5 – 150 min), pH (2 – 12), and temperature (303 – 323

K). This involved using varying amounts of adsorbent, pre-determined contact durations, pH levels, and specific temperatures. Subsequently, the mixtures of dye and adsorbent in the flasks were filtered, and the absorbance of the filtrate was measured using a UV-visible scanning spectrophotometer at the specified absorption wavelength, λ_{max} (464.5 nm) of methyl orange dye (22).

The quantity of dye adsorbed per unit mass of adsorbent, denoted as q (mg/g), was calculated using formulas 1 and 2.

$$q_e = \frac{(C_o - C_e) \times v}{m} \tag{1}$$

$$q_t = \frac{(C_o - C_t) \times v}{m} \tag{2}$$

In this context, q_e and q_t denote the quantity of dye adsorbed (in mg/g) at equilibrium and at a specific time t , respectively. C_o , C_e , and C_t (measured in mg/L)

represent the initial dye concentration (at $t=0$), dye concentration at equilibrium, and dye concentration at a given time $t=t$, respectively. V refers to the volume of the solution (in liters), while m indicates the mass of the adsorbent (in grams).

3. RESULTS AND DISCUSSION

3.1 Characterization

Figure 2 depicts the FTIR spectra of the adsorbent both before and after the adsorption of dye. The FTIR spectrum of activated carbon from gingerbread plum seed shell is composite, featuring multiple absorption peaks even prior to dye adsorption. Reflective of different functional groups, which are potential sites for adsorption of adsorbate (9). Following the adsorption of methyl orange, shifts in band positions of frequencies were evident in the FTIR spectrum of the adsorbent after adsorption (Table 1). These shifts in adsorption bands imply potential interaction between the surface of adsorbent and dye molecules.

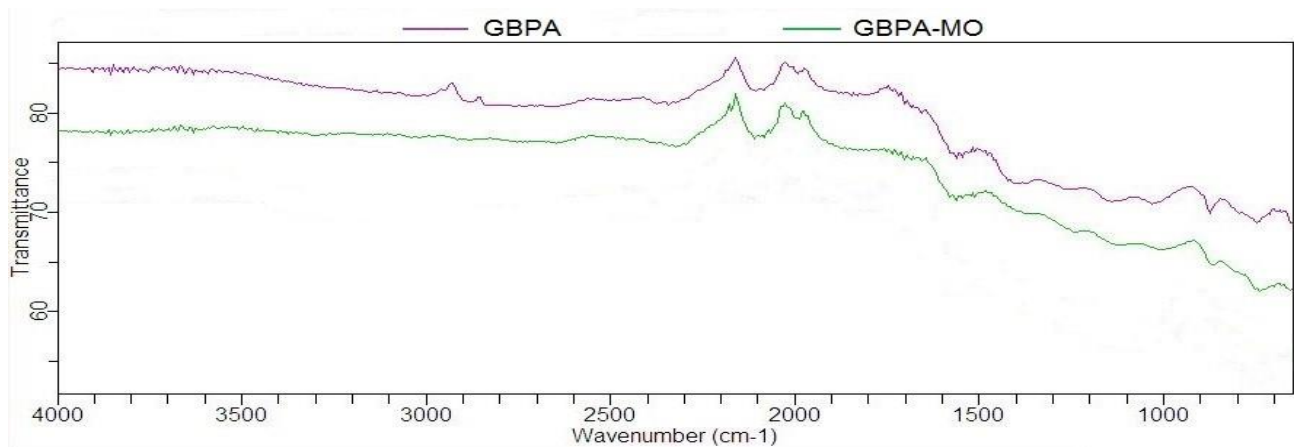


Figure 2: FTIR Analysis before (GBPA) and after Adsorption of MO (GBPA-MO).

Table 1: Functional group observed before and after adsorption of Methyl orange.

Functional group	Vibration Frequency (cm ⁻¹)	Observed Frequency (cm ⁻¹)	
		Before Adsorption	After Adsorption
O-H stretching vibration in alcohol	3700-3584	3661	3674
C-H stretching vibration in alkane	3000-2840	2880	2850
C ≡ C stretching vibration in alkyne	2260-2100	2191	2258
C ≡ C stretching vibration in alkyne	2260-2100	2107	2173
C=C=C stretching of allene	2000-1900	1994	1990
N-O stretching of nitro groups	1550-1500	1547	1562
C-O stretching of aliphatic ether	1150-1085	1140	1165
C-H bending of 1,3-disubstituted	880±20	870	866
C-H bending of monosubstituted	750±20	755	749

Additional characterization results are presented in Figure 3. The scanning electron micrograph of the adsorbent at $\times 1000$ magnification (Figure 3a) displays an irregular and porous surface texture. This characteristic surface structure could signify a

favorable attribute for an effective adsorbent with a substantial surface area. This surface was smoothed by the presence of dye molecules after the adsorption process (Figure 3b) (16,23).

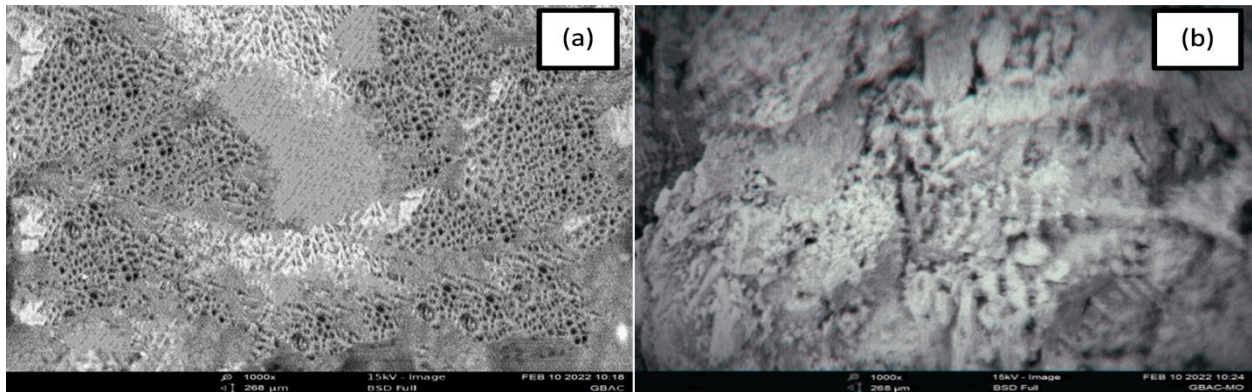


Figure 3: SEM Micrograph (a) before and (b) Adsorption of Methyl orange.

In Figure 4, the point of zero charge (pH_{zpc}) is depicted and found to be 5.60. Below this pH, the surface of the adsorbent carries a positive charge, which attracts negatively charged species in the

solution. Conversely, above the pH_{zpc} , the surface carries a negative charge, thereby attracting cations (24,25).

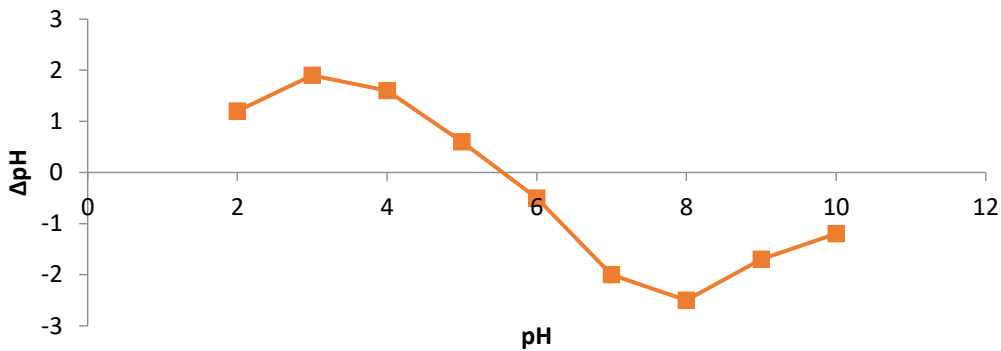


Figure 4: pH at point of zero charge of the adsorbent.

3.2 Influence of Solution pH

The pH level of an aqueous system plays a pivotal role in determining the chemical state and degree of ionization of the adsorbate during the adsorption process. This renders it a critical factor in wastewater treatment via adsorption. Figure 5 illustrates the influence of pH on the adsorption of methyl orange onto the adsorbent. The adsorption capacity (q_e) demonstrated a pronounced increase under acidic pH conditions, gradually diminishing as the pH level rose. This trend may be attributed to the heightened presence of OH^- ions, which compete with the anion

groups on the dye for available adsorption sites on the adsorbent, especially with increasing pH. Moreover, when the pH is below the adsorbent's point of zero charge (pH_{zpc}), the adsorbent's surface holds a positive charge, facilitating the attraction of anionic dyes through electrostatic forces. This phenomenon amplifies the adsorption of methyl orange. (26,27) have also reported similar findings concerning the increased adsorption capacity of acid dyes in acidic pH conditions.

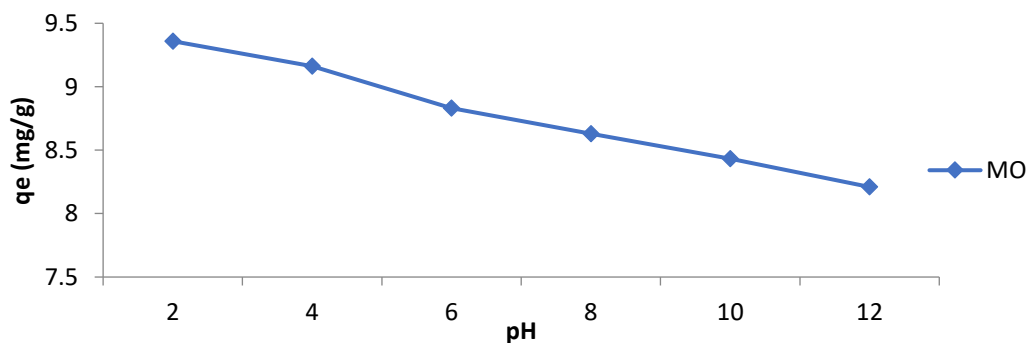


Figure 5: Effect of pH on adsorption of methyl orange.

3.3 Impact of Adsorbent Dosage

The quantity of methyl orange adsorbed per unit mass of adsorbent, indicated as q_e , decreased as the

adsorbent dosage increased across various adsorbate systems (single, binary, and ternary), as shown in Figure 6a. With an increase in the adsorbent dose from 0.1 to 0.6 g, the adsorption capacity (q_e) consistently decreased from 9.70 to 8.99 mg/g in the single dye system containing only methyl orange, from 9.388 to 9.95 mg/g in the binary system with methyl orange and methylene blue (MO + MB), and from 8.30 to 7.599 mg/g in the binary system with methyl orange and Congo red (MO + CR). A

reduction in the adsorption density (from 8.801 to 8.09 mg/g) was also observed in the ternary system containing all three dyes. These findings suggest that at lower doses, the active sites on the surface of the adsorbent were effectively utilized, but with an increase in the adsorbent dose, a significant portion of these active sites likely overlapped, resulting in a decrease in the specific uptake.

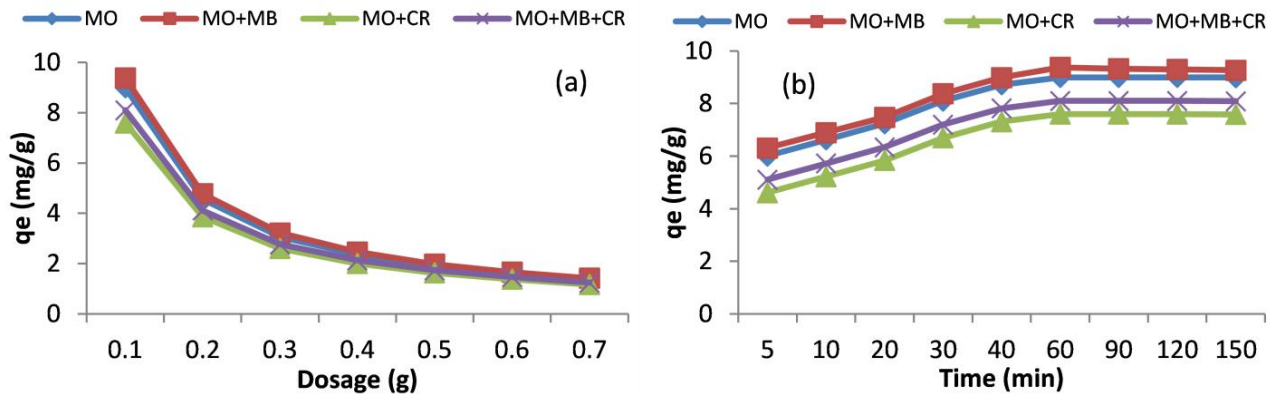


Figure 6: Effect of a) dosage, b) contact time.

3.4 Impact of Initial Concentration

To investigate how the initial concentration of methyl orange affects its absorption by the adsorbent, four different adsorbate systems were studied: (i) Methyl orange by itself (single system), (ii) Methyl orange combined with Methylene Blue (MO+MB, binary system), (iii) Methyl orange combined with Congo Red (MO+CR, binary system), and (iv) a mixture of methyl orange along with methylene blue and Congo red (MO + MB + CR, ternary system). The adsorbent's capacity for methyl orange, indicating the quantity of methyl orange adsorbed per unit mass of adsorbent, increased as the initial concentration of methyl orange increased in all types of adsorbate-adsorbent systems: single, binary, or ternary (Figure 6b).

As the initial concentration of methyl orange ranged from 20 – 500 mg/L, the values rose from 9.04 to 92.60 mg/g in the single system (MO), from 9.34 to 100.77 mg/g in the MO+MB binary system, from 7.64 to 57.60 mg/g in the MO+CR binary system, and from 8.54 to 80.10 mg/g in the ternary dye system. The observed increase in dye uptake with higher initial dye concentrations in all systems is likely due to the lower availability of dye molecules at lower concentrations. However, at higher concentrations, the abundance of dye molecules overcomes resistance to mass transfer.

Additionally, when starting with the same initial concentrations of methyl orange and other competing dyes, there were slight fluctuations in the adsorption capacity of all the systems. For example, at an initial concentration of 20 mg/L for methyl orange, the adsorption capacity of the adsorbent was 9.04, 9.34, 7.64, and 8.54 mg/g for the single, MO+MB, MO+CR, and MO+MB+CR systems,

respectively. This behavior can be attributed to the competitive nature of the adsorption processes.

3.5 Influence of Contact Time and Kinetics

The adsorption of methyl orange exhibited a rise in the single, binary, and ternary dye systems as the contact time was extended, eventually reaching equilibrium (Figure 6b). This research delved into adsorption dynamics, which assesses the speed at which the solute is taken up, thereby influencing how long the adsorbate remains at the interface between solid and solution. The kinetics of methyl orange adsorption were explored using both the pseudo-first-order model and the pseudo-second-order equation. The mathematical expressions for these models are provided by equations 3 and 4 (28).

The pseudo-first-order equation:

$$\ln(q_e - q_t) = \ln q_e - k_1 t \quad (3)$$

The pseudo-second-order equation:

$$\frac{t}{q_t} = \frac{1}{k_2 q_e^2} + \frac{t}{q_e} \quad (4)$$

In this context, q_t (mg/g) represents the adsorption capacity at time t , k_1 (min^{-1}) stands for the rate constant of pseudo-first-order adsorption, and k_2 (g/mg/min) denotes the pseudo-second-order rate constant. Graphs depicting these equations can be found in Figure 7 (a and b), and the resulting rate parameters are listed in Table 2. Across all adsorbate systems (single, binary, and ternary), the adsorption kinetics were most accurately described by the pseudo-second-order rate model, with R^2 values exceeding 0.99. Additionally, both the experimental and calculated q_e values demonstrated better agreement with the pseudo-second-order model as opposed to the pseudo-first-order model. The conformity of sorption kinetics to the pseudo-second-

order equation implies that chemisorption likely plays a role in the rate-limiting step of the process (20).

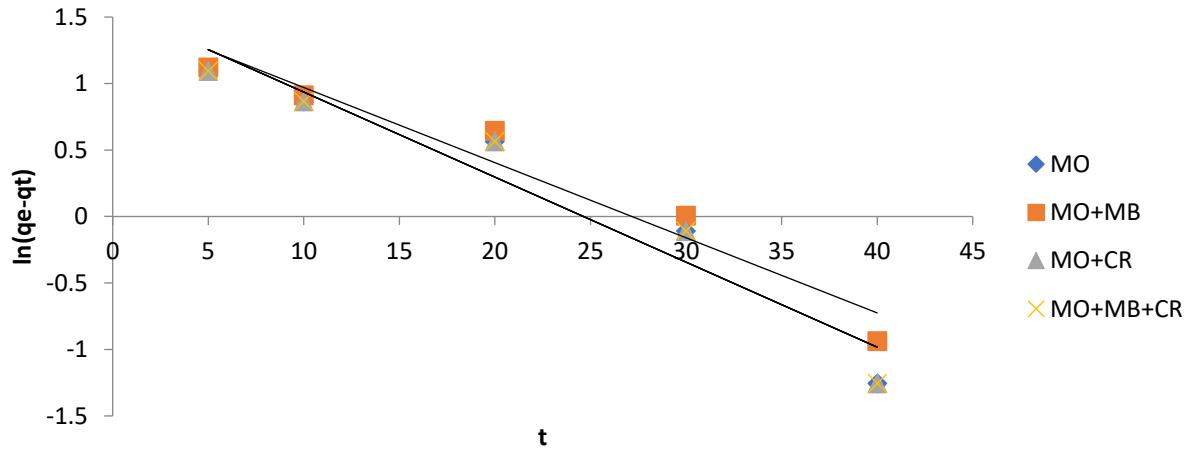


Figure 7: Pseudo-first order plot.

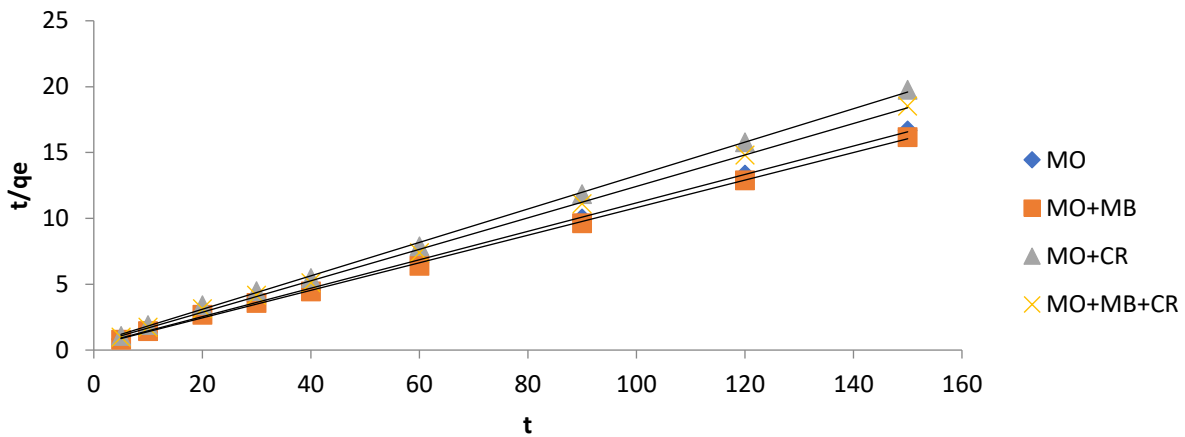


Figure 7b: Pseudo-second order plot.

Table 2: Kinetic parameters.

Kinetic Model	Parameters	MO	MO+MB	MO+CR	MB+MO+CR
Pseudo-first order	k_1	0.046	0.057	0.063	0.063
	$q_{e \text{ exp}}$	9.00	9.38	7.60	8.10
	$q_{e \text{ cal}}$	4.83	4.64	4.83	4.83
	R^2	0.9353	0.9459	0.9820	0.9353
Pseudo-second order	k_2	0.030	0.031	0.028	0.29
	$q_{e \text{ exp}}$	9.00	9.38	7.60	8.10
	$q_{e \text{ cal}}$	9.26	9.56	7.88	8.70
	R^2	0.9994	0.9993	0.9991	0.9999

3.6 Adsorption Isotherms

The adsorption equilibrium isotherm describes the connection between adsorbates in the liquid phase and those on the surface of the adsorbent under a consistent temperature. In this investigation, we employed linearized versions of the isotherm equations to fit the equilibrium concentrations of the remaining methyl orange dye solution (C_e) and the amounts of dye adsorbed onto the adsorbent surface (q_e) in single, binary, and ternary systems. This was carried out to characterize the equilibrium association under a constant temperature. The

suitability of the isotherm models was evaluated based on the correlation coefficients (R^2) obtained from linear plots. The mathematical formulations utilized in this study are provided below:

$$\frac{1}{q_e} = \frac{1}{q_{max}K_L C_e} + \frac{1}{q_{max}} \tag{5}$$

$$R_L = \frac{1}{1 + K_L C_0} \tag{6}$$

Freundlich;

$$\ln q_e = \ln K_f + \frac{1}{n} \ln C_e \quad (7)$$

$$\text{Temkin} \quad q_e = b_T \ln C_e + b_T \ln K_T \quad (8)$$

where C_e stands for the equilibrium adsorbate concentration (mg/L), q_e represents the quantity of adsorbate absorbed per unit mass of adsorbent (mg/g), q_m and K_L are Langmuir constants associated with monolayer adsorption capacity and adsorbent affinity, respectively. R_L (L/mg) is a dimensionless Langmuir constant, and C_0 (mg/L) is the highest initial concentration. K_F is the Freundlich constant indicating adsorption capacity and intensity on the adsorbent or surface heterogeneity, while K_T and B_T are constants for the Temkin model. Additionally, R represents the universal gas constant (8.314 J mol⁻¹K), and T denotes the temperature in kelvin (29,30).

The equilibrium isotherm parameters and their corresponding correlation coefficients for the adsorption processes are provided in Table 3. The high values of the correlation coefficients (R^2) across the three isotherm models indicate distinct characteristics of the adsorption processes at different stages, thereby influencing the final mechanism. This suggests that the adsorption of methyl orange is a complex process.

Langmuir Isotherm Model: The Langmuir isotherm model posits that adsorption occurs as a monolayer on a finite number of surface sites without the adsorbate moving within the surface plane (31). For this study, the dimensionless (R_L) obtained for the

entire system is less than 1, indicating favorable adsorption.

Freundlich Model: R^2 values for the adsorption processes were high, suggesting a potentially heterogeneous adsorbent surface and the likelihood of multilayer adsorption. The n values (Freundlich constant) above 1 for all adsorption processes indicate favorable adsorption (32).

Temkin Model: The Temkin isotherm was used to explore the energy relationship between adsorbate and adsorbent interactions. High R^2 values from the isotherm equation plots indicated model suitability. This suggests that the energy associated with methyl orange adsorption decreases linearly with coverage, in line with the Temkin model's assumption (33). This hints at adsorbate-adsorbate interactions in the studied adsorption processes.

The b_T constant, linked to adsorption energy, ranged from 1.99 to 3.92 kJ/mol. This range is lower than the 8–16 kJ/mol range associated with bonding energy in ion-exchange mechanisms. This implies that methyl orange and adsorbent interaction might involve physisorption rather than ion exchange. However, this doesn't rule out the possibility of chemisorption, as not all chemical interactions follow ion-exchange mechanisms. The alignment with the pseudo-second-order rate model suggests a role for chemisorption, particularly in the rate-determining step (34).

Table 3: Adsorption isotherm parameters.

Isotherm	Parameters	MO	MO+MB	MO+CR	MO+MB+CR
Langmuir	q_m (mg/g)	48.54	47.17	42.19	47.85
	K_L (L/mg)	0.11	0.18	0.05	0.07
	R_L	0.31	0.22	0.50	0.42
	R^2	0.9274	0.8979	0.9691	0.9491
Freundlich	K_F	6.83	7.94	4.32	3.23
	(mg/g)(L/mg) ^{1/n}				
	n	2.22	2.27	2.22	2.00
	$1/n$	0.45	0.44	0.45	0.0.50
Temkin	R^2	0.9935	0.9909	0.9886	0.9940
	A_T	16.35	16.77	11.70	15.15
	B_T	2.52	1.99	3.92	3.27
	R^2	0.8923	0.8698	0.9540	0.9170

3.7 Impact of Temperature and Thermodynamics

The influence of temperature on the adsorption process of Acid Blue 161 was investigated through batch adsorption experiments conducted at four distinct temperatures, 303 K, 313 K, 323 K, and 333 K, for both single and mixed systems. The outcomes are presented graphically in Figure 8. The figure clearly demonstrates that the adsorbent's adsorption capacity (q_e) for methyl orange dye decreases with

increasing temperature in the single, binary, and ternary systems. This suggests that elevating the temperature reduces the adsorption of methyl orange dye, indicating that the adsorption process is more favorable at lower temperatures. Moreover, the rise in temperature likely induced changes in the morphology of the adsorbent, potentially causing destabilization of adsorbed adsorbate molecules (35).

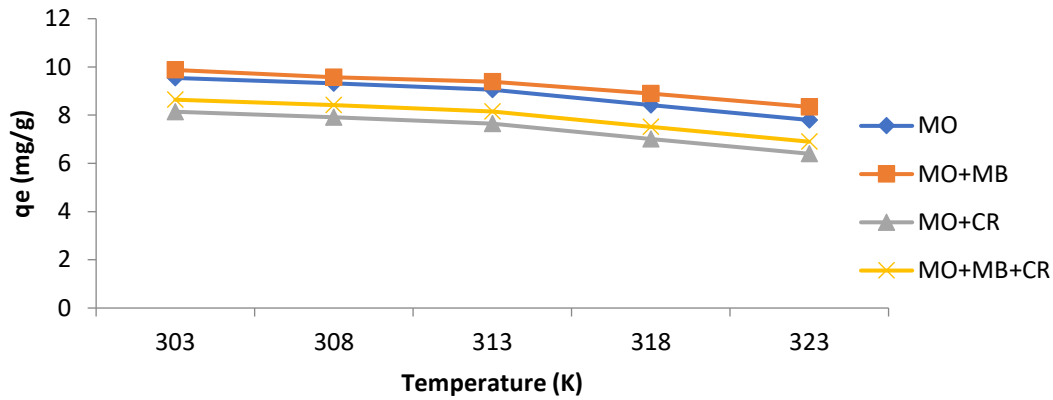


Figure 8: Effect of temperature.

The changes in free energy (ΔG), enthalpy (ΔH), and entropy (ΔS) were assessed as thermodynamic parameters from the batch adsorption results at different temperatures. The following equations were utilized:

$$K_c = \frac{c_{ads}}{c_e} \tag{9}$$

$$\Delta G = \Delta H - T\Delta S \tag{10}$$

$$\ln K_c = \frac{\Delta S}{R} - \frac{\Delta H}{RT} \tag{11}$$

In these equations, K_c represents the sorption distribution coefficient, ΔG (kJ/mol) stands for the

free energy of adsorption, T (Kelvin) denotes the absolute temperature, R is the universal gas constant, ΔH (kJ/mol) indicates the heat of adsorption, and ΔS (J/K) signifies the entropy change (36).

Figure 9 illustrates the $\ln K_c$ versus $1/T$ plots for methyl orange adsorption in both single and mixed systems at various temperatures. Enthalpy change (ΔH) and entropy change (ΔS) were determined from slopes and intercepts, while free energy changes (ΔG) were assessed using equation 9. All corresponding values are presented in Table 4.

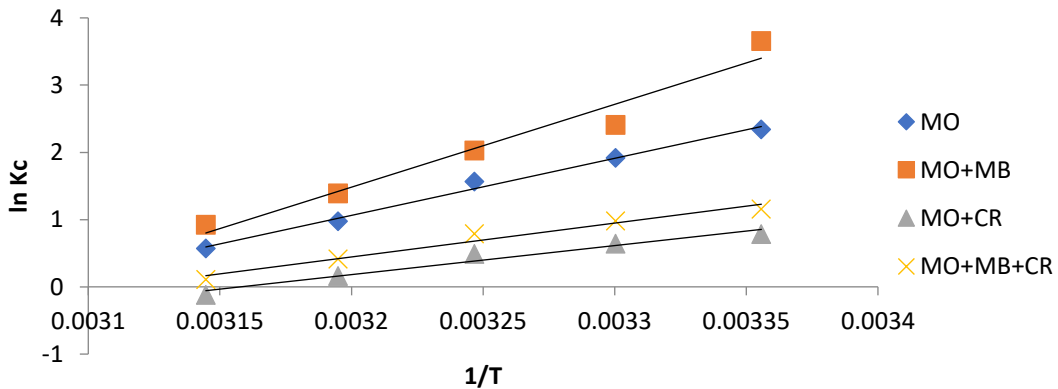


Figure 9: Thermodynamic plot.

Table 4: Thermodynamic parameters.

System	- ΔH (kJ/mol)	- ΔS (J/K)	- ΔG (kJ/mol)				
			303 K	308 K	313 K	318 K	323 K
MO	54.63	159.42	6.453	5.656	4.861	4.066	3.271
MO+MB	12.62	382.62	10.415	8.542	6.632	4.722	2.812
MO+CR	17.94	054.43	2.186	1.926	1.666	1.406	1.146
MO+MO+MB	22.58	064.55	3.190	2.870	2.550	2.230	1.910

The Gibbs free energy change (ΔG) for dye adsorption in all examined systems demonstrates a negative value, indicating spontaneous and thermodynamically feasible sorption processes (37). With decreasing temperatures, the feasibility of adsorption also increased in each system. Likewise,

the adsorption processes in all systems were exothermic, as evidenced by their negative enthalpy values. This implies that heat was released during the interaction between the dye and the adsorbent surface. The entropy change (ΔS) exhibited negativities for all systems (Table 3). Negative ΔS

values suggest reduced randomness at the adsorbent and dye(s) interface in both single and mixture systems.

4. CONCLUSION

This investigation shows the effectiveness of gingerbread plum seed shell-activated carbon in removing methyl orange from aqueous solutions, encompassing single, binary, and ternary adsorbate systems. Various experimental parameters, including contact time, initial adsorbate concentration, adsorbent dosage, solution pH, and reaction temperature, were explored. The adsorption processes adhere to pseudo-second-order kinetics, while the Freundlich, Langmuir, and Temkin isotherm models exhibit high correlation coefficients (>0.9) in certain cases, indicating distinct characteristics at different stages that influence the final mechanism. All adsorption processes were confirmed to be spontaneous and thermodynamically viable, as evidenced by negative ΔG values. Additionally, they were exothermic in nature, leading to reduced randomness with negative ΔS values.

5. REFERENCES

- Vatanpour V, Karimi H, Imanian Ghazanlou S, Mansourpanah Y, Ganjali MR, Badii A, et al. Anti-fouling polyethersulfone nanofiltration membranes aided by amine-functionalized boron nitride nanosheets with improved separation performance. *J Environ Chem Eng* [Internet]. 2020 Dec 1;8(6):104454. Available from: [<URL>](#).
- Khan MA, Khan MI, Zafar S. Removal of different anionic dyes from aqueous solution by anion exchange membrane. *Membr Water Treat* [Internet]. 2017 May 25;8(3):259–77. Available from: [<URL>](#).
- Bhatia D, Sharma NR, Singh J, Kanwar RS. Biological methods for textile dye removal from wastewater: A review. *Crit Rev Environ Sci Technol* [Internet]. 2017 Oct 2;47(19):1836–76. Available from: [<URL>](#).
- Ragupathy S, Manikandan V, Devanesan S, Ahmed M, Ramamoorthy M, Priyadharsan A. Enhanced sun light driven photocatalytic activity of Co doped SnO₂ loaded corn cob activated carbon for methylene blue dye degradation. *Chemosphere* [Internet]. 2022 May 1;295:133848. Available from: [<URL>](#).
- Bulgariu L, Escudero LB, Bello OS, Iqbal M, Nisar J, Adegoke KA, et al. The utilization of leaf-based adsorbents for dyes removal: A review. *J Mol Liq* [Internet]. 2019 Feb 15;276:728–47. Available from: [<URL>](#).
- George A, Magimai Antoni Raj D, Venci X, Dhayal Raj A, Albert Irudayaraj A, Josephine RL, et al. Photocatalytic effect of CuO nanoparticles flower-like 3D nanostructures under visible light irradiation with the degradation of methylene blue (MB) dye for environmental application. *Environ Res* [Internet]. 2022 Jan 1;203:111880. Available from: [<URL>](#).
- Noreen S, Bhatti HN, Nausheen S, Sadaf S, Ashfaq M. Batch and fixed bed adsorption study for the removal of Drimarine Black CL-B dye from aqueous solution using a lignocellulosic waste: A cost affective adsorbent. *Ind Crops Prod* [Internet]. 2013 Oct 1;50:568–79. Available from: [<URL>](#).
- Nausheen S, Bhatti HN, Sadaf S, Farrukh Z, Noreen S. Equilibrium Modeling of Removal of Drimarine Yellow HF-3GL Dye from Aqueous Solutions by Low Cost Agricultural Waste. *J Chem Soc Pakistan* [Internet]. 2014;36(1):177–90. Available from: [<URL>](#).
- Sadaf S, Bhatti HN, Nausheen S, Noreen S. Potential Use of Low-Cost Lignocellulosic Waste for the Removal of Direct Violet 51 from Aqueous Solution: Equilibrium and Breakthrough Studies. *Arch Environ Contam Toxicol* [Internet]. 2014 May 28;66(4):557–71. Available from: [<URL>](#).
- Das P, Debnath A. Reactive orange 12 dye adsorption onto magnetically separable CaFe₂O₄ nanoparticles synthesized by simple chemical route: kinetic, isotherm and neural network modeling. *Water Pract Technol* [Internet]. 2021 Oct 1;16(4):1141–58. Available from: [<URL>](#).
- Das P, Debnath P, Debnath A. Enhanced sono-assisted adsorptive uptake of malachite green dye onto magnesium ferrite nanoparticles: Kinetic, isotherm and cost analysis. *Environ Nanotechnology, Monit Manag* [Internet]. 2021 Dec 1;16:100506. Available from: [<URL>](#).
- Das P, Nisa S, Debnath A, Saha B. Enhanced adsorptive removal of toxic anionic dye by novel magnetic polymeric nanocomposite: optimization of process parameters. *J Dispers Sci Technol* [Internet]. 2022 May 2;43(6):880–95. Available from: [<URL>](#).
- Deb A, Debnath A, Saha B. Sono-assisted enhanced adsorption of eriochrome Black-T dye onto a novel polymeric nanocomposite: kinetic, isotherm, and response surface methodology optimization. *J Dispers Sci Technol* [Internet]. 2021 Aug 31;42(11):1579–92. Available from: [<URL>](#).
- Olajire AA, Giwa AA, Bello IA. Competitive adsorption of dye species from aqueous solution onto melon husk in single and ternary dye systems. *Int J Environ Sci Technol* [Internet]. 2015 Mar 9;12(3):939–50. Available from: [<URL>](#).
- Giwa AA, Oladipo MA, Abdulsalam KA. Adsorption of Rhodamine B from single, binary and ternary dye systems using sawdust of *Parkia biglobosa* as adsorbent: isotherm, kinetics and thermodynamics studies. *J Chem Pharm Res* [Internet]. 2015;7(2):454–75. Available from: [<URL>](#).
- Husaini M, Usman B, Ibrahim MB. Adsorption Studies of Methylene Blue using Activated Carbon Derived from Sweet Detar Seed Shell. *ChemSearch J* [Internet]. 2023 Jul 27;14(1):21–32. Available from: [<URL>](#).
- Ibrahim MB, Umar A. Adsorption thermodynamics of some basic dyes uptake from aqueous solution using *Albizia lebbek* shells. *ChemSearch J* [Internet]. 2016 Jul 27;7(1):43–51. Available from: [<URL>](#).
- Moharm AE, El Naeem GA, Soliman HMA, Abd-Elhamid AI, El-Bardan AA, Kasseem TS, et al. Fabrication and Characterization of Effective Biochar Biosorbent Derived from Agricultural Waste to Remove Cationic Dyes from Wastewater. *Polymers (Basel)* [Internet]. 2022 Jun 26;14(13):2587. Available from: [<URL>](#).
- Husaini M, Bashir Ibrahim M. Investigation of Inhibition Potential Effect of Organic Compound for the Corrosivity of Phosphoric Acid on Aluminium. *Int J Eng Manuf* [Internet]. 2020 Feb 8;10(1):41–53. Available from: [<URL>](#).
- Husaini M, Bashir Ibrahim M. Thermodynamic and Kinetic Study on the Corrosion of Aluminium in Hydrochloric Acid

using Benzaldehyde as Corrosion Inhibitor. *Int J Eng Manuf* [Internet]. 2019 Nov 8;9(6):53–64. Available from: [<URL>](#).

21. Ekpete OA, Horsfall MJ. Preparation and Characterization of Activated Carbon derived from Fluted Pumpkin Stem Waste (*Telfairia occidentalis* Hook F). *Res J Chem Sci*. 2011;1(3):10–7.

22. Ibrahim MB. Comparative analysis of the thermodynamics and adsorption isotherms for the adsorption of some metal ions from aqueous solution using sawdust material. *Int J Res Chem Environ* [Internet]. 2011;1(1):179–85. Available from: [<URL>](#).

23. Saranya KS, Vellora Thekkae Padil V, Senan C, Pilankatta R, Saranya K, George B, et al. Green Synthesis of High Temperature Stable Anatase Titanium Dioxide Nanoparticles Using Gum Kondagogu: Characterization and Solar Driven Photocatalytic Degradation of Organic Dye. *Nanomaterials* [Internet]. 2018 Dec 4;8(12):1002. Available from: [<URL>](#).

24. Kim JR, Kan E. Heterogeneous photo-Fenton oxidation of methylene blue using CdS-carbon nanotube/TiO₂ under visible light. *J Ind Eng Chem* [Internet]. 2015 Jan 25;21:644–52. Available from: [<URL>](#).

25. Husaini M, Usman B, Ibrahim MB. Competitive Adsorption of Congo red Dye from Aqueous Solution onto Activated Carbon Derived from Black Plum Seed Shell in Single and Multicomponent System. *African J Manag Eng Technol Cit* [Internet]. 2023;2023(2):76–89. Available from: [<URL>](#).

26. Giwa ARA, Abdulsalam KA, Wewers F, Oladipo MA. Biosorption of Acid Dye in Single and Multidye Systems onto Sawdust of Locust Bean (*Parkia biglobosa*) Tree. *J Chem* [Internet]. 2016;2016:6436039. Available from: [<URL>](#).

27. Husaini M, Usman B, Ibrahim MB. Modeling and Equilibrium Studies for the Adsorption of Congo red Using Detarium microcarpum Seed Shell Activated Carbon | *Applied Journal of Environmental Engineering Science*. *Appl J Environ Eng Sci* [Internet]. 2023 [cited 2024 Feb 28];9(3):147–62. Available from: [<URL>](#).

28. Ho Y. Review of second-order models for adsorption

systems. *J Hazard Mater* [Internet]. 2006 Aug 25;136(3):681–9. Available from: [<URL>](#).

29. Langmuir I. The adsorption of gases on plane surfaces of glass, mica and platinum. *J Am Chem Soc* [Internet]. 1918 Sep 1;40(9):1361–403. Available from: [<URL>](#).

30. Freundlich H. Über die Adsorption in Lösungen. *Zeitschrift für Phys Chemie* [Internet]. 1907 Oct 1;57U(1):385–470. Available from: [<URL>](#).

31. Temkin MI. Kinetics of ammonia synthesis on promoted iron catalysts. *Acta Physiochim* [Internet]. 1940;12:327–56. Available from: [<URL>](#).

32. Sekar M, Sakthi V, Rengaraj S. Kinetics and equilibrium adsorption study of lead(II) onto activated carbon prepared from coconut shell. *J Colloid Interface Sci* [Internet]. 2004 Nov 15;279(2):307–13. Available from: [<URL>](#).

33. Juang LC, Wang CC, Lee CK, Hsu TC. Dyes adsorption onto organoclay and MCM-41. *J Environ Eng Manag* [Internet]. 2007;17(1):29–38. Available from: [<URL>](#).

34. Giwa A, Olajire A, Adeoye D, Ajibola T. Kinetics and Thermodynamics of Ternary Dye System Adsorption on to Melon (*Citrillus lanatus*) Seed Husk. *Am Chem Sci J* [Internet]. 2015 Jan 10;7(1):7–25. Available from: [<URL>](#).

35. Tian W, Lin J, Zhang H, Duan X, Wang H, Sun H, et al. Kinetics and mechanism of synergistic adsorption and persulfate activation by N-doped porous carbon for antibiotics removals in single and binary solutions. *J Hazard Mater* [Internet]. 2022 Feb 5;423:127083. Available from: [<URL>](#).

36. Husaini M, Usman B, Ibrahim MB. Inhibitive Effect of Glutaraldehyde on the Corrosion of Aluminum in Hydrochloric Acid Solution. *J Sci Technol* [Internet]. 2019 Dec 30;11(2):8–16. Available from: [<URL>](#).

37. Husaini M, Usman B, Ibrahim MA, Ibrahim MB. Effect of Aniline as Corrosion inhibitor on the Corrosion of Aluminium in Hydrochloric Acid Solution. *Res J Chem Environ*. 2020;24(2):99–106.



Large-scale Production of Few-Layer Reduced Graphene Oxide by the Rapid Thermal Reduction of Graphene Oxide and Its Structural Characterization

Osman Eksik^{1*} 

¹Gebze Technical University, Institute of Nanotechnology, Kocaeli, 41400, Turkey

Abstract: Graphene, a carbon allotrope, is a two-dimensional honeycomb of carbon atoms. Although graphene is a thin material, it is the strongest material known on Earth thanks to the strong carbon bonds in its structure. It is stated that the strength of these carbon bonds in graphene is about 100 times stronger than steel. In this study, graphite was first converted into graphene oxide (GO) by the Improved Hummers method, which is one of the methods suitable for large-scale production. Reduced graphene oxide (RGO) was obtained from the synthesized GOs by thermal reduction. TGA, FTIR, XRD, XPS, Raman, BET, and SEM analyses were used to characterize GO produced using the improved Hummers method and RGO reduced by thermal methods. TGA measurements show that RGO produced using the thermal approach had a lower mass loss than graphite oxidized using the improved Hummers process. This shows that the GO sample prepared using the improved Hummers approach contains a considerable number of distinct oxygen-containing groups. The novelty of the modified Hummers' method lies in its enhanced efficiency in producing graphene oxide through reduced thermal reaction times and improved scalability compared to the original approach in the literature. The C:O ratio of the GO and RGO samples was determined by XPS to be 1.88 and 11.17, respectively. The I_D/I_G ratio obtained by Raman analysis was 0.973. In addition, RGO's BET surface area was discovered to be $543.6 \text{ m}^2 \text{ g}^{-1}$. These findings demonstrated that graphite was successfully oxidized by an improved Hummers method, and the resulting GO was thermally converted to few-layer RGO.

Keywords: Graphene, Reduced Graphene Oxide, Thermal Reduction, Graphene Oxide, Structural Characterization

Submitted: July 15, 2023. **Accepted:** January 3, 2024.

Cite this: Eksik O. Large-scale Production of Few-Layer Reduced Graphene Oxide by the Rapid Thermal Reduction of Graphene Oxide and Its Structural Characterization. JOTCSA. 2024;11(2):665-xxx.

DOI: <https://doi.org/10.18596/jotcsa.1327988>

***Corresponding author.** E-mail: oeksik@gtu.edu.tr

1. INTRODUCTION

The arrangement of carbon atoms in a hexagonal structure in a single plane gives graphene, an allotrope of carbon, its two-dimensional structure. Graphene, a new two-dimensional material with unique electrical and structural properties, has received a lot of interest. This structure of graphene gives it extraordinary properties. The specific surface area of graphene is extraordinarily high relative to its mass ratio (theoretically, $2650 \text{ m}^2 \text{ g}^{-1}$), a very high thermal conductivity ($5300 \text{ Wm}^{-1} \text{ K}^{-1}$, ten times higher than copper), and an optical transmittance of 98%. Another interesting property of graphene is that it is flexible and very durable. Due to a bond shape called sp^2

hybridization, it is as resistant to forces in certain directions as a diamond and has a high Young's modulus (1150 GPa). Due to these extraordinary properties of graphene, it enables applications in different fields of use (1-6). Today, intensive scientific research on graphene is being carried out to improve the application areas and production methods of graphene in daily life (7-8). However, there are still difficulties in producing graphene at a low cost and in large quantities. The oxidation of graphite is one of the most promising processes for producing graphene. The first example of graphene oxide synthesis was Brodie's discovery of graphite structure in 1859. One of his reactions was adding potassium chlorate (KClO_3) to a graphite slurry in strong nitric acid (HNO_3). (HNO_3) (9). According to

Brodie's findings, the compound that is produced contains carbon, hydrogen, and oxygen in increasing proportions as the overall weight of graphite increases. With a successful oxidizer treatment, he discovered that the oxygen concentration increased to the limit value after four reactions. Brodie found that this material could be dispersed in pure or normal water but not in acidic media. This led him to define the material as "graphite acid". Staudenmaier improved upon Brodie's oxidation of graphite in 1898 by gradually adding potassium chlorate (KClO_3) to fuming nitric acid (HNO_3) and concentrated sulfuric acid (H_2SO_4). (10). Later, Hofmann synthesized graphene oxide using concentrated nitric acid (HNO_3) instead of the fuming nitric acid used in Staudenmaier and Brodie's method (10). About 60 years after Staudenmaier, to achieve the same degree of oxidation, Hummers came up with a technique that involved the reaction of graphite with a combination of potassium permanganate (KMnO_4) and strong sulfuric acid (H_2SO_4) (10). The Brodie, Staudenmaier, and Hofmann approaches generally used KClO_3 , concentrated HNO_3 , and H_2SO_4 . Nitric acid is a widely used oxidizer, and its strong interactions with aromatic carbon surfaces, including carbon nanotubes, are known. The reaction produces numerous oxygen-containing groups, including carboxyls, lactones, and ketones. Nitric acid-induced oxidation results in the emission of NO_2 and/or N_2O_4 gases (11). At the same time, KClO_3 is also a strong oxidizer. Potassium permanganate (KMnO_4) and sulfuric acid (H_2SO_4) are used in the Hummers technique. Potassium permanganate is a strong oxidizer, and this property makes the GO structure hydrophilic by containing different oxygen groups (carboxyl, hydroxyl, epoxy, etc.) on the surface of activated graphene oxide (12).

A few-layer RGO can be produced by chemical and heat reduction of GO. Many thermal and chemical approaches have been proposed for the reduction of GO. The thermal reduction methods used in graphene synthesis are thermal annealing, microwave, and photoreduction (13-14). Rapid GO heating in thermal annealing causes CO and CO_2 gases to develop between the graphene layers and rapidly expand. This process is carried out at 1050 °C, and at this temperature, the bulk graphene oxide layers separate from each other to form graphene sheets (10).

Modified Hummers' method for graphene oxide and following thermal reduction offers a relatively efficient and scalable approach for producing graphene nanoplatelets compared to other methods. The disadvantages of Modified Hummers' method of using chemicals, including the use of strong acids and harsh chemicals, pose environmental and safety risks. Another method used in graphene production is chemical reduction. The chemical reduction method mainly consists of chemical separator reduction, photocatalytic reduction, and electrochemical reduction (15-16). The modified

method achieves a more controlled and reproducible synthesis of graphene oxide through alterations in reaction conditions and parameters, such as temperature, time, and precursor materials.

In this study, naturally occurring, inexpensive graphite powder was used as a starting material for the oxidation of graphite, and graphite was oxidized using an improved Hummers method. A few layers of RGO were produced by the thermal reduction of GO.

2. MATERIALS AND METHODS

2.1 Spectroscopic and Microscopic Characterization of GO and rGO

Scanning electron microscopy (SEM; JEOL JEM 1011), X-ray diffraction analysis with the Bruker D8 Discover X-Ray diffraction system, XPS analysis with the Thermo K-Alpha X-Ray Photoelectron Spectrometer, Raman analysis with the Renishaw Invia instrument, surface area analysis with the Micromeritics ASAP 2020 HD accelerated surface area and porosimetry analyzer, FTIR analysis with the Thermo Scientific iS10, and TGA analysis with the TA Instruments were used.

2.2. GO Synthesis Using an Improved Hummers Method

In the improved Hummers method, the oxidation of graphite is carried out in two stages. After the graphite pre-oxidation process, it undergoes a second oxidation process where it fully oxidizes and becomes graphite oxide (12). In the pre-oxidation step, graphite powder was treated with strong oxidizing agents such as H_2SO_4 , P_2O_5 , and $\text{K}_2\text{S}_2\text{O}_8$. In this step, 98% H_2SO_4 (25 mL) was heated to 90°C in an oil bath. Then, 5 g of $\text{K}_2\text{S}_2\text{O}_8$ and 5 g of P_2O_5 were added. After the reaction temperature was reduced to 80°C, 3 g of graphite powder was slowly added to the mixture. Since outgassing was observed at this stage, adding graphite powder to the hot mixture was carried out very carefully and slowly. The heating process was terminated after stirring the reaction mixture at 80°C for 5 hours. The mixture was added to deionized water, left to stand on its own for one night, and filtered using a vacuum filter. In order to remove the acidity of the solid sample obtained, it was washed with deionized water until the pH value was neutral. Finally, the synthesized pre-oxidized graphite structure was allowed to dry at room temperature for one day. The pre-oxidized graphite is oxidized to graphene oxide with the help of KMnO_4 . Since the reactions in this process are highly exothermic, all processes were carried out in an ice bath at a temperature not exceeding 10°C. Pre-oxidized graphite powder was added to 98% H_2SO_4 (240 mL) and kept in the ice bath with stirring. Then KMnO_4 (30g) was added to the mixture and dissolved. During this process, care was taken not to exceed 10°C. After this step was completed, the mixture's temperature was raised to 35 °C and stirring was continued for 4 hours. In all these processes, it is critical that the temperature not exceed 50°C. After this time, 500 mL of

deionized water was added to the mixture. The mixture was stirred for 1 hour, and 40 mL of 35% H₂O₂ was added dropwise to complete the oxidation process. The final mixture was kept at room temperature for one day and then subjected to filtration. The resulting product was washed with a 10% HCl solution to remove metal ions. In the last step, the mixture was washed with acetone until the pH value was neutral. The graphene oxide obtained was dried in an oven at 60°C.

2.3. RGO Synthesis by Thermal Reduction

Graphene oxide can be thermally reduced to yield monolayer and multilayer graphene. In the thermal reduction technique, the GO sample was placed in the tube furnace system at 1050°C under argon gas flow for a short time (45 seconds), and RGO was obtained by thermal shock reduction. During heat reduction, the functional groups in GO oxide containing oxygen (carboxyl, epoxy, hydroxyl, etc.) are removed from the structure. The CO and CO₂ gases formed between the layers undergo thermal exfoliation, creating high pressure and expanding. These processes are shown schematically in Figure 1.

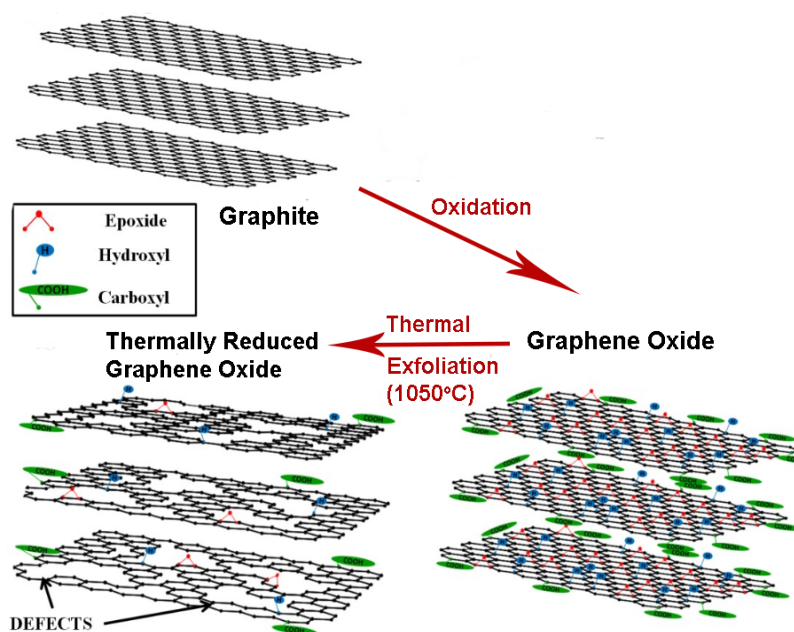


Figure 1: Thermal reduction of GO

3. RESULTS AND DISCUSSION

3.1. Graphite, GO, and RGO TGA Analysis

Figure 2 shows the thermal properties of graphite, GO, and RGO by TGA analysis. When the thermal properties of graphite were examined, no weight change was observed in graphite due to temperature change (Figure 2). On the other hand, GO obtained using the improved Hummers method showed three-stage degradation. In the first stage, between 50 and 150 °C, graphene oxide lost mass due to moisture loss (17). The second stage is

between 150 °C and 400 °C. The mass loss here can be explained as removing oxygen-containing groups such as hydroxyl, epoxy, and carboxyl in the GO structure from the graphene oxide structure. In the third stage, at temperatures above 400 °C, mass loss occurred due to the degradation of unstable carbon structures in the nitrogen gas environment. The RGO obtained using the thermal reduction method lost 25% of its weight. This is due to the removal of oxygen-containing groups remaining in the structure of RGO (17-18).

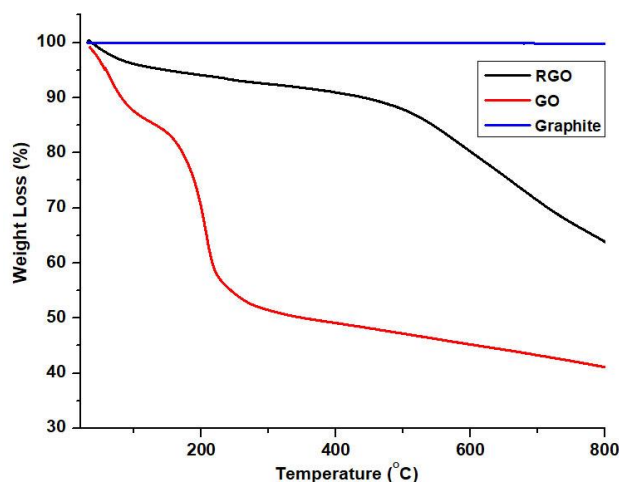


Figure 2: The TGA outcomes for graphite, GO, and RGO

3.2. Graphite and GO, Analyzed by X-Ray Diffraction

Figure 3 shows the XRD analysis of graphite and GO, respectively. Figure 3 shows a peak for graphite at $2\theta = 26.5^\circ$; the peak value of graphene oxide appears as $2\theta = 10.3^\circ$. In line with the values from the literature, these peaks are known to be 26.48° for graphite and 10.90° for graphene oxide,

respectively (19). When the obtained data are compared with the literature data, it is seen that the oxidation process was successful. Considering the interlayer distances, 0.3 nm is for pure graphite, and 0.83 nm is for graphene oxide. The increase in the distance between graphene oxide layers due to the oxidation process indicates that the oxidation process was successful.

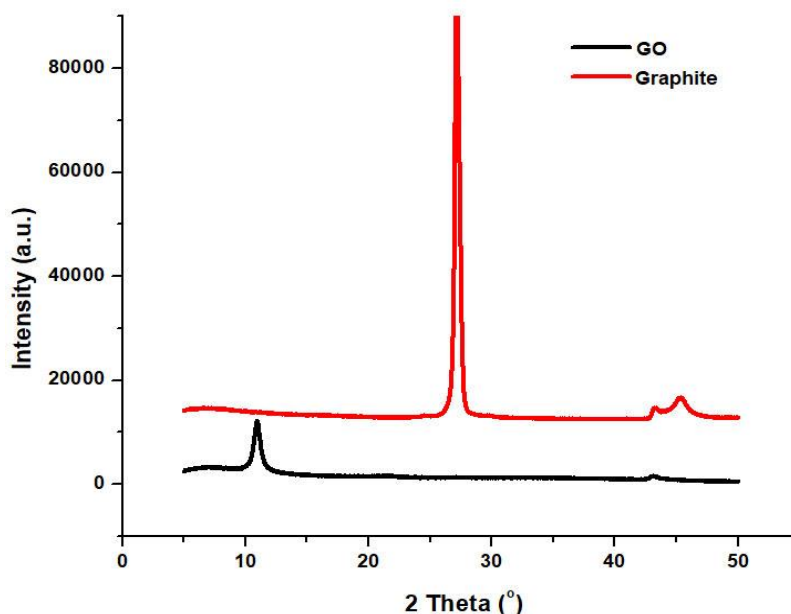


Figure 3: XRD spectrum of a graphite and GO sample

3.3. FTIR Analysis of Graphite, GO, and Reduced Graphene

FTIR spectroscopy analysis was performed to determine the functional groups such as epoxy, carboxyl, and hydroxy that are expected to be included in the structure as a result of the oxidation of graphite. As seen in Figure 4, OH stress vibration was measured at 3106 cm^{-1} , C=O stress vibration at 1714 cm^{-1} , C=C stress vibration at 1602 cm^{-1} , and C-O stress vibration at 1020 cm^{-1}

¹. As a result of the literature research, OH stress vibration was found to be 3191 cm^{-1} , C=O stress vibration 1718 cm^{-1} , C=C stress vibration $1600\text{--}1660\text{ cm}^{-1}$, and C-O stress vibration 1040 cm^{-1} (20). The graphite sample does not have any of these vibrations. These functional groups included in the structure as a result of the oxidation of graphite indicate that graphene oxide has been successfully synthesized.

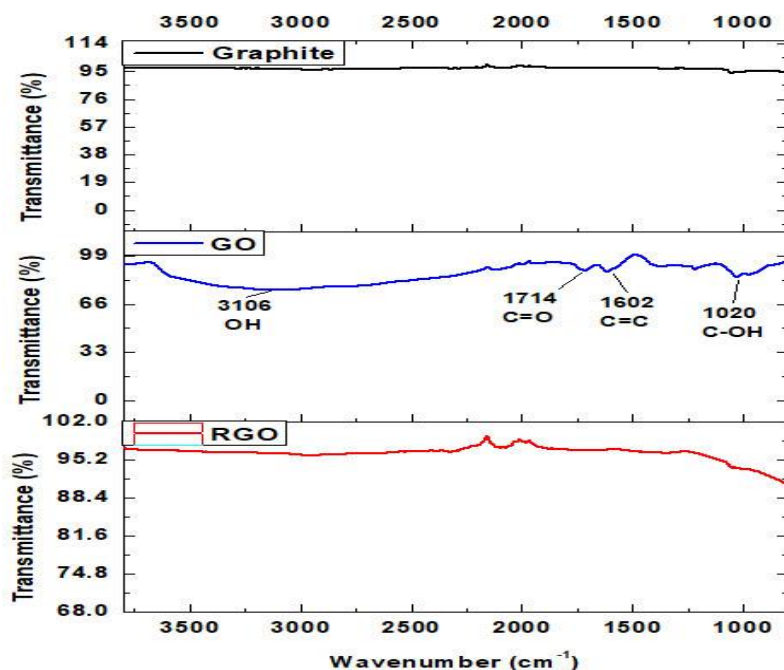


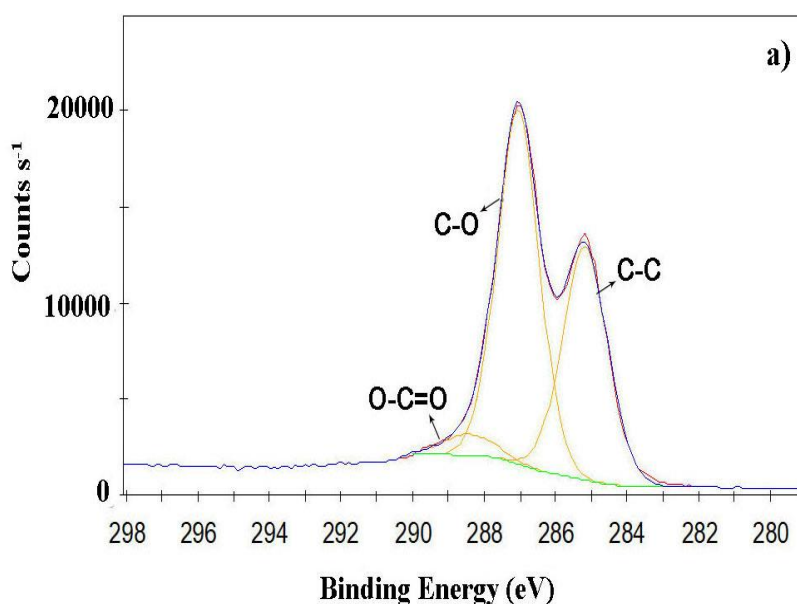
Figure 4: FTIR spectrum of graphite, GO, and RGO

The effect of thermal reduction was also investigated under the conditions studied. As can be seen in Figure 4, the characteristic peaks of graphene oxide disappear when the thermal method is used as a reductant (21).

3.4. XPS Analysis of GO and RGO

The results of the XPS analysis of GO and RGO are given in Figures 5. GO and RGO C1s XPS spectra are displayed in Figure 5. C-C peak at 284.7 eV, C-O peak at 286 eV, and O-C=O peak at 288.8 eV is all well visible in the C1s spectra of the GO sample (22). A large peak for RGO was found at 284.7 eV, corresponding to graphitic carbon, which makes up 69.1% of RGO and 23.7% of GO. The C-O atom,

which makes up 22.79% of the RGO structure, is the source of the peak at 286 eV. This percentage is less than the GO percentage (37.6%). In RGO (288.5 eV), another oxygen-containing group, O-C=O, was found in extremely low amounts compared to GO. The percentage of carbon and oxygen elements in graphene oxide composition obtained as a result of XPS analysis is given in Table 1. The C:O ratio of GO was determined as 1.88. This ratio indicates that the graphene oxide process subjected the graphene layers to strong oxidation. Oxygenated functional groups are removed from the GO structure as a result of reduction by the thermal method. The C:O ratio of RGO was found to be 11.17.



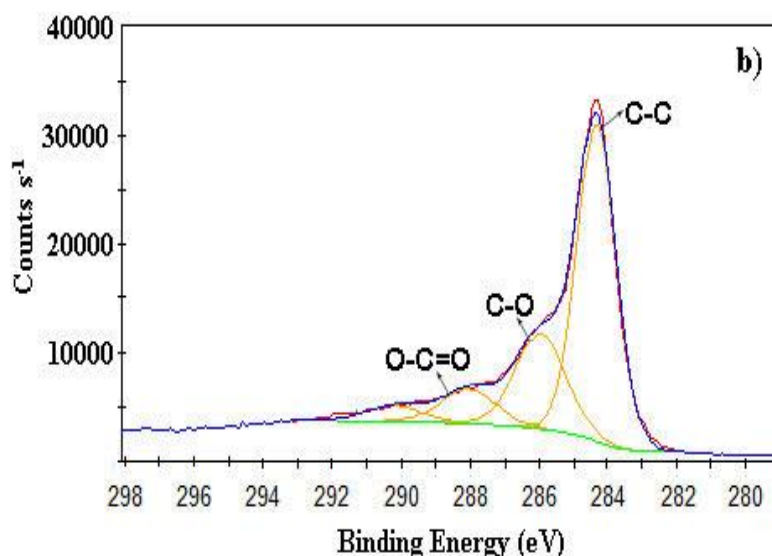


Figure 5: C1s. XPS spectra of GO (a), RGO (b)

Table 1: C:O ratios of GO and RGO samples according to XPS analysis data

Element	GO	RGO
Atomic C, %	65.3	91.8
Atomic O, %	34.7	8.3
C:O ratio	1.88	11.2

3.5. Raman Analysis of RGO Synthesized by the Thermal Reduction Method

Following the chemical oxidation of graphite, RGO was obtained by removing the oxygenated groups from GO by thermal reduction (thermal exfoliation). The crystal structure and properties of the obtained RGO were investigated by Raman spectroscopy. As expected in the Raman pattern of graphene, the D peak is observed at 1360 cm^{-1} , the G peak at 1580 cm^{-1} , and the 2D peak at 2675

cm^{-1} (Figure 6). The intensity of the D band (I_D) in the Raman pattern shows the irregularities in the structure, the intensity of the G band (I_G) shows the regular structures in the structure, and the 2D band shows the characteristic peak of graphene. The D, G, and 2D peak values of the graphene synthesized in the study are consistent with the literature (23-24).

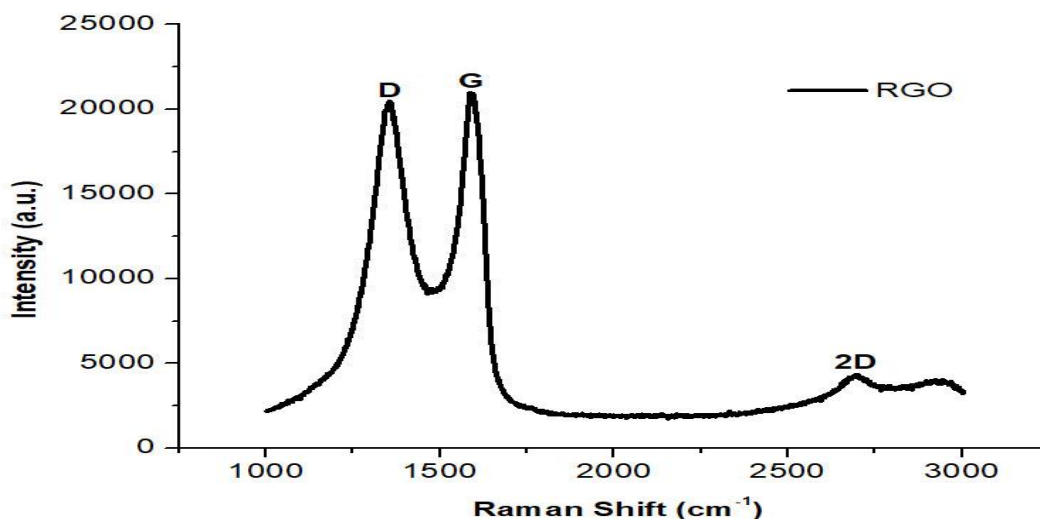


Figure 6: Raman spectra of RGO

3.6. SEM Analysis of Graphite, GO, and RGO

The surface properties of graphite, GO, and RGO samples were investigated by SEM analysis (Figure 7). From the SEM images, oxygenated groups on GO were removed as a result of the thermal

reduction reaction, resulting in less layered, wrinkled RGO structures (25). SEM images of GO often depict irregular, crumpled, or wavy sheet-like structures with wrinkles and folds. GO layers are generally thicker due to the presence of oxygen-

containing groups and water molecules trapped between the layers, leading to a more expanded and layered structure than pristine graphene. SEM images of rGO display smoother, more continuous, and less corrugated sheets than GO. rGO tends to

have thinner layers than GO due to removing oxygen groups and water molecules, leading to a more compact and less layered structure.

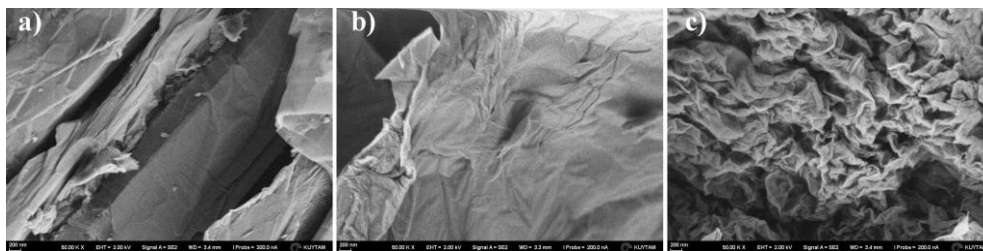


Figure 7: SEM images of graphite (a), GO (b), RGO (c)

3.7. Evaluation of BET Results

The surface area analysis of graphene samples synthesized by the thermal reduction method was

performed by the Brunauer, Emmet, and Teller (BET) method. Table 2 displays the outcomes of the BET study of RGO.

Table 2: BET analysis results for RGO

Element	RGO
BET surface area (m ² /g)	543.64
Volume (cc/g)	1.005
Pore diameter (4V/S Angstrom)	90.26

As a result of BET analysis of the sample of the graphene study produced by the thermal method, the surface area of graphene was 543.64 m²g⁻¹. The reason for this is that the oxygenated groups are separated more effectively during the production of graphene by thermal inversion of the improved Hummers-GO, forming a more porous structure and providing a high surface area. Reduced graphene oxide (rGO) produced through thermal reduction methods, particularly at high temperatures like 1050 °C, tends to exhibit a higher Brunauer-Emmett-Teller (BET) surface area compared to lower temperature reduction processes and chemical reduction processes. The high temperature facilitates the removal of oxygen-containing functional groups from graphene oxide, resulting in a more extensive restoration of the sp² carbon network, which contributes to a higher surface area.

4. CONCLUSION

This research focused on producing GO and RGO with a few layers from flake graphite. In addition, the characterization methods of GO and RGO were investigated. First of all, graphite was converted into GO by the improved Hummers technique, which is one of the methods suitable for extensive production. The obtained GO samples were reduced using the thermal method. GO and RGO samples were characterized by TGA, XRD, FTIR, XPS, SEM, Raman, and BET analysis. FTIR spectroscopy results indicate the existence of functional groups that include oxygen (OH, C=O, and C-OH) in the synthesized graphene oxide. XRD analysis revealed interlayer distances of 0.32 nm for graphite and 0.85 nm for graphene oxide. These results indicate that the oxidation process

was successful. The results of the XPS spectrum analysis show that the atomic C:O ratios in the chemical structures of GO and RGO are approximately 1.88 and 11.17, respectively. Raman analysis of RGO samples showed that the amount of ordered crystal structure increased. Transparent and wrinkled RGO structures were detected from SEM images. As a result of BET analysis of reduced graphene oxide samples, it was determined that the surface area was approximately 543.64 m²g⁻¹. This indicates that the synthesized RGOs have a few-layered structure. Thermal methods for producing graphene with high amounts and high surface areas can further optimize its properties, making it more cost-effective, scalable, and suitable for various industrial applications. Such as high surface area, graphene can be utilized in supercapacitors and batteries; it can be used as a catalyst support or even as a catalyst itself in various chemical reactions, including hydrogen production, environmental remediation, and organic synthesis; its use in gas sensors, biosensors, and environmental monitoring devices and graphene can be employed in water filtration and desalination processes.

5. CONFLICT OF INTEREST

There are no conflicts that need to be reported.

6. ACKNOWLEDGMENTS

This study was supported by Gebze Technical University BAP Unit Project No. 2022-A-113-04.

7. REFERENCES

1. Geim AK, Novoselov KS. The rise of graphene. *Nat Mater* [Internet]. 2007 [cited 2023 Jul 14];6(3):183–91. Available from: [URL](#)
2. Chen W, Lv G, Hu W, Li D, Chen S, Dai Z. Synthesis and applications of graphene quantum dots: a review. *Nanotechnol Rev* [Internet]. 2018;7(2):157–85. Available from: [URL](#)
3. Coroş M, Pogăcean F, Măgeruşan L, Socaci C, Pruneanu S. A brief overview on synthesis and applications of graphene and graphene-based nanomaterials. *Front Mater Sci* [Internet]. 2019;13(1):23–32. Available from: [URL](#)
4. Afroj S, Tan S, Abdelkader AM, Novoselov KS, Karim N. Highly conductive, scalable, and machine washable graphene-based E-textiles for multifunctional wearable electronic applications. *Adv Funct Mater* [Internet]. 2020;30(23):2000293. Available from: [URL](#)
5. Razaq A, Bibi F, Zheng X, Papadakis R, Jafri SHM, Li H. Review on graphene-, graphene oxide-, reduced graphene oxide-based flexible composites: From fabrication to applications. *Materials (Basel)* [Internet]. 2022 [cited 2023 Jul 14];15(3):1012. Available from: [URL](#)
6. Smaisim GF, Abed AM, Al-Madhhachi H, Hadrawi SK, Al-Khateeb HMM, Kianfar E. Graphene-based important carbon structures and nanomaterials for energy storage applications as chemical capacitors and supercapacitor electrodes: A review. *Bionanoscience* [Internet]. 2023;13(1):219–48. Available from: [URL](#)
7. Vivaldi FM, Dallinger A, Bonini A, Poma N, Sembranti L, Biagini D, et al. Three-dimensional (3D) laser-induced graphene: Structure, properties, and application to chemical sensing. *ACS Appl Mater Interfaces* [Internet]. 2021;13(26):30245–60. Available from: [URL](#)
8. Guo H, Zhao H, Niu H, Ren Y, Fang H, Fang X, et al. Highly thermally conductive 3D printed graphene filled polymer composites for scalable thermal management applications. *ACS Nano* [Internet]. 2021;15(4):6917–28. Available from: [URL](#)
9. Dreyer DR, Todd AD, Bielawski CW. Harnessing the chemistry of graphene oxide. *Chem Soc Rev* [Internet]. 2014 [cited 2023 Jul 14];43(15):5288–301. Available from: [URL](#)
10. Poh HL, Šaněk F, Ambrosi A, Zhao G, Sofer Z, Pumera M. Graphenes prepared by Staudenmaier, Hofmann and Hummers methods with consequent thermal exfoliation exhibit very different electrochemical properties. *Nanoscale* [Internet]. 2012 [cited 2023 Jul 14];4(11):3515–22. Available from: [URL](#)
11. Shahriary L, Athawale AA. Graphene Oxide Synthesized by using Modified Hummers Approach. *Int. J. Energy Environ. Eng.* 2012;2(1):58-63. Available from: [URL](#)
12. Gilje S, Han S, Wang M, Wang KL, Kaner RB. A chemical route to graphene for device applications. *Nano Lett* [Internet]. 2007;7(11):3394–8. Available from: [URL](#)
13. Acik M, Lee G, Mattevi C, Chhowalla M, Cho K, Chabal YJ. Unusual infrared-absorption mechanism in thermally reduced graphene oxide. *Nat Mater* [Internet]. 2010 [cited 2023 Jul 14];9(10):840–5. Available from: [URL](#)
14. Sharma S, Ganguly A, Papakonstantinou P, Miao X, Li M, Hutchison JL, et al. Rapid microwave synthesis of CO tolerant reduced graphene oxide-supported platinum electrocatalysts for oxidation of methanol. *J Phys Chem C Nanomater Interfaces* [Internet]. 2010;114(45):19459–66. Available from: [URL](#)
15. Akhavan O. Photocatalytic reduction of graphene oxides hybridized by ZnO nanoparticles in ethanol. *Carbon N Y* [Internet]. 2011;49(1):11–8. Available from: [URL](#)
16. Wang Z, Zhou X, Zhang J, Boey F, Zhang H. Direct electrochemical reduction of single-layer graphene oxide and subsequent functionalization with glucose oxidase. *J Phys Chem C Nanomater Interfaces* [Internet]. 2009;113(32):14071–5. Available from: [URL](#)
17. Alam SN, Sharma N, Kumar L. Synthesis of graphene oxide (GO) by improved hummers method and its thermal reduction to obtain reduced graphene oxide (rGO). *Graphene* [Internet]. 2017 [cited 2023 Jul 14];06(01):1–18. Available from: [URL](#)
18. Losic D, Farivar F, Yap PL, Karami A. Accounting carbonaceous counterfeits in graphene materials using the thermogravimetric analysis (TGA) approach. *Anal Chem* [Internet]. 2021;93(34):11859–67. Available from: [URL](#)
19. Muzyka R, Kwoka M, Smędowski Ł, Díez N, Gryglewicz G. Oxidation of graphite by different improved Hummers methods. *New Carbon Mater* [Internet]. 2017;32(1):15–20. Available from: [URL](#)
20. Manoratne CH, Rosa SRD, Kottegodda IRM. XRD-HTA, UV Visible, FTIR and SEM interpretation of reduced graphene oxide synthesized from high purity vein graphite. *Mater. Sci. Res. India.* 2017;14(1):19:30. Available from: [URL](#)
21. Oliveira AEF, Braga GB, Tarley CRT, Pereira AC. Thermally reduced graphene oxide: synthesis, studies and characterization. *J Mater Sci* [Internet]. 2018;53(17):12005–15. Available from: [URL](#)
22. Al-Gaashani R, Najjar A, Zakaria Y, Mansour S, Atieh MA. XPS and structural studies of high quality graphene oxide and reduced graphene oxide prepared by different chemical oxidation methods. *Ceram Int* [Internet]. 2019;45(11):14439–48. Available from: [URL](#)
23. Farah S, Farkas A, Madarász J, László K. Comparison of thermally and chemically reduced graphene oxides by thermal analysis and Raman spectroscopy. *J Therm Anal Calorim* [Internet]. 2020;142(1):331–7. Available from: [URL](#)
24. Lee AY, Yang K, Anh ND, Park C, Lee SM, Lee TG, et al. Raman study of D* band in graphene oxide and its correlation with reduction. *Appl Surf Sci* [Internet]. 2021;536(147990):147990. Available from: [URL](#)
25. Saleem H, Haneef M, Abbasi HY. Synthesis route of reduced graphene oxide via thermal reduction of chemically exfoliated graphene oxide. *Mater Chem Phys* [Internet]. 2018;204:1–7. Available from: [URL](#)



Insight into D-galactose Oxidation: Kinetic and Mechanistic Analysis with Imidazolium Fluorochromate

Ashish Tomar^{1*}, Unik Arora¹, Jai Veer Singh²

¹Department of Chemistry, Meerut College, 250001 Meerut (U.P.), India

²Department of Chemistry, Nehru College, Chhibramau-209721, Kannauj (U.P.) India

Abstract: In a 50% (v/v) aqueous acetic acid medium, a study on the oxidation kinetics of D-galactose by imidazolium fluorochromate (IFC) was conducted. The study revealed unit-order dependence on [D-galactose], [IFC], and [perchloric Acid]. The reaction was catalyzed by perchloric acid, and followed a 1:1 stoichiometric ratio. Adding sodium hyperchlorate (VII) salt did not affect the reaction. Polymerization of acrylonitrile was not observed in the oxidation process. The oxidation rates were retarded on adding Mn^{2+} ions in the mixture, and rates increased as the reaction medium's dielectric constant (D) decreased. The observed results follow the Amis and Kirkwood plots $\{\log k_1 \text{ vs. } (1/D) \text{ and } ((D-1/2D+1))\}$. Several thermodynamic variables were determined by analyzing the kinetic data across a temperature range. Arabinose and formic acid were formed as the products of the reaction. A mechanistic path involving the formation of an ester followed by hydride ion transfer was proposed.

Keywords: Oxidation, Kinetics, Mechanism, D-galactose, Imidazolium Fluorochromate

Submitted: November 7, 2023. **Accepted:** February 2, 2024.

Cite this: Tomar A, Arora U, Singh JV. Insight into D-galactose Oxidation: Kinetic and Mechanistic Analysis with Imidazolium Fluorochromate. JOTCSA. 2024;11(2):673-682.

DOI: <https://doi.org/10.18596/jotcsa.1387416>

***Corresponding author.** E-mail: ashisht.chemistry@mcm.ac.in, ashishtomar1983@yahoo.co.in

1. INTRODUCTION

Chromium (VI), in the form of chromate or dichromate, is highly toxic and soluble in water, but generally insoluble in most organic solvents (1). However, sugars and their derivatives can influence chromium chemistry due to their reducing properties (2). It was observed that oxidation process could convert potentially hazardous Cr (VI) into environmentally benign and non-toxic Cr (III)/Cr (IV) oxidation states (3). Therefore, various Cr (VI) complexes like pyridinium chlorochromate (4), tetraethylammonium chlorochromate (5), quinolinium chlorochromate (6), quinolinium fluorochromate (7), pyridinium fluorochromate

(8), and tributylammonium chlorochromate (9) have been developed to oxidize some biologically important organic molecules, including sugars (10). D-galactose, a specific type of reducing sugar, plays an important role as a primary energy source for mammalian infants during their exclusive dependence on milk. The primary origin of galactose is lactose, found in dairy products, which undergoes hydrolysis to form glucose and galactose. Moreover, small amounts of galactose can be found in certain vegetables and fruits. Recent researches have suggested potential therapeutic applications for galactose, including its use in the treatment of diseases like Alzheimer's and nephrotic syndrome (11–15). Given its crucial role in neonates' metabolism and

therapeutic benefits, a study on oxidation kinetics was performed. To control selectivity and over-oxidation of products, imidazolium fluorochromate (IFC) (16,17), a recently developed Cr (VI) complex was used as an oxidant in the reaction. Previous literature studies illustrated that oxidation study of D-galactose with IFC has not been reported yet (17,18). Considering this, the kinetic and mechanistic characteristics of the oxidation of D-galactose with IFC oxidant are described here.

2. EXPERIMENTAL SECTION

2.1 Materials and methods

IFC oxidant has been prepared by the reported method (17). The purity of oxidant was confirmed by using dichromatic method. Commercially provided D-galactose was employed as the substrate. To ensure consistency, the D-galactose solution was always prepared fresh in a 50% (v/v) aqueous acetic acid solvent medium. Sodium hyperchlorate (VII) salt was added to maintain an unaltered ionic strength throughout the reaction mixture. Perchloric acid was used as a source of active H⁺ ions in the reaction. All TLC experiments were performed on an activated cellulose MN 300 G layer plate, as stated in the published method

(19). All other chemicals and solvents were used without any further purification.

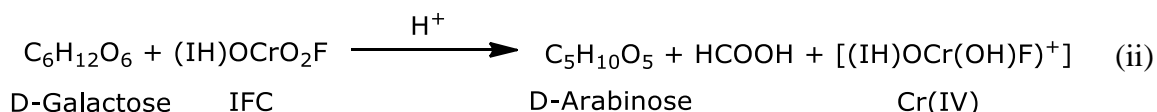
2.2 Kinetic analysis

The kinetics were studied under pseudo-first-order conditions when [D-galactose] is in excess over [IFC]. A 50% (v/v) aqueous acetic acid served as the solvent, unless specified differently. The reaction advancement was tracked by assessing absorbance at 350 nm through a visible spectrophotometer, reaching 70-80% completion. Pseudo-first order velocity constants (denoted as k_1) were evaluated from the slope of the linear plot between $\log_e (A_0/A_t)$ and time (t) {Here, A_0 represents absorbance value when the reaction commenced, and A_t signifies the absorbance at any specific time}. Second-order rate constants (k_2) were computed using the given expression (i):

$$k_2 = \frac{k_1}{[D\text{-galactose}]} \quad (i)$$

2.3 Stoichiometry

It was established through a mixture where [D-galactose] was in excess of [IFC], kept in darkness at 303 K to attain a complete reaction. The remaining Cr (VI) was determined by dichromatic approach. A 1:1 stoichiometric ratio was observed in the reaction, consistent with the stated expression (ii):



2.4 Product analysis

For product assessment, a 1:1 molar ratio of D-galactose and IFC was prepared and equilibrated for 24 hours. The products were separated using trichloromethane (CHCl₃) and dried over anhydrous MgSO₄ (20). The oxidation product

was identified as D-arabinose by comparing its R_f value with authentic sugar samples (Table 1). The formation of a phenylhydrazone derivative also supports the formation of D-arabinose. Further, formic acid was detected as a side product through spot test analysis (20–22).

Table 1: The R_f values of standard sugars in comparison with product

Sugars	R _f (Std. sugar)	R _f (Product)
Galactose	0.34	-
Mannose	0.47	-
Fructose	0.46	-
Arabinose	0.52	0.52
Xylose	0.68	-
Glucose	0.42	-
Ribose	0.71	-

3. RESULTS AND DISCUSSION

3.1 Effect on varying [oxidant]

At constant [D-galactose], [HClO₄], ionic strength, and temperature, the reaction was

examined at different [IFC], and pseudo-first-order rate constants (k_1) were computed. It was observed that k_1 remained constant irrespective of [IFC], which implies a first-order nature of the reaction concerning [IFC] (Table 2). The same

conclusion is also noticeable from a linear plot between ($\log_e (A_0/A_t)$) and time (Figure 1).

3.2 Effect of varying [substrate]

The rate constants (k_1) were calculated at constant [IFC], [HClO_4], ionic strength, and temperature. The observed k_1 values were elevated and demonstrated a direct proportionality with [D-galactose] (Figure 2(a)), indicating a first-order relationship between substrate and the reaction rate (Table 2). Further, the slope of the plot between ($\log k_1$)

and ($\log [\text{D-galactose}]$) is 0.9875, which also justifies the observed result (Figure 2(b)).

3.3 Effect of varying [perchloric acid]

The k_1 was evaluated at different [HClO_4], keeping all other reaction conditions the same. The study revealed that the rates increased with the base to the power of one in [HClO_4], which suggests the reaction is first order concerning [HClO_4], as illustrated in Figure 3(a). In addition, the gradient of the observed linear plot between ($\log k_1$) and ($\log [\text{HClO}_4]$) is 1.0024, corroborating the findings (Figure 3(b)).

Table 2: Rate constants (k_1 & k_2) for oxidation process of D-galactose by IFC at 303 K.

[IFC] x 10 ³ M	[D-galactose] x 10 ² M	[HClO ₄] M	k ₁ x 10 ⁴ (s ⁻¹)	k ₂ x 10 ² (M ⁻¹ x s ⁻¹)	R ²
0.66	2.66	0.89	7.46		0.9911
1.33	2.66	0.89	7.69	2.89	0.9942
2.66	2.66	0.89	7.57		0.9899
4.00	2.66	0.89	7.76		0.9927
1.33	1.33	0.89	3.63	2.73	0.9781
1.33	4.00	0.89	11.05	2.76	0.9942
1.33	5.33	0.89	14.76	2.77	0.9958
1.33	6.66	0.89	18.27	2.74	0.9967
1.33	8.00	0.89	22.21	2.78	0.9844
1.33	2.66	0.668	5.82		0.9901
1.33	2.66	1.113	9.85		0.9959
1.33	2.66	1.316	11.38		0.9983
1.33	2.66	1.558	13.87		0.9979
1.33	2.66	1.781	15.29		0.9936
1.33	2.66	2.004	17.48		0.9966

3.4 Effect of adding salt

The reaction was examined across various NaClO_4 concentrations, from 1.33×10^{-2} to 4.66×10^{-2} M. Interestingly, the reaction rates remain constant, indicating the involvement of primary and secondary salt effects, potentially nullifying each other. A literature study also supports the observed findings (23–25).

3.5 Effect of incorporating a radical precursor

To understand the reaction pathway, acrylonitrile, a radical forming species, was introduced into the mixture. The absence of acrylonitrile polymerization in the reaction

indicates that the formation of free radicals was unlikely during the reaction.

3.6 Effect of adding Mn²⁺ ions

Mn^{2+} ions were introduced into the reaction mixture to investigate the potential involvement of Cr^{4+} as an intermediate in the oxidation process. A study previously recognized Mn^{2+} as a reliable agent for trapping Cr^{4+} intermediates (26). Increasing [Mn^{2+}] led to a decrease in the reaction rates (Table 3), indicating the participation of Cr^{4+} with Mn^{2+} , as illustrated in expression (iii):

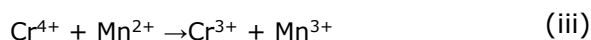


Table 3: Mn^{2+} ion-based rate constants (k_1) for the D-galactose oxidation by IFC oxidant in a 50% (v/v) aqueous acetic acid medium at 303 K. [IFC] = 1.33×10^{-3} M, [D-galactose] = 2.66×10^{-2} M, [HClO_4] = 0.89 M, [NaClO_4] = 0.13 M

[MnSO ₄] x 10 ² M	k ₁ x 10 ⁴ (s ⁻¹)	R ²
0.00	7.69	0.9942
2.66	7.45	0.9928
5.33	7.26	0.9969
10.66	6.92	0.9914
16.00	6.54	0.9918

3.7 Effect of varying solvent composition

Kinetics was analyzed in solvents with different acetic acid: water compositions to gain insight

into the interaction between the reacting species. A decrease in rate was observed in solvents with high dielectric constants (Table 4).

Table 4: Solvent based rate constants (k_1) for the oxidation of D-galactose by IFC reagent at 303 K. [IFC] = 1.33×10^{-3} M, [D-galactose] = 2.66×10^{-2} M, [HClO₄] = 0.89 M, [NaClO₄] = 0.13 M

CH ₃ COOH: H ₂ O	$k_1 \times 10^4$ (s ⁻¹)	R ²	1000/D	D-1/2D+1
40:60	5.92	0.9923	20	0.485
50:50	7.69	0.9942	24	0.482
60:40	10.82	0.9958	28	0.479
70:30	14.71	0.9903	36	0.473
80:20	22.36	0.9875	48	0.465

The positive gradient of the linear Amis plot ($\log k_1$ and $1/D$) and the linear Kirkwood plot ($\log k_1$ and $(D-1/2D+1)$) suggest ion-dipole interactions in the reaction's suggested mechanistic pathway {Here, D denotes the dielectric constant of the reaction medium} (Figure 4(a) and 4(b)) (27,28).

$$\Delta H^\ddagger = E_a - 2RT \quad (\text{iv})$$

Free energy and entropy of activation (ΔG^\ddagger and ΔS^\ddagger) were computed using Eyring's equation for reaction rates (expression (v)) (24,25,29).

$$k_2 = K_t \frac{K_b T}{h} e^{-\frac{\Delta G^\ddagger}{RT}} \quad (\text{v})$$

3.8 Effect of varying temperatures

A temperature-dependent trend in second-order rate constants (k_2) was studied by recording kinetics over different temperature ranges (T). The k_2 values showed an increase with rising temperatures, as depicted in Table 5. The activation energy (E_a), followed by enthalpy of activation (ΔH^\ddagger) were determined from the linear plot between ($\log_e k_2$) and ($1/T$) (Figure 5) and expression (iv).

The observed negative value of entropy of activation (ΔS^\ddagger) indicates that the intermediate complex is more polar compared to the initial reactants. The overall decrease in entropy during complex formation is typically due to the loss of translational energy required to bring multiple reactants together at the transition state (23, 30, 31).

Table 5: Temperature-based rate constants (k_2) and thermodynamic parameters for the D-galactose oxidation by IFC oxidant in a 50% (v/v) aqueous acetic acid medium. [IFC] = 1.33×10^{-3} M, [D-galactose] = 2.66×10^{-2} M, [HClO₄] = 0.89 M, [NaClO₄] = 0.13 M

Temp (K)	$k_2 \times 10^2$ (M ⁻¹ x s ⁻¹)	E_a (kJ/mol)	$\log_e A$ (M ⁻¹ x s ⁻¹)	ΔG^\ddagger (kJ/mol)	ΔH^\ddagger (kJ/mol)	$-\Delta S^\ddagger$ (J K ⁻¹ mol ⁻¹)
293	1.49	56.11	18.82	81.99	51.24	104.94
303	2.89		18.73	83.20	51.07	106.03
313	5.78		18.71	84.22	50.91	106.42
323	11.26		18.71	85.21	50.74	106.71
Mean:			18.74 ± 0.03	83.66 ± 0.69	50.99 ± 0.11	106.03 ± 0.39

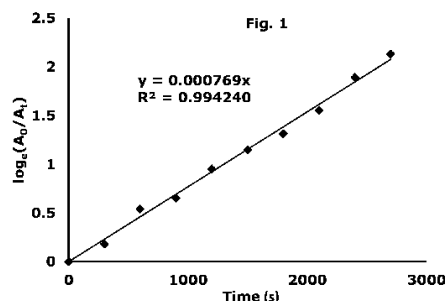


Figure 1: Plot between $\log_e (A_0/A_t)$ and Time (s) for oxidation of D-galactose by IFC oxidant in a 50% (v/v) aqueous acetic acid medium at 303 K. [IFC] = 1.33×10^{-3} M, [D-galactose] = 2.66×10^{-2} M, [HClO₄] = 0.89 M, [NaClO₄] = 0.13 M

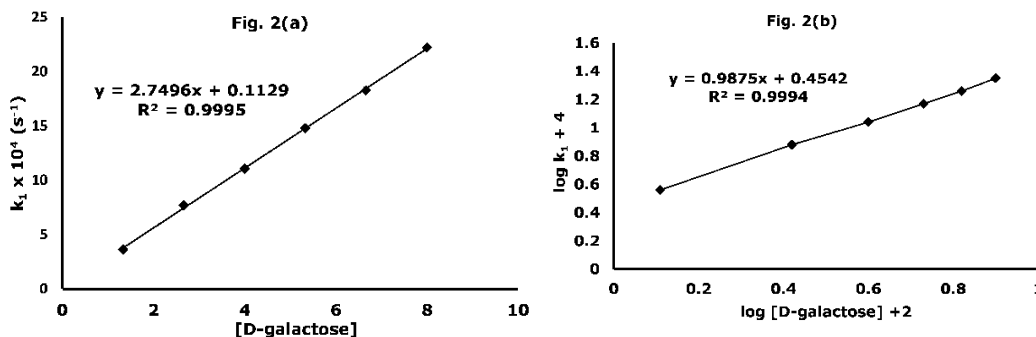


Figure. 2(a): Plot between (k_1) and ([D-galactose]), **2(b):** Plot between ($\log k_1 + 4$) and ($\log [D-galactose] + 2$) for oxidation of D-galactose by IFC oxidant in a 50% (v/v) aqueous acetic acid medium at 303 K. [IFC] = 1.33×10^{-3} M, [HClO₄] = 0.89 M, [NaClO₄] = 0.13 M

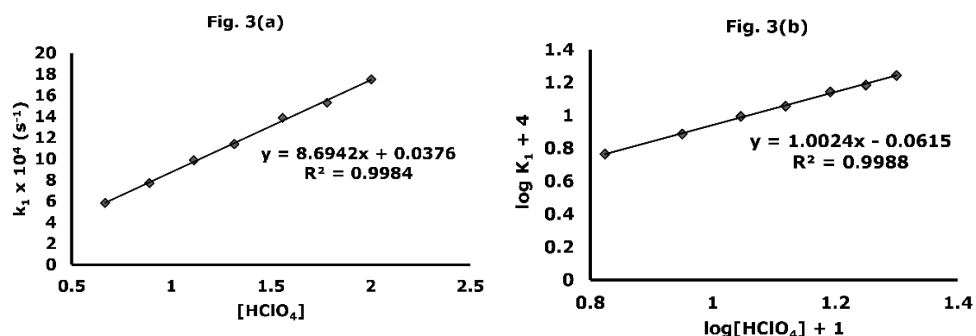


Figure 3(a): Plot between (k_1) and ([HClO₄]), **3(b):** Plot between ($\log k_1 + 4$) and ($\log [HClO_4] + 1$) for oxidation of D-galactose by IFC oxidant in a 50% (v/v) aqueous acetic acid medium at 303 K. [IFC] = 1.33×10^{-3} M, [D-galactose] = 2.66×10^{-2} M, [NaClO₄] = 0.13 M

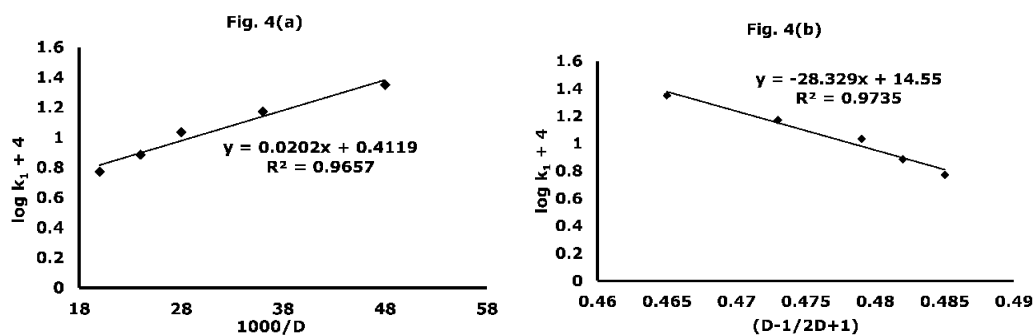


Figure 4 (a): Plot between ($\log k_1 + 4$) and ($1000/D$) (Amis plot), **4 (b):** Plot between ($\log k_1 + 4$) and ($D-1/2D+1$) (Kirkwood plot) for the oxidation of D-galactose by IFC oxidant at 303 K. [IFC] = 1.33×10^{-3} M, [D-galactose] = 2.66×10^{-2} M, [HClO₄] = 0.89 M, [NaClO₄] = 0.13 M

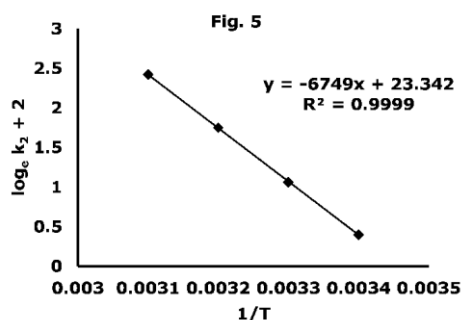


Figure 5: Plot between $(\log_e k_2 + 2)$ and $(1/T)$ for D-galactose oxidation by IFC oxidant in a 50% (v/v) aqueous acetic acid medium. $[IFC] = 1.33 \times 10^{-3} \text{ M}$, $[D\text{-galactose}] = 2.66 \times 10^{-2} \text{ M}$, $[\text{HClO}_4] = 0.89 \text{ M}$, $[\text{NaClO}_4] = 0.13 \text{ M}$

3.9 Mechanism of the reaction

In an acidic aqueous condition, D-galactose primarily adopts a cyclic hemiacetal, resulting in

mixture of α - and β -pyranose ring forms that constantly interconvert with the rare open-chain structure (Scheme 1) (32). Among these, the prevalent form is β -D-galactopyranose (Table 6).

Table 6: Percentage Composition of different galactose configurations (33)

Aldose	$[\alpha\text{-Pyranose}] (\%)$	$[\beta\text{-pyranose}] (\%)$	Open chain (%)
Galactose	~35	~65	0.085

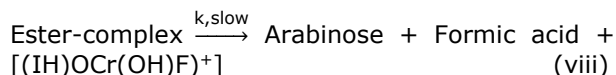
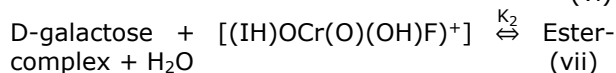
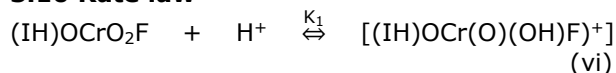
Reaction involving monosaccharides proceeds through the acyclic configuration, probably feasible by converting the chain form to open-chain form through a less favorable equilibrium step (34). A comparative kinetic study on the reactivity of several sugars with Cr(VI) revealed that their reactivity increased proportionally with an increasing amount of open-chain configuration of the sugar (33,35). Some reports also suggest that cyclic pyranose forms have increased exposure to interact with Cr(VI), which can actively participate in oxidation processes (36–38). Therefore, it is rational to infer that the rate constant (k_1) encompasses the combined influence of the cyclic and acyclic forms, both of which persist in a state of dynamic equilibrium.

In the presence of acid, IFC (A) is protonated; species (B) is formed by selectively capturing the released H^+ ion from the dissociation of HClO_4 (Scheme 2). Additionally, the first-order reliance on $[\text{HClO}_4]$ and the catalytic impact of perchloric acid on reaction rates signifies that the oxidation process exclusively takes place under acidic conditions, and the equilibrium constant for the protonation step is low.

Notably, no fractional order kinetics dependence on $[\text{Substrate}]$ and the absence of spectrophotometric proof indicate the absence of the proposed complex. Nonetheless, these findings do not conclusively dismiss the possibility of the proposed complex. It was hypothesized that the rate constants governing the complex formation step are very small, explaining the absence of observable kinetic and spectrophotometric evidence (34, 39–41). Previous studies on the oxidation process of various organic compounds using Cr(VI)-based oxidants have reported an ester complex formation mechanism (40–43). Considering all

these facts into account, it is postulated that the charged version of IFC interacts with the cyclic β -form of galactose and an ester-like complex is formed. Subsequently, this ester complex undergoes a hydride ion transfer in the rate-limiting step of the reaction, followed by $\text{C}_1\text{-C}_2$ bond cleavage, resulting in the formation of the products outlined in Scheme 3.

3.10 Rate law



The rate equation for the proposed mechanism was formulated by using expression (viii), which serves as the rate-determining step of the reaction.

$$\frac{-d[\text{IFC}]}{dt} = k[\text{ester-complex}] \quad (\text{ix})$$

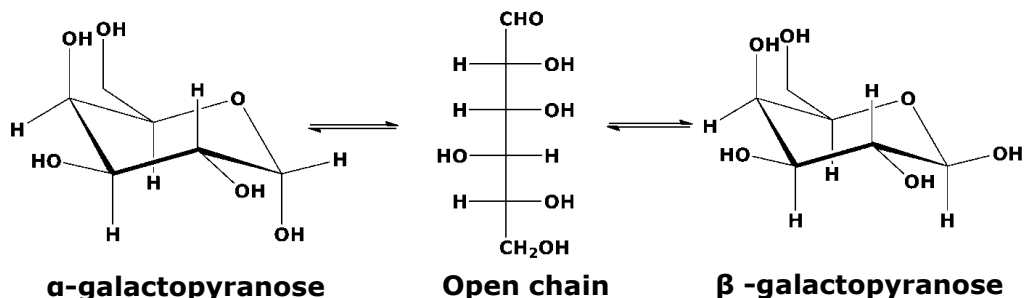
On applying the approximation condition in expression (vii) and using expression (vi), expression (ix) could be written as,

$$\frac{-d[\text{IFC}]}{dt} = \frac{kK_1K_2[\text{D-galactose}][\text{IFC}]_t[\text{H}^+]}{(1+K_1K_2[\text{D-galactose}][\text{H}^+])} \quad (\text{x})$$

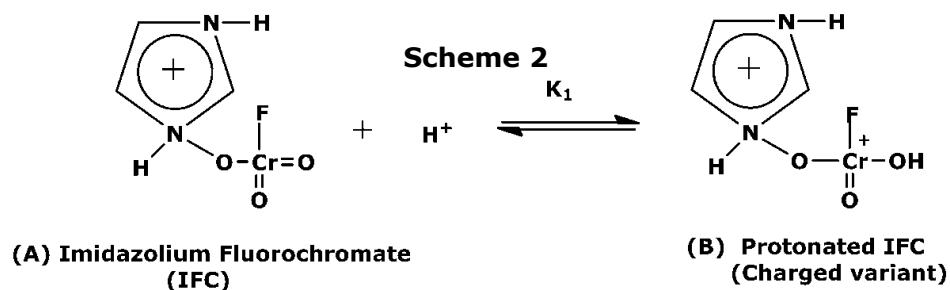
In expression (x), $[\text{IFC}]_t = [\text{IFC}] + [\text{ester-complex}]$. Taking into account the previously discussed small values of K_1 and K_2 , it is logical to assume that $1 \gg (K_1K_2[\text{D-galactose}][\text{H}^+])$ and $[\text{IFC}]_t = [\text{IFC}]$. This assumption gives rise to the following rate law (expression (xi)), explaining the experimental results observed.

$$\frac{-d[\text{IFC}]}{dt} = kK_1K_2[\text{D-galactose}][\text{IFC}][\text{H}^+] \quad (\text{xi})$$

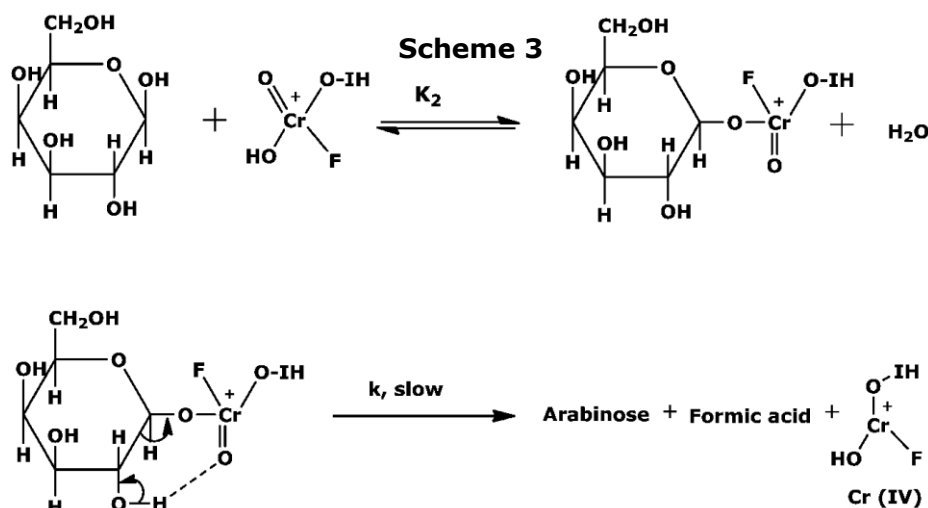
Scheme 1



Scheme 1: Interconversion of α -galactopyranose to β -galactopyranose via open chain form



Scheme 2: Structure of IFC and its Protonated form



Scheme 3: Reaction mechanism

4. CONCLUSION

The oxidation kinetics of D-galactose by IFC oxidant in a 50% (v/v) aqueous acetic acid medium were investigated at 303 K using spectrophotometric method. The reaction depicted a first-order relationship regarding [substrate], and [oxidant]. The presence of H^+ ions acted as a catalyst, also exhibiting a unit-order relationship with $[H^+]$. The oxidation process showed sluggishness in adding Mn^{2+} ions

to the reaction blend, pointing towards the involvement of Cr(IV) species as an intermediate. The possibility of a free radical intermediate was eliminated, as there was no observed polymerization of acrylonitrile. Considering all the above facts, it was proposed that protonated IFC would interact with D-galactose and form an ester-like intermediate, which further undergoes a hydride ion elimination during the slowest step of the reaction to produce the final products.

5. CONFLICT OF INTEREST

Authors have no conflict of interest to declare.

6. ACKNOWLEDGEMENT

Thanks to the financial support provided by the Higher Education Department, Uttar Pradesh, in the form of a minor research project under the "Research and Development Scheme" by Government order no. 107/2021/2584/सत्तर-4-2021-4(28)/2021 dated-28/12/2021.

7. REFERENCES

- Saha R, Nandi R, Saha B. Sources and toxicity of hexavalent chromium. *J Coord Chem*. 2011 May 20;64(10):1782–806. Available from: [<URL>](#)
- Khan Z, Kabir-ud-din. Kinetics and mechanism of D-glucose by chromium(VI) in perchloric acid. *Indian J Chem*. 2000 May;39A:522–7. Available from: [<URL>](#)
- Ukhurebor KE, Aigbe UO, Onyancha RB, Nwankwo W, Osibote OA, Paumo HK, et al. Effect of hexavalent chromium on the environment and removal techniques: A review. *J Environ Manage*. 2021 Feb;280:111809. Available from: [<URL>](#)
- Piancatelli G, Scettri A, D'Auria M. Pyridinium Chlorochromate: A Versatile Oxidant in Organic Synthesis. *Synthesis*. 1982;1982(04):245–58. Available from: [<URL>](#)
- Singh JV. Tetraethylammonium Chlorochromate: A Novel Oxidant, Kinetic and Mechanistic Aspect. *Acta Cienc Indica [Internet]*. Available from: [<URL>](#)
- Singh J, Kad GL, Vig S, Sharma M, Chhabra BR. Selective oxidation of primary alcohols with quinolinium chlorochromate. *Indian J Chem*. 1997 Mar;36 B:272–4. Available from: [<URL>](#)
- Chaudhuri MK, Chettri SK, Lyndem S, Paul PC, Srinivas P. Quinolinium Fluorochromate (QFC), C₉H₇NH[CrO₃F]: An Improved Cr(VI)-Oxidant for Organic Substrates. *Bull Chem Soc Jpn*. 1994 Jul;67(7):1894–8. Available from: [<URL>](#)
- Bhattacharjee MN, Chaudhuri MK, Purkayastha S. Some aspects of pyridinium fluorochromate, C₅H₅NhCrO₃F (pfc), oxidations. stoichiometry of oxidation of alcohols, evidence for oxygen transfer, and the identity of the reduced chromium species. *Tetrahedron*. 1987 Jan;43(22):5389–92. Available from: [<URL>](#)
- Ghammamy S, Mazareey M. Tributylammonium chlorochromate, (C₄H₉)₃NH[CrO₃Cl] (TriBACC): A new, mild and stable oxidant for organic substrates. *J Serb Chem Soc*. 2005;70(5):687–93. Available from: [<URL>](#)
- Singh JV, Awasthi A, Dipti, Tomar A, Singh D. Kinetics and Mechanism of Oxidation of Reducing Sugars: A Review. *Asian J Chem*. 2013;25(2):595–611. Available from: [<URL>](#)
- Reasons why galactose is good for you [Internet]. International Dairy Federation; Available from: [<URL>](#)
- Coelho AI, Berry GT, Rubio-Gozalbo ME. Galactose metabolism and health. *Curr Opin Clin Nutr Metab Care*. 2015 Jul;18(4):422–7. Available from: [<URL>](#)
- Schaafsma G. Lactose and lactose derivatives as bioactive ingredients in human nutrition. *Int Dairy J*. 2008 May;18(5):458–65. Available from: [<URL>](#)
- Waisbren SE, Potter NL, Gordon CM, Green RC, Greenstein P, Gubbels CS, et al. The adult galactosemic phenotype. *J Inheret Metab Dis*. 2012 Mar;35(2):279–86. Available from: [<URL>](#)
- Berry G. The rate of de novo galactose synthesis in patients with galactose-1-phosphate uridylyltransferase deficiency. *Mol Genet Metab*. 2004 Jan;81(1):22–30. Available from: [<URL>](#)
- Tomar A, Singh JV. Imidazolium Fluorochromate: A Novel Chromium (VI) Oxidant, Mechanistic and Synthetic Aspects. *Int J Anal Exp Modal Anal*. 2023 Jan;15(1):356–81. Available from: [DOI](#)
- Pandurangan A, Rajcumar GA, Arabindoo B, Murugesan V. Imidazolium fluorochromate (IFC): A new, mild, stable and selective chromium(VI) oxidant. *Indian J Chem*. 1999 Jan;38B:99–100. Available from: [<URL>](#)
- Katre SD. Recent Advances in the Oxidation Reactions of Organic Compounds using Chromium (VI) Reagents. *Res J Chem Environ*. 2020 Jan;24(1):130–51. Available from: [<URL>](#)
- S. Chidan Kumar C, Chandraju S, Mythily R, Ahmad T, M. Made Gowda N. Extraction of Sugars from Black Gram Peels by Reversed-Phase Liquid Chromatography Systems and Identification by TLC and Mass Analysis. *Adv Anal Chem Sci Acad Publ*. 2012 Aug 9;2(4):32–6. Available from: [<URL>](#)
- Agarwal GL, Tiwari S. Kinetics and mechanism of the oxidation of d-mannose with pyridinium chlorochromate. *React Kinet Catal Lett*. 1993 Jun;49(2):361–7. Available from: [<URL>](#)
- Tomar A, Kumar A. Kinetic and Mechanistic Study of the Oxidation of D-mannose by Tetraethylammonium Chlorochromate in Aqueous Acetic Acid Medium. *Asian J Chem*. 2006;18(4):3073–80. Available from: [<URL>](#)
- Feigl F, Anger V. *Spot Tests in Organic Analysis*. 7th ed. Amsterdam: Elsevier Science; 2014. ISBN: 978-0-444-59797-7
- Mardhanpally AK, Kodali SB, Jakku NR, Kamatala CR, Yerraguntla RR. Potassium hydrogen sulfate mediated kinetics and mechanism of oxidation of certain polyols by Quinolinium bound Cr(VI) reagents.

- SN Appl Sci. 2020 Oct;2(10):1747. Available from: [<URL>](#)
24. Laidler KJ, Meiser JH, Sanctuary BC. Physical chemistry. 4th ed. Boston: Houghton Mifflin; 2003. 1060 p. ISBN: 978-0-618-12341-4
25. Espenson JH. Chemical kinetics and reaction mechanisms. 2nd ed. repr. New York [etc.]: McGraw-Hill Custom Publishing; 2007. ISBN: 978-0-07-288362-6
26. Panday D, Jain H, Kalal R. Evaluation of kinetic parameters for oxidation of thioacids by benzimidazolium dichromate: A mechanistic study. J Indian Chem Soc. 2022 Apr;99(4):100390. Available from: [<URL>](#)
27. Amis ES. Solvent effects on reaction rates and mechanisms: Tab. New York: Acad. Pr; 1967. 326 p. ISBN: 978-0-12-057350-9
28. Kirkwood JG. Theory of Solutions of Molecules Containing Widely Separated Charges with Special Application to Zwitterions. J Chem Phys. 1934 Jul 1;2(7):351-61. Available from: [<URL>](#)
29. Glasstone S, Laidler KJ, Eyring H. The Theory of Rate Processes. New York: McGraw-Hill; 1941. ISBN: 978-0-07-023360-7
30. Arnaut L. Enzymatic catalysis. In: Chemical Kinetics [Internet]. Elsevier; 2021 [cited 2023 Nov 4]. p. 409-39. Available from: [<URL>](#) ISBN: 978-0-444-64039-0
31. Mardhanpally AK, Kamatala CR, Pulusu V, Kodali SB, Jakku NR, Yerraguntla RR. Cornforth's and Corey-Suggs Cr(VI) compounds as efficient reagents for selective oxidation of certain polyols in aqueous KHSO₄ medium –A kinetic and mechanistic approach. Chem Data Collect. 2022 Jun;39:100847. Available from: [<URL>](#)
32. Bruice PY. Organic chemistry. Eighth edition, global edition. Harlow: Pearson; 2017. 1336 p. ISBN: 978-1-292-16034-4
33. Fadnis AG, Shrivastava SK. Kinetics of oxidation of aldoses by thallium(III) in acid perchlorate medium. Carbohydr Res. 1982 Apr;102(1):23-9. Available from: [<URL>](#)
34. Saha B, Das M, Mohanty RK, Das AK. Micellar Effect on the Reaction of Chromium(VI) Oxidation of L-Sorbose in the Presence and Absence of Picolinic Acid in Aqueous Acid Media: A Kinetic Study. J Chin Chem Soc. 2004 Apr;51(2):399-408. Available from: [<URL>](#)
35. Virtanen POI, Lindroos-Heinänen R. Comparison of the kinetics of oxidation of monosaccharides by Ce (IV), Cr (VI) and V (V). Acta Chem Scand. 1988 Jul 1;42:411-3. Available from: [<URL>](#)
36. Sen Gupta KK, Nath Basu S, Sen Gupta S. Kinetics and mechanism of oxidation of d-fructose and l-sorbose by chromium(VI) and vanadium(V) in perchloric acid medium. Carbohydr Res. 1981 Nov;97(1):1-9. Available from: [<URL>](#)
37. Rizzotto M, Frascaroli MI, Signorella S, Sala LF. Oxidation of l-rhamnose and d-mannose by chromium(VI) in aqueous acetic acid. Polyhedron. 1996 May;15(9):1517-23. Available from: [<URL>](#)
38. Sala LF, Signorella SR, Rizzotto M, Frascaroli MI, Gandolfo F. Oxidation of L -rhamnose and D -mannose by Cr(VI) in perchloric acid. A comparative study. Can J Chem. 1992 Jul 1;70(7):2046-52. Available from: [<URL>](#)
39. Daier V, Signorella S, Rizzotto M, Frascaroli MI, Palopoli C, Brondino C, et al. Kinetics and mechanism of the reduction of Cr^{VI} to Cr^{III} by D -ribose and 2-deoxy-D -ribose. Can J Chem. 1999 Jan 1;77(1):57-64. Available from: [<URL>](#)
40. Sen Gupta KK, Basu SN. Kinetics and mechanism of oxidation of d-erythrose and dL-glyceraldehyde by chromium(VI) and vanadium(V) in perchloric acid medium. Carbohydr Res. 1980 Nov;86(1):7-16. Available from: [<URL>](#)
41. Sengupta KK, Samanta T, Basu SN. Kinetics and mechanism of oxidation of ethanol, isopropanol and benzyl alcohol by chromium(VI) in perchloric acid medium. Tetrahedron. 1986 Jan;42(2):681-5. Available from: [<URL>](#)
42. Kali Sen Gupta K, Dey S, Sen Gupta S, Adhikari M, Banerjee A. Evidence of esterification during the oxidation of some aromatic aldehydes by chromium (VI) in acid medium and the mechanism of the oxidation process. Tetrahedron. 1990 Jan;46(7):2431-44. Available from: [<URL>](#)
43. Tomar A, Kumar A. Kinetics and mechanism of oxidation of D-fructose by tetraethylammonium chlorochromate in aqueous acetic acid. J Indian Chem Soc. 2006 Nov 30;83:1153-7. Available from: [<URL>](#)



Synthesis, Spectroscopic Characterization, Crystal Structure, and DNA Docking Studies of A New Trans-Platinum Saccharinate Complex Containing Aqua and Dimethyl Sulfoxide Ligands

Ceyda İçsel^{1*} 

¹Department of Chemistry, Faculty of Science, Karadeniz Technical University, Trabzon, 61080, Türkiye.

Abstract: A new trans-platinum complex, trans-[Pt(sac)₂(H₂O)(DMSO)] (sac= saccharinate; DMSO= dimethyl sulfoxide), was synthesized and characterized by elemental analysis, UV, FTIR, NMR spectroscopy and X-ray single-crystal diffraction. In the mononuclear complex, the platinum(II) cation was coordinated by two N-coordinated sac ligands in the trans position, the sulfur atom of the DMSO ligand, and an aqua ligand, forming a distorted square planar coordination geometry. The interaction of the platinum(II) complex with DNA was studied using molecular docking. The complex successively docked into the minor groove of DNA via intermolecular hydrogen bonds with the adenine, cytosine, and guanine bases.

Keywords: Platinum(II) complex, saccharinate, X-ray crystallography, DNA docking.

Submitted: December 4, 2023. **Accepted:** February 7, 2024.

Cite this: İçsel C. Synthesis, Spectroscopic Characterization, Crystal Structure, and DNA Docking Studies of A New Trans-Platinum Saccharinate Complex Containing Aqua and Dimethyl Sulfoxide Ligands. JOTCSA. 2024;11(2):683-90.

DOI: <https://doi.org/10.18596/jotcsa.1399962>

***Corresponding author's E-mail:** cydyilmaz@ktu.edu.tr

1. INTRODUCTION

Saccharin (sacH, 1,1-dioxo-1,2-benzothiazol-3-one or benzosulfimide) is an artificial sweetener and is commercially available in the forms of sodium or calcium salts. SacH is a weak acid with a pK_a of about 2 and readily loses the imine proton in aqueous solutions. The saccharinate anion (sac) acts as a polyfunctional ligand towards various metal ions through the imine N, carbonyl, and sulfonyl O donor groups, displaying mono-, bi-, and tridentate chelating and bridging coordination modes (1).

Platinum(II) complexes such as cisplatin, oxaliplatin, and carboplatin are extensively used in cancer chemotherapy. Since they display serious side effects and drug resistance, increasing attention was paid to the development of other platinum anticancer agents. Over the last two decades, many Pt(II) complexes were prepared and evaluated in vitro and in vivo anticancer activity (2–6). The first palladium(II) and platinum(II) complexes of sac were reported by Henderson et al. (7). *cis*-[Pt(sac)₂(NH₃)₂] (8) and {K[Pt(sac)₃(H₂O)]·H₂O}₂ (9) complexes were also reported by Al-Jibori et al. and Cavicchioli et al., respectively. In the last two decades, our research group prepared a number of

palladium(II) and platinum(II) complexes of sac with polypyridyl ligands (10–17) and phosphine ligands (18–23). Some of these complexes displayed potent in vitro/in vivo anticancer activity and were documented in recent reviews (24–27).

Since DNA is one of the main targets of many drugs, the interaction of metal complexes with DNA has long been the subject of intensive research. The metal complexes bind to DNA through covalent and non-covalent modes (28,29). The anticancer platinum(II) drug, cisplatin, forms covalent bonds with the nitrogen of two adjacent guanine bases on the same DNA strand (30). On the other hand, the non-covalent modes of the metal complex–DNA interactions were classified as intercalative, groove binding, and electrostatic (31). The intercalation of metal complexes typically occurs via the insertion of planar aromatic rings of the coordinated ligands between the base pairs of DNA (32), while groove binding takes place at the grooves of DNA, and the electrostatic mode is associated with the attractive force between metal complex cations and the anionic sugar-phosphate backbone of DNA.

In this study, a new *trans*-platinum sac complex containing aqua and dimethyl sulfoxide ligands,

namely *trans*-[Pt(sac)₂(H₂O)(DMSO)], has been synthesized and characterized by elemental analysis, FTIR, NMR, and X-ray single-crystal diffraction methods. The platinum(II) aqua complexes usually exist in aqueous solutions and were rarely obtained in the solid state (33–38). Therefore, the present platinum(II) complex will be a new example containing aqua ligand in the crystalline state. In addition, the interaction of the new platinum(II) complex with DNA was studied using *in silico* methods such as molecular docking since platinum(II) aqua complexes display a high affinity towards DNA.

2. EXPERIMENTAL SECTION

2.1. Materials and Measurements

cis-[PtCl₂(DMSO)₂] was synthesized by following a method reported by Price et al. (39). All other chemicals were purchased and used as received. Elemental analyses (C, H, and N) were obtained using a Costech elemental analyzer. UV and IR spectra were recorded on a Perkin Elmer Lambda 35 and a Perkin Elmer Spectrum Two FT-IR spectrophotometer, respectively. NMR spectra were performed using a Bruker Ascend 400 MHz spectrometer in DMSO-*d*₆. Melting point was measured using a Thermo Scientific Electrothermal Digital Melting Point. The conductivity measurement was performed in MeOH using a HANNA HI 5521 pH/conductometer.

2.2. Synthesis of *trans*-[Pt(sac)₂(H₂O)(DMSO)]

The solid Na(sac)·2H₂O (120.6 mg, 0.5 mmol) was added to the aqueous solution (30 mL) of *cis*-[PtCl₂(DMSO)₂] (105.6 mg, 0.25 mmol) with stirring. 5 mL MeOH was added to the solution. After 6 h refluxing at 55 °C, the solution was filtrated and evaporated to remove the solvents. The solid was crystallized from a mixture of H₂O, MeOH, and DMSO (1:1:1).

Colorless crystals. Yield: 134.4 mg, 82%. M.p. 115–117 °C. Anal. Calcd. for C₁₆H₁₆N₂O₈PtS₃ (%): C, 29.31; H, 2.46; N, 4.27. Found C, 29.14; H, 2.60; N, 4.51. UV-vis (MeOH), λ_{max} (nm) ε_{max} (M⁻¹cm⁻¹): 272 (6700), 283 (5900). IR (cm⁻¹) ν: 3437broad (OH-aqua), 3094w, 3019w (CH-Ph), 2925w (CH-DMSO), 1669m (C=O), 1594w (CN), 1461w, 1422vw, 1338w (CNS)_{sym}, 1289vs, 1250s (SO₂)_{asym}, 1174s, 1157vs (SO₂)_{sym}, 1123s, 1057w, 1027m, 972s (CNS)_{asym}, 798w, 752s (γCH), 718w, 677s γ(ring-Ph), 594vs, 563vs, 537s, 520vs. ¹H NMR (400 MHz, DMSO-*d*₆, δ, ppm): 8.01–7.52 (m, 8H, sac), 3.45 (s, 6H, DMSO, ³J_{Pt-H} = 36.0 Hz). ¹³C NMR (100 MHz, DMSO-*d*₆, δ, ppm): 162.9 (s, C₇-sac), 142.2 (s, C₁-sac), 133.9 (s, C₃-sac), 132.2 (s, C₆-sac), 131.6 (s, C₄-sac), 123.8 (s, C₅-sac), 120.5 (s, C₂-sac), 40.8 (s, DMSO). Molar conductivity, Λ_M (MeOH, 298 K, 1 mM) 44 S cm² mol⁻¹ (nonelectrolyte).

2.3. X-ray Crystallography

Single crystal X-ray diffraction data of *trans*-[Pt(sac)₂(H₂O)(DMSO)] were collected on a Rigaku Xcalibur X-ray diffractometer with EOS CCD detector using Mo-Kα radiation (0.71073 Å) with ω-scan mode. The data collection, cell refinement, and data

reduction were performed using CrysAlispro (40). Using Olex2 (41), the structure was solved with the ShelXT structure solution program (42) using Intrinsic Phasing and refined with the ShelXL refinement package (43) using Least-Squares minimization. Except for nitrogen atoms, all non-hydrogen atoms were refined with anisotropic thermal displacement parameters, while all hydrogen atoms were located at calculated positions and refined using the riding model. Since the two nitrogen atoms are disordered, they were refined isotropically to obtain better refinement results. The crystal structure of the complex was determined as a non-merohedral twin with a fractional contribution of 0.72 from the main twin component. Due to the very high mosaicity of the crystals of the complex, the crystal is of very low quality, causing the vibration amplitudes of the atoms to be quite large. To eliminate the problems arising from this, EADP constraints and a set of ISOR/SADI/RIGU restraints were applied to improve some disordered atoms or parts of the molecular structure.

The details of data collection and refinement are presented in Table S1. Crystallographic data are deposited at the Cambridge Crystallographic Data Centre with a CCDC number 2311770. Copy of the data can be obtained free of charge via www.ccdc.cam.ac.uk/data_request/cif, or by emailing data_request@ccdc.cam.ac.uk.

2.4. Molecular Docking

The crystal structures of DNA (PDB ID: 1BNA and 1AIO) were obtained from the Protein Data Bank (PDB). The Autodock/Vina was employed for docking evaluations (44). The water molecules were removed from 1BNA, and cisplatin was removed from 1AIO together with water molecules. The binding site was centered on DNA, and a grid box was created with 60 × 60 × 60 points and a 0.375 Å grid spacing. For each docking calculation, 9 different poses were required within the energy range of 2 kcal mol⁻¹, and then, the pose with the lowest energy and best docking was selected. All other parameters were kept at their default values. The docked molecules were visualized by Discovery Studio 3.5 software.

3. RESULTS AND DISCUSSION

3.1. Synthesis and Spectroscopic Characterization

trans-[Pt(sac)₂(H₂O)(DMSO)] was synthesized by the reaction of *cis*-[PtCl₂(DMSO)₂] with Na(sac)·2H₂O in aqueous solution. A DMSO ligand and the two chloride ligands in *cis*-[PtCl₂(DMSO)₂] were substituted by an aqua ligand and two sac ligands, yielding the title platinum(II) complex. The experimental elemental analyses agree well with the calculated values. The complex is air-stable and highly soluble in common organic solvents and moderately soluble in water. The complex is non-electrolyte as evidenced by the conductivity measurements.

The platinum(II) complex was characterized using UV-Vis, IR and NMR spectral data Figures (S1–S3). Two distinct absorption bands were observed in the

UV region at 272 and 283 nm, attributed to intraligand transitions. In the IR spectrum, the broad band centered at 3437 cm^{-1} is due to the OH stretching of the aqua ligand with hydrogen bonding. The aromatic and aliphatic CH vibrations were observed as weak bands at 3019 and 2925 cm^{-1} , respectively. The band at 1669 cm^{-1} is characteristic for the carbonyl group of sac. The antisymmetric and symmetric stretching vibrations of the sulfonyl group of sac occurred at 1250 and 1157 cm^{-1} as sharp bands. The ^1H NMR spectrum displayed the signals of the aromatic protons of sac as a multiplet in the range of 8.01 - 7.52 ppm. The protons of the Me groups of DMSO appeared as a singlet at 3.45 ppm. In the ^{13}C NMR spectrum, the signals appeared at 163 and 142 ppm were characteristic to the C=O and C-S groups of sac, respectively. The other C signals of the Ph ring occurred in the range of 134 - 120 ppm. and The signal of the Me groups of DMSO was observed at ca. 41 ppm.

3.2. Description of the X-ray Structure

trans-[Pt(sac)₂(H₂O)(DMSO)] crystallizes in the monoclinic crystal system with the $P2_1/n$ space group. The molecular structure of the platinum(II) complex is illustrated in Figure 1a, and selected bond distances and angles are given in Table 1. The bond angles suggest a distorted square planar coordination geometry around the platinum(II) cation. Two sac ligands are N-coordinated and occupy the *trans* positions, while DMSO is S-bonded in accord with the hard-soft acid-base definition. The Pt-N bond distances of $1.879(13)$ and $1.949(13)$ Å compares well with those in reported platinum(II) sac complexes (7 - 23 , 45). On the other hand, the Pt-S bond distance of Pt-S bond distance of typical as observed in *cis*-[PtCl₂(DMSO)₂] (46). The Pt-OH₂ bond distance is $2.043(15)$ Å, being comparable with those found in aqua platinum complexes: $2.052(8)$ Å in *cis*-[Pt(NH₃)₂(H₂O)(1-methylcytosine)](NO₃)₂·H₂O (33), $2.078(6)$ Å in [Pt(*N,N'*-dimethylethylenediamine)(H₂O)(SO₄)]·H₂O (34) and $2.016(7)$ Å in *trans*-[Pt{HN=C(O)-Bu^t}₂(H₂O)₂].1/3H₂O (35). Longer Pt-O bond distances were observed in other $2.099(5)$ Å in [Pt{1,1-bis(aminomethyl)cyclohexane}(H₂O)(SO₄)]·H₂O

(36), $2.12(2)$ Å in *trans*-[PtCl₂(H₂O)(PPh₃)] (37) and $2.200(5)$ Å in [Pt{(CH(CH₂C₆F₅)(CH₂CH₂CH=CH₂))(C₆F₅)(H₂O)] (38).

In the crystalline state, two molecules of *trans*-[Pt(sac)₂(H₂O)(DMSO)] are doubly bridged through strong OH...O hydrogen bonds involving the aqua ligands in neighboring molecules (Figure 1b). The hydrogen bonded dimers are further connected via π ... π stacking interactions ($3.659(5)$ Å) between the phenyl rings of sac in the adjacent molecules (Figure 1b).

3.1. Docking of *trans*-[Pt(sac)₂(H₂O)(DMSO)] with DNA

The DNA binding of *trans*-[Pt(sac)₂(H₂O)(DMSO)] was studied using molecular docking modelling. The lowest energy docked pose showing interactions between the platinum(II) complex and DNA (PDB ID: 1BNA) is illustrated in Figure 2. The molecular docking analysis indicated that the platinum(II) complex binds to the minor groove of DNA through the non-covalent binding interactions, including relatively strong hydrogen bonds with adenine (A), cytosine (C) and guanine (G) bases of DNA (Table 2). Consequently, these interactions between the platinum(II) complex and DNA results in the binding energy of $-36.40\text{ kJ}\cdot\text{mol}^{-1}$. The results suggest that the complex display a greater affinity towards DNA compared to the reported platinum(II) complexes of sac (19 - 21 , 23).

Since the Pt-OH₂ bond was suggested to undergo the ligand substitution reactions (47), the possibility of the covalent binding of *trans*-[Pt(sac)₂(H₂O)(DMSO)] with DNA (PDB ID: 1AIO) after removal of the aqua ligand was also studied. The docking analysis showed that the approach of the [Pt(sac)₂(DMSO)] moiety to the N donor sites of the G base was sterically hindered by the two sac ligands, resulting in a Pt-N bond distance of 5.31 Å, which cancels the presence of any covalent bonding. The binding energy of the [Pt(sac)₂(DMSO)] moiety with DNA was computed as $-33.47\text{ kJ}\cdot\text{mol}^{-1}$, being remarkably lower than that of the parent platinum(II) complex.

Table 1: Selected geometrical parameters for *trans*-[Pt(sac)₂(H₂O)(DMSO)].

Bond distances (Å)		Bond angles (°)	
Pt1-N1	1.879(13)	N1- Pt1-N2	177.8(5)
Pt1-N2	1.949(13)	N1- Pt1-O1W	88.1(6)
Pt1-O1W	2.043(15)	N1- Pt1-S3	92.4(4)
Pt1-S3	2.211(6)	N2- Pt1-O1W	89.9(7)
		N2- Pt1-S3	89.6(4)
		O1W- Pt1-S3	179.3(6)

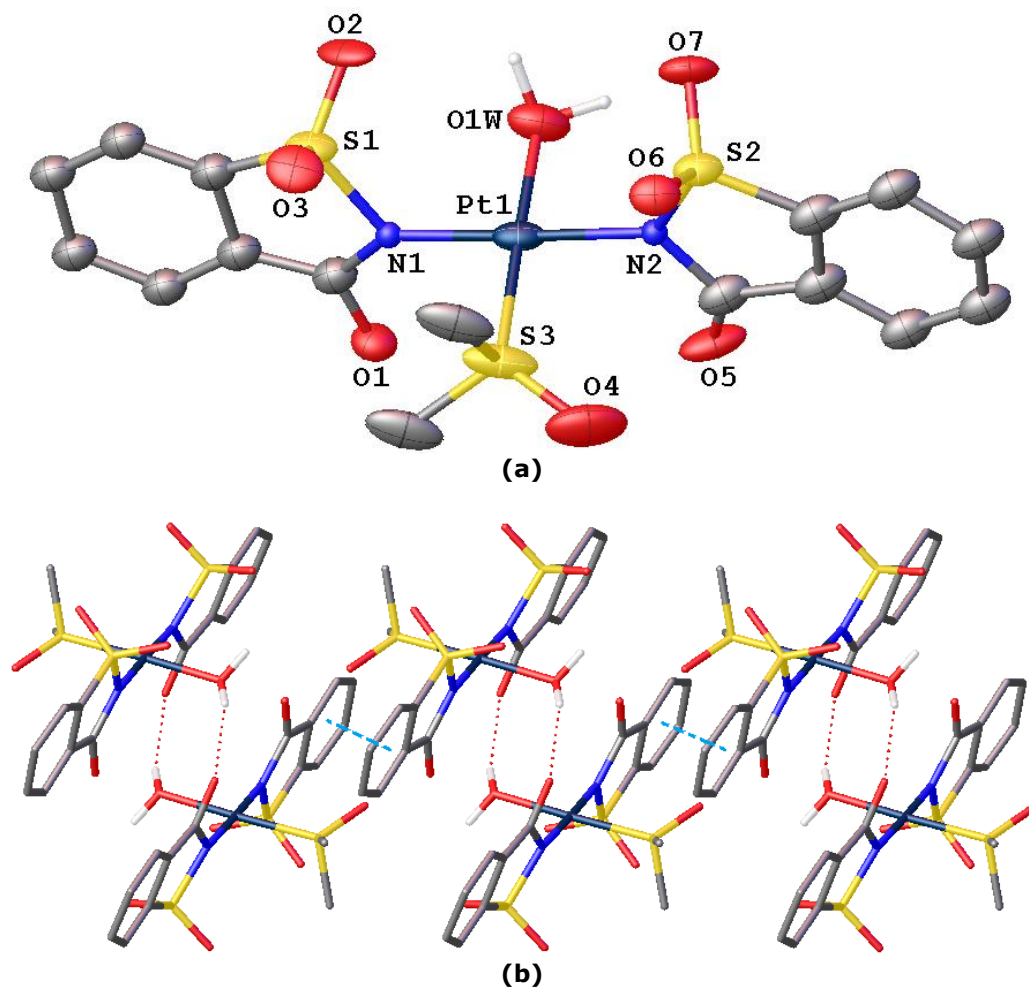


Figure 1: (a) The molecular structure of *trans*-[Pt(sac)₂(H₂O)(DMSO)] with the atom numbering. The CH hydrogens were omitted for clarity. (b) The hydrogen bonds and π - π stacking interactions between the molecules of *trans*-[Pt(sac)₂(H₂O)(DMSO)].

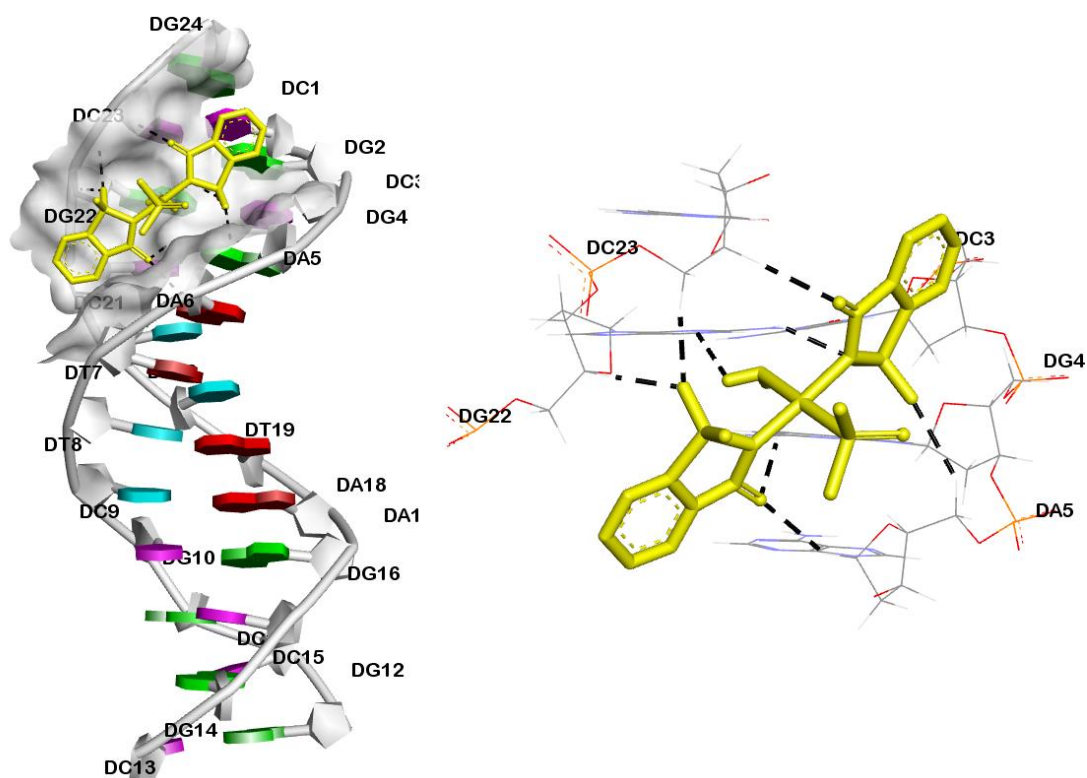


Figure 2: Docking of *trans*-[Pt(sac)₂(H₂O)(DMSO)] with DNA (1BNA), showing intermolecular interactions of the platinum(II) complex with DNA bases at the minor groove.

Table 2: The intermolecular interactions between *trans*-[Pt(sac)₂(H₂O)(DMSO)] and DNA (1BNA).

Hydrogen bonds	Distance (Å)	Binding energy (kJ mol ⁻¹)
G22(CH ₂)...O (sac sulfonyl)	2.15; 2.44	-36.40
G4(NH ₂)...O (sac carbonyl)	2.26	
C23(CH ₂)...O (sac sulfonyl)	2.37	
A5(CH)...O (sac carbonyl)	2.54	
C23(CH)...O (sac carbonyl)	2.54	
A5(CH ₂)...O (sac sulfonyl)	2.75	
OH ₂ ... N (G22)	2.76	

4. CONCLUSION

In this study, a new *trans*-configured complex, namely *trans*-[Pt(sac)₂(H₂O)(DMSO)], was synthesized and characterized by spectroscopic methods. The crystal structure of the platinum(II) complex was identified by single-crystal spectroscopy. The present complex is an interesting example of the rare platinum(II) complexes bearing the aqua ligand. The DNA binding of the complex was studied using molecular docking modeling. The results indicated that the complex shows a great binding affinity towards DNA with a binding preference for the minor groove.

5. CONFLICT OF INTEREST

There is no conflict of interest.

6. ACKNOWLEDGMENTS

I wish to thank Assoc. Prof. Dr. Muhittin Aygün at Dokuz Eylül University for his assistance in X-ray crystallographic measurements.

7. REFERENCES

- Baran EJ, Yilmaz VT. Metal complexes of saccharin. *Coord Chem Rev* [Internet]. 2006 Aug;250(15-16):1980-99. Available from: [<URL>](#).
- Brabec V, Hrabina O, Kasparkova J. Cytotoxic platinum coordination compounds. DNA binding agents. *Coord Chem Rev* [Internet]. 2017 Nov;351:2-31. Available from: [<URL>](#).
- Cai L, Yu C, Ba L, Liu Q, Qian Y, Yang B, et al. Anticancer platinum-based complexes with non-classical structures. *Appl Organomet Chem* [Internet]. 2018 Apr 11;32(4):e4228. Available from: [<URL>](#).
- Jin S, Guo Y, Guo Z, Wang X. Monofunctional Platinum(II) Anticancer Agents. *Pharmaceuticals* [Internet]. 2021 Feb 7;14(2):133. Available from: [<URL>](#).
- Sharma R, Singh VJ, Chawla PA. Advancements in the Use of Platinum Complexes as Anticancer Agents. *Anticancer Agents Med Chem* [Internet]. 2022 Mar;22(5):821-35. Available from: [<URL>](#).
- Štarha P, Křikavová R. Platinum(IV) and platinum(II) anticancer complexes with biologically active releasable ligands. *Coord Chem Rev*

[Internet]. 2024 Feb;501:215578. Available from: [<URL>](#).

7. Henderson W, Nicholson BK, McCaffrey LJ. Platinum(II) and palladium(II) saccharinate complexes. *Inorganica Chim Acta* [Internet]. 1999 Feb;285(1):145-8. Available from: [<URL>](#).

8. Al-Jibori SA, Al-Jibori GH, Al-Hayaly LJ, Wagner C, Schmidt H, Timur S, et al. Combining anti-cancer drugs with artificial sweeteners: Synthesis and anti-cancer activity of saccharinate (sac) and thiosaccharinate (tsac) complexes cis - [Pt(sac)₂(NH₃)₂] and cis-[Pt(tsac)₂(NH₃)₂]. *J Inorg Biochem* [Internet]. 2014 Dec;141:55-7. Available from: [<URL>](#).

9. Cavicchioli M, Massabni AC, Castellano EE, Sabeh LPB, Costa-Neto CM. Synthesis and X-ray structure of the dinuclear platinum(II) complex with saccharin {K[Pt(sac)₃(H₂O)]·H₂O}₂: Studies on its antiproliferative activity in aqueous solution. *Inorganica Chim Acta* [Internet]. 2007 Jun;360(9):3055-60. Available from: [<URL>](#).

10. Guney E, Yilmaz VT, Kazak C. Bis(saccharinato)palladium(II) and platinum(II) complexes with 2,2'-bipyridine: Syntheses, structures, spectroscopic, fluorescent and thermal properties. *Polyhedron* [Internet]. 2010 Mar;29(4):1285-90. Available from: [<URL>](#).

11. Guney E, Yilmaz VT, Sengul A, Buyukgungor O. Platinum(II) and palladium(II) saccharinato complexes with 2,2':6',2"-terpyridine: Synthesis, characterization, crystal structures, photoluminescence and thermal studies. *Inorganica Chim Acta* [Internet]. 2010 Jan;363(2):438-48. Available from: [<URL>](#).

12. Yilmaz VT, Ertem A, Guney E, Buyukgungor O. Palladium(II) and Platinum(II) Saccharinate Complexes with 2-Aminomethylpyridine and 2-Aminoethylpyridine: Synthesis, Characterization, Crystal Structures, and Thermal Properties. *Zeitschrift für Anorg und Allg Chemie* [Internet]. 2010 Mar 16;636(3-4):610-5. Available from: [<URL>](#).

13. Guney E, Yilmaz VT, Buyukgungor O. Neutral and cationic palladium(II) and platinum(II) complexes of 2,2'-dipyridylamine with saccharinate: Syntheses, spectroscopic, structural, fluorescent and thermal studies. *Inorganica Chim Acta* [Internet]. 2010 Aug;363(11):2416-24. Available from: [<URL>](#).

14. Guney E, Kaya Y, Yilmaz VT, Gumus S. Synthesis, experimental and theoretical characterization of palladium(II) and platinum(II) saccharinate complexes with 2-(2-pyridyl)benzimidazole. *Spectrochim Acta Part A Mol Biomol Spectrosc* [Internet]. 2011 Sep;79(5):1171–8. Available from: [<URL>](#).
15. Guney E, Yilmaz VT, Buyukgungor O. Palladium(II) and platinum(II) saccharinate complexes containing pyridine and 3-acetylpyridine: Synthesis, crystal structures, fluorescence and thermal properties. *Polyhedron* [Internet]. 2011 Aug;30(12):1968–74. Available from: [<URL>](#).
16. Guney E, Yilmaz VT, Ari F, Buyukgungor O, Ulukaya E. Synthesis, characterization, structures and cytotoxic activity of palladium(II) and platinum(II) complexes containing bis(2-pyridylmethyl)amine and saccharinate. *Polyhedron* [Internet]. 2011 Jan;30(1):114–22. Available from: [<URL>](#).
17. Ari F, Aztopal N, Icsel C, Yilmaz VT, Guney E, Buyukgungor O, et al. Synthesis, structural characterization and cell death-inducing effect of novel palladium(II) and platinum(II) saccharinate complexes with 2-(hydroxymethyl)pyridine and 2-(2-hydroxyethyl)pyridine on cancer cells in vitro. *Bioorg Med Chem* [Internet]. 2013 Nov;21(21):6427–34. Available from: [<URL>](#).
18. Yilmaz VT, Icsel C, Turgut OR, Aygun M, Erkisa M, Turkdemir MH, et al. Synthesis, structures and anticancer potentials of platinum(II) saccharinate complexes of tertiary phosphines with phenyl and cyclohexyl groups targeting mitochondria and DNA. *Eur J Med Chem* [Internet]. 2018 Jul;155:609–22. Available from: [<URL>](#).
19. Icsel C, Yilmaz VT, Cevatemre B, Aygun M, Ulukaya E. Structures and anticancer activity of chlorido platinum(II) saccharinate complexes with mono- and dialkylphenylphosphines. *J Inorg Biochem* [Internet]. 2019 Jun;195:39–50. Available from: [<URL>](#).
20. Icsel C, Yilmaz VT, Cevatemre B, Aygun M, Ulukaya E. Cytotoxic platinum(II) complexes derived from saccharinate and phosphine ligands: synthesis, structures, DNA cleavage, and oxidative stress-induced apoptosis. *JBIC J Biol Inorg Chem* [Internet]. 2020 Feb 26;25(1):75–87. Available from: [<URL>](#).
21. Icsel C, Yilmaz VT, Aygun M, Ulukaya E. Trans-Pd/Pt(II) saccharinate complexes with a phosphine ligand: Synthesis, cytotoxicity and structure-activity relationship. *Bioorg Med Chem Lett* [Internet]. 2020 May;30(9):127077. Available from: [<URL>](#).
22. Icsel C, Yilmaz VT, Aygun M, Cevatemre B, Alper P, Ulukaya E. Palladium(II) and platinum(II) saccharinate complexes with bis(diphenylphosphino)methane/ethane: synthesis, S-phase arrest and ROS-mediated apoptosis in human colon cancer cells. *Dalt Trans* [Internet]. 2018;47(33):11397–410. Available from: [<URL>](#).
23. Yilmaz VT, Icsel C, Aygun M, Erkisa M, Ulukaya E. Pd(II) and Pt(II) saccharinate complexes of bis(diphenylphosphino)propane/butane: Synthesis, structure, antiproliferative activity and mechanism of action. *Eur J Med Chem* [Internet]. 2018 Oct;158:534–47. Available from: [<URL>](#).
24. Medici S, Peana M, Nurchi VM, Lachowicz JI, Crisponi G, Zoroddu MA. Noble metals in medicine: Latest advances. *Coord Chem Rev* [Internet]. 2015 Feb;284:329–50. Available from: [<URL>](#).
25. Fanelli M, Formica M, Fusi V, Giorgi L, Micheloni M, Paoli P. New trends in platinum and palladium complexes as antineoplastic agents. *Coord Chem Rev* [Internet]. 2016 Mar;310:41–79. Available from: [<URL>](#).
26. Alam MN, Huq F. Comprehensive review on tumour active palladium compounds and structure–activity relationships. *Coord Chem Rev* [Internet]. 2016 Jun;316:36–67. Available from: [<URL>](#).
27. Paprocka R, Wiese-Szadkowska M, Janciauskiene S, Kosmalski T, Kulik M, Helmin-Basa A. Latest developments in metal complexes as anticancer agents. *Coord Chem Rev* [Internet]. 2022 Feb;452:214307. Available from: [<URL>](#).
28. Keene FR, Smith JA, Collins JG. Metal complexes as structure-selective binding agents for nucleic acids. *Coord Chem Rev* [Internet]. 2009 Aug;253(15–16):2021–35. Available from: [<URL>](#).
29. Pages BJ, Ang DL, Wright EP, Aldrich-Wright JR. Metal complex interactions with DNA. *Dalt Trans* [Internet]. 2015;44(8):3505–26. Available from: [<URL>](#).
30. Sherman SE, Gibson D, Wang AHJ, Lippard SJ. Crystal and molecular structure of cis-[Pt(NH₃)₂[d(pGpG)]], the principal adduct formed by cis-diamminedichloroplatinum(II) with DNA. *J Am Chem Soc* [Internet]. 1988 Oct 1;110(22):7368–81. Available from: [<URL>](#).
31. Smith JA, Keene FR, Li F, Collins JG. Noncovalent DNA Binding of Metal Complexes. In: Reedijk J, Poeppelemeier K, editors. *Comprehensive Inorganic Chemistry II* [Internet]. Elsevier; 2013. p. 709–50. Available from: [<URL>](#).
32. Liu HK, Sadler PJ. Metal Complexes as DNA Intercalators. *Acc Chem Res* [Internet]. 2011 May 17;44(5):349–59. Available from: [<URL>](#).
33. Britten JF, Lippert B, Lock CJL, Pilon P. Platinum(II) complexes with terminal hydroxo and aqua groups: crystal structures of hydroxo-cis-diammine(1-methylcytosine-N³)platinum(II) nitrate dihydrate, [Pt(OH)(NH₃)₂(C₅H₇N₃O)]NO₃·2H₂O, and cis-diammineaqua(1-methylcytosine-N³)platinum(II) dinitrate hydrate, [Pt(NH₃)₂(H₂O)(C₅H₇N₃O)](NO₃)₂·H₂O. *Inorg Chem* [Internet]. 1982 May 1;21(5):1936–41. Available from: [<URL>](#).
34. Rochon FD, Melanson R. Molecular and crystal structure of a platinum(II) complex with aquo and

- sulfate ligands: aquo(N,N'-dimethylethylenediamine)(sulfato)platinum(II) hydrate. *Inorg Chem* [Internet]. 1987 Apr 1;26(7):989–92. Available from: [<URL>](#).
35. Intini FP, Lanfranchi M, Natile G, Pacifico C, Tiripicchio A. Synthesis and Crystal Structure of a *trans*-Diaquabis(amidato) Complex of Platinum(II). *Inorg Chem* [Internet]. 1996 Jan 1;35(6):1715–7. Available from: [<URL>](#).
36. Meinema HA, Verbeek F, Marsman JW, Bulten EJ, Dabrowiak JC, Krishnan BS, et al. The synthesis and characterization of 1,1-bis(aminomethyl)cyclohexaneplatinum(II) compounds and the crystal structure determination of 1,1-bis(aminomethyl)-cyclohexaneaquosulphatoplatinum(II) monohydrate. *Inorganica Chim Acta* [Internet]. 1986 Apr;114(2):127–35. Available from: [<URL>](#).
37. Rath NP, Fallis KA, Anderson GK. Structure of *trans*-aquadichloro(triphenylphosphine)platinum(II). *Acta Crystallogr Sect C Cryst Struct Commun* [Internet]. 1993 Dec 15;49(12):2079–81. Available from: [<URL>](#).
38. Deacon GB, Drago PR, Göbbels D, Wickleder MS, Meyer G. A Novel Alkene(alkyl)(aqua)(aryl)platinum(II) Complex - [Pt{CH(CH₂C₆F₅)CH₂CH₂CH=CH₂}(C₆F₅)(OH₂)]. *Zeitschrift für Anorg und Allg Chemie* [Internet]. 2001 May;627(5):811–3. Available from: [<URL>](#).
39. Price JH, Williamson AN, Schramm RF, Wayland BB. Palladium(II) and platinum(II) alkyl sulfoxide complexes. Examples of sulfur-bonded, mixed sulfur- and oxygen-bonded, and totally oxygen-bonded complexes. *Inorg Chem* [Internet]. 1972 Jun 1;11(6):1280–4. Available from: [<URL>](#).
40. Rigaku Oxford Diffraction, CrysAlisPro Software System, Version 1.171.38.46, Rigaku Corporation, Oxford, UK, 2015.
41. Dolomanov O V., Bourhis LJ, Gildea RJ, Howard JAK, Puschmann H. *OLEX2*: a complete structure solution, refinement and analysis program. *J Appl Crystallogr* [Internet]. 2009 Apr 1;42(2):339–41. Available from: [<URL>](#).
42. Sheldrick GM. *SHELXT* – Integrated space-group and crystal-structure determination. *Acta Crystallogr Sect A Found Adv* [Internet]. 2015 Jan 1;71(1):3–8. Available from: [<URL>](#).
43. Sheldrick GM. Crystal structure refinement with *SHELXL*. *Acta Crystallogr Sect C Struct Chem* [Internet]. 2015 Jan 1;71(1):3–8. Available from: [<URL>](#).
44. Trott O, Olson AJ. AutoDock Vina: Improving the speed and accuracy of docking with a new scoring function, efficient optimization, and multithreading. *J Comput Chem* [Internet]. 2010 Jan 30;31(2):455–61. Available from: [<URL>](#).
45. İçsel C. Synthesis, characterization and crystal structures of platinum(II) saccharinate complexes with 1,5-cyclooctadiene. *Turkish J Chem* [Internet]. 2020;44(3):736–45. Available from: [<URL>](#).
46. Melanson R, Rochon FD. The Crystal Structure of *cis*-Dichlorobis(dimethylsulfoxide)platinum(II). *Can J Chem* [Internet]. 1975 Aug 15;53(16):2371–4. Available from: [<URL>](#).
47. Olusegun MA, Reddy D, Jaganyi D. An investigation of comparative substitution behavior of bifunctional *trans*-platinum(II) complexes with symmetric and asymmetric alkylamine ligands. *Int J Chem Kinet* [Internet]. 2020 Dec 4;52(12):884–92. Available from: [<URL>](#).



***In Vitro* Inhibitory Effects of Some Antiviral, Antidiabetic, and Non-Steroidal Anti-Inflammatory Drug Active Compounds on α -Glucosidase and Myeloperoxidase Activities**

Fatma Yaşar Boztaş^{1,2} , Sevim Tunalı^{2*} 

¹İstanbul University-Cerrahpaşa, Institute of Graduate Studies, Avcılar, 34320 İstanbul, Türkiye.

²İstanbul University-Cerrahpaşa, Department of Chemistry, Biochemistry Division, Avcılar, 34320, İstanbul, Türkiye.

Abstract: In recent decades, interest in enzyme inhibition, such as myeloperoxidase (MPO) and glycosidases, has dramatically increased, mainly because these enzymes play a vital role in many biological processes. Based on the biological potential associated with these enzymes, instead of several glycosidase and myeloperoxidase (MPO) inhibitors that have been developed, there are not enough studies on the inhibition effects of widely used types of antivirals (aciclovir, tenofovir), oral antidiabetics (glibenclamide, glibornuride, glurenorm, metformin), and non-steroidal anti-inflammatory drugs (NSAIDs) active substances (benzylamine HCl, diclofenac, indomethacin, ketorolac tromethamine, paracetamol, salicylic acid) today. For that reason, the aim of our study is to investigate the inhibition effects of these 12 different drug active substances on α -glucosidase and MPO activities. According to the obtained results, the screened drug active substances acyclovir, glibornuride, and paracetamol inhibited α -glucosidase with the lowest IC₅₀ value, while similarly low values for MPO were found by tenofovir, glurenorm, and indomethacin. In our study, we can suggest that these active pharmaceutical ingredients may contribute to the pharmaceutical industry due to their inhibitory effects on α -glucosidase and MPO *in vitro*.

Keywords: α -Glucosidase, myeloperoxidase, enzyme inhibition, drug active compounds.

Submitted: December 13, 2023. **Accepted:** February 5, 2024.

Cite this: Yaşar Boztaş F, Tunalı S. *In Vitro* Inhibitory Effects of Some Antiviral, Antidiabetic, and Non-Steroidal Anti-Inflammatory Drug Active Compounds on α -Glucosidase and Myeloperoxidase Activities. JOTCSA. 2024;11(2):691-8.

DOI: <https://doi.org/10.18596/jotcsa.1404431>.

***Corresponding author. E-mail:** stunali@iuc.edu.tr

1. INTRODUCTION

Enzyme inhibitors are key molecules that regulate the velocity of enzymatic reactions in metabolism. A possible correlation between enzyme activity and diseases is an important reason for increasing interest in inhibition research. Examination of different antiviral, antidiabetic, and nonsteroidal anti-inflammatory drug (NSAIDs) active compounds demonstrated their inhibitory effect on the two important enzymes α -glucosidase and myeloperoxidase (MPO).

Glycosidases are enzymes responsible for the hydrolysis of glycosidic bonds in glycoconjugates, that are found in almost all living organisms (1). Today, wide structural diversity of carbohydrates, stable character of glycosidic bonds and catalytic rates of up to 10¹⁷ times have led to increased

interest in glycosidases (2). Although catalysis of carbohydrates by these enzymes is biologically common, glycosidases also take part in various intracellular functions, such as the formation of signaling molecules or glycoconjugate catabolism (3).

Since glycosidases are enzymes responsible for the breakdown of di-, oligo- and polysaccharides and glycoconjugates, they appear in every aspect of life. Inhibition of starch hydrolysis to slow down the absorption of glucose in starchy foods is an effective way to prevent type 2 diabetes. Recently, glycosidase inhibitors, synthesized or isolated from various plant sources, are used for several purposes, such as elucidating the mechanisms catalyzed by various types of glycosidases, in addition to being used in treatments (4). Besides being involved in the digestion of carbohydrates in the intestines,

glycosidases are involved in many biochemical processes, such as the catabolization of glycoconjugates in lysosomes and the processing of glycoproteins through post-translational modifications. Glycosidase inhibitors are important both in understanding the biological functions of glycoproteins and in investigating the structures and reaction mechanisms of glycosidases (5).

Myeloperoxidase (MPO) is an inflammatory enzyme that triggers both oxidative stress and neuroinflammation in damage resulting from pathological processes such as cerebral ischemia-reperfusion and is also a therapeutic target (6). MPO is one of the major proteins of the antimicrobial system in mammalian neutrophils (7). Since the surface of MPO molecule contains numerous lysine and arginine residues, which make the MPO a highly cationic molecule ($PI \sim 10$), the interaction of MPO with a multitude of compounds or cells that have a negatively charged surface (or domain) including bacterial cells (8), endothelial cells (9), extracellular matrix components, particularly polyanionic glycosaminoglycans (9), apolipoprotein B-100 (10) and apolipoprotein A-I (11), albumin (12), cytokeratin I (13), $\alpha 1$ -antitrypsin (14) and ceruloplasmin (15). It is reported that in physiological conditions, when MPO is binding to endothelial cells and glycosaminoglycans, it is inhibited by heparin and the multi-functional copper containing protein ceruloplasmin, which may be explained these molecules as anti-inflammatory (16, 17).

Apart from infiltrated neutrophils, MPO is also located in activated microglial cells, astrocytes, and neurons in the ischemic brain. Activation of MPO can catalyze the reaction of chloride and H_2O_2 to produce HOCl. Induced MPO activity in tissues also causes the production of reactive oxygen species (ROS) and reactive nitrogen species (RNS), activation of polarization and inflammation-related signaling pathways in microglia and neutrophils, and consequent oxidative stress. Therefore, inhibition of MPO may also be therapeutically targeted for ischemic stroke and attenuation of neuroinflammation. It has been observed that targeting MPO both at the genetic expression level and in terms of catalytic inhibition is important in reducing possible neurological problems and brain infarction (6).

In this paper, we investigate the inhibitory effect of 12 different drug active substances on α -glucosidase and MPO activities *in vitro*. Moreover, in addition to the antiviral, blood glucose lowering and anti-inflammatory effects of these drug active ingredients, which are already widely used, we also aimed to emphasize to what extent they have the potential to inhibit these two enzymes.

2. EXPERIMENTAL SECTION

2.1. Inhibition of α -glucosidase

α -Glucosidase inhibition assay was performed according to the method of Tao et al. (18). 5 μ L of different concentrations of inhibitory solution and 20

μ L of 0.15 U/mL enzyme solution were added to 75 μ L of 0.1 M phosphate buffer (pH 7.4) and mixed. In the control sample, 5 μ L of distilled water were taken instead of the inhibitor solution. The same amount of distilled water and buffer was added to the blind instead of the inhibitor and enzyme solutions, and the same amount of buffer solutions were added to the color-blind instead of the enzyme. After 10 minutes of incubation at 37 °C, 20 μ L of 0.005 M *p*-nitrophenylglycopyranoside (PNG) was added to all samples and the absorbance values at 410 nm were read. Acarbose was used as a positive control. The inhibition (%) values were calculated with the help of the following formula.

$$\alpha\text{-Glucosidase Inhibition (\%)} = ([A-B]/A) \times 100$$

A: The absorbance value of the control solution in the spectrophotometer.

B: The absorbance value of the solution containing the sample in the spectrophotometer.

2.2. Inhibition of MPO

Rat gastric tissue homogenates were used as the enzyme source. The gastric tissues were homogenized in 0.9% saline to make up a 10% (w/v) homogenate. The homogenate was centrifuged at 3000 rpm for 30 minutes at +4 °C, and the supernatant was used for enzyme inhibition experiments. MPO enzyme inhibitory activity was determined spectrophotometrically according to Wei and Frenkel's method (19). In a test tube, 1.3 mL of 4-aminoantipyrine (25 mM in 2% phenol) and 1.5 mL of hydrogen peroxide solutions (1.7 mM) were shaken for 4 min, and 0.1 mL inhibition solution were added and stirred. The reaction was started by adding 0.2 mL of homogenate. Then, the change in absorbance was measured at 510 nm for 5 min. Reference measurements were performed without inhibitors (control value). Rutin hydrate was used as a standard. The potent inhibition of MPO activity (%) was calculated as follows:

$$\text{MPO Inhibition (\%)} = (A-B)/A \times 100$$

A is the enzyme activity without inhibitor. B is the activity in presence of inhibitor.

The IC_{50} was determined as the concentration of drug active compound required to inhibit α -glucosidase and MPO activities by 50%. The results are given as half maximal inhibitory concentrations (IC_{50}), whose value could be used to assess the inhibitory efficiency of the inhibitor calculated from the regression equations prepared from the concentrations of the samples. All measurements were done in triplicate. The percentage of inhibition was calculated from the residual activity in comparison to the control sample. Low IC_{50} values indicate higher enzyme inhibitory activity.

3. RESULTS AND DISCUSSION

The inhibitory effects of antiviral drug active compounds and standard compounds on α -glucosidase and MPO are given in Table 1.

Table 1: α -Glucosidase and MPO inhibitory activities of antiviral drug active compounds at different concentrations.

Enzyme	Drug active compounds	Drug active compounds conc. (mM)	Inhibition (%) *	IC ₅₀ (mM) *
α -Glucosidase	Acyclovir	10.0	12.25±1.61	58.41±16.73
		15.0	19.81±2.73	
		25.0	25.21±2.67	
	Tenofovir	0.5	10.96±3.19	184.65±35.23
		5.0	17.89±1.66	
		50.0	23.53±1.51	
	Acarbose	2.5	21.83±0.65	10.57±0.57
		5.0	26.77±2.77	
		7.5	40.20±1.77	
MPO	Acyclovir	10.0	5.8±2.40	321.03±214.03
		15.0	6.0±0.57	
		20.0	6.6±1.06	
	Tenofovir	10.0	16.7±2.90	52.90±0.68
		25.0	31.2±2.62	
		50.0	47.1±0.57	
	Rutin hydrate	2.5	31.3±1.77	13.00±2.67
		5.0	38.9±0.78	
		10.0	43.3±2.97	

*Mean±SD

The studied two antiviral drug active compounds, acyclovir and tenofovir, have shown inhibitory effects on both α -glucosidase (IC₅₀= 58.41±16.73 mM for acyclovir and 204.40±30.29 for tenofovir) and MPO (IC₅₀= 321.03±214.03 mM for acyclovir and 52.90±0.68 for tenofovir) when compared to standard drugs acarbose and rutin hydrate (IC₅₀=10.57±0.57 for α -glucosidase; IC₅₀=13.00±2.67 for MPO). According to Table 1, acyclovir is a more potent inhibitor on α -glucosidase than MPO, while tenofovir inhibits MPO more effectively. The inhibitory effects of antiviral drug active compounds and standard on α -glucosidase decreased activity are in the following order: acarbose > acyclovir > tenofovir. Similarly, for MPO, this order is as follows: rutin hydrate > tenofovir > acyclovir.

The inhibitory effects of antidiabetic drug active compounds and standard compounds on α -glucosidase and MPO are given in Table 2.

According to Table 2, glibornuride and glurenorm showed the lowest IC₅₀ values for α -glucosidase (IC₅₀=0.29±0.04) and MPO (IC₅₀=4.11±0.26), respectively. Both enzymes were inhibited at the lowest rate by metformin (IC₅₀=142.59±46.64 for α -glucosidase; IC₅₀=151.05±149.81 for MPO). The highest inhibition values of the antidiabetic drug active compounds and standards for α -glucosidase are as follows: glibornuride > glurenorm > glibenclamide > acarbose > metformin; and for MPO, glurenorm > rutin hydrate > glibenclamide > glibornuride > metformin, respectively (Table 2).

α -Glucosidase and MPO inhibitory activities of NSAIDs compounds and standard compounds are

given in Table 3.

Among NSAIDs, paracetamol was found to be the most potent α -glucosidase enzyme inhibitor (IC₅₀=4.02±0.20), while salicylic acid was identified as the weakest α -glucosidase enzyme inhibitor (IC₅₀=206.23±15.28). While indomethacin did not show any inhibitory effect on α -glucosidase, on the contrary, it was found to strongly inhibit MPO at the highest rate (IC₅₀=3.3×10⁻⁵ ±0.03×10⁻⁵). Inhibition rate of NSAIDs and standard compounds, for α -glucosidase is: paracetamol > acarbose > ketorolac > diclofenac > benzidamine HCl > salicylic acid; and for MPO is indomethacin > diclofenac > paracetamol > rutin hydrate > ketorolac tromethamine > salicylic acid > benzidamine HCl, respectively.

Given their multitude of roles *in-vivo*, inhibition of α -glucosidase and MPO in a number of different processes is very important. α -Glucosidase inhibition has potential in the treatment of lysosomal storage diseases, diabetes, and viral infections, including influenza and HIV. On the other hand, suppressing the catalytic activity of MPO prevents the accumulation of reactive oxygen species that cause tissue damage in some inflammatory diseases such as rheumatoid arthritis, atherosclerosis, multiple sclerosis, and cerebral ischemia-reperfusion. (6,20). Therefore, MPO and its downstream inflammatory pathways might be attractive targets for both prognostic and therapeutic intervention in the prophylaxis of all mentioned illnesses. Besides that, α -glucosidase inhibitors can play an important role in controlling the postprandial blood glucose levels of diabetics and keeping the blood glucose levels in a suitable range by delaying the digestion of carbohydrates and diminishing the absorption of

monosaccharides (21-23).

In recent years, in addition to different sugar-based inhibitory molecules being designed (24), extracts obtained from different parts of various plants have also been reported to exhibit inhibitory activity against glucosidase (25-27). Most of the α -glucosidase inhibitors in these plants are secondary metabolites such as alkaloids, phenolic acids, flavonoids, terpenoids, anthocyanins, and their glycosides, and these have been suggested to have much stronger inhibitory potentials than the inhibitory effect obtained from acarbose (28).

Among the antiviral agents, acyclovir is used in the treatment of diseases such as herpes viruses, genital herpes, chickenpox, shingles, and dermal infections. Instead of this, in the studies conducted with various antiviral drugs for the prevention of the SARS CoV-2 pandemic, two antiviral drugs, muglistat and catastanospermine (the prodrug of celgosivir) are used for the inhibition of α -glucosidase (I and II) involved in the early stages of glycoprotein N-linked oligosaccharide processing in the endoplasmic reticulum (ER) where acyclovir inhibition is not examined (29, 30). On the other hand, another antiviral drug, tenofovir, is available for the treatment of HIV and HBV infections (31). No previous studies were found based on *in vitro* inhibition of α -

glucosidase and MPO by acyclovir and tenofovir. However, Olojede et al., (2022) demonstrated in their research that tenofovir disoproxil fumarate loaded on silver nanoparticles successfully reduced the blood sugar level of diabetic rats through the inhibition of α -glucosidase and α -amylase in the gastrointestinal tract *in vivo*. (32). In our study, we have found that acyclovir inhibited α -glucosidase more effectively than tenofovir, with an inhibition rate of $IC_{50}=58.41\pm 16.73$ mM. On the other hand, tenofovir reduced MPO activity more effectively ($IC_{50}=52.90\pm 0.68$ mM) than acyclovir ($IC_{50}=321.03\pm 214.03$ mM).

α -Glucosidase inhibitors are oral antihyperglycemic drugs that inhibit upper gastrointestinal enzymes that break down complex carbohydrates into glucose. Most conventional glycosidase inhibitors mimic the structures of monosaccharides or oligosaccharides and are well accepted by organisms. As a result, the absorption of glucose is delayed, postprandial glucose is reduced, and glycemic control is improved (33). Widely used two types of oral antidiabetics in the treatment of hyperglycemia are biguanides (metformin) and the second generation of sulphonylureas (glibenclamide, glibornuride, and gliquidon (glurenorm)).

Table 2: α -Glucosidase and MPO inhibitory activities of antidiabetic drug active compounds at different concentrations.

Enzyme	Drug active compounds	Drug active conc. (mM)	Inhibition (%)*	IC ₅₀ (mM)*
α -Glucosidase	Glibenclamide	0.05	8.52±0.78	4.62±3.50
		0.25	11.21±1.96	
		0.50	14.20±3.40	
	Glibornuride	0.001	2.24±0.77	0.29±0.04
		0.01	13.15±0.68	
		0.1	21.53±2.33	
	Glurenorm	0.1	20.33±1.30	0.86±0.05
		0.5	29.02±2.02	
		0.75	49.03±1.44	
	Metformin	10.0	10.17±4.04	142.59±46.64
		25.0	12.85±1.58	
		50.0	23.32±3.59	
	Acarbose	2.5	21.83±0.65	10.57±0.57
		5.0	26.77±2.77	
		7.5	40.20±1.77	
MPO	Glibenclamide	2.5	4.5±3.18	48.7±9.93
		5.0	7.3±1.98	
		10.0	12.1±0.21	
	Glibornuride	5.0	5.3±0.78	119.85±34.86
		12.5	7.4±2.33	
		25.0	13.8±2.83	
	Glurenorm	2.5x10 ⁻¹	1.1±0.71	4.11±0.26
		0.5	3.3±0.71	
		1.0	10.5±1.27	
	Metformin	2.5	3.7±3.39	151.05±149.81
		5.0	6.0±2.47	
		10.0	8.2±2.19	

	2.5	31.3±1.77	
Rutin hydrate	5.0	38.9±0.78	13.00±2.67
	10.0	43.3±2.97	

*Mean±SD

Table 3: α -Glucosidase and MPO inhibitory activities of NSAIDs compounds at different concentrations.

Enzyme	Drug active compounds	Drug active conc. (mM)	Inhibition (%)*	IC ₅₀ (mM)*
α -Glucosidase	Benzydamine HCl	50	23.09±1.01	73.19±2.16
		60	33.75±3.26	
		70	46.81±2.27	
	Diclofenac	15	8.33±0.57	52.28±1.21
		25	24.51±1.35	
		45	41.20±1.02	
	Indomethacin	-	-	-
	Ketorolac-tromethamine	2.5	26.13±0.58	22.56±1.92
		10	30.70±0.35	
		15	43.20±2.72	
	Paracetamol	0.1	16.1±1.40	4.02±0.20
		1.0	39.1±0.48	
		5.0	54.9±1.70	
	Salicylic acid	25	3.31±0.80	206.23±15.28
		40	6.43±3.08	
100		22.39±1.66		
Acarbose	2.5	21.83±0.65	10.57±0.57	
	5.0	26.77±2.77		
	7.5	40.20±1.77		
MPO	Benzydamine HCl	2.5	2.7±2.83	153.17±102.15
		5.0	3.5±0.99	
		10.0	5.3±2.69	
	Diclofenac	3.4x10 ⁻³	19.4±11.81	5.6x10 ⁻³ ±0.0003
		5.1x10 ⁻³	44.5±2.05	
		8.4x10 ⁻³	85.9±4.03	
	Indomethacin	2.8x10 ⁻⁸	18.5±2.12	3.3x10 ⁻⁵ ±0.03x10 ⁻⁵
		2.8x10 ⁻⁶	20.3±2.33	
		1.4x10 ⁻⁵	41.6±21.4	
	Ketorolac-tromethamine	1.25	3.3±2.97	24.92±2.74
		2.5	9.4±1.34	
		5.0	11.3±3.04	
	Paracetamol	6.6x10 ⁻³	1.3±0.14	0.032±0.004
		9.9x10 ⁻³	19.7±11.6	
		1.7x10 ⁻²	22.3±3.54	
Salicylic acid	5.0	5.4±2.05	83.69±5.64	
	10.0	6.8±0.07		
	20.0	13.7±2.26		
Rutin hydrate	2.5	31.3±1.77	13.00±2.67	
	5.0	38.9±0.78		
	10.0	43.3±2.97		

*Mean±SD

Especially, sulfonylureas are widely used in medicine as potent blood glucose-reducing agents for the treatment of diabetes. Sulfonylureas alter the plasma membrane of cells to increase their responsiveness to insulin action, by increasing the number of insulin receptors (34). Today, a wide variety of sulfonylurea derivatives continue to be synthesized and

recommended as adjunctive agents in treatments to reduce diabetes symptoms. Although it has been emphasized that the mechanism of action of sulfonylureas in diabetes is on insulin secretion in the pancreas., Bui et al., (2021) demonstrated in their research that different new synthesized sulfonylurea derivatives exhibited significant α -glucosidase

inhibition compared to commercially available acarbose and glipizide (35). Similarly, in our study, we found that glubornuride and glurenorm, also inhibited α -glucosidase more strongly than acarbose ($IC_{50} = 0.29 \pm 0.04$ mM; $IC_{50} = 0.86 \pm 0.05$ mM). On the other hand, when examined with various diabetes models after the formation of diabetes, it is observed that MPO activity clearly increases in various diabetic tissues (36-38). Although, a broad and chemically heterogeneous group of molecules (alkylindoles, fluoroindoles, indazonoles, dapson, bis-arylalkamines, nitroxides, and phenolic compounds) have been found to successfully inhibit MPO, no data were found regarding *in vitro* inhibition with oral antihyperglycemic drugs (39). Our research showed that each examined antihyperglycemic drug in Table 2 inhibited MPO at different rates, but the highest inhibition was observed to be achieved by glurenorm ($IC_{50} = 4.11 \pm 0.26$ mM). However, if we need to make a comparison between both groups, it was found that sulfonylurea group oral antidiabetic agents are more effective inhibitors of both studied enzymes, α -glucosidase and MPO, than metformin, which is a biguanide type.

The NSAIDs are among the most widely prescribed drugs worldwide (40), and these components were investigated for their ability to affect the chlorinating activity of human MPO and to scavenge HOCl, which is the main MPO system product (41). In our study, although NSAIDs showed an inhibitory effect on the α -glucosidase, it was observed that this effect was actually more effective on MPO. Moreover, indomethacin was found to be the strongest MPO inhibitor with the lowest IC_{50} value ($IC_{50} = 3.3 \times 10^{-5} \pm 0.03 \times 10^{-5}$), whereas on α -glucosidase, it was observed to be unaffected (Table 3). Supporting this, in an *in-vitro* study using murine neutrophils, it was found that indomethacin and NSAIDs inhibited HOCl formation in MPO (42). Similarly, Zurbier et al., (1990) demonstrated that, in isolated MPO from human polymorphonuclear neutrophils, diclofenac inhibited the enzyme during the reaction cycle of MPO with H_2O_2 (43). Supporting these findings, we also found in our study that diclofenac inhibits MPO very effectively. ($IC_{50} = 5.6 \times 10^{-3} \pm 0.0003$ mM).

4. CONCLUSION

Despite the discovery of different novel α -glucosidase and MPO inhibitors as potential novel therapeutic interventions for many diseases, in existing literature there is a lack of information about the inhibitory effects of 12 commonly used drug active compounds studied in our research. Among the scanned different antiviral, antidiabetic, and NSAIDs active compounds, it was found that these selected ingredients are effective inhibitors of α -glucosidase as well as MPO *in-vitro*, except indomethacin, which is not effective on α -glucosidase activity in contrast to MPO. Therefore, we can suggest that these drugs, which are used as antidiabetics, antivirals, and NSAIDs in the field of health, can contribute to the pharmaceutical industry due to their α -glucosidase and MPO inhibition effects.

5. CONFLICT OF INTEREST

There are no conflicts to declare.

6. ACKNOWLEDGMENTS

Research Fund of Istanbul University-Cerrahpaşa financed this study (Project No: FDK-2022-36259).

7. REFERENCES

1. Rempel BP, Withers SG. Covalent inhibitors of glycosidases and their applications in biochemistry and biology. *Glycobiology* [Internet]. 2008 May 14;18(8):570–86. Available from: [<URL>](#).
2. Wolfenden R, Lu X, Young G. Spontaneous hydrolysis of glycosides. *J Am Chem Soc* [Internet]. 1998 Jun 13;120(27):6814–5. Available from: [<URL>](#).
3. Compain P. Multivalent effect in glycosidase inhibition: The end of the beginning. *The Chemical Record* [Internet]. 2020 Jan 17;20(1):10–22. Available from: [<URL>](#).
4. Gloster TM, Davies GJ. Glycosidase inhibition: assessing mimicry of the transition state. *Org Biomol Chem* [Internet]. 2010 Dec 23;8(2):305–20. Available from: [<URL>](#).
5. Wadood A, Ghufuran M, Khan A, Azam SS, Jelani M, Uddin R. Selective glycosidase inhibitors: A patent review (2012–present). *Int J Biol Macromol* [Internet]. 2018 May;111:82–91. Available from: [<URL>](#).
6. Chen S, Chen H, Du Q, Shen J. Targeting myeloperoxidase (MPO) mediated oxidative stress and inflammation for reducing brain ischemia injury: Potential application of natural compounds. *Front Physiol* [Internet]. 2020 May 19;11:528444. Available from: [<URL>](#).
7. Peng Y, Wu X, Zhang S, Deng C, Zhao L, Wang M, et al. The potential roles of type I interferon activated neutrophils and neutrophil extracellular traps (NETs) in the pathogenesis of primary Sjögren's syndrome. *Arthritis Res Ther* [Internet]. 2022 Dec 19;24(1):170. Available from: [<URL>](#).
8. Ling S, Xu JW. NETosis as a pathogenic factor for heart failure. *Oxid Med Cell Longev* [Internet]. 2021 Feb 23;2021:6687096. Available from: [<URL>](#).
9. Hawkins CL, Davies MJ. Role of myeloperoxidase and oxidant formation in the extracellular environment in inflammation-induced tissue damage. *Free Radic Biol Med* [Internet]. 2021 Aug 20;172:633–51. Available from: [<URL>](#).
10. Carr AC, Myzak MC, Stocker R, McCall MR, Frei B. Myeloperoxidase binds to low-density lipoprotein: potential implications for atherosclerosis. *FEBS Lett* [Internet]. 2000 Dec 29;487(2):176–80. Available from: [<URL>](#).
11. Zheng L, Nukuna B, Brennan ML, Sun M, Goormastic M, Settle M, et al. Apolipoprotein A-I is a

- selective target for myeloperoxidase-catalyzed oxidation and functional impairment in subjects with cardiovascular disease. *J Clin Invest* [Internet]. 2004 Aug 16;114(4):529–41. Available from: [<URL>](#).
12. Tiruppathi C, Naqvi T, Wu Y, Vogel SM, Minshall RD, Malik AB. Albumin mediates the transcytosis of myeloperoxidase by means of caveolae in endothelial cells. *Proc Natl Acad Sci* [Internet]. 2004 May 18;101(20):7699–704. Available from: [<URL>](#).
13. Astern JM, Pendergraft WF, Falk RJ, Jennette JC, Schmaier AH, Mahdi F, et al. Myeloperoxidase interacts with endothelial cell-surface cytokeratin 1 and modulates bradykinin production by the plasma kallikrein-kinin system. *Am J Pathol* [Internet]. 2007 Jul 1;171(1):349–60. Available from: [<URL>](#).
14. Bouriche H, Salavei P, Lessig J, Arnhold J. Differential effects of flavonols on inactivation of α 1-antitrypsin induced by hypohalous acids and the myeloperoxidase–hydrogen peroxide–halide system. *Arch Biochem Biophys* [Internet]. 2007 Mar 1;459(1):137–42. Available from: [<URL>](#).
15. Segelmark M, Persson B, Hellmark T, Wieslander J. Binding and inhibition of myeloperoxidase (MPO): a major function of ceruloplasmin? *Clin Exp Immunol* [Internet]. 2003 Oct 29;108(1):167–74. Available from: [<URL>](#).
16. Ndrepepa G. Myeloperoxidase – A bridge linking inflammation and oxidative stress with cardiovascular disease. *Clin Chim Acta* [Internet]. 2019 Jun 1;493:36–51. Available from: [<URL>](#).
17. Wang J, Li J, Cui Z, Zhao M. Deglycosylation influences the oxidation activity and antigenicity of myeloperoxidase. *Nephrology* [Internet]. 2018 Jan 17;23(1):46–52. Available from: [<URL>](#).
18. Tao Y, Zhang Y, Cheng Y, Wang Y. Rapid screening and identification of α -glucosidase inhibitors from mulberry leaves using enzyme-immobilized magnetic beads coupled with HPLC/MS and NMR. *Biomed Chromatogr* [Internet]. 2013 Feb 5;27(2):148–55. Available from: [<URL>](#).
19. Wei H, Frenkel K. In vivo formation of oxidized DNA bases in tumor promoter-treated mouse skin. *Cancer Res* [Internet]. 1991;51(16):4443–9. Available from: [<URL>](#).
20. Gloster TM, Davies GJ. Glycosidase inhibition: assessing mimicry of the transition state. *Org Biomol Chem* [Internet]. 2010;8(2):305–20. Available from: [<URL>](#).
21. Shen Q, Shao J, Peng Q, Zhang W, Ma L, Chan ASC, et al. Hydroxycoumarin derivatives: Novel and potent α -glucosidase inhibitors. *J Med Chem* [Internet]. 2010 Dec 9;53(23):8252–9. Available from: [<URL>](#).
22. Nakao Y, Maki T, Matsunaga S, Van Soest RWM, Fusetani N. Penasulfate A, a new α -glucosidase inhibitor from a marine sponge *Penares* sp. *J Nat Prod* [Internet]. 2004 Aug 1;67(8):1346–50. Available from: [<URL>](#).
23. Zhang X, Li G, Wu D, Yu Y, Hu N, Wang H, et al. Emerging strategies for the activity assay and inhibitor screening of α -glucosidase. *Food Funct* [Internet]. 2020 Jan 29;11(1):66–82. Available from: [<URL>](#).
24. Ferjancic Z, Bihelovic F, Vulovic B, Matovic R, Trmcic M, Jankovic A, et al. Development of iminosugar-based glycosidase inhibitors as drug candidates for SARS-CoV-2 virus via molecular modelling and in vitro studies. *J Enzyme Inhib Med Chem* [Internet]. 2024 Dec 31;39(1):2289007. Available from: [<URL>](#).
25. Tunalı S, Yaşar Boztaş F, Yanardağ R. The inhibitory effects of plant extracts, vitamins and amino acids on myeloperoxidase activity. *İstanbul J Pharm* [Internet]. 2020 Aug 30;50(2):125–30. Available from: [<URL>](#).
26. Zhang L, Tu Z cai, Xie X, Wang H, Wang H, Wang Z xing, et al. Jackfruit (*Artocarpus heterophyllus* Lam.) peel: A better source of antioxidants and α -glucosidase inhibitors than pulp, flake and seed, and phytochemical profile by HPLC-QTOF-MS/MS. *Food Chem* [Internet]. 2017 Nov 1;234:303–13. Available from: [<URL>](#).
27. Park D, Barka GD, Yang EY, Cho MC, Yoon JB, Lee J. Identification of QTLs controlling α -glucosidase inhibitory activity in pepper (*Capsicum annuum* L.) leaf and fruit using genotyping-by-sequencing analysis. *Genes (Basel)* [Internet]. 2020 Sep 23;11(10):1116. Available from: [<URL>](#).
28. Assefa ST, Yang EY, Chae SY, Song M, Lee J, Cho MC, et al. Alpha glucosidase inhibitory activities of plants with focus on common vegetables. *Plants* [Internet]. 2019 Dec 18;9(1):2. Available from: [<URL>](#).
29. Williams SJ, Goddard-Borger ED. α -glucosidase inhibitors as host-directed antiviral agents with potential for the treatment of COVID-19. *Biochem Soc Trans* [Internet]. 2020 Jun 30;48(3):1287–95. Available from: [<URL>](#).
30. Rajasekharan S, Milan Bonotto R, Nascimento Alves L, Kazungu Y, Poggianella M, Martinez-Orellana P, et al. Inhibitors of protein glycosylation are active against the coronavirus severe acute respiratory syndrome coronavirus SARS-CoV-2. *Viruses* [Internet]. 2021 Apr 30;13(5):808. Available from: [<URL>](#).
31. Marrazzo JM, Ramjee G, Richardson BA, Gomez K, Mgodi N, Nair G, et al. Tenofovir-based preexposure prophylaxis for HIV infection among African women. *N Engl J Med* [Internet]. 2015 Feb 5;372(6):509–18. Available from: [<URL>](#).
32. Olojede SO, Lawal SK, Dare A, Naidu ECS, Rennie CO, Azu OO. Evaluation of tenofovir disoproxil fumarate loaded silver nanoparticle on testicular morphology in experimental type-2 diabetic rats. *Artif Cells, Nanomedicine, Biotechnol* [Internet]. 2022 Dec 31;50(1):71–80. Available from: [<URL>](#).
33. Hedrington MS, Davis SN. Considerations when

using alpha-glucosidase inhibitors in the treatment of type 2 diabetes. *Expert Opin Pharmacother* [Internet]. 2019 Dec 12;20(18):2229–35. Available from: [<URL>](#).

34. Mikada A, Narita T, Yokoyama H, Yamashita R, Horikawa Y, Tsukiyama K, et al. Effects of miglitol, sitagliptin, and initial combination therapy with both on plasma incretin responses to a mixed meal and visceral fat in over-weight Japanese patients with type 2 diabetes. "The MASTER randomized, controlled trial." *Diabetes Res Clin Pract* [Internet]. 2014 Dec 1;106(3):538–47. Available from: [<URL>](#).

35. Bui TT, Tran VL, Ngo DQ, Tran VC, Tran VS, Tran TPT. Synthesis and evaluation of α -glucosidase inhibitory activity of sulfonyleurea derivatives. *Zeitschrift für Naturforsch B* [Internet]. 2021 Apr 27;76(3–4):163–71. Available from: [<URL>](#).

36. Nessler K, Grzybczak R, Nessler M, Zalewski J, Gajos G, Windak A. Associations between myeloperoxidase and paraoxonase-1 and type 2 diabetes in patients with ischemic heart disease. *BMC Cardiovasc Disord* [Internet]. 2022 Dec 3;22(1):521. Available from: [<URL>](#).

37. Unubol M, Yavasoglu I, Kacar F, Guney E, Omurlu IK, Ture M, et al. Relationship between glycemic control and histochemical myeloperoxidase activity in neutrophils in patients with type 2 diabetes. *Diabetol Metab Syndr* [Internet]. 2015 Dec 30;7(1):119. Available from: [<URL>](#).

38. Ozel AB, Dagsuyu E, Aydın PK, Bugan I, Bulan OK, Yanardag R, et al. Brain boron level, DNA content, and myeloperoxidase activity of metformin-

treated rats in diabetes and prostate cancer model. *Biol Trace Elem Res* [Internet]. 2022 Mar 15;200(3):1164–70. Available from: [<URL>](#).

39. Valadez-Cosmes P, Raftopoulou S, Mihalic ZN, Marsche G, Kargl J. Myeloperoxidase: Growing importance in cancer pathogenesis and potential drug target. *Pharmacol Ther* [Internet]. 2022 Aug 1;236:108052. Available from: [<URL>](#).

40. Abdel-Azeem AZ, Abdel-Hafez AA, El-Karamany GS, Farag HH. Chlorzoxazone esters of some non-steroidal anti-inflammatory (NSAI) carboxylic acids as mutual prodrugs: Design, synthesis, pharmacological investigations and docking studies. *Bioorg Med Chem* [Internet]. 2009 May 15;17(10):3665–70. Available from: [<URL>](#).

41. Nève J, Parij N, Moguilevsky N. Inhibition of the myeloperoxidase chlorinating activity by non-steroidal anti-inflammatory drugs investigated with a human recombinant enzyme. *Eur J Pharmacol* [Internet]. 2001 Apr 6;417(1–2):37–43. Available from: [<URL>](#).

42. Shacter E, Lopez RL, Pati S. Inhibition of the myeloperoxidase-H₂O₂-Cl⁻ system of neutrophils by indomethacin and other non-steroidal anti-inflammatory drugs. *Biochem Pharmacol* [Internet]. 1991 Mar 15;41(6–7):975–84. Available from: [<URL>](#).

43. Zuurbier KWM, Bakkenist ARJ, Fokkens RH, Nibbering NMM, Wever R, Muijsers AO. Interaction of myeloperoxidase with diclofenac. *Biochem Pharmacol* [Internet]. 1990 Oct 15;40(8):1801–8. Available from: [<URL>](#).



Adsorption Performance of Acidic Modified Fly Ash: Box–Behnken Design

İlhan Küçük^{1*}, Pınar Üstündağ²

¹Department of Chemistry, Faculty of Arts and Sciences, Muş Alparslan University, Muş, Türkiye.

²Health Sciences, Muş Alparslan University, Muş, Türkiye.

Abstract: Fly ash (FA) and modified fly ash (mFA) were used as adsorbents to remove methylene blue (MB) dye from aqueous solutions. The adsorbents were characterized using crystal structures with XRD, surface functional groups with FTIR, and surface morphologies with SEM. Response surface methodology (RSM) with Box-Behnken design (BBD) was used to optimize adsorption parameters such as MB dye concentration (A: 10-20 mg/L), solution pH (B: 3-11), and contact time (C: 30-180 min). ANOVA analysis shows the significant interactions between initial concentration, solution pH value, and solution pH value, contact time was found to be significant in the removal of MB (p -value= $\leq 0.0001, 0.0040$), whereas between the effect of initial concentration and contact time was not significant (p -value = 0.0881). The adsorption kinetics followed the pseudo-second-order (PSO) kinetic model and the adsorption isotherm followed the Langmuir model. At 28°C, the adsorption capacity of fly ash-HNO₃ for MB was found to be 7.67 mg/g.

Keywords: Fly Ash, ANOVA, Adsorption, Box–Behnken design, Methylene blue.

Submitted: September 26, 2023. **Accepted:** February 19, 2024.

Cite this: Küçük İ, Üstündağ P. Adsorption Performance of Acidic Modified Fly Ash: Box–Behnken Design. JOTCSA. 2024;11(2):699-708.

DOI: <https://doi.org/10.18596/jotcsa.1366346>

***Corresponding author's E-mail:** i.kucuk@alparslan.edu.tr

1. INTRODUCTION

Fly ash (FA) is a product made from coal-burning power plants. Every year, EU countries produce around two million tons of fly ash, but only a small portion of it is utilized (1). FA has numerous applications, including its use in cementitious products, construction sites such as highway road bases, and as an effective sorbent for eliminating heavy metals, organics, and dyes from water (2). Although FA has many positive uses, its production rate exceeds its consumption rate. So, FA disposal poses a significant problem due to its detrimental impact on air, water, and soil (3).

FA can be used as an inexpensive adsorbent to eliminate dyes, heavy metals, and organics from wastewater (4). This is due to its low cost, availability, and environmentally friendly features (5). However, the low surface area and crystalline structure of FA waste result in a low adsorption capacity. To improve the adsorption efficiency of dye-contaminated wastewater, the modification of FA with chemical and physical methods has been studied. Many researchers have experimented with various methods to modify FA to adsorb different

dyes. Treatment with different methods has been found to increase the adsorption capacity (6).

Every day, clean water supplies are at risk of being contaminated by harmful substances like synthetic dyes, heavy metals, medicines, pesticides, and other pollutants. Synthetic dyes, in particular, can be extremely dangerous even in small amounts, as they can cause cancer and mutations (7). These dyes are commonly used in various industries such as textiles, paper, pulp, tanneries, and pharmaceuticals due to their affordability, vibrant hues, ability to withstand environmental factors, and ease of application (8). The widespread use of these dyes has led to a significant amount of pollution being released into water systems. This pollution has harmful impacts on the environment and poses a threat to human health (9). Efficient treatment of dye effluent is necessary before it can be released into a water body. Several methods have been devised for removing dyes from industrial wastewater, such as electrocoagulation (10), coagulation (11), photocatalysis (12), cation-exchange membrane (13), and adsorption (14). Out of all the different treatment methods available, adsorption is considered to be the most favorable

due to its easy implementation, high removal efficiency, and minimal secondary pollution (15).

The research aims to enhance the adsorption capacity of FA, which is produced in large quantities in our country and around the world, for methylene blue through acidic modification. The study involved characterizing the modified FAs and conducting tests using the modification that demonstrated the highest adsorption capacity, as well as kinetic and isotherm equations. Additionally, the Box-Behnken design (BBD) was utilized to optimize the adsorption of MB dye statistically and maximize its efficiency.

2. METHODS AND MATERIALS

2.1. Materials and Reagents

The FA was obtained from a thermal power plant (Afşin, Elbistan, Türkiye). Hydrochloric acid (HCl, 0.5 M, J.T. Baker, Poland), sulfuric acid (H₂SO₄, ~96-99%, Merck Germany), and nitric acid (HNO₃, ~65%, Merck, Germany) were procured. Methylene blue

(Isolab, Türkiye, λ_{max}, 663 nm) was used in the adsorption process as adsorbates.

2.2. Preparation of the FA

The fly ash obtained from Afşin/Elbistan was washed with distilled water and dried at 105 °C in the oven until constant weight was reached. The dried fly ash earned a stable weight and was thoroughly ground using an agate mortar. Three different conical flask samples, each weighing 25 grams, were added to the obtained fly ash, and 0.1 M H₂SO₄, HCl, and HNO₃ were added to each sample. Partial carbon dioxide release was observed. The mixture was stirred at 400 rpm at room temperature for 6 hours. The mixture was then filtered through filter paper (coarse filter paper), and the resulting modified fly ash was washed with distilled water until it reached a pH of 7.

The Box-Behnken method was studied with the help of the Design Expert -13 program and working conditions are given in Table 1.

Table 1. Adsorption conditions.

Run	A: Initial Concentration	B: pH	C: Contact time	Response: Adsorption amount
1	10	3	105	5.1
2	10	7	30	5
3	20	7	180	9.7
4	15	11	180	10.3
5	15	7	105	7
6	15	7	105	7.2
7	15	3	180	5.5
8	20	11	105	12
9	10	7	180	6.7
10	15	7	105	6.7
11	15	7	105	7.1
12	15	3	30	4.5
13	15	11	30	7.6
14	10	11	105	7.3
15	20	3	105	5.4
16	20	7	30	7.2
17	15	7	105	7.1

2.3. Adsorption Procedure

For the adsorption study, 0.5 g of methylene blue (C₁₆H₁₈ClN₃S, λ_{max} = 663 nm) was taken and dissolved in 1000 mL of distilled water to prepare the stock solution. This stock solution was used in all adsorption processes. Isotherm studies were conducted at three different temperatures (301, 310, and 321 K) with initial concentrations ranging from 5 to 25 ppm for a duration of 3 h. Additionally, kinetic studies were carried out for initial concentrations ranging from 10 to 20 ppm for a duration of 3 h. Equation 1 was used to determine the results.

$$qe = \frac{(Co - Ce)V}{W} \quad (1)$$

pH adjustments were made with 0.01, 0.1 M HCl, and 0.01 and 0.1 M NaOH solutions.

2.4. Fly Ash Analysis

The surface morphologies of fly ash were determined using SEM (scanning electron microscope model LEO-EVO 40). FTIR analysis was analyzed in an Agilent Cary 630 Infrared Spectrophotometer

equipped with a spectrum range of 400-4000 cm⁻¹, resolution 2 cm⁻¹, to observe different functional groups. XRD spectrum of the fly ash was analyzed in a PANalytical Empyrean equipped with a spectrum range of 10-80 2θ, X-ray generator 4 kW to observe crystallization. UV-Vis Analysis was performed with an Agilent Cary 60 device.

3. RESULTS AND DISCUSSION

3.1. Characterization of FAs

FT-IR analysis is a widely used method to investigate structural modifications in substances (16). This particular study analyzed the infrared spectra of FA and mFA. The spectra were evaluated in four distinct regions that correspond to vibrations of Si-Al, C, S, and OH bonds. The number of vibrations in each wavelength was assessed to identify any differences between them. The results from FTIR analysis helped to determine the surface structures of molecules, which are depicted in Figure 1 A. The Si-O bonds associated with Al-O vibrations occur at frequencies

of 593 and 604 cm^{-1} . Additionally, CO_3^{2-} can be seen at 1426 cm^{-1} (17).

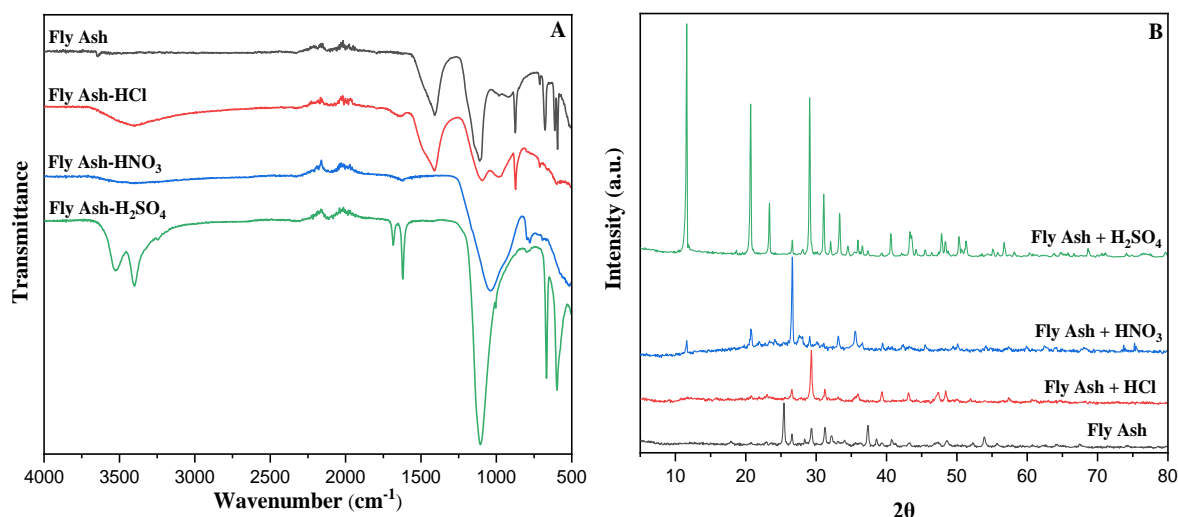


Figure 1: A. FT-IR spectrum **B.** X-ray diffraction spectrum.

Meanwhile, the vibrations of Si-O bonds in cage assemblies are observed at a frequency of 908 cm^{-1} , and vibrations of Si-O-Si bonds are observed at a frequency of 1040 cm^{-1} (18). The band at about 1430 cm^{-1} is from sodium carbonate inclusion due to the reaction of residual sodium with atmospheric CO_2 (16). Additionally, the weak peaks at 1660 may be due to unburned carbons in fly ash, caused by C=O

and C=C stretching and bending (16). The broad band at 3490–3390 cm^{-1} corresponded to stretching vibrations of (Al)O-H and (Si)O-H bonds (19). The peaks in the untreated sample were slightly increased after modification which illustrates the attachment of the carboxylic group to the surface of fly ash. This is an indication that carboxylic groups are attached to the surface of fly ash.

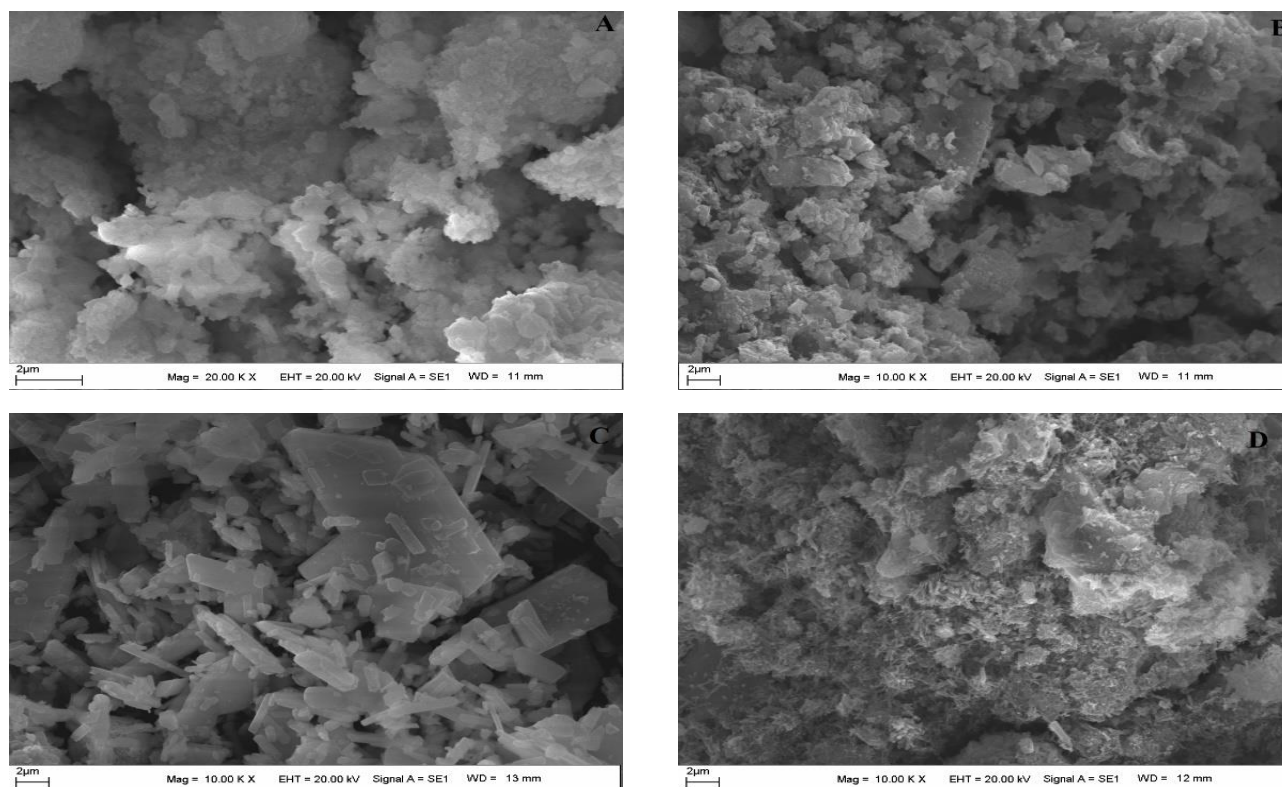


Figure 2: A. Fly Ash **B.** Fly Ash + HNO₃ **C.** Fly Ash + H₂SO₄ **D.** Fly Ash + HCl.

The X-ray diffraction pattern presented in Figure 1 B determined crystallographic information about the FAs. The peaks within the 2θ angle range of 5 to 80 were identified based on peak position data. The diffractogram of FAs exhibits various peaks related to the primary chemical components, namely oxides.

These components include quartz, corundum, mullite, and hematite, along with other complex crystalline phases such as anorthite, goethite, albite, portlandite, gibbsite, and magnesium hydroxide (20). Most of the peaks in the fly ash diffractogram and modified fly ash were between 20-45.

Furthermore, the quartz and corundum peaks with the highest intensities were located between 20 and 30. The characteristic peaks of quartz and corundum are: 21°, 27°, 37° and 26°, 35°, 39° respectively. Mullite and hematite structures exhibit peaks at approximately 25-40° and 34-38°, respectively. Based on the results obtained, it is evident that the structure contains a high concentration of oxides.

SEM images reveal material morphology and surface texture. Figure 2 shows micrographs of fly ash and modified fly ash. Modifying fly ash brings about alterations in its surface appearance. The HNO₃ modification causes the structure to adopt a more particulate form, whereas the H₂SO₄ modification leads to the emergence of more pronounced and abundant crystal formations within the structure. Additionally, crystal structures are partially formed through the HCl modification.

3.2. Box–Behnken design

MB adsorption tests were designed using Design Expert 13.0 software, and a quadratic polynomial regression model was utilized to predict the response (Equation 2).

$$Y = \beta_0 + \sum \beta_i X_i + \sum \beta_{ii} X_i^2 + \sum \sum \beta_{ij} X_i X_j \quad (2)$$

Y shows the response factor; β_0 is the constant; X_i and X_j are coded as the factors; β_i , β_{ii} , and β_{ij} are coefficients of studied factors. BBD provided 17 experiments for optimizing factors affecting MB dye removal including A: Initial concentration (10–20 mg/g), B: pH (3–11), and C: Contact time (30–180 min). Table 1 presents data obtained from BBD regarding the removal of MB dye.

Table 2: ANOVA analysis.

Source	Sum of Squares	df	Mean Square	F-value	p-value
Model	61.96	9	6.88	168.78	< 0.0001
A-Initial Concentration	13.01	1	13.01	318.86	< 0.0001
B-pH	34.86	1	34.86	854.74	< 0.0001
C-Contact Time	7.80	1	7.80	191.27	< 0.0001
AB	4.84	1	4.84	118.67	< 0.0001
AC	0.1600	1	0.1600	3.92	0.0881
BC	0.7225	1	0.7225	17.71	0.0040
A ²	0.3853	1	0.3853	9.45	0.0180
B ²	0.0684	1	0.0684	1.68	0.2362
C ²	0.1253	1	0.1253	3.07	0.1231
Residual	0.2855	7	0.0408		
Lack of Fit	0.1375	3	0.0458	1.24	0.4059
Pure Error	0.1480	4	0.0370		
Cor Total	62.24	16			

BBD was used to design 17 experiments (as shown in Table 1) for testing three independent parameters that may significantly affect MB removal. BBD in RSM was used to investigate the effects of three independent variables on MB removal: Initial concentration (A), pH (B), and Contact time (C). The ANOVA analysis of experimental data for MB removal is presented in Table 2. ANOVA results were analyzed using p-values, sum of squares, and F-values to determine significant factors. The model's statistically significant F-value of 168.78 for MB removal has a corresponding p-value < 0.0001 (21). The adjusted R² of 0.989 and R² value of 0.995 indicate a strong correlation between predicted and actual values. According to Table 2, model term values with Prob > F < 0.0500 indicate that factors are significant under the chosen conditions. The significant model terms are linear terms of A, B, and C, quadratic terms of A², B², and C², and interaction

between AB, AC, and BC. To enhance the model fit, insignificant terms with p-value > 0.05 were excluded. Equation (4) expresses the polynomial relationship between examined parameters and MB removal.

$$\text{MB removal (mg/g)} = 8,59 - 0,55 A - 0,56 B + 0,002 C + 0,055 AB + 0,0005 AC + 0,001 BC + 0,012A^2 + 0,008 B^2 - 3,06 \times 10^{-5} C^2$$

The interactions between initial concentration (A), solution pH value (B), and solution pH value (B), contact time (C) were found to be significant on the removal of MB (p-value=< 0.0001, 0.0040), whereas between the effect of initial concentration (A) and contact time (C) was not significant (p-value = 0.0881). The three-dimensional (3D) surface for interaction between initial concentration (A), solution pH (B), and contact time (C) was given in Figure 3.

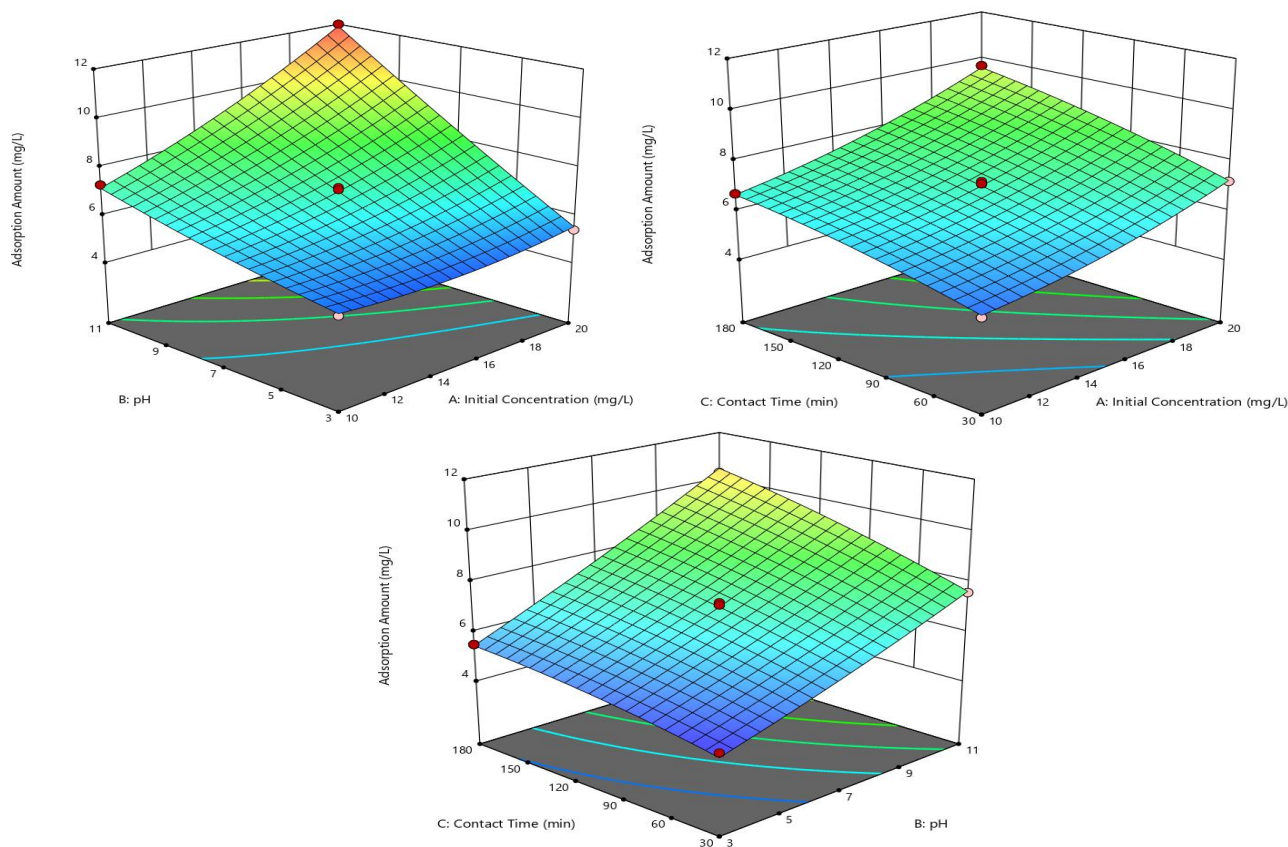


Figure 3: 3D response surface plot of MB removal.

The graph in Figure 4 illustrates how MB adsorption changes with varying initial concentrations, pH, and contact times. The concentration of the pollutant significantly affects the adsorption capacity of the adsorbent. The initial concentration of the MB was varied from 10 mg/L to 20 mg/L, resulting in an increase in uptake from 6.6 mg/g to 7.7 mg/g onto FA-HNO₃. Enhancement in adsorption capacity can be explained by the higher concentration of MB, which offers more molecules to be diffused into internal pores of FA-HNO₃ and reach active adsorption sites (22). The pH of an adsorption system significantly affects the adsorbent's surface characteristics, as well as the adsorbate's ionization and speciation. The effect of pH on the uptake of MB was studied across a pH range of 3 to 11. A significant increase in adsorption capacity occurs from pH 3 to 11, with a nearly two-fold increase in capacity. At low pH, the electron-rich active site on the sorbent surface was easily protonated, so less

available for MB cations adsorption. So, at low pH levels, its ability to adsorb is significantly reduced, causing a decrease in its adsorption capacity (23). The adsorption capacity of the adsorbent is significantly impacted by the duration of the pollutant's contact with the system. The adsorption of MB was initially very fast, with approximately 60% of the dye being adsorbed within the first 30 min. As the contact time between adsorbate and adsorbent increased, the uptake of MB dye gradually increased up to 180 min. The fast initial adsorption rate may be attributed to a higher number of available active sites, in terms of functional groups and pores, on the surface of the adsorbent during the initial stage of the adsorption process. However, as the adsorption process continues, the build-up of dye molecules on the surface of the adsorbent hinders the diffusion of molecules into pores, which leads to a slower adsorption rate (24).

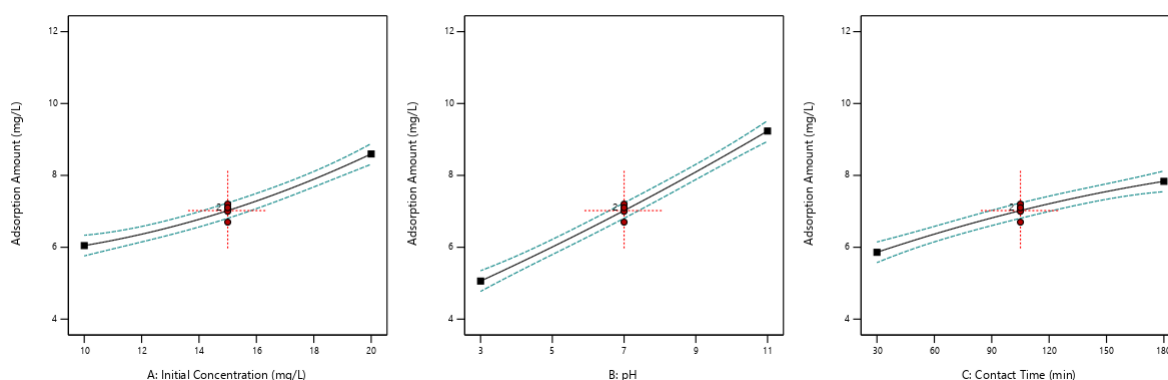


Figure 4: BBD of the effect of initial concentration, pH, and contact time.

3.3. Adsorption Studies

3.3.1 Adsorption isotherms

Understanding the interaction between Fly ash- HNO₃ and MB dye requires analyzing the adsorption isotherm. To determine the ability of Fly ash-HNO₃ to adsorb MB dye, the experimental data was fitted using linear forms of Langmuir, Freundlich, Temkin, and D-R models (25). These models are expressed by Eqs. (3)–(6) and help determine the adsorption capacity of Fly ash-HNO₃.

$$\frac{C_e}{q_e} = \frac{1}{K_L q_m} + \frac{C_e}{q_m} \quad (3)$$

$$\log q_e = \log K_F + \frac{1}{n} \log C_e \quad (4)$$

$$q_e = \frac{RT}{B_T} \ln K_T + \frac{RT}{B_T} \ln C_e \quad (5)$$

$$\ln q_e = \ln q_s - k_{ad} \varepsilon^2 \quad (6)$$

K_L (L/mg) is Langmuir isotherm constant, q_m (mg/g) is maximum adsorption capacity, K_F (mg/g) is Freundlich constant, T (K) is temperature in Kelvin, n is adsorption intensity, K_T (L/mg) is Temkin constant; b_T (J/mol) is heat of adsorption; R (8.314 J/mol·K) is universal gas constant; ε , is polanyi constant.

In Figure 5, the plot and function of isotherms are illustrated, while their detailed information is presented in Table 3. According to Table 3, it was observed that Langmuir isotherm was the most appropriate model for describing the homogeneous surface and monolayer adsorption of MB onto the adsorbent surface, with the highest R² value of 0.99. At a temperature of 28 °C, the maximum adsorption capacity (q_m) of the adsorbent for MB was determined to be 7.67 mg/g.

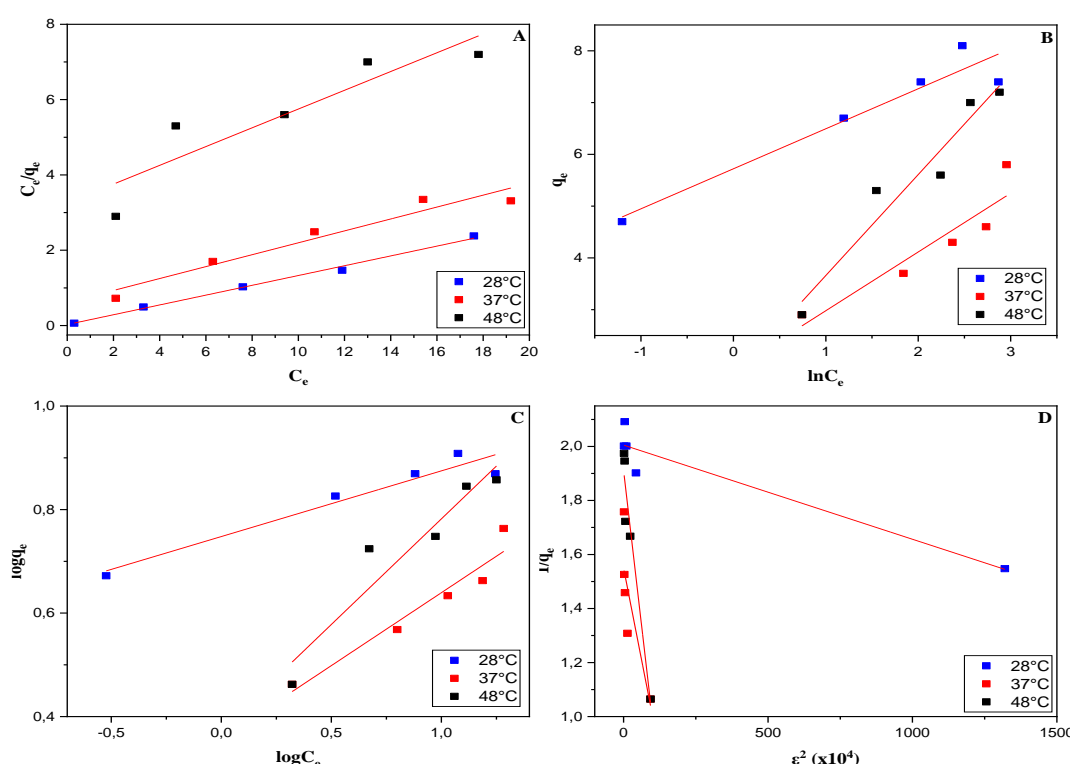


Figure 5: A. Langmuir B. Temkin C. Freundlich D. D-R.

Table 3. Isotherm constant.

°C	Langmuir			Freundlich			
	q_m	K_L	R^2	K_F	n	R^2	
28	7.67	4.96	0.997	5.59	7.88	0.966	
37	6.32	0.25	0.969	2.27	3.55	0.965	
48	4.01	0.07	0.911	2.36	2.45	0.953	
°C	D-R			Temkin			
	q_s	K_{ad}	E	R^2	B_T	K_T	R^2
28	7.42	3.4×10^{-4}	37.87	0.956	3237	1637	0.960
37	4.70	5.4×10^{-3}	9.57	0.835	2270	5.07	0.928
48	6.75	9.2×10^{-3}	7.41	0.972	1368	2.40	0.969

3.3.2 Adsorption kinetics

The kinetics of adsorption can provide valuable insights into the mechanism of MB adsorption. To determine the mechanism of adsorption of MB onto fly ash and modified fly ash, we applied kinetic models such as the pseudo-first-order (PFO),

Elovich, and pseudo-second-order (PSO) models. We examined experimental results of varying initial MB concentrations. The linear equations for PFO, Elovich, and PSO, models are explained in equations 7, 8, and 9, respectively (26).

$$\ln(q_e - q_t) = \ln q_e - k_1 t \tag{7}$$

$$q_e = \frac{1}{b} \ln(ab) + \frac{1}{b} \ln(t) \tag{8}$$

$$\frac{t}{q_t} = \frac{1}{k_2 q_e^2} + \frac{t}{q_e} \tag{9}$$

q_e (mg/g) is the amount of MB adsorbed by fly ash at equilibrium, q_t (mg/g) is the amount of MB adsorbed by fly ash at the time (t); k_1 (1/min) and k_2 (g/mg min) are rate constants of PFO and PSO respectively; a, b is Elovich constant.

In Figure 6, the plot and function of isotherms are illustrated, while their detailed information is presented in Table 4. In Table 4, the R^2 correlation coefficients from the pseudo-second-order model were found to be over 0.995, higher than those of

the pseudo-first-order model. This indicates that the pseudo-second-order model best describes the kinetics of MB adsorbed onto FA. Additionally, the calculated q_e , cal values from the pseudo-second-order model closely match the experimental q_e , exp values, whereas the q_e , cal values from the pseudo-first-order model are lower than the q_e , exp values. These results further support that the adsorption of MB onto FA from aqueous solution follows the pseudo-second-order model well. Similar phenomena have been observed in MB adsorption on other natural products. The pseudo-second-order model assumes that the rate-determining step involves chemical adsorption with valence forces through the sharing or exchange of electrons between the adsorbent and the adsorbate.

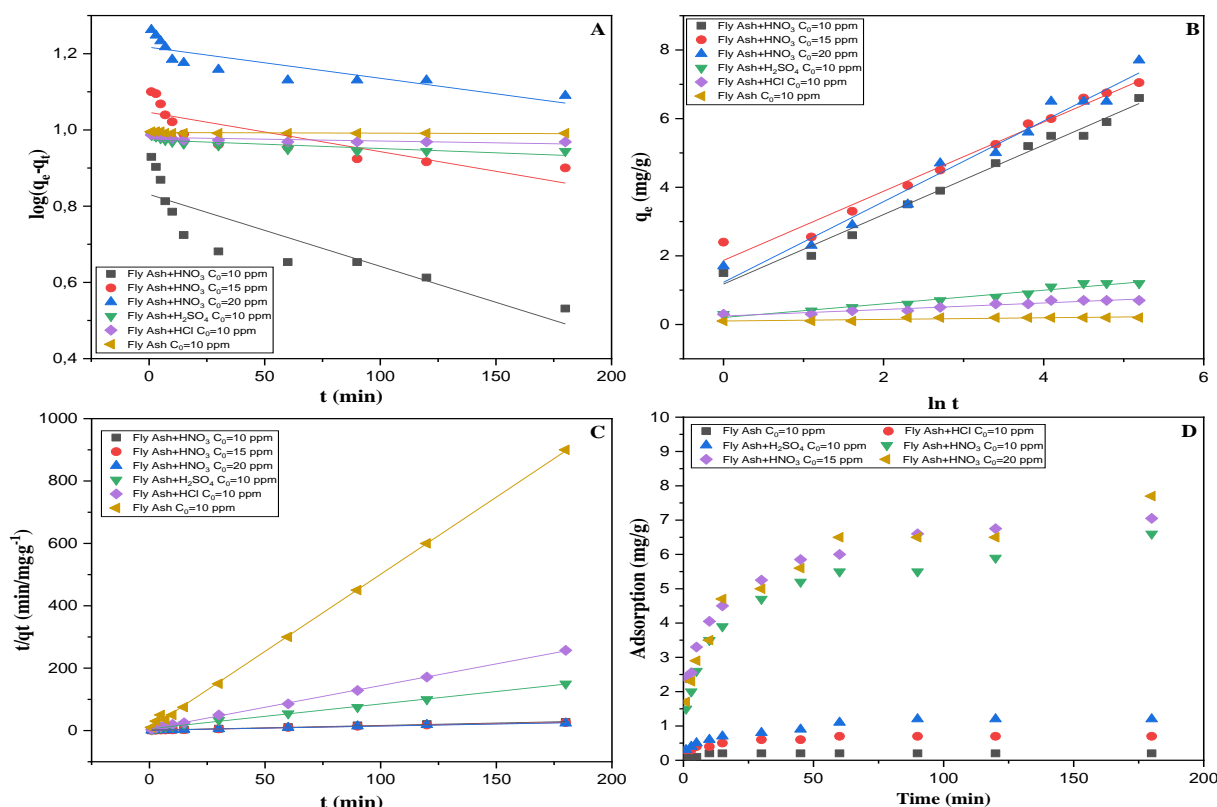


Figure 6: A. PFO B. Elovich C. PSO D. Effect of initial concentration and contact time.

Table 4. Kinetic Constant.

Adsorbent	C ₀	Pseudo-First Order			Pseudo-Second Order		
		k ₁	q _e	R ²	k ₂	q _e	R ²
Fly ash-HNO ₃	10	1.8x10 ⁻³	2.29	0.871	0.019	6.57	0.996
Fly ash-HNO ₃	15	1.0x10 ⁻³	2.84	0.847	0.023	7.14	0.999
Fly ash-HNO ₃	20	8.1x10 ⁻⁴	3.37	0.857	0.015	7.57	0.995
Fly ash-H ₂ SO ₄	10	2.2x10 ⁻⁴	2.64	0.842	0.109	1.25	0.999
Fly ash-HCl	10	9.6x10 ⁻⁵	2.66	0.764	0.385	0.71	0.999
Fly ash	10	1.6x10 ⁻⁵	2.69	0.481	3.715	0.20	0.999
Elovich							
Adsorbent	C ₀	a	b	R ²			
Fly ash-HNO ₃	10	3.26	0.98	0.993			
Fly ash-HNO ₃	15	6.44	0.99	0.989			
Fly ash-HNO ₃	20	3.35	0.85	0.985			
Fly ash-H ₂ SO ₄	10	1.02	5.03	0.979			
Fly ash-HCl	10	1.26	10.49	0.967			
Fly ash	10	1.74	42.55	0.832			

Table 5 presents a comparison of the maximum adsorption capacity, referred to as q_m , for the adsorption of dyes onto different types of fly ash (FA). In this study, the q_x values obtained for the adsorption of dyes were found to be comparable to those reported in previous research. However, it is noteworthy that the q_m values observed for the dyes in this study were relatively lower when compared to

findings from other investigations. Despite the relatively lower adsorption capacity exhibited by the fly ash examined in this study, its potential as an adsorbent for dye removal remains of interest. This is primarily due to its advantageous characteristics such as being cost-effective and readily available as a waste material.

Table 5. Comparison of dye adsorption on fly ash.

Dye	Fly ash type	q_m (mg/g)	References
Acid red 1	Coal FA	92.59	(27)
Acid red 1	Coal FA-NaOH	12.66	(27)
Acid red 91	FA	1.46	(28)
Acid Blue 9	FA	4.31	(28)
Acid Blue193	FA	22.08	(29)
Acid Black 1	FA	18.94	(29)
Reactive Red 23	FA	5.04	(29)
Reactive Black 5	FA	7.94	(30)
Reactive Red 198	Coal FA	47.26	(31)
Reactive Yellow 84	Coal FA	37.26	(31)
Methylene Blue	FA	7.67	This study

4. CONCLUSION

Fly ash and modified fly ash were applied for the removal of MB. Response surface methodology (RSM) was used to optimize key adsorption parameters, and an analysis of variance (ANOVA) was performed. The interactions between initial concentration (A), solution pH value (B), and solution pH value (B), contact time (C) were found to be significant in the removal of MB (p-value= < 0.0001 , 0.0040), whereas the effect of initial concentration (A) on contact time (C) was not significant (p-value = 0.0881). Equilibrium data obtained at various temperatures fit well with the Langmuir isotherm model, as compared to the Freundlich and Temkin isotherm models. The maximum monolayer adsorption capacities were found to be 7.67, 6.32, and 4.01 mg/g at 28, 37, and 48 °C, respectively, and were spontaneous at all studied temperatures. This material has the potential for wider applications, including the removal of heavy metals, pesticides, and other colorless organic pollutants in water.

5. ACKNOWLEDGEMENTS

This project is funded by TUBITAK 2209-A program.

6. REFERENCES

- Buema G, Harja M, Lupu N, Chiriac H, Forminte L, Ciobanu G, et al. Adsorption Performance of Modified Fly Ash for Copper Ion Removal from Aqueous Solution. Water [Internet]. 2021 Jan 16;13(2):207. Available from: [<URL>](#).
- Gao M, Ma Q, Lin Q, Chang J, Ma H. A novel approach to extract SiO₂ from fly ash and its considerable adsorption properties. Mater Des [Internet]. 2017 Feb;116:666–75. Available from: [<URL>](#).

- Ohenoja K, Pesonen J, Yliniemi J, Illikainen M. Utilization of Fly Ashes from Fluidized Bed Combustion: A Review. Sustainability [Internet]. 2020 Apr 8;12(7):2988. Available from: [<URL>](#).
- Zhang M, Mao Y, Wang W, Yang S, Song Z, Zhao X. Coal fly ash/CoFe₂O₄ composites: a magnetic adsorbent for the removal of malachite green from aqueous solution. RSC Adv [Internet]. 2016;6(96):93564–74. Available from: [<URL>](#).
- Taufiq A, Hidayat P, Hidayat A. Modified coal fly ash as low cost adsorbent for removal reactive dyes from batik industry. Ma'mun S, Tamura H, Purnomo MRA, editors. MATEC Web Conf [Internet]. 2018 Feb 28;154:01037. Available from: [<URL>](#).
- Hussain Z, Chang N, Sun J, Xiang S, Ayaz T, Zhang H, et al. Modification of coal fly ash and its use as low-cost adsorbent for the removal of directive, acid and reactive dyes. J Hazard Mater [Internet]. 2022 Jan;422:126778. Available from: [<URL>](#).
- Acisli O, Acar I, Khataee A. Preparation of a fly ash-based geopolymer for removal of a cationic dye: Isothermal, kinetic and thermodynamic studies. J Ind Eng Chem [Internet]. 2020 Mar;83:53–63. Available from: [<URL>](#).
- Chandarana H, Subburaj S, Kumar PS, Kumar MA. Evaluation of phase transfer kinetics and thermodynamic equilibria of Reactive Orange 16 sorption onto chemically improved Arachis hypogaea pod powder. Chemosphere [Internet]. 2021 Aug;276:130136. Available from: [<URL>](#).
- Malek NNA, Jawad AH, Ismail K, Razuan R, ALothman ZA. Fly ash modified magnetic chitosan-polyvinyl alcohol blend for reactive orange 16 dye removal: Adsorption parametric optimization. Int J Biol Macromol [Internet]. 2021 Oct;189:464–76. Available from: [<URL>](#).
- Hendaoui K, Trabelsi-Ayadi M, Ayari F. Optimization and mechanisms analysis of indigo dye removal using

- continuous electrocoagulation. Chinese J Chem Eng [Internet]. 2021 Jan;29:242-52. Available from: [<URL>](#).
11. Demissie H, An G, Jiao R, Ritigala T, Lu S, Wang D. Modification of high content nanocluster-based coagulation for rapid removal of dye from water and the mechanism. Sep Purif Technol [Internet]. 2021 Mar;259:117845. Available from: [<URL>](#).
12. Ahmad Rafeaie H, Mohd Yusop NF, Azmi NF, Abdullah NS, Ramli NIT. Photocatalytic degradation of methylene blue dye solution using different amount of ZnO as a photocatalyst. Sci Lett [Internet]. 2021 Jan 3;15(1):1-12. Available from: [<URL>](#).
13. Pakalapati H, Show PL, Chang JH, Liu BL, Chang YK. Removal of dye waste by weak cation-exchange nanofiber membrane immobilized with waste egg white proteins. Int J Biol Macromol [Internet]. 2020 Dec;165:2494-507. Available from: [<URL>](#).
14. Jawad AH, Abd Rashid R, Ismail K, Sabar S. High surface area mesoporous activated carbon developed from coconut leaf by chemical activation with H₃PO₄ for adsorption of methylene blue. Desalin Water Treat [Internet]. 2017;74:326-35. Available from: [<URL>](#).
15. Abdulhameed AS, Mohammad AT, Jawad AH. Application of response surface methodology for enhanced synthesis of chitosan tripolyphosphate/TiO₂ nanocomposite and adsorption of reactive orange 16 dye. J Clean Prod [Internet]. 2019 Sep;232:43-56. Available from: [<URL>](#).
16. Tüzün E, Karakuş S. Ultrasound-Assisted Adsorption of Basic Blue 41 onto Salda mud: Optimization and Error Analysis. J Turkish Chem Soc Sect A Chem [Internet]. 2021 Feb 28;8(1):57-68. Available from: [<URL>](#).
17. Karaca H, Altıntiğ E, Türker D, Teker M. An evaluation of coal fly ash as an adsorbent for the removal of methylene blue from aqueous solutions: kinetic and thermodynamic studies. J Dispers Sci Technol [Internet]. 2018 Dec 2;39(12):1800-7. Available from: [<URL>](#).
18. Li H, Dai M, Dai S, Dong X, Li F. Methylene blue adsorption properties of mechanochemistry modified coal fly ash. Hum Ecol Risk Assess An Int J [Internet]. 2018 Nov 17;24(8):2133-41. Available from: [<URL>](#).
19. Zhou J, Xia K, Liu X, Fang L, Du H, Zhang X. Utilization of cationic polymer-modified fly ash for dye wastewater treatment. Clean Technol Environ Policy [Internet]. 2021 May 14;23(4):1273-82. Available from: [<URL>](#).
20. Burduhos Nergis DD, Abdullah MMAB, Sandu AV, Vizureanu P. XRD and TG-DTA Study of New Alkali Activated Materials Based on Fly Ash with Sand and Glass Powder. Materials (Basel) [Internet]. 2020 Jan 11;13(2):343. Available from: [<URL>](#).
21. Abdulhameed AS, Jawad AH, Mohammad AT. Synthesis of chitosan-ethylene glycol diglycidyl ether/TiO₂ nanoparticles for adsorption of reactive orange 16 dye using a response surface methodology approach. Bioresour Technol [Internet]. 2019 Dec;293:122071. Available from: [<URL>](#).
22. Surip SN, Abdulhameed AS, Garba ZN, Syed-Hassan SSA, Ismail K, Jawad AH. H₂SO₄-treated Malaysian low rank coal for methylene blue dye decolorization and cod reduction: Optimization of adsorption and mechanism study. Surfaces and Interfaces [Internet]. 2020 Dec;21:100641. Available from: [<URL>](#).
23. Hassan R, Arida H, Montasser M, Abdel Latif N. Synthesis of New Schiff Base from Natural Products for Remediation of Water Pollution with Heavy Metals in Industrial Areas. J Chem [Internet]. 2013;2013:240568. Available from: [<URL>](#).
24. Choudhary M, Kumar R, Neogi S. Activated biochar derived from Opuntia ficus-indica for the efficient adsorption of malachite green dye, Cu⁺² and Ni⁺² from water. J Hazard Mater [Internet]. 2020 Jun;392:122441. Available from: [<URL>](#).
25. Al-Ghouti MA, Da'ana DA. Guidelines for the use and interpretation of adsorption isotherm models: A review. J Hazard Mater [Internet]. 2020 Jul;393:122383. Available from: [<URL>](#).
26. Wang J, Guo X. Adsorption kinetic models: Physical meanings, applications, and solving methods. J Hazard Mater [Internet]. 2020 May;390:122156. Available from: [<URL>](#).
27. Hsu T. Adsorption of an acid dye onto coal fly ash. Fuel [Internet]. 2008 Oct;87(13-14):3040-5. Available from: [<URL>](#).
28. Ramakrishna KR, Viraraghavan T. Dye removal using low cost adsorbents. Water Sci Technol [Internet]. 1997;36(2-3):189-96. Available from: [<URL>](#).
29. Sun D, Zhang X, Wu Y, Liu X. Adsorption of anionic dyes from aqueous solution on fly ash. J Hazard Mater [Internet]. 2010 Sep;181(1-3):335-42. Available from: [<URL>](#).
30. Eren Z, Acar FN. Adsorption of Reactive Black 5 from an aqueous solution: equilibrium and kinetic studies. Desalination [Internet]. 2006 Jun;194(1-3):1-10. Available from: [<URL>](#).
31. Dizge N, Aydinler C, Demirbas E, Kobya M, Kara S. Adsorption of reactive dyes from aqueous solutions by fly ash: Kinetic and equilibrium studies. J Hazard Mater [Internet]. 2008 Feb;150(3):737-46. Available from: [<URL>](#).



Chemical Composition and Phytochemical Screening of *Juniperus Phoenicea* L.: Evaluation of Antioxidant Activity, Minerals, and Bioactive Compounds

Khaled Muftah Elsherif^{1*}, Marwa A. Sulaiman², Adel Mlitan^{3*}

¹ Libyan Authority for Scientific Research, Tripoli, Libya

² Chemistry Department, Faculty of Arts and Science, El-Mergib University, Msallata, Libya

³ Chemistry Department, Faculty of Science, Misurata University, Misurata, Libya

Abstract: The purpose of the research was to determine *Juniperus phoenicea* L.'s elemental content, antioxidant activity, and phytochemical composition. Phytochemical screening was performed on four plant extracts (water, ethanol, chloroform, and ether). The aqueous and ethanol extracts were also analyzed for their total phenols, total flavonoids, and total antioxidant contents. The levels of macroelements (Na, Mg, Ca) and microelements (Fe, Cu, Zn) in the plant were determined by flame photometry and atomic absorption spectrometry. Moisture, ash, total protein, and total alkaloids were also determined. The results showed that the aqueous and ethanol extracts contained various phytochemicals, such as carbohydrates, proteins, phenols, tannins, flavonoids, alkaloids, coumarins, anthocyanins, saponins, and glycosides. The ethanol extract had higher concentrations of most phytochemicals than the aqueous extract, except for carbohydrates and proteins. The chloroform and ether extracts had lower concentrations of phytochemicals than the aqueous and ethanol extracts. The moisture, ash, total protein, and total alkaloid contents of the plant were 13%, 5.52%, 10.78%, and 1.84%, respectively. The total phenol contents, total flavonoid contents, and total antioxidant activity of the ethanol extract were 49.36±5.24 mg/g, 20.61±2.08 mg/g, and 34.82±2.44 mg/g, respectively. The corresponding values for the aqueous extract were 46.26±2.47 mg/g, 14.80±1.12 mg/g, and 37.32±3.29 mg/g, respectively. The order of abundance for macroelements was Ca (26860±950 mg/kg) > Na (1705.4±85 mg/kg) > Mg (944.4±38 mg/kg), whereas for microelements it was Fe (315.4±18 mg/kg) > Cu (55.52±3 mg/kg) > Zn (35.66±2 mg/kg). These results indicate that *Juniperus phoenicea* L. is a rich source of phytochemicals and elements that may have potential health benefits.

Keywords: *Juniperus phoenicea* L., Phytochemical composition, Antioxidant activity, Elemental content, Medicinal plant, Traditional medicine

Submitted: July 23, 2023. **Accepted:** February 9, 2024.

Cite this: Elsherif KM, Sulaiman MA, Mlitan A. Chemical Composition and Phytochemical Screening of *Juniperus Phoenicea* L.: Evaluation of Antioxidant Activity, Minerals, and Bioactive Compounds. JOTCSA. 2024;11(2):709-22.

DOI: <https://doi.org/10.18596/jotcsa.1330273>

***Corresponding author.** E-mail: elsherif27@yahoo.com

1. INTRODUCTION

Herbal medicinal plants are still used in traditional diabetes therapy and have long been a major source of healthcare in developing countries. These plants offer unique benefits because they have a wide range of pharmacological properties, including antioxidant, antiviral, anticancer, antibacterial, antifungal, and antiparasitic properties, and they also contain a large number of medicinal phytochemicals that may help in the

creation of novel medications (1). Particularly abundant in these plant extracts are polyphenols, which have the ability to bind with proteins and reduce the activity of enzymes (2). Herbal medicinal plants have the potential to transform healthcare by providing natural alternatives to traditional treatments due to their various bioactive components (3). Furthermore, polyphenols' capacity to selectively interact with certain enzymes makes them appealing candidates for drug development since they may be utilized to

construct focused medicines with few adverse effects (4). As a result, herbal medicinal plants have piqued the interest of academics who are investigating their therapeutic potential and creating novel medications based on their active components. Herbal medicinal plant use in medicine is a fast-emerging sector with bright possibilities for the future of healthcare (5).

Because of its secondary metabolites, which have positive effects and are widely employed in Libyan folk and traditional medicine, *Juniperus phoenicea* L. is regarded as a medicinal plant in Libya (6,7). This plant, which is a member of the *Cupressaceae* family, is also referred to as Ar'ar in Arabic and Phoenician Juniper in English. It is a naturally occurring shrub or small tree that is extensively dispersed throughout Europe, northern Africa, and the Canary Islands. It thrives in Mediterranean coastal regions (8). For centuries, people have used the antiviral, antibacterial, antiseptic, and inflammatory qualities of *Juniperus phoenicea* leaves and fruits. In Libyan traditional medicine, they are also utilized as a natural treatment for digestive, respiratory, and urinary tract issues (9,10). Several studies have reported that *Juniperus phoenicea* L. is rich in a diverse range of compounds, including diterpenoids, flavonoids, lignans, phenylpropanoid glucosides, furanone glucosides, bis-furanone derivatives, norterpenes, and sesquiterpene glucosides (11,12).

Because of its antioxidant activity—that is, its capacity to stop or slow down the oxidation of other molecules by free radicals—it has therapeutic benefits. Free radicals are very reactive, unstable chemicals that may harm DNA, lipids, proteins, and organisms. By giving electrons or hydrogen atoms to free radicals, antioxidants can neutralize them and shield the organism against oxidative stress and inflammation (13). Natural products, especially those produced from plants, have long been considered a valuable source of medicinal compounds. Plants' medicinal and aromatic characteristics were found gradually via trial and error, with some successes and disappointments. Vitamin E (tocopherol), vitamin C (ascorbate), and polyphenols are examples of antioxidant compounds having strong antioxidant activity against free radicals. These substances function by scavenging and neutralizing these radicals, converting them into stable molecules or ions (14, 15). The presence of hydroxyl groups in their phenolic structures increases their capacity to efficiently prevent radical processes. Because of their favorable impacts on human health, phenolic compounds, a broad collection of natural chemicals, have been the subject of substantial investigation. They are crucial in preventing and treating conditions including cancer, diabetes, hypertension, and Alzheimer's disease because they counteract oxidative stress (16). The antioxidant capacity of essential oils and extracts of *Juniperus phoenicea* L. derived from various plant parts, including leaves, berries, and seeds, has been documented in a number of

investigations. The essential oil of red juniper (*Juniperus phoenicea* L.) leaves, for instance, exhibited strong radical-scavenging action against DPPH (2,2-diphenyl-1-picrylhydrazyl), a stable free radical that is frequently used to gauge a substance's antioxidant capacity, according to Aouadi et al. (17). The high amount of α -pinene (74.14%), a monoterpene molecule with shown antioxidant and anti-inflammatory capabilities, was attributed by the scientists to this action. An additional investigation by Elmhdwi et al. (18) found that the Moroccan *Thymus satureioides* leaves, which are related to *Juniperus phoenicea* L., had a significant antioxidant activity against DPPH and another synthetic free radical called ABTS (2,2'-azino-bis(3-ethylbenzothiazoline-6-sulfonic acid)). The authors proposed that the extract's phenolic components, which include tannins and flavonoids, were the cause of this action. Certain trace elements are present in live organisms in incredibly low quantities and have a substantial impact on physiological processes that are common to all living systems. Based on evidence from several processes, including hormone production, enzyme activity, and acid-base balance, their function is thought to be catalytic (19). Given their involvement in the body's synthesis of active chemical components, it is important to comprehend the impact of trace elements in medicinal plants on human health. Furthermore, a crucial area of study is the relationship between the elemental profiles of medicinal plants and the historic uses of those plants for healing (20).

This investigation sought to assess the chemical constituents and possible medicinal qualities of *Juniperus phoenicea* L., which was harvested from the Libyan Msallata region. Total phenols, total flavonoids, total antioxidant activity, ash, moisture, and mineral content (Na, K, Ca, Mg, Zn, Fe, and Cu) were all measured. Moreover, phytochemical screening was performed on four distinct extracts (aqueous, ethanolic, chloroformic, and ether) of *Juniperus phoenicea* L. to detect the presence of several bioactive components. The findings of this study may help create new therapeutic compounds made from *Juniperus phoenicea* L. and offer significant new insights into the plant's possible medical uses.

2. EXPERIMENTAL SECTION

2.1. Plant sampling and processing

Between February and May 2022, the aerial part of *Juniperus phoenicea* was collected from the Msallata area of Libya. A specialist in plants from the Misurata University Faculty of Science's Botany Department recognized the plant samples based on their morphology. The voucher specimens were retained at the department's Laboratory of Plant Science. The gathered plant samples were washed, then left to air dry on lab tables for 15 days at ambient temperature (24–25°C). An air conditioner in the laboratory area helped to keep the temperature steady as the material dried. After

that, the dehydrated plant material was blended into a uniform powder and kept for later use in an airtight container. About 50.0 g of dried material from the plant was prepared and stored in airtight containers for further analysis. To avoid deterioration and maintain their genetic integrity, the dried plant samples were kept in opaque, airtight containers at -18°C.

2.2. Plant Extraction

A modified version of the process described in the literature (3, 21) was used to manufacture the extracts. In summary, 100 mL of a chosen solvent (water, ethanol, chloroform, or ether) was combined with 10 g of dried powdered plant material, and the mixture was allowed to extract for 72 hours at room temperature while being continuously shaken. The resultant extracts were concentrated at 40°C under vacuum using a rotary evaporator (Buchi R-215, Switzerland) after being filtered using Whatman filter paper (No. 4). For a maximum of one month, the concentrated extracts were kept in the dark at 4°C to avoid deterioration and maintain their efficacy.

2.3. Phytochemical screening

The main classes of phytochemicals found in extracts from *Juniperus phoenicea*, such as alkaloids, flavonoids, saponins, terpenoids, phenols, tannins, glycosides, carbohydrates, proteins, coumarins, and anthocyanins, were qualitatively examined using conventional analytical techniques (22–24).

2.4. Quantitative analysis

2.4.1. Determination of yield

To calculate the yield of each extract, dried samples were weighed, and the weight of the soluble constituents was determined. The yield of the extract under investigation was calculated using the equation provided by (25):

$$\text{Yield (\%)} = \frac{W_2}{W_1} \times 100 \quad (1)$$

The weight of the concentrated plant extract obtained by evaporation is denoted by w_1 in the equation above, and the weight of the dried plant material used for extraction with each solvent is indicated by w_2 .

2.4.2. Determination of Moisture and ash

After weighing 3.00 g of the fresh plant sample in a clean, dry crucible, it was dried for three hours at 100°C in an oven. The crucible was reweighed after 15 minutes of cooling it in a desiccator. Until a steady weight was achieved, this procedure was repeated. Using equation (26), where w_1 and w_2 represent the sample weights before and after drying, respectively, we were able to calculate the moisture content of fresh samples:

$$\% \text{ Moisture} = \frac{W_1 - W_2}{W_1} \times 100 \quad (2)$$

3.0 mg of the plant sample, weighed in a dry, clean porcelain crucible, were heated to 550°C for three hours in a muffle furnace in order to ascertain the amount of ash present. The crucible was reweighed after 15 minutes of cooling it in a

desiccator. Equation (27) was used to determine the ash content.

$$\% \text{ Ash} = \frac{\text{weight of ash}}{\text{weight of sample}} \times 100 \quad (3)$$

2.4.3. Determination of total protein

To estimate the protein content in plant samples, the Kjeldahl method was utilized with certain modifications. In this method, the plant material is oxidized with concentrated sulfuric acid, which oxidizes all the components except for the nitrogen present in proteins. The nitrogen is subsequently reduced to ammonia, which is determined through back titration in the presence of a methyl red indicator (28). The total protein content of plants can be calculated by converting the percentage of nitrogen using the equation below:

$$\text{Total protein} \left(\frac{g}{100 \text{ mL}} \right) = \text{Nitrogen content} \left(\frac{g}{100 \text{ mL}} \right) \times 6.25 \quad (4)$$

2.4.4. Determination of total alkaloids

To estimate total alkaloids, the gravimetric technique with certain adjustments (29) was used. First, 200 mL of 10% acetic acid in ethanol was poured into a 250 mL flask containing 5.00 g of the dried plant powder. After letting the combination remain for four hours, it was filtered and concentrated to a fourth of its original volume in a water bath. Gradually adding concentrated ammonium hydroxide, the precipitation was allowed to finish. Following a centrifugation of the mixture, the precipitate was recovered, cleaned with diluted ammonium hydroxide, and filtered once more. The precipitate was dried, weighed, and the proportion of alkaloids was computed. The residual product generated from this operation represents the alkaloids.

2.4.5. Determination of total phenols

The total phenolic content of the plant under study was ascertained by applying specific modifications to the Folin-Ciocalteu technique (30) in order to extract the plant's water and ethanol. In order to use this procedure, 0.2 mL of the extract and 1 mL of 10% diluted Folin-Ciocalteu reagent were combined, and the mixture was then incubated for 4 minutes in the dark. After that, 0.8 mL of a 7.5% sodium carbonate solution was added, and solvent was used to raise the volume to 10 mL. After 30 minutes, the solution's absorbance at 765 nm was determined. A standard calibration curve was created using different amounts of gallic acid (10–60 mg/L) and used to quantify the total phenolic contents. As a benchmark, gallic acid was used, and the outcomes were presented as gallic acid equivalents.

2.4.6. Determination of total flavonoids

The amount of flavonoids present overall in the plant extracts was determined using the modified aluminum chloride technique (31). Rutin equivalent was utilized to express the total flavonoid content, with rutin serving as the standard reference. Several rutin concentrations (ranging from 1 to 60 mg/L) were used to create a standard calibration curve. The whole flavonoid

content of the plant's water and ethanol extracts under study was determined using this approach.

In order to perform the experiment, 0.3 mL of sodium nitrite solution (NaNO₂), 4 mL of distilled water, and 1 mL of the extract (ethanol, water, or rutin solution) were mixed. After five minutes, the mixture was allowed for six minutes before 0.3 mL of aluminum chloride solution was added. After that, 2 mL of a 1 M sodium hydroxide solution was added, and after 10 minutes, the volume was increased to 10 mL using distilled water. Next, the solution's absorbance was calculated at 510 nm.

2.4.7. Total antioxidants (DPPH radical scavenging assay)

The free radical scavenging ability of aqueous and ethanolic extracts was measured using the technique reported by Al-Mustafa et al. (32) using ascorbic acid as a reference. Each extract was mixed with 2.0 mL of methanolic DPPH solution to perform the experiment. Following a 30-minute dark incubation period at room temperature, the preparations' absorbance at 517 nm was determined. Using the following formula, the antioxidant activity of the plant extracts was determined:

$$\% I = \frac{A_{\text{blank}} - A_{\text{sample}}}{A_{\text{blank}}} \times 100 \quad (5)$$

A_{sample} is the absorbance of the tested plant extract, % I is the inhibition in DPPH absorbance, and A_{blank} is the absorbance of the control reaction (containing all reagents except the plant extract). The plot of inhibition (%) against extract concentration was also used to determine the extract concentrations that gave 50% inhibition (I_{C50}). Three copies of each sample were used.

2.4.8. Determination of micro and macro elements

Mineral element concentrations, including those of Fe, Zn, Mn, Cu, and Mg, were measured with an atomic absorption spectrophotometer (VARIAN 220 FS), while Ca and Na were measured with a flame photometer (PFP7 Jenway). To eliminate all organic matter in the plant material, the wet digestion method was employed, which involved the use of nitric acid and hydrogen peroxide (33,34).

1.00 g of plant powder and around 10 mL of concentrated nitric acid were mixed in a beaker, and the mixture was heated for 10 minutes until the vapors disappeared in order to complete the plant material digestion process. An extra 10 mL of acid is added and heated once more if the brown odors continue. After adding 10 mL of hydrogen peroxide solution, the mixture was heated to a boil, at which point the solution turned clear and colorless. Following cooling, the mixture was moved to a 100 mL volumetric flask and filtered using filter paper. Then, deionized water was added to get the amount up to 100 mL.

2.4.9. Statistical analysis

Each measurement was made for three replicates and the mean value was reported. The results were reported as the mean ± standard error of the mean (SEM) attained from several parallel measurements. Excel statistical software package developed by Microsoft Office 2016 was used for statistical analysis and database management.

3. RESULTS AND DISCUSSION

3.1. Phytochemical screening

Table 1: Phytochemical screening results

Solvent				Bioactive compounds
Ether	Chloroform	Ethanol	Water	
-	-	++	+++	Carbohydrates
-	-	++	+++	Proteins
-	+	+++	+++	Phenols
-	+	+++	+++	Tannins
-	-	+++	++	Flavonoids
+	-	++	+	Alkaloids
+	+	++	++	Coumarins
-	-	+	+	Anthocyanin
-	-	+++	++	Saponins
-	+	++	+++	Glycosides
+	++	-	-	Steroids
+	+	-	-	Terpenoids

(+++ visible change occurred, (++) moderate change, (+) very slight change, (-) no change occurred

Table 1 displays the phytochemical screening results of four solvent extracts of *Juniperus phoenicea* L. The aqueous and ethanol extracts were found to contain carbohydrates, proteins, phenols, tannins, flavonoids, coumarins, anthocyanins, saponins, and glycosides. These phytochemicals have essential biological functions, such as providing energy, serving as structural components or signaling molecules, and exhibiting antioxidant, anti-inflammatory, antimicrobial, and pharmacological effects on the nervous system. Saponins can lower cholesterol, modulate the immune system, and inhibit tumor growth, while glycosides can have various effects, including cardiac, antidiabetic, and anticancer effects (31,35).

Table 1 indicates that the ethanol extract contains higher concentrations of most phytochemicals compared to the aqueous extract, except for carbohydrates and proteins. This suggests that ethanol is a superior solvent to water for extracting phytochemicals from *Juniperus phoenicea* L. due to its ability to dissolve both polar and non-polar compounds. On the other hand, the ether extract has more alkaloids than the chloroform extract, while the chloroform extract has larger quantities of phenols, tannins, and glycosides. This may suggest that chloroform is more effective than ether for extracting phenols, tannins, and

glycosides from *Juniperus phoenicea* L., while ether is more effective than chloroform for extracting alkaloids from the plant material. This is because chloroform can dissolve both polar and non-polar compounds, whereas ether can only dissolve non-polar compounds, making it better suited for extracting alkaloids.

These results are in line with some previous studies, such as the one by Hamzal et al. (2016), (36) which reported the presence of saponins, flavonoids, tannins, and alkaloids in *Juniperus phoenicea* L. Another study by Amalich et al. (2016) (37) detected various phenols, tannins, flavonoids, steroids, and terpenes, but not alkaloids or saponins, in the leaves. However, a study by El-Sawi et al. (2014) (38) found no tannins, coumarins, or alkaloids in *Juniperus phoenicea* L. leaves, which contradicts the current study's results. Nevertheless, both studies agreed on the presence of carbohydrates, glycosides, terpenes, steroids, flavonoids, and saponins. The current study also concurred with a study by Bouassida et al. (2018) (39) that identified alkaloids, terpenes, and tannins in *Juniperus phoenicea* L. leaves but differed in the absence of glycosides.

3.2. Yield, moisture, and ash contents

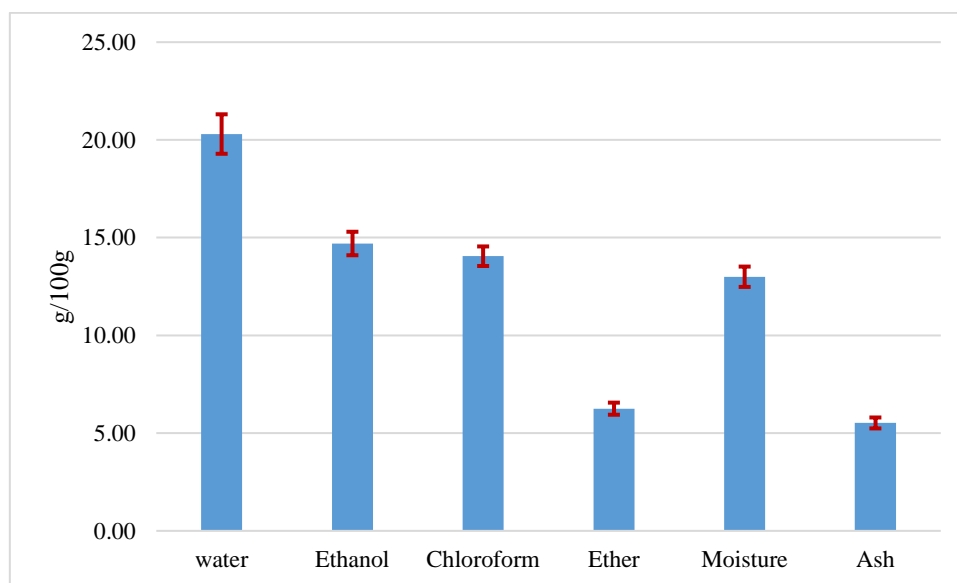


Figure 1: Yield, moisture, and ash contents of *Juniperus phoenicea* leaves

Figure 1 showcases the moisture, ash, and yield values of *Juniperus phoenicea* leaves, obtained through the use of four different solvents: aqueous, ethanol, chloroform, and ether. The results indicate that the ethanol extract exhibited the highest yield, measuring $20.30 \pm 0.40\%$ with a 95% confidence interval ranging from 19.98% to 20.62%. Following that, the aqueous extract displayed a yield of $14.70 \pm 0.27\%$ with a 95% confidence interval spanning from 14.44% to 14.96%. The chloroform extract showed a yield of $14.05 \pm 0.39\%$ with a 95% confidence interval

ranging from 13.73% to 14.37%. Lastly, the ether extract demonstrated the lowest yield at $6.09 \pm 0.18\%$ with a 95% confidence interval of 6.09% to 6.41%. The leaves' moisture content was found to be $13.00 \pm 0.13\%$, with a 95% confidence range that fell between 12.88% and 13.12%. Furthermore, the results showed that the ash content was $5.52 \pm 0.22\%$, with a 95% confidence interval that included 5.32% and 5.72%.

Previous studies have examined the yield, moisture, and ash content of *Juniperus phoenicea*

leaves or fruits using various solvents and methods. Dane et al. (40) reported a yield of 20.98% for the ethyl acetate extract, which aligns with the findings of the present study. However, Farahat (2020) (41) reported a yield of 9.8% for *Juniperus phoenicea* leaves collected from Egypt using methanol as the solvent. Bouassida et al. (2018) (39) reported a yield of 12.5% for leaves collected from Tunisia using a hydroalcoholic solvent. In a separate study, Amalich et al. (2016) (37) reported a yield of 0.4% for *Juniperus phoenicea* fruits collected from Morocco through hydrodistillation. El-Sawi et al. (2014) (38) documented a moisture content of 7.5% and an ash content of 3.5% for *Juniperus phoenicea* leaves collected from Egypt.

The yield, moisture, and ash of *Juniperus phoenicea* leaves can vary depending on the solvent, method, location, and collection season. Ethanol extract had a higher yield, suggesting better extraction of bioactive compounds than water, chloroform, or ether. Moisture content was higher than in some previous studies, indicating incomplete drying or moisture absorption during storage or transportation. The ash content was also higher, suggesting higher mineral content or impurities. However, these values may vary depending on the location, season, and method of harvesting. For example, the yield and moisture of *Juniperus phoenicea* were higher in the coastal areas than in the inland areas, and lower in the summer than in the winter. The ash content of *Juniperus phoenicea* was also affected by the soil type, with higher values in clayey soils than in sandy soils.

3.3. Total protein content

Analysis results show that *Juniperus phoenicea* has a considerable amount of total protein, $10.78 \pm 0.44\%$, with a 95% confidence interval between 10.43% and 11.13%. In addition to being an essential macromolecule for plant growth, development, and stress response, protein has nutritional and therapeutic advantages for both people and animals.

Previous research on *Juniperus phoenicea* or related plants from the Cupressaceae family can provide a basis for comparing total protein levels. For instance, El-Gohary et al. (2015) (42) found that the total protein of *Juniperus phoenicea* leaves collected from Egypt was slightly lower at 8.7% compared to the current study. Similarly, Al-Mustafa et al. (2021) (32) reported that the total protein of *Juniperus phoenicea* leaves collected from Jordan was 9.3%, which is also lower than the current result. In contrast, Dzialuk et al. (2011) (43) reported a higher total protein content of 11.9% for *Juniperus communis* needles collected from Poland.

3.4. Total alkaloids content

The current investigation reveals that *Juniperus phoenicea* exhibits a comparatively reduced level of total alkaloids, constituting approximately

$1.84 \pm 0.08\%$ with a 95% confidence interval ranging from 1.77% to 1.91%. This proportion is notably lower when compared to other plant species. Alkaloids, which encompass nitrogen-containing compounds, possess the potential to impact the nervous system and exhibit various pharmacological characteristics. These properties may encompass analgesic, stimulant, sedative, and hallucinogenic effects. A comparison of the total alkaloid levels of *Juniperus phoenicea* or Cupressaceae plants can be based on previous research on these plants. For instance, Al-Mustafa et al. (2021) (32) found that the total alkaloids of *Juniperus phoenicea* leaves collected from Jordan were lower at 0.9% compared to the current study. Similarly, Bajes et al. (2021) (44) reported that the total alkaloids of *Juniperus phoenicea* leaves collected from Jordan were 0.7%, which is lower than the current result. In addition, Shaboun et al. (2021) (45) reported a lower total alkaloid content of 0.8% for *Juniperus phoenicea* leaves collected from Libya.

The extraction method, the plant part, and the environmental conditions were the main factors that influenced the total alkaloids content (TAC) of *Juniperus phoenicea* in our study. We obtained a higher TAC (1.84%) than previous studies (0.70-0.90%) by using a gravimetric technique, which was more efficient and selective than other methods. We also used the leaves of the plant, which had a higher TAC than other parts.

3.5. Total phenols content

The results obtained from the analysis of aqueous and ethanolic extracts are as follows: The aqueous extract exhibited a value of 46.26 ± 2.47 mg/g, with a 95% confidence interval ranging from 43.67 mg/g to 48.85 mg/g. Conversely, 49.36 ± 5.24 mg/g was the value shown by the ethanolic extract, with a 95% confidence range covering 43.75 mg/g to 54.97 mg/g. Figure 2 shows a visual representation of these numbers. An indication of the amount and diversity of phenolic chemicals found in a plant or plant extract is the total phenol content. The capacity of phenolic compounds to donate electrons or hydrogen atoms to free radicals or reactive oxygen species makes them known for their antioxidant properties. Important biomolecules like proteins, lipids, and DNA are shielded from oxidative damage by this mechanism, which also successfully neutralizes these dangerous substances (46).

Previous studies that used different solvents or methods to assess the total phenol content of *Juniperus phoenicea* leaves or fruits can provide a basis for comparison with the current findings. The total phenolic content of the ethyl extracts of *Juniperus phoenicea* L. came within the same range as found in our investigation, according to Shaboun et al. (45). The authors reported that the total phenols ranged from 21.36 to 84.55 mg/g for different extract concentrations. Also, El-Gohary et al. (2015) (42) found that the total phenol content of *Juniperus phoenicea* leaves collected from Egypt

using methanol as a solvent was much higher at 136.1 mg/g compared to the current study. Al-Mustafa et al. (2021) observed that the total phenol content of *Juniperus phoenicea* leaves collected from Jordan using methanol as a solvent was greater, at 103.6 mg/g. In comparison, *Juniperus phoenicea* fruits gathered from Morocco

using hydrodistillation had a substantially lower total phenol concentration (3.8 mg/g) according to Amalich et al. (2016) (37). El-Sawi et al. (2014) (38) found that the total phenol content of *Juniperus phoenicea* leaves collected from Egypt using ethanol as a solvent was lower at 16.1 mg/g compared to the current study.

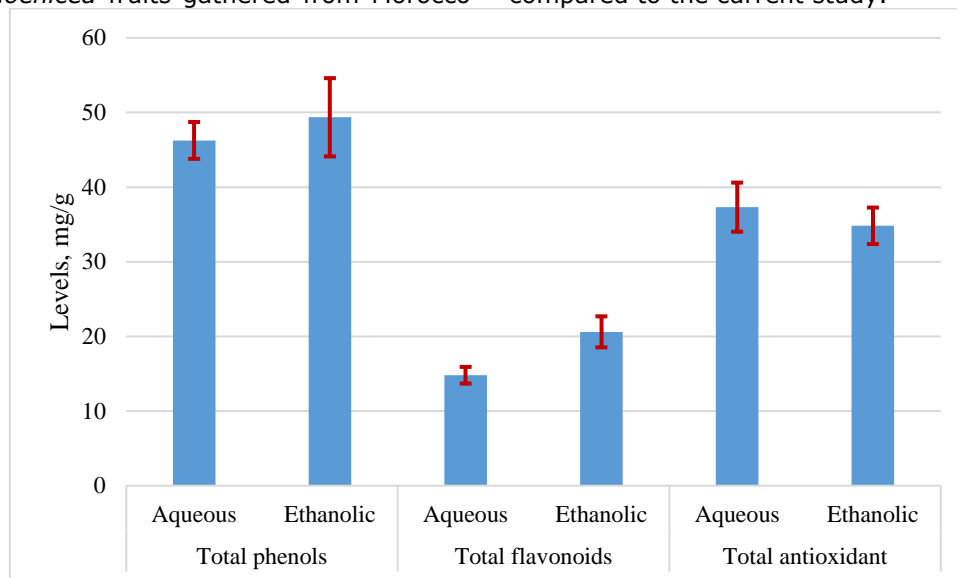


Figure 2: Levels of total phenols, total flavonoids, and total antioxidants in ethanolic and aqueous extracts of *Juniperus phoenicea*

3.6. Total flavonoids content

With a 95% confidence range spanning from 13.77 mg/g to 15.83 mg/g, the total flavonoid concentration in the aqueous extract was found to be 14.80 ± 1.12 mg/g. By contrast, the total flavonoid concentration of the ethanolic extract was greater at 20.61 ± 2.08 mg/g, with a 95% confidence interval that included the range of 18.55 mg/g to 22.67 mg/g. Figure 2 presents these findings. Given that the ethanolic extract had a higher total flavonoid content than the aqueous extract, it appears that ethanol is a better solvent for removing flavonoid components from *Juniperus phoenicea* leaves.

Among the many pharmacological characteristics of flavonoids is their antioxidant activity, which scavenges free radicals and reactive oxygen species to help shield biomolecules like proteins, lipids, and DNA from oxidative damage. Additionally, they have anti-inflammatory properties that can control the release or function of inflammatory mediators such as leukotrienes, prostaglandins, and cytokines. Moreover, flavonoids possess antibacterial properties that can impede the development of bacteria by altering their cell walls, membranes, or enzyme activity. Furthermore, flavonoids have an antidiabetic effect, which may enhance insulin sensitivity or glucose metabolism through changes in signaling, absorption, or transport (47, 48).

Previous studies have reported the total flavonoid contents of *Juniperus phoenicea* leaves or fruits

using different solvents or methods, allowing for a comparison with the current findings. For example, Al-Mustafa et al. (2021) (32) discovered that, in comparison to the current investigation, the total flavonoid content of *Juniperus phoenicea* leaves collected from Jordan utilizing methanol as a solvent was much greater at 101.1 mg/g. Comparing the current results with Shaboun et al. (2021) (45), the total flavonoid content of *Juniperus phoenicea* leaves collected from Libya using ethyl acetate as a solvent was found to be lower, at 17.44 mg/g. On the other hand, 0.9 mg/g of total flavonoids were found in *Juniperus phoenicea* fruits that were hydrodistilled and harvested from Morocco, according to Amalich et al. (2016) (37). El-Sawi et al. (2014) (38) found that the total flavonoid content of *Juniperus phoenicea* leaves collected from Egypt using ethanol as a solvent was higher at 27.13 mg/g than in the current study.

3.7. Determination of antioxidant activity: DPPH radical scavenging assay

The aqueous extract, as shown in Figure 2, has an overall antioxidant content of 37.32 ± 3.29 mg/g, with a 95% confidence range that spans from 34 mg/g to 40.64 mg/g. On the other hand, the ethanolic extract had a somewhat reduced total antioxidant content, measuring 34.82 ± 2.44 mg/g with a 95% confidence range that included 31.28 mg/g to 38.36 mg/g. Moreover, for both the ethanolic and aqueous extracts, the concentration needed to inhibit 50% of DPPH radicals (IC_{50}) was found. With a 95% confidence range spanning

from 0.117 mg/mL to 0.131 mg/mL, the aqueous extract's IC₅₀ value was determined to be 0.124±0.007 mg/mL. Additionally, the IC₅₀ value of the ethanolic extract was determined to be 0.133±0.009 mg/mL, with a 95% confidence interval spanning from 0.124 mg/mL to 0.142 mg/mL. Figure 3 provides an illustration of these values. The findings demonstrated the considerable antioxidant activity of both *Juniperus phoenicea* extracts; however, the aqueous extract's activity was marginally greater than that of the ethanolic extract. This result contrasts with other research (32, 49) that found that ethanolic extracts of *Juniperus phoenicea* had higher total phenolic content and antioxidant activity than aqueous extracts. Nonetheless, a few other investigations have also discovered that aqueous extracts of *Juniperus* species exhibit more antioxidant activity than ethanolic extracts (45). This disparity might result from various extraction techniques, solvents, plant components, or sample origins. Non-phenolic substances like alkaloids, terpenoids, anthraquinones, or glycosides may have additive or synergistic effects with phenolic compounds, which might account for the aqueous extract's comparatively larger overall antioxidant concentration. These compounds, along with phenolic compounds, could modulate the redox status of cells or inhibit oxidative enzymes, thereby enhancing the overall antioxidant activity of the extract (32).

The antioxidant activity of the *Juniperus phoenicea* aqueous extract in this investigation was found to be lower than that of the same species' methanolic extract, as reported by Al-Mustafa et al. (32). El Jemli et al. observed that it showed more antioxidant activity than other *Juniperus* species' aqueous extracts (49). However, the ethanolic extract of *Juniperus phoenicea* in our investigation showed lesser antioxidant activity than the methanolic extract of *Juniperus phoenicea* published by Al-Mustafa et al. (32) but equal antioxidant activity to the aqueous extract of *Juniperus oxycedrus* reported by El Jemli et al. (49). Additionally, compared to the ethanolic extract of the same species published by Menaceur et al. (50), who used a different extraction technique and a different plant component, the ethanolic extract of *Juniperus phoenicea* in our investigation showed reduced antioxidant activity. It is significant to note that the IC₅₀ values in our study were lower than those reported by Fadel et al. (51), who found that the extracts of *J. Oxycedrus* and *J. Phoenicea* had IC₅₀ values of 0.404 and 0.481 mg/ml, respectively. Rahhal et al. (52) observed a similar IC₅₀ level of 0.14 mg/mL for the same species; however, Chelouati et al. (13) reported an IC₅₀ level of 0.26 mg/mL for *J. phoenicea*.

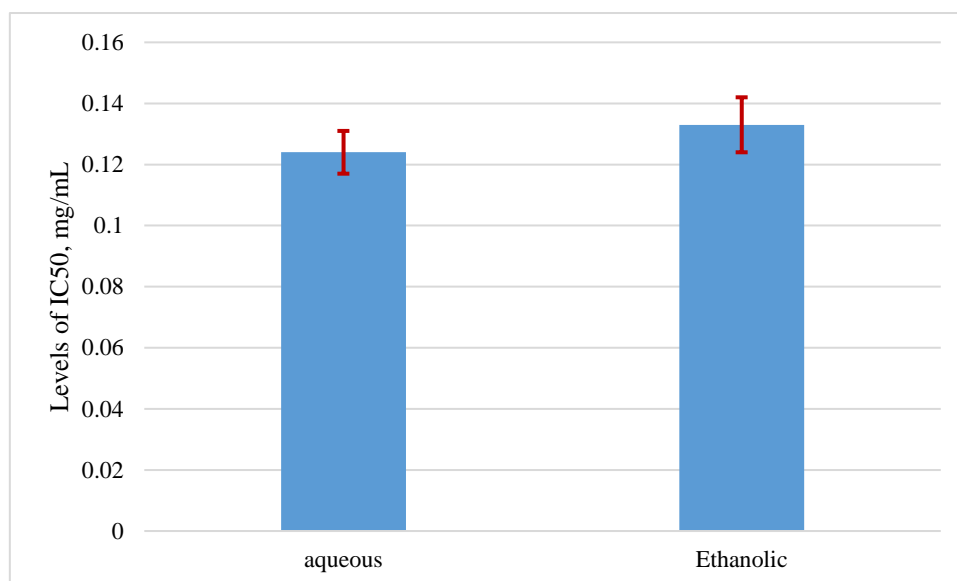


Figure 3: Levels of IC₅₀ in ethanolic and aqueous extracts of *Juniperus phoenicea*

3.8. Micro and macro elements contents

The following findings were obtained from measuring the amounts of macroelements (Na, Mg, Ca) and microelements (Fe, Cu, Zn) in *Juniperus phoenicea*: Ca (26860±950 mg/kg) > Na (1705.4±85 mg/kg) > Mg (944.4±38 mg/kg) was the order of abundance for macroelements, whereas the order for microelements was Fe

(315.4±18 mg/kg) > Cu (55.52±3 mg/kg) > Zn (35.66±2 mg/kg). The highest level among all the elements analyzed was Ca, which was found to be much higher than Na and Mg. Similarly, Fe had the highest level among the microelements, followed by Cu and Zn, respectively. The levels of these elements are depicted in Figures 4 & 5.

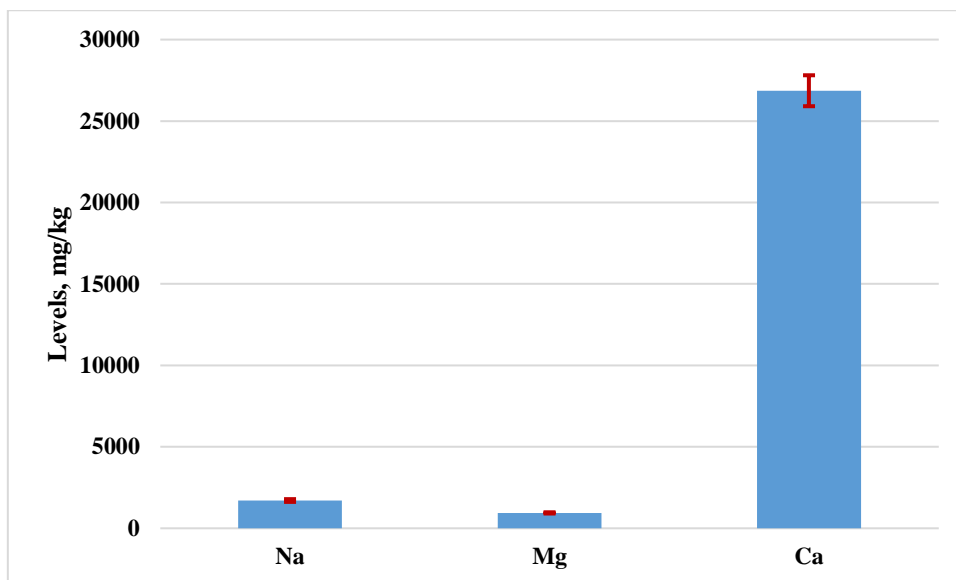


Figure 4: Levels of macroelements in *Juniperus Phoenicea*

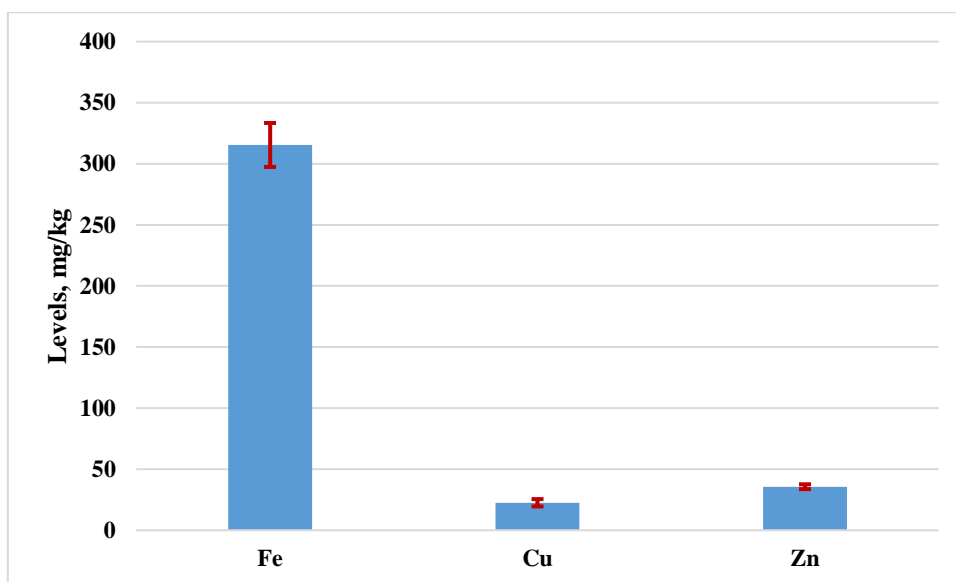


Figure 5: Levels of microelements in *Juniperus phoenicea*

Each element's concentration in *Juniperus phoenicea* shows both its potential influence on human health and its significance for the growth and development of plants. Calcium is a vital macronutrient for plant growth, and it is also essential for human health, especially for bone and tooth formation. Sodium and magnesium are also needed for plant growth, and they have important roles in various physiological processes in humans, such as nerve and muscle function. Iron is a crucial micronutrient for plant growth, and it is required for the synthesis of chlorophyll. In humans, iron is important for the formation of hemoglobin, which transports oxygen in the blood. Copper and zinc are also critical micronutrients for plant growth, and they have important roles in enzyme function

in humans. Overall, the amount of these elements in *Juniperus phoenicea* indicates that it may have potential health benefits for humans, particularly for bone and tooth formation, nerve and muscle function, and enzyme activity (53, 54).

The current study's findings show differences in the identified metals' concentrations. Environmental variables such as soil type, temperature, and altitude might be blamed for these variances (55, 56). Table 2 (57–60) compares the amounts of macroelements and microelements found in this study with those documented in the literature for other *Juniperus phoenicea* in order to give more context.

Table 2: Comparing the levels of macro and micro elements in *Juniperus phoenicea* with previous research studies

Na (mg/kg)*	Mg (mg/kg)*	Ca (mg/kg)*	Fe (mg/kg)*	Cu (mg/kg)*	Zn (mg/kg)*	Ref.
1705.4±85	944.4±38	26860±950	315.4±18	55.52±3	35.66±2	This study
1607.6-1803.2**	900.5-988.3**	25763.8-27956.2**	294.6-336.2**	52.06-58.98**	33.35-37.97**	
52.13±4.76	-	1600±0.10	430±.20	-	15.60±0.70	57
6.50±0.87	-	51.61±1.16	0.43±0.06	3.00±0.27	-	58
-	-	-	168.07±0.03	31.51±0.03	40.71±0.03	59
-	-	-	190.11±0.04	71.86±0.10	13.72±0.11	
602	370	828	13	9	7	60
681	479	972	22	7	8	
630	1107	1036	16	15	8	
638	652	946	17	11	11	

*Mean ± SD, **95% Confidence intervals

Through a comparison of mineral concentrations in *Juniperus phoenicea* with the recommended daily intakes (RDIs) for adults, specifically for men and women aged between 19-50, it was found that consuming 100 g of *Juniperus phoenicea* would fulfill and surpass the RDIs for calcium, iron, and copper. However, it would not meet the RDIs for sodium, magnesium, and zinc (RDIs: 750 mg/day for Ca, 2000 mg/day for Na, 300-350 mg/day for Mg, 6-7 mg/day for Fe, 1.3-1.6 mg/day for Cu, 6.2-12.7 mg/day for Zn) (61, 62).

4. CONCLUSION

In summary, this investigation uncovered the elemental content, antioxidant capacity, and phytochemical makeup of the traditional medicine plant *Juniperus phoenicea*. Numerous phytochemicals found in the plant, including glycosides, alkaloids, flavonoids, and phenols, have shown strong antioxidant activity. In addition, the plant had moderate amounts of salt and magnesium and high amounts of calcium and iron—all of which are vital for human health. These findings suggest that *Juniperus phoenicea* may have potential health benefits and therapeutic applications. To validate the biological actions of the plant extracts and their separated components in vivo, more research is required.

5. CONFLICT OF INTEREST

The authors disclose that the research was carried out without any financial or commercial relationships that may be seen as having a conflict

of interest. The writers do not belong to or are associated with any organization or institution that has a financial or non-financial interest in the topics or sources covered in this paper. There are no academic, professional, or personal ties between the writers and their work that may slant or affect it. The writers have disclosed no conflicting interests.

6. ACKNOWLEDGMENTS

For providing the resources and encouragement for this study, the authors would like to sincerely thank the Chemistry Department of Misurata University's Faculty of Science.

7. REFERENCES

- Batool Z, Singh K, Gairola S. Medicinal plants are traditionally used in the health care practices by the indigenous communities of the Trans-Himalayan region of Ladakh, India. *J Ethnopharmacol.* 2023;317:116837. Available from: [URL](#)
- Kar A, Mahar D, Biswas S, Chakraborty D, Efferth T, Panda S. Phytochemical profiling of polyphenols and thyroid stimulatory activity of *Ficus religiosa* leaf extract in 6-propyl-thiouracil-induced hypothyroid rats. *J Ethnopharmacol.* 2023;313:116479. Available from: [URL](#)
- Elsherif KMM, Ewlad-Ahmed AM, Alhlbad EAA. Evaluation of some Chemical and Biochemical Constituents in *Ocimum Basilicum* Available in Msallata City- Libya. *Adv J Chem B.* 2023;5(2):197-212. Available from: [URL](#)

4. Rani P, Yu X, Liu H, Li K, He Y, Tian H, Kumar R. Material, antibacterial and anticancer properties of natural polyphenols incorporated soy protein isolate: A review. *Eur Polym J.* 2021;152:110494. Available from: [URL](#)
5. Dailah HG. The ethnomedicinal evidence pertaining to traditional medicinal herbs used in the treatment of respiratory illnesses and disorders in Saudi Arabia: A review. *Saudi J Biol Sci.* 2022;29(9):103386. Available from: [URL](#)
6. Mssillou I, Bakour M, Slighoua M, Laaroussi H, Saghrouchni H, Amrati FE-Z, Lyoussi B, Derwich E. Investigation on wound healing effect of Mediterranean medicinal plants and some related phenolic compounds: A review. *J Ethnopharmacol.* 2022;298:115663. Available from: [URL](#)
7. Abubaker N, Ali A. Health Information System and Their Impact on The Quality of Health Care at Benghazi Medical Center. *Alq J Med Appl Sci.* 2021;4(1):132-145.
8. Laouar A, Klibet F, Bourogaa E, Benamara A, Boumendjel A, Chefrour A, Messarah M. Potential antioxidant properties and hepatoprotective effects of *Juniperus phoenicea* berries against CCl₄ induced hepatic damage in rats. *Asian Pac J Trop Med.* 2017;10(3):263-269. Available from: [URL](#)
9. Ait-Ouazzou A, Lorán S, Arakrak A, Laglaoui A, Rota C, Herrera A, Pagán R, Conchello P. Evaluation of the chemical composition and antimicrobial activity of *Mentha pulegium*, *Juniperus phoenicea*, and *Cyperus longus* essential oils from Morocco. *Food Res Int.* 2012;45(1):313-319. Available from: [URL](#)
10. Ali M, El shatshat S. Ecological study of *Juniperus phoenicea* L. in EL-Gabal El-Akhdararea, Libya. *Eur J Exp Biol.* 2015;5(7):71-76.
11. Nedjimi B, Beladel B, Guit B. Multi-element determination in medicinal Juniper tree (*Juniperus phoenicea*) by instrumental neutron activation analysis. *J Radiat Res Appl Sci.* 2015;8(2):243-246. Available from: [URL](#)
12. Keskes H, Mnafgui K, Hamden K, Damak M, El Feki A, Allouche N. In vitro anti-diabetic, anti-obesity and antioxidant properties of *Juniperus phoenicea* L. leaves from Tunisia. *Asian Pac J Trop Biomed.* 2014;4(Suppl 2):649-655. Available from: [URL](#)
13. Chelouati T, Lafraxo S, Bouslamti M, El Barnossi A, Chebaibi M, Akhazzane M, Salamatullah A, Nafidi H, Bourhia M, Lyoussi B, Benjelloun A. Study on antioxidant and antimicrobial potential of chemically profiled essential oils extracted from *Juniperus phoenicea* (L.) by use of in vitro and in silico approaches. *Open Chem.* 2023;21(1):20220333. Available from: [URL](#)
14. Shahar B, Dolma N, Chongtham N. Phytochemical analysis, antioxidant activity and identification of bioactive constituents from three wild medicinally important underutilized plants of Ladakh, India using GCMS and FTIR based metabolomics approach. *Food Hum.* 2023;1:430-439. Available from: [URL](#)
15. Ait Bouzid H, Oubannin S, Ibourki M, Bijla L, Hamdouch A, Sakar EH, Harhar H, Majourhat K, Koubachi J, Gharby S. Comparative evaluation of chemical composition, antioxidant capacity, and some contaminants in six Moroccan medicinal and aromatic plants. *Biocatal Agric Biotechnol.* 2023;47:102569. Available from: [URL](#)
16. Sari KRP, Ikawati Z, Danarti R, Hertiani T. Micro-titer plate assay for measurement of total phenolic and total flavonoid contents in medicinal plant extracts. *Arab J Chem.* 2023;16(9):105003. Available from: [URL](#)
17. Aouadi M, Msaada K, Sebai E, Wannas WA, Abbassi MS, Akkari H. Antioxidant, anthelmintic and antibacterial activities of red juniper (*Juniperus phoenicea* L.) essential oil. *J Essent Oil Res.* 2022;34(2):163-172. Available from: [URL](#)
18. Elmhdwi MF, Attitalla IH, Khan BA, Mena F. Evaluation of Antibacterial Activity and Antioxidant Potential of Different Extracts from the Leaves of *Juniperus Phoenicea*. *J Plant Pathol Microbiol.* 2015;6(9). Available from: [URL](#)
19. Prasathkumar M, Anisha S, Dhriya C, Becky R, Sadhasivam S. Therapeutic and pharmacological efficacy of selective Indian medicinal plants – A review. *Phytomedicine Plus.* 2021;1(2):100029. Available from: [URL](#)
20. Dim LA, Funtua II, Oyewale AO, Grass F, Umar IM, Gwozd R, Borylo A, Parus JL. Determination of some elements in *Ageratum conyzoides*, a tropical medicinal plant, using instrumental neutron activation analysis. *J Radioanal Nucl Chem.* 2004;261:225-228. Available from: [URL](#)
21. Abubakar AR, Haque M. Preparation of medicinal plants: Basic extraction and fractionation procedures for experimental purposes. *J Pharm Bioallied Sci.* 2020;12(1):1-10. Available from: [URL](#)
22. Kumaran A, Karunakaran RJ. In vitro antioxidant activities of methanol extracts of five *Phyllanthus* species from India. *LWT-Food Sci Technol.* 2007;40(2):344-352. Available from: [URL](#)
23. Elsherif KMM, Aljaroushi AM. Biochemical Properties Evaluation of some Libyan dates. *Chem Rev Lett.* 2021;4(4):213-220. Available from: [URL](#)
24. Najah Z, Elsherif KM. Analytical and Phytochemical Studies on *Zizphus Lotus*. *Eur J Biomed Pharm Sci.* 2016;3(7):574-577.
25. Najah Z, Elsherif KM, Kawan E, Farah N. Phytochemical screening and heavy metals contents of *Nicotiana glauca* plant. *Int J Pharm Pharm Res.* 2015;4(3):82-91.
26. Yaghi MM, Mohammed MY, Towier NA, Elsherif KM. Analysis of Potato Chips: Evaluation of Sodium, Potassium and Chloride Contents. *Int J Multidiscip Sci Adv Technol.* 2021;1(Special Issue):92-97. Available from: [URL](#)
27. Elsherif KM, Abu Khater RA, Hegaig FA. Determination of major and minor elements in dairy products produced in Misurata city – Libya. *Maghrebian J Pure Appl Sci.* 2017;3(2):9-17.
28. Di Marzo L, Pranata J, Barbano DM. Measurement of casein in milk by Kjeldahl and sodium dodecyl sulfate-polyacrylamide gel electrophoresis. *J Dairy Sci.* 2021;104(7):7448-7456. Available from: [URL](#)
29. Gracelin DHS, De Britto AJ, Kumar PBJR. Qualitative and quantitative analysis of phytochemicals in five *Pteris*

- species. *Int J Pharm Pharm Sci.* 2013;5(Suppl 1):105-107.
30. Rumpf J, Burger R, Schulze M. Statistical evaluation of DPPH, ABTS, FRAP, and Folin-Ciocalteu assays to assess the antioxidant capacity of lignins. *Int J Biol Macromol.* 2023;233:123470. Available from: [URL](#)
31. Shraim AM, Ahmed TA, Rahman MM, Hijji YM. Determination of total flavonoid content by aluminum chloride assay: A critical evaluation. *LWT - Food Sci Technol.* 2021;150:111932. Available from: [URL](#)
32. Al-Mustafa A, Al-Tawarah M, Al-Sheraideh MS, Al-Zahrany FA. Phytochemical analysis, antioxidant and in vitro β -galactosidase inhibition activities of *Juniperus phoenicea* and *Calicotome villosa* methanolic extracts. *BMC Chem.* 2021;15(1):55. Available from: [URL](#)
33. Yaghi MM, Elsherif KM, El Ziani NO. Heavy Metals Analysis of Baby Cereal Available in the Libyan Markets. *Libyan J Basic Sci.* 2022;19(3):1-12.
34. Alkherraz A, Hashad O, Elsherif K. Heavy metals contents in some commercially available coffee, tea, and cocoa samples in Misurata City–Libya. *Prog Chem Biochem Res.* 2019;2(3):99-107.
35. Barnawi IO, Nasr FA, Noman OM, Alqahtani AS, Al-zharani M, Alotaibi AA, Daradka HM, Al-Mishari AA, Alobaid WA, Alqahtani A, Herqash RN. Induction of apoptosis and cell cycle arrest by chloroform fraction of *Juniperus phoenicea* and chemical constituents analysis. *Open Chem.* 2021;19:119-127. Available from: [URL](#)
36. Hamzal A, Bouzidi N, Bekhechi C, Fernandez X. Phytochemical screening and antioxidant activity of Algerian *Juniperus phoenicea* L. extracts. *J Appl Pharm Sci.* 2016;6(1):87-96. Available from: [URL](#)
37. Amalich S, Fadili K, Fahim M, Hilali FE, Zaïr T. Polyphenols content and antioxidant power of fruits and leaves of *Juniperus phoenicea* L. from Tounfite (Morocco). *Mor J Chem.* 2016;4(4):2177-2186. Available from: [URL](#)
38. El-Sawi SA, Motawae HM, Sleem MA-f, El-Shabrawy ARO, Sleem A, Ismail MA. Phytochemical screening, investigation of carbohydrate contents, and antiviral activity of *Juniperus phoenicea* L. growing in Egypt. *J Herbs Spices Med Plants.* 2014;20(1):83-91. Available from: [URL](#)
39. Zouari Bouassida K, Makni S, Tounsi A, Jlaïel L, Trigui M, Tounsi S. Effects of *Juniperus phoenicea* hydroalcoholic extract on inflammatory mediators and oxidative stress markers in carrageenan-induced paw oedema in mice. *BioMed Res Int.* 2018;2018:3069487. Available from: [URL](#)
40. Dane Y, Mouhouche F, Canela-Garayoa R, Delpino-Rius A. Phytochemical Analysis of Methanolic Extracts of *Artemisia absinthium* L. 1753 (Asteraceae), *Juniperus phoenicea* L., and *Tetraclinis articulata* (Vahl) Mast, 1892 (Cupressaceae) and evaluation of their biological activity for stored grain protection. *Arab J Sci Eng.* 2016;41:2147-2158. Available from: [URL](#)
41. Farahat EA. Age structure and static life tables of the endangered *Juniperus phoenicea* L. in North Sinai Mountains, Egypt: implication for conservation. *J Mountain Sci.* 2020;17(10):2170-2178. Available from: [URL](#)
42. El-Gohary MA, El-Hady MA, El-Sayed MM. Phytochemical screening, investigation of carbohydrate contents, and antioxidant activity of *Juniperus phoenicea* L. growing in Egypt. *J Appl Sci Res.* 2015;11(1):1-9. Available from: [URL](#)
43. Dzialuk A, Mazur M, Boratyńska K, Montserrat JM, Romo A, Boratyński A. Population genetic structure of *Juniperus phoenicea* (Cupressaceae) in the western Mediterranean Basin: gradient of diversity on a broad geographical scale. *Ann For Sci.* 2011;68(8):1341-1350. Available from: [URL](#)
44. Bajes HR, Oran SA, Bustanji YK, Al-Zahrany FA. Chemical composition and antiproliferative and antioxidant activities of essential oil from *Juniperus phoenicea* L. Cupressaceae. *Res J Pharm Technol.* 2021;14(8):4464-4470. Available from: [URL](#)
45. Shaboun S, Almajbri MM, Elmshiti BM, El Aali NM, Towier NH. The contents of total phenolic, flavonoid and antioxidant activity of ethyl acetate extract of *Juniperus phoenicea* L. (Cupressaceae) leaves growing in East Libya. *Lebda Med J.* 2021;8:292-297.
46. Camacho MdM, Zago M, García-Martínez E, Martínez-Navarrete N. Free and bound phenolic compounds present in orange juice by-product powder and their contribution to antioxidant activity. *Antioxidants.* 2022;11:1748. Available from: [URL](#)
47. Ullah A, Munir S, Badshah SL, Khan N, Ghani L, Poulson BG, Emwas AH, Jaremko M. Important Flavonoids and Their Role as a Therapeutic Agent. *Molecules.* 2020;25:5243. Available from: [URL](#)
48. Panche AN, Diwan AD, Chandra SR. Flavonoids: an overview. *J Nutr Sci.* 2016;5:e47. Available from: [URL](#)
49. El Jemli M, Kamal R, Marmouzi I, Zerrouki A, Cherrah Y, Alaoui K. Radical-scavenging activity and ferric reducing ability of *Juniperus thurifera* (L.), *J. oxycedrus* (L.), *J. phoenicea* (L.) and *Tetraclinis articulata* (L.). *Adv Pharmacol Pharm Sci.* 2016;2016:6392656. Available from: [URL](#)
50. Menaceur F, Benchabane A, Hazzit M, Baaliouamer A. Chemical Composition and Antioxidant Activity of Algerian *Juniperus phoenicea* L. Extracts. *J Biologically Active Prod Nat.* 2013;3(1):87-96. Available from: [URL](#)
51. Fadel H, Benayache F, Benayache S. (2016). Antioxidant properties of four Algerian medicinal and aromatic plants *Juniperus oxycedrus* L., *Juniperus phoenicea* L., *Marrubium vulgare* L., and *Cedrus atlantica* (Manetti ex Endl). *Der Pharm Lett.* 2016;8(3):72-79.
52. Rahhal R, EL Hajjouji H, Gmouh S, Hsaine M, Fougrach H, Badri W. Chemical composition, antioxidant and antibacterial activities of the essential oils of *Juniperus phoenicea*, *Juniperus thurifera* and *Juniperus oxycedrus*. *Mediterranean J Chem.* 2019;9(3):190-198. Available from: [URL](#)
53. Mazari K, Bendimerad N, Bekhechi C, Fernandez X. Chemical composition and antimicrobial activity of essential oils isolated from Algerian *Juniperus phoenicea* L. and *Cupressus sempervirens* L. *J Med Plants Res.* 2010;4(10):959-964. Available from: [URL](#)
54. Bajes HR, Oran SA, Bustanji YK. Chemical Composition and Antiproliferative and Antioxidant Activities of Essential Oil from *Juniperus phoenicea* L.

Cupressaceae. Res J Pharm Technol. 2022;15(1):153-159. Available from: [URL](#)

55. Koutsaviti A, Tzakou O, Galati EM, Certo G, Germanò MP. Chemical Composition of *Juniperus phoenicea* and *J. Drupacea* Essential Oils and their Biological Effects in the Choriallantoic Membrane (CAM) Assay. Nat Prod Commun. 2017;12(3):449-452.

56. Aljaiyash A, Ghanmi M, Satrani B, Labiad H, Echchel A, Chaouch A. Chemical Composition and Antimicrobial Activities of Ripe and Unripe Berries and Leaves of *Juniperus Phoenicea* L. Int J Emerg Eng Res Technol. 2016;4(10):7-1.

57. Nedjimi B, Beladel B, Guit B. Multi-element determination in medicinal Juniper tree (*Juniperus phoenicea*) by instrumental neutron activation analysis. J Radiat Res Appl Sci. 2015;8(2):243-246. Available from: [URL](#)

58. Ali RFM, Alaila AK. Morpho-Chemical Composition Characteristics of *Juniperus* and *Pistacia* Genera as Bio-Indicator of Construction Dust in Al-Jabal Al-Akhder-Libya. Haya Saudi J Life Sci. 2019;4(8):245-249. Available from: [URL](#)

59. Abu-darwish MS, Ofir R. Heavy metals content and essential oil yield of *Juniperus phoenicea* L. in different origins in Jordan. Environ Eng Manag J. 2014;13(12):3009-3014. Available from: [URL](#)

60. Nasri N, Tlili N, Elfalleh W, Cherif E, Ferchichi A, Khaldi A, Triki S. Chemical compounds from Phoenician juniper berries (*Juniperus phoenicea*). Nat Prod Res. 2011;25:1733-1742. Available from: [URL](#)

61. Kim MH, Choi MK. Seven Dietary Minerals (Ca, P, Mg, Fe, Zn, Cu, and Mn) and Their Relationship with Blood Pressure and Blood Lipids in Healthy Adults with Self-Selected Diet. Biol Trace Elem Res. 2013;153:69-75. Available from: [URL](#)

62. Paz S, Rubio C, Gutiérrez ÁJ, González-Welleer D, Hardisson A. Dietary Intake of Essential Elements (Na, K, Mg, Ca, Mn, Zn, Fe, Cu, Mo, Co) from Tofu Consumption. Biol Trace Elem Res. 2021;199:382-388. Available from: [URL](#)



Fatty Acid Composition, Antioxidant, and Enzyme Inhibition Activities of *Cachrys crassiloba* (Boiss.) Meikle Fruit and Leaf Extracts

Tugsen Buyukyildirim^{1,2*} , Yavuz Bagci³ , Nuraniye Eruygur¹ , Muhammed Rasit Bakir⁴ 

¹Department of Pharmacognosy, Faculty of Pharmacy, Selcuk University, Konya 42150, Türkiye.

²Graduate School of Health Science, Gazi University, Ankara 06640, Türkiye.

³Department of Pharmaceutical Botany, Faculty of Pharmacy, Selcuk University, Konya 42150, Türkiye.

⁴Department of Analytical Chemistry, Faculty of Pharmacy, Selcuk University, Konya 42150, Türkiye.

Abstract: The genus *Cachrys* L. (Apiaceae) is distributed in the Mediterranean region and contains 11 species. *C. crassiloba* (Boiss.) Meikle is a species that grows in Southwest and Western Anatolia. Considering the literature studies, there were not enough studies on *C. crassiloba*. In this study, fatty acid composition, total phenol/flavonoid contents, antioxidant and acetyl-butrylcholinesterase, tyrosinase, and α -glucosidase enzyme inhibition activities of n-hexane and ethanol extracts prepared from *C. crassiloba* fruits and leaves were investigated by spectrophotometric methods at different concentrations. When the results were evaluated, it was found that the hexane extract of *C. crassiloba* leaf (123.92 ± 4.62 GA mg/g extract) had the highest total phenol content, while the ethanol extract of *C. crassiloba* fruit (134.38 ± 0.98 QE mg/g extract) had the highest flavonoid content. *C. crassiloba* hexane and ethanol leaf extracts ($IC_{50} = 8.04 \pm 1.31$ μ g/mL; 10.30 ± 3.15 μ g/mL) showed good antioxidant activity compared to the ascorbic acid ($IC_{50} = 14.59 \pm 1.96$ μ g/mL) in DPPH assay. *C. crassiloba* leaf ethanol extract ($IC_{50} = 17.38 \pm 5.02$ μ g/mL) has the highest ABTS scavenging activity. *C. crassiloba* extracts have moderate cholinesterase inhibitory activity. *C. crassiloba* leaf ethanol extract ($IC_{50} = 196.65 \pm 1.94$ μ g/mL) has good tyrosinase enzyme inhibition activity. *C. crassiloba* leaf hexane extract ($36.35\% \pm 1.13$) was found to have significant inhibitory activity against α -glucosidase. In conclusion, besides its antioxidant activity, *C. crassiloba* may be effective against neurodegenerative diseases and skin disorders such as hyperpigmentation and diabetes mellitus, but further phytochemical analysis studies are required.

Keywords: *Cachrys crassiloba*, Apiaceae, Fatty acid composition, Antioxidant activity, Enzyme inhibition activity.

Submitted: November 13, 2023. **Accepted:** February 20, 2024.

Cite this: Buyukyildirim T, Bagci Y, Eruygur N, Bakir, MR. Fatty Acid Composition, Antioxidant, and Enzyme Inhibition Activities of *Cachrys crassiloba* (Boiss.) Meikle Fruit and Leaf Extracts. JOTCSA. 2024;11(2):723-30.

DOI: <https://doi.org/10.18596/jotcsa.1390152>

***Corresponding author's E-mail:** tugsen095@gmail.com, tugsen.dogru@selcuk.edu.tr

1. INTRODUCTION

Plant extracts and plant-derived compounds have important potential as drug precursors with neuroprotective activity. They are potential drug candidates for the treatment of Alzheimer's disease (AD), especially with cholinesterase inhibition (such as galantamine and Huperzin A) (1). AD, a neurodegenerative disease, is characterized by low levels of the neurotransmitter acetylcholine in the brain. So, inhibition of acetylcholinesterase (AChE) and butyrylcholinesterase (BChE) is considered a promising strategy for the treatment of AD (2). Therefore, it is important to investigate medicinal

plants and natural compounds with potential cholinesterase inhibitory activity.

The hydroxylation of tyrosine to O-diphenols and the oxidation of O-diphenols to O-quinones are carried out by the enzyme tyrosinase (TYR). The melanin is created from these quinones. The excessive production of melanin pigment in human skin results in skin color changes, wrinkles, and eventually skin aging. TYR inhibitors are preferred in cosmetic products as active compounds used for skin whitening in recent years (3,4).

Diabetes mellitus (DM) is a serious life-threatening disease that causes many complications. In these

patients, as a result of insufficient insulin or insensitivity to insulin, the blood sugar level increases, resulting in the deterioration of carbohydrate metabolism as well as fat and protein metabolism (5). The α -glucosidase enzyme breaks down large carbohydrates to release glucose. Therefore, anti-diabetic drugs with α -glucosidase inhibitory properties such as acarbose, voglibose, miglitol, and emigrate are commercially available for the treatment of DM (6). However, due to their existing side effects, researchers are looking for new natural drug candidates with high inhibitory potential and minimal side effects. Enzymes play a role in the pathophysiology of many important diseases (such as Alzheimer's-acetyl/butyrylcholinesterase, diabetes-glucosidase, Parkinson's, or skin lightening effect-tyrosinase). Therefore, suppressing some enzymes slows the progression of some diseases and becomes a therapeutic target in the drug industry.

Reactive oxygen species and oxygen-centered free radicals cause tissue damage followed by cell death by oxidizing lipids, proteins, and DNA. This condition triggers many chronic diseases, such as cancer, neurodegenerative diseases, and diabetes, and accelerates the aging process (7). Many medicinal plants contain large amounts of antioxidant substances such as flavonoids, phenolic compounds, and phenolic diterpenes (8). Since the synthetic antioxidants used have side effects such as liver damage and carcinogenesis, the use of plants and phytochemicals as antioxidants have become widespread (9).

The Apiaceae family includes the recognized genus *Cachrys*, which is widespread in Mediterranean nations and is found in southern Europe, northern Africa, and Asia (10). The genus contains 11 species. In Turkey, the *Cachrys* genus is represented by two species, namely *C. crassiloba* and *C. cristata*. Considering the ethnobotanical uses of the genus *Cachrys*, *C. alpine* M. Bieb is used as an aphrodisiac (11), while *C. libanotis* L. is used in the treatment of rheumatism (12). In Turkey, *C. cristata* DC. is added to a traditional soup (10, 13). *Cachrys* species are a rich source of coumarins, primarily furanocoumarins

(14), and other phytochemicals such as terpenes, fatty acids, phytosterols, and flavonoids, have also been identified. Some *Cachrys* species have been investigated in terms of essential oil content. The main components of *C. sicula* L. essential oil were found to be β -pinene (17.9%), sabinene (17.8%), myrcene (12%), and α -pinene (11.4%). (15). *Cachrys* species have various biological activities such as antioxidant, antimicrobial, anti-inflammatory, cytotoxic, and photocytotoxic (16,17). *C. crassiloba* (syn: *Hippomarathrum crassilobum* Boiss.) is a perennial herb that grows mostly in Southwestern and Western Anatolia (18) and grows primarily in the subtropical biome.

There are few biological activity studies on *C. crassiloba*. In this study, fatty acid composition, acetyl/butyrylcholinesterase, tyrosinase, and α -glucosidase enzyme inhibitory and antioxidant activities (DPPH and ABTS radical) of *C. crassiloba* fruit and leaf extracts were evaluated.

2. EXPERIMENTAL SECTION

2.1. Plant Material

The fruits and leaves of *C. crassiloba* were harvested in August 2020 from the Antalya province of Türkiye (C3 Antalya: Akseki, Murtiçi (Old Murtiçi), 600 m, roadside, 21.08.2020). The plants were identified by the botanist professor Yavuz Bağcı at the faculty of Pharmacy, Selcuk University. Voucher specimens are deposited in the Herbarium of the Faculty of Science under accession code Bağcı 4197 (KNYA Herb.).

2.2. Preparation of the Extracts

The fruits and leaves of the plant material were divided into two parts and dried in the shade. After the samples were pulverized, they were left to macerate with hexane and ethanol. After maceration, they were filtered with filter paper via Whatman No. 1 filter paper. The filtrates were evaporated to dryness in a rotary evaporator at 40 °C. The obtained extracts were stored in a deep freezer until biological activity studies were carried out. The yields of the extracts are given in Table 1.

Table 1: % Yield of the extracts from *C. crassiloba*.

Plant material	Plant parts	Solvent	%Yield of the extracts (w/w)
<i>C. crassiloba</i>	Fruit	Hexane	6.67
		Ethanol	13.32
	Leaf	Hexane	3.50
		Ethanol	11.31

2.3. Preparation of Fatty Acid Methyl Esters

The fatty acid methyl esters (FAMES) of the oil extracts of each plant were prepared according to the method recommended by the EU regulation (19). For this purpose, 0.10 g of each extract was weighed into a glass tube. The weighed samples were dissolved in 10 mL of hexane. 100 μ L of potassium hydroxide solution (2 N) prepared in methanol was added to each sample and shaken for 1 minute. The samples were centrifuged at 2500 x g for 5 min to separate the phases. From the samples whose phases were completely separated, the supernatant was taken,

filled into vials, and stored at +4 °C to be injected into GC-FID.

2.4. FAME Analysis by GC-FID

GC analysis was performed using an Agilent 6890N (Agilent Technologies Inc., Wilmington, DE, USA) gas chromatography system with FID. Automatic split-splitless injection was performed using the Agilent 7683 series autosampler. Helium gas was used as a carrier gas. The column used for the separations was HP-88 (100 m x 0.25 mm x 0.2 μ m) cyanopropyl capillary column. The temperature of the injection

and detector was set at 250°C. The column furnace temperature was initially held at 45 °C for 4 minutes. Afterward, the temperature was increased to 175 °C by increasing 13 °C per minute and was kept at this temperature for 27 minutes. It was programmed to be increased to 215 °C with an increase of 4 °C per minute and kept there for 35 minutes. Samples were injected in splitless injection mode (1 µL). H₂ and dry air flow rates for the detector were set at 30 and 300 mL per minute, respectively. Chromatograms were recorded using the Agilent 1200 Series-B.03.02 software program. Identification of each FA was performed by comparing the GC retention time with that of approved pure commercial standards for 37 FAME mixtures. The area under each FA peak relative to the total area of all FA peaks was used to quantify the FAs identified, and the results were expressed as a percentage of FA.

2.5. Antioxidant Activity Assays

2.5.1. Total phenol content (TPC)

The Folin Ciocalteu (F-C) method was used according to the Clarke et al. method for TPC measurements in extracts (20). Reagent F-C (1:10) was added to 10 µL of extract. Then 100 µL of 7.5% Na₂CO₃ was added and incubated for 60 minutes. Measurements were measured at 650 nm absorbance with a microplate reader (Multiscan Sky). All analyses were performed in triplicate, and the calibration curve of absorbance versus concentration was estimated as mg gallic acid (GA)/equivalent g extract ($y=0.0027x+0.0084$, $r^2=0.9966$).

2.5.2. Total flavonoid content (TFC)

TFC in the extracts was determined using the aluminum chloride colorimetric technique (21). 2% AlCl₃ was added to 150 µL of extract (0.3 mg/mL). After 15 min of incubation, absorbances were measured at 435 nm in a microplate reader. Total flavonoid content was calculated as mg quercetin (QE) equivalent/g extract ($y=0.0346x+0.2221$, $r^2=0.9773$).

2.5.3. 2,2-Diphenyl 1-picrylhydrazyl (DPPH) radical scavenging activity

180 µL of DPPH solution was combined with 20 µL of test solution on a 96-well plate. After 15 minutes of dark incubation, the plate was measured at 540 nm using an Elisa reader (Multiscan Sky, USA) (20). The positive control was ascorbic acid.

2.5.4. 2,2'-azino-bis-(3-ethylbenzothiazoline-6-sulfonic) acid (ABTS) radical scavenging activity

ABTS radical scavenging activity was performed with minor modifications to the method of Re et al. (22). ABTS•⁺ stock solution was prepared from 15 mL of 7 mM ABTS and 264 µL of 140 mM potassium persulfate solution for 16 hours of mix incubation prior to the experiment. The stock solution was diluted with 80% MeOH to set its absorbance at 0.70 ± 0.02 at 734 nm. 50 µL of extracts and 100 µL of ABTS⁺ solution were combined on a 96-well plate. After 10 minutes at room temperature, absorbance was measured at 734 nm. Butylated hydroxytoluene (BHT) was used as an antioxidant standard to compare the ABTS⁺ radical scavenging activity of extracts.

The antioxidant activity of all extracts, negative and positive controls, was assessed in triplicate. Calculations were made according to the following formula:

$$\text{Inhibition \%} = 100 - \left[\left(\frac{A_1}{A_2} \right) \times 100 \right] \quad (1)$$

A_1 = Absorbance of sample solutions
 A_2 = Average absorbance of negative control solutions

2.6. Enzyme Inhibition Activity Assay

2.6.1. AChE/BChE inhibition assay

Cholinesterase enzyme inhibition activities were performed according to the method of Ellman et al. with some modifications (Ellman et al., 1961) (23). Briefly, 20 µL of the test sample, 140 µL of 200 mM phosphate buffer (pH 7.7), 10 µL of 5,5-dithio-bis-(2-nitrobenzoic acid (DTNB)), and 20 µL of enzyme were mixed and incubated for 15 min (at room temperature). 10 µL of substrate (0.71 mM acetyl/0.2 mM butyrylthiocholine iodide) was added. Then 10 µL of DTNB was mixed. The absorbance of the yellow color formed was measured at 412 nm. Galantamine was used as a positive control.

2.6.2. TYR enzyme inhibition activity

TYR inhibitor activities of the extracts were performed according to the method of Yang et al. (24). Briefly, 20 µL of extract, 100 µL of phosphate buffer, and 20 µL of TYR were mixed in a 96-well plate. After 10 min of incubation at room temperature, 20 µL of L-tyrosine was added. Absorbances were measured at 492 nm. Kojic acid was used as a positive control.

2.6.3. α -glucosidase enzyme inhibition activity

With a few minor modifications, the spectrophotometric approach (24) described before was used to assess the inhibitory effect on α -glucosidase. In a 96-well microplate, 20 µL extracts were combined with 20 µL of a 0.08 U/mL α -glucosidase solution in 0.25 M phosphate buffer (pH 6.5). Before adding 40 µL of 0.375 mM 4-nitrophenyl- α -D-glucopyranoside (pNPG) to each well, the mixture was incubated at 37°C for 10 min. The reaction was stopped by adding 80 µL of 1 M Na₂CO₃ to this mixture after 30 min of incubation at 37°C. At 405 nm, the released 4-nitrophenol's absorbance was measured using a Multiscan microplate reader (USA). The positive control utilized was acarbose. The enzyme inhibition activity of all extracts, negative and positive controls, was performed in triplicate. Calculations were made according to the following formula:

$$\text{Inhibition \%} = 100 - \left[\left(\frac{A_1}{A_2} \right) \times 100 \right] \quad (2)$$

A_1 = Absorbance of sample solutions
 A_2 = Average absorbance of negative control solutions

3. RESULTS AND DISCUSSION

3.1. Fatty Acid Composition

Fatty acids have various biological activities in the human body and are the main components of biological matter. They are either saturated or unsaturated according to their chemical structure.

Especially unsaturated fatty acids are very valuable for maintaining a healthy state (25). Polyunsaturated fatty acids influence neurological controls, regulate gene expression, maintain skin water balance, and modulate immune function. Monounsaturated fatty acids lower blood cholesterol levels, reduce the risk of heart disease, and regulate immune function (26). In this study, the fatty acid compositions of *C. crassiloba* extracts are given in Table 2. Upon evaluation of the results, it was observed that the percentage of linoleic acid in *C. crassiloba* leaf ethanol and fruit hexane extracts was higher than

that of other fatty acids (28.04 and 33.78%, respectively). Linoleic acid is a polyunsaturated fatty acid that is the precursor to arachidonic acid, which produces eicosanoids that increase the production of pro-inflammatory cytokines (27). Several case-control studies have shown that low linoleic acid content in blood, platelets, erythrocytes, and adipose tissue is associated with an increased risk of ischemic stroke (28). While palmitic acid (26.48%) was abundant in *C. crassiloba* leaf hexane extract, the total of behenic acid and gamma-linolenic acid in *C. crassiloba* fruit ethanol extract was 23.90%.

Table 2: Fatty acid composition (%).

Fatty Acids	<i>C. crassiloba</i> leaf		<i>C. crassiloba</i> fruit		
	Ethanol	Hexane	Ethanol	Hexane	
C11:0	Undecanoic acid	11.35± 0.12	nd	1.94± 0.01	3.34± 0.02
C12:0	Lauric acid	nd	1.98± 0.01	nd	nd
C13:0	Tridecanoic acid	nd	nd	8.32± 0.07	nd
C14:0	Myristic acid	nd	8.69± 0.02	2.3± 0.01	3.59± 0.01
C16:0	Palmitic acid	22.94± 0.56	26.48± 0.43	9.33± 0.22	26.91± 0.35
C18:0	Stearic acid	nd	3.68± 0.01	nd	nd
C18:1 cis	Oleic acid	26.16± 1.04	13.65± 0.29	7.12± 0.36	14.63± 0.91
C18:2 trans	Linoleic acid	nd	nd	nd	nd
C18:2 cis	Linoleic acid	28.04± 0.78	15.28± 0.28	13.64± 0.17	33.78± 1.02
C18:3n6	Gamma linoleic acid	nd	2.20± 0.02	nd	nd
C18:3n3	Alpha linoleic acid	nd	5.29± 0.01	2.68± 0.10	6.22± 0.32
C21:0	Heneicosanoic acid	nd	nd	16.19± 0.34	4.44± 0.17
C22:0 + C20:3n6	Behenic acid + gamma linoleic acid	nd	4.49± 0.07	23.90± 0.48	7.04± 0.09
C22:1	Erucic acid	nd	nd	10.21± 0.18	nd
C24:0	Lignoceric acid	nd	18.27± 0.17	2.71± 0.02	nd
C24:1	Nervonic acid	11.49± 0.53	nd	1.63± 0.01	nd

nd; not detected

3.2. Antioxidant Activity of Extracts

Phenolic compounds are among the most common secondary metabolite groups in plants. They are responsible for many biological activities, especially antioxidant activity (29). To eliminate the harmful effects of free radicals, they can act by giving hydrogen atoms to oxidant molecules or by repairing cell damage, inhibiting oxidant enzymes, and stimulating the antioxidant mechanism (30). When the results were evaluated, it was found that the hexane extract of *C. crassiloba* leaf (123.92 ± 4.62 GA mg/g extract) had the highest total phenol content, while the ethanol extract of *C. crassiloba* fruit (134.38 ± 0.98 QE mg/g extract) had the highest flavonoid content. Hexane extracts of *C. crassiloba* fruit and leaf have nearly the same total flavonoid content (Fig. 1-2). *C. crassiloba* leaf hexane ($IC_{50} = 8.04 \pm 1.31$ µg/mL) and ethanol ($IC_{50} = 10.30 \pm 3.15$ µg/mL) extracts showed high and close DPPH radical scavenging activity, while *C. crassiloba* leaf ethanol extract ($IC_{50} = 17.38 \pm 5.02$ µg/mL) showed the highest ABTS scavenging activity. *C. crassiloba* leaf extracts showed strong antioxidant activity compared to the positive control group, ascorbic acid in the DPPH assay. As a result, the hexane extract of *C. crassiloba* fruit showed

moderate antioxidant activity, while other extracts had high antioxidant activity (Table 3). The fact that the TPC content of *C. crassiloba* fruit hexane extract is lower than the others may explain the lower antioxidant activity. In the correlation between antioxidant activity parameters, it is seen that TPC has a strong positive correlation with DPPH radical ($r = 0.95$, $p < 0.0001$) and ABTS radical ($r = 0.89$, $p < 0.0001$) radical scavenging activity (Fig. 3). However, there was a negative correlation between TFC and other antioxidant activity parameters. In the correlation, the antioxidant activities of the extracts were calculated in terms of ascorbic acid and BHT equivalent, which are the positive control groups. In another study, the DPPH radical scavenging activity of *C. crassiloba* (67.611% and 81.281%) was found to be high (31). In a study on another species of the genus *Cachrys*, TPC/TFC values of different extracts of *C. cristata* aerial parts and fruits were found to be between 22.60-166.97 mg GAE / g extract and 8.91-46.02 mg QE / g extract, respectively. DPPH radical scavenging activity was highest in the water extract of *C. cristata* fruit ($IC_{50} = 1.784$ mg/mL). Acetone extract of *C. cristata* aerial part showed strong ABTS scavenging activity (3.42 ± 0.005 mg vitamin CE/g) (32).

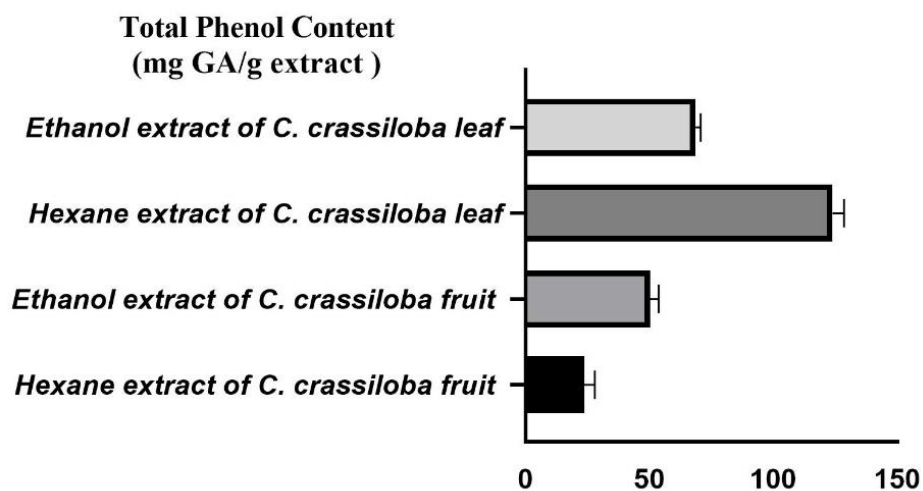


Figure 1: TPC of *C. crassiloba* extracts.

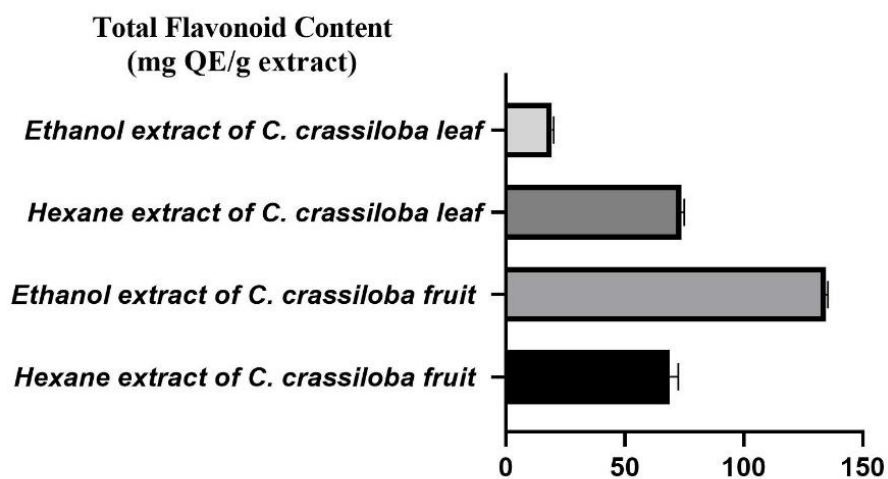


Figure 2: TFC of *C. crassiloba* extracts.

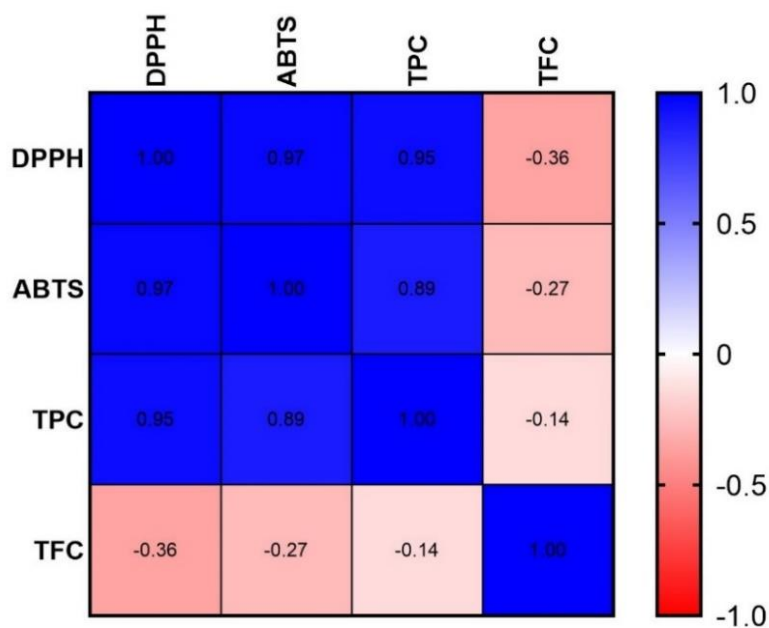


Figure 3: Heatmap of correlations between the analyzed antioxidant parameters.

Table 3: Antioxidant activities of *C. crassiloba* extract.

Plant	Solvent	DPPH radical scavenging activity (percentage \pm S.D. ^a) 1 mg/mL ^b	ABTS radical scavenging activity (percentage \pm S.D. ^a) 1 mg/mL ^b
<i>C. crassiloba</i> fruit	Hexane	32.89 \pm 0.05	16.87 \pm 4.35 ^c
	Ethanol	63.96 \pm 2.27 (IC ₅₀ = 47.97 \pm 2.33 μ g/mL)	77.58 \pm 0.83 (IC ₅₀ = 99.32 \pm 4.11 μ g/mL)
<i>C. crassiloba</i> leaf	Hexane	86.03 \pm 0.22 (IC ₅₀ = 8.04 \pm 1.31 μ g/mL)	87.38 \pm 0.38 (IC ₅₀ = 41.32 \pm 2.21 μ g/mL)
	Ethanol	80.24 \pm 0.11 (IC ₅₀ = 10.30 \pm 3.15 μ g/mL)	86.13 \pm 0.29 (IC ₅₀ = 17.38 \pm 5.02 μ g/mL)
References		94.13 \pm 0.02 ^d (IC ₅₀ = 14.59 \pm 1.96 μ g/mL)	87.61 \pm 0.27 ^e (IC ₅₀ = 10.45 \pm 4.85 μ g/mL)

^a: standard deviation, ^b: stock concentration, ^c: 2 mg/mL, ^d: Ascorbic acid, ^e: BHT

3.3. Enzyme Inhibition Activity of Extracts

C. crassiloba leaf and fruit extracts showed moderate/high cholinesterase inhibitory activity. *C. crassiloba* fruit ethanol extract showed the strongest acetylcholinesterase inhibitory activity (IC₅₀= 74.26 \pm 4.31 μ g/mL), while *C. crassiloba* fruit hexane (IC₅₀= 31.95 \pm 0.13 μ g/mL) and ethanol (IC₅₀= 39.93 \pm 3.45 μ g/mL) extract showed high butyrylcholinesterase inhibitory activity. *C. crassiloba* leaf ethanol extract (IC₅₀= 196.65 \pm 1.94 μ g/mL) showed the highest inhibitory activity against TYR enzyme. The α -glucosidase inhibitory activity of

C. crassiloba leaf hexane extract (36.35% \pm 1.13) was found to be significantly good activity. All enzyme inhibition results are given in Table 4. No previous enzyme inhibition activity study has been performed on extracts of *C. crassiloba*. In a previous study, a mild acetylcholinesterase inhibitor (IC₅₀=169.91 \pm 0.00 μ g/mL) and a good butyrylcholinesterase inhibitory effect (IC₅₀= 91.90 \pm 0.00 μ g/mL) of *C. sicula* L. essential oil were found. In the same study, the antioxidant activity was found to be high in the ABTS method (IC₅₀= 81.93 \pm 0.00 μ g/mL) (15).

Table 4: Enzyme inhibition activities of *C. crassiloba* extracts.

Plant	Solvent	AChE (percentage \pm S.D. ^a) 1 mg/mL ^b	BChE (percentage \pm S.D. ^a) 1 mg/mL ^b	TYR (percentage \pm S.D. ^a) 1 mg/mL ^b	α -glucosidase (percentage \pm S.D. ^a) 2 mg/mL ^b
<i>C. crassiloba</i> fruit	Hexane	40.98 \pm 5.38 (IC ₅₀ = 91.20 \pm 6.43 μ g/mL)	62.42 \pm 5.36 (IC ₅₀ = 31.95 \pm 0.13 μ g/mL)	28.47 \pm 3.91	- ^c
	Ethanol	60.56 \pm 6.39 (IC ₅₀ = 74.26 \pm 4.31 μ g/mL)	78.53 \pm 0.87 (IC ₅₀ = 39.93 \pm 3.45 μ g/mL)	14.35 \pm 5.64	19.18 \pm 3.70
<i>C. crassiloba</i> leaf	Hexane	34.46 \pm 7.84 (IC ₅₀ = 139.38 \pm 7.77 μ g/mL)	38.65 \pm 6.94 (IC ₅₀ = 157.20 \pm 0.28 μ g/mL)	34.03 \pm 0.09	36.35 \pm 1.13
	Ethanol	33.51 \pm 1.99 ^d	-	62.66 \pm 1.09 (IC ₅₀ = 196.65 \pm 1.94 μ g/mL)	3.91 \pm 1.13
Positive control		99.28 \pm 1.01 ^e	87.63 \pm 4.43 ^e	76.77 \pm 3.3 ^f	47.09 \pm 3.49 ^g

^a: standard deviation, ^b: stock concentration ^c: not effect ^d: 2 mg/mL, ^e: galantamine, ^f: kojic acid, ^g: acarbose.

4. CONCLUSION

Scientific understanding of plant chemical components and biological activity has advanced significantly in recent years. However, several species of the genus have yet to be completely defined, suggesting that more research is required. Although some bioactivity studies have been conducted on *Cachrys*, the chemical components in *Cachrys* may have additional bioactivities that have yet to be found and analyzed. In this study, *C. crassiloba* extracts were found to be potent

antioxidants due to the higher amount of phenolic compounds. These findings support the use of *C. crassiloba* in traditional medicine. In conclusion, the effectiveness of *C. crassiloba* extracts for human well-being and enzyme activity-guided isolation of active compounds should be complemented by further studies.

5. CONFLICT OF INTEREST

The authors declare that there are no known competing financial interests or personal

relationships that influenced the results reported in this paper.

6. ACKNOWLEDGMENTS

The authors thank the Faculty of Pharmacy, Selcuk University Konya, for supporting the instruments.

7. REFERENCES

1. Tamfu AN, Kucukaydin S, Yeskaliyeva B, Ozturk M, Dinica RM. Non-Alkaloid Cholinesterase Inhibitory Compounds from Natural Sources. *Molecules* [Internet]. 2021 Sep 14;26(18):5582. Available from: [<URL>](#).
2. Adewusi EA, Moodley N, Steenkamp V. Medicinal plants with cholinesterase inhibitory activity: A Review. *African J Biotechnol* [Internet]. 2010;9(49):8257–76. Available from: [<URL>](#).
3. Senol Deniz FS, Orhan IE, Duman H. Profiling cosmeceutical effects of various herbal extracts through elastase, collagenase, tyrosinase inhibitory and antioxidant assays. *Phytochem Lett* [Internet]. 2021 Oct 1;45:171–83. Available from: [<URL>](#).
4. Hong X, Luo X, Wang L, Gong D, Zhang G. New Insights into the Inhibition of Hesperetin on Polyphenol Oxidase: Inhibitory Kinetics, Binding Characteristics, Conformational Change and Computational Simulation. *Foods* [Internet]. 2023 Feb 20;12(4):905. Available from: [<URL>](#).
5. Sihoglu Tepe A, Ozaslan M. Anti-Alzheimer, anti-diabetic, skin-whitening, and antioxidant activities of the essential oil of *Cinnamomum zeylanicum*. *Ind Crops Prod* [Internet]. 2020 Mar 1;145:112069. Available from: [<URL>](#).
6. Papoutsis K, Zhang J, Bowyer MC, Brunton N, Gibney ER, Lyng J. Fruit, vegetables, and mushrooms for the preparation of extracts with α -amylase and α -glucosidase inhibition properties: A review. *Food Chem* [Internet]. 2021 Feb 15;338:128119. Available from: [<URL>](#).
7. Eruygur N, Ucar E, Akpulat HA, Shamsavari K, Safavi SM, Kahrizi D. In vitro antioxidant assessment, screening of enzyme inhibitory activities of methanol and water extracts and gene expression in *Hypericum lydiu*m. *Mol Biol Rep* [Internet]. 2019 Apr 14;46(2):2121–9. Available from: [<URL>](#).
8. Sharma SK, Singh L, Singh S. A review on medicinal plants having antioxidant potential. *Indian J Res Pharm Biotechnol* [Internet]. 2013;1(3):404–9. Available from: [<URL>](#).
9. Krishnaiah D, Sarbatly R, Nithyanandam R. A review of the antioxidant potential of medicinal plant species. *Food Bioprod Process* [Internet]. 2011 Jul 1;89(3):217–33. Available from: [<URL>](#).
10. Musolino V, Perri MR, Conforti F, Gliozzi M, Marrelli M, Mollace V. *Cachrys L.* Genus: A Comprehensive Review on Botany, Phytochemistry and Biological Properties. *Plants* [Internet]. 2023 Jan 26;12(3):565. Available from: [<URL>](#).
11. Tunçtürk M, Özgökçe F. Chemical composition of some Apiaceae plants commonly used in cheese in Eastern Anatolia. *Turkish J Agric For* [Internet]. 2015 Jan 1;39(1):55–62. Available from: [<URL>](#).
12. Aouachria S, Boumerfeg S, Benslama A, Boussoualim N, Trabsa H, Baghiani A. Phenolics Contents, Xanthine Oxidoreductase Inhibitory Potential, Antibacterial and Antioxidant Activities of *Cachrys libanotis L.* Root Extracts. *J Drug Deliv Ther* [Internet]. 2020 Aug 15;10(4-s):71–9. Available from: [<URL>](#).
13. Özek G, Özek T, Başer KHC, Hamzaoglu E, Duran A. Composition of the Essential Oil of *Hippomarathrum cristatum* (DC.) Boiss. *J Essent Oil Res* [Internet]. 2007 Nov;19(6):540–2. Available from: [<URL>](#).
14. Kuran F, Karavuş Ş, Miski M. *Cachrys cristata* DC. Isolation of Furanocoumarin Derived Compounds from Root Dichloromethane Extract. In: XXIV Symposium on Plant Originated Crude Drugs. Ankara, Türkiye; 2022. p. 270–1.
15. Tahar S, Hamdi B, Flamini G, Mehmet Ö, Duru ME, Bruno M, et al. Chemical composition, antioxidant and anticholinesterase activity of the essential oil of algerian *cachrys sicula L.* *Nat Prod Res* [Internet]. 2022 Aug 18;36(16):4094–102. Available from: [<URL>](#).
16. Perri MR, Pellegrino M, Aquaro S, Cavaliere F, Lupia C, Uzunov D, et al. *Cachrys* spp. from Southern Italy: Phytochemical Characterization and JAK/STAT Signaling Pathway Inhibition. *Plants* [Internet]. 2022 Oct 29;11(21):2913. Available from: [<URL>](#).
17. Marrelli M, Perri MR, Amodeo V, Giordano F, Statti GA, Panno ML, et al. Assessment of Photo-Induced Cytotoxic Activity of *Cachrys sicula* and *Cachrys libanotis* Enriched-Coumarin Extracts against Human Melanoma Cells. *Plants* [Internet]. 2021 Jan 8;10(1):123. Available from: [<URL>](#).
18. Duran A, Doğan B, Ay H. *Bilacunaria aksekiensis* (Apiaceae), a new species from South Anatolia, Turkey. *Ann Bot Fenn* [Internet]. 2011;48(4):361–7. Available from: [<URL>](#).
19. Commission EU. Regulation EEC 2568/91 on the characteristics of olive oil and olive-residue oil and on the relevant methods of analysis. *Off J Eur Communities L.* 1991;1991:248.
20. Clarke G, Ting K, Wiart C, Fry J. High Correlation of 2,2-diphenyl-1-picrylhydrazyl (DPPH) Radical Scavenging, Ferric Reducing Activity Potential and Total Phenolics Content Indicates Redundancy in Use of All Three Assays to Screen for Antioxidant Activity of Extracts of Plants from the Malaysian Rainforest. *Antioxidants* [Internet]. 2013 Jan 4;2(1):1–10. Available from: [<URL>](#).
21. Yang H, Dong Y, Du H, Shi H, Peng Y, Li X. Antioxidant Compounds from Propolis Collected in Anhui, China. *Molecules* [Internet]. 2011 Apr 21;16(4):3444–55. Available from: [<URL>](#).
22. Re R, Pellegrini N, Proteggente A, Pannala A, Yang M, Rice-Evans C. Antioxidant activity applying an improved ABTS radical cation decolorization assay. *Free Radic Biol Med* [Internet]. 1999 May 1;26(9–10):1231–7. Available from: [<URL>](#).
23. Ellman GL, Courtney KD, Andres V, Featherstone RM. A new and rapid colorimetric determination of acetylcholinesterase activity. *Biochem Pharmacol* [Internet]. 1961 Jul 1;7(2):88–95. Available from: [<URL>](#).
24. Yang Z, Wang Y, Wang Y, Zhang Y. Bioassay-guided screening and isolation of α -glucosidase and tyrosinase inhibitors from leaves of *Morus alba*. *Food Chem* [Internet]. 2012 Mar 15;131(2):617–25. Available from: [<URL>](#).
25. Albakry Z, Karrar E, Ahmed IAM, Oz E, Proestos C, El Sheikha AF, et al. Nutritional Composition and Volatile

- Compounds of Black Cumin (*Nigella sativa* L.) Seed, Fatty Acid Composition and Tocopherols, Polyphenols, and Antioxidant Activity of Its Essential Oil. *Horticulturae* [Internet]. 2022 Jun 24;8(7):575. Available from: [<URL>](#).
26. Ayyildiz HF, Topkafa M, Kara H, Sherazi STH. Evaluation of Fatty Acid Composition, Tocols Profile, and Oxidative Stability of Some Fully Refined Edible Oils. *Int J Food Prop* [Internet]. 2015 Sep 2;18(9):2064–76. Available from: [<URL>](#).
27. Kiecolt-Glaser JK, Epel ES, Belury MA, Andridge R, Lin J, Glaser R, et al. Omega-3 fatty acids, oxidative stress, and leukocyte telomere length: A randomized controlled trial. *Brain Behav Immun* [Internet]. 2013 Feb 1;28:16–24. Available from: [<URL>](#).
28. Iso H, Sato S, Umemura U, Kudo M, Koike K, Kitamura A, et al. Linoleic Acid, Other Fatty Acids, and the Risk of Stroke. *Stroke* [Internet]. 2002 Aug 1;33(8):2086–93. Available from: [<URL>](#).
29. Sakthidevi G, Mohan VR. Total Phenolic, Flavonoid Contents and In vitro Antioxidant Activity of *Dioscorea alata* L. Tuber. *Artic J Pharm Sci Res* [Internet]. 2013;5(5):115–9. Available from: [<URL>](#).
30. Varela-López A, Bullón P, Giampieri F, Quiles J. Non-Nutrient, Naturally Occurring Phenolic Compounds with Antioxidant Activity for the Prevention and Treatment of Periodontal Diseases. *Antioxidants* [Internet]. 2015 Jun 24;4(3):447–81. Available from: [<URL>](#).
31. Duran A, Uslu N, Doğan B, Musa Özcan M, Çelik M. Antioxidant Activity and Phenolic Contents of 30 Selected Medicinal Plants. *J Agroalimnet Process Technol* [Internet]. 2015;21(2):136–41. Available from: [<URL>](#).
32. Matejic J, Dzamic A, Mihajilov-Krstev T, Randjelovic V, Mileski K, Marin P. Total phenolic and flavonoid contents and biological activities of *Cachrys cristata* DC. extracts. *Arch Biol Sci* [Internet]. 2014;66(3):1117–23. Available from: [<URL>](#).



A Systematic Review of Synthesis MgO Nanoparticles and Their Applications

Hadia Hemmami^{1,2,3} , Ilham Ben Amor^{1,2*} , Soumeia Zeghoud^{1,2}, Salah Eddine Laouini^{1,4}, Emmanuel Chile Nleonu⁵ , Pawel Pohl⁶ , Jesus Simal-Gandara⁷ 

¹Department of Process Engineering and Petrochemical, Faculty of Technology, University of El Oued, El Oued 39000, Algeria.

²Renewable Energy Development unit in Arid Zones (UDERZA), University of El Oued, El Oued 39000, Algeria.

³Laboratory of Applied Chemistry and Environment, Faculty of Exact Sciences, University of El Oued, P.O. Box 789, El Oued 39000, Algeria.

⁴Laboratory of Biotechnology Biomaterials and Condensed Materials, faculte de la technologie, , University of El Oued, P.O. Box 789, El Oued 39000, Algeria.

⁵Department of Chemistry, Federal Polytechnic Nekede, P.M.B. 1036, Owerri, Imo State, Nigeria.

⁶Department of Analytical Chemistry and Chemical Metallurgy, Faculty of Chemistry, University of Science and Technology, Wyspianskiego 27, 50-370 Wroclaw, Poland.

⁷Universidade de Vigo, Nutrition and Bromatology Group, Analytical Chemistry and Food Science Department, Faculty of Science, E32004 Ourense, Spain.

Abstract: Recently, nanoscale biotechnology has emerged as an essential field of contemporary science and a new era in the study of materials. It draws the attention of many scientists from all over the world due to its versatility in various fields. Many physical, chemical, and biological processes are used to create biomaterials. Among the materials of interest is magnesium oxide (MgO), which can be widely used in medical and biotechnological applications due to its non-toxicity and environmental friendliness. This review article discusses various methods for the synthesis of magnesium oxide nanoparticles (MgONPs), with particular emphasis on recent developments and applications of these nanomaterials.

Keywords: MgONPs, Synthesis techniques, applications.

Submitted: February 4, 2023. **Accepted:** February 28, 2024.

Cite this: Hemmami H, Ben Amor I, Zeghoud S, Laouini SE, Nleonu EC, Pohl, P, Simal-Gandara J. A Systematic Review of Synthesis MgO Nanoparticles and Their Applications. JOTCSA. 2024;11(2):731-50.

DOI: <https://doi.org/10.18596/jotcsa.1247385>

***Corresponding author's E-mail:** ilhambenamor97@gmail.com

1. INTRODUCTION

Nanotechnology is a main driver behind the advancement of different disciplines of study that offers promise for numerous advances. Science and technology, deal with the synthesis, characterization, and development of applications of materials with at least one nanometer-scale dimension (1, 2).

Nanoparticles (NPs) are subgroups of particles with a size range of 1-100 nanometers that make up nanomaterials, which are structural components with a size range of 1-1000 nm (3, 4). Conical, spiral, flat, hollow, and other shapes and structures are just a few examples of the many different forms that can exist. Certainly, they exhibit exceptional physical

traits when compared to their bulk form, which gives them unique mechanical strength, improved stability, and many other advantages, and opens up the possibility for a range of unique applications (5, 6).

MgONPs are gaining more attention than other metal oxide nanoparticles that are frequently used in a variety of fields due to their high strength-to-weight ratio, low density, good functionality, nontoxicity, and hygroscopic properties. Because of their biocompatibility, they are very promising structural materials for implants and other biological systems. These characteristics of MgONPs boost their usefulness in several ways and provide additional benefits. It should not be surprising that MgONPs

have numerous commercial and biological applications in addition to their use in bone regeneration-assisting cryoinjury, antibacterial and antimicrobial inhibition, catalysis, lithium-ion battery production, and elimination of hazardous wastes (3, 7-11).

Because the synthesis method and its course determine the properties of the obtained nanomaterial and its subsequent use, the goal of this review study is to look into the methods involved in the synthesis of MgO NPs, with a particular emphasis on the most recent advancements in their various applications.

2. MAGNESIUM OXIDE NANOPARTICLE SYNTHESIS

Several methods are available for producing MgONPs, as shown in Figure 1. The most popular biological and chemical synthesis methods follow the bottom-up approach (12), and they are shown in Figure 1. Specifically, these methods include solve-/hydrothermal (13), sol-gel (14), co-precipitation (15), and combustion (16) processes. A special place among these methods is occupied using chemical reactions mediated by the use of plant extracts and microorganism media and fluids, the so-called green synthesis processes (17). In general, the bottom-up approach is advantageous because of its simplicity and ability to control the size and shape of the nanoparticles (18).

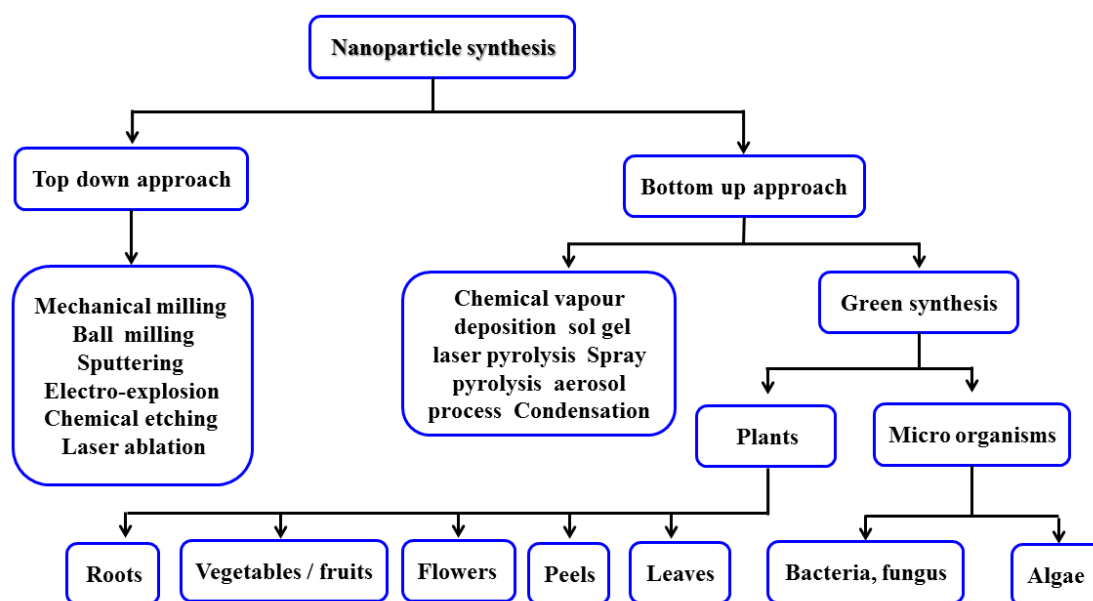


Figure 1: Different processes for creating nanoparticles.

2.1. Sol-Gel Technique

One of the simplest ways for synthesizing new material structures in the presence of an organic solvent and an inorganic precursor is the sol-gel method (19). Typically, this method is used to produce inorganic compounds like metal oxides and others that are comparable. In the middle of the 19th century, silica gel was first made using the sol-gel process (20). Metal alkoxides can be used to prepare homogeneous solutions, colloidal suspensions (sol), and integrated networks (gel), which, depending on the drying method, can subsequently be converted into xerogels or aerogels.

Mustuli *et al.* (21) focused on the production of nanostructured MgONPs using the sol-gel technique. They discovered that using Mg acetate in combination with a complexing agent in the form of oxalic acid and tartaric acid, the crystal growth could be inhibited.

Sutapa *et al.* (22) also produced MgONPs using Mg acetate. These researchers achieved the creation of cubic-shaped crystals, which were verified, using a scanning electron microscope (SEM), to have the highest texture coefficient value (0.98 in the crystal

plane (222)). They also characterized stress, strain, and crystal energy.

Wahab *et al.* (23), synthesized MgONPs using $\text{Mg}(\text{NO}_3)_2$ and NaOH. The sol-gel method described in their work resulted in the production of cubic-shaped MgONPs with a size of 50-60 nm.

In contrast, using Mg ribbons as a precursor, Boddu *et al.* (24) documented the synthesis of MgONPs having a coralline structure. In this case, hydrolysis, supercritical drying, and heat activation processes were carried out after a solution of Mg methoxide was obtained. This applied method resulted in the fabrication of 200–300 nm-sized particles having the aforementioned structure. To produce a nanopowder from MgO xerogel, Mg methoxide was employed by Dercz *et al.* (25) as a precursor, and the hydrolysis in the presence of toluene, followed by the addition of methanol was carried out. In this way, a specific surface area of 138 m^2/g and an average crystallite size of 7.5 nm were attained for these MgONPs.

Rani *et al.* (26) employed $\text{Mg}(\text{NO}_3)_2$, which dissolved in distilled water. SEM examinations showed that the final particles, produced *via* gel grinding and

subsequent annealing, had an average size of 60 nm. Nassar *et al.* (27) employed a mixed sol-gel combustion technique to produce nanostructured MgONPs as well. The scientists discovered that the kind of fuel had no discernible impact on the size and shape of the crystallites when utilizing $\text{Mg}(\text{NO}_3)_2$ in combination with oxalic acid, urea, and citric acid (citric acid was used to create the lowest crystallite size, which was about 12 nm).

2.2. Co-Precipitation

The synthesis of NPs with this method is based on the idea of precipitation, and frequently uses liquid-phase synthesis (28), while vapor-phase synthesis is applied less frequently (29). The precipitating agent is frequently NaOH (30, 31), and two processes, i.e., nucleation and nuclei growth, make up together the homogeneity of the precipitation reaction and the quality of the final nanomaterial product (32). Three basic concepts are taken into account: (i) the diffusion-based single nucleation and the homogeneous growth; (ii) the smaller subunits formation, development, and assemblage; and (iii) the numerous nucleation and the Ostwald ripening growth (33).

Mashad *et al.* (34) produced MgONPs by co-precipitation and evaluated the effects of various reaction parameters, such as temperature, pH, and the molar ratio of precursor (magnesium nitrate), on the quality of the products. They obtained nanoparticles and nanorods with a reasonably high specific surface area (231 m^2/g for nanoparticles and 176 m^2/g for nanorods) and a particle size of 50 nm.

$\text{Mg}(\text{NO}_3)_2$ was used as the precursor, while an NH_4OH solution served as the precipitating agent in work by Kumar *et al.* (35). As a result, MgONPs having an average size of around 11 nm were produced. The impact of the polyethylene glycol (PEG) content on the characteristics of MgONPs produced by the co-precipitation method was also investigated by Karthikeyan *et al.* (36). In this work, $\text{Mg}(\text{NO}_3)_2$ was used as a precursor while NaOH as a precipitation agent. When PEG was additionally used, it resulted in doubling the size of crystallites, according to XRD measurements (8.6 nm vs. 14.8–15.9 nm without and with PEG, respectively). What is more, PEG-modified MgONPs exhibited a flake-like structure, while pure MgONPs were spherical.

By calcining MgCO_3 , which Frantina *et al.* (37) initially obtained by combining $(\text{NH}_4)_2\text{CO}_3$ and MgCl_2 , MgONPs were also produced. The XRD data suggested a cubic structure with an average crystallite size of 24 nm. With negligible changes in the particle size, the spherical shape of the resulting MgONPs was confirmed using SEM, while their average size was 50.9 nm.

MgONPs reported by Kushwaha *et al.* (38) were produced by several distinct techniques (sol-gel, solution combustion, and a solution of cetyltrimethylammonium bromide (CTAB)), as well as the co-precipitation technique. Their findings demonstrated that 4.9 eV bandgap MgONPs were produced using the chemical method. The crystallite

size was shown by XRD to be 14.8 nm, and the authors also reported a hydrodynamic particle size of 100 nm. MgO nanotubes were also prepared by Tandon and Chauhan (32) using Mg acetate and NaOH. Using XRD, the average crystal size was calculated to be 34 nm. The field emission (FE)SEM data showed that the resulting nanomaterial had a tubular shape, with an inner diameter of 31 nm and an estimated outside diameter of 78 nm. Additionally, a greater bandgap of MgONPs in comparison to the prior example (5.73 eV) was reported.

2.3. Combustion Technique

Due to its effectiveness and affordability, the combustion process is commonly utilized to manufacture metal oxide nanoparticles (39). Two strategies can be used for that, including so-called "self-propagating synthesis" and the "volume combustion synthesis" (40). In the case of "self-propagating synthesis", the production of solid products occurs without the need for the energy input (41), because spontaneous redox reactions occur between the precursor (oxidizer) and the reductant (fuel) combined at the molecular level in solution. These reactions are initiated by an outside source. In the second case ("volume combustion synthesis"), the sample is heated until the reaction starts, spreading across its whole volume. The latter approach is especially recommended for moderate exothermic reactions that require preheating before the ignition, even though this sort of preparation is more difficult to control (42).

Accordingly, when urea was used as a fuel and $\text{Mg}(\text{NO}_3)_2$ as an oxidizer, it was possible to produce MgONPs with a cubic structure and a crystallite size of around 22 nm, according to the XRD data (43). The resulting MgONPs were uniformly sized and spherical, as established by SEM. Interestingly, the synthesized nanomaterial exhibited a bandgap of just 2.9 eV, which is much lower as compared to earlier research. The same raw ingredients were utilized by Rao *et al.* (44), who tested the impact of the fuel-to-oxidizer ratio on the quality of the produced nanomaterial. The findings showed that except for the percentage of oxidizer was 0.75, manufactured MgONPs have larger crystallite sizes (18–53 nm) when the fuel contribution increases. Changes in the burn rate, enthalpy, or ignition temperature might be responsible for this.

Ranjan *et al.* (45) reported a variation of this procedure, using $\text{Mg}(\text{NO}_3)_2$ as the precursor and glycine as the fuel. The estimated crystallite size, based on the XRD measurements, was 20.8 nm in this case.

On the other hand, Therami *et al.* (46) used citric acid as fuel. The authors examined how the specified parameters of MgONPs were impacted by the concentration of this acid. The most significant changes obtained were observed for the particle size of MgONPs (it decreased from 35 to 20 nm), their bandgap (it increased from 4.72 to 5.35 eV), and their morphology (vacuolar, flower-like, and flake-like).

MgONPs were also obtained by Kumar *et al.* (47), who used $\text{Mg}(\text{NO}_3)_2$ and a parthenium plant extract. The primary objective was to analyze the impact of the fuel quantity on the bandgap width (5.3–5.45 eV) and the crystallite size (27–35 nm). However, the variation of both parameters was not as pronounced as it was reported in other works.

2.4. Solvo- and Hydrothermal Method

Another popular technique for regulating the formation of crystals in a variety of materials is the solvothermal approach (48). The required products are generated when a precursor and a suitable solvent are put in an autoclave and exposed simultaneously to a high temperature and a high pressure (49). In contrast to the co-precipitation approach, these reaction conditions (temperature and pressure) enable to obtain the high crystallinity materials (50). Solvents other than water are typically utilized in the "solvothermal" technique, including alcohols or other organic or inorganic solvents. When water is used as the solvent, this process can be referred to as "hydrothermal."

Devaraja *et al.* (51) used $\text{Mg}(\text{NO}_3)_2$ and NaOH to produce a nanocrystalline MgO powder and evaluated its quality. The MgONPs produced by them were porous, with an average crystallite size of 25 nm and an optical energy bandgap of 5.5 eV. Al-Hazmi *et al.* (52), on the other hand, obtained nanofibers by the direct interaction of urea and Mg acetate. These fibers had an average crystallite size of 6 nm, which corresponded to their diameter, and the length of 10 nm, as measured by TEM.

Ding *et al.* reported the synthesis of rod- and tube-shaped $\text{Mg}(\text{OH})_2$, which was subjected to thermal decomposition to fabricate MgONPs (53). The author's findings demonstrated that the hydrothermal approach could be used to manipulate the crystallite size of the resultant MgONPs, and their shape and structure. The material for the synthesis was either Mg powder, $\text{Mg}(\text{SO}_4)_2$, or $\text{Mg}(\text{NO}_3)_2$. Due to various experimental circumstances, numerous morphologies (lamellar, needle-like, and rod-like) of MgONPs were achieved. The resultant nanomaterials were 20 to 600 nm in size and had a specific surface area of more than 100 m^2/g .

Rukh *et al.* (54) used Mg powder as the precursor for the MgONPs synthesis. The reaction medium for the synthesis was a mixture of H_2O_2 and de-ionized water. Using this method, MgONPs with an 18 nm crystallite size were obtained. Nanoplates are another form of nanostructured MgO that was reported to be produced by Duong *et al.* (54). Additionally, the scientists utilized sodium dodecyl sulfate (SDS), PEG, CTAB, and $\text{Mg}(\text{NO}_3)_2$ to regulate the morphology of the resulting nanomaterials. MgONPs produced using the hydrothermal process in conjunction with SDS were the most intriguing since they had the largest specific surface area (126 m^2/g) and the ideal disc shape (thickness 5 nm, diameter 40–60 nm).

2.5. Green Synthesis of MgO Nanoparticles

Researchers have shown a growing interest in the production of MgONPs through biological processes over the past ten years. The development and significance of this synthesis type are mostly related to the possibility of the use of much fewer chemicals, making this less cost-effective and more environmentally friendly (55–57).

The traditional chemically- or physically-based techniques for the synthesis of MgONPs are less practical and less ecologically benign than their biologically-based alternatives, also known as (56, 58). Consequently, the term "green synthesis" is frequently used to describe biological techniques. The large-scale synthesis of nanoparticles utilizing the green methods is always a difficult undertaking, and these are only performed at laboratory-scale processes. However, thanks to advancements in the understanding of the nature of the biological extract composition and the reaction with metal ions, large-scale preparation may soon be feasible without the need for any powerful machines (59).

To lessen the hazardous nature of the nanoproductions, biological substrates such as plants, bacteria, algae, and fungi are frequently utilized in place of chemical compounds used as stabilizers and solvents (59). The greener way to produce MgONPs involved the use of the available precursors, such as $\text{Mg}(\text{NO}_3)_2$, MgCl_2 , Mg acetate, and $\text{Mg}(\text{SO}_4)_2$, and different biological agents, including plants, microorganisms, and biomolecules. The precursor was combined with the previously produced biological extracts of plants, microorganisms, or templates to prepare homogeneous mixtures, which were then subjected to thermal treatment (60–62).

There are several papers on the production of MgONPs. The information on the various synthetic processes used to produce nanostructured MgO reported in the literature is given in Table 2. Many biological templates were employed for the production of MgONPs, as can be seen from the data given. The production of MgONPs with various sizes and morphologies was ultimately achieved by the variation in the reaction time, the concentration of the Mg precursors, pH, and the temperature of the reactants.

For instance, it was established that the particle size of MgONPs grows along with the increasing dose of the biological substrate (63). According to the Mie hypothesis, the absorbance of light is proportional to the particle size of the metal nanoparticles formed. However, it was discovered (64) that when the extract of *Amaranthus tricolor* and Mg acetates ($\text{Mg}(\text{C}_2\text{H}_3\text{O}_2)_2$) were used, the MgONPs produced were found to deviate from the Mie theory, showing the lower absorbance and the increased particle size when the amount of the biological substrate was higher. When they added 5 mL of the *Amaranthus tricolor* extract and Mg acetate, they found that the product had a little variation from the Mie theory; it had decreased absorbance and increased particle size. Smaller-sized MgONPs resulted from the addition of 10 and 15 mL of the *Amaranthus tricolor*

extract to the same precursor. This demonstrated how the presence of the biological substrates affects the size of MgONPs. According to scientists, the addition of capping agents could also improve the production of MgONPs. Smaller amounts of the capping agents caused the particles to adhere to one another and, to larger extents, the formation of larger particles. It is also obvious that the use of lower concentrations of the biological substrates would produce more homogeneous and bigger nanoparticles, whereas higher concentrations of the biological substrates would produce less stable nanoparticles. It is also evident that the presence of flavanoids in the biological substrates is responsible for these modifications. The development of MgO NPs is also influenced by reaction time. Additionally, the size of the product rises along with the response time. Numerous pH reports at 3.2, 5.2, 7.2, and 9.2 are available. It is clear from examining the impact of pH reports that a pH of 3.2 results in good particle size. The biological templates' active components, like flavonoids and polyphenols, are particularly effective at reducing metal ions at this pH level (65).

Khan *et al.* (66) noticed that the temperature also has an impact on the formation of MgONPs. The authors conducted the reaction at temperatures between 30 and 70 °C while holding all other variables constant. Generally speaking, the appropriate temperature should be kept for the formation of MgONPs with phytochemical support (Flavonoids, phenols, and other species). Otherwise, the phytochemicals utilized to synthesize MgONPs could alter their structure. The highest absorbance (81%) range of methylene blue (MB) dye was achieved at 30 °C. Additionally, it was noticed that when the temperature was raised, product agglomeration occurred, while product formation was prevented. Furthermore, the production of the final product was hampered by precursor concentrations greater than 0.001 mol/L. The final loss of chemicals, energy, and time will occur from the addition of an excessive concentration of the precursors. The physicochemical properties of MgONPs can be altered depending on the conditions of the green synthesis conditions (see details in Table 2).

Table 1: Individual ingredients and reaction circumstances for the bottom-up production of nanostructural MgO using various techniques.

Sol-Gel Technique							
Precursor	Solvent(s)	Drying temperature (°C)	Temperature of calcination (°C)	Time of calcination (h)	Size (nm)	Expected applications	Ref.
Mg(NO ₃) ₂	C ₆ H ₈ O ₇ , C ₂ H ₂ O ₄ , NH ₂ CONH ₂	350	550, 800	2	12	catalyst	(27)
Mg(CH ₃ COO) ₂	C ₄ H ₆ O ₆ , NaOH	-	600	6	-	-	(21)
Mg(CH ₃ COO) ₂	C ₂ H ₂ O ₄	200	950	6	-	-	(22)
Mg(NO ₃) ₂	NaOH	300	500	2	50-60	adsorber	(23)
Mg(OCH ₃) ₂	CH ₃ OH, C ₇ H ₈	-	500	5	200-300	-	(24)
Mg(OCH ₃) ₂	CH ₃ OH; C ₇ H ₈	60	450	-	Ca.8	-	(25)
Mg(NO ₃) ₂	H ₂ O	150	500	2	60	-	(26)
Co-Precipitation Technique							
Precursor	Precipitation agent	Reaction temperature (°C)	Temperature of calcination (°C)	Time of calcination (h)	Size (nm)	Expected applications	Ref.
Mg(NO ₃) ₂	NaOH	Room	Room	-	78	antibacterial agent	(32)
Mg(NO ₃) ₂	NaOH	-	440	4.5	-	catalyst	(38)
Mg(NO ₃) ₂	NH ₄ OH	60, 70, 80	550	2	50	-	(34)
Mg(NO ₃) ₂	NH ₄ OH	100	600	4-6	11	antibacterial agent	(35)
Mg(NO ₃) ₂	NaOH	Room	500	4	14-16	antibacterial agent	(36)
Combustion Technique							
Oxidizer	Fuel	Ignition temperature	Temperature of calcination (°C)	Time of calcination (h)	Size (nm)	Expected applications	Ref.
Mg(NO ₃) ₂	Parthenium extract	400	-	-	27-35	photocatalyst	(47)
		70-80	500	3	22	adsorber	(43)
	NH ₂ CONH ₂	100	300	2	18-53	-	(44)
	NH ₂ CH ₂ COOH	170	600	2	Ca.21	fuel additive	(45)
	C ₆ H ₈ O ₇	100	400	15 min	20-35	antibacterial agent	(46)
Solvo- and Hydrothermal Technique							
Oxidizer	Solvent	Autoclave temperature	Temperature of calcination (°C)	Time of calcination (h)	Size (nm)	Expected applications	Ref.
Mg(NO ₃) ₂	NaOH	100	500	4	40-60	adsorber	(67)
Mg	H ₂ O ₂	220	-	-	18	antibacterial	(54)
MgSO ₄	NH ₃ H ₂ O; en-H ₂ O	180	280-450	1;2	100-200	catalyst	(53)

Mg(NO ₃) ₂	NaOH	130	400-800	2	25	-	(51)
Mg(CH ₃ COO)	NH ₂ CONH ₂	180	600	1	6	antibacterial	(52)
Mg(NO ₃) ₂	NaOH	80	280-450	1;2	50	catalyst	(53)
Green Synthesis							
Precursor solution	Reagent extract	Reaction temperature	Temperature of calcination (°C)	Time of calcination (h)	Size (nm)	Expected applications	Ref.
Mg(NO ₃) ₂	<i>Nepheium lappaceum</i>	80	450	-	55	-	(68)
	<i>Trigonella foenum-graecum</i>	80	600	4	14	antibacterial agent	(69)
	<i>Rosa foribunda</i>	90	-	-	10	antibacterial agent	(70)
Bulk MgO	<i>Rosmarinus officinalis</i>	70	-	-	8.8	antibacterial agent	(71)
Mg(NO ₃) ₂	<i>Dalbergia sissoo</i>	30-70	-	-	50	photocatalyst	(66)
	<i>Saussurea costus</i>	80	450	3	30	photocatalyst	(72)
	<i>Swertia chirayaita</i>	55	400	4	< 20	antibacterial agent	(73)
MgCl ₂	<i>Moringa oleifera</i>	90	600	5	21	antibacterial agent	(74)
Mg(NO ₃) ₂	<i>Tecoma stans</i>	90	550	6	20-50	adsorber	(75)

Table 2: Reported processes for making MgO NPs through green synthesis.

Material used	Particle size (nm)	Morphology of nanomaterial	Activity carried	Ref.
<i>Citrus limon</i> leaf extract	12-80	nanoflakes	nil	(58)
<i>Rosmarinus officinalis</i>	<20	nanoflowers	antibacterial activity	(71)
<i>Nepheium lappaceum</i>	60-70	cubic	nil	(76)
<i>Solanum trilobatum</i>	30 and 42	spherical	antibacterial and antioxidant activity	(77)
<i>Mucuna pruiens</i> seeds	35	spherical	antibacterial and photocatalytic activity	(78)
<i>Rhizophora lamarckii</i>	20 and 50	hexagonal and spherical	antibacterial activity	(79)
<i>Aloe vera</i>	8.6	dense rock-shaped flakes	antibacterial and photocatalytic activity	(80)
<i>Amaranthus blitum</i> and <i>aloe vera</i>	26-50	spherical	water treatment	(81)
Mushroom extract	20-15	cubic	seed germination	(82)
<i>Aspergillus tubingensis</i>	2.8	sphere	nil	(83)
<i>Aspergillus niger</i>	43-91	sphere	antibacterial activity	(84)
<i>Lactobacillus plantarum</i>	30	cubic	anticancer activity	(85)
<i>Lactobacillus sporogenes</i>				
<i>Aspergillus fumigatus</i>	0.3-94	nil	nil	(86)
<i>Manihot esculenta</i>	37	hexagonal	nil	(87)
<i>Sargassum wightii</i>	69	cubic	antimicrobial and photocatalytic activity	(88)
<i>Artemisia abrotanum</i> herb	10	clusters	photocatalytic and antioxidant activity	(89)
<i>Rhododendron arboretum</i>	nil	nil	antibacterial activity	(62)
<i>Ocimum sanctum</i>	50-100	nanoflakes	antibacterial and antioxidant activity	(81)
<i>Chamaemelum nobile</i> flower extract	20-40	nanoflakes	insect repellent	(90)
<i>Curcumin</i>	35	rod-like and spherical - like shape	catalytic properties	(91)
<i>Acacia</i> gum	50-78	nanoflowers, cubic	catalytic properties	(92)
<i>Brassica olercea</i> and <i>Punica granatum</i>	30-65	spherical	photocatalytic and anticancer activity	(93)

Orange peel extract	>10	spherical	antibacterial and antimicrobial activity	(94)
Curry leaves	20	spherical	photocatalytic activity	(95)
<i>Swertia chirayaita</i>	<20	spherical	antibacterial activity	(73)
<i>Pisidium guvajava</i> and <i>aloe vera</i>	50-90	cubic	antibacterial activity	(96)
<i>Lepidium sativum</i>	33	nanoflakes	photocatalytic activity	(97)
<i>Matricaria chamomilla</i> L. extract	18 and 16	disc-shape	antibacterial activity	(98)

3. RESOURCES THAT CAN BE USED AS A MAGNESIUM SOURCE TO PREPARE MgO NPs

MgO nanoparticles with superior properties are important in industry, and these particles can be prepared from different sources using different methods. Table 3 shows the resources that can be

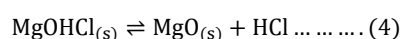
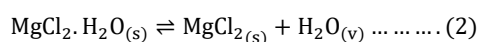
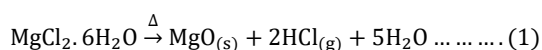
used to manufacture MgO NPs as a source of magnesium in a direct way. As for the indirect method, an intermediate is extracted and subsequently treated to produce magnesium oxide (Table 4). The following chemical equations (1-4) explain the mechanism of transformation of the medium into magnesium oxides.

Table 3: There are several resources that may be employed to manufacture MgO NPs as a magnesium source.

Resources	Presses	Intermediate reactant	Temperature of calcination (°C)	Yield%	Purity%	Size (nm)	Ref.
Dolomite CaMg(CO ₃) ₂	Pyrohydrolysis process	HCl CO ₂	600	98.10	98.86	100	(99)
Dolomite: CaMg(CO ₃) ₂]	Pyrohydrolysis process	HCl MgCl ₂	500	--	95.48	--	(100)
Dolime (CaO.MgO)	Pyrohydrolysis process			--	87.80	--	
Serpentine;		(NH ₄) ₂ SO ₄ NaHSO ₄	1300	--	high purity	62	(101)
Dolomite : poly(acrylate) magnesium hydroxide	Pyrohydrolysis process	poly(acrylate) Na ₂ S ₂ O ₈ MgCl ₂ NaOH	500	--	high purity	20	(102)
Sea water	Pyrohydrolysis process	MgCl ₂ NaOH	1400	43	56	--	(103)

Table 4: Various resources that may be employed to prepare an intermediate reactant using a magnesium source.

Resources	Technique	Reactants	Temperature of reaction (°C)	Yield %	Purity %	Size (nm)	Ref.
serpentine mineral	precipitation	NH ₄ OH HNO ₃	80	--	high purity	30	(104)
Serpentine 4MgCO ₃ .Mg(OH) ₂ . 4H ₂ O	precipitation	NH ₃ .H ₂ O NH ₄ HCO ₃	40~70	96.3	high purity	--	(105)



mode. Mono-coordinated hydroxyl (-OH) groups are indicated at 3100–3500 cm⁻¹. The stretching frequency of H-O-H is linked to a wide band at roughly 3461 cm⁻¹. At roughly 673 cm⁻¹, the wide band stretching vibration matches the Mg-O stretching vibration. The stretching vibration of magnesium oxide is shown by a prominent peak with a center of 433–769 cm⁻¹.

4. CHARACTERISTICS MgO NPs

Magnesium oxide may also be identified and structurally characterized using Fourier transform infrared spectroscopy (FTIR)(106, 107). Depending on the wavelength of the incoming light, transmittance or absorbance are the most typical interpretations. Figure 2a displays typical FTIR spectra for magnesium oxide in the absorbance

Using X-ray diffraction (XRD) (JCPDS Standard No. 01-089-7746), it is possible to characterize the crystal structure of magnesium oxide. Important peaks can be assigned near the 2θ values of 36.8, 42.9, 62.19, 74.6, and 78.58°, which can be indexed to the lattice planes (111), (200), (220), (311), and (222), respectively. Comparable findings have been frequently reported(108) (Figure 2b). The most

popular method in the literature for interpreting XRD data to calculate the crystallite size of produced nanostructures is the Scherrer equation(109). Nevertheless, the average crystallinity size up to around 200 nm(110) is the limiting factor in terms of employing the Scherrer equation. This is caused by the fact that when crystallite size increases, the diffraction peak's widening reduces(111). Hence, it is challenging to distinguish between the widening of the peak caused by crystallite size and the

broadening caused by other causes (e.g., size distributions and shape of the crystallites)(106).

In addition to the methods mentioned above, UV-Vis spectroscopy (UV-Vis) and spectra are taken between 200 nm and 800 nm. They may also be used to analyze MgO, especially to establish the bandgap energy(112, 113). Tauc plots and absorbance spectra are both utilized for this. To measure the bandgap width, the photoluminescence technique(114) is usually employed.

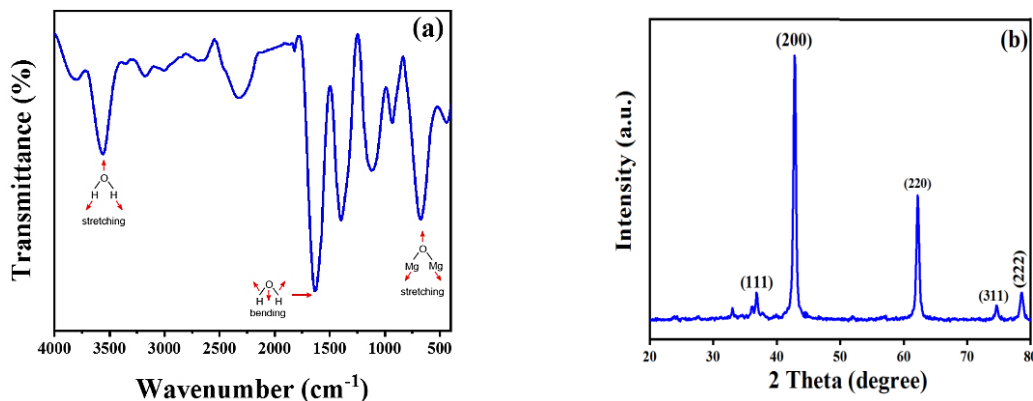


Figure 2: FTIR spectra (a) and an XRD pattern(b) used to characterize the structural properties of MgONPs (redrawn and adapted from the results presented in(115)).

Depending on several variables, including the synthesis process, the synthesis circumstances, and the post-treatment techniques, MgO structures can have a variety of morphologies. Typical morphological variations between MgO formations include the following:

Particle size and shape: The synthesis technique utilized can have a significant impact on the size and form of MgO particles. For instance, sol-gel processes may yield a range of morphologies, including nanowires and sheets, whereas precipitation methods usually produce spherical particles with a restricted size distribution(116).

Surface area: Depending on their form, MgO structures' surface areas can also change. Larger particles often have lower surface areas than nanoparticles or nanowires, which might be crucial for applications like catalysis(117).

Porosity: Depending on the synthesis technique employed, MgO structures can be either very porous

or non-porous. For instance, although hydrothermal synthesis may yield structures with a high degree of crystallinity and little porosity, flame synthesis can produce very porous structures, such as hollow spheres(118).

Crystal structure: The crystal formations of MgO can be cubic, hexagonal, or tetragonal. The material's chemical and physical characteristics can be affected by the crystal structure(119).

Surface chemistry: Depending on their form, MgO structures' surfaces can have different chemical compositions. For instance, exposed crystal planes or surface flaws might influence the reactivity of MgO in catalytic processes(120).

The morphology and properties of the prepared MgONPs differ and depend on the synthesis route and processing conditions. Figure 3 illustrates the various morphologies that can be seen in MgO nanoparticles.

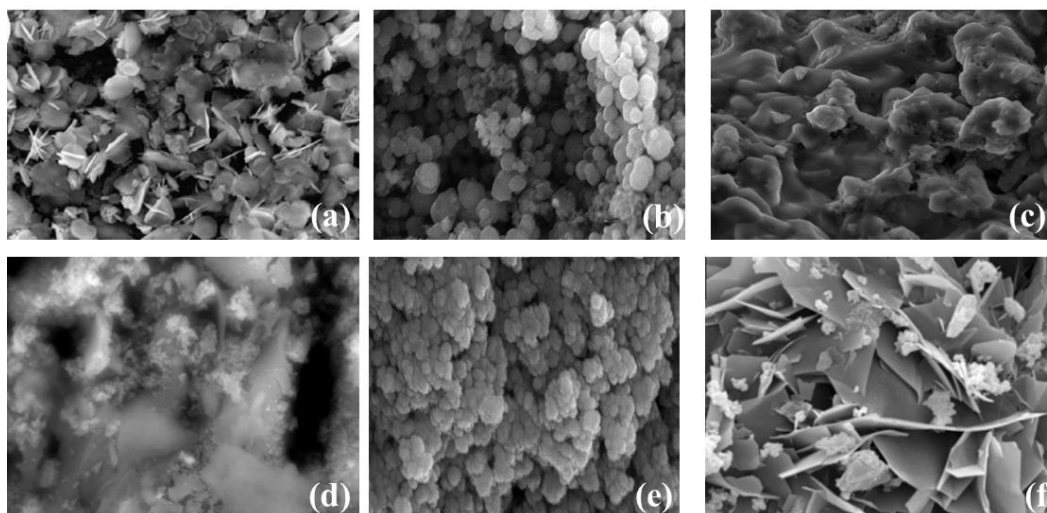


Figure 3. Different morphologies of MgO NPs: (a) flower-like(121), (b) spherical(115),(c) irregular shaped flakes(97),(d) Clusters(122),(e) Hexagonal(87),(f) flakes shape(87).

5. APPLICATIONS

MgONPs have a large specific area, a broadband gap, and good physical and chemical properties, providing them with strong technological applications. Additionally, MgONPs exhibit a propensity to generate superoxides when they are in contact with O_2 found in bacterial cell walls. The bacterial cell walls

and their phospholipids are promptly destroyed by these superoxides, which are highly responsive to them. MgONPs can also be used in many applications, as displayed in Figure 4, including the production and/or modification of fuel cells, ceramics, batteries, supercapacitors, and electronics, in addition to environment and agriculture purposes.

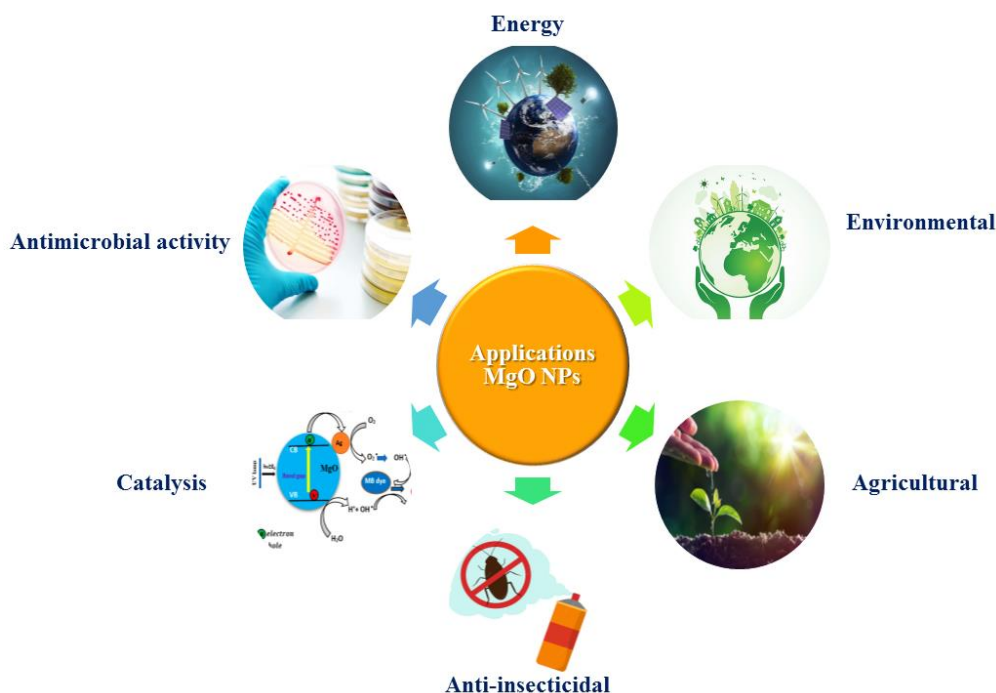


Figure 4: Different applications of MgONPs.

5.1. Energy

Recently, the global world has seen a surge in air pollution, global warming, and sea level rise as a result of the depletion of fossil fuels. Therefore, it is critical to locate a substitute for these changes. Fuel cells, solar cells, and batteries as fossil fuel alternatives could be a very good remedy. In addition to the production of H_2 , which is a good fuel and a superior substitute for carbon-based bi-products, they will also release water as a byproduct. Magnesium performs better than other metals in the storage of H_2 . The storage of H_2 is stated to benefit

from the use of chemical hydrides such $NaAlH_4$, $LiBH_4$, and $LiNH_2$ as well as metal hydrides like $Pd@H$, $V@H$, alloys like $TiFeH_2$, $LaNi_5H_6$, $Ti@V@Mn@H$, Mg_2NiH_4 , and certain complicated hydrides. Compared to the other hydrides, Mg has the benefit of being extremely abundant in the earth's crust, having a higher capacity to store H_2 , and having an ecologically benign and cost-effective nature (123). There are numerous reports of these MgO-based batteries that use polymers (124), pigments like acetylene black (125), metals like Na (126), Li, V (127), carbon substrates (128), and B. These energy

storage technologies are reliable, safe, affordable, and ecologically benign.

5.2. Catalysis

MgONPs are also frequently used in heterogeneous catalysis for several chemical reactions, including the oxidative coupling of CH₄, the dehydration of alcohols, the benzylation of aromatics, the dehydrohalogenation of halogenated hydrocarbons, the production of pyranopyrazole and its derivatives, the benzylation of aromatics, the dehydrohalogenation of halogenated hydrocarbons. In this case, nano-structured MgO is utilized as a support for catalysts due to its structure, basicity, and electronic and electrochemical properties, making it easier to move the electrons across the catalyst surface (129, 130). Vegetable oils were recently trans-esterified using MgO as a catalyst (131). Other reactions, *i.e.*, Wittig (132), Cyanosilylation (81), Aldol (133), Mannich (134), aza-Michael (135), Baylis-Hillman (136, 137), were

also catalyzed with the aid of MgONPs. The enormous surface area and the distinctive morphology of MgO are thought to be the cause of its observed high catalytic activity (138).

5.3. Agricultures

MgONPs are also known to offer several benefits, including low phytotoxicity, non-genotoxicity, and non-biotoxicity to people, and thermal stability, which open up a wide range of potential applications of this nanomaterial for plant protection (139). Along with the aforementioned qualities, MgONPs also possess several additional traits that make them particularly useful in a variety of different agricultural applications, as illustrated in Figure 5 (140). Additionally, these nanoparticles aid in the development of seedling and plant growth and are utilized as an authorized food supplement, a food additive, a color retentate, and also in increasing the agricultural production of peanuts (141, 142).

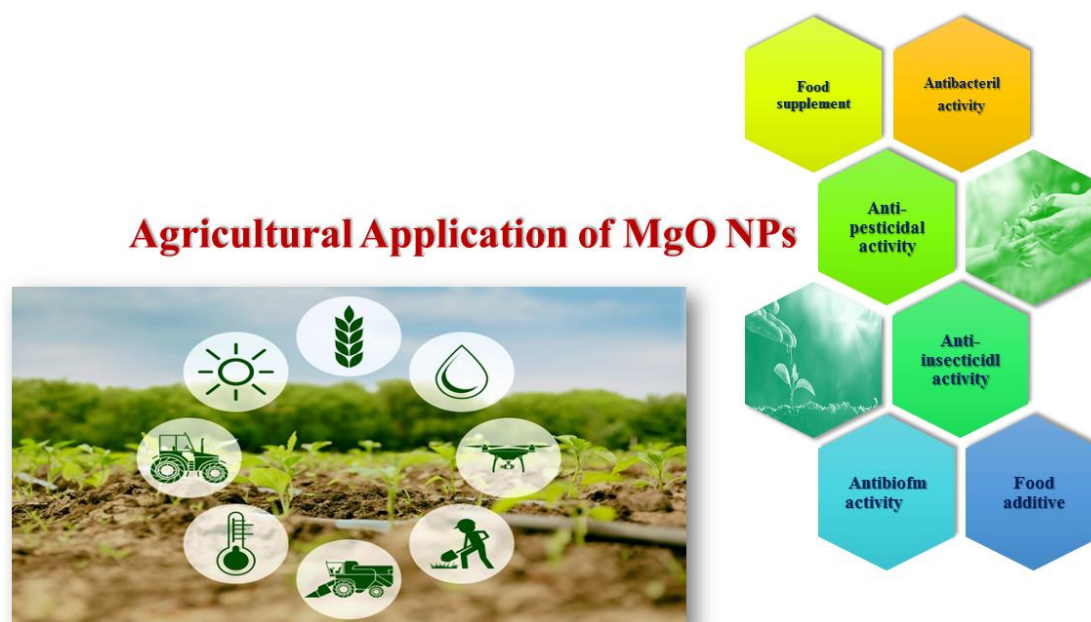


Figure 5: Potential applications for MgO NPs in the agricultural domain.

5.4. Biomedical

Because of their high absorption capability, high reaction activity, active catalysis property, and enzyme immobilization, MgONPs are used in the development of the diagnosis of cancer and the guidance of the cure plan through medical imaging. For use in dentistry, surgery, bacterial suppression, tissue engineering, and bone mending, bioactive glass is currently being developed (143, 144). Research findings support the addition of MgONPs to several medicinally valuable chemicals due to their various qualities, including antibacterial, anticancer, biocompatibility, nontoxicity, and cheap cost. MgO also seems to have several safe and useful medicinal applications. Given the potential for negative impacts from exposure to MgONPs, we must have the best method to both reap the benefits of MgONPs and prevent any negative effects that may arise (145).

5.5. Anti-microbial Activity

By inducing a breach in their cell membrane and eventually resulting in their death, MgO NPs have antibacterial action against food-borne pathogens such as *E. coli* and *Salmonella enteritidis* (146). The bacterial strain *Acidovorax oryzae* is the source of the illness known as the bacterial brown stripe, which is known to spread among rice and entirely ruin rice farming. As a result, Ogunyemi *et al.* reported on the biosynthesis of MgO NPs utilizing *Matricaria chamomilla L.*, which showed a good inhibitory impact on the development of *Acidovorax oryzae* bacteria (98). The worst wilt disease in *R. solanacearum* is caused by phytopathogenic bacteria, which were found to have a favorable antibacterial response to MgO NPs in another study (147). Accordingly, MgO NP nanoflowers were also developed because they possess the ability to inhibit bacterial infections and shield crops from harmful attacks (148). Due to the role of Mg in the

pathogenesis, plant defense, and other physiological processes, as well as the importance of this metal for maintaining balanced nutrition in plants, MgO NPs are known to have a strong antifungal action even at low fungicidal concentrations (149-152).

5.6. Anti-biofilm Activity and Anti-insecticidal

Cry genes are proteins produced by *Bacillus thuringiensis* that function as an insecticide against a variety of insects, including nematodes. However, this protein is released into the soil by water, which hinders its insecticidal effectiveness. By adhering this protein to MgO NPs and subsequently transferring them to the surface of cotton leaves, Rao *et al.* (153) indicated increased insect fatality rates across the board. As a result, cry protein was transferred *via* MgO NPs, which enhanced their use as bioinsecticides (154). By limiting the development of the biofilms, MgO NPs are known to promote systemic resistance against the gram-negative, plant-pathogenic bacterium *R. solanacearum*. They can also start the signaling of pathways for phytohormones like jasmonic acid and salicylic acid, which are crucial components of the plant's defense mechanisms. Therefore, it should be noted that MgONPs are highly efficient anti-microbial, antibiofilm agents, and anti-insecticidal in agricultural fields (155, 156).

5.7. Environmental

The major issue of environmental pollution affects both developed and developing countries worldwide. There are several ways to deal with this global problem, but one downside is that certain cleaning chemicals have side effects that make them act as contaminants themselves. Nanoparticles appear to be a fantastic replacement for several various environmental applications (Figure 4). MgONPs are effective in a variety of environmental remediation. These metal oxide NPs are utilized as a possible adsorber of harmful gases, including NO₂ and SO₂, due to their strong adsorbing characteristics, wide surface area, and high reaction capacity (157-160).

5.7.1. Dye removal

2,4-Dichlorophenol (2,4-DCP) is a hazardous substance that is often discharged from paper companies into various water sources, functioning as a main effluent in water. This chlorophenol compound (2,4-DCP) is known to have negative effects on people, animals, and plants who consume it, but treatment with MgO NPs has resulted in its rapid degradation because magnesium oxide acts as a catalyst in the degradation of this dye through the ionization Technique (161).

Acid Red 73 dye, a water contaminant released in large quantities from the textile industry, was removed by S. Jorfi *et al.*, and B.J.H. Ng *et al.* showed that the activity of ferrate VI, which oxidizes the Blue 203 dye (a water-contaminating dye from the leather and cosmetic industries), is enhanced by MgO NPs (162). Numerous other industries, like the fabric and clothing sectors, employ a variety of dyes to color clothing, with indigo carmine, a water effluent, being one of the most often used ones. MgO NPs were created by A. Bagheri GH *et al.* and used

as a photocatalyst for the photocatalytic decolorization of indigo carmine(163).

5.7.2. Heavy metal ion removal and detection

MgO NPs have been shown by Y. Cai *et al.* to be a novel possibility for the removal of heavy metals like lead (Pb²⁺) and cadmium (Cd²⁺)(164). Nanocomposites such as magnesium oxide-copper oxide nanocomposites and magnesium oxide-manganese oxide nanocomposites, which compete with other nanoparticles involved in the removal of heavy metals from water, are effective adsorbents and have demonstrated high adsorbing properties towards heavy metal ions such as lead, arsenic, and mercury(165).

Improved MgO NPs' sensitivity, By demonstrating the exceptional detection of heavy metals like nickel, copper, and cadmium that are present in significant concentrations in well water, tap water, as well as seawater, these nanoparticles, when modified with graphene oxide, demonstrate (166).

5.7.3. Chemical toxin detection and elimination

Magnesium oxide nanoparticles' ability to act as detoxifying agents is widely exploited in many different contexts, one of which is the identification and elimination of chemical pollutants. When treated with MgO NPs, the highly toxic chemical bis(2-chloroethyl) sulfide, also known as sulfur mustard and typically used as a biological warfare agent, can be broken down into non-harmful products like divinyl sulfide, thiodiglycol, and 2-chloroethyl vinyl sulfide, which are the byproducts of elimination and nucleophilic substitution reactions, respectively (167). According to S. Ali *et al.*, 2,4,6-trinitrophenyl, a very hazardous pollutant known to induce tumors, liver malfunctions, skin-related problems, etc., is degraded in MgO NPs, and ZnO NPs(168).

5.7.4. degradation of pesticides and hydrogen peroxide sensors

Although pesticides serve to increase agricultural productivity by preventing pests and insects from destroying crops, when these chemicals leak from the field into other water sources, they cause several dangerous illnesses to both plants and people. According to L.E. Lange *et al.*, etching MgO NPs combined with polypropylene improves the chemical stability of the reactive sites present in the nanoparticles that break down methyl parathion, an organophosphate insecticide (169). Aluminum oxide and MgO NPs have been discovered to reduce the harmful effects of the diazinon herbicide, which the Environmental Protection Agency has prohibited due to its high toxicity toward both plants and people(170).

Hydrogen peroxide, a consequence of highly selective oxidative processes, has numerous important uses in a wide range of industries and disciplines, including medicinal, therapeutic, environmental, agricultural, industrial, and many more. As a result, its identification by a sensitive and precise approach is required(171). MgO NPs, an inorganic substance, and chitosan, an organic polymer, are used to create biosensor devices for the

detection of hydrogen peroxide(172). Nanosensors are created for the detection of hydrogen peroxide in milk using magnesium oxide nanoparticles. The created nano biosensor is inexpensive, quick, and very sensitive, able to pick up even the tiniest amount of H₂O₂ (173).

Despite the numerous uses for MgO NPs already mentioned, there are still many more. For example, very small amounts of these particles are sufficient to improve the ability of polyurethane films to resist

corrosion, and these particles, along with nanofiltration membranes, can remove pollutants like nitrogen species, organic matter, bacteria, heavy metals, and suspended solid particles to make water safe for drinking(174). Due to their unique qualities, such as high recovery and repeatability, electrostatic, attraction abrasiveness, and oxidizing power, which work together to increase biocidal capabilities, these nanoparticles have become widely used in wastewater treatment in Figure 6 (175).



Figure 6: Environmental applications for MgO NPs.

6. CONCLUSION

Physical, chemical, and biological approaches to the synthesis of MgONPs are surveyed in the present review. Chemical and physical methods typically utilize toxic materials and are related to high energy consumption. Biological methods are currently being advocated by researchers due to their simplicity, cost-effectiveness, and environmental friendliness. Therefore, it is important to put a greater emphasis on more widespread greener methods to produce MgONPs, since this activity will be associated to some extent with the reduction of environmental pollution. MgONPs have various industrial applications, which can change energy production and protect crops from diseases caused by plant pathogens. The major problem of nanostructured MgO, as synthesized using different routes, is the occurrence of a wide band gap. Therefore, there is a crucial need to develop the synthesis method that will enable obtaining MgONPs of a narrow bandgap, making a much wider industrial application of this nanomaterial.

7. CONFLICT OF INTEREST

The authors possessed no relevant financial or non-financial interests.

8. ACKNOWLEDGMENTS

Funding open access charges: Universidade de Vigo/CISUG.

9. REFERENCES

1. Silva GA. Introduction to nanotechnology and its applications to medicine. *Surg Neurol* [Internet]. 2004 Mar 1;61(3):216–20. Available from: [<URL>](#).
2. Zeghoud S, Hemmami H, Ben Seghir B, Ben Amor I, Kouadri I, Rebiai A, et al. A review on biogenic green synthesis of ZnO nanoparticles by plant biomass and their applications. *Mater Today Commun* [Internet]. 2022 Dec 1;33:104747. Available from: [<URL>](#).
3. Yang W, Peters JI, Williams RO. Inhaled nanoparticles—A current review. *Int J Pharm* [Internet]. 2008 May 22;356(1–2):239–47. Available from: [<URL>](#).
4. Buzea C, Pacheco II, Robbie K. Nanomaterials and nanoparticles: Sources and toxicity. *Biointerphases* [Internet]. 2007 Dec 1;2(4):MR17–71. Available from: [<URL>](#).
5. Imani MM, Safaei M. Optimized Synthesis of Magnesium Oxide Nanoparticles as Bactericidal

- Agents. *J Nanotechnol* [Internet]. 2019 Apr 1;2019:6063832. Available from: [<URL>](#).
6. Ben Amor I, Emran TB, Hemmami H, Zeghoud S, Laouini SE. Nanomaterials based on chitosan for skin regeneration: an update. *Int J Surg* [Internet]. 2023 Mar 1;109(3):594–6. Available from: [<URL>](#).
7. Tang ZX, Lv BF. MgO nanoparticles as antibacterial agent: preparation and activity. *Brazilian J Chem Eng* [Internet]. 2014 Sep 1;31(3):591–601. Available from: [<URL>](#).
8. Sirota V, Selemenev V, Kovaleva M, Pavlenko I, Mamunin K, Dokalov V, et al. Synthesis of Magnesium Oxide Nanopowder by Thermal Plasma Using Magnesium Nitrate Hexahydrate. *Phys Res Int* [Internet]. 2016 Feb 17;2016:6853405. Available from: [<URL>](#).
9. Krishnamoorthy K, Moon JY, Hyun HB, Cho SK, Kim SJ. Mechanistic investigation on the toxicity of MgO nanoparticles toward cancer cells. *J Mater Chem* [Internet]. 2012 Nov 13;22(47):24610–7. Available from: [<URL>](#).
10. Anu Mary Ealia S, Saravanakumar MP. A review on the classification, characterisation, synthesis of nanoparticles and their application. *IOP Conf Ser Mater Sci Eng* [Internet]. 2017 Nov 1;263(3):032019. Available from: [<URL>](#).
11. Haldorai Y, Shim JJ. An efficient removal of methyl orange dye from aqueous solution by adsorption onto chitosan/MgO composite: A novel reusable adsorbent. *Appl Surf Sci* [Internet]. 2014 Feb 15;292:447–53. Available from: [<URL>](#).
12. Ngô C, Van de Voorde M. *Nanotechnology in a Nutshell* [Internet]. Paris: Atlantis Press; 2014. Available from: [<URL>](#).
13. Feng SH, Li GH. Hydrothermal and Solvothermal Syntheses. In: Ruren X, Yan X, editors. *Modern Inorganic Synthetic Chemistry* [Internet]. Elsevier; 2017. p. 73–104. Available from: [<URL>](#).
14. Sakka S. *Handbook of Sol-gel Science and Technology, Processing Characterization and Applications. Volume 1 Sol-Gel Processing*. Dordrecht, Netherlands: Kluwer Academic Publishers; 2005.
15. Rane AV, Kanny K, Abitha VK, Thomas S. Methods for Synthesis of Nanoparticles and Fabrication of Nanocomposites. In: *Synthesis of Inorganic Nanomaterials* [Internet]. Elsevier; 2018. p. 121–39. Available from: [<URL>](#).
16. Sereni JGR. Reference module in materials science and materials engineering. 2016;
17. Pal G, Rai P, Pandey A. Green synthesis of nanoparticles: A greener approach for a cleaner future. In: Kumar Shukla A, Irvani S, editors. *Green Synthesis, Characterization and Applications of Nanoparticles* [Internet]. Elsevier; 2019. p. 1–26. Available from: [<URL>](#).
18. Escudero A, Carrillo-Carrión C, Romero-Ben E, Franco A, Rosales-Barrios C, Castillejos MC, et al. Molecular Bottom-Up Approaches for the Synthesis of Inorganic and Hybrid Nanostructures. *Inorganics* [Internet]. 2021 Jul 17;9(7):58. Available from: [<URL>](#).
19. Soytas SH, Oğuz O, Menceloğlu YZ. Polymer Nanocomposites With Decorated Metal Oxides. In: Pielichowski K, Majka TM, editors. *Polymer Composites with Functionalized Nanoparticles* [Internet]. Elsevier; 2019. p. 287–323. Available from: [<URL>](#).
20. Danks AE, Hall SR, Schnepf Z. The evolution of 'sol-gel' chemistry as a technique for materials synthesis. *Mater Horizons* [Internet]. 2016 Feb 29;3(2):91–112. Available from: [<URL>](#).
21. Mastuli MS, Ansari NS, Nawawi MA, Mahat AM. Effects of Cationic Surfactant in Sol-gel Synthesis of Nano Sized Magnesium Oxide. *APCBEE Procedia* [Internet]. 2012 Jan 1;3:93–8. Available from: [<URL>](#).
22. Sutapa IW, Wahid Wahab A, Taba P, Nafie NL. Dislocation, crystallite size distribution and lattice strain of magnesium oxide nanoparticles. *J Phys Conf Ser* [Internet]. 2018 Mar 1;979(1):012021. Available from: [<URL>](#).
23. Wahab R, Ansari SG, Dar MA, Kim YS, Shin HS. Synthesis of Magnesium Oxide Nanoparticles by Sol-Gel Process. *Mater Sci Forum* [Internet]. 2007 Oct;558–559:983–6. Available from: [<URL>](#).
24. Boddu VM, Viswanath DS, Maloney SW. Synthesis and Characterization of Coralline Magnesium Oxide Nanoparticles. *J Am Ceram Soc* [Internet]. 2008 May 6;91(5):1718–20. Available from: [<URL>](#).
25. Dercz G, Prusik K, Pająk L, Pielaszek R, Malinowski JJ, Pudło W. Structure studies on nanocrystalline powder of MgO xerogel prepared by sol-gel method. *Mater Sci* [Internet]. 2009;27(1):201–7. Available from: [<URL>](#).
26. Rani N, Chahal S, Chauhan AS, Kumar P, Shukla R, Singh SK. X-ray Analysis of MgO Nanoparticles by Modified Scherer's Williamson-Hall and Size-Strain Method. *Mater Today Proc* [Internet]. 2019 Jan 1;12(3):543–8. Available from: [<URL>](#).
27. Nassar MY, Mohamed TY, Ahmed IS, Samir I. MgO nanostructure via a sol-gel combustion synthesis method using different fuels: An efficient nano-adsorbent for the removal of some anionic textile dyes. *J Mol Liq* [Internet]. 2017 Jan 1;225:730–40. Available from: [<URL>](#).
28. Mantzaris N V. Liquid-phase synthesis of nanoparticles: Particle size distribution dynamics and control. *Chem Eng Sci* [Internet]. 2005 Sep 1;60(17):4749–70. Available from: [<URL>](#).
29. Swihart MT. Vapor-phase synthesis of nanoparticles. *Curr Opin Colloid Interface Sci*

- [Internet]. 2003 Mar 1;8(1):127–33. Available from: [<URL>](#).
30. Benrabaa R, Boukhlof H, Bordes-Richard E, Vannier RN, Barama A. Nanosized nickel ferrite catalysts for CO₂ reforming of methane at low temperature: effect of preparation method and acid-base properties. In: *Studies in Surface Science and Catalysis* [Internet]. Elsevier; 2010. p. 301–4. Available from: [<URL>](#).
31. Huang G, Lu CH, Yang HH. Magnetic Nanomaterials for Magnetic Bioanalysis. In: Wang X, Chen X, editors. *Novel Nanomaterials for Biomedical, Environmental and Energy Applications* [Internet]. Elsevier; 2019. p. 89–109. Available from: [<URL>](#).
32. Hornak J. Synthesis, Properties, and Selected Technical Applications of Magnesium Oxide Nanoparticles: A Review. *Int J Mol Sci* [Internet]. 2021 Nov 25;22(23):12752. Available from: [<URL>](#).
33. Tartaj P, Morales M a del P, Veintemillas-Verdaguer S, Gonzalez-Carretero T, Serna CJ. The preparation of magnetic nanoparticles for applications in biomedicine. *J Phys D Appl Phys* [Internet]. 2003 Jul 7;36(13):R182–97. Available from: [<URL>](#).
34. Alaei M, Jalali M, Alimorad A. Simple and Economical Method for the Preparation of MgO Nanostructures with Suitable Surface Area. *J Chem Chem Eng* [Internet]. 2014;33(1):21–8. Available from: [<URL>](#).
35. Kumar R, Sharma A, Kishore N. Preparation and Characterization of MgO Nanoparticles by Co-Precipitation Method. *Int J Chem Phys Astron* [Internet]. 2016 Sep;70:33–41. Available from: [<URL>](#).
36. Karthikeyan V, Dhanapandian S, Manoharan C. Characterization and Antibacterial Behavior of MgO-PEG Nanoparticles Synthesized via Co-Precipitation Method. *Int Lett Chem Phys Astron* [Internet]. 2016 Sep;70:33–41. Available from: [<URL>](#).
37. Frantina YI, Fajaroh F, Nazriati, Yahmin, Sumari. Synthesis of MgO/CoFe₂O₄ nanoparticles with coprecipitation method and its characterization. In: *AIP Conference Proceedings* [Internet]. American Institute of Physics Inc.; 2021. p. 070003. Available from: [<URL>](#).
38. Kushwaha A, Bagchi T. MgO NPs synthesis, capping and enhanced free radical effect on the bacteria and its cell morphology. In: *AIP Conference Proceedings* [Internet]. American Institute of Physics Inc.; 2018. p. 030010. Available from: [<URL>](#).
39. Varma A, Mukasyan AS, Rogachev AS, Manukyan K V. Solution Combustion Synthesis of Nanoscale Materials. *Chem Rev* [Internet]. 2016 Dec 14;116(23):14493–586. Available from: [<URL>](#).
40. Mukasyan AS, Manukyan KV. One- and Two-Dimensional Nanostructures Prepared by Combustion Synthesis. In: Pottathara YB, editor. *Nanomaterials Synthesis* [Internet]. Elsevier; 2019. p. 85–120. Available from: [<URL>](#).
41. Stojanovic BD, Dzunuzovic AS, Ilic NI. Review of methods for the preparation of magnetic metal oxides. In: Stojanovic BD, editor. *Magnetic, Ferroelectric, and Multiferroic Metal Oxides* [Internet]. Elsevier; 2018. p. 333–59. Available from: [<URL>](#).
42. Mukasyan AS, Dinka P. Novel approaches to solution-combustion synthesis of nanomaterials. *Int J Self-Propagating High-Temperature Synth* [Internet]. 2007 Mar;16(1):23–35. Available from: [<URL>](#).
43. Balakrishnan G, Velavan R, Mujasam Batoo K, Raslan EH. Microstructure, optical and photocatalytic properties of MgO nanoparticles. *Results Phys* [Internet]. 2020 Mar 1;16:103013. Available from: [<URL>](#).
44. Rao KV, Sunandana CS. Structure and microstructure of combustion synthesized MgO nanoparticles and nanocrystalline MgO thin films synthesized by solution growth route. *J Mater Sci* [Internet]. 2008 Jan 29;43(1):146–54. Available from: [<URL>](#).
45. Ranjan A, Dawn SS, Jayaprabakar J, Nirmala N, Saikiran K, Sai Sriram S. Experimental investigation on effect of MgO nanoparticles on cold flow properties, performance, emission and combustion characteristics of waste cooking oil biodiesel. *Fuel* [Internet]. 2018 May 15;220:780–91. Available from: [<URL>](#).
46. Tharani K, Jegatha Christy A, Sagadevan S, Nehru LC. Fabrication of Magnesium oxide nanoparticles using combustion method for a biological and environmental cause. *Chem Phys Lett* [Internet]. 2021 Jan 16;763:138216. Available from: [<URL>](#).
47. Kumar D, Yadav LSR, Lingaraju K, Manjunath K, Suresh D, Prasad D, et al. Combustion synthesis of MgO nanoparticles using plant extract: Structural characterization and photoluminescence studies. In: *AIP Conference Proceedings* [Internet]. American Institute of Physics Inc.; 2015. p. 050145. Available from: [<URL>](#).
48. Ng JJ, Leong KH, Sim LC, Oh WD, Dai C, Saravanan P. Environmental remediation using nano-photocatalyst under visible light irradiation: the case of bismuth phosphate. In: *Nanomaterials for Air Remediation* [Internet]. Elsevier; 2020. p. 193–207. Available from: [<URL>](#).
49. Williams MJ, Corr SA. Magnetic Nanoparticles for Targeted Cancer Diagnosis and Therapy. In: Summers H, editor. *Nanomedicine* [Internet]. Amsterdam, Netherlands: Elsevier; 2013. Available from: [<URL>](#).
50. Chircov C, Grumezescu AM, Holban AM. Magnetic Particles for Advanced Molecular Diagnosis. *Materials (Basel)* [Internet]. 2019 Jul 5;12(13):2158. Available from: [<URL>](#).
51. Devaraja PB, Avadhani DN, Prashantha SC, Nagabhushana H, Sharma SC, Nagabhushana BM, et

- al. Synthesis, structural and luminescence studies of magnesium oxide nanopowder. *Spectrochim Acta Part A Mol Biomol Spectrosc* [Internet]. 2014 Jan 24;118:847–51. Available from: [<URL>](#).
52. Al-Hazmi F, Alnowaiser F, Al-Ghamdi AA, Al-Ghamdi AA, Aly MM, Al-Tuwirqi RM, et al. A new large – Scale synthesis of magnesium oxide nanowires: Structural and antibacterial properties. *Superlattices Microstruct* [Internet]. 2012 Aug 1;52(2):200–9. Available from: [<URL>](#).
53. Ding Y, Zhang G, Wu H, Hai B, Wang L, Qian Y. Nanoscale Magnesium Hydroxide and Magnesium Oxide Powders: Control over Size, Shape, and Structure via Hydrothermal Synthesis. *Chem Mater* [Internet]. 2001 Feb 1;13(2):435–40. Available from: [<URL>](#).
54. Rukh S, Sofi AH, Shah MA, Yousuf S. Antibacterial activity of magnesium oxide nanostructures prepared by hydrothermal method. *Asian J Nanosci Mater* [Internet]. 1999 Nov 30;2(4):425–30. Available from: [<URL>](#).
55. Jeevanandam J, Chan YS, Danquah MK. Biosynthesis and characterization of MgO nanoparticles from plant extracts via induced molecular nucleation. *New J Chem* [Internet]. 2017 Mar 27;41(7):2800–14. Available from: [<URL>](#).
56. Das RK, Pachapur VL, Lonappan L, Naghdi M, Pulicharla R, Maiti S, et al. Biological synthesis of metallic nanoparticles: plants, animals and microbial aspects. *Nanotechnol Environ Eng* [Internet]. 2017 Dec 9;2(1):18. Available from: [<URL>](#).
57. Ali MI, Sharma G, Kumar M, Dut Jasuja N. Biological approach of magnesium oxide nanoparticles synthesize by *Spirulina platensis*. *World J Pharm Res* [Internet]. 2015;4(7):1234–41. Available from: [<URL>](#).
58. Awwad AM, Ahmad AL. Biosynthesis, characterization, and optical properties of magnesium hydroxide and oxide nanoflakes using Citrus limon leaf extract. *Arab J Phys Chem*. 2014;1(2):66.
59. Bandeira M, Giovanela M, Roesch-Ely M, Devine DM, da Silva Crespo J. Green synthesis of zinc oxide nanoparticles: A review of the synthesis methodology and mechanism of formation. *Sustain Chem Pharm* [Internet]. 2020 Mar 1;15:100223. Available from: [<URL>](#).
60. Das B, Moumita S, Ghosh S, Khan MI, Indira D, Jayabalan R, et al. Biosynthesis of magnesium oxide (MgO) nanoflakes by using leaf extract of *Bauhinia purpurea* and evaluation of its antibacterial property against *Staphylococcus aureus*. *Mater Sci Eng C* [Internet]. 2018 Oct 1;91:436–44. Available from: [<URL>](#).
61. Jadhav AH, Lim AC, Thorat GM, Jadhav HS, Seo JG. Green solvent ionic liquids: structural directing pioneers for microwave-assisted synthesis of controlled MgO nanostructures. *RSC Adv* [Internet]. 2016 Mar 29;6(38):31675–86. Available from: [<URL>](#).
62. Singh A, Joshi NC, Ramola M. Magnesium oxide Nanoparticles (MgONPs): Green Synthesis, Characterizations and Antimicrobial activity. *Res J Pharm Technol* [Internet]. 2019 Oct 1;12(10):4644–6. Available from: [<URL>](#).
63. Cai L, Liu M, Liu Z, Yang H, Sun X, Chen J, et al. MgONPs Can Boost Plant Growth: Evidence from Increased Seedling Growth, Morpho-Physiological Activities, and Mg Uptake in Tobacco (*Nicotiana tabacum* L.). *Molecules* [Internet]. 2018 Dec 19;23(12):3375. Available from: [<URL>](#).
64. Wrigglesworth EG, Johnston JH. Mie theory and the dichroic effect for spherical gold nanoparticles: an experimental approach. *Nanoscale Adv* [Internet]. 2021 Jun 15;3(12):3530–6. Available from: [<URL>](#).
65. El-Seedi HR, El-Shabasy RM, Khalifa SAM, Saeed A, Shah A, Shah R, et al. Metal nanoparticles fabricated by green chemistry using natural extracts: biosynthesis, mechanisms, and applications. *RSC Adv* [Internet]. 2019 Aug 8;9(42):24539–59. Available from: [<URL>](#).
66. Khan MI, Akhtar MN, Ashraf N, Najeeb J, Munir H, Awan TI, et al. Green synthesis of magnesium oxide nanoparticles using *Dalbergia sissoo* extract for photocatalytic activity and antibacterial efficacy. *Appl Nanosci* [Internet]. 2020 Jul 25;10(7):2351–64. Available from: [<URL>](#).
67. Duong THY, Nguyen TN, Oanh HT, Dang Thi TA, Giang LNT, Phuong HT, et al. Synthesis of Magnesium Oxide Nanoplates and Their Application in Nitrogen Dioxide and Sulfur Dioxide Adsorption. *J Chem* [Internet]. 2019 May 26;2019:4376429. Available from: [<URL>](#).
68. Yuvakkumar R, Hong SI. Green Synthesis of Spinel Magnetite Iron Oxide Nanoparticles. *Adv Mater Res* [Internet]. 2014 Oct 27;1051:39–42. Available from: [<URL>](#).
69. Vergheese M, Vishal Sk, Mary Vergheese C. Green synthesis of magnesium oxide nanoparticles using *Trigonella foenum-graecum* leaf extract and its antibacterial activity. *J Pharmacogn Phytochem* [Internet]. 2018;7(3):1193–200. Available from: [<URL>](#).
70. Younis IY, El-Hawary SS, Eldahshan OA, Abdel-Aziz MM, Ali ZY. Green synthesis of magnesium nanoparticles mediated from *Rosa floribunda* charisma extract and its antioxidant, antiaging and antibiofilm activities. *Sci Rep* [Internet]. 2021 Aug 19;11(1):16868. Available from: [<URL>](#).
71. Abdallah Y, Ogunyemi SO, Abdelazez A, Zhang M, Hong X, Ibrahim E, et al. The Green Synthesis of MgO Nano-Flowers Using *Rosmarinus officinalis* L. (Rosemary) and the Antibacterial Activities against *Xanthomonas oryzae* pv. *oryzae*. *Biomed Res Int* [Internet]. 2019 Feb 17;2019:5620989. Available from: [<URL>](#).

72. Amina M, Al Musayeib NM, Alarfaj NA, El-Tohamy MF, Oraby HF, Al Hamoud GA, et al. Biogenic green synthesis of MgO nanoparticles using *Saussurea costus* biomasses for a comprehensive detection of their antimicrobial, cytotoxicity against MCF-7 breast cancer cells and photocatalysis potentials. Mishra YK, editor. *PLoS One* [Internet]. 2020 Aug 14;15(8):e0237567. Available from: [<URL>](#).
73. Sharma G, Soni R, Jasuja ND. Phytoassisted synthesis of magnesium oxide nanoparticles with *Swertia chirayaita*. *J Taibah Univ Sci* [Internet]. 2017 May 16;11(3):471–7. Available from: [<URL>](#).
74. Fatiqin A, Amrulloh H, Simanjuntak W. Green synthesis of MgO nanoparticles using *Moringa oleifera* leaf aqueous extract for antibacterial activity. *Bull Chem Soc Ethiop* [Internet]. 2021 May 7;35(1):161–70. Available from: [<URL>](#).
75. Nguyen DTC, Dang HH, Vo DVN, Bach LG, Nguyen TD, Tran T Van. Biogenic synthesis of MgO nanoparticles from different extracts (flower, bark, leaf) of *Tecoma stans* (L.) and their utilization in selected organic dyes treatment. *J Hazard Mater* [Internet]. 2021 Feb 15;404:124146. Available from: [<URL>](#).
76. Suresh J, Yuvakkumar R, Sundrarajan M, Hong SI. Green Synthesis of Magnesium Oxide Nanoparticles. *Adv Mater Res* [Internet]. 2014 May;952:141–4. Available from: [<URL>](#).
77. Narendhran S, Manikandan M, Shakila PB. Antibacterial, antioxidant properties of *Solanum trilobatum* and sodium hydroxide-mediated magnesium oxide nanoparticles: a green chemistry approach. *Bull Mater Sci* [Internet]. 2019 Jun 25;42(3):133. Available from: [<URL>](#).
78. Rahmani-Nezhad S, Dianat S, Saedi M, Hadjiakhoondi A. Characterization and Catalytic Activity of Plant-Mediated MgO Nanoparticles Using *Mucuna Pruriens* L. Seed Extract and Their Biological Evaluation. *J Nanoanalysis* [Internet]. 2017;4(4):290–8. Available from: [<URL>](#).
79. Prasanth R, Kumar SD, Jayalakshmi A, Singaravelu G, Govindaraju K, Kumar VG. Green synthesis of magnesium oxide nanoparticles and their antibacterial activity. *IJMS Vol48(08)* [August 2019] [Internet]. 2019;48(08):1210–5. Available from: [<URL>](#).
80. Anantharaman A, Sathyabhama S, George M. Green synthesis of magnesium oxide nanoparticles using *Aloe Vera* and its applications. *IJSRD—International J Sci Res Dev*. 2016;4(9):20.
81. Abinaya S, Kavitha HP, Prakash M. Sustainable Chemistry and Pharmacy.
82. Jhansi K, Jayarambabu N, Reddy KP, Reddy NM, Suvarna RP, Rao KV, et al. Biosynthesis of MgO nanoparticles using mushroom extract: effect on peanut (*Arachis hypogaea* L.) seed germination. *3Biotech* [Internet]. 2017 Aug 25;7(4):263. Available from: [<URL>](#).
83. Raliya R, Tarafdar JC, Choudhary K, Mal P, Raturi A, Gautam R, et al. Synthesis of MgO Nanoparticles Using *Aspergillus Tubingensis* TFR-3. *J Bionanoscience* [Internet]. 2014 Feb 1;8(1):34–8. Available from: [<URL>](#).
84. Ibrahim E, Thalij K, Badawy A. Antibacterial Potential of Magnesium Oxide Nanoparticles Synthesized by *Aspergillus niger*. *Biotechnol J Int* [Internet]. 2017 Jan 10;18(1):1–7. Available from: [<URL>](#).
85. Mohanasrinivasan V, Subathra Devi C, Mehra A, Prakash S, Agarwal A, Selvarajan E, et al. Biosynthesis of MgO Nanoparticles Using *Lactobacillus* Sp. and its Activity Against Human Leukemia Cell Lines HL-60. *Bionanoscience* [Internet]. 2018 Mar 5;8(1):249–53. Available from: [<URL>](#).
86. Kaul RK, Kumar P, Burman U, Joshi P, Agrawal A, Raliya R, et al. Magnesium and iron nanoparticles production using microorganisms and various salts. *Mater Sci* [Internet]. 2012 Sep 14;30(3):254–8. Available from: [<URL>](#).
87. Essien ER, Atasié VN, Okefor AO, Nwude DO. Biogenic synthesis of magnesium oxide nanoparticles using *Manihot esculenta* (Crantz) leaf extract. *Int Nano Lett* [Internet]. 2020 Mar 23;10(1):43–8. Available from: [<URL>](#).
88. Pugazhendhi A, Prabhu R, Muruganantham K, Shanmuganathan R, Natarajan S. Anticancer, antimicrobial and photocatalytic activities of green synthesized magnesium oxide nanoparticles (MgONPs) using aqueous extract of *Sargassum wightii*. *J Photochem Photobiol B Biol* [Internet]. 2019 Jan 1;190:86–97. Available from: [<URL>](#).
89. Dobrucka R. Synthesis of MgO Nanoparticles Using *Artemisia abrotanum* Herba Extract and Their Antioxidant and Photocatalytic Properties. *Iran J Sci Technol Trans A Sci* [Internet]. 2018 Jun 2;42(2):547–55. Available from: [<URL>](#).
90. Ghidan AY, Al-Antary TM, Awwad AM. Green synthesis of magnesium oxide (MgONPs) nanoparticles using *Chamaemel umnobile* flowers extract: Effect on Green Peach Aphid. In: *The 3rd International Nanotechnology Conference and Expo Italy Madridge Journal Nanotechnology Science*. 2018. p. 67.
91. Subhan MA, Chandra Saha P, Uddin N, Sarker P. Synthesis, Structure, Spectroscopy and Photocatalytic Studies of Nano Multi-Metal Oxide MgO·Al₂O₃·ZnO and MgO·Al₂O₃·ZnO·Curcumin Composite. *Int J Nanosci Nanotechnol* [Internet]. 2017 Feb 1;13(1):69–82. Available from: [<URL>](#).
92. Srivastava V, Sharma YC, Sillanpää M. Green synthesis of magnesium oxide nanoflower and its application for the removal of divalent metallic species from synthetic wastewater. *Ceram Int* [Internet]. 2015 Jun 1;41(5):6702–9. Available from: [<URL>](#).

93. Sugirtha P, Divya R, Yedhukrishnan R, Suganthi KS, Anusha N, Ponnusami V, et al. Green Synthesis of Magnesium Oxide Nanoparticles Using Brassica oleracea and Punica granatum Peels and their Anticancer and Photocatalytic Activity. *Asian J Chem* [Internet]. 2015 Jul 1;27(7):2513–7. Available from: [<URL>](#).
94. Munjal S, Singh A, Kumar V. Synthesis and characterization of MgO nanoparticles by orange fruit waste through green method. *Int J Adv Res Comput Sci*. 2017;4(9):36–42.
95. Kumara KNS, Nagaswarupa HP, Mahesh KR V, Mylarappa M, Prashantha SC, Siddeshwara DMK, et al. Synthesis and characterization of ZnO/MgO nano particles by curry leaves through green approach and their photocatalytic applications. *Int J Adv Res*. 2016;4(10):1958–62.
96. Umaralikhhan L, Jamal Mohamed Jaffar M. Green Synthesis of MgO Nanoparticles and its Antibacterial Activity. *Iran J Sci Technol Trans A Sci* [Internet]. 2018 Jun 7;42(2):477–85. Available from: [<URL>](#).
97. Anantharama NA, Sheethal KS, Mary G. Green synthesis and its applications of magnesium oxide nanoparticles from the seeds of lepidium sativum. *Int J Recent Sci Res*. 2016;7:14029–32.
98. Ogunyemi SO, Zhang F, Abdallah Y, Zhang M, Wang Y, Sun G, et al. Biosynthesis and characterization of magnesium oxide and manganese dioxide nanoparticles using *Matricaria chamomilla* L. extract and its inhibitory effect on *Acidovorax oryzae* strain RS-2. *Artif Cells, Nanomedicine, Biotechnol* [Internet]. 2019 Dec 4;47(1):2230–9. Available from: [<URL>](#).
99. Yildirim M, Akarsu H. Preparation of magnesium oxide (MgO) from dolomite by leach-precipitation-pyrohydrolysis process. *Physicochem Probl Miner Process* [Internet]. 2010;44:257–72. Available from: [<URL>](#).
100. Mustafa AMK, Al-Dahan DK, Khachik T V. Laboratory wtudy of MgO preparation from Iraqi dolomite by leach-precipitation–Pyrohydrolysis process. *Iraqi Bull Geol Min*. 2014;10(3):83–107.
101. Kulikova SA, Vinokurov SE, Khamizov RK, Vlasovskikh NS, Belova KY, Dzhendloda RK, et al. The Use of MgO Obtained from Serpentinite in the Synthesis of a Magnesium Potassium Phosphate Matrix for Radioactive Waste Immobilization. *Appl Sci* [Internet]. 2020 Dec 28;11(1):220. Available from: [<URL>](#).
102. Mantilaka MMMGPG, Pitawala HMTGA, Karunaratne DGGP, Rajapakse RMG. Nanocrystalline magnesium oxide from dolomite via poly(acrylate) stabilized magnesium hydroxide colloids. *Colloids Surfaces A Physicochem Eng Asp* [Internet]. 2014 Feb 20;443:201–8. Available from: [<URL>](#).
103. Jassim AK, Salmtori SA, Jassam JA. Sustainable manufacturing process applied to produce magnesium oxide from sea water. *IOP Conf Ser Mater Sci Eng* [Internet]. 2020 Mar 1;757(1):012021. Available from: [<URL>](#).
104. Sirota V, Selemenev V, Kovaleva M, Pavlenko I, Mamunin K, Dokalov V, et al. Preparation of crystalline Mg(OH)₂ nanopowder from serpentinite mineral. *Int J Min Sci Technol* [Internet]. 2018 May 1;28(3):499–503. Available from: [<URL>](#).
105. Chen Y, Yang X, Wu L, Tong L, Zhu J. Recovery of Mg from H₂SO₄ Leaching Solution of Serpentine to Precipitation of High-Purity Mg(OH)₂ and 4MgCO₃·Mg(OH)₂·4H₂O. *Minerals* [Internet]. 2023 Feb 23;13(3):318. Available from: [<URL>](#).
106. Ben Amor I, Hemmami H, Laouini SE, Mahboub MS, Barhoum A. Sol-Gel Synthesis of ZnO Nanoparticles Using Different Chitosan Sources: Effects on Antibacterial Activity and Photocatalytic Degradation of AZO Dye. *Catalysts* [Internet]. 2022 Dec 8;12(12):1611. Available from: [<URL>](#).
107. Ben Amor I, Hemmami H, Laouini SE, Abdelaziz AG, Barhoum A. Influence of chitosan source and degree of deacetylation on antibacterial activity and adsorption of AZO dye from water. *Biomass Convers Biorefinery* [Internet]. 2023 Jan 11;1:1–11. Available from: [<URL>](#).
108. Diachenko OV, Opanasuyk AS, Kurbatov DI, Opanasuyk NM, Kononov OK, Nam D, et al. Surface Morphology, Structural and Optical Properties of MgO Films Obtained by Spray Pyrolysis Technique. *Acta Phys Pol A* [Internet]. 2016 Sep;130(3):805–10. Available from: [<URL>](#).
109. Alexander L, Klug HP. Determination of Crystallite Size with the X-Ray Spectrometer. *J Appl Phys* [Internet]. 1950 Feb 1;21(2):137–42. Available from: [<URL>](#).
110. Holzwarth U, Gibson N. The Scherrer equation versus the “Debye-Scherrer equation”. *Nat Nanotechnol* [Internet]. 2011 Aug 28;6(9):534. Available from: [<URL>](#).
111. Al-Tabbakh AA, Karatepe N, Al-Zubaidi AB, Benchaabane A, Mahmood NB. Crystallite size and lattice strain of lithiated spinel material for rechargeable battery by X-ray diffraction peak-broadening analysis. *Int J Energy Res* [Internet]. 2019 Apr 1;43(5):1903–11. Available from: [<URL>](#).
112. Kimiagar S, Abrinaei F. Effect of temperature on the structural, linear, and nonlinear optical properties of MgO-doped graphene oxide nanocomposites. *Nanophotonics* [Internet]. 2018 Jan 26;7(1):243–51. Available from: [<URL>](#).
113. Verma R, Naik KK, Gangwar J, Srivastava AK. Morphology, mechanism and optical properties of nanometer-sized MgO synthesized via facile wet chemical method. *Mater Chem Phys* [Internet]. 2014 Dec 15;148(3):1064–70. Available from: [<URL>](#).
114. Li J, Khalid A, Verma R, Abraham A, Qazi F, Dong X, et al. Silk Fibroin Coated Magnesium Oxide Nanospheres: A Biocompatible and Biodegradable Tool for Noninvasive Bioimaging Applications.

- Nanomaterials [Internet]. 2021 Mar 10;11(3):695. Available from: [<URL>](#).
115. Ben Amor I, Hemmami H, Laouini SE, Temam H Ben, Zaoui H, Barhoum A. Biosynthesis MgO and ZnO nanoparticles using chitosan extracted from *Pimelia Payraudi* Latreille for antibacterial applications. *World J Microbiol Biotechnol* [Internet]. 2023 Jan 21;39(1):19. Available from: [<URL>](#).
116. Yarbrough R, Davis K, Dawood S, Rathnayake H. A sol-gel synthesis to prepare size and shape-controlled mesoporous nanostructures of binary (II-VI) metal oxides. *RSC Adv* [Internet]. 2020 Apr 6;10(24):14134-46. Available from: [<URL>](#).
117. Sainudeen SS, Asok LB, Varghese A, Nair AS, Krishnan G. Surfactant-driven direct synthesis of a hierarchical hollow MgO nanofiber-nanoparticle composite by electrospinning. *RSC Adv* [Internet]. 2017 Jul 13;7(56):35160-8. Available from: [<URL>](#).
118. Guo Y, Hu J, Wan L. Nanostructured Materials for Electrochemical Energy Conversion and Storage Devices. *Adv Mater* [Internet]. 2008 Aug 4;20(15):2878-87. Available from: [<URL>](#).
119. Sayle DC, Seal S, Wang Z, Mangili BC, Price DW, Karakoti AS, et al. Mapping Nanostructure: A Systematic Enumeration of Nanomaterials by Assembling Nanobuilding Blocks at Crystallographic Positions. *ACS Nano* [Internet]. 2008 Jun 1;2(6):1237-51. Available from: [<URL>](#).
120. Stark J V., Park DG, Lagadic I, Klabunde KJ. Nanoscale Metal Oxide Particles/Clusters as Chemical Reagents. Unique Surface Chemistry on Magnesium Oxide As Shown by Enhanced Adsorption of Acid Gases (Sulfur Dioxide and Carbon Dioxide) and Pressure Dependence. *Chem Mater* [Internet]. 1996 Jan 1;8(8):1904-12. Available from: [<URL>](#).
121. Sutradhar N, Sinhamahapatra A, Pahari SK, Pal P, Bajaj HC, Mukhopadhyay I, et al. Controlled Synthesis of Different Morphologies of MgO and Their Use as Solid Base Catalysts. *J Phys Chem C* [Internet]. 2011 Jun 30;115(25):12308-16. Available from: [<URL>](#).
122. Dobrucka R. Synthesis of MgO Nanoparticles Using *Artemisia abrotanum* Herba Extract and Their Antioxidant and Photocatalytic Properties. *Iran J Sci Technol Trans A Sci* [Internet]. 2018 Jun 2;42(2):547-55. Available from: [<URL>](#).
123. Sheng O, Jin C, Luo J, Yuan H, Huang H, Gan Y, et al. Mg₂B₂O₅ Nanowire Enabled Multifunctional Solid-State Electrolytes with High Ionic Conductivity, Excellent Mechanical Properties, and Flame-Retardant Performance. *Nano Lett* [Internet]. 2018 May 9;18(5):3104-12. Available from: [<URL>](#).
124. Shao Y, Rajput NN, Hu J, Hu M, Liu T, Wei Z, et al. Nanocomposite polymer electrolyte for rechargeable magnesium batteries. *Nano Energy* [Internet]. 2015 Mar 1;12:750-9. Available from: [<URL>](#).
125. Sun W, Sun X, Peng Q, Wang H, Ge Y, Akhtar N, et al. Nano-MgO/AB decorated separator to suppress shuttle effect of lithium-sulfur battery. *Nanoscale Adv* [Internet]. 2019 Apr 9;1(4):1589-97. Available from: [<URL>](#).
126. Zhang R, Tutusaus O, Mohtadi R, Ling C. Magnesium-Sodium Hybrid Battery With High Voltage, Capacity and Cyclability. *Front Chem* [Internet]. 2018 Dec 10;6:611. Available from: [<URL>](#).
127. Saha P, Datta MK, Velikokhatnyi OI, Manivannan A, Alman D, Kumta PN. Rechargeable magnesium battery: Current status and key challenges for the future. *Prog Mater Sci* [Internet]. 2014 Oct 1;66:1-86. Available from: [<URL>](#).
128. Wang J, Wang C, Gong S, Chen Q. Enhancing the Capacitance of Battery-Type Hybrid Capacitors by Encapsulating MgO Nanoparticles in Porous Carbon as Reservoirs for OH⁻ Ions from Electrolytes. *ACS Appl Mater Interfaces* [Internet]. 2019 Jun 19;11(24):21567-77. Available from: [<URL>](#).
129. Julkapli NM, Bagheri S. Magnesium oxide as a heterogeneous catalyst support. *Rev Inorg Chem* [Internet]. 2016 Jan 1;36(1):1-41. Available from: [<URL>](#).
130. Scarsella M, de Caprariis B, Damizia M, De Filippis P. Heterogeneous catalysts for hydrothermal liquefaction of lignocellulosic biomass: A review. *Biomass and Bioenergy* [Internet]. 2020 Sep 1;140:105662. Available from: [<URL>](#).
131. Almerindo GI, Probst LFD, Campos CEM, de Almeida RM, Meneghetti SMP, Meneghetti MR, et al. Magnesium oxide prepared via metal-chitosan complexation method: Application as catalyst for transesterification of soybean oil and catalyst deactivation studies. *J Power Sources* [Internet]. 2011 Oct 1;196(19):8057-63. Available from: [<URL>](#).
132. Vickers NJ. Animal Communication: When I'm Calling You, Will You Answer Too? *Curr Biol* [Internet]. 2017 Jul 24;27(14):R713-5. Available from: [<URL>](#).
133. Kantam ML, Pal U, Sreedhar B, Choudary BM. An Efficient Synthesis of Organic Carbonates using Nanocrystalline Magnesium Oxide. *Adv Synth Catal* [Internet]. 2007 Jul 2;349(10):1671-5. Available from: [<URL>](#).
134. Yang XF, Zhang MJ, Hou XL, Dai LX. Stereocontrolled Aziridination of Imines via a Sulfonium Ylide Route and a Mechanistic Study. *J Org Chem* [Internet]. 2002 Nov 1;67(23):8097-103. Available from: [<URL>](#).
135. Mastuli MS, Kamarulzaman N, Nawawi MA, Mahat AM, Rusdi R, Kamarudin N. Growth mechanisms of MgO nanocrystals via a sol-gel synthesis using different complexing agents. *Nanoscale Res Lett* [Internet]. 2014 Dec 21;9(1):134. Available from: [<URL>](#).

136. Kumar D, Reddy VB, Mishra BG, Rana RK, Nadagouda MN, Varma RS. Nanosized magnesium oxide as catalyst for the rapid and green synthesis of substituted 2-amino-2-chromenes. *Tetrahedron* [Internet]. 2007 Apr 9;63(15):3093–7. Available from: [<URL>](#).
137. Kantam ML, Chakrapani L, Ramani T. Synthesis of α -diazo- β -hydroxy esters using nanocrystalline MgO. *Tetrahedron Lett* [Internet]. 2007 Aug 27;48(35):6121–3. Available from: [<URL>](#).
138. Chintareddy VR, Lakshmi Kantam M. Recent Developments on Catalytic Applications of Nano-Crystalline Magnesium Oxide. *Catal Surv from Asia* [Internet]. 2011 Jun 19;15(2):89–110. Available from: [<URL>](#).
139. Singh RP. Application of Nanomaterials Toward Development of Nanobiosensors and Their Utility in Agriculture. In: *Nanotechnology* [Internet]. Singapore: Springer Singapore; 2017. p. 293–303. Available from: [<URL>](#).
140. Khot LR, Sankaran S, Maja JM, Ehsani R, Schuster EW. Applications of nanomaterials in agricultural production and crop protection: A review. *Crop Prot* [Internet]. 2012 May 1;35:64–70. Available from: [<URL>](#).
141. Singh RP. Utility of Nanomaterials in Food Safety. In: *Food Safety and Human Health* [Internet]. Elsevier; 2019. p. 285–318. Available from: [<URL>](#).
142. Rao Kandregula G, Rao KG, Ashok CH, Rao KV, Chakra CS. Structural properties of MgO Nanoparticles: Synthesized by Co-Precipitation Technique. *Int J Sci Res ISSN* [Internet]. 2014;3(12):43–6. Available from: [<URL>](#).
143. Al-Noaman A, Rawlinson SCF, Hill RG. The role of MgO on thermal properties, structure and bioactivity of bioactive glass coating for dental implants. *J Non Cryst Solids* [Internet]. 2012 Nov 1;358(22):3019–27. Available from: [<URL>](#).
144. Boys AJ, McCorry MC, Rodeo S, Bonassar LJ, Estroff LA. Next generation tissue engineering of orthopedic soft tissue-to-bone interfaces. *MRS Commun* [Internet]. 2017 Sep 3;7(3):289–308. Available from: [<URL>](#).
145. Fahmy HM, El-Hakim MH, Nady DS, Elkaramany Y, Mohamed FA, Yasien AM, et al. Review on MgO nanoparticles multifunctional role in the biomedical field: Properties and applications. *Nanomedicine J* [Internet]. 2022 Jan 1;9(1):1–14. Available from: [<URL>](#).
146. He Y, Ingudam S, Reed S, Gehring A, Strobaugh TP, Irwin P. Study on the mechanism of antibacterial action of magnesium oxide nanoparticles against foodborne pathogens. *J Nanobiotechnology* [Internet]. 2016 Dec 27;14(1):54. Available from: [<URL>](#).
147. Cai L, Chen J, Liu Z, Wang H, Yang H, Ding W. Magnesium Oxide Nanoparticles: Effective Agricultural Antibacterial Agent Against *Ralstonia solanacearum*. *Front Microbiol* [Internet]. 2018 Apr 25;9:335574. Available from: [<URL>](#).
148. Ibrahim E, Fouad H, Zhang M, Zhang Y, Qiu W, Yan C, et al. Biosynthesis of silver nanoparticles using endophytic bacteria and their role in inhibition of rice pathogenic bacteria and plant growth promotion. *RSC Adv* [Internet]. 2019 Sep 17;9(50):29293–9. Available from: [<URL>](#).
149. Abdallah ESH, Mahmoud MM, Abdel-Rahim IR. *Trichosporon jirovecii* infection of red swamp crayfish (*Procambarus clarkii*). *J Fish Dis* [Internet]. 2018 Nov 26;41(11):1719–32. Available from: [<URL>](#).
150. Huber DM, Jones JB. The role of magnesium in plant disease. *Plant Soil* [Internet]. 2013 Jul 11;368(1–2):73–85. Available from: [<URL>](#).
151. Wang WN, Tarafdar JC, Biswas P. Nanoparticle synthesis and delivery by an aerosol route for watermelon plant foliar uptake. *J Nanoparticle Res* [Internet]. 2013 Jan 10;15(1):1417. Available from: [<URL>](#).
152. Chen J, Peng H, Wang X, Shao F, Yuan Z, Han H. Graphene oxide exhibits broad-spectrum antimicrobial activity against bacterial phytopathogens and fungal conidia by intertwining and membrane perturbation. *Nanoscale* [Internet]. 2014 Jan 16;6(3):1879–89. Available from: [<URL>](#).
153. Kumar K, Sridhar J, Choudhary VK, Singh HK, Parameshwari B, Senthil Kumar KM, et al. New Innovations and Approaches for Biotic Stress Management of Crops. In: *Ghost PK, Kumar P, Chakraborty D, Mandal D, Sivalingam PN, editors. Innovations in Agriculture for a Self-Reliant India* [Internet]. London: CRC Press; 2021. p. 265–92. Available from: [<URL>](#).
154. Rao W, Zhan Y, Chen S, Xu Z, Huang T, Hong X, et al. Flowerlike Mg(OH)₂ Cross-Nanosheets for Controlling Cry1Ac Protein Loss: Evaluation of Insecticidal Activity and Biosecurity. *J Agric Food Chem* [Internet]. 2018 Apr 11;66(14):3651–7. Available from: [<URL>](#).
155. Imada K, Sakai S, Kajihara H, Tanaka S, Ito S. Magnesium oxide nanoparticles induce systemic resistance in tomato against bacterial wilt disease. *Plant Pathol* [Internet]. 2016 May 18;65(4):551–60. Available from: [<URL>](#).
156. Radzig MA, Nadtochenko VA, Koksharova OA, Kiwi J, Lipasova VA, Khmel IA. Antibacterial effects of silver nanoparticles on gram-negative bacteria: Influence on the growth and biofilms formation, mechanisms of action. *Colloids Surfaces B Biointerfaces* [Internet]. 2013 Feb 1;102:300–6. Available from: [<URL>](#).
157. Wang T, Liu X, Zhao D, Jiang Z. The unusual electrochemical characteristics of a novel three-dimensional ordered bicontinuous mesoporous carbon. *Chem Phys Lett* [Internet]. 2004 May 11;389(4–6):327–31. Available from: [<URL>](#).

158. Camtakan Z, Erenturk S (Akyil), Yusan S (Doyurum). Magnesium oxide nanoparticles: Preparation, characterization, and uranium sorption properties. *Environ Prog Sustain Energy* [Internet]. 2012 Dec 15;31(4):536–43. Available from: [<URL>](#).
159. Park JY, Lee YJ, Jun KW, Baeg JO, Yim DJ. Chemical Synthesis and Characterization of Highly Oil Dispersed MgO Nanoparticles. *J Ind Eng Chem* [Internet]. 2006;12(6):882–7. Available from: [<URL>](#).
160. Štengl V, Bakardjieva S, Maříková M, Bezdička P, Šubrt J. Magnesium oxide nanoparticles prepared by ultrasound enhanced hydrolysis of Mg-alkoxides. *Mater Lett* [Internet]. 2003 Aug 1;57(24–25):3998–4003. Available from: [<URL>](#).
161. Mohammadi L, Bazrafshan E, Noroozifar M, Ansari-Moghaddam A, Barahuie F, Balarak D. Removing 2,4-dichlorophenol from aqueous environments by heterogeneous catalytic ozonation using synthesized MgO nanoparticles. *Water Sci Technol* [Internet]. 2017 Dec 6;76(11):3054–68. Available from: [<URL>](#).
162. Tara N, Siddiqui SI, Rathi G, Chaudhry SA, Inamuddin, Asiri AM. Nano-engineered Adsorbent for the Removal of Dyes from Water: A Review. *Curr Anal Chem* [Internet]. 2020 Jan 8;16(1):14–40. Available from: [<URL>](#).
163. Bagheri GH A, Sabbaghan M, Mirgani Z. A comparative study on properties of synthesized MgO with different templates. *Spectrochim Acta Part A Mol Biomol Spectrosc* [Internet]. 2015 Feb 25;137:1286–91. Available from: [<URL>](#).
164. Wu D, Bai Y, Wang W, Xia H, Tan F, Zhang S, et al. Highly pure MgO₂ nanoparticles as robust solid oxidant for enhanced Fenton-like degradation of organic contaminants. *J Hazard Mater* [Internet]. 2019 Jul 15;374:319–28. Available from: [<URL>](#).
165. Askari P, Faraji A, Khayatian G, Mohebbi S. Effective ultrasound-assisted removal of heavy metal ions As(III), Hg(II), and Pb(II) from aqueous solution by new MgO/CuO and MgO/MnO₂ nanocomposites. *J Iran Chem Soc* [Internet]. 2017 Mar 2;14(3):613–21. Available from: [<URL>](#).
166. Khayatian G, Jodan M, Hassanpoor S, Mohebbi S. Determination of trace amounts of cadmium, copper and nickel in environmental water and food samples using GO/MgO nanocomposite as a new sorbent. *J Iran Chem Soc* [Internet]. 2016 May 21;13(5):831–9. Available from: [<URL>](#).
167. Štengl V, Maříková M, Bakardjieva S, Šubrt J, Opluštil F, Olšanská M. Reaction of sulfur mustard gas, soman and agent VX with nanosized anatase TiO₂ and ferrihydrite. *J Chem Technol Biotechnol* [Internet]. 2005 Jul 14;80(7):754–8. Available from: [<URL>](#).
168. Ali S, Farrukh MA, Khaleeq-ur-Rahman M. Photodegradation of 2,4,6-trinitrophenol catalyzed by Zn/MgO nanoparticles prepared in aqueous-organic medium. *Korean J Chem Eng* [Internet]. 2013 Nov 6;30(11):2100–7. Available from: [<URL>](#).
169. Lange LE, Obendorf SK. Effect of Plasma Etching on Destructive Adsorption Properties of Polypropylene Fibers Containing Magnesium Oxide Nanoparticles. *Arch Environ Contam Toxicol* [Internet]. 2012 Feb 18;62(2):185–94. Available from: [<URL>](#).
170. Behnam R, Morshed M, Tavanai H, Ghiaci M. Destructive Adsorption of Diazinon Pesticide by Activated Carbon Nanofibers Containing Al₂O₃ and MgO Nanoparticles. *Bull Environ Contam Toxicol* [Internet]. 2013 Oct 4;91(4):475–80. Available from: [<URL>](#).
171. Singh RP, Tiwari A, Pandey AC. Silver/Polyaniline Nanocomposite for the Electrocatalytic Hydrazine Oxidation. *J Inorg Organomet Polym Mater* [Internet]. 2011 Dec 13;21(4):788–92. Available from: [<URL>](#).
172. Lu L, Zhang L, Zhang X, Wu Z, Huan S, Shen G, et al. A MgO Nanoparticles Composite Matrix-Based Electrochemical Biosensor for Hydrogen Peroxide with High Sensitivity. *Electroanalysis* [Internet]. 2010 Feb 4;22(4):471–7. Available from: [<URL>](#).
173. Dong X xiu, Li M ying, Feng N nan, Sun Y ming, Yang C, Xu Z lin. A nanoporous MgO based nonenzymatic electrochemical sensor for rapid screening of hydrogen peroxide in milk. *RSC Adv* [Internet]. 2015 Oct 13;5(105):86485–9. Available from: [<URL>](#).
174. An Y, Zhang K, Wang F, Lin L, Guo H. Removal of organic matters and bacteria by nano-MgO/GAC system. *Desalination* [Internet]. 2011 Oct 17;281(1):30–4. Available from: [<URL>](#).
175. Ramanujam K, Sundrarajan M. Biocidal activities of monochlorotriazine-β-cyclodextrine with MgO modified cellulosic fabrics. *J Text Inst* [Internet]. 2015 Nov 2;106(11):1147–53. Available from: [<URL>](#).



Reference Materials: A review

Meriem Outaki^{1*}, Sarah Loukmas², Said Gmouh³, Ebrahim Kerak⁴

¹University Hassan I, Faculty of Sciences and Technologies Settat, Laboratory of applied chemistry and environment, Settat, 26000, Morocco.

²University Mohamed V, Rabat, 10000, Morocco.

³University Hassan II, Faculty of sciences Ben M'Sik, Laboratory of engineering and materials (LIMAT), Casablanca, 20000, Morocco.

⁴University Hassan II, Faculty of sciences and technologies Mohammedia, Laboratory of materials, catalysis and natural resources valorization, Mohammedia, 20650, Morocco.

Abstract: Several factors have increased the use of reference materials in laboratories. This can be explained by the fact that the reference materials have several roles, namely: the confirmation of the identity of unknown materials and/or the determination of their properties; the calibration of measuring equipment; the validation of methods; the realization of proficiency tests; etc. To be able to produce and use them, a set of standards and guidelines concerning the subject of reference materials has been established. There are several producers of reference materials in many fields, but finding the right choice is sometimes considered difficult given the multitude of materials to be analyzed that do not correspond perfectly to the reference material, especially in the case of matrices. This makes the market always seek new materials. To develop them, five steps are essential: material preparation, homogeneity study, stability study, characterization, and evaluation of measurement uncertainties. These steps are equally important; the fact of highlighting less than one of them will imply a significant decrease in the quality of the reference material developed. This review seeks to furnish the scientific community with a paper elucidating the functions of these materials in research laboratories, the normative references devised to standardize their production and utilization, the factors influencing their production, and the essential steps for their development.

Keywords: Reference material, Homogeneity study, Stability study, Characterization, Evaluation of measurement uncertainties.

Submitted: October 15, 2023. **Accepted:** February 16, 2024.

Cite this: Outaki M, Loukmas S, Gmouh S, Kerak E. Reference materials: A review. JOTCSA. 2024;11(2):751-64.

DOI: <https://doi.org/10.18596/jotcsa.1361004>

***Corresponding author's E-mail:** meriem.outaki@gmail.com

1. INTRODUCTION

Throughout the world, the results of measurements and testing are considered as a base to be able to control industrial production, affirm or disconfirm scientific hypotheses, make diagnoses in the medical field, assess the nature and degree of pollution in the environment, assess the nutritional quality of foods, etc. In this perspective, incorrect measurements and testing can be the source of incorrect decisions and thus generate additional costs or risks. Therefore, accurate measurements are of paramount importance for the functioning of society in all sectors: industry, health, environment, agri-food, etc.

Decision-making is based on the knowledge of information, which in most cases, in the field of research, rests on the results of measurements and testing delivered by the laboratories (1). These results, aiming mainly to answer research questions, are supposed to be of high quality (trueness, precision) to guarantee a relevant interpretation by the researchers. As a result, the prescribers of measurements and testing, who are increasingly aware, have increased their requirements about the reliability of the results provided by the laboratories (2). Measurements and testing results alone, not accompanied by information on their quality and traceability, are no longer considered sufficient and satisfactory; laboratories are obliged to prove the reliability of their measurements and testing at all

stages, from sampling until the delivery of the final report (2).

In this perspective, modalities aiming at ensuring good quality assurance of the measurements and testing and accuracy of the produced data have been established. This includes setting up good laboratory practices and requirements of accreditation organizations (3) as well as participation in interlaboratory comparisons (4) and the use of reference materials. The use of the latter is considered a means for quality control of the results provided since they make it possible to join them to known quantities (4). The certified reference materials are considered an essential link of a metrological traceability chain to ensure that the unity of the result is universal (1). Their use makes the results of measurements and testing comparable to the recognized reference values and those obtained by the international scientific community. Reference materials are of paramount importance when the accuracy and reliability of the measurement and testing results must be guaranteed.

This review aims to provide the scientific community with a paper detailing the roles of these materials in research laboratories, the normative references developed to standardize their production and use, the elements that govern their production, as well as the steps necessary for their development.

2. TERMS AND DEFINITIONS

ISO Guide 30:2015 (5) defines a reference material (RM) and a certified reference material (CRM) as follows :

- Reference material: "material, sufficiently homogeneous and stable concerning one or more specified properties, which has been established to be fit for its intended use in a measurement process". Properties can be quantitative or qualitative (e.g., identity of substances or species). Uses may include the calibration of a measurement system, assessment of a measurement procedure, assigning values to other materials, and quality control.
- Certified reference material: "RM characterized by a metrologically valid procedure for one or more specified properties, accompanied by an RM certificate that provides the value of the specified property, its associated uncertainty, and a statement of metrological traceability".

That said, the difference between an RM and a CRM is that parameters in the CRM are guaranteed by the producer and are known with great trueness (2).

Different categories of RMs may be encountered: primary RM, secondary RM, and in-house or working RM. By going from first to last, uncertainty increases (6). An RM that is characteristic of a real sample is called matrix RM (examples: soil, drinking water, blood) according to ISO Guide 30:2015 (5). Matrix RM may be obtained directly from biological,

environmental, or industrial sources. They may also be prepared by spiking the component(s) of interest into an existing material.

3. NORMATIVE REFERENCES

A panoply of standards and guidelines concerning the topic of RM are established whether by the International Organization for Standardization (ISO) or by other organizations. Below is a non-exhaustive list of these references:

- ISO Guide 30:2015: Reference materials - Selected terms and definitions (5);
- ISO Guide 31:2015: Reference materials - Contents of certificates, labels, and accompanying documentation (7);
- ISO Guide 33:2015: Reference materials - Good practice in using reference materials (8);
- ISO Guide 35:2017: Reference materials - Guidance for characterization and assessment of homogeneity and stability (9);
- ISO 17034:2016: General requirements for the competence of reference material producers (10);
- ISO Guide 80:2014: Guidance for the in-house preparation of quality control materials (QCMs) (11);
- ISO/TR 16476:2016: Reference materials -- Establishing and expressing metrological traceability of quantity values assigned to reference materials (12);
- ISO/TR 79:2015: Reference materials - Examples of reference materials for qualitative properties (13);
- ISO/TR 10989:2009: Reference materials -- Guidance on, and keywords used for, RM categorization (14);
- ISO 11095:1996: Linear calibration using reference materials (15);
- ISO/TR 11773:2013: Global distribution of reference materials (16);
- ISO 15194:2009: In vitro diagnostic medical devices - Measurement of quantities in samples of biological origin - Requirements for certified reference materials and the content of supporting documentation (17);
- ISO/FDIS 33407: Guidance for the production of pure organic substance certified reference materials (under development) (18);
- LAB MR REF 02 established by the Cofrac (Comité français d'accréditation) (19). It's a document concerning the requirements for accreditation of producers of RMs;
- APLAC TC 012: Guidelines for acceptability of chemical reference materials and commercial chemicals for calibration of equipment used in chemical testing (20) established by the APLAC (Asia Pacific Laboratory Accreditation Cooperation).

4. ROLE OF REFERENCE MATERIALS

Several fields, such as chemistry, biology, agri-food, health, environment, etc., use the RMs. These latter

allow the realization of certain practices ensuring the quality of the measurements, namely:

- The determining of the properties of a material (e.g., quantity, hardness, etc.) and/or the confirmation of its identity (1).
- The calibration of certain methods allows to establish the substance signal-quantity interaction (e.g., UV spectroscopy, colorimetry, atomic emissions, chromatography, etc.). The calibration should be done by using the RMs and taking into account the nature of the matrix as much as possible (21). This makes it possible to obtain quantitative results through the comparison of the sample signals and those of the RM(22). The purity of the RM as well as the uncertainty of this purity must be known (22).
- Calibration of measurement equipment (1–3,6,23).
- The development and validation of methods (2,3,6,24) as well as the validation of the modifications applied to the method (3): the validation as one of the requirements of ISO/IEC 17025:2017 (25) should be performed whenever non-standard methods, internally developed methods, or methods outside their intended scope are used. The estimation of the bias (difference between the measured value and the reference value) can be done by using the RM within the limits of the uncertainty of the certified value and the method submitted to validation (1).
- The internal quality control for the monitoring of an analytical process (1–3,6,23,24): the verification of the long-term reproducibility of a method is performed by using the RMs in statistical control systems while creating control charts (a graphical representation of the results obtained from an RM over time, the system is out of control if the upper or lower control limit is exceeded, among others) (3). The RMs thus allow monitoring of the stability of testing (2).
- The comparison of the performances of the methods in the same laboratory (3) by comparing the testing results by using the same RM and several methods.
- The realization of proficiency tests (1,3,6,24): the laboratory that organizes the proficiency test sends an RM to the participating laboratories. The comparison of the testing results of the RM of a laboratory with those of other laboratories using the same technique allows for evaluation of the performance of the laboratory with this technique (3).
- The uncertainty estimation (1–3,6): the realization of the design of experiments by using RMs is necessary for the estimation of all components of the measurement uncertainties and for estimating the uncertainty of measurement by intra-laboratory reproducibility (2). The uncertainty associated with the purity of the RM contributes to the total uncertainty of the measurement (6).
- The traceability of measurement (24): CRMs are used for quantitative measurements, which makes them "traceable" to these CRMs. However, this approach is not always reliable because, in many cases, the CRM does not have the same

matrix as the unknown sample (3).

- Materials intended to test the step(s) of a method (3): the method, that contains steps where the sample is physically destroyed (e.g., acid digestion, fusions, dry ash) or the analyte to be determined is extracted from the matrix, can be verified using a CRM with a matrix (matrix CRM) similar to the unknown sample. The use of CRM allows us to demonstrate if there are losses or contaminations by applying the method. The presence of errors in this method can be affirmed or disconfirmed by comparing the certified value of the CRM and the value determined by the laboratory.

5. PRODUCTION OF REFERENCE MATERIALS

5.1. Producers of Reference Materials

To meet the requirements of prescribers for reliable measurements, it is essential to produce RMs in a wide variety of fields. As a result, the RMs market is considered a very active market (1). For the different areas of measurements and testing, there are several RMs and CRM providers. There is a need to ensure the availability of sufficient quantities of these materials as well as their availability in the long term, even if their production is long and expensive (21). The main organizations distributing RMs are (26):

- NIST: National Institute of Standards and Technology, United States;
- NIBSC: National Institute for Biological Standards and Control (WHO international laboratory for biological standards), United Kingdom;
- CENAM: Centro Nacional de Metrología, Mexico;
- IRMM: Institute for Reference Materials and Measurements, European Union;
- LGC: LGC Limited, United Kingdom;
- HECTEF: HECTEF Standard Reference Center Foundation, Japan.

Given the growth of the RM market and the diversity of producers, finding the right choice has become difficult for users. Databases were developed to assist laboratories in finding the CRM that they need by providing information on the available CRM. However, the COMAR (Code of Reference Materials) remains the main source of information on RMs (3). It was produced at the end of 1970 by the LNE (laboratoire national de métrologie et d'essai, France). Formal cooperation between LNE, NPL (National Physical Laboratory, United Kingdom), and BAM (Bundesanstalt für Materialforschung und-Prüfung, Germany) was then established to improve and propagate the database (27). The use of the latter is free.

The COMAR database lists information on thousands of CRMs produced by more than 200 producers in 26 countries.

Figure 1 shows the distribution of the RMs according to their area of use. The biological and clinical domains have the lowest percentage. For the other domains, the distribution is very close, with a dominance of the industrial sector.

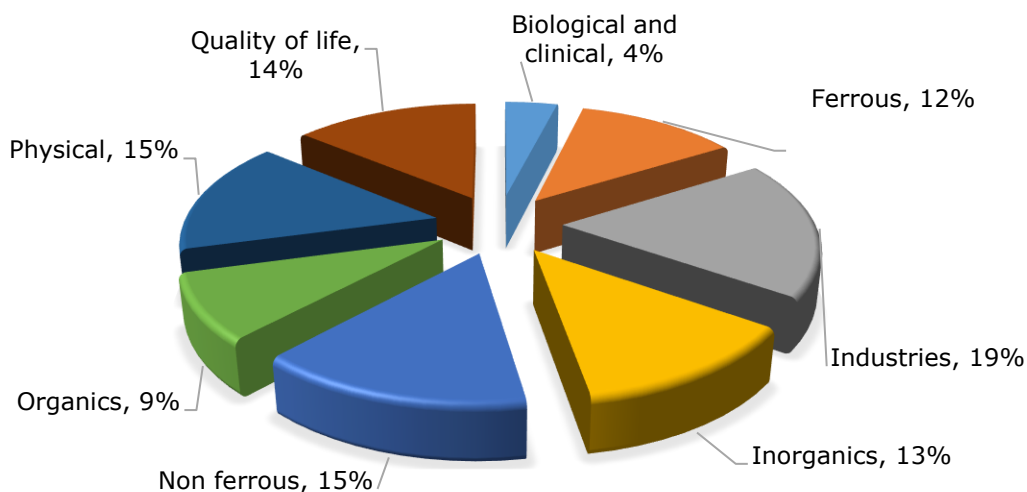


Figure 1: Percentage distribution of CRM by fields of application (27).

Below are some examples of RMs in the environmental, food, and clinical fields (3):

- Environmental analysis: river, lake, estuarine, and marine sediments, as well as fresh-, ground-, and seawater certified for trace elements or trace organics, are some examples of existing CRMs.
- Food analysis: matrices for human nutrition (e.g., meats, cereals, and milk) are usually analyzed for their content of toxic organic (e.g., PAHs, PCBs) or inorganic substances (e.g., heavy metals, major elements), nitrates, pesticides, toxin, and mycotoxins. Nutritional quality and nutritional properties (e.g., fatty acids, sterols, total fat, proteins,

carbohydrate oils, fat-soluble vitamins, etc.) are also taken into account during the preparation of certain matrices.

- Clinical analysis: RMs of serum and blood (in lyophilized form) are most often used for the quality control of, for example, toxic elements (e.g., Cd, Pb) or main group elements (e.g., Ca, Li, Mg) and hormones (e.g., cortisol, progesterone). Proteins or enzymes that are partially or highly purified are also used.

Based on the consultation of the COMAR database, a distribution of the origins of the produced RMs is presented in Figure 2.

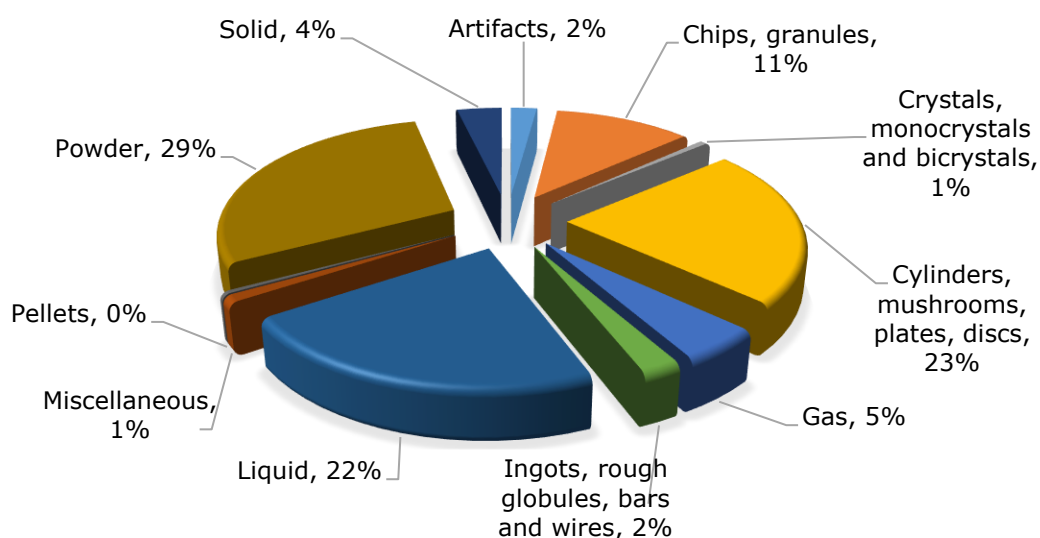


Figure 2: Origin of RMs at the level of COMAR database (27).

For each RM, the available information is the name, status (available or not), year, country, producer, general description, fields of application, and certified properties (27).

The selection of an RM by the user depends on his needs and objectives (2). The choice of an RM by the user takes into account the nature of the matrix, its concentration, availability, lifetime, and cost.

5.2. Constraints Related to The Production of Reference Materials

The production and certification of the RMs require enormous costs. These latter are linked to the initial investment for the purchase of the equipment, the time required for their development, the costs related to the certification procedure, as well as those about the production of a large stock needed to ensure the continuity of the availability of a specific lot over several years (23). Having accurate information on producer turnover and the cost price of the RMs is not easy. Nevertheless, the cost of R&D in the case of an RM is weakly echoed by the cost price in the case of the national metrology laboratories (1). This situation remains valid even for the big CRM producers such as NIST and IRMM (1). RM users are confronted with the problem of identifying the appropriate material to use. Users are expected to look for an available RM, that also meets their needs (e.g., components, uncertainty, etc.) (28). In many cases, the available RMs are not

suitable since they are not sufficiently similar to the real sample (3). The RMs that are available and adapted to the complexity and multiplicity of testing are insufficient (3). Also, new complex matrices need to be analyzed, and the producers are unable to rapidly produce CRMs for these new samples (3). As a result, CRM request exceeds supply in terms of availability and nature of materials. This encourages users and accreditation organizations to understand the limits of the RMs used (6).

5.3. Accreditation of Reference Materials Producers

The producers of RMs can be accredited by the standard ISO 17034 which specifies the general requirements for the competence of the producers of RMs. To get an overview of this standard in process form, we propose a process mapping bringing together all the elements covered by ISO 17034:2016 (10) (Figure 3).

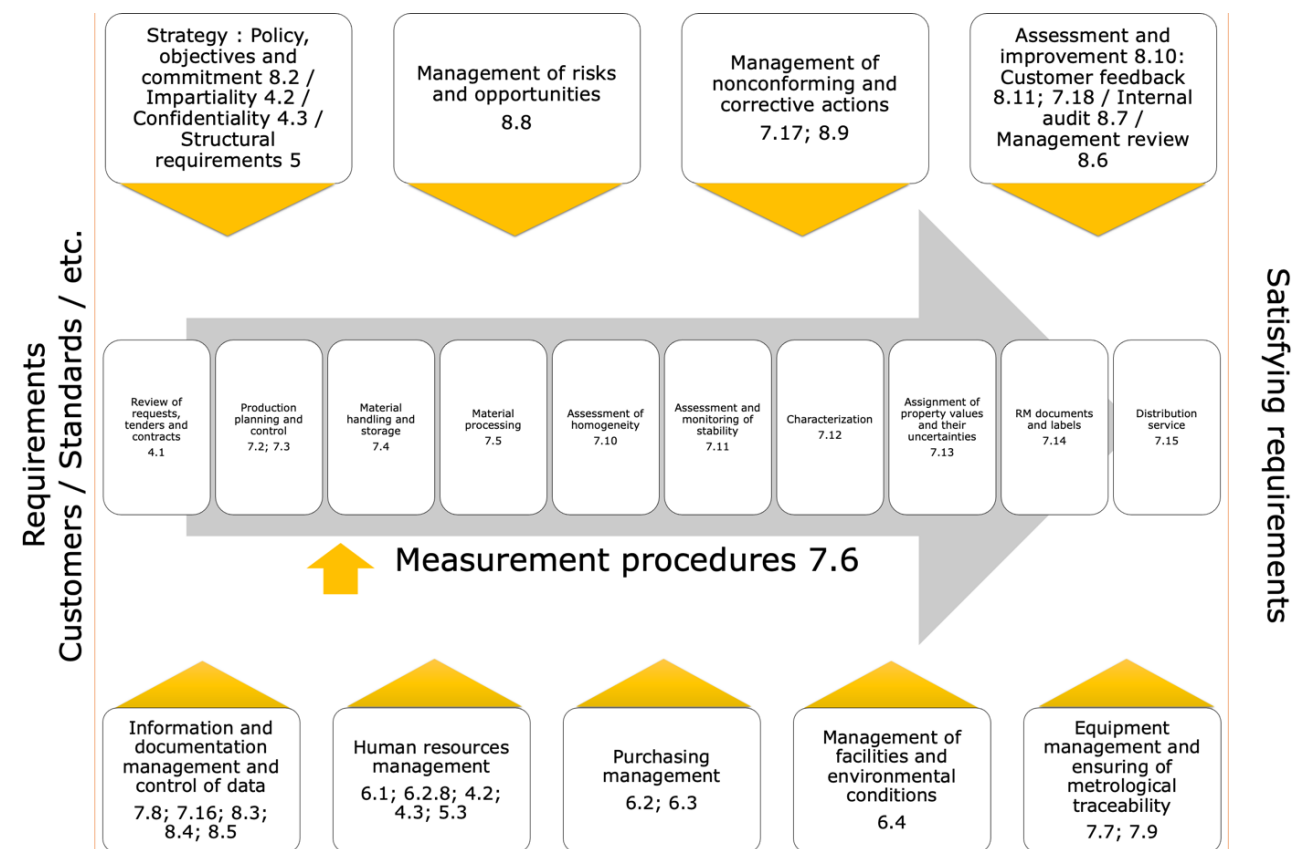


Figure 3: Process mapping bringing together all the elements covered by ISO 17034:2016.

ISO/IEC 17025 is considered indispensable for the application of the ISO 17034 standard which is aligned with the relevant requirements (10). Reference materials producers that comply with this international standard (ISO 17034) will also operate generally by the principles of ISO 9001 (10). The

Cofrac, an accrediting organization, also takes into account the requirements of the standards ISO/IEC 17025 (25) and/or ISO 15189 (29) to accredit these producers (19). Table 1 presents common elements between ISO 17034:2016 (10), ISO/IEC 17025:2017 (25), and ISO 9001:2015 (30).

Table 1: Common elements between ISO 17034:2016, ISO/IEC 17025:2017, and ISO 9001:2015.

ISO 17034:2016	ISO/IEC 17025:2017	ISO 9001:2015
4.1 Contractual matters	7.1 Review of requests, tenders, and contract	-
4.2 Impartiality	4.1 Impartiality	-
4.3 Confidentiality	4.2 Confidentiality	-
5 Structural requirements	5 Structural requirements	-
6.1 Personnel	6.2 Personnel	-
6.2 Subcontracting	6.6 Externally provided products and services	-
6.3 Provision of equipment, services, and supplies		
6.4 Facilities and environmental conditions	6.3 Facilities and environmental conditions	-
7.6 Measurement procedures	7.2 Selection, verification, and validation of methods 7.3 Sampling 7.7 Ensuring the validity of results	-
7.7 Measuring equipment	6.4 Equipment	-
7.8 Data integrity and evaluation	7.11 Control of data and information management	-
7.9 Metrological traceability of certified values	6.5 Metrological traceability	-
7.16 Control of quality and technical records	7.5 Technical records	-
7.17 Management of non-conforming work	7.10 non-conforming work	-
7.18 Complaints	7.9 Complaints	-
8.2 Quality policy	8.2 Management system documentation	5.2 Policy 6.2 Quality objectives and planning to achieve them
8.3 General management system documentation	8.3 Control of management system documents	7.5 Documented information
8.4 Control of management system documents	8.4 Control of records	
8.5 Control of records		
8.6 Management review	8.9 Management review	9.3 Management review
8.7 Internal audits	8.8 Internal audits	9.2 Internal audits
8.8 Actions to address risks and opportunities	8.5 Actions to address risks and opportunities	6.1 Actions to address risks and opportunities
8.9 Corrective actions	8.7 Corrective actions	10.2 non-conformity and corrective actions
8.10 Improvement	8.6 Improvement	10.3 Continual improvement
8.11 Feedback from customers	8.6 Improvement	9.1.2 Customer satisfaction

Among the mandatory requirements of ISO 17034:2016 (10) about the production of RMs, there are requirements for subcontractors. If the organization decides to call on the services of a

subcontractor, the standard specifies the services that may or may not be subcontracted. These services are presented in Table 2.

Table 2: Services that can be subcontracted or not.

Activities that can be subcontracted	Processes should not be subcontracted
Sampling	Production planning
Processing an RM	Selection of subcontractors
Handling an RM	Assignment of proper values and their uncertainties
Homogeneity and stability testing	Authorization of property values and their uncertainties
Characterization	Authorization of RM documents
Storage of RM	
Distribution of RM	

When a reference material producer calls on a subcontractor to carry out part of the production, it must have procedures in place to ensure that the subcontractors' experience and technical competence are sufficient for the tasks entrusted to them and that they comply with the relevant sections of ISO 17034:2016 (10) and other appropriate standards.

6. DEVELOPMENT OF REFERENCE MATERIALS: KEY STEPS

6.1. Preparation of The Material

The RM preparation is performed in a manner that minimizes heterogeneity and instability (31). Ensuring RM stabilization is the most sensitive and difficult step (3). Many operations can be performed to avoid material changes (e.g., to avoid chemical or microbiological changes in the material, drying, sterilization by irradiation, and/or freezing can be used, among others). The nature of the material and the purpose of its use guide the choice of the method to be adopted (3). This choice must be made to respect, as far as possible, the integrity of the material (3). To avoid contamination, measures must be taken not to cause inhomogeneity in a material that is already homogeneous (31). Also, precautions must be taken to prevent any negative influence from the environment. After homogenizing the material, its storage must be done in suitable containers (3) (waterproof and inert (31)).

Homogeneity and stability are two primordial characteristics of an RM. The most important measures taken to ensure them are those taken during the selection, preparation, and packaging of the material (32). The testing realized at a later step over a limited period of some units of the RM can only verify the success or failure of previously performed steps (32).

The 2017 version of ISO Guide 35 (9) leaves to the RMs producers the judgment of the need or not to carry out experimental studies of homogeneity and stability based on several elements, namely (32):

- The knowledge of the physical, chemical, and/or biological properties of the material as well as the knowledge of the variation of these properties over time based on the scientific literature;
- The analysis of previous experimental data or monitoring data of stability;
- The absence of anomalies detected by the producer and the users further to cumulative observations on complete lifetimes;
- The tests were performed on the effect of the packaging.

6.2. Homogeneity Study

There are two types of homogeneity tests (5):

- Within-unit homogeneity, which represents the uniformity of a specified property value within each unit of an RM;
- Between-unit homogeneity represents the uniformity of a specified property value among units of an RM.

For the development of RMs, a within-unit and between-unit homogeneity study is carried out (4). The objective is to ensure that the content is the same in one unit and from one unit to another (3).

Different designs can be used for homogeneity studies, namely: simple randomized design, randomized block design, and nested design (9). Concerning the number of samples, it is recommended to take 10 to 30 samples from the batch of material, ISO Guide 35:2017 proposes a formula to calculate this number (9). Three repetitions per sample are advised; it is recommended to analyze them in a random order and not in the same order (4). The analyses must be carried out following the conditions of repeatability. The types of sampling to be performed can be systematic, random, or stratified random (4).

The study of homogeneity is carried out after placing the material in the containers (33). The authors evaluated the between-unit homogeneity by analyzing samples whose number varied between 6 and 16; this number was between 2 and 5 concerning the sub-samples used for the study of the within-unit homogeneity (34–43). The kind of sampling used is random (35–38,40,41,43) or stratified random (34,39). For the homogeneity study, internal (42,44) or external (33,34) standards can be used. The testing of samples is performed in a random order to distinguish between an analytical drift and a possible tendency in the filling sequence (37).

Homogeneity can be assessed using the ANOVA test (33,35–39,41,44–47). Other authors have used the Student's t-test to evaluate significant differences between averages obtained from within-unit and between-unit analysis (34,48). The outliers in the homogeneity study can be detected by visual inspection (9) or using the Grubbs test (9,37,38,44–46). Some authors used regression analysis to reject the drift of the measurement (36). The standard ISO 13528:2022 (49) recommends the use of the Cochran test for repetitions. Other standards provide several methods for identifying outliers, namely: ISO 5725-2:2019(50) (which describes Grubbs tests) and ISO 16269-4(51) (which describes graphical outlier tests and other tests for multiple outliers).

Concerning uncertainty associated with heterogeneity (W_{hom}), further to ISO Guide 35:2017 (9), it can be calculated by Formula:

$$u_{hom} = \sqrt{u_{bb}^2 + u_{wb}^2}$$

With,

u_{bb} : standard uncertainty associated with between-unit variability

u_{wb} : standard uncertainty associated with within-unit heterogeneity

If a basic design and one-way analysis of variance are used to evaluate homogeneity (figure 4), s_{bb}^2 (between-unit variance from a homogeneity study), is identical to the (squared) between-unit

homogeneity contribution to the uncertainty, u_{bb}^2 (9). In the case presented in Figure 4, the s_{bb}^2 we will obtain from ANOVA 1 in the case of within-unit

homogeneity will be equivalent to s_{wb}^2 (the second component of the uncertainty u_{hom} (u_{wb}^2)).

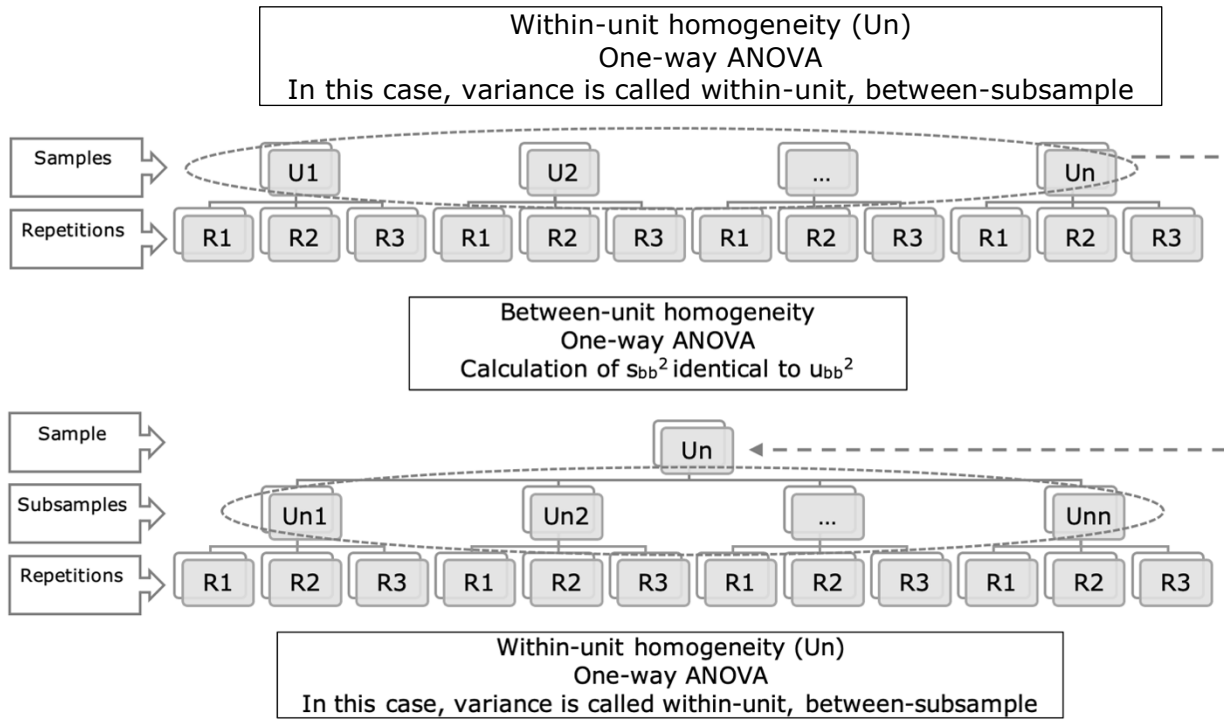


Figure 4: Diagram of a basic plan for carrying out a between-unit and within-unit homogeneity study.

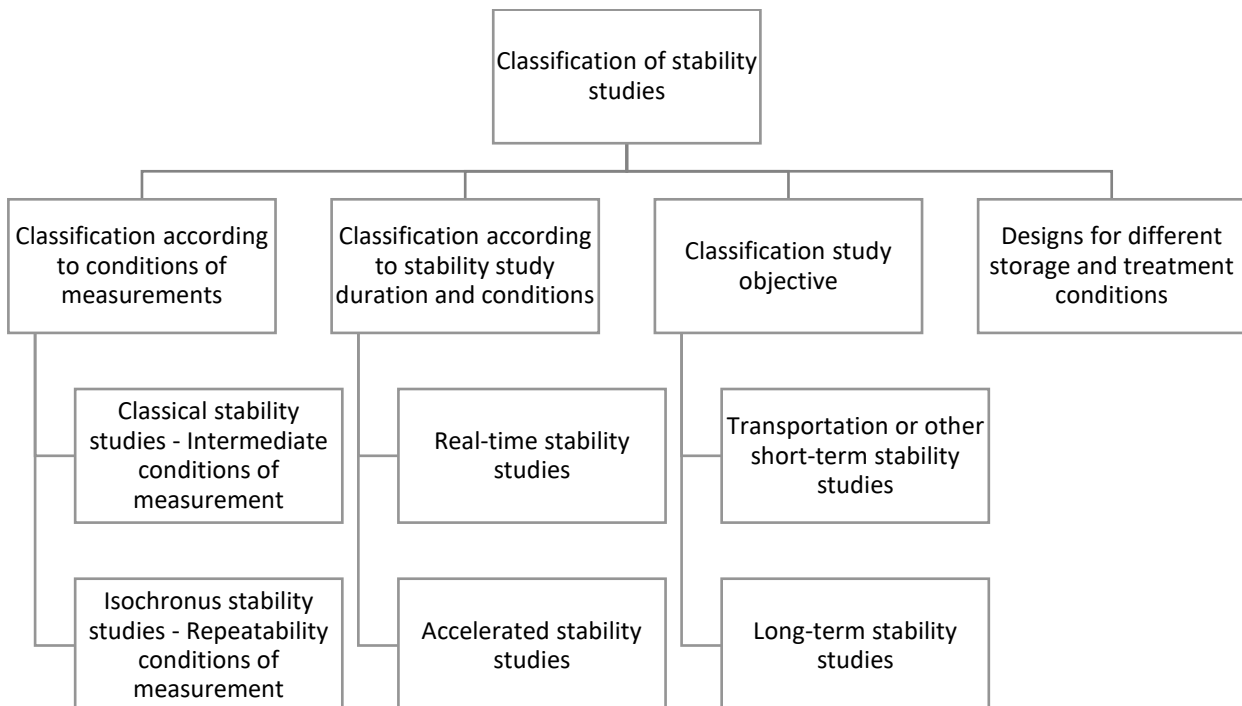


Figure 5: Classification of stability studies according to ISO Guide 35:2017.

Some authors (37) have used the method described by Van Der Veen, Linsinger, & Pauwels (52) to calculate the uncertainty due to possible inhomogeneity which can be masked by the repeatability of the method.

6.3. Stability Study

The properties of the material and the parameters studied should remain unchanged over long periods (3). For that purpose, a stability study is performed to evaluate the behavior of the material under various conditions. In general, a series of measurements realized at different times is performed to accomplish a stability study (31). Figure 5 presents the classification of stability studies according to ISO Guide 35:2107 (9).

ISO 17034:2016 (10) requires stability to be assessed under the proposed conditions of transport and the proposed conditions of storage. This assessment can be carried out either accelerated or in real-time, using a classical or isochronous study. The latter is defined by ISO Guide 35:2017 (9) as an "experimental study of reference material stability in which units exposed to different storage conditions and times are measured in a short period".

A short-term stability study is generally performed to determine conditions during delivery (3,37,41,44,46). Habitually high temperatures (between 35 and 40 °C) are used to assess predictable degradation under the most unfavorable conditions, such as during transport (3). The long-term stability helps to identify optimal storage conditions for the RM (37,41,44). An accelerated stability study (where some samples are exposed to extreme conditions in comparison to desired storage or transport conditions) has the advantage of reducing the total time required for the study of experimental stability (32). Some authors suppose that a "sample stable at + 40 °C during one year may be stable at + 20 °C for a longer period (Arrhenius)" (3). Other authors judge the simulation of long-term storage under difficult conditions as inappropriate, given the possibility of modification of the degradation mechanism (31). Therefore, using extrapolation to estimate stability data from higher temperatures using the Arrhenius equation is not recommended (31).

To study the stability of the RM, the authors analyzed samples of the RM stored at expected temperatures for storage, extreme temperatures (e.g., 40 °C, 60 °C), and temperatures where it is supposed to have very weak or negligible variations of the RM (e.g., -20 °C, -70° C, and -80° C) (3,31,33–35,37,46). The stability study can also be performed by modifying other conditions, such as light, or darkness (53) and/or humidity. The short-term stability was assessed by the authors over periods ranging from 0, 1, and 2 weeks, then over regular intervals of one month to 4 months (33–35,37,38). The study of long-term stability has been carried out between 3 months and 2 years for some authors (33–

35,37,38,46,54,55). The number of samples analyzed at each time/temperature pair varied between 1 (56), 2 (33,57), 3 (46), 5 (35) and 6 (37) samples. Certain authors use an external calibration for the study of stability (33). The evaluation of stability is carried out by comparing the obtained results in the initial time with those obtained in each period (35). Some authors (34,37,57,58) used the isochronous approach (59) to assess the stability of the RM.

The stability study is performed by analyzing samples chosen randomly (33,46). Increasing the number of repetitions per time and increasing the duration of the stability study allow us to reduce the influence of the analytical variation (31). To assess stability, certain authors have used the F test (54). The Grubbs test is used by other authors to identify outliers (37,44). The latter also performed linear regression analysis as a function of time and for each temperature. These same authors tested the slopes for their significance using a t-test proposed also by ISO Guide 35:2017 (9). The uncertainty of the stability has been estimated by some authors (37,44) "as the uncertainty of the regression line with a slope of zero multiplied by the envisaged shelf-life of the material", as described by Thomas P.J. Linsinger et al. (60).

6.4. Characterization and Evaluation of Measurement Uncertainty

According to ISO Guide 30:2015 (5), the characterization of an RM is the "determination of the property values or attributes of a reference material, as part of the production process". It aims to obtain a metrologically valid estimation of the real value of the property (61).

There are several valid characterization approaches (61):

- A single (primary) method in a single laboratory;
- Two or more independent reference methods in one or several laboratories;
- One or more methods of demonstrable accuracy, performed by a network of competent laboratories;
- An approach providing method-specific, operationally defined property values, using a network of competent laboratories.

The Consultative Committee for Amount of Substance (CCQM) defined the primary method of measurement as a "method having the highest metrological qualities, whose operation can be completely described and understood, for which a complete uncertainty statement can be written down in terms of SI units, and whose results are, therefore, accepted without reference to a standard of the quantity being measured" (62). The VIM (63) defined the primary reference measurement procedure as a "reference measurement procedure used to obtain a measurement result without relation to a measurement standard for a quantity of the same kind".

Some authors consider that the primary method is completely understood, so they judge that a single value from a single laboratory is sufficient since an unknown laboratory or method bias can be excluded (61). Other authors say that the laboratory may have a bias, and therefore, by using only one method in a single laboratory, the certified value may be wrong (3). In addition, an estimation of the uncertainty may not be correct by choosing the use of the results of one method in a single laboratory (3).

On the other hand, the reference method is defined in ISO Guide 30:2015 (5) as a "measurement method, that has been shown to have the appropriate trueness and precision for its intended use and has been officially defined as reference method by a competent body". The VIM (63) defines the reference measurement procedure as a "measurement procedure accepted as providing measurement results fit for their intended use in assessing the measurement trueness of measured quantity values obtained from other measurement procedures for quantities of the same kind, in calibration, or in characterizing reference materials".

The use of several independent methods is the most commonly adopted approach (3,21).

The choice of the characterization of the samples by several laboratories is within the scope of the interlaboratory comparisons. This involves sending the same entity or similar entities to the selected laboratories for analysis. Further to the obtained results by the different laboratories, a statistical analysis is planned to identify the assigned values and their associated uncertainties. ISO 13528 presents the statistical methods that can be used in proficiency testing by interlaboratory comparison. Interlaboratory comparisons allow us to verify the trueness of the methods of analysis (2).

The number of chosen laboratories (6, 11,24), the number of used methods (1, 2, 3), the number of analyzed samples (2), the number of repetitions per sample (1, 2, 6) as well as the period of analysis (2 days, 3 days) differ from one author to another (4,41,44). Some authors chose to do the repetitions under intermediate precision conditions (4). For the control of the measurements, the authors have chosen to send also two samples of a "standard certified calibration" for analysis (41). The selected laboratories must use validated methods and be able to ensure the traceability of results (4).

Evaluation of the uncertainty is carried out following the characterization. This assessment takes into account the uncertainty of the testing having allowed the determining of reference values (characterization) as well as those related to within-unit and between-unit homogeneity and stability (2,39). These last two uncertainties may not appear in the uncertainties budget if the contribution of the one related to homogeneity is shown to be negligible and if the stability of the property value of the material can be insured (64).

To help RM producers in preparing the documentation that will accompany them, the ISO has established ISO Guide 31 (7) which lists the information that must be included on a certificate of a CRM, on the label attached to the container, and also on the product information sheets. This information will help the users to confirm the adequacy of the chosen CRM.

7. CONCLUSION

The importance of the reference materials has pushed among others the ISO to the establishment of several standards concerning the development and use of the reference materials.

The development of the reference materials consists of four steps mainly: preparation, realization of the homogeneity study, carrying out the stability study, and characterization. These steps are equally important; the fact of highlighting less than one of them will imply a significant decrease in the quality of the reference material developed.

The production of reference materials is governed by many different factors and may differ from one country to another. The introduction of quality assurance in laboratories, the implementation of a quality approach by ISO/IEC 17025, the regulatory framework which sometimes imposes thresholds for certain elements as well as the demand of industrialists can be considered elements encouraging the production of the reference materials. These latter are of paramount importance in analysis laboratories since they have several roles, namely calibration of equipment, development, and validation of methods, and realization of interlaboratory comparisons among others. Certainly, the laboratories need more and more reference materials, however finding the appropriate ones is not easy. In several cases, the available reference materials do not correspond 100 % to the sample to be analyzed because of the variety of compounds, concentrations, and matrices; this makes the development of new reference materials a necessity. This expensive operation requiring technical knowledge and important experience makes the price of these reference materials high, which makes their use limited in the laboratories.

The outlook for the reference materials development market will depend on several factors, including the rapid development of analytical technologies using cutting-edge analytical methods, and the expansion of the biotechnology, nanotechnology, and renewable energy sectors. Demand for sustainably produced reference materials could increase as environmental concerns gain in importance. Increasingly stringent standards and regulations, economic change, and scientific developments could lead to a customization of demand for reference materials tailored to the specific needs of certain fields.

8. CONFLICT OF INTEREST

Nothing to report.

9. ACKNOWLEDGMENTS

Nothing to report.

10. REFERENCES

1. Charlet P, Hervouët G. Nouvelles demandes en matériaux de référence Certifiés cas de secteurs émergents: Environnement: Biologie et Autres. Lab Natl d'essai, Paris. 2001.
2. Lafargue M, Seiller MP. Les matériaux de référence: définitions, disponibilité, sélection et utilisation. *Spectra Anal.* 2004;240:33-7.
3. Günzler H, editor. Accreditation and Quality Assurance in Analytical Chemistry [Internet]. Berlin, Heidelberg: Springer Berlin Heidelberg; 1996. Available from: [<URL>](#).
4. Daugey G, Soule P, Hakim K, Hewitt A, Prunet T, Nicolas M, et al. Production d'un échantillon de référence certifié: du prélèvement au dimensionnement des essais de certification. *Cah des Tech l'INRA* [Internet]. 2015;1(84):1-8. Available from: [<URL>](#).
5. ISO. ISO Guide 30:2015 Reference Materials - Selected Terms and Definitions. 2015.
6. King B. The selection and use of reference materials - a basic guide for laboratories and accreditation bodies. *Accredit Qual Assur* [Internet]. 2003 Sep 1;8(9):429-33. Available from: [<URL>](#).
7. ISO. ISO Guide 31:2015 Reference Materials - Contents of Certificates, Labels and Accompanying Documentation. 2015.
8. ISO. ISO Guide 33:2015 Reference Materials - Good Practice in Using Reference Materials. 2015.
9. ISO. ISO Guide 35:2017 Reference Materials - Guidance for Characterization and Assessment of Homogeneity and Stability. 2017.
10. ISO. ISO 17034:2016 General Requirements for the Competence of Reference Material Producers. 2016.
11. ISO. ISO Guide 80:2014 Guidance for the in-House Preparation of Quality Control Materials (QCMs). 2014.
12. ISO. ISO/TR 16476:2016 Reference Materials - Establishing and Expressing Metrological Traceability of Quantity Values Assigned to Reference Materials. 2016.
13. ISO. ISO/TR 79:2015 Reference Materials - Examples of Reference Materials for Qualitative Properties. 2015.
14. ISO. ISO/TR 10989:2009 Reference Materials - Guidance on, and Keywords Used for, RM Categorization. 2009.
15. ISO. ISO 11095:1996 Linear Calibration Using Reference Materials. 1996.
16. ISO. ISO/TR 11773:2013 Global Distribution of Reference Materials. 2013.
17. ISO. ISO 15194:2009 In Vitro Diagnostic Medical Devices - Measurement of Quantities in Samples of Biological Origin - Requirements for Certified Reference Materials and the Content of Supporting Documentation. 2009.
18. ISO. ISO/FDIS 33407 Guidance for the Production of Pure Organic Substance Certified Reference Materials.
19. Cofrac. Exigences pour l'accréditation des producteurs de matériaux de référence LAB MR REF 02 - Révision 02. 2019.
20. APLAC. Guidelines for Acceptability of Chemical Reference Materials and Commercial Chemicals for Calibration of Equipment Use in Chemical Testing APLAC TC 012. 2009.
21. Vialle J, Linet P, Maier EA. La métrologie en chimie. Quelques principes et beaucoup d'incertitudes. *Analisis* [Internet]. 1999 Jul 1;27(6):479-90. Available from: [<URL>](#).
22. Borges R, Meyer VR. The uncertainty of purity of reference materials must be known. *J Pharm Biomed Anal* [Internet]. 2013 Apr 15;77:40-3. Available from: [<URL>](#).
23. Jenks PJ, Henk Boekholt A, Maaskant JFN, Rucinski RD. Are certified reference materials a victim of quality systems? The need for working matrix-certified reference materials. *Fresenius J Anal Chem* [Internet]. 1998 Feb 1;360(3-4):366-9. Available from: [<URL>](#).
24. Majcen N. A need for clearer terminology and guidance in the role of reference materials in method development and validation. *Accredit Qual Assur* [Internet]. 2003 Apr 1;8(3-4):108-12. Available from: [<URL>](#).
25. ISO. ISO/IEC 17025 General Requirements for the Competence of Testing and Calibration Laboratories. 2017.
26. Vassault A, Giroud C, Arnaud J. Traceability of the standards and calibrations. *Ann Biol Clin (Paris)*. 2010 Dec;68(1):295-303.
27. BAM - RRR - Home [Internet]. 2017 [cited 2018 Jul 14]. Available from: [<URL>](#).
28. Steiger T, Pradel R. COMAR: the international database for certified reference materials—an overview. *Accredit Qual Assur* [Internet]. 2015 Feb 12;20(1):47-52. Available from: [<URL>](#).
29. ISO. ISO 15189:2022 Medical Laboratories -- Requirements for Quality and Competence. 2022.
30. ISO. ISO 9001:2015 Quality Management Systems — Requirements. 2015.

31. Linsinger TPJ, Pauwels J, van der Veen AMH, Schimmel H, Lambert A. Homogeneity and stability of reference materials. *Accredit Qual Assur* [Internet]. 2001 Jan 9;6(1):20–5. Available from: [<URL>](#).
32. Ellison SLR, Botha A. Principles for the assessment of homogeneity and stability in the new ISO Guide 35:2017. *Accredit Qual Assur* [Internet]. 2018 Feb 25;23(1):47–51. Available from: [<URL>](#).
33. Ng SY, Dewi F, Wang J, Sim LP, Shin RYC, Lee TK. Development of a cosmetic cream certified reference material: Certification of lead, mercury and arsenic mass fractions in cosmetic cream. *Int J Mass Spectrom* [Internet]. 2015 Oct 15;389:59–65. Available from: [<URL>](#).
34. Chew G, Sim LP, Ng SY, Ding Y, Shin RYC, Lee TK. Development of a mushroom powder Certified Reference Material for calcium, arsenic, cadmium and lead measurements. *Food Chem* [Internet]. 2016 Jan 1;190:293–9. Available from: [<URL>](#).
35. Valente A, Sanches-Silva A, Albuquerque TG, Costa HS. Development of an orange juice in-house reference material and its application to guarantee the quality of vitamin C determination in fruits, juices and fruit pulps. *Food Chem* [Internet]. 2014 Jul 1;154:71–7. Available from: [<URL>](#).
36. Espinoza M, Azar CO, Massiff G, Villa A. Development of a reference material for copper and iron in wine. *J Food Compos Anal* [Internet]. 2008 Dec 1;21(8):684–8. Available from: [<URL>](#).
37. Zeleny R, Emteborg H, Charoud-Got J, Schimmel H, Nia Y, Mutel I, et al. Development of a reference material for *Staphylococcus aureus* enterotoxin A in cheese: Feasibility study, processing, homogeneity and stability assessment. *Food Chem* [Internet]. 2015 Feb 1;168:241–6. Available from: [<URL>](#).
38. Gong N, Zhang B, Hu F, Du H, Du G, Gao Z, et al. Development of a new certified reference material of diosgenin using mass balance approach and Coulometric titration method. *Steroids* [Internet]. 2014 Dec 15;92:25–31. Available from: [<URL>](#).
39. Yarita T, Otake T, Aoyagi Y, Kuroda Y, Numata M, Iwata H, et al. Development of soybean certified reference material for pesticide residue analysis. *Talanta* [Internet]. 2014 Feb 15;119:255–61. Available from: [<URL>](#).
40. Otake T, Yarita T, Aoyagi Y, Kuroda Y, Numata M, Iwata H, et al. Development of apple certified reference material for quantification of organophosphorus and pyrethroid pesticides. *Food Chem* [Internet]. 2013 Jun 1;138(2–3):1243–9. Available from: [<URL>](#).
41. Köppen R, Bremser W, Stephan I, Klein-Hartwig K, Rasenko T, Koch M. T-2 and HT-2 toxins in oat flakes: development of a certified reference material. *Anal Bioanal Chem* [Internet]. 2015 Apr 16;407(11):2997–3007. Available from: [<URL>](#).
42. Kinumi T, Goto M, Eyama S, Kato M, Kasama T, Takatsu A. Development of SI-traceable C-peptide certified reference material NMIJ CRM 6901-a using isotope-dilution mass spectrometry-based amino acid analyses. *Anal Bioanal Chem* [Internet]. 2012 Jul 20;404(1):13–21. Available from: [<URL>](#).
43. Takahashi K, Matsuyama S, Kato H, Kinugasa S. Development of the Certified Reference Material of Poly(ethylene glycol) Nonylphenyl Ether by Supercritical Fluid Chromatography. *Int J Polym Anal Charact* [Internet]. 2012 Apr;17(3):208–17. Available from: [<URL>](#).
44. Zeleny R, Schimmel H, Ulberth F, Emons H. Development of a certified reference material for the content of nitroimidazole parent drugs and hydroxy metabolites in pork meat. *Anal Chim Acta* [Internet]. 2009 Feb 23;634(2):237–42. Available from: [<URL>](#).
45. Kim MJ, Kim M, Kim S, Lee K, Kim Y, Kim J, et al. Feasibility study on the homogeneity and stability of megastigmatrienone isomers for the development of certified reference material. *J Food Compos Anal* [Internet]. 2023 Oct 1;123:105573. Available from: [<URL>](#).
46. Sin DWM, Chan P kwan, Cheung STC, Wong YL, Wong S kay, Mok C shing, et al. Development of a candidate certified reference material of cypermethrin in green tea. *Anal Chim Acta* [Internet]. 2012 Apr 6;721:110–4. Available from: [<URL>](#).
47. Mazánová M, Kačur M. Homogeneity evaluation of liquid reference material developed for nuclear decommissioning. *Appl Radiat Isot* [Internet]. 2023 Jul 1;197:110775. Available from: [<URL>](#).
48. Shimizu Y, Ohte Y, Kato K. Development of a certified reference material for calibration of DSC and DTA below room temperature: NMIJ CRM 5401-a, Cyclohexane for Thermal Analysis. *Thermochim Acta* [Internet]. 2013 Sep 20;568:61–6. Available from: [<URL>](#).
49. ISO. ISO 13528:2022 Statistical Methods for Use in Proficiency Testing by Interlaboratory Comparison. 2022.
50. ISO. ISO 5725-2:2019 Accuracy (Trueness and Precision) of Measurement Methods and Results — Part 2: Basic Method for the Determination of Repeatability and Reproducibility of a Standard Measurement Method. 2019.
51. ISO. ISO 16269-4:2010 Statistical Interpretation of Data — Part 4: Detection and Treatment of Outliers. 2010.
52. van der Veen AMH, Linsinger TP, Pauwels J. Uncertainty calculations in the certification of reference materials. 2. Homogeneity study. In: Bièvre P, Günzler H, editors. *Measurement Uncertainty in Chemical Analysis* [Internet]. Berlin, Heidelberg: Springer Berlin Heidelberg; 2001. p. 94–8. Available from: [<URL>](#).

53. Cuadros-Rodríguez L, Bosque-Sendra JM, de la Mata-Espinosa AP, González-Casado A, Rodríguez-García FP. Elaboration of Four Olive Oil Certified Reference Materials: InterOleo-CRM 2006 Certification Study. *Food Anal Methods* [Internet]. 2008 Dec 13;1(4):259–69. Available from: [<URL>](#).
54. Hon PYT, Chu PWS, Cheng C ho, Lee TCL, Chan P kwan, Cheung STC, et al. Development of melamine certified reference material in milk using two different isotope dilution mass spectrometry techniques. *J Chromatogr A* [Internet]. 2011 Sep 28;1218(39):6907–13. Available from: [<URL>](#).
55. Gab-Allah MA, Getachew Lijalem Y, Yu H, Lee S, Baek SY, Han J, et al. Development of a certified reference material for the accurate determination of type B trichothecenes in corn. *Food Chem* [Internet]. 2023 Mar 15;404:134542. Available from: [<URL>](#).
56. Ortega-Gavilán F, García-Mesa JA, Marzal-Fernández JC, Moreno-Ballesteros FJ, Rodríguez-García FP, González-Casado A, et al. Innovative and thorough practice to certify reference materials for sensory defects of olive oil. *Food Chem* [Internet]. 2022 Jun 30;380:132195. Available from: [<URL>](#).
57. Paleari R, Muñoz A, Mosca A. Towards the development of a certified reference material for hemoglobin A 2. *cclm* [Internet]. 2010 Nov 1;48(11):1611–8. Available from: [<URL>](#).
58. Grimalt S, Harbeck S, Shegunova P, Seghers J, Sejerøe-Olsen B, Emteborg H, et al. Development of a new cucumber reference material for pesticide residue analysis: feasibility study for material processing, homogeneity and stability assessment. *Anal Bioanal Chem* [Internet]. 2015 Apr 28;407(11):3083–91. Available from: [<URL>](#).
59. Lamberty A, Schimmel H, Pauwels J. The study of the stability of reference materials by isochronous measurements. *Fresenius J Anal Chem* [Internet]. 1998 Feb 1;360(3–4):359–61. Available from: [<URL>](#).
60. Linsinger TPJ, Pauwels J, Lamberty A, Schimmel HG, van der Veen AMH, Siekmann L. Estimating the uncertainty of stability for matrix CRMs. *Fresenius J Anal Chem* [Internet]. 2001 Jun 1;370(2–3):183–8. Available from: [<URL>](#).
61. Linsinger TPJ, Emons H. Characterization of reference materials: proposal for a simplification of the options listed in ISO Guide 34. *Accredit Qual Assur* [Internet]. 2013 Apr 12;18(2):149–52. Available from: [<URL>](#).
62. Milton MJT, Quinn TJ. Primary methods for the measurement of amount of substance. *Metrologia* [Internet]. 2001 Aug 1;38(4):289–96. Available from: [<URL>](#).
63. ISO. ISO/IEC Guide 99:2007 International Vocabulary of Metrology — Basic and General Concepts and Associated Terms (VIM). 2007.
64. Trapmann S, Botha A, Linsinger TPJ, Mac Curtain S, Emons H. The new International Standard ISO 17034: general requirements for the competence of reference material producers. *Accredit Qual Assur* [Internet]. 2017 Dec 26;22(6):381–7. Available from: [<URL>](#).



Structural and Dielectric Properties of Eu^{3+} , B^{3+} co-doped CoNb_2O_6 Ceramic

Mustafa İlhan^{1*}, Mete Kaan Ekmekçi², Kadir Esmer³

¹Department of Environmental Engineering, Faculty of Engineering, Marmara University, Maltepe, 34854, Istanbul, Turkey.

²Marmara University, Department of Chemistry, Faculty of Science, Marmara University, Kadıköy, 34722, Istanbul, Turkey.

³Department of Physics, Faculty of Science, Marmara University, Kadıköy, 34722, Istanbul, Turkey.

Abstract: The boron co-doped $\text{CoNb}_2\text{O}_6:\text{xEu}^{3+}, \text{yB}^{3+}$ ($\text{x}=1, 3, 6, 9, 12$ mol%, $\text{y}=10$ mol%) ceramics were obtained by the molten salt method, which has advantageous properties such as short reaction time, low sintering temperature, improved homogeneity, and crystallinity. The ceramic samples were examined by structural and dielectric analyses. In X-ray diffractions, the orthorhombic columbite type CoNb_2O_6 structure was obtained, and also a minor EuNbO_4 phase was detected with increasing Eu^{3+} doping concentrations. Additionally, increasing Eu^{3+} concentration led to a slight increase in crystallite size, and two theta peak shifts occurred towards higher angles associated with shrinkage in the lattice or reduction in the lattice constant. In SEM examinations, a slight increase was observed in grain sizes from 1 to 9 mol% Eu^{3+} in the range of 1-30 μm , while some decrease occurred in grain sizes at 12 mol%, and there was an evident increase in plate-shaped and elongated grains. The dielectric constant (ϵ') of the ceramic samples increased with increasing Eu^{3+} concentration and reached approximately 35 and 0.24 at 20 Hz for 9 mol% Eu^{3+} , respectively. The increase in dielectric loss with increasing Eu^{3+} was associated with an increase in ionic conductivity, in which Eu^{3+} substitution does not suppress oxygen vacancies or make them more ordered.

Keywords: CoNb_2O_6 , XRD, SEM, Eu^{3+} doping, dielectric properties.

Submitted: November 29, 2023. **Accepted:** February 24, 2024.

Cite this: İlhan M, Ekmekçi MK, Esmer K. Structural and Dielectric Properties of Eu^{3+} , B^{3+} co-doped CoNb_2O_6 Ceramic. JOTCSA. 2024;11(2):765-74.

DOI: <https://doi.org/10.18596/jotcsa.1397311>

***Corresponding author's E-mail:** mustafa.ilhan@marmara.edu.tr

1. INTRODUCTION

Materials exhibiting high dielectric constant are widely used in electronic industries such as capacitors, memory devices, and filters. In practical applications, materials with a high dielectric constant are desired to exhibit low dielectric loss and relatively weak frequency and temperature dependence (1-3). Luminescent dielectrics can be obtained from host materials doped with RE ions. Among the rare earth (RE) ions, the trivalent europium ion is considered an excellent red activator for the luminescence centers of red phosphors due to its $^5\text{D}_0 \rightarrow ^7\text{F}_J$ ($J=0, 1, 2, 3, 4$) transitions (4-6) and is also widely used in dielectric-related research (7-10). There are some studies on the secondary phase effect on the dielectric properties of rare earth ion-doped host materials. Wang et al (11) investigated the microstructure, and dielectric properties of $(\text{Nd}_{0.5}\text{Nb}_{0.5})_{\text{x}}\text{Ti}_{1-\text{x}}\text{O}_2$ ceramics, and revealed that the secondary phase is beneficial

to increase the grain boundary resistance and the material keeps low dielectric loss and improved the temperature stability. In another study, Zhao and Wu (12) examined the dielectric behavior of the $(\text{Dy}_{0.5}\text{Nb}_{0.5})_{\text{x}}\text{Ti}_{1-\text{x}}\text{O}_2$ structure, where the secondary phases are induced by Dy enrichment, and largely facilitate the decreased dielectric loss.

The columbite-type structure with orthorhombic symmetry can be expressed as MNB_2O_6 ($\text{M} = \text{Co}, \text{Mg}, \text{Sr}, \text{Mn}, \text{Ni}, \text{Cd}, \text{etc}$). The MNB_2O_6 structure has a significant advantage in that it can host guest ions with ionic sizes comparable to the Nb and divalent M^{2+} ions found in the structure. As MNB_2O_6 structure, cobalt niobate (CoNb_2O_6) has been studied due to its magnetic (13-16), neutron scattering (17), luminescence (18-21), dielectric (22,23) gas sensing (24,25) and magnetic-thermodynamic (26,27) properties. Singh et al (22) reported the dielectric and ferroelectric properties of Ti^{4+} doped CoNb_2O_6

where Ti^{4+} substitution in $CoNb_2O_6$ lattice enhances the dielectric constant of the material. The dielectric constant (ϵ') for undoped $CoNb_2O_6$ is found to be 500, whereas $CoNb_{1.95}Ti_{0.05}O_6$ is 700 and $CoNb_{1.9}Ti_{0.1}O_6$ is 14000 at 100 Hz frequency at 200 °C. Zhang et al (23) also studied the sintering behavior and microwave dielectric properties of B_2O_3 doped $CoNb_2O_6$, where the 1.5 wt% B_2O_3 doped $CoNb_2O_6$ sintered at 1000 °C exhibited microwave dielectric properties with an ϵ' of 22.4, a high Qxf of 43.979 GHz, and a τ_f of -46.2 ppm/°C. In addition, there are studies on the effect of boron on grain morphology and its improvement in dielectric properties in which the doping of boron has the effect of increasing the bulk properties to some extent and can reduce the grain boundaries in the structure (28-30). Moreover, there are also studies on the morphology of lanthanide ion-doped structures with boron addition and the luminescence-enhancing properties of boron (31-33).

In this paper, the structural and dielectric properties of $CoNb_2O_6:xEu^{3+},yB^{3+}$ ($x=1, 3, 6, 9, 12$ mol%, $y=10$ mol%) ceramics fabricated at 900 °C were investigated by doping boron to $CoNb_2O_6:xEu^{3+}$ ($x=1, 3, 6, 9, 12$ mol%) powders produced by the molten salt method at 800 °C. The structural and dielectric analyses were performed by XRD, SEM-EDS, and impedance analyzer.

2. EXPERIMENTAL

The $CoNb_2O_6:xEu^{3+}$ ($x=0.01, 0.03, 0.06, 0.09,$ and 0.12 or $x=1, 3, 6, 9, 12$ mol%) powders were fabricated by the molten salt route. In the synthesis, cobalt nitrate hexahydrate ($Co(NO_3)_2 \cdot 6H_2O$) (Sigma-Aldrich, 98.5%), niobium oxide (Nb_2O_5) (Alpha Aesar, 99.9%), and europium oxide (Eu_2O_3) (Alpha Aesar, 99.9%) were used. For the synthesis, Li_2SO_4/Na_2SO_4 (salt/salt), and $Li_2SO_4+Na_2SO_4/CoO+Nb_2O_5+Eu_2O_3$ (salt/oxide) molar ratio were taken as 0.635/0.365 and 2/1 weight ratio, respectively. The oxide mixtures and salt mixtures were prepared according to their stoichiometric ratios and mixed well in an agate mortar to provide homogeneity. The resulting mixtures were subsequently placed in an alumina crucible and sintered for 4 h at 800 °C in an air atmosphere using an electric furnace. After the sintering, the ceramic powders were washed down several times with bi-distilled water to get rid of the ionic salts and filtered using a vacuum pump several times. The remnants of Cl^- ions in the solution were controlled by qualitative analysis. To investigate the structural and dielectric properties, the 10 mol% boron in the form of H_3BO_3 was added to the synthesized powders, pelletized, and sintered in an electric furnace at 900 °C for 6 hours.

The phase structure of the ceramics was investigated by X-ray diffractometer (XRD; Panalytical Empirical, Malvern Panalytical Ltd., UK) using $Cu-K\alpha$ (1.5406 Å) radiation in between $2\theta=20-70$ °C with scan speed 2 °C/min. The grain morphology of the ceramics was examined by scanning electron microscopy (FE-SEM; Gemini 500, Zeiss Corp., Germany). The elemental

compositions were determined by scanning electron microscopy (SEM, JEOL, Tokyo, Japan, JSM-5910LV) equipped with energy dispersive spectroscopy (EDS, OXFORD Instruments, Abingdon, England, INCA-Sight 7274; 133 eV resolution 5.9 keV) after Au (gold) coating. Frequency-dependent changes of real and imaginary permittivity and loss factor were investigated using dielectric equations:

$$\epsilon' = \frac{C}{C_0}, \quad \epsilon'' = \frac{G}{\omega C_0}, \quad C_0 = \epsilon_0 \frac{A}{d} \quad \text{and} \quad \tan\delta = \frac{\epsilon''}{\epsilon'}$$

where C_0 is vacuum capacitance, C is capacitance, ω is angular frequency and G is conductance. The dielectric properties of the ceramic samples were carried out using an impedance analyzer (Wayne Kerr 6500 B Precision; between frequency 40 Hz–100 kHz, UK) at 1 Vrms potential at room temperature.

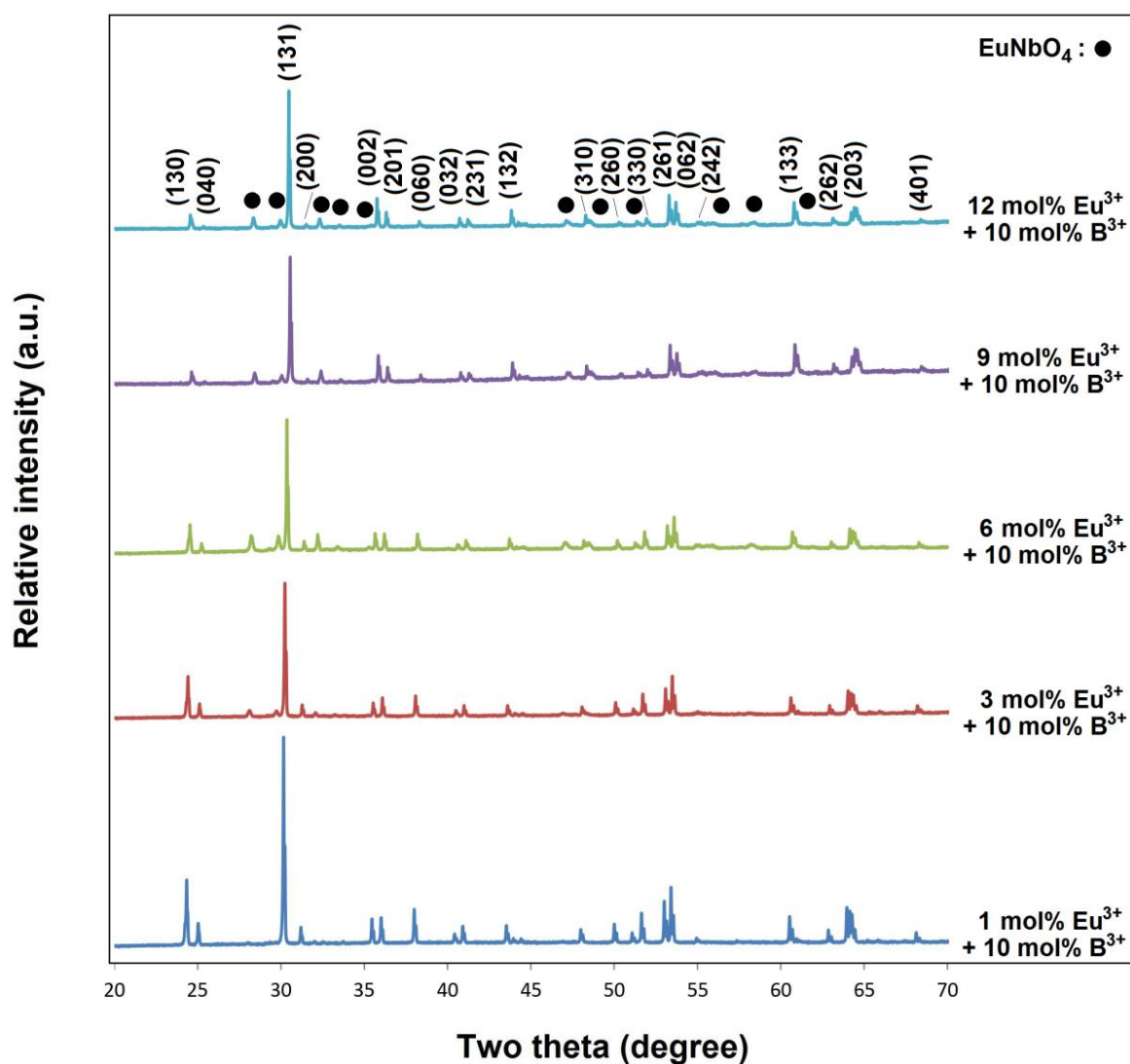
3. RESULTS AND DISCUSSION

3.1. XRD and SEM-EDS Results

Figure 1 presents the X-ray diffraction patterns of Eu^{3+} , and B^{3+} co-doped $CoNb_2O_6$ samples. XRD results of the ceramic samples were defined by orthorhombic columbite symmetry (JCPDS no: 32-0304) with space group $Pbcn60$. As seen in Figure 1, while 1 mol% concentration exhibits a single-phase $CoNb_2O_6$ structure, the $EuNbO_4$ secondary phase (JCPDS no: 22-1099) appears with increasing Eu^{3+} concentration. Additionally, the absence of boron-related reflections in the XRD results may be attributed to the dissolution of boron in the columbite structure, and similar studies have been reported (32,33). The schematic representation of the $CoNb_2O_6$ crystal structure consisting of corner-shared and edge-shared NbO_6 and CoO_6 octahedral is shown in Figure 2. In the columbite structure, there are three vacant octahedral sites labeled $4a$, $4b$, and $8d$, where the $4a$ sites are the most favorable for Eu^{3+} occupancy (32-35). The XRD peaks of the (131) reflection are shown in Figure 3. With increasing Eu^{3+} concentration, a shift of the (131) peak to higher two theta angles was observed, which may be associated with a decrease in the lattice constant or the shrinkage of the lattice. The decrease in the lattice continued up to 9 mol%, while the shift to the left at 12 mol% indicated an expansion. Accordingly, the doping of Eu^{3+} ions will likely affect the charge balance due to the shrinkage of the lattice and cause some defects in the structure. Table 1 summarizes the lattice parameters of the samples, in which the a , b , c , and V data from 1 to 12 changed to 14.4995, 5.5857, 5.0559 Å, 409.47 Å³ and 14.2362, 5.6138, 4.9888 Å, 398.70 Å³, respectively. In addition, the cell data of orthorhombic $CoNb_2O_6$ are reported as $a=14.167$ Å, $b=5.714$ Å, $c=5.046$ Å, and $V=408.47$ Å³ (27), which are consistent with the lattice parameters in this study. The average crystallite sizes of the samples from the Scherrer Eq. were found between 28.07 and 33.91 nm. The slight increase in crystallite size can be associated with the formation of a secondary $EuNbO_4$ phase due to the increased presence of Eu^{3+} and thus the development of crystallinity as a result of maintaining the charge balance in the structure.

Table 1: Cell parameters and crystallite sizes for Eu^{3+} , B^{3+} co-doped CoNb_2O_6 ceramics.

Sample (mol%)	Lattice parameters					Crystallite size
	a (Å)	b (Å)	c (Å)	c/a	V (Å) ³	D (nm)
Ref. [27]	14.1670	5.7140	5.0460	-	408.47	-
1 Eu^{3+} , 10 B^{3+}	14.4995	5.5857	5.0559	0.3487	409.47	28.07
3 Eu^{3+} , 10 B^{3+}	14.4058	5.5927	5.0492	0.3505	406.80	28.08
6 Eu^{3+} , 10 B^{3+}	14.2683	5.6033	5.0391	0.3532	402.87	29.79
9 Eu^{3+} , 10 B^{3+}	14.1471	5.6208	4.9822	0.3522	396.18	33.92
12 Eu^{3+} , 10 B^{3+}	14.2362	5.6138	4.9888	0.3504	398.70	33.91

**Figure 1:** X-ray diffractions of $\text{CoNb}_2\text{O}_6:x\text{Eu}^{3+},y\text{B}^{3+}$ ($x=1, 3, 6, 9, 12$ mol% Eu^{3+} , $y=10$ mol%) co-doped CoNb_2O_6 samples.

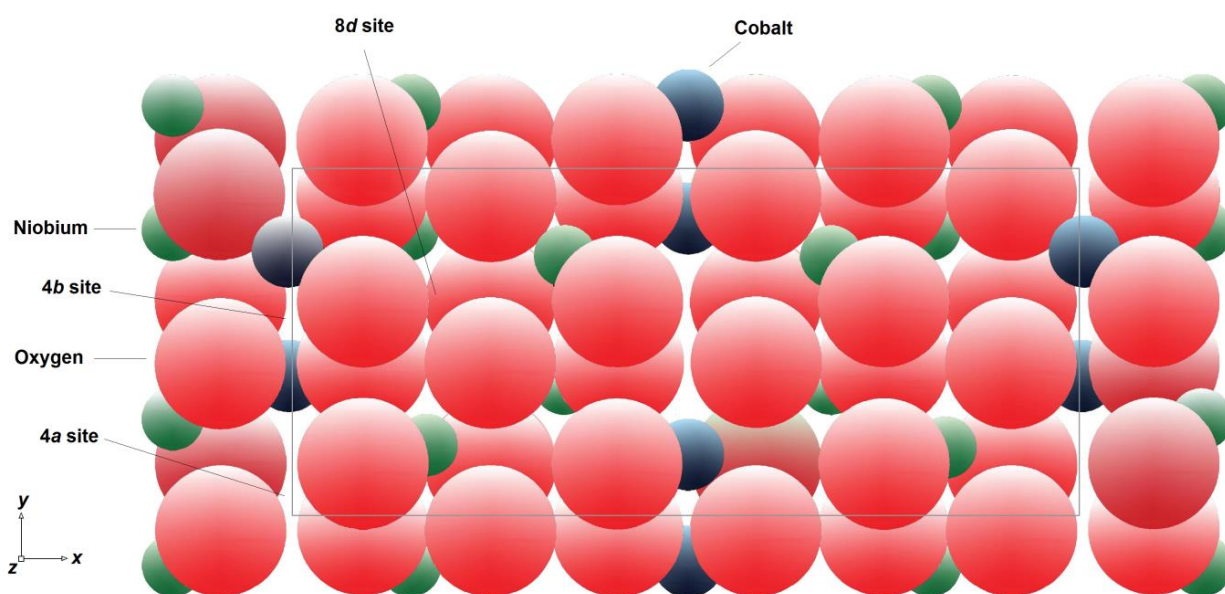


Figure 2: Schematic illustration of the CoNb_2O_6 crystal structure.

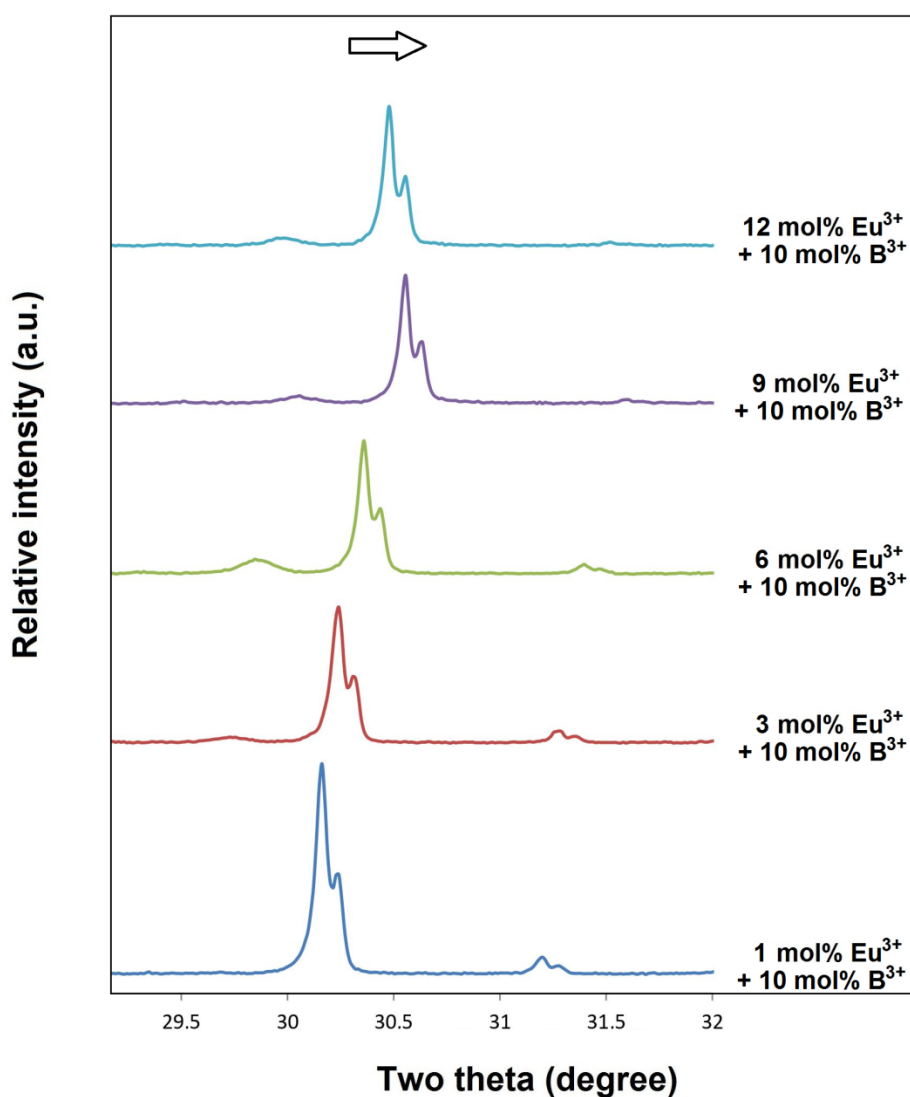


Figure 3: XRD two theta angles (131) shifted to higher angles with Eu^{3+} concentration.

Figure 4(a-e) shows the SEM micrographs at 5000x magnification for 1, 3, 6, 9 and 12 mol% Eu^{3+} , B^{3+} co-doped samples, respectively. In SEM micrographs, there was a slight increase in the grain

sizes of the ceramic samples with the increasing Eu^{3+} concentration from 1 to 9 mol% which ranged between 1-30 μm . There was some decrease in grain sizes at 12 mol% concentration, while an increase

occurred in plate-shaped and elongated grains. Also, as seen in SEM micrographs in Figure 4(a-e), increasing Eu^{3+} concentration promotes the formation of collapses and holes in the grains. Moreover, it has been previously reported that the grain sizes of powder samples produced by the molten salt method at 800 °C are in the range of

0.05-2 μm (20). However, in this study, boron was subsequently added and the temperature was increased to 900 °C after pelletization. As a result, the morphology of the grains was affected by the 10 mol% boron doping, and increasing the temperature from 800 to 900 °C, a significant increase in grain sizes occurred.

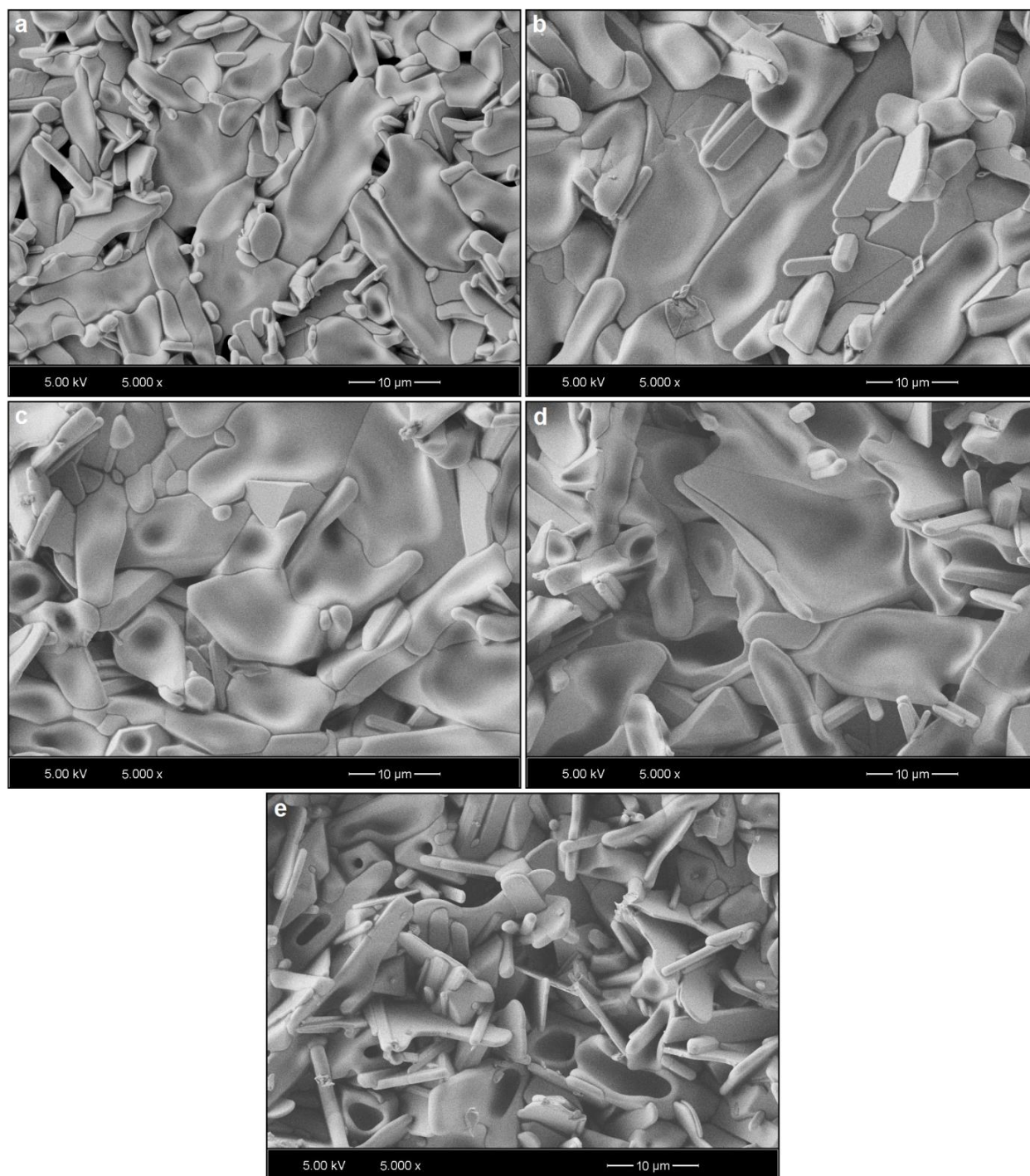


Figure 4: SEM micrographs of (a) 1, (b) 3, (c) 6, (d) 9, (e) 12 mol% Eu^{3+} , 10 mol% B^{3+} co-doped samples at 5000 \times magnifications and 5 kV acceleration voltage.

SEM-EDS analysis was performed to reveal phase structures and elemental compositions. Figure 5a shows an SEM micrograph for 6 mol% Eu^{3+} , 10 mol% B^{3+} co-doped sample, at 15000 \times magnification under 20 kV acceleration voltage. The elemental composition differences between CoNb_2O_6 main phase and EuNbO_4 minor phase were detected by

EDS analysis, where the point-1 (Figure 5b) and point-2 (Figure 5c) show Eu^{3+} doped CoNb_2O_6 and EuNbO_4 grains, respectively. As seen from the EDS results, the atomic compositions (%) of the main and minor phases agree with the theoretical compositions (%).

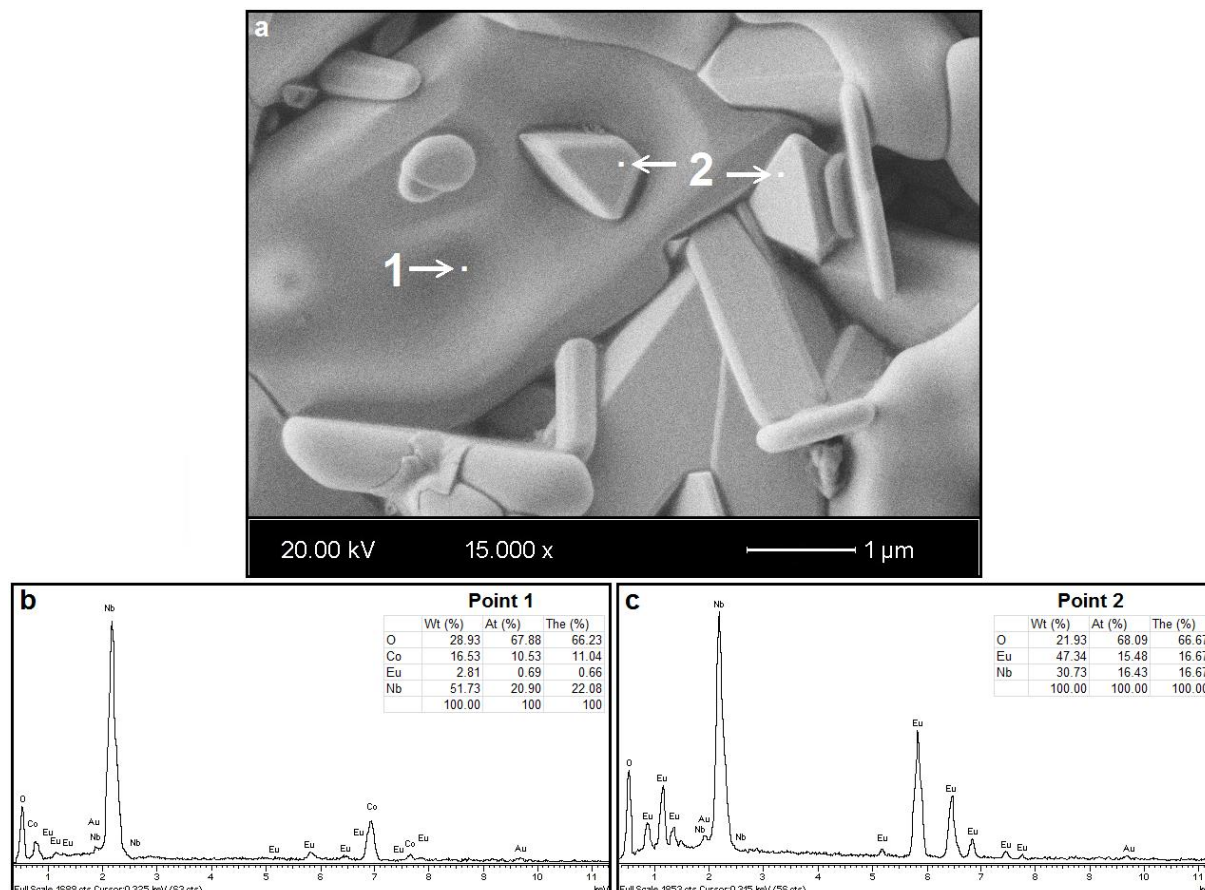


Figure 5: (a) SEM micrograph, and EDS spectrums with weight%, atomic% elemental compositions, and theoretical atomic% values, (b) main phase-point 1 (c) EuNbO_4 phase-point 2 for 6 mol% Eu^{3+} , 10 mol% B^{3+} co-doped sample.

3.2. Dielectric Behavior of Eu^{3+} , B^{3+} co-doped CoNb_2O_6 Ceramics

Figure 6 shows the dielectric constants (ϵ') of ceramic samples measured between 20 Hz– 10^7 Hz. The dielectric constants of Eu^{3+} , and B^{3+} co-doped CoNb_2O_6 ceramics varied between approximately 34.8 and 24.5 at 20 Hz. As seen in Figure 6, the dielectric constant depends on frequency, the ϵ' value was almost constant in the high-frequency range, and it increased in the low-frequency range. Regarding this, with increasing frequency, the ability of electron exchange to follow the applied field, and therefore the dielectric constant decreases. At very high frequencies the field reverses before the motion of the space charge carriers and as a result, does not contribute to polarization, and so the ϵ' value is almost constant at high frequencies (36-38). In Figure 6, increasing Eu^{3+} concentration led to an increase in the dielectric constant up to 9 mol% and then decreased to 12 mol%. In a study conducted by Betinelli et al (39) on BaTiO_3 , similar to this study, an increase in crystallite size and ϵ' value occurred with increasing Eu^{3+} concentration. So, Eu^{3+} ions are introduced into the host lattice as trivalent cations, giving rise to more point defects when increasing the dopant concentration, where the increasing ϵ' value with Eu^{3+} doping into the BaTiO_3 structure is attributed to the lattice defects caused by the dopant and is explained as the higher the lattice defects added to the host lattice with increasing dopant concentration, the higher the value of the dielectric constant. Accordingly, as seen in Figure 2 and Table

1, the shift to the right in the XRD peaks with increasing Eu^{3+} concentration can be associated with the presence of increasing defects in the lattice and the dielectric property improving up to 9 mol%. Moreover, the c/a ratio (40.41), which can be attributed to the distortion in the lattice, varies between 0.3487 and 0.3522 from 1 mol% to 9 mol%. On the other hand, as seen in Figure 2, the Eu^{3+} ions included in the structure caused a shift to the left or smaller two theta angles in the XRD peaks and expansion of the lattice, so a decrease occurred in the ϵ' value and c/a ratio at 12 mol% concentration. Based on this result, it is likely that a decrease in the dielectric constant occurred at 12 mol% Eu^{3+} concentration due to the presence of reduced point defects in the lattice. On the other hand, since the dielectric constant is grain size-related or sensitive to grain size and is affected externally, this phenomenon is explained based on the Maxwell-Wagner theory of extrinsic factors. According to this theory, the dielectric constant is directly proportional to the grain size of the sample, where an increase in grain size causes the polarization ability of atoms and the ϵ' value to increase (42-46). A slight increase in grain size in SEM examinations supports the improvement of the dielectric constant, which can be attributed to the absence of additional grain boundaries that prevent polarization. In addition, in the XRD results, it was previously stated that the formation of the EuNbO_4 secondary phase due to the increased presence of Eu^{3+} prevents the decrease in grain size by maintaining the charge balance in the

structure. This may be associated with a slight increase in the crystallite size, which supports the improved bulk feature and increased polarization. So, this increase in dielectric constant is considered to be consistent with the increase in grain size and crystallite size. As the amount of dopant increases, the grain size decreases, and the grain boundaries increase. At the same time, excessive grain boundary barrier weakens the electron transfer between grain boundaries and increases the interfacial polarization between grain and grain boundary, leading to deterioration of dielectric property (11). Of course, increasing dopant concentration will also increase the possibility of secondary phase formation, as in this study. The secondary phase effect is emphasized in detail in different studies in the literature (11,12). In

a study on $(\text{Nd}_{0.5}\text{Nb}_{0.5})_x\text{Ti}_{1-x}\text{O}_2$ by Wang et al (11), the secondary NdTiNbO_6 phase containing RE ions formed at $x=3\%$ level and continued up to $x=7\%$ concentration. Thus, the decrease in the dielectric constant after increasing up to $x=3\%$ may be attributed to the tolerance of the secondary phase in the structure to some extent. In addition, the dielectric property of the secondary phase may affect the dielectric property of the main phase, like RENbO_4 ceramics which offer excellent dielectric properties (47). Therefore, the fact that the secondary phase of EuNbO_4 has dielectric properties, its increased presence in the structure or at grain boundaries may be ascribed to some extent being tolerated by the structure or reducing its deteriorating effect on the dielectric property.

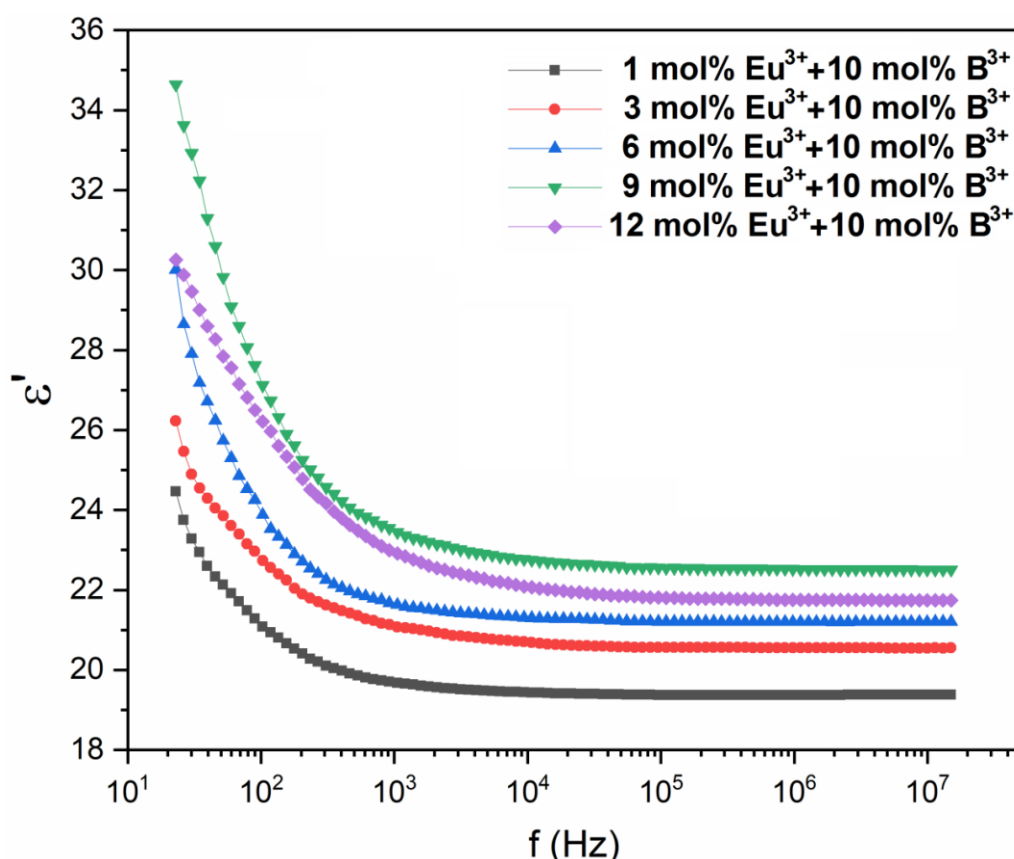


Figure 6: Dielectric constants of $\text{CoNb}_2\text{O}_6:x\text{Eu}^{3+}, y\text{B}^{3+}$ ($x=1, 3, 6, 9, 12$ mol%, $y=10$ mol%) ceramics.

Figure 7 shows the variation of dielectric loss ($\tan \delta$) with frequency for Eu^{3+} doped CoNb_2O_6 samples. It is seen that dielectric loss increases continuously as the frequency decreases in the range of $20-10^5$ Hz. In the low-frequency range corresponding to high resistance, more energy is required for polarization due to the grain boundary, while in the high-frequency range associated with low resistance, very little energy will be needed for electron transfer because of the grain boundary, and the energy loss will be less (48-50). The $\tan \delta$ factor shows an increasing trend with increasing concentration up to 9 mol% Eu^{3+} . Different studies in the literature relate the dielectric loss factor in ferroelectrics to oxygen vacancies, which are responsible for dielectric loss or leakage current (50-53). The randomization or

disorder of oxygen vacancies results in a decrease in the energy required for oxygen to jump from an occupied lattice site to an unoccupied site, so the oxygen vacancies in the structure undergo an order-disorder transition. This situation leads to an increase in ionic conductivity (53). Consequently, the increased dielectric loss may be related to Eu^{3+} substitution, which probably does not suppress oxygen vacancies or make them more ordered. This result led to an increase in ionic conductivity, and so increased dielectric loss or leakage current due to Eu^{3+} substitution. In addition, the decrease in dielectric loss at 12 mol% Eu^{3+} concentration may be associated with the Eu^{3+} substitution suppressing or making the oxygen vacancies more ordered.

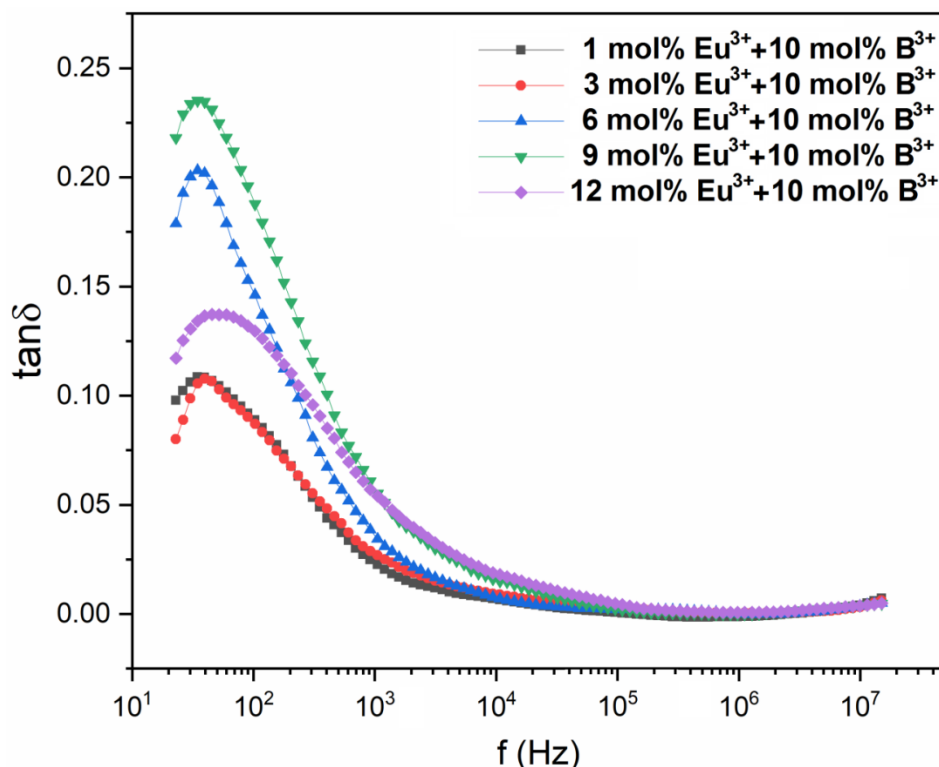


Figure 7: Dielectric losses of $\text{CoNb}_2\text{O}_6:x\text{Eu}^{3+}, y\text{B}^{3+}$ ($x=1, 3, 6, 9, 12$ mol%, $y=10$ mol%) ceramics.

4. CONCLUSION

In the study, the structural and dielectric properties of orthorhombic columbite Eu^{3+} , and B^{3+} co-doped CoNb_2O_6 ceramics were examined. The powders were synthesized by the molten salt method at 800 °C, to improve the bulk property, boron was added and the sintering temperature was raised to 900 °C. In XRD results, the CoNb_2O_6 phase maintained up to 12 mol%, and also the EuNbO_4 minor phase was detected in which ceramic samples have slightly enhanced crystallinity. SEM micrographs showed that the Eu^{3+} increase led to a somewhat increase in grain sizes, while the formation of the plate-shaped and elongated morphology occurred in high Eu^{3+} concentrations. In EDS results, the atomic compositions (%) of the main and EuNbO_4 phases were agreed with the theoretical compositions (%). The dielectric constants of the Eu^{3+} , B^{3+} co-doped CoNb_2O_6 were determined in the range of 34.8 and 24.5 at 20 Hz, while increased Eu^{3+} caused an increase in the ϵ' value up to 9 mol% and then decreased for 12 mol%. Based on the evaluation of the Maxwell-Wagner theory, this increase in dielectric constant was considered to be consistent with the increase in grain size and crystallite size. The dielectric loss increased with increased Eu^{3+} concentration up to 9 mol%. The increased $\tan \delta$ with increasing Eu^{3+} was attributed to Eu^{3+} substitution, which did not suppress oxygen vacancies or make them more ordered, and so this situation was associated with increased ionic conductivity and increased dielectric loss or leakage current.

5. CONFLICT OF INTEREST

There is no conflict of interest.

6. REFERENCES

1. Krohns S, Lunkenheimer P, Meissner S, Reller A, Gleich B, Rathgeber A, et al. The route to resource-efficient novel materials. *Nat Mater* [Internet]. 2011 Dec 23;10(12):899–901. Available from: [<URL>](#).
2. Wersing W, Steele BCH. *Electronic Ceramics*. New York: Elsevier; 1991.
3. Hao S, Li J, Yang P, Wei L, Yang Z. Enhanced electrical properties and strong red light-emitting in Eu^{3+} -doped $\text{Sr}_{1.90}\text{Ca}_{0.15}\text{Na}_{0.9}\text{Nb}_5\text{O}_{15}$ ceramics. *J Am Ceram Soc* [Internet]. 2017 Dec;100(12):5620–8. Available from: [<URL>](#).
4. İlhan M, Ekmekçi MK, Keskin İÇ. Judd–Ofelt parameters and X-ray irradiation results of $\text{MNb}_2\text{O}_6:\text{Eu}^{3+}$ (M= Sr, Cd, Ni) phosphors synthesized *via* a molten salt method. *RSC Adv* [Internet]. 2021;11(18):10451–62. Available from: [<URL>](#).
5. İlhan M, Katı Mİ, Keskin İÇ, Güteryüz LF. Evaluation of structural and spectroscopic results of tetragonal tungsten bronze $\text{MTa}_2\text{O}_6:\text{Eu}^{3+}$ (M= Sr, Ba, Pb) phosphors and comparison on the basis of Judd-Ofelt parameters. *J Alloys Compd* [Internet]. 2022 Apr;901:163626. Available from: [<URL>](#).
6. İlhan M, Keskin İÇ. Photoluminescence, radioluminescence and thermoluminescence properties of Eu^{3+} doped cadmium tantalate phosphor. *Dalt Trans* [Internet]. 2018;47(39):13939–48. Available from: [<URL>](#).
7. Mahapatro J, Agrawal S. Effect of Eu^{3+} ions on electrical and dielectric properties of barium hexaferrites prepared by solution combustion method. *Ceram Int* [Internet]. 2021 Jul;47(14):20529–43. Available from: [<URL>](#).
8. Evangeline T G, Annamalai A R, Ctibor P. Effect of Europium Addition on the Microstructure and Dielectric Properties of CCTO Ceramic Prepared Using Conventional and Microwave Sintering. *Molecules* [Internet]. 2023 Feb

8;28(4):1649. Available from: [<URL>](#).

9. Chakrabarti A, Tarafder A, Molla AR. Synthesis of Eu^{3+} -doped $\text{BaBi}_2\text{Ta}_2\text{O}_9$ based glass-ceramic nanocomposites: Optical and dielectric properties. *J Am Ceram Soc* [Internet]. 2018 Jan 18;101(1):231–43. Available from: [<URL>](#).

10. Fu J, Zhao J, Sa T, Qin N, Bao D. Photoluminescent and dielectric properties of Eu^{3+} -doped LaAlO_3 thin films fabricated by chemical solution deposition method. *Appl Surf Sci* [Internet]. 2013 Dec;286:1–6. Available from: [<URL>](#).

11. Wang Z, Chen H, Nian W, Fan J, Li Y, Wang X, et al. Grain boundary effect on dielectric properties of $(\text{Nd}_{0.5}\text{Nb}_{0.5})_x\text{Ti}_{1-x}\text{O}_2$ ceramics. *J Alloys Compd* [Internet]. 2019 May;785:875–82. Available from: [<URL>](#).

12. Zhao C, Wu J. Effects of Secondary Phases on the High-Performance Colossal Permittivity in Titanium Dioxide Ceramics. *ACS Appl Mater Interfaces* [Internet]. 2018 Jan 31;10(4):3680–8. Available from: [<URL>](#).

13. Sarvezuk PWC, Kinast EJ, Colin C V., Gusmão MA, da Cunha JBM, Isnard O. New investigation of the magnetic structure of CoNb_2O_6 columbite. *J Appl Phys* [Internet]. 2011 Apr 1;109(7):07E160. Available from: [<URL>](#).

14. Scharf W, Weitzel H, Yaeger I, Maertense I, Wanklyn BM. Magnetic structures of CoNb_2O_6 . *J Magn Magn Mater* [Internet]. 1979 Sep;13(1–2):121–4. Available from: [<URL>](#).

15. Lei S, Wang C, Guo D, Gao X, Cheng D, Zhou J, et al. Synthesis and magnetic properties of MNb_2O_6 (M= Fe, Co, Ni) nanoparticles. *RSC Adv* [Internet]. 2014 Oct 13;4(95):52740–8. Available from: [<URL>](#).

16. Xu Y, Wang LS, Huang YY, Ni JM, Zhao CC, Dai YF, et al. Quantum Critical Magnetic Excitations in Spin-1/2 and Spin-1 Chain Systems. *Phys Rev X* [Internet]. 2022 Apr 26;12(2):021020. Available from: [<URL>](#).

17. Ringler JA, Kolesnikov AI, Ross KA. Single-ion properties of the transverse-field Ising model material CoNb_2O_6 . *Phys Rev B* [Internet]. 2022 Jun 27;105(22):224421. Available from: [<URL>](#).

18. Erdem R, İlhan M, Ekmekçi MK, Erdem Ö. Electrospinning, preparation and photoluminescence properties of $\text{CoNb}_2\text{O}_6:\text{Dy}^{3+}$ incorporated polyamide 6 composite fibers. *Appl Surf Sci* [Internet]. 2017 Nov;421:240–6. Available from: [<URL>](#).

19. Ekmekçi MK, İlhan M, Güleriyüz LF, Mergen A. Study on molten salt synthesis, microstructural determination and white light emitting properties of $\text{CoNb}_2\text{O}_6:\text{Dy}^{3+}$ phosphor. *Optik (Stuttg)* [Internet]. 2017 Jan;128:26–33. Available from: [<URL>](#).

20. İlhan M, Güleriyüz LF, Ekmekçi MK. Structural Properties, Photoluminescence, and Judd-Ofelt Parameters of Eu^{3+} -Doped CoNb_2O_6 Phosphor. *J Turkish Chem Soc Sect A Chem* [Internet]. 2023 Aug 30;10(3):745–56. Available from: [<URL>](#).

21. Ekmekçi MK, Erdem M, Başak AS. Molten salt synthesis, visible and near-IR region spectral properties of europium or neodymium doped CoNb_2O_6 columbite niobate. *Dalt Trans* [Internet]. 2015;44(12):5379–85. Available from: [<URL>](#).

22. Singh N, Kumar K, Singh P. Synthesis of single phase Ti^{4+} substituted Trirutile CoNb_2O_6 Ceramic: evolution of Relaxor type ferroelectricity and high k dielectricity. *J*

Electroceramics [Internet]. 2023 Oct 18;51(2):133–45. Available from: [<URL>](#).

23. Zhang Y, Liu S, Zhang Y, Xiang M. Microwave dielectric properties of low-fired CoNb_2O_6 ceramics with B_2O_3 addition. *J Mater Sci Mater Electron* [Internet]. 2016 Nov 29;27(11):11293–8. Available from: [<URL>](#).

24. Liu F, Wang B, Yang X, Guan Y, Sun R, Wang Q, et al. High-temperature stabilized zirconia-based sensors utilizing MNb_2O_6 (M: Co, Ni and Zn) sensing electrodes for detection of NO_2 . *Sensors Actuators B Chem* [Internet]. 2016 Sep;232:523–30. Available from: [<URL>](#).

25. Balamurugan C, Maheswari AR, Lee DW. Structural, optical, and selective ethanol sensing properties of p-type semiconducting CoNb_2O_6 nanopowder. *Sensors Actuators B Chem* [Internet]. 2014 Dec;205:289–97. Available from: [<URL>](#).

26. Liang T, Koochpayeh SM, Krizan JW, McQueen TM, Cava RJ, Ong NP. Heat capacity peak at the quantum critical point of the transverse Ising magnet CoNb_2O_6 . *Nat Commun* [Internet]. 2015 Jul 6;6(1):7611. Available from: [<URL>](#).

27. Hanawa T, Shinkawa K, Ishikawa M, Miyatani K, Saito K, Kohn K. Anisotropic Specific Heat of CoNb_2O_6 in Magnetic Fields. *J Phys Soc Japan* [Internet]. 1994 Jul 15;63(7):2706–15. Available from: [<URL>](#).

28. Zhang X, Wang B, Huang W, Chen Y, Wang G, Zeng L, et al. Synergistic Boron Doping of Semiconductor and Dielectric Layers for High-Performance Metal Oxide Transistors: Interplay of Experiment and Theory. *J Am Chem Soc* [Internet]. 2018 Oct 3;140(39):12501–10. Available from: [<URL>](#).

29. Mazumder R, Seal A, Sen A, Maiti HS. Effect of Boron Addition on the Dielectric Properties of Giant Dielectric $\text{CaCu}_3\text{Ti}_4\text{O}_{12}$. *Ferroelectrics* [Internet]. 2005 Oct;326(1):103–8. Available from: [<URL>](#).

30. Li Z, Zhou W, Su X, Luo F, Huang Y, Wang C. Effect of boron doping on microwave dielectric properties of SiC powder synthesized by combustion synthesis. *J Alloys Compd* [Internet]. 2011 Jan;509(3):973–6. Available from: [<URL>](#).

31. İlhan M, Güleriyüz LF. Boron doping effect on the structural, spectral properties and charge transfer mechanism of orthorhombic tungsten bronze $\beta\text{-SrTa}_2\text{O}_6:\text{Eu}^{3+}$ phosphor. *RSC Adv* [Internet]. 2023;13(18):12375–85. Available from: [<URL>](#).

32. İlhan M, Ekmekçi MK, Güleriyüz LF. Effect of boron incorporation on the structural, morphological, and spectral properties of $\text{CdNb}_2\text{O}_6:\text{Dy}^{3+}$ phosphor synthesized by molten salt process. *Mater Sci Eng B* [Internet]. 2023 Dec;298:116858. Available from: [<URL>](#).

33. Başak AS, Ekmekçi MK, Erdem M, İlhan M, Mergen A. Investigation of Boron-doping Effect on Photoluminescence Properties of $\text{CdNb}_2\text{O}_6:\text{Eu}^{3+}$ Phosphors. *J Fluoresc* [Internet]. 2016 Mar 11;26(2):719–24. Available from: [<URL>](#).



34. Ekmekçi MK, İlhan M, Ege A, Ayvacıklı M. Microstructural and Radioluminescence Characteristics of Nd^{3+} Doped Columbite-Type SrNb_2O_6 Phosphor. *J Fluoresc* [Internet]. 2017 May 13;27(3):973–9. Available from: [<URL>](#).

35. İlhan M, Ekmekçi MK. Synthesis and photoluminescence properties of Dy^{3+} doped white light emitting CdTa_2O_6 phosphors. *J Solid State Chem* [Internet]. 2015 Mar;226:243–9. Available from: [<URL>](#).

36. Tan YQ, Yu Y, Hao YM, Dong SY, Yang YW. Structure and dielectric properties of $\text{Ba}_5\text{NdCu}_{1.5}\text{Nb}_{8.5}\text{O}_{30-\delta}$ tungsten bronze ceramics. *Mater Res Bull* [Internet]. 2013 May;48(5):1934–8. Available from: [<URL>](#).
37. Esha IN, Al-Amin M, Toma FTZ, Hossain E, Khan MNI, Maria KH. Synthesis and analysis of the influence of Eu^{3+} on the structural, ferromagnetic, dielectric and conductive characteristics of $\text{Ni}_{0.4}\text{Zn}_{0.45}\text{Cu}_{0.15}\text{Fe}_{(2-x)}\text{Eu}_x\text{O}_4$ composites using conventional double sintering ceramic method. *J Ceram Process Res* [Internet]. 2019 Oct;20(5):530–9. Available from: [<URL>](#).
38. Shah MR, Akther Hossain AKM. Structural and dielectric properties of La substituted polycrystalline $\text{Ca}(\text{Ti}_{0.5}\text{Fe}_{0.5})\text{O}_3$. *Mater Sci* [Internet]. 2013 Jan 25;31(1):80–7. Available from: [<URL>](#).
39. Bettinelli M, Speghini A, Seliman SI, Battisha IK. Structural and dielectrical properties of nano-structure BaTiO_3 powders doped with Eu^{3+} ions prepared by sol-gel process. *Fiz A a J Exp Theor Phys* [Internet]. 2004 Mar 1;13(1):11–22. Available from: [<URL>](#).
40. Kim L, Jung D, Kim J, Kim YS, Lee J. Strain manipulation in $\text{BaTiO}_3/\text{SrTiO}_3$ artificial lattice toward high dielectric constant and its nonlinearity. *Appl Phys Lett* [Internet]. 2003 Mar 31;82(13):2118–20. Available from: [<URL>](#).
41. Feng L, Ye ZG. Phase Diagram and Phase Transitions in the Relaxor Ferroelectric $\text{Pb}(\text{Fe}_{2/3}\text{W}_{1/3})\text{O}_3\text{-PbTiO}_3$ System. *J Solid State Chem* [Internet]. 2002 Feb;163(2):484–90. Available from: [<URL>](#).
42. Wagner KW. Zur Theorie der unvollkommenen Dielektrika. *Ann Phys* [Internet]. 1913 Jan 14;345(5):817–55. Available from: [<URL>](#).
43. Maxwell JC. A treatise on electricity and magnetism. London: Caleredon press, Oxford University; 1873.
44. Kadam AA, Shinde SS, Yadav SP, Patil PS, Rajpure KY. Structural, morphological, electrical and magnetic properties of Dy doped Ni–Co substitutional spinel ferrite. *J Magn Magn Mater* [Internet]. 2013 Mar;329:59–64. Available from: [<URL>](#).
45. Yuan WX, Luo Z, Wang C. Investigation on effects of CuO secondary phase on dielectric properties of $\text{CaCu}_3\text{Ti}_4\text{O}_{12}$ ceramics. *J Alloys Compd* [Internet]. 2013 Jun;562:1–4. Available from: [<URL>](#).
46. Zheng Q, Fan H, Long C. Microstructures and electrical responses of pure and chromium-doped $\text{CaCu}_3\text{Ti}_4\text{O}_{12}$ ceramics. *J Alloys Compd* [Internet]. 2012 Jan;511(1):90–4. Available from: [<URL>](#).
47. Liu L, Chen Y, Feng Z, Wu H, Zhang X. Crystal structure, infrared spectra, and microwave dielectric properties of the EuNbO_4 ceramic. *Ceram Int* [Internet]. 2021 Feb;47(3):4321–6. Available from: [<URL>](#).
48. Gul IH, Maqsood A. Influence of Zn–Zr ions on physical and magnetic properties of co-precipitated cobalt ferrite nanoparticles. *J Magn Magn Mater* [Internet]. 2007 Sep;316(1):13–8. Available from: [<URL>](#).
49. Ganguly P, Jha AK. Enhanced characteristics of $\text{Ba}_5\text{SmTi}_3\text{Nb}_7\text{O}_{30}$ ferroelectric nanocrystalline ceramic prepared by mechanical activation process: A comparative study. *Mater Res Bull* [Internet]. 2011 May;46(5):692–7. Available from: [<URL>](#).
50. Sati PC, Kumar M, Chhoker S, Jewariya M. Influence of Eu substitution on structural, magnetic, optical and dielectric properties of BiFeO_3 multiferroic ceramics. *Ceram Int* [Internet]. 2015 Mar;41(2):2389–98. Available from: [<URL>](#).
51. Chakrabarti A, Bera J. Effect of La-substitution on the structure and dielectric properties of $\text{BaBi}_4\text{Ti}_4\text{O}_{15}$ ceramics. *J Alloys Compd* [Internet]. 2010 Sep;505(2):668–74. Available from: [<URL>](#).
52. Kumar P, Kar M. Effect of structural transition on magnetic and optical properties of Ca and Ti co-substituted BiFeO_3 ceramics. *J Alloys Compd* [Internet]. 2014 Jan;584:566–72. Available from: [<URL>](#).
53. Kendall KR, Thomas JK, Loye HC. Synthesis and ionic conductivity of a new series of modified Aurivillius phases. *Chem Mater* [Internet]. 1995 Jan 1;7(1):50–7. Available from: [<URL>](#).



Phytochemical, Pharmacological, Phyto-cosmeceutical, Toxicity, and *In silico* Toxicological Evaluations of *Vernonia amygdalina* Delile – A Review

Olubunmi ATOLANI¹ , Priyanka BANERJEE², Adedamola Elizabeth AYENI¹, Muhammed Abubakar USMAN¹, Opeyemi Jamiu ADEJUMO¹, Ochuko L. ERUKAINURE³, Robert PREISSNER², Jean Baptiste SOKOUDJOU⁴, Mary Olufunmilayo OLOGE⁵, Muhammad Torequl ISLAM⁶, Oluoyomi Stephen ADEYEMI⁷, Ifeoluwa Samuel ADEDOTUN^{1,8} 

¹Department of Chemistry, University of Ilorin, PMB 1515, Ilorin, Nigeria

²Institute of Physiology, Charite University of Medicine, Berlin 10117, Germany

³Department of Pharmacology, University of the Free State, Bloemfontein 9300, South Africa

⁴Research Unit of Microbiology and Antimicrobial substances, Faculty of Science, University of Dschang, P.O. Box 67, Dschang, Cameroon.

⁵Department of Pharmacology and Therapeutics, University of Ilorin, Ilorin, Nigeria

⁶Department of Pharmacy, Life Science Faculty, Bangabandhu Sheikh Mujibur Rahman Science and Technology University, Gopalganj-8100, Bangladesh

⁷Department of Biochemistry, Medicinal Biochemistry, Infectious Diseases, Nanomedicine & Toxicology Laboratory, Landmark University, PMB 1001, Omu-Aran 251101, Kwara State, Nigeria.

⁸Department of Pure and Applied Chemistry, Osun State University, P.M.B 4494, Osogbo, Nigeria.

Abstract: *Vernonia amygdalina* Delile, which is in the Asteraceae family, is used as food and medicine all over the world, especially in Africa and Asia. This review reports the phytochemical, ethnopharmacological, phyto-cosmeceutical, and toxicological potentials of the plant. Recent scientific exploration of the plant has mainly focused on both its nutritional potential and ethnopharmacological properties. The antioxidant, anti-inflammatory, antidiabetic, hepatoprotective, hematological, anti-plasmodial, antimicrobial, anticancer, neurological, cosmeceutical, and other pharmacological values of *V. amygdalina* continue to be extensively explored. Many empirical studies of the therapeutic potential of the plant have attributed the ethnomedicinal properties of the plant to its phytochemical constituents, which include glycosides, saponins, tannins, terpenoids, etc. Compounds obtained from the leaves, root, stem, and flowers, which include vernoniosides, vernoamiosides, vernoniomyosides, vernoniosides, vernolide, vernodalol, vernodalol, vernomenin, vernomygdin, vernodalinol, epivernodalol, vernolepin, coumarins, luteolin, edotides, etc. have been identified as bioactive constituents responsible for numerous pharmacological activities of the plant. In addition, the toxicological evaluation of the plant revealed that it is safe for consumption at relatively high concentrations.

Keywords: Medicinal plant; nutraceuticals; antidiabetic; antioxidant; vemoniosides; bioactives

Submitted: February 04, 2023. **Accepted:** September 12, 2023.

Cite this: Atolani O, Banerjee P, Ayeni AE, Usman MA, Adejumo OJ, Erukainure OL, et al. Phytochemical, Pharmacological, Phyto-cosmeceutical, Toxicity, and *In silico* Toxicological Evaluations of *Vernonia amygdalina* Delile – A Review. JOTCSA. 2024;11(2):775-802.

DOI: <https://doi.org/10.18596/jotcsa.1247620>.

***Corresponding authors. E-mails:** ifeoluwa.adedotun@uniosun.edu.ng, atolani.o@unilorin.edu.ng

1. INTRODUCTION

Medicinal plants form the fulcrum of folk medicine due to their numerous economic, pharmacological, nutritional, and tremendous health benefits to humans. The utilization and relevance of medicinal plants, particularly in the drug development and food industries, cannot be overemphasized. Their medicinal and pharmacological properties have been

attributed to the presence of phytoconstituents, which are typically bioactive compounds capable of producing definite physiological action in humans (1). Since ancient practice, medicinal plants have been adopted ethnobotanically for medicine, food, clothing, hunting, and, in some religious ceremonies, even though their primary use has been for health care (2). Different parts of medicinal plants have been used to cure specific ailments.

Recently, a gradual renewal of interest in the use of medicinal plants in developing countries was rekindled because herbal medicines are reported to be safe and have fewer adverse side effects when carefully prepared in comparison with conventional drugs (1, 2). Among the edible plants whose parts are highly valued in ethnomedicine is *V. amygdalina* (Figure 1).

V. amygdalina, a tree or shrub of the family Asteraceae and genus *Vernonia*, is well known in the tropics, particularly in Africa and Asia. The perennial plant is characterized by the bitter taste of the sap from the leaf, and this has been widely explored for its ethnobotanical applications in traditional medicine (3, 4). The plant has been found to be rich in minerals, especially phosphorus, calcium, potassium, magnesium, zinc, iron, and vitamins A, C, and E. Scientific and pharmacological studies have revealed the antihyperglycemic action of the roots of *V. amygdalina* (5). In addition, there is an increasing dependence on the use of this medicinal plant, as bioactives are prepared as nutraceuticals and chemotherapeutics for conventional applications (2). In addition, findings have suggested that the plant is a reservoir for potent phytochemicals of pharmaceutical importance (6). The overall therapeutic properties of plants are often based on the phytochemical constituents of the plant (7, 8).

V. amygdalina extracts are traditionally used as an antidiabetic, anti-helminthic, antimalarial, laxative, digestive tonic, appetizer, and febrifuge agents (4, 9). In some African countries, including Ethiopia, *V. amygdalina* is among the medicinally significant plants used against malaria, helminth infections, gastrointestinal disorders, and fever. This species is also used to promote wound healing and treat microbial infections (9). The main bioactive constituents of the leaves were reported as sesquiterpene lactones. Some of them include

vernonioside A1, vernonioside A2, vernonioside B1, vernonioside B2, vernodalin, vernolepin, vernomygdin, vernodalol, and vernodalinol (10).



© authors

Figure 1: Photograph of *V. amygdalina*.

2. BOTANICAL OVERVIEW

V. amygdalina of the family Asteraceae or Compositae is an African and Asia renowned shrub or tree with valuable medicinal principles. The plant, otherwise called bitter leaf, is well known in countries that include Cameroon, Nigeria, Egypt, Uganda, Tanzania, and others where it thrives around water paths, forest zones, and home plantations (11). In Africa, the rough brown bark plant often reaches a height of 7 m as the semioblong leaves attain an average size of 10 x 4 cm. The plant produces off-white to cream-colored clusters of flowers that are axillary and terminal with sweet smell (11). The taxonomic classification of *V. amygdalina* is presented in Table 1.

Table 1: Taxonomical classification of *V. amygdalina*.

Classification	Taxonomy
Kingdom	Plantae
Clade	Angiospermae
Order	Asterales
Family	Asteraceae
Genus	<i>Vernonia</i>
Species	<i>V. amygdalina</i>

3. ETHNOBOTANICAL AND MEDICINAL USES

In Africa, *V. amygdalina* is adopted for various ethnobotanical and medicinal purposes on account of economic reasons (12). During childbirth, the leaf aqueous extract orally administered is used to induce overdue labor as a result of its capability to stimulate uterine motility (11). Parasites such as ringworms are expelled by applying leaf extract, which is also used to control various infections when taken orally (11). In addition, leaf decoction has been used to manage coughs and colds as well as enhance milking in lactating women. The leaf is notable for its culinary purpose as well. As a staple

vegetable, it is often used for the preparation of special soup and stew in Africa. The soup prepared from the leaf is consumed as both food and medicine (13). *V. amygdalina* contains both major and trace elements that are responsible for some of the observed pharmacological properties (14).

Stem and root bark are used as chewing sticks in some parts of Africa to serve as cleansing agents and antimicrobial agents in oral applications. Antihelminthic, antimalarial, and anti-tumorigenic properties have been properly reported for extracts from this plant. Other studies have demonstrated hypoglycaemic and hypolipidaemic effects of leaf

extract in experimental animals (4). Since ancient times, medicinal plants such as *V. amygdalina* have been widely used in traditional medicine for the prevention and curation of various disease conditions due to their potency, affordability, and ready availability (15).

V. amygdalina has also been used in human and veterinary medicine against several pathological infections (16). In the ancient world, ill chimpanzees were known to suck the stalk of the plant to derive some health remedies while enhancing their body fitness, lost strength, or appetite. Stalk juice is also known to reduce indigestion or bowel looseness in animals. Likewise, birds fed with the leaf extract reportedly indicated reduced mortality compared to those that were not fed with the leaf extract (11). Virtually all parts of the plant possess bioactives of pharmacological relevance in the management of various disease conditions (4, 17).

4. PHYTOCHEMISTRY

A plethora of bioactive phytochemicals have been identified in various parts of *V. amygdalina*. Several studies have reported the isolation and characterization of some bioactive compounds, such as flavonoids, saponins, alkaloids, tannins, phenolics, terpenes, steroidal glycosides, triterpenoids, and several types of sesquiterpene lactones (18-22). Some of the isolated and characterized bioactive compounds are shown (Figure 2). Sesquiterpene lactones, including vernodalol, vernolepin, vernodalinol, vernomygdin, hydroxyvernolide, and vernolide, have been identified in the plant (21, 23-25). In addition, various vernoniosides and steroidal glucosides have also been identified as major types of compounds in plants (26, 20). In fact, *V. amygdalina* is well known for its bitter taste due to the presence of vernoniosides A1, A2, A3, and A4. However, vernoniosides B1, B2, and B3, which were equally present, are not characterized by any bitter taste (27). Recently, stigmastane-type steroid saponins, including vernoniamyosides A-D, vernonioside B, and vernoamyoside D, were reportedly in *V. amygdalina* (28). Vernoamyosides A-D and

stigmastane-type steroid saponins have also been characterized as compounds isolated from the leaves of *V. amygdalina* (20).

Other steroidal saponins have been identified in the plant, with flavonoids, tannins, saponins, and triterpenoids in the plant reported to possess antioxidant and hypolipidaemic effects (10, 29-31). Igile et al. (1994) (32) accounted for the presence of the flavonoids; luteolin, luteolin 7-O- β -glucuronide, and luteolin 7-O- β -glucoside in the leaves of *V. amygdalina*. Other researchers have also affirmed the presence of flavonoids like luteolin, etc, in the plant (33-35).

Other phytochemicals present in the leaves of *V. amygdalina* include terpenes, coumarins, phenolic acids, lignans, xanthenes, phytate, alkaloids, saponins, tannins, oxalate, cardiac glycosides, and anthraquinones without cyanogenic glycosides (34, 36-39). Isorhamnetin, a flavonoid and tricosane, a hydrocarbon, were obtained in flower extracts of *V. amygdalina* (9, 40). Likewise, the presence of bioactive peptides called edotides in the leaves of *V. amygdalina* has also been reported (12, 41). Recently, compounds (Figure 2) that included 4 α -hydroxy-n-pentadecanoic acid, 10-geranylanyl-O- β -D-xyloside, 11 α -hydroxyus-5,12-dien-28-oic acid-3 α ,25-olide, 1-heneicosenol-O- β -D-glucopyranoside, glucuronolactone, and vernoniaolideglucoside were reportedly isolated from the stem bark of the plant (42,43). The phytochemicals of the plant are reportedly responsible for corrosion inhibition when applied to metals (44) and as antifungal agents (45) on surfaces. Among other phytochemicals, saponins and glycosides in the leaf are responsible for bitterness (46). Phenolic compounds identified in the plant can be grouped into flavonoids, tannins, and caffeoyl quinic acid (47). Other compounds, including phytol, stigmastadienol, α -tocopherol, and decanamide, have also been detected in the plant (48). Tannins, glycosides, and saponins have been obtained as the primary phytochemicals from the root and stem bark extracts of *V. amygdalina* (45). A summary of the phytochemicals present in *V. amygdalina* is iterated (Table 2).

Table 2: Phytochemical constituents of *V. amygdalina* and their bioactivities.

Compounds in <i>V. amygdalina</i>	Class of compound	Part of the plant	Uses	References
Vernolide	Sesquiterpene lactone	Aerial part/root/pith/leaf	Antimicrobial, antioxidant, antitumor, antiplasmodial, antischistosomal, antibacterial	(25,49)

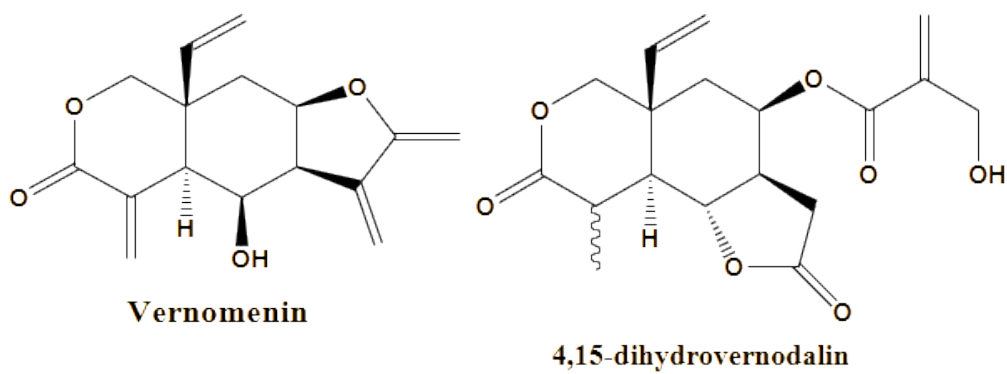
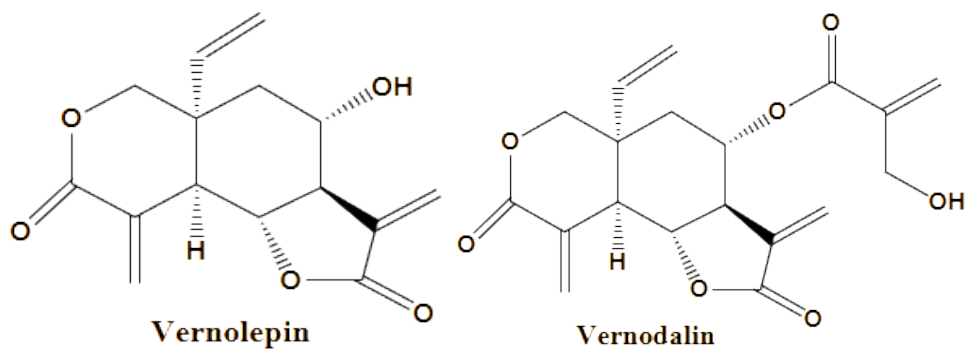
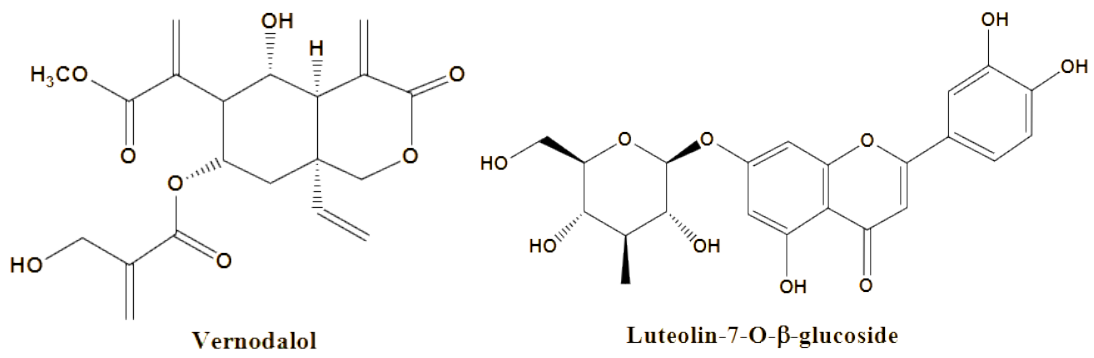
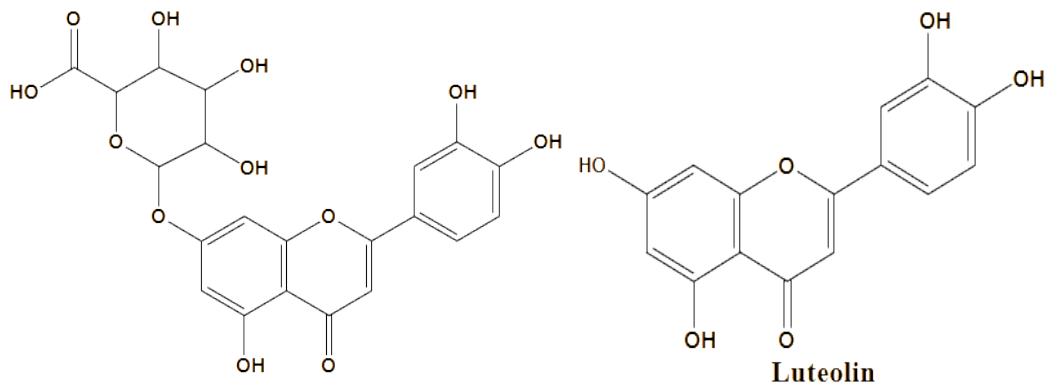
Compounds in <i>V. amygdalina</i>	Class of compound	Part of the plant	Uses	References
Vernodalol	Sesquiterpene lactone	Aerial part/root/pith/leaf	Antimicrobial, antioxidant, antitumoral, antiplasmodial, antischistosomal, antibacterial	(21,50)
Vernodalin	Sesquiterpene lactone	Aerial parts/root/leaf	Antitumor, insecticidal, antileishmanial	(24,51-53)
Vernomygdin	Sesquiterpene lactone	Aerial part	Anticancer	(21, 52, 54)
Vernodalinol	Sesquiterpene lactone	parts/root/pith	Anticancer	(21, 52, 54)
Epivernodalol	Sesquiterpene lactone	Aerial parts	Anticancer	(21, 52, 54)
Vernolepin	Sesquiterpene lactone	Aerial parts/root/pith	Antiplatelet, anticancer, antibacterial	(24, 55, 56)
Vernomenin	Sesquiterpene lactone	Aerial parts/root/pith	Anticancer, antibacterial	(51)
11,13-Dihydrovernodalol	Sesquiterpene lactone	Aerial parts/root/pith	Insecticidal	(53)
Hydroxyvernolide	Sesquiterpene lactone	Aerial parts/root/pith	Antiplasmodial, antitumor, antischistosomal, antileishmanial, antiprotozoal	(57,58)
3'Deoxyvernodalol	Sesquiterpene lactone	Aerial parts/root/pith	Anti-inflammatory and antioxidant	(49)
Luteolin	Flavonoid	Leaf/whole plant	Anticancer, antioxidant	(33, 34, 43, 59)
Luteolin 7-O- β -glucuroniside	Flavonoid	Leaf/whole plant	Antioxidant	(33, 34, 43)
Luteolin 7-O- β -glucoside	Flavonoid	Leaf/whole plant	Antioxidant	(33, 34, 43)
Isorhamnetin	Flavonoid	Flower	Antioxidant and antibacterial	(40)
Vemonioside A1	Steroid Glucoside	Leaf/stem/pith/Root	Antiplasmodial, antischistosomal	(51, 57, 60)
Vemonioside A2	Steroid Glucoside	Leaf/stem/pith/Root	Antiplasmodial, antischistosomal	(51, 57, 60)
Vemonioside A3	Steroid Glucoside	Leaf/stem/pith/Root	Antiplasmodial, antischistosomal	(51, 57, 60)
Vemonioside A4	Steroid Glucoside	Leaf/stem/pith/Root	Antiplasmodial, antischistosomal	(57, 60)
Vemonioside B1	Steroid Glucoside	Leaf/stem/pith/Root	Antiplasmodial, antischistosomal	(51, 57, 60)
Vemonioside B2	Steroid Glucoside	Leaf/stem/pith/Root	Antiplasmodial, antischistosomal, antitumor	(51, 57, 60)
Vemonioside B3	Steroid Glucoside	Leaf/stem/pith/Root	Antiplasmodial, antischistosomal	(57, 60)
Vemonioside D1	Steroid Glucoside	Leaf/stem/pith/Root	Antiplasmodial, antischistosomal	(57, 60)
Vemonioside D2	Steroid	Leaf/stem/pith/	Antiplasmodial,	(57, 60)

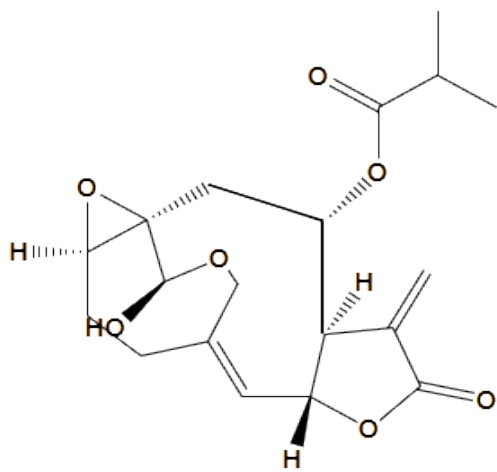
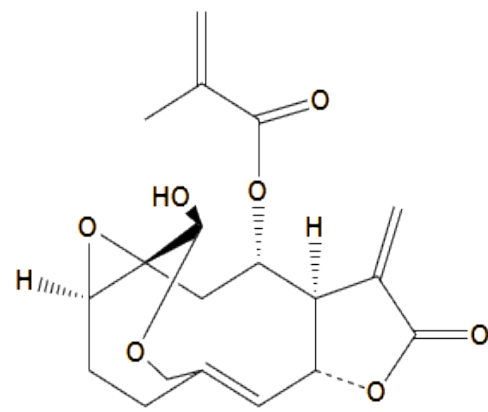
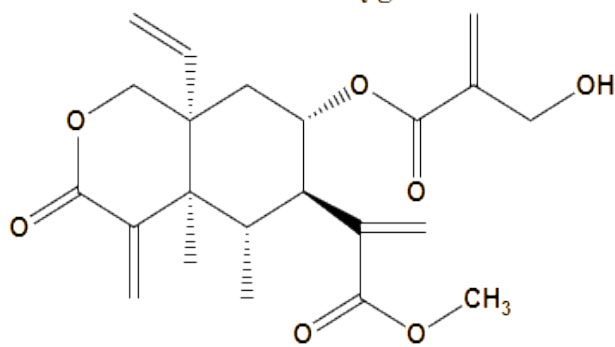
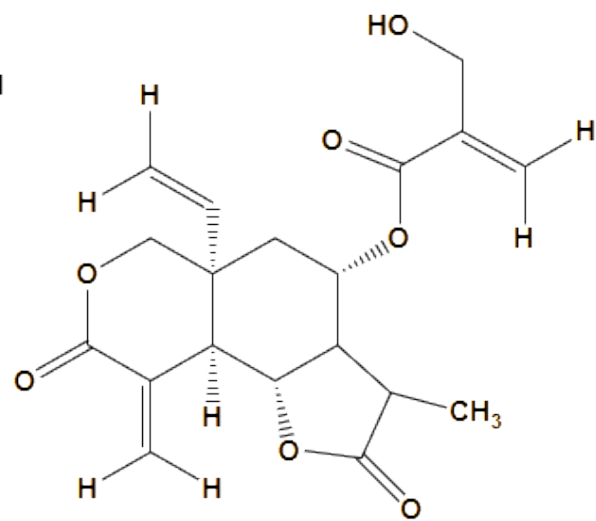
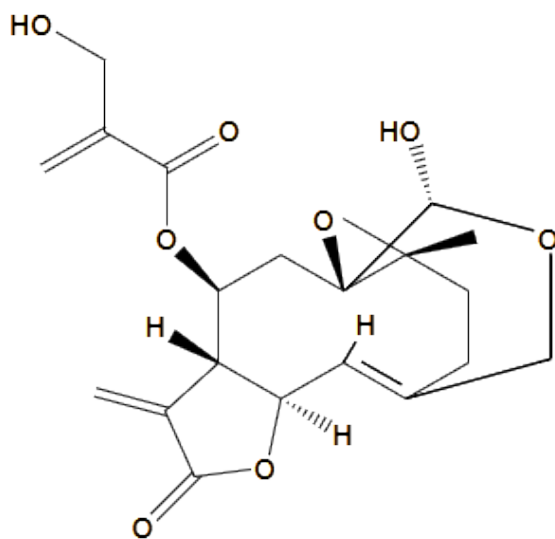
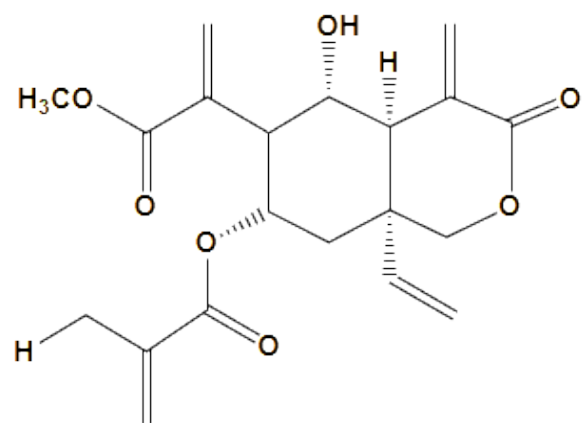
Compounds in <i>V. amygdalina</i>	Class of compound	Part of the plant	Uses	References
	Glucoside	Root	antischistosomal	
Vemonioside E	Steroid Glucoside	Leaf/stem/pith/ Root	Antiplasmodial, antischistosomal	(57, 60)
Vernoamyosides A	Steroid saponins	Leaf	Anti-inflammatory	(20)
Vernoamyosides B	Steroid saponins	Leaf	Anti-inflammatory	(20)
Vernoamyosides C	Steroid saponins	Leaf	Anti-inflammatory	(20)
Vernoamyosides D	Steroid saponins	Leaf	Anti-inflammatory, antitumor	(20, 28)
Vernoniamyoside A	Steroid saponins	Leaf	Antitumor	(28)
Vernoniamyoside B	Steroid saponins	Leaf	Antitumor	(28)
Vernoniamyoside C	Steroid saponins	Leaf	Antitumor	(28)
Vernoniamyoside D	Steroid saponins	Leaf	Antitumor	(28)
Edotides	Peptides	Leaf/root		(41,61)
4 α -Hydroxy-n-pentacanoic acid	Hydroxy fatty acid	Stem bark	Anti-plasmodial	(42)
10-geranilanyl-O- β -D-xyloside	Terpene glycoside	Stem bark	Anti-plasmodial	(42)
11 α -Hydroxy-5,12-dien-28-oic acid-3 α ,25-olide	Steroid	Stem bark	Anti-plasmodial	(42)
1-Heneicosenol-O- β -D-glucoopyranoside	Fatty acid glycoside	Stem bark	Anti-plasmodial	(42)
Vernoniaolideglucoside	Fatty-keto glycoside	Stem bark	Anti-plasmodial	(42)
Glucoronolactone	Lactone	Stem bark	Anti-plasmodial	(42)
Others	Terpenes, coumarins, phenolic acid, lignans, xanthenes, and anthraquinones	Leaf		(34)

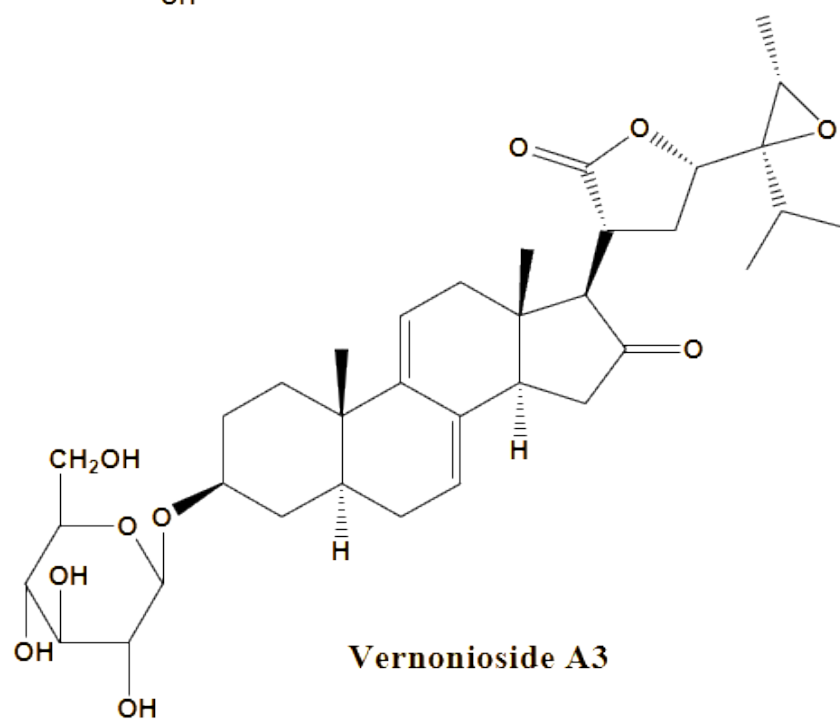
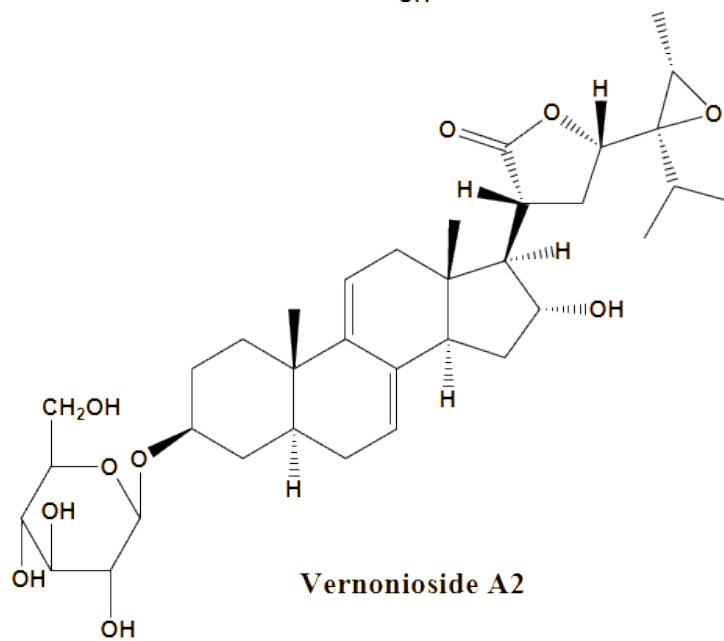
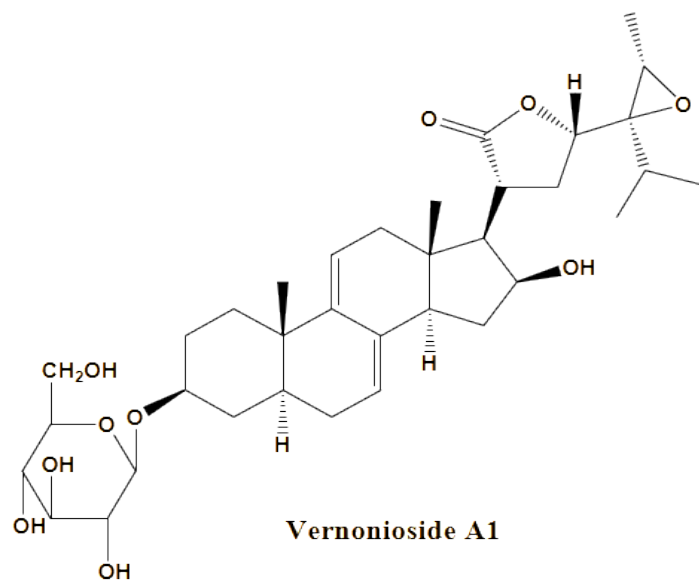
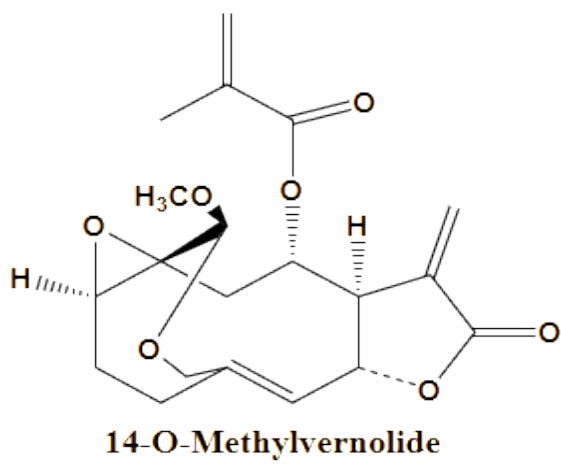
5. ESSENTIAL OIL FROM *V. amygdalina*

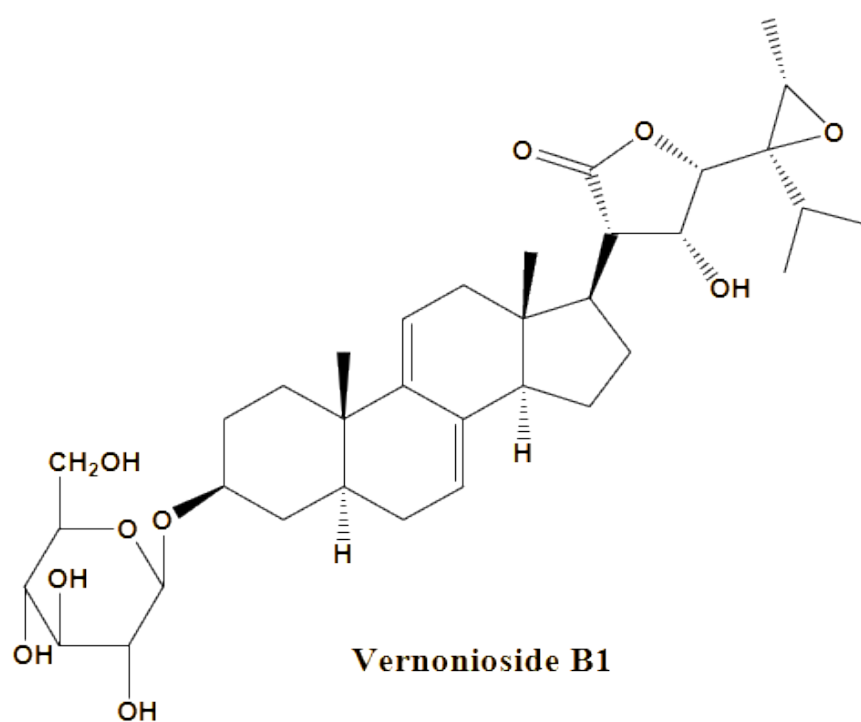
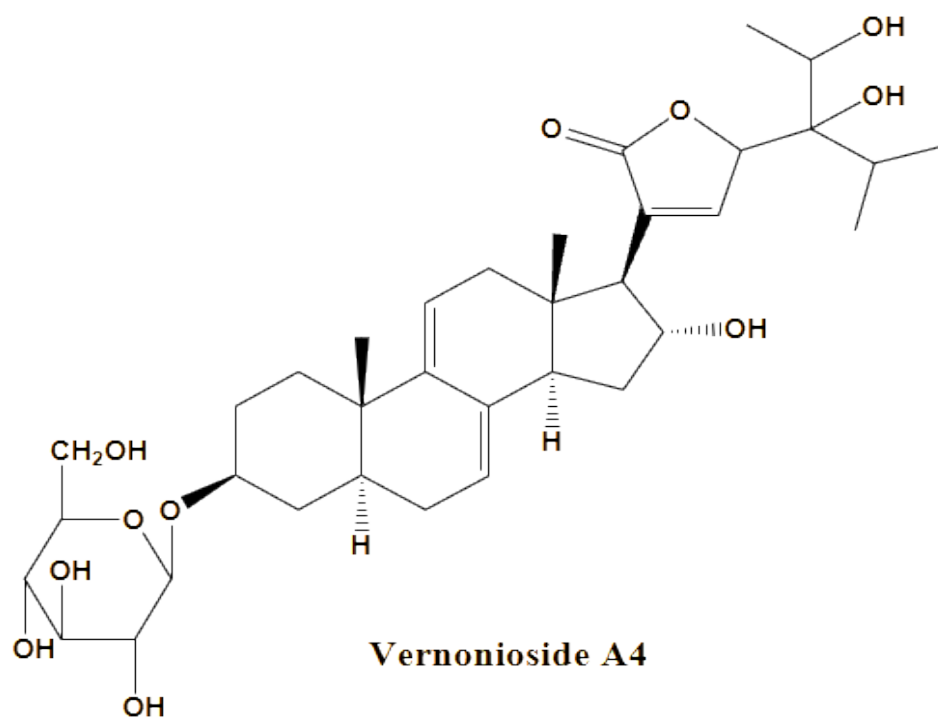
Essential oil obtained from the leaves of *V. amygdalina* via hydrodistillation contained eucalyptol (1,8-cineol, 25%), β -pinene (14.5%), and myrtenal (6.5%) as the major constituents, along with other minor constituents. α -muurolol (45.7%) was the major essential oil extracted from the aerial part (62, 63). Twenty-two percent palmitic acid, 21.5% α -linoleic acid (Omega-3) and 15.8% linoleic acid (Omega-6) were the main fatty

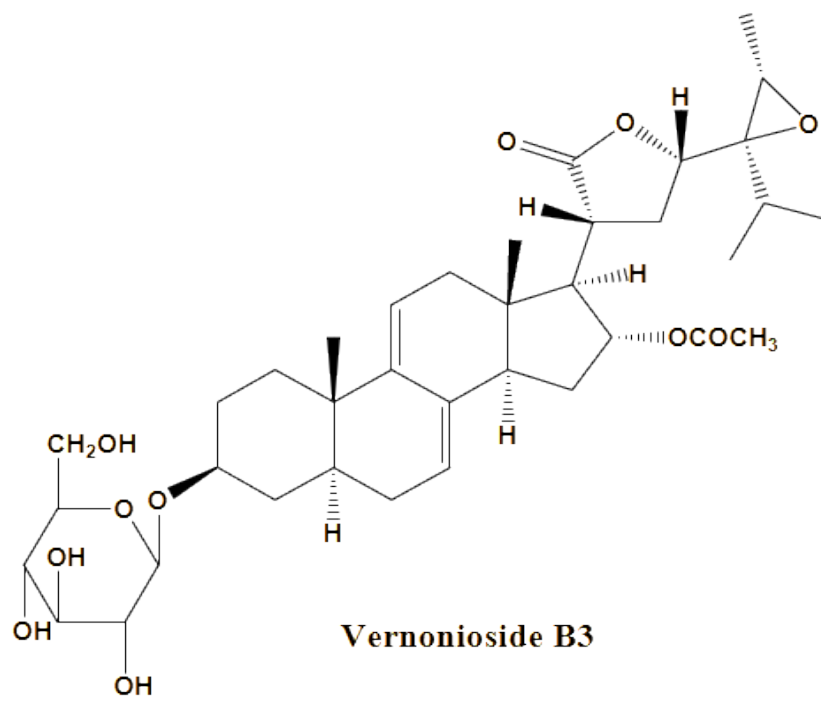
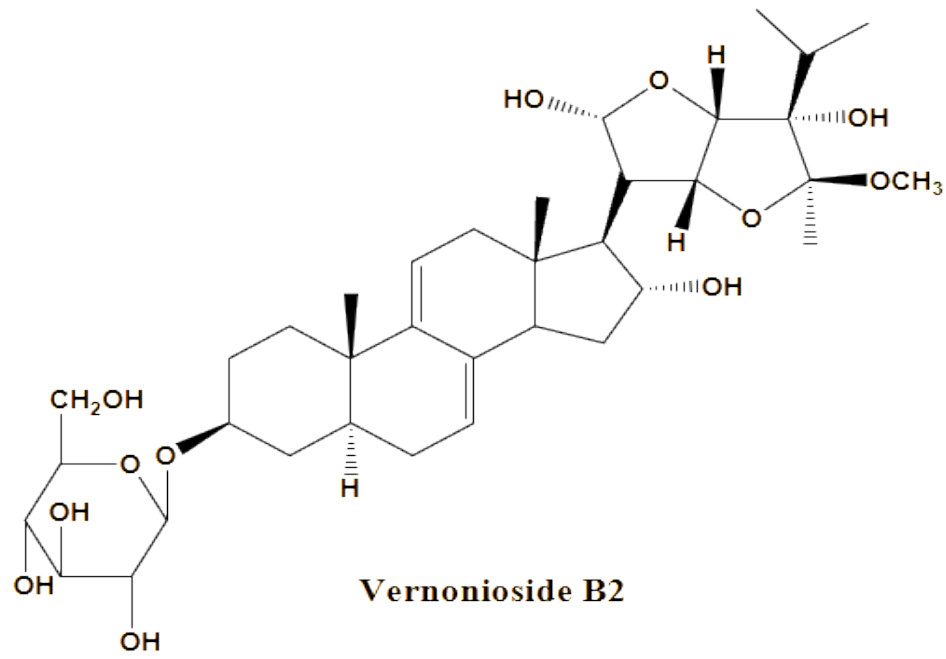
acids obtained from the hexane/isopropanol extract of *V. amygdalina* leaves (64). Furthermore, another report of the composition of the essential oil of the plant indicated that the major constituents include α -muurolol (45.7%), thymol (27.0 %), phytol (15.7 %), *o*-cymene (12.7 %), β -selinene (8.1 %), γ -terpinene (4.4 %), β -caryophyllene (3.9 %), and apiole (3.8 %) (65). While more than 40 compounds have been identified in the essential oil of the plant, the main constituent of oils from the plant obtained in Nigeria was α -muurolol (45.7%) (63).

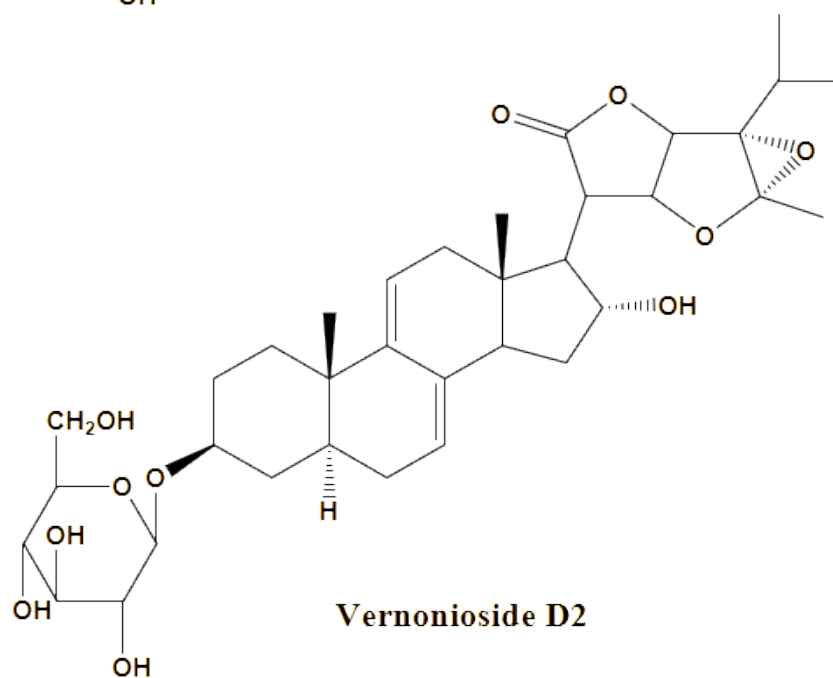
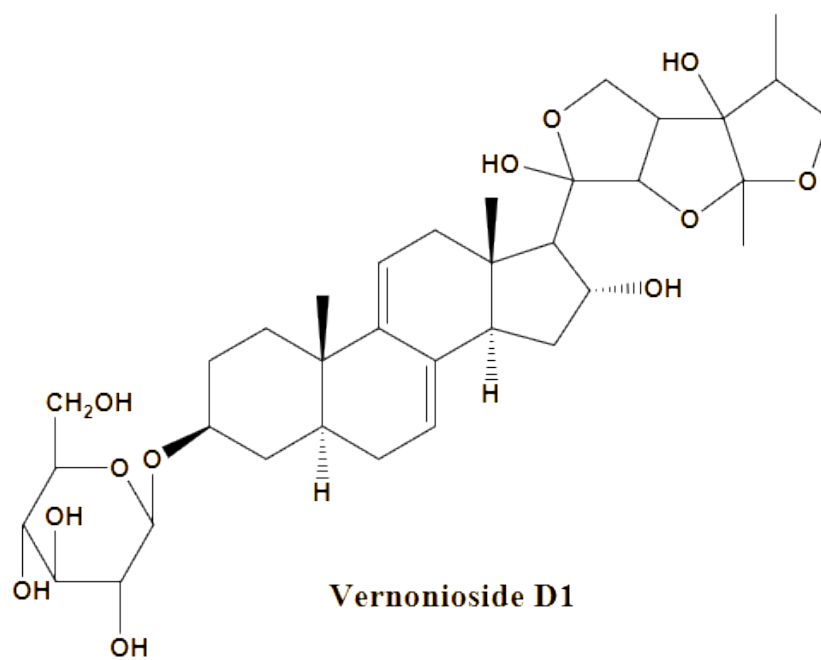


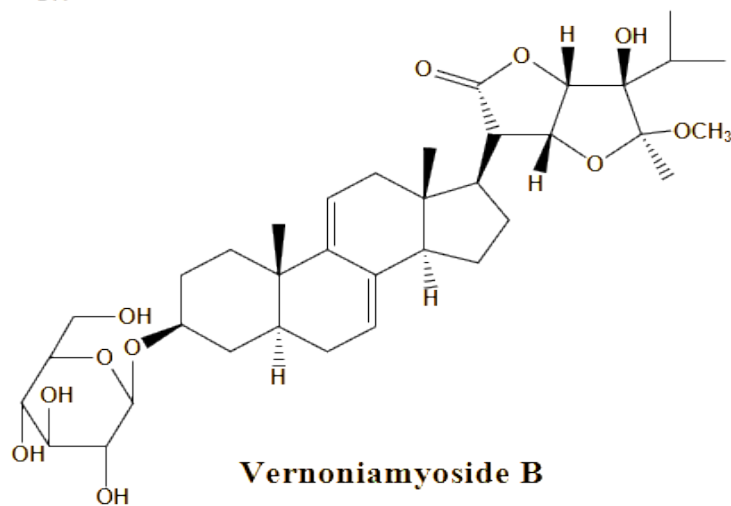
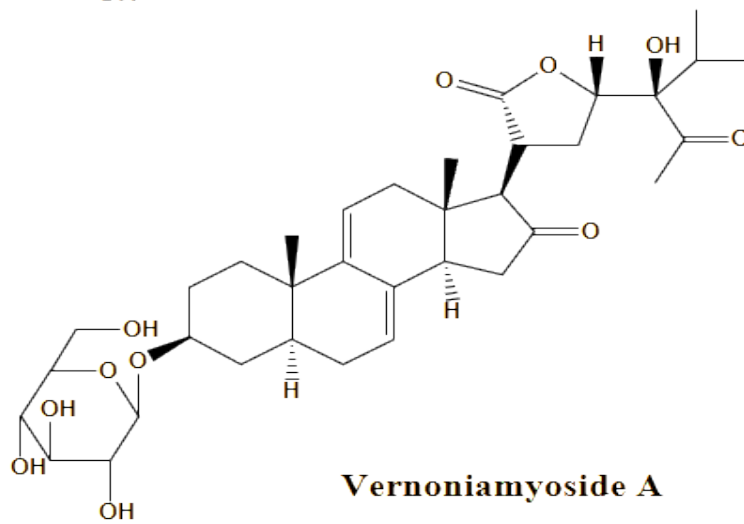
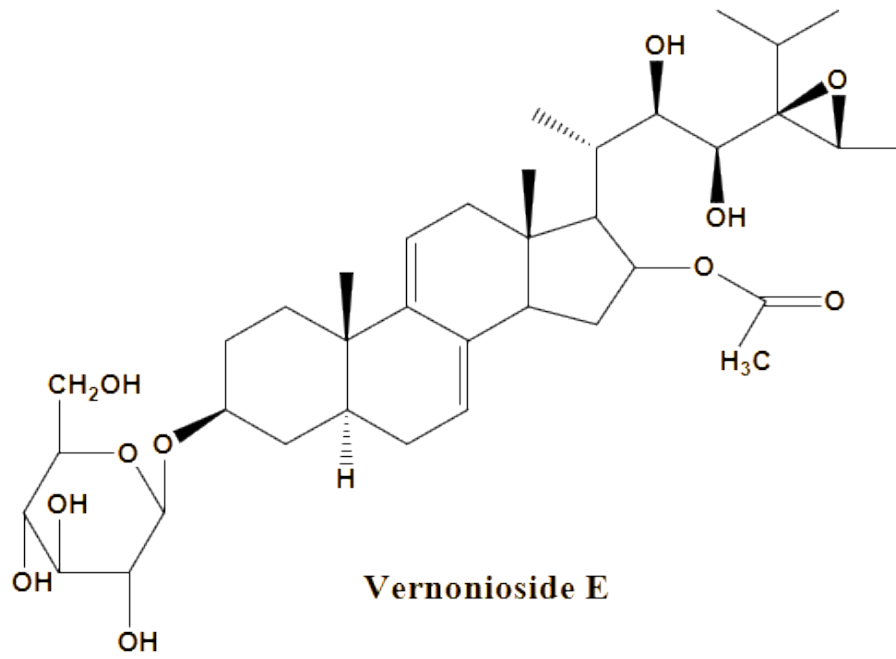
**Vernomygdin****Vernolide****Epivernodalol****11,13-dihydrovernodalol****Hydrovernolide****3'-deoxyvernodalol**

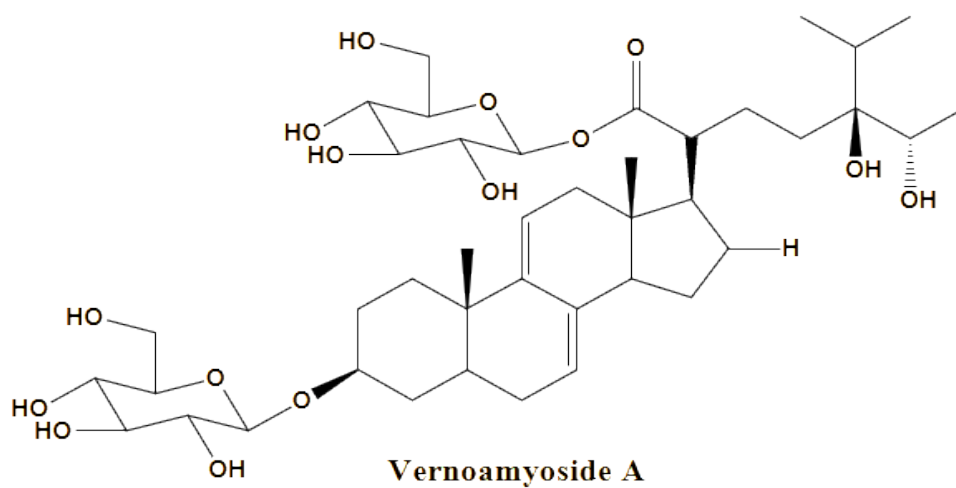
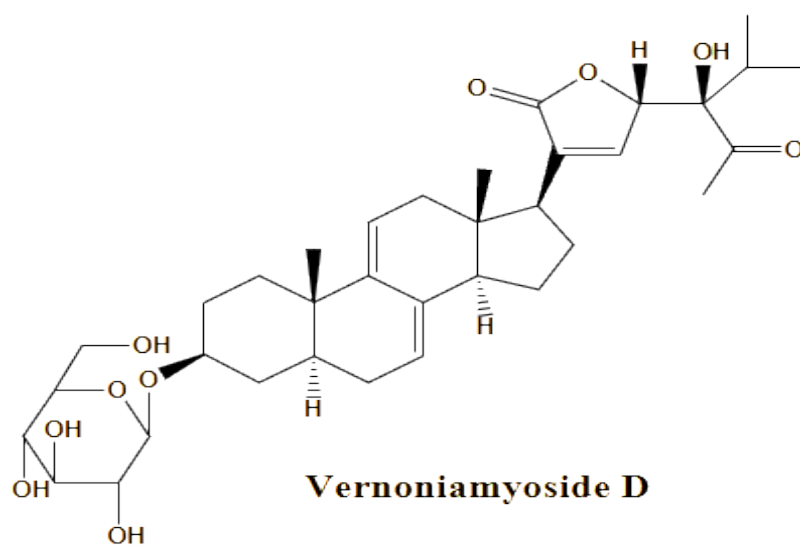
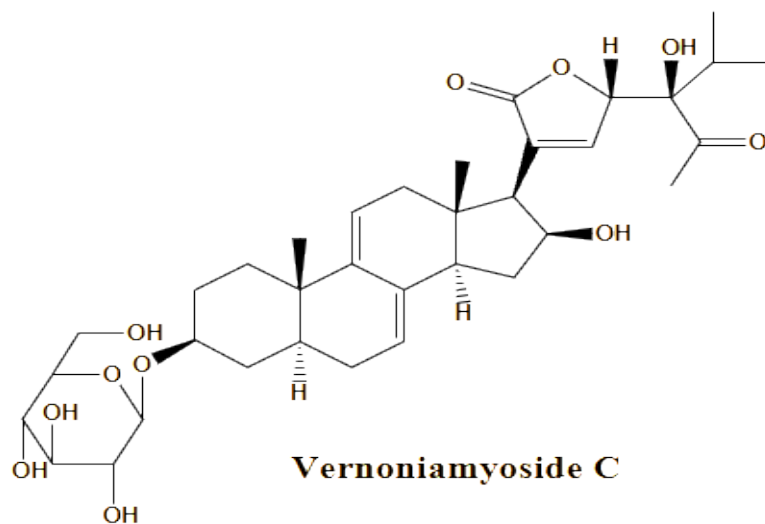


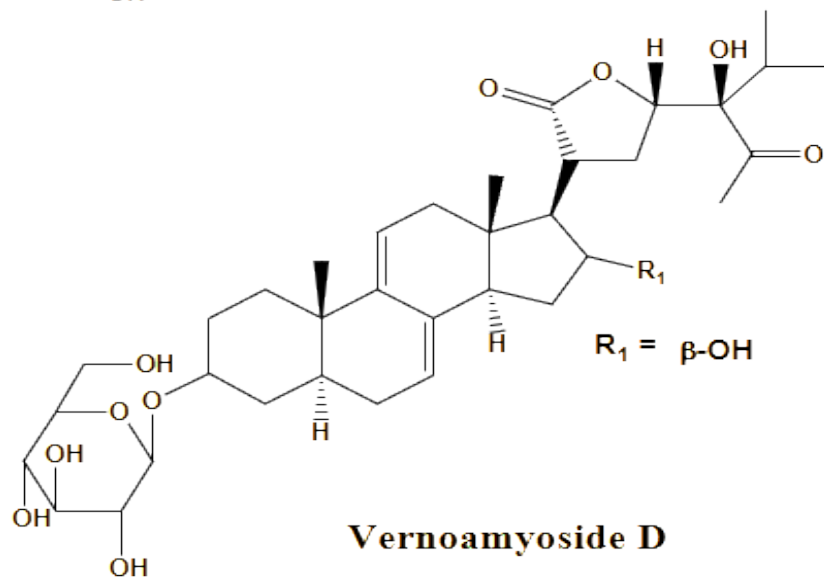
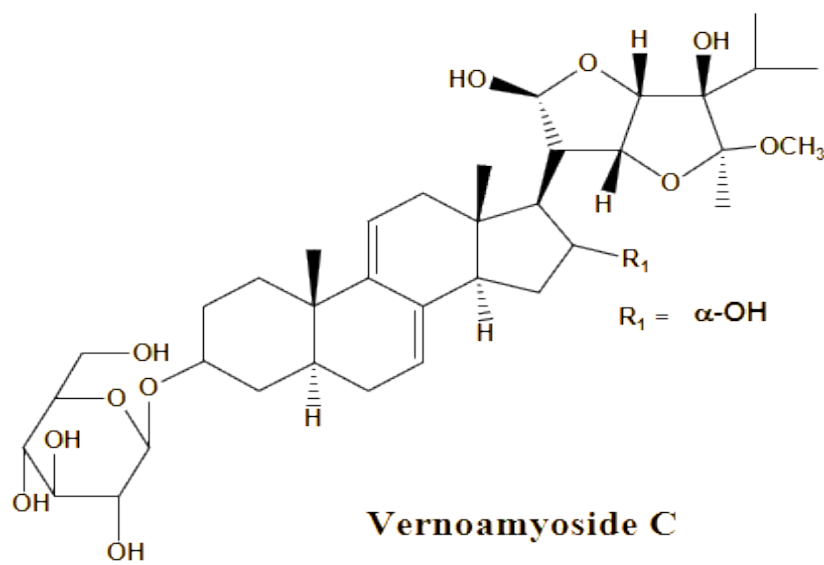
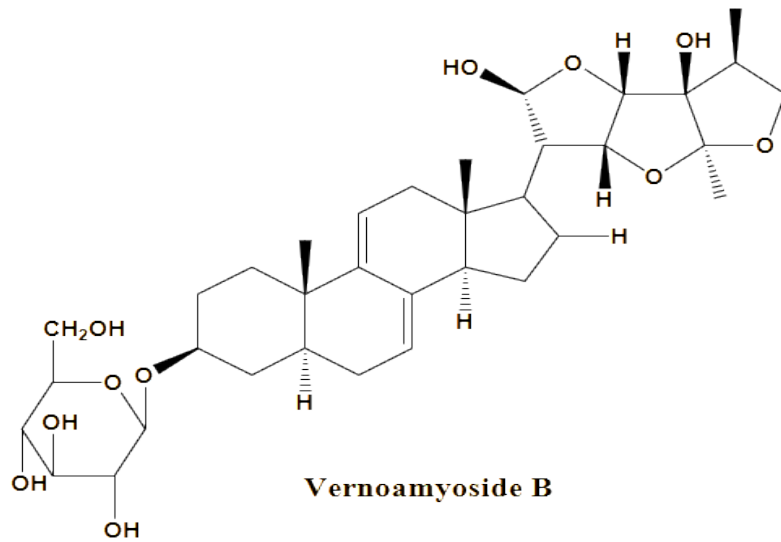


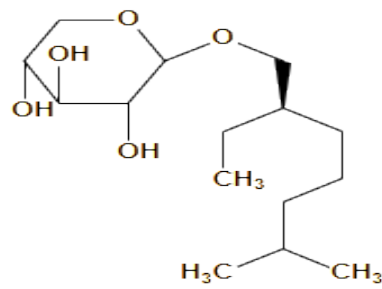
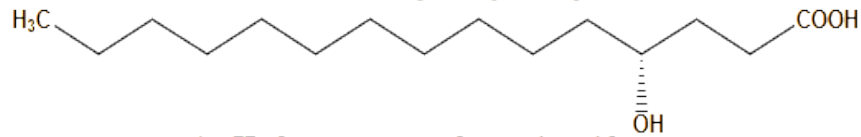
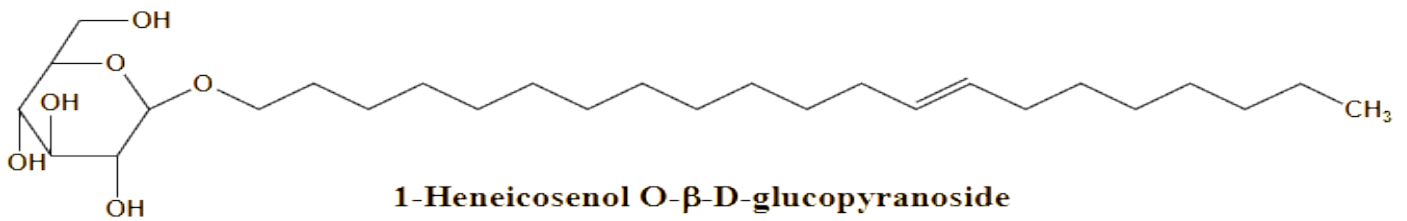
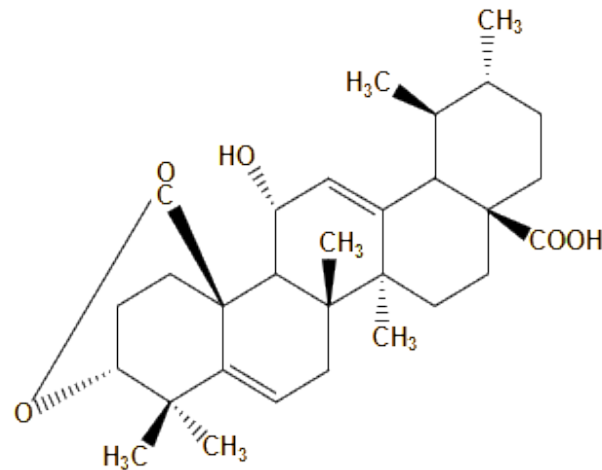
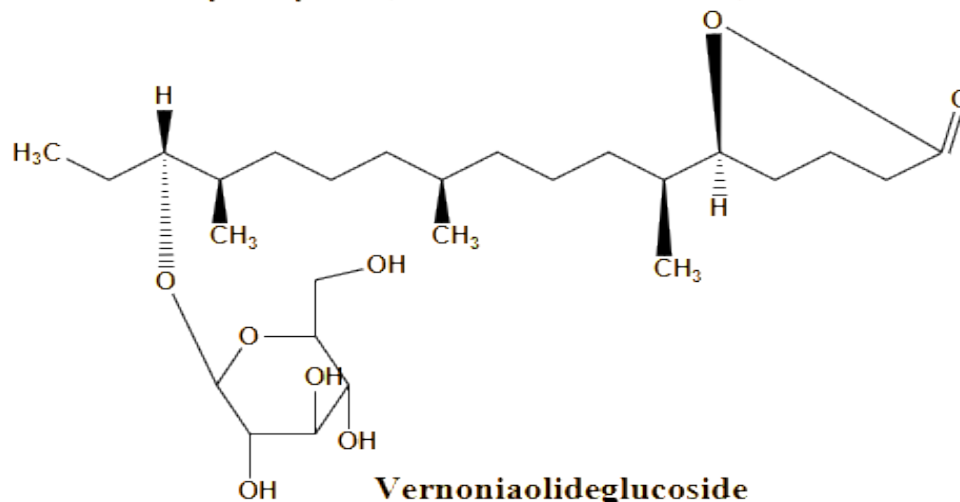










**10-Geranylanyl O- β -D-xyloside****4 α -Hydroxy-n-pentadecanoic acid****1-Heneicosenol O- β -D-glucopyranoside****11 α -Hydroxyurs-5, 12-dien-28-oic acid-3 α , 25-olide****Vernoniaolideglucoside**

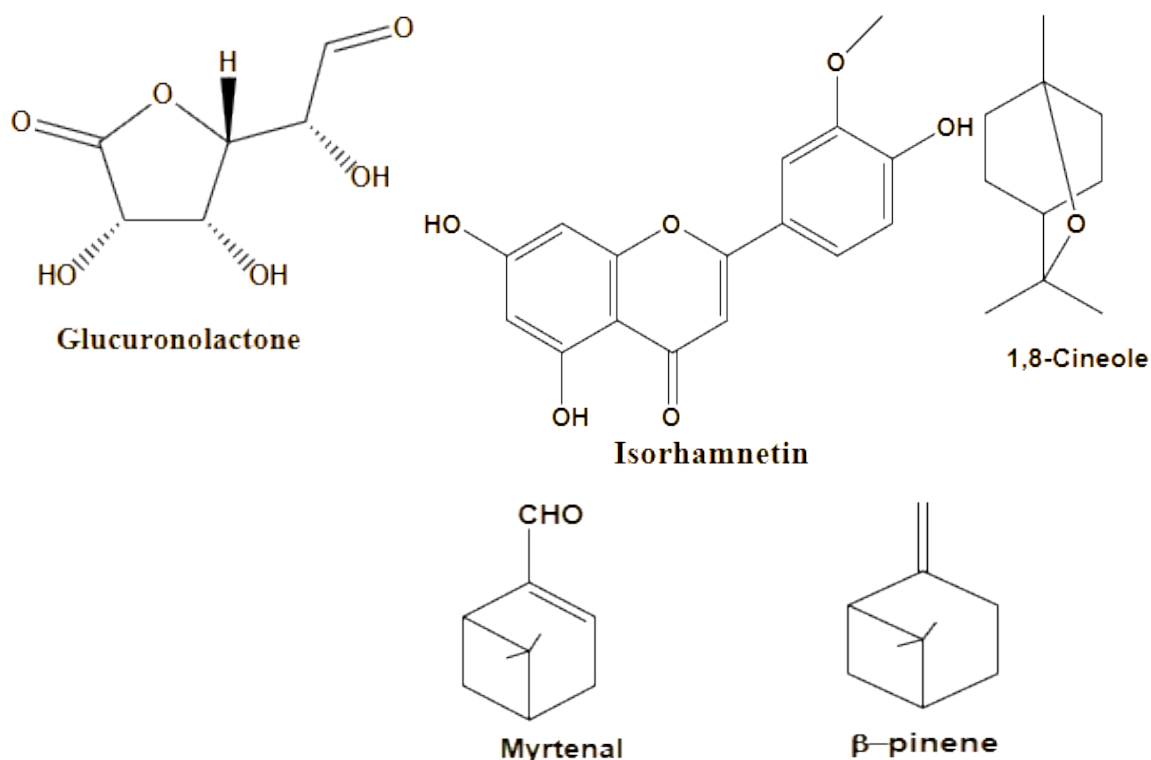


Figure 2: Structures of some phytochemicals isolated from *V. amygdalina*.

6. PHARMACOLOGICAL ACTIVITIES OF *V. amygdalina*

The pharmacological properties of *V. amygdalina* have been investigated to validate the wide traditional uses of the plant as a therapeutic agent. Several studies have indicated that *V. amygdalina* possesses anticancer, antidiabetic, antimalarial, anti-inflammatory, cathartic, hepatoprotective, antimicrobial, antioxidant, chemoprotective and cytotoxic, analgesic, anthelmintic, antipyretic, hypolipidemic, hemolytic, antimutagenic, antileishmanial, spermatogenic, antiplatelet and abortifacient activities (12, 66-68). The bioactive compounds in the plants could act independently or in synergy with each other to exert the pharmacological activities of interest or otherwise (43).

6.1. Antioxidant Activity

Since many synthetic antioxidants, such as butylated hydroxytoluene (BHT) and butylated hydroxyanisole (BHA), are suspected to be tumorigenic (69, 70), plant sources have been viable sources of antioxidants (70-75). The health-promoting activity of *V. amygdalina* is linked to the antioxidant capacity of flavonoids and luteoin. It has been reported that *V. amygdalina* glucosides luteolin 7-O- β -glucuronide and luteolin 7-O- β -glucoside possess significant antioxidant activities. Luteolin is reported as a strong antioxidant compound (32, 76). Studies have revealed that the aqueous and ethanol extracts of the plants' leaves, at about 200 mg/kg dosage, exhibit antioxidant properties, including scavenging free radicals, inhibiting the bleaching of β -carotene, and ameliorating serum malondialdehyde in both in vitro and rat models (38, 77-81).

6.2. Antidiabetic Activity

The aqueous extract of the leaves of *V. amygdalina* at about 80 mg/kg dosage has been reported to have significantly lower blood sugar (82-84). This claim was corroborated by many other reports from similar research on the plant that used various standards and *in vivo* assays (85-91). The sugar-lowering potential of the plant was observed to be independent of the mode of extract administration (92). Furthermore, the administration of the combined extracts of *V. amygdalina* and *Azadirachta indica* A. Juss. was reported to produce synergistic effects that attenuated blood glucose levels, regardless of the diabetic status of test animals (rats) (93).

The fermented extract of the plant exhibited significant antihyperglycemic potency in a rat model (94). The effect was further enhanced with the incorporation of *Ocimum gratissimum* L. leaf extract, suggesting that the potential of *V. amygdalina* leaf extract to inhibit diabetes progression could be synergistically improved with selected plant extracts.

Erukainure *et al.* (2018) examined the potential of *V. amygdalina* leaf infusion to inhibit α -glucosidase and intestinal glucose absorption (95). This inhibition was demonstrated as a potent antidiabetic mechanism, attenuating the breakdown of dietary carbohydrates and slowing the postprandial rise in blood glucose levels. The leaf infusion consequently stimulated muscular glucose absorption and conversion both in the absence and presence of insulin (95). This underscores the importance of glucose uptake and utilization by the muscles, a

major mechanism shared with many conventional antidiabetic drugs, such as metformin.

6.3 Anti-inflammatory Potential

V. amygdalina has also been reported to have anti-inflammatory activities *in vitro* and *in vivo*. A stigmastane-type steroidal saponin, isolated from the leaves and stem barks of the genus, exhibited anti-inflammatory activity (96, 97). The coadministration of *V. amygdalina* and *Azadirachta indica* extracts on normal and diabetic rats yielded a positive anti-inflammatory response (98). The aqueous extract of *V. amygdalina* leaves reportedly inhibited carrageenan-induced rat paw edema and xylene-induced ear edema in treated animals (99). Likewise, 100 µg/mL ethanolic extract of *V. amygdalina* exacerbated polymorphonuclear and mononuclear cell activities without impairing structural cell integrity (100). Young and old leaf extracts of the plant reportedly exhibited anti-inflammatory potential in a carrageenan-induced inflammation model in rats (101). The leaf extract reportedly repressed inflammatory potentials through reductions in leucocyte migration and lipid peroxidation in a mouse model (102). Additionally, *V. amygdalina* leaf extract, which contained compounds including vernonioside D, caffeoyl-quinic acids, luteolin, flavanone-O-rutinoside, and apigenin derivative, suppressed inflammation, collagenases, pain, and cartilage degradation while improving cartilage matrix synthesis when examined in cartilage explant assays and a postmenopausal osteoarthritis (OA) animal model (103). Furthermore, vernonioside V from the leaf extract strongly attenuated the secretion of inflammatory cytokines, including IL-6, IL-8 and TNF α , at a low dose (104).

6.4 Anticancer, Antiproliferative, and Cytotoxic Activities of *V. amygdalina*

The cytotoxicity and anticancer activity of *V. amygdalina* have been widely investigated (105, 106). It was further reported that the aqueous leaf extracts of the plant induced cell death in human hepatoblastoma (HBL), human breast tumors (MCF-7), and urinary bladder carcinoma (UBC) cell lines via a pathway that involved a reduction in the extracellular signal, among others (105). Similarly, peptides from plant leaves have been shown to exert anticancer activity, activating protein kinases (42, 107).

Other studies have shown the potency of plant extracts against cells, including MCF-7, BT-549, and human breast cancer cells (108-111). Vernoniomyosides A and B and vernonioside B₂ isolated from leaves of *V. amygdalina* exhibited strong cytotoxicity towards BT-549 cell lines, while vernoniomyoside C, vernoniomyoside D, and vernoamyoside D exhibited different levels of cytotoxic activities on HeLa, MCF-7, and MDA-MB-231 cells (20). The ethyl acetate extract of the leaves exhibited anticancer activity on 4T1 breast cancer cells via the induction of apoptosis, facilitated cell accumulation in G₂/M phases of the cell cycle, and attenuated the secretion of mTOR and PI3K (112). The cytotoxicity and

antiproliferative potential of the plant continued to be explored (113).

6.5 Neuroprotective Properties of *V. amygdalina*

Neurodegenerative diseases such as Alzheimer's and Parkinson's diseases are of major public health concern globally. These diseases are associated with neuronal death and have tremendous effects on movement, speech, intelligence, sleep, memory, and appetite (114). The neuroprotective role of *V. amygdalina* has been reported in several studies (54, 115). It was also reported that the aqueous leaf extract of *V. amygdalina* improved learning and memory in rats by modulating cholinergic neurotransmission (115). The leaves were demonstrated (116) to exert protective effects against neurodegeneration in the rat brain by modulating the activities of Na⁺/K⁺ ATPase, ecto-5'-nucleotidase, monoamine oxidase (MAO), acetylcholinesterase, butyrylcholinesterase, and oxidative stress. The methanolic extract of the leaves has been reported to protect against gamma radiation in the brain by improving antioxidant status and tissue morphology in the brains of rats exposed to gamma rays (54). It was demonstrated that leaf infusions stimulate glucose uptake and utilization in isolated brains (117). The neuroprotective potential of alkaloid-rich leaf extract has been reported in transgenic fruit fly (*Drosophila melanogaster*) model and scopolamine-induced amnesia rats (118).

6.6 Antibacterial and Anti-fungal Properties of *V. amygdalina*

Extensive investigation, particularly on the stem bark and leaf extracts of *V. amygdalina*, adds credibility to the folkloric claim of the antibacterial and antifungal potencies of the plant (119, 120). In a study, ethanolic and aqueous extracts of *V. amygdalina* leaves exhibited significant MIC inhibitions on *Streptococcus mutans* at 25 and 55 mg/mL, respectively. Ethanolic and aqueous extracts of *V. amygdalina* parts (leaf, bark, root, and honey) exhibited significant *in vitro* antibacterial and antifungal effects against various human pathogens, including *Pseudomonas aeruginosa*, *Staphylococcus aureus*, *Candida albicans*, *Klebsiella pneumoniae*, *Bacillus subtilis*, *Aspergillus niger*, and *Escherichia coli* (17).

In addition, the stem bark or wood of *V. amygdalina* has been recommended for use as a chewing stick due to the confirmed activities of the extract against a broad spectrum of human pathogenic bacteria (121). The recommendation is in tandem with the documented traditional use of the plant as a chewing stick for maintaining clean and healthy teeth. The antidermatophytic and antimycoplasmal properties of *V. amygdalina* have also been reported (122, 123).

6.7 Antiviral Activities

Antiviral activities are not common properties of the family. However, a few antiviral studies have been reported for *V. amygdalina*. The ethanolic extract of

the plant's leaf is reportedly potent against some viral infections, including poliovirus (124).

6.8 Antimalarial Properties

Traditionally, *V. amygdalina* is used for the prevention and management of malaria (125-127). While *in vitro* anti-plasmodium activities have been reported (128-130,43) and *in vivo* potential has been confirmed (131-133), clinical trials have also been reported in some cases (134,135) and reported that the aqueous extract of the leaves of *V. amygdalina* inhibited 73% of *Plasmodium berghei* in mice when given 200 mg/kg daily for 4 days. Antihelminthic and antimalarial properties, as well as anti tumorigenic properties, have also been reported for extracts from the plant (17).

6.9 Hepato- and Nephroprotective Properties of *V. amygdalina*

Aqueous and ethanolic leaf extracts of *V. amygdalina* reportedly protect against tetrachloromethane-, alcohol- and aflatoxin-induced hepatotoxicity, among others, in mouse and rat models (78, 136-138). The extracts also had the potential to reverse hepatic damage in rats (46). Supplementation of a rat diet with the leaves of *V. amygdalina* was associated with no acute hepatotoxicity (139). However, a report indicated that the extract could trigger hyponatremia in rats (89). It was further confirmed that other selected plant extracts co-administered with the *V. amygdalina* extract reversed hyponatremia but exacerbated hypophosphatemia, which was diabetes-induced (140). In aspirin-triggered gastric ulcers in rats, leaf extract was observed to induce gastroprotection and prevent renal damage (141, 142).

7. ZOO-PHARMACOLOGY

In instances of severe parasitic infestations, including nematodes, some wild animals, such as chimpanzees, are known to deliberately ingest the leaves of *V. amygdalina* for treatment (143, 144). Pigs and other animals are also fed with the plant to expel parasites such as helminths (22, 143, 145). Some experimental research output added credence to the claim of the use of the leaves of the plant for the expulsion of parasites in animals (24).

8. PHYTO-COSMECEUTICAL APPLICATIONS

Phyto-cosmetics are primarily plant-derived products applied to improve the external look, radiance, beauty, and general health of skin, hair, and teeth. Generally, phytocosmeceuticals, as herbal products, contain bioactive phytochemicals that retard skin aging, acne, and skin wrinkling, among others (71, 74, 75, 146, 147). Prominent phytochemicals with bioactive properties, such as antioxidant, anti-inflammatory, and antityrosinase properties, include phenolics, flavonoids, terpenoids, saponins, and lipids (73, 148-150). *V. amygdalina* has been reported for its cosmetic application due to the presence of a great variety of phytochemicals, including phenolics and saponins, that support its usage in the preparation of traditional cosmetics,

astringents, emollients, skin moisturizers, photoprotection, or excipients in cosmetic preparations (151).

The leaf extract of *V. amygdalina* is used in Eastern Cameroon for the preparation of hair cream (151). Additionally, in the southwestern part of Nigeria, the leaves are said to be used as body cream after being dried, crushed into fine powder, and mixed with oil of choice (146). As a result of its antimicrobial potency, the stem and root are chewed in Nigeria for oral hygiene and prevention of dental decay (152). It was reported that the use of the chewing stick made from *V. amygdalina* resulted in fewer incidences of oral lesions compared to those who used toothbrushes (153).

9. OXYTOCIC POTENTIAL OF *V. amygdalina*

Traditionally, *V. amygdalina* aqueous leaf extract is used in child delivery to enhance uterine dilation and motility (154). Hence, some studies have confirmed the oxytocic potential in animal models (155, 156). The administration of the plant extract reportedly enhanced uterine motility and initiated contraction in rabbits, thereby confirming the oxytocic capability. Furthermore, *V. amygdalina* aqueous extract improved milk production while enhancing uterine contraction in an animal model (157). The results obtained add credence to oxytocic potency, as acclaimed by local midwives.

10. TOXICOLOGICAL EVALUATIONS OF *V. amygdalina*

The toxicity of the various parts of *V. amygdalina* has been severely investigated (158). The toxicity of the plant has been reported by various authors. The acetone extract reportedly showed toxicity only at higher dosages with an LD₅₀ of 824.6 mg/kg, while the methanol extract did not show any toxicity up to 2000 mg/kg in albino mice (159). The essential oils of the plant exerted a good measure of toxicity against *Sitophilus zeamais* Motschulsky (160). The polar extract of the plant attenuated Cd-induced hepatic injury in a wistar rat model (161).

10.1. *In silico* Toxicological Evaluation

The safety of plants in folk medicine is often based on the toxicity profile of the phytochemical compounds in the plant. In order to predict toxicity, various *in silico* approaches exist. Here, we performed *in silico* toxicity evaluations of the compounds using the ProTox-II and SuperCYPsPred platforms developed at Charite, University of Medicine. These computational platforms incorporate molecular similarity, fragment propensities, most frequent features, and machine-learning algorithms to predict 46 endpoints (models) in total. Various toxicity endpoints, such as acute toxicity, hepatotoxicity, cytotoxicity, carcinogenicity, mutagenicity, immunotoxicity, adverse outcome (Tox21) pathways, toxicity targets, and cytochrome inhibition prediction of five major CYP isoforms, 3A4, 2C19, 2C9, 2D6, and 1A2, were identified. Based on these predictions (Table 3), the compounds were found to be safe (inactive

for toxicity endpoints) and had no relevant interactions with cytochromes. Table 3 reports the acute toxicity class profiles of these compounds. The ProTox-II acute toxicity prediction classes are defined according to the globally harmonized system of classification and labelling of chemicals (GHS). LD₅₀ values are given in [mg/kg]:

Class I: fatal if swallowed (LD₅₀ ≤ 5); Class II: fatal if swallowed (5 < LD₅₀ ≤ 50); Class III: toxic if swallowed (50 < LD₅₀ ≤ 300); Class IV: harmful if swallowed (300 < LD₅₀ ≤ 2000); Class V: may be harmful if swallowed (2000 < LD₅₀ ≤ 5000); Class VI: nontoxic (LD₅₀ > 5000).

Table 3: Acute toxicity class (predicted LD₅₀ oral in rat) analysis of the compounds using ProTox-II computational platform.

Name	ProTox-Acute Toxicity class	Prediction score (%)	Predicted LD ₅₀ value (mg/kg)
Vernolide	3	75.0	100
Vernodalol	4	69.80	1335
Vernolepin	3	68.07	150
Vernomenin	3	69.36	150
11,13-Dihydrovernodalol	4	69.46	452
Hydroxyvernolide	2	69.26	7
3'Deoxyvernodalol	NA	NA	NA
Luteolin	5	70.95	3919
Luteolin 7-O-β- glucuroniside	NA	NA	NA
Luteolin 7-O-β-glucoside	5	70.97	5000
Isorhamnetin	5	70.67	5000
Vemonioside A1	5	69.26	4000
Vemonioside A2	5	69.26	4000
Vemonioside A3	5	69.26	4000
Vemonioside A4	3	69.71	52
Vemonioside B1	5	69.26	4000
Vemonioside B2	6	70.01	8000
Vemonioside B3	5	69.26	4000
Vemonioside D1	6	69.26	8000
Vemonioside D2	5	78.00	3220
Vemonioside E	6	79.55	8000
Vernoamyosides A	4	73.34	1500
Vernoamyosides B	5	77.75	3220
Vernoamyosides C	3	73.43	53
Vernoamyosides D	3	71.77	52
Vernoniamyoside A	5	77.08	4000

Vernoniomyoside B	6	76.68	8000
Vernoniomyoside C	NA	NA	NA
Vernoniomyoside D	4	75.36	4000
Edotides	NA	NA	NA

NA: Not available.

From the data obtained (**Table 3**), all the compounds except hydroxyvernonolide were classified into classes III to VI, implying that most compounds were saved at $50 < LD_{50} \leq 5000$. These results apparently showed the relative safety of the plant when consumed at moderate doses. Hydroxyvernonolide, a sesquiterpene lactone obtained from the aerial part of *V. amygdalina* and from the leaf of *Vernonia cinerascens Sch.Bip.*, is reported to possess antitumor, antitrypanosomal, antiprotozoan, antileishmanial, and antiplasmodial activities (57, 58,162).

11. OTHER APPLICATIONS

It is apparent that numerous *in vitro* and *in vivo* have been done on the plant. *V. amygdalina* leaf extract was reported to exhibit strong antidiarrheal activity in a diarrheal model that was castor oil-induced. It was found to delay the onset of diarrhea and attenuate the frequency of stools and the weight of feces at 400 mg/kg bw (163). Other authors have also investigated the potential of various extracts of *V. amygdalina* to inhibit diarrhea (164). The plant is also reported for its cathartic (165), antitrypanosomal and antileishmanial (166), antiplaque (167), antinociceptive (102), antiphlogistic (99), antileukemia (106) and antiquorum sensing activities (168).

12. CONCLUSION

V. amygdalina is obviously a multimedicinal plant with high nutritional and pharmacological value. The plant is greatly endowed with important phytoconstituents that could be a source of lead candidates for drug development in the pharmaceutical industry. Plants that are used as vegetables in many climes hold potential for the ready and affordable management and prevention of chronic diseases such as diabetes and other cardiovascular-related diseases. The renowned activities of the plant, which include antioxidant, anti-inflammatory, anticancer, and antidiabetic activities, cannot be overemphasized. The high safety threshold of the plant makes it a candidate for further exploration. The underexplored parts, which include the root and flowers, need more scientific investigation.

13. CONFLICTS OF INTEREST

The authors declare no conflicts of interest.

7. REFERENCES

- Alara OR, Nour HA, Chinonso IU, and Nassereldeen AK. Extraction and Characteristics of bioactive compounds In *Vernonia Amygdalina* leaf Ethanoic extract comparing soxhlet and microwave-assisted Extraction techniques. Journal of taibah university for science. 2019; 13 (1): 414-422. Available from: [<DOI>](#)
- Odangowei IO, Dienize GG and Ngozi GE. Ethnopharmacological properties of *Vernonia amygdalina* (Bitter leaf). Journal of Medicinal Plants Studies. 2019; 7(2): 175-181.
- Yeap SK, Ho WY, Beh BK, Liang WS, Ky H, Hadi A, Alitheen NB. *Vernonia amygdalina* Ethnoveterinary an Ethnomedical used Green Vegetable with Multiple Bio-activities. Journal of Medicinal Plants Research. 2010; 4(25): 2787-2812. Available from: [<DOI>](#)
- Halim A M, Sirajuddin S, Bahar B, Jafar N, Syam A, Masni. The effect of African leaf herbal tea on fast blood glucose on centration of pre-diabetes teachers in Makassar city. Enfermeria Clinica. 2020; 30: 261-264. Available from: [<DOI>](#).
- Nwaoguikpe RN. The effect of extract of bitter leaf (*Vernonia amygdalina*) on blood glucose levels of diabetic rats. International Journal of Biological and Chemical Sciences. 2010. 4(3): 721-729. Available from: [<DOI>](#)
- Oladunmoye MK, Afolami OI, Oladejo BO, Amoo IA, Osho BI. Identification and Quantification of Bioactive Compounds present in the plant *Vernonia amygdalina* Delile using GC-MS Technique. Natural products Chemistry and Research. 2019; 7(1): 1-5. Available from: [<DOI>](#).
- Atolani O and Olatunji GA: Comprehensive scientific demystification of *Kigelia africana*: A review. African Journal of Pure and Applied Chemistry. 2009; 3 (9): 158-164. Available from: [<URL>](#)
- Islam MT, Hasan J, Hossain-Snidgha HMS, Ali ES, Sharifi-Rad J, Martorell M, Mubarak MS. Chemical profile, traditional uses, and biological activities of *Piper chaba* Vahl: A review. Journal of Ethnopharmacology. 2020; 257: 1-10. Available from: [<DOI>](#)
- Habtamu A, Melaku Y. Antibacterial and Antioxidant Compounds from the Flower Extracts of *Vernonia amygdalina*. Hindawi Advances in Pharmacological sciences. 2018; 2018(4803736): 1-6. Available from: [<DOI>](#)
- Alara OR, Abdurahman NH, Abdul Mudalip SK, Olalere OA. A Review: Phytochemical and Pharmacological Properties of *Vernonia amygdalina*. Journal of Chemical Engineering and Industrial Biotechnology. 2017; 2: 80-96. Available from: [<DOI>](#).
- Asuzu CU. Bitter herbs of eastern Nigeria (*Gongronema latifolium*, *Vernonia amygdalina* and *Vitex doniana*). African Journal of Traditional, Complementary

- and Alternative Medicines. 2018; 15 (3): 47-56. Available from: [<DOI>](#).
12. Divneet K, Navpreet K, Anuja C. A comprehensive review on phytochemistry and pharmacological activities of Vernonia amygdalina. Journal of pharmacognosy and Phytochemistry. 2019; 8(3): 2629-2636.
 13. Kigigha LT, Onyema E. Antibacterial activity of bitter leaf (*Vernonia amygdalina*) soup on *Staphylococcus aureus* and *Escherichia coli*. Sky Journal of Microbiology Research. 2015; 3(4): 41-45.
 14. Zaharaddeen NG, Samuel O. The effect of different drying methods on the elemental and nutritional composition of Vernonia amygdalina. Science. 2019; 13(1): 396-401. Available from: [<DOI>](#).
 15. Ogunrinola OO, Fajana OO, Adu OB, Otutuloro AM, Moses TA, Lediju K, Agbabiaka OA, Elemo BO. The effects of Vernonia amygdalina leaves on lipid profile in cadmium-induced rat. MedCrave online Journal of Toxicology. 2019; 5(2): 83-88
 16. Zubairu AY, Mukhtar M, Saidu I, Ibrahim Z, Isah S, Garga MA, Kebbi HS. Antibacterial activity of methanolic extract of bitter leaf (*Vernonia amygdalina*) from various component fractions using column Chromatography. GSC Biological and pharmaceutical sciences. 2019; 7(2): 16-21. Available from: [<DOI>](#).
 17. Olaoluwa JO, Orjiakor PI, Olowe BM, Ukhureigbe OM, Oguntoye DO. Antimicrobial Potentials of Vernonia amygdalina and Honey on Vancomycin-Resistant *Staphylococcus aureus*. Clinical and Environmental. 2019; 6(5): 1-13. Available from: [<URL>](#).
 18. Adedapo AA, Aremu OJ and Oyagbemi AA. Antioxidant, Anti-inflammatory and Antinociceptive Properties of the Acetone Leaf Extract of Vernonia amygdalina in Some Laboratory Animals. Advanced Pharmaceutical Bulletin. 2014; 4: 591-598. Available from: [<DOI>](#).
 19. Alara OR, Abdurahman NH, Olalere OA. Ethanol extraction of flavonoids, phenolics and antioxidants from Vernonia amygdalina leaf using two-level factorial design. Journal of King Saud University – Science. 2020; 32 (1): 7-16. Available from: [<DOI>](#).
 20. Quasie O, Zhang Y, Zhang H, Luo J, Kong L. Four new steroid saponins with highly oxidized side chains from the leaves of Vernonia amygdalina. Phytochemistry letters. 2016; 15: 16-20. Available from: [<DOI>](#).
 21. Luo X, Jiang Y, Fronczek FR, Lin C, Izevbigie EB, Lee S, Lee KS. Isolation and Structure Determination of a Sesquiterpene Lactone (Vernodalinol) from Vernonia amygdalina Extracts. Pharmaceutical Biology. 2011; 49(5): 464-470. Available from: [<DOI>](#).
 22. Oyeyemi IT, Akinlabi AA, Adewumi A, Aleshinloye AO, Oyeyemi OT. A review on Vernonia amygdalina: A folkloric herb with anthelmintic properties. Beni-Suef University Journal of Basic and Applied Sciences. 2018; 7: 43-49. Available from: [<DOI>](#).
 23. Amodu A, Itodo SE, Musa DE. Nigerian Foodstuffs with Tumour Chemosuppressive Polyphenols. International Journal of Pharmaceutical Science Invention. 2013; 2(1): 12-17.
 24. Jisaka M, Ohigashi H, Takegawa K, Huffman MA, Koshmizu K. Antinutritional and antimicrobial activities of bitter sesquiterpene lactones of Vernonia amygdalina a possible medicinal plant used by wild chimpanzee. Bioscience, Biotechnology, and Biochemistry. 1993; 57: 833-834. Available from: [<DOI>](#).
 25. Erasto P, Grierson DS, Afolayan AJ. Bioactive sesquiterpene lactones from the leaves of Vernonia amygdalina. Journal of Ethnopharmacology. 2006; 106: 117-120. Available from: [<DOI>](#).
 26. Huffman MA, Gotoh S, Izutsu D, Koshimizu K, Kalunde MS. Further observations on the use of the medicinal plant Vernonia amygdalina (Del.), by a wild chimpanzee, its possible effect on parasite load, and its phytochemistry. African Study Monographs. 1993 14(4):227-240.
 27. Osinubi AAA. Effects of Vernonia amygdalina and chlorpropamide on blood glucose. Medical Journal of Islamic World Academic Sciences. 2007; 16: 115-119.
 28. Wang J, Song H, Wu X, Zhang S, Gao X, Li F, Zhu X, Chen Q. Steroidal Saponins from Vernonia amygdalina Del. and Their Biological Activity Molecules 2018; 23: 579. Available from: [<DOI>](#).
 29. Erasto P, Grierson DS, Afolayan AJ. Evaluation of Antioxidant Activity and the Fatty Acid Profile of the Leaves of Vernonia amygdalina growing in South Africa. Food Chemistry. 2007a; 104: 636-642. Available from: [<DOI>](#).
 30. Farombi EO and Owoeye O. Antioxidative and Chemopreventive Properties of Vernonia amygdalina and Garcinia biflavonoid. International Journal of Environmental Research and Public Health. 2011; 8: 2533-2555. Available from: [<DOI>](#).
 31. Atangwho IJ, Egbung GE, Ahmad M, Yam MF, Asmawi MZ. Antioxidant versus anti-diabetic properties of leaves from Vernonia amygdalina Del. growing in Malaysia. Food Chem. 2013; 141: 3428-3434. Available from: [<DOI>](#).
 32. Igile GO, Oleszek W, Jurzysta M, Burda S, Fanfunso M, Fasanmade AA. Flavonoids from Vernonia amygdalina and their antioxidant activities. Journal Agriculture for Food Chemicals. 1994; 42: 2445-2448. Available from: [<DOI>](#).
 33. Udensi EA, Ijeh II, Ogbonna U. Effect of traditional processing on the phytochemical and nutrient composition of some local Nigerian leafy vegetables. Journal of Science Technology. 2002; 8: 37-40.
 34. Tona L, Cimanga RK, Mesia K, Musuamba CT, De Bruyne T, Apers S, Hermans N, Van Miret S, Pieters L, Totte J, Vlietink AJ. In vitro antiplasmodial activity of extracts and fractions of seven medicinal plants used in the Democratic Republic of Congo. Journal of Ethnopharmacology. 2004; 93: 27-32. Available from: [<DOI>](#).
 35. Dagnon S, Novkova Z, Bojilov D, Nedialkov P, Kouassi C. Development of surrogate standards approach for the determination of polyphenols in Vernonia amygdalina Del. Journal of food composition and analysis. 2019; 82:103231. Available from: [<DOI>](#).
 36. Tsaku AP, Ibrahim T, Ekeleme IK, Nkenne IH, Oti VB, Abimiku RH. Phytochemical and Antibacterial analysis of aqueous and alcoholic extracts of Vernonia amygdalina (del.) Leaf. World journal of Pharmaceutical Research. 2018; 7: 9-17. Available from: [<DOI>](#).
 37. Ayoola GA, Coker HAB, Adesegun SA, Adepoju-Bello AA, Obaweve K, Ezennia EC, Atangbayila TO.

- Phytochemical screening and antioxidant activities of some selected medicinal plants used for malaria therapy in Southwestern Nigeria. *Trop. J. Pharm. Res.* 2008; 7:1019-1024. Available from: [<DOI>](#).
38. Nwanjo HU. Efficacy of aqueous leaf extract of *Vernonia amygdalina* on plasma lipoprotein and oxidative status in diabetic rat models. *Nigeria Journal of Physiological Sciences.* 2005; 20: 39-42.
39. Ogundipe OO, Moody JO, Akinyemi TO, Raman A. Hypoglycemic potentials of methanolic extracts of selected plant foods in alloxanized mice. *Plant Foods and Human Nutrition.* 2003; 58: 1-7.
40. Céspedes CL, Avila JG, Martínez A, Serrato B, Calderón-Mugica JC, Salgado-Garciglia R. Antifungal and Antibacterial Activities of Mexican Tarragon (*Tagetes lucida*). *Journal of Agricultural and Food Chemistry.* 2006; 54(10), 3521–3527. Available from: [<DOI>](#).
41. Izevbigie EB. Discovery of water-soluble anticancer agents (edotides) from a vegetable found in Benin City, Nigeria. *Experimental Biology and Medicine.* 2003; 228: 293-298. Available from: [<DOI>](#).
42. Ejiolor II, Das A, Mir SR, Ali M, Zaman K. Novel phytocompounds from *Vernonia amygdalina* with antimalarial potentials. *Pharmacognosy Research.* 2020; 12(1): 53-59. Available from: [<DOI>](#).
43. Ijeh II, Ejike CE. Current perspective on the medicinal potentials of *Vernonia amygdalina*. *Journal of Medicinal Plants Research.* 2011; 5(7): 1051-1061. Available from: [<URL>](#).
44. Odiongenyi AO, Odoemelam SA, Eddy NO. Corrosion inhibition and adsorption properties of ethanol extract of *Vernonia amygdalina* for the corrosion of mild steel in H₂SO₄. *Portugaliae Electrochimica Acta.* 2009; 27: 33-45.
45. Nduagu C, Ekefan EJ, Nwankiti AO. Effect of some crude plant extracts on growth of *Colletotrichum capsici* (Synd) Butler and Bisby, causal agent of pepper anthracnose. *J. Appl. Biosci.* 2008; 6: 184-190.
46. Arhoghro EM, Ekpo KE, Anosike EO, Ibeh GO. Effect of aqueous extract of bitter leaf (*Vernonia amygdalina* Del) on carbon tetrachloride induced liver damage in albino wistar rats. *Eur. J.Sci. Res.* 2009; 26: 122-130. Available from: [<URL>](#).
47. Salawu SO, Akindahunsi AA. Protective effect of some tropical vegetables against CCl₄ – induced hepatic damage. *J. Med. Food.* 2007; 10: 350-355. Available from: [<DOI>](#).
48. Fairuz SY, Ismail SI, Farhanah FH, Mahmud TMM. Phytochemical composition in hexane and methanolic leaf extract of *Vernonia amygdalina*. *Malaysian Applied Biology.* 2019; 48(5): 11-17.
49. Sinisi A, Munoz E, Abay SM, Habluetzel A, Appendino G, Millan E. Poly electrophilic sesquiterpene lactones from *Vernonia amygdalina*: new members and differences in their mechanism of thiol trapping and inbioactivity. *Journal of Natural Product.* 2016; 78(7): 1618–1623. Available from: [<DOI>](#).
50. Abay SM, Lucantoni L, Dahiya N, Dori G, Dembo EG, Lupidi G. Plasmodium transmission blocking activities of *Vernonia amygdalina* extracts and isolated compounds. *Malaria Journal.* 2015; 14: 288. Available from: [<DOI>](#).
51. Jisaka M, Ohigashi H, Takegawa K, Hirota M, Irie R, Huffman MA, Koshmizu K. Steroid glucosides from *Vernonia amygdalina*, a possible chimpanzee medicinal plant. *Phytochemistry.* 1993; 34: 409-413. Available from: [<DOI>](#).
52. Kupchan SM, Hemingway RJ, Karim A, Werner D. Tumor inhibitors XLVII Vernodalin and vernomygdin, two new cytotoxic sesquiterpene lactones from *Vernonia amygdalina* Del. *Journal of Organic Chemistry.* 1969; 34: 3908-3911. Available from: [<DOI>](#).
53. Ganjian I, Kubo I, Fludzinski P. Insect antifeedant elemanolide lactones from *Vernonia amygdalina*. *Phytochemistry.* 1983; 22: 2525-2526. Available from: [<DOI>](#).
54. Owoeye O, Yousuf S, Akhtar MN, Qamar K, Dar A, Farombi EO, Choudhary MI. Another Anticancer Elemanolide from *Vernonia amygdalina* Del. *International Journal of Biology and Chemical Sciences.* 2010; 4: 226–234. Available from: [<DOI>](#).
55. Laekeman GM, Mertens J, Totte J, Bult H, Vlietinck AJ, Herman AG. Isolation and pharmacological characterization of vernolepin. *Journal of Natural Product.* 1983; 46: 161-169. Available from: [<DOI>](#).
56. Laekeman GM, De Clerck F, Vlietinck AJ, Herman AG. Vernolepin: an antiplatelet compound of natural origin. *NaunynSchmiedeberg's Archives Pharmacology.* 1985; 331: 108-113. Available from: [<DOI>](#).
57. Ohigashi H. Toward the chemical ecology of medicinal plant use in chimpanzees: The case of *Vernonia amygdalina*, a plant used by wild chimpanzees, possibly for parasite-related diseases. *Journal of Chemistry Ecology.* 1994; 20: 541–553. Available from: [<DOI>](#).
58. Koshimizu K, Ohigashi H, Huffman MA. Use of *Vernonia amygdalina* by wild chimpanzee: Possible Roles of Its Bitter and Related Constituents. *Physiology and Behavior.* 1994; 56(6): 1209-1216. Available from: [<DOI>](#).
59. Galati G, Teng S, Moridani MY, Chan TS, O'Brien PJ. Cancer chemoprevention and apoptosis mechanisms induced by dietary polyphenolics. *Drug Metabolism and Drug Interaction.* 2000; 17: 311–349. Available from: [<DOI>](#).
60. Huffman MA. Self-medicative behavior in the African great apes: an evolutionary perspective into the origins of human traditional medicine. *Bioscience.* 2001; 51: 651–661. Available from: [<DOI>](#).
61. Clement E, Erharuyi O, Vincent I, Joy A, Christopher A, et al. Significance of Bitter Leaf (*Vernonia amygdalina*) In Tropical Diseases and Beyond: A Review. *Malarial Chemotherapy Control.* 2014; 3(1): 1-10. Available from: [<DOI>](#).
62. Asawalam EF, Emosairue SO, Hassanali A. Contribution of different constituents to the toxicity of the essential oil constituents of *Vernonia amygdalina* (compositae) and *xylopia aetiopica* (annonaceae) on maize weevil, *Sitophilus zeamais motschulsky* (coleoptera: Curculionidae). *African Journal of Biotechnology.* 2006; 7(16): 2957-2962.
63. Ogunbinu AO, Flamini G, Cioni PL, Ogunwande IA, Okeniyi, SO. Essential oil constituents of *Eclipta prostrata* (L.) L. and *Vernonia amygdalina* delile. *Natural Product Communications.* 2009; 4(3): 421-424. Available from: [<DOI>](#).

64. Erasto P, Grierson DS, Afolayan AJ. Antioxidant constituents in *Vernonia amygdalina* leaves. *Pharmaceutical Biology*. 2007b; 45(3): 195-199. Available from: [<DOI>](#).
65. Sonibare OO, Sonibare MA, Adesanya EO. Essential oil composition of *Vernonia amygdalina* del. from Southwestern Nigeria. *Journal of Essential Oil-Bearing Plants*. 2009; 12(1): 55-58. Available from: [<DOI>](#).
66. Okpe O, Habila N, Ikwebe J, Upev VA, Okoduwa SIR, Isaac OT. Antimalarial Potential of *Carica papaya* and *Vernonia amygdalina* in Mice Infected with *Plasmodium berghei*. *Journal of Tropical Medicine*. art. no. 8738972. 2016;1-6. Available from: [<DOI>](#).
67. Ajayi EIO, Adeleke MA, Adewumi TY, Adeyemi AA. Antiplasmodial activities of ethanol extracts of *Euphorbia hirtawhole* plant and *Vernonia amygdalina* leaves in *Plasmodium berghei* -infected mice *Journal of Taibah University for Science*. 2017; 11(6): 831-835. Available from: [<DOI>](#).
68. Alawa CBI, Adamu AM, Gefu JO, Ajanusi OJ, Abdu PA, Chiezey NP, Alawa JN, Bowman DD. In vitro screening of two Nigerian medicinal plants (*Vernonia amygdalina* and *Annona senegalensis*) for anthelmintic activity. *Veterinary Parasitology*. 2003; 11(1): 73-81. Available from: [<DOI>](#).
69. Ito N, Fukushima S, Fukushima H. Carcinogenicity and modification of the carcinogenicity response by BHA and BHT and other antioxidants. *CRC Crit. Rev. Food Technology*. 1985; 15: 109-125. Available from: [<DOI>](#).
70. Atolani O, Olabiyi ET, Issa AA, Azeez HT, Onoja EG, Ibrahim SO, Zubair MF, Oguntoye OS, Olatunji GA. Green synthesis and characterization of natural antiseptic soaps from the oils of underutilized tropical seed. *Sustainable Chemistry and Pharmacy*. 2016; 4: 32-39. Available from: [<DOI>](#).
71. Atolani O, Olatunji GA. Chemical Composition, Antioxidant and Cytotoxicity Potential of *Daniellia oliveri* (Rolfe) Hutch. & Dalz. *Turkish Journal of Pharmaceutical Sciences*. 2016; 13(1): 41-46.
72. Atolani O, Olorundare OE, Anoka AN, Osin AO, Biliaminu SA. Antioxidant, Proteinase Inhibitory and Membrane Stabilization Potentials of *Moringa oleifera* Seed Oil. *FABAD Journal of Pharmaceutical Sciences*. 2018; 43(2): 1-13.
73. Atolani O, Areh ET, Oguntoye OS, Zubair MF, Fabiyi OA, Oyegoke RA, Tarigha DE, Adamu N, Adeyemi OS, Kambizi L, Olatunji GA. Chemical Characterization, Antioxidant, Cytotoxicity, Anti-Toxoplasma gondii and Antimicrobial Potentials of the *Citrus sinensis* Seed Oil for Sustainable Cosmeceutical Production. *Heliyon*. 2020; 6: 2e03399. Available from: [<DOI>](#).
74. Zubair MF, Atolani O, Ibrahim SO, Oguntoye OS, Abdulrahim HA, Oyegoke RA, Olatunji, GA. Chemical and biological evaluations of potent antiseptic cosmetic products obtained from *Momordica charantia* seed oil. *Sustainable Chemistry and Pharmacy*. 2018; 9: 35-41. Available from: [<DOI>](#).
75. Zubair MF, Atolani O, Ibrahim SO, Oguntoye OS, Oyegoke RA, Olatunji GA. Fatty acids Composition, Antimicrobial Potential and Cosmeceutical Utilization of *Prosopis africana* Seed Oil. *Journal of Mexican Chemistry Society*. 2019; 62(3): 1. Available from: [<DOI>](#).
76. Torel J, Cillard J, Cillard P. Antioxidant activity of flavonoids and reactivity with peroxy radical. *Phytochemistry*. 1986; 25: 383-385. [<DOI>](#).
77. Adaramoye OA, Akintayo O, Achem J, Fafunso MA. Lipid lowering effects of methanolic extracts of *Vernonia amygdalina* leaves in rats fed on high cholesterol diet. *Vascular Health and Risk Management*. 2008; 4: 236-241. DOI: [<DOI>](#).
78. Iwalokun BA, Efedede BU, Alabi-Sofunde JA, Oduala T, Magbagveola OA, Akinwande AI. Hepato-protective and antioxidant activities of *Vernonia amygdalina* on acetaminophen-induced hepatic damage in mice. *Journal of Medicinal Food*. 2006; 9(4): 524-530. Available from: [<DOI>](#).
79. Owolabi MA, Jaja SI, Oyekanmi OO, Olatunji J. Evaluation of the antioxidant activity and lipid peroxidation of the leaves of *Vernonia amygdalina*. *Journal of Complimentary and Integrative Medicine*. 2008; 5(1): 21. Available from: [<DOI>](#).
80. Kambizi L, Bakare-Odunola MT, Oladiji AT, Kola-Mustapha AT, Amusa TO, Atolani O, Njinga NS, Quadri AL. Proteinase inhibition, membrane stabilization, antioxidant and phytochemical evaluations of leaves, seeds and calyces of four selected edible medicinal plants. *Cogent Chemistry*. 2017; 3: 1314064. Available from: [<DOI>](#).
81. Da Costa FM, Lemos COT, Arvelos S, Traczynski MR, Da Silva EA, Cardozo-Filho L, Hori CE, Watanabe EO. Evaluation of supercritical carbon dioxide extraction to obtain bioactive compounds from *Vernonia amygdalina* delile leaves. *Chemical Industry and Chemical Engineering Quarterly*. 2020; 26(2): 113-124. Available from: [<DOI>](#).
82. Akah PA, Okafor CL. Blood sugar lowering effect of *V. amygdalina* del. in an experimental rabbit model. *Phytotherapy Resources*. 1992; 6: 171-173. Available from: [<DOI>](#).
83. Gbolade AA. Inventory of antidiabetic plants in selected districts of Lagos State, Nigeria. *Journal of Ethnopharmacology*. 2009; 121: 135-139. Available from: [<DOI>](#).
84. Anh HLT, Vinh LB, Lien LT, Cuong PV, Arai M, Ha TP, Lin HN, Dat TTH, Cuong LCV, Kim YH. In vitro study on α -amylase inhibitory and α -glucosidase of a new stigmastane-type steroid saponin from the leaves of *Vernonia amygdalina*. *Natural Product Research*. 2019; 35(5): 873-879.
85. Osinubi AAA. Effects of *Vernonia amygdalina* and chlorpropamide on blood glucose. *Medical Journal of Islamic World Academic Sciences*. 1996; 16: 115-119.
86. Nwanjo HU, Nwokoro EA. Antidiabetic and biochemical effects of aqueous extract of *Vernonia amygdalina* leaf in normoglycaemic and diabetic rats *Journal of Innovational Life Science*. 2004; 7: 6-10.
87. Uhuegbu FO, Ogbuehi KJ. Effect of aqueous extract (crude) of leaves of *Vernonia amygdalina* (Del.) on blood glucose, serum albumin and cholesterol levels in diabetic albino rats. *Global Journal Pure and Applied Science*. 2004; 10: 189-194. Available from: [<DOI>](#).
88. Atangwho IJ, Ebong PE, Egbung GE, Eteng MU, Eyong EU. Effect of *Vernonia amygdalina* Del. on liver function in alloxan-induced hyper glycaemic rats. *J. Pharm. Bioresour*. 2007a; 4:25-31. Available from: [<URL>](#).

89. Atangwho IJ, Ebong PE, Eteng MU, Eyong EU, Obi AU. Effects of *Vernonia amygdalina* Del. leaf on kidney function of diabetic rats. *International Journal of Pharmacology*. 2007b; 3:143-148.
90. Atangwho IJ, Ebong PE, Eyong MU, Eteng MU, Uboh FE. *Vernonia amygdalina* Del.: a potential prophylactic Antidiabetic agent in lipids complication. *Global Journal of Pure and Applied Science*. 2007c; 13: 103-106.
91. Ekpo A, Eseyin OA, Ikpeme AO, Edoho EJ. Studies on some biochemical effects of *Vernonia amygdalina* in rats. *Asia Journal of Biochemistry*. 2007; 2: 193-197. Available from: [<URL>](#).
92. Okolie UV, Okeke CE, Oli JM, Ehiemere IO. Hypoglycemic indices of *Vernonia amygdalina* on post prandial blood glucose concentration of healthy humans. *African Journal of Biotechnology*. 2008; 7(24): 4581-4585.
93. Atangwho IJ, Ebong PE, Eyong EU, Eteng MU. Combined administration of extracts of *Vernonia amygdalina* (Del) and *Azadirachta indica* (A. Juss) mimic insulin in time-course body weight and glucose regulation in diabetic and non-diabetic rats." *Nigerian Journal of Biochemistry and Molecular Biology*. 2010; 25:44-49.
94. Okafor GI, Okoli CO, Odo AS, Kelechi NR. Studies on the effect of processing methods on the antihyperglycemic activity of herbal teas from leaves of *Vernonia amygdalina* Del. *Pharmacognosy Research*. 2009; 1(5): 256.
95. Erukainure OL, Chukwuma CI, Sanni O, Matsabisa MG, Islam MS. Histochemistry, phenolic content, antioxidant, and anti-diabetic activities of *Vernonia amygdalina* leaf extract. *Journal of Food Biochemistry*. 2018; 43(1): 1-11. Available from: [<DOI>](#).
96. Cioffi G, Sanogo R, Diallo D, Romussi G, De Tommasi N. New compounds from an extract of *Vernonia colorata* leaves with anti-inflammatory activity. *Journal of Natural Products*. 2004; 67: 389-394. Available from: [<DOI>](#).
97. Liu J, Liu Y, Si Y, Yu S, Qu J, Xu S, Hu Y, Ma S. New vernocuminosides from the stem barks of *Vernonia cumingiana* Benth. *Steroids*. 2009; 74: 51-61. Available from: [<DOI>](#).
98. Eyong EU, Atangwho IJ, David-Oku E, Agiang MA, Ebong PE. Haematological and immunological effect of co-administration of extracts of *Vernonia amygdalina* and *Azadirachta indica* on normal and diabetic rats. *African Journal of Biotechnology*. 2011; 10: 10258-10262. Available from: [<DOI>](#).
99. Iroanya O, Okpuzor J, Mbagwu H. Anti-nociceptive and anti-phlogistic actions of a polyherbal decoction. *International Journal of Pharmacology*. 2010; 6(1): 31-36.
100. Koko WS, MESAİK MA, Yousaf S, Galal M, Choudhary MI. In vitro immunomodulating properties of selected Sudanese medicinal plants. *Journal of Ethnopharmacology*. 2008; 118: 26-34. Available from: [<DOI>](#).
101. Asante DB, Henneh IT, Acheampong DO, Kyei F, Adokoh CK, Ofori EG, Domey NK, Adakudugu E, Tangella LP, Ameyaw EO. Anti-inflammatory, anti-nociceptive and antipyretic activity of young and old leaves of *Vernonia amygdalina*. *Biomedicine and Pharmacotherapy*. 2019; 111: 1187-1203. Available from: [<DOI>](#).
102. Onasanwo SA, Oyebanjo OT, Ajayi AM, Olubori MA. Anti-nociceptive and anti-inflammatory potentials of *Vernonia amygdalina* leaf extract via reductions of leucocyte migration and lipid peroxidation. *Journal of Intercultural Ethnopharmacology*. 2017; 6(2): 192-198. Available from: [<DOI>](#).
103. Wang W, Liao S, Wu Z, Chang C, Wu J. Simultaneous study of antioxidant activity, DNA protection and anti-inflammatory effect of *Vernonia amygdalina* leaves extracts. *PloS One*. 2020; 15(7): e0235717. Available from: [<DOI>](#).
104. Nguyen TXT, Dang DL, Ngo VQ, Trinh TC, Trinh QN, Do TD, Thanh TTT. Anti-inflammatory activity of a new compound from *Vernonia amygdalina*. *Natural Product Research*. 2020; 2020(7)1-6. Available from: [<DOI>](#).
105. Opatá MM, Izevbigie EB. Aqueous *Vernonia amygdalina* extracts alter MCF-7 cell membrane permeability and efflux. *International Journal of Environmental Research and Public Health*. 2006. Available from: [<DOI>](#).
106. Khalafalla MM, Abdellatef E, Daffalla HM, Nassarallah AA, Aboul- Enein KM, Lightfoot DA, Cocchetto A, El-Shemy HA. Antileukemia activity from root cultures of *Vernonia amygdalina*. *Journal of Medicinal Plants Research*. 2009; 3(8): 556-562. Available from: [<URL>](#).
107. Izevbigie EB, Byrant JL, Walker A. A novel natural inhibitor of extracellular signal-regulated kinases and human breast cancer cell growth. *Experimental Biology and Medicine*. 2004; 229: 163-169. Available from: [<DOI>](#).
108. Howard CB, Izevbigie EB, Opatá MM. Inhibition paclitaxel resistant MCF-7Rag cell growth by *Vernonia amygdalina* extract. 1st AACR Int Conference on Mol. Diagnostics in Cancer Ther. Dev. 2006; 12-15.
109. Yedjou CG, Rogers C, Brown E, Tchounwou PB. Differential effect of ascorbic acid and N-acetyl 1-cysteine on arsenic trioxide mediated oxidative stress in human leukemia (HL-60) cells. *Journal of Biochemistry and Molecular Toxicology*. 2008; 22: 85-92. Available from: [<DOI>](#).
110. Gresham LJ, Ross J, Izevbigie EB. *Vernonia amygdalina*: anticancer activity, authentication and adulteration detection. *International Journal of Environmental Research and Public Health*. 2008; 5(5): 342-348. Available from: [<DOI>](#).
111. Oyugi DA, Luo X, Lee KS, Hill B, Izevbigie EB. Activity markers of the anti-breast carcinoma cell growth fractions of *Vernonia amygdalina* extracts. *Experimental Biology and Medicine*. 2009; 234(4): 410-417. Available from: [<DOI>](#).
112. Hasibuan PAZ, Harahap U, Sitorus P, Satria D. The anticancer activities of *Vernonia amygdalina* Delile. Leaves on 4T1 breast cancer cells through phosphoinositide 3-kinase (PI3K) pathway. *Heliyon*. 2020; 6(7): e0449. Available from: [<DOI>](#).
113. Siew YY, Yew HC, Neo SY, Tan CH, Koh HL. Evaluation of anti-proliferative activity of medicinal plants used in Asian Traditional Medicine to treat cancer. *Journal of Ethnopharmacology*. 2019; 235: 75-87. Available from: [<DOI>](#).

114. Berman T, Bayati A. What are neurodegenerative diseases and how do they affect the brain? *Front Young Minds*. 2018; 6:70. Available from: [<DOI>](#).
115. Ebuehi O, Ajagun-Ogunleye MO. Neurochemical impact of the aqueous extract of *Vernonia amygdalina* and *Talinum triangulare* on learning and memory in male Wistar rats. *International Journal of Brain and Cognitive Sciences*. 2017; 6: 81-88.
116. Ademosun AO, Oboh G, Oyeleye SI, Ejakpovi II, Adewuni TM. Modulation of cholinergic, monoaminergic, and purinergic enzymes of the brain functions by bitter (*Vernonia amygdalina*) and water bitter (*Struchium sparganophora*) leaves extracts: comparison of phenolic constituents versus nootropic potentials. *Comparative Clinical Pathology*. 2017; 26(6): 1267-1272. Available from: [<DOI>](#).
117. Erukainure OL, Oyebo OA, Ibeji CU, Koorbanally NA, Islam MS. *Vernonia amygdalina* Del. stimulated glucose uptake in brain tissues enhances antioxidative activities; and modulates functional chemistry and dysregulated metabolic pathways. *Metabolic Brain Disease*. 2019; 34(3): 721-732. Available from: [<DOI>](#).
118. Oboh G, Adedayo BC, Adetola MB, Oyeleye IS, Ogunsuyi OB. Characterization and neuroprotective properties of alkaloid extract of *Vernonia amygdalina* Delile in experimental models of Alzheimer's disease. *Drug and Chemical Toxicology*. 2020; 43: 1-11. Available from: [<DOI>](#).
119. Ijeh II, Nwugo VO, Obidoa O. Comparative studies on the nutritive, phytochemical and antimicrobial properties of two varieties of *Vernonia amygdalina*. *Plant Processing Research Community*. 1996; 1: 71-75.
120. Akinpelu DA. Antimicrobial activity of *Vernonia amygdalina* leaves. *Fitoterapia*. 1999; 70: 432-434. Available from: [<DOI>](#).
121. Kola OM. Anti-inflammatory activity of ethanolic leaf extract from *Vernonia amygdalina* on the immune system of Swiss Albino rats dosed with *Clostridium sporogenes* (NC13532). *Research Journal of Medical Sciences*. 2007; 1(2): 127-131.
122. Muraina IA, Auda AO, Mamman M, McGaw LJ, Eloff JN. Antimycoplasmal activity of some plant species from northern Nigeria compared to the currently used therapeutic agent. *Pharmaceutical Biology*. 2010; 48(10): 1103-1107. Available from: [<DOI>](#).
123. Sit NW, Chan YS, Lai SC, Khoo KS, Ong HC. In vitro antidermatophytic activity and cytotoxicity of extracts derived from medicinal plants and marine algae. *Journal de Mycologie Medicale*. 2018; 28(3): 561-567. Available from: [<DOI>](#).
124. Vlietinck AJ, Hoof LV, Totte J, Lasure A, Berghe DV. Screening of hundred Rwandese medicinal plants for antimicrobial and antiviral properties. *Journal of Ethnopharmacology*. 1995; 46: 31-47. Available from: [<DOI>](#).
125. Kraft C, Jenett-Siems K, Siems K, Jakupovic J, Mavi S et al. In vitro antiplasmodial evaluation of medicinal plants from Zimbabwe. *Phytotherapeutic Research*. 2003; 17: 123-128. Available from: [<DOI>](#).
126. Toyang N, Verpoorte R. A review of the medicinal potentials of plants of the genus *Vernonia* (Asteraceae). *Journal of Ethnopharmacology*. 2013; 146: 681-723. Available from: [<DOI>](#).
127. Oladeji OS, Oluyori AP, Bankole DT, Afolabi TY. Natural products as sources of antimalarial drugs: Ethnobotanical and ethnopharmacological studies. *Scientifica*. 2020; 2020(1): 1-22. Available from: [<DOI>](#).
128. Masaba SC. The antimalarial activity of *Vernonia amygdalina* Del (Compositae). *Transactions of Royal Society of Tropical Medicine Hygiene*. 2000; 94: 694-695. Available from: [<DOI>](#).
129. Omoregie ES, Pal A, Darokar MP, Chanda D, Sisodia B. In vitro and in vivo antiplasmodial activity and cytotoxicity of extracts from *Vernonia amygdalina* Del. leaves. *Malaria Journal*. 2010; 9(2): 30. Available from: [<DOI>](#).
130. Lacroix D, Prado S, Kamoga D, Kasenene J, Namukobe J, Krief S. Antiplasmodial and cytotoxic activities of medicinal plants traditionally used in the village of Kiohima, Uganda. *Journal of Ethnopharmacology*. 2011; 133: 850-855. Available from: [<DOI>](#).
131. Iwalokun BA. Enhanced antimalarial effects of chloroquine by aqueous *Vernonia amygdalina* leaf extract in mice infected with chloroquine-resistant and chloroquine-sensitive *Plasmodium berghei* strains. *African Health Science*. 2008; 8(1): 25-35.
132. Abosi AAO, Raseroka BHB. In vivo antimalarial activity of *Vernonia amygdalina*. *British Journal of Biomedical Science*. 2003; 60(2): 89-91. Available from: [<DOI>](#).
133. Melariri P, Campbell W, Etusim P, Smith P. In vitro and in vivo antiplasmodial activities of extracts of *Cymbopogon citratus* Staph and *Vernonia amygdalina* Delile leaves. *Journal of Natural Product*. 2011; 4: 164-172. Available from: [<URL>](#).
134. Challand S, Willcox M. A clinical trial of the traditional medicine *Vernonia amygdalina* in the treatment of uncomplicated malaria. *Journal of Alternative Complementary Medicine*. 2009; 15: 1231-1237. Available from: [<DOI>](#).
135. Njan AA, Adzu B, Agaba AG, Byarugaba D, Díaz-Llera S, Bangsberg DR. The analgesic and antiplasmodial activities and toxicology of *Vernonia amygdalina*. *Journal of Medicinal Food*. 2008; 11(3): 574-581. Available from: [<DOI>](#).
136. Ijeh II, Obidoa O. Effect of dietary incorporation of *Vernonia amygdalina* Del. on AFB1-induced hepatotoxicity in weanling albino rats. *Jamaican J. Sci. Tech*. 2004; 15: 32-36.
137. Ogunlade B, Akunna GG, Fatoba OO, Ayeni OJ, Adegoke AA, Adelakun SA. Aqueous extract of *Vernonia amygdalina* protects against alcohol-induced hepatotoxicity in Wistar rats. *World J. Young Res*. 2012; 2: 70.
138. Singh M, Hussain T, Firdous H, Shaikh S, Rizvi SMD, Moin A, Khan M, Kamal MA. Preclinical hepatoprotective effect of herbalism against ethanol induced hepatotoxicity: A review. *Current Drug Metabolism*. 2018; 19(12): 1002-1011. Available from: [<DOI>](#).
139. Ijeh II, Obidoa O. Effects of dietary incorporation of two varieties of *Vernonia amygdalina* leaves on mean relative organ weight of weanling albino rats. *Nigeria*

- Journal of Biochemistry and Molecular Biology. 2001; 16: 50-51.
140. Atangwho IJ, Ebong PE, Egbung GE, Ani IF. Effects of co-administration of Vernonia amygdalina and Azadirachta indica extracts on serum electrolyte profile of diabetic and non-diabetic rats. Australia Journal of Basic Applied Sciences. 2009; 3: 2974-2978.
141. Achuba FI. Role of bitter leaf (Vernonia amygdalina) extract in prevention of renal toxicity induced by crude petroleum contaminated diets in rats. International Journal of Veterinary Science and Medicine. 2018; 6 (2): 172-177. Available from: [<DOI>](#).
142. Adefisayo MA, Akomolafe RO, Akinsomisoye SO, Alabi QK, Ogundipe OL, Omole JG, Olamilosoye KP. Gastro-protective effect of methanol extract of Vernonia amygdalina (del.) leaf on aspirin-induced gastric ulcer in Wistar rats. Toxicology Reports. 2017; 4: 625-633. Available from: [<DOI>](#).
143. Huffman MA, Seifu M. "Observations on the illness and consumption of a possibly medicinal plant Vernonia amygdalina (Del.), by a wild chimpanzee in the Mahale Mountains National Park, Tanzania". Primates. 1989; 30: 51-63. Available from: [<DOI>](#).
144. Huffman MA, Page JE, Sukhadeo MVK, Gotoh S, Kalunde MS, Towers GH. Leaf swallowing by chimpanzees: A behavioural adaptation for the control of strong nematode infections. International Journal of Rrimatology. 1996; 72: 475-503. Available from: [<DOI>](#).
145. Engel C. Zoopharmacognosy. Veterinary Herbal Medicine. 2007; 2: 7-15.
146. Fred-Jaiyesimi A, Ajibesin KK, Odeyemi T, Ogundokun G. Ethnobotanical studies of folklore phytocosmetics of South West Nigeria. Pharmaceutical Biology. 2015; 53(3): 313-318. Available from: [<DOI>](#).
147. Mohammad IS, Naveed M, Ijaz S, Shumzaid M, Hassan S, Muhammad KS, Rasool F, Akhtarh N, Ishaq HF, Khan HMS. Phytocosmeceutical formulation development, characterization and its in-vivo investigations. Biomedicine & Pharmacotherapy. 2018; 107: 806-817. Available from: [<DOI>](#).
148. Atolani O, Oguntoye H, Areh ET, Adeyemi OS, Kambizi L. Chemical composition, anti-toxoplasma, cytotoxicity, antioxidant, and anti-inflammatory potential of Cola gigantea seed oil. Pharmaceutical Biology. 2019a; 57(1): 154-160. Available from: [<DOI>](#).
149. Atolani O, Areh ET, Oguntoye OS, Zubair MF, Fabiyi OA, Oyegoke RA, Tarigha DE, Adamu N, Adeyemi OS, Kambizi L, Olatunji GA. Chemical composition, antioxidant, anti-lipoxygenase, antimicrobial, anti-parasite and cytotoxicity of Polyalthia longifolia seed oil. Medicinal Chemistry research. (2019b); 28 (3): 515-527. Available from: [<DOI>](#).
150. Osho A, Otuechere CA, Adeosun CB, Oluwagbemi T, Atolani O. Phytochemical, sub-acute toxicity, and antibacterial evaluation of Cordia sebestena leaf extracts. Journal of basic and clinical physiology and pharmacology. 2015; 27(2): 163-170. Available from: [<DOI>](#).
151. Fongnzossie EF, Tize Z, Fogang Nde PJ, Nyangono Biyegue CF, Bouelet Ntsama IS, Dibong SD, Nkongmeneck BA. Ethnobotany and pharmacognostic perspective of plant species used as traditional cosmetics and cosmeceuticals among the Gbaya ethnic group in Eastern Cameroon. South African Journal of Botany. 2017; 112: 29-39. Available from: [<DOI>](#).
152. Oloke J, Odelade K, Oladeji O. Characterization and Antimicrobial Analysis of Flavonoids in Vernonia Amygdalina: A Common Chewing Stick In South-Western Nigeria. Bulletin of Pharmaceutical Research. 2017; 7(3): 149. DOI: 10.21276/bpr.2017.7.3.2
153. Ndukwe K, Okeke IN, Lamikanra A, Adesina SK, Aboderin O. Antibacterial activity of aqueous extracts of selected chewing sticks. Journal of Contemporary Dental Practice. 2005; 6(3): 1-8.
154. Bullough CHW, Leary WP. Herbal medicines used by traditional birth attendants in Malawi. Tropical and Geographical Medicine. 1982; 34: 81-85.
155. Kamatenesi-Mugisha M. Medicinal plants used in reproductive health care in Western Uganda: Documentation, phytochemical and bioactivity evaluation. PhD Thesis in Botany, Makerere University, Kampala, Uganda. 2004.
156. Kamatenesi-Mugisha M, Oryem-Origa H, Makawiti OO. Ethnopharmacological screening of Vernonia amygdalina and Cleome gynandra traditionally used in childbirth in Western Uganda. Proc 11th NAPRECA Symposium, Antanarivo, Madagascar. 2005; 110-122. Available from: [<URL>](#).
157. Ijeh II, Igwe KK, Ejike CECC. Effect of leaf aqueous extracts of Vernonia amygdalina Del. on contraction of mammary gland and uterus of guinea pig dams. Journal of Herbs, Spices and Medicinal Plants. 2010; 1: 107-116. Available from: [<URL>](#).
158. Ibrahim G, Abdurahman E, Ibrahim H, Ibrahim N, Magaji M. Toxicity and analgesic effects of Vernonia amygdalina Del. (Asteraceae) leaf extract on mice. International Journal of Advanced Pharmaceutical and Biological Sciences. 2011; 1: 1-4.
159. Lelago A, Ekeru D, Keshebo DL. Isolation of Sesquiterpene from the Leaves Extract of Vernonia amygdalina and Its Acute Toxicity to the Albino Mice. Chemistry and Materials Research. 2016; 8(6): 56-60.
160. Asawalam EF, Emosairue SO, Hassanali A. Contribution of different constituents to the toxicity of the essential oil constituents of Vernonia amygdalina (compositae) and xylopia aetiopica (annonaceae) on maize weevil, Sitophilus zeamais motschulsky (coleoptera: Curculionidae). African Journal of Biotechnology 2008; 7(16): 2957-2962.
161. Imafidon CE, Olukiran OS, Ogundipe DJ, Eluwole AO, Adekunle IA, Oke GO. Acetonic extract of Vernonia amygdalina (Del.) attenuates Cd-induced liver injury: Potential application in adjuvant heavy metal therapy. Toxicology Reports. 2018; 5: 324-332. Available from: [<DOI>](#).
162. Kimani NM, Matasyoh JC, Kaiser M, Brun R, Schmidt TJ. Sesquiterpene lactone from Vernonia cinerascens Sch. Bip. and their in vitro antitrypanosomal activity. Molecule. 2018; 23(2):248. Available from: [<DOI>](#).
163. Degu A, Kefale B, Alemayehu D, Tegegne GT. Evaluation of the Antidiarrheal Activity of Hydromethanol Crude Extracts of Ruta chalepensis and Vernonia amygdalina in Mice. Evidence-based Complementary and

Alternative Medicine. 2020; 2020(2): 1-6. Available from: [<DOI>.](#)

164. Olayemi AA, Temitope AO, David KB. Evaluation of antidiarrheal activity of the ethanolic stem bark extract of *Vernonia amygdalina* in experimental animals. *Journal of Natural Sciences Research*. 2016; 6 (10): 61-66.

165. Awe SO, Makinde JM, Olajide OA. Cathartic effect of the leaf extract of *Vernonia amygdalina*. *Fitoterapia*. 1999; 70(2): 161-165. Available from: [<DOI>.](#)

166. Obbo CJD, Kariuki ST, Gathirwa JW, Cheplogoi PK, Mwangi EM. In vitro antiplasmodial, antitrypanosomal and antileishmanial activities of selected medicinal plants from Ugandan flora: Refocusing into multi-component potentials. *Journal of Ethnopharmacology*. 2019; 229: 127-136. Available from: [<DOI>.](#)

167. Ocheng F, Bwanga F, Joloba M, Softrata A, Azeem M, Pütsep K, Borg-Karlson AK, Obua C, Gustafsson A. Essential oils from ugandan aromatic medicinal plants: Chemical composition and growth inhibitory effects on oral pathogens. *Evidence-Based Complementary and Alternative Medicine*. 2015; 2015(4): 1-10. Available from: [<DOI>.](#)

168. Bacha K, Tariku Y, Gebreyesus F, Schmitz RA, Mulat M. Antimicrobial and anti-Quorum Sensing activities of selected medicinal plants of Ethiopia: Implication for development of potent antimicrobial agents. *BioMed Central Microbiology*. 2016; 16 (1): 139. Available from: [<DOI>.](#)



Tris(pentafluorophenyl)corrolatoindium(III) – A Long-awaited Metalloporphyrin: Synthesis and Characterization

Ali Tuna^{1,2*} , Pekka Peljo¹ , Roberto Paolesse³ , Günther Knör^{4*} 

¹Department of Mechanical and Materials Engineering, University of Turku (UTU), Vesilinnantie 5, FI-20014 Turku, Finland.

²Institute of Chemical Sciences and Engineering (ISIC), Ecole Polytechnique Fédérale de Lausanne (EPFL), Rue de l'Industrie 17, Case Postale 440, Sion CH-1951, Switzerland.

³Department of Chemical Science and Technologies, University of Rome "Tor Vergata" (UniRoma2), Via della Ricerca Scientifica 1, Roma I-00133, Italy.

⁴Department of Environmental Technology Magistrate Linz, Hauptplatz 1-5, Linz A-4041, Austria.

Abstract: The first attempts at the synthesis of an indium corrole compound were synthesized in the late 80s, but it has not been possible to obtain and characterize such complex completely, and the indium part of metalloporphyrin's periodic table remained unfilled. In this work, an efficient insertion of indium into the 5,10,15-tris(pentafluorophenyl)corrole was achieved. The obtained 5,10,15-tris(pentafluorophenyl)corrolatoindium(III) derivatives has been successfully characterized by relevant analytical techniques and some photophysical and electrochemical features were studied and investigated for the first time. As a novel research, ¹⁹F-¹⁹F COSY NMR technique was employed for the first time in corrole chemistry and the obtained results were further compared to the geometry-optimized molecular structure via density functional theory (DFT) calculations.

Keywords: corrole, indium, metalloporphyrin, NMR, ¹⁹F-¹⁹F COSY

Submitted: January 26, 2024. **Accepted:** March 2, 2024.

Cite this: Tuna A, Peljo P, Paolesse R, Knör G. Tris(pentafluorophenyl)corrolatoindium(III) – A Long-awaited Metalloporphyrin: Synthesis and Characterization. JOTCSA. 2024;11(2):803-12.

DOI: <https://doi.org/10.18596/jotcsa.1425456>

***Corresponding author's E-mail:** ali.tuna@utu.fi, knoer.guenther@web.de

1. INTRODUCTION

Corroles are ring-contracted porphyrin derivatives, with a conjugated 18 π -electron aromatic ring system carrying one direct pyrrole-pyrrole linkage. Many metal complexes of corrole ligands have been successfully synthesized in the last decades, and their molecular as well as electrochemical and photophysical properties have been investigated (1).

The coordination chemistry behavior of corrole is quite different from the corresponding porphyrin derivatives (Figure 1) and most of these variations can be related to the ligand charge, being while porphyrins are dianionic species, free-base corrole molecules are trianionic ligands, and to the contracted size and electron-rich character of the corrole ring. These features have important consequences for the stability and chemical properties of the corresponding metalated corrole derivatives (1).

For example, the coordinated central ions of metalloporphyrins are better stabilized in their high-valent oxidation states, due to the triply negative charge of the fully deprotonated ligand core. The available size of the metal-binding cavity is a second important criterion of distinction between corrole and porphyrin molecules, which leads to modified coordination chemistry (2).

In many cases, the contracted core and the electron distribution of the trianionic corrole ligand joined with the positive charge of the coordinated metal cation may induce a ligand-to-metal type re-distribution of electron density, which is characteristic for the non-innocent behavior of corrole as a ligand. This feature has caused a difficult elucidation of the dominant electronic structure of various metal complexes of corrole (2).

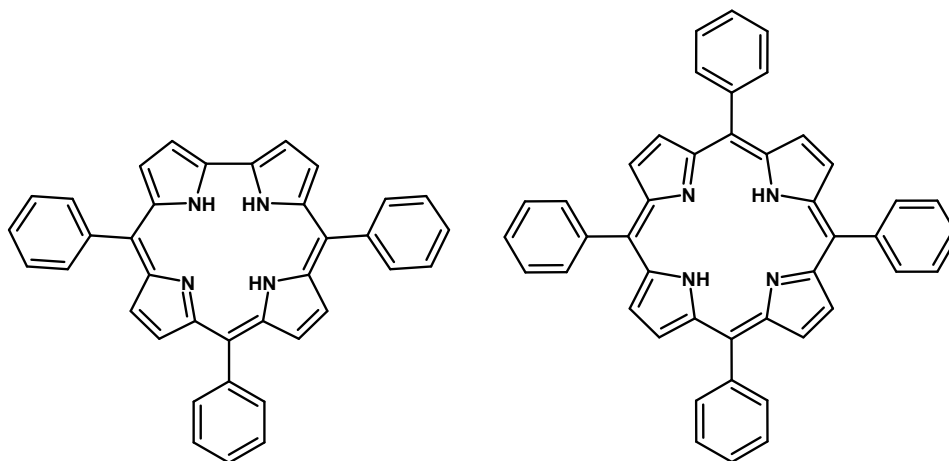


Figure 1: The basic molecular structures of 5,10,15-triphenylcorrole (left) and 5,10,15,20-tetraphenylporphyrin (right).

The characterization of different types of main group and transition metal corrole complexes has been reported, and their diverse properties have been investigated by many specialized research groups active in the field (2,3).

These efforts also include several examples of group 13 elements (B, Al, and Ga), which are already very well characterized. The corresponding corrole complexes of the heavier elements of this main group of the periodic table, however, are still mainly unexplored. Although first systematic attempts to synthesize such compounds started quite early in the field (4), a detailed characterization of an indium corrole molecule has not been published in the literature so far. We herein wish to report our recent progress in this direction.

2. EXPERIMENTAL

5,10,15-Tris(pentafluorophenyl)corrole as free base ligand molecule was synthesized from the condensation reaction between 2,3,4,5,6-pentafluorobenzaldehyde and freshly distilled pyrrole in acidic media and the obtained free-base corrole ligand was purified according to the published procedure (5).

Indium(III) chloride was purchased from ABCR Chemie, Germany. All NMR solvents were purchased from ARMAR Isotopes, Germany. Other solvents, chemicals and supplements were purchased from VWR, Finland and Magasin EPFL, Switzerland. Commercially available reagents were used without further purifications.

The obtained indium corrole species were characterized by UV-vis (Specord plus, Analytik Jena), MS (Q-TOF, Bruker and Orbitrap, Exploris), CV (Gamry 600+ Potentiostat/Galvanostat), IR (Vertex 70 FTIR-ATR, Bruker), Fluorescence (FLS1000 spectrofluorometer, Edinburgh Instruments) and NMR (400 MHz, Bruker) techniques. Full details are given in the supporting information.

2.1. Synthesis of bis(*d*₅-pyridine)-5,10,15-tris(pentafluorophenyl)corrolatoindium(III)

To a solution of 5,10,15-tris(pentafluorophenyl)corrole (51 mg, 64 μmol, 1 eq) in *d*₅-pyridine (15 mL), an excess amount of indium(III) chloride was added and the reaction mixture was refluxed under Ar atmosphere. The reaction was monitored by UV-vis spectroscopy. Once metalation completed as no further spectral change observed, the reaction mixture was cooled down to room temperature and the reaction mixture was purified by microcolumn chromatography using silica gel and *d*₅-pyridine as an eluent to give bis(*d*₅-pyridine)-5,10,15-tris(pentafluorophenyl)corrolatoindium(III) as a dark green solution. The obtained indium corrole molecule was characterized by various analytical techniques.

¹H-NMR (400 MHz, 278 K, *d*₅-py, ppm): δ= 9.12-8.99 (m, 5H), 8.97-8.82 (m, 3H); ¹⁹F NMR (376 MHz, 278 K, *d*₅-py, ppm): δ= -137.4-139 (m, 6F, o-Ar-F), -153-156.2 (m, 3F, p-Ar-F), -163.2-164.2 (m, 6F, m-Ar-F); UV/Vis (pyridine, nm, ε (mol⁻¹dm³cm⁻¹)): λ_{max}= 411 (39700), 433 (174000), 516 (6740), 544 (9300), 585 (16000), 610 (19700); fluorescence (pyridine): λ_{ex}= 410 nm; λ_{em}= 617, 669.5 nm; MS: m/z calcd for [M-(*d*₅-py)+H]⁺: 993.0357, found: 993.0366; m/z calcd. for [M+H]⁺: 1077.1093, found: 1077.1112; FTIR (*d*₅-py): ν̃= 1790 (s) cm⁻¹ (In-N=C).

2.2. Synthesis of 5,10,15-tris(pentafluorophenyl)corrolatoindium(III)

Previously obtained solution of bis(*d*₅-pyridine)-5,10,15-tris(pentafluorophenyl)corrolatoindium(III) in *d*₅-pyridine was slowly evaporated in a two-necked round bottom flask under reduced pressure at room temperature, then *d*-chloroform was added via the septum to give 5,10,15-tris(pentafluorophenyl)corrolatoindium(III) as a dark green solution. The obtained indium corrole molecule was characterized by various analytical techniques.

¹H-NMR (400 MHz, 278 K, *d*₃-AcN, ppm): δ= 8.87 (s, 2H), 8.73 (s, 2H), 8.56 (s, 2H), 8.44 (s, 2H); ¹⁹F NMR (278 MHz, 263 K, *d*₃-AcN, ppm): δ= (m, 6F, Ar-F); UV/Vis (acetonitrile, nm, ε (mol⁻¹dm³cm⁻¹)): λ_{max}= 411 (178500), 549 (39400), 600 (37100), 656 (28800), 708 (22600); fluorescence (acetonitrile):

$\lambda_{\text{ex}} = 410 \text{ nm}$; $\lambda_{\text{em}} = 617, 661.5, 718 \text{ nm}$; MS: m/z calcd for $[M+H]^+$: 908.9621, found: 908.9417.

2.3. NMR Measurements

The 1D- and 2D-NMR experiments were performed using AVANCE 400 MHz Bruker NMR spectrometers equipped with relevant (cryo) probes. D_5 -pyridine (d_5 -py) or d_3 -acetonitrile (d_3 -AcN) were used as the solvent and relevant corrole compounds were dissolved in 300-500 μL of the solvent and placed in a high accuracy 500 mm (7-inch) NMR tubes with PTFE septum. The NMR spectra were observed in various temperatures from 253 K to 298 K in order to study kinetic peak resolutions. At the end, we only report the NMR spectra were observed at around 278 K (approximately 5°C).

The ^{19}F - ^{19}F COSY experiments were performed using AVANCE-III-HD 400 MHz Bruker NMR spectrometer equipped with a BBO2: BB {1H} 5mm (ATMA) (Z136881/10) probe. D_5 -pyridine or d_3 -acetonitrile were used as the solvent, and 5,10,15-tris(pentafluorophenyl)corrole and/or relevant indium corrole complexes were dissolved in 400 μL of the solvent and placed in a high accuracy 500 mm (7-inch) NMR tubes with PTFE septum.

The resulting spectra were processed using TOPSPIN (Bruker) software. The FID was Fourier transformed using relevant commands and window functions, and the resulting spectrum was phase-corrected, baseline-corrected, and referenced to the d-TFA and CFCl_3 resonances. The ^{19}F - ^{19}F COSY spectrum was analyzed to determine the correlations between different sets of fluorine nuclei in the sample. The chemical shifts and coupling constants were measured, and the resulting data were used to determine the molecular structure and aid in the characterization of the compound.

2.4. Photophysical Measurements

The UV-Vis measurements were performed in a quartz fluorescence cuvette at room temperature in pyridine or chloroform. Steady-state fluorescence intensity (365 nm or 410 nm) and excitation (at 650 nm) measurements were performed using FLS1000 spectrofluorometer (Edinburgh Instruments) with an excitation source of a pulsed (μsec) Xe-arc lamp at ambient temperature with a same cuvette in pyridine or chloroform. The emission spectra were set to limit at 850 nm due to the saturation of the detector (no peak formation). The obtained photophysical data were evaluated and visualized over Origin and Microsoft Excel.

2.5. Electrochemical Measurements

The cyclic voltammetry experiments were performed in Gamry 600+ Potentiostat/Galvanostat using a four-hole-three-electrode glass cell (24 mm x 62 mm, 10 mL). Cyclic voltammograms were obtained at room temperature under Ar atmosphere (10 minutes of purging) using with 3 mm glassy carbon as working electrode, Pt wire as counter (auxiliary) electrode and Ag wire dipped in 100 mM AgNO_3 (in anhydrous pyridine) as reference electrode, together with 100 mM tetrabutylammonium perchlorate

(TBAP) as supporting electrolyte and ferrocene (Fc) as an internal standard. The data were analyzed over Echem Analyst (Gamry) software.

2.6. Computational Methods

The DFT calculations were performed with the Gaussian 16 using the hybrid functional B3LYP along with the basis set of LANL2DZ as well as fine integration grids and tight SCF and geometry optimization criteria were used throughout with the implicit effects from pyridine taken into account (6–9). TD-NMR values were calculated using the method implemented in the Gaussian 16 and GaussView 6.0 software was used for the visualization (10). For more details on the DFT calculations please see the supporting information.

3. RESULTS AND DISCUSSION

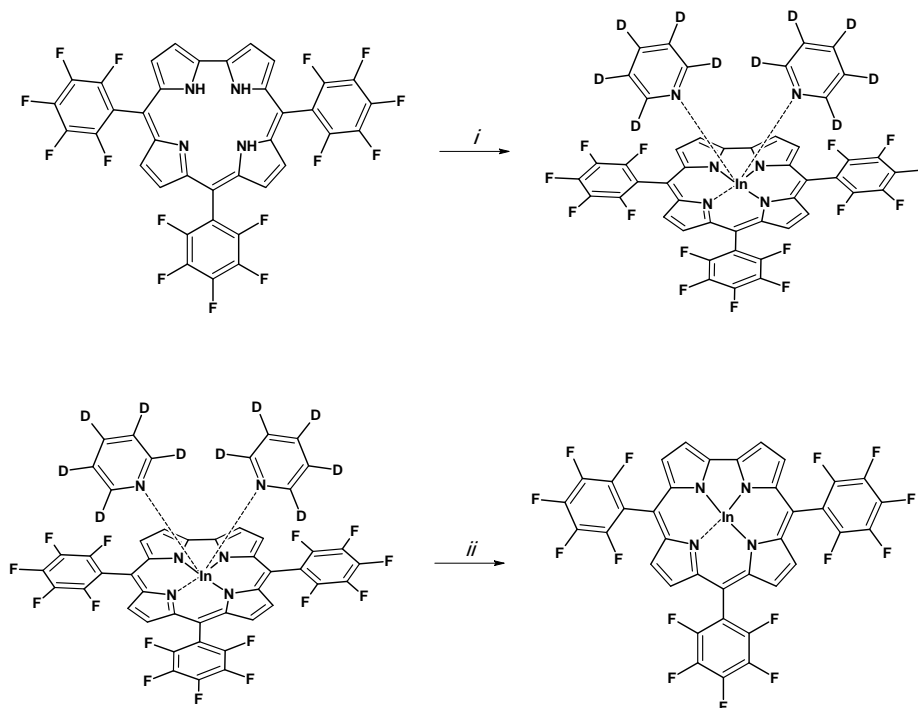
The 5,10,15-tris(pentafluorophenyl)corrolatoindium (III) and a corresponding bis(d_5 -pyridine) coordinated complex were successfully synthesized and characterized with different spectroscopic techniques (Scheme 1).

The synthetic methodologies were modified systematically and, the preparation strategy was optimized and repeated several times to study the influence of different reaction conditions with variations in solvents, reagents, optimal temperature, and reaction time.

In contrast to our initial assumptions derived from the well-known properties of aluminum- and gallium-corrole complexes (11), it turned out that the corresponding indium compound could be obtained and characterized without the attachment of additional axial ligands such as pyridine.

Our experimental studies and analytical results revealed that 5,10,15-tris(pentafluorophenyl)corrolatoindium(III) exists as either in a six-coordinate pyramidal with two d_5 -pyridine units on the same side or four-coordinate parent complex in non-coordinating solvents such as chloroform and that it is metastable under certain conditions, as could be clearly demonstrated by MS and NMR techniques.

Such structural motif seems to be quite common for heavier main group element corrolato complexes with tricationic central ions, as already observed with bismuth as the central metal, where a four-coordinate species was isolated and crystallized (12). Although different crystallization techniques (solvent diffusion, under oil treatment, slow solvent evaporation, etc.) were also tried out several times in the case of the indium corrolato complex, unfortunately, no successful formation of a sample suitable for single crystal diffraction was achieved up to now. The solidified and dried green compound showed decomposition to give a mixture of white indium oxide/hydroxide and green residue as free base corrole ligand in the presence of air. However, it was possible to characterize 5,10,15-tris(pentafluorophenyl)corrolatoindium(III) in solution.



Scheme 1: The syntheses of indium corrole molecules; bis(d_5 -pyridine)-5,10,15-tris(pentafluorophenyl)corolatoindium(III) (top, i: InCl_3 in d_5 -pyridine) and 5,10,15-tris(pentafluorophenyl)corolatoindium(III) (bottom, ii: vacuum at r.t.)

Metalation of the free-base corrole with an excess of indium salts was performed in pyridine solution. As soon as 5,10,15-tris(pentafluorophenyl)corrole was dissolved in pyridine, we observed a deprotonation of the free-base corrole ligand indicated by the absorption spectroscopic signature of the corresponding corrolato anion. This observation was further corroborated by analyzing the ^1H -NMR spectra in d_5 -pyridine, where the characteristic signals of the inner protons experiencing a strong shielding effect of the macrocyclic aromatic ring current of the corrole core were disappearing. A similar phenomenon in porphyrin chemistry can be

also seen in the course of porphyrinato anion formation under alkaline conditions (13,14).

For our present study of new indium compounds with a fluorinated macrocyclic ligand system, we introduced a relevant ^{19}F - ^{19}F COSY NMR technique, which to the best of our knowledge was not used before for any corrole complex in accordance to today's known literature. With this technique, we characterized both our free-base corrole ligand of 5,10,15-tris(pentafluorophenyl)corrole and its two new indium complexes to understand and analyze the correlations between all F atoms (Figure 2).

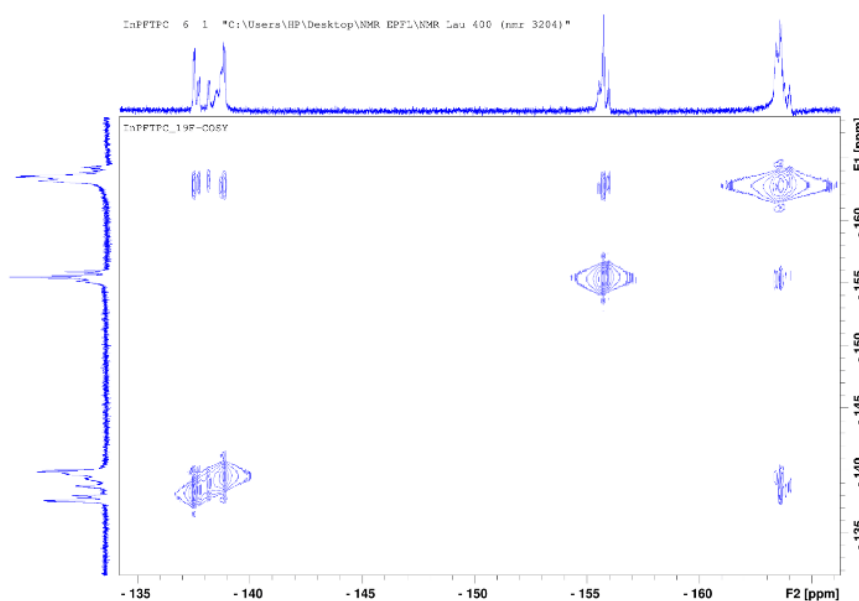


Figure 2: The ^{19}F - ^{19}F COSY NMR spectrum of bis(d_5 -pyridine)-5,10,15-tris(pentafluorophenyl)corolatoindium(III) in d_5 -pyridine.

After insertion of indium, the $^1\text{H-NMR}$ and $^{19}\text{F-NMR}$ peaks of the axially coordinated d_5 -pyridine complex of the 5,10,15-tris(penta-fluorophenyl)corrolato indium(III) molecule formed were unequally distributed indicating a top-sitting complex structure where two d_5 -pyridine molecules were actually placed on the same side. However, when losing both axial d_5 -pyridine ligands, in deuterated chloroform a $^1\text{H-NMR}$ spectrum of 5,10,15-tris(pentafluorophenyl)corrolatoindium(III) was obtained, indicating a more symmetrical structure resembling the one of 5,10,15-tris(pentafluorophenyl)corrolatobismuth (III).

The possible exploitation of the In-NMR technique for the characterization of the corrole complex has been considered. However, indium has naturally abundant two NMR active nuclei, ^{113}In and ^{115}In which both present a quadrupolar (with 9/2 spin) behavior. In most cases, NMR measurements yield in very broad signals which give an increased signal width over the chemical shift range even if the molecules have highly symmetric chemical environments. All these properties limit to study the chemical environment of indium as giving too broad signals and requiring very long measurement times together with very fast relaxation times (μs) which are not suitable for indium peak observation by an In-NMR spectroscopy (15,16).

Considering all experimental and instrumental parameters, it was concluded that the use of In-NMR technique is not applicable for our molecular system due to molecular asymmetry. In order to understand the effect of this asymmetry, we did run $^{19}\text{F-}^{19}\text{F}$ COSY NMR spectroscopy measurements and found that the

geminal pyridine molecules were localized on the same side and as a result the asymmetry was increased to be yielded in the formation of unequal F peaks as well as having different atomic interactions between the F atoms of meso-aryl units and D atoms of axially coordinated pyridine molecules.

In the same group elements, as Al and Ga corrole complexes, this phenomenon occurs somewhat two pyridine molecules are positioned axially but in opposite directions such one is up and one is down. This situation can be associated with the size of the ionic diameter. In rare cases, axial units can be positioned in the same direction which can be also exemplified by obtaining some tantalum, tungsten, molybdenum, uranium, and thorium corrole molecules in a monomeric or dimeric form(s) (17–19).

During the prediction, if two pyridine molecules were positioned relative to their surroundings (above and below), a symmetrical structure would emerge as they would interact equally with the F atoms of the corrole ligand and the pyrrole H in the beta position. A similar interaction was also observed in the $^1\text{H-NMR}$ spectrum, where H peaks interacted to different degrees with pyridine molecules in the same direction (geminal). However, all H and F atoms of the formed indium corrole structure with two axial pyridine ligands were distributed unequally, which indicates that an asymmetric molecule as we deceived was present. This situation was further simulated geometry-optimization molecular structure via density functional theory (DFT) calculations (Figure 3).

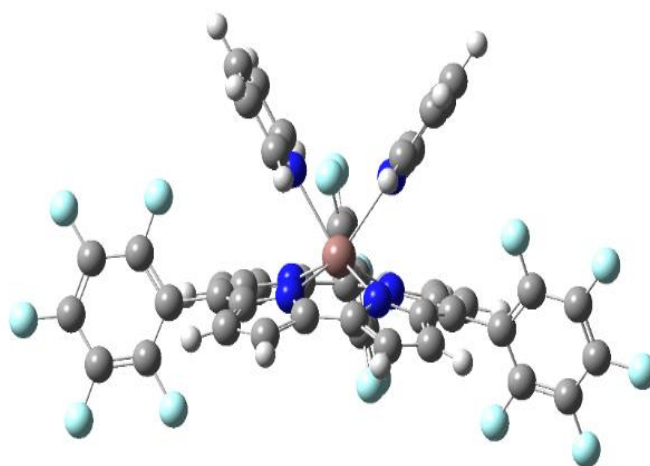


Figure 3: The DFT optimized molecular structure of bis(pyridine)-5,10,15-tris(pentafluorophenyl)corrolatoindium(III) in pyridine.

Considering the structure of geminal two pyridine-coordinated indium corrole, the optimized distance between the closest F and the D atom of the one pyridine units of two geminal pyridine is approximately 3.231 Å, while this distance with the H atom in the beta position is approximately 4.029 Å.

As a result, $^{19}\text{F-}^{19}\text{F}$ COSY experiment is more favorable than $^1\text{H-}^1\text{H}$ COSY experiment due to the

considered bond lengths where D atoms of axial pyridine ligand(s) have more impact on F atoms on meso positions.

The DFT-assisted obtained $^{19}\text{F-NMR}$ spectrum also showed very similar images that F atoms interacted differently in the same ring which cause different peak formations in the obtained both experimental and theoretical spectrum (Figure 4).

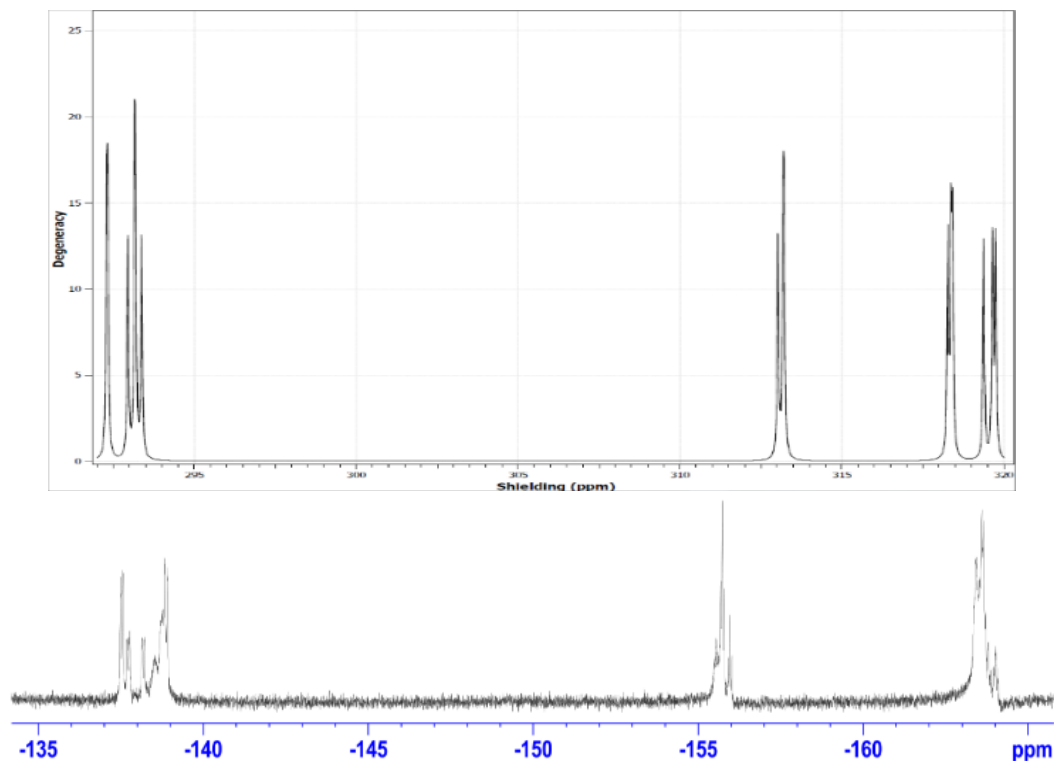


Figure 4: The DFT ^{19}F -NMR spectrum of the optimized molecular structure of bis(pyridine)-5,10,15-tris(pentafluorophenyl)corrolatoindium(III) in pyridine (top) and experimental ^{19}F -NMR spectrum of bis(d_5 -pyridine)-5,10,15-tris(pentafluorophenyl)corrolatoindium(III) in d_5 -pyridine (bottom).

As it can be easily seen that the similarity between DFT and experimental ^{19}F -NMR spectra of two pyridine coordinated 5,10,15-tris(pentafluorophenyl)corrolatoindium(III) structure in pyridine, two pyridine units are coordinated on the same side instead of axially to create unsymmetrical interactions through meso-substituted aryl-fluorine atoms as well as they are yielded in more peak formations.

A preliminary study of indium corrole luminescence spectra could also be carried out. The emission properties of bis(d_5 -pyridine)-5,10,15-tris(pentafluorophenyl)corrolatoindium(III) in pyridine solution at room temperature are shown (Figure 5), together with the corresponding excitation spectrum.

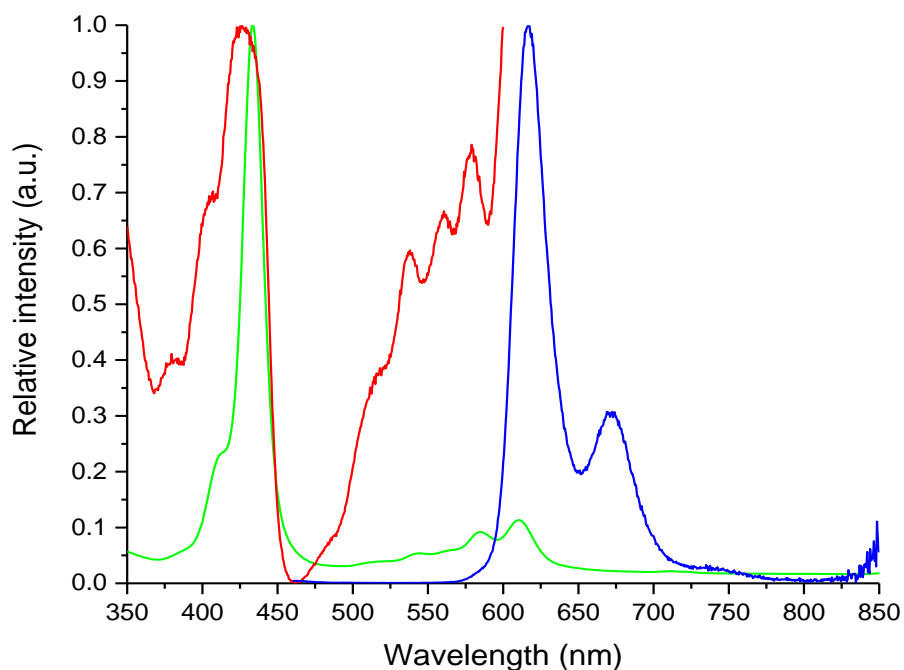


Figure 5: Absorbance (green), excitation (red), and fluorescence (blue) spectra of bis(d_5 -pyridine)-5,10,15-tris(pentafluorophenyl)corrolatoindium(III) in pyridine.

All luminescence features reported here were checked for authenticity by analyzing the corresponding excitation spectra of Figure 5 above. Remarkably, in addition to the expected Soret- and

Q-band patterns of the indium corrole complex, the fluorescence excitation spectrum shows an additional shoulder at around 482 nm, which is not dominant in the absorption spectrum below (Figure 6).

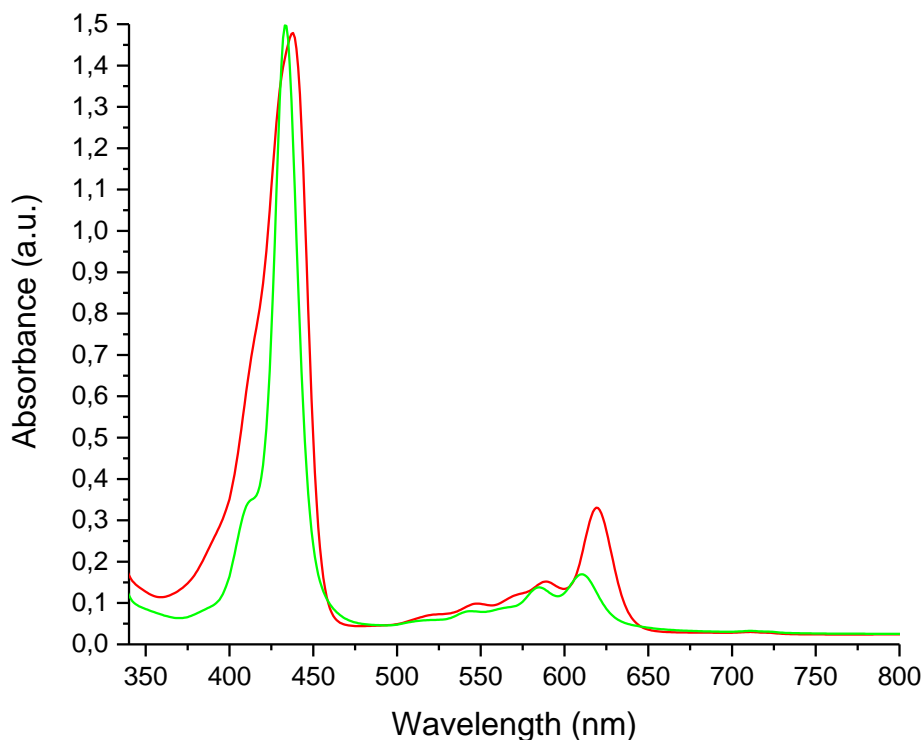


Figure 6: UV-Vis spectra of the 5,10,15-tris(pentafluorophenyl)corrolato anion (red) and of bis(d_5 -pyridine)-5,10,15 tris(pentafluorophenyl)corrolato indium(III) (green) in pyridine.

The indium corrole complex displays a normal-type ligand-centered fluorescence arising from the lowest π - π^* excited singlet state with a quantum yield of $\phi = 0.25$ and electronic energy level of $E_{0-0}(S_1) = 2.06$ eV.

At the same time, the Stokes-shift of the fluorescence band is calculated to be found around 200 cm^{-1} in d_5 -pyridine. Due to the general reactivity trends in the main group 13 element series with an increasing oxidation power of the heavier trivalent cations, it can be rationalized that this unique feature of In(III)-corrole might indicate the presence of a low-lying ligand-to-metal charge transfer (LMCT) excited state level in the visible spectral region, which is not accessible in the case of the related Al(III)- and Ga(III)-corrole derivatives.

Although more detailed studies will be necessary to finally corroborate such a tentative assignment, the currently available luminescence results seem to indicate the accessibility of lower oxidation states of the central metal. Therefore, a reversible metal centered two-electron photoredox chemistry, as typical for heavier main group element derivatives containing tetrapyrrole ligands might also be expected in the case of indium corrole complexes (12,20,21).

To explore the possibility of reaching lower oxidation states at the central metal, the new compounds were investigated by cyclic voltammetry. All electrochemical experiments were carried out in Ar-purged anhydrous pyridine and performed versus Ag/AgNO₃ in the presence of TBAP as a supporting electrolyte. In contrast to more common solvents usually preferred for cyclovoltammetry studies, pyridine is limited to a rather narrow potential window (22), but had to be chosen in our case due to the much better stability of the indium complexes in this solvent as we obtained the mass spectra of mono- and di-pyridine coordinated indium corrole complexes.

For the indium corrole complex carrying axial pyridine, except from axial ligand reduction, only one irreversible cathodic peak at -1.51 V was obtained. Interestingly, this peak shifted to -1.42 V after addition of ferrocene as an internal standard, while at the same time a pseudo-reversible electron transfer behavior occurred. This might indicate an unexplored switch in electron transfer pathways via interaction of the corrole complex with ferrocene. The first oxidation of the indium corrole complex in pyridine solution occurs at an anodic peak potential around 0.6 V . All cyclovoltammetric waves were compared with the literature data available for the Al and Ga complexes of 5,10,15-tris(pentafluorophenyl)corrole, respectively (Table 1).

Table 1: Comparison of redox potentials of the tris(pentafluorophenyl)corrole complexes of Al, Ga, and In.

	Al	Ga	In
2nd Oxidation	-	1.14 V*	-
1st Oxidation	0.55 V*	0.68 V*	~ 0.6**
1st Reduction	- 0.88 V*	- 0.81 V*	- 0.78 V**
2nd Reduction	-1.58 V*	-1.55 V*	-1.51 V** (-1.42 V***)

(*: in dichloromethane (22), **: in pyridine versus Ag/AgNO₃ in pyridine, ***: after ferrocene addition in pyridine versus Ag/AgNO₃ in pyridine.

From the first oxidation peak and the data given in Table 1, an approximately calculated HOMO-LUMO gap of ~2.1 V can be derived, which is in good agreement with our spectroscopic results and the electrochemical data of other group 13 metallocorrole complexes such as 5,10,15-tris(pentafluorophenyl)corrolatoaluminum(III) (23).

Along with the photophysical data obtained, the redox properties of the indium corrole complex in the first excited singlet state can also be estimated. A clear trend can be observed for all known values in the series Al, Ga and In, where the indium corrole derivative is the one which is easier to reduce and harder to oxidize (22,23). This can also be seen from the possible oxidation states of the metal center, indium can have In(I), In(II), and In(III) oxidation states but for gallium and aluminum, these are quite exceptional in special conditions.

In our attempts to characterize the onset of the ring-centered reductions of the indium corrole system by measuring further into the cathodic region of the given solvent window, we observed very interesting results indicating the accessibility of metal-centered electron transfer steps.

According to the literature on main group element tetrapyrroles, the first electrochemical reduction should occur at the macrocyclic ligand system to form an In(III)-corrole π -radical anion. These species may then interconvert into a redox-isomeric In(II)-corrole complex with an open-shell s₁-electronic configuration at the central metal, thus forming a short-lived radical intermediate. In general, such types of In(II) complexes can be stabilized by an intermolecular disproportionation process or undergo dimerization, however, we did not observe any dimerization in our studies. In addition, a further In(II)/In(I) reduction may easily occur by capturing an electron in follow-up chemical steps due to the close redox potentials. This finally leads to a low-valent diamagnetic complex with an In(I) oxidation state and a "carbene-analogous" s₂-electron configuration at the central metal (24–26).

In our preliminary studies, unfortunately, the electron transfer steps following the first metal-centered redox process in solution were not fully reversible and resulted in demetallation of the indium corrole complex and we observed cyclic voltammograms indicating some deposition of elemental indium on the working electrode (25). This lack of stability in the low-valent form is probably due

to the fact that In(I) becomes too large for the corrole ligand system and no longer fits well into the macrocyclic core. The indium redox behaviors were also compared to the standard electrode potential values (27). It should also be outlined here that more comprehensive electro-chemical investigations necessary were not yet within the scope of our present study.

Moreover, we are planning to further explore the very interesting metal-centered redox processes not accessible with the lighter group 13 central metals, and to study the potential presence of low-lying charge transfer (CT) excited states that could be populated by visible light excitation. These efforts are mainly motivated by the importance of controlled formation of low-valent indium complexes and to study the potential of driving In(I)/In(III) interconversion processes as a further example main group element related two-electron redox chemistry. This might become quite useful for the (photo)catalysis of multielectron conversions with carbon-based substrates (e.g. CO₂ reduction, C-C coupling etc.) and interesting other applications in the future.

4. CONCLUSIONS

As a result, two new 5,10,15-tris(pentafluorophenyl)corrolatoindium(III) complexes were successfully synthesized and characterized their structures and basic properties by several analytical techniques. The synthetic approach was refined several times to optimize the minimum conditions for successful indium corrole formation.

In addition to one-dimensional ¹H- and ¹⁹F-NMR techniques, ¹⁹F-¹⁹F COSY NMR technique was employed for the first time in corrole chemistry. Thus, we were able to better understand the characteristic peaks and to compare our new indium corrole complexes with the free-base corrole ligand in different deuterated solvents. By means of NMR-spectroscopy, we could characterize the formation of a pyramidal top-sitting indium corrole complex in d₅-pyridine which gives several and different proton and fluorine peaks in accordance the atomic interactions.

Our ESI-MS results also showed the presence of one and two axially linked d₅-pyridine units to the indium corrole. Once we removed these pyridines under reduced pressure, we also observed 5,10,15-tris(pentafluorophenyl)corrolatoindium(III) as a

four-coordinate species and it showed different analytical responses than its pyridine derivatives.

Cyclic voltammetry technique was attempted in order to understand redox behavior of the formed indium corrole molecule in pyridine. Unfortunately, we observed immediate decomposition of indium corrole molecules in dichloromethane, benzonitrile, acetonitrile, tetrahydrofuran, and toluene. Although the bis(*d*₅-pyridine)-5,10,15-tris(pentafluorophenyl)corrolatoindium(III) and 5,10,15-tris(pentafluorophenyl)corrolatoindium(III) complexes are readily soluble in chloroform, unfortunately it did not allow us to perform any further electrochemical measurements.

To increase our knowledge on group 13 metallocorroles, we also have aimed to synthesize a series of different other indium complexes. The formation of some new indium corrole complexes had been just and recently confirmed by some preliminary spectroscopic data. We are currently conducting our experimental and theoretical studies for further investigations, however in this study, we report successful synthesis and characterization of two new indium corrole molecules together with DFT-assisted calculations.

5. AUTHOR CONTRIBUTIONS

Tuna A: Data curation, formal analysis, investigation, methodology, validation, visualization, writing – original draft, writing – review & editing.

Peljo P: Resources, supervision, validation, writing – review & editing.

Paolesse R: Conceptualization, supervision, resources, validation, writing – review & editing.

Knör G: Conceptualization, data curation, investigation, supervision, validation, writing – original draft, writing – review & editing.

6. CONFLICTS OF INTEREST

All authors read and commented on the manuscript, and have no conflicts of interest to declare.

7. ACKNOWLEDGEMENTS

We would like to thank to the Academy of Finland (Suomen Akatemia, Funding Decision Number 334828), University of Turku (UTU) and the École Polytechnique Fédérale de Lausanne (EPFL) to support our PhD student, Ali Tuna for his projects. We would also like to thank to Dr. Jeremy Weaver, University of Wisconsin – Madison, USA) who carried out his PhD thesis on the investigation of indium corrole formation and discussions, and NMR specialists Aurélien Bornet (EPFL, Switzerland) and Jani Rahkila (Bruker, Finland) for establishing ¹⁹F-¹⁹F COSY NMR technique for detailed analytical characterization, and Dr. Ian Pompermayer Machado (UTU, Finland) for fluorescence spectroscopy measurements.

8. REFERENCES

- Kadish K, Smith KM, Guillard R. The Porphyrin Handbook, Volume 2. New York, USA: Academic Press; 1999.
- Nardis S, Mandoj F, Stefanelli M, Paolesse R. Metal complexes of corrole. *Coord Chem Rev* [Internet]. 2019 Jun 1;388:360–405. Available from: [<URL>](#).
- Mahammed A, Gross Z. Milestones and Most Recent Advances in Corrole's Science and Technology. *J Am Chem Soc* [Internet]. 2023 Jun 14;145(23):12429–45. Available from: [<URL>](#).
- Paolesse R, Licoccia S, Boschi T. Towards the periodic table of metallocorrolates: synthesis and characterization of main group metal complexes of octamethylcorrole. *Inorganica Chim Acta* [Internet]. 1990 Dec 3;178(1):9–12. Available from: [<URL>](#).
- Orłowski R, Gryko D, Gryko DT. Synthesis of Corroles and Their Heteroanalogues. *Chem Rev* [Internet]. 2017 Feb 22;117(4):3102–37. Available from: [<URL>](#).
- Frisch MJ, Trucks GW, Schlegel HB, Scuseria GE, Robb MA, Cheeseman JR, et al. Gaussian 16, Revision C. 01. Wallingford, CT: Gaussian, Inc.; 2016.
- Becke AD. Density-functional thermochemistry. III. The role of exact exchange. *J Chem Phys* [Internet]. 1993 Apr 1;98(7):5648–52. Available from: [<URL>](#).
- McLean AD, Chandler GS. Contracted Gaussian basis sets for molecular calculations. I. Second row atoms, Z = 11–18. *J Chem Phys* [Internet]. 1980 May 15;72(10):5639–48. Available from: [<URL>](#).
- Tomasi J, Mennucci B, Cammi R. Quantum Mechanical Continuum Solvation Models. *Chem Rev* [Internet]. 2005 Aug 1;105(8):2999–3094. Available from: [<URL>](#).
- Reed AE, Curtiss LA, Weinhold F. Intermolecular interactions from a natural bond orbital, donor-acceptor viewpoint. *Chem Rev* [Internet]. 1988 Sep 1;88(6):899–926. Available from: [<URL>](#).
- Kowalska D, Liu X, Tripathy U, Mahammed A, Gross Z, Hirayama S, et al. Ground- and Excited-State Dynamics of Aluminum and Gallium Corroles. *Inorg Chem* [Internet]. 2009 Mar 16;48(6):2670–6. Available from: [<URL>](#).
- Reith LM, Stiftinger M, Monkowius U, Knör G, Schoefberger W. Synthesis and Characterization of a Stable Bismuth(III) A₃-Corrole. *Inorg Chem* [Internet]. 2011 Jul 18;50(14):6788–97. Available from: [<URL>](#).
- Shen J, Ou Z, Shao J, Gałęczowski M, Gryko DT, Kadish KM. Free-base corroles: determination of deprotonation constants in non-aqueous media. *J Porphyr Phthalocyanines* [Internet]. 2007 Apr 25;11(04):269–76. Available from: [<URL>](#).

14. Weaver J. Corroles [PhD Thesis]. [California, USA]: Technical University of California; 2005.
15. McGarvey BR, Trudell CO, Tuck DG, Victoriano L. Coordination compounds of indium. 37. Indium-115 NMR studies of anionic indium species in nonaqueous solution. *Inorg Chem* [Internet]. 1980 Nov 1;19(11):3432–6. Available from: [<URL>](#).
16. NMR Lab [Internet]. 2023 [cited 2024 Jan 23]. NMR Lab. Available from: [<URL>](#).
17. Ward AL, Buckley HL, Lukens WW, Arnold J. Synthesis and Characterization of Thorium(IV) and Uranium(IV) Corrole Complexes. *J Am Chem Soc* [Internet]. 2013 Sep 18;135(37):13965–71. Available from: [<URL>](#).
18. Ziegler JA, Buckley HL, Arnold J. Synthesis and reactivity of tantalum corrole complexes. *Dalton Trans* [Internet]. 2017 Jan 17;46(3):780–5. Available from: [<URL>](#).
19. Vazquez-Lima H, Conradie J, Johansen MAL, Martinsen SR, Alemayehu AB, Ghosh A. Heavy-element–ligand covalence: ligand noninnocence in molybdenum and tungsten Viking-helmet Corroles. *Dalt Trans* [Internet]. 2021 Sep 28;50(37):12843–9. Available from: [<URL>](#).
20. Knör G. Photocatalytic reactions of porphyrin-based multielectron transfer sensitizers. *Coord Chem Rev* [Internet]. 1998 Apr 1;171:61–70. Available from: [<URL>](#).
21. Schöfberger W, Lengwin F, Reith LM, List M, Knör G. Lead corrole complexes in solution: Powerful multielectron transfer reagents for redox catalysis. *Inorg Chem Commun* [Internet]. 2010 Oct 1;13(10):1187–90. Available from: [<URL>](#).
22. Fang Y, Ou Z, Kadish KM. Electrochemistry of Corroles in Nonaqueous Media. *Chem Rev* [Internet]. 2017 Feb 22;117(4):3377–419. Available from: [<URL>](#).
23. Mahammed A, Gross Z. Corroles as triplet photosensitizers. *Coord Chem Rev* [Internet]. 2019 Jan 15;379:121–32. Available from: [<URL>](#).
24. Tuck DG. The lower oxidation states of indium. *Chem Soc Rev* [Internet]. 1993 Jan 1;22(4):269. Available from: [<URL>](#).
25. Hill MS, Hitchcock PB, Pongtavornpinyo R. Oxidative Addition Reactions of Alkyl Halides with the Group 13 Carbene Analogue [In{N(Dipp)C(Me)}₂CH] (Dipp = 2,6- i Pr₂ C₆ H₃). *Inorg Chem* [Internet]. 2007 Apr 30;46(9):3783–8. Available from: [<URL>](#).
26. Hill MS, Hitchcock PB. A mononuclear indium(i) carbene analogue. *Chem Commun* [Internet]. 2004 Aug 9;2004(16):1818–919. Available from: [<URL>](#).
27. Cramer SD, Covino BS, editors. Electrochemical Series. In: *Corrosion: Materials* [Internet]. ASM International; 2005. p. 665–71. Available from: [<URL>](#).



Preparation of Poly (N-Isopropylacrylamide) -Poly (2-Ethyl-2-Oxazoline) and Their Self-Assembly Properties with Dicarboxylic Acid

Perihan Yilmaz Erdogan¹ , Fatma Bilge Emre^{2*} , Turgay Seçkin³ 

¹Gaziantep University, Department of Chemistry, Sehitkamil, 27310 Gaziantep, Türkiye

²İnönü University, Faculty of Education, Department of Mathematics and Science Education, 44280, Battalgazi/Malatya, Türkiye

³İnönü University, Faculty of Science and Literature, Department of Chemistry, 44280, Battalgazi/Malatya, Türkiye

Abstract: This study reports the synthesis of copolymers that contain thermally responsive polymers, namely poly(N-isopropylacrylamide) (PNIPAM) and poly(2-ethyl-2-oxazoline) (PEOX), as well as biodegradable side groups that are water-soluble and capable of hydrogen bonding. The assay aims to produce heat-responsive PNIPAM and PEOX polymers with di-carboxylic acid (DCA) controlled structuring of the resulting pH-sensitive nano-structured polymers. These will be used as a template in the synthesis of inorganic materials. The study demonstrated the impact of pH, salt concentration, and temperature on the polymer/DCA. This fragment describes the functional groups of the thermosensitive polymers PNIPAM and PEOX. These polymers have carboxylic acid functional groups at both ends, are water soluble, and are capable of hydrogen bonding. The structure of these polymers can be recognized with small molecules of DCA in an aqueous solution at different pH, salt concentrations, and temperatures with H-bonds. Additionally, these polymers can be used as templates to synthesize hollow silica polymers. The synthesized monomers and polymers were structurally characterized using Fourier transform infrared spectrophotometer (FT-IR). The resulting structured polymers were identified by scanning electron microscopy and atomic force microscopy (SEM, AFM). UV-VIS spectrophotometer and Differential Scanning Calorimetry (DSC) were used to determine the Lower Critical Solution temperature of the polymers.

Keywords: Self-organization, pH-sensitivity, nano-structured material, template.

Submitted: November 25, 2022. **Accepted:** February 5, 2024.

Cite this: Yilmaz Erdogan P, Emre FB, Seçkin T. Preparation of Poly (N-Isopropylacrylamide) -Poly (2-Ethyl-2-Oxazoline) and Their Self-Assembly Properties with Dicarboxylic Acid. JOTCSA. 2024;11(2):813-24.

DOI: <https://doi.org/10.18596/jotcsa.1150117>

***Corresponding author.** E-mail: fatma.emre@inonu.edu.tr

1. INTRODUCTION

Smart polymeric materials, also known as stimuli-responsive polymers, have emerged as a dynamic and innovative class of materials that can adapt their physical and chemical properties in response to external stimuli and have vast potential for technological applications (1). The remarkable feature of these systems is that they respond dramatically (solubility, shape, volume, surface properties, etc.) to slight changes in the surrounding environment, such as temperature, pH, ionic power, electrical potential, and light (2). This distinguishing feature of materials lies in rapid and drastic changes in structures and physical properties and their reversal. For some applications, a physical stimulus such as temperature is preferred to

increase the number of degenerations. It offers high-potential applications such as thermo-reactive block copolymers, temperature sensors, thermo-responsive gels, actuators, and suspending agents for distribution systems (3,4).

The thermal sensitivity of these materials is usually based on a sharp change in solubility. On heating or cooling, that is, the lower critical solution temperature (LCST) (5) or upper critical solution temperature (UCST), two distinct phase transition phenomena observed in certain polymer solutions (6). They refer to specific temperature points at which significant changes in the solution's properties occur. These phase transitions can be finely tuned by adjusting factors such as polymer chemistry, molecular weight, and the nature of the solvent. The

LCST and UCST properties of polymer solutions have found applications in a variety of fields, including drug delivery (7), thermoresponsive materials (8), and biomaterials (9), where precise control over phase behavior is essential for specific functions and applications.

PNIPAM and PEOX are well-known polymers exhibiting LCST behavior in aqueous solutions (10). LCST behavior is characterized by a phase transition from a soluble, single-phase state to a phase-separated state as the temperature of the solution is increased. PNIPAM's LCST behavior has been extensively studied and is widely used in various applications, including drug delivery systems (7), temperature-responsive hydrogels (11), and a model system for understanding LCST behavior in polymers. PEOX is less commonly studied than PNIPAM but has potential applications in drug delivery, responsive materials, and other areas (12) where LCST behavior can be advantageous. It's worth noting that the LCST behavior of these polymers can be influenced by factors such as polymer molecular weight, concentration, and the presence of additives or salts in the solution.

Polymers with carboxyl groups (-COOH) and polymers with amide groups (-CONH-) both engage in hydrogen bonding (H-bonding) interactions, but their H-bonding behaviors differ due to variations in their chemical structures (13). Carboxyl groups possess dual functionality, serving as both H-bond donors (via the -OH group) and acceptors (via the carbonyl oxygen, C=O). This dual nature results in the formation of strong H-bonds, contributing to the high-water solubility and ionization behavior of carboxyl-containing polymers. In contrast, amide groups contain both H-bond donor (-NH) and acceptor (C=O) sites, facilitating moderately strong H-bonds. These interactions play a role in the structural stability and biological compatibility of polymers featuring amide groups, such as poly(lactic-co-glycolic acid) (PLGA), which is widely employed in drug delivery and tissue engineering applications. In summary, while carboxyl groups form robust H-bonds, amide groups form moderately strong H-bonds, each imparting unique properties and applications to the respective polymers. The layer-by-layer (LbL) film formation method separates the aqueous solution of the polymer with amide groups from the aqueous solution of the polymer with carboxyl groups and alternately solid surface. It provides relatively more regular layer-to-layer film formation on solid surfaces by allowing it to be adsorbed on them, but these films do not form spontaneous (ordered) nanostructures because the polymers adsorbed on the surfaces are kinetically trapped and their mobility is limited (14). However, water-soluble polymers can be made with weak physical interactions in dilute solutions. It is known that amide groups can form H-bond with carboxyl groups in aqueous solutions (15). In light of the information that this interaction can be successfully used in layer-by-layer pH-sensitive film formation and the

water-soluble polymers can be made with weak physical interactions in dilute solutions (16). PNIPAM and PEOX polymers were chosen as the model system. PNIPAM and PEOX are heat-reactive polymers that exhibit subcritical solution behavior. PNIPAM is highly soluble in water, and the solution appears clear and homogeneous. Above the LCST (above approximately 32°C), the polymer undergoes a phase transition, becoming increasingly insoluble in water. This results in the formation of polymer-rich aggregates or a separate polymer-rich phase, leading to cloudiness or phase separation in the solution. Similar to PNIPAM, PEOX exhibits LCST behavior in aqueous solutions. Below the LCST, PEOX is soluble in water, and the solution is clear. Above the LCST (above approximately 61°C), PEOX undergoes a phase transition, leading to reduced solubility and phase separation. Both polymers are completely dissolved in water under LCST, and polymer chain conformations can be controlled between the two expanded and contracted endpoints (17). On the LCST, the polymer chains are in the form of globules. As a result of breaking the H-bonds formed with water on the LCST, phase separation is observed, and the solution becomes cloudy. Poly(2-ethyl-2-oxazoline) self-assembles in a phase-decomposed solution on LCST and forms copolymer (18). When looking at the structuring of PEOX in aqueous solutions, it has been shown that crystalline PEOX polymers were formed on LCST. The basic mechanism in the formation of these crystalline polymers is the orientation of the amid dipoles in the PEOX chains as a result of strong dipolar interactions. PNIPAM is stable in aqueous solution above and below the LCST and is not structured (19,20).

Maleic acid, a dicarboxylic organic acid, possesses several properties that make it of interest in applications involving LCST behavior and responsive polymers. The pKa1 and pKa2 values of maleic acid are important in understanding its behavior in LCST systems, especially when it influences the pH of the solution and thereby impacts the LCST of responsive polymers. Maleic acid has two pK, which are pKa1 (the first ionization constant), which was approximately 1.9, and pKa2 (the second ionization constant), which was approximately 6.3. These pKa values indicate the pH levels at which specific ionization states of maleic acid occur. The first pKa (pKa1) corresponds to the ionization of the first carboxyl group (-COOH) in maleic acid, resulting in the formation of the maleate anion (-COO-). The second pKa (pKa2) represents the ionization of the second carboxyl group in maleic acid, leading to the formation of the dihydrogen maleate anion (-HCOO-). In LCST systems, maleic acid can be added to solutions to adjust the pH, and this adjustment can influence the LCST behavior of responsive polymers like PNIPAM and PEOX. Depending on the pH of the solution, the ionization states of maleic acid can vary, which, in turn, can affect the interactions between maleic acid and the polymers, leading to alterations in the LCST. By knowing the pKa1 and pKa2 values of maleic acid, researchers can control

and tailor the pH conditions in LCST systems, allowing for precise manipulation of the LCST behavior of responsive polymers, which is particularly useful in applications such as drug delivery systems and responsive materials. Figure 1

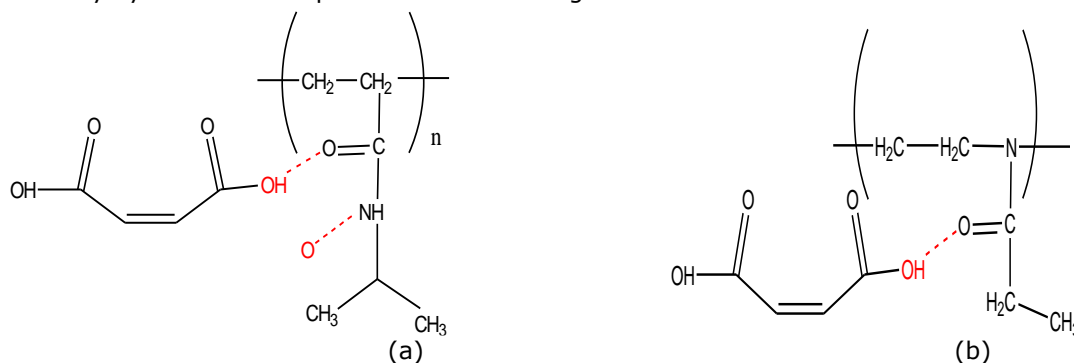


Figure 1: H-bonds of maleic acid with thermally reactive polymers in the range $pK_{a1} < pH < pK_{a2}$: a) PNIPAM, b) PEOX.

Both polymers have amide (= N-C = O) functional groups. It is well-known and widely studied that amide groups make H-bonds with carboxylic acid (-COOH) groups (21). In the amide group, both carbonyl (-C = O) and nitrogen (N) groups can be H-accepting (H-acceptor) H-bonds. Secondary amine-NH groups in PNIPAM are also H-donors. PEOX has tertiary amine -N = groups, no H-donor (-CH₃ and =CH₂ do not act as H-donors in aqueous solution). Intermolecular and intramolecular H-bonds are formed due to the co-presence of H-acceptor and H-donor groups in PNIPAM. These H-bonds are the reason for the hysteresis observed in the thermal reaction transition around the LCST in PNIPAM aqueous solutions (22). Working together on the self-assembly of PNIPAM and PEOX with DCAs and comparing the results with each other will enable us to understand the effects of different polymer chemical structures and different thermal response behaviors (having different LCST) on self-assembly in aqueous solutions.

Poly(N-isopropylacrylamide) (PNIPAM), poly(2-ethyl-2-oxazoline) (PEOX), and maleic acid are substances that have garnered significant scientific interest due to their pivotal roles in lower critical solution temperature (LCST) behavior, which triggers remarkable phase transitions in response to environmental changes. LCST represents a critical point at which these polymers switch from being soluble to forming aggregates or phase-separated structures, rendering them invaluable in applications requiring precise control over responses to factors like temperature and pH. Understanding the interplay between these compounds and their influence on LCST is paramount, as it underpins innovations in drug delivery systems, responsive materials, and a myriad of fields where controlled phase transitions are crucial for functionality and performance.

This study aimed to synthesize copolymers containing thermally responsive polymers ((poly (N-isopropylacrylamide) (PNIPAM) and poly (2-ethyl-2-

shows the H-bonds maleic acid will make with thermally reactive polymers in the range $pK_{a1} < pH < pK_{a2}$.

oxazoline) (PEOX)) and biodegradable side groups which are water soluble and capable of hydrogen bonding for using biomedical applications.

2. EXPERIMENTAL SECTION

2.1. Materials and Equipment

NIPAM ($\geq 97\%$, 113.16 g/mol), PEOX (MW: 200.000 g/mol), maleic acid ($\geq 99\%$, HPLC, 116.07 g/mol), Potassium persulfate (ACS reagent, $\geq 99.0\%$, 270.32 g/mol), Sodium iodide (ACS reagent, $\geq 99.0\%$, 149.89 g/mol), Sodium chloride (ACS reagent, $\geq 99.0\%$, 58.44 g/mol), Sodium sulfate (ACS reagent, $\geq 99.0\%$, anhydrous, granular, 142.04 g/mol) and Sodium carbonate (ACS reagent powder, $\geq 99.5\%$, 105.99 g/mol) were purchased from Sigma Aldrich. All chemicals were used without purification.

Perkin Elmer model Fourier Transform Infrared Spectrophotometer (FT-IR), Leo EV40 SEM, Park Systems XE-100E label AFM, Shimadzu UV-1601 model UV-VIS spectrophotometer, and Shimadzu DSC-60 model Differential Scanning Calorimetry were used.

2.2. Synthesis of Poly (N-isopropylacrylamide) (PNIPAM)

To synthesize 0.02 mol PNIPAM, 2.5 g of NIPAM was placed in a tube, and 31.25 mL of distilled water was added to it. NIPAM was mixed with a magnetic stirrer at room temperature until completely dissolved. Then, 0.125 g of Potassium persulfate initiator was added, the tube was placed in the oil bath, and it was kept in the oil bath and magnetic stirrer for 2 hours at a constant temperature (70 °C) for the polymerization to occur. In this way, PNIPAM polymer is obtained.

2.3. Characterization

Perkin Elmer model FT-IR was used for the structural characterization of the synthesized monomers and polymers. During these analyses, FT-IR measurements were made in the 400-4000

cm^{-1} wave number range and with an ATR surface scanning system. Leo EV40 SEM device was used for surface properties to magnify the image. Park Systems XE-100E brand AFM was used to determine the surface topography of the polymers obtained. Shimadzu UV-1601 brand UV-vis spectrophotometer and Shimadzu DSC-60 brand Differential Scanning Calorimeter were used to determine the subcritical solution temperature of the polymers.

3. RESULTS AND DISCUSSION

3.1. Self-assembly of PNIPAM and PEOX Polymers with Dicarboxylic Acid Solution

Figure 2 illustrates the different amounts of 0.02 mol PNIPAM (a: 2 mg, b: 4 mg, c: 6 mg, d: 8 mg, e: 10 mg) in 0.8M maleic acid solution at different pH (2, 4, 6, 8, 10) configuration. The structuring of PNIPAM and PEOX polymers in aqueous solution was

carried out through H-bonds with maleic acid. To do this, we either use the polymer chain in the range $\text{pKa}_1 < \text{pH} < \text{pKa}_2$ as described above, and the chain of electrostatic interactions is stretched, or we need to find the pH where the pH is less than pKa_1 and the corresponding pH where a carboxylic acid is protonated. Maleic acid solutions were prepared at different pH (2, 4, 6, 8, 10) values and were used for this. A constant amount of this solution was put into the tube. PNIPAM maleic acid structuring was examined by adding different amounts of 0,02 mol PNIPAM (2-10 mg). Figure 2 shows no structuring at pH 2 and pH 4, while self-assembly takes place at pH 6, pH 8, and pH 10. As the polymer amount increases, the structuring between the polymer and DCA increases even more. As seen in Figure 2, the most suitable maleic acid pH for the structuring of PNIPAM has been determined as pH 6.

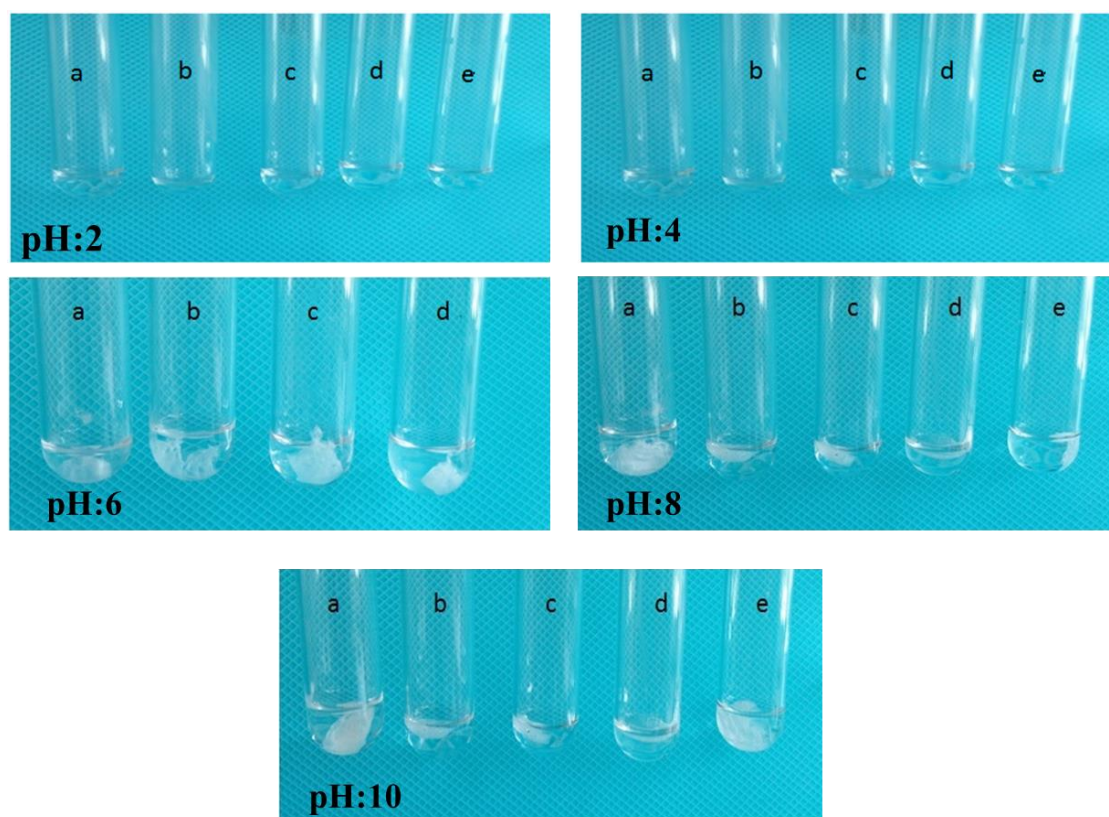


Figure 2: Structuring of a specific amount of PNIPAM polymers (a: 2 mg, b: 4 mg, c: 6 mg, d: 8 mg, e: 10 mg) in maleic acid solution with varying pH values (2, 4, 6, 8, 10).

PEOX polymer was analyzed by combining solutions of maleic acid at varying pH values. It was demonstrated in Figure 3 shows the configuration of the PEOX polymer in the maleic acid solution at

three different pH values (a: 6, b: 8, c: 10). As a result of the experiments, we see that the structuring of PEOX in maleic acid started at pH 8.

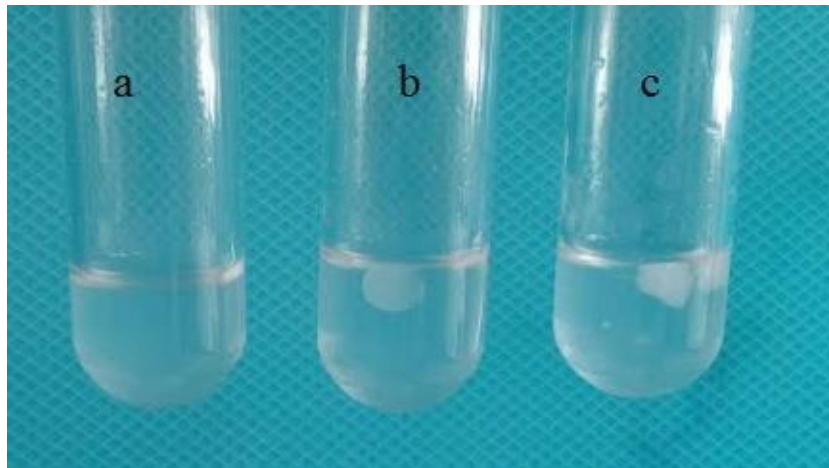


Figure 3: Structuring of the PEOX polymer in maleic acid solution at different pH (a: 6, b: 8, c: 10).

3.2. Self-assembly of Maleic Acid and PEOX and PNIPAM Mix

The structuring of PEOX and PNIPAM polymers in maleic acid was examined separately. Copolymerization of NIPAM with special pH value-responsive and strong hydrophilic ability of PEOX results in dual pH and temperature-stimuli-

responsive hydrogels. The determined LCST values of the copolymer obtained from different ratios of PEOX and PNIPAM in maleic acid solution are given in Table 1. Table 1 can be used to determine the optimal gel ratio and temperature for *in vivo* research or biomedical applications.

Table 1: Gel ratio of PEOX - PNIPAM blend.

Blend	% (V/V)	LCST (°C)
1.PEOX-PNIPAM	90-10	32
2.PEOX-PNIPAM	80-20	32
3.PEOX-PNIPAM	70-30	34
4.PEOX-PNIPAM	60-40	35
5.PEOX-PNIPAM	50-50	35
6.PEOX-PNIPAM	40-60	36
7.PEOX-PNIPAM	30-70	36
8.PEOX-PNIPAM	20-80	37
9.PEOX-PNIPAM	10-90	40

Figure 4 shows the structuring of the blend of PEOX and PNIPAM in maleic acid solution at different pH (a) pH:5, b) pH:5.3, c) pH:5.6, d) pH:5.8, e) pH:6,

f) pH:8, g) pH:10). The structuring of PEOX and PNIPAM blend in maleic acid solution at different pH starts at approximately pH 5.8.

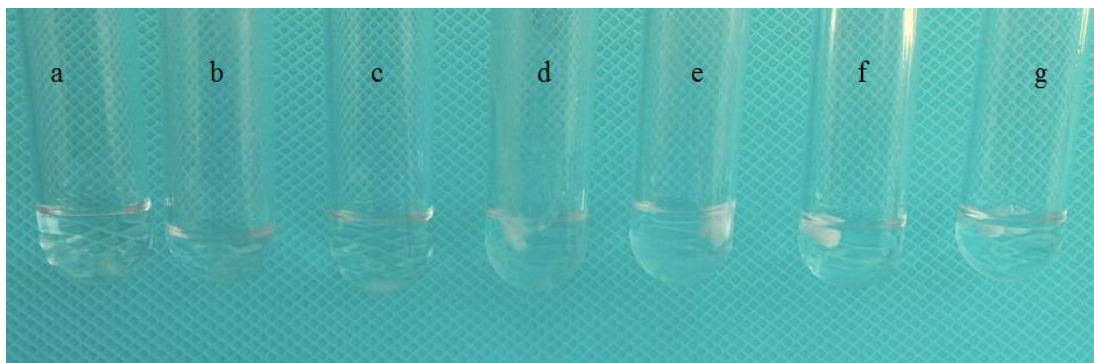


Figure 4: Maleic acid structuring of PEOX and PNIPAM blend at different pH; a) pH:5, b) pH:5.3, c) pH:5.6, d) pH:5.8, e) pH:6, f) pH:8, g) pH:10).

3.3. Determination of Sub-Critical Solution Temperature of PNIPAM and PEOX Polymers

"Smart" materials, in other words, materials that can react to stimuli, represent one of the darkest classes of materials (23). There are two basic types of thermo-reactive polymers; The first presents the LCST, while the second presents the UCST (24). For example, a polymer solution below MAP is a clear, homogeneous solution; A polymer solution above

LCST looks cloudy (also known as LCST's cloud point). Figure 5 a show a 32 ° C LCST of PNIPAM. This temperature is close to body temperature. This proximity is a very useful temperature for biomedical applications. Figure 5 b shows a 61 ° C LCST of PEOX. Figure 5 c shows the LCST behavior of the PEOX-PNIPAM blend against temperature. LCST temperature of 20-80% PEOX-PNIPAM blend was determined as 37 ° C.

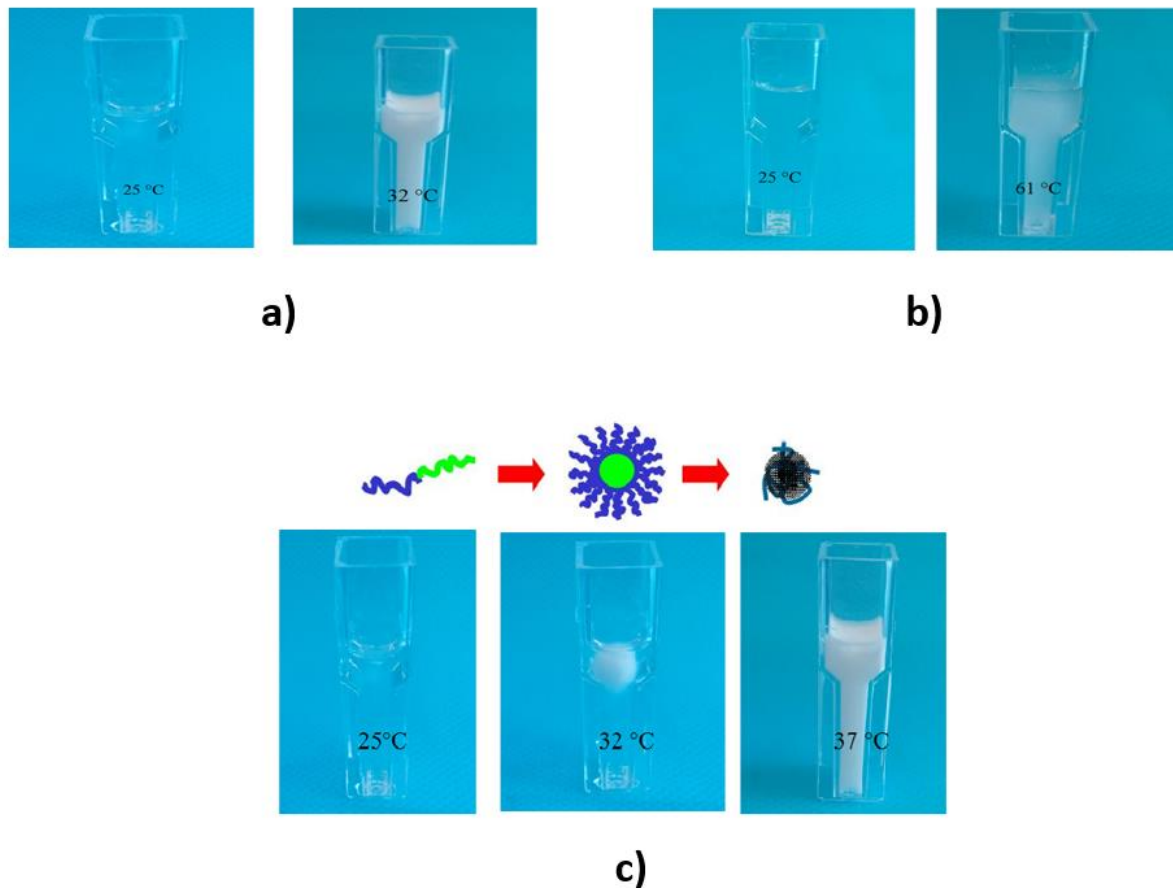


Figure 5: LCST behavior with temperature a) PNIPAM's, b) PEOX, and c) PEOX-PNIPAM blend.

3.4. Characterization

Figure 6a show the FT-IR spectrum of PNIPAM. 3292 cm^{-1} (secondary amide NH stretch) (25), 2970 cm^{-1} ($-\text{CH}_3$ asymmetric stretch) (26), 1650 cm^{-1} (secondary amide C = O stretch, amide bond) (27) and 1550 cm^{-1} O stretch, amide II bond). Figure 6b shows the FT-IR spectrum for PNIPAM-DCA configuration. Considering the polymeric structures made with DCA, the peak changes occurring - C = O peaks are seen in 1660-1735 cm^{-1} . N-H peak is seen

in 3292 cm^{-1} (28) and the aliphatic C-H strain peak is seen in 2850-2950 cm^{-1} . Possible peaks for these polymers, which are made with a hydrogen bond, are seen where expected. In these structures where structural change is observed, the structures formed due to hydrogen bonding are seen around 2300 cm^{-1} . The peaks of different shapes of hydrogen bonds indicate that the embodiment is in different shapes and some regions within the polymeric chain.

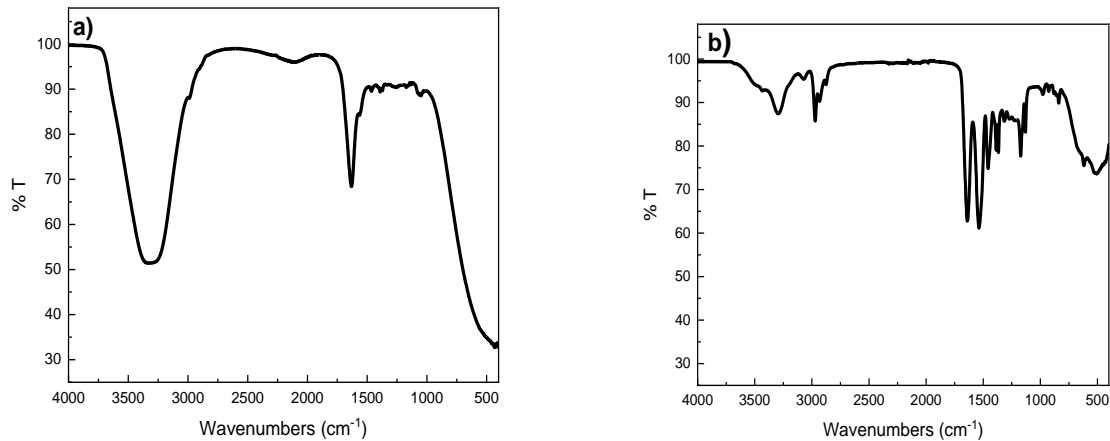


Figure 6: FT-IR spectrum of a) PNIPAM and b) Self-assembly of PNIPAM-DCA.

Figure 7 shows the UV-VIS graphic for PNIPAM. As a result of the studies, the LCST UV-VIS spectrophotometer measurement technique is determined for PNIPAM. For PNIPAM, LCST is available at 32 °C. Figure 7 b shows the DSC results

for PNIPAM. For PNIPAM, LCST is measured this time with the DSC technique. For PNIPAM, LCST also supports literature and the UV-VIS spectrophotometer measurement technique, which is determined to be 32 °C (29).

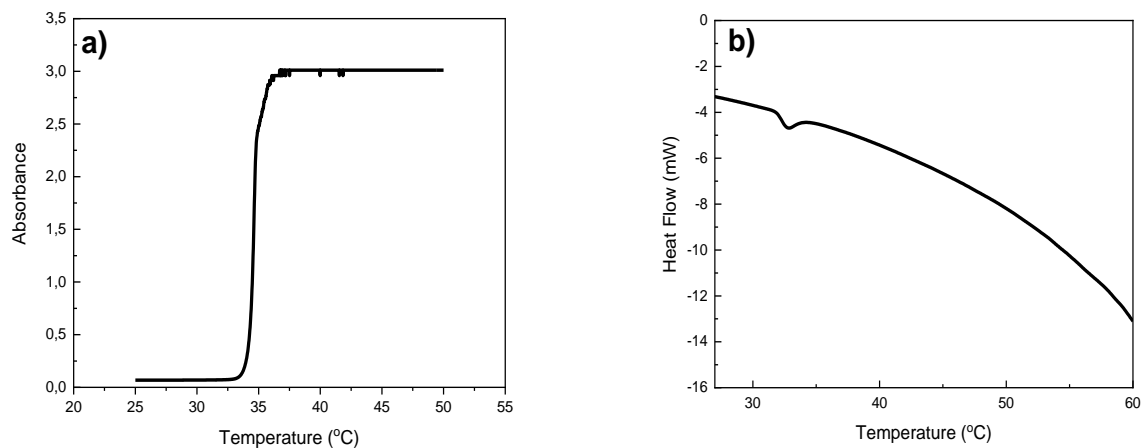


Figure 7: a) UV-VIS and b) DSC thermogram of PNIPAM structure

Figure 8 shows AFM images at different magnifications for PNIPAM-DCA configuration. When AFM images of the gel structures obtained in the studies are examined, it is thought that possible configurations are caused by interactions such as van der Waals forces, electrostatic interactions, entropic forces, steric forces, and external volume

repulsion (30). The stability of the colloidal system is used in the sense of suspending the particles in the solution, that is, suspending. Stability decreases with aggregation and precipitation phenomenon. These facts are disclosed due to the tendency to reduce surface energy. Reduced surface tension ensures colloidal particles are stable.

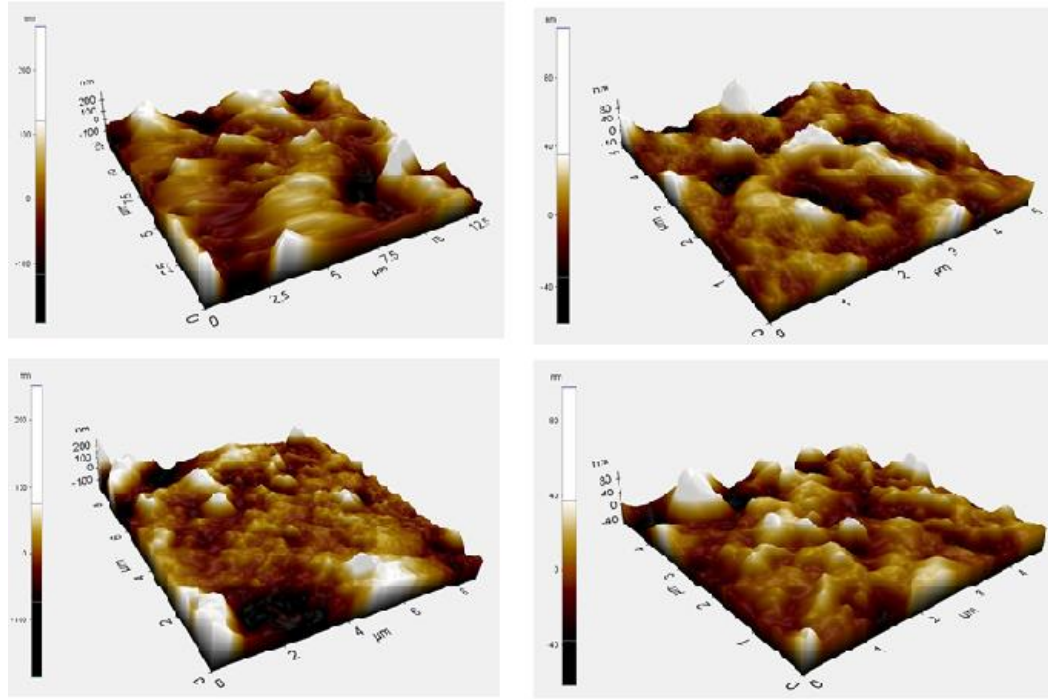


Figure 8: AFM images for PNIPAM-DCA configuration.

Clumping is actually the sum of the forces of attraction between the particles. If the gravitational forces, for example, van der Waals, are greater than the thrust forces, the particles come together to clump together. Electrostatic and steric settling prevents the agglomeration and collapse of the

particle. Therefore, it is understood that possible interactions arise from these forces. AFM images are capable of supporting this. The initial structure and possible pore diameters change after the interaction process, and the formation of nanostructures are given in AFM images (31).

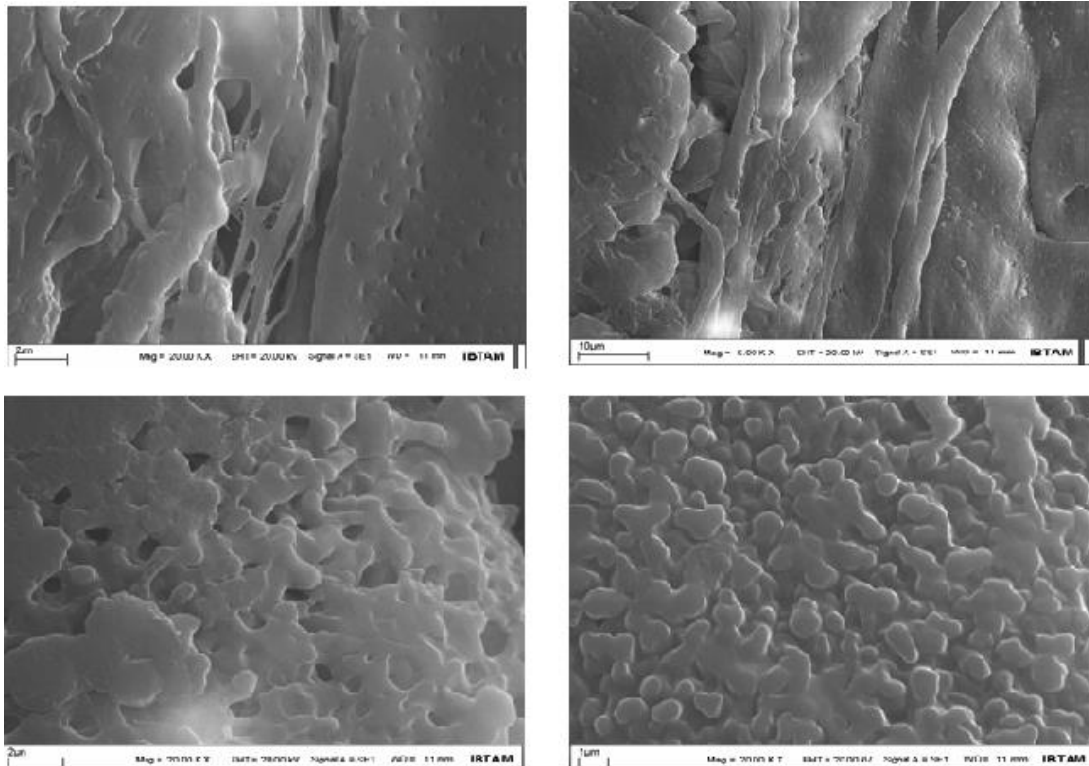


Figure 9: SEM images of self-assembly of PNIPAM-DCA (20.00 KX magnification).

Figure 9 shows SEM images in different magnifications for PNIPAM-DCA structuring. When

SEM images are examined, it is seen that PNIPAM structures with DCA functionality are constructed in

the form of bars and there are gaps in the intermediate segments. When the results of SEM structural analysis are interpreted as equivalent to AFM images, the effect of the constructions on the morphology is understood. Among the polymeric embodiments, the regional hydrogen bond shows that the structure interacts with the overlap and ball. Globule formations can be converted back to the old heap by changing the environment

variables. The most important evidence of this transformation is that the structural dissolution event and the clarification and collapse, i.e. self-structuring, are reversible. It is clearly seen that when the high magnifications of the building are reached, their surfaces have a clear gap. All these properties prove that the synthesized structures have porous morphology.

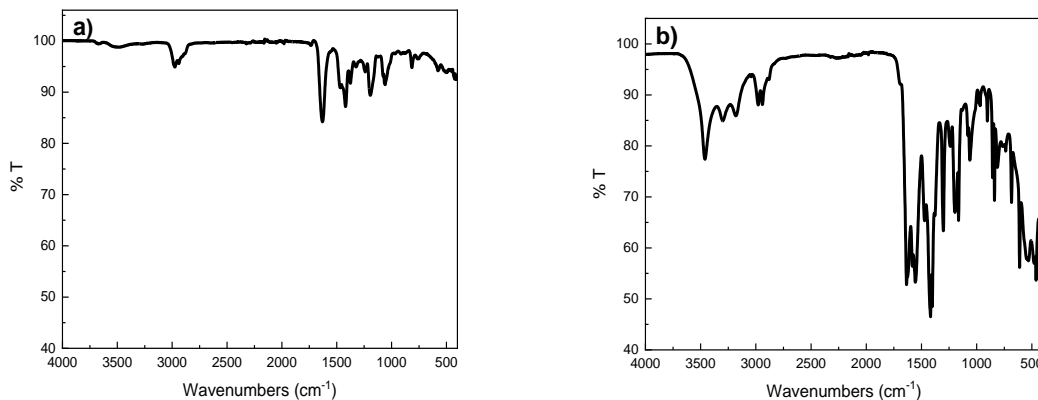


Figure 10: FT-IR spectrum of a) PEOX b) Self-configuration of PEOX-DCA.

Figure 10a show the FT-IR spectrum of the PEOX structure. At 2820-3100 cm^{-1} we see the peak caused by the aliphatic C-H groups in the structure, at 1620 cm^{-1} we see the carbonyl stress peak vibration. In addition, the C-C tensile peak at 1370 cm^{-1} and aliphatic CH_2 vibration peak from CH_2 groups are seen at 1180 cm^{-1} (32). All these structures are compatible with the literature, and the desired PEOX structure has been reached.

Figure 10 b shows the FT-IR spectrum for the PEOX-DCA configuration. In this structure, we also see carbonyl stress vibrations caused by DCA attached to the structure. The secondary carbonyl peak at 1520 cm^{-1} was included in the spectrum (33). In addition, the characteristic structure of the C-H tension peak in the structure has changed, and this change proves that DCA is connected to the structure.

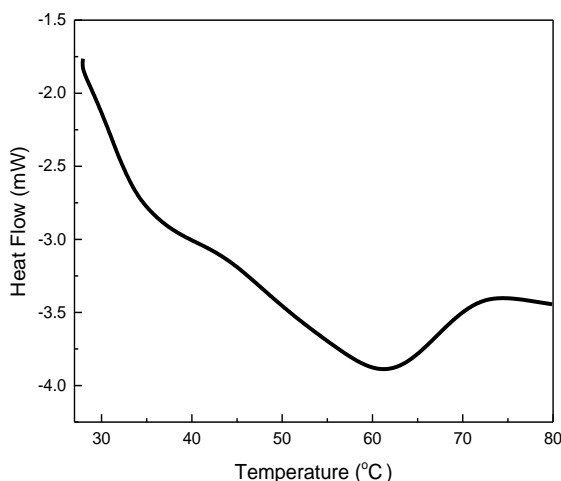


Figure 11: DSC thermogram for PEOX.

Figure 11 shows the DSC thermogram for PEOX. The LCST of the PEOX structure was determined as 61.78 $^{\circ}\text{C}$. The behavior of the building against temperature is reversible. Figure 12 shows the different magnification AFM images of the polymers

obtained by connecting DCA to the PEOX structure. Homogeneous and smooth porosity was determined in the structure at different magnifications. The gaps in Figure 12 show us that DCA and PEOX form a very regular structure.

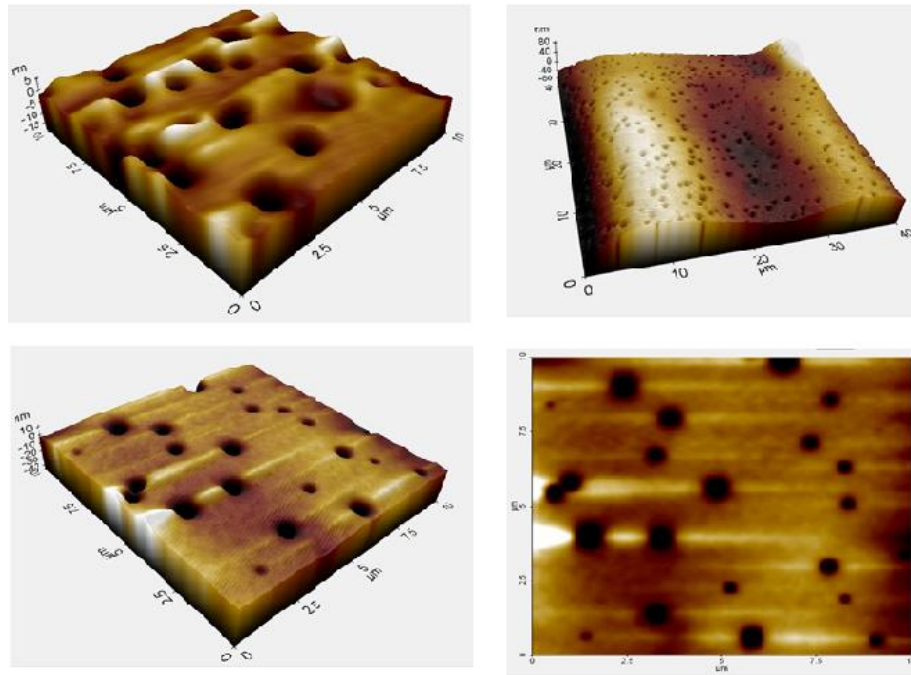


Figure 12: AFM images for PEOX-DCA structuring.

The FT-IR spectrum of the PEOX-PNIPAM blend is presented in Figure 13a. The FT-IR spectrum of the DCA configuration of the PEOX-PNIPAM blend is presented in Figure 13b. The spectrum shows that the most significant change is the carbonyl peak at 1520 cm^{-1} , originating from the DCA structure.

Additionally, there are carbonyl tensile vibrations at 1620 cm^{-1} from PNIPAM and at 1630-1620 cm^{-1} from the PEOX structure (34). It is important to note that all three carbonyl peaks are desired to coexist in the structure.

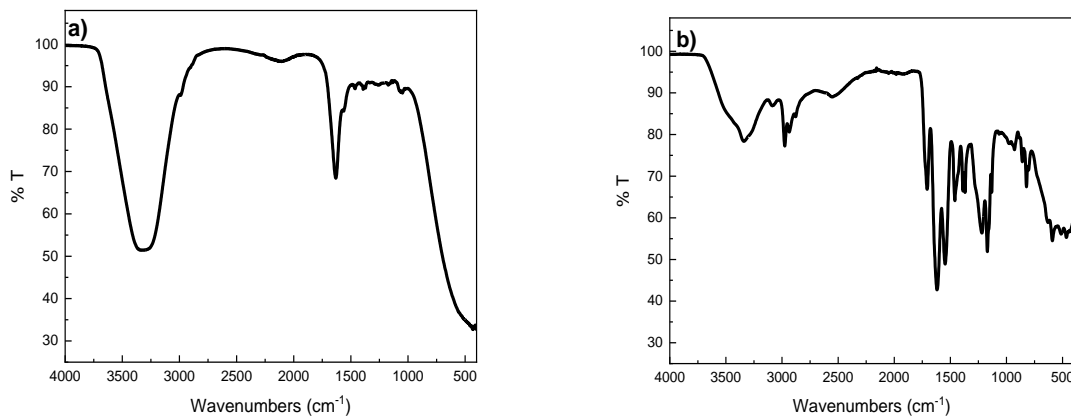


Figure 13: FT-IR spectrum of a) PEOX-PNIPAM blend, b) PEOX-PNIPAM-DCA structuring.

Figure 14 displays the AFM images for the DCA configuration of the PEOX - PNIPAM blend. The clusters on the surface and the rough surface image

indicate that DCA is connected to the PEOX-PNIPAM structure, as shown in the AFM images.

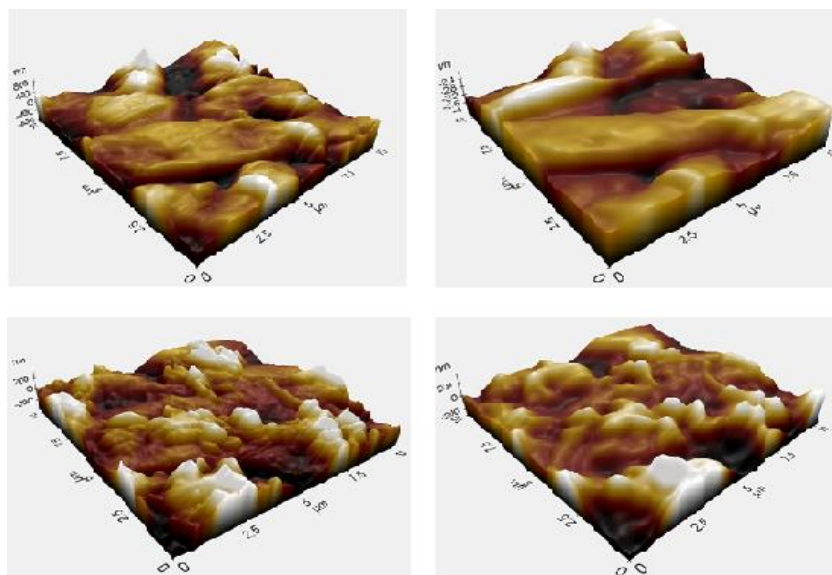


Figure 14: AFM images of PEOX – PNIPAM blend DCA structuring.

4. CONCLUSION

After synthesizing PNIPAM and conducting structural characterization, the LCST value was determined using DSC and UV-VIS. The structuring of PNIPAM with maleic acid (DCA) was then examined. PNIPAM and PEOX polymers were blended in specific proportions, and their LCST behaviors were systematically analyzed. It was discovered that changes greatly influenced the LCST behavior of the blend in hydrophobicity. The addition of PEOX to PNIPAM increased the LCST value. The repeating units of PNIPAM have both hydrophobic and hydrophilic parts. At low temperatures, strong hydrogen bonds form between hydrophilic groups in the polymer and water molecules, which counteract the unwanted free energy caused by the interaction of hydrophobic groups with water molecules. This allows the polymer to dissolve well in water. As the temperature increases, hydrophobic interactions between hydrophobic side groups become stronger while hydrogen bonding weakens. At temperatures above the LCST, interactions between hydrophobic groups dominate. Entropy-induced failure and phase separation are observed in polymer chains. The decrease in the movement of the polymer chains is compensated for by the increase in entropy resulting from the separation of the polymer from a high order around its hydrophobic groups. Therefore, increasing or decreasing the hydrophilic content of PNIPAM results in an increase or decrease in the LCST value, respectively. It is important to understand that the LCST is dependent on both the salt concentration and the molecular mechanisms that cause this behavior. This understanding is crucial for adjusting the LCST as desired for various applications. The present study examined the structures of PNIPAM, PEOX, and PEOX-PNIPAM blends with maleic acid and determined their pH sensitivity.

5. CONFLICT OF INTEREST

The authors state no conflict of interest.

6. ACKNOWLEDGMENTS

This work was supported by Inonu University, BAP 2016-13





7. REFERENCES

1. Pino-Ramos VH, Ramos-Ballesteros A, López-Saucedo F, López-Barriguete JE, Varca GHC, Bucio E. Radiation grafting for the functionalization and development of smart polymeric materials. In: Applications of Radiation Chemistry in the Fields of Industry, Biotechnology and Environment. Springer; 2017. p. 67–94.
2. Wei M, Gao Y, Li X, Serpe MJ. Stimuli-responsive polymers and their applications. *Polym Chem.* 2017;8(1):127–43. Available from: [URL](#)
3. Karimi M, Sahandi Zangabad P, Ghasemi A, Amiri M, Bahrami M, Malekzad H, et al. Temperature-responsive smart nanocarriers for delivery of therapeutic agents: applications and recent advances. *ACS Appl Mater Interfaces.* 2016;8(33):21107–33. Available from: [URL](#)
4. Li J, Kikuchi S, Sato S ichiro, Chen Y, Xu L, Song B, et al. Core-First Synthesis and Thermoresponsive Property of Three-, Four-, and Six-Arm Star-Shaped Poly (N, N-diethylacrylamide) s and Their Block Copolymers with Poly (N, N-dimethylacrylamide). *Macromolecules.* 2019;52(19):7207–17. Available from: [URL](#)
5. Al-Zaidi AT, Al-Dokheily ME, Al-Atabi SH. Low critical solution temperatures and water swelling ratios of some new PNIPAAm copolymers synthesized by free radical polymerization. In: AIP Conference Proceedings. AIP Publishing LLC; 2020. p. 20176.
6. Tseng W, Fang T, Chen C, Hsieh Y, Lai W. Upper Critical Solution Temperature-Type Thermal Response of Soluble Multi-l-Arginyl-Poly-l-Aspartic Acid (cyanophycin) Conjugated with Maltodextrin. *J Polym Sci A Polym Chem.* 2019;57(19):2048–55. Available from: [URL](#)

7. Pasparakis G, Tsitsilianis C. LCST polymers: Thermoresponsive nanostructured assemblies towards bioapplications. *Polymer*, 2020; 211: 123146. Available from: [URL](#)
8. Marsili L, Dal Bo M, Berti F, Toffoli G. Chitosan-Based Biocompatible Copolymers for Thermoresponsive Drug Delivery Systems: On the Development of a Standardization System. *Pharmaceutics*. 2021; 13(11): 1876. Available from: [URL](#)
9. Kocak G, Tuncer C, Bütün V. Stimuli-Responsive Polymers Providing New Opportunities for Various Applications. *Hacettepe J. Biol. & Chem.*, 2020; 48(5): 527-574. Available from: [URL](#)
10. Konefař R, Spěvák J, Černoch P. Thermoresponsive poly (2-oxazoline) homopolymers and copolymers in aqueous solutions studied by NMR spectroscopy and dynamic light scattering. *Eur Polym J*. 2018; 100: 241-52. Available from: [URL](#)
11. Tang Q, Qian S, Chen W, Song X, Huang J. Preparation and characterization of temperature-responsive Ca-alginate/poly(N-isopropylacrylamide) hydrogel. *Polym Int*, 2023; 72: 252-262. Available from: [URL](#)
12. Lusina A, Nazim T, Cegłowski M. Poly(2-oxazoline)s as Stimuli-Responsive Materials for Biomedical Applications: Recent Developments of Polish Scientists. *Polymers*. 2022; 14(19):4176. Available from: [URL](#)
13. Mizusaki M, Endo T, Nakahata R, Morishima Y, Yusa S ichi. pH-induced association and dissociation of intermolecular complexes formed by hydrogen bonding between diblock copolymers. *Polymers (Basel)*. 2017;9(8):367. Available from: [URL](#)
14. Zhu YG, Wang Y, Shi Y, Wong JI, Yang HY. CoO nanoflowers woven by CNT network for high energy density flexible micro-supercapacitor. *Nano Energy*. 2014;3:46-54. Available from: [URL](#)
15. Altıntaş Z, Adatoz EB, Ijaz A, Miko A, Demirel AL. Self-assembled poly (2-ethyl-2-oxazoline)/malonic acid hollow fibers in aqueous solutions. *Eur Polym J*. 2019;120:109222. Available from: [URL](#)
16. Kocak G, Tuncer C, Bütün V. pH-Responsive polymers. *Polym Chem*. 2017;8(1):144-76. Available from: [URL](#)
17. Hendessi S, Güner PT, Miko A, Demirel AL. Hydrogen bonded multilayers of poly (2-ethyl-2-oxazoline) stabilized silver nanoparticles and tannic acid. *Eur Polym J*. 2017;88:666-78. Available from: [URL](#)
18. Oleszko-Torbus N, Utrata-Wesołek A, Bochenek M, Lipowska-Kur D, Dworak A, Wałach W. Thermal and crystalline properties of poly (2-oxazoline)s. *Polym Chem*. 2020;11(1):15-33. Available from: [URL](#)
19. Ohnsorg ML, Ting JM, Jones SD, Jung S, Bates FS, Reineke TM. Tuning PNIPAm self-assembly and thermoresponse: roles of hydrophobic end-groups and hydrophilic comonomer. *Polym Chem*. 2019;10(25):3469-79. Available from: [URL](#)
20. Gandhi A, Paul A, Sen SO, Sen KK. Studies on thermoresponsive polymers: Phase behaviour, drug delivery and biomedical applications. *Asian J Pharm Sci*. 2015;10(2):99-107. Available from: [URL](#)
21. Adams N, Schubert US. Poly (2-oxazolines) in biological and biomedical application contexts. *Adv Drug Deliv Rev*. 2007;59(15):1504-20. Available from: [URL](#)
22. Gaertner FC, Luxenhofer R, Blechert B, Jordan R, Essler M. Synthesis, biodistribution and excretion of radiolabeled poly (2-alkyl-2-oxazoline) s. *Journal of Controlled Release*. 2007;119(3):291-300. Available from: [URL](#)
23. Dutta K, De S. Smart responsive materials for water purification: an overview. *J Mater Chem A Mater*. 2017;5(42):22095-112. Available from: [URL](#)
24. Zou H, Wu Q, Li Q, Wang C, Zhou L, Hou XH, et al. Thermo-and redox-responsive dumbbell-shaped copolymers: from structure design to the LCST-UCST transition. *Polym Chem*. 2020;11(4):830-42. Available from: [URL](#)
25. Chen JJ, Ahmad AL, Ooi BS. Poly (N-isopropylacrylamide-co-acrylic acid) hydrogels for copper ion adsorption: Equilibrium isotherms, kinetic and thermodynamic studies. *J Environ Chem Eng*. 2013;1(3):339-48. Available from: [URL](#)
26. Wang J, Sutti A, Lin T, Wang X. Thermo-responsive PNIPAM hydrogel nanofibres photocrosslinked by azido-POSS. In: *Fiber Society Spring 2013 Technical Conference*. Fiber Society; 2013. Available from: [URL](#)
27. Li G, Song S, Zhang T, Qi M, Liu J. pH-sensitive polyelectrolyte complex micelles assembled from CS-g-PNIPAM and ALG-gP (NIPAM-co-NVP) for drug delivery. *Int J Biol Macromol*. 2013;62:203-10. Available from: [URL](#)
28. Lai H, Wang Z, Wu P. Structural evolution in a biphasic system: poly (N-isopropylacrylamide) transfer from water to hydrophobic ionic liquid. *RSC Adv*. 2012;2(31):11850-7. Available from: [URL](#)
29. Saad A, Mills R, Wan H, Mottaleb MA, Ormsbee L, Bhattacharyya D. Thermo-responsive adsorption-desorption of perfluoroorganics from water using PNIPAm hydrogels and pore functionalized membranes. *J Memb Sci*. 2020;599:117821. Available from: [URL](#)
30. Rusen L, Dinca V, Mustaciosu C, Icriverzi M, Sima LE, Bonciu A, et al. Smart Thermoresponsive Surfaces Based on pNIPAm Coatings and Laser Method for Biological Applications. *Modern Technologies for Creating the Thin-film Systems and Coatings*. 2017;10. Available from: [URL](#)
31. Mourdikoudis S, Pallares RM, Thanh NTK. Characterization techniques for nanoparticles: comparison and complementarity upon studying nanoparticle properties. *Nanoscale*. 2018;10(27):12871-934. Available from: [URL](#)
32. Niranjnathurthi L, Park C, Lim KT. Synthesis and characterization of graphene oxide/poly (2-ethyl-2-oxazoline) composites. *Molecular Crystals and Liquid Crystals*. 2012;564(1):206-12. Available from: [URL](#)
33. Minkova LI, Miteva T, Sek D, Kaczmarczyk B, Magagnini PL, Paci M, et al. Reactive blending of a functionalized polyethylene with a semiflexible liquid crystalline copolyester. *J Appl Polym Sci*. 1996;62(10):1613-25. Available from: [URL](#)
34. Kuo SW. Hydrogen bonding in polymeric materials. *John Wiley & Sons*; 2018. Available from: [URL](#)



Synthesis and Characterization of Calcium Oxide Nanoparticles (CaO NPS) from Snail Shells Using Hydrothermal Method

Wisdom Chukwuemeke Ulakpa^{1*} , Ijara Maryjane Adaeze², Ohiri Augustine Chimezie³, Ayodeji Arnold Olaseinde⁴, Eyide Odeworitse⁵, Erhinyodavwe Onoriode⁶, Oluwatosin Azeez Sarafa⁷ , Moses Aderemi Olutoye⁷ , Paul Dim⁷, Mohammad Siddique⁸ 

¹Department of Chemical Engineering, Delta State University of Science and Technology, Ozoro, 334111, Nigeria.

²Department of Environment, Delta State Ministry of Environment, Asaba, 320109, Nigeria.

³Department of Health, Health and Safety Environment, Promasidor Nigeria Limited, Lagos, 100271, Nigeria.

⁴Department of Materials Science and Engineering, College of Engineering, Computing and Applied Sciences, Clemson University, South Carolina, 29631, USA.

⁵Department of Chemical Engineering, University of Delta, Agbor, 321105, Nigeria.

⁶Department of Mechanical Engineering, University of Delta, Agbor, 321105, Nigeria.

⁷Department of Chemical Engineering, Federal University of Technology, Minna, 920211, Nigeria.

⁸Department of Chemical Engineering BUITEMS, Quetta, 87300, Pakistan.

Abstract: Calcium oxide (CaO) holds significant importance as a catalyst and effective chemisorbent for hazardous gases. This study presents the synthesis of CaO nanoparticles (NPs) using the hydrothermal technique with snail shells' calcium carbonate (CaCO₃) as the starting material. The hydrothermal method offers several advantages over alternative approaches for producing metal oxide NPs, including its simplicity, cost-effectiveness, and ability to operate at low temperatures and pressures. By utilizing waste materials like snail shells as a precursor, the entire process becomes more economical, environmentally friendly, and sustainable. The synthesized NPs were analyzed using various techniques, including Fourier transform infrared spectroscopy (FTIR), X-ray powder diffraction (XRD), scanning electron microscope (SEM), transmission electron microscope (TEM), the Barrett-Joyner-Halenda (BJH) model for pore structure quantification, Brunauer-Emmett-Teller (BET) for surface area calculation, and thermo gravimetric analysis (TGA/DTA-DSC). XRD analysis confirmed that the size of the synthesized CaO NPs was 43.14 nm, determined using the Debye-Scherrer equation. The transmission electron microscopy (TEM) image provided valuable insight into the morphology of the nano-catalyst. The analysis revealed that the nano-catalyst displayed a spherical shape, with an average particle size measuring 50 nanometers. The FTIR and XRD results unequivocally demonstrated the successful conversion of calcium carbonate (CaCO₃) derived from snail shells into calcium oxide (CaO). TGA exhibited a significant weight loss peak at 700 °C, indicating the transformation of CaCO₃ into CaO. The DTA-DSC curve exhibited sharp endothermic peaks at 700 °C, suggesting a decomposition reaction and the formation of a new compound. SEM images displayed porous, rough, and fragile surfaces that became agglomerated at higher temperatures. In other words, the FE-SEM images of NPs illustrated that the particles were predominantly spherical in morphology. Hence, waste snail shells hold promise as a valuable source of calcium for various applications in different fields.

Keywords: Calcium oxide NPs, hydrothermal, snailshell, X-ray diffraction, Transmission electron microscope, Brunauer-Emmett-Teller.

Submitted: January 8, 2024. **Accepted:** March 20, 2024.

Cite this: Chukwuemeke Ulakpa W, Maryjane Adaeze I, Augustine Chimezie O, Arnold Olaseinde A, Odeworitse E, Onoriode E, Azeez Sarafa O, Aderemi Olutoye M, Dim P, Siddique M. Synthesis and Characterization of Calcium Oxide Nanoparticles (CaO NPS) from Snail Shells Using Hydrothermal Method. JOTCSA. 2024;11(2):825-34.

DOI: <https://doi.org/10.18596/jotcsa.1416214>

***Corresponding author's E-mail:** ulakpa.wisdom@yahoo.com

1. INTRODUCTION

The escalating volume of solid waste presents a significant obstacle to establishing a sustainable world. Inadequate waste management practices lead to issues concerning public health and the environment (1). A substantial quantity of solid waste, encompassing municipal, industrial, and hazardous waste, is generated globally. Among these waste products are snail shells, which contribute to environmental degradation and originate from households and restaurants. Snail shells predominantly consist of natural calcium carbonate with limited permeability (1). However, these unwanted materials can be changed to high-quality by-products. Snail shells can serve as a spring of calcium carbonate (CaCO_3) for various applications (2). Unfortunately, the prevailing method of managing waste snail shells involves landfilling, which gives rise to environmental problems. The biodegradation process in landfills, including those that handle food waste, often results in the emission of unpleasant odors. Additionally, the presence of membranes in landfills attracts worms and insects. However, utilizing snail shells can offer several benefits, not only in terms of addressing environmental concerns but also by helping to free up valuable landfill space. The development of nanoparticles has garnered increased awareness due to their superior effectiveness in enhanced surface area. Indeed, scientists have confirmed that nanotechnology has brought about a significant revolution in the field of science. The application of nanotechnology at the nanoscale has indeed unlocked new possibilities and advancements across various scientific disciplines. This progress can be primarily attributed to the unique properties exhibited by nanoparticles (NPs). These properties include an increased surface-to-volume ratio, particle size, charge, shape, and magnetic properties, which differ from their bulk counterparts. Such distinct characteristics of nanoparticles have paved the way for innovative research and applications in fields such as medicine, electronics, materials science, and more, where NPs demonstrate enhanced chemical effectiveness and feasibility at lower temperatures (3). The realm of nanotechnology has made significant strides (4), with NPs finding applications in optical and catalytic domains (3).

In general, materials that have at least one geometrical dimension ranging from 1- 100 nm are typically categorized as nanomaterials (5). Nanocatalysts play a crucial role in various industries because their characteristics are enhanced when they exist in nanosized form. This enhancement is attributed to the larger surface-to-volume ratio of smaller catalysts. Increased pore size and the presence of a vast surface area in nanocatalysts result in a higher number of active sites. As a result, this leads to enhanced catalytic activity and selectivity, along with a longer lifespan and a reduced amount of energy needed to initiate chemical

reactions (6). Furthermore, the utilization of nanocatalysts enables the execution of processes under mild reaction conditions (7).

Calcium oxide is a type of oxide belonging to the group of alkali-earth metals that holds significant potential in various applications. One of its notable advantages is its easy and cost-effective production as nanoparticles (NPs) (4). Calcium oxide nanoparticles (CaO NPs) have been effectively employed as catalysts in numerous reactions (3). Additionally, calcium oxide (CaO) finds applications as a pellet for CO_2 capture and kinetic analysis, as a remediation agent for toxic waste, as an additive in refractory and paint industries, as an antimicrobial agent, as a facilitator for drug delivery, and finding applications in diverse biomedical fields. (8). Its excellent speed and impressive ability to trap carbon dioxide, coupled with its cost-effectiveness and efficiency even in situations with low CO_2 levels, make it a highly promising candidate for carbon capture (9). Furthermore, it can be utilized for the desulfurization of flue gas and as an emission control to combat pollution, as well as for the purification of hot gases. However, it is important to note that CaO is susceptible to air instability and gradually reverts to CaCO_3 when cooled to room temperature (8).

The synthesis procedures for calcium oxide nanoparticles (NPs) vary, and the process that yields the optimum performance in terms of surface area is always preferred (1). There exist numerous techniques for the production of CaO nanoparticles, encompassing sol-gel, thermal decomposition, hydrothermal technique, combustion method, co-precipitation technique, biogenic method, precipitation method, two-step thermal decomposition technique, one-step multi-component synthesis, and microwave synthesis (8). These methods offer the opportunity to customize the physical and chemical properties of nano- CaO , such as its morphology, specific surface area, and capturing efficiency, under specific synthesis conditions (8). However, most of these methods have limitations such as the use of organic solvents (10), high temperatures, lengthy processing times, and complex equipment (10). Typically, CaO nanoparticles are produced by thermally treating precursors like $\text{Ca}(\text{OH})_2$ or CaCO_3 (10). In the synthesis of catalysts through thermal hydration-dehydration, three factors significantly impact the catalytic performance of CaO catalyst: hydration duration, recalcination temperature, and recalcination duration. The basicity of the CaO catalyst, which is directly related to the length of its hydration process (11), can be utilized to estimate its catalytic performance. The objective of this research is to develop calcium oxide (CaO) nanoparticles with high surface area and small particle size using snail shell as a precursor through the hydrothermal method (calcination-hydration-dehydration), to obtain a highly active heterogeneous nanocatalyst. The synthesized particles were characterized using scanning electron microscopy (SEM), X-ray diffraction (XRD), and

Chukwuemeke Ulakpa W et al. JOTCSA. 2024; 11(2): 825-834
transmission electron microscopy (TEM), as well as BET (Brunauer-Emmett-Teller) and thermogravimetric-differential scanning calorimetry (TG-DSC) techniques to determine their suitability for industrial applications.

2. EXPERIMENTAL SECTION

2.1. Materials and Methods

The snail shells were obtained from a nearby restaurant and market, specifically from a dealer who specializes in snail shells. For the experiments, deionized water (H₂O) was utilized with a remarkable purity level of 99%. Furthermore, all the chemicals employed in the experiments were of analytical grade.

2.2. Synthesis of Calcium Oxide Nanoparticles (CaO NPs)

The synthesis of calcium oxide nanoparticles (CaO NPs) involved the preparation of a highly active CaO catalyst through a series of steps including calcination, hydration, and dehydration using snail shells. To begin, the snail shells were thoroughly washed to remove any unwanted materials adhering to their surface. They were then rinsed with distilled water. The washed shells were dried in a hot air oven at a temperature of 110°C for a duration of 12 hours. After drying, the shells were crushed into smaller pieces using a blender, ensuring they could pass through a 60µm sieve. Subsequently, the crushed shells were calcined in a muffle furnace under static air conditions at a temperature of 900°C for a period of 3 hours. This process aimed to transform the calcium species within the shells into CaO particles.

The CaO derived from the shells was then subjected to refluxing in water at a temperature of 80°C. The mixture was stirred for 2 hours using a magnetic stirrer set at 350 rpm and allowed to settle for 12 hours. The resulting whitish product was ground, filtered, and subsequently dried in a hot air oven overnight at a temperature of 120°C. To convert the hydroxide form of the product into its oxide form, the solid product underwent dehydration through recalcination at a temperature of 700°C for a duration of 3 hours. This process yielded a finely powdered white catalyst of nano CaO. To ensure the stability of the obtained product, it was stored in a desiccator to prevent reactions with carbon dioxide and humidity in the air before use. Finally, the samples were subjected to characterization to analyze their properties.

2.3. Characterization of The Synthesized Nanoparticles (NPs)

For this study, several scientific techniques were employed. Fourier-transform infrared spectroscopy (FTIR), thermogravimetric analysis (TGA-DTG-DSC), X-ray diffraction (XRD), Brunauer-Emmett-Teller

RESEARCH ARTICLE

(BET/BJH), scanning electron microscope (SEM), and transmission electron microscope (TEM) were utilized. To conduct crystal structural analysis, X-ray diffraction (XRD) was employed. The diffraction angles (2θ) used ranged from 10 to 90 degrees. Cu Kα radiation (λ = 1.5406 Å) was used as the source of radiation for this analysis. To examine the size, shape, and surface morphology of the nanoparticle, a field emission scanning electron microscope (FE-SEM) with a coater (Quorum Q150T ES/10 mA, 120 s Pt coating) was used. The accelerating voltage for this microscope was set at 10 kV. To determine the different functional groups present in the synthesized nanoparticle, FTIR spectroscopy (FT-IR) (6700 FTIR) was employed. The specific surface area, pore size, and pore volume of the nanocatalyst were measured using N₂ adsorption/desorption isotherm. This analysis was performed using a BET surface area analyzer (Micromeritics ASAP 2020V1.05 software). Powder X-ray diffraction (XRD) was carried out using a Rigaku MiniFlex-300/600 to determine the catalytic phases. The diffractogram was developed within a 2θ range of 10°-80° with a scan rate of 10°/min. The obtained XRD data was compared with the database of the 'Joint Committee on Powder Diffraction Standards' (JCPDS) to confirm the exact catalyst phase. Finally, the chemical analysis of the synthesized CaO nanoparticle was performed using an X-ray fluorescence spectrometer (Shimadzu, Japan).

3. RESULTS AND DISCUSSION

3.1. Fourier Transform Infrared Analysis (FTIR) of CaONPs

Figure 1 illustrates the results of the Fourier Transform Infrared (FTIR) analysis conducted on calcium oxide (CaO) nanoparticles. The spectra revealed several absorption bands at specific wavenumbers: 3716.2, 2512.2, 2113.4, 1982.9, 1897.2, 1796.6, 1394.0, 872.2, 711.9, and 663.5 cm⁻¹. The sharp absorption band observed at 2512.2 cm⁻¹ can be attributed to the stretching vibrations of hydroxyl (O-H) groups. This band is a result of the formation of calcium hydroxide (Ca(OH)₂) through the hydration process of CaO (12). Furthermore, the broad peak at 2113.4 cm⁻¹ indicates the presence of physically adsorbed water molecules attached to the nanoparticles, as it signifies the -OH stretching vibrations (13). Additionally, absorption bands at 1982.9 and 1796.6 cm⁻¹ correspond to the absorption of CO₂ on the nanoparticle's surface and the stretching vibrations of the Ca-OH bonds, respectively (14). The most prominent peaks observed at 1394.0, 872.2, and 711.9 cm⁻¹ confirm the presence of calcium oxide nanoparticles, as they are assigned to the vibrations of the Ca-O bonds (12, 14).

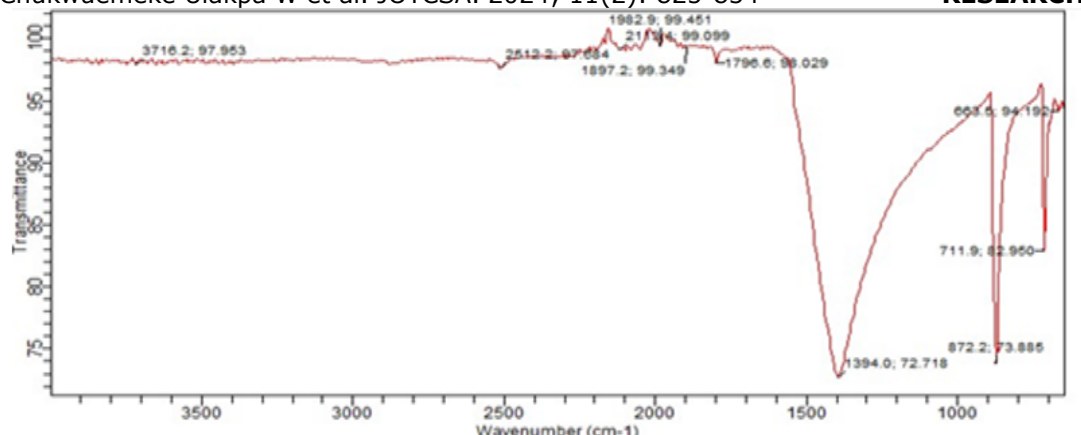


Figure 1: Fourier Transform Infrared analysis (FTIR) of CaONPs.

3.2. X-ray Fluorescence (XRF) Analysis

The chemical makeup of the CaO NPs in this investigation can be found in Table 1. The primary constituents of the catalyst include oxygen (O), calcium (Ca), aluminum (Al), titanium (Ti), and magnesium (Mg). Additionally, it comprises various metallic oxides, namely silicon dioxide (SiO₂), vanadium pentoxide (V₂O₅), chromium trioxide (Cr₂O₃), manganese oxide (MnO), iron oxide (Fe₂O₃), cobalt oxide (Co₃O₄), nickel oxide (NiO), copper

oxide (CuO), niobium oxide (Nb₂O₃), tungsten trioxide (WO₃), diphosphorus pentoxide (P₂O₅), sulfur trioxide (SO₃), calcium oxide (CaO), magnesium oxide (MgO), potassium oxide (K₂O), barium oxide (BaO), aluminum oxide (Al₂O₃), tantalum pentoxide (Ta₂O₅), titanium dioxide (TiO₂), zinc oxide (ZnO), silver oxide (Ag₂O), chlorine (Cl), zirconium dioxide (ZrO₂), and tin dioxide (SnO₂). These components are also believed to serve as the primary active sites of the catalyst (15).

Table 1: X-ray fluorescence (XRF) of synthesized CaONPs.

Elements	Weight/Concentration (wt%)		
O	29.113	Fe	0.072
Mg	0.000	Co	0.051
Al	1.872	Ni	0.028
Si	0.087	Cu	0.044
P	0.000	Zn	0.006
S	0.091	Zr	0.073
Cl	0.256	Nb	0.291
K	0.057	Ag	0.000
Ca	67.178	Sn	0.571
Ti	0.021	Ba	0.052
V	0.013	Ta	0.063
Cr	0.001	W	0.046
Mn	0.014	Total	100.00

3.3. Brunauer-Emmett-Teller-BET-(Textural Properties Analysis)/Barrett-Joyner-Halenda (BJH) Method

The results obtained from the BET and BJH analyses of the artificially produced nano-CaO revealed that it had a surface area of 5.11 square meters per gram, an average pore diameter of 1.1 nanometers, and a pore volume of 0.002556 cubic centimeters per gram. On the other hand, the reported average pore diameter of the nanoparticles (NPs) ranged from greater than 2 nanometers to 50 nanometers, indicating the presence of both microspores and active sites on the external surface of the nano-CaO catalyst. It is worth noting that the total surface area

often plays a crucial role in determining the catalytic performance of a catalyst. Therefore, in this study, we measured the surface areas of the synthesized catalysts to understand the impact of the total surface area on the catalytic reaction. Figure 2 displays the BET plot of the synthesized CaO NPs, while Figures 3(a) and 3(b) represent the nitrogen adsorption-desorption isotherms and pore distribution of the synthesized CaO NPs, respectively. The NPs exhibited a characteristic type III isotherm with a hysteresis loop of H3 type, indicative of a micro-porous structure. This implies that the prepared NPs possess a micro-porous structure, which further supports the presence of microspores on the catalyst's surface.

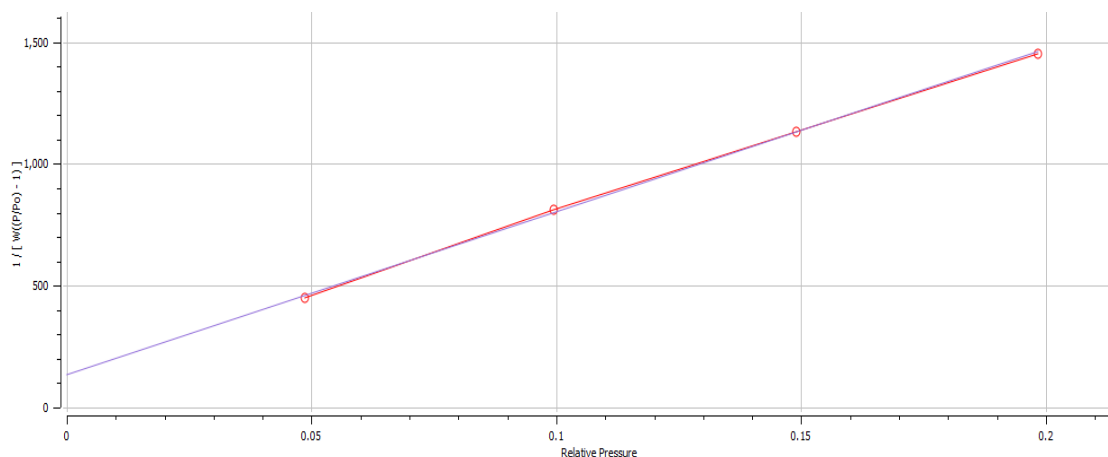


Figure 2: BET plot of CaO NPs.

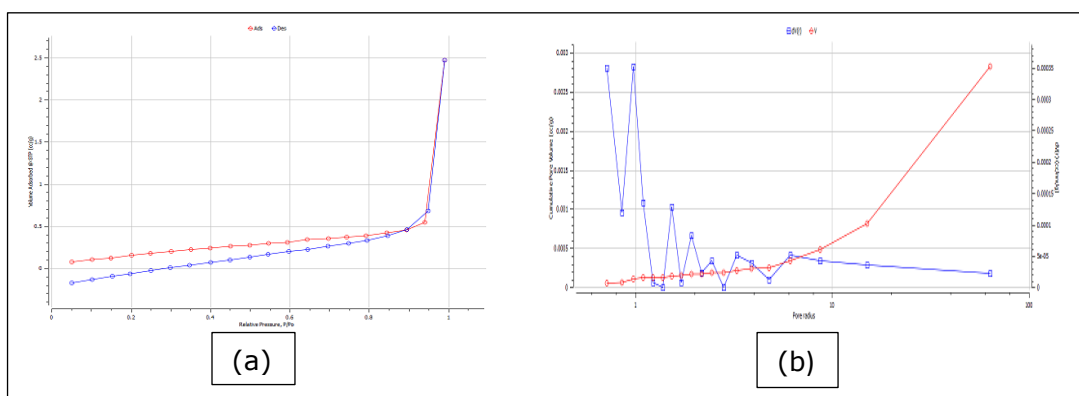


Figure 3: (a): N_2 adsorption-desorption isotherm of CaO NPs, (b): Barrett-Joyner-Halenda (BJH) pore size and pore volume distribution (desorption isotherm) of CaO NPs.

3.4. X-ray Diffraction (XRD) Analysis

X-ray diffraction analysis (XRD) was employed for the characterization of the catalysts (16). As the samples were in the form of polycrystalline powder, the XRD analysis focused on identifying specific lattice planes that generated peaks at corresponding angular positions, known as 2θ , as determined by Bragg's law (16). The 2θ peaks observed for CaO nanoparticles were found at angles of 23.09° , 29.44° , 31.45° , 36.06° , 39.44° , 43.19° , 47.53° , 48.53° , 56.20° , 57.41° , 58.12° , 60.67° , 61.44° , 63.16° , 64.70° , 65.64° , 69.16° , 70.28° , 72.92° , 76.29° , 77.16° , 81.53° , 83.75° , and 84.90° . These peaks displayed a significant resemblance to the standard ICDD (The International Centre for Diffraction Data) file for CaO (JCPDS: 00-005-0586), with corresponding values of (h k l) as (0 1 2), (1 0 4), (0 0 6), (1 1 0), (1 1 3), (2 0 2), (0 1 8), (1 1 6), (2 1 1), (1 2 2), (1 0 1), (2 1 4), (1 1 9), (1 2 5), (3 0 0), (0 0 1), (2 1 7), (0 2 1), (1 2 8), (2 2 0), (1 1

1), (2 1 1), (1 3 4), and (2 2 6), respectively. These planes corresponded to the calcite phase and were observed in the nano CaO catalyst prepared through thermal-hydration-dehydration treatment. The XRD pattern confirmed the formation of calcium oxide in the cubic phase (17, 18), which aligned with the findings of previous studies (19, 20). The average crystallite sizes (D) were determined using the full width at half maximum (FWHM) of the XRD peaks, following Debye-Scherrer's equation: $D = K\lambda/(\beta \cos\theta)$, where β represents the full width at half maximum (FWHM) in radians and θ is the position of the maximum diffraction peak (incident angle of the X-ray). The shape factor, K, typically around 0.9, was also considered. In this study, the X-ray wavelength (λ) used was 1.5406 \AA for Cu K α . Applying Debye-Scherrer's equation, the average crystallite size of the CaO nanoparticles was calculated to be 43.14 nm, while the particle size of the synthesized nanoparticles ranged from 20.07 to 70.25 nm.

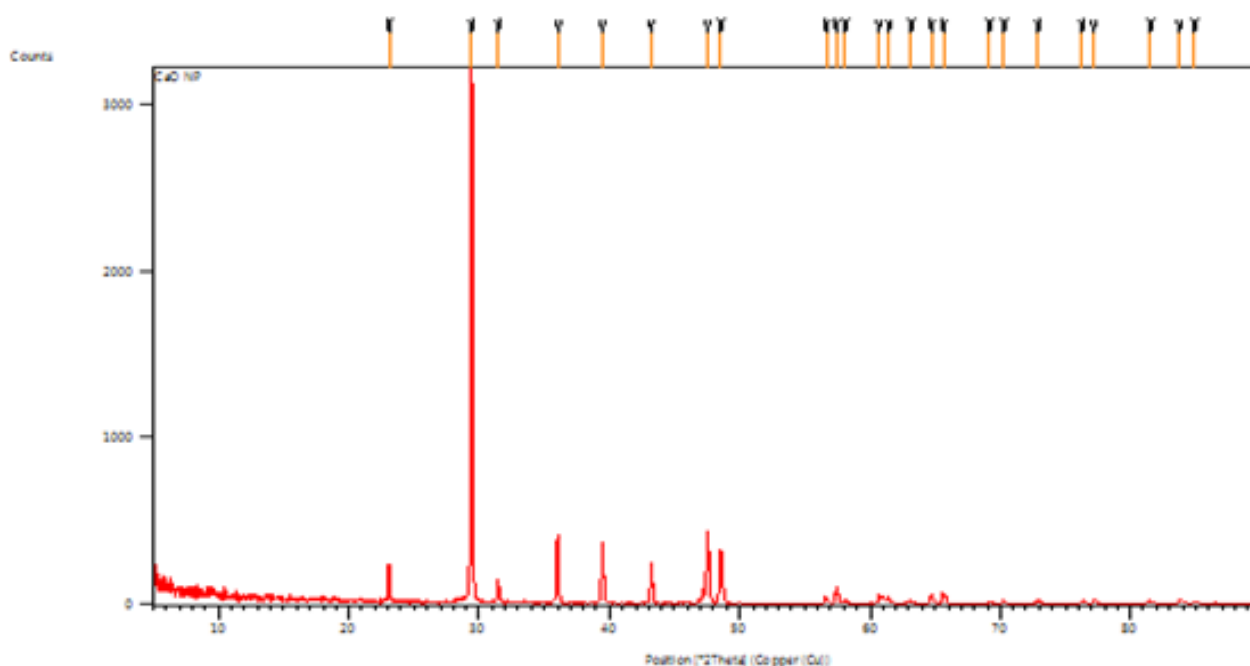


Figure 4: XRD pattern of synthesized CaO NPs.

Table 2: Peak angles and their corresponding (h k l) planes, peak height, full width at half maximum, d-spacing, relative intensity, and crystallite sizes of CaO NPs.

Peak number	Peak Pos.(2 θ°)	Miller indices (h k l)	Peak-Height (cts)	FWHM (2 θ°)	d-spacing (Å)	Rel. Int. (%)	D *. nm	Average D (nm)
1	23.0923	(0 1 2)	223.73	0.1476	3.85166	6.97	56.10	43.14
2	29.4474	(1 0 4)	3209.89	0.1476	3.03329	100.00	56.10	
3	31.4552	(0 0 6)	137.26	0.1476	2.84411	4.28	56.16	
4	36.0610	(1 1 0)	387.89	0.1771	2.49073	12.08	46.92	
5	39.4463	(1 1 3)	366.73	0.1771	2.28442	11.42	46.92	
6	43.1931	(2 0 2)	239.36	0.2066	2.09455	7.46	41.16	
7	47.5289	(0 1 8)	416.78	0.1476	1.91310	12.98	56.23	
8	48.5328	(1 1 6)	322.68	0.1476	1.87585	10.05	56.10	
9	56.6280	(2 1 1)	32.08	0.1771	1.62541	1.00	46.86	
10	57.4113	(1 2 2)	80.52	0.1771	1.60508	2.51	46.84	
11	58.1288	(1 0 1)	19.56	0.2362	1.58697	0.61	35.13	
12	60.6790	(2 1 4)	57.46	0.1181	1.52624	1.79	70.25	
13	61.4462	(1 1 9)	32.39	0.1771	1.50901	1.01	46.87	
14	63.1679	(1 2 5)	13.66	0.3542	1.47196	0.43	23.41	
15	64.7045	(3 0 0)	56.14	0.1181	1.44067	1.75	70.25	
16	65.6424	(0 0 1)	63.44	0.1476	1.42234	1.98	56.21	
17	69.1648	(2 1 7)	9.16	0.3542	1.35826	0.29	23.42	
18	70.2817	(0 2 1)	19.50	0.3542	1.33939	0.61	23.42	
19	72.9271	(1 2 8)	22.30	0.3542	1.29719	0.69	23.42	
20	76.2934	(2 2 0)	10.16	0.2362	1.24812	0.32	35.12	
21	77.1636	(1 1 1)	21.77	0.4133	1.23621	0.68	20.07	
22	81.5328	(2 1 1)	18.18	0.1771	1.18065	0.57	46.87	
23	83.7588	(1 3 4)	20.64	0.2952	1.15485	0.64	28.10	
24	84.9228	(2 2 6)	8.15	0.3542	1.14197	0.25	23.42	

* D: The crystallite size (nm)

3.5. Scanning Electron Microscopy (SEM) Analysis

The image displayed in Figure 5 illustrates the physical appearance of the CaO nanoparticles that were synthesized. The scanning electron microscopy (SEM) image reveals that the particles have an irregular shape with a rough surface and fractured texture. Additionally, the particles tend to have a

spherical shape and possess a porous structure with numerous cavities, similar to a porous material. This porous structure is believed to contribute to the increased presence of basic sites on the catalyst, as mentioned in reference (21). The porosity observed in the CaO nanoparticles is attributed to the release of a significant amount of gaseous water molecules

during the decomposition of $\text{CaCO}_3 \cdot \text{H}_2\text{O}$, as reported in reference (12).

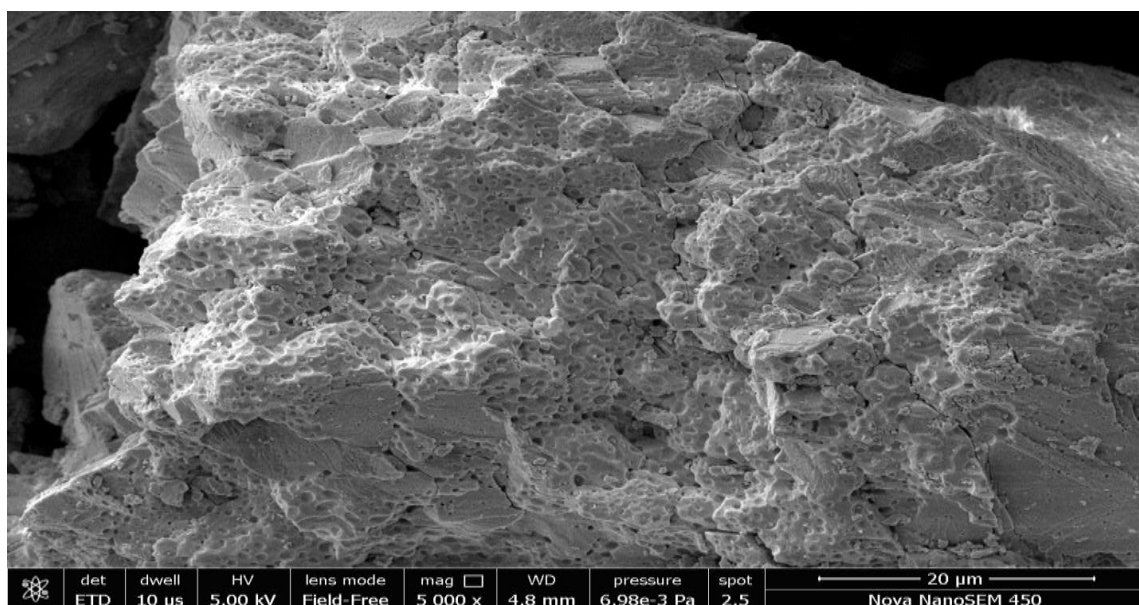


Figure 5: Scanning electron microscope of synthesized CaO NPs.

3.6. High-Resolution Transmission Electron Microscopy (HRTEM)

The high-resolution transmission electron microscope (HR-TEM) is a valuable technique for determining the characteristics of particles, such as their morphology, phase, and structural properties. It also provides crystallographic information. Additionally, HR-TEM is useful for identifying the mesoporous structure of nanoparticles. Figure 6 illustrates the HRTEM image of CaO nanoparticles.

Upon analyzing the high-resolution TEM micrograph (Figure 6), it was discovered that the CaO

nanoparticles exhibited a particulate morphology, with particle sizes smaller than 50 nm. Notably, the nano-CaO particles tended to agglomerate, forming larger and spherical particles, as depicted in Figure 6. The particle size observed using TEM corresponds well with the average crystallite size estimated by X-ray diffraction (XRD). This finding aligns with the results reported by (22).

Furthermore, the presence of crystallites contributes to an increase in the surface area, thereby enhancing the interaction between reactants and the catalyst surface.

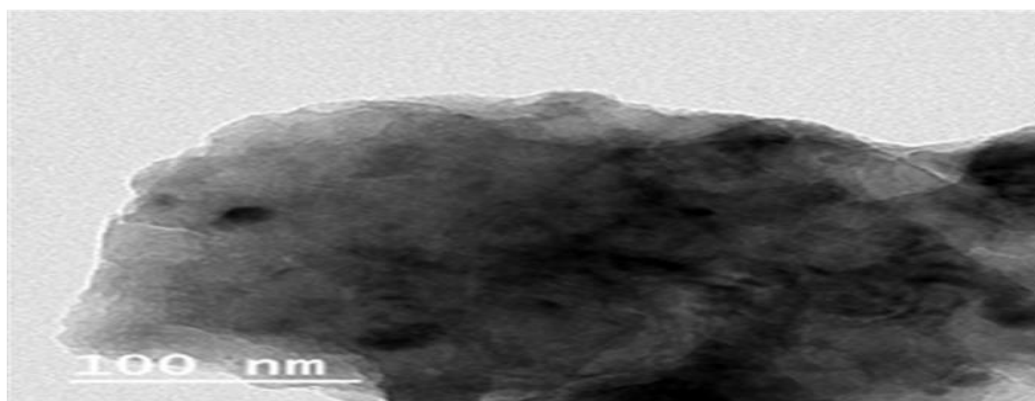


Figure 6: HRTEM image of CaO NPs.

3.7. Thermogravimetric Analysis (TGA)/Differential Thermal Analysis (DTA/DSC)

The synthesized calcium oxide nanoparticles (CaO NPs) were subjected to thermal gravimetric analysis (TGA) and differential thermal analysis (DTA)/differential scanning calorimetry (DSC) to comprehend the influence of elevated temperatures on their thermal ability to withstand heat, as well as to identify the thermal transitions occurring during

the process. Figure 7 presents the TGA/DTA-DSC curve of the CaO NPs. The TGA curve demonstrates a significant weight loss of the catalyst (approximately 43%) at higher temperatures (700 °C). The weight reduction can be ascribed to the disintegration of carbonic material, resulting in the formation of carbon monoxide (CO) and carbon dioxide (CO_2), as well as the elimination of water from calcium hydroxide ($\text{Ca}(\text{OH})_2$) and the

decomposition of calcium carbonate (CaCO₃) (12). Furthermore, the DTA/DSC curve supports these findings by revealing sharp endothermic peaks within the temperature range of 700-800 °C. These peaks indicate decomposition reactions and the formation

of new compounds. Therefore, the TGA/DTA-DSC results conclusively confirm that a high temperature is necessary for the calcination process of CaO nanoparticles.

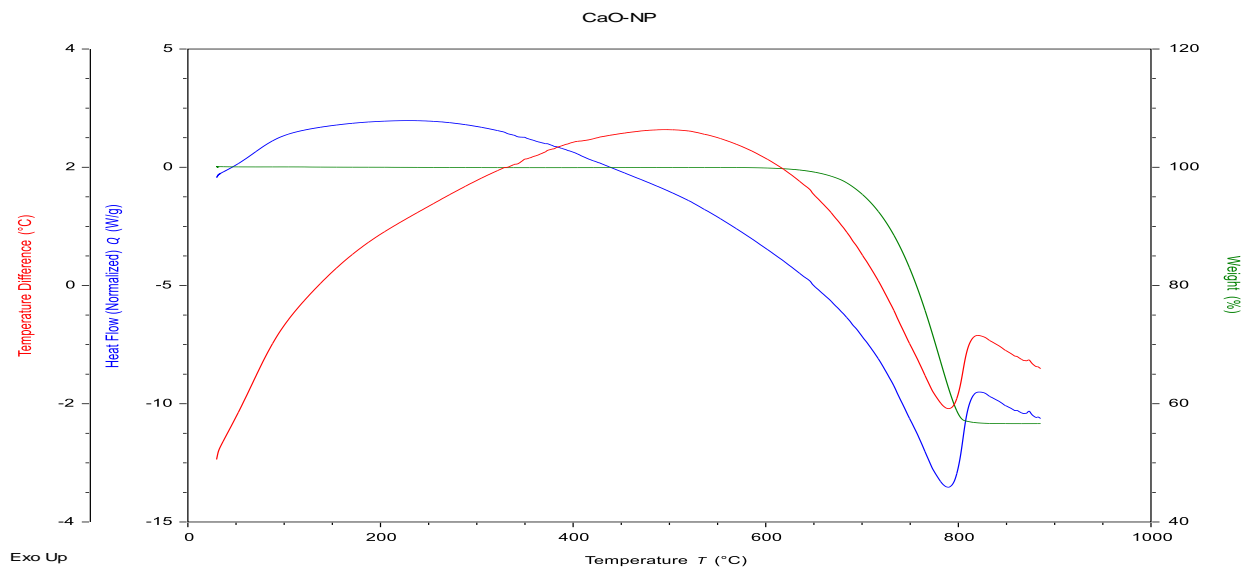


Figure 7: TGA/DTA-DSC of CaO NPs.

3.8. X-ray Photoelectron Spectroscopy (XPS) Analysis of CaONPs

A comprehensive examination using X-ray photoelectron spectroscopy (XPS) was conducted to ascertain the chemical composition and bonding state of the CaO nanoparticle catalysts. The XPS full survey spectrum, displayed in Figure 8, provides insights into the presence of oxygen (O), calcium (Ca), and carbon (C) on the catalyst's surface. By deconvoluting the C 1s spectra, two distinct peaks were observed at 284.36eV and 289.31eV binding

energy, with a full width at half maximum (FWHM) of 2.7eV. These peaks indicate the existence of metal carbonates, specifically C-C and C=O bonds. The O1s spectrum shows a peak at 530.95 eV, suggesting the presence of metal oxide. Furthermore, the deconvoluted Ca2p spectrum exhibits peaks at 346.28 eV and 350.12 eV, indicating the occurrence of calcium oxide (CaO) and calcium carbonate (CaCO₃), respectively. Detailed information about the XPS survey peaks can be found in Table 3.

Table 3: XPS survey Peaks of CaO NPs.

	Name	Peak Binding Energy (eV)	FWHM eV	Area (P) CPS.eV	Atomic %
CaO NPs	O1s	530.95	2.76	1814758.72	47.19
	C1s	284.36, 289.14	2.7	617465.92	38.83
	Ca2p	346.28, 350.12	2.72	1273838.92	13.97

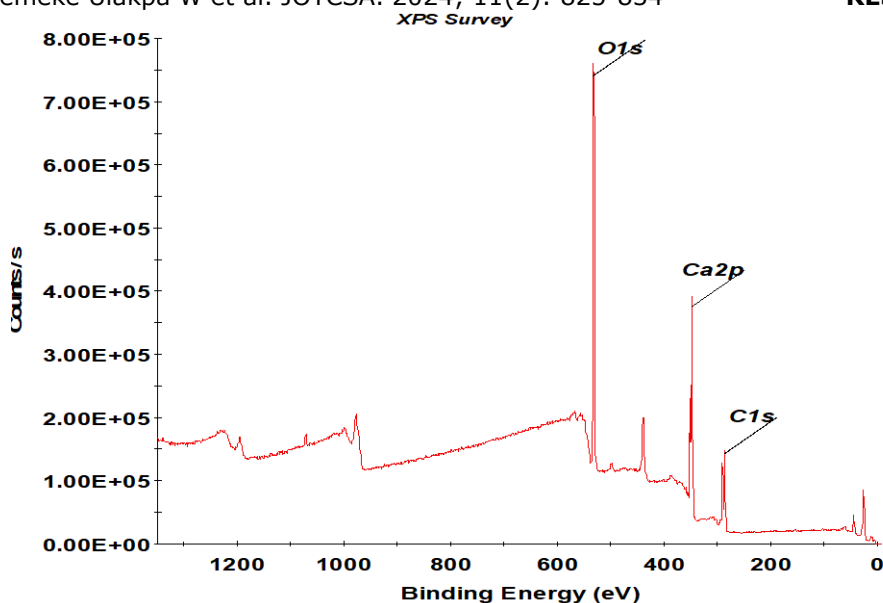


Figure 8: XPS full survey spectrum of CaO NPs.

4. CONCLUSION

In conclusion, this research demonstrates that calcium oxide (CaO) nanoparticles can be successfully produced using the hydrothermal method with calcium carbonate (CaCO_3) as a precursor. The process involves heating the CaCO_3 at a temperature of 900 °C for 3 hours and then recalcining it at 700 °C for another 3 hours. The resulting CaO nanoparticles exhibit a nearly spherical morphology, as observed through scanning electron microscopy (SEM) images.

Furthermore, the BET (Brunauer-Emmett-Teller) analysis reveals that the prepared nanoparticles possess micropore range porosity. This indicates their potential for various applications. X-ray diffraction investigations validate the polycrystalline characteristic of the CaO nanoparticles. The proposed method is both simple and convenient, eliminating the need for organic solvents, expensive raw materials, or complex equipment. As a result, it offers an economical approach to synthesizing calcium oxide particles on a large scale, utilizing snail shells as a sustainable source of calcium carbonate. The findings of this research highlight the promising capabilities of CaO nanoparticles in serving as effective drug carriers, given their bioactive and biocompatible properties. Furthermore, the particle surfaces exhibit micropores with a surface area of 5.11 m^2/g , an average pore diameter of 1.1 nm, and a pore volume of 0.00255 cm^3/g . These characteristics further enhance the nanoparticles' potential for various applications.

In addition, this research contributes to the conversion of agricultural waste into valuable resources. The hydrothermal treatment of snail shells, combined with the synthesized catalyst, results in the formation of calcium oxide (CaO). This not only provides a sustainable solution for waste management but also presents an opportunity for resource utilization.

In summary, this study demonstrates the successful production of CaO nanoparticles using a hydrothermal method. The nanoparticles exhibit desirable properties, making them suitable for various applications, including drug delivery. Furthermore, the incorporation of snail shells as a primary resource aids in the promotion of sustainable agricultural waste management.

5. CONFLICT OF INTEREST

The authors declare no conflict of interest.

6. ACKNOWLEDGMENTS

The authors are grateful to the Department of Agricultural and Bioresources Engineering, Futminna for their assistance in carrying out the research work in their Laboratory. The authors are also grateful to Scientium analyze solutions, India.

7. REFERENCES

- Habte L, Shiferaw N, Mulatu D, Thenepalli T, Chilakala R, Ahn J. Synthesis of Nano-Calcium Oxide from Waste Eggshell by Sol-Gel Method. Sustainability [Internet]. 2019 Jun 7;11(11):3196. Available from: [<URL>](#).
- Cree D, Rutter A. Sustainable Bio-Inspired Limestone Eggshell Powder for Potential Industrialized Applications. ACS Sustain Chem Eng [Internet]. 2015 May 4;3(5):941–9. Available from: [<URL>](#).
- Alobaidi YM, Ali MM, Mohammed AM. Synthesis of Calcium Oxide Nanoparticles from Waste Eggshell by Thermal Decomposition and their Applications. Jordan J Biol Sci [Internet]. 2022 Jun 1;15(2):269–74. Available from: [<URL>](#).
- Bano S, Pillai S. Green synthesis of calcium oxide nanoparticles at different calcination temperatures. World J Sci Technol Sustain Dev [Internet]. 2020 May 19;17(3):283–95. Available from: [<URL>](#).

5. Bensebaa F. Nanoparticle Fundamentals. In: Interface Science and Technology [Internet]. Elsevier; 2013. p. 1–84. Available from: [<URL>](#).
6. Banković–Ilić IB, Miladinović MR, Stamenković OS, Veljković VB. Application of nano CaO–based catalysts in biodiesel synthesis. *Renew Sustain Energy Rev* [Internet]. 2017 May 1;72:746–60. Available from: [<URL>](#).
7. Serp P, Philippot K. Nanomaterials in Catalysis [Internet]. Serp P, Philippot K, editors. *Nanomaterials in Catalysis: First Edition*. Wiley; 2013. Available from: [<URL>](#).
8. Khine EE, Koncz-Horvath D, Kristaly F, Ferenczi T, Karacs G, Baumli P, et al. Synthesis and characterization of calcium oxide nanoparticles for CO₂ capture. *J Nanoparticle Res* [Internet]. 2022 Jul 1;24(7):139. Available from: [<URL>](#).
9. Granados-Pichardo A, Granados-Correa F, Sánchez-Mendieta V, Hernández-Mendoza H. New CaO-based adsorbents prepared by solution combustion and high-energy ball-milling processes for CO₂ adsorption: Textural and structural influences. *Arab J Chem* [Internet]. 2020 Jan 1;13(1):171–83. Available from: [<URL>](#).
10. Mirghiasi Z, Bakhtiari F, Darezereshki E, Esmaeilzadeh E. Preparation and characterization of CaO nanoparticles from Ca(OH)₂ by direct thermal decomposition method. *J Ind Eng Chem* [Internet]. 2014 Jan 25;20(1):113–7. Available from: [<URL>](#).
11. Asikin-Mijan N, Taufiq-Yap YH, Lee HV. Synthesis of clamshell derived Ca(OH)₂ nano-particles via simple surfactant-hydration treatment. *Chem Eng J* [Internet]. 2015 Feb 15;262:1043–51. Available from: [<URL>](#).
12. Gaurav K, Kumari S, Dutta J. Utilization of Waste Chicken Eggshell as Heterogeneous CaO Nanoparticle for Biodiesel Production. *J Biochem Technol* [Internet]. 2021 Jun 17;12(1):49–57. Available from: [<URL>](#).
13. Sumathi N. Optical characterization of calcium oxide nanoparticles. *Int J Adv Technol Eng Sci*. 2017;5(2):63–7.
14. Kalanakoppal Venkatesh Y, Mahadevaiah R, Haraluru Shankaraiah L, Ramappa S, Sannagoudar Basanagouda A. Preparation of a CaO Nanocatalyst and Its Application for Biodiesel Production Using Butea monosperma Oil: An Optimization Study. *J Am Oil Chem Soc* [Internet]. 2018 May 19;95(5):635–49. Available from: [<URL>](#).
15. Rajkumari K, Rokhum L. A sustainable protocol for production of biodiesel by transesterification of soybean oil using banana trunk ash as a heterogeneous catalyst. *Biomass Convers Biorefinery* [Internet]. 2020 Dec 28 [cited 2024 Mar 22];10(4):839–48. Available from: [<URL>](#).
16. Charles Ugbede A, Elizabeth Jumoke E, Abdullahi Abdullahi M. Development and Application of Heterogeneous Catalyst from Snail Shells for Optimization of Biodiesel Production from *Moringa Oleifera* Seed Oil. *Am J Chem Eng* [Internet]. 2021;9(1):1–17. Available from: [<URL>](#).
17. Almutairi FM. Biopolymer Nanoparticles: A Review of Prospects for Application as Carrier for Therapeutics and Diagnostics. *Int J Pharm Res Allied Sci* [Internet]. 2019;8(1):25–35. Available from: [<URL>](#).
18. Babaei H, Sepahy AA, Amini K, Saadatmand S. The effect of titanium dioxide nanoparticles synthesized by bacillus tequilensis on clb gene expression of colorectal cancer-causing Escherichia coli. *Arch Pharm Pract*. 2020;11(1):22–31.
19. Gupta J, Agarwal M. Preparation and characterization of CaO nanoparticle for biodiesel production. *AIP Conf Proc* [Internet]. 2016 Apr 13;1724(1):020066. Available from: [<URL>](#).
20. Bet-Moushoul E, Farhadi K, Mansourpanah Y, Nikbakht AM, Molaei R, Forough M. Application of CaO-based/Au nanoparticles as heterogeneous nanocatalysts in biodiesel production. *Fuel* [Internet]. 2016 Jan 15;164:119–27. Available from: [<URL>](#).
21. Simpen IN, Winaya INS, Subagia IDGA, Suyasa IWB. Green Nano-Composite of CaO/K-Sulfated TiO₂ and Its Potential as a Single-Step Reaction Solid Catalyst for Biofuel Production. *KnE Life Sci* [Internet]. 2022 Jun 7;2022:382-392–382–392. Available from: [<URL>](#).
22. Kodeh FS, El-Nahhal IM, Elkhair EA, Darwish AH. Synthesis of CaO–Ag-NPs @CaCO₃ Nanocomposite via Impregnation of Aqueous Sol Ag-NPs onto Calcined Calcium Oxalate. *Chem Africa* [Internet]. 2020 Sep 14;3(3):679–86. Available from: [<URL>](#).



Copper Oxide Nano Biochar from Spent Coffee Grounds for Phosphate Removal and its Application as an Antibacterially Active Entity

Biruk Bezabeh Yimam^{1*} , Gamada Begna Sisay¹ , Eskedar Getachew Feleke¹

¹Chemistry Department, Mizan Tepi University P.O.Box 121, Tepi, Ethiopia

Abstract: From the viewpoint of both eutrophication and sustainable use of phosphate, the removal and recovery of phosphate from wastewater are important. Adsorption is seen as a viable alternative for effective phosphate removal, even at low concentrations. It is very simple to operate and cheaper. Among the various adsorbents tested, biomass-derived nanomaterials, such as nanobiochar, have shown promising efficiency. However, the use of pristine biochar is often less effective and difficult to recycle. In the present study, copper oxide-modified nanobiochar from spent coffee grounds is presented as an effective phosphate adsorbent. The adsorbent was prepared by the acid digestion of spent coffee grounds, followed by the co-precipitation of copper metal. The developed adsorbent was characterized by BET, FTIR, and XRD. Batch mode adsorption studies were conducted to assess the adsorption efficiency of the developed adsorbent and to investigate the effect of pH, initial concentration, contact time, and adsorbent dose. It was observed that acidic conditions favored the adsorption of phosphate, with maximum adsorption efficiency (93%) at pH 3. The maximum equilibrium phosphate adsorption capacity in this study was 50.2 mg/g at 25 °C, pH 3, a phosphate concentration of 20 mg/L, and an adsorbent dose of 35 mg/mL. The batch experimental data fit the Freundlich isotherm with regression ($R^2 = 0.991$), which signifies that the surface of the adsorbent is heterogeneous. Adsorption kinetic data were best fitted with the pseudo-second-order kinetic model ($R^2 = 0.996$), indicating that the adsorption process was dominated by chemisorption. The copper oxide nanoparticles and Cu/NBC showed relatively higher zone inhibition in gram-positive bacteria than in gram-negative bacteria at similar concentrations. This might be due to the higher activity of the nanoparticle extract on gram-positive bacteria, as most nanoparticle extracts were more active in gram-positive bacteria. This difference may be explained by the difference in the structure of the cell wall in gram-positive bacteria, which consists of a single layer, and in gram-negative bacteria, which has a multi-layered structure and is quite complex. In the majority of test bacteria, Cu/NBC showed better activity. The higher activity of this nanomaterial might be associated with the number of bioactive metabolites and their synergistic activities.

Keywords: Adsorption, Antibacterial activity, Copper oxide nano biochar, Phosphate, Spent coffee

Submitted: October 5, 2023. **Accepted:** February 13, 2024.

Cite this: Yimam BB, Sisay GB, Feleke EG. Copper Oxide Nano Biochar from Spent Coffee Grounds for Phosphate Removal and its Application as an Antibacterially Active Entity. JOTCSA. 2024;11(2):835-44.

DOI: <https://doi.org/10.18596/jotcsa.1369920>

***Corresponding author.** E-mail: birukbezabeh04@gmail.com

1. INTRODUCTION

Phosphorus is necessary for the growth of plants and is essential for all living things. Rock phosphate is a finite resource that is tapped into for fertilizer production, food production, and contemporary farming (1). Phosphate accumulates in water systems due to industrial and agricultural discharge. They can result in the phosphate enrichment of water bodies, which is occurring worldwide and is known as eutrophication (2). Hence, from the viewpoint of both eutrophication

and sustainable use of phosphate, the removal and recovery of phosphate from wastewater, manure, and sludge are important (3).

To date, many different methodologies have been mapped out for the mitigation of aqueous phosphates, such as anion exchange (4), chemical precipitation, adsorption, etc. Chemical precipitation is the most commonly used technique; however, it is limited by the generation of large amounts of sludge; the separation of chemically bonded phosphate can be difficult and

costly; and it is unsuitable for small-scale plants (5). Adsorption is considered a promising alternative for the effective removal and recovery of phosphate, even at low concentrations (6). Hence, the design of an effective adsorbent with economic feasibility is very important. Various adsorbents, such as polymers (7), metal oxides/hydroxides (8), and biomass-derived adsorbents such as activated carbon and biochar (9), have been studied, and promising results have been reported.

The material mentioned in the above paragraph requires expensive raw materials for their preparation and difficulty in their operation. Therefore, establishing an economical adsorbent is imperative (10). In contrast, biochar, which is a carbon-rich biomass source formed by thermochemical conversion has elicited much attention due to its kindness to the environment and economics. For the present study, coffee grounds were selected as sources of biomass. However, most of the biochar has a low adsorption capacity for phosphate because of its anion-dominated surface. Hence, it's important to modify the biochar by converting macrobiochar to nanobiochar with size reduction followed by co-precipitation of cationic metals, such as $\text{Fe}^{2+}/\text{Fe}^{3+}$, Mg^{2+} , and Mg/Al , on the nanobiochar to enhance its affinity towards phosphate. Compared to pristine nanobiochar (NBC), metal-modified nanobiochar has the maximum phosphate adsorption capacity because the surface of the adsorbent becomes cations-dominated, which makes it suitable for upcoming phosphate. So in this study, copper oxide modifies the surface of nanobiochar made from coffee grounds.

Copper oxide nanoparticles and copper oxide nanoparticle nanobiochar (Cu/NBC) show strong antibacterial properties against pathogens. It can inhibit the growth of these microorganisms due to the damage they cause to the membrane of bacterial cells (11, 12). The application of nanomaterials as new antimicrobials should provide new modes of action and/or different cellular targets compared with existing antibiotics, which somehow promote multiple drug-resistant microbes (12). To the best of our knowledge, this is the first adsorbent reported by combining the nano-scale feature of biochar with copper metal modification.

The main objective of this study is to develop copper-modified nanobiochar from spent coffee

grounds for phosphate recovery, and its antibacterial activity.

2. EXPERIMENTAL

2.1. Chemicals and Materials

Analytical-grade chemicals and reagents were all employed in this research project without further purification. Ammonium molybdate tetrahydrate (CAS 12054-85-2), $(\text{NH}_4)_6\text{Mo}_7\text{O}_{24}\cdot 4\text{H}_2\text{O}$ (99%), copper nitrate hexahydrate (CAS 13478-38-1), $(\text{Cu}(\text{NO}_3)_2\cdot 6\text{H}_2\text{O})$ (99%), potassium dihydrogen phosphate (CAS 7778-77-0), (KH_2PO_4) (98%), antimony potassium tartrate (CAS 28300-74-5), $(\text{C}_8\text{H}_4\text{K}_2\text{O}_{12}\text{Sb}_2\cdot 3\text{H}_2\text{O})$ (99.5%), were purchased from Research Lab Fine Chemicals, Mumbai, India. Mueller-Hinton Agar (CAS 9002-18-0, MHA) and Dimethyl Sulfoxide (CAS 67-68-5, Hi-Media Laboratories Pvt. Ltd., India)

Characterization was performed by Brunauer – Emmett – Teller (BET) (SA-9600, USA), a Fourier transform infrared spectrometer (FT-IR, iS50ABX Thermo Scientific, Germany), an X-ray diffraction spectrometer (XRD-700 X-RAY, Germany), and a UV-Vis spectrophotometer (Biochrom, UK).

2.2. Preparation of Copper Oxide Nano Biochar

First, spent coffee grounds from nearby coffee shops were gathered, cleaned, and oven-dried. At various temperatures (250, 350, and 450 °C), the cleaned spent coffee grounds were treated to gradual pyrolysis in a muffle furnace. To create uniform-sized particles, the obtained biochar was mashed in a mortar and pestle and sieved using a 150.0 μm mesh (5, 13). The size of the biochar particles was reduced by acid digestion in a hydrothermal autoclave reactor. The process was typically allowed to finish in a fume hood after 1.0 g of the resulting biochar was put into a hydrothermal autoclave reactor holding 60.0 mL of concentrated HNO_3 and H_2SO_4 (1:3 ratio). Finally, the product was collected, filtered, washed, and stored for further experiments (1,5). The co-precipitation of metal ions allowed for the modification of nanobiochar. Typically, 200.0 mL of solutions containing $\text{CuSO}_4\cdot 6\text{H}_2\text{O}$ (0.2 M) in a 2:1 ratio were added to 0.4 g of nanobiochar. After that, 1.0 M NaOH was added drop by drop while being stirred rapidly for 1 hr. After allowing the reaction mixture to sit for 24 hrs, the precipitate was ultimately removed, cleaned, and kept for later investigations as shown in Figure 1(13).

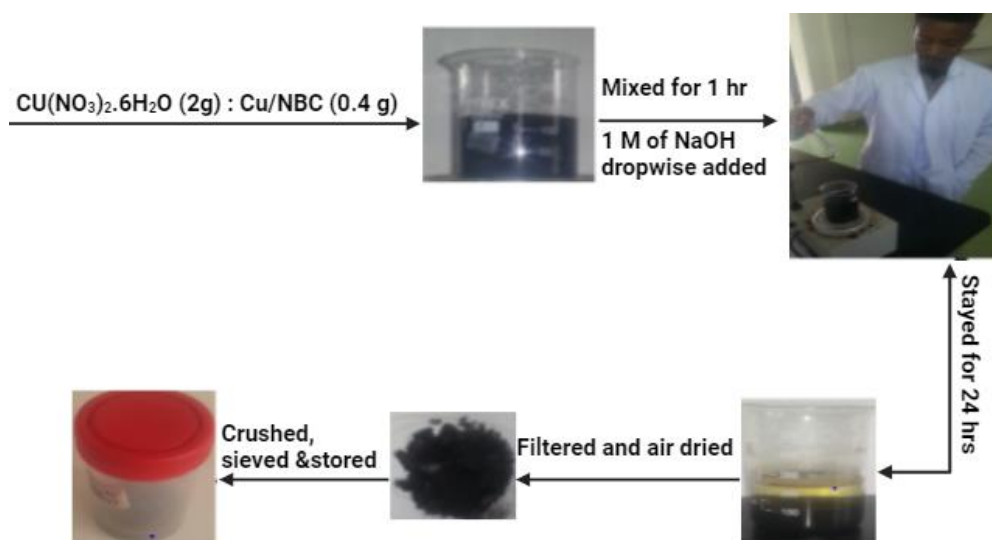


Figure 1: The schematic representation of the preparation of Cu/NBC.

2.3. Adsorption study

In batch-mode adsorption studies, the material capacity for phosphate adsorption was evaluated. In a series of batch mode tests, factors affecting the efficiency of the adsorption, such as pH (3–12) and a dose of adsorbent (15–35 mg), were investigated using the one factor-at-a-time approach. Quantification of the residual phosphate concentration was measured by the ascorbic acid method (Method, 1978) using a calibration curve from phosphate external standards (1, 11, 12, 14). The removal efficiency and the amount of phosphate adsorbed were determined by using equations (1) and (2), respectively.

$$\% \text{ removal} = \frac{C_o - C_f}{C_o} \times 100 \quad (\text{Eq. 1})$$

$$\text{Adsorption capacity} = \frac{C_o - C_f}{\frac{V}{m}} \quad (\text{Eq. 2})$$

Where C_o and C_f are the initial and final phosphate concentrations, q_t is the amount of phosphate adsorbed at time t , V is the volume solution, and m is the mass of the adsorbent used. The adsorption isotherm was done by fitting the equilibrium data into the linear form of the Langmuir (Eq. (3)) and Freundlich (Eq. (4)) isotherm models.

$$q_e = \frac{q_m k_L C_e}{1 + k_L C_e} \quad (\text{Eq. 3})$$

$$q_e = k_f C_e^{1/n} \quad (\text{Eq. 4})$$

where q_e (mg g^{-1}) and C_e (mg L^{-1}) are equilibrium adsorption capacity and equilibrium concentration, respectively; $1/n$ is the intensity of adsorption; K_f (mg g^{-1}) (Lmg^{-1}) $^{1/n}$ is the Freundlich adsorption constant; q_m (mg g^{-1}) is the maximum adsorption capacity; and K_L (L mg^{-1}) is a Langmuir constant (12). Similarly, the kinetics study was done by fitting the equilibrium data into pseudo-first (Eq.

(5)) and second-order (Eq. (6)) kinetic models shown below.

$$q_e = q_e(1 - e^{-k_1 t}) \quad (\text{Eq. 5})$$

$$q_e = \frac{k_2 q_e^2}{1 + k_2 q_e} t \quad (\text{Eq. 6})$$

Where q_e and q_t (mg g^{-1}) are the amounts of phosphate adsorbed at equilibrium and at time t , respectively; k_1 (min^{-1}), and k_2 ($\text{g mg}^{-1} \text{min}^{-1}$), are the rate constants of the corresponding models.

2.4. Antibacterial analysis of copper-modified nano biochar

2.4.1. Bacterial test organisms and standard antibacterial disc

The standard American Type Cell Culture (ATCC) bacterial species of Salmonella typhi, Escherichia coli, Staphylococcus aureus, and Streptococcus pneumoniae were obtained from the Department of Biology at Mizan-Tepi University, Ethiopia. The standard antibacterial disc used for the study was gentamicin.

2.4.2. Antibacterial activity

The Mueller-Hinton Agar (MHA) used was made according to previously reported literature (15–17), which called for mixing 38.0 g of powder media with 1.0 L of distilled water, sealing the mixture in a container, and autoclaving it at 121°C for 15 minutes. After that, the media were put on sterilized Petri dishes. After the media had solidified, 100.0 mL of the working stock culture was distributed with a sterile cotton swab, and stainless steel cork borer wells were formed in each Petri dish. Then different concentrations of nano copper oxide particles and nanobiochar (100 $\mu\text{g/mL}$, 250 $\mu\text{g/mL}$, and 500 $\mu\text{g/mL}$) were prepared by dilution of the stock solution in DMSO (negative control) and poured into the well using a micropipette. The plates were incubated for 24 hours at 37°C (16, 17). The extracts were tested in triplicate, and the findings were shown as the

mean standard deviation. The diameter of the zone of inhibition was measured in millimeters (mm).

3. RESULT AND DISCUSSION

3.1. Preparation and Characterization of Cu/NBC

The nanobiochar was obtained by first optimizing pyrolysis and then acid digestion. Co-precipitation modifies it with copper metal. Table 1 represents the nitrogen adsorption and desorption isotherms of adsorbents at room temperature. As shown in the table, the copper modification considerably increased the adsorbent's specific surface area. Since the specific surface area refers to both the total surface pore and external surfaces, the obtained result shows that Cu/NBC is more favorable for the adsorption process and antibacterial.

Table 1: BET Specific Surface Area of the nano biochar from nano biochar and after Cu²⁺ modification.

Adsorbent	BET (m ² /g)
NBC	7.09
Cu ²⁺ /NBC	124.9

XRD was used to determine the crystallinity of the prepared adsorbent material. The peaks at 32.06°, 35.69°, 38.996°, and 48.93°, corresponding to (110), (002), (111), and (202) planes, can be assigned to the monoclinic structure of CuO (JCPDS, file no. 801268), respectively, as shown in Figure 2.b. The broad peak is centered at 24.5°, indicating the amorphous carbon phase in the nano-biochar, as shown in Figure 2.a. Hence, the XRD study confirms the availability of crystalline metallic phases of Cu on the adsorbent.

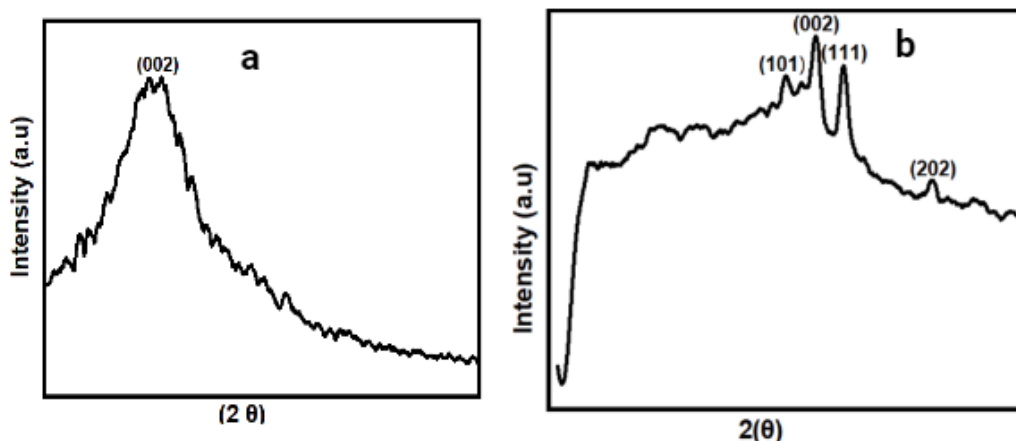


Figure 2: XRD peaks of (a), NBC; (b), CuO/NBC.

The surface functional groups involved were checked by FTIR (Fig. 3a-c). As seen in Fig. 3a, the FTIR spectrum of the NBC consists of absorption bands at 1716 cm⁻¹, 1546 cm⁻¹, and 1156 cm⁻¹ which correspond to C=O, C=C, and C-O stretching vibrations, respectively. After modification, a peak appears at 602 cm⁻¹ which

corresponds to the CuO (Fig. 3c). This is in agreement with the XRD data and shows that the metal is successfully loaded on the NBC surface. After adsorption, two new bands appear at 1163 cm⁻¹, and 765 cm⁻¹ which can be assigned P-O stretching and P-O-P bending modes, respectively (1).

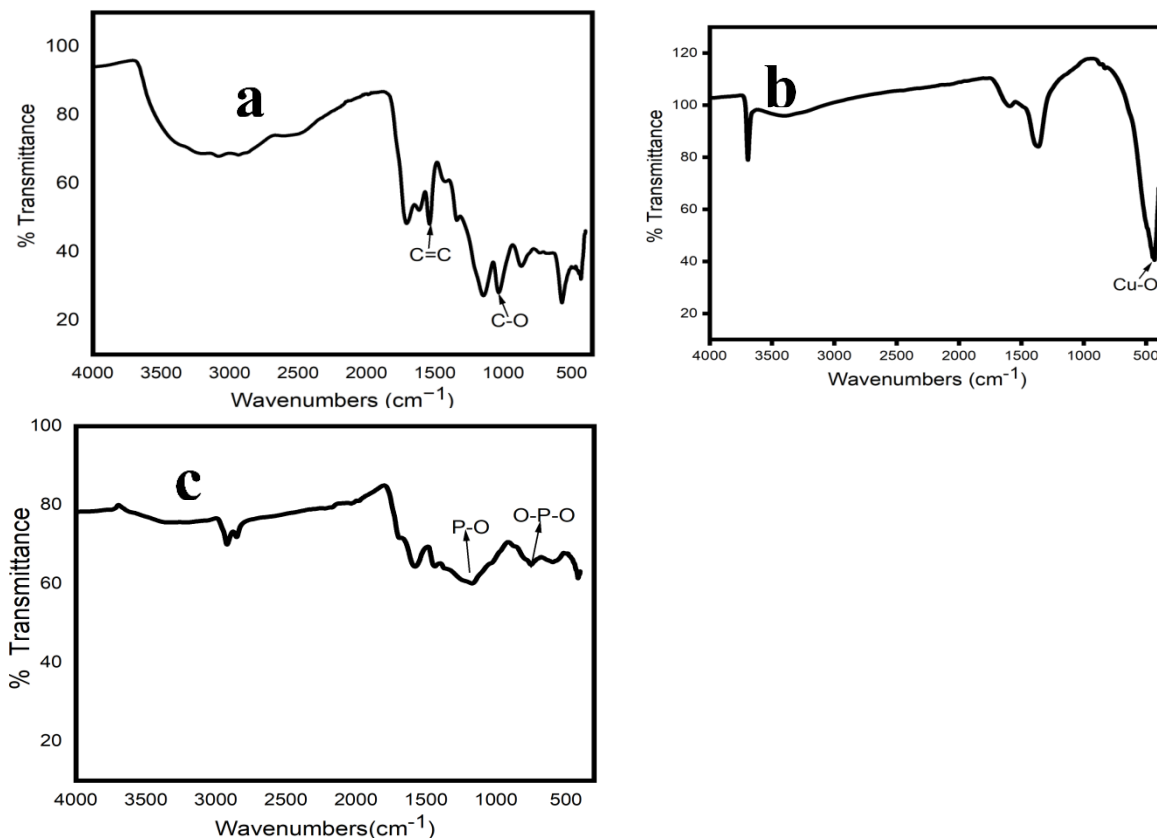


Figure 3: FTIR spectra of the adsorbents (a) NBC ; (b)Cu/NBC before adsorption ; (c) Cu/NBC after adsorption.

3.2 Adsorption Studies

The effect of pH, dose of adsorbent, contact time, and initial concentration on the adsorption efficiency was systematically studied in a batch-mode adsorption study by varying one factor at a time. The effect of pH on the adsorption of phosphate was studied by varying the pH of the solution from 3–12 while fixing other parameters. As shown in Fig. 4a, the phosphate removal efficiency reached its maximum (93%) at pH 3. The maximum adsorption capacity at pH 3 suggests that, in addition to the electrostatic attraction, there is precipitation of copper phosphate. This is because, for pH less than 2, H_3PO_4 and $\text{H}_2\text{PO}_4^{-1}$ are dominant species that trigger the precipitation of copper phosphate (18). This trend obtained is in agreement with previous studies on phosphate removal by Mg/Zr-spent coffee nano biochar adsorbents (Sisay *et al.*). Figure 4b shows the percentage of phosphate removal at various adsorbent doses. As seen in the figure, the percent removal increased with the adsorbent dose and reached its optimum (96.2%), and 19.24 mg/L of phosphate adsorbed at 35

mg of Cu/NBC, indicating that 35 mg of Cu/NBC could effectively remove 20 mg/L phosphates at pH 3. The increase in adsorption efficiency with an adsorbent dose can be attributed to the availability of additional active sites that could take up the phosphate anions.

The effect of contact time on phosphate adsorption by Cu/NBC was investigated by varying the contact time from 25- 100 minutes in batch mode adsorption experiments. As shown in Figure 4.d the adsorption process was very fast initially with more than 98 % of the adsorbate being removed in 25 minutes. The % removal continued to increase and started to stabilize after 85 minutes of contact time suggesting the attainment of the adsorption equilibrium. Thus 85 minutes is the optimal time for the study. The effect of initial concentration on the adsorption process was studied by conducting batch mode experiments at different initial concentration levels of phosphate (10-50 mg/L) while maintaining the rest three parameters constant. As shown in Figure 4.c the percent of adsorption was found to decrease with an increase in the initial concentration of adsorbate.

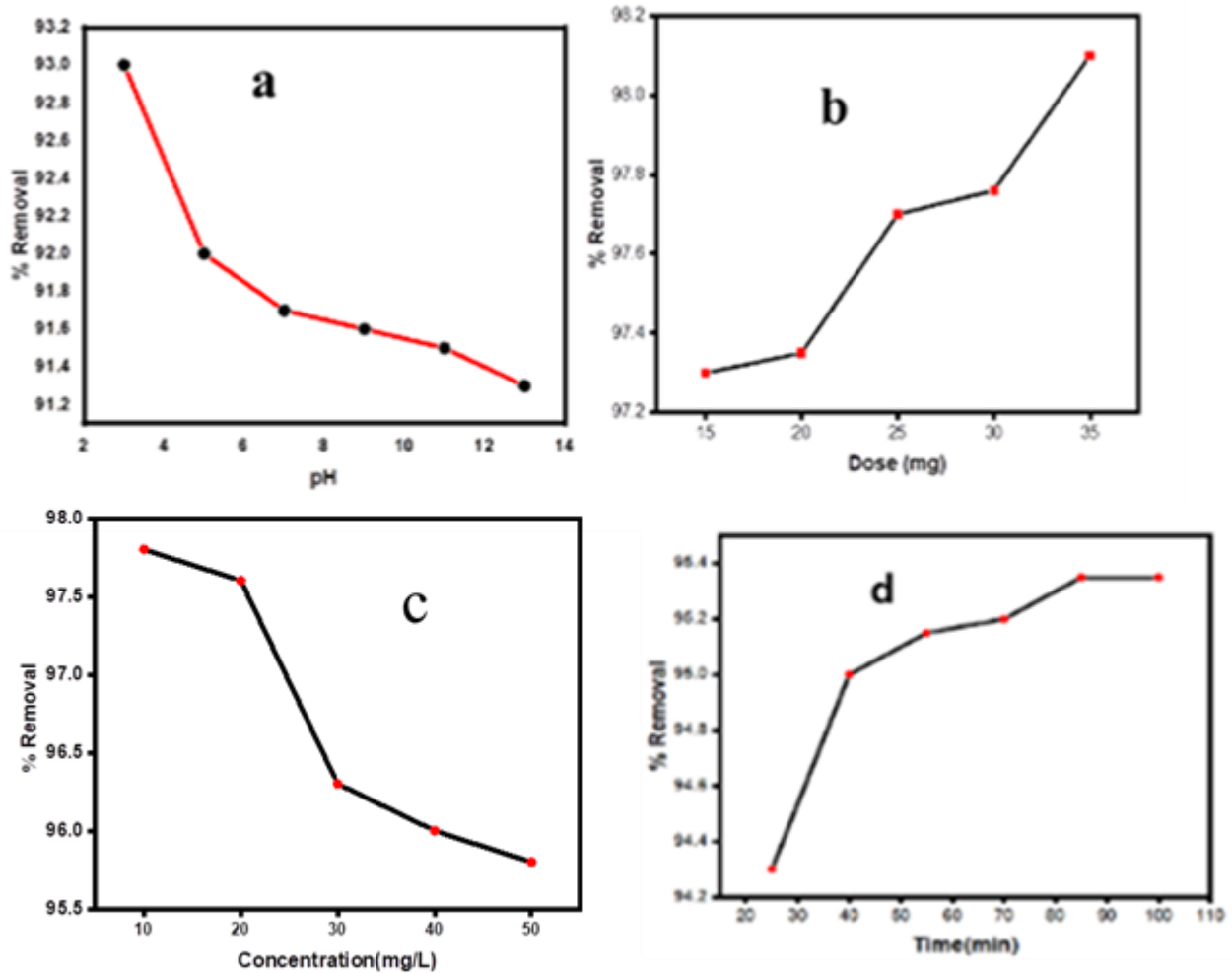


Figure 4: Effect of (a) pH; (b) effect of dose ; (c) initial concentration; and (c) effect of contact time of adsorbent on the adsorption efficiency.

3.2.1 Adsorption isotherm

The equilibrium data obtained at different phosphate concentrations (10–50 mg/L) at a fixed mass of adsorbent were fitted into Langmuir and Freundlich adsorption isotherm models (equations

3&4 respectively). As seen in Fig. 5a-b and Table 2, the Freundlich isotherm model better conforms to the equilibrium data ($R^2 = 0.991$).

Table 2: Freundlich and Langmuir Adsorption Parameters for PO_4^{3-} adsorption on Cu/NBC.

Langmuir model			Freundlich model		
K_L (L/mg)	q_m (mg/g)	R^2	K_F (mg/g)	N	R^2
1.57	142.9	0.984	50.2	1.27	0.991

The above results suggest that the adsorption of phosphate on Cu/NBC follows the heterogeneous surface and multilayer adsorption process.

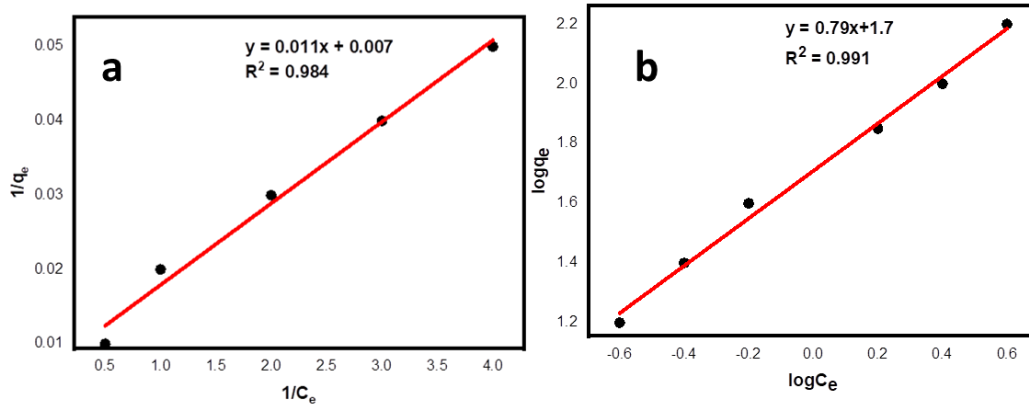


Figure 5: Phosphate adsorption isotherm of Cu/NBC; (a) Langmuir adsorption ; (b) Freundlich isotherm model.

3.2.2. Adsorption kinetics

As shown in Table 3, and Figure 6 the pseudo-first-order kinetic model is not applicable, since the correlation coefficient ($R^2 = 0.952$) obtained with this approximation is relatively low and the calculated $q_{e, cal}$ values did not match the experimental q_e values well. This is because near

equilibrium the experimental data deviate notably from the previous data obtained during the first stage of the experiment(19). The correlation coefficient obtained with the pseudo-second-order is, however, much higher (0.996), and the calculated q_e values show a good agreement with the experimental q_e values as seen in Table 3.

Table 3: Pseudo first order and Pseudo second order parameters for PO_4^{3-} adsorption on Cu/NBC.

Pseudo first order				Pseudo second order			
q_e exp (mg/g)	q_e , cal (mg/g)	k_1 (min^{-1})	R^2	q_e , exp (mg/g)	q_e , cal (mg/g)	K_2 (g/mg min)	R^2
26.2	0.06	0.05	0.952	26.2	26.3	0.0987	0.996

The above results suggest that the adsorption process was mainly controlled by the chemical reaction process due to either the sharing or exchange of electrons, rather than mass transfer. In this study metallic-modified nanobiochars have

an abundant active site this is the reason why chemisorption is the dominant mechanism. Similar results were reported in the study of phosphorus removal and recovery in phosphate by Mg/Zr nano biochar (1).

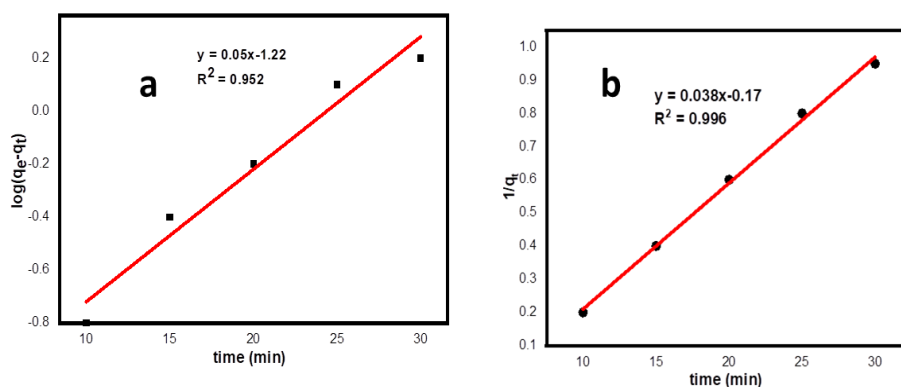


Figure 6: Adsorption kinetics of phosphate on Cu/NBC: (a) pseudo-first-order model; (b) pseudo-second-order model.

3.2.3. Comparison of Cu/NBC adsorption capacity with adsorbents

The adsorption capacity (mg/g) of Cu/NBC found in this study was compared with other metal-modified adsorbents for phosphate removal

reported by other authors as shown in **Table 4**. It can be seen from the table that the Cu/NBC has by far better adsorption capacity than most of the recently reported materials for phosphate adsorption.

Table 4: The comparison of the adsorption capacity of Cu/NBC with other adsorbents.

S/N	Adsorbent	Adsorption capacity ($\frac{mg}{g}$)	Reference
1	Lanthanum-doped silica	47.89	8
2	Mg-biochar	14.33	20
3	Mg-Fe layered double hydroxides	16.31	21
4	Ca (OH) ₂ -biochar	36.74	22
5	Magnetic Carbon Nanofibers	7.26	23
9	Mg-Zr NBC	39.4	1
10	Cu/NBC	50.2	This work

3.3. Antibacterial Analysis of Copper Oxide Nanoparticles and Nano Biochar

3.3.1. Antibacterial screening results

In this investigation, the antibacterial activities of copper oxide nanoparticles and Cu/NBC were evaluated using the agar well diffusion method at a concentration of 100, 250, and 500 μ g/mL as shown in Table 5. The maximum zone of inhibition for the Cu/NBC was achieved for *S. aureus* at 17.31 ± 0.19 mm at the concentration of 500 mg/mL, while the minimum antibacterial activity for the copper oxide nanoparticles for *S. typhi* and *E. coli* was obtained at 7.0 ± 0.29 mm and 7.00 ± 0.40 mm at a concentration of 10 mg/mL respectively.

The copper oxide nanoparticles and Cu/NBC have shown antibacterial activity based on the different concentrations that are explained in different

literature (20,21). The copper oxide nanoparticles and Cu/NBC extract show greater antibacterial activity against gram-negative and gram-positive bacterial tests. The result is in agreement with the findings of, (20,21) who reported that *E.coli* and *S.typhi* were present respectively (Fig 7).

The copper oxide nanoparticles and Cu/NBC showed relatively higher zone inhibition in gram-positive bacteria than in gram-negative bacteria at similar concentrations. This might be due to the higher activity of the nanoparticle extract on gram-positive bacteria as most nanoparticle extracts were more active in gram-positive bacteria. This difference may be explained by the difference in the structure of the cell wall in gram-positive bacteria which consists of a single layer and the gram-negative bacteria, which is a multi-layered structure and quite complex (15-17).

Table 5: Antibacterial activities of copper nanoparticles and nano biochar against gram-negative and gram-positive bacteria.

Test bacteria	Nanoparticles	Concentration of extracts Zone of inhibition in diameter (mm)				
		100 μ g/mL	250 μ g/mL	500 μ g/mL	(+) control	(-) control
<i>S. typhi</i>	CuO	7.0 ± 0.29	8.19 ± 0.70	10 ± 0.33	15 ± 0.59	NA
	Cu/NBC	9.21 ± 0.39	11.21 ± 0.29	13.44 ± 0.30		
<i>E. Coli</i>	Cu	7.00 ± 0.40	10.41 ± 0.19	12.00 ± 0.11	16.33 ± 0.27	NA
	Cu/NBC	8.37 ± 0.59	11.01 ± 0.79	12.46 ± 0.45		
<i>S. Aureu</i>	Cu	7.91 ± 0.71	11.61 ± 0.21	15.24 ± 0.33	18.71 ± 0.59	NA
	Cu/NBC	10.25 ± 0.33	13.51 ± 0.35	17.31 ± 0.19		
<i>S. pneumoniae</i>	Cu	7.21 ± 0.45	12.3 ± 0.33	14.19 ± 0.27	19.82 ± 0.47	NA
	Cu/NBC	11.45 ± 0.35	14.21 ± 0.72	17.38 ± 0.56		

Values are expressed as mean \pm SD (n = 3). NA = no activity, (+) control (gentamicin), and (-) control = negative control (DMSO).

In the majority of test bacteria, the Cu/NBC showed of bioactive metabolites and their synergetic better activity. The higher activity of these extracts activities. and fractions might be associated with the number



Figure 7: Activity of the copper oxide nanoparticles and Cu/NBC extracts against E.coli and E.coli respectively.

4. CONCLUSION

In conclusion, Cu-modified NBC from spent coffee grounds was prepared by pyrolysis and subsequent acid digestion. The acid digestion method is simple and nanobiochar of size down to nanoscale. The resulting Cu-modified NBC was used as an effective adsorbent for phosphate removal and subsequent utility as an antibacterial agent. Batch mode adsorption studies showed phosphate adsorption on Cu/NBC followed pseudo-second-order kinetic and Freundlich isotherm models. The adsorption capacity was calculated to be 50.2 mg/g at 35 mg of Cu/NBC in 85 min at pH 3. Compared with other Cu-based biochar, the prepared Cu/NBC offered higher adsorption capacity. This is due to the increased effective surface area of the nanobiochar than its micro-sized counterparts. Cu/NBC showed better activity in the majority of test bacteria. The increased activity of this nanoparticle could be attributed to the presence of more bioactive metabolites and their synergistic effects.

5. CONFLICTS OF INTEREST

The authors declare that they have no conflicts of interest.

6. ACKNOWLEDGMENTS

The authors would like to thank the Mizan-Tepi University, Ethiopia for their support.

7. REFERENCES

- Sisay GB, Atisme TB, Workie YA, Negie ZW, Mekonnen ML. Mg/Zr modified nanobiochar from spent coffee grounds for phosphate recovery and its application as a phosphorous release fertilizer. *Environmental Nanotechnology, Monitoring & Management*. 2023 May 1;19:100766. Available from: [<URL>](#)
- Jiang D, Chu B, Amano Y, Machida M. Removal and recovery of phosphate from water by Mg-laden biochar: Batch and column studies. *Colloids and Surfaces A: Physicochemical and Engineering Aspects*. 2018 Dec 5;558:429-37. Available from: [<URL>](#)
- Nobaharan K, Bagheri Novair S, Asgari Lajayer B, van Hullebusch ED. Phosphorus removal from wastewater: The potential use of biochar and the key controlling factors. *Water*. 2021 Feb 17;13(4):517. Available from: [<URL>](#)
- Seo YI, Hong KH, Kim SH, Chang D, Lee KH, Do Kim Y. Phosphorus removal from wastewater by ionic exchange using a surface-modified Al alloy filter. *Journal of Industrial and Engineering Chemistry*. 2013 May 25;19(3):744-7. Available from: [<URL>](#)
- Mbamba CK, Lindblom E, Flores-Alsina X, Tait S, Anderson S, Saagi R, Batstone DJ, Gernaey KV, Jeppsson U. Plant-wide model-based analysis of iron dosage strategies for chemical phosphorus removal in wastewater treatment systems. *Water research*. 2019 May 15;155:12-25. Available from: [<URL>](#)
- Liu X, Shen F, Qi X. Adsorption recovery of phosphate from aqueous solution by CaO-biochar composites prepared from eggshell and rice straw. *Science of the total environment*. 2019 May 20;666:694-702. Available from: [<URL>](#)
- Gusain R, Gupta K, Joshi P, Khatri OP. Adsorptive removal and photocatalytic degradation of organic pollutants using metal oxides and their composites: A comprehensive review. *Advances in colloid and interface science*. 2019 Oct 1;272:102009. Available from: [<URL>](#)
- Huang W, Zhu Y, Tang J, Yu X, Wang X, Li D, Zhang Y. Lanthanum-doped ordered mesoporous hollow silica spheres as novel adsorbents for efficient phosphate removal. *Journal of Materials Chemistry A*. 2014;2(23):8839-48. Available from: [<URL>](#)
- De Gisi S, Lofrano G, Grassi M, Notarnicola M. Characteristics and adsorption capacities of low-cost sorbents for wastewater treatment: A review. *Sustainable Materials and Technologies*. 2016 Sep 1;9:10-40. Available from: [<URL>](#)
- Zhu D, Chen Y, Yang H, Wang S, Wang X, Zhang S, Chen H. Synthesis and characterization of magnesium oxide nanoparticle-containing biochar composites for efficient phosphorus removal from aqueous solution. *Chemosphere*. 2020 May 1;247:125847. Available from: [<URL>](#)
- Kizito S, Wu S, Kirui WK, Lei M, Lu Q, Bah H, Dong R. Evaluation of slow pyrolyzed wood and rice husks

- biochar for adsorption of ammonium nitrogen from piggery manure anaerobic digestate slurry. *Science of the Total Environment*. 2015 Feb 1;505:102-12. Available from: [<URL>](#)
12. Tavakoli S, Kharaziha M, Ahmadi S. Green synthesis and morphology dependent antibacterial activity of copper oxide nanoparticles. *Journal of Nanostructures*. 2019 Jan 1;9(1):163-71. Available from: [<URL>](#)
 13. Kassaw S, Tamir A, Yimam BB. Phytochemical Investigation and Determination of Antibacterial Activities of the Fruit and Leaf Crude Extract of *Ficus palmata*. *Sch Int J Chem Mater Sci*. 2022;5(4):61-6. Available from: [<URL>](#)
 14. Sisay GB, Mekonnen ML. Mg modified nanobiochar from spent coffee grounds: Evaluation of the phosphate removal efficiency and its application as a phosphorous release fertilizer. *Chemistry Select*. 2023; 8(47):e202302288. Available from: [<URL>](#)
 15. Wang J, Guo X. Adsorption isotherm models: Classification, physical meaning, application and solving method. *Chemosphere*. 2020 Nov 1;258:127279. Available from: [<URL>](#)
 16. Bekele T, Yimam BB. Phytochemical Screening and Antimicrobial Activity of Stem Bark Extracts of *Schinus molle* *linens*. *Sch Int J Chem Mater Sci*. 2023;6(5):108-14. Available from: [<URL>](#)
 17. Melkamu WW, Feleke EG. Green Synthesis of Copper Oxide Nanoparticles Using Leaf Extract of *Justicia Schimperiana* and their Antibacterial Activity. *Research Square*. 2022. Available from: [<URL>](#)
 18. Legesse BA, Tamir A, Bezabeh B. Phytochemical screening and antibacterial activity of leaf extracts of *Dovyalis abyssinica*. *J Emerg Technol Innov Res*. 2019;6(6):453-65.
 19. Yin Q, Ren H, Wang R, Zhao Z. Evaluation of nitrate and phosphate adsorption on Al-modified biochar: influence of Al content. *Science of the Total Environment*. 2018 Aug 1;631:895-903. Available from: [<URL>](#)
 20. Deng W, Zhang D, Zheng X, Ye X, Niu X, Lin Z, Fu M, Zhou S. Adsorption recovery of phosphate from waste streams by Ca/Mg-biochar synthesis from marble waste, calcium-rich sepiolite and bagasse. *Journal of Cleaner Production*. 2021 Mar 15;288:125638. Available from: [<URL>](#)
 21. Shin H, Tiwari D, Kim, DJ. Phosphate adsorption/desorption kinetics and P bioavailability of Mg-biochar from ground coffee waste, *Journal of Water Process Engineering*. 2020;37: 101484. Available from: [<URL>](#)
 22. Kim TH, Lundehøj L, Nielsen UG. An investigation of the phosphate removal mechanism by MgFe layered double hydroxides. *Applied Clay Science*. 2020;189:105521. Available from: [<URL>](#)
 23. Humayro A, Harada H, Naito KJJOAC. Environment, adsorption of phosphate and nitrate using modified spent coffee ground and its application as an alternative nutrient source for plant growth. *Journal of Agricultural Chemistry and Environment*. 2020;10(1):80-90. Available from: [<URL>](#)



New Generation Nanoadsorbents and Conventional Techniques for Arsenic Removal from Waters

Veyis KARAKOÇ^{1*}  and Erol ERÇAĞ² 

¹Vocational School of Health Services, Çankırı Karatekin University, Çankırı, 18200, Türkiye,

²Department of Chemistry, Faculty of Engineering, İstanbul University-Cerrahpaşa, İstanbul, 34320, Türkiye

Abstract: Nowadays, with excessive use due to rapid population growth, growing industry, and technological developments, environmental pollution is also increasing and is reaching a point where it threatens the health of humans. The alarming increase in environmental pollution is mostly seen in the form of water pollution. Water pollution has reached levels that threaten human health. There are difficulties in accessing clean water in many parts of the world as a result of restricting the use of natural water resources polluted by both human activities and natural causes. Therefore, intense efforts are made to remove especially heavy metals and other harmful substances that pollute water. Among these toxic heavy metals threatening the health of humans, arsenic is at the top of the list as the most dangerous one. In recent years, many methods and techniques have been developed in addition to classical methods for removing pollutants from water. In this study, conventional methods used in the treatment of arsenic-contaminated waters, the difficulties encountered in the removal process, and the advantages and disadvantages of the methods were critically reviewed in the light of current and past information. In addition, detailed comparative information is given about nano-sized adsorbents, which is an innovative approach used in the adsorption method, one of the arsenic removal methods.

Keywords: Arsenic, arsenic removal, removal methods, nanoadsorbents, adsorption

Submitted: February 18, 2024. **Accepted:** March 03, 2024.

Cite this: Karakoç V, Erçağ E. New Generation Nanoadsorbents and Conventional Techniques for Arsenic Removal from Waters. JOTCSA. 2024;11(2):845-68.

DOI: <https://doi.org/10.18596/jotcsa.1438869>.

***Corresponding author. E-mail:** veyiskarakoc@karatekin.edu.tr.

1. INTRODUCTION

The presence of arsenic in water sources is a common problem in the world. Arsenic is one of the 20 most abundant natural elements in the earth's crust. Arsenic is an odorless and tasteless semi-metal with atomic number 33 and atomic weight 74.91. Arsenic is found as a basic component in more than 200 minerals. Arsenic is mostly found in sulfur and oxides of different minerals. Arsenic is found in sulfur minerals such as arsenic sulfide or orpiment (As_2S_3), realgar (AsS), arsenopyrite ($FeAsS$) (1-3).

Arsenic level in water is increasing due to natural and anthropogenic reasons. Arsenic pollutes water through the erosion and dissolution of rocks, minerals and ores in the soil or through natural events such as geothermal and volcanic activities. In addition, arsenic and its compounds are used in various industrial activities such as production of medicines, agricultural chemicals, colorants and dyes, soaps, ceramic, glass, timber, wood, animal skins, cellulose

and paper, battery plates, semiconductor production and petroleum refining and electroplating processes. Even natural events are the most important cause of arsenic pollution in water, the discharge of wastewater from various industrial enterprises, agricultural practices and mining activities into the environment without being subjected to adequate treatment processes is also a very important factor (3).

Arsenic exists in nature as both organic and inorganic compounds. Inorganic arsenic compounds are the most common. Arsenic is commonly seen in water in two oxidation states: arsenite (As^{3+}) and arsenate (As^{5+}). In natural waters, under different redox conditions, arsenic exists in (3-), (0), (3+) and (5+) oxidation stages (1).

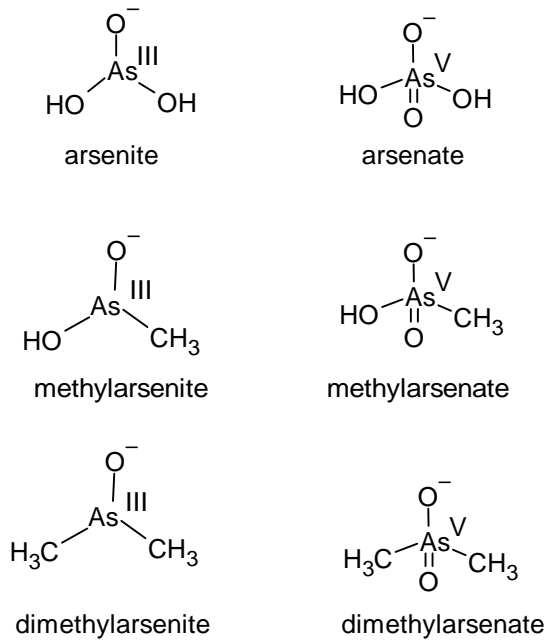


Figure 1: Arsenic species commonly found in water. Figure republished with permission from Ref. (9).

Depending on the pH of the medium, while in oxidizing conditions arsenic ions are found in waters as arsenate [As(V)] species H_3AsO_4 , H_2AsO_4^- , HAsO_4^{2-} , and in reducing conditions it is found as arsenite [As(III)] species H_3AsO_3 , H_2AsO_3^- , HAsO_3^{2-} (1).

Which species of arsenic will be dominant in the aquatic medium depends on the pH value and redox potential (Eh) of the water. Generally, arsenic is present in surface waters in the form of As(V), and As(III) is present in groundwater in anaerobic conditions with low oxygen content (2). In choosing the arsenic removal method, it is very important which species of arsenic is in the medium.

Table 1: Different species of Arsenic found in aqueous media depending on the pH of the medium. Figure reproduced with permission from Ref. (4).

Reaction	pKa
As (V)	
$\text{H}_2\text{AsO}_4^- + \text{H}^+ \rightarrow \text{H}_3\text{AsO}_4$	2.24
$\text{H}_2\text{AsO}_4^{2-} + \text{H}^+ \rightarrow \text{H}_2\text{AsO}_4^-$	6.96
$\text{H}_2\text{AsO}_4^{3-} + \text{H}^+ \rightarrow \text{H}_2\text{AsO}_4^{2-}$	11.50
As (III)	
$\text{H}_2\text{AsO}_3^- + \text{H}^+ \rightarrow \text{H}_3\text{AsO}_3$	9.22
$\text{H}_2\text{AsO}_3^{2-} + \text{H}^+ \rightarrow \text{H}_2\text{AsO}_3^-$	12.11
$\text{AsO}_3^{3-} + \text{H}^+ \rightarrow \text{HAsO}_3^{2-}$	13.41

In this graph, also known as the "Pourbaix diagram" in Figure 3, the pH value of the solution is given on the horizontal axis, and the redox potential (Eh) is given in volts on the vertical axis. According to the diagram, arsenite is mostly found in groundwater and arsenate is found in surface waters (1, 3).

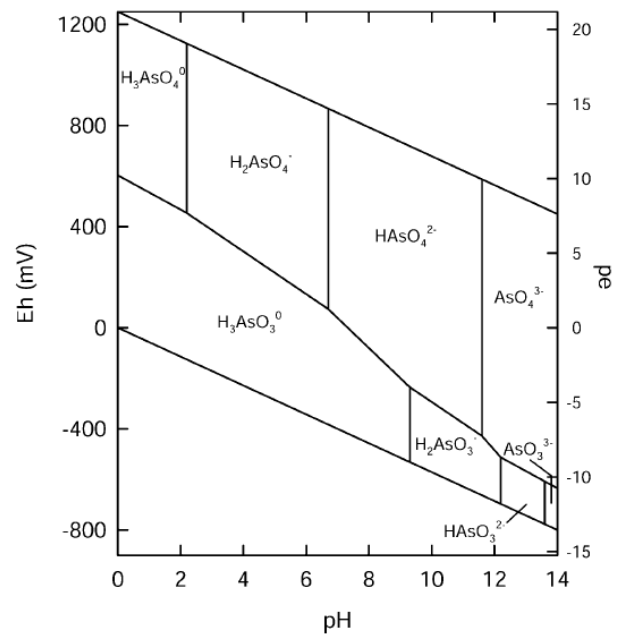


Figure 2: Eh-pH diagram of arsenic species in water in the As-O₂ - H₂O system (25 °C temperature and 1 bar total pressure). Figure republished with permission from Ref. (1).

It is very difficult to remove uncharged arsenite ions at the pH levels of drinking water. Arsenate is present in water as oxyanions. These oxyanions can be easily removed from solution by precipitation, adsorption, ion exchange and some other methods. Therefore, in order to remove arsenite, it must first be oxidized to arsenate. In other words, uncharged arsenite must be made charged. Removal of arsenic species from solution does not depend only on the oxidation stage of arsenic. In addition, it also depends on other factors such as the presence of other ions in the solution (2, 3).

1.1. Arsenic Pollution and Its Effects on Health
 Arsenic pollution is a major problem in natural water resources around the world. High levels of arsenic contamination in underground and surface waters have been reported in many countries such as the United States, Argentina, Bangladesh, China, India, Japan, Cambodia, Canada, Mexico, Mongolia, Nepal, Pakistan, Chile, Thailand, Taiwan, Turkey, Vietnam and New Zealand. Bangladesh and the West Bengal region of India are the most populated regions exposed to arsenic from groundwater (2).

Although it was used in the past to treat diseases such as syphilis and amoebic dysentery, arsenic is now listed among the first group of carcinogenic compounds by the World Health Organization (WHO) and the International Agency for Research on Cancer (IARC). Based on research, the World Health Organization determined the maximum amount of arsenic in drinking water as 10 µg/L in 1993 and declared that water containing arsenic above this value is toxic (3,4). As(III), one of the most common inorganic arsenic species found in water, is the most toxic form of arsenic. Arsenite is 60 times more toxic than arsenate, and inorganic arsenic is 100 times more toxic than organic arsenic. The toxicity level of arsenic is listed as "Arsine > arsenite As(III)>

Organic As(III)> arsenate As(V)> organic As (V)> arsonium" (3).

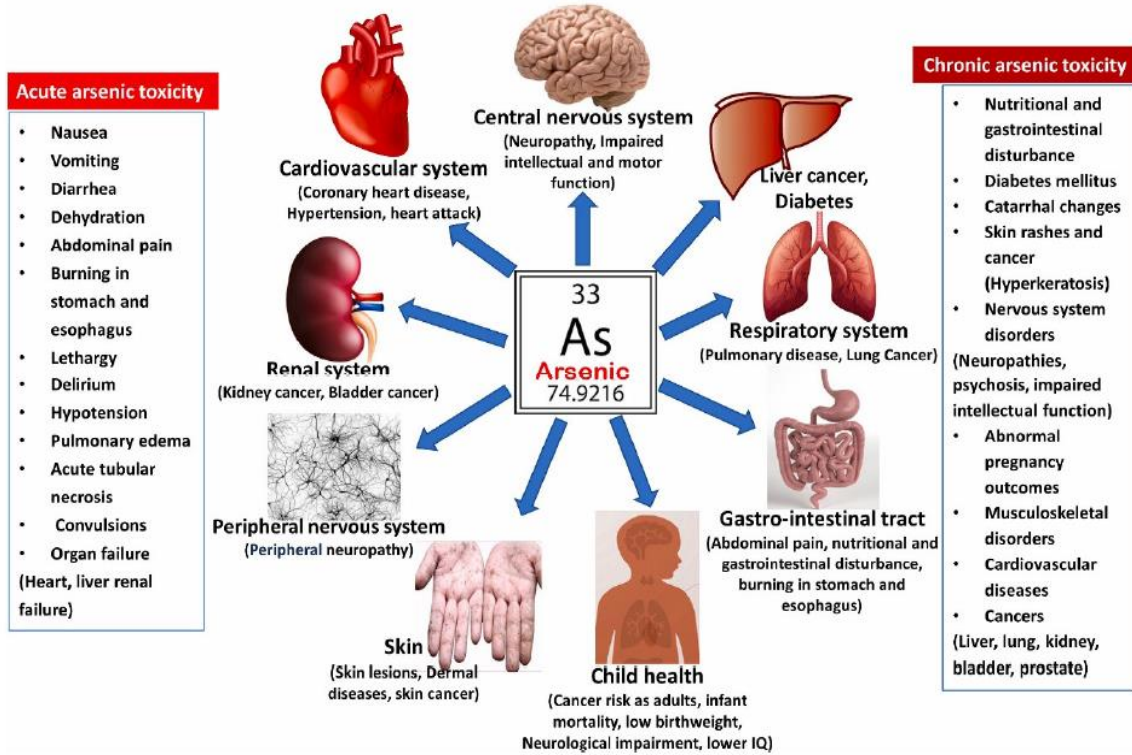


Figure 3: Human health effects of exposure to arsenic. Figure republished with permission from Ref. (12).

Arsenic is generally taken into the human body through drinking water and accumulates in tissues over time. Arsenic disrupts the structure of enzymes and proteins in the body, renders them dysfunctional, and even causes damage to molecules such as DNA and RNA in long-term high intakes. The disease symptoms that occur when water contaminated with arsenic is drunk for several years are called arsenicosis. The effects of exposure to arsenic through drinking water include various skin lesions, neurological effects, hypertension, cardiovascular diseases, respiratory disorders, diabetes, edema, gangrene, ulcers, skin and other types of cancer, miscarriage, stillbirth, premature births, weakness, weight loss, lethargy, anemia, and damage to the immune system (3-6).

thiol groups in the protein part of some enzymes, inhibits the enzymes and so renders them inoperable (3, 7, 8).

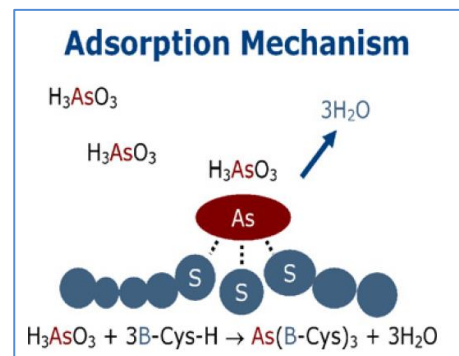


Figure 4: Schematic representation of the complex formed by an arsenic atom with 3 -SH thiol molecules. Figure republished with permission from Ref. (6).

Arsenic combines with some enzymes in the body and disrupts cellular metabolism. The fact that arsenic has a special affinity for sulfur is the main reason why it is toxic to the body. Arsenic, by binding to the free

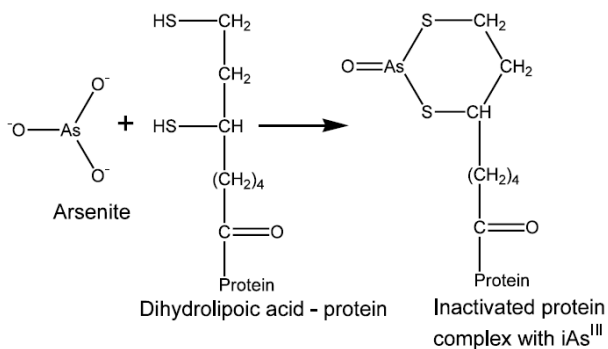


Figure 5: Arsenic blocks the enzyme system. Figure republished with permission from Ref. (3).

Arsenic shows its effects by causing the cells' mitochondrial enzymes to lose their activity. As(III) compounds have a high affinity for sulfhydryl groups found in proteins and form chelation with these groups. As(V) competes with phosphate in cell reactions and prevents ATP formation by separating oxidative phosphorylation (8-10).

2. ARSENIC REMOVAL METHODS FROM WATERS

Drinking water is often treated to remove turbidity and kill microorganisms. There are many technologies developed for the removal of arsenic from drinking and groundwater. These technologies are used effectively today, with arsenic removal of up to 95% in various sizes, from household to classical treatment plant scale. The chemical properties and composition of arsenic-contaminated water and the intended use of the treated water are among the factors that determine which technologies should be used in purification. Especially when arsenic removal is aimed, different processes are applied depending on the flow rate and application location. When choosing an effective arsenic removal process, pH should be taken into account depending on the species of arsenic. If As(III) is present in the medium, the uncharged As(III) must be oxidized with oxidizers such as Cl₂, NaOCl, KMnO₄, O₃ etc. to As(V) through a pre-treatment process. Since groundwater is generally anaerobic, all arsenic compounds are generally found in the As(III) form, depending on the conditions of the medium. Since As(III) is uncharged at the natural pH level and As(V) is negative at the natural pH level, removal of As(V) is easier (4-6, 9).

Technologies traditionally applied to remove arsenic species from water are oxidation, coagulation-flocculation, adsorption, ion exchange and membrane techniques.

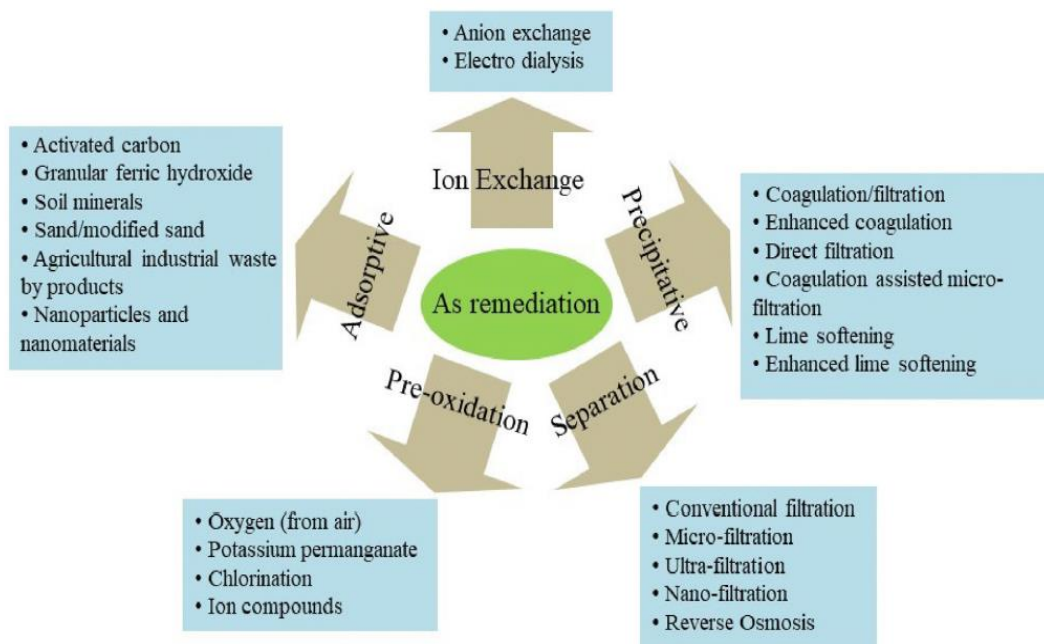


Figure 6: Conventional arsenic removal methods from water. Figure republished with permission from Ref. (5).

Coagulation-sedimentation and filtration processes are also used for the purpose of remove arsenic at the source in high-flow drinking water treatment. For small flow rates and points of use, membrane purification processes such as adsorption, ion exchange, reverse osmosis and nanofiltration can be applied. Below, all arsenic removal processes are discussed with their positive and negative aspects (2, 5, 11).

Considering the disadvantages of the processes used in arsenic removal, it could be said that an alternative arsenic treatment process which has some important properties should be developed. The followings could be given as an example to these properties; 1) it should have high arsenic removal efficiency and high effectiveness in removing both species of arsenic, 2) it should not require pre-oxidation process and additional chemicals, 3) it should not create secondary pollutants in the treated water, 4) it should

creates less treatment sludge and waste, 5) it should have low operation and maintenance-repair costs (12, 13).

2.1. Overview of Common Arsenic Removal Methods as Removal Technologies

2.1.1. Arsenic removal by coagulation

The most commonly used methods for removing arsenic from drinking water are coagulation-precipitation and filtration methods. Chemical precipitation is the most used method on industrial scale because it is highly effective, relatively easy to apply and low cost. Arsenic removal by chemical precipitation method is based on the principle of formation of a poorly soluble common salt. Arsenic becomes dissolved in the medium and precipitates by adsorption on the surface of metal hydroxides or by mixing with the structure during floc formation (14). With this type of purification method, in addition to arsenate, many solid substances such as turbidity, iron, manganese, phosphate and fluoride are also removed. The most commonly used coagulants in this method include Fe^{3+} and aluminum salts. Additionally, this technique is used in large-scale treatment processes such as urban treatment plants by adding lime softener (10, 15). The most commonly used chemicals are lime ($\text{Ca}(\text{OH})_2$), ferric chloride ($\text{FeCl}_3 \cdot n\text{H}_2\text{O}$) and aluminum sulfate ($\text{Al}_2(\text{SO}_4)_3 \cdot n\text{H}_2\text{O}$). It is possible to remove arsenic at

a rate of 90% with lime, 90% with aluminum sulfate and 95% with iron compound (16).

In the chemical precipitation process, heavy metal ions are precipitated by converting them into insoluble salts with a chemical agent added to the medium. By adding coagulant to water, the ability of colloidal particles to come together in water is increased. With the added coagulants, aluminum or iron hydroxide microflocs are rapidly formed. The flocs grow until they reach sufficient weight and then precipitate. Thus, it is purified from the water medium. Gravitational force and friction force are effective on the precipitated particles (16, 17).

Studies have been conducted investigating the pH effectiveness of different coagulants in arsenic removal. However $\text{Al}_2(\text{SO}_4)_3$ and FeCl_3 exhibited equal performance in arsenic removal in waters with pH below 7.3, it was observed that FeCl_3 was a more effective coagulant in waters with pH greater than 7.3. While aluminum hydroxide is stable in the neutral pH range, iron hydroxide is stable in a wider pH range. Additionally, since iron hydroxides have a high affinity for arsenic, co-precipitation of arsenic with iron hydroxide occurs. If As(III) is present in the water, first As(III) is converted to As(V) by oxidation and pH adjustment, and then As(V) is removed by the coagulation-filtration process (16-18).

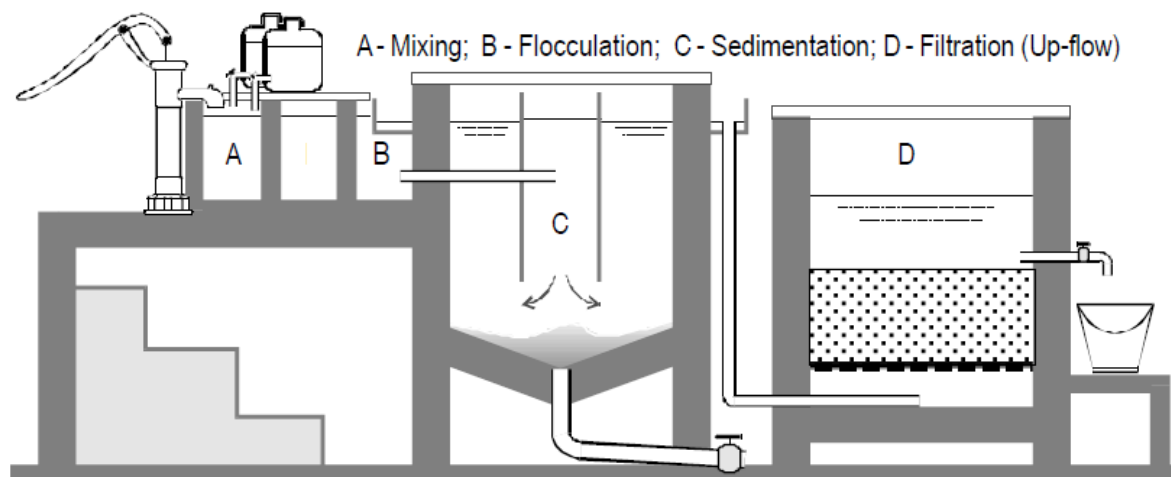


Figure 7: A facility where coagulation-sedimentation and filtration processes can be carried out simultaneously. Figure republished with permission from Ref. (19).

Coagulation- Filtration process produces sludge (if a sedimentation tank is used) and backwash water (if a filter is used) as waste. The water content of the sludge coming from the sedimentation ponds is quite high, so the solids content is quite low ($\text{SM} < 1\%$). For this reason, it is recommended to increase the solids content with sludge thickeners before dewatering. The solids content can be increased to 35-50% with a filter press and 15-30% with a centrifuge. Depending on the arsenic content, the resulting sludge can be disposed of by dumping it on land or by burying it in regular storage facilities. Lime-Soda method is a chemical treatment process in which coagulation, flocculation and precipitation processes are applied. Lime softening is another economical, conventional treatment process that is effective for arsenic removal. In the lime soda

softening method, the optimum pH for As(V) and As(III) purification is expressed as approximately 10.5 and 11, respectively. Arsenic as a result of the lime-soda process, sludge emerges as waste and pH adjustment is needed again. Typical sludge concentration contains 1-4% arsenic waste (10, 18, 19).

2.1.2. Oxidation

The chemical form of arsenic is important in its purification. Since arsenic in groundwater is generally found in the uncharged As(III) form, it must first be converted to As(V) form in order to be effectively removed from the water. Arsenic in water is not removed by oxidation, but arsenite is oxidized to arsenate and removed in subsequent processes (chemical precipitation, filtration, membrane

processes, etc.). Adding oxidants such as chlorine, permanganate, ozone, chlorine dioxide and hydrogen peroxide helps to increase the oxidation rate of arsenic. Among these, chlorine is a fast and effective oxidant for arsenic due to its easy accessibility. However, it is known that chlorine may create some toxic by-products (trihalides) as a result of its reaction with organic substances (18, 19).

When native iron is present in groundwater, oxidation and coprecipitation are followed by cost-effective filtration that removes waste. In oxidation by coprecipitation, iron is oxidized from Fe^{2+} to Fe^{3+} and arsenic is oxidized from As(III) to As(V) and they are filtered from water. Iron and arsenic As(III) are oxidized, then arsenic As(V) is adsorbed to iron hydroxide compounds and retained in the filters. The ratio between iron and arsenic should be 20:1 (10, 12). The appropriate pH range for the retention of arsenic compounds with iron is stated as 5.5 – 8.5. While oxygen is only sufficient for iron, it cannot oxidize arsenic. Ozone (O_3) is used for disinfection, oxidation, odor and taste removal (10).

2.1.3. Arsenic removal with membrane processes

Another effective treatment technology used in removing arsenic from water is membrane technologies. Membrane processes are generally used to purify groundwater and drinking water where clogging is not observed due to sediment formation. In these processes, separation is carried out according to the molecular size, shape or charge of the substance. For example, if the important criterion is the molecule size, while water and other small molecules can pass through the membrane, molecules and particles larger than water cannot pass (10, 17). In porous membranes, the separation process is achieved by passing mixture which has

more than one component through the membrane. Membranes are an effective method for arsenic treatment. What is expected from the membrane process is that even low amounts of arsenic species in the water can be eliminated from the water with high efficiency.

Such techniques have advantages such as high removal efficiency, easy operation, and minimal toxic sludge generated during the process. However, the initial investment and operating costs are relatively high, and high pressure is usually needed to pass contaminated water through the membranes. In addition, in the membrane process, discharge of concentrate, membrane clogging and flux reduction are generally inevitable (20-23).

Generally, four different membrane processes are applied in water treatment. These are microfiltration (MF), ultrafiltration (UF), nanofiltration (NF) and reverse osmosis (RO). These processes differ from each other due to the difference in pore size. As the selectivity of the membrane increases, the pressure used in the process also increases. While separation is achieved through mechanical sieving at low pressure for MF and UF membranes, separation occurs by capillary flow or solution diffusion at high pressure for NF and RO membranes. UF and MF membranes are generally used for particle and removal of pathogens. UF membranes can remove disinfection by-products to a large extent. MF membranes have on average ten times larger pores than UF membranes. MF membranes are designed to remove micrometer-level contaminants. It has a pore structure between 0.05 and 5 micrometers. While UF membranes can purify viruses, viruses can pass through the pores of MF membranes (22).

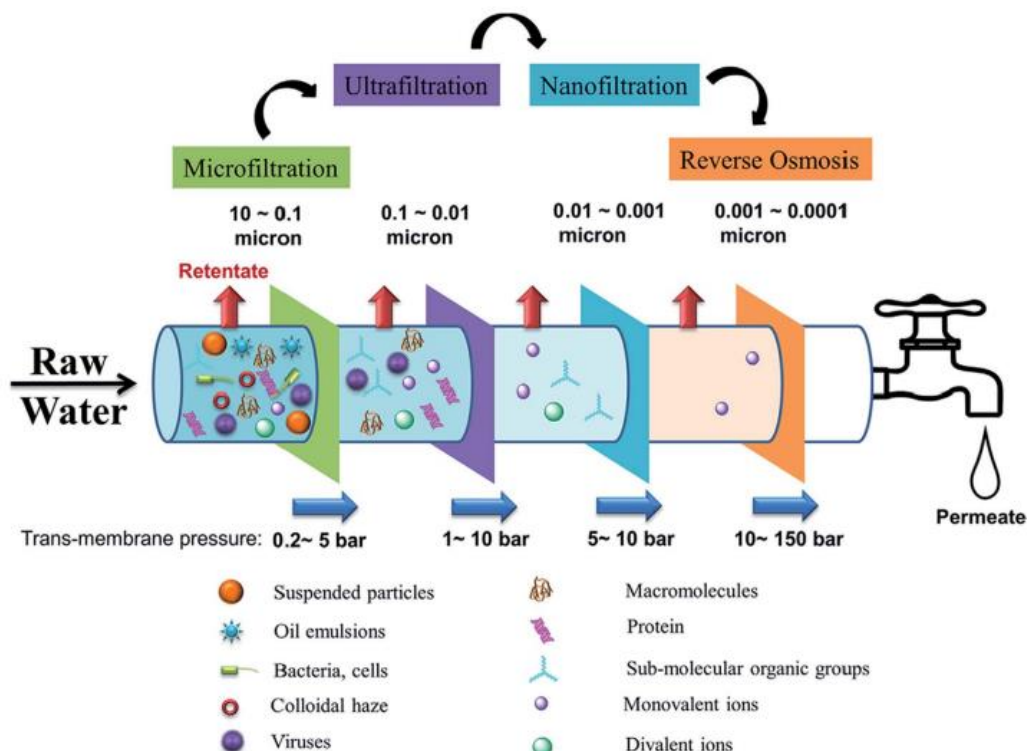


Figure 8: Membrane technologies. Figure republished with permission from Ref. (20)

Nanofiltration is also a very effective method in arsenic purification. However, investment and operating costs are high and it generates wastewater. Since it can remove all pollutants from water at a high rate, it provides quality drinking water production. Cellulose (cellulose acetate (CA) or cellulose triacetate CTA) membranes are generally used in nanofiltration. The largest advantage of these membranes is that they are resistant to chlorinated water. Despite this, they are adversely affected by alcoholic liquids and some bacteria. Membrane performance can be increased by appropriate pre-treatment of raw water with coagulation chemicals, pre-filtration and hardness removal methods (19, 24).

Osmosis; in nature, it occurs by the transfer of water from one to the other between two liquids of different concentrations, between which there is a semi-permeable membrane that allows only water to pass through and impermeable to other substances, and this process continues until balance is achieved on both sides. Osmotic pressure occurs with the static height difference caused by the volume change in the liquids on both sides of the membrane. Reverse osmosis, on the other hand, is a membrane technology and is the process of passing mineral-rich water with reduced minerals to the other side of a semi-permeable membrane by using osmotic pressure. Many minerals, bacteria and viruses in water can be removed with this method up to 99% purity. Reverse osmosis is relatively simple compared to similar technologies (23, 24).

Factors affecting the performance of the membrane process are suspended solids, high molecular weight dissolved solids, organic compounds and colloids, oxidation species of arsenic and temperature. High molecular weight particles in the membrane feed water can cause clogging of the membrane. Before the membrane process, pre-oxidation of arsenic species in the water to be treated will increase the treatment efficiency. As(III) compounds are smaller than As(V) compounds and pass through the membrane more easily than arsenate. Membrane technology can also be used as a polishing step after other treatment technologies in cases where solids are removed from the precipitation process and lower arsenic concentrations are required (19, 24).

2.1.4. Arsenic removal by ion exchange

Ion exchange technology is a physical and chemical process in which ions held by electrostatic forces on the surface of the resin are replaced by ions with similar charge values in the water. It is a method based on the principle of keeping the anions and cations desired to be purified from wastewater in a column filled with a suitable anion and/or cation exchanger (19). In ion exchange, arsenic is purified by exchanging the ions dissolved in water with an ion in the ion exchanger. Ions with a strong bond structure are replaced by ions with a weak bond structure in the water medium. Resins used in ion exchange are resins made from synthetic organic, inorganic or natural polymeric materials. There are two types of resins: anion and cation resins. Anion

resins are generally used for chlorine and anionic pollutants, while cation resins are used for sodium, potassium and cationic pollutants. Mixed resins are used in cases where both types of pollutants are present. The resin is generally placed in the column, and as the arsenic water passes through the column, the arsenic ions are replaced by ions such as chloride or hydroxide on the resin surface, depending on the type of resin used. Anion exchange resins used in the removal of arsenic from water are resin systems in which As(V) ions are removed by effectively replacing the H_2AsO_4^- , HAsO_4^{2-} and AsO_4^{3-} oxy-anionic species of arsenate with the anionic charged functional group of the resin. Since arsenite is generally found as a neutral molecule, an oxidation step is applied as a pre-treatment for using the ion exchange method. Common competitive anions such as sulfate, phosphate and nitrate are important in the removal of Arsenic by ion exchange. Ion exchange resin must be regenerated periodically (19, 25).

Various strong base-based ion exchange resins are easily available in the market and are used effectively to remove arsenate from water. As a result of removal, arsenic concentration can be reduced below 1 $\mu\text{g/L}$. Although nitrate-selective resins also remove arsenic, classical sulfate-selective resins are particularly suitable for arsenate removal (25). Generally, resins are pretreated with HCl acid to generate chloride ions on the surface. These resins can also be made ready for use with other anions such as bromide or acetate. Chloride is easily replaced by As(V). After arsenite is converted to As(V), it is eliminated very efficiently with anion exchange resins. As the pH of the water medium increases from pH 6.5 to pH 8.5, the adsorption capacity of the ion exchanger decreases. As(V) removal is relatively independent of pH and inlet water concentration. On the other hand, among anions, especially sulfate has a strong effect. Because the ion exchange resin prefers to retain sulfate before arsenate. Therefore, it is preferred to have low sulfate concentration in raw water (2, 19).

2.1.5. Adsorption

Adsorption is the process of adhesion of ions, atoms or molecules to the surface of a solid material. Adsorption processes are one of the most useful methods preferred in purification. This method is based on the principle of removing ions from the water medium by adhering to a solid adsorbent surface in water purification processes. In this method, the interaction between the adsorbent substance and analyte ions is generally reversible (2, 4, 19).

In adsorption purification technology, adsorbent is placed in the column. While water containing arsenic passes through the column, the pollutant adsorbed to the adsorbent surface with the help of physical and chemical forces, thus removing arsenic from the water. Arsenic adsorption largely depends on the concentration of the system, its pH, and the type of adsorbent used (12, 19). Many materials are used as adsorbents. Many organic or inorganic substances can be given as examples of these adsorbents such

as activated alumina, activated carbon, granular ferric hydroxide, pulp coated with ferric hydroxide, sand coated with iron oxide, sand mixed with iron fillings, green sand filtration (potassium permanganate coated gluconite), copper-zinc granules, zeolite modified with surfactant, dried hyacinth root, jute, red ash, fly ash, sawdust, and newspaper pulp. Adsorbents used in the adsorption process must be stable, economical, regenerable and reusable. The surface area of the adsorbent used in adsorption, the volume and size distribution of the pores are important because they affect the adsorption capacity and duration. In addition, the surface properties of the adsorbent determine the selectivity of adsorption (19, 26, 27).

Adsorption processes are operations with high efficiency, low cost, ease of use and simple operation. There is no need to add additional reagents to the medium. They do not create by-products and hazardous waste sludge. One of the important advantages of the adsorption method is that the working conditions are flexible and can be adjusted according to need. The regeneration process of the adsorbent is carried out by using appropriate desorption agents, thus it is allowed to reuse of the adsorbent. The reusability of the adsorbent provides a significant economic advantage. Due to all these advantages, adsorption is considered the best available technology (BAT) by EPA (19, 27, 28).

While technologies of adsorption are less used in large-scale classical treatment plants, they are frequently used in treatment technologies used especially for domestic and smaller population settlements. The adsorption method is also applied as a final polishing step in classical treatment systems (12, 19).

3. NANOADSORBENTS FOR ARSENIC REMOVAL FROM WATERS

Advances in nanoscience and nanotechnology have enabled the development of various nanomaterials for environmental applications and the remediation of arsenic-contaminated water. Nanoparticles are atomic clusters smaller than 100 nm (29). Nanoadsorbents are materials that are used in the widely preferred adsorption method in arsenic treatment and are promising for future studies with their unique physical and chemical properties. Properties such as large surface area, high specificity, high reactivity and catalytic potential make nanoparticles excellent candidates for water purification applications (29, 30). The low surface area and slow adsorption speed of conventional adsorbents limit their application. Due to their high surface area, nanoadsorbents allow reaching high adsorption capacities in a much shorter time than micron-scale adsorbents. Among the nanoadsorbents, especially polymeric adsorbents, can be used again and again because they enable surface modification and can be regenerated. Nanoadsorbents have been the most used and researched adsorbents in the treatment of arsenic-contaminated water in recent years (12, 15, 16, 29, 31).

There are different methods in the literature for water treatment applications of nanoadsorbents. Adsorption processes with nanoparticles have generally been applied in the batch method instead of fixed bed column due to the very small size of nanoparticles. There are experiments in which the column inlets and outlets were closed with glass wool to prevent the escape of nanoparticles into the purified water, but no effective results were obtained (27, 32).

Another approach to the applicability of nanoadsorbents in the removal of arsenic from water is the immobilization of nanoadsorbents on appropriate supports. This method, which does not require an additional separation step, causes a decrease in the adsorption ability of the nanoadsorbent. Studies on different solid porous materials such as silica, carbons, polymers, exchange resins, bentonite, kaolinite, zeolites or chitosan beads have been reported (33-37).

From studies related to this approach, Savina et al. produced polymeric composite materials in which iron nanoparticles were embedded in the walls of a macroporous polymer. and the study examining their efficiency in removing As(III) from aqueous media is a good example (38).

Similar to this approach, the study conducted by Önnby et al. is a study on arsenic removal from water with cryogel columns. In the study where cryogels with 3 different properties were synthesized, in the first of the prepared cryogel columns, the surface of the column was prepared by embedding aluminum nanoparticles, the second column was prepared by embedding molecularly imprinted polymers, and the last column was prepared by functionalizing the surface of the cryogel with thiol. The stability of the nanoparticles was ensured by embedment into the polymeric column, and it was reported that maximum adsorption capacities were reached in the pH range of 2-8 in the adsorption carried out in both composite columns (39, 40).

In another study conducted by Gurbuz et al. on arsenic removal with cryogels, they succeeded in removing up to 95.4% of arsenic from groundwater with the cryogel column they prepared. They reported that the poly (HEMA-co-GMA) cryogel hybrid column they synthesized adsorbed As(III) 11.44 and As(V) 5.79 mg/g at pH: 7, respectively. They managed to bring the arsenic level they measured in groundwater between 44.96 and 219.04 µg/L to drinkable levels by adsorption (100).

A similar study was conducted by Saha and Sarkar. In this study, an arsenic adsorbent consisting of alumina nanoparticles dispersed in a polymer matrix was developed and its arsenic adsorption properties were examined. In the study, the arsenic removal mechanism with alumina-loaded polymer beads was governed by both electrostatic adsorption and complexation. When As(V) removal is optimum at pH 7.2, the free amino group (-NH₂) in alumina nanoparticle dispersed chitosan-graftpolyacrylamide (CTS-g-PA) can exist in equilibrium with the protonated amino group in acidic aqueous solution.

Therefore, arsenate ions can interact with the polymer through electrostatic interactions / complexation (protonated amino group) and hydrogen bonds (unprotonated amino group). The positively charged Al^{3+} on the surface of the biosorbent will attract the negatively charged $\text{HAsO}_4/\text{H}_2\text{AsO}_4$ through electrostatic attraction. The maximum adsorption capacity of the nano-alumina loaded CTS-g-PA adsorbent prepared in batch studies was reported as 6.56 mg/g (35).

The most important disadvantages of nanoadsorbents are their high production costs, the difficult and costly separation of these very small adsorbents from the adsorption medium after the adsorption process, and their escape back into the treated water medium (33, 41, 42). In the current literature, there are various methods reported for the separation of nanoparticles after the adsorption process, such as magnetic separation, filtration and

centrifugation method (41, 43, 44). Centrifugal separation of nanoparticles has been found to be a more effective method for non-magnetic nanoparticles due to its high efficiency, scalable production ability, lack of nanoparticle aggregation, and high density (43). In general, a centrifuge with a speed of 20,000-50,000 rpm has the capacity to remove nanoparticles from water (45-47).

External magnetic field and membrane filtration methods are frequently used to separate nanoparticles from aqueous solution (30). In particular, magnetic nanoadsorbent can be easily removed from the adsorption medium by applying a high magnetic field from outside. Separation by filtration has been done by various researchers using a 0.45 μm membrane filter. Considering the size and type of membranes, the filtration process has been chosen by many researchers to separate nanoparticles (48).

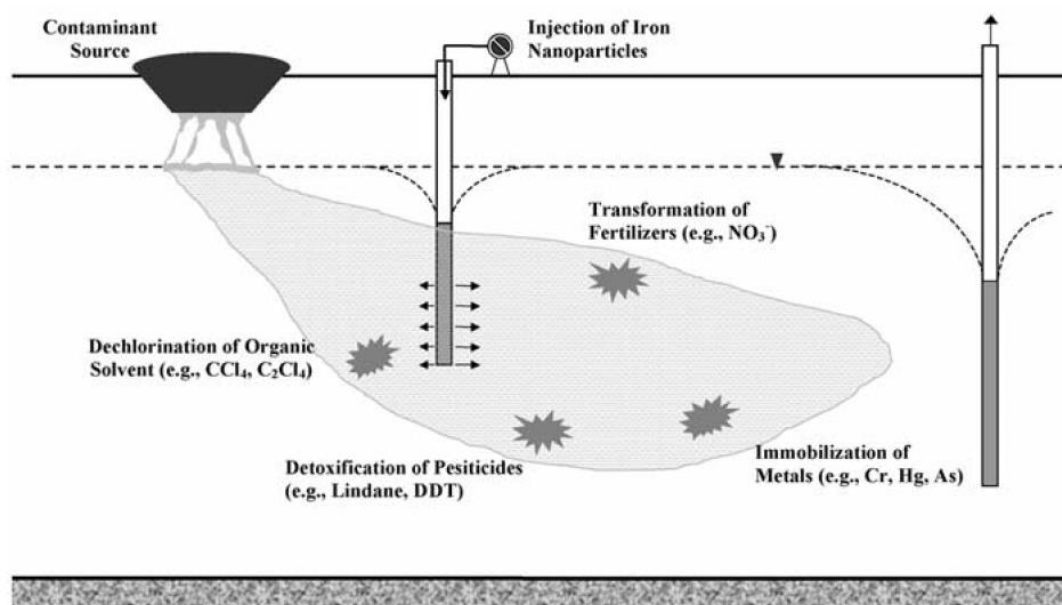


Figure 9: In-situ adsorption and magnetic separation. Figure republished with permission from Ref. (49).

Research has been conducted on in-situ applications as well as process applications for arsenic removal with nanoparticles. For example, nanoparticles can be easily used in sludge reactors to treat contaminated soils, sediments, and solid waste. Alternatively, nanoparticles can be attached to a solid matrix such as activated carbon and/or zeolite for improved treatment of water, wastewater, or gaseous process streams. Direct subsurface injection under gravity-fed or pressurized conditions has been shown to effectively transform chlorinated organic compounds (49).

However, nanoparticles without a stabilizer or surface modifier tend to rapidly aggregate into micron-scale or larger aggregates. As a result, the specific surface area and arsenic adsorption capacity of the adsorbent are greatly reduced. Therefore, to prevent the agglomeration of nanoparticles, stabilizers such as starch and carboxymethyl cellulose have been found to be effective in facilitating the size control of various metal and metal oxide-based nanoparticles (50).

4. NEW GENERATION DIFFERENT NANO ADSORBENTS FOR ARSENIC REMOVAL

Nanoparticles can generally be classified according to their chemical properties as organic (carbon-based), inorganic and composite. The most common inorganic nanoparticles used in water treatment are transition metal and metal oxide-based nanoparticles. These generally consist of Fe, Al, Ti, Si, Cu, Co, Zr, Ag and Zn and their oxides. Organic nanoadsorbents are classified as carbon nanotubes, graphene/graphene oxides, dendrimers and polymers due to their different shapes and chemical properties (31, 32). In order to benefit from the superior properties of inorganic nanoadsorbents such as magnetism, composite nanoadsorbents have been synthesized through surface functionalization processes. For this purpose, composite nanoadsorbents have been created by coating metal oxides such as Fe_3O_4 with polymer or by functionalizing them with organic molecules such as $-\text{NH}_2$, $-\text{COOH}$ or $-$

SO₃H on the surface, and positive results have been reported in water purification studies such as arsenic removal (33, 34).

These nanoadsorbents, nanospheres, nanotubes, nanowires and nanorods, prepared in various forms, have larger surface areas and allow high-capacity adsorption to remove arsenic ions from water.

According to literature nanoparticles used in water treatment should offer a high adsorption capacity and the used products should be easily separated from water and should not cause any harmful effects on the treated water. The fact that adsorbents are regenerable makes the adsorption process economically feasible. pH has an important role in the regeneration of adsorbents (30-32).

Criteria for ideal nanoadsorbent materials for water and wastewater remediation purposes are described by many researchers in literature (27-34, 41-47):

1. Nanoadsorbent materials should be non-toxic.
2. Nanoadsorbent materials should have high adsorption capacities and high selectivity to remove low concentrations of contaminants.
3. The surface of nanoadsorbent materials should be easily reactivated. So, it must be regenerable.
4. Nanoadsorbents should be easily separated from the adsorption medium and should not cause leaching.

4.1. Inorganic Nanoadsorbents

4.1.1. Metal/Metal Oxides

Nano-sized metal/metal oxide nanoadsorbents used in arsenic removal have attracted attention and have become the most studied adsorbents due to reasons such as being economical, non-toxic, widely available in nature and environmentally friendly. In particular, transition metals and their oxides have been widely synthesized at nanoscales and studied in water treatment processes (32, 43, 51). The magnetic properties of metals such as Fe, Co and Ni and their oxides make it easier to remove the adsorbent from the medium, especially after the adsorption process. Iron and iron oxides, which are metal and metal oxide-based nanoadsorbents, have been widely used in the removal of arsenic and a lot of research has been done on them. Especially iron-based adsorbents, which are non-toxic, low-cost and easily accessible in large quantities, offer promising results for arsenic removal from water (43).

Alumina (Al₂O₃), one of the nano-sized metal oxides used to remove arsenic, occurs in natural soils and has many structural forms such as α , β , γ , θ and χ . In traditional methods, α -Al₂O₃ is used as a natural adsorbent with greater stability. Alumina, is a popular sorbent because it has interesting properties; for example thermal conductivity, compressive strength, corrosion resistance, and extremely high electrical insulation. Aluminum oxides are very important adsorbents in arsenic removal due to their various nanostructured properties and low cost (31, 32).

Studies in the literature have revealed the importance of Al₂O₃ nanoparticles in the removal of

arsenic by adsorption. Patra et al. synthesized a mesoporous adsorbent by self-assembling Al₂O₃ nanoparticles with a maximum size of 10 nm. The adsorbent they synthesized had high surface areas (231–497 m²/g). They managed to remove arsenic with 86% efficiency at pH: 6.0 from solutions with 100 ppb AsO₂ concentration (52). Ghosh et al. synthesized Al₂O₃ nanoparticles for arsenic removal from water. In the adsorption experiments carried out in the batch system at room temperature, the arsenic adsorption capacity from As(III) and As(V) solutions at 400 µg/L concentrations with the synthesized Al₂O₃ adsorbate was 693.76 µg/g for the As(III) ion and 743.84 µg/g for the As(V) ion. At these rates, removal efficiency of 87.69% and 93.91% for arsenite and arsenate was obtained at pH:6.8 (53).

Another metal oxide that has been studied in the removal of arsenic from water is copper oxide (CuO) nanoparticles. There are many studies in the literature on the removal of arsenic from water with copper oxide CuO nanoparticles. Martinson and Reddy tried to remove As(III) and As(V) ions from groundwater with the CuO nanoparticles. The synthesized nanoparticles have a diameter range of 12–18nm and a surface area of 85m²/g. In the pH range of 6 and 10, the maximum adsorption was 26.9 mg/g for As(III) and 22.6 mg/g for As(V). In studies conducted in the presence of competitive ions, the sulfate and silicate ions in water did not affect As(V) adsorption, but reduced As(III) adsorption. In addition, it was observed that only the phosphate ion reduced the adsorption of arsenic (54). Goswami et al. measured the surface area of the CuO nanoparticles they prepared for arsenic adsorption as 52.11 m²/g. In their experimental study, with an adsorbent dose of 1 g/L from arsenic solution at a concentration of 200 ppb, 100% adsorption was achieved within 300 min interaction time. at pHs where the surface of the adsorbent is deprotonated, that is, at basic pHs, while 75% As removal was achieved at acidic values below pH:8. In arsenic adsorption carried out in the presence of phosphate and sulfate ions, it was observed that phosphate ion reduced arsenic adsorption by 20% and sulfate ion reduced the adsorption of arsenic by 10% (55).

Titanium dioxide (TiO₂) nanoparticles have also been used as adsorbents in several studies to evaluate the adsorption potential for the removal of arsenic from drinking water. Due to the low toxicity, chemical stability, resistance to corrosion and low cost of titanium-based nanoparticles, TiO₂ is a widely used adsorbent in water or wastewater treatment, as well as a semiconductor photocatalyst in UV light or sunlight. TiO₂ nanoparticles degrade organic contaminants and inactivate pathogens (56). Jegadeesan et al. investigated the effect of nano-sized amorphous and crystalline TiO₂ nanoparticles on the adsorption behavior of As(III) and As(V) ions in amorphous or crystalline structure. In experimental studies, samples were centrifuged and filtered through 0.45 mm Nylon filters. In experimental studies, adsorption reached its maximum value in the neutral pH range: 7-8. As a result of X-ray absorption spectroscopic analysis, they observed that As(III) ion

prefers the amorphous structure over crystal surfaces in adsorption. It was determined that As(V) ion was adsorbed more on crystal surfaces. It was observed that silicate and phosphate ions had a negative effect on arsenic adsorption (57). Deng et al. investigated arsenic ions adsorption with TiO₂ nanoparticles. H-Fe₃O₄ microspheres with a hollow porous structure were synthesized from Fe₃O₄ with a size of 280 nm. Then, they coated the hollow Fe₃O₄ magnetic microspheres they synthesized with TiO₂ and obtained mesopores on the surface. The surface area of the synthesized adsorbent was measured as 179.98 m²/g. In experimental studies, the maximum adsorption capacity of the adsorbent was 18.22 mg/g for As(III) ion, while As(V) ion was 7.74 mg/g. Maximum adsorption values were reached at pH: 3.0 for the As(V) ion and in the pH:3-10 range for the As(III) ion (58).

Zinc oxide nanoparticles are among the metal oxides that have been studied in the removal of arsenic from water. Singh et al. used ZnO nanoparticles functionalized with acetic acid to remove arsenic from contaminated water. They measured the dimensions of the synthesized ZnO nanomaterials as a maximum 60 nm. They observed that nanoparticles prepared from zinc acetate removed arsenic from water more effectively than those prepared from zinc chloride, zinc nitrate, and zinc sulfate. They think that acetate ions on the surface of ZnO adsorb arsenic via an oxo-coordination mechanism. In the experimental studies, arsenic adsorption reached a plateau at the 15th minute and at pH:5.8, and they managed to remove 99.92% of the arsenic from the medium by adsorption. In addition, in leaching studies, they reported that ZnO dissolved at low pH with HCl added to the medium and dissolved as AsCl₃ (59). Additionally, Rehman et al. carried out studies on the removal of arsenic from groundwater with the ZnO nanoparticles they synthesized. The size range of the synthesized ZnO nanoparticles varies between 3.6 nm and 12.7 nm. Arsenic adsorption was maximum at pH values lower than 5.0 (60).

Zirconium oxide nanoparticles are among the metal oxides studied in the literature for arsenic removal. Cui et al. synthesized ZrO₂ nanospheres with an average size of 7 nm and a surface area of 98 m²/g and carried out As(III) and As(V) adsorption studies in a fixed bed reactor. The synthesized ZrO nanoparticles were treated with powder agar and micron-sized spheres were obtained. They carried out continuous system work using fixed bed columns. They interacted the ZrO₂ spheres they synthesized, which are non-toxic, extremely stable and resistant to acid and alkali, with water containing 300 ppb arsenic in a fixed bed column system for 10 minutes. Thus, they managed to reduce the amount of arsenic in the medium below 10 ppb (61). Zheng et al. in their As(III) removal studies with zirconia nanoparticles synthesized in the 60 – 90 nm size range, they managed to adsorb As(III) ions at 1.85 mmol-As/g in the pH range of 8-9 without pre-oxidation. In studies investigating the effect of competitive ions on adsorption, the presence of humic acid or typical anions (e.g., fluoride, silicate, phosphate, and sulfate) did not have substantially

negative effects on As(III) adsorption. However, the adsorption of As(III) was inhibited due to the presence of bicarbonate ions (62).

Iron-based nanoparticles are the most studied metal/oxide nanoadsorbents in arsenic removal compared to other metal/oxide nanoparticles. In addition to being a suitable adsorbent for arsenic removal, nZVI, an iron-based nanoparticle, has attracted attention because it is a strong reductant and shows promise in the elimination of many pollutants. In addition, the fact that iron oxides have magnetic properties and can be controlled by an external magnetic field has made them among the popular nanoadsorbents, and magnetic Fe₃O₄ has become the most studied adsorbent. Due to the importance of iron-based nanoadsorbents, they are examined under a separate subheading (63).

4.1.1.1 Iron Based Nanoparticles

Studies conducted in recent years have revealed that iron-based adsorbents, which are low-cost and easily accessible in large quantities, can be easily used in the removal of arsenic from water, as iron does not have any known toxicity. Studies in the literature have shown that iron-based adsorbents can be developed in various ways and can be used with high efficiency in removing arsenic species from water (30-341.43). Although iron-based nanoadsorbents consist of nZVI and iron oxides, in some cases they are also prepared from mixtures of iron and different metals. Iron-based nanoadsorbents are increasingly used to remove both organic and inorganic pollutants from water. In addition, iron-based nanoparticles especially provide opportunities for in situ treatment applications. In addition to the high surface areas of iron-based nanoadsorbents and their high affinity for arsenic ions, the easy magnetic separation of some iron nanoadsorbents such as magnetite (Fe₃O₄) and maghemite (γ-Fe₂O₃) has made them very popular adsorbents in arsenic treatment (64).

The low release of arsenic back into the medium after the adsorption process from iron compounds such as hematite, goethite, iron oxide coated materials and granular ferric hydroxide (GFR) makes them important. Except for the PO₄³⁻, Cl⁻, NO₃⁻, SO₄²⁻ and CO₃²⁻ ions do not have serious negative effects on the arsenic adsorption capacities of iron-based adsorbents in arsenic removal studies. Some adsorbents, such as ferric hydroxide and zerovalent iron, have been produced on an industrial scale as commercial adsorbents (63-65).

4.1.1.2. Nanozerovalent iron (nZVI)

Zero-valent iron (nZVI) is elemental iron that has an oxidation state of 0 and is written as Fe⁰. nZVI attracts attention due to its high stability, large surface area, non-toxicity, reducing ability and with high adsorption capacity. nZVI is prepared by reducing iron or iron salts with various reducing agents, primarily NaBH₄, and using suitable capping agents such as organic surfactants and stabilizers. In recent years, nZVI, in addition to being an effective reductant, has attracted attention for its ability to degrade or oxidize other organic pollutants by combining with H₂O₂. nZVI can form soluble Fe(II)

ions by reducing dissolved inorganics in water and these ions can then be oxidized to Fe(III) ions (66, 67).

In many studies in the literature, it is seen that nZVI is used as a catalyst in the removal of heavy metal ions and the oxidation of oxidizable organic and inorganic impurities in wastewater. To prevent oxidation, nZVI particles are alloyed or doped with other metal atoms such as Ag and Cu (63). Alloyed metals prevent iron from corroding. Iron nanoparticles can also be stabilized by incorporating them into some polymeric matrices.

Recent studies show that nZVI is effective in removing arsenic from contaminated water. The basis of nZVI's arsenic removal mechanism is the corrosion of zero-valent iron in the medium. Essentially, in arsenic removal, when oxygenated water comes into contact with nZVI, nZVI corrodes and provides the formation of various by-products such as Fe^{II} and Fe^{III} hydroxides, which can oxidize and remove arsenic. It is generally accepted that arsenic removal by ZVI involves adsorption, reduction, surface precipitation, and co-precipitation with various iron corrosion products such as iron/ferric (hydr)oxides (63, 65, 66).

Aggregation is a major problem of iron-based nanoparticles, and to overcome this, various polymers (e.g., neutral or charged polysaccharides) and other coatings have been used to stabilize nZVI particles. nZVI is characterized by a high tendency to agglomerate in water, high mobility, lack of stability and low reduction specificity, and therefore should be used in conjunction with surface stabilizers such as chitosan, alginate, activated carbon and other porous structures (49, 67). Therefore, Mosaferi et al. carried out an adsorption study by stabilizing nZVI with iron starch and carboxymethylcellulose for arsenic removal. In this study, they prevented agglomeration with their application and reported that the adsorption capacity increased by 36.5% for As(V) and 30% for As(III) (50). Yin et al. they managed to remove As(V) by 99.9% and As(III) by more than 70.9% in groundwater at 100 µg/L arsenic concentration with the 48 ± 9 nm sized nZVI nanoparticles they synthesized. In a study investigating the effect of common ions on adsorption, they reported that phosphate and carbonate ions decreased the adsorption efficiency (68). Morgada et al. conducted a study to investigate the effect of humic acid and UV light on the removal of arsenic from water with commercial nZVI (NanoFe1) in the 5-15 nm size range and 63 m²/g surface area. From experimental studies, they found that nZVI removed arsenic with 90% efficiency in 150 min of interaction, and humic acid reduced arsenic removal by 50% in the dark. In studies investigating the effect of UV light, adsorption experiments were carried out in the presence and absence of humic acid. As a result of the experiments, it was observed that UV light doubled the adsorption of arsenic and that almost all arsenic was removed in a humic acid medium in 4 hours (69).

4.1.1.3. Magnetic Nanoadsorbents

Magnetic nanoadsorbents are one of the most important advanced nanomaterials that combine the superior properties of magnetic separation and nanotechnology in removing impurities from water. Nanosized magnetic Fe₃O₄ are an important member of magnetic nanoadsorbents. Magnetic separation technique is preferred in environmental applications because magnetic adsorbents can be easily removed from the environment by externally applied magnetic field high gradient magnetic separation (HGMS) technique at the end of the adsorption process (43, 64).

In general, magnetic nanoparticles contain elements such as iron, nickel and cobalt and their oxides. Iron oxide-based nanoadsorbents are basically divided into three forms: These are iron nanoparticles such as magnetite (Fe₃O₄), maghemite (γ-Fe₂O₃) and hematite (α-Fe₂O₃). Additionally, these particles are environmentally friendly as they are biodegradable (70). Besides favorable magnetic properties, low toxicity and price, iron oxide nanoparticles exhibit high surface/volume ratios and have high adsorption capacity for the adsorption of toxic pollutants in water purification procedures when associated with their surface chemical modification capabilities (71). Separation of contaminant-loaded adsorbents from water has always been considered a major challenge in drinking water treatment processes. Separating pollutant-saturated adsorbents from reactors and distribution systems is important to prevent secondary environmental pollution through the disposal of these materials. Magnetite nanoparticles are promising adsorbents for the removal of arsenic due to their high adsorption capacity and easy separation from water under external magnetic field (63).

Magnetic nanoparticles have a relatively larger surface area, biocompatibility, chemical stability, minimal toxicity and easy dispersion ability. Therefore, magnetic nanoparticles are more reliable, convenient and cost-effective to apply in water treatment (43, 72).

Mamindy-Pajany et al. studied arsenate adsorption on goethite, hematite and magnetite and found that arsenic adsorption was related to the iron content of the adsorbents and the adsorption rate increased in the order goethite < hematite < magnetite < ZVI. Moreover, desorption experiments show that arsenic is strongly adsorbed onto hematite and ZVI. They reported that among adsorbents, hematite appears to be the most suitable for the removal of arsenate in the natural medium, as it is effective over wide pH and arsenic concentration ranges (70). Mayo et al. compared the arsenic ions adsorption capacity of the 12 nm sized magnetic Fe₃O₄ nanoparticles they synthesized and the commercial 300 nm sized magnetic Fe₃O₄, and observed an approximately 200-fold increase in the adsorption capacity, depending on the size. They carried out the adsorption experiments by applying an external magnetic field to columns filled with stainless-steel wool. In this study, carried out using a high gradient magnetic field column separator, 99,2% separation was

achieved with 12 nm-sized bare Fe_3O_4 nanoparticles from an As(III) solution at a concentration of 500 $\mu\text{g/L}$, while 90.9% of 20 nm-sized and 24.9% of As(III) ions were removed with 300 nm-sized

particles. Under the same conditions, they were able to remove As(V) ion as 98.4% with 12 nm particles, 96.5% with 20 nm particles, and 29.2% with 300 nm commercial nanoparticles (73).

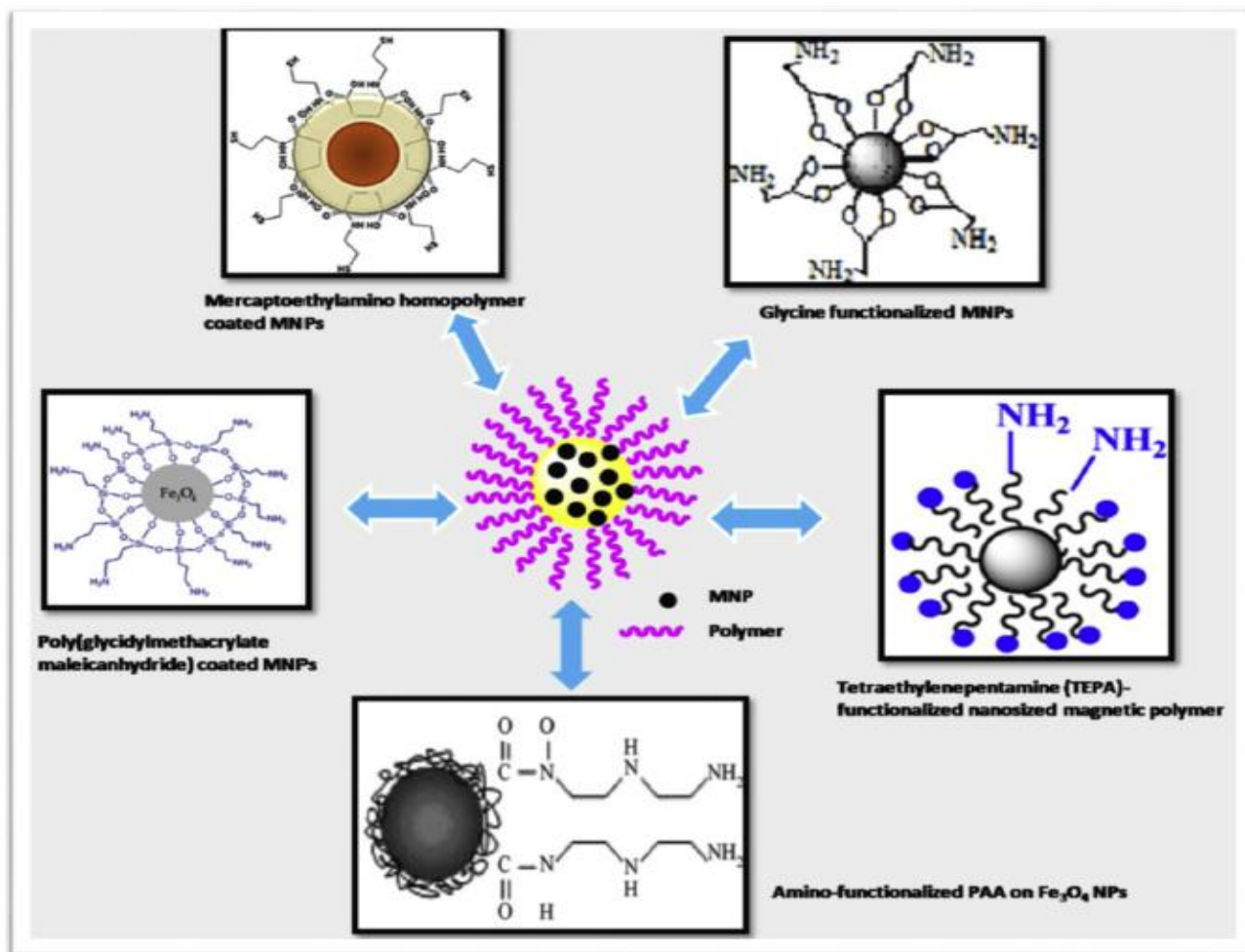


Figure 10: Surface functionalization of the of magnetic nanoparticles using polymers or organic molecules. Figure republished with permission from Ref. (43).

According to literature references, various adsorption forces such as electrostatic interactions, ion exchange and ion association tendencies, and complex formations play a role in the arsenic adsorption mechanism on the surfaces of oxide forms of iron. These properties of adsorbents play an important role in the affinity of pollutants to the surface of the adsorbent (63, 71-76).

4.1.1.4. Iron oxy-hydroxides

Many different materials have a high affinity for arsenic, but iron oxy-hydroxides are the most researched due to their easy accessibility. Commonly used iron oxy-hydroxides such as akaganeite ($\beta\text{-FeOOH}$), goethite ($\alpha\text{-FeOOH}$), lepidocrocite ($\gamma\text{-FeOOH}$) and ferrihydrites ($\text{Fe}_{10}\text{O}_{14}(\text{OH})_2$) can be chemically synthesized by precipitation of Fe(II) or Fe(III) salts through hydrolysis and oxidation processes (76).

Deliyanni et al. synthesized akaganeite with a nanocrystalline hybrid surface, which is an innovative adsorbent for the removal of arsenate ions from dilute solution. They observed that, unlike

nanocrystalline akaganeite, the hybrid adsorbent prepared using cationic surfactant had a significantly higher arsenate adsorption capacity (approximately 180 mg As(V)/g) than pure akaganeite (approximately 120 mg As(V)/g) in the pH range of 4-10 (77).

4.1.2. Zeolite nanoadsorbents

Zeolites are aluminosilicate minerals with a surface structure containing numerous electrostatic holes occupied by cations and water molecules. Cations and water molecules have a significant choice of motion, allowing ion exchange and reversible dehydration. The normal size of zeolite is micro-scale, but nanozeolite can be produced in the range of 10-500 nm. Nano-scale zeolite has larger adsorption capacity, higher density of adsorption sites, and higher surface area (400-1000 m^2/g) than conventional zeolite (2, 27). Therefore, nano-zeolite has a great affinity and effective property against pollutants. It has been known since 1980 that zeolite is used together with silver (33).

Zeolites have been used extensively in separation and recovery processes for many years due to their

highly porous structure. 1A and 2A group metal ions can be moved within their frameworks to balance the negatively charge between Si(IV) and Al(III). However, today, zeolites are used in the form of nanoparticles, which are more suitable for adsorption since they have a large surface area and therefore high adsorption capacity. (78). Attia et al. prepared a new zeolite (MNCZ) adsorbent coated with magnetic nanoparticle (γ -Fe₂O₃) to remove arsenic ions from aqueous solution. The results showed that MNCZ was effective in removing arsenic from aqueous solution, and the removal percentage of arsenic could reach over 95.6% within 15 min at pH 2.5. In this study, the adsorption capacity of MNCZ particles was reported to be 19.39 mg/g (78). Pizarro et al. studied arsenate removal from water with a composite adsorbent they synthesized from 50 nm magnetic Fe₃O₄ and zeolite. In this study, in which zeolite was used as support material; the maximum arsenate adsorption was 5.1 mg/g (37).

4.1.3. Silica-based nanoadsorbent

Nanosized silica oxides, which constitute another group of inorganic nanoadsorbents, have unique properties such as large surface area, controllable surface properties and well-defined pore size. Therefore, it has great potential in water treatment processes. In addition, nanosilica is an environmentally friendly adsorbent that has no toxic effects on health. In addition, adsorption capacity and selectivity can be increased by modification of their surfaces with functional groups such as -NH₂ and -SH. (79). Studies have shown that naturally occurring adsorbents such as iron-coated sand are cost-effective arsenic treatment technologies.

Jamali-Behnam et al. synthesized 100 nm-sized magnetic Fe₃O₄ nanoparticles to remove As(III) and coated these magnetic nanoparticles with silica. While magnetic nanoparticles tended to aggregate, such a behavior was not observed in silica-coated ones and they removed more than 99% of arsenic from the medium. The maximum adsorption was 33.36 µg/g for MNPs and 32.10 µg/g for Si-MNPs (80).

4.2. Organic (Carbon Based) Nanoadsorbents

Carbon-based functional materials are among the most important nanoadsorbents used in water treatment due to their distinctive physical and chemical properties and functionalizable surface properties. Carbon-based nanoadsorbents enable selective adsorption studies because their dimensions and surface properties can be adjusted, and they attract the attention of researchers due to these features. For a long time, research has been carried out to obtain various carbon-based nanoadsorbents such as graphene, activated carbon, carbon nanotubes, carbon-based nanocomposites and their derivatives for the removal of various types of pollutants from water (30, 31, 79).

Activated carbon is widely used today for the removal of metallic impurities. Activated carbons are of great interest in the removal of heavy metal ions from water due to their large surface area (27). Scientific research continues to obtain cheap and effective

activated carbon from carbon-based materials and to use it in removing heavy metals from water. However, activated carbon poorly adsorbs arsenic species due to its negatively charged surface (81). For this reason, composites are prepared. Rodriguez et al. tested the ability of activated carbon modified with iron hydroxides to adsorb arsenic from water. They reported that activated carbon modified with FeOOH- which has a surface area of up to 1101 m² adsorbed As(V) up to a maximum of 1250 µg/g in the range of pH: 6-8. In the study conducted on groundwater samples, they observed that adsorption decreased in the presence of Cl⁻, SO₄²⁻ and F⁻ ions (81).

4.2.1. Carbon Nanotubes

Carbon nanotubes are carbon nanostructures with a cylindrical form. Based on the synthesis process, carbon nanotubes are classified as single-walled or multi-walled nanotubes. Carbon nanotubes due to their cylindrical hollow structure have higher surface area, electrical conductivity, high adsorption sites, and tunable surface chemistry. Carbon nanotubes are divided into two main groups: single-walled (SWCNTs) and multi-walled (MWCNTs) (82).

Carbon nanotubes can be applied to determine the preliminary concentration and reveal pollutants as it can be applied, especially, to remove organic pollutants. The interaction between carbon nanotubes and metal cations is achieved through electrostatic attraction and chemical bonding. In studies conducted in the literature, the mechanism of removing oil from wastewater using carbon nanotubes has been clearly explained. Although carbon nanotubes have significant advantages over activated carbon, using them to treat large amounts of wastewater on an industrial scale is currently not feasible due to high production costs. However, carbon nanotube application will be more competitive in the short term (2, 31).

Despite these positive properties of carbon nanotubes, the adsorption capacity of metal ions using raw carbon nanotubes is very low, but their adsorption capacity can be significantly increased after oxidation of carbon nanotubes using HNO₃, NaClO and KMnO₄ solutions. Carbon nanotubes in different forms (single-walled or multi-walled closed or open-ended CNTs) have been used for the removal of various contaminants (79). The modification technique of carbon nanotubes should be selected according to the contaminant. Metal oxide-modified materials combine the adsorption properties of metal oxides and the outstanding properties of carbon nanotubes, such as large surface area, evenly distributed pores, and the presence of functional groups on the surface (83).

The hydrophobic surface properties of carbon nanotubes cause stabilization through particle aggregation in aqueous solution to prevent decreases in surface activity. There are numerous reports regarding oxidation and surface modification (2, 27, 31, 32, 79). In addition to the fact that oxidation and surface modification processes provide carbon nanotubes with sufficient adsorption sites, carbon

nanotubes also serve as a good support material for other adsorbents.

Imran Ali carried out As(III) and As(V) removal studies with multi-walled carbon nanotubes (MWCNTs) that he synthesized with dimensions of 10–40 nm and a surface area of 9.1 m²/g. He carried out adsorption studies at pH: 6.0 at a concentration of 40 µg/L and managed to remove As(III) with 91% efficiency and As(V) with 92% efficiency. He also carried out experimental studies as batch and column studies. He carried out experimental studies

separately as batch and column studies. One of the two 25 cm long glass columns, separated by a glass filter with 20 µm pore size, was filled with carbon nanotubes and the other was filled with river sand and treated with arsenic water with the help of a peristaltic pump at a flow rate of 45 min per minute. In experimental studies, maximum adsorption occurred at pH 6.0, 92.0% for As(V) and 91.5% for As(III). Additionally, from column studies, the capacity of the adsorbent to remove arsenic ions was determined as 13.5 µg/g for As(III) and 14.0 µg/g for As(V) (84).

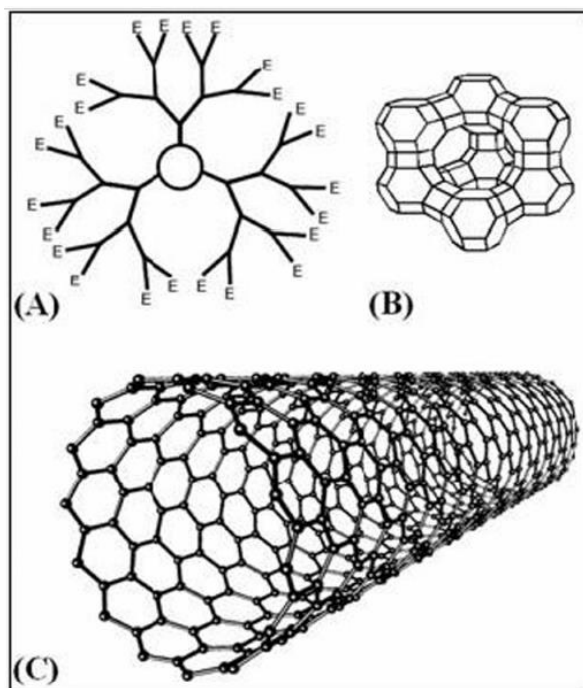


Figure 11: Nanosorbents structures for adsorption processes: (A) dendrimer, (B) zeolite and (C) carbon nanotube. Figure republished with permission from Ref. (79).

4.2.2. Graphene/graphene oxide nanomaterials

Graphene (G) and graphene oxide (GO) have attracted great attention since the discovery of graphene. Graphene and graphene-based nano-adsorbents have been prepared and used for the removal of pollutants in water, including metal ions and organic compounds. Graphene, another member of carbon-based nano-adsorbents, has received significant attention especially in the field of water remediation. Graphite oxides can be easily synthesized on a large scale from low-cost natural graphite. Additionally, graphite oxide is much more applicable than pure graphite, as hybrid multifunctional materials can be synthesized with iron-based nano-adsorbents (28).

The presence of oxygen-containing functional moieties on the surface of graphene oxide provides it with a strong hydrophilic structure, and this leads to its dispersion in water. Graphene oxide can be used effectively in wastewater treatment processes due to its high surface area as well as the functional groups it has on its surface. These nano-adsorbents are preferred in the removal of various pollutants in wastewater. Removal of heavy metal ions by

adsorption occurs through complexation with the oxide binding site in graphene (79). Tabatabaiee Bafrooe et al. (2021) modified the surface of the adsorbent they prepared with EDA by embedding magnetic Fe₃O₄ between the GO layers they synthesized to remove As(III) from water. The As(III) removal capacity of the functionalized magnetic graphene oxide composite adsorbent they prepared was 13.3 mg/g. They reported that at 10 mg/L arsenic concentration, As(III) adsorption occurred as 60% in the first 5 minutes, and removal occurred with 80% efficiency at pH:8.0 by forming a complex on the adsorbent surface (85).

4.2.3. Polymeric nano-adsorbents

In recent years, polymeric adsorbents have emerged as alternatives to traditional adsorbents in terms of their large surface area, tunable surface chemistry, excellent mechanical properties, adjustability of dimensions, applicability under harsh conditions and allowing regeneration (86). Polymer-based nano-adsorbents are preferred for the selective removal of impurities due to the hydroxyl, amine, amide and carboxyl functional groups on their surfaces. Specific interactions between functional groups attached to polymeric matrices and the target ion are effective in

the adsorption capacity and selectivity of synthetic polymers against metal ions (29). In removing arsenic from water, the redox structures of these materials, their adsorption abilities, and their tendency to form complexes and/or precipitate against various pollutants should be taken into consideration.

The low surface area and slow adsorption rate of conventional adsorbents pose a limitation to their applications. Meanwhile, metal/metal oxide nanoparticles have large surface area, but lack functional groups on their surface to chelate metal ions. The development and application of polymer-based nanoadsorbents and nanocomposites provide an alternative opportunity for effective removal of impurities in water (30, 79). As nanoadsorbents, polymeric nanoparticles and polymer-supported nanocomposites, metal/oxide nanoadsorbents have large surface areas and multifunctional groups on the surface compared to other adsorbents.

Polymers are also used especially in surface modification to obtain selective and higher adsorption capacities of magnetic nanoparticles. In addition, polymeric coating provides important advantages to nanoparticles such as chemical stability, mechanical strength and biocompatibility (31, 32). Polymeric nanoadsorbents can generally be prepared in the form of spheres or membranes. Nanofibrous membranes have become preferred in membrane systems due to their well-defined porous structures, higher permeability, small interfiber pore sizes and large surface areas. They have high strength, tunable surface functional groups and the ability to be easily degraded. These features make them an excellent choice among adsorbents. The adsorption process on the polymeric membrane surface composed of nanofibers involves the retention of metal ions by functional groups on the membrane surface and the penetration of wastewater through the membrane (86). The presence of special functional groups such as $-NH_2$, $-COOH$, $-SO_3H$ etc. in polymers can be achieved by the use of different monomers or surface modification while synthesizing the polymer. These groups that the polymer has determine the adsorption capacity and selectivity of the nanoadsorbent (2, 31, 32). Spherical polymeric nanoparticles among polymeric nanoadsorbents can be prepared in different forms such as polymer nanofibers, polymer nanocrystals and polymer nanorods. Polymer-based nanoadsorbents can be categorized as biobased or synthetic on the material used. Synthetic organic polymers or biopolymers, namely cellulose, alginate and chitosan, carrying multifunctional groups such as $-NH_2$, $-SH$, $-OH$, $-COOH$ etc. on the surface, are used to effectively adsorb arsenic ions in water (79).

4.2.4. Chitosan nanoadsorbents

Chitosan is a hydrophilic, biocompatible, non-toxic, environmentally friendly polymer that can form complexes with metal ions with its amino and hydroxyl groups. Adsorption on chitosan occurs not only electrostatically with the functional groups on the surface, which can be charged depending on the pH of the environment, but also by interaction with

metal ions through chelation. In addition, the functionalization process for adsorption efficiency and selectivity also stabilizes chitosan in an acidic environment and increases its mechanical properties (87, 88).

Min et al. synthesized Fe-doped chitosan electrospun nanofibers to remove As(V) from water. They reported that the maximum As(V) adsorption of the chitosan nanofiber they synthesized with a diameter of 128 nm to 153 nm was 11.2 mg/g at pH 7.2. In their XPS and FTIR analyses, they observed that $-NH$, $-OH$ and $C-O$ functional groups in the structure of chitosan were effective in As(V) adsorption. Additionally, in examining the effect of other ions on adsorption, they reported that while arsenic adsorption decreased with increasing solution ionic strength, Cl^- and SO_4^{2-} anions up to 1 mM did not affect the adsorption of arsenate, but SiO_3^{2-} and PO_4^{2-} ions had a significant negative effect on adsorption (89).

4.2.5. Cellulose-based nanoadsorbents

Dendrimers are organic polymeric adsorbents containing high amounts of chelating amine functional groups and are a nanomaterial that is being researched for metal adsorption. These adsorbents provide advantages because they are based on natural cellulose, are non-toxic and economical (28).

Chaia et al. carried out an arsenic removal study with pH-sensitive nanocellulose-based nanoparticles that they synthesized by using polyethyleneimine and glutaraldehyde as cross-linkers. With the cellulose nanoparticles they synthesized, they managed to quickly adsorb As(V) ions at a maximum capacity of 255.19 mg/g in acidic conditions, especially at pH: 3.0. Then, they could easily regenerate the adsorbent using NaOH (90).

4.2.6. Dendrimer nanoadsorbent

Dendrimers are organic polymeric adsorbents containing highly chelating amine functional groups and another potential nanomaterial for metal adsorption. Typically, dendrimers are symmetrical around the core and often have a spherical three-dimensional morphology. Dendrimers, which have repeatedly branched molecules, are considered an excellent example for their effectiveness in removing organic and inorganic pollutants. The general properties of dendrimers are determined by the functional groups they have on their surface, but there are also examples of dendrimers with functionality within the structure (28, 31, 91).

Prabu et al. synthesized graphene oxide-polyamidoamine dendrimer (up to 2nd generation, (GO-gen2) adsorbents) by the grafting method to remove As(V). They then functionalized the surface of the adsorbent with aromatic triazine rings which is rich in aromatic nitrogen. They entrapped ZrO in this synthesized adsorbent and examined its adsorption behavior of AsO_3 ion from water. The maximum adsorption capacity of the dendrimer composite adsorbent in GO sheet form was 1.075 mmol/g for AsO_3 (91). Yavari et al evaluated the effect of

polyamidoamine dendrimer generation 3 (PAMAM G3) as an adsorbent in the removal of As(V) from aqueous solutions. They carried out their experimental studies in the pH range of 2-10 and the maximum adsorption was 233.17 mg/g at a concentration of 1000 mg/L at pH:7.0. They reported that the adsorption mechanism occurs through the electrostatic interaction of negatively charged arsenic ions with the positively charged dendrimer surface at pH = 7.0 (92).

4.3. Composite Nanoadsorbents

Each of the organic and inorganic adsorbents used in the removal of toxic pollutants from water has superior properties but also shortcomings. Although metal/metal oxide nanoadsorbents are natural and inexpensive, they have disadvantages such as specificity, stability and aggregation. Despite their superior properties such as having different functional groups that allow interactions on their surfaces and being regenerable, organic adsorbents have disadvantages such as being relatively expensive to synthesize compared to inorganic ones, difficult to remove from adsorption medium and costly to use. Researchers have focused on developing new composite adsorbents that have the superior properties of organic and inorganic adsorbents. Researchers have carried out studies to develop composite adsorbents with superior properties by combining the superior properties of carbon-based adsorbents, such as allowing the physico-chemical properties of the adsorbent used to be modified and maintaining its stability under harsh conditions, and the superior properties of magnetic adsorbents, such as being easy to separate because they are natural, economical and magnetic. In this way, the tendency of inorganic adsorbents to form aggregates can be prevented. In addition, the leakage of metals into the adsorption medium is prevented (93). There are studies in the literature to remove arsenic from water with various composites consisting of carbon nanotubes, graphene oxide, activated carbons and iron oxide nanoparticles (41, 43). In addition to this approach, there are many studies on arsenic removal from water with composite nanoadsorbents embedded in polymeric nanoadsorbents. Composite studies, in particular, where magnetic properties are utilized and Fe₃O₄ nanoparticles are surface modified with molecules having functional groups such as -NH₂ -COOH or -SO₃H, are among the areas where researchers focus on (31).

4.3.1. Organic polymer supported nanocomposites

Magnetic nanoparticles, which are the most common inorganic nanoadsorbent used in arsenic treatment, can be prepared as composites by coating them with polymers, embedding them in the polymeric structure, or bonding organic molecules to their surfaces. In addition to the important developments in the synthesis of magnetic nanoadsorbents, preserving their stability by preventing their agglomeration and precipitation is also an important issue. To overcome these shortcomings, bare magnetic nanoparticles can be functionalized with different molecules. Surface modification of magnetic nanoparticles increases the selectivity and adsorption

capacity towards certain metal ion, as well as increases the stability of magnetic Fe₃O₄ against oxidation (79).

In functionalization, polymeric coating using polyethylene glycol (PEG), polyvinyl alcohol (PVA) and polyvinylpyrrolidone (PVP), etc., provides complex formation, chemical bonding and ligand combination in addition to the electrostatic and Van der Waals interactions responsible for metal ion adsorption on the adsorbent surface of magnetic nanoparticles. Thanks to coating polymers, agglomeration of magnetic nanoparticles can be prevented (41).

This process provides a larger surface area/volume ratio and promotes better dispersion of magnetic nanoparticles in solution. Functionalization of the surfaces of magnetic nanoparticles allows specific adsorption of metal ions. In addition to coating magnetic nanoparticles with polymers, many studies have also been conducted on functionalizing them with biological molecules or functional molecules (71-76).

Polymeric nanocomposites are also categorized in terms of the incorporation of inorganic nanoparticles into a polymer matrix. Organic polymer-supported nanocomposites are formed by preparing organic polymers together with inorganic nanoadsorbents such as Fe/TiO₂/Fe₃O₄. Polymers covering the surfaces of metallic nanoadsorbents can be examined under two different groups: synthetic polymer-supported nanocomposites and biopolymer-supported nanocomposites. The first group includes synthetic polymers such as polyaniline (PAN), polystyrene, polyhydroxybutyrate (PHB), poly(tetrafluoroethylene), polyethylene (PE), and nafion. Biopolymer-supported nanocomposites are prepared with biological polymers such as cellulose, chitosan and alginate or resin (31).

Türkmen et al. embedded the nano-sized Fe₃O₄ magnetic nanoparticles they synthesized into the polymer to remove arsenic. They synthesized polymeric nanoparticles with the -SH functional group on their surface using the molecular imprinting technique. With the nanoparticles they synthesized, they managed to adsorb the As(III) ion as 76.83 mg/g nanoparticles and the As(V) ion as 87.57 mg/g nanoparticles at pH: 5.0. It can be seen from SEM analysis that the sizes of the magnetic Fe₃O₄ containing nanoparticles they synthesized are in the range of 30-40 nm (94).

Metal oxide nanoadsorbents have a tendency to aggregate, which causes a decrease in their surface area and, as a result, a decrease in adsorption capacity is observed. However, adsorption capacities can be increased by functionalizing them with polymers and preparing their composites. However, modification of the metal oxide surface contributes to both increasing the adsorption capacity of the nanoadsorbent and increasing its selectivity. In particular, the oxidation tendencies of iron nanoparticles can also be controlled by alloying it

with another stable metal or coating them with some polymers.

Alginate, a biopolymer, has also been applied as a biopolymer support in the construction of nanocomposites to remove toxic elements from water. Haris et al. carried out an As(III) removal study with the 12 nm-size bare and alginate encapsulated super paramagnetic nanoparticles they synthesized. The dimensions of the alginate-coated and bare super paramagnetic nanoparticles were 25-30 nm and the maximum adsorption occurred at pH:7.0. They succeeded in removing 90% of arsenic from the solution at 6.5 mg/L As(III) concentration with bare iron oxide nanoparticles and 99% with alginate-coated ones (95). Chitosan nanoparticles have faster adsorption rates and higher adsorption capacities compared to micro-chitosan materials. Abdollahi et al. synthesized chitosan nanoparticles containing magnetic Fe_3O_4 to remove arsenic from water. They determined that chitosan-coated nanoparticles were 10 nm in size. They reported that the adsorption behavior obeyed the Langmuir adsorption isotherm model and reached a maximum of 10.5 mg/g at pH: 9.0. They also reported that at 10 mg/L As(III) concentration, As(III) ion adsorption was 74.59 mg/g for bare Fe_3O_4 nanoparticles and 87.46 mg/g for Chitosan-coated Fe_3O_4 nanoparticles (96).

4.3.2. Nanoparticles functionalized with organic/biomolecules

Functionalization of magnetic nanoadsorbents with organic/biomolecules not only increases the adsorption capacity, but also enables their safe and environmentally friendly use in the purification process of metal ions. Many researchers have investigated the use of magnetic nanoadsorbents functionalized with biomolecules in the adsorption of heavy metals as well as arsenic ions. Functional groups on the surfaces of nanoparticles whose surfaces are functionalized with organic molecules greatly increase the adsorption capacity and also provide selectivity to inorganic nanoadsorbents by forming complexes with metal ions (31, 41, 42, 97).

Tripathy et al. functionalized the surfaces of the Fe_3O_4 magnetic nanoparticles they synthesized with L-cysteine (an amino acid). Thus, they developed a dispersible adsorbent that can be collected magnetically. Later, they used this adsorbent to remove As(III) and As(V) ions from water. They reported that the cysteine-functionalized mesoporous magnetic Fe_3O_4 nanoparticles they synthesized adsorbed 20.0 mg/g As(III) and 34.0 mg/g As(V) ions. In their studies, they managed to adsorb approximately 93% of As(III) (at pH: 7.0 and 9.0) and 95% of As(V) (at pH: 5.0) onto the surface of Fe_3O_4 -cysteine. Functionalizing the surface with L-cysteine not only increased the dispersibility of Fe_3O_4 nanoparticles in aqueous suspensions, but also effectively prevented iron ions from leaking into the solution (98).

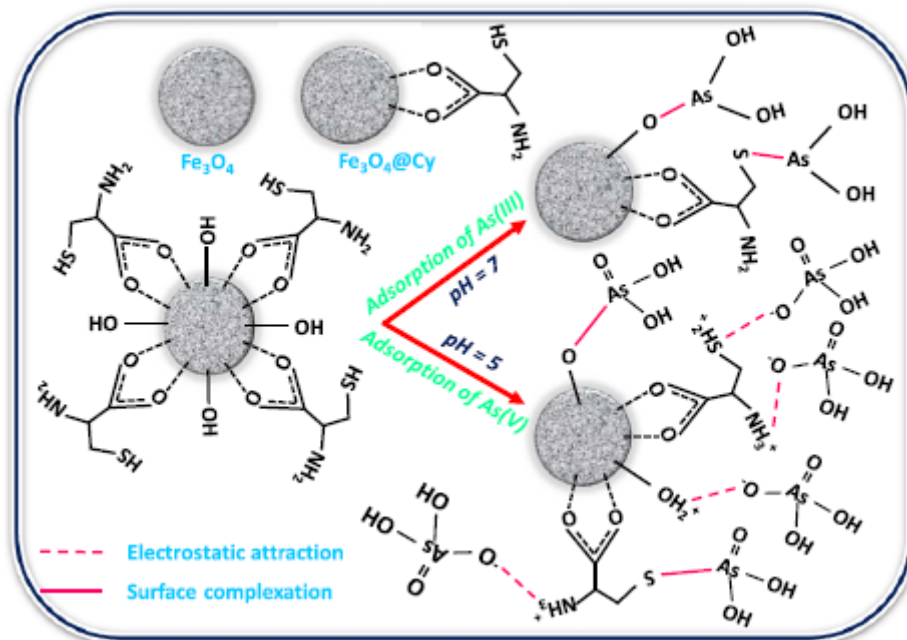


Figure 12: Schematic representation of the arsenic ions adsorption mechanism of Fe_3O_4 nanoparticles functionalized with cysteine. Figure republished with permission from Ref. (98).

5. FACTORS AFFECTING ARSENIC ADSORPTION

The most important parameter in metal adsorption studies is the ambient pH. In metal adsorption processes, at low pH, electrostatic repulsions between protonated functional parts and metal

cations on the surface of the adsorbents cause a decrease in adsorption. In addition, H^+ and H_3O^+ ions, which increase in the medium due to the decrease in pH, compete with metal cations in adsorption. However, at intermediate pH values, the amount of adsorption increases due to the decrease

in electrostatic repulsion due to deprotonation of functional groups. We can state that medium pH is suitable for the removal of toxic metal ions because in this case the adsorbent surface is deprotonated, which causes an increase in negatively charged regions. This causes increased electrostatic attractions between the adsorbent surface and metal cations, leading to an increase in adsorption capacity. In basic conditions, hydroxylated complexes of metal ions in the medium are formed (42, 74, 93).

The situation here is slightly different in removing arsenic from water. In aqueous media, As(III) and As(V) ions exist in the form of oxyanions and vary depending on the pH of the medium. As the pH of the medium increases, the negative charge value of As(V) ions in the negatively charged oxyanion form increases, but in acidic media, the uncharged As(III) form turns into a negatively charged form after pH: 9.0. At pH values below 9.0, where it is uncharged, arsenite ions can be removed from the medium by complexing with the adsorbent rather than electrostatic interactions (32, 43).

Another parameter that affects adsorption is the dose amount of the adsorbent. As the adsorbent dose amount of nanoparticles in the medium increases, the adsorption capacity increases. However, the high amount of adsorbent added to the medium causes the nanoadsorbents to form aggregates, which leads to a decrease in the surface area and a decrease in adsorption, and therefore a decrease in the adsorption capacity (43, 79).

Another factor affecting adsorption is metal ion concentration. The adsorption rate increases with the increase of metal ion concentration to a certain degree at the beginning, but more increase causes the removal efficiency to decrease. This may be because the optimum metal ion concentration must be present in the solution for a certain amount of adsorbent. The presence of a low concentration of metal ions in the medium means fewer metal ions available for adsorption, leading to a low removal rate, but if the concentration increases, it causes an increase in the amount of ions available for adsorption and an increase in the interaction with the binding sites, resulting in a higher adsorption rate (28).

Especially in metal ion adsorption on large scales, the contact time between metal ions in solution and adsorbents is important and time plays an important role in economical wastewater treatment processes. Since it is easier for analyte ions to access the active areas of nano-sized adsorbents with high surface areas, reaching equilibrium in adsorption occurs in a shorter time and thus maximum adsorption capacities are reached in a short time (32, 75).

Another point that affects the adsorption is the temperature of the adsorption medium. Adsorption medium temperature is also an important parameter in the adsorption process. In general, the increase in initial temperature reduces the viscosity of the solution, resulting in increased diffusion rate of the analyte across the adsorbent surface, leading to

higher adsorption efficiency. Adsorption phenomenon is an exothermic phenomenon and as the temperature increases, the kinetic energy of the analyte increases and adsorption decreases. The change in temperature affects adsorption in two different ways, depending on whether the system exhibits heat absorption or heat dissipation behavior. In an exothermic process, the adsorption capacity decreases with increasing temperature, while in an endothermic process it increases (72).

Ion diversity in the medium also affects adsorption. Especially, depending on the affinity of the functional groups on the adsorbent surface to the target metal ion, the adsorption of the target ion is affected by the presence of competitive ions in the medium. Since competing ions in the medium occupy active sites by creating chelation on the surface, there is a decrease in the adsorption of the target metal ion. In addition, for selective adsorption, it is necessary to specifically design the adsorbent surface or use selectivity-oriented techniques such as molecular imprinting (29, 94). During arsenic removal processes from water, the presence of anions such as PO_4^{3-} , Cl^- , NO_3^- , SO_4^{2-} and CO_3^{2-} ions in the medium affects the adsorption of arsenate and arsenite ions, which are in the form of negatively charged oxyanions. Studies in the literature have reported that especially the PO_4^{3-} ion significantly affects adsorption (43, 65).

6. CONCLUSION

In recent years, developments in nanoscience and nanotechnology have enabled the development of efficient, economical and environmentally friendly approaches to environmental remediation. Nowadays, nanomaterials as adsorbents with large specific surface area, functionalized surfaces for more and selective adsorption, and less tendency to agglomerate have attracted great attention in the decontamination of water. Particularly prepared nanocomposites have become promising adsorbents for water treatment due to their physicochemical properties (34).

Scientists have extensively reported studies on various nanostructured materials such as metal/metal oxide, carbon-based and composite materials used as adsorbents in the removal of heavy metal ions. Moreover, recent literature searches show that research focuses on surface functionalization and modification of adsorbents for their better dispersion and easy separation in the adsorption medium. To improve their surface properties of nanoadsorbents in the functionalization different molecules such as inorganic, organic, polymeric, biomolecules, etc. are used (31, 44).

Research and adaptation studies for the treatment of arsenic from water continue at both laboratory and industrial scales. However, the instability of some nanoadsorbents and the difficulty of removing them from purified water and regenerating them have limited their commercial use. The biggest disadvantage of using nanosized adsorbents is the high cost (49, 65). In addition to the fact that there are difficulties in removing nanoadsorbents from the

adsorption medium, another disadvantage is that the toxic effects of toxic metal-loaded nanoadsorbents remaining in the medium have not been clearly elucidated.

Considering the various studies reported so far, it is concluded that composite magnetic nanoparticles may be a better option for removing arsenic from waters. In the selection of nano adsorbents for arsenic removal, factors such as adsorption potential, high surface area, physical and chemical stability, ease of production and applicability, solubility product of the adsorbent, easy separation of the adsorbent from water, leachability to the water medium, its toxic effect, cost and regenerability and in-situ applicability should be taken into consideration (30, 63, 65, 75, 99).

Although nanoadsorbents have unique properties, most of the adsorption studies are at laboratory scale and their industrial applications are quite few. Laboratory studies by the scientists to develop nanoadsorbents with desired properties and suitable for use in industrial systems are still continuing. Researchers have concerns due to the uncertainties about the health problems that nanoadsorbents may cause due to problems in their recovery from the medium (33). Detailed studies on the design and development, surface modification and applications of new generation adsorbents are continuing intensively, and these adsorbents are promising in environmental applications and water treatment. The use of nanoparticles for water purification at laboratory scale has shown promising results, but further improvement of their physicochemical properties appears to be needed for full-scale application (44, 49).

7. REFERENCES

1. Smedley PL, Kinniburgh DG. A Review of the Source, Behavior and Distribution of Arsenic in Natural Waters. *Applied Geochemistry*. 2002; 17(5): 517-568. Available from: [<DOI>](#)
2. Mohan D, Pittman CU. Arsenic removal from water/wastewater using adsorbents A critical review, *Journal of Hazardous Materials*. 2007; 142(1-2):1-53. Available from: [<DOI>](#)
3. Mandal BK, Suzuki KT. Arsenic round the world: a review. *Talanta*. 2002; 58(1): 201-235. Available from: [<DOI>](#)
4. Sharma VK, Sohn M. Aquatic arsenic: toxicity, speciation, transformations, and remediation. *Environment international*. 2009; 35(4): 743-759
5. Weerasundara L, Ok YS, Bundschuh J. Selective removal of arsenic in water: A critical review, *Environmental Pollution*. 2021; 268: 115668 Available from: [<DOI>](#)
6. Teixeira MC, Ciminelli VST, Dantas MSS, Diniz SF, Duarte HA Raman Spectroscopy and DFT Calculations of As(III) Complexation with a Cysteine-Rich Biomaterial. *Journal of Colloid and Interface Science*. 2007; 315(1): 128-134 Available from: [<DOI>](#)
7. Patel K S, Pandey P K, Martín-Ramos P, Corns WT, Varol S, Bhattacharya P, Zhu Y. A review on arsenic in the environment: contamination, mobility, sources, and exposure. *RSC Advances*, 2023; 13(13): 8803-8821.
8. Shen S, Li XF, Cullen WR, Weinfeld M, Le XC. Arsenic binding to proteins. *Chemical Reviews* 2013; 113(10): 7769-7792. Available from: [<DOI>](#)
9. Mudhoo A, Sharma S K, Garg V K, Tseng CH. Arsenic: an overview of applications, health, and environmental concerns and removal processes. *Critical Reviews in Environmental Science and Technology*, 2011; 41(5): 435-519. Available from: [<DOI>](#).
10. Choong TS, Chuah TG, Robiah Y, Koay FG, Azni I. Arsenic toxicity, health hazards and removal techniques from water: an overview. *Desalination*. 2007; 217(1-3): 139-166. Available from: [<DOI>](#).
11. Altowayti WAH, Othman N, Shahir S, Alsharif AF, Al-Gheethi AA, Al-Towayti FAH, Haris SA. Removal of arsenic from wastewater by using different technologies and adsorbents: A review. *International Journal of Environmental Science and Technology*. 2021; 19:9243-9266. Available from: [<DOI>](#)
12. Dilpazeer F, Munir M, Baloch MYJ, Shafiq I, Iqbal J, Saeed M, Mahboob I. A Comprehensive Review of the Latest Advancements in Controlling Arsenic Contaminants in Groundwater. *Water*. 2023; 15(3): 478. Available from: [<DOI>](#)
13. Rathi BS, Kumar PS. A review on sources, identification and treatment strategies for the removal of toxic Arsenic from water system. *Journal of Hazardous Materials* 2021; 418: 126299. Available from: [<DOI>](#)
14. Singh R, Singh S, Parihar P, Singh VP, Prasad SM. Arsenic contamination, consequences and remediation techniques: a review. *Ecotoxicology and environmental safety*. 2015; 112: 247-270. Available from: [<DOI>](#)
15. Mahamallik P, Swain R. A mini-review on arsenic remediation techniques from water and future trends. *Water Science and Technology*. 2023; 87(12): 3108-3123. Available from: [<DOI>](#)
16. Alka S, Shahir S, Ibrahim N, Ndejiko MJ, Vo DVN, Abd Manan F. Arsenic removal technologies and future trends: A mini review. *Journal of Cleaner Production*. 2021; 278, 123805. Available from: [<DOI>](#)
17. Rahidul Hassan, H. A review on different arsenic removal techniques used for decontamination of drinking water. *Environmental Pollutants and Bioavailability*, 2023; 35(1): 2165964. Available from: [<DOI>](#)
18. Nicomel NR, Leus K, Folens K, Van Der Voort P, Du Laing G. Technologies for arsenic removal from water: current status and future perspectives.

International journal of environmental research and public health. 2016; 13(1): 62. Available from: [<DOI>](#).

19. Ahmed MF. An overview of arsenic removal technologies in Bangladesh and India. In Proceedings of BUET-UNU international workshop on technologies for arsenic removal from drinking water, Dhaka. 2001; 5-7.
20. Selatile MK, Ray SS, Ojijo V, Sadiku R. Recent developments in polymeric electrospun nanofibrous membranes for seawater desalination. RSC Advances, 2018; 8(66): 37915-37938. Available from: [<DOI>](#)
21. Kirisenage PM, Zulqarnain SM, Myers JL, Fahlman BD, Mueller A, Marquez I. Development of Adsorptive Membranes for Selective Removal of Contaminants in Water. Polymers, 2022; 14(15): 3146. Available from: [<DOI>](#)
22. Moreira VR, Lebron YAR, Santos LVS, de Paula EC, Amaral MCS. Arsenic contamination, effects and remediation techniques: A special look onto membrane separation processes. Process Safety and Environmental Protection. 2021; 148, 604-623. Available from: [<DOI>](#)
23. Chen M, Shafer-Peltier K, Randtke S J, Peltier E. Modeling arsenic (V) removal from water by micellar enhanced ultrafiltration in the presence of competing anions. Chemosphere. 2018; 213: 285-294. Available from: [<DOI>](#)
24. Chia RJJ, Lau WJ, Yusof N, Shokravi H, Ismail AF. Adsorptive Membranes for Arsenic Removal–Principles, Progress and Challenges. Separation & Purification Reviews, 2023; 52(4): 379-399. [<DOI>](#)
25. Awual MR, Hossain MA, Shenashen M. Evaluating of arsenic(V) removal from water by weak-base anion exchange adsorbents. Environmental science and pollution research international. 2013; 20:421-430. Available from: [<DOI>](#)
26. Wang Y, Tsang DC. Effects of solution chemistry on arsenic (V) removal by low-cost adsorbents. Journal of Environmental Sciences. 2013; 25(11): 2291-2298. Available from: [<DOI>](#).
27. Crini G, Lichtfouse E, Wilson LD, Morin-Crini N. Conventional and non-conventional adsorbents for wastewater treatment. Environmental Chemistry Letters, 2019; 17, 195-213. Available from: [<DOI>](#)
28. Liu B, Kim KH, Kumar V, Kim S. A review of functional sorbents for adsorptive removal of arsenic ions in aqueous systems. Journal of hazardous materials, 2020; 388, 121815. Available from: [<DOI>](#)
29. Kyzas GZ, Matis KA. Nanoadsorbents for pollutants removal: a review. Journal of Molecular Liquids. 2015; 203, 159-168. Available from: [<DOI>](#)
30. Ali I. New generation adsorbents for water treatment. Chemical Reviews, 2012; 112(10): 5073-5091. Available from: [<DOI>](#)
31. Habuda-Stanić M, Nujić M. Arsenic removal by nanoparticles: a review. Environ Sci Pollut Res. 2015; 22: 8094–8123. Available from: [<DOI>](#)
32. Lata S, Samadder SR. Removal of arsenic from water using nano adsorbents and challenges: A review, Journal of Environmental Management. 2016;166: 387-406. Available from: [<DOI>](#).
33. Mohmood I, Lopes CB, Lopes I, Ahmad I, Duarte AC, Pereira E. Nanoscale materials and their use in water contaminants removal—a review. Environmental science and pollution Research. 2013; 20: 1239-1260. Available from: [<DOI>](#)
34. Khan NA, Khan SU, Ahmed S, Farooqi IH, Dhingra A, Hussain A, Changani F. Applications of nanotechnology in water and wastewater treatment: A review. Asian Journal of Water, Environment and Pollution. 2019; 16(4): 81-86. Available from: [<DOI>](#)
35. Saha S, Sarkar P. Arsenic remediation from drinking water by synthesized nano-alumina dispersed in chitosan-grafted polyacrylamide. Journal of hazardous materials. 2012; 227-228: 68-78. Available from: [<DOI>](#)
36. Yürüm A, Kocabaş Ataklı ZÖ, Sezen M, Semiat R, Yürüm Y. Fast deposition of porous iron oxide on activated carbon by microwave heating and arsenic (V) removal from water. Chemical Engineering Journal. 2014; 242: 321-332. Available from: [<DOI>](#).
37. Pizarro C, Rubio MA, Escudey M, Albornoz MF, Muñoz D, Denardin J, Fabris JD. Nanomagnetite-zeolite composites in the removal of arsenate from aqueous systems. Journal of the Brazilian Chemical Society. 2015; 26: 1887-1896. Available from: [<DOI>](#)
38. Savina IN, English CJ, Whitby RL, Zheng Y, Leistner A, Mikhalovsky SV, Cundy AB. . High efficiency removal of dissolved As (III) using iron nanoparticle-embedded macroporous polymer composites. Journal of hazardous materials. 2011; 192(3): 1002-1008. Available from: [<DOI>](#)
39. Önnby L, Svensson C, Mbundi L, Busquets R, Cundy A, Kirsebom H. . γ -Al₂O₃-based nanocomposite adsorbents for arsenic (V) removal: Assessing performance, toxicity and particle leakage. Science of the total environment. 2014; 473-474: 207-214. Available from: [<DOI>](#)
40. Önnby L, Pakade V, Mattiasson B, Kirsebom H. Polymer Composite Adsorbents Using Particles of Molecularly Imprinted Polymers or Aluminium Oxide Nanoparticles for Treatment of Arsenic Contaminated Waters. Water. Res 2012; 46: 4111-4120. Available from: [<DOI>](#)
41. Siddiqui SI, Naushad M, Chaudhry SA. Promising prospects of nanomaterials for arsenic water remediation: A comprehensive review. Process

Safety and Environmental Protection. 2019; 126: 60-97. Available from: [<DOI>](#)

42. Lu F, Astruc D. Nanomaterials for removal of toxic elements from water. *Coordination Chemistry Reviews*. 2018; 356: 147-164. Available from: [<DOI>](#)
43. Wadhawan S, Jain A, Nayyar J, Mehta SK. . Role of nanomaterials as adsorbents in heavy metal ion removal from waste water: A review. *Journal of Water Process Engineering*. 2020; 33: 101038. Available from: [<DOI>](#)
44. Mostafa MG, Hoinkis J. . Nanoparticle adsorbents for arsenic removal from drinking water: a review. *International Journal of Environmental Science, Management and Engineering Research*, 2012; 1(1): 20-31.
45. Khin MM, Nair AS, Babu VJ, Murugan R, Ramakrishna S. A review on nanomaterials for environmental remediation. *Energy & Environmental Science*, 2012; 5(8): 8075-8109. Available from: [<DOI>](#) .
46. Wong W, Wong HY, Badruzzaman ABM, Goh HH, Zaman M. . Recent advances in exploitation of nanomaterial for arsenic removal from water: a review. *Nanotechnology*. 2016; 28(4), 042001. Available from: [<DOI>](#).
47. Alidokht L, Anastopoulos I, Ntarlagiannis D, Soupios P, Tawabini B, Kalderis D, Khataee A. Recent advances in the application of nanomaterials for the remediation of arsenic-contaminated water and soil. *Journal of Environmental Chemical Engineering*, 2021; 9(4): 105533. Available from: [<DOI>](#)
48. Picón D, Torasso N, Baudrit JRV, Cerveny S, Goyanes S. Bio-inspired membranes for adsorption of arsenic via immobilized L-Cysteine in highly hydrophilic electrospun nanofibers. *Chemical Engineering Research and Design*. 2022; 185: 108-118. Available from: [<DOI>](#).
49. Zhang WX. Nanoscale iron particles for environmental remediation: an overview. *Journal of Nanoparticle Research*, 2003; 5: 323-332. Available from: [<DOI>](#)
50. Mosaferi M, Nemati S, Khataee A, Nasser S, Hashemi AA. Removal of Arsenic (III, V) from aqueous solution by nanoscale zero-valent iron stabilized with starch and carboxymethyl cellulose. *Journal of Environmental Health Science and Engineering*. 2014; 12: 1-11. Available from: [<DOI>](#)
51. Ersan G, Brienza M, Mulchandani A, Apul OG, Garcia-Segura S. . Trends on arsenic species removal by metal-based nanoadsorbents. *Current Opinion in Environmental Science & Health*. 2023;34: 100478. Available from: [<DOI>](#)
52. Patra AK, Dutta A, Bhaumik A. Self-assembled mesoporous γ -Al₂O₃ spherical nanoparticles and their efficiency for the removal of arsenic from water. *Journal of hazardous materials*. 2012; 201-202: 170-177. Available from: [<DOI>](#)
53. Ghosh S, Prabhakar R, Samadder SR. Performance of γ -aluminium oxide nanoparticles for arsenic removal from groundwater. *Clean technologies and environmental policy*. 2019; 21: 121-138. Available from: [<DOI>](#)
54. Martinson CA, Reddy KJ. Adsorption of arsenic (III) and arsenic (V) by cupric oxide nanoparticles. *Journal of colloid and interface science*, 2009; 336(2): 406-411. Available from: [<DOI>](#)
55. Goswami A, Raul PK, Purkait MK. Arsenic adsorption using copper (II) oxide nanoparticles. *Chemical Engineering Research and Design*, 2012; 90(9): 1387-1396. Available from: [<DOI>](#)
56. Ashraf S, Siddiqa A, Shahida S, Qaisar S. . Titanium-based nanocomposite materials for arsenic removal from water: A review. *Heliyon*, 2019; 5(5): e01577 Available from: [<DOI>](#)
57. Jegadeesan G, Al-Abed SR, Sundaram V, Choi H, Scheckel KG, Dionysiou DD. Arsenic sorption on TiO₂ nanoparticles: size and crystallinity effects. *Water research*, 2010; 44(3): 965-973. Available from: [<DOI>](#)
58. Deng M, Chi M, Wei M, Zhu A, Zhong L, Zhang Q, Liu Q. A facile route of mesoporous TiO₂ shell for enhanced arsenic removal. *Colloids and Surfaces A: Physicochemical and Engineering Aspects*, 2021; 627, 127138. Available from: [<DOI>](#)
59. Singh N, Singh SP, Gupta V, Yadav HK, Ahuja T, Tripathy SS, Rashmi. A process for the selective removal of arsenic from contaminated water using acetate functionalized zinc oxide nanomaterials. *Environmental Progress & Sustainable Energy*, 2013; 32(4): 1023-1029. Available from: [<DOI>](#)
60. Rehman H, Ali Z, Hussain M, Gilani SR, Shahzady TG, Zahra A, Farooq MU. Synthesis and characterization of ZnO nanoparticles and their use as an adsorbent for the arsenic removal from drinking water. *Digest Journal of Nanomaterials and Biostructures*, 2019; 14(4): 1033-1040.
61. Cui H, Su Y, Li Q, Gao S, Shang JK. Exceptional arsenic (III, V) removal performance of highly porous, nanostructured ZrO₂ spheres for fixed bed reactors and the full-scale system modeling. *Water research*, 2013; 47(16): 6258-6268. Available from: [<DOI>](#)
62. Zheng YM, Yu L, Wu D, Chen JP. Removal of arsenite from aqueous solution by a zirconia nanoparticle. *Chemical engineering journal*, 2012; 188: 15-22. Available from: [<DOI>](#)
63. Litter MI. A short review on the preparation and use of iron nanomaterials for the treatment of pollutants in water and soil. *Emergent Materials*, 2022; 5(2): 391-400. Available from: [<DOI>](#)
64. Ahmaruzzaman M. Magnetic nanocomposite adsorbents for abatement of arsenic species from water and wastewater. *Environmental Science and Pollution Research*. 2022; 29(55): 82681-82708 Available from: [<DOI>](#)

65. Siddiqui SI, Chaudhry SA. Iron oxide and its modified forms as an adsorbent for arsenic removal: A comprehensive recent advancement. *Process Safety and Environmental Protection*. 2017; 111: 592-626. Available from: [<DOI>](#)
66. Rashid US, Saini-Eidukat B, Bezbaruah AN. Modeling arsenic removal by nanoscale zero-valent iron. *Environmental monitoring and assessment*. 2020; 192: 1-7. Available from: [<DOI>](#)
67. Xue W, Li J, Chen X, Liu H, Wen S, Shi X, Xu Y. Recent advances in sulfidized nanoscale zero-valent iron materials for environmental remediation and challenges. *Environmental Science and Pollution Research*, 2023; 30(46): 101933-101962. Available from: [<DOI>](#)
68. Yin L, Liu L, Lin S, Owens G, Chen Z. Synthesis and characterization of Nanoscale Zero-Valent Iron (nZVI) as an adsorbent for the simultaneous removal of As (III) and As (V) from groundwater. *Journal of Water Process Engineering*, 2022; 47: 102677. Available from: [<DOI>](#)
69. Morgada ME, Levy IK, Salomone V, Farías SS, Lopez G, Litter MI. Arsenic (V) removal with nanoparticulate zerovalent iron: effect of UV light and humic acids. *Catalysis Today*, 2009; 143(3-4), 261-268. Available from: [<DOI>](#)
70. Mamindy-Pajany Y, Hurel C, Marmier N, Roméo M. Arsenic (V) adsorption from aqueous solution onto goethite, hematite, magnetite and zero-valent iron: effects of pH, concentration and reversibility. *Desalination*, 2011; 281: 93-99. Available from: [<DOI>](#)
71. Chowdhury SR, Yanful EK. Arsenic removal from aqueous solutions by adsorption on magnetite nanoparticles. *Water and Environment Journal*, 2011; 25(3): 429-437. Available from: [<DOI>](#)
72. Jain R. Recent advances of magnetite nanomaterials to remove arsenic from water. *RSC advances*, 2022; 12(50): 32197-32209. Available from: [<DOI>](#)
73. Mayo JT, Yavuz C, Yean S, Cong L, Shipley H, Yu W, Colvin VL. The effect of nanocrystalline magnetite size on arsenic removal. *Science and technology of advanced materials*. 2007; 8(1-2): 71. Available from: [<DOI>](#)
74. Arora R. Nano adsorbents for removing the arsenic from waste/ground water for energy and environment management- a review, *Materials Today: Proceedings*. 2021; 45(6): 4437-4440. Available from: [<DOI>](#).
75. Ahmaruzzaman Md. Recent developments of magnetic nanoadsorbents for remediation of arsenic from aqueous stream, *Journal of Environmental Science and Health, Part A*. 2022; 57(12): 1058-1072. Available from: [<DOI>](#)
76. Polowczyk I, Cyganowski P, Ulatowska J, Sawiński W, Bastrzyk A. Synthetic iron oxides for adsorptive removal of arsenic. *Water, Air, & Soil Pollution*, 2018; 229: 1-10. Available from: [<DOI>](#)
77. Deliyanni EA, Lazaridis NK, Matis KA. Arsenates Sorption by Nanocrystalline Hybrid Surfactant-Akaganéite, *Separation Science and Technology*, 2012; 47(16): 2331-2339. Available from: [<DOI>](#)
78. Salem Attia TM, Hu XL, Yin DQ. Synthesised magnetic nanoparticles coated zeolite (MNCZ) for the removal of arsenic (As) from aqueous solution. *Journal of Experimental Nanoscience*, 2014; 9(6): 551-560. Available from: [<DOI>](#)
79. El-Sayed ME. Nanoadsorbents for water and wastewater remediation. *Science of the Total Environment*, 2020; 739: 139903. Available from: [<DOI>](#)
80. Jamali-Behnam F, Najafpoor AA, Davoudi M, Rohani-Bastami T, Alidadi H, Esmaily H, Dolatabadi M. Adsorptive removal of arsenic from aqueous solutions using magnetite nanoparticles and silica-coated magnetite nanoparticles. *Environmental Progress & Sustainable Energy*, 2018; 37(3): 951-960. [<DOI>](#)
81. Vitela-Rodriguez AV, Rangel-Mendez JR. Arsenic removal by modified activated carbons with iron hydro (oxide) nanoparticles. *Journal of environmental management*, 2013; 114: 225-231. Available from: [<DOI>](#)
82. Gupta VK, Moradi O, Tyagi I, Agarwal S, Sadegh H, Shahryari Ghoshekandi R, Makhlof ASH, Goodarzi M, & Garshasbi A. Study on the removal of heavy metal ions from industry waste by carbon nanotubes: Effect of the surface modification: a review, *Critical Reviews in Environmental Science and Technology*, 2016; 46(2): 93-118. Available from: [<DOI>](#)
83. Liu X, Wang M, Zhang S, Pan B. Application potential of carbon nanotubes in water treatment: a review. *Journal of Environmental Sciences*, 2013; 25(7): 1263-1280. Available from: [<DOI>](#)
84. Ali I. Microwave assisted economic synthesis of multi walled carbon nanotubes for arsenic species removal in water: batch and column operations. *Journal of molecular liquids*, 2018; 271: 677-685. Available from: [<DOI>](#)
85. Tabatabaiee Bafrooe AA, Moniri E, Ahmad Panahi H, Miralinaghi M, Hasani AH. Ethylenediamine functionalized magnetic graphene oxide (Fe₃O₄@GO-EDA) as an efficient adsorbent in Arsenic (III) decontamination from aqueous solution. *Research on Chemical Intermediates*, 2021; 47: 1397-1428. Available from: [<DOI>](#)
86. Bhaumik M, Noubactep C, Gupta VK, McCrindle RI, Maity A. Polyaniline/Fe₀ composite nanofibers: An excellent adsorbent for the removal of arsenic from aqueous solutions. *Chemical Engineering Journal*, 2015; 271: 135-146. Available from: [<DOI>](#)
87. Pontoni L, Fabbricino M. Use of chitosan and chitosan-derivatives to remove arsenic from aqueous solutions—a mini review. *Carbohydrate*

- research, 2012; 356, 86-92. Available from: [<DOI>](#)
88. Singh P, Bajpai J, Bajpai AK, Shrivastava RB. Fixed-bed studies on removal of arsenic from simulated aqueous solutions using chitosan nanoparticles. *Bioremediation journal*, 2011; 15(3): 148-156. Available from: [<DOI>](#)
89. Min LL, Zhong LB, Zheng YM, Liu Q, Yuan ZH, Yang LM. Functionalized chitosan electrospun nanofiber for effective removal of trace arsenate from water. *Scientific reports*, 2016; 6(1): 32480. Available from: [<DOI>](#)
90. Chai F, Wang R, Yan L, Li G, Cai Y, Xi C. Facile fabrication of pH-sensitive nanoparticles based on nanocellulose for fast and efficient As(V) removal. *Carbohydrate polymers*, 2020; 245: 116511. Available from: [<DOI>](#)
91. Prabhu SM, Pawar RR, Sasaki K, Park CM. A mechanistic investigation of highly stable nano ZrO₂ decorated nitrogen-rich azacytosine tethered graphene oxide-based dendrimer for the removal of arsenite from water. *Chemical Engineering Journal*, 2019; 370: 1474-1484. Available from: [<DOI>](#)
92. Yavari Z, Amin MM, Izanloo H, Rahimi S, Mohamadi F. Using Generation 3 Polyamidoamine Dendrimer as Adsorbent for the Removal of Pentavalent Arsenic from Aqueous Solutions. *J Environ Health Sustain Dev*, 2016; 1(1): 28-36.
93. Kumar A, Joshi H, Kumar A. Remediation of arsenic by metal/metal oxide-based nanocomposites/nanohybrids: contamination scenario in groundwater, practical challenges, and future perspectives. *Separation & Purification Reviews*, 2021; 50(3): 283-314. Available from: [<DOI>](#)
94. Türkmen D, Özkaya-Türkmen M, Akgönüllü S, Denizli A. Development of ion imprinted based magnetic nanoparticles for selective removal of arsenic (III) and arsenic (V) from wastewater. *Separation Science and Technology*, 2022; 57(6): 990-999. Available from: [<DOI>](#)
95. Haris SA, Dabagh S, Mollasalehi H, Ertas YN. Alginate coated superparamagnetic iron oxide nanoparticles as nanocomposite adsorbents for arsenic removal from aqueous solutions. 2023; *Separation and Purification Technology*, 310, 123193. Available from: [<DOI>](#)
96. Abdollahi M, Zeinali S, Nasirimoghaddam S, Sabbaghi S. Effective removal of As(III) from drinking water samples by chitosan-coated magnetic nanoparticles. *Desalination and Water Treatment*, 2015; 56(8): 2092-2104. Available from: [<DOI>](#)
97. Morillo D, Uheida A, Pérez G, Muhammed M, Valiente M. Arsenate removal with 3-mercaptopropanoic acid-coated superparamagnetic iron oxide nanoparticles. *Journal of colloid and interface science*, 2015; 438, 227-234. Available from: [<DOI>](#)
98. Tripathy M, Padhiari S, Hota G. L-Cysteine-Functionalized Mesoporous Magnetite Nanospheres: Synthesis and Adsorptive Application toward Arsenic Remediation. *Journal of Chemical Engineering Data*. 2020; 65(8): 3906-3919. Available from: [<DOI>](#)
99. Biftu WK, Ravindhranath K, Ramamoorthy M. New research trends in the processing and applications of iron-based nanoparticles as adsorbents in water remediation methods. *Nanotechnology for Environmental Engineering*, 2020; 5: 1-12. Available from: [<DOI>](#)
100. Gurbuz F, Akpınar Ş, Özcan S, Acet Ö, Odabaşı M. Reducing arsenic and groundwater contaminants down to safe level for drinking purposes via Fe 3+-attached hybrid column. *Environmental monitoring and assessment*, 2019;191, 1-14. Available from: [<DOI>](#)



Terpene Derivatives: A Comprehensive Computational Insights in Drug-likeness and ADMT Properties, and DFT Study

Goncagül Serdaroğlu^{1*}

¹Sivas Cumhuriyet University, Faculty of Education, Math. and Sci. Edu., 58140, Sivas, Turkey

Abstract: In this study, the terpene-like compounds were investigated to explore the possible reactivity tendency using DFT/B3LYP/6-311G** level and evaluation of absorption, distribution, and metabolism characteristics. The lipophilicity indexes of terpenes revealed that the T1 and T2 molecules were more lipophilic than the other molecules, whereas the T5 and T6 molecules were less lipophilic. The water solubility scores obtained from ALI and ESOL approaches indicated that T5 and T6 functionalized with the -C=O group's most soluble compounds, while T2 was the least soluble among the compounds. Regarding absorption, the T5 molecule was determined to be a promising structure among the compounds. Also, all compounds' VD (L/kg) values were determined in the optimal range of 0.04-20 L/kg. The terpenes T1-T3 would exhibit a BBB Penetration at a medium level, while they would not be suitable structures for PPB %. The terpenes T4-T6 could be quite promising in distribution except for BBB Penetration. T6 structure was determined to be more suitable in terms of metabolism than the other terpenes. NBO analyses revealed that $\sigma \rightarrow \sigma^*$ interactions for T1-T4 would lower the stabilization energy, predicted at 7.04 kcal/mol. In contrast, the resonance ($\pi \rightarrow \pi^*$) interaction for T5 was predicted with the energy of 20.26 kcal/mol, which was the highest contributed interaction to $E^{(2)}$. FMO analyses indicated that T5 (0.204 au) could prefer electron donation more than terpenes, while T4 (0.108 au) would prefer electron donation less. MEP plots implied that the surround of the oxygen atom for T3-T6 molecules would be the electron-rich region for the electrophiles, whereas the around of the double bonds of T1 and T2 would be possible sites for the electrophiles. According to the NPA approach, the atomic charge of the O1 atom of terpenes T4-T6 was predicted at -0.76279, -0.55670, and -0.55395, whereas the O28 atom' charge was found to be at -0.77131, remarkable. The findings from this study are anticipated to provide invaluable insights into the relationship between electronic structure, ADM properties, and toxicity. This could potentially guide the future discovery, development, and refinement of terpene-based therapeutics.

Keywords: Terpene, ADMT study, FMO, MEP

Submitted: June 9, 2023. **Accepted:** February 20, 2024.

Cite this: Serdaroğlu G. Terpene derivatives: A comprehensive computational insights in drug-likeness and ADMT properties, and dft study. JOTCSA. 2024;11(2):869-88.

DOI: <https://doi.org/10.18596/jotcsa.1311965>

***Corresponding author.** E-mail: goncagul.serdaroglu@gmail.com

1. INTRODUCTION

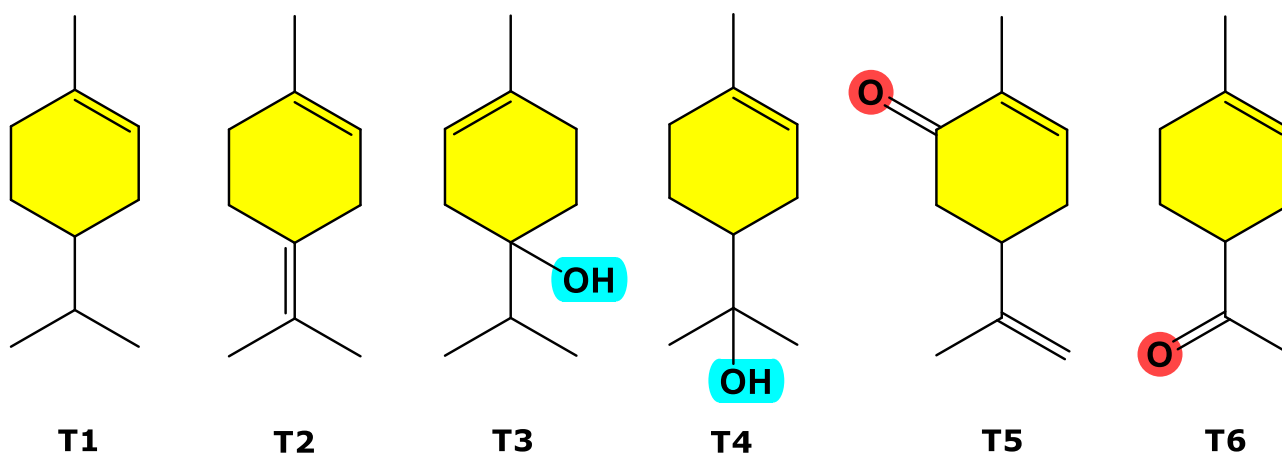
Terpenes and terpenoids are a broad and diverse class of naturally occurring organic compounds produced by a wide variety of plants, fungi, and bacteria (1-3). Due to their strong odors, they play a critical role in plant biology, especially in defense mechanisms against herbivores and in plant-to-plant and plant-to-environment interactions (4). Furthermore, they have been found to possess a broad range of biological activities (5), including anti-inflammatory (6), antiviral (7), antibacterial (8), and anticancer (9,10). Thus, the application of terpenes

is extensive and extends to fields like pharmaceuticals, food additives (11,12), cosmetics (13,14), and even biofuels (15,16). In this regard, Pahima et al. (16) presented a model that combined theoretical and statistical approaches to calculate the thermodynamic properties of terpenes, a promising biofuel. It accurately computes key properties using advanced computational methods, offering a cost-effective strategy for identifying potential petroleum substitutes without expensive experiments. In this regard, coumarin and its nitrile-modified derivative have been investigated by using electrochemical tools and DFT computations to explore the possible

inhibition potency on mild steel surfaces (17). Furthermore, the key interactions between purine metabolism products and DNA have also been investigated by using electrochemical techniques and DFT computational tools (18). Recently, the highly selective fluorescent ligand 3-(1H-benzimidazol-2-yl)quinolin-2(1H)-one monohydrate has been designed and explored in terms of sequential sensing of Cu(II) and HS⁻ ions in the solution (19). In recent work, Maspero and co-workers have reported a novel strategy to explore the possible enhancement of fluorescence characteristics of the biocompatible difluoro boron-functionalized biindoleketonates: they have also performed TD-B3LYP-D3 computations to characterize the $s_0 \rightarrow s_1$ transition (20). Carvomenthene, Limonene, 4-Terpinenol, α -terpineol, and Carvone are also key members of the terpene family, characterized by unique structures, all of which are constructed from isoprene units and reflecting the inherent structural design of terpenes (21). Namely, limonene, a monocyclic monoterpene, is one of the most common terpenes. It is known for its citrusy aroma and is a principal constituent in citrus peel oils (22). 4-Terpinenol, α -terpineol, and carvomenthene, like limonene, are monoterpenes with distinctive structural arrangements and biochemical characteristics. Conversely, carvone is a monoterpene ketone, presenting as two

mirror-image forms or enantiomers, each with a distinct minty or caraway aroma (23).

To understand the biological activity and physicochemical properties of terpenes (Scheme 1), it's important to delve into their structural composition and molecular behavior. In this regard, computational chemistry, specifically Density Functional Theory (DFT), has shown promising results. DFT has been extensively used to study terpenes' molecular geometries, electronic structures, and reaction mechanisms (24-26). Such theoretical studies aid in revealing the fundamental structure-activity relationships, paving the way for the development of new applications and fine-tuning existing uses of these fascinating molecules. In a recent work on carvone, Yankova et al. focused on the electronic properties and chemical activity of carvone by using a B3LYP level with a 6-311++G(2d,2p) basis set; they performed the NBO, FMO, and MEP studies as well as the Hirshfeld surface (27). Also, Mekkaoui and co-workers (28) synthesized the optically active limonaketone with a 92% yield, a high-value monoterpene, from natural and inexpensive limonene and explored the chemoselectivity in the Zinc-deoxygenation reaction and its corresponding mechanistic pathway using density functional theory (DFT) calculations at the M06-2X/6-311G(d,p) (LANL2DZ for Zinc) level.



Scheme 1: The chemical structures of terpenes: The abbreviations and common names are as follows

- T1:** 4-isopropyl-1-methylcyclohex-1-ene (Carvomenthene)
T2: 1-methyl-4-(propan-2-ylidene)cyclohex-1-ene (Limonene)
T3: 1-isopropyl-4-methylcyclohex-3-en-1-ol (4-Terpinenol)
T4: 2-(4-methylcyclohex-3-en-1-yl)propan-2-ol (α -terpineol)
T5: 2-methyl-5-(prop-1-en-2-yl)cyclohex-2-en-1-one (Carvone)
T6: 1-(4-methylcyclohex-3-en-1-yl)ethan-1-one (Limonaketone)

Terpenes such as carvomenthene (T1), limonene (T2), 4-terpineol (T3), α -terpineol (T4), carvone (T5), and limonaketone (T6) are prime examples of the diverse structural composition and inherent design of terpenes. Understanding their unique structures and molecular behavior is key to revealing their biological activity and physicochemical properties. In this perspective, the DFT computational tools have been particularly effective in studying the molecular geometries, electronic structures, and reaction mechanisms of terpenes and related compounds. Also, the application of computational

methods like DFT enables researchers to delve deeper into the complex world of these molecules, promoting their potential in various applications and helping address global challenges such as the need for renewable energy sources. The main idea of this paper is to present a comprehensive overview of the compounds T1-T6 structurally related to the terpenes, covering their structures, biological importance, and possible harmful effects in terms of both medicinal and environmental. By the advantages of the DFT computations, this work will be hoped to support the smart molecule design,

introducing the electronic and related properties that are important in developing or modifying the molecular systems.

2. COMPUTATIONAL METHODS

2. 1. DFT Study

All DFT computations at the B3LYP (29,30) /6-311G** (31,32) level of theory maintaining default (33,34) settings were performed using the G09W (35), which were also utilized by GaussView 6.0.16 (36) for demonstrating the optimized structures and FMO plots. The water phase simulations were conducted using the PCM "Polarized Continuum Model" (37,38).

It is well-established that the evaluation of thermodynamic quantities is guided by the principles of quantum statistics (39,40). Namely, the total partition function 'Q' is instrumental in the determination of thermodynamic properties via specific equations outlined herein. In systems typified as asymmetric tops, the vibrational degree of freedom amounts to 3N-6, attributable to the molecular systems having three translational freedom degrees and three rotation freedom degrees along separate axes. Therefore, it is imperative to understand that variations in the quantities of thermodynamic properties across all molecular systems originate remarkably from vibrational movements since the contributions from translational and rotational movements remain consistent. The formulation of the vibrational partition function, as presented below, plays a vital role in contributing to thermodynamic properties and, by extension, is crucial in the evaluation of chemical properties (39-42).

$$Q = Q_{trans} \times Q_{rot} \times Q_{vib} \times Q_{elec}.$$

$$Q_{vib} = \prod_{j=1}^{3N-6} \frac{e^{-\theta_{v,j}/2T}}{(1 - e^{-\theta_{v,j}/T})}$$

Here, E_{vib} . "vibrational thermal energy", S_{vib} . "vibrational entropy", and C_{vib} . "vibrational heat capacity" are calculated by the following equations (39-41).

$$E_{vib} = Nk \sum_{j=1}^{3N-6} \left(\frac{\theta_{v,j}}{2} + \frac{\theta_{v,j} e^{-\theta_{v,j}/T}}{(1 - e^{-\theta_{v,j}/T})} \right)$$

$$S_{vib} = Nk \sum_{j=1}^{3N-6} \left[\frac{\theta_{v,j}/T}{(e^{\theta_{v,j}/T} - 1)} - \ln(1 - e^{-\theta_{v,j}/T}) \right]$$

$$C_{vib} = Nk \sum_{j=1}^{3N-6} \left[\left(\frac{\theta_{v,j}}{T} \right)^2 \frac{e^{\theta_{v,j}/T}}{(e^{\theta_{v,j}/T} - 1)^2} \right]$$

The terms disclosed as $\theta_{v,j} = \frac{hv_j}{k}$ "the vibrational temperature", $h \rightarrow$ "Planck constant", $k \rightarrow$ "Boltzmann constant", and $v_j \rightarrow$ "jth fundamental frequency".

Koopmans' theorem delineates the parameters of 'ionization energy' (I) and 'electron affinity' (A) (43), contingent on the energies of the frontier molecular orbitals. After the derivation of I and A values, the computation of global reactivity indices

can be achieved through the employment of the ensuing equations.

$$I = -E_{HOMO}$$

$$A = -E_{LUMO}$$

$$\chi = -\left(\frac{I+A}{2}\right)$$

$$\eta = \frac{I-A}{2}$$

$$\omega = \frac{\mu^2}{2\eta}$$

$$\Delta N_{max} = \frac{I+A}{2(I-A)}$$

$$\omega^+ \approx (I+3A)^2/(16(I-A))$$

$$\omega^- \approx (3I+A)^2/(16(I-A))$$

$$\Delta E_{back-donation} = -\frac{\eta}{4}$$

The symbols denoted that $\chi \rightarrow$ "electronic chemical potential", $\eta \rightarrow$ "global hardness", $\omega \rightarrow$ "electrophilicity", $\Delta N_{max} \rightarrow$ "the maximum charge transfer capability index" (44-49), ω^- "the electron donating power" and ω^+ "the electron accepting power" (50), and $\Delta E_{back-donat}$. "back-donation energy" (51).

The "second-order-perturbation" energy analyses and NPA "Natural population analysis" of terpenes T1-T6 were performed using the NBO code (52) implemented in the G09W. Accordingly, the lowering stabilization energy depending on the $q_i \rightarrow$ "the donor orbital occupancy", ϵ_i and $\epsilon_j \rightarrow$ "donor and acceptor orbital energies (diagonal elements)", $F_{ij} \rightarrow$ "the off-diagonal NBO Fock matrix element" is defined as follows (53-56):

$$E^{(2)} = \Delta E_{ij} = q_i \frac{(F_{ij})^2}{(\epsilon_j - \epsilon_i)}$$

In addition to the NPA approach, MPA "Mulliken Population Analysis" (57) is used to evaluate the partial charges of terpenes.

2. 2. Lipophilicity and water solubility

The estimation of lipophilicity indices was comprehensively undertaken employing a suite of five distinct methodologies, namely, ILOGP (58), XLOGP3 (59), WLOGP (60), MLOGP (61), and SILICOS-IT (62). The execution of these methodologies was facilitated via the SwissADME tool (63). It is widely recognized in scientific discourse that the parameter for lipophilicity, denoted as Log P, is inherently based on the ratio of the concentration of a specific neutral molecular system in an octanol medium (C_o) to its concentration in a water medium (C_w). This principle is encapsulated in the following mathematical formulation.

$$\text{Log } P_{o/w} = \text{Log } \frac{C_o}{C_w}$$

The calculation of water solubility, represented as Log S, was carried out using distinct methodologies as delineated by Delaney et al. (64) and Ali et al. (55). Here, the 'Estimated SOLubility' (ESOL) method defined by Delaney et al. (44) is employed, which derives its calculation based on specific molecular characteristics. These characteristics include 'Molecular Weight' (MWT), 'Rotatable Bonds

(RB), and 'Aromatic Proportion' (AP). The following equations delineate this approach.

$$\text{Log Sw} = 0.16 - 0.63 \text{ clogP} - 0.0062 \text{ MWT} + 0.066 \text{ RB} - 0.74 \text{ AP (ESOL)}$$

Furthermore, a robust benchmark study by Ali et al. (65) demonstrated a notable correlation between water solubility and specific phenolic parameters, such as the number of aromatic hydroxyls (-OH) groups. Additional factors, including the melting point and Topological Polar Surface Area (TPSA), were also found to impact water solubility significantly, as explained in the following equations.

$$\text{logS} = -1.0239 \text{ logP} - 0.0148 \text{ TPSA} - 0.0058 \text{ (m.p. (C) - 25)} + 0.3295 \text{ aroOHdel} + 0.5337 \text{ (ALI)}$$

2. 3. Absorption, Distribution, Metabolism, and Toxicity

Evaluation of the drug-like properties of **T1-T6** was comprehensively undertaken, guided by a selection of established rules and parameters as defined by Lipinski (61), Ghose (66), Veber (67), Egan (68), and Muegge (69). In addition, the Abbott bioavailability score (70) was employed as an instrumental tool in assessing the potential bioavailability of **T1-T6** with the aid of the SwissADME platform (63). To gain a holistic understanding of the dataset's pharmacokinetic properties, its absorption, distribution, metabolism, and potential toxicity characteristics were delineated utilizing the capabilities of ADMETLab 2.0 (71).

3. RESULT AND DISCUSSION

3. 1. Calculated Thermochemical and Physical Properties

Within the complex domain of molecular characterization, thermochemical and physical parameters serve as fundamental constituents. Thermochemical components, incorporating parameters such as heat capacity, enthalpy, and entropy, elucidate the molecule's stability and reactivity and delineate potential energy profiles. Concurrently, physical indices, including molecular weight, geometric configuration, and polarity, provide a detailed representation of the molecule's intrinsic physical compartment, influencing attributes such as solubility and reactivity (72-75). Thereby, they facilitate a holistic comprehension of

molecular properties and, then, the conceptualization and advancement of novel molecular structures across diverse scientific and industrial spheres. In this regard, the calculated thermodynamic quantities of the optimized molecules T1-T6 (Figure 1) and physical constants are presented in Table 1.

In the gas phase, the DM (D) and α (au) values of T1-T6 were found to be in the orders of T2 (0.205) < T1 (0.216) < T4 (1.562) < T3 (1.659) < T6 (2.729) < T5 (2.981) and T6 (98.979) < T5 (111.613) < T1 (112.485) < T2 (114.182) < T3 (114.749) < T4 (115.705), respectively, the water phase revealed the same orders for both properties. ΔG_{sol} (kJ/mol) order was determined as T5 (18.879) > T6 (17.78) > T4 (14.26) > T3 (11.94) > T2 (5.97) > T1 (4.64), which indicated that T5 and T6 would gain more stability in water than the others, probably due to the presence of the -C=O (ketone) group. ΔE_{sol} and ΔH_{sol} (kJ/mol) values of T1-T6 were found to be as T5 (18.92) > T6 (18.13) > T4 (14.25) > T3 (11.67) > T2 (6.14) > T1 (4.62) and T5 (18.97) > T6 (18.19) > T4 (14.21) > T3 (11.52) > T2 (6.16) > T1 (4.59), respectively. The main participation of both entropy and heat capacity was sourced from the vibrational freedom degrees, as expected. The $\Delta E_{\text{thermal}}$ (kcal/mol) for T1 was determined to be 168.523 kcal/mol by the vibrational contribution of 166.746 kcal/mol, which is remarkable. Similarly, the Cv quantity of T6 was found to be 39.643 cal/molK by the vibrational contribution of 33.681 cal/molK. From Table 1, the $\Delta E_{\text{thermal}}$ (kcal/mol) and Cv (cal/molK) of the T1-T6 were estimated as the orders of T3 (171.915) > T4 (171.789) > T1 (168.523) > T2 (153.413) > T5 (142.2367) > T6 (138.568) and T4 (48.251) > T3 (48.173) > T1 (43.428) > T2 (42.390) > T5 (43.277) > T6 (39.643), respectively. Also, the S (cal/molK) values of the compounds were calculated as T4 (106.316) > T3 (105.776) > T5 (105.187) > T2 (103.073) > T1 (102.074) > T6 (100.069), and vibrational freedom degrees of all compounds constituted one-third of entropy. By analyzing and comparing these parameters, the obtained results not only provide a deeper understanding of the physical and chemical properties of these compounds but also present valuable insights into their behavior under diverse environmental conditions. Thus, they can effectively guide the design and development of new materials that possess desired and tailored properties for a wide range of applications.

Table 1: The calculated physiochemical values.

	T1	T2	T3	T4	T5	T6	
Gas	DM (debye)	0.216	0.205	1.659	1.562	2.981	2.729
	α (au)	112.485	114.182	114.749	115.705	111.613	98.979
	ΔE (au)	-	-	-	-	-	-
		391.753938	390.549241	466.990430	466.990042	464.603006	426.509962
	ΔH (au)	-	-	-	-	-	-
		391.741759	390.537018	466.977195	466.976767	464.590580	426.498496
	ΔG (au)	-	-	-	-	-	-
		391.790258	390.585991	467.027453	467.027281	464.640557	426.546042
	$\Delta E_{\text{thermal}}$ (kcal/mol)					142.236	138.568
	ΔE_{vib} (kcal/mol)	168.523	153.413	171.915	171.789		
	C_v (cal/molK)	166.746	151.635	170.138	170.012	140.459	136.790
	$C_{v_{\text{vib}}}$ (cal/molK)	43.428	42.390	48.173	48.251	43.277	39.643
	S (cal/molK)	37.466	36.428	42.211	42.290	37.315	33.681
S_{vib} (cal/molK)	102.074	103.073	105.776	106.316	105.187	100.069	
	31.473	32.600	34.580	34.946	33.917	29.807	
Water	DM (debye)	0.338	0.323	2.142	2.098	4.094	3.825
	α (au)	148.303	150.294	150.970	151.762	147.378	129.850
	ΔE (au)	-	-	-	-	-	-
		391.755697	390.551580	466.994876	466.995468	464.610213	426.516866
	ΔH (au)	-	-	-	-	-	-
		391.743508	390.539364	466.981582	466.982180	464.597806	426.505424
	ΔG (au)	-	-	-	-	-	-
		391.792027	390.588264	467.032000	467.032712	464.647746	426.552815
	$\Delta E_{\text{thermal}}$ (kcal/mol)					142.066	138.412
	ΔE_{vib} (kcal/mol)	168.193	153.144	171.581	171.494		
	C_v (cal/molK)	166.415	151.366	169.804	169.717	140.288	136.635
	$C_{v_{\text{vib}}}$ (cal/molK)	43.528	42.470	48.342	48.355	43.287	39.661
	S (cal/molK)	37.567	36.508	42.380	42.394	37.326	33.699
S_{vib} (cal/molK)	102.117	102.918	106.115	106.353	105.109	99.742	
	31.515	32.443	34.914	34.978	33.839	29.485	
Solvation energies							
ΔE_{sol} (kJ/mol)	4.62	6.14	11.67	14.25	18.92	18.13	
ΔH_{sol} (kJ/mol)	4.59	6.16	11.52	14.21	18.97	18.19	
ΔG_{sol} (kJ/mol)	4.64	5.97	11.94	14.26	18.87	17.78	

3.2. Lipophilicity and water solubility

In the field of pharmaceutical research and development, two crucial factors that come into play are the hydrophobicity (fat-solubility) and hydrophilicity (water-solubility) of organic compounds (76). Hydrophobicity significantly impacts the processes of drug absorption, distribution, metabolism, and excretion (77), and highly hydrophobic drugs carry the risk of accumulating in the body's adipose tissues and causing toxicity (78). Conversely, hydrophilicity plays a pivotal role in drug formulation, delivery, and bioavailability, posing challenges when a drug exhibits excessively high or low water solubility. Both hydrophobicity and hydrophilicity contribute to drug-drug interactions and chemical stability, ultimately influencing drug effectiveness, safety, and overall suitability (79). In this respect, the calculated lipophilic and water solubility characteristics and physicochemical values of T1-T6 are given in Table 2.

Log Po/w (iLOGP) indices were determined in the following order T1 (2.74) > T2 (2.71) > T3 (2.51) > T5 (2.27) > T4 (2.09) > T6 (2.03), while the lipophilicity index depending on (XLOGP3) approach was estimated as T1 (3.42) > T2 (4.47) > T4 (3.39) > T3 (3.26) > T5 (2.71) > T6 (1.34). On the other hand, the WLOGP approach to determine the lipophilicity revealed the following order: T2 (3.45) > T1 (3.39) > T3 (2.50) \geq T4 (2.50) > T5 (2.49) > T6 (2.32), whereas the Log Po/w based on MLOGP. the approach was predicted as T1 (4.29) > T2 (3.27) > T3 (2.30) \geq T4 (2.30) > T5 (2.10) > T6 (1.89). The mean of the lipophilicity indices changed in the following order: T2 (3.40) > T1 (3.36) > T3 (2.60) > T4 (2.49) > T5 (2.44) > T6 (1.98). Although the approaches used to calculate the lipophilicity index had different rankings, it could be said that the lipophilicity of the T1 and T2 molecules was higher than the other molecules.

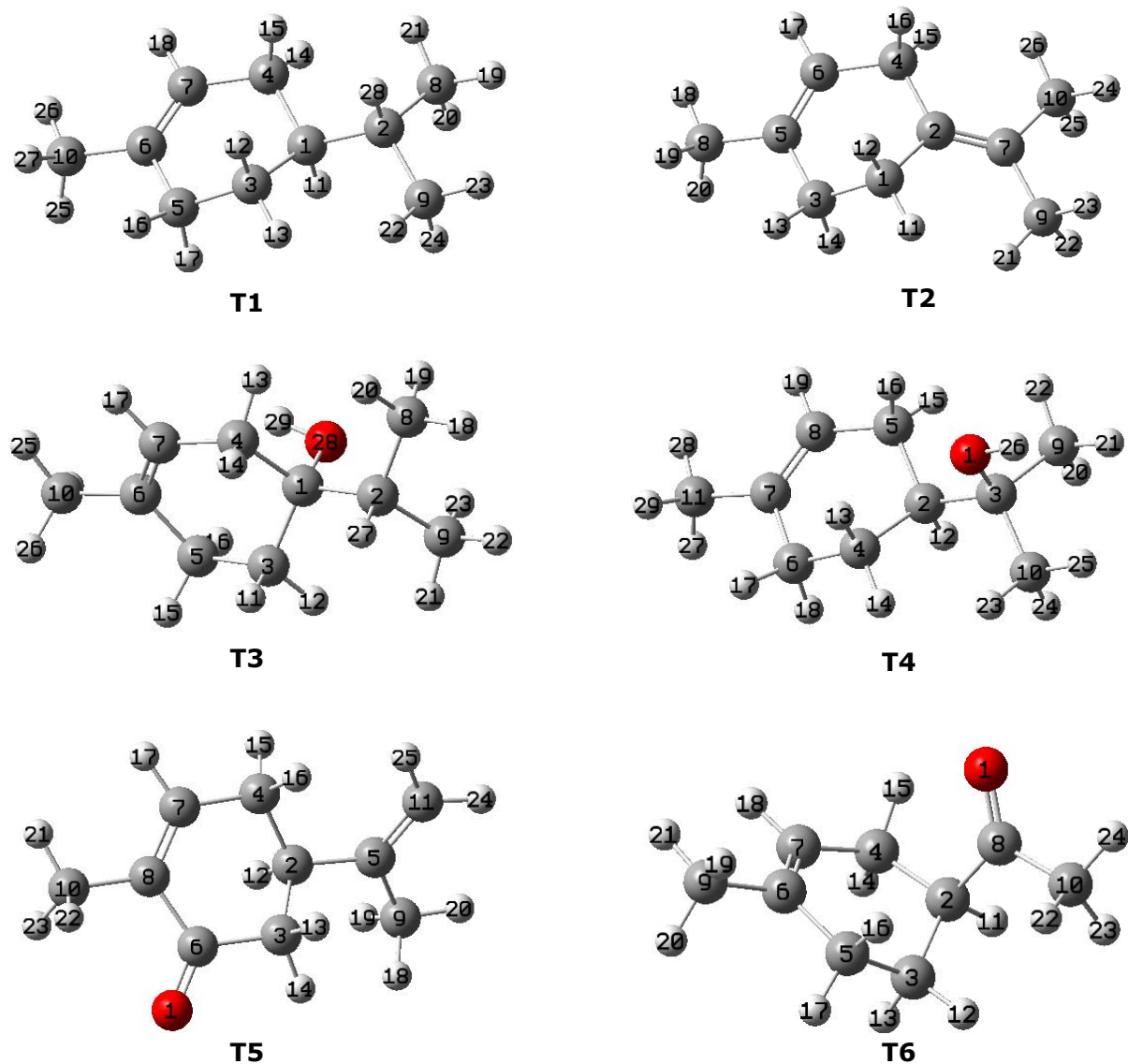


Figure 1: The optimized structures of the terpenes.

Conversely, it should be noted from Table 2 that the water solubility of the T6 molecule would be considerably higher than that of other molecules due to the $-C=O$ group located on the aliphatic chain of the compound. Namely, the ESOL ($\text{mg/mL} \times 10^{-1}$) method for the water-solubility of the compounds denoted the order of $T6 (46.3) > T5 (5.81) > T3 (2.54) > T1 (2.26) > T4 (2.10) > T2 (0.43)$, while the Log S (Ali) ($\text{mg/mL} \times 10^{-2}$) gave the following order $T6 (692) > T5 (28.5) > T1 (11.0) > T3 (6.75) > T4 (4.95) > T2 (0.880)$. According to the ALI and ESOL approaches, T2 would have medium-level solubility since the sp^2 hybridized group as the bridge between the aliphatic chain and ring chain probably

made the compound more likely to prefer intramolecular interactions instead of acting towards the outer system. On the other hand, the T4 could be more soluble among the molecules according to the SILICOS-IT approach. Although there were different orders of solubility of the compounds, the presence of $-C=O$ and $-OH$ groups in the molecule especially contributed to an increase in the water solubility. Also, the position of these groups on the molecule caused the change of the water solubility of the compounds. Namely, the solubility of T6 functionalized with the $-C=O$ group on the chain part could be higher than that of the T5, including this group on the ring.

Table 2: Physicochemical properties, lipophilicity, and water solubility features.

<i>Physicochemical properties</i>	T1	T2	T3	T4	T5	T6
Formula	C10H18	C10H16	C10H18O	C10H18O	C10H14O	C9H14O
Molecular weight (g/mol)	138.25	136.23	154.25 g	154.25	150.22	138.21
Num. heavy atoms	10	10	11	11	11	10
Num. arom. heavy atoms	0	0	0	0	0	0
Fraction Csp3	0.80	0.60	0.80	0.80	0.50	0.67
Num. rotatable bonds	1	0	1	1	1	1
Num. H-bond acceptors	0	0	1	1	1	1
Num. H-bond donors	0	0	1	1	0	0
Molar Refractivity	47.60	47.12	48.80	48.80	47.32	42.99
TPSA (Å ²)	0.00	0.00	20.23	20.23	17.07	17.07
<i>Lipophilicity</i>						
Log <i>P</i> _{o/w} (iLOGP)	2.74	2.71	2.51	2.09	2.27	2.03
Log <i>P</i> _{o/w} (XLOGP3)	3.42	4.47	3.26	3.39	2.71	1.34
Log <i>P</i> _{o/w} (WLOGP)	3.39	3.45	2.50	2.50	2.49	2.32
Log <i>P</i> _{o/w} (MLOGP)	4.29	3.27	2.30	2.30	2.10	1.89
Log <i>P</i> _{o/w} (SILICOS-IT)	2.96	3.08	2.44	2.17	2.64	2.31
Consensus Log <i>P</i> _{o/w}	3.36	3.40	2.60	2.49	2.44	1.98
<i>Water Solubility</i>						
Log <i>S</i> (ESOL)	-2.79	-3.50	-2.78	-2.87	-2.41	-1.48
Solubility (mg/mL)x10 ⁻¹	2.26	0.43	2.54	2.10	5.81	46.3
Class	S	S	S	S	S	VS
Log <i>S</i> (Ali)	-3.10	-4.19	-3.36	-3.49	-2.72	-1.30
Solubility (mg/mL)x10 ⁻²	11.0	0.880	6.75	4.95	28.5	692
Class	S	MS	S	S	S	VS
Log <i>S</i> (SILICOS-IT)	-2.25	-2.46	-1.91	-1.69	-2.16	-1.76
Solubility (mg/mL)	0.781	0.473	1.92	3.17	1.04	2.40
Class	S	S	S	S	S	S

"TPSA "topological polar surface Area" was calculated based on polar fragments that contributed to the polar surface. S, soluble; MS, moderate soluble; and VS, very soluble."

3.3. Absorption, Distribution, Metabolism, and Bioavailability

The ADM-DL study "Absorption, Distribution, Metabolism, Drug-likeness", in essence, is fundamental for the optimization of pharmacokinetic properties and therapeutic efficacy of drug candidates, allowing the design of more effective and safer therapeutic agents. By investigating these factors, it can predict the drug's behavior inside the body, minimize adverse effects, and enhance its therapeutic efficiency. In this respect, the calculated ADM scores and BOILED-EGG and pharmacokinetic radar graphs were represented in Table 3 and Figure 2, respectively.

Accordingly, all compounds were determined in the optimal range (>-5.15 Log unit) in terms of Caco-2 Pe scores that were calculated as T5 (-4.532) < T2 (-4.428) < T6 (-4.369) < T1 (-4.264) < T4 (-4.245) < T3 (-4.191). The MDCK Pe. (x10⁻⁵) cm/s were determined as T5 (2.8) > T6(2.1) > T1 = T3 (2.0) > T4 (1.9) > T2 (1.7), which would display high-level passive permeability (>20x10⁻⁶ cm/s) for the MDCK Pe. The compound T2 (0.159) could be more potent in terms of the Pgp-inh., whereas the T6 (0.015) could present higher Pgp-subst. potency, relatively. The T3, T4, and T6 (0.004) might display the same

capability for HIA, whereas the T5 (0.006) would have relatively higher potency for HIA. In terms of bioavailability, the T5 and T3 could be promising agents with the F_{20%} scores at 0.029 and 0.681 (moderate-size), respectively, while the others gave the red alarm about the bioavailability with the scores being determined between 0.897- 0.966. On the other hand, T3 (0.035), T4 (0.19), and T5 (0.003) would denote good bioavailability with the F_{30%} scores, while T1 (0.873), T2 (0.818), and T6 (0.744) might no bioavailable agent.

The T4 (82.50%), T5 (58.77%), and T6 (80.86%) would present sensible PPB scores (<90%), while T1 (94.62%), T2 (95.54%), and T3 (90.26%) would have higher PPB % scores which might cause the low therapeutic index. Here, the -C=O group located on the ring of the T5 would be more important in the PPB potency than both the -OH and -C=O substitutions on the aliphatic chain. The VD scores for all compounds were calculated in the range of optimal values (0.04-20 L/kg) and found to order of T2 (5.905) > T1(3.887) > T3 (2.457) > T5 (1.650) > T6 (1.650) > T4 (1.497), which implied the compounds would have a sensible volume distribution. Also, T1-T3 would have a BBB Pen. scores in the range of 0.314- 0.576 (in yellow alarm

limits), while the T4-T6 could present the red alarm with BBB Pen. scores in 0.727- 0.971. The portion of the T1 and T2 unbonded in the plasma was calculated with low size at 4.737% and 4.586%, respectively, whereas T3 would be distributed in the plasma as unbonded at a moderate level with a Fu% of 9.940. The T4-T6 could dissolve as unbonded in the plasma at a high level with Fu% changed in 19.13-50.58.

In terms of the metabolism of the compounds, -C=O-modified molecule T6 could have been more promising than the other terpenes, while T4 modified with the -OH group could be a less suitable agent among terpenes. Namely, the CYP1A2 inh. and CYP1A2 subs. values of the compounds were calculated in the orders of T2 (0.925)> T1 (0.757)> T3(0.558)> T6 (0.523)> T5 (0.329)> (0.124) and T6 (0.762)> T1 (0.450)> T5 (0.435)> T3 (0.346)> T2 (0.263)> T4 (0.162), respectively. Also,

CYP2C19 inh. and CYP2C19 subs. scores of the compounds changed in 0.064-0.361 and 0.632-0.790, which could be interpreted to mean that the substrate potency of the compounds was higher than those of the inhibitor potency for CYP2C19.

Similarly, the substrate potencies of the compounds for CYP2C9, CYP2D6, and CYP3A4 were also greater than those of the inhibition potencies. Namely, the scores of inhibitor and substrate potency for CYP2C9 were predicted at 0.468-0.867 and 0.036-0.345, respectively. These results are significant as they provide a nuanced understanding of the interaction of these compounds with various cytochrome P450 enzymes. Understanding these interactions can help predict drug metabolism and potential drug-drug interactions and inform drug design and dosage recommendations.

Table 3: Absorption, Distribution, and Metabolism indices.

	T1	T2	T3	T4	T5	T6
Absorption						
Caco-2 Pe.	-4.264	-4.428	-4.191	-4.245	-4.532	-4.369
MDCK Pe. (x10 ⁻⁵) cm/s	2	1.7	2	1.9	2.8	2.1
Pgp-inh.	0.001	0.159	0.0	0.001	0.067	0.001
Pgp-subs.	0.009	0.002	0.006	0.002	0.001	0.015
HIA	0.003	0.003	0.004	0.004	0.006	0.004
F _{20%}	0.966	0.960	0.681	0.897	0.029	0.959
F _{30%}	0.873	0.818	0.035	0.19	0.003	0.744
Distribution						
PPB %	94.62	95.54	90.26	82.50	58.77	80.86
VD (L/kg)	3.887	5.905	2.457	1.497	1.650	1.638
BBB Pen.	0.561	0.314	0.576	0.727	0.968	0.971
Fu %	4.737	4.586	9.940	20.43	50.58	19.13
Metabolism						
CYP1A2 inh.	0.757	0.925	0.558	0.124	0.329	0.523
CYP1A2 subs.	0.450	0.263	0.346	0.162	0.435	0.762
CYP2C19 inh.	0.230	0.361	0.179	0.064	0.300	0.215
CYP2C19 subs.	0.790	0.602	0.816	0.639	0.837	0.632
CYP2C9 inh.	0.290	0.345	0.089	0.052	0.052	0.036
CYP2C9 subs.	0.797	0.867	0.843	0.775	0.468	0.859
CYP2D6 inh.	0.016	0.021	0.037	0.009	0.031	0.011
CYP2D6 subs.	0.351	0.254	0.252	0.243	0.608	0.845
CYP3A4 inh.	0.082	0.040	0.059	0.020	0.036	0.030
CYP3A4 subs.	0.295	0.208	0.252	0.202	0.263	0.238

"Permeability, Pe; Penetration, Pen, Inhibitor, Inh; Substrate, subs"

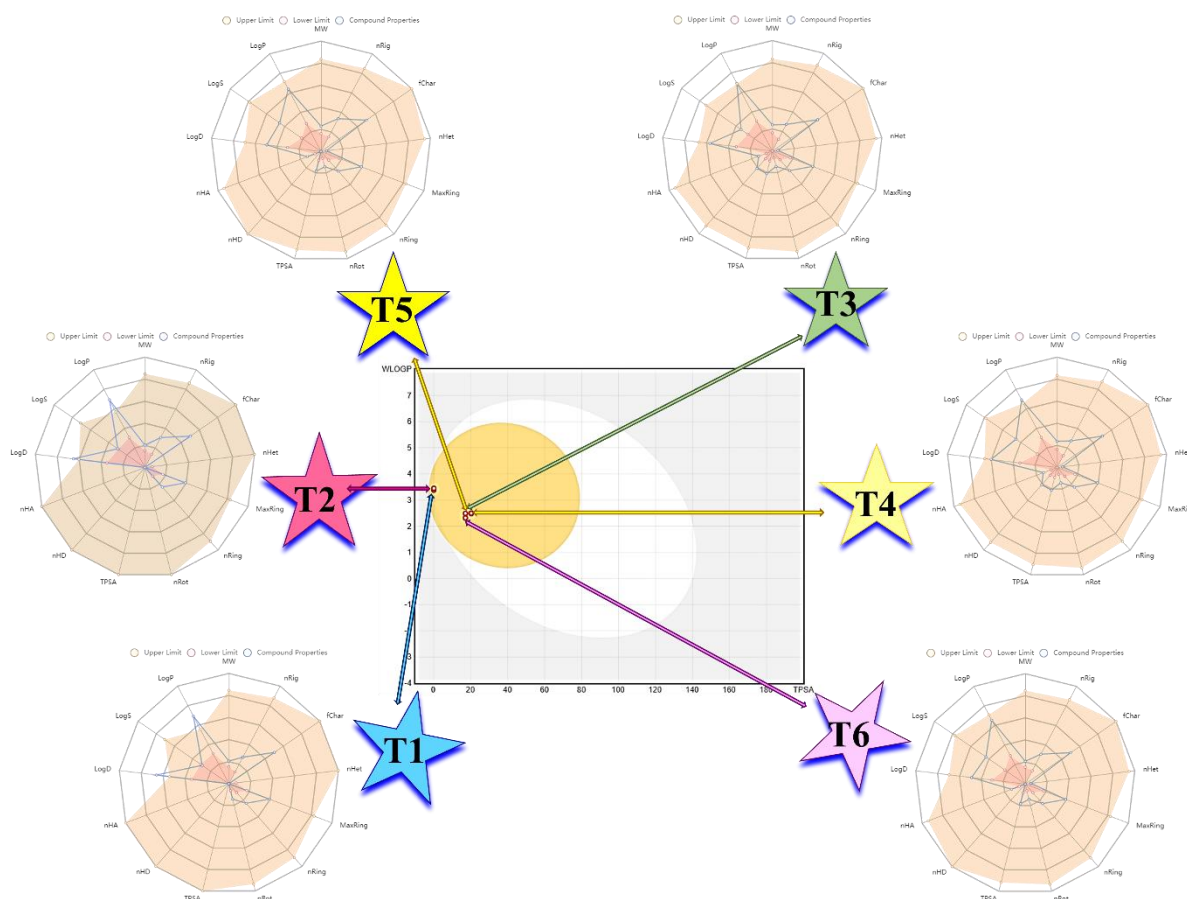


Figure 2: BOILED-Egg model and pharmacokinetic radar graphs.

3.4. Toxicity Study

A fundamental objective in the field of drug discovery and development is the identification of therapeutic agents that are not only effective but also safe to enhance patient outcomes. This process necessitates an exhaustive assessment of the toxicity of potential drug candidates, as well as an evaluation of their 'drug-likeness'. Computational tools come into play here, providing predictive measures of toxicity scores, which encompass both medicinal and environmental risk factors. These tools also assist in the identification of optimal pharmacokinetic and pharmacodynamic properties, which are key indicators of a drug's behavior within the body. In this context, we have provided the calculated toxicity results in Table 4. These results present a quantitative analysis of potential risk factors associated with each drug candidate, demonstrating their suitability or otherwise for further development.

In considering the possible harmful effect of the compounds T1-T4 and T6 related to the hERG Blockers, H-HT, DILI, AMES, Rat Oral Acute, and FDAMDD (except for T4) the results implied that the compounds would not have a toxic effect on them, due to the calculated scores for all them were close to zero. Here, the FDAMDD indexes of the T4 and T6 were determined at 0.546 and 0.667, which indicated that it could cause a moderate-level toxic effect. Even though the T5 would have been harmful

to FDAMDD (0.874) and H-HT (0.698) at a moderate level, it would not have also been a toxic effect related to the hERG Blockers (0.021), DILI (0.046), AMES (0.013), and Rat Oral Acute (0.027). Furthermore, T6 could cause an unwanted effect with a high possibility on skin (0.905), carcinogenicity (0.902), eye corrosion (0.984) and, irritation (0.988), and respiratory (0.884). Except for T2 (0.597) and T3 (0.698), which would have been an adverse effect at a medium level, the other compounds would also have been adversely in terms of skin sensitization. The carcinogenicity scores of the compounds were estimated as $T4=T6 (0.902) > T2 (0.874) > T5 (0.837) > T1 (0.824) > T3 (0.543)$; the T3 would have medium-level toxicity, but the others could have toxic potency at a high level. Furthermore, the compounds T1 (0.965), T5 (0.951), and T6 (0.984) implied that they would have undesired effects in terms of eye corrosion, whereas the unwanted effect of the compounds T2 (0.483), T3 (0.664), and T4 (0.696) would be a moderate size. All compounds could irritate the eye due to the high indexes predicted in the range of 0.977-0.992.

Furthermore, the BCF scores of all compounds were computed lower than that of threshold value $\log BCF < 3.3$ (80,81), which meant that they would have no risk in terms of secondary poisoning potential on the environment. From Table 4, the IGC₅₀, LC₅₀FM, and LC₅₀DM values of the compounds

varied in the following orders of T5 (2.899) > T1 (2.808) > T3 (2.565) > T2 (2.521) > T6 (2.418) > T4 (2.294), T5 (4.263) > T2 (3.501) > T1 (3.170) > T6 (2.984) > T3 (2.970) > T4 (2.854), and T2 (4.798) > T1 (4.746) > T3 (4.423) > T5 (4.365) > T6 (4.239) > T4 (3.836), respectively. In recent work, the in-silico toxicity analyses of volatile compounds that are among the components of *Piper acutifolium* have been reported (82); the IGC₅₀, LC₅₀FM, and LC₅₀DM scores of the terpenes in the investigated essential oil have been predicted in the ranges of 3.080-4.471, 3.674-5.331, and 4.107-5.948, respectively. Although there are some reports that the excessive use of glyphosate caused adverse effects on soils and water (83-85), glyphosate can still be used for comparison purposes due to being considered non-toxic. In this regard, the IGC₅₀, LC₅₀FM, and LC₅₀DM values of glyphosate have been determined as 2.351, 3.794, and 3.503, respectively (82). Regarding IGC₅₀, the studied terpenes, except for T4, could be less toxic than the glyphosate (IGC₅₀ > 2.351). Moreover, the T5 and T6 could be less toxic than glyphosate (LC₅₀FM > 3.794), while the other terpenes, T1-T4

could be more toxic than glyphosate. Fortunately, all terpenes would be less toxic (LC₅₀FM > 3.503) than glyphosate.

In view of the Tox21 pathway scores, the T1, T3, T4, and T6 would have no risk in terms of all parameters given in Table 4. Namely, the NR-AR, NR-AR-LBD, and NR-AhR scores of compounds T1-T6 were calculated in the ranges of 0.005-0.096, 0.003-0.008, and 0.011-0.071, respectively, which meant that there would have no any risk potency. The compound T5 could present a moderate-level risk on NR-Aromatase (0.394) and SR-ARE (0.483), whereas the T2 could cause a toxic effect only for NR-ER (0.606). Accordingly, compounds T1, T3, T4, and T6 demonstrated negligible risk based on various parameters, including low NR-AR, NR-AR-LBD, and NR-AhR scores. However, compound T5 indicated a moderate risk level for NR-Aromatase and SR-ARE, and T2 posed a potential toxicity risk for NR-ER. Despite the majority of compounds showing minimal risk, T5 and T2 should have needed further examination due to their potential risk factors.

Table 4: Toxicity scores.

	T1	T2	T3	T4	T5	T6
Medicinal						
hERG Blockers	0.022	0.020	0.015	0.010	0.021	0.017
H-HT	0.185	0.213	0.075	0.138	0.698	0.362
DILI	0.241	0.185	0.054	0.039	0.046	0.219
AMES Tox.	0.013	0.004	0.006	0.005	0.013	0.053
Rat Oral Acute Tox.	0.018	0.009	0.017	0.020	0.027	0.082
FDAMDD	0.067	0.032	0.020	0.546	0.874	0.667
Skin Sens.	0.889	0.597	0.698	0.726	0.940	0.905
Carcinogenicity	0.824	0.874	0.543	0.902	0.837	0.902
Eye Corrosion	0.965	0.483	0.664	0.696	0.951	0.984
Eye Irritation	0.982	0.977	0.985	0.984	0.992	0.988
Respiratory Tox.	0.053	0.020	0.026	0.083	0.889	0.884
Environmental						
BCF	2.383	2.135	1.147	0.748	0.754	0.660
IGC ₅₀	2.808	2.521	2.565	2.294	2.899	2.418
LC ₅₀ FM	3.170	3.501	2.970	2.854	4.263	2.984
LC ₅₀ DM	4.746	4.798	4.423	3.836	4.365	4.239
Tox21 Pathway						
NR-AR	0.009	0.013	0.034	0.005	0.014	0.096
NR-AR-LBD	0.003	0.003	0.003	0.004	0.004	0.008
NR-AhR	0.012	0.026	0.011	0.018	0.071	0.015
NR-Aromatase	0.004	0.006	0.009	0.005	0.394	0.007
NR-ER	0.124	0.606	0.064	0.119	0.079	0.176
NR-ER-LBD	0.201	0.232	0.005	0.007	0.013	0.038
NR-PPAR-gamma	0.003	0.005	0.004	0.003	0.004	0.005
SR-ARE	0.016	0.021	0.024	0.021	0.483	0.025
SR-ATAD5	0.003	0.004	0.003	0.004	0.011	0.009
SR-HSE	0.075	0.274	0.028	0.022	0.222	0.028
SR-MMP	0.016	0.013	0.032	0.021	0.038	0.015
SR-p53	0.003	0.007	0.008	0.003	0.063	0.006

"The abbreviations are defined as: Tox, Toxicity; sens, Sensitization; BCF, the unit of bioconcentration factors, IGC₅₀, LC₅₀FM, and LC₅₀DM is given in -Log₁₀[(mg/L)/(100xMW)]."

3.5. NBO study

The NBO method is also fairly used to estimate the key intramolecular interactions that have a critical role in lowering the stabilization energy and thus evaluating the chemical behavior of the molecular systems (86-88). Here, the selected interactions of terpenes were given in Table 5; full data of interactions was given in Table S1 (suppl. data).

Here, it should be noted that the studied systems are not aromatic, and mainly, the possible interactions would have related to the less familiar interactions such as anomeric, cieplak, negative hyperconjugation, etc. Among the terpenes, the resonance interaction was only determined for the T5 structure. Namely, the resonances of n O7-C8 ($ED_i=1.86177e$) \rightarrow n^* C1-C6 ($ED_j=0.13989e$) and n O1-C6 ($ED_i=1.97064e$) \rightarrow n^* C7-C8 ($ED_j=0.08951e$) for T5 was predicted with the energies of 20.26 and 5.96 kcal/mol, respectively. Furthermore, the anomeric interactions would play a remarkable role in stabilizing the T5 molecule: the charge transfers from LP (2) O1 ($ED_i=1.89090e$) to unfilled orbitals σ^* C3-C6 ($ED_j=0.05893e$) and σ^* C6-C8 ($ED_j=0.07124e$) was calculated with the energies of 19.67 and 18.66 kcal/mol, respectively. In addition, the energy of the hyperconjugation σ C3-H13 ($ED_i=1.95935e$) \rightarrow n^* O1-C6 ($ED_j=0.13989e$) was calculated as 6.90 kcal/mol. From Table S1 (see suppl. data), the other hyperconjugation energies for the T5 compound were calculated in the range of 2.01-5.29 kcal/mol. Also, the negative hyperconjugations ($n \rightarrow \sigma^*$) for T5 could be remarkable in lowering the stabilization energy predicted in the range of 2.07-3.51 kcal/mol (Table S1). Moreover, the cieplak interactions occurred in the T5 molecule σ C7-H17 \rightarrow σ^* C6-C8 ($E^{(2)}=6.31$ kcal/mol), σ C11-H24 \rightarrow σ^* C2-C5 ($E^{(2)}=7.82$ kcal/mol), and σ C11-H25 \rightarrow σ^* C5-C9 ($E^{(2)}=6.96$ kcal/mol) would have responsibility on the stabilization of the molecule. For the molecule T5, the energies of the other cieplak interactions would be in the range of 2.84-4.56 kcal/mol. From Table 5, the highest portion of the lowering the stabilization for T6 would source from the anomeric interactions LP (2) O1 \rightarrow σ^* C2-C8 ($ED_j=0.07531e$) and LP (2) O1 \rightarrow σ^* C8-C10 ($ED_j=0.05710e$) with the $E^{(2)}$ of 20.63 and 20.51 kcal/mol, respectively. Furthermore, the highest energy hyperconjugation for T6 was found to be σ C2-H11 \rightarrow n^* O1-C8 ($E^{(2)}=6.41$ kcal/mol) and C10-H22 \rightarrow n^* O1-C8 ($E^{(2)}=6.27$ kcal/mol), and the orbital occupancies of them were with the remarkable. Energies of the other hyperconjugative interactions were calculated in the range of 2.70-4.71 kcal/mol (Table S1). Moreover, the negative σ -conjugations would have an important role in lowering the energy; the energies of the interactions n C6-C7 ($ED_i=1.93464e$) \rightarrow σ^* C5-H16 ($ED_j=0.02157e$) and n C6-C7 \rightarrow σ^* C4-H15 ($ED_j=0.01707e$) for T6 were estimated in 3.75 and 2.05 kcal/mol, respectively. The calculated energies for the cieplak interactions were changed in the range of 2.55-7.25 kcal/mol; the highest energy interaction was σ C7-H18 \rightarrow σ^* C5-C6, and the lowest energy one would be σ C2-C4 \rightarrow σ^* C8-C10.

Moreover, the T3 and T4 molecules functionalized with the -OH group on the ring exhibited that the conjugative interactions could have a critical role in terms of stability. For T3, the hyperconjugations σ C5-H16 ($ED_i=1.96644e$) \rightarrow n^* C6-C7 ($ED_j=0.09324e$) and σ C4-H14 ($ED_i=1.96389e$) \rightarrow n^* C6-C7 ($ED_i=1.96389e$) were predicted with the energies of 5.10 and 4.46 kcal/mol, respectively. On the other hand, the energies of the negative σ -conjugations for the compounds T3 and T4 were determined in the ranges of 2.22-3.97 kcal/mol and 2.12-3.75 kcal/mol, respectively. The interaction σ C7-H17 \rightarrow σ^* C5-C6 for T3 was estimated with the energy of 7.04 kcal/mol, whereas the corresponding interaction for T4 was predicted as σ C8-H19 \rightarrow σ^* C6-C7 with the same energy. Similarly, the same cieplak interaction for T1 and T2 molecules would be responsible for the stabilization of the system with the same energy (7.04 kcal/mol).

3.6. Atomic Charges

The prediction of the atomic charges (74,75,89) also provides a useful viewpoint in the evaluation of the local reactivity site (s) of the molecular systems. Herein, the calculated atomic charges of the compounds obtained from MPA and NPA approaches were summarized in Table 6; the whole data was given in Tables S2 and S3, respectively.

For the T1 and T2 without heteroatom, the lowest charges were determined for the Cs of the methyl groups due to the existence of the electron-donating Hs. Namely, the charges of the C8, C9, and C10 atoms of T1 were predicted as -0.270782, -0.264074, and -0.252332 by MPA and -0.57090, -0.56977, and -0.58350 by NPA methods. Furthermore, the charges of the atoms C8, C9, and C10 for T2 by MPA and NPA methods were found to be -0.251532, -0.256386, -0.255652, and -0.58311, -0.58721, -0.58941, respectively. According to the results of the MPA approach, the charges of all C atoms for T1 and T2 were found to be negative values, while the C atoms' charges for T3 were calculated in positive value except for C7 (-0.051884). On the other hand, the NPA method depends on the NBO method, which considers the non-covalent interactions in the relevant molecular system and thus reveals a different charge distribution. Especially, the presence of the electronegative oxygen atom makes the charge distribution on the surface different from MPA. Namely, the C1 charge for T3 by MPA and NPA was determined as 0.401289 and 0.33652, respectively; the non-covalent interactions aforementioned in the NBO section would be responsible for the decrease of the charge density on the C1 atom. MPA calculated the partial charge of the O28 atom of T3 at -0.593646, which was bigger than that of -0.77131 predicted by NPA, as expected from the basics of this approach that care of the non-covalent interactions.

Furthermore, O1 charge for T4-T6 molecules was estimated by the MPA at -0.401483, -0.302913, and -0.293275, respectively, while it was determined by

the NPA method as -0.76279, -0.55670, and -0.55395. For all terpenes, the O atom that was a part of the alcohol or ketone group exhibited more negative charge distribution as an indicator of the electron abundance region, as expected. Also, the H' charge of the -OH group for T3 and T4 were determined by MPA as 0.234756 (H29) and 0.233889 (H26), respectively, while NPA estimated them as 0.45585 and 0.44580. On the other hand,

the C6 (T5) and C8 (T6) charges were estimated by the MPA method at 0.201871 and 0.221130, respectively, whereas the NPA method revealed these charges at 0.56430 and 0.60869, respectively. For both methods, the Hs' charges for all terpenes were determined to be higher than zero, as expected from the electropositive nature of the atom (Tables S2 and S3).

Table 5. The second-order perturbative energy analyze, at B3LYP/6-311G(d,p) in gas phase.

Donor(i)	ED _i /e	Acceptor (j)	ED _j /e	E ⁽²⁾ / kcalmol ⁻¹	E(j)-E(i)/ a.u	F(i,j)/ a.u
T1						
σ C1-C3	1.97439	σ* C2-C8	0.01470	2.29	0.97	0.042
σ C4-H14	1.97091	π* C6-C7	0.09146	2.71	0.55	0.035
σ C5-H17	1.96779	π* C6-C7	0.09146	4.84	0.55	0.047
π C6-C7	1.93549	σ* C4-H14	0.01578	2.00	0.68	0.033
		σ* C4-H15	0.02255	3.84	0.66	0.045
σ C7-H18	1.97579	σ* C5-C6	0.02967	7.04	0.93	0.072
T2						
σ C1-C3	1.97198	π* C2-C7	0.10885	2.17	0.67	0.035
π C2-C7	1.91864	σ* C4-H16	0.02484	3.84	0.65	0.045
σ C4-H16	1.95867	π* C2-C7	0.10885	4.89	0.56	0.048
π C5-C6	1.93711	σ* C4-H15	0.01574	2.11	0.68	0.034
σ C6-H17	1.97582	σ* C3-C5	0.02910	7.04	0.93	0.072
T3						
σ C1-C3	1.97260	σ* C2-C8	0.01502	2.28	0.98	0.042
σ C4-H13	1.97025	π* C6-C7	0.09324	2.45	0.55	0.033
σ C5-H16	1.96644	π* C6-C7	0.09324	5.10	0.55	0.048
π C6-C7	1.93482	σ* C4-H14	0.02093	3.97	0.67	0.047
		σ* C5-H15	0.01658	2.22	0.68	0.035
σ C7-H17	1.97622	σ* C5-C6	0.02971	7.04	0.93	0.072
LP (2) O28	1.95436	σ* C1-C3	0.04278	7.80	0.67	0.065
T4						
σ C5-C8	1.97669	σ* C2-C3	0.04022	2.22	0.98	0.042
σ C5-H15	1.97058	π* C7-C8	0.09223	2.77	0.55	0.036
σ C6-H18	1.96830	π* C7-C8	0.09223	4.84	0.56	0.047
π C7-C8	1.93603	σ* C5-H15	0.01567	2.03	0.67	0.033
		σ* C6-H18	0.02139	3.75	0.66	0.045
σ C8-H19	1.97564	σ* C6-C7	0.02968	7.04	0.93	0.072
LP (2) O1	1.95531	σ* C3-C9	0.03255	5.37	0.66	0.053
		σ* C3-C10	0.03294	5.98	0.67	0.056
T5						
π O1-C6	1.97064	σ* C3-H13	0.01579	2.07	0.76	0.036
σ C3-H13	1.95935	π* O1-C6	0.13989	6.90	0.52	0.055
σ C4-H15	1.97289	π* C7-C8	0.08951	2.01	0.86	0.047
π C7-C8	1.86177	π* O1-C6	0.13989	20.26	0.30	0.070
σ C11-H24	1.98240	σ* C2-C5	0.03618	7.82	0.94	0.077
LP (2) O1	1.89090	σ* C3-C6	0.05893	19.67	0.65	0.102
		σ* C6-C8	0.07124	18.66	0.71	0.104
T6						
σ C2-C4	1.97443	σ* C8-C10	0.05710	2.55	0.98	0.045
σ C2-H11	1.95033	π* O1-C8	0.08421	6.41	0.51	0.052
σ C5-H17	1.97195	π* C6-C7	0.09008	2.70	0.56	0.035
π C6-C7	1.93464	σ* C4-H15	0.01707	2.05	0.69	0.034
		σ* C5-H16	0.02157	3.75	0.66	0.045
σ C7-H18	1.97498	σ* C5-C6	0.02978	7.25	0.92	0.073
LP (2) O1	1.88596	σ* C2-C8	0.07531	20.63	0.65	0.104
		σ* C8-C10	0.05710	20.51	0.64	0.104

Table 6: The selected atomic charges of terpenes in gas phase.

	<i>T1</i>	<i>T2</i>	<i>T3</i>			<i>T4</i>	<i>T5</i>	<i>T6</i>
MPA								
C1	-0.189984	-0.200904	0.401289		O1	-0.401483	-0.302913	-0.293275
C2	-0.185028	-0.102881	0.118172		C2	-0.184721	-0.222480	-0.265890
C3	-0.190141	-0.166907	0.018783		C3	-0.014241	-0.187501	-0.220248
C4	-0.150511	-0.118736	0.024100		C4	-0.182113	-0.159843	-0.145180
C5	-0.170717	-0.115804	0.077870		C5	-0.147422	-0.101527	-0.189606
C6	-0.124793	-0.111715	0.054923		C6	-0.173012	0.201871	-0.107730
C7	-0.094971	-0.141937	-0.051884		C7	-0.125081	-0.080330	-0.084984
C8	-0.270782	-0.251532	0.025376		C8	-0.094835	-0.130282	0.221130
C9	-0.264074	-0.256386	0.024556		C9	-0.240234	-0.239866	-0.252887
C10	-0.252332	-0.255652	0.074607		C10	-0.225768	-0.229155	-0.301834
O28			-0.593646		C11	-0.252679	-0.173070	0.136967
H29			0.234756		H26	0.233889		
NPA								
C1	-0.20078	-0.39032	0.33652		O1	-0.76279	-0.55670	-0.55395
C2	-0.18840	-0.01097	-0.21065		C2	-0.22279	-0.22540	-0.29387
C3	-0.37225	-0.39335	-0.40359		C3	0.33880	-0.46133	-0.36614
C4	-0.40755	-0.42643	-0.44550		C4	-0.37461	-0.41905	-0.40852
C5	-0.39956	-0.00110	-0.41055		C5	-0.41211	0.01828	-0.41049
C6	0.00179	-0.19087	-0.00048		C6	-0.39879	0.56430	-0.00448
C7	-0.19484	-0.00311	-0.20882		C7	-0.00080	-0.10130	-0.18752
C8	-0.57090	-0.58311	-0.57416		C8	-0.19188	-0.11580	0.60869
C9	-0.56977	-0.58721	-0.57217		C9	-0.60281	-0.59115	-0.58307
C10	-0.58350	-0.58941	-0.58492		C10	-0.60096	-0.58472	-0.67271
O28			-0.77131		C11	-0.58303	-0.39175	0.21764
H29			0.45585		H26	0.44580		

3.7. FMO (Frontier Molecular Orbital) Analysis and MEP (Molecular Electrostatic Potential)

Nowadays, global reactivity descriptors play an inevitable role in computational chemistry and molecular physics. They provide a quantitative means to evaluate the overall reactivity of a molecular system, giving invaluable insights into its behavior and interactions with other molecules (86-88, 90,91). Thus, they help to design new chemical compounds and predict potential outcomes in drug design and other chemical synthesis processes.

By using the *I* and *A* values given in Table 7, the calculated reactivity indices of T1-T6 changed in the gas phase in the following orders. According to ΔE order, T1 would tend to interact with the external system rather than intramolecular actions, whereas

T5 could prefer intramolecular interactions more than acting with the outer system. On the other hand, the T5 would be more stable electronically than the others, and vice versa for T4, depending on the μ . T1 was predicted to be the hardest molecule, while the soft compound would be T5. ω scores denoted that T5 could have bigger electrophilicity than the others and vice versa for T1 and T4. In addition, T5 would present more electron-donating or electron-accepting potency than the other compounds, and vice versa for T4. Supportingly, the charge transfer potency of T5 could be bigger than the others, and vice versa for T4. Moreover, the T1 would have gained more stability by the back donation than the others, and T5 was determined to have gained less stability relatively.

H (-*I*) (eV): T2 (-6.091) > T4 (-6.209) > T1 (-6.324) > T6 (-6.385) > T3 (-6.619) > T5 (-6.667)

L (-*A*) (eV): T1 (0.652) > T4 (0.643) > T2 (0.514) > T3 (0.344) > T5 (-1.478) > T6 (-0.516)

ΔE (L-H) (eV): T1 (6.976) > T3 (6.963) > T4 (6.852) > T2 (6.605) > T6 (5.869) > T5 (5.189)

μ (eV): T5 (-4.073) < T6 (-3.451) < T3 (-3.138) < T1 (-2.836) < T2 (-2.788) < T4 (-2.783)

η (eV): T1 (3.488) > T3 (3.482) > T4 (3.426) > T2 (3.303) > T6 (2.934) > T5 (2.594)

ω (eV): T5 (0.117) > T6 (0.075) > T3 (0.052) > T2 (0.043) > T1=T4 (0.042)

$\omega+$ (au): T5 (0.055) > T6 (0.025) > T3 (0.010) > T2 (0.007) > T1=T4 (0.006)

$\omega-$ (au): T5 (0.204) > T6 (0.151) > T3 (0.126) > T1 (0.111) > T2 (0.110) > T4 (0.108)

$\Delta N_{\max.}$ (eV): T5 (1.570) > T6 (1.176) > T3 (0.901) > T2 (0.844) > T1 (0.813) > T4 (0.812)
 $\Delta E_{\text{back.}}$ (eV): T1 (-0.872) < T3 (-0.870) < T4 (-0.856) < T2 (-0.826) < T6 (-0.734) < T5 (-0.649)

In the water phase, the ΔE , μ , η , ω , $\omega+$, and $\Delta E_{\text{back.}}$ indexes gave the same order as those in the gas phase. On the other hand, $\omega-$ (au) values changed as T5 (0.212) > T6 (0.157) > T3 (0.122) > T1=T2=T4 (0.113); here, the electron donating potencies of T1, T2, and T4 approximately were calculated close to each other. Moreover, $\Delta N_{\max.}$ (eV) values varied in the order of T5 (1.601) > T6 (1.216) > T3 (0.877) > T2 (0.858) > T4 (0.827) > T1 (0.826); the T1 would gain the less stability via back donation comparison to other compounds.

Over the years, FMO and MEP graphs have established themselves as indispensable theoretical tools in the realm of computational chemistry. These plots enable a visual examination of the electronic structure and reactivity of molecules,

thereby trying to light on their complex behavior and characteristics. From Figure 3, the HOMO density for all molecules was concentrated around the double bonds, whereas it for T3-T6 was distributed on neighboring bonds around the oxygen atom. Moreover, the LUMO for T1 and T3-T5 expanded on the hexene ring mainly, while it for T6 expanded over the aliphatic part mainly and on the ring slightly and, the LUMO for T2 covered all molecular surfaces. For T4, the red color as a function of the negative electrostatic potential ($V < 0$) appeared on the oxygen atom and double bonds for the electrophiles, whereas the blue color ($V > 0$) was seen on the H atom for the nucleophiles. For T1 and T2, the area around the double bond was covered in red.

Table 7: The chemical reactivity indices

		T1	T2	T3	T4	T5	T6
Gas	H (-I) (eV)	-6.324	-6.091	-6.619	-6.209	-6.667	-6.385
	L (-A) (eV)	0.652	0.514	0.344	0.643	-1.478	-0.516
	ΔE (L-H) (eV)	6.976	6.605	6.963	6.852	5.189	5.869
	μ (eV)	-2.836	-2.788	-3.138	-2.783	-4.073	-3.451
	η (eV)	3.488	3.303	3.482	3.426	2.594	2.934
	ω (eV)	0.042	0.043	0.052	0.042	0.117	0.075
	$\omega+$ (au)	0.006	0.007	0.010	0.006	0.055	0.025
	$\omega-$ (au)	0.111	0.110	0.126	0.108	0.204	0.151
	$\Delta N_{\max.}$ (eV)	0.813	0.844	0.901	0.812	1.570	1.176
	$\Delta E_{\text{back.}}$ (eV)	-0.872	-0.826	-0.870	-0.856	-0.649	-0.734
Water	H (-I) (eV)	-6.385	-6.170	-6.551	-6.361	-6.805	-6.442
	L (-A) (eV)	0.608	0.471	0.430	0.602	-1.571	-0.629
	ΔE (L-H) (eV)	6.993	6.641	6.982	6.963	5.234	5.813
	μ (eV)	-2.888	-2.850	-3.061	-2.879	-4.188	-3.535
	η (eV)	3.497	3.320	3.491	3.481	2.617	2.906
	ω (eV)	0.044	0.045	0.049	0.044	0.123	0.079
	$\omega+$ (au)	0.007	0.008	0.009	0.007	0.058	0.027
	$\omega-$ (au)	0.113	0.113	0.122	0.113	0.212	0.157
	$\Delta N_{\max.}$ (eV)	0.826	0.858	0.877	0.827	1.601	1.216
	$\Delta E_{\text{back.}}$ (eV)	-0.874	-0.830	-0.873	-0.870	-0.654	-0.727

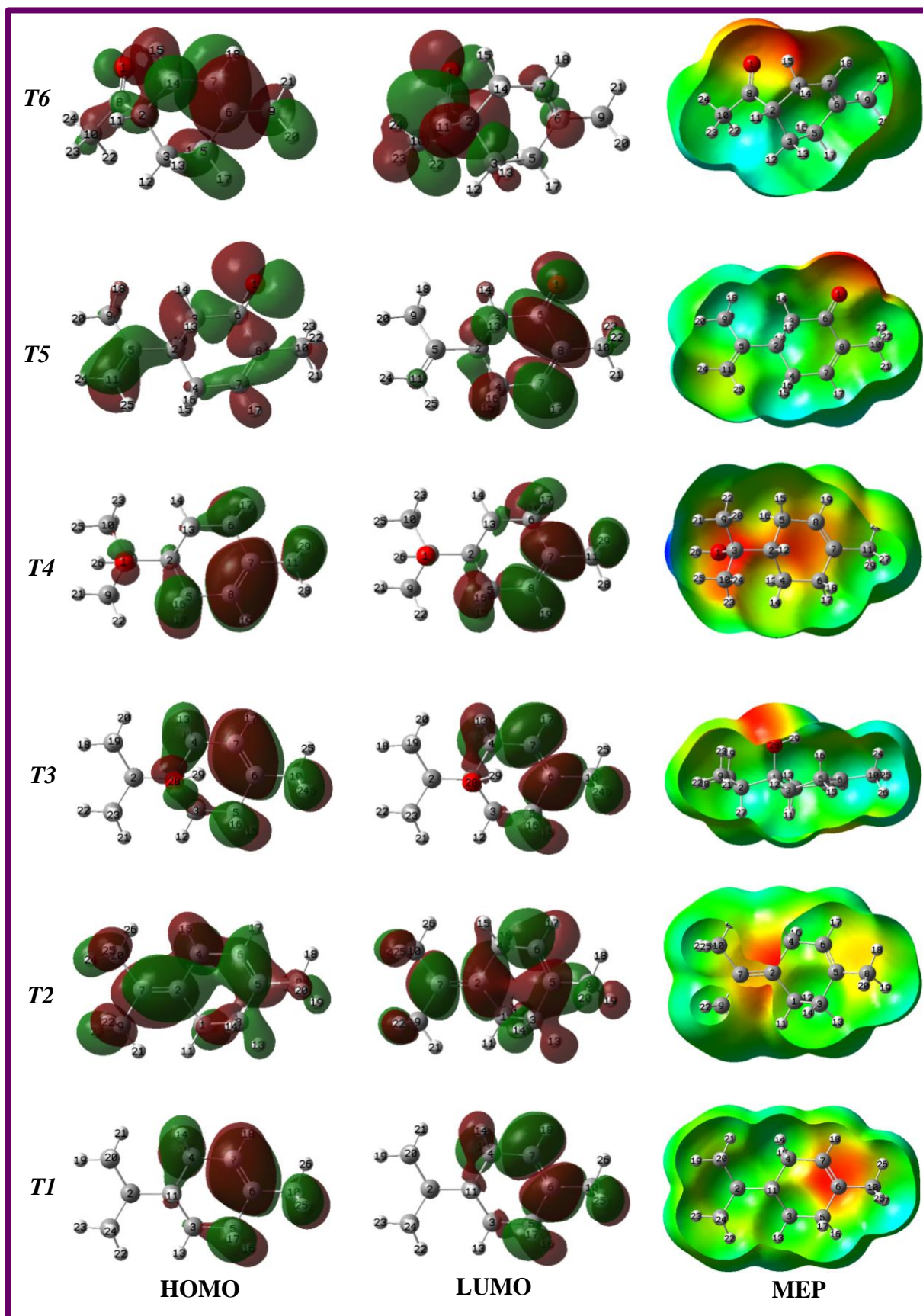


Figure 3: HOMO& LUMO, and MEP visualizations of T1-T6.

4. CONCLUSION

In this work, the DFT/DFT/B3LYP/6-311G** level computations were performed to predict the physicochemical and electronic characteristics of the terpenes T1-T6. In this regard, the FMO and MEP analyses were used to predict the possible reactivity direction and site(s). Moreover, the NBO analyses and atomic charges of the compounds were determined to evaluate the intramolecular interactions and charge distribution on the whole surface, which would be important to provide insight into the possible bioactivity, drug-likeness, toxicity, etc. In conclusion, the key points obtained from the computational tools of this work can be summarized as follows:

The T1 and T2 molecules were more lipophilic than the other molecules, whereas T5 and T6 molecules were found to be less lipophilic.

T5 and T6 functionalized with the -C=O group's most soluble compounds, while T2 was the less soluble one among the compounds, depending on results obtained from ALI and ESOL approaches.

VD (L/kg) values of all compounds were estimated in the optimal range of 0.04-20 L/kg, which would be very important in terms of the distribution of each of them.

NBO analyses revealed that $\sigma \rightarrow \sigma^*$ interactions for T1-T4 would be important to lowering the stabilization energy, predicted at 7.04 kcal/mol. In contrast, the resonance ($\pi \rightarrow \pi^*$) interaction for T5 was predicted with the energy of 20.26 kcal/mol which was the highest contributed interaction to E(2).

FMO analyses indicated that T5 (0.204 au) could prefer electron donation more than the other terpenes, while T4 (0.108 au) would prefer electron donation less than the others.

MEP plots implied that the surround of the oxygen atom for T3-T6 molecules would be the electron-rich region for the electrophiles, whereas the around of the double bonds of T1 and T2 would be possible sites for the electrophiles.

The NPA approach revealed that the atomic charge of the O1 atom of terpenes T4-T6 was predicted at -0.76279, -0.55670, and -0.55395, whereas the O28 atom' charge was found to be at -0.77131, remarkable.

It is hoped that the findings derived from this study will shed light on the interplay between ADM attributes, toxicity, and electronic structure, thereby contributing to the discovery, development, and refinement of prospective pharmaceutical agents.

5. ACKNOWLEDGMENTS

All calculations have been carried out at TUBITAK ULAKBIM, High Performance and Grid Computing Center (TR-Grid e-Infrastructure). The author thanks to Scientific Research Projects Department of Cumhuriyet University (Project No: EGT-2023-098).

6. REFERENCES

- McGarvey DJ, Croteau R. Terpenoid metabolism. *Plant Cell*. 1995;7(7):1015-1026. Available from: [<URL>](#).
- Masyita A, Sari RM, Astuti AD, Yasir B, Rumata NR, Emran TB, et al. Terpenes and terpenoids as main bioactive compounds of essential oils, their roles in human health and potential application as natural food preservatives. *Food Chem X*. 2022;13:100217. Available from: [<URL>](#).
- Brahmkshatriya PP, Brahmkshatriya PS. Terpenes: Chemistry, Biological Role, and Therapeutic Applications. In: Ramawat K, Mérillon JM, eds. *Natural Products*. Berlin, Heidelberg: Springer; 2013. Available from: [<URL>](#).
- Pichersky E, Gershenzon J. The formation and function of plant volatiles: perfumes for pollinator attraction and defense. *Curr Opin Plant Biol*. 2002;5(3):237-243. Available from: [<URL>](#).
- Bakkali F, Averbeck S, Averbeck D, Idaomar M. Biological effects of essential oils – A review. *Food Chem Toxicol*. 2008;46(2):446-475. Available from: [<URL>](#).
- Del Prado-Audelo ML, Cortés H, Caballero-Florán IH, González-Torres M, Escutia-Guadarrama L, Bernal-Chávez SA, et al. Therapeutic Applications of Terpenes on Inflammatory Diseases. *Front Pharmacol*. 2021;12:704197. Available from: [<URL>](#).
- Wen CC, Kuo YH, Jan JT, Liang PH, Wang SY, Liu HG, et al. Specific plant terpenoids and lignoids possess potent antiviral activities against severe acute respiratory syndrome coronavirus. *J Med Chem*. 2007;50(17):4087-4095. Available from: [<URL>](#).
- Guimarães AC, Meireles LM, Lemos MF, Guimarães MCC, Endringer DC, Fronza M, et al. Antibacterial Activity of Terpenes and Terpenoids Present in Essential Oils. *Molecules*. 2019;24(13):2471. Available from: [<URL>](#).
- Ansari IA, Akhtar MS. Current Insights on the Role of Terpenoids as Anticancer Agents: A Perspective on Cancer Prevention and Treatment. In: Swamy M, Akhtar M, eds. *Natural Bio-active Compounds*. Singapore: Springer; 2019. Available from: [<URL>](#).
- Kamran S, Sinniah A, Abdulghani MAM, Alshawsh MA. Therapeutic Potential of Certain Terpenoids as Anticancer Agents: A Scoping Review. *Cancers*. 2022;14(5):1100. Available from: [<URL>](#).
- Fan M, Yuan S, Li L, Zheng J, Zhao D, Wang C, et al. Application of Terpenoid Compounds in Food and Pharmaceutical Products. *Fermentation*. 2023;9(2):119. Available from: [<URL>](#).
- Gutiérrez-del-Río I, López-Ibáñez S, Magadán-Corpas P, Fernández-Calleja L, Pérez-Valero Á, Tuñón-Granda M, et al. Terpenoids and Polyphenols as Natural Antioxidant Agents in Food Preservation. *Antioxidants*. 2021;10(8):1264. Available from: [<URL>](#).
- Yang W, Chen X, Li Y, Guo S, Wang Z, Yu X. Advances in Pharmacological Activities of Terpenoids. *Nat Prod Commun*. 2020;15(3):1-13. Available from: [<URL>](#).
- Mani V, Park S, Kim JA, Lee SI, Lee K. Metabolic Perturbation and Synthetic Biology Strategies for Plant

- Terpenoid Production—An Updated Overview. *Plants*. 2021;10(10):2179. Available from: [<URL>](#).
15. Zhang Y, Song X, Lai Y, Mo Q, Yuan J. High-Yielding Terpene-Based Biofuel Production in *Rhodobacter capsulatus*. *ACS Synth Biol*. 2021;10(6):1545-1552. Available from: [<URL>](#).
16. Pahima E, Hoz S, Ben-Tziona M, Majo DT. Computational design of biofuels from terpenes and terpenoids. *Sustainable Energy Fuels*. 2019;3:457-466. Available from: [<URL>](#).
17. Alper Fitoz, Hasan Nazır, Mehtap Özgür (nee Yakut), Emel Emregül, Kaan C. Emregül, "An experimental and theoretical approach towards understanding the inhibitive behavior of a nitrile substituted coumarin compound as an effective acidic media inhibitor", *Corrosion Science*. 2018;133:451-464. Available from: [<URL>](#).
18. Alper Fitoz, Zehra Yazan, "Experimental and theoretical approaches to interactions between DNA and purine metabolism products", *International Journal of Biological Macromolecules*. 2023;248:125961. Available from: [<URL>](#).
19. A. Kalavathi, P. Saravana Kumar, K. Satheeshkumar, K.N. Vennila, S. Ciattini, L. Chelazzi, Kuppanagounder P. Elango, "Spectroscopic and TD-DFT studies on sequential fluorescent detection of Cu(II) and HS⁻ ions in an aqueous solution", *Inorganica Chimica Acta*. 2023;550:121447. Available from: [<URL>](#).
20. Maspero, A.; Vavassori, F.; Nardo, L.; Vesco, G.; Vitillo, J.G.; Penoni, A. Synthesis, Characterization, Fluorescence Properties, and DFT Modeling of Difluoroboron Biindoleketonates. *Molecules*. 2023;28:4688. Available from: [<URL>](#).
21. McGarvey DJ, Croteau R. Terpenoid metabolism. *Plant Cell*. 1995;7(7):1015-1026. Available from: [<URL>](#).
22. Vekiari SA, Protopapadakis EE, Papadopoulou P, Papanicolaou D, Panou C, Vamvakias M. Composition and seasonal variation of the essential oil from leaves and peel of a Cretan lemon variety. *J Agric Food Chem*. 2002;50(1):147-153. Available from: [<URL>](#).
23. Al-Basheer W. Linear and nonlinear chiro-optical properties of carvone molecule mirror-image configurations. *Proc SPIE*. 2019;11026:110260Z. Available from: [<URL>](#).
24. Sato H, Hashishin T, Kanazawa J, Miyamoto K, Uchiyama M. DFT Study of a Missing Piece in Brasilane-Type Structure Biosynthesis: An Unusual Skeletal Rearrangement. *J Am Chem Soc*. 2020;142(47):19830-19834. Available from: [<URL>](#).
25. Sato H, Li BX, Takagi T, Wang C, Miyamoto K, Uchiyama M. DFT Study on the biosynthesis of verrucosane diterpenoids and mangicol sesterterpenoids: Involvement of secondary-carbocation-free reaction cascades. *JACS Au*. 2021;1(8):1231-1239. Available from: [<URL>](#).
26. Zhu XK, Zheng YQ, Liu JB. A Computational Mechanistic Study of Cp*Co(III)-Catalyzed Three-Component C–H Bond Addition to Terpenes and Formaldehydes: Insights into the Origins of Regioselectivity. *J Phys Chem A*. 2021;125(23):5031-5039. Available from: [<URL>](#).
27. Yankova R, Dimov M, Dobрева K, Stoyanova A. Electronic structure, reactivity, and Hirshfeld surface analysis of carvone. *J Chem Res*. 2019;43(9-10):319-29. Available from: [<URL>](#).
28. Mekkaoui AA, El Ayouchia H, Anane H, Chahboun R, El Firdoussi L, El Houssame S. Viable route and DFT study for the synthesis of optically active limonaketone: A barely available natural feedstock in *Cedrus atlantica*. *J Mol Struct*. 2021;1235:130221. Available from: [<URL>](#).
29. Becke AD. A new mixing of Hartree–Fock and local density-functional theories. *J Chem Phys*. 1993;98:1372-1377. Available from: [<URL>](#).
30. Lee C, Yang W, Parr RG. Development of the Colle-Salvetti correlation-energy formula into a functional of the electron density. *Phys Rev B*. 1988;37:785-789. Available from: [<URL>](#).
31. Raghavachari K, Binkley JS, Seeger R, Pople JA. Self-Consistent Molecular Orbital Methods. 20. Basis set for correlated wave-functions. *J Chem Phys*. 1980;72(1):650-654. Available from: [<URL>](#).
32. McLean AD, Chandler GS. Contracted Gaussian-basis sets for molecular calculations. 1. 2nd row atoms, Z=11-18. *J Chem Phys*. 1980;72(9):5639-5648. Available from: [<URL>](#).
33. Li X, Frisch MJ. Energy-represented DIIS within a hybrid geometry optimization method. *J Chem Theory Comput*. 2006;2(3):835-839. Available from: [<URL>](#).
34. Kudin KN, Scuseria GE, Cancès E. A black-box self-consistent field convergence algorithm: One step closer. *J Chem Phys*. 2002;116(19):8255-8261. Available from: [<URL>](#).
35. Frisch MJ, Trucks GW, Schlegel HB, Scuseria GE, Robb MA, Cheeseman JR, et al. Gaussian 09W, Revision D.01, Gaussian, Inc, Wallingford CT, 2013.
36. Dennington R, Keith TA, Millam JM. GaussView, Version 6. Semichem Inc., Shawnee Mission, KS, 2016.
37. Cossi M, Barone V, Cammi R, Tomasi J. Ab initio study of solvated molecules: A new implementation of the polarizable continuum model. *Chem Phys Lett* 1996;255:327-335. Available from: [<URL>](#).
38. Tomasi J, Mennucci B, Cammi R. Quantum mechanical continuum solvation models. *Chem Rev*. 2005;105:2999-3093. Available from: [<URL>](#).
39. McQuarrie DA. *Statistical Thermodynamics*. Harper & Row Publishers, 1973.
40. Hill TL. *An Introduction to Statistical Thermodynamics*. Addison-Wesley Publishing, 1962.
41. Herzberg, G. *Molecular Spectra and Molecular Structure III (1st ed.)*. D. Van Nostrand Company, Inc., 1964.
42. Serdaroglu G, Durmaz S. DFT and statistical mechanics entropy calculations of diatomic and polyatomic molecules. *Indian J Chem* 2010; 49: 861-866. ISSN: 0376-4710
43. Koopmans T. Über die Zuordnung von Wellenfunktionen und Eigenwerten zu den Einzelnen Elektronen Eines Atoms. *Physica* 1934;1:104-113. Available from: [<URL>](#).

44. Perdew JP, Parr RG, Levy M, Balduz JL, et al. Density-Functional Theory for Fractional Particle Number: Derivative Discontinuities of the Energy. *Phys Rev Lett* 1982;49(23):1691-1694. Available from: [<URL>](#).
45. Janak JF. Proof that $\partial E/\partial n_i = \epsilon_i$ in density-functional theory. *Phys Rev B*. 1978;18(12):7165-7168. Available from: [<URL>](#).
46. Perdew JP, Levy M. Physical Content of the Exact Kohn-Sham Orbital Energies: Band Gaps and Derivative Discontinuities. *Phys Rev Lett*. 1983;51(20):1884-1887. Available from: [<URL>](#).
47. Parr RG, Pearson RG. Absolute hardness: companion parameter to absolute electronegativity. *J Am Chem Soc*. 1983;105:7512-7516. Available from: [<URL>](#).
48. Pearson RG. Absolute electronegativity and hardness correlated with molecular orbital theory. *Proc Natl Acad Sci USA*. 1986;83:8440-8441. Available from: [<URL>](#).
49. Parr RG, Szentpaly LV, Liu S. Electrophilicity Index. *J Am Chem Soc*. 1999;121:1922-1924. Available from: [<URL>](#).
50. Gazquez JL, Cedillo A, Vela A. Electrodonating and Electroaccepting Powers. *J Phys Chem A*. 2007;111(10):1966-1970. Available from: [<URL>](#).
51. Gomez B, Likhanova NV, Domínguez-Aguilar MA, Martínez-Palou R, Vela A, Gazquez JL. Quantum Chemical Study of the Inhibitive Properties of 2-Pyridyl-Azoles. *J Phys Chem B*. 2006;110(18):8928-8934. Available from: [<URL>](#).
52. NBO Version 3.1, E. D. Glendening, A. E. Reed, J. E. Carpenter, F. Weinhold.
53. J. P. Foster and F. Weinhold, "Natural hybrid orbitals", *J. Am. Chem. Soc.*, 102 (1980):7211-7218.
54. Reed, A.E., Weinstock, R.B. and Weinhold, F. Natural Atomic Orbitals and Natural Population Analysis. *Journal of Chemical Physics*. 1985;83:735-746. Available from: [<URL>](#).
55. A. E. Reed and F. Weinhold, "Natural localized molecular orbitals", *J. Chem. Phys*. 1985;83:1736-1740.
56. A. E. Reed, L. A. Curtiss and F. Weinhold, "Intermolecular interactions from a natural bond orbital, donor-acceptor viewpoint", *Chem. Rev*. 1988;88(6):899-926.
57. Mulliken RS. Chemical bonding. *Annual Review of Physical Chemistry*. 1978;29(1):1-31.
58. Daina A, Michielin O, Zoete V. iLOGP: A Simple, Robust, and Efficient Description of n-Octanol/Water Partition Coefficient for Drug Design Using the GB/SA Approach. *J Chem Inf Model*. 2014;54(12):3284-3301. Available from: [<URL>](#).
59. Cheng T, Zhao Y, Li X, Lin F, Xu Y, Zhang X, Li Y, Wang R. Computation of Octanol-Water Partition Coefficients by Guiding an Additive Model with Knowledge. *J Chem Inf Model*. 2007;47(6):2140-2148. Available from: [<URL>](#).
60. Wildman SA, Crippen GM. Prediction of Physicochemical Parameters by Atomic Contributions. *J Chem Inf Comput Sci*. 1999;39:868-873. Available from: [<URL>](#).
61. Lipinski CA, Lombardo F, Dominy BW, Feeney PJ. Experimental and computational approaches to estimate solubility and permeability in drug discovery and development settings. *Adv Drug Deliv Rev*. 2001;46:3-26. Available from: [<URL>](#).
62. Silicos-it. (n.d.). Available from: [<URL>](#).
63. Daina A, Michielin O, Zoete V. SwissADME: a free web tool to evaluate pharmacokinetics, druglikeness and medicinal chemistry friendliness of small molecules. *Sci Rep*. 2017;7:42717. Available from: [<URL>](#).
64. Delaney JS. ESOL: Estimating Aqueous Solubility Directly from Molecular Structure. *J Chem Inf Comput Sci*. 2004;44:1000-1005. Available from: [<URL>](#).
65. Ali J, Camilleri P, Brown MB, Hutt AJ, Kirton SB. In Silico Prediction of Aqueous Solubility Using Simple QSPR Models: The Importance of Phenol and Phenol-like Moieties. *J Chem Inf Model*. 2012;52:2950-2957. Available from: [<URL>](#).
66. Ghose AK, Viswanadhan VN, Wendoloski JJ. A Knowledge-Based Approach in Designing Combinatorial or Medicinal Chemistry Libraries for Drug Discovery. 1. A Qualitative and Quantitative Characterization of Known Drug Databases. *J Comb Chem*. 1999;1:55-68. Available from: [<URL>](#).
67. Veber DF, Johnson SR, Cheng H-Y, Smith BR, Ward KW, Kopple KD. Molecular Properties That Influence the Oral Bioavailability of Drug Candidates. *J Med Chem*. 2002; 45: 2615-2623. Available from: [<URL>](#).
68. Egan WJ, Merz KM Jr, Baldwin JJ. Prediction of Drug Absorption Using Multivariate Statistics. *J Med Chem*. 2000; 43: 3867-3877. Available from: [<URL>](#).
69. Muegge I, Heald SL, Brittelli D. Simple Selection Criteria for Drug-like Chemical Matter. *J Med Chem*. 2001;44(12):1841-1846. Available from: [<URL>](#).
70. Martin YC. A Bioavailability Score. *J Med Chem*. 2005;48:3164-3170. Available from: [<URL>](#).
71. ADMETlab 2.0.
72. Serin S. A comprehensive DFT study on organosilicon-derived fungicide flusilazole and its germanium analogue: A computational approach to Si/Ge bioisosterism. *J Indian Chem Soc*. 2023;100:100939. Available from: [<URL>](#).
73. Serdaroğlu G, Ortiz JV. Ab Initio Calculations on some Antiepileptic Drugs such as Phenytoin, Phenobarbital, Ethosuximide and Carbamazepine. *Struct Chem*. 2017;28(4):957-964. Available from: [<URL>](#).
74. Serdaroğlu G. DFT and Ab initio computational study on the reactivity sites of the GABA and its agonists, such as CACA, TACA, DABA, and muscimol: In the gas phase and dielectric media. *Int J Quantum Chem*. 2011;111(14):3938-3948. Available from: [<URL>](#).
75. Serdaroğlu G. A DFT study of determination of the reactive sites of the acetylcholine and its agonists: In the gas phase and dielectric medium. *Int J Quantum Chem*. 2011;111(10):2464-2475. Available from: [<URL>](#).

76. Serin S, Kaya G, Utku T. Insights into solvent effects on molecular properties, physicochemical parameters, and NLO behavior of brinzolamide, a bioactive sulfonamide: A computational study. *J Indian Chem Soc.* 2022;99:100738. Available from: [<URL>](#).
77. Lin JH, Lu AY. Role of Pharmacokinetics and Metabolism in Drug Discovery and Development. *Pharmacol Rev.* 1997;49(4):403-449. Available from: [<URL>](#).
78. Jackson E, Shoemaker R, Larian N, Cassis L. Adipose Tissue as a Site of Toxin Accumulation. *Compr Physiol.* 2017;7(4):1085-1135. Available from: [<URL>](#).
79. Carpenter JF, Pikal MJ, Chang BS, Randolph TW. Rational design of stable lyophilized protein formulations: Theory and practice. *Pharm Biotechnol.* 1997;9:189-227. Available from: [<URL>](#).
80. McGeer JC, Brix KV, Skeaff JM, DeForest DK, Brigham SI, Adams WJ, Green A. Inverse relationship between bioconcentration factor and exposure concentration for metals: implications for hazard assessment of metals in the aquatic environment. *Environ Toxicol Chem.* 2003;22(5):1017-1037. Available from: [<URL>](#).
81. Nendza M, Müller M. Screening for low aquatic bioaccumulation. 1. Lipinski's 'Rule of 5' and molecular size. *SAR QSAR Environ Res.* 2010;21(5-6):495-512. Available from: [<URL>](#).
82. Cuadros-Siguas CF, Herrera-Calderon O, Batiha GES, Almohmad, NH, Aljarba NH, Apesteguia-Infantes JA, ... & Pari-Olarte JB. Volatile Components, Antioxidant and Phytotoxic Activity of the Essential Oil of *Piper acutifolium* Ruiz & Pav. from Peru. *Molecules.* 2023;28(8):3348.
83. Rezende ECN, Carneiro FM, de Moraes JB, Wastowski IJ. Trends in science on glyphosate toxicity: a scientometric study. *Environ Sci Pollut Res.* 2021;28:56432-56448. Available from: [<URL>](#).
84. Rivas-Garcia, T.; Espinosa-Calderón, A.; Hernández-Vázquez, B.; Schwentesius-Rindermann, R. Overview of Environmental and Health Effects Related to Glyphosate Usage. *Sustainability.* 2022;14:6868. Available from: [<URL>](#).
85. Deeksha Rawat, Aarti Bains, Prince Chawla, Ravinder Kaushik, Rahul Yadav, Anil Kumar, Kandi Sridhar, Minaxi Sharma, Hazardous impacts of glyphosate on human and environment health: Occurrence and detection in food, *Chemosphere.* 2023;329:138676. Available from: [<URL>](#).
86. Erdogan M, Serdaroglu G. New Hybrid (E)-4-((pyren-1-ylmethylene)amino)-N-(thiazol-2-yl)benzenesulfonamide as a Potential Drug Candidate: Spectroscopy, TD-DFT, NBO, FMO, and MEP Studies. *Chemistry Select.* 2021;6:9369-9381. Available from: [<URL>](#).
87. Serdaroglu G. Harmine derivatives: a comprehensive quantum chemical investigation of the structural, electronic (FMO, NBO, and MEP), and spectroscopic (FT-IR and UV-Vis) properties. *Research on Chemical Intermediates.* 2020;46(1):961-982.
88. Uludağ N, Serdaroglu G. An efficient studies on C-2 cyanomethylation of the indole synthesis: The electronic and spectroscopic characterization (FT-IR, NMR, UV-Vis), antioxidant activity, and theoretical calculations. *Journal of Molecular Structure.* 2022;1247:131416.
89. Sigfridsson E, Ryde U. Comparison of methods for deriving atomic charges from the electrostatic potential and moments. *Journal of Computational Chemistry.* 1998;19(4):377-395. Available from: [<URL>](#).
90. Serin S. DFT-based computations on some structurally related N-substituted piperazine. *J Indian Chem Soc.* 2022;99:100766. Available from: [<URL>](#).
91. Hsissou R, Benhiba F, Echihi S, Benzidia B, Cherrouf S, Haldhar R, Alvi PA, Kaya S, Serdaroglu G, Zarrouk A. Performance of curing epoxy resin as potential anticorrosive coating for carbon steel in 3.5 NaCl medium: Combining experimental and computational approaches. *Chem Phys Lett.* 2021;783:139081. Available from: [<URL>](#).



Investigation of Thermodynamic and Morphological Properties of Crystalline 4-HPG (4-hydroxyphenylglycine) Using Raman, PXRD and DTA/TGA

M. Fatih Ergin* 

Department of Chemical Engineering, Engineering Faculty, Istanbul University- Cerrahpasa, Istanbul / Turkey

Abstract: This study focuses on the detailed physical characterization of 4-HPG, a significant impurity found in some of the most commonly prescribed β -lactam antibiotics worldwide. Various analytical techniques, including X-ray powder diffractometry, dynamic light scattering, scanning electron microscopy, Fourier-transform infrared, and Raman spectroscopy, were employed to characterize the properties of 4-HPG crystals. XRD analysis revealed the crystallinity and small crystallite sizes of 4-HPG particles, supported by DLS and SEM analyses. FT-IR and Raman spectroscopy results exhibited excellent agreement, providing insight into the structural characterization of 4-HPG. Thermal analysis revealed a two-stage degradation feature of 4-HPG. Overall, this study contributes to a better understanding of 4-HPG's structure and its impact on antibiotic stability.

Keywords: 4-hydroxyphenylglycine, impurity, crystallization, pharmaceutical analysis, stability

Submitted: October 02, 2023. **Accepted:** March 25, 2024.

Cite this: Ergin MF. Investigation of Thermodynamic and Morphological Properties of Crystalline 4-HPG (4-hydroxyphenylglycine) Using Raman, PXRD and DTA/TGA. JOTCSA. 2024;11(2):889-98.

DOI: <https://doi.org/10.18596/jotcsa.1369980>.

*Corresponding author. E-mail: mfergin@iuc.edu.tr.

1. INTRODUCTION

Today, studies on the physical characterization of active pharmaceutical ingredients (APIs) examine drug stability (1) in detail within formulation programs that encompass analytical tests (2) and the physical properties of the drug substance (3-7). Understanding the properties of APIs, as well as their impurities, is equally crucial for comprehending their effects on pharmaceutical structure. A sufficiently detailed physical framework of both the API and its impurities serves as a vital starting point in addressing undesirable crisis situations stemming from raw materials. Thermal analysis methods provide information on the material's physical characteristics depending on its temperature.

Combining thermal analysis (TG, DTA) (8) with electron microscopy (SEM), Raman and FT-IR spectroscopy, and X-ray powder diffractometry (XRD) offers a comprehensive view of the chemical and physical changes occurring in pharmaceuticals (9, 10).

An analog of tyrosine, an amino acid with intriguing photophysical activity in a peptide chain, is 4-hydroxyphenylglycine (4-HPG) (Figure 1) (11). Additionally, 4-hydroxyphenylglycine is one of the main components of Complestatin, a neuroprotective agent (12). Furthermore, surface-functionalized single-walled carbon nanotubes with azomethine ylide groups and fixed phenol structures are created using 4-HPG (13).

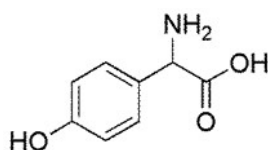


Figure 1: Molecular structure of 4-hydroxyphenylglycine.

Chiral amino acid derivatives, such as D(-)/L(+) - 4-Hydroxyphenylglycine, exhibit easy accessibility, multiple metal binding sites, and versatile binding modes, making them ideal candidates for forming compounds. Li et al. formed complexes with D/L -4-HPG, Pb(II), Cu(II), and Cd(II) metals, showcasing the structural diversity and potential of D/L-4-HPG in synthesizing coordination compounds with intriguing structures (14). HPG, known for its large specific surface area and strong cohesion strength with catalyst nanoparticles, was utilized alongside $\text{Co}_{0.85}\text{Se}$ in the electrochemical water cracking process in alkaline solution by Zhong et al (15). Mostaghazi et al. prepared Fe_3O_4 -HPG-FA nanoparticles, demonstrating their

potential as efficient nanotheranostic devices for eliminating cancer cells (16). Liu et al. developed 3D HPG-supported high-performance $\text{Pt/NiCo}_2\text{O}_4$ for glycerol electrooxidation (17). He et al. synthesized Fe_3O_4 /HPG-COOH nanoparticles and highlighted their effectiveness as an adsorbent to remove cationic dyes from water (18).

Moreover, 4-HPG is widely used as an acyl donor in the enzymatic synthesis of Amoxicillin trihydrate (AMCT), a cephalosporin-type β -lactam antibiotic (19, 20). However, regardless of the production method used (Figure 2), it is inevitable that 4-HPG will appear as an impurity along with the desired AMCT (21, 22).

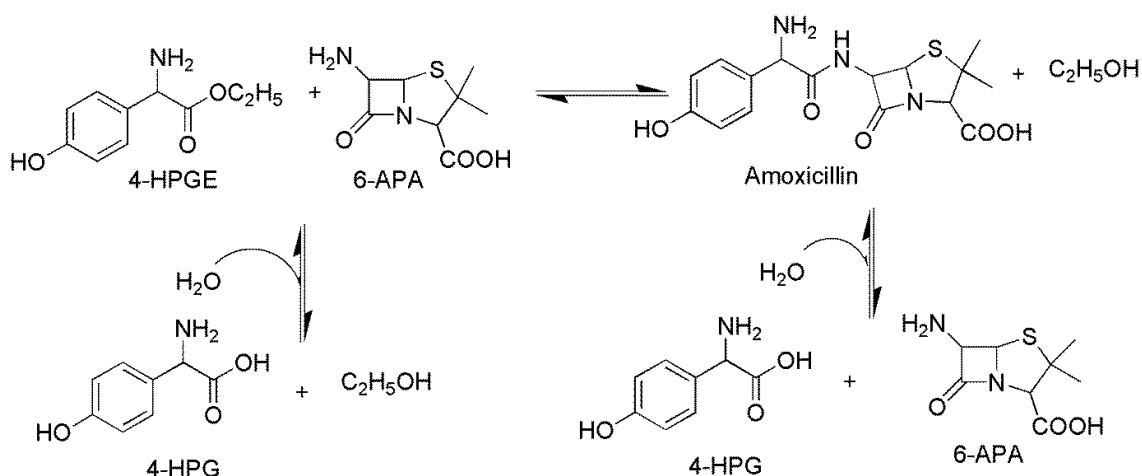


Figure 2: Enzymatic synthesis for the production of AMCT.

Impurities in β -lactam crystallization adversely affect nucleation and growth rate. Hence, considerable attention has been given in the literature to identifying and purifying impurity products of AMCT, especially 4-HPG (23-26). The quantitative measurement of organic and medicinal components, as well as completed goods and contaminants, is carried out using various methodologies (27-29). The presence of degradation products of AMCT, especially 4-HPG, reduces synthesis efficiency and affects downstream purification and separation processes. Therefore, detailed physical characterization of 4-HPG is essential to avoid adverse effects on the AMCT process. Ergin and Yasa developed a fast, simple, and specific UV-spectrophotometric method for determining 4-HPG and 6-APA (30). This study takes a step towards understanding the effects of 4-hydroxyphenylglycine (4-HPG), a significant impurity in some of the world's most commonly prescribed beta-lactam antibiotics such as amoxicillin trihydrate, by providing a comprehensive physical characterization. By shedding light on the role of 4-HPG in pharmaceutical products, enhancing quality control, and optimizing production efficiency, this research aims to illuminate the latest developments in the industry. It represents a stride forward in the pharmaceutical industry towards

producing safer, more effective, and more reliable medications.

2. EXPERIMENTAL SECTION

4-HPG purchased from Sigma Aldrich (USA) was of analytical purity and used without additional purification steps. The Milli-Q system (Millipore, USA) was employed to produce distilled water throughout the study. Hydrochloric acid and sodium hydroxide from Sigma-Aldrich were used to prepare 1.0 M HCl and 5.0 M NaOH solutions, respectively.

2.1. Crystallization

In this study, a pre-designed Büchner glass funnel was used to easily obtain crystals without losing them and to operate at the desired temperature (24, 30, 31). The temperature of the process was set to room temperature with a circulating water bath (VWR Science 1150) and the system was operated at the same temperature for 30 minutes. All solvents were kept at the specified temperature (room temperature) in the water bath during the process to stabilize the system. 5.0 g of 4-HPG and 100 mL of deionized water were added to the jacketed reactor and stirred at 300 rpm with a mechanical stirrer (Ika RW 16) for 5 min. Then, 1 M HCl was fed into a jacketed reactor at the same

temperature as the solution (pH: 1.9, about 45 mL HCl) until all 4-HPG was dissolved. The undissolved solids were eliminated using 0.45 m Whatman Nylon filter paper. The solution was then fed with 5 M NaOH solution until pH reaches 5.0 and then allowed to crystallize for 30 min. A pH meter was used to continuously monitor the pH of the HCl and NaOH stages (Fischer Scientific AE 150, USA). The crystals obtained were filtered using Whatman Nylon filter paper with a pore size of 0.2 m. The resulting crystal samples were gently removed and dried for use in the experiments (Figure 3).

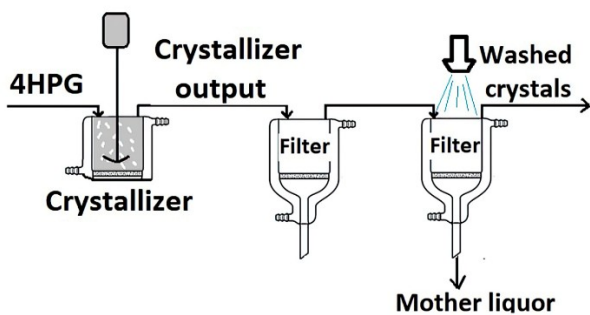


Figure 3: Schematic presentation of the 4-HPG crystallization process.

2.2. Thermogravimetric Analysis (TGA-DTG)

The thermal degradation behavior was analyzed using a Shimadzu DTG 60H instrument under airflow, with a heating rate of 10 °C min⁻¹, from room temperature to 800 °C in platinum crucibles.

The heating rate of 10 °C min⁻¹ signifies how rapidly the temperature of the sample increases during the analysis. This parameter influences the rate of thermal degradation and provides insight into the stability of the material under investigation. A higher heating rate may accelerate the degradation process, whereas a lower rate allows for a more detailed observation of degradation behavior.

The analysis conducted under airflow indicates that continuous air circulation around the sample was maintained during heating. This airflow helps remove volatile degradation products and maintains consistent temperature conditions throughout the analysis. However, inert atmospheres such as nitrogen or argon were not preferred due to their potential impact on the degradation behavior of the sample.

Overall, the detailed parameters of thermal analysis, including heating rate, atmosphere conditions, and sample preparation, play a significant role in accurately characterizing the thermal degradation behavior of the material under investigation.

2.3. X-ray Diffraction (XRD)

The crystallographic structure analysis was performed using a Rigaku D/max-2200 X-ray diffractometer

equipped with CuK α radiation. The scan rate was set at 2 θ = 0.01°/s over the angular range of 2° to 40°. During XRD analysis, the sample preparation involved finely grinding the crystalline material to a powder form and uniformly spreading it onto a sample holder. The sample holder was then positioned in the X-ray beam path, and the diffraction pattern was recorded as the sample was rotated.

The obtained diffraction pattern consists of peaks corresponding to the crystal lattice planes of the material. The positions and intensities of these peaks provide information about the spacing between lattice planes and the arrangement of atoms in the crystal structure.

To analyze the data, the diffraction pattern is compared to standard reference patterns available in powder diffraction files (PDFs) from the International Centre of Diffraction Data (ICDD). By matching the observed peaks with those in the reference patterns, qualitative phase analysis can be performed to identify the crystalline phases present in the sample.

$$n\lambda = 2d \cdot \sin \theta \quad (\text{Eq. 1})$$

$$d = (0.94\lambda) / (\beta \cos \theta) \quad (\text{Eq. 2})$$

Crystallite sizes were estimated using the Scherrer equation (Equation 2), with d representing crystallite size, λ representing X-ray wavelength, β representing full-width at half maximum (FWHM), and θ representing the diffraction angle. The average d -spacing, d (Å), was calculated using Bragg's equation (Equation 1) (32). Crystallite size was calculated based on the peak (100).

2.4. Raman Spectrometer

A Raman spectrometer (Model Thermo DXR) with a spectral range of 3200–400 cm⁻¹ was used for the analysis of 4-HPG. Ideal Raman conditions were determined as 532 nm, 10.0 mW, 10, 4.0 s, 2 and 50 m pinholes, respectively.

2.5. Fourier Transform Infrared Spectroscopy (FT-IR)

The FT-IR spectra of the samples synthesized in this study were recorded in the Thermo Nicolet 380 FT-IR brand spectrometer, in the range of 4000–400 cm⁻¹.

2.6. Particle Size Analysis

Particle sizes were determined using Dynamic Light Scattering (DLS) with a Brookhaven 90 Plus submicron particle size analyzer.

In DLS analysis, the sample, either a solution or dispersion, is illuminated with a monochromatic laser beam. This light is scattered by the particles in the sample. The DLS analyzer measures the properties of this scattering and calculates the particle size distribution using these data.

2.7. Scanning Electron Microscope (SEM)

Thermo Fisher Scientific's FEI FEG Quanta 250 scanning electron microscope (SEM) with energy-dispersive X-ray spectroscopy was used to analyze the microstructures of 4-HPG.

3. RESULTS AND DISCUSSION

3.1. Thermogravimetric Analysis

To date, only a limited number of studies have been conducted on the thermal behavior of amoxicillin in its pure form and in combination with specific excipients (31-33). Additionally, Bhattacharya et al. (1994) mentioned the determination of the melting point of HPG in their study on the synthesis of D-4-Hydroxyphenylglycine, but they did not provide any data or graphs regarding this (34). This study presents, for the first time, the Thermogravimetric Analysis (TGA) and Differential Thermal Analysis (DTA) spectra demonstrating the thermal properties of 4-hydroxyphenylglycine (4-HPG), a common impurity found in amoxicillin.

This study highlights the critical role of 4-HPG's thermal behavior as a prevalent impurity in amoxicillin.

Understanding the impact of 4-HPG's presence on the quality and stability of pharmaceutical products is crucial. The TGA and DTA spectra reveal a distinct two-step decomposition characteristic of 4-HPG. The structure of 4-HPG remains stable at room temperature, with no observed mass loss up to 210 °C, indicating its thermal stability until this temperature threshold. Upon reaching 210 °C, drug molecules acquire sufficient energy for orderly crystallization, followed by immediate melting and subsequent degradation of the molecules. The abrupt decrease in weight loss (~40%) observed in the temperature range of 210-255 °C is attributed to the elimination of the -COOH group (Table 1). Furthermore, a gradual reduction in mass is observed between 440 and 597 °C, accounting for approximately 54% of the mass, due to the decomposition of other groups remaining in the structure.

The examination of TGA and DTA spectra provides valuable information about the stability and decomposition properties of 4-HPG. The findings indicate that 4-HPG exhibits resistance to heat and possesses a stable structure. This understanding may contribute to discerning the potential impact of 4-HPG on the quality and stability of pharmaceutical products.

Table 1: Thermogravimetric data for compound 4-HPG.

Compound	Step	Temperature Range (°C)	Weight loss (%)	Residue
4-HPG	1 st	210-255	39.51	60.49
	2 nd	440-597	54.42	-

3.2. X-ray Diffraction (XRD) Analysis

Powder XRD (PXRD) was utilized to explore the crystal structure properties of 4-HPG. PXRD models of 4-HPG are depicted in Figure 5, presented for the first time in the literature, providing detailed insight into the crystal structures of 4-HPG. This analysis constitutes a novel contribution to the existing literature. Furthermore, comparative analysis with previous studies underscores

the significance of our findings. Additionally, while Bathori et al. (2009) utilized 4-hydroxyphenylglycine to acquire D(-)-amino-(4-hydroxyphenyl) acetate crystals, subsequently analyzed through X-ray diffraction, our study expands upon this research by offering a comprehensive examination of 4-HPG's crystal structures (13).

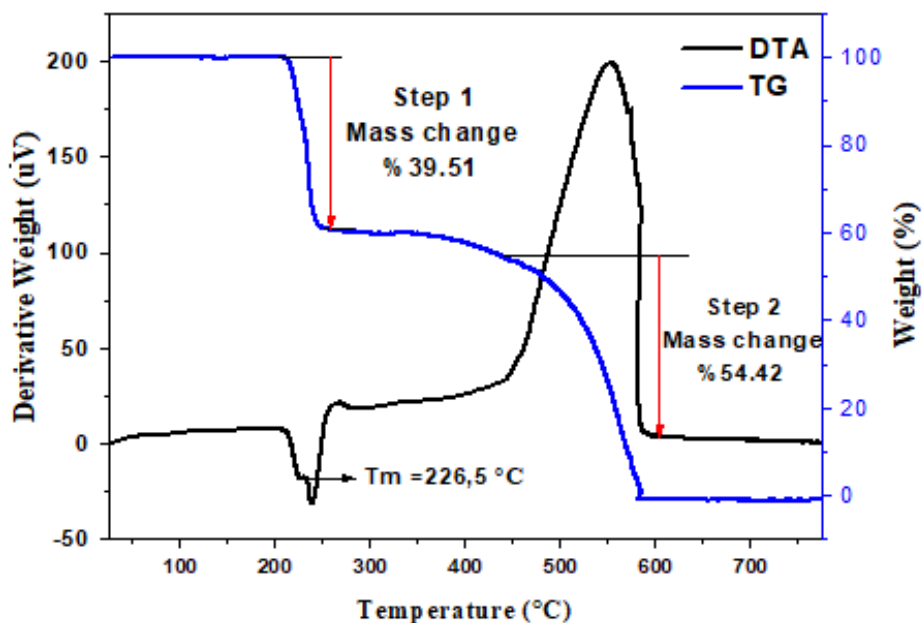


Figure 4: TGA-DTA graphics of the 4-hydroxyphenylglycine.

The highest intensity peak value of the 4-HPG particles was observed at 2θ : 20.51° , corresponding to the scattering from the (100) plane. Other peaks in the structure delineate the crystal structure of 4-HPG, with 2θ values of 20.51° , 27.50° , 35.66° , 40.07° , and 41.97° corresponding to crystalline (h k l) Miller indices (100), (101), (110), (111), and (012), respectively, indicative of the hexagonal phase 4-HPG crystals. 4-HPG exhibits relatively intense and sharp peaks with good crystallinity. The d-spacing values of 4-HPG were

calculated in accordance with Bragg's equation and are detailed in Table 2, with a calculated value of 0.43 nm. Additionally, the intensity of XRD peaks of the sample clearly indicates the crystalline nature of 4-HPG particles, with broad diffraction peaks suggesting small crystallite sizes. The crystallite sizes of 4-HPG particles were determined to be approximately ~43 nm. Furthermore, it is noteworthy to mention that the crystal structure properties of 4-HPG serve as a significant source of information for researchers in the field.

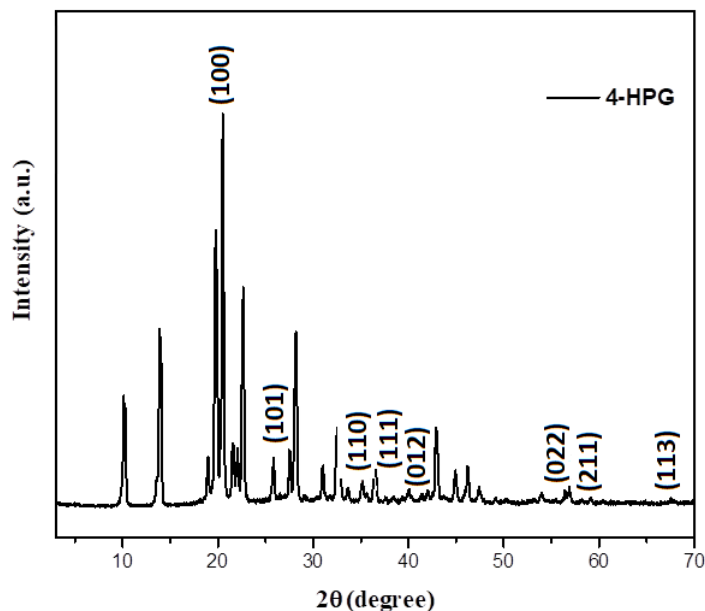


Figure 5: X-rays powder diffractograms of 4-HPG structure.

3.3. Fourier Transform Infrared Spectroscopy (FT-IR) and Raman Analysis

Figure 6 shows the characteristic FT-IR spectrum of 4-HPG crystals in detail. Between 3200 cm^{-1} and 2500 cm^{-1} and between 1700 cm^{-1} and 400 cm^{-1} wavenumbers,

variations in transmission spectroscopy data were noted. These results are in accordance with the amoxicillin literature (33, 35). It is also compatible with the graph given by Yokozeki et al. (1987) for d-4-hydroxyphenylglycine (36). Figure 7 shows the characteristic Raman spectrum of 4-HPG crystals. The Raman spectrum of 4-HPG was shown for the first time in the literature in this study and examined in detail. Thus, it will shed light on the work of many researchers.

O-H stretching of COOH, phenolic OH, and NH stretching vibrations cause an overlap of peaks in the wide band envelope between 2000 and 3500 cm^{-1} . Due to their shared characteristics, the N-H and O-H groups superimpose and were located at 3212 cm^{-1} in the FT-IR and 3192 cm^{-1} in the Raman spectrum. Asymmetric vibrations of C-H at 2967 cm^{-1} and C-H bond the of aromatic ring at 3061 cm^{-1} were also seen in FT-IR, and

at 3070 cm^{-1} and 2958 cm^{-1} in the Raman spectrum, respectively. Since amino acids exist in the form of zwitter ions, they contain amine and carboxylate salts in their structure. Ammonium ion was detected at 1605 cm^{-1} and 1523 cm^{-1} in FT-IR, and 1603 and 1523 cm^{-1} in Raman, respectively. COO⁻ stretching vibration is lower than the free acid group. It gives strong asymmetric peak at 1626 cm^{-1} and 1405 cm^{-1} in FT-IR, at 1626 cm^{-1} and 1405 cm^{-1} in Raman spectrum. The vibrations of the para-substituted benzoic ring produce peaks of high intensity at 847 cm^{-1} in FT-IR, at 868 cm^{-1} in Raman spectrum.

It is seen in Figure 8 that the FT-IR and Raman spectrum values support each other with great agreement. In addition, it is in harmony with the structure. Thus, they will shed light on the work of many researchers and may also be useful for the quantitative analysis of the phase composition of the pharmaceutical material (37).

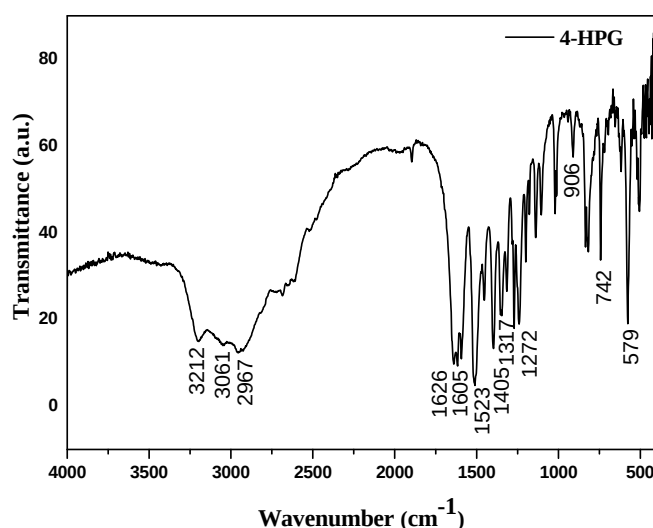


Figure 6: FT-IR spectra of 4-HPG structure.

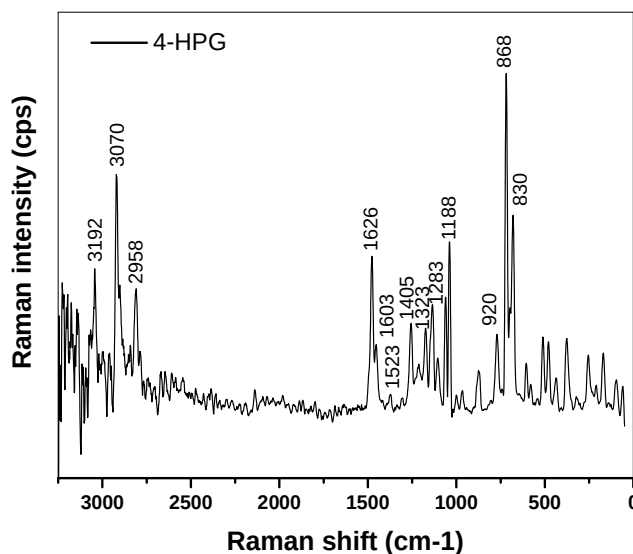


Figure 7: Raman spectra of 4-HPG.

Table 2: Peak search report of 4-HPG structure from X-rays powder pattern.

2-Theta	d-spacing (nm)	Height	I%	Area	Area%	FWHM	Crystallite Sizes (nm)	Miller indices (h k l)
10.13	0.87	880	28.7	13183	34.4	0.254	34	
13.91	0.63	1410	46.0	24942	65.0	0.301	28	
18.17	0.48	23	0.7	271	0.7	0.205	44	
18.98	0.46	355	11.6	5263	13.7	0.252	34	
19.78	0.44	2098	68.4	33995	88.6	0.275	31	
20.51	0.43	3068	100.0	38358	100.0	0.213	43	(1 0 0)
21.56	0.41	397	12.9	5858	15.3	0.251	35	
22.07	0.40	392	12.8	6262	16.3	0.271	32	
22.66	0.39	1714	55.9	23906	62.3	0.237	37	
25.84	0.34	331	10.8	4563	11.9	0.234	38	
27.50	0.32	363	11.8	3923	10.2	0.184	53	(1 0 1)
28.20	0.31	1339	43.6	21732	56.7	0.276	31	
29.14	0.30	41	1.3	435	1.1	0.178	55	
31.05	0.28	274	8.9	4318	11.3	0.268	33	
32.52	0.27	573	18.7	12762	33.3	0.378	22	
33.62	0.26	95	3.1	1234	3.2	0.220	42	
35.22	0.25	144	4.7	2945	7.7	0.347	25	
35.66	0.25	54	1.8	1054	2.7	0.329	26	(1 1 0)
36.51	0.24	374	12.2	6197	16.2	0.281	31	
37.63	0.23	33	1.1	271	0.7	0.141	84	
38.52	0.23	43	1.4	494	1.3	0.193	50	
39.38	0.22	36	1.2	265	0.7	0.125	>100	
40.07	0.22	106	3.5	1824	4.8	0.292	30	(1 1 1)
41.37	0.21	43	1.4	363	0.9	0.142	84	
41.97	0.21	64	2.1	934	2.4	0.248	37	(0 1 2)
42.88	0.21	566	18.4	9106	23.7	0.274	33	
44.92	0.20	241	7.9	3648	9.5	0.257	36	
46.22	0.19	279	9.1	4050	10.6	0.247	38	
47.40	0.19	117	3.8	1990	5.2	0.291	31	
49.18	0.18	41	1.3	417	1.1	0.171	63	
50.18	0.18	31	1.0	629	1.6	0.342	26	
53.99	0.17	73	2.4	1345	3.5	0.314	29	
55.49	0.16	26	0.8	301	0.8	0.193	54	
56.40	0.16	100	3.3	1286	3.4	0.219	46	(0 2 2)
56.88	0.16	129	4.2	2468	6.4	0.326	29	
59.12	0.15	43	1.4	533	1.4	0.212	49	(2 1 1)
67.51	0.13	41	1.3	907	2.4	0.372	26	(1 1 3)

3.4. Morphology and The Particular Size of 4-HPG

Many studies in the literature have focused on examining the SEM image of pure AMCT or its mixtures. The SEM results obtained revealed the long acicular rectangular prismatic structure of AMCT crystals (38). Although 4-HPG is one of the most critical impurities of AMCT mentioned in the USP (39), SEM images showing 4-HPG are still not available in the literature. This study is very important as it is the first to use SEM images to reveal the surface and morphology of 4-HPG crystals in detail (Figure 9a, 9b, and 9c). It also enabled the

identification of 4-HPG present as an impurity in the AMCT crystal lattice (Figure 9d).

In SEM images and DLS analysis of 4-HPG crystals, it was observed that the average particle size is between 500 nm and 1500 nm (Figure 10), rectangular prisms, and sharp-edged structures with regular geometric shapes. In addition, it was determined that the particles of 4-HPG were smaller than the crystals of amoxicillin, which were impurities.

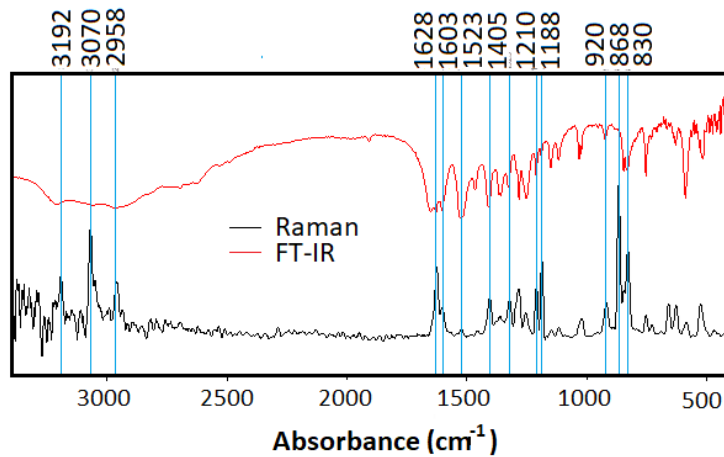


Figure 8: Comparison of FT-IR and Raman spectra.

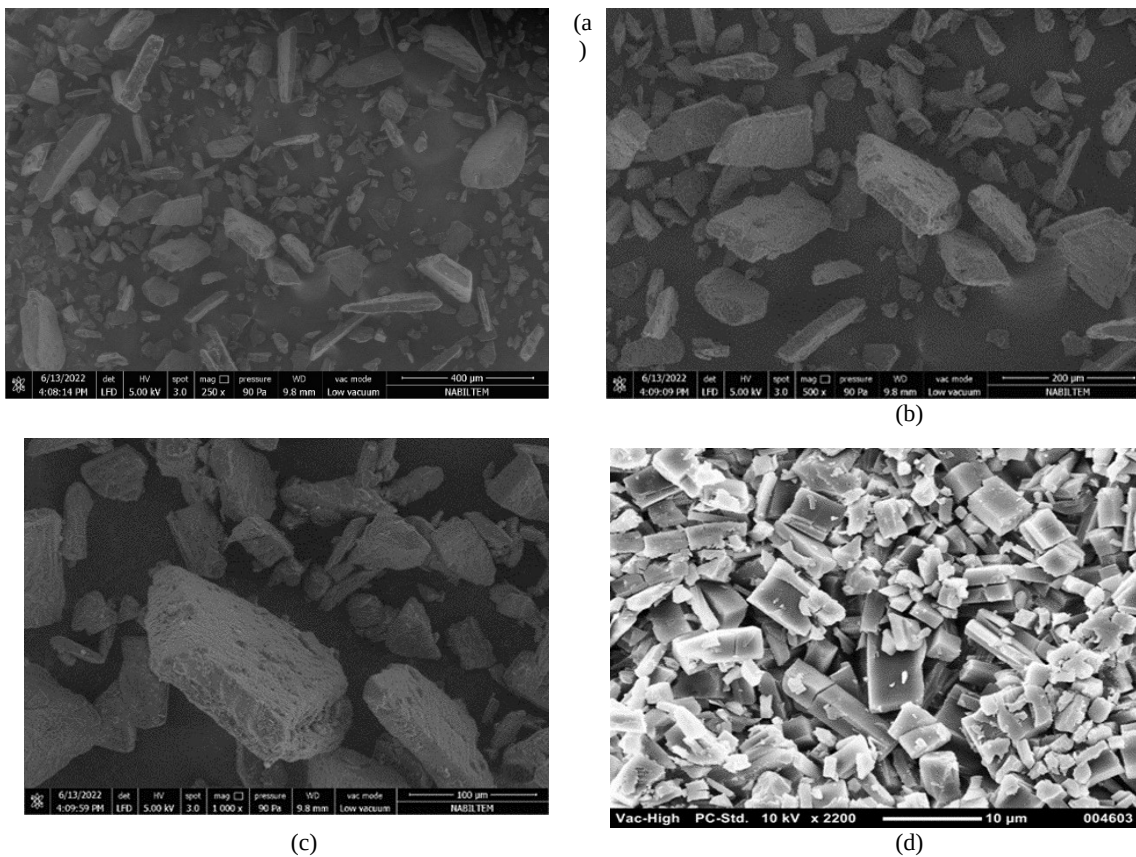


Figure 9: a,b,c) SEM images of 4-HPG and d) AMCT with impurities.

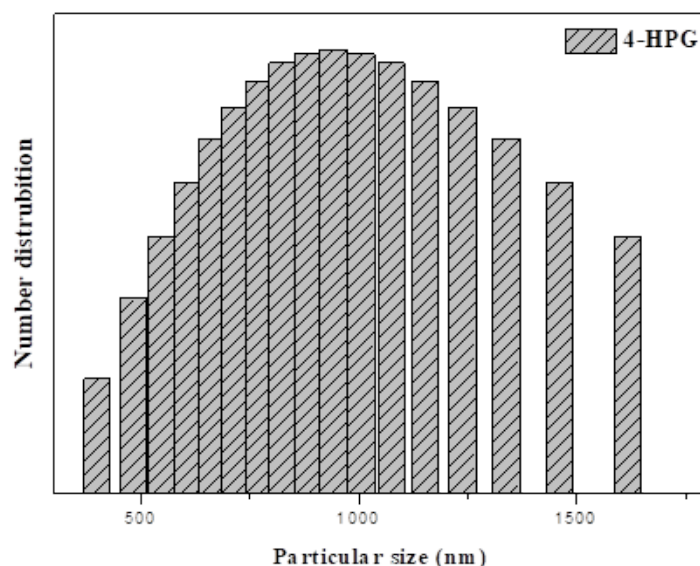


Figure 10: The particle size of 4-HPG crystals.

4. CONCLUSION

In an environment where competition is always intense in the pharmaceutical industry, one of the most important questions to address is how to achieve high yield rates and ensure product quality without compromising it. The fundamental solution to this issue, particularly in obtaining a pure product, lies in fully identifying and eliminating impurities that degrade quality. This study focuses on the detailed thermal, morphological, and physical characterization of 4-HPG, a significant impurity found in some of the most commonly prescribed β -lactam antibiotics worldwide, such as Amoxicillin, amoxicillin salt, amoxicillin trihydrate, cefadroxil, cefoperazone, cephalosporin, and cephalosporin hydroxylamine.

The study has helped us better understand the potential effects of 4-HPG on industrial applications and the quality of pharmaceutical products. Thermal analysis results have provided important insights into the thermal resistance and stability of 4-HPG, which can affect the stability and shelf life of relevant pharmaceutical products. XRD analysis has thoroughly revealed the structural properties of 4-HPG crystals, and this information can assist in understanding the crystal structures of relevant products and optimizing production processes. FT-IR and Raman spectroscopy shed light on the molecular structure of 4-HPG and provide a basis for understanding the potential effects of impurities on the quality of pharmaceutical products. These findings can play a significant role in the industrial applications of 4-HPG and the development of pharmaceutical products.

Given that 4-HPG significantly affects the shelf life and stability of antibiotics in which it is present, it is crucial to define its structure in detail.

7. REFERENCES

1. McGinity JW. Drug Stability: Principles and Practices. *Journal of Pharmaceutical Sciences*. 1991;80(1):98.
2. Ohannesian L, Streeter A. Handbook of pharmaceutical analysis: CRC Press; 2001.
3. Fiese E, Hagen T. Preformulation In: The Theory and Practice of Industrial Pharmacy. Lachman L, Lieberman HA, Kanig JL. Varghese Publishing House; 1990.
4. Wadke DA, Serajuddin AT, Jacobson H. Preformulation testing. *Pharmaceutical dosage forms: Tablets*. 1989;1:1-73.
5. Carstensen JT. *Pharmaceutical preformulation*: crc Press; 1998.
6. Gibson M. Pharmaceutical preformulation and formulation. *Drugs the pharmaceutical sciences*. 2001;199:199.
7. Adeyeye MC, Brittain H. Drug-excipient interaction occurrences during solid dosage form development. *THE PHARMACEUTICAL SCIENCES*. 2008;178:357.
8. Leite RS, Macedo RO, Torres SM, Batista CCN, Baltazar LO, Neto SL, et al. Evaluation of thermal stability and parameters of dissolution of nifedipine crystals. *Journal of thermal analysis calorimetry*. 2013;111(3):2117-23.
9. Kocevská S, Maggioni GM, Crouse SH, Prasad R, Rousseau RW, Grover MA. Effect of ion interactions on the Raman spectrum of NO₃⁻: Toward monitoring of low-activity nuclear waste at Hanford. *Chemical Engineering Research Design*. 2022;181:173-94.
10. Lagerman CE, Grover MA, Rousseau RW, Bommarius AS. Reactor Design and Optimization of α -Amino Ester Hydrolase-Catalyzed Synthesis of Cephalexin. *Frontiers in Bioengineering Biotechnology*. 2022;10.
11. Wiesław W, Krystyna S, Cezary C, Leszek Ł, Alicja M. Photophysical properties of (p-hydroxy) phenylglycine. *Journal*

- of Photochemistry Photobiology A: Chemistry. 1997;102(2-3):189-95.
12. Kaneko I, Fearon DT, Austen K. Inhibition of the alternative pathway of human complement in vitro by a natural microbial product, complestatin. *Journal of immunology*. 1980;124(3):1194-8.
 13. Báthori NB, Bourne SA. Crystal Structure of D (-)-amino-(4-hydroxyphenyl) acetate, the Zwitter Ionic Form of Biologically Active D (-)-4-hydroxyphenylglycine. *Journal of Chemical Crystallography*. 2009;39:539-43.
 14. Li S, Cao M, Li Y, Yang J, Zhao M, Song H. Three pairs of Pb (II), Cd (II) and Cu (II) enantiomeric coordination compounds based on D-(-)-and L-(+)-4-Hydroxyphenylglycine: Synthesis, structures and properties. *Journal of Molecular Structure*. 2022;1255:132451.
 15. Zhong Q-S, Xia W-Y, Liu B-C, Xu C-W, Li N. Co0. 85Se on three-dimensional hierarchical porous graphene-like carbon for highly effective oxygen evolution reaction. *International Journal of Hydrogen Energy*. 2019;44(21):10182-9.
 16. Mostaghazi E, Zarepour A, Zarrabi A. Folic acid armed Fe3O4-HPG nanoparticles as a safe nano vehicle for biomedical theranostics. *Journal of the Taiwan Institute of Chemical Engineers*. 2018;82:33-41.
 17. Liu B-C, Chen S-L, Ling X-Y, Li Q-X, Xu C-W, Liu Z-L. High activity of NiCo 2 O 4 promoted Pt on three-dimensional graphene-like carbon for glycerol electrooxidation in an alkaline medium. *RSC advances*. 2020;10(41):24705-11.
 18. He Y, Cheng Z, Qin Y, Xu B, Ning L, Zhou L. Facile synthesis and functionalization of hyperbranched polyglycerol capped magnetic Fe3O4 nanoparticles for efficient dye removal. *Materials Letters*. 2015;151:100-3.
 19. Kosmidis J, Williams J, Andrews J, Goodall J, Geddes A. Amoxicillin-pharmacology, bacteriology and clinical studies. *Brit J Clin Practice*. 1972;26(7):341-6.
 20. Chen C-X, Wu Q, Liu B-K, Lv D-S, Lin X-F. Anhydrous tert-pentanol as a novel media for the efficient enzymatic synthesis of amoxicillin. *Enzyme microbial technology*. 2008;42(7):601-7.
 21. Youshko MI, Moody HM, Bukhanov AL, Boosten WH, Švedas VK. Penicillin acylase-catalyzed synthesis of β -lactam antibiotics in highly condensed aqueous systems: Beneficial impact of kinetic substrate supersaturation: *Biotechnology bioengineering*. 2004;85(3):323-9.
 22. Giron D, Goldbronn C, Mutz M, Pfeiffer S, Piechon P, Schwab P. Solid state characterizations of pharmaceutical hydrates. *Journal of thermal analysis calorimetry*. 2002;68:453-65.
 23. Ergin M. Purification of amoxicillin trihydrate in the presence of degradation products by different washing methods. *CrystEngComm*. 2021;23(46):8121-30.
 24. ERGİN M. Yıkama Metodu Kullanılarak Saflaştırılan Amoksisilin Trihidratın Taguchi Yöntemi ile Optimizasyonu. *Journal of the Institute of Science Technology*. 2022;12(2):933-45.
 25. Hsi KH, Kenny M, Simi A, Myerson AS. Purification of structurally similar compounds by the formation of impurity-coformer complexes in solution. *Crystal growth design*. 2013;13(4):1577-82.
 26. Hsi KHY, Concepcion AJ, Kenny M, Magzoub AA, Myerson AS. Purification of amoxicillin trihydrate by impurity-coformer complexation in solution. *CrystEngComm*. 2013;15(34):6776-81.
 27. YAŞA H. Synthesis, characterization, and evaluation of antioxidant activity of new γ - and δ -imino esters. *Turkish Journal of Chemistry*. 2018;42(4):1105-12.
 28. Onar HÇ, Vardar BA. Synthesis and antioxidant activity of novel 8-formyl-4-substitued coumarins. *Bulletin of the Chemical Society of Ethiopia*. 2018;32(1):175-8.
 29. YAŞA H, Ergin MF, ERGİN A, ALKAN G. Importance of inert gases for chemical transportation. *Proceedings Book*. 2016:825.
 30. Ergin M, Yasa H. Determination of amoxicillin trihydrate impurities 4-HPG and 6-APA by means of ultraviolet spectroscopy. *Methods Applications in Fluorescence*. 2022.
 31. Celik Onar H, Ergin MF, Yasa H. Investigating the Role of Citric Acid as a Natural Acid on the Crystallization of Amoxicillin Trihydrate. *ACS Omega*. 2023;8(39):36344-54.
 32. Nugrahani I, Asyarie S, Soewandhi SN, Ibrahim S. Solid state interaction between amoxicillin trihydrate and potassium Clavulanate. *Malays J Pharm Sci*. 2007;5(1):45-57.
 33. Bisson-Boutelliez C, Fontanay S, Finance C, Kedzierewicz F. Preparation and physicochemical characterization of amoxicillin β -cyclodextrin complexes. *Aaps Pharmscitech*. 2010;11:574-81.
 34. Bhattacharya A, Araullo-Mcadams C, Meier MB. Crystallization induced asymmetric transformation: synthesis of Dp-hydroxyphenylglycine. *Synthetic communications*. 1994;24(17):2449-59.
 35. Fogazzi GB, Cantu M, Saglimbeni L, Daudon M. Amoxycillin, a rare but possible cause of crystalluria. *Nephrology Dialysis Transplantation*. 2003;18(1):212-4.
 36. Yokozeki K, Nakamori S, Eguchi C, Yamada K, Mitsugi K. Screening of Microorganisms Producing d-p-Hydroxyphenylglycine from DI-5-(-Hydroxyphenyly) hydantoin. *Agricultural biological chemistry*. 1987;51(2):355-62.
 37. Bhat SA, Ahmad SJoMS. FTIR, FT-Raman and UV-Vis spectral studies of d-tyrosine molecule. 2016;1105:169-77.
 38. Feng S, Shan N, Carpenter KJ. Crystallization of amoxicillin trihydrate in the presence of degradation products. *Organic process research development*. 2006;10(6):1212-8.
 39. Pharmacopeia U. USP 39-NF34. The United States Pharmacopeial. 2016.



Omnipotent Plant Sources Assisted Green Synthesis of Silver Nanoparticles: A Promising Chemical Sensing Tool

Anitha Selvaraj^{1,3} , Kannan Mukundamurthy^{2*} , Rangasamy Rajmohan³ 

¹Department of Chemistry, Sri Sairam Engineering College, Chennai, 600044, India

²Department of Chemistry, Ramakrishna Mission Vivekananda College, Chennai, 600004, India

³Department of Chemistry, Guru Nanak College, Chennai, 600042, India

Abstract: This article aims to analyze the various sensor applications of silver nanoparticles synthesized from green materials, particularly plant-based sources. The current shape in the field of nanotechnology is the synthesis of metal nanoparticles via environmentally friendly and more reliable green materials. The green route synthesis is found to be a promising method because of its congenial properties. It is economical, affable, and reproducible. Heavy metals have been dispersed widely in the environment, and they are well known for their virulent effects. Numerous methods are available to sense and detect those metals. The headway in the domain of nanotechnology is to synthesize AgNPs from green plants and to steer clear of the hazardous effects of metals. Efficacious synthetic routes via plant-mediated synthesized AgNPs open up easy and efficient sensing of hazardous metals in the environment. AgNPs have attracted many researchers because they have good biocompatibility and other outstanding properties. Remarkable electronic, catalytic, and optical properties have enabled AgNPs to be used as sensors in medical, biological, and chemical fields. This review highlights the application of PAGES-AgNPs as a chemical sensor for detecting heavy metals and organic compounds in the environment.

Keywords: Green synthesis; silver nanoparticles; plant extracts; sensor; plant material-assisted green synthesis; applications.

Submitted: October 4, 2023. **Accepted:** January 16, 2024.

Cite this: Selvaraj A, Mukundamurthy K, Rajmohan R. Omnipotent Plant Sources Assisted Green Synthesis of Silver Nanoparticles: A Promising Chemical Sensing Tool. JOTCSA. 2024;11(2):899-918.

DOI: <https://doi.org/10.18596/jotcsa.1370240>

***Corresponding author. E-mail:** kannanchem@rkmvc.ac.in.

1. INTRODUCTION

Nanomaterials have gained significant attention and are in high demand nowadays since they possess innate properties that deviate from the bulk. Particle dimensions ranging from 100 nm to less than 100 nm are categorised as nanoparticles. As the size of NPs decreases, a pronounced change in properties arises that makes them suitable materials that can be used in a wide variety of fields. Quantum effects and surface behaviour come into play in the above size range (1-3). A well-tunability of properties can be achieved by means of quantum effects. A researcher can fine-tune the material to bring about a drastic change in its optical and electrical properties, melting point, boiling point, fluorescence, and many others, as shown in Figure 1 (4-6). The surface-to-volume ratio

also plays a crucial role in catalytic studies and sensing properties. Controlling the agglomeration of nanoparticles is crucial to maintaining the properties mentioned above. A significant lead of nanomaterials over bulk materials in various fields like biomedical, drug delivery, bioimaging, tissue engineering, DNA nanotechnology, environmental remediation, agriculture, and catalytic fields is due to their significant surface modification along with their tunable physical properties (7). Several researchers have reported different metal-based nanoparticles for several biomedical applications, environmental remediation, and catalytic functions. Attributable to their remarkable characteristics and utility, MNPs like silver, gold, and copper were mainly focused on (8-9).

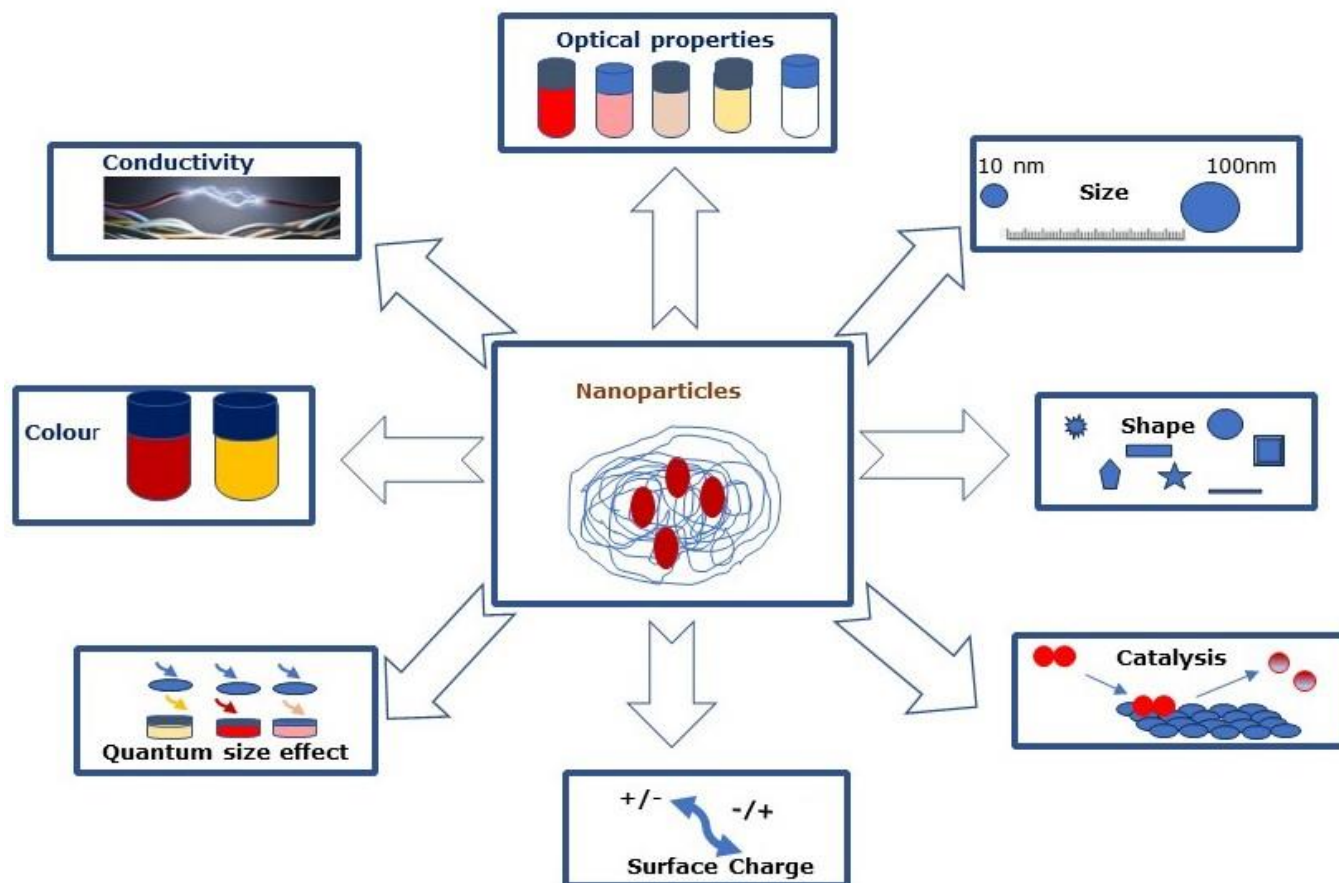


Figure 1: Properties of metal nanoparticles (NPs).

The main pathways for synthesizing nanoparticles traditionally adhered to by researchers are the bottom-up method and top-down method, i.e., building nanoparticles from molecular components by the self-assembly method and constructing nanoparticles from larger entities, respectively, as shown in Figure 2. The above-mentioned methods provide large-scale production and a well-controlled size and shape. But the negative impact of these methods is related to environmental issues and economic concerns. Furthermore, conventional methods require hazardous chemicals and solvents that cannot be used in the medical and clinical fields. To resolve this problem, researchers nowadays prefer to use green route synthesis over conventional methods. The blooming of green protocols for the synthesis of nanoparticles rebuffs the use of hazardous chemicals and solvents and the production of by-products (10-12).

The greener route is the safest and non-hazardous route for the synthesis of MNPs. It has many strategic and prospective advantages over other methods due to its eco-friendly nature and inexpensiveness. Moreover, the greener route of synthesis does not incorporate any hazardous chemicals, high temperature, or pressure. In addition, the framework and stabilization were achieved by the slow crystallization of MNPs (13). Many researchers have reported that plants seem to be the best contenders compared to

microorganisms for the synthesis of MNPs on a larger scale. Various plant parts, such as fruits, stems, roots, flowers, gums, seeds, and leaves, contain numerous biomolecules that can act as reducing and stabilizing agents for the synthesis of nanoparticles at a faster rate compared to the use of microorganisms. It can also be used to produce nanoparticles of different sizes and shapes (14-15).

A miscellany of metabolites found in plants, including carbohydrates, polypeptides, terpenoids, flavonoids, enzymes, alkaloids, phenolic compounds, and vitamins, possess many vital functionalities. These functionalities serve as ligands, anchoring the organic moiety onto the NPs (16). The various plant sources used to synthesize MNPs are shown in Figure 3. The plant materials are rich in phytochemical constituents like flavonoids and polyphenols. These chemicals are natural antioxidants and can serve as reducing agents. The functional molecules within plant materials react with metal ions, initiating the nucleation step of nanoparticle formation and further assisting in the reduction of metal ions to their zero-valent state, facilitating the formation of metal NPs. The various functional, natural polymeric moieties present in the plant materials, such as polypeptide and polysaccharide units, adhere to the surface of the AgNPs as a capping agent, thus preventing the agglomeration of the nanoparticles and aiding in the stabilization of silver nanoparticles.

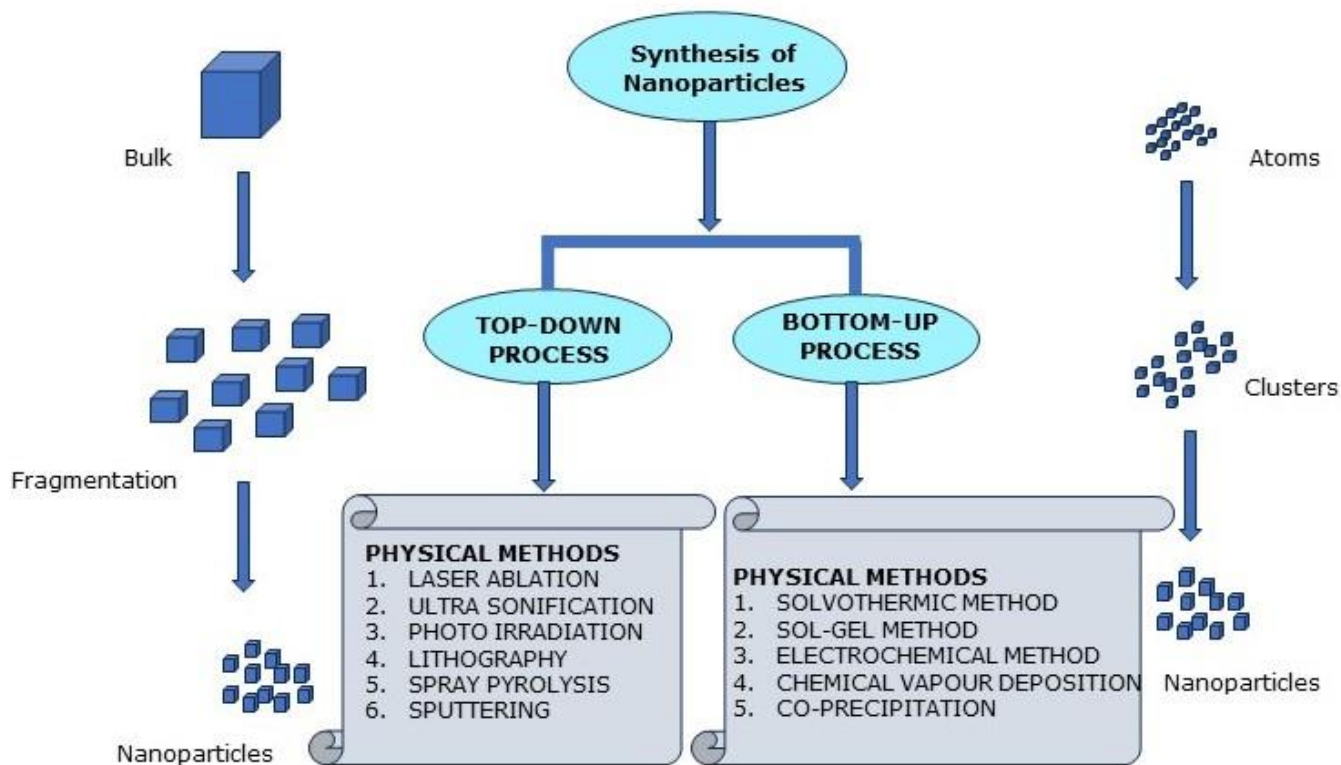


Figure 2: General methods of nanoparticle synthesis.

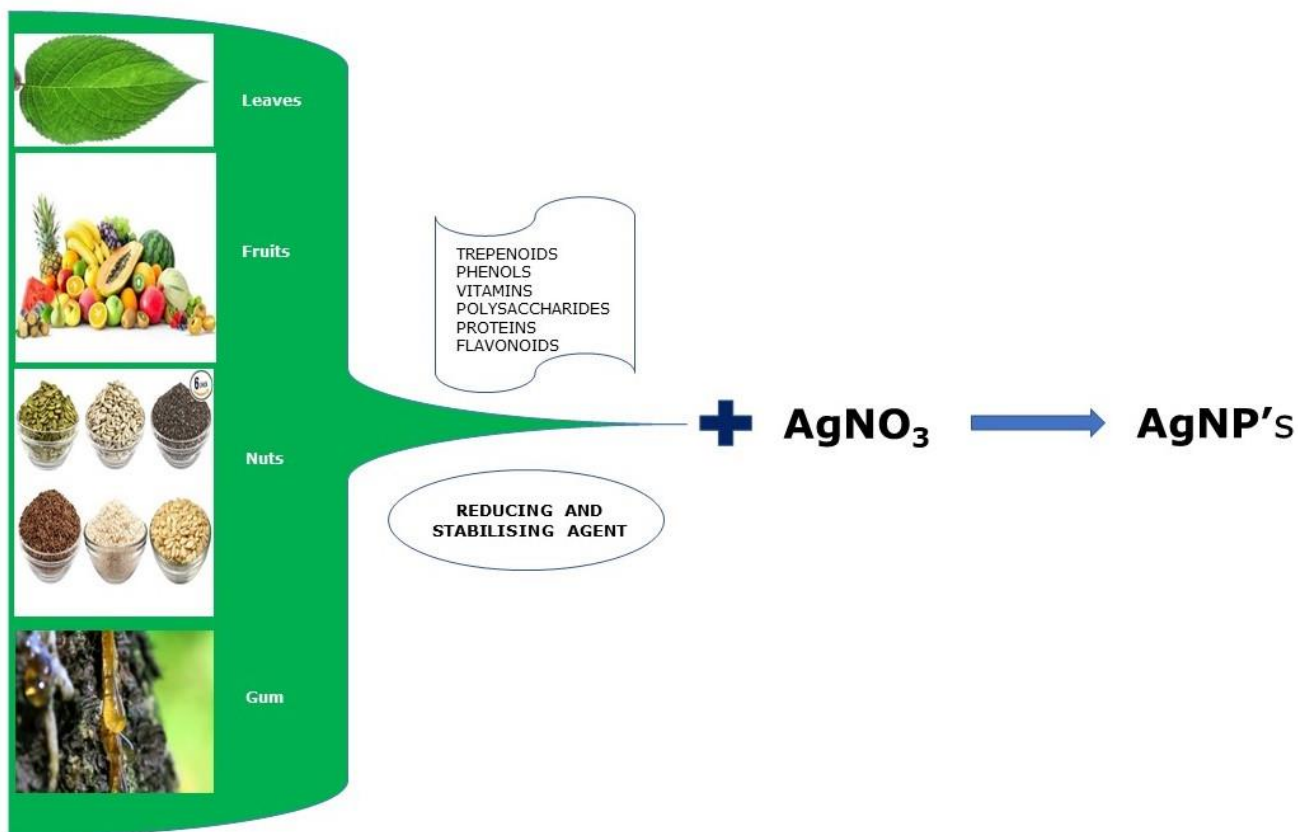


Figure 3: Various plant sources for silver nanoparticle synthesis.

This article discusses the literature based on the sensing applications of AgNPs. In particular, the plant material-assisted green synthesized AgNPs are focused. These PAGES-AgNPs serve as efficient, tiny functional materials and are used as a sensing tool. In this review, the greener route for the synthesis of AgNPs is briefly elaborated. The greener route is inclined towards the Sustainable Development Goals (SDG) because it is performed in ambient conditions and products are environment-friendly (SDG-3), cost-effective and safe (SDG-7), and fast and easy to scale up (SDG-9).

PAGES-AgNPs offer many features to serve as an excellent probing tool for sensing applications. We aimed to spotlight a few literature findings under this category. The prominent characteristics of the NPs are the surface plasmon resonance (SPR) and their absorption peak in the UV-Visible spectra. Changes in this SPR behaviour of the PAGES-AgNPs were analyzed by the researchers for the sensing of the probe. All AgNPs have a unique colour, and variation of this colour upon addition of a selective metal-ion/chemical was employed for its detection purpose. Researchers also monitored the alteration in the electrochemical characteristics of the PAGES-AgNPs by adding H_2O_2 , phenol, and nitrobenzene and utilizing them for sensing applications. In the literature, PAGES-AgNPs show significant fluorescence. The FRET process in the presence of metal ions was resorted to for sensing purposes.

2. EXPERIMENTAL SECTION

2.1. Characterisation of Green Synthesised Nanoparticles

The characterization of green synthesized MNPs can be carried out using numerous techniques, as shown in Figure 4 (17-18). This article tries to enlighten us about the application of green synthesized AgNPs as sensors in various fields.

2.2. Greener Strategy for AgNPs Synthesis

MNPs have potential roles in the biomedical field, environmental remediation, food packaging, electronic components, catalytic agents, and semiconductors (19-21). Among the various MNPs available, AgNPs are found to be a fascinating nanomaterial for environmental systems and biomedical applications. It plays a crucial role in the diagnosis and treatment of viral diseases. AgNPs act as biosensors for sensing metal ions, pesticides, and fungicides in the environment. It also plays a key role in the degradation of harmful synthetic organic dyes, which are very hazardous to humans and the environment. Moreover, MNPs have been used in antiparasitic, antiviral, antifungal, anti-diabetic, and anticancer therapies. For wound repair and bone healing, AgNPs show bactericidal effects (22-29). Plant-based sources for AgNPs synthesis dominate the literature in the greener approach. Recent reviews based on the green synthesis of AgNPs are listed in Table 1. The various plant-based methodologies were discussed in the references therein.

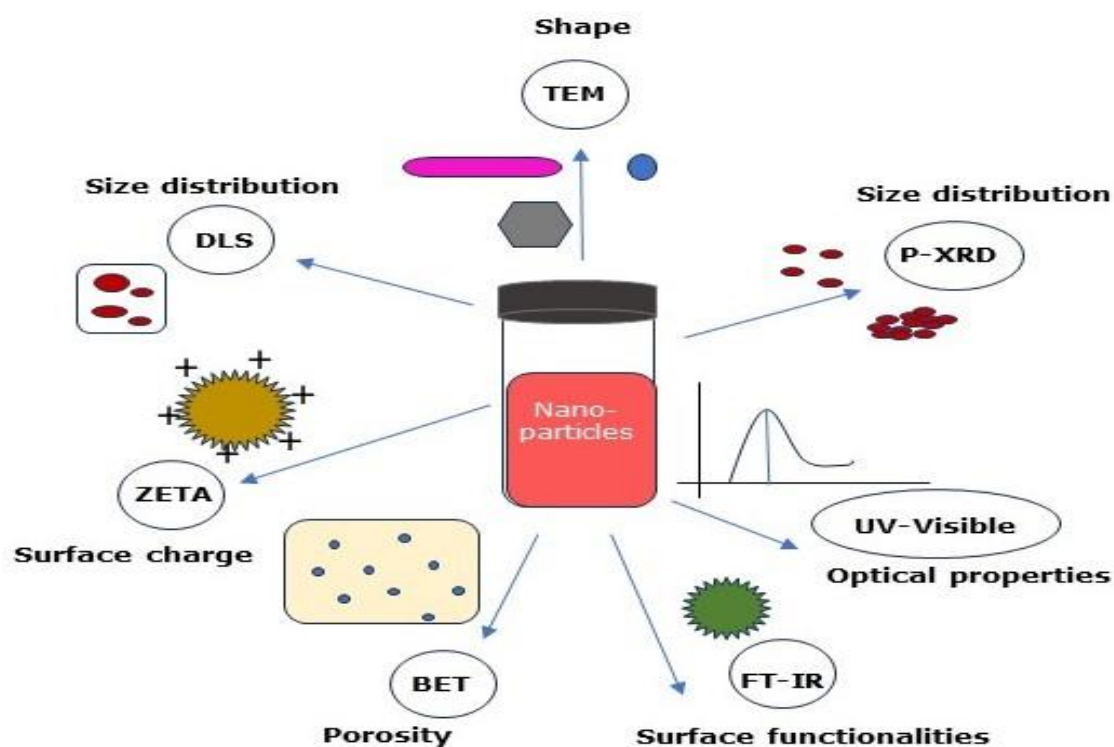


Figure 4: General characterisation techniques of metal nanoparticles (MNPs).

Table 1: Literature reviews based on the green synthesis of AgNPs.

Green synthesis methodology	Remarks	References cited therein Plant-based synthesis (total synthesis-based)	Ref.
Discussed biological approaches	Bio-medical applications Nano bio-sensors Agricultural engineering Applications in clothing and fabrics	90 (134)	30
Various biological approaches (both from plant extract and microorganisms)	Bioactivities	38 (60)	31
Major focus based on plant sources Discussed Extract preparation Steps involved Mechanism Factors	Characterization techniques Biological applications	>40	32
Discussed biological approaches	Bioactivities	78 (120)	33
Exclusively based on fruit and vegetable sources	Factors affecting synthesis	33	34

This review assessed recent advancements in the environmentally friendly synthesis of silver nanoparticles (AgNPs) and their potential applications in sensing. PAGS is reviewed exclusively due to their precise control over NPs size, shape, and composition. AgNPs are produced from various plant parts, such as leaves, roots, gums, flowers, seeds, stems, and fruits. Research has shown that biomolecules, including alkaloids, phenolic compounds, terpenoids, enzymes, co-enzymes, proteins, polysaccharides, lipids, etc., are present in the plant extract. These molecules act as both reducing and capping agents for the synthesis of AgNPs. In literature reports, the general procedure for synthesizing AgNPs is mixing silver nitrate solution with reducing agents extracted from plants. Plant extracts are obtained using the below-mentioned standard procedure Flow chart-1.

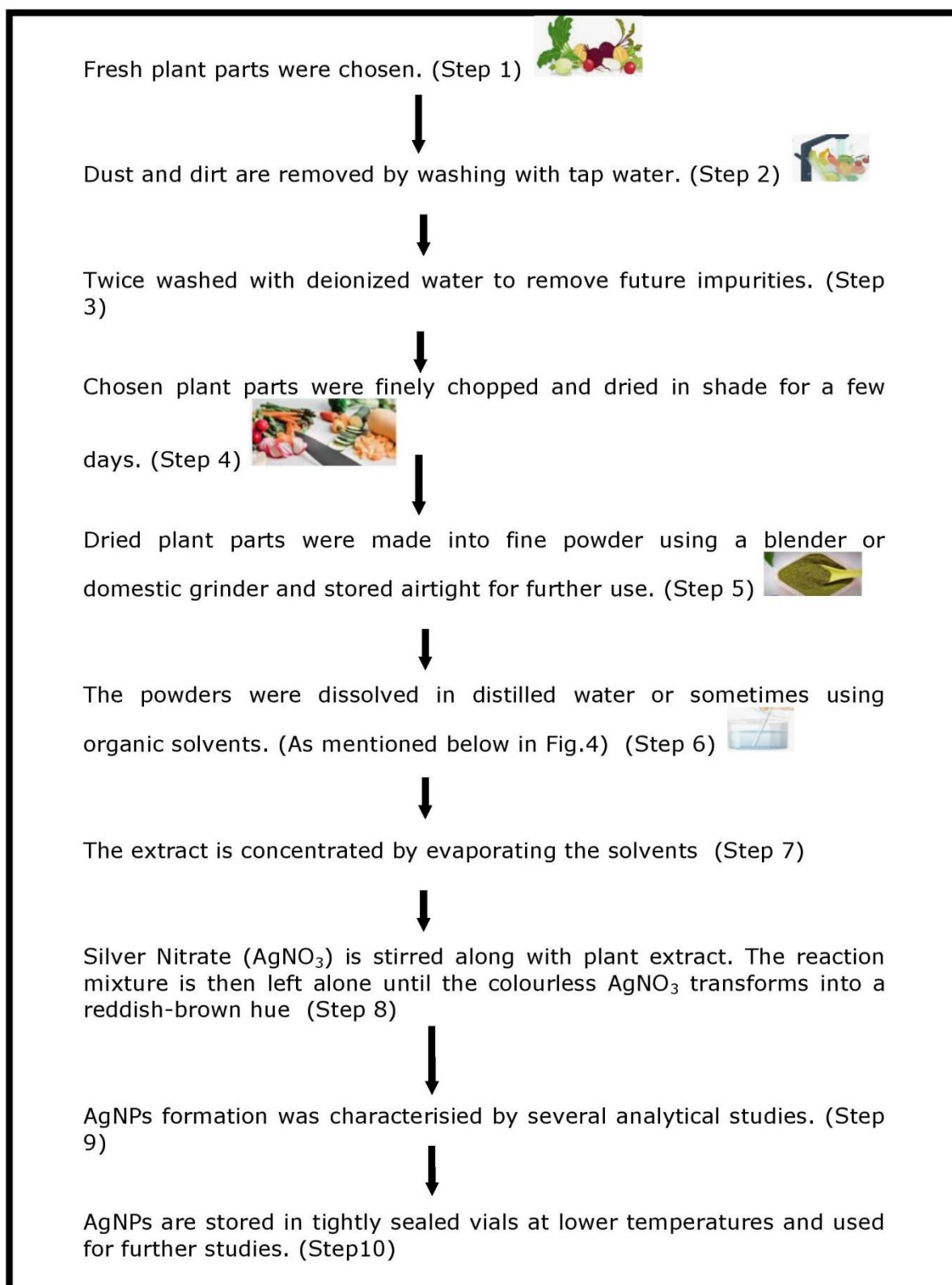
Earlier literature reports confirm the AgNPs formation by the colour change of the reaction medium to brownish or brown-orange colour (30-34). In 2022, Deepa and co-researchers reported that the presence of phenolic acid and flavonoids in the vegetable peels of pea (*Pisum sativum*) and bottle gourd (*Lagenaria siceraria*) constitutes potential functional groups contributing to the stability of nanoparticle synthesis (35). Lakshmanan et al. (2017) reported that rich concentrations of both enzyme and non-enzyme-based antioxidant molecules, including ascorbic acid, glutathione-S-transferase, superoxide dismutase, peroxidase, and polyphenol oxidase, were present in the *C. viscosa* fruit extract. Reduced glutathione, flavonoids, and a-tocopherol are present in *C. viscosa*

fruit extract, which acts as a capping and reducing agents in the synthesis of silver nanoparticles (36). The study by Samrot and coworkers shows that *Azadirachta indica* gum contains complex polysaccharides that act as capping and reducing agents in the synthesis of silver nanoparticles (37). Anthocyanin-containing purple heart-shaped ornamental plant was utilized by M. Saquib Hasnain et al. in 2019. It is anticipated to help with the reduction of silver ions during the anthocyanin-mediated synthesis of silver nanoparticles (38). Manik et al. (2020) revealed that bio compounds such as flavonoids, alkaloids, and polyphenols present in the leaves of *Artocarpus heterophyllus* and *Azadirachta indica* act as reducing and stabilizing agents for AgNPs synthesis (39). Sandhanasamy Devanesan et al. (2021) synthesized spherical AgNPs from *Abelmoschus esculentus* (L.) freshly picked flowers (40). Biomolecules such as polyphenolic compounds, catechins, flavanol, and tannins are responsible for the reduction and stability of AgNPs.

2.2.1. Stepwise procedure for plant-material assisted green synthesis (PAGS) of silver nanoparticles (AgNPs).

The step-by-step procedure used by several researchers to create AgNPs utilizing plant extracts is illustrated in Flow Chart 1.

Literature methods available in the extraction of plant material (Figure 5).



Flow chart 1: Procedural sequence of PAGES-AgNPs synthesis.

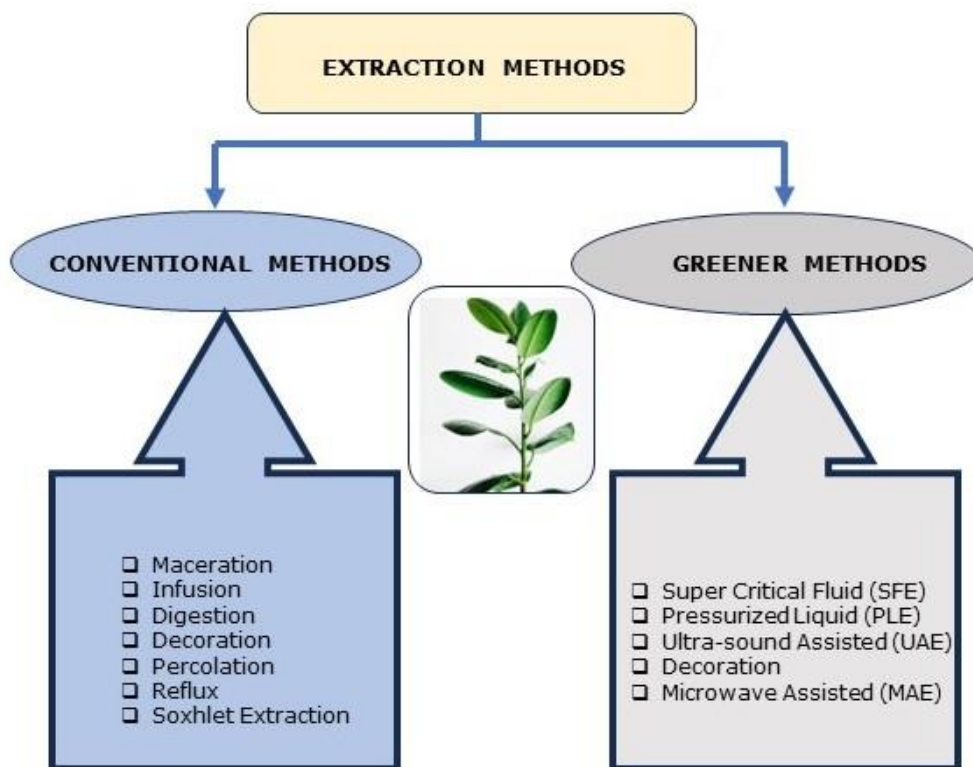


Figure 5: General plant extraction techniques.

2.3. Mechanism of Synthesis of AgNPs from Plant Sources.

Several researchers have reported a disparate variety of plant sources for synthesizing AgNPs. The phytochemical constituents act as reducing agents and stabilize the nanoparticles from agglomeration. Most literature studies show that no additional reducing agents are required (41).

The following steps are involved in the synthesis of AgNPs as shown in Figure 6.

a) Organic moieties present in the plant material add electrons to the Ag^+ .

b) Reduction of Ag^+ to Ag^0 followed by nucleation, occurs.

c) The agglomerating agent present in plants stabilizes the formed nanoparticles.

The agglomeration of nanoparticles occurs due to the attraction and adhesion of particles using weak vanderwals forces. It is reported in the literature that small nanosized particles agglomerate faster compared to larger-sized nanoparticles. The phytochemical constituents in plant extract not only act as a reducing agent but also help to control the agglomeration by sticking to the nanoparticle surface.

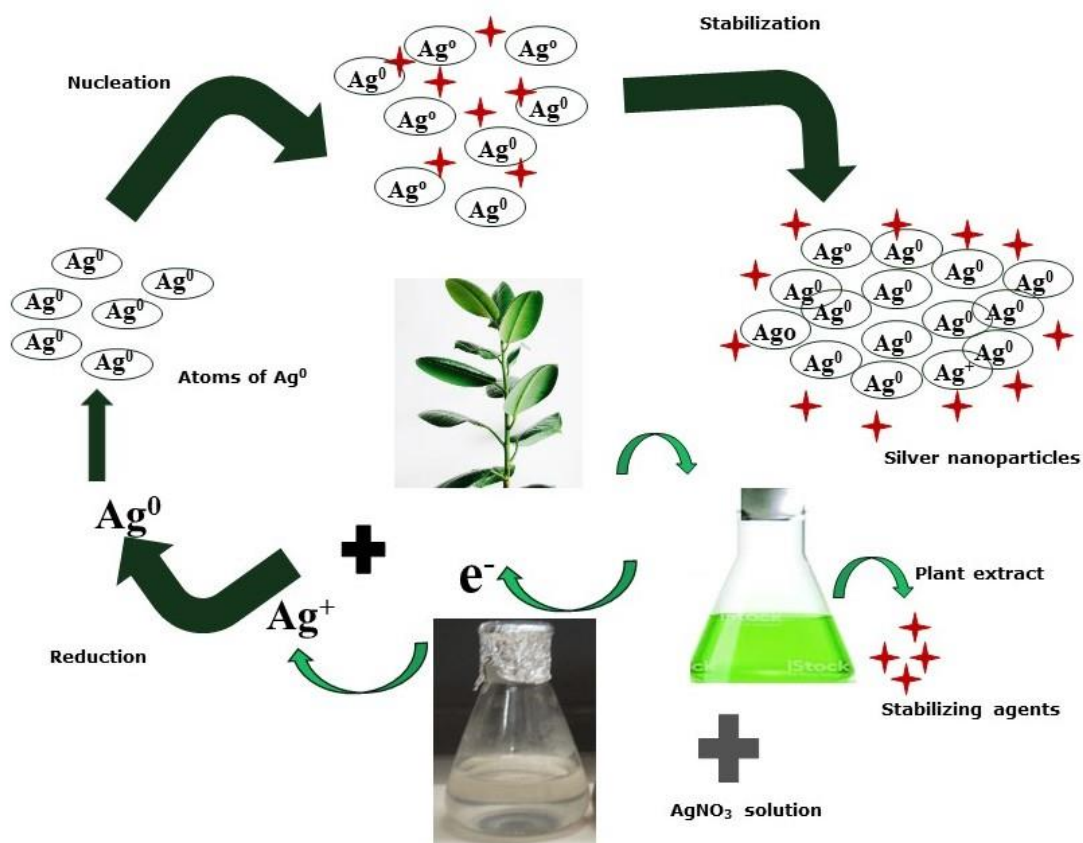


Figure 6. General mechanism for the formation of PAGES-AgNPs.

3. RESULTS AND DISCUSSION

3.1. Applications of PAGES-AgNPs

Researchers were attracted by the astounding properties of AgNPs compared to their bulk analogs and included them in numerous applications. Due to their excellent biocompatibility, size, and shape, AgNPs find their applications in the fields of solar cells, bio-sensing, image sensing, catalysis, nano-device fabrication, optical detectors, drug delivery, and so on (42-43). There have been several reviews in the past on the applications of AgNPs in various fields. A few of them are highlighted here. The author presents a bird's-eye view of the therapeutic application of green synthesized AgNPs (44). Kareem et al. (2020) shed light on the photocatalytic applications of AgNPs in a recent review (45). The review report by Mousavi et al. (2018) reveals that PAGES-AgNPs are more preferred for antimicrobial, antibacterial, and anticancer activity (46). The synthesis and application of various PAGES-AgNPs are reviewed by Jaffri and Shahzad Ahmad (47). The adaptability of PAGES-AgNPs in various medical fields was highlighted by Ill-Min Chung et al. in their review (48). A comprehensive review by Moradi et al., exclusively addressing AgNPs synthesized from medicinal plant materials and correlating plant materials and their correlation of plant biological constituents with

various applications, is well presented in the literature (49). Fahimirad et al. discussed the superiority of the green synthesis method compared to physio-chemical methods and also considered it a better candidate for medical applications (50). PAGES-AgNPs applications in cancer diagnosis and treatment were exclusively reviewed by Rath et al. (51).

3.2. Application of PAGES-AgNPs as Sensors.

Faraday & Philos, in 1857, were the first to recognize the fact that colloidal suspension has strong light absorption and scattering, resulting in intense colors. The optical excitation of the surface plasmon resonance (SPR) originates from the absorbed light. It excites the electrons in the conduction band of the nanoparticle. This absorption attains large molar extinction coefficients and relevant scattering as the particles reach a size larger than a few hundred atoms/molecules (nanometers). This optical scattering property is utilized in biosystems for imaging detection methods and is also applied as a diagnostic tool in various biological systems, such as cancer cells. The plasmon resonance response sensitivity can be enhanced by varying the geometries with the purpose of finding the best nanoparticle configuration. The same is exemplified in many theoretical and experimental studies of metal nanoparticles.

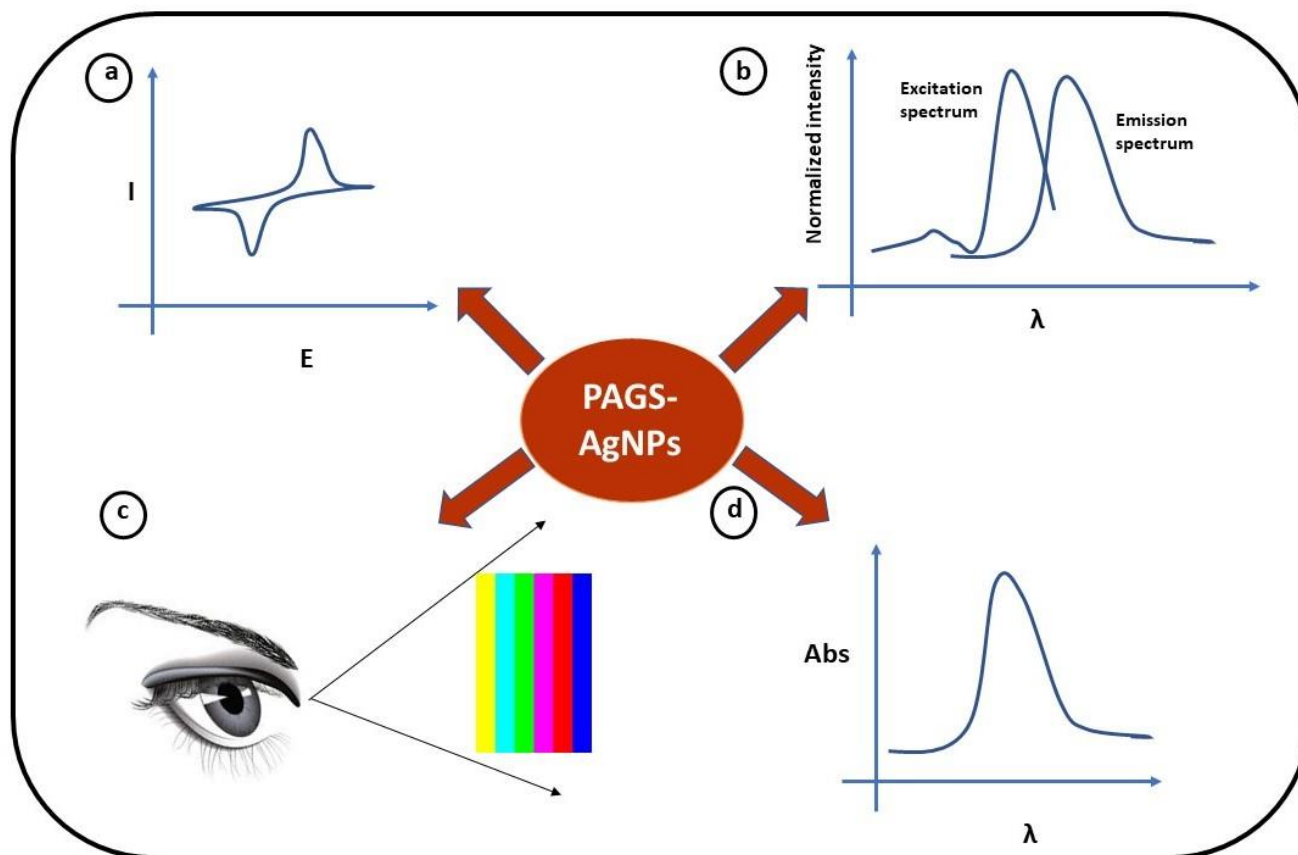


Figure 7: Scheme representing sensing methods by PAGS-AgNPs.

a) Electrochemical techniques **b)** Fluorimetry **c)** Naked eye detection **d)** UV-Visible spectrometry.

The sensing application of silver nanoparticles (AgNPs) was well documented in the form of several reviews. Various modifications of electrodes for electrochemical sensing of chemicals are discussed in detail in the recent review (52). A review in 2021 highlighted AgNP-modifier-based electrochemical sensors as systematic tools for detecting various organic pollutants in water (53). The utility of AgNPs as an electrochemical biosensor is also highlighted in the review (54). Pomal et al. exclusively reviewed the sensing of mercury ions by colorimetric and fluorimetric methods by PAGS-AgNPs (55). Jouybana and Rahimpour extensively reviewed the spectro-chemical sensing of pharmaceutical compounds by the LSPR of AgNPs (56). The chemical contaminants in the food are sensed by various NPs, including AgNPs, as presented in the review of 2019 (57). The focus of the current review is only on four sensing platforms for the detection of specific chemicals, which are schematically represented in Figure 7.

3.3. PAGS-AgNPs Sensor for H₂O₂ Detection.

The literature recently reported the naked-eye detection of H₂O₂ using a sucrose solution in an alkaline medium (58). Even though the synthesized AgNPs were not from a plant-mediated route, the method adopted shows a close resemblance to a plant-mediated route. Since sucrose is a plant derivative and does not violate the greener route, the utility of the AgNPs can be extended for plant-mediated routes with minor modifications. The authors analyzed the colour change based on the red,

blue, and green color intensity variations. Since the AgNPs are yellow, their complementary blue color was monitored. The authors were able to show a significant change in the blue color intensity at 1×10^{-3} M concentration of H₂O₂, which is the detection limit in most of the literature reports. The simplified scheme for analyte detection by the colorimetric method is represented in Figure 9.

Researchers cast the cellulose fibers with AgNPs for H₂O₂ detection (59). It is an attempt to extend the plant-mediated AgNPs towards the paper-based technical application end to detect hydrogen peroxide. Literature shows that green silver nanoparticles synthesized using *Mangifera indica* leaf extracts were characterized by UV-Visible spectroscopy and TEM. These PAGS-AgNPs are drop-casted on the cellulose substrate and applied for sensing H₂O₂. The change in colour of the substrate from yellow to white upon increasing the concentration from μ M to mM confirms its presence.

Researchers also successfully fabricated the optical fiber using plant-mediated AgNPs for sensing purposes (60). They also demonstrated the effect of the concentration of the anchoring agent locust bean gum (LGB) on the synthesized AgNPs absorbance, showing a decrease in the absorbance of AgNPs by increasing the concentration of LGB. They concluded that the above effect may be due to the strong capping of the anchoring agent and, consequently, the deep burying of the NPs beneath the anchoring

agent, thus reducing the absorbance. The fabricated optical fiber shows effective sensing properties for H_2O_2 detection. The power output was significantly lowered by the mM concentration of H_2O_2 solution. The added H_2O_2 decreases the concentration of AgNPs, which is a consequence of oxidation and, in turn, a decrease in the back scattering of light from AgNPs. These results open up plant-mediated AgNPs applications in the field of optical fiber-based sensing. The concentrations of H_2O_2 were measured as the output voltage of the optical fiber immersed in the AgNPs and H_2O_2 mixture. The observed results were the consequence of the degradation of AgNPs by the addition of H_2O_2 to the solution. As the NP concentration diminished, an alteration of the colour and refractive index of the medium was observed. The decrease in backscattering light intensity from AgNPs acts as a mirror, and as a result, power output also decreases. This phenomenon was utilized for the sensing purpose of H_2O_2 . The utility of the environmentally friendly renewable source, ambient conditions, and its sensing features further widen the scope of green nanoparticle synthesis.

Researchers showed that the AgNPs synthesized using *Atalantia monophylla* leaf extracts show H_2O_2 sensing characteristics besides their antimicrobial activity against pathogenic microorganisms (61). The authors characterized the AgNPs by various spectroscopic techniques like Ultraviolet-Visible spectroscopy, photo-luminescence spectroscopy, SEM with EDAX, and TEM. The anchoring of the plant extract constituents was analyzed by FTIR studies, confirming the functional group on silver nanoparticles. They have also highlighted that the antimicrobial activity of AgNPs was found to be superior to that of the standard antibiotics.

Researchers also prepared stable AgNPs by using azadirachtin as an anchoring and reducing agent (62). The authors modified the glassy carbon electrode (GCE) with PAGES-AgNPs and used it for the sensing purpose of H_2O_2 . The modified GCE sensitivity was retained for H_2O_2 detection for 100 days, even after exposure to air. The AgNPs attached to the GC were more stable than the unmodified NPs and the sensitivity was not diminished. The sensitivity was measured for tap water using the AgNPs-modified GC. The results showed an increase in the recovery percentage as the concentration increased. The simplified scheme for the detection of analytes by the electrochemical method is represented in Figure 8.

Researchers observed the change in optical characteristics of the colloidal AgNPs at a wavelength of 425 nm (63). The SPR decreases with an increase in hydrogen peroxide concentration. The observed phenomenon was due to the formation of Ag_2O with the addition of H_2O_2 at the expense of AgNPs. The change of colour to yellow from brownish red was observed by the addition of 30 mM H_2O_2 solution. Even the colour change was evident to the naked eye, which was further confirmed by the UV-Visible spectrometer measurements. The summary of the PAGES-AgNPs as H_2O_2 sensors is tabulated in Table 2.

3.4. PAGES-AgNPs Sensor for NH_3 Detection

In 2021, researchers reported the detection of H_2O_2 and NH_3 in water from the tannery outlet near University, Khon Kean, Thailand, using the plant-mediated AgNPs synthesized (63). The reports revealed that 2 mL of the environmental water contained 50 mM of hydrogen peroxide and 30 ppm of ammonia, respectively. The result was a significant step towards plant-mediated AgNPs for sensing hydrogen peroxide and ammonia in water resources.

In 2019, a research group used a leaf extract of *C. cneorum* in an aqueous medium to synthesize stable AgNPs (64). They drop-cast the filter paper with PAGES-AgNPs and used it for sensing purposes after drying. The changes in the surface plasmon resonance (SPR) peak of the PAGES-AgNPs were used for the detection of ammonia through the UV-Visible spectrophotometer. The authors varied the concentration of ammonia from 5 – 300 ppm, and the SPR spectra showed an increase in intensity as concentration increased, accompanied by a blue shift of the peak. The blue shift is due to the accumulation of positive charge by the formation of the coordination complex $[Ag(NH_3)_2]^+$ and also to the change in the dielectric constant of the solution.

Rapid sensing of ammonia in an aqueous medium up to a detection limit of 1 ppm at ambient conditions was published by researchers (65). AgNPs synthesized using an aqueous solution of polysaccharide from *Cyamopsis tetragonaloba*, commonly known as guar gum (GG), act as a reducing and capping agent. The uniformity of the particle size was well characterized by the available techniques. The ammonia in an aqueous medium was detected using the surface plasmon resonance (SPR) of the AgNPs. This optical method of sensing ammonia in an aqueous medium at lower limits can prove vital in the field of biomedical applications in the future. Since the sensing parameter can be useful in the clinical and medical diagnostics of ammonia detection in biological fluids like sweat, plasma, cerebrospinal fluid, and saliva, it can serve as a better sensor for biological samples. A report on optical sensing of ammonia by the PAGES-AgNPs, synthesized using chemically modified guar gum (carboxymethyl guar gum), is available (66).

Very recently, researchers reported plant-mediated AgNPs for sensor studies based on the SPR properties of the nanoparticles. The synthesized AgNPs that exhibit good sensing features with quick response and relaxation are claimed to be a simple and affordable material for industrial production (67). Researchers were successful in producing monodisperse AgNPs from durian fruit shells as anchoring agents. This material, if developed, can be a future candidate in the field of sensors for the diagnostics of biological samples.

Table 2. Literature Summary of PAGS-AgNPs as H₂O₂ sensors.

Plant material	Significance / relevant property	Detection limit	Technique used	Ref
Sucrose solution	Naked eye / (RGB) color values	1×10^{-3} M	Colorimetric detection	58
Leaves of <i>Mangifera indica</i>	Paper based technique	Significant only above mM	Colorimetric detection	59
LBG extracted from the seeds of <i>Ceratonia siliqua</i>	Fiber based sensor	0.1 mM	Photo detector / Out voltage measured in the fiber	60
<i>Atalantia monophylla</i> leaf extracts	Antimicrobial activity is also studied	40 mM	UV spectroscopy (Fluorescence also measured for AgNP alone)	61
Neem kernel extract	GC electrode	1 mM	Amperometry	62
Sugarcane leaves extract	Water resource from tannery tested / SPR	30 mM	UV-Visible spectrophotometer	63

The research group used AgNPs synthesized from the aqueous fruit extract of *T. Chebul* (68). These PAGES-AgNPs showed excellent optical sensing features for ammonia detection, exhibiting linear changes in the SPR with the concentration of NH₃ in the medium. The authors highlighted the change in intensity of the peak along with the blue shift caused by the significant change in the NH₃ concentration of the medium. The authors confirmed the reduction in the size of the AgNPs from 30 nm to 50 nm in the control experiment with the addition of NH₃, using the TEM images. The reduction in the size of NPs was stated to be due to the formation of soluble diamine complexes with phenolate ions present in the fruit extract. The role of the phenolate ion is to speed up the nucleation step prior to the size reduction.

Researchers reported the viability of large-scale production of plant-mediated AgNPs using the fresh aqueous extract of *D. erecta* fruits. They used the synthesized AgNPs for colorimetric sensing of Cr⁶⁺ and NH₃ (69). The sensing characteristics of the AgNPs were attributed to the constituent organic moieties, such as the bulky hydroxyl groups found in polyphenols and flavonoids from the plant extracts. The SPR-based sensing showed a detection limit of 0.5 ppm and a fast response time for AgNPs. It can pave the way for sensors in the field of medical diagnostics to have lower detection limits in the future. The summary of the PAGES-AgNPs as NH₃ sensors is tabulated in Table 3.

Table 3: Literature summary of PAGES-AgNPs as NH₃ sensors.

Plant material	Detection limit (ppm)	Significance / property	Technique used	Ref
Sugarcane leaves extract	5	Water resource from tannery tested / SPR	UV-Visible spectrophotometry	63
Leaf extract <i>C. cneorum</i>	5	Sensing strip / novel cellulose filter paper-based AgNPs	Colorimetry	64
Polysaccharide GG	1	Applicable for biological fluids / SPR	UV-Visible spectrophotometry	65
Durian fruit shell extract	500	Applicable for biological fluids / SPR	UV-Visible spectrophotometry	67
Fruit extract of <i>T. chebula</i>	100	Size reduction / SPR	UV-Visible spectrophotometry	68
<i>D. erecta</i> fruit extract	0.5	Detection of Cr ⁶⁺ also	Colorimetry	69

3.5. PAGES-AgNPs Sensor for Phenol Detection

Very recently, researchers reported the synthesis of AgNPs using five different leaf sources, such as basil, geranium, eucalyptus, melia, and ruta by a greener route (70). Among them, AgNPs using *Melia azedarach* (AgNPs-M) were found to show exciting electrochemical properties, that the research group has captured toward selective sensitivity for phenol. The AgNPs-M-modified GCE electrode was used for phenol sensing. This group has fabricated the novel GCE by drop-casting the AgNPs-M onto the surface of glassy carbon transducers and using them as modified nanosensors. The AgNPs-M modified GCE showed good selectivity for sensing phenol, bisphenol A, and catechol. Particularly, the sensitivity of phenol was significant and excellent since its limit of detection is about 0.42 μM. The authors also showed reproducibility and sensitivity with the RSD values.

The applicability of AgNPs-M modified GCE as a phenol sensor was also successfully tested for tap and mineral water. The test was conducted with a water sample and a phosphate buffer solution with 5–8 μM phenol added to the buffer solution. The employed modified GCE produced excellent results with a recovery percentage >100. This work has enough potential to be adopted as a sustainable large-scale production of the AgNPs-M modified GCE nanosensor since the material production is simple, cost-effective, enormously available, and environmentally friendly. The authors showed adequate results for proving the potential of the novel material as a nanosensor and with minor surface engineering, it can prove to be a future candidate for phenol sensing in water quality monitoring. The simplified scheme for the detection of analyte by electrochemical method is represented in Figure 8.

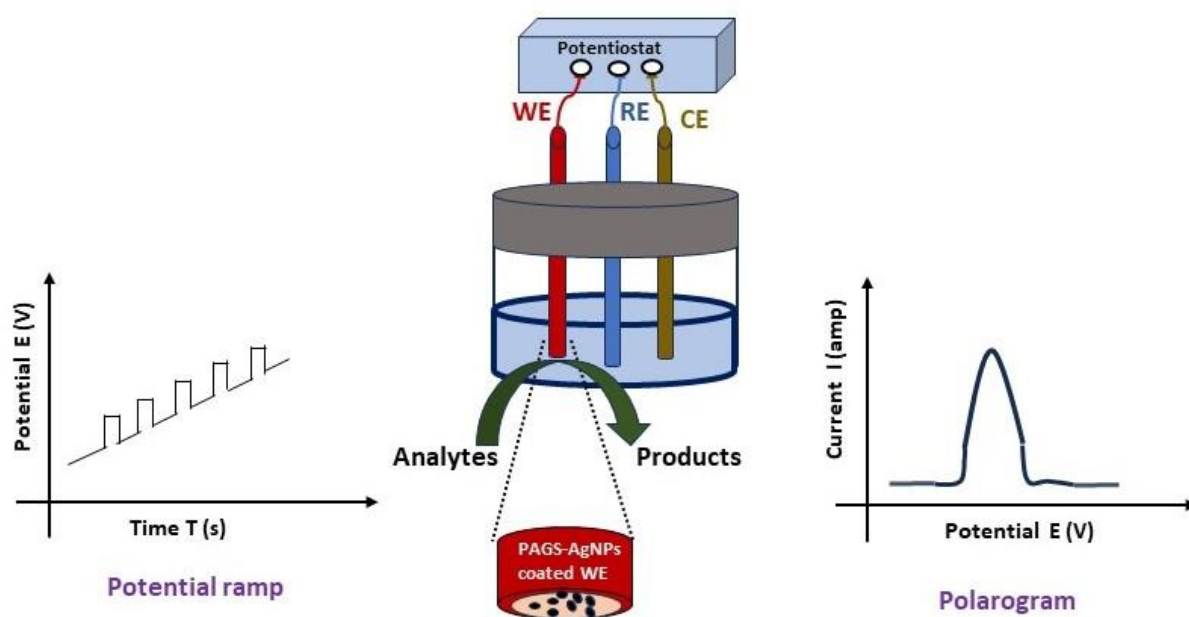


Figure 8: Scheme representing electrochemical sensing method by PAGS-AgNPs.

3.6. PAGS-AgNPs Sensor for Nitrobenzene Detection

Nitrobenzene (NB) was used as a reagent in many organic industries. The surface water gets contaminated with the NB by the release of untreated effluent from the organic industries. The World Health Organization (WHO) prescribed the limit for the concentration of nitrobenzene as 2 mg/L in water bodies, and beyond this limit, it becomes hazardous to the environment. Hence, the continuous assessment of the NB level in the environmental water becomes inevitable. Also, economically viable detection methods are the focus of the current research. In that connection, researchers reported the synthesis of silver nanoparticles (AgNPs) by microwave using a Eucalyptus extract from the bark of the tree as a reducing and stabilizing agent. These

3.7. PAGS-AgNPs Sensor for Metal Ion Detection

Many of the heavy metals are known to be environmental contaminants. Monitoring their limits has become essential in the modern world. Their detection, particularly in water, becomes a matter of prime importance because of the ever-increasing health hazards related to them. Many research groups focus on that aspect and produce commendable results, but the search for better sensing material is still not over. Plant-mediated AgNPs are a promising candidate in this field because of their low-cost production. Plant material-assisted synthesis of AgNPs has thrown up a brand-new, environmentally-friendly pathway for metal sensing probes. *Artemisia vulgaris* mediated silver nanoparticles (AgNPs) are employed as colorimetric analyzers for mercury, a hazardous metal in an aqueous solution (72). In an aqueous solution, the *Artemisia*-modified reddish-brown AgNPs solution was selectively decolourized by the addition

AgNPs coated on the GCE were used for the electrochemical sensing of nitrobenzene (71). Hemicellulose, present in the bark of the Eucalyptus tree, acts as a reducing agent for synthesis. The AgNPs synthesized using hemicellulose were used to modify GCE and were further utilized for sensing NB in water. The authors exhibited many advantages of AgNPs/GCE electrodes, such as good sensitivity in the range of 5–40 μM , a minimal LOD of 0.027 μM and specific detection of NB in the presence of other interfering species widely ranging from organic nature (aniline, toluene, phenol), inorganic compounds (urea) and many inorganic salts (ammonium nitrate, ammonium chloride, calcium chloride, sodium sulfate, potassium chloride, and sodium chloride). The authors also showed good recovery results for NB, which argues for the emulation of the method as the front-runner for practical applicability studies.

of Hg^{2+} . The color change was evident with the unaided eyes, whereas the remaining metal solution did not undergo any discernible colour change. This plant-mediated nanoparticle can serve as a probe for the sensing activity toward Hg^{2+} . It also shows an excellent catalytic-reducing property in a short time of 8 min by converting 4-nitrophenol to aminophenol. This plant mediated AgNPs is environment friendly because of its dual behaviour of Hg sensing and reduction of 4-nitrophenol. When fine-tuned, it could serve as a future material for several industrial applications.

Researchers have reported the use of an extract from *Diospyros discolor Willd* (Bisbul) leaves for synthesizing silver nanoparticles (73). Several research groups have utilized silver nanoparticles (AgNPs) as a material for sensing various heavy metals. Reports suggest that the AgNPs obtained from plant sources

can be developed into materials for the detection of heavy metals in the environment. The color change of the plant-mediated AgNPs up to the addition of metal ions is utilized for detection by the colorimetric method. In the report, the presence of various metal ions, namely Mg^{2+} , Mn^{2+} , Pb^{2+} , Zn^{2+} , Co^{2+} , and Fe^{2+} was analyzed by AgNPs obtained from a biosynthetic approach using bisbul leaves, commonly known as antler orchid and it selectively detected the presence of Fe^{2+} . The report showed a solution discoloration ranging from brownish to greenish, a distinct colour change when the synthesized AgNPs were added to Fe^{2+} ion solution in concentrations ranging from 0.1 – 1000 mg/L. AgNPs agglomerate with the addition of excess Fe^{2+} . This detection method can be enhanced and refined to find Fe^{2+} metal ions in the surrounding environment. These biosynthetic AgNPs were assessed using analytical methods such as particle size analysis (PSA).

Recently, researchers used *Sapindus mukorossi* extract (SME) to produce AgNPs and applied them for effective sensing of Fe^{2+} and Fe^{3+} ions in solution (74). The detailed analysis includes various metal ion interferences in the sensing of Fe^{2+} and Fe^{3+} ions. They examined the interference by adding 1000 μM concentrations of Li^+ , Na^+ , Ca^{2+} , K^+ , Mg^{2+} , Cr^{3+} , Ba^{2+} , Mn^{2+} , Ni^{2+} , Co^{2+} , Cd^{2+} , Cu^{2+} , Pb^{2+} and Zn^{2+} to 100 μM concentrated Fe^{2+} and Fe^{3+} solutions. Real-time analysis using river water and bottled water spiked with Fe^{2+} and Fe^{3+} ions was also performed. Interestingly, the presence of Fe^{2+} ions drove the AgNPs solution's SPR band intensity to rise. In contrast, the presence of Fe^{3+} ions caused it to drop, with no noteworthy changes seen for other metal ions. While the AgNPs absorption peak remained unaltered when additional metal ions were added, the addition of Fe^{2+} and Fe^{3+} ions alone caused a shift in colour to black and white, respectively, indicating the selectivity nature of SME@AgNPs towards colorimetric detection.

The reduction of any Ag^+ in the medium by Fe^{2+} ions as well as Fe^{2+}/Fe^{3+} hydroxides to elemental silver and the Ligand to Metal Charge-Transfer process plays a major role in the red shift that occurred as the concentration of Fe^{2+} ions rises. The literature showed the AgNP could be used to sense eight metal ions in water by colour change; the sensitivity is also confirmed by the UV-visible spectrometry (75). Even though the synthetic route was not plant-mediated, it is worthwhile to mention these green-synthesized AgNPs here to gauge the future prospects of PAGES AgNPs.

Hg^{2+} and Pb^{2+} are the most hazardous contaminants in water. Their complete ignorance of usage is not possible since both of these metals play a major role in many of the industrial processes. Probing their presence and analyzing their quantity in water bodies has become highly unavoidable. Researchers have shown their potential for the detection of these two metals with low detection limits. Various literatures have highlighted the capacity of plant-mediated AgNPs as a colorimetric probe for detecting heavy metals. In that regard, AgNPs synthesized utilizing the extract from the environmentally beneficial root *Bistorta amplexicaulis* serve as a dual Hg^{2+}/Pb^{2+} colorimetric sensor (76). Changes in absorption spectrum of plant-mediated AgNPs were analyzed for the detection of common heavy metal cations. This report proved that the colorimetric sensor based on AgNPs could be applied for detecting Hg^{2+} and Pb^{2+} with detection limits in 0.1 mM range. The Pb^{2+} ions decrease the absorbance of AgNPs significantly, and a hypsochromic shift in the SPR band of AgNPs and the Hg^{2+} ions, causing the naked eye's detection of it by the colour change to bright yellow from dark brown, confirms its role as a colorimetric sensor. The simplified scheme for analyte detection by the colorimetric method is represented in Figure 9.

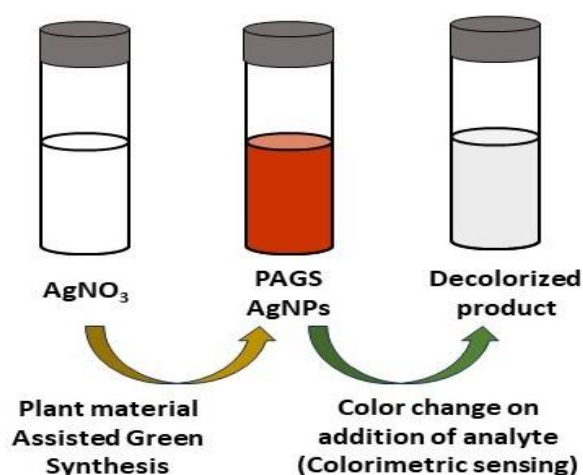


Figure 9: Scheme representing colorimetric sensing method by PAGES-AgNPs.

A gum acacia-mediated, simple, and environmentally friendly technique for generating silver nanoparticles was reported in the literature (77). The synthesized AgNPs demonstrated good sensitivity towards $Hg(II)$

and S^{2-} . The reported plant-mediated AgNPs exhibit a fluorescence band around 500-600 nm when excited at 300 nm. The fluorescence intensity was enhanced by the addition of nano-molar concentrations of

Hg(II), which showed a downward trend by the addition of micromolar concentrations of S^{2-} ions and malachite green dye. The authors demonstrated the fluorescence variation of the AgNPs with variations in Hg(II), S^{2-} and the dye. The results highlight the material utilized for the future development of an Ag@Hg nanoalloy. The literature reports of PAGES-AgNPs as phenol, nitrobenzene, and metal ion sensors are summarized in Table 4.

4. CONCLUSION

The remarkable features of nanoparticles have made them important in various industries. Technologies utilizing the nanoparticles have considerable potential because they can transform unstable, poorly soluble, and poorly absorbed physiologically active compounds into viable deliverable chemicals. Compared to conventional biosensors, the performance of nano-biochemical sensors is good in terms of sensitivity, selectivity, linearity, stability, response time, and repeatability. The current review offers a brief and informative overview of greener synthetic routes for the generation of AgNPs. The plant material-assisted AgNPs synthetic route is an extensive area and a complex phenomenon. This route often displays diverse behaviors, selectivity, and sensitivity. This complexity can be used as an advantage to extrapolate the research to newer limits. In the literature, many researchers used the plant material without purification for the synthesis of PAGES-AgNPs, which contains various phytochemical constituents like flavonoids, terpenoids, alkaloids, polysaccharides, polyphenols etc. The activity of a particular phytochemical residue may support or reinforce other constituents, potentially providing advantages in sensing applications and opening up opportunities for further investigations and inventions.

Plant material-assisted AgNPs were functionalized by the functionalities present in the plant materials. These functional nanoparticles offer various advantages due to their versatile characteristics:

- a) In sensing applications, the functionality present on the surface of NPs plays a prominent role in determining the selectivity and specificity of the analyte detected.
- b) Nanoparticles with functional moieties can easily be adsorbed on the substrate for application as a sensing probe, like electrodes, fibers, paper, etc.
- c) Researchers have the advantage of experimenting with the controllables towards the size of the NPs, and as a consequence, the current LOD limits can be lowered further by varying the concentration of the plant material in the synthetic step.

The review takes the opportunity to combine various viewpoints and terminologies used in PAGES-AgNPs-based sensors towards H_2O_2 , ammonia, phenol, nitrobenzene, and metal ion sensing. The literature reports cited here highlight the advantages of the respective materials, which leads to potential directions for additional advances to be investigated for future research and developments to be explored,

emphasizing the challenges for PAGES-AgNPs-based flexible sensors. This review presents four sensing platforms explored by PAGES-AgNPs as sensors. UV-visible spectroscopy, calorimetry, electrochemical, and fluorescence are the four prominently used techniques by researchers in the literature. Among them, electrochemical sensing seems to be more versatile in terms of the diversity of the chemical nature of the analyte. Naked eye detection (including colorimetry and UVV spectrometry) is the simplest one, covering a wider range of publications, and its simplicity might attract many applications in the future. The fluorescence PAGES-AgNPs sensors have limited publications, but the cost-effective synthetic route has an edge over current fluorescent probes in biochemical sensors.

Table 4. Literature Summary of PAGES-AgNPs as Phenol, Nitrobenzene and Metal ion sensors.

Plant material	Detection limit	Significance / property / analyte	Technique	Ref.
leaf extracts of <i>Melia</i>	0.42 μM	Drop cast modified GCE Phenol	Differential pulse voltammetry (DPV)	70
<i>Eucalyptus</i> bark extract	0.027 μM	Drop cast modified GCE Nitrobenzene	Differential pulse voltammetry (DPV)	71
<i>Artemisia vulgaris</i> leaf extract	20–600 μL (Hg^{2+})	Catalytic activity studied	UV-Visible spectrophotometry	72
Extract of <i>Diospyros discolor</i> Willd. (Bisbul) leaves	0.1 mg /L (Fe^{2+})	Visual detection without any aid	Colorimetric detection	73
<i>Sapindus mukorossi</i> pericarp extract	1 μM - 5 μM (Fe^{2+} , Fe^{3+})	Visual detection without any aid	Colorimetric detection	74
Sodium citrate	1×10^{-5} M	Eight metal ions detection	UV-Visible spectrophotometry	75
Roots extract of <i>Bistorta amplexicaulis</i>	0.8 μM (Hg^{2+}) and 0.2 μM (Pb^{2+})	Dual sensor for Hg^{2+} and Pb^{2+}	Colorimetric detection	76
Gum acacia (<i>Acacia senegal</i>)	2.1 nmol L^{-1} (Hg^{2+}) 1.3 $\mu\text{mol L}^{-1}$ (S^{2-}) 1.6 $\mu\text{M L}^{-1}$ (Malachite green)	Dual sensor for Hg^{2+} and S^{2-}	Fluorescence spectroscopy	77

5. CONFLICT OF INTEREST

The authors have no conflicts of interest.

6. ABBREVIATIONS

MNPs – metal nanoparticles,
NPs – nanoparticles
PAGS – plant-assisted green synthesis
AgNPs – silver nanoparticles
SPR – surface plasmon resonance
GCE – glassy carbon electrode

7. REFERENCES

- Ghaedi M, Yousefinejad M, Safarpour M, Khafri HZ, Purkait MK. Rosmarinus officinalis leaf extract mediated green synthesis of silver nanoparticles and investigation of its antimicrobial properties. J Ind Eng Chem [Internet]. 2015;31:167–72. Available from: [<URL>](#)
- Joudeh N, Linke D. Nanoparticle classification, physicochemical properties, characterization, and applications: a comprehensive review for biologists. J Nanobiotechnology [Internet]. 2022;20(1). Available from: [<URL>](#)
- Tran QH, Nguyen VQ, Le A-T. Corrigendum: Silver nanoparticles: synthesis, properties, toxicology, applications and perspectives (Adv. Nat. Sci: Nanosci. Nanotechnol . 4 033001). Adv Nat Sci Nanosci Nanotechnol [Internet]. 2018;9(4):049501. Available from: [<URL>](#)
- Pérez-Beltrán CH, García-Guzmán JJ, Ferreira B, Estévez-Hernández O, López-Iglesias D, Cubillana-Aguilera L, et al. One-minute and green synthesis of magnetic iron oxide nanoparticles assisted by design of experiments and high energy ultrasound: Application to biosensing and immunoprecipitation. Mater Sci Eng C Mater Biol Appl [Internet]. 2021;123(112023):112023. Available from: [<URL>](#)
- Goudarzi M, Salavati-Niasari M, Yazdian F, Amiri M. Sonochemical assisted thermal decomposition method for green synthesis of CuCo₂O₄/CuO ceramic nanocomposite using Dactylopius Coccus for anti-tumor investigations. J Alloys Compd [Internet]. 2019;788:944–53. Available from: [<URL>](#)
- Samuel MS, Suman S, Venkateshkannan, Selvarajan E, Mathimani T, Pugazhendhi A. Immobilization of Cu₃(btc)₂ on graphene oxide-chitosan hybrid composite for the adsorption and photocatalytic degradation of methylene blue. J Photochem Photobiol B [Internet]. 2020;204(111809):111809. Available from: [<URL>](#)
- Mahmoodi NO, Ghavidast A, Amirmahani N. A comparative study on the nanoparticles for improved drug delivery systems. J Photochem Photobiol B [Internet]. 2016;162:681–93. Available from: [<URL>](#)
- Gupta R, Xie H. Nanoparticles in daily life: Applications, toxicity and regulations. J Environ Pathol Toxicol Oncol [Internet]. 2018;37(3):209–30. Available from: [<URL>](#)
- Azharuddin M, Zhu GH, Das D, Ozgur E, Uzun L, Turner APF, et al. A repertoire of biomedical applications of noble metal nanoparticles. Chem Commun (Camb) [Internet]. 2019;55(49):6964–96. Available from: [<URL>](#)
- Ying S, Guan Z, Ofoegbu PC, Clubb P, Rico C, He F, et al. Green synthesis of nanoparticles: Current developments and limitations. Environ Technol Innov [Internet]. 2022;26(102336):102336. Available from: [<URL>](#)
- Alsammarraie FK, Wang W, Zhou P, Mustapha A, Lin M. Green synthesis of silver nanoparticles using turmeric extracts and investigation of their antibacterial activities. Colloids Surf B Biointerfaces [Internet]. 2018;171:398–405. Available from: [<URL>](#)
- Sone BT, Diallo A, Fuku XG, Gurib-Fakim A, Maaza M. Biosynthesized CuO nano-platelets: Physical properties & enhanced thermal conductivity nanofluidics. Arab J Chem [Internet]. 2020;13(1):160–70. Available from: [<URL>](#)
- Shah M, Fawcett D, Sharma S, Tripathy S, Poinern G. Green synthesis of metallic nanoparticles via biological entities. Materials (Basel) [Internet]. 2015;8(11):7278–308. Available from: [<URL>](#)
- Zhang D, Ma X-L, Gu Y, Huang H, Zhang G-W. Green synthesis of metallic nanoparticles and their potential applications to treat cancer. Front Chem [Internet]. 2020;8. Available from: [<URL>](#)
- Rauwel P, Küünal S, Ferdov S, Rauwel E. A review on the Green synthesis of silver nanoparticles and their morphologies studied via TEM. Adv Mater Sci Eng [Internet]. 2015;2015:1–9. Available from: [<URL>](#)
- Giri AK, Jena B, Biswal B, Pradhan AK, Arakha M, Acharya S, et al. Green synthesis and characterization of silver nanoparticles using Eugenia roxburghii DC. extract and activity against biofilm-producing bacteria. Sci Rep [Internet]. 2022;12(1). Available from: [<URL>](#)
- Erdogan O, Abbak M, Demirbolat GM, Birtekocak F, Aksel M, Pasa S, et al. Green synthesis of silver nanoparticles via Cynara scolymus leaf extracts: The characterization, anticancer potential with photodynamic therapy in MCF7 cells. PLoS One [Internet]. 2019;14(6):e0216496. Available from: [<URL>](#)
- Joy Prabu H, Johnson I. Plant-mediated biosynthesis and characterization of silver nanoparticles by leaf extracts of Tragia involucrata, Cymbopogon citronella, Solanum verbascifolium and Tylophora ovata. Karbala Int J Mod Sci [Internet]. 2015;1(4):237–46. Available from: [<URL>](#)
- Singh P, Kim YJ, Wang C, Mathiyalagan R, El-Agamy Farh M, Yang DC. Biogenic silver and gold nanoparticles synthesized using red ginseng root extract, and their applications. Artif Cells Nanomed Biotechnol [Internet]. 2015;1–6. Available from: [<URL>](#)
- Raja S, Ramesh V, Thivaharan V. Green biosynthesis of silver nanoparticles using Calliandra haematocephala leaf extract, their antibacterial activity and hydrogen peroxide sensing capability. Arab J Chem [Internet]. 2017;10(2):253–61. Available from: [<URL>](#)
- Singh J, Dutta T, Kim K-H, Rawat M, Samddar P, Kumar P. 'Green' synthesis of metals and their oxide nanoparticles: applications for environmental remediation. J Nanobiotechnology [Internet]. 2018;16(1). Available from: [<URL>](#)

22. Montes-Hernandez G, Di Girolamo M, Sarret G, Sarah Bureau, Fernandez-Martinez A, Lelong C, et al. In situ formation of silver nanoparticles (Ag-NPs) onto textile fibers. ACS Omega [Internet]. 2021;6(2):1316-27. Available from: [<URL>](#)
23. Burduşel A-C, Gherasim O, Grumezescu AM, Mogoantă L, Ficăi A, Andronescu E. Biomedical applications of silver nanoparticles: An up-to-date overview. Nanomaterials (Basel) [Internet]. 2018;8(9):681. Available from: [<URL>](#)
24. Nakamura S, Sato M, Sato Y, Ando N, Takayama T, Fujita M, et al. Synthesis and application of silver nanoparticles (Ag NPs) for the prevention of infection in healthcare workers. Int J Mol Sci [Internet]. 2019;20(15):3620. Available from: [<URL>](#)
25. Kale SK, Assistant Professor, Department of First Year Engineering, Pimpri Chinchwad College of Engineering, Pune, Maharashtra, India, Parishwad GV, Husainy ASN, Patil AS, Principal, Pimpri Chinchwad Collge of Engineering, Pune, Maharashtra, India, et al. Emerging agriculture applications of silver nanoparticles. ES Food Agrofor [Internet]. 2021; Available from: [<URL>](#)
26. Naing AH, Kim CK. Application of nano-silver particles to control the postharvest biology of cut flowers: A review. Sci Hortic (Amsterdam) [Internet]. 2020;270(109463):109463. Available from: [<URL>](#)
27. Bouafia A, Laouini SE, Ahmed ASA, Soldatov AV, Algarni H, Feng Chong K, et al. The recent progress on silver nanoparticles: Synthesis and electronic applications. Nanomaterials (Basel) [Internet]. 2021;11(9):2318. Available from: [<URL>](#)
28. Bruna T, Maldonado-Bravo F, Jara P, Caro N. Silver nanoparticles and their antibacterial applications. Int J Mol Sci [Internet]. 2021;22(13):7202. Available from: [<URL>](#)
29. Terenteva EA, Apyari VV, Kochuk EV, Dmitrienko SG, Zolotov YA. Use of silver nanoparticles in spectrophotometry. J Anal Chem [Internet]. 2017;72(11):1138-54. Available from: [<URL>](#)
30. Rafique M, Iqra SM, Rafique S, Tahir BM. (2017) A review on green synthesis of silver nanoparticles and their applications, Artif Cells Nanomed Biotechnol [Internet]. 2017;45(7): 1272-1291. Available from: [<URL>](#)
31. Ahmad S, Munir S, Zeb N, Ullah A, Khan B, Ali J, Bilal M, Omer M, Alamzeb M, Salman SM, Ali S. Green nanotechnology: a review on green synthesis of silver nanoparticles — an ecofriendly approach. Int J Nanomedicine. [Internet]. 2019;14:5087-5107 Available from: [<URL>](#)
32. Sharma NK, Vishwakarma J, Rai S, Alomar TS, Masoud, NA, Bhattarai A. Green Route Synthesis and Characterization Techniques of Silver Nanoparticles and Their Biological Adeptness. ACS Omega [Internet]. 2022;7 (31):27004-27020. Available from: [<URL>](#)
33. Srikar S, Giri D, Pal D, Mishra P, Upadhyay, S. (2016) Green Synthesis of Silver Nanoparticles: A Review. Green sustain. chem. [Internet]. 2016;6:34-56. Available from: [<URL>](#)
34. Desai R, Dutta S. Fruit and Vegetable Mediated Green Synthesis of Silver Nanoparticles – A Review. Chem Sci Rev Lett. [Internet]. 2022;11(43):303-310.
35. Deepa, Ameen F, Amirul IM., Dhanker R. Green synthesis of silver nanoparticles from vegetable waste of pea Pisum sativum and bottle gourd Lagenaria siceraria: Characterization and antibacterial properties. Front. Environ. Sci. [Internet] 2022;10 (941554). Available from: [<URL>](#)
36. Lakshmanan G, Sathiyaseelan A, Kalaichelvan PT, Murugesan K. Plant-mediated synthesis of silver nanoparticles using fruit extract of Cleome viscosa L.: Assessment of their antibacterial and anticancer activity. KIJOMS [Internet]. 2018;4(1): 61-68, Available from: [<URL>](#)
37. Samrot AV, Angalene JLA, Roshini SM, Raji P, Stefi SM, Preethi R, Selvarani AJ, Madankumar A. Bioactivity and Heavy Metal Removal Using Plant Gum Mediated Green Synthesized Silver Nanoparticles. J Clust Sci [Internet] 2019;30:1599-1610. Available from: [<URL>](#)
38. Saquib HM, Md. Noushad J, Md. Sabir A, Poonam R, Sanjay R, Sadath A, Amit Kumar N, Sarwar B. Purple heart plant leaves extract-mediated silver nanoparticle synthesis: Optimization by Box-Behnken design. Mater. Sci. Eng.C. [Internet]. 2019;99:1105-1114. Available from: [<URL>](#)
39. Manik, U., Nande, A., Raut, S., & Dhoble, S.J. (2020). Green synthesis of silver nanoparticles using plant leaf extraction of Artocarpus heterophyllus and Azadirachta indica. Results Mater. [Internet]. 2020;6:100086, Available from: [<URL>](#)
40. Devanesan S, AlSalhi MS. Green Synthesis of Silver Nanoparticles Using the Flower Extract of Abelmoschus esculentus for Cytotoxicity and Antimicrobial Studies. Int J Nanomedicine. [Internet]. 2021;16:3343-3356. Available from: [<URL>](#)
41. Alshehri AH, Jakubowska M, Młozniak A, Horaczek M, Rudka D, Free C, et al. Enhanced electrical conductivity of silver nanoparticles for high frequency electronic applications. ACS Appl Mater Interfaces [Internet]. 2012;4(12):7007-10. Available from: [<URL>](#)
42. Sharma N, Kaushik S. Synthesis of bio nano particles with special reference to gold and silver metal. Mater Today [Internet]. 2020;29:477-80. Available from: [<URL>](#)
43. Paknejad SA, Mannan SH. Review of silver nanoparticle based die attach materials for high power/temperature applications. Microelectron Reliab [Internet]. 2017;70:1-11. Available from: [<URL>](#)
44. Simon S, Sibuyi NRS, Fadaka AO, Meyer S, Josephs J, Onani MO, et al. Biomedical applications of plant extract-synthesized silver nanoparticles. Biomedicines [Internet]. 2022;10(11):2792. Available from: [<URL>](#)
45. Kareem MA, Bello IT, Shittu HA, Awodele MK, Adedokun O, Sanusi YK. Green synthesis of silver nanoparticles (AgNPs) for optical and photocatalytic applications: a review. IOP Conf Ser Mater Sci Eng [Internet]. 2020;805(1):012020. Available from: [<URL>](#)
46. Mousavi SM, Hashemi SA, Ghasemi Y, Atapour A, Amani AM, Savar Dashtaki A, et al. Green synthesis of silver nanoparticles toward bio and medical applications: review study. Artif Cells Nanomed Biotechnol [Internet]. 2018;46(sup3):855-72. Available from: [<URL>](#)
47. Jaffri SB, Ahmad KS. Phytofunctionalized silver nanoparticles: green biomaterial for biomedical and

- environmental applications. *Rev Inorg Chem* [Internet]. 2018;38(3):127–49. Available from: [<URL>](#)
48. Chung I-M, Park I, Seung-Hyun K, Thiruvengadam M, Rajakumar G. Plant-mediated synthesis of silver nanoparticles: Their characteristic properties and therapeutic applications. *Nanoscale Res Lett* [Internet]. 2016;11(1). Available from: [<URL>](#)
49. Moradi F, Sedaghat S, Moradi O, Arab Salmanabadi S. Review on green nano-biosynthesis of silver nanoparticles and their biological activities: with an emphasis on medicinal plants. *Inorg Nano-met Chem* [Internet]. 2021;51(1):133–42. Available from: [<URL>](#)
50. Fahimirad S, Ajallouei F, Ghorbanpour M. Synthesis and therapeutic potential of silver nanomaterials derived from plant extracts. *Ecotoxicol Environ Saf* [Internet]. 2019;168:260–78. Available from: [<URL>](#)
51. Jain N, Jain P, Rajput D, Patil UK. Green synthesized plant-based silver nanoparticles: therapeutic prospective for anticancer and antiviral activity. *Micro Nano Syst Lett* [Internet]. 2021;9(1). Available from: [<URL>](#)
52. Abbas A, Amin HMA. Silver nanoparticles modified electrodes for electroanalysis: An updated review and a perspective. *Microchem J* [Internet]. 2022;175(107166):107166. Available from: [<URL>](#)
53. Zahran M, Khalifa Z, Zahran MA-H, Abdel Azzem M. Recent advances in silver nanoparticle-based electrochemical sensors for determining organic pollutants in water: a review. *Mater Adv* [Internet]. 2021;2(22):7350–65. Available from: [<URL>](#)
54. Yu C-X, Xiong F, Liu L-L. Electrochemical biosensors with silver nanoparticles as signal labels. *Int J Electrochem Sci* [Internet]. 2020;15(5):3869–90. Available from: [<URL>](#)
55. Pomal NC, Bhatt KD, Modi KM, Desai AL, Patel NP, Kongor A, et al. Functionalized silver nanoparticles as colorimetric and fluorimetric sensor for environmentally toxic mercury ions: An overview. *J Fluoresc* [Internet]. 2021;31(3):635–49. Available from: [<URL>](#)
56. Jouyban A, Rahimpour E. Optical sensors based on silver nanoparticles for determination of pharmaceuticals: An overview of advances in the last decade. *Talanta* [Internet]. 2020;217(121071):121071. Available from: [<URL>](#)
57. Li Y, Wang Z, Sun L, Liu L, Xu C, Kuang H. Nanoparticle-based sensors for food contaminants. *Trends Analyt Chem* [Internet]. 2019;113:74–83. Available from: [<URL>](#)
58. Fetalbero Reyes D. Green-synthesized silver nanoparticles as sensor probes for the naked-eye detection of hydrogen peroxide. *Orient J Chem* [Internet]. 2020;36(04):640–4. Available from: [<URL>](#)
59. Koshy O. Green synthesis of silver nanoparticles using aqueous plant extracts and its application as optical sensor. *Int J Biosens Bioelectron* [Internet]. 2017;2(3). Available from: [<URL>](#)
60. Tagad CK, Dugasani SR, Aiyer R, Park S, Kulkarni A, Sabharwal S. Green synthesis of silver nanoparticles and their application for the development of optical fiber based hydrogen peroxide sensor. *Sens Actuators B Chem* [Internet]. 2013;183:144–9. Available from: [<URL>](#)
61. Mahadevan S, Vijayakumar S, Arulmozhi P. Green synthesis of silver nano particles from *Atalantia monophylla* (L) Correa leaf extract, their antimicrobial activity and sensing capability of H₂O₂. *Microb Pathog* [Internet]. 2017;113:445–50. Available from: [<URL>](#)
62. Shukla VK, Yadav RS, Yadav P, Pandey AC. Green synthesis of nanosilver as a sensor for detection of hydrogen peroxide in water. *J Hazard Mater* [Internet]. 2012;213–214:161–6. Available from: [<URL>](#)
63. Srikhao N, Kasemsiri P, Lorwanishpaisarn N, Okhawilai M. Green synthesis of silver nanoparticles using sugarcane leaves extract for colorimetric detection of ammonia and hydrogen peroxide. *Res Chem Intermed* [Internet]. 2021;47(3):1269–83. Available from: [<URL>](#)
64. Ismail M, Khan MI, Akhtar K, Seo J, Khan MA, Asiri AM, et al. Phytosynthesis of silver nanoparticles; naked eye cellulose filter paper dual mechanism sensor for mercury ions and ammonia in aqueous solution. *J Mater Sci: Mater Electron* [Internet]. 2019;30(8):7367–83. Available from: [<URL>](#)
65. Pandey S, Goswami GK, Nanda KK. Green synthesis of biopolymer–silver nanoparticle nanocomposite: An optical sensor for ammonia detection. *Int J Biol Macromol* [Internet]. 2012;51(4):583–9. Available from: [<URL>](#)
66. Gupta AP, Verma DK. Carboxymethylguar-gum-silver nanocomposite: green synthesis, characterization and an optical sensor for ammonia detection. *Adv Nat Sci Nanosci Nanotechnol* [Internet]. 2014;5(3):035018. Available from: [<URL>](#)
67. Alzahrani E. Colorimetric detection of ammonia using synthesized silver nanoparticles from durian fruit shell. *J Chem* [Internet]. 2020;2020:1–11. Available from: [<URL>](#)
68. Edison TNJI, Atchudan R, Lee YR. Optical sensor for dissolved ammonia through the Green synthesis of silver nanoparticles by fruit extract of *Terminalia chebula*. *J Cluster Sci* [Internet]. 2016;27(2):683–90. Available from: [<URL>](#)
69. Ismail M, Khan MI, Akhtar K, Khan MA, Asiri AM, Khan SB. Biosynthesis of silver nanoparticles: A colorimetric optical sensor for detection of hexavalent chromium and ammonia in aqueous solution. *Physica E Low Dimens Syst Nanostruct* [Internet]. 2018;103:367–76. Available from: [<URL>](#)
70. Jebiril S, Fdhila A, Dridi C. Nanoengineering of eco-friendly silver nanoparticles using five different plant extracts and development of cost-effective phenol nanosensor. *Sci Rep* [Internet]. 2021;11(1). Available from: [<URL>](#)
71. Shivakumar M, Dharmaprakash MS, Manjappa S, Nagashree KL. Green synthesis of silver nanoparticles (SNPs)-modified electrode for electrochemical detection of nitrobenzene. *J Iran Chem Soc* [Internet]. 2020;17(4):893–900. Available from: [<URL>](#)
72. Adhikari A, Lamichhane L, Adhikari A, Gyawali G, Acharya D, Baral ER, et al. Green synthesis of silver nanoparticles using *Artemisia vulgaris* extract and its application toward catalytic and metal-sensing activity. *Inorganics* [Internet]. 2022;10(8):113. Available from: [<URL>](#)
73. Handayani W, Intan Pratiwi N, Yulkifli, Ramli, Benti Etika S, Imawan C. A silver nanoparticle-based colorimetric

detection of Fe²⁺. J Phys Conf Ser [Internet]. 2019;1317(1):012093. Available from: [<URL>](#)

74. Dayanidhi K, Sheik Eusuff N. Distinctive detection of Fe²⁺ and Fe³⁺ by biosurfactant capped silver nanoparticles via naked eye colorimetric sensing. New J Chem [Internet]. 2021;45(22):9936–43. Available from: [<URL>](#)

75. Tamilselvan S, Soniya RM, Vasantharaja R, Kannan M, Supriya S, Dass Batvari BP. Silver nanoparticles based spectroscopic sensing of eight metal ions in aqueous solutions. Environ Res [Internet]. 2022;212:113585. Available from: [<URL>](#)

76. Ahmed F, Kabir H, Xiong H. Dual colorimetric sensor for Hg²⁺/Pb²⁺ and an efficient catalyst based on silver nanoparticles mediating by the root extract of *Bistorta amplexicaulis*. Front Chem [Internet]. 2020;8. Available from: [<URL>](#)

77. Abbasi A, Hanif S, Shakir M. Gum acacia-based silver nanoparticles as a highly selective and sensitive dual nanosensor for Hg(ii) and fluorescence turn-off sensor for S²⁻ and malachite green detection. RSC Adv [Internet]. 2020;10(6):3137–44. Available from: [<URL>](#)